NASA CONTRACTOR REPORT 185138

PROPFAN TEST ASSESSMENT (PTA)
FINAL PROJECT REPORT

B. H. Little, D. T. Poland, H. W. Bartel, C. C. Withers
Lockheed Aeronautical Systems Company
Marietta, Georgia

P. C. Brown
Hamilton Standard Division
United Technologies Corporation
Windsor Locks, Connecticut

July 1989

Prepared for
Lewis Research Center
Under Contract NAS3-24339



National Aeronautics and
Space Administration

(NASA-CR-185138) PROPFAN TEST ASSESSMENT (PTA) Final Report (Lockheed Aeronautical Systems Co.) 378 p CSCL 21E

N90-11739

Unclas
G3/07 0255600

NASA CONTRACTOR REPORT 185138

PROPFAN TEST ASSESSMENT (PTA) FINAL PROJECT REPORT

B. H. Little, D. T. Poland, H. W. Bartel, C. C. Withers
Lockheed Aeronautical Systems Company
Marietta, Georgia

P. C. Brown
Hamilton Standard Division
United Technologies Corporation
Windsor Locks, Connecticut

July 1989

Prepared for
Lewis Research Center
Under Contract NAS3-24339

NASA
National Aeronautics and
Space Administration

FOREWORD

The Propfan Test Assessment (PTA) Program involved modification of an existing aircraft to provide a testbed for an advanced high-speed propfan, subsequent tests of that propfan over a wide range of flight conditions, and analysis of resulting blade stress and acoustics data. This document is the Final Project Report for that program in fulfillment of DRD 251.

This work was performed under contract from the NASA-Lewis Research Center. The NASA Project Manager for the major portion of the work was E. J. Graber, Jr.

This report is also identified as Lockheed Aeronautical Systems Company Engineering Report LG89ER0064.

PRECEDING PAGE BLANK NOT FILMED

PAGE ___ INTENTIONALLY BLANK

Lockheed

TABLE OF CONTENTS

Section	Title	Page
	FOREWORD	iii-1
	TABLE OF CONTENTS	v
	LIST OF FIGURES	xi
	LIST OF SYMBOLS AND ABBREVIATIONS	xxxiii
1.0	SUMMARY	1
2.0	INTRODUCTION	3
	2.1 Background	3
	2.2 Objectives and Requirements	3
	2.3 Scope	9
	2.4 Significance of the PTA Program	11
3.0	SYSTEM DESIGN	13
	3.1 Major Components	13
	3.1.1 Aircraft	13
	3.1.2 Large-Scale Advanced Propfan (LAP)	13
	3.1.3 Propfan Drive System	20
	3.2 Aircraft Modification	23
	3.2.1 Wing Modification	23
	3.2.2 Fuselage Modifications	30
	3.2.3 Nacelle Design	38
	3.2.4 Aircraft Systems	52
	3.3 Drive System Design and Qualification	56
	3.3.1 Power Section	56
	3.3.2 Gearbox	60
	3.3.3 Torquemeter	65
	3.3.4 Controls, Subsystems, and Accessories	65
	3.3.5 Mounts	70
	3.3.6 Installation	70
	3.3.7 Maintainability	77
	3.3.8 Qualification	79

PRECEDING PAGE BLANK NOT FILMED

PAGE IV INTENTIONALLY BLANK

TABLE OF CONTENTS (CONT'D)

Section	Title	Page
	3.4 Instrumentation	87
	3.4.1 Data System General Description	87
	3.4.2 Aircraft Flight Instrumentation	89
	3.4.3 Drive System Instrumentation	89
	3.4.4 Acoustics Instrumentation	89
	3.4.5 Propfan Blade Instrumentation	92
4.0	MODEL TESTS	109
	4.1 Stability and Control/Performance/Acoustics Testbed Model Testing	109
	4.1.1 Objectives	109
	4.1.2 Models	109
	4.1.3 Test Facilities	110
	4.1.4 Instrumentation	110
	4.1.5 Supporting Analysis	113
	4.1.6 Test Results	113
	4.1.7 Results and Conclusions	130
	4.2 Flutter Model Tests	135
	4.2.1 Objectives	135
	4.2.2 Test Facilities and Procedures	135
	4.2.3 Model Description	135
	4.2.4 Instrumentation	139
	4.2.5 Results	139
	4.2.6 Conclusions	142
	4.3 Inlet Model Testing	142
	4.3.1 Objectives	142
	4.3.2 Test Apparatus	143
	4.3.3 Test Results	143
	4.3.4 Conclusions	151
5.0	ANALYSES	153
	5.1 Propfan Performance Analyses	153
	5.1.1 Engine Inlet Design Analysis	153
	5.1.2 Engine Exhaust Nozzle Sizing	157
	5.1.3 Predicted Drive System Performance	157

Lockheed

TABLE OF CONTENTS (CONT'D)

Section	Title	Page
	5.2 Aircraft Aerodynamics	157
	5.2.1 Aircraft Drag Prediction	157
	5.2.2 Aircraft Performance	163
	5.3 Aircraft Stability and Control Analysis	163
	5.3.1 Basic Aerodynamic Characteristics	163
	5.3.2 Stability and Control Evaluation	171
	5.3.3 Conclusions	191
	5.4 Acoustic Analyses	200
	5.4.1 Initial Test Planning	200
	5.4.2 Acoustic Test Capability Assessment	210
	5.5 Structural Analysis	216
	5.5.1 Airframe Structural Integrity	216
	5.5.2 Forward Nacelle Structural Analysis	245
	5.5.3 Aft Nacelle	250
	5.5.4 Nacelle Sonic Fatigue	255
	5.6 Safety Analyses	263
	5.6.1 Failure Modes and Effects Analysis	263
	5.6.2 Safety Analysis	264
6.0	PROPFAN PROPULSION SYSTEM STATIC TEST	267
	6.1 Test Objectives	267
	6.2 Test Hardware and Facility Description	267
	6.2.1 Test Assembly	267
	6.2.2 Control System	267
	6.2.3 Test Limits	269
	6.3 Test Facility	270
	6.4 Instrumentation	274
	6.4.1 Propfan	274
	6.4.2 Drive System and Nacelle	281
	6.4.3 Acoustics	281
	6.4.4 Ambient Conditions and Facility Data	281

TABLE OF CONTENTS (CONT'D)

Section	Title	Page
	6.5 Test Procedures and Results	281
	6.5.1 Functional Checkout	282
	6.5.2 Propfan Balancing	282
	6.5.3 Low Power Governing Check	284
	6.5.4 Stress Survey	284
	6.5.5 Transient Tests	289
	6.5.6 Endurance Test	295
	6.5.7 Reverse Thrust Test	304
	6.5.8 Propfan Auxiliary Pump Motor Test	304
	6.5.9 Acoustics Tests	308
	6.5.10 Propfan Performance	328
	6.5.11 Drive System	333
	6.5.12 Subsystems Performance	338
	6.5.13 System Vibration Characteristics	345
	6.6 Conclusions	348
7.0	AIRCRAFT PROCUREMENT AND MODIFICATION	351
8.0	AIRCRAFT CHECKOUT TESTS	371
	8.1 Ground Tests	371
	8.1.1 Nacelle/Wing Proof Tests	371
	8.1.2 Ground Vibration Test	372
	8.1.3 Acoustic and Vibration Tests	379
	8.1.4 Systems Functional	382
	8.1.5 Propfan Structural Integrity	383
	8.2 Flight Checkout Tests	427
	8.2.1 Propfan Off	427
	8.2.2 Flight Airworthiness - With Propfan Blades	429
9.0	FLIGHT RESEARCH TESTS	453
	9.1 Propfan Blade Structural Evaluation Tests	454
	9.1.1 Objectives and Scope	454
	9.1.2 Test Procedures	454
	9.1.3 Results and Discussion	454
	9.2 Near-Field Noise Tests	481
	9.2.1 Objectives and Scope	481
	9.2.2 Test Procedures	481
	9.2.3 Results and Discussion	487

TABLE OF CONTENTS (CONT'D)

Section	Title	Page
	9.3 Low Altitude Tests	509
	9.3.1 Objectives and Scope	509
	9.3.2 Test Procedures	515
	9.3.3 Results and Discussions	515
	9.4 Cabin Noise Tests	541
	9.4.1 Objectives and Scope	541
	9.4.2 Test Procedures	541
	9.4.3 Results and Discussion	541
	9.5 Cabin Acoustic Treatment Test	551
10.0	CONCLUDING REMARKS	555
	REFERENCES	557
APPENDIX A	ACOUSTIC REFLECTION CONTAMINATION TESTS IN THE NASA-LANGLEY 16-FOOT TRANSONIC TUNNEL	A-1
APPENDIX B	REVERSE ROTATION DESIGN STUDY	B-1
APPENDIX C	LOW-SPEED, FULL-SCALE WIND TUNNEL TESTS	C-1
APPENDIX D	PREDICTED AIRPORT PERFORMANCE - PTA AIRCRAFT	D-1
APPENDIX E	SAMPLE OF A COMPUTERIZED SAFETY TRACKING LOG	E-1

LIST OF FIGURES

Figure	Title	Page
1	Large-Scale Advanced Propeller (LAP)	4
2	PTA Aircraft	5
3	Flight Test Envelope	7
4	PTA Program Schedule	10
5	Gulfstream Aerospace GII Aircraft	14
6	LAP Assembly	15
7	Features of the SR-7L Blade Construction	16
8	LAP Control Schematic	19
9	Model 570 Engine Features	21
10	Torquemeter Assembly	24
11	PTA Aircraft Modifications	25
12	Research Instrumentation	26
13	On-Board Data System Installation	27
14	Left Wing Modifications	28
15	Skate Angles on GII Wing	29
16	Wing Leading Edge Modifications	31
17	Acoustic Boom Installation	32
18	Spoiler Modification	33
19	Right Wing Modifications	34
20	Fuselage Modifications	35
21	Flight Station Modifications	37
22	Predicted Propfan Excitation Factor	40
23	PTA Nacelle Features	40
24	Size and Location of Engine Inlet	42

PRECEDING PAGE BLANK NOT FILMED

PAGE X INTENTIONALLY BLANK

LIST OF FIGURES (CONT'D)

Figure	Title	Page
25	PTA Nacelle General Arrangement	43
26	QEC Nacelle Primary Structure	44
27	QEC Nacelle Secondary Structure	44
28	Nacelle Tilt Fitting	45
29	Nacelle Tilt Range	45
30	QEC Internal Arrangement	46
31	Air Inlet and Outlet for Oil Cooler	48
32	Oil Cooler Air Outlet Flap	48
33	Aft Nacelle Basic Dimensions	49
34	Aft Nacelle Structure	50
35	Aft Nacelle Exit Region	50
36	Acoustic Tailpipe Assembly	51
37	Nacelle/Wing Fillets	51
38	AC Electrical System Modification	53
39	Model 501-M78 Power Section	57
40	Power Section Lubrication System Change	59
41	Lubrication and Vent System	59
42	Power Section First Stage Vane Reset	61
43	Power Section Containment Ring Restraint Blocks	61
44	T56 Gearbox Features	62
45	Model 501-M78 Gearbox Modifications	62
46	Reversing Accessory Drive Idler Gear	64
47	Gearbox Estimated Life Limit	64
48	Propfan Speed Control Block Diagram	66

LIST OF FIGURES (CONT'D)

Figure	Title	Page
49	Propfan Speed Control Actuator Mounting Arrangement	66
50	Functional Diagram of 501-M78 Control System	68
51	501-M78 Control System Input/Outputs	68
52	Gearbox Mounts	72
53	Bleed Air System Modification for Air Start	72
54	Oil Cooler Design	74
55	Oil Cooler System Performance	74
56	QEC Fire Detector Elements	75
57	Propfan Fire Suppression System	75
58	Stub Tailpipe	76
59	Turbine Containment Ring Installation	76
60	Nacelle Cooling and Venting	78
61	Drive System Test Plan Overview	80
62	Schematic of Power Unit Test Setup	81
63	501-M78 Power Section Component Tests	81
64	Power Section Altitude Test Envelope	82
65	Allison Gearbox Test Arrangement	82
66	Nose-to-Nose Gearbox Test Rig	86
67	Gearbox Component Testing	86
68	Gearbox Component Test Time Distribution	88
69	PTA Data System	90
70	Aircraft Flight Instrumentation	93
71	Aircraft Airspeed System	94
72	Flutter Accelerometer Locations	95

LIST OF FIGURES (CONT'D)

Figure	Title	Page
73	Wing Surface Static Pressures	96
74	Typical Wing Pressure Tap Distribution	97
75	QEC Air Temperature Measurements	98
76	QEC Structural Temperature Measurements	99
77	Drive System Air, Oil, and Surface Temperature Measurements	100
78	Subsystem and Engine Research Pressure Measurements	101
79	Aft Nacelle Ambient Temperature Measurements	102
80	Aft Nacelle Structural Temperature Measurements	103
81	Drive System Vibration and Strain Gages	104
82	Vibration and Pickup Locations	105
83	Typical Fuselage Microphone Installation	106
84	Typical Wing Microphone Installation	107
85	typical Boom Microphone Installation	107
86	PTA Model in 4M x 7M Wind Tunnel	111
87	High-Speed Flow Field Model	112
88	Flow Survey Rake	114
89	Lift/Pitching Moment Correlation with Theory	115
90	Lift Curves for PTA Buildup	115
91	Effect of Mach Number on PTA Lift	116
92	Drag Due to PTA Modifications	118
93	Drag of PTA Components at High Speed	119
94	Airfoil Section Modification for LEX	119
95	Effect of LEX on PTA Drag	120
96	Wing Surface Pressure Distributions - Mach 0.4	121

LIST OF FIGURES (CONT'D)

Figure	Title	Page
97	Wing Surface Pressure Distributions - Mach 0.7	122
98	Effect of PTA Nacelle on Wing Pressures - Mach 0.7	122
99	Effect of Mach Number on Wing Pressures	124
100	Effects of PTA Modifications on Lift and Pitching Moment	124
101	Effects of Propfan Power on Aerodynamic Characteristics in Pitch	125
102	Effects of PTA Modifications on Side Force, Yawing Moment, and Rolling Moment	127
103	Effects of Power on Aerodynamic Characteristics in Pitch	128
104	Mach Number Effects on Lift Characteristics	129
105	Axial Velocity Rake Data - Mach 0.6	131
106	Vertical Velocity Rake Data - Mach 0.6	132
107	Lateral Velocity Rake Data - Mach 0.6	133
108	Thrust Coefficient Data - Mach 0.4	134
109	Power Coefficient Data - Mach 0.4	134
110	Flutter Model in Langley Transonic Dynamics Wind Tunnel	136
111	Flutter Model Test Envelope	137
112	Model Design Scales	138
113	Flutter Test Envelope and Results	140
114	Calculated vs. Measured Flutter Boundary - PTA Configuration with Destabilizing Boom	141
115	PTA Inlet Duct Test Hardware	144
116	PTA Inlet Duct - Major Dimensions and Design Parameters	145
117	QUADPAN Pressure Distribution Predictions	146

LIST OF FIGURES (CONT'D)

Figure	Title	Page
118	Inlet Duct Test Apparatus	147
119	View of Simulated Engine Compressor Face	148
120	Predicted and Measured Static Pressure Distributions	149
121	Total Pressure Recovery at the Compressor Face	150
122	Flow Distortion Relative to Allison Envelope	152
123	Propfan Blade Excitation for Several Inlet Configurations	154
124	Inlet Diffuser Model Test Results	154
125	Predicted and Measured Cowl Pressures	156
126	Impact of Boundary Layer Diverter Height on Inlet Pressure Recovery	158
127	Impact of Exhaust Nozzle Size on SHP and Thrust	158
128	Predicted Drive System Performance	159
129	Estimated Nacelle Drag Increment	161
130	Estimated Drag Polars - Mach 0.4	161
131	Estimated Drag Polars - Mach 0.8	162
132	Original and Revised Aircraft Drag Predictions	162
133	Predicted Speed for Best Rate of Climb	164
134	Predicted Climb Performance	165
135	Predicted Long Range Cruise Performance	166
136	Predicted Sea Level Loiter Performance	167
137	Predicted Speed-Altitude Envelope	168
138	Predicted Test Times	169
139	Comparison of QUADPAN Predictions with GII Data	170
140	Speed-Altitude Envelope for S&C Evaluation	172

LIST OF FIGURES (CONT'D)

Figure	Title	Page
141	Center of Gravity Envelope for S&C Evaluation	173
142	Elevator Angle Required for Trim - Low Altitude	175
143	Elevator Angle Required for Trim - High Altitude	176
144	Elevator Tab Angle Required for Trim - Low Altitude	177
145	Elevator Tab Angle Required for Trim - High Altitude	178
146	Directional Trim Requirements	179
147	Lateral Trim Requirements	180
148	Static Longitudinal Stability	181
149	Static Longitudinal Stability - Mach 0.5	183
150	Static Longitudinal Stability - Mach 0.7	185
151	Low Altitude Maneuvering Stability - Elevator Gradient	187
152	High Altitude Maneuvering Stability - Elevator Gradient	188
153	Longitudinal Dynamic Stability - Short Period Frequency	189
154	Longitudinal Dynamic Stability - Damping Ratios	190
155	Maximum Level Flight Speeds	192
156	Dive Speeds	193
157	Upset Analysis for Determination of Dive Speed	194
158	Single Engine Control	195
159	Lateral-Directional Dynamic Stability - Dutch Roll Mode	196
160	Lateral-Directional Dynamic Stability - Spiral Mode	197
161	Lateral Dynamic Stability - Roll Mode	198
162	Roll Response to Lateral Control	199

LIST OF FIGURES (CONT'D)

Figure	Title	Page
163	Propfan Performance Map for Far-Field Noise Tests	202
164	Predicted Peak Flyover Noise Spectra with Propfan at High Power	203
165	Propfan Performance Map for High-Altitude, Near-Field Noise Tests	205
166	Acoustic Geometry and Baseline Cruise Conditions	207
167	Operational Map of Predicted Near-Field, Free-Field Noise	208
168	Fuselage Surface Predicted Noise Levels - Baseline Cruise	209
169	Fuselage Surface Predicted Noise Levels - Worst Case	211
170	Fluctuating Pressure Levels on Wing and Nacelle - Worst Case	212
171	Flight Path Gradient with Spey Engines at Flight Idle	214
172	Thrust Trade-Offs for Level Flight	215
173	Finite Element Model for Structural Analysis	218
174	Weight-CG Envelope for Structural Analysis	218
175	Maximum Airspeeds for Structural Design	220
176	Wing Load Envelope - WS 120 Left	220
177	Wing Load Envelope - WS 200 Left	222
178	Margins of Safety - Left Wing Upper Cover	222
179	Margins of Safety - Left Wing Lower Cover	224
180	Dynamic Balance Boom	224
181	Static Balance Boom	225
182	Wing Load Envelope - WS 399 Right	226
183	Wing Load Envelope - WS 280 Right	228

LIST OF FIGURES (CONT'D)

Figure	Title	Page
184	Margins of Safety - Right Wing Upper Cover	228
185	Margins of Safety - Right Wing Lower Cover	229
186	Horizontal Tail Load Envelope - BL 32	229
187	Vertical Tail Load Envelope - WL 180	231
188	Drag Shear Web and Link Loads Envelope	232
189	Wing-Fuselage Attachment Loads - Front Spar (FS 345.875)	234
190	Forward Fuselage Load Envelope - FS 288	235
191	Aft Fuselage Load Envelope - FS 451	236
192	Fuselage Protection - Steel Plate Installation	237
193	Flutter Clearance Program	239
194	Predicted Flutter Boundaries	239
195	Predicted Flutter Boundaries with Drive System Failures	241
196	Predicted Flutter Boundaries with Loss of Dynamic Balance Boom	242
197	Airframe Structure Design Life	244
198	Flap Sonic Fatigue Analysis	244
199	Inertia Forces for Nacelle Design	246
200	QUADPAN Paneling for Nacelle Loads	248
201	QEC Finite Element Model	248
202	Aft Nacelle External Aerodynamic Pressures	251
203	Predicted Aft Nacelle Internal Pressures	253
204	Aft Nacelle Finite Element Model	254
205	QEC/Aft Nacelle Interface Loads	254
206	Inboard Skin Stresses - WS 145, NT = +3°	256

LIST OF FIGURES (CONT'D)

Figure	Title	Page
207	Inboard Skin Stresses - WS 145, NT = -5°	256
208	Aft Nacelle Materials and Fasteners	257
209	Aft Nacelle Maximum Operating Temperatures	257
210	Summary of Aft Nacelle Safety Margins	258
211	Sonic Fatigue Substantiation of Inlet	258
212	Sonic Fatigue Substantiation of Upper Cowling Panels	259
213	Sonic Fatigue Substantiation of Side Cowling Panels	259
214	Random Fatigue Shaker Testing	260
215	Test Specimen and Instrumentation	260
216	Typical Large-Bay Skin Panel	261
217	Skin Panel Sonic Fatigue Analysis Example	261
218	Aft Nacelle Sonic Fatigue Analysis Conclusions	262
219	Risk Assessment Matrix	265
220	Propfan Propulsion System Static Test Assembly	268
221	Propfan Operating Limits	271
222	Rohr Brown Field Test Facility	272
223	PTA Propulsion System on Rohr Test Stand	273
224	Acoustic Data Field	275
225	Acoustic Data Field with Barrier in Forward Position	276
226	Acoustic Data Field with Barrier in Aft Position	277
227	Propfan Blade Strain Gages	278
228	Static Engine Test Operating Limits	283
229	Stress Survey Conditions Selected for Data Analysis	286
230	Tip Bending Strain Variation with Torque	286

LIST OF FIGURES (CONT'D)

Figure	Title	Page
231	SR-7L Torque Change with Blade Angle	287
232	Tip Bending Gage Strain Variation with Blade Angle	287
233	Vibratory Strain Distribution	288
234	Frequency Content of the Tip Bending Gage 13	288
235	Predicted and Measured Blade Natural Frequencies	290
236	Inboard Bending Vibratory Strain	291
237	Mid-Board Bending Vibratory Strain	291
238	Tip Bending Vibratory Strain	292
239	Speed Transient Conditions	293
240	Power Transient Conditions	294
241	Response to 4-Second Speed Lever Traverse - 87.5 to 100% Np; 2238 kw (3000 hp)	296
242	Response to 2-Second Speed Lever Traverse - 87.5 to 100% Np; 2238 kw (3000 hp)	297
243	Response to Step Increase in Power - 1268 kw to 2089 kw (1700 to 2800 hp), 87.5% Np	298
244	Response to Step Reduction in Power - 2089 kw to 1268 kw (2800 to 1700 hp), 87.5% Np	299
245	Response to Step Increase in Power - 1350 kw to 2700 kw (1810 to 3620 hp), 95% Np	300
246	Response to Step Reduction in Power - 2700 kw to 1350 kw (3620 to 1810 hp), 95% Np	301
247	Fast Speed Lever Transient - 2240 kw (3000 hp)	302
248	Fast Power Lever Transient - 95% Np	303
249	Effects of Endurance Test on Gas Generator Speed	305
250	Effects of Endurance Test on Correct MGT	306
251	Effects of Endurance Test on Fuel Flow	307

LIST OF FIGURES (CONT'D)

Figure	Title	Page
252	Ground Level Noise Spectrum	309
253	Ground Level Noise Spectrum with High Resolution (10x) Frequency Analysis	310
254	Ground Level One-Third Octave Noise Spectrum	312
255	Ground Level One-Third Octave Noise Spectrum	314
256	Ground Level Subjective Noise Level - Minimum Test Powers	315
257	Ground Level Subjective Noise Level - 105% Np	316
258	Ground Level First Order Blade Noise Dependence on Power	317
259	Ground Level First Order Blade Noise Dependence on Thrust	318
260	Ground Level Random Noise Dependence on Power	319
261	Ground Level Random Noise Dependence on Thrust	320
262	Ground Level Random Noise Relationsnip to Thrust Coefficient	321
263	Ground Level Random Noise Relationship to Power Coefficient	323
264	Ground Level Compressor/Propfan Interaction Tone Noise Dependence on Power	324
265	Near-Field Microphone Locations Relative to Aircraft Fuselage	325
266	Near-Field Noise Levels at Equivalent Fuselage Stations for Different Powers	326
267	Near-Field Noise Levels at Equivalent Fuselage Stations for Different Tip Speeds	327
268	Near-Field Sound Pressure Time Histories Centerline Height Sound Pressures	329
269	Instantaneous and Average Pressure Wave Samples	330
270	Propfan Power Coefficient vs Blade	331

LIST OF FIGURES (CONT'D)

Figure	Title	Page
271	Propfan Thrust Coefficient vs Power Coefficient	332
272	Revised Static Operating Envelope	334
273	Installation Effects on Unity Ram Gas Generator Speed	335
274	Installation Effects on Unity Ram MGT	336
275	Installation Effects on Unity Ram Fuel Flow	337
276	Installation Effects on Corrected Gas Generator Speed	339
277	Installation Effects on Corrected MGT	340
278	Installation Effects on Corrected Fuel Flow	341
279	PTA Static Test Propfan Fluid Temperature	342
280	PTA Static Test Drive System Oil Temperature	344
281	Propfan Relative Vertical Acceleration on the Static Test Stand	346
282	Propulsion System Vibration Mode Shape at Np = 94%	347
283	QEC Mockup and Drive System Mockup	352
284	Wing from GII S/N 245	353
285	Wing Structural Modification	354
286	Wing After Primary Modification	355
287	Modified Wing with Aft Nacelle Buildup Jig	356
288	Estimated Two-Year Operating Costs of Candidate Aircraft	358
289	Completed QEC/Drive System Assembly	359
290	Fabrication of Acoustic Tailpipe at Rohr	360
291	Mating of S/N 245 Wing with S/N 118 Aircraft	361
292	Buildup of Aft Nacelle on Wing	362
293	Rear View of Aft Nacelle Buildup	363

LIST OF FIGURES (CONT'D)

Figure	Title	Page
294	Aircraft Cabin Modified to Test Configuration	364
295	PTA Modifications in Wing Leading Edge	366
296	Mounting of Acoustic Boom on Wing	367
297	Mounting of Wing Tip Boom	368
298	Mating of QEC with Wing and Aft Nacelle	369
299	Completed Propfan Drive System Installation	370
300	Proof Test Loads	373
301	Measured Boom Frequencies	376
302	Control Surface Rotation Frequencies	376
303	Summary of Measured Modes	377
304	Block Diagram of the Vibration Excitation System	380
305	Block Diagram of the Acoustic Excitation System	381
306	Crosswind Test Conditions	384
307	Crosswind Testing Using a C-130 as a "Blower" Aircraft	385
308	Power Lever Traverse During Calm Wind Conditions	387
309	Calm Wind Governing Tests	388
310	Variation of Tip Bending Strain with Torque	389
311	Tip Bending Strain During Static Operation	391
312	Tip Bending Gage Response Spectra at 100% N_p	392
313	Comparison of Static Boundaries for SR-7L and SR-7A	393
314	Torque Variation with Blade Angle While Governing	394
315	Tip Bending Strain Variation with Blade Angle	395
316	Radial Strain Distribution for Two Torque Values	397
317	Visicorder Plots of Strain Gage Signals	398

LIST OF FIGURES (CONT'D)

Figure	Title	Page
318	Blade Strain Amplitude Spectrum - 100% Np	399
319	Blade Strain Amplitude Spectrum - 85% Np	400
320	Blade Natural Frequencies from PTA Ground Tests	401
321	Tip Bending Strain During Calm Wind Power Lever Traverse	403
322	Mid-Blade Bending Strain During Calm Wind Power Lever Traverse	404
323	Inboard Bending Strain During Calm Wind Power Lever Traverse	405
324	Shank Flatwise Moment During Calm Wind Power Lever Traverse	406
325	Shank Edgewise Moment During Calm Wind Power Lever Traverse	407
326	Power Lever Traverse During 225° Crosswind Tests	408
327	Governing Conditions During 225° Crosswind Tests	409
328	Power Lever Traverse During 270° Crosswind Tests	410
329	Governing Conditions During 270° Crosswind Tests	411
330	Power Lever Traverse During 135° Crosswind Tests	412
331	Governing Conditions During 135° Crosswind Tests	413
332	Wind Direction and Speed Recorded During 225° Crosswind Tests	414
333	Wind Speed During the 225° Power Lever Traverse	415
334	Wind Speed During the 270° Power Lever Traverse	416
335	Wind Speed During the 135° Crosswind Power Lever Traverse	417
336	Power Lever Traverse During Crosswind Conditions	419
337	Tip Vibratory Response in a Crosswind Environment	420

LIST OF FIGURES (CONT'D)

Figure	Title	Page
338	Shank Edgewise Response in a Crosswind Environment	421
339	Shank Flatwise Response in a Crosswind Environment	422
340	Tip Bending Strain Variation with Blade Angle - 225° Crosswind	423
341	Tip Bending Strain Variation with Blade Angle - 270° Crosswind	424
342	Tip Bending Strain Variation with Blade Angle - 135° Crosswind	425
343	Effect of Taxi Speed on the Buffet Boundary	426
344	Nose Boom Position Error Correction	430
345	Engine Tailpipe Extension	433
346	Flight Envelope Clearance Points for Blade Stress	436
347	Effect of Airspeed on Vibratory Loads in Stabilized Flight	438
348	Blade Vibratory Load vs Indicated Airspeed	439
349	Blade Vibratory Loading vs Indicated Airspeed	440
350	Comparison of the 1P Component and Total IRP Shank Moment	441
351	Vibratory Loading vs Altitude (Maximum Continuous Torque)	442
352	Vibratory Loading vs RPM (Constant Torque)	443
353	Vibratory Loads in a Sideslip Maneuver	444
354	Spectral Plot, Blade Shank Flatwise Vibratory Bending Moment, Sideslip Maneuver	446
355	Vibratory Response to an Elevator Doublet	447
356	Spectral Plot, Blade Shank Flatwise Vibratory Bending Moment Elevator Doublet	448
357	Vibratory Loading During Feathering and Shutdown	449

LIST OF FIGURES (CONT'D)

Figure	Title	Page
358	Visicorder Traces During Shutdown and Feathering	450
359	Second Peak Visicorder Traces During Shutdown and Feathering	451
360	High-Altitude Flight Test Envelope, NT = -1°	455
361	High-Altitude Flight Test Envelope, NT = -3°, +2°	456
362	High-Altitude Flight Test Envelope, Yaw Conditions	457
363	Inboard Bending Vibratory Strain, NT = -3°	458
364	Inboard Bending Vibratory Strain, NT = -1°	459
365	Inboard Bending Vibratory Strain, NT = +2°	460
366	Typical Frequency Spectrum for an Inboard Bending Strain Gage	461
367	Radial Distr bution of 1P and 2P Strain, NT = -3°	463
368	Radial Distribution of 1P and 2P Strain, NT = -1°	464
369	Radial Distribution of 1P and 2P Strain, NT = +2°	465
370	Radial Distribution of 3P and 4P Strain, NT = -1°	466
371	Effect of Airspeed on Blade Response at Low Altitude	468
372	Effect of Airspeed on Blade Response at High Altitude	469
373	Propfan Relative Excitation Factor	470
374	Effect of Nacelle Tilt on Blade Response at Low Speed	471
375	Effect of Nacelle Tilt on Blade Response at High Speed	472
376	Effect of Torque on Blade Response	474
377	Calculated Camber Change with Torque	475
378	Effect of Rotational Speed on Blade 1P and 2P Response at Low Speed	477

LIST OF FIGURES (CONT'D)

Figure	Title	Page
379	Effect of Rotational Speed on Blade 1P, 2P, and 3P Response at High Speeds	478
380	Effect of Rotational Speed on Blade 3P and 4P Shank Edgewise Response	479
381	Effect of Mach Number on Blade Response at Constant Airspeed	480
382	Comparison of Measured and Predicted Propfan Performance, Mach 0.8, J = 3.07	482
383	Comparison of Measured and Predicted Propfan Performance, Mach 0.7, J = 2.75	483
384	Comparison of Measured and Predicted Propfan Performance, Mach 0.5, J = 2.70	484
385	High-Altitude Flight Test Envelope - Propfan Off	485
386	High-Altitude Flight Test Envelope for Cabin Noise Surveys	486
387	Effects of Near Side Spey Engine on Fuselage Noise - Prop On	488
388	Effects of Near Side Spey Engine on Fuselage Noise - Prop Off	488
389	Sound Pressure Spectra on Fuselage and Acoustic Boom	489
390	Sound Pressure Distribution on Fuselage	490
391	Circumferential Distribution of SPL on Fuselage	491
392	Effects of Power Variation at Constant Tip Speed on Fuselage SPL	493
393	Effects of Propfan Thrust and Tip Speed on Fuselage SPL Measurements	494
394	Effects of C_p and J on Fuselage SPL Measurements	494
395	Variation of SPL on Fuselage over Flight Envelope	495
396	Differences Between Fuselage SPLs at BPF1 and BPF2	496
397	Effect of Propfan Helical Tip Mach Number on Fuselage SPL	496

LIST OF FIGURES (CONT'D)

Figure	Title	Page
398	Test Conditions for Altitude Scaling Validation	497
399	Results from Altitude Scaling Validation Tests	497
400	Expected Influence on Near-Field Noise of Propfan Inflow Angle and Direction of Rotation	499
401	Effect of Nacelle Tilt on Fuselage and Boom SPLs	499
402	Propfan Near-Field Acoustic Prediction Methodology	500
403	Summary of Fuselage Predicted and Measured SPLs	500
404	Summary of SPL Prediction Accuracy	501
405	Fuselage Axial Distribution of SPL	501
406	Comparison of Predicted and Measured SPL Spectra on Fuselage	503
407	Effects of Rotational Speed on Fuselage SPL	504
408	Effect of Nacelle Tilt on Fuselage SPL	504
409	Spectrum of Fluctuating Pressure on Wing Lower Surface	505
410	Spectra of Wing FPL in Four Quadrants	506
411	Distribution of FPL on Wing Lower Surface	507
412	Distribution of FPL on Wing Upper Surface	507
413	Chordwise Distribution of Wing FPL	508
414	Effects of Propfan Rotational Speed and Power on Wing Inboard FPLs	510
415	Effects of Propfan Rotational Speed and Power on Wing Outboard FPLs	510
416	Variation of FPLM over Flight Envelope	511
417	Relation Between Wing FPLM and Fuselage SPLM	512
418	Effect of Nacelle Tilt on Wing FPLs in Four Quadrants	512

LIST OF FIGURES (CONT'D)

Figure	Title	Page
419	Fluctuating Pressure Prediction Methodology	513
420	Summary of Predicted Wing FPLs	513
421	Effects of Propfan Power and Tip Speed on Wing FPLs	514
422	Low-Altitude Flight Test Conditions	516
423	Low-Altitude Test Procedure with Propfan Blades Removed	517
424	Typical Far-Field Noise Time History	518
425	Typical 1/3-Octave Band Spectra	519
426	Azimuthal Noise Directivity at Blade Passage Frequency	521
427	Polar Noise Directivity at Blade Passage Frequency	522
428	Effects of Power and Helical Tip Mach Number on OASPL	523
429	Effects of Power and Nacelle Tilt on Peak OASPL	526
430	Comparison of Predicted and Measured Peak OASPL	528
431	Comparison of Predicted and Measured Time Histories	529
432	Comparison of Predicted and Measured Noise Spectra	530
433	Effects of Shaft Horsepower on Predicted and Measured Noise at the Nominal Conditions of: Altitude = 305 m (1000 ft); V_{ROT} = 213 m/s (700 fps); M_{TH} = 0.7; NT = -1°; Angle of Attack = 4.3°; Sideslip Angle = -1°	532
434	Effects of Tip Speed on Predicted and Measured Noise at the Nominal Conditions of: Altitude = 305 m (1000 ft); Power = 4320 kw (5790 PSHP); NT = -1°; Angle of Attack = 4.3°; Sideslip Angle = -1°	534
435	Effect of Nacelle Tilt on Far-Field Noise	536
436	Calculation Procedure for Lateral Noise Attenuation	537
437	Lateral Attenuation as a Function of Elevation Angle - Port Side	538

LIST OF FIGURES (CONT'D)

Figure	Title	Page
438	Lateral Attenuation as a Function of Elevation Angle - Starboard Side	539
439	Summary of Lateral Attenuation Results	540
440	Cabin Acoustic Measurement Area	542
441	Identification and Location of Cabin Microphones	543
442	Comparison of Interior and Exterior Cabin Noise Spectra	544
443	Lateral and Axial Distribution of Cabin Noise	545
444	Spatial Variation of Cabin Noise in the Propfan Plane	546
445	Effect of Fuselage Pressurization on Cabin Noise	548
446	Effects of Flight Conditions on Cabin Noise	548
447	Effects of Propfan Power and Tip Speed on Cabin Noise	549
448	Predicted Structureborne Noise and Measured Cabin Total Noise	550
449	Noise Reduction Required at BPF to Achieve 80 dBA in Cabin	552
450	Assembly of the Advanced-Acoustic-Wall Cabin Enclosure for PTA Flight Tests	553

LIST OF SYMBOLS AND ABBREVIATIONS

ABN	Airborne noise
AC	Alternating current
AGL	Above ground level
AL	Acceleration level
BL	Aircraft butt line
BPF	Blade passage frequency
c	Speed of sound
C	Centigrade
CBFM	Constant bandwidth frequency modulation
CCW	Counterclockwise
CG	Center of gravity
C_L	Lift coefficient
C_{L_α}	Lift curve slope
cm	Centimeters
C_M	Pitching moment coefficient
C_{MO}	Pitching moment coefficient at zero lift
C_P	Propfan power coefficient
CRT	Cathode ray tube
C_T	Propfan thrust coefficient
CVG	Compressor variable geometry system
CW	Clockwise
dB	Decibels
dBA	"A"-weighted noise
dBOA	Overall noise
DC	Direct current

LIST OF SYMBOLS AND ABBREVIATIONS (CONT'D)

D_p	Propfan diameter
DSA	Data sample average
ECU	Electronic control unit
EF	Excitation factor
EPNL	Effective perceived noise level
F	Fahrenheit
FFT	Fast Fourier transform
FL	Input force level
FM	Frequency modulation
FPL	Fluctuating pressure level
FPLM	Maximum FPL in an area
fps	Feet per second
FS	Aircraft fuselage station
ft	Feet
g	Acceleration due to gravity
gal.	gallons
GPM	Gallons per minute
H	Altitude
hp	Horsepower
Hz	Frequency, Hertz
IL	Insertion loss
in.	Inches
IRIG	Intermediate range instrumentation group
IRP	Infrequently repeating peak
J	Propfan advance ratio

LIST OF SYMBOLS AND ABBREVIATIONS (CONT'D)

KCAS	Knots, calibrated air speed
KEAS	Knots, equivalent airspeed
kg	kilograms
kHz	KiloHertz
KIAS	Knots, indicated airspeed
km	Kilometers
kN	Kilonewtons
KR	Radial distortion coefficient
KTHETA	Circumferential distortion coefficient
kts	Knots
KVA	Kilovolt-amperes
kw	Kilowatts
LADS	Lockheed Airborne Data System
LAP	Large-Scale Advanced Propfan
lb	pounds
LEX	Leading edge extension
m	Meters
M	Mach number
M_D	Dive Mach number
M_{DF}	Functional dive Mach number
MGT	Measured gas temperature at power turbine entrance
M_H	Maximum level flight Mach number
mm	Millimeters
MN	Mach number
mph	Miles per hour

LIST OF SYMBOLS AND ABBREVIATIONS (CONT'D)

mps	meters per second
M_{ROT}	Propfan rotational Mach number
M_{TH}	Propfan tip helical Mach number
M_X	Aircraft bending moment
M_x	Positive vertical bending moment
M_Y	Aircraft torsion moment
M_y	Positive torsion moment
M_z	Positive lateral bending moment
N	Newtons
Ng	Gas generator rotational speed
N_G	Gas generator speed
NM	Nautical miles
N_P	Turbine speed
NR	Noise reduction
NT	Nacelle tilt angle
OASPL	Overall sound pressure level
p	Static pressure
P	Per revolution (as in 1P)
PCM	Pulse code modulation
PNdB	Perceived noise level
PNLT	Tone-corrected perceived noise levels
PSHP	Propeller shaft horsepower
psi	Pounds per square inch

LIST OF SYMBOLS AND ABBREVIATIONS (CONT'D)

PTA	Propfan Test Assessment
PTH	Pressure time histories
P_x	Positive aft load
P_y	Positive left load
P_z	Positive up load
q	Freestream dynamic pressure
QEC	Quick engine change
rms	Root-mean-square
rpm	Revolutions per minute
RSS	Root sum squared
RVDT	Rotary variable differential transformer
S/N	Serial Number
SBN	Structureborne noise
sec	seconds
shp	Shaft horsepower
SPL	Sound pressure level
SPLM	Maximum SPL in an area
t	Time
TEU	Trailing edge up
TED	Trailing edge down
T/R	Transformer rectifier
T_C	Thrust coefficient
TDT	Transonic Dynamics Tunnel
TGT	Turbine gas temperature

LIST OF SYMBOLS AND ABBREVIATIONS (CONT'D)

TRAM	Cabin traversing microphone boom
V_1, V_2, etc.	Acceleration at various points on the gearbox
VA	Volt, amperes
VAC	AC voltage
V_C	Cruise speed
V_D	Dive velocity
VDC	DC voltage
V_{DF}	Functional dive speed
V_E	Equivalent airspeed
V_K	Wind tunnel airspeed
V_{MC}	Minimum control speed
V_{rms}	Root mean square
V_{ROT}	Propfan rotational velocity
V_S	Stall speed
V_{TIP}	Propeller tip speed
WL	Water line
WPAFB	Wright-Patterson Air Force Base
WS	Aircraft wing station
1P, 2P, etc.	Once per revolution, twice per revolution, etc.
1P/1E, etc.	E or F denotes edgewise or flatwise bending modes

Greek Symbols:

α	Aircraft angle of attack
β	Propeller blade angle
ρ	Freestream air density
ϕ	Azimuthal angle
ψ	Propeller inflow angle
η_p	Propfan efficiency

1.0 SUMMARY

The objectives of the Propfan Test Assessment (PTA) Program were to validate in flight the structural integrity of large-scale propfan blades and to measure noise characteristics of the propfan in both near and far fields. All program objectives were met or exceeded, on schedule and under budget. To accomplish these objectives, a Gulfstream Aerospace Corporation GII aircraft was modified to provide a testbed for the 2.74m (9 ft) diameter Hamilton Standard SR-7 propfan which was driven by a 4475 kw (6000 shp) turboshaft engine mounted on the left-hand wing of the aircraft. Provision was made for changing the tilt angle of the forward nacelle in order to vary dynamic loads on the propfan blades.

Flight research tests were performed for 20 combinations of speed and altitude within a flight envelope that extended to Mach numbers of 0.85 and altitudes of 12,192m (40,000 ft). Propfan blade stress, near-field noise on aircraft surfaces, and cabin noise were recorded. Primary variables were propfan power and tip speed, and the nacelle tilt angle.

Extensive low altitude far-field noise tests were made to measure flyover and sideline noise and the lateral attenuation of noise. In cooperation with the FAA, tests were also made of flyover noise for the aircraft at 6100m (20,000 ft) and 10,668m (35,000 ft). A final series of tests were flown to evaluate an advanced cabin wall noise treatment that was produced under a separate program by NASA-Langley Research Center.

The propfan was well-behaved structurally over the entire operating envelope. Vibratory blade response, which was dominated by once-per-revolution loads, followed predicted trends with airspeed, nacelle tilt, power, and tip speed. Blade inboard vibratory response was slightly less than predicted.

Noise measurements were dominated by tones at blade passage frequency. For near-field and cabin noise, higher order harmonics were also significant. Propfan noise was: strongly directional in both polar and azimuthal planes, strongly affected by power and tip Mach number, and significantly affected by nacelle tilt angle. Cabin noise was primarily airborne (as opposed to structureborne).

2.0 INTRODUCTION

2.1 BACKGROUND

In response to national emphases on fuel conservation, the Advanced Turboprop (ATP) Project Office was established at NASA-Lewis Research Center in the mid-1970s. The major objective of this office was to extend the excellent low-speed propulsive efficiency of the propeller to higher subsonic speeds. At Mach numbers up to 0.6, turboprop propulsion systems were much more fuel efficient than turbofans, but at higher speeds, conventional propellers rapidly lost that advantage.

Working with Hamilton Standard, the SR (single rotation) series of high-speed propellers were developed and were dubbed "propfans." Wind tunnel model tests indicated that the best of the propfans would permit fuel savings of greater than 20 percent for medium range transport aircraft cruising at Mach numbers of 0.8. Furthermore, these tests showed the propfans, with their thin, highly swept blades, to be much quieter than high-speed propellers developed earlier.

Prior to declaration that propfans were ready for application, NASA determined that two further steps were necessary. First, there must be assurance that the propfan blades--representing a radical departure in geometry from earlier blades--could be operated with the infinite-fatigue-life properties necessary for commercial aircraft. Second, more knowledge was needed about the noise characteristics of propfans to determine if: (a) the cabin noise treatment weight penalties were acceptable, and (b) propfan-powered aircraft could meet community noise standards.

To answer these questions, NASA established the Large-Scale Advanced Propeller, or LAP, Program (Reference 1) and the Propfan Test Assessment, or PTA, Program. In the LAP Program, Hamilton Standard designed and built a large-scale version of their SR-7 propfan; and in the PTA Program, the Lockheed Aeronautical Systems Company developed a flying test platform for the LAP and performed a series of flight research tests.

The LAP rotor, as shown in Figure 1, consisted of eight thin, highly swept blades, with tips designed to operate at helical Mach numbers of almost 1.2 at the design flight speed of Mach 0.8 at 10,668m (35,000 ft). The PTA aircraft, shown in Figure 2, was a Gulfstream II business jet that was modified to mount the propfan propulsion system on the left-hand wing. The propfan was powered by an Allison 501-M78 turboshaft engine rated at 4475 kw (6000 hp). The aft-mounted Spey engines were retained as the primary power plants for the PTA aircraft. The aircraft was extensively arrayed with microphones, pressure transducers, and accelerometers for the measurement of the desired research data.

2.2 OBJECTIVES AND REQUIREMENTS

The NASA-defined objectives of the PTA Program were to evaluate, through the development of a flightworthy drive system and subsequent ground and flight testing of a large-scale propfan:

PRECEDING PAGE BLANK NOT FILMED

PAGE 2 INTENTIONALLY BLANK

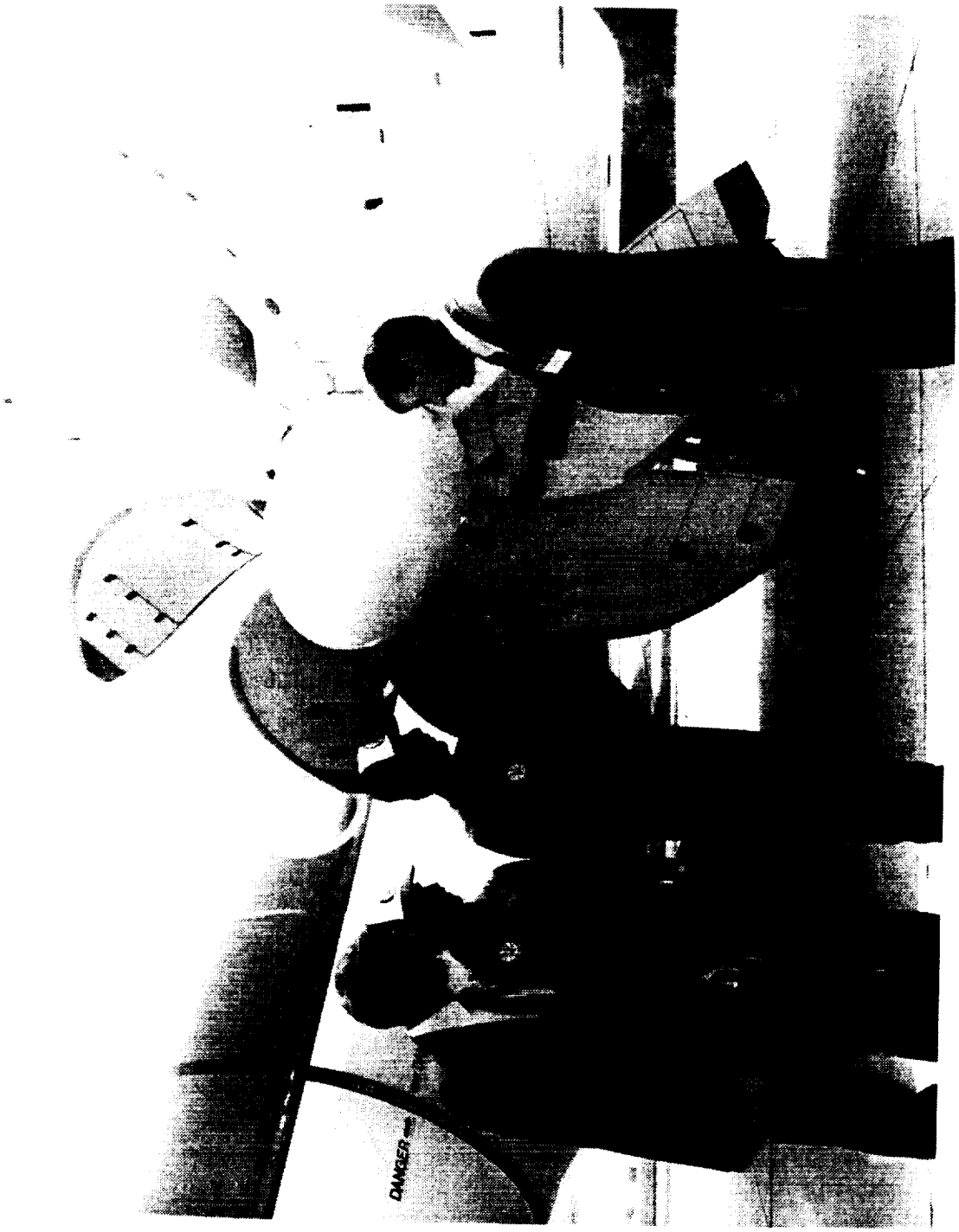


Figure 1. Large-Scale Advanced Propeller (LAP)

ORIGINAL PAGE
BLACK AND WHITE PHOTOGRAPH

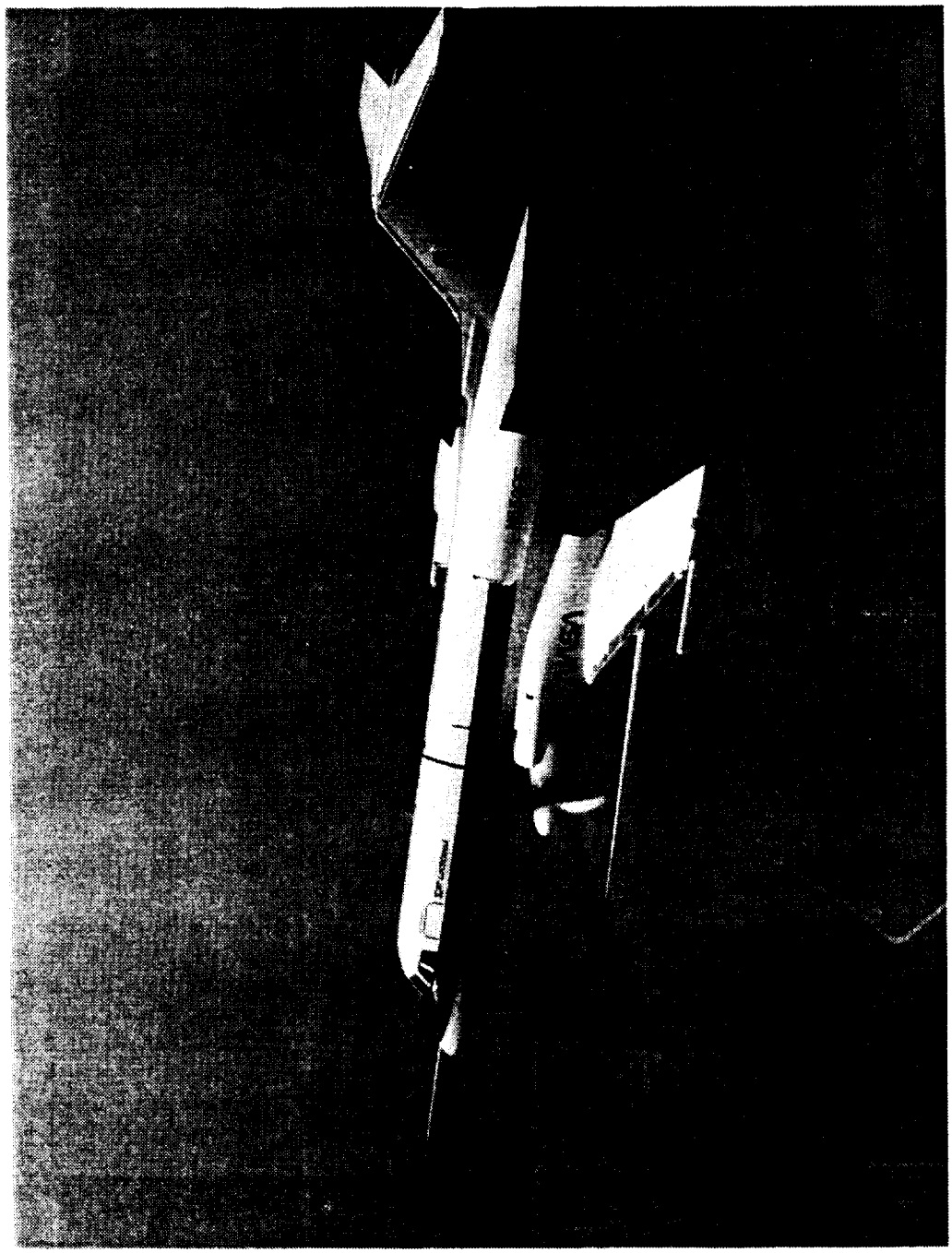


Figure 2. PTA Aircraft

ORIGINAL PAGE
BLACK AND WHITE PHOTOGRAPH

- o Propfan structural integrity
- o Propfan source noise
- o Associated propfan-related cabin noise and vibration
- o FAR-36 community noise
- o En route cruise noise (ground)

The LAP test article was designated the SR-7L, and the LAP assembly included the blades, hub and blade retention system, pitch change and control system, spinner, and instrumentation. The SR-7L was designed to operate with the blades moving upwards on the inboard side of the nacelle with the nacelle on the left wing of the aircraft.

The propfan drive system was the Allison Model 501-M78. It was required that it be geared and controlled so that propfan tip speeds of 183 mps (600 fps), 213 mps (700 fps), and 244 mps (800 fps) could be tested. A fourth tip speed of 256 mps (840 fps) was desired. Power loadings were desired to range from the point of peak propfan efficiency up to maximum power. A maximum power loading (P/D_p^2) of 321 kw/m² (40 hp/ft²) was desired at the Mach 0.8, 10,668m (35,000 ft) design flight condition. The design power loading at this flight condition, as specified by Hamilton Standard, was 257 Kw/m² (32 hp/ft²).

The flight test envelope that was defined for the major portion of the research tests is shown in Figure 3. It was required that tests include the full range of power and tip speed variation at the Mach 0.8 design point, and it was desired that data be obtained in the extended envelope to Mach 0.85 at 12,192m (40,000 ft). At the Mach 0.8 design point, it was also required that the test aircraft have a cruise test mission duration in excess of one hour.

The PTA contract required that the testbed aircraft be capable of flying safely from takeoff to cruise to landing within the operational envelope for a condition of one engine failed, the other main engine operating up to maximum power, and the propfan windmilling or feathered. For handling quality, CAR-4b and MIL-F-8785C were specified as guides.

It was specified that flight research tests include four altitudes above 1524m (5000 ft), selected to cover the normal flight envelope of Figure 3 and, if possible, the extended flight envelope. At each altitude, at least four Mach numbers were to be selected. It was also specified that low altitude tests should be conducted at a minimum of two altitudes to define far-field, propfan-generated noise at stations consistent with the FAR Part 36 noise measurement locations.

Furthermore, it was required that the test vehicles provide a range of propfan excitation factors from 2.0 to 4.0 (4.5 desired), and that the higher-order harmonic loads of the propfan be in the range of 12 to 30 percent of the total dynamic loads. Excitation factor is a parameter developed by Hamilton Standard as a measure of unsteady aerodynamic loads on propeller blades caused by flow field distortion. The PTA contract

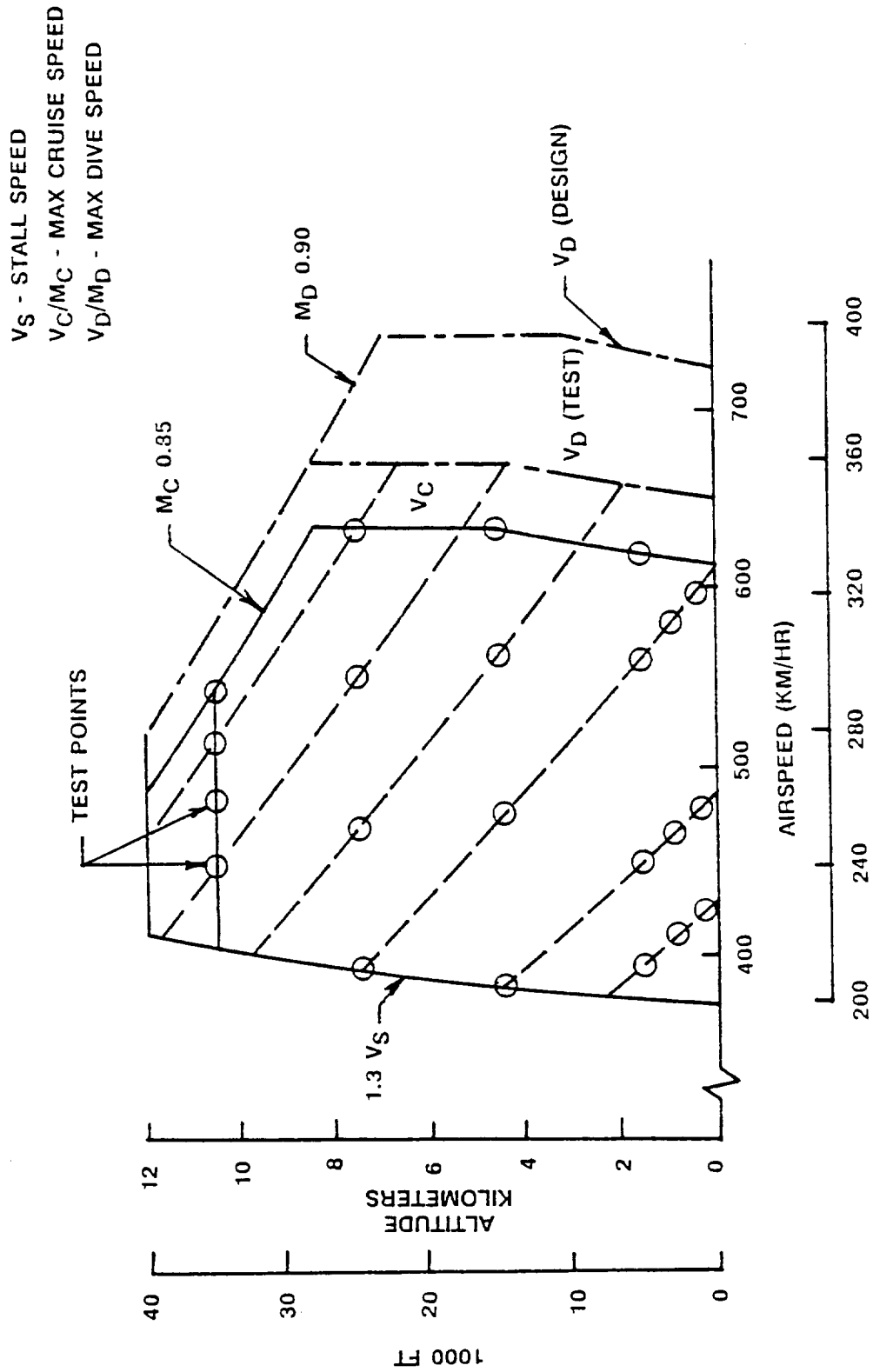


Figure 3. Flight Test Envelope

stipulated that aircraft yaw could not be used as the primary means of attaining the required variation of excitation factor.

Wind tunnel and other scale model tests were required to minimize technical risks associated with the program. These included aerodynamic drag/stability and control model tests as well as flutter model tests and tests of the propfan inlet duct. Other wind tunnel tests were specified to obtain baseline acoustics on the small-scale model, and particularly on the effects of propfan direction of rotation. These tests, unfortunately, were precluded by problems with the hardware of the small scale model. Some valuable data were obtained, however, on acoustic signal reflections in a transonic wind tunnel, and these are described in Appendix A.

A propfan propulsion system static test of the full-scale system was required to:

- Provide a functional checkout test of the complete system
- Verify safe and stable operation of the propfan and drive system over the full range of power loadings
- Provide a functional checkout of all instrumentation
- Define propfan and drive system noise
- Provide data to verify predicted sea level static performance

Ground tests of the assembled aircraft were required to:

- Verify satisfactory operation of normal aircraft systems
- Determine vibration modes of the modified aircraft in order to validate the analytical models used in flutter analysis
- Evaluate the relationship between wing excitation and cabin noise
- Verify predicted load paths for critical nacelle loads
- Assess cross wind effects on propfan blade vibratory loads
- Screen for incipient propfan stall flutter in taxi tests

Flight checkout tests were required to:

- Shake down and check out all aircraft and instrumentation systems
- Verify adequate handling characteristics with and without the propfan installed
- Verify adequate flutter margins with and without the propfan installed
- Verify the propfan drive system and system instrumentation

- Evaluate propfan blade aeroelastic characteristics sufficient to clear the test envelope

There were also requirements in the original contract for preliminary design of a twin engine testbed aircraft, with the drive system on the right-hand wing capable of rotating in either direction. The results of this activity are reported in Appendix B.

Another requirement, that later became superfluous, was for tests of the assembled PTA aircraft in the NASA Ames 40-Ft x 80-Ft Wind Tunnel. This requirement was originally included as a preliminary to flight tests and to obtain data on structureborne noise, but was deleted in favor of expanding flight tests and acoustic data analysis. The work performed in preparation for the wind tunnel tests is reported in Appendix C.

2.3 SCOPE

To meet the PTA Program objectives and requirements, the following tasks were performed:

- Selection of basic system components
- Design of components
- Developmental tests to support and validate design
- Component fabrication and aircraft modification
- System assembly
- System checkout
- Flight research tests
- Data analysis and reporting

Highlights of the PTA Program schedule are shown in Figure 4. The program began in October 1984, and the Detail Design Review was held in December 1985. Concurrent with system design at Lockheed, Allison Gas Turbine Division of General Motors was engaged in fabrication, assembly, and test of the propfan drive system, while Rohr, Inc., designed and built the forward nacelle (or QEC). The drive system was installed in the QEC in early 1986, and static tests of the complete propulsion system (with LAP) took place in June 1986.

A number of small-scale models were designed and tested in this time period with final wind tunnel tests occurring in September 1986.

The GII aircraft was procured in March 1986 and flown to Gulfstream Aerospace Corporation for modification. It was mated with the reinforced wing on which the aft nacelle was mounted and completely modified to the PTA configuration by March 1987. First flight occurred that same month, and flight research tests began in June 1987. Flight research tests for the basic PTA Program were completed in November 1987, and flight tests for the acoustic enclosure add-on were completed in March 1988.

Figure 4. PTA Program Schedule

ORIGINAL PAGE
BLACK AND WHITE PHOTOGRAPH

Analysis of flight research results continued through October 1988. An industry-wide review of those results was presented in November 1988.

2.4 SIGNIFICANCE OF THE PTA PROGRAM

The PTA Program accomplished all of its technical objectives. It demonstrated that advanced technology, high-speed propellers can be developed that will operate safely through the entire operating range of high-speed, subsonic commercial aircraft. It also provided near- and far-field noise data on a full-scale propfan that can be used to update predictions that earlier were based on small-scale wind tunnel tests.

Another accomplishment that may have greater long-range significance than either of the above, however, was the acquisition of a large amount of high quality noise data for which test parameters were systematically varied. The data analyses already performed have shown a good many areas where noise prediction methods are inadequate, and in some cases have pointed the way to needed improvements in analytical methods. It is expected that further analysis of this data base can be very beneficial in developing better noise prediction methods.

An example of new insight that has been gained is the recognition, on the basis of PTA data analysis, of the significance of inflow angularity on propeller noise; the prediction codes used did not adequately account for this variable. The PTA data not only provide insight for improvement of the codes, but also provide the systematic data base against which improved codes can be evaluated.

3.0 SYSTEM DESIGN

3.1 MAJOR COMPONENTS

3.1.1 Aircraft

The Gulfstream Aerospace Corporation GII aircraft, shown in Figure 5, is a high-performance, low-wing jet aircraft designed to seat a maximum of 19 passengers in a fully-pressurized cabin environment. It can cruise at Mach numbers up to 0.85 and has a range greater than 3000 NM. Ramp weight with full fuel and payload is 30,000 kg (66,000 lb).

The GII is powered by two Rolls Royce 511-8 Spey turbine engines mounted on the aft fuselage. Each engine develops 48,930N (11,400 lb) of thrust at static sea level standard day conditions.

Primary flight controls for the GII consist of hydraulically boosted elevators and ailerons and fully powered rudder and spoilers. The control column and pedals are directly connected to the primary control surfaces by means of conventional cables and pushrods providing manual reversion capability. The longitudinal control system consists of full-span conventional elevators with a sealed internal balance area ahead of the hinge line. Trim is accomplished with half-span irreversible trailing edge tabs. The entire stabilizer is movable with the incidence geared to the wing flaps to provide additional rotational moment during takeoff and landing. The lateral control system consists of outboard ailerons and midspan spoilers.

Secondary controls consist of a single-segment, double-slotted flap mounted on trailing edge flap tracks. A ground-operable spoiler is located inboard of the flight-operable spoiler on each wing.

3.1.2 Large-Scale Advanced Propfan (LAP)

3.1.2.1 General Description

The large-scale advanced propfan shown in Figure 6 is a 2.74m (9 ft) diameter, 8-bladed, tractor-type propeller rated for 4476 kw (6000 shp) at 1698 rpm. It is designed to be mounted on a standard 60A splined propeller shaft. The LAP has a hydraulically actuated blade pitch change system and a hydromechanical pitch control that allows the propfan to operate in a speed governing mode. The design of the actuator and control is based on proven technology used in Hamilton Standard's military and commercial propellers. A brief description of each of the major elements of the LAP as depicted in Figure 6 is presented below.

3.1.2.2 SR-7L Blade

Features of the structural configuration of the SR-7L blade are shown in Figure 7. These include a central aluminum spar which forms the structural "backbone" of the blade, a multi-layered, glass-cloth-reinforced shell overhanging the leading and trailing edge of the spar, a nickel

PRECEDING PAGE BLANK NOT FILMED

PAGE 12 INTENTIONALLY BLANK

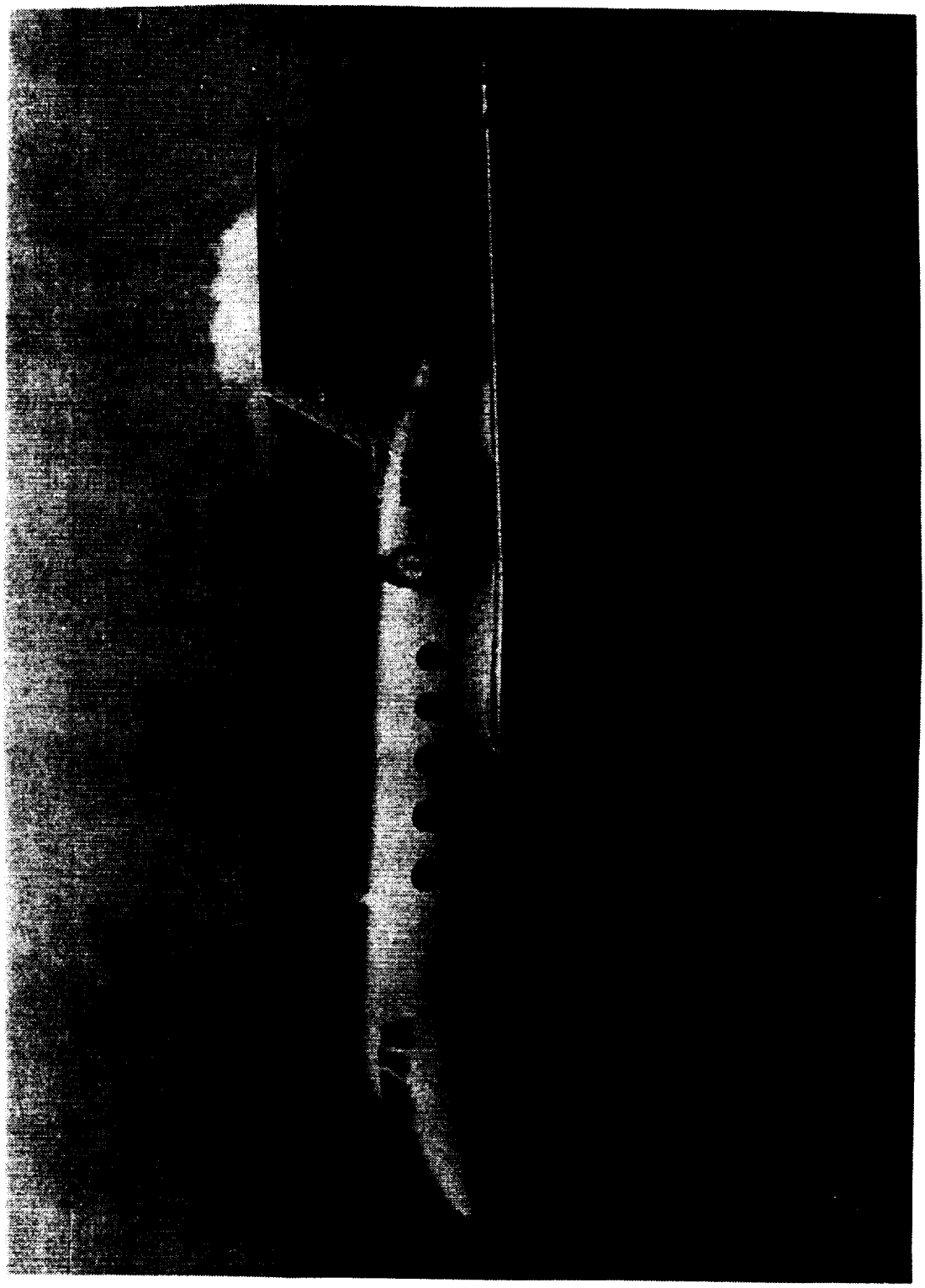


Figure 5. Gulfstream Aerospace GII Aircraft

ORIGINAL PAGE
BLACK AND WHITE PHOTOGRAPH

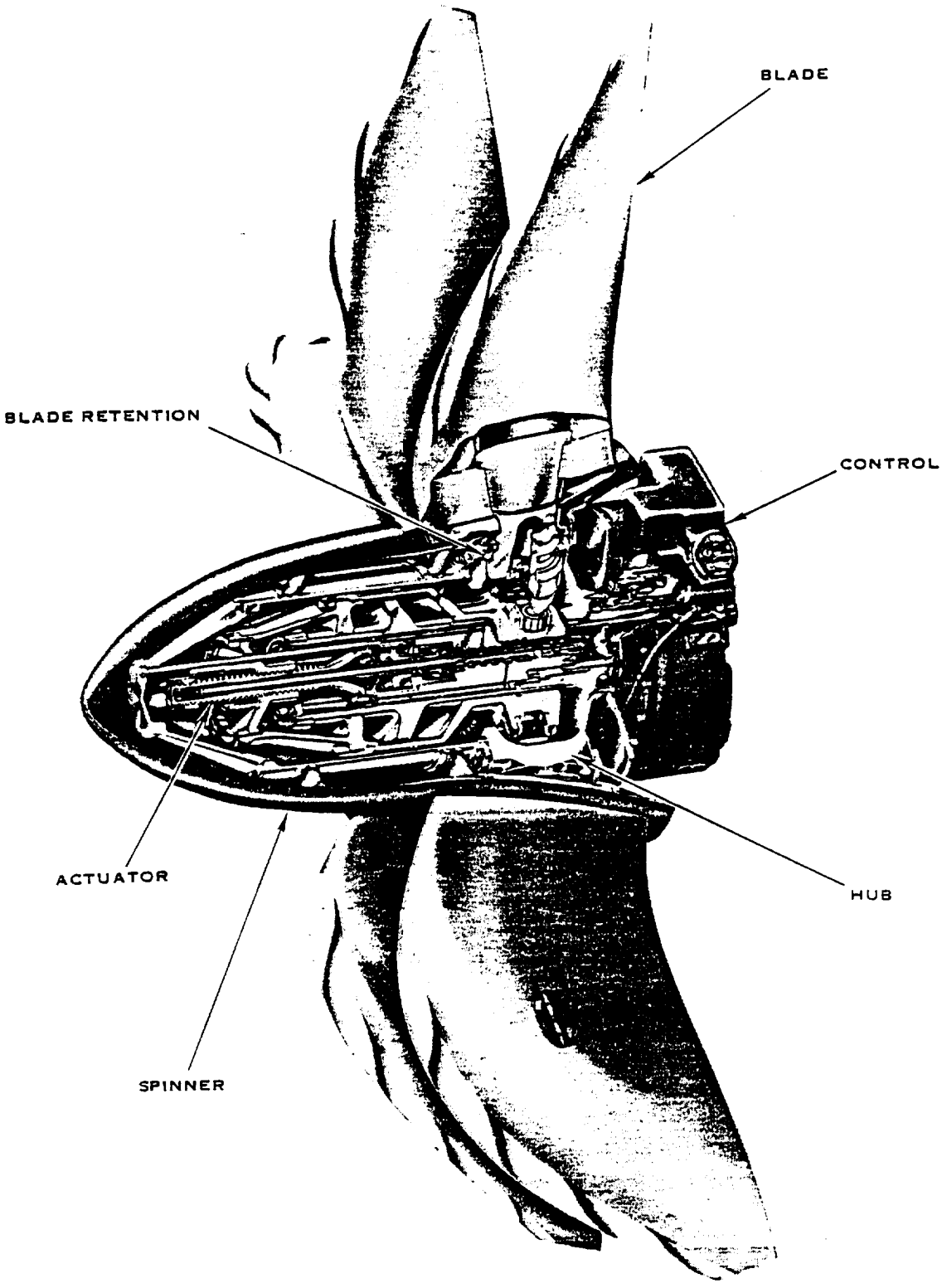


Figure 6. LAP Assembly

ORIGINAL PAGE
BLACK AND WHITE PHOTOGRAPH

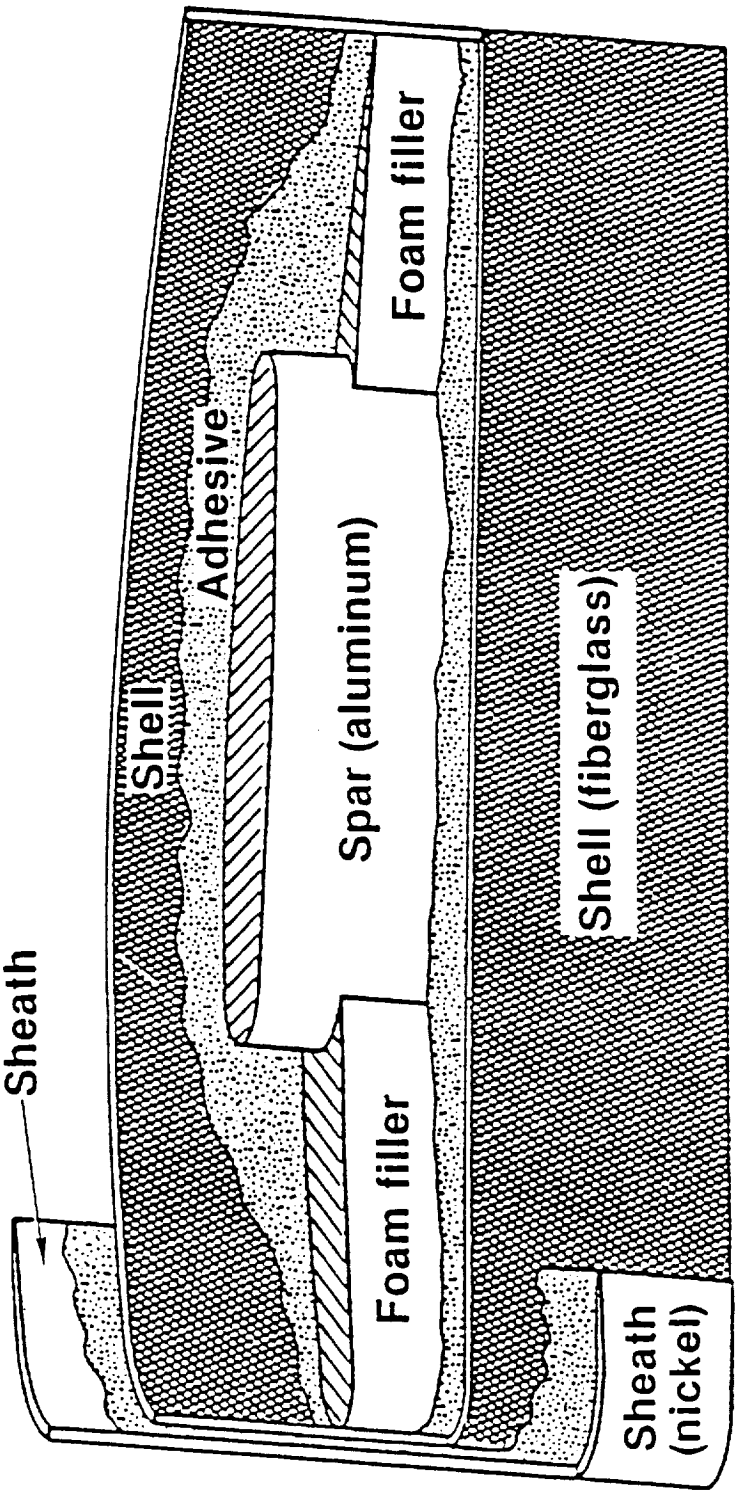


Figure 7. Features of the SR-7L Blade Construction

sheath which covers the leading edge of the outer two-thirds of the blade, and a nonoperational integral heater in the inboard leading edge area. Though the scope of the LAP testing never included utilization of the blade heaters, it was decided to install the heaters to evaluate the structural response of a blade closely resembling that of a typical blade configuration. The remaining internal cavities are filled with low-density rigid foam. The outboard portion of the spar is intentionally moved toward the blade leading edge to increase stability by reducing overhung mass in the tip trailing edge, while at the same time increasing the integrity of the leading edge from the standpoint of resistance to foreign object damage.

The blade design makes use of a NACA Series 16 airfoil outboard and a Series 65 circular arc airfoil inboard. Each blade has an activity factor of 227.3 with 45 degrees of leading edge sweep at the tip. The blades were designed with predeflection so that they assume the desired aerodynamic shape at the cruise operating condition.

Although some improvements in sweep/stress/stability trade-offs were predicted through the use of advanced composites, it was decided not to include these in the final blade design. Their use would require the development of new manufacturing technology, both in terms of suitable construction methods and processes, and lengthy development of design allowables to reflect the manufacturing process.

It was felt that the scope of the program would be best served by utilizing the service-proven combination of an aluminum spar enveloped with a fiberglass shell for which processes and stress allowables are well known.

3.1.2.3 Hub and Blade Retention

The LAP hub assembly forms a semi-rigid link between the blades, which provide the thrust, and the engine shaft, which provides the torque. The hub and tailshaft is a one-piece forged component which is carburized, heat treated, and machined. A single-row bearing retains each of the eight blades in the hub, while the tailshaft secures the propfan to the engine shaft through two cone seats that are preloaded against each other by the propfan retaining nut. The hub also forms the support for the pitch change actuator system, the control, and the spinner.

The retention transmits the loads from the blades to the hub while accommodating changes in blade pitch. The single-row ball bearing retention provides ease of maintenance by allowing individual blade replacement without disassembly of the hub. It has a through-hardened inner race which seats against the aluminum blade shank and an outer race which is integral with the barrel. The outer race is carburized to achieve the hardness necessary to support the ball loads. The balls are kept apart from each other by an elastomeric separator. The rotational speed of the propfan keeps the retention submerged in oil which is contained in the hub by eight blade seals.

3.1.2.4 Pitch Change

The pitch change system is comprised of two components, a pitch change actuator and a control. The pitch change actuator is the prime mover for blade angle change and is located with the propfan hub as shown in Figure 6. The pitch change control, which generates and regulates the system hydraulic pressures for the pitch change actuator, is a modified version of an existing turboprop integral oil control and is mounted on the hub tailshaft, also as shown in Figure 6.

Pitch Change Actuator - The hub-mounted pitch change actuator assembly consists of an internal stationary piston, a translating outer cylinder with an integral yoke to engage the blade trunnions, and a pitchlock and servo assembly. The pitchlock and servo assembly meters the main hydraulic pressure, upon command from the pitch control, to produce increase-pitch or decrease-pitch pressure for the actuator. The pitch change mechanism was designed such that all malfunctions will either cause the system to pitchlock or go to feather. An additional safety feature on the LAP is a ground adjustable low pitch stop. This limits the minimum blade angle under all circumstances.

The actuator was designed to present state-of-the-art technology and low development risk technique that have been used on a number of existing propeller systems. The design uses mostly steel for the load carrying members, and all surfaces subject to sliding seal wear are chrome plated to increase durability. The actuator was designed to conservative stress and deflection levels to minimize development effort while maintaining a reasonable but not minimum weight.

Pitch Change Control - The control for the LAP, as illustrated in Figure 8, is a modified 54H60 Integral Oil Control unit. The 54H60 is a hydromechanical control in use on the Lockheed C-130 and P-3 aircraft. Since the first production unit was placed in service in 1956, there have been over 11,000 built, and they have logged over 73 million hours. The 54H60 is very similar to the 54460 unit presently in service on the Grumman E-2/C-2 aircraft. It provides the constant speed governing function and the capability to either manually or electrically feather the propeller. Because of physical restraints on the installation, no beta, i.e., direct blade angle, control is provided. An engine-supplied overspeed electrical signal is available in the event of a malfunction of the on speed governor. The control utilizes this signal through the feather solenoid to cause the blade angle to increase until the propeller speed is at the overspeed setting and modulates there.

The primary functions of the blade pitch control are to generate the hydraulic pressure for the actuator and establish the increase or decrease pitch hydraulic pressure signal transmitted to the pitchlock and servo assembly. Hydraulic pressure is produced by two pumps contained in the stationary control and driven by the propeller shaft. A pump, driven by an auxiliary electric motor, provides hydraulic pressure for blade angle change when the propfan is not rotating. The increase/decrease pitch hydraulic signal is produced by a flyweight governor and a governor valve, which senses changes in rotational speed and sets the hydraulic pressure

ORIGINAL PAGE IS
OF POOR QUALITY

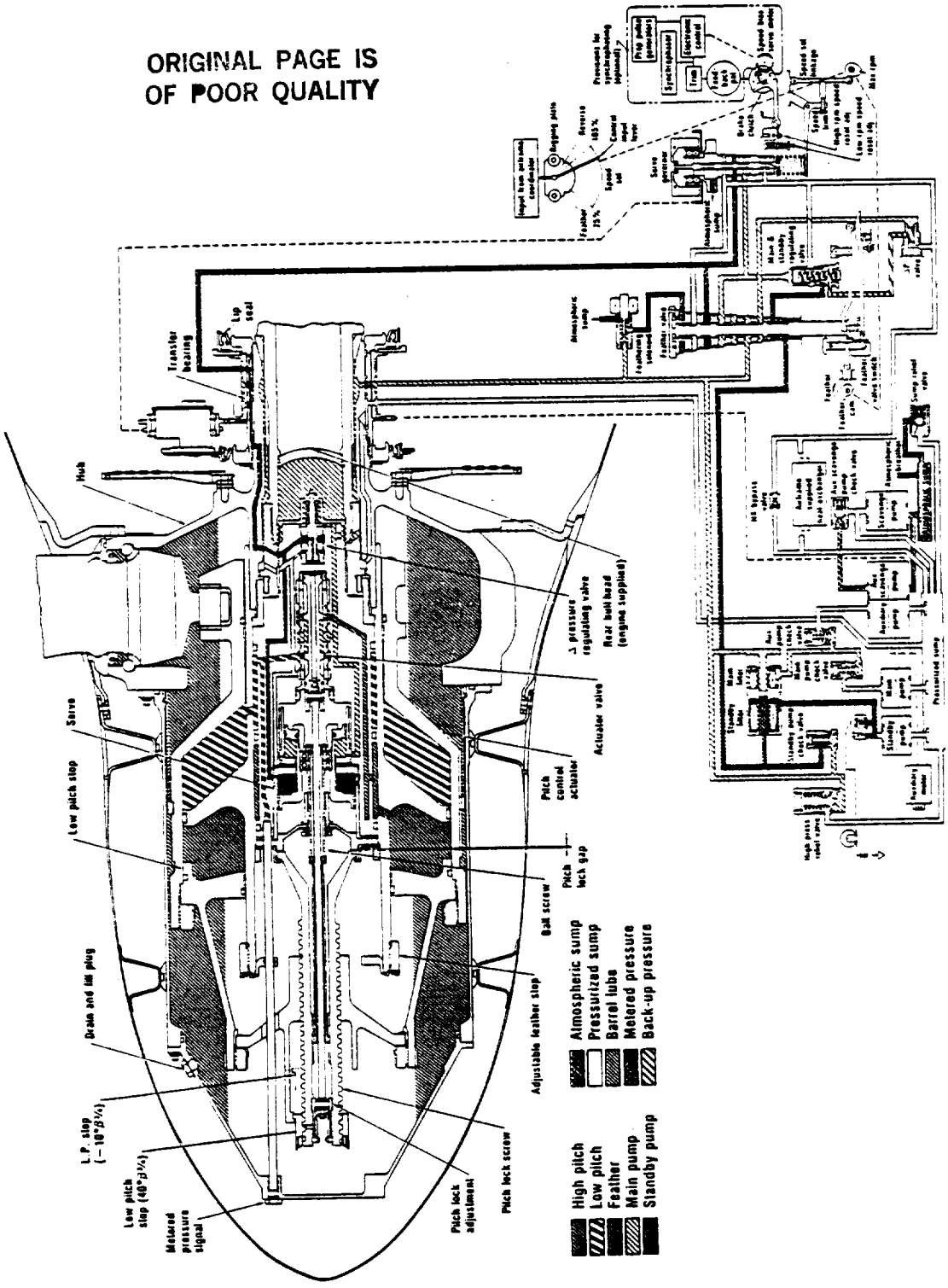


Figure 8. LAP Control Schematic

signal accordingly to reestablish the set point speed. This results in a blade pitch angle rate of change that is proportional to the difference between the actual rpm and the set point rpm.

The control has a single mechanical input positioned by an electro-mechanical actuator mounted on the Allison gearbox. This input signal will set the governing speed, feather the propeller, and reset the governor for reverse. The reverse blade angle is set by the pitch change mechanism. The output of the control is metered pressure to a half area servo piston in the pitch change mechanism. The control also includes an electrical feather override which will feather the propeller upon command or in the event of overspeed, regardless of the position of the mechanical pitch control input. Increasing metered pressure will cause the propeller to decrease pitch. Decreasing pressure will cause the propeller to increase pitch. Feather is accomplished by dumping metered pressure to drain.

3.1.2.5 Spinner

The LAP spinner and rear bulkhead assembly is essentially a reinforced fiberglass/epoxy shell, supported by the hub and actuator, and incorporating an aerodynamic shape to facilitate proper airflow around the blade roots. Its primary function is to insure proper propfan aerodynamic performance. The rear bulkhead, which mounts on the rear of the hub arms, is the main structural support for the spinner and provides a mounting surface for much of the instrumentation hardware in the rotating field.

3.1.3 Propfan Drive System

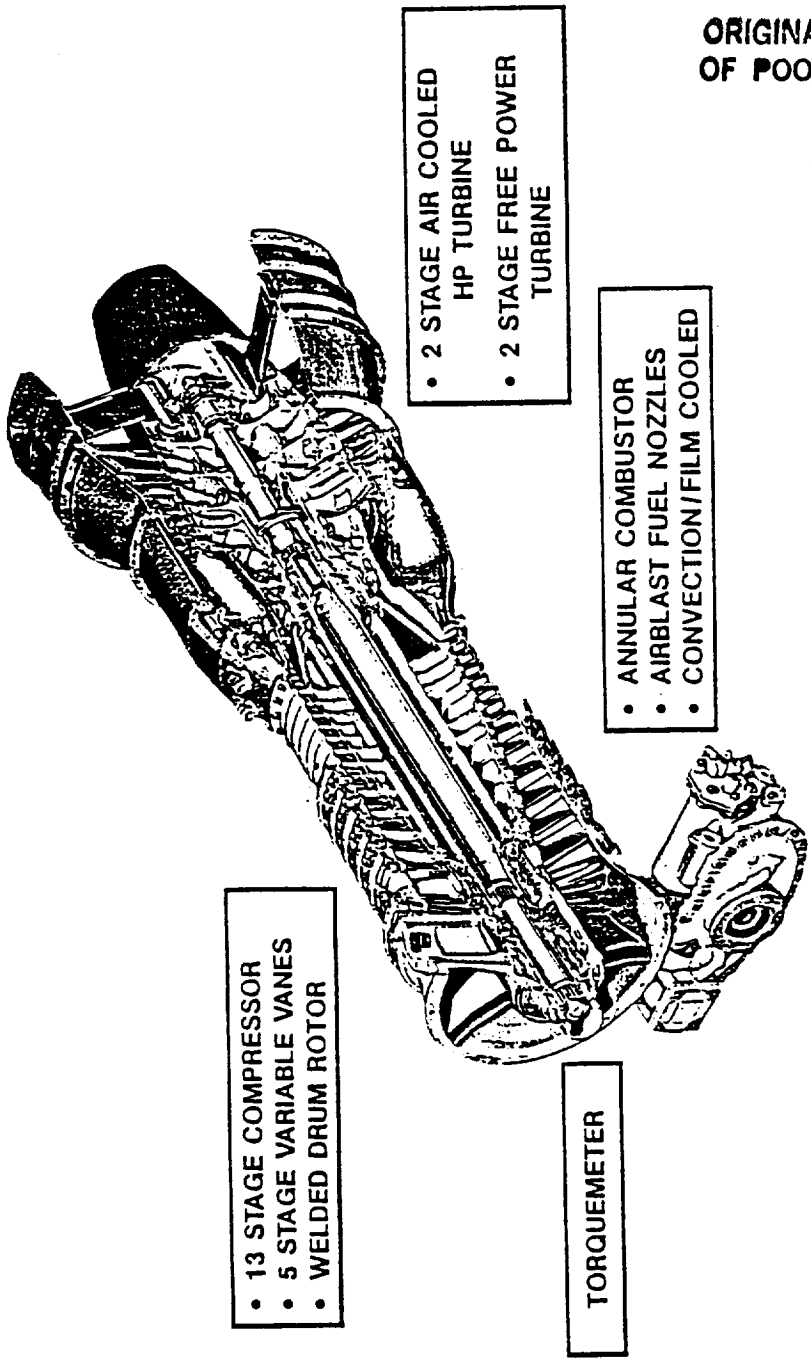
3.1.3.1 M570 Engine

The propfan drive system comprised the engine and gearbox and the connecting torquemeter. The engine selected was the Allison Model 570, 6000 hp class industrial engine. This engine, however, had an aircraft background since it derived from the Model XT701 engine developed for the U.S. Army Heavy Lift Helicopter program. To convert from the XT701 to the 570 models, provisions for compressor bleed were eliminated, and the titanium compressor case was replaced with one of steel. The Model 570 power section is shown in Figure 9.

The compressor of the M570 engine is a 13-stage axial flow assembly with variable inlet guide vanes and 5 stages of variable stator vanes. The compressor variable geometry (CVG) system is used to position the vanes at their optimum angle at any operating condition. In addition to preventing stall during start-ups, this system allows the compressor to operate at high efficiency even at part load conditions.

The diffuser/combustor assembly incorporates a triple-pass diffuser and annular combustor. The combustor contains 16 airblast fuel nozzles and 4 spark igniters which are turned off after combustion occurs.

The power section consists of a two-stage gas generator turbine and a two-stage power turbine. The turbine case is designed to contain any single



ORIGINAL PAGE IS
OF POOR QUALITY

Figure 9. Model 570 Engine Features

turbine blade failure. To further minimize damage in the event of overspeed conditions, the failure order is as follows: turbine blades, wheel lugs, and finally wheels. If a blade failure occurs, the rotor will no longer accelerate and the risk of wheel failure is low.

All of the engine accessories are driven by the accessory gearbox that is mounted on the bottom of the air inlet housing. These accessories include the oil pump, centrifugal breather, and fuel pump. The accessory gearbox also serves as the gearbox through which the engine starter drives.

3.1.3.2 Reduction Gearbox

The reduction gearbox for the PTA drive system was adapted from the Allison T56-A-14 gearbox that was used on the Lockheed P-3 Orion. This gearbox had two stages of reduction gearing and an overall gear ratio of 13.54:1. This produced an output shaft speed of 1020 rpm, whereas propfan rotational speed of the order of 1700 rpm was needed for the PTA application. For the PTA gearbox, the first stage gears were changed to produce an overall gear ratio of 6.8:1.

The direction of rotation of the output shaft on the M570 engine was opposite that of the T56 engines and with the T56 gearbox would produce counterclockwise looking forward rotation of the propshaft. This together with the desire to have the propfan rotate upwards on the inboard side of the propfan installation established the location of the PTA propfan on the left hand wing. This combination of engine and gearbox, however, caused the gearbox accessory drive to rotate in the wrong direction, so it was necessary to install a reversing idler gear in that drive train.

Altogether, it was determined that the following changes to the T56 gearbox were needed to make it suitable for the PTA application.

- New pinion gear
- New main drive gear
- New pressure pump assemblies
- Modified prop brake
- Accessory drive reversing idler gear
- Reworked front and rear housing
- Redirected oil supply to the pinion and sun gear teeth

These were all considered feasible and well within the scope of the PTA schedule constraints.

3.1.3.3 Torquemeter

There was no torquemeter that could be modified for the PTA application because the distance between engine and gearbox was different from that on other T56 engine/gearbox combinations. The design for the PTA, however, was similar in all major respects to that of the T56-A-14 configuration except for minor dimension changes.

As shown in Figure 10, the torquemeter assembly consisted of a housing for the torquemeter that also serves as one of the structural members of the engine/gearbox assembly. The torquemeter shaft consisted of two concentric shafts--the inner being a solid shaft that transmits torque to the gearbox. The outer shaft was keyed to the inner at the aft end and provided then a reference by which torsional deflection of the inner shaft could be measured by a magnetic pickup.

3.2 AIRCRAFT MODIFICATION

A photograph of the PTA aircraft after modifications were completed was shown in Figure 2, and the modifications are highlighted in Figure 11. The major modification, of course, was the installation of the propfan drive system, and a major feature of the drive system design was the ability to vary the tilt angle of the propfan centerline. As will be discussed in Section 3.2.3, Nacelle Design, this tilt angle variation was needed to provide the required range of propfan blade dynamic loading.

The propfan propulsion system was mounted on the left wing of the aircraft with the thrust line at BL 4.191m (165.0 in.). This necessitated deactivation of the inboard wing spoiler panels. The left wing was strengthened to accommodate the weight and overhung moment of the propfan propulsion system, and a dynamic balance boom was located at the left wing tip to assure adequate flutter margin. The left flap in the wake region of the propfan was strengthened to avoid sonic fatigue.

A microphone boom was installed on the left wing at a distance outboard of the propfan centerline equal to the distance between the propfan centerline and the nearest fuselage surface. The microphones on this boom recorded essentially free-field noise data. On the right hand wing tip, a static balance boom was located for lateral balance. This required that the right hand wing also be strengthened to withstand taxi and gust loads.

Instrumentation was installed as indicated in Figure 12 to measure over 600 parameters plus propfan operational data. The fuselage cabin interior trim and furnishings were removed aft of the cockpit, and data systems were installed for acquisition and monitoring of data by test personnel at consoles in the front and rear of the cabin as shown in Figure 13.

3.2.1 Wing Modification

3.2.1.1 Left Wing

The modification of the GII left wing assembly is illustrated in Figure 14. An existing streamwise rib at BL 368.3 cm (145.0 in.) was strengthened to withstand loads transmitted through the inboard side of the aft nacelle and a new rib was installed at BL 469.9 cm (185.0 in.) to react the nacelle loads transmitted through the outboard side of the aft nacelle. The nacelle was then secured to the upper and lower surfaces of the wing through dual-element skate angles which may be seen in Figure 15.

A 0.318 cm (0.125 in.) thick external reinforcing doubler was installed on the wing front beam, and a 0.254 cm (0.100 in.) thick aluminum doubler was

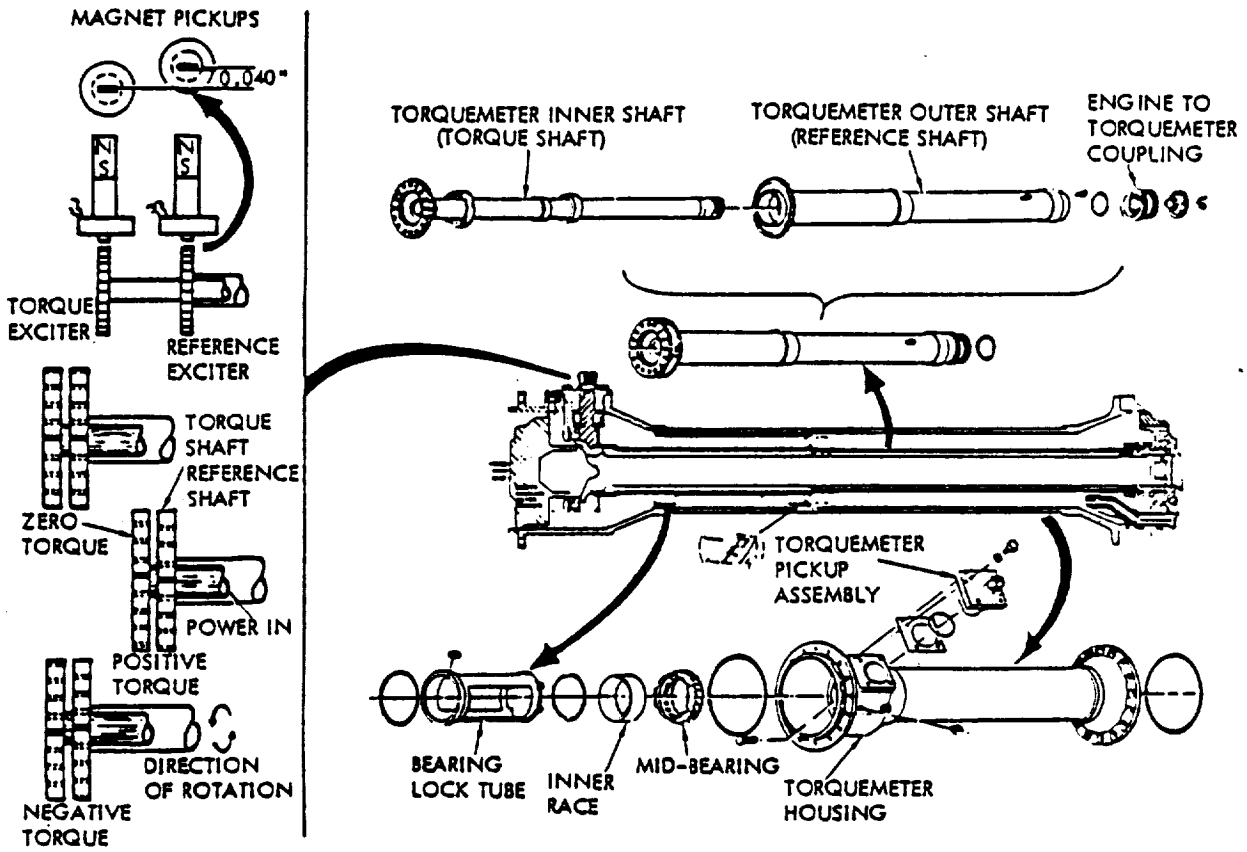


Figure 10. Torquemeter Assembly

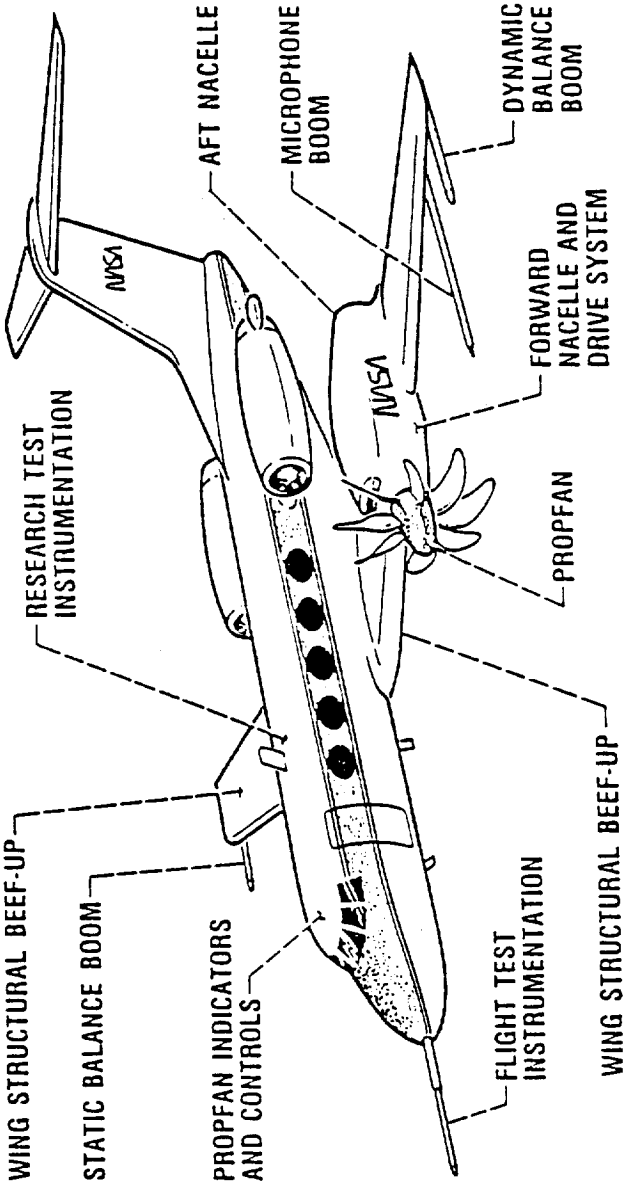


Figure 11. PTA Aircraft Modifications

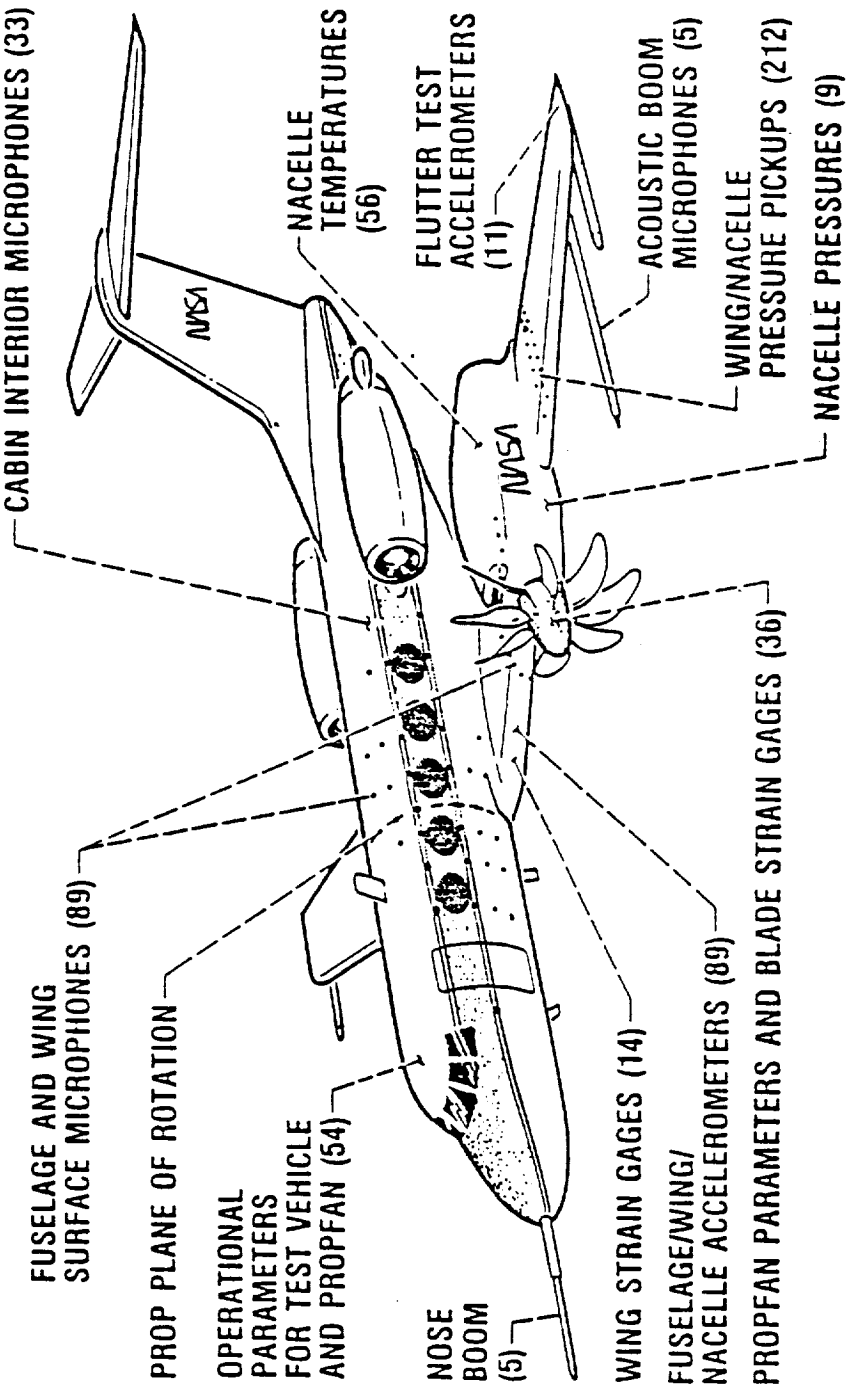


Figure 12. Research Instrumentation

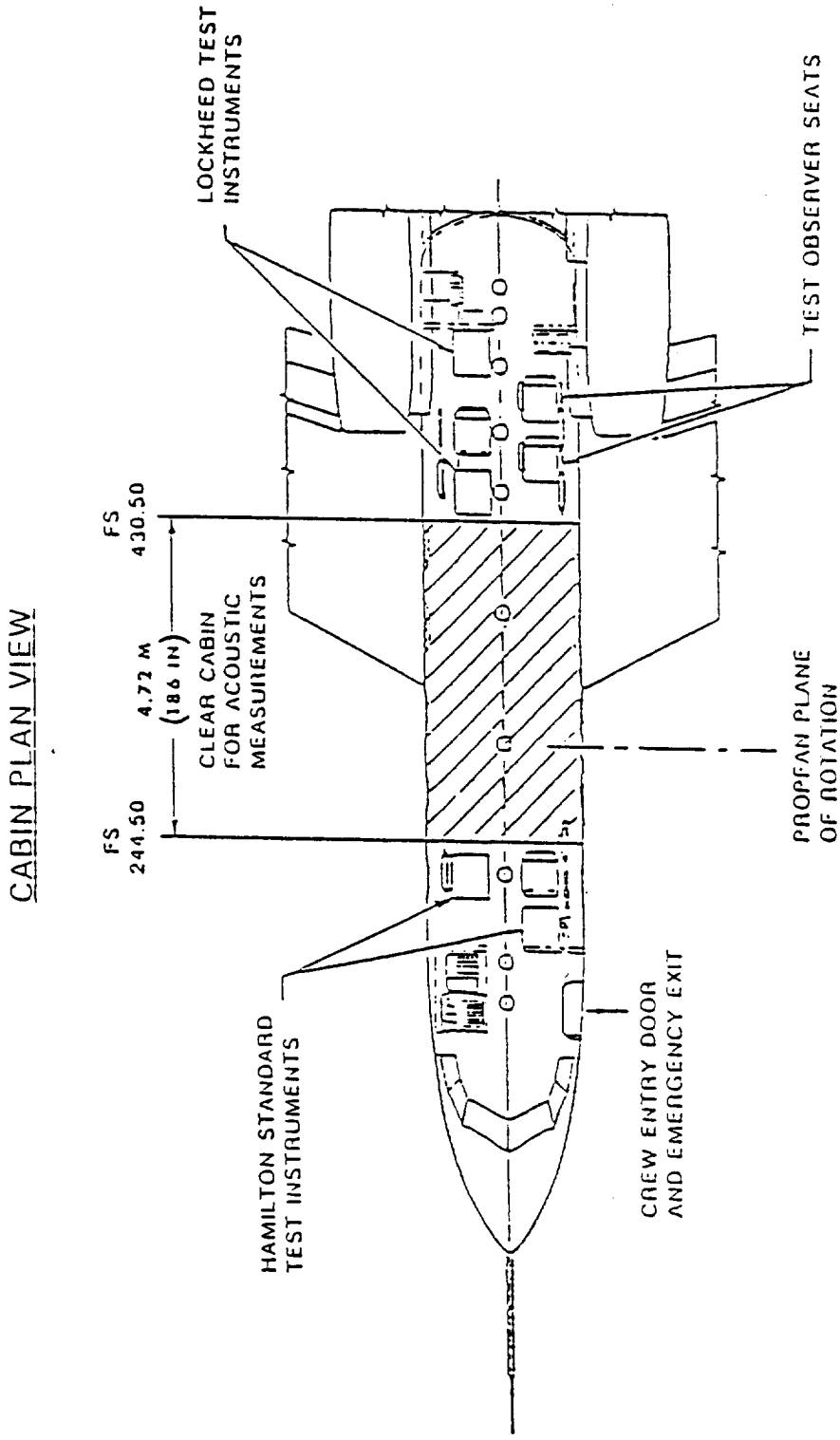


Figure 13. On-Board Data System Installation

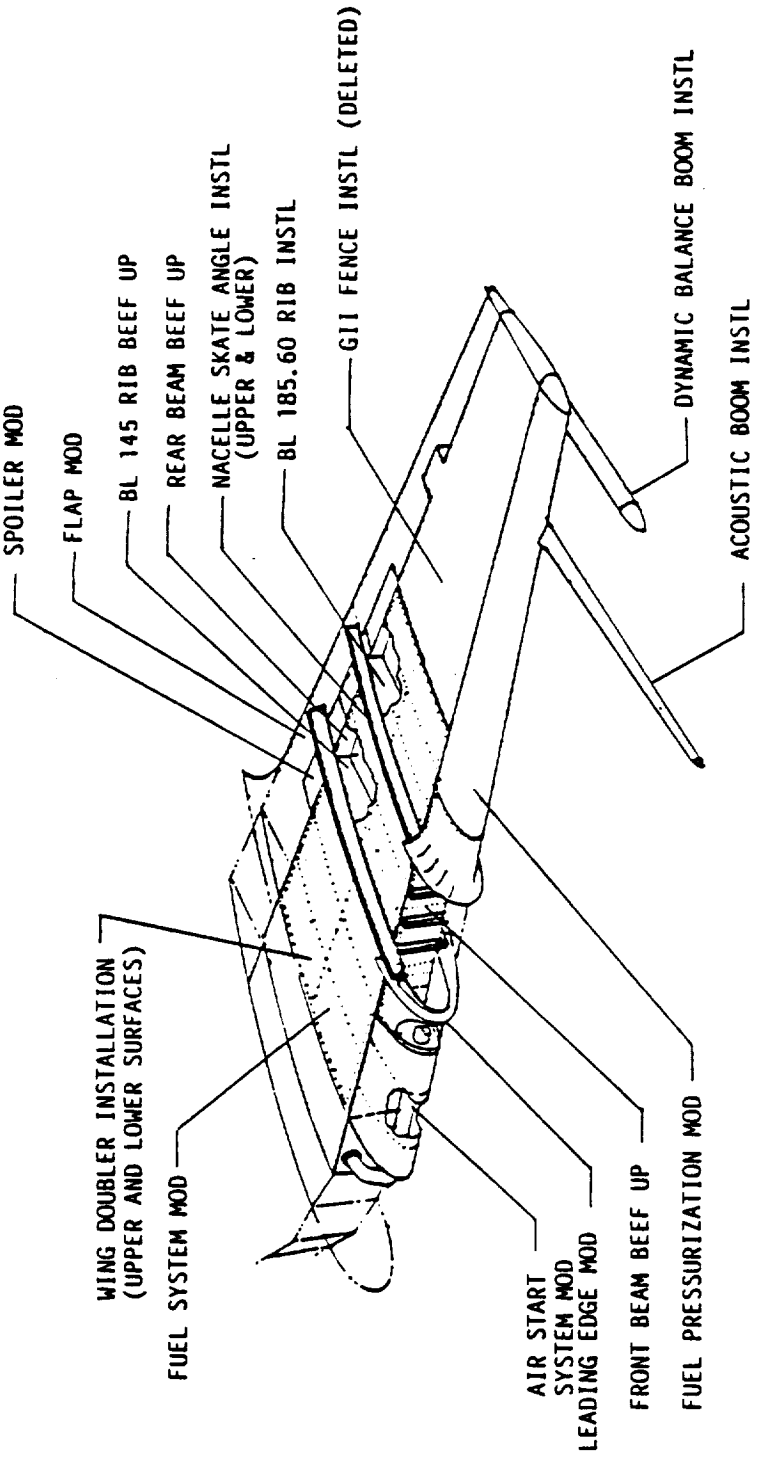


Figure 14. Left Wing Modifications

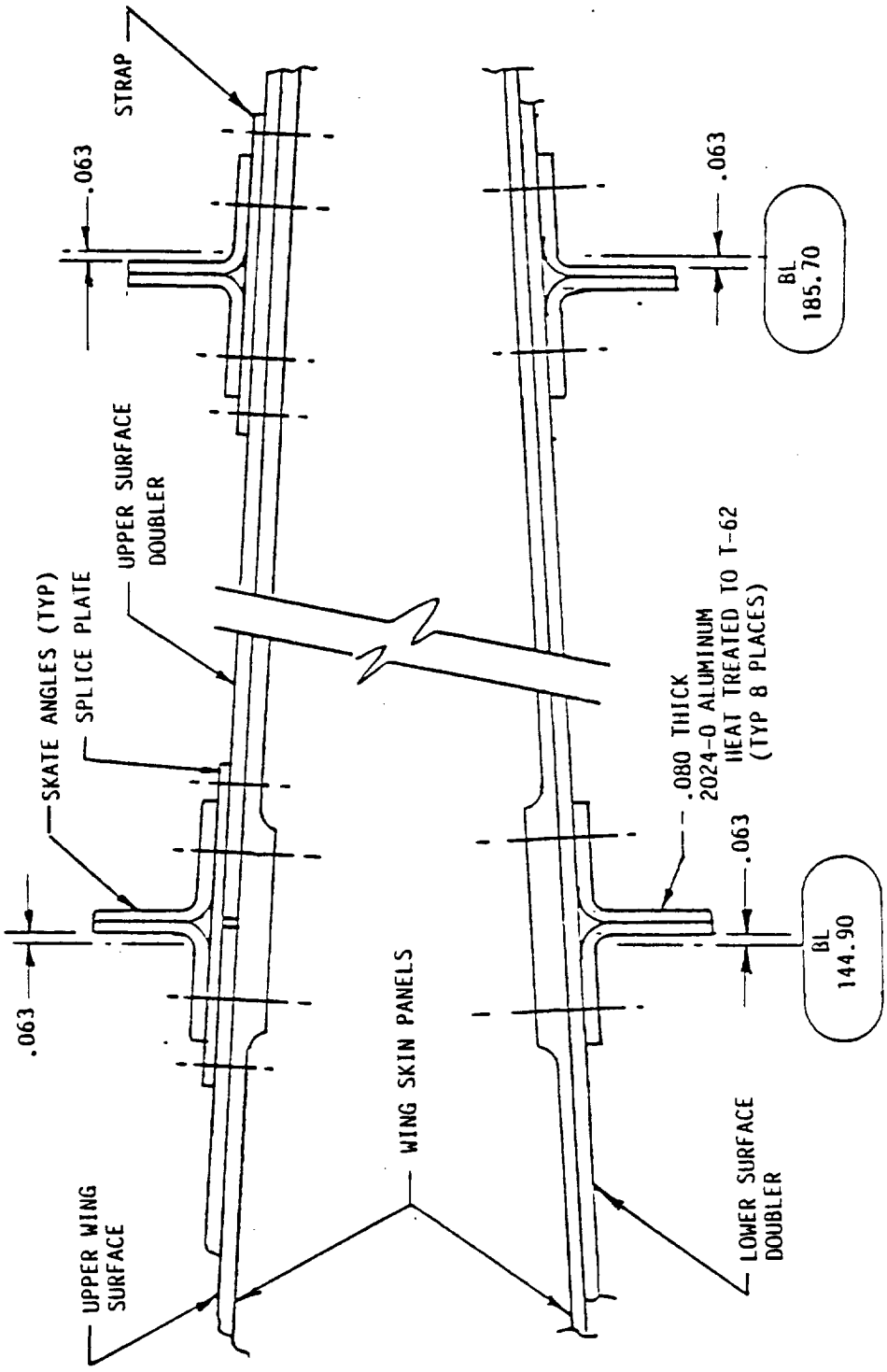


Figure 15. Skate Angles on GII Wing

installed on the internal surface of the rear beam with aluminum nacelle tie-in fittings.

The leading edge of the wing was modified as shown in Figure 16. New splice ribs and leading edge assemblies accommodated the intersection with the propfan nacelle. Tapered fiberglass fairings were added on the wing surface to provide a smooth fairing to the 0.229 cm (0.090 in.) skin doublers.

The acoustic boom, depicted in Figure 17, was installed on the left wing at BL 12.293m (283.965 in.) and was constructed primarily of carbon reinforced epoxy material. The boom tapered from 18.8 cm (7.4 in.) diameter at the wing front beam to 2.9 cm (1.4 in.) diameter at the tip. The purpose of the boom was to position a row of five microphones outboard of the propfan diametrically opposite a similar row on the fuselage and thus allow investigation of the acoustic impact of upward versus downward propeller motion in the wing/nacelle flow field.

The dynamic balance boom on the left wing tip was supported from existing GII wing tank support fittings. It contained a lead plug which could be positioned to accurately control the location of the boom center of gravity. A steel nose, wooden tail fairing, and fiberglass boom-to-wing fairing completed the assembly.

A new flap was provided for the left wing. It was externally identical to the original GII flap but had thickened skins and an increased number of internal ribs to withstand sonic fatigue in the propfan wake. The wing fixed trailing edge behind the rear beam was also stiffened to withstand sonic fatigue by doubling the skin gage and adding stiffeners.

The propfan aft nacelle overlapped the two inboard wing spoilers, as shown in Figure 18. These two spoiler panels were deactivated by deletion of the actuation linkage and addition of a fixed link to hold them in the faired position. This eliminated the use of ground spoilers for lift-dumping and reduced the spoiler contribution to roll control.

3.2.1.2 Right Wing

As depicted in Figure 19, the modifications to the right wing included installation of a 136 kg (300 lb) static balance boom at the wing tip. This boom also contained a lead plug which could be positioned to control the center of gravity. The tip boom assembly weighed 969 kg (2137 lb). The G-II wing was not designed to take landing loads with this type weight, so it was necessary to add skin doubler to strengthen the right wing also.

3.2.2 Fuselage Modifications

3.2.2.1 Cabin

The fuselage modifications are depicted in Figure 20. All passenger cabin furnishings and interior trim were removed, and the flight station was modified to accommodate the propfan controls and instrumentation.

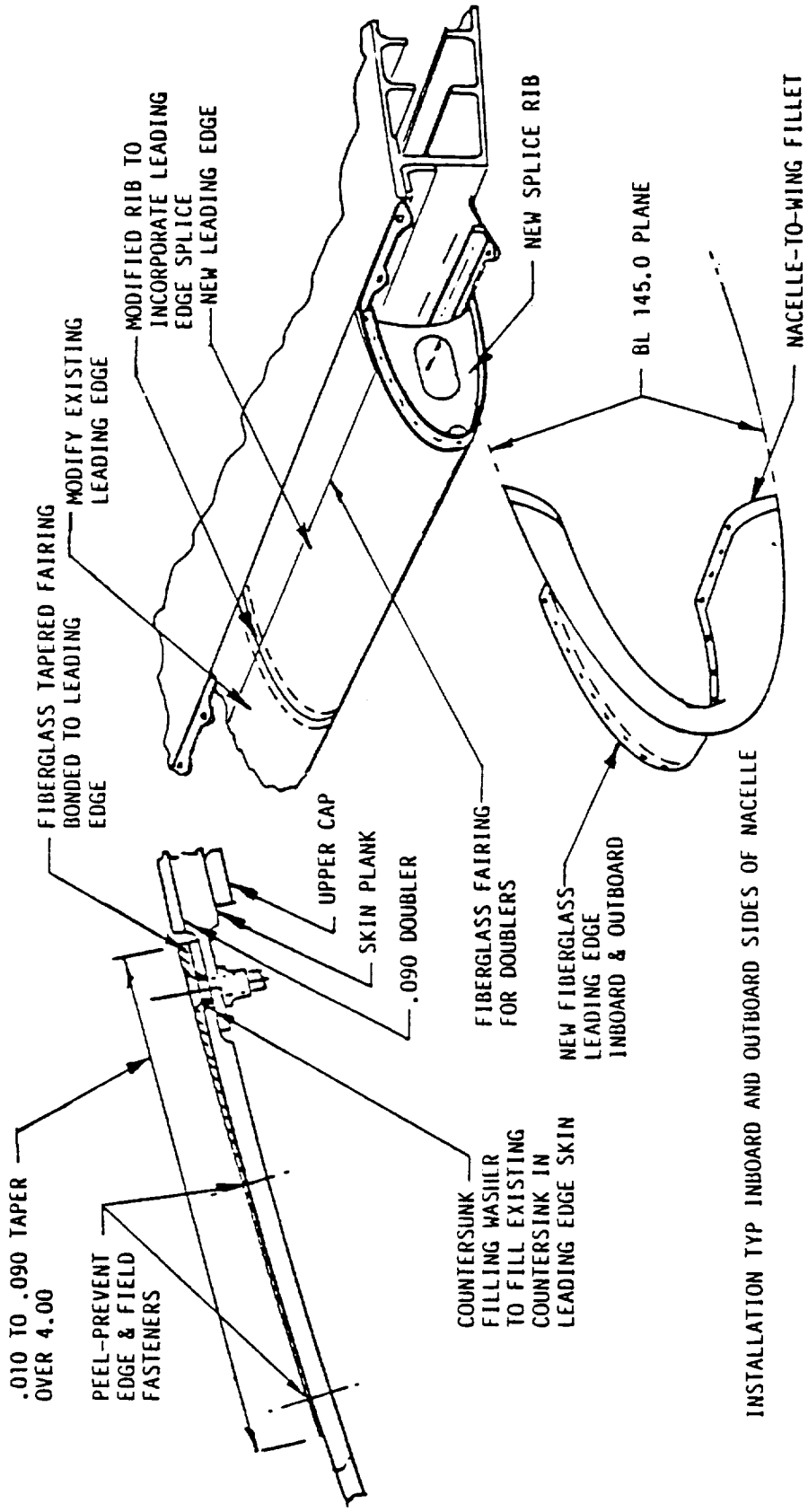


Figure 16. Wing Leading Edge Modifications

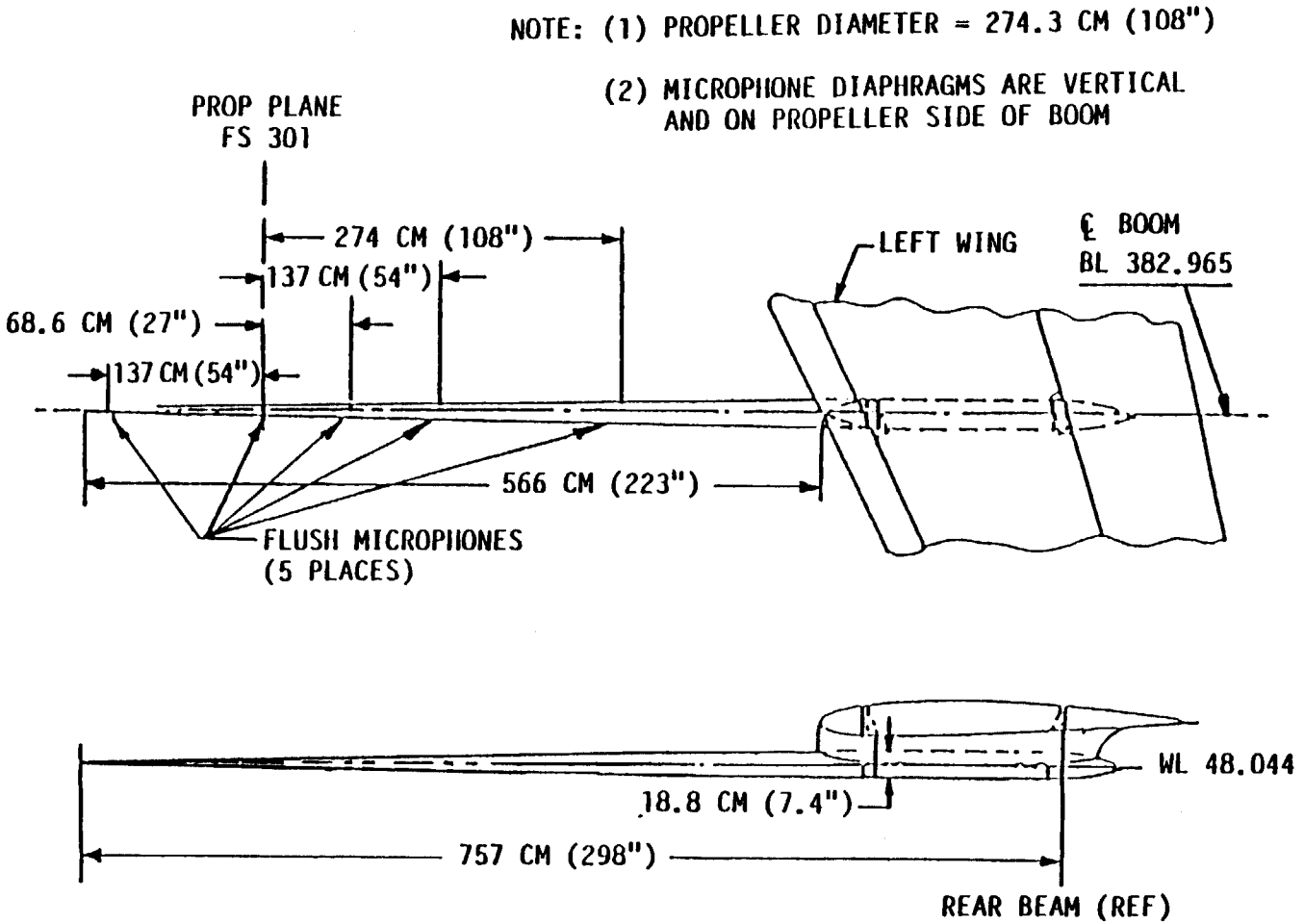
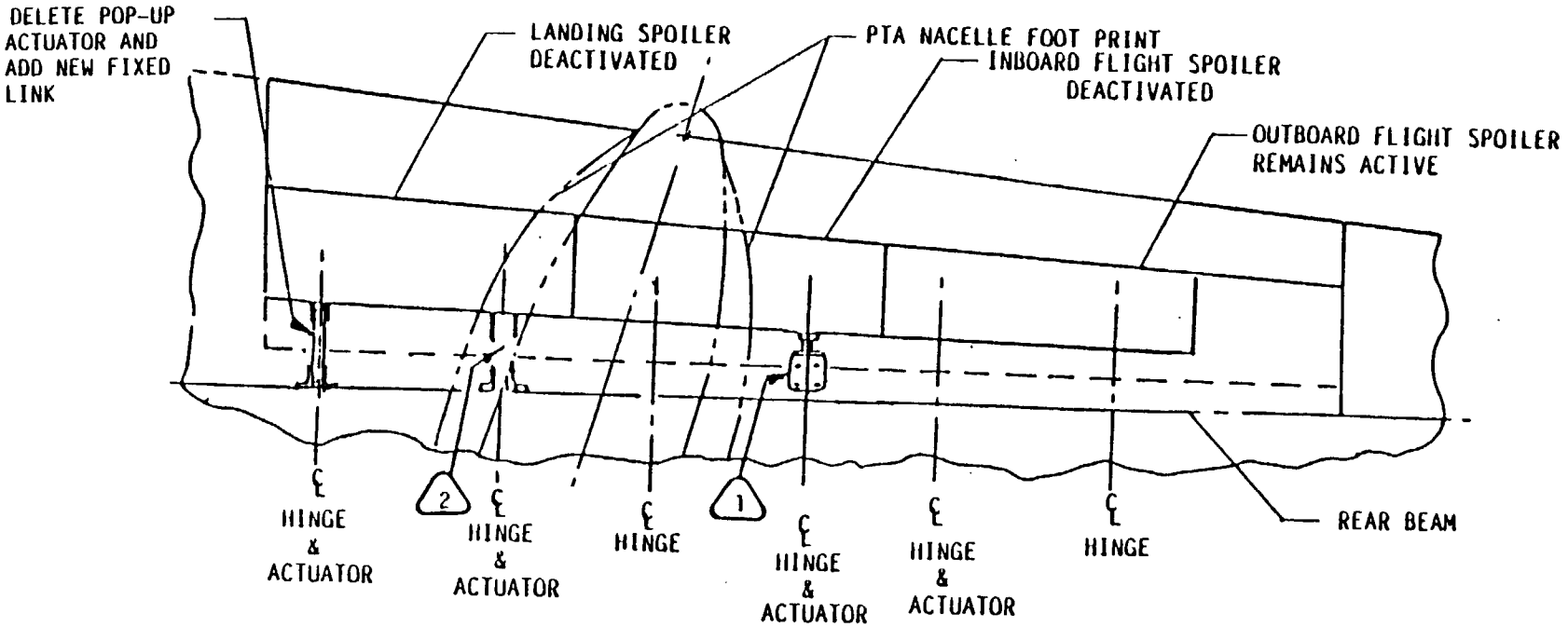


Figure 17. Acoustic Boom Installation



(1) DELETE ACTUATION ROD BETWEN SPOILER AND DEPLOYMENT MECHANISM. ADD NEW SPOILER LOCK FITTING BETWEEN SPOILER ACTUATION LUG AND FLAP SUPPORT FITTING

(2) DELETE ACTUATION ROD BETWEEN SPOILER AND DEPLOYMENT MECHANISM, INBOARD FLAP WILL BE RETAINED BY POP-UP ACTUATOR REPLACING FIXED LINK. NOTE: GII INBOARD FLAP WAS RETAINED AND ACTUATED AT INBOARD LOCATION PRIOR TO INCORPORATION OF POP-UP ACTUATOR

Figure 18. Spoiler Modification

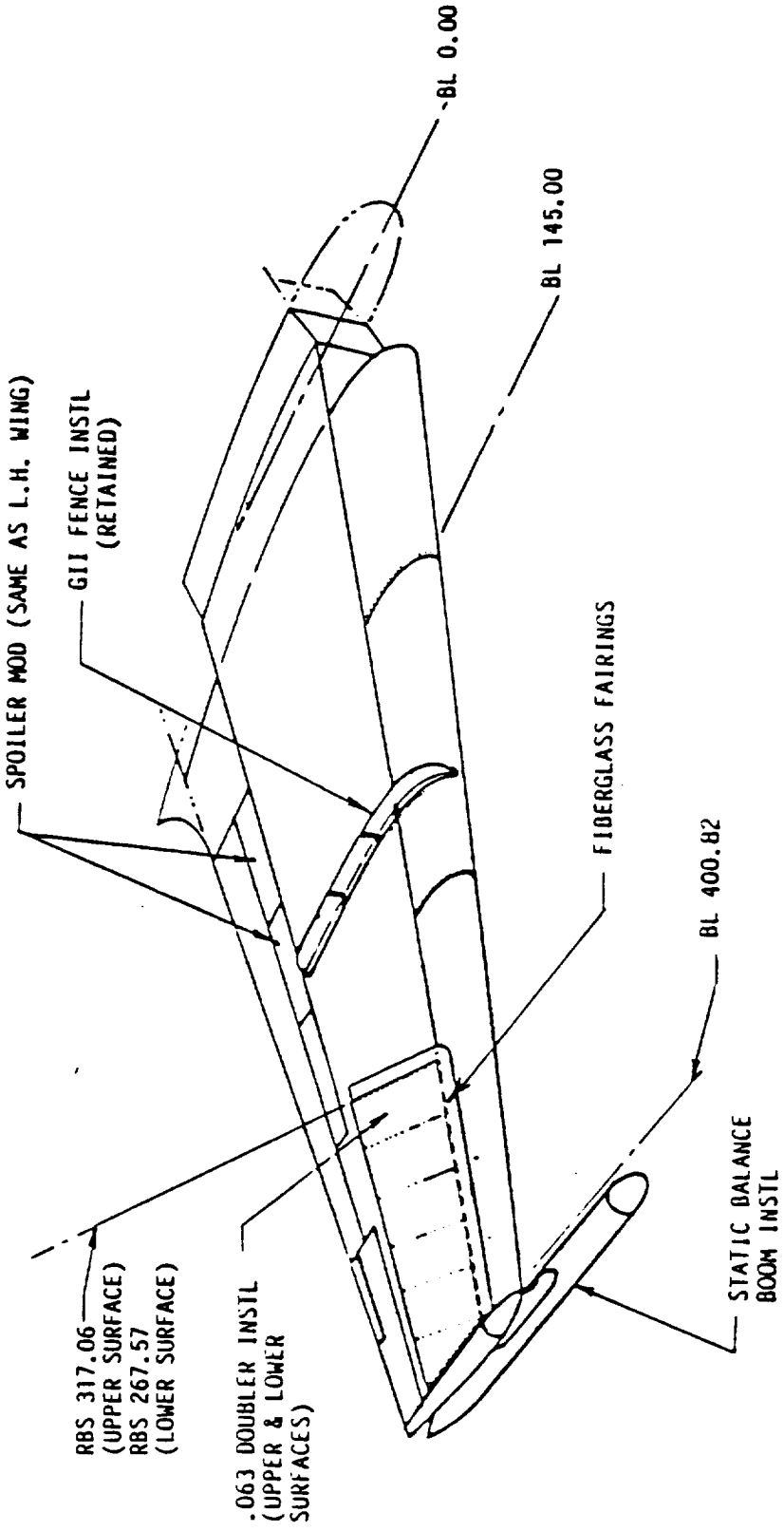


Figure 19. Right Wing Modifications

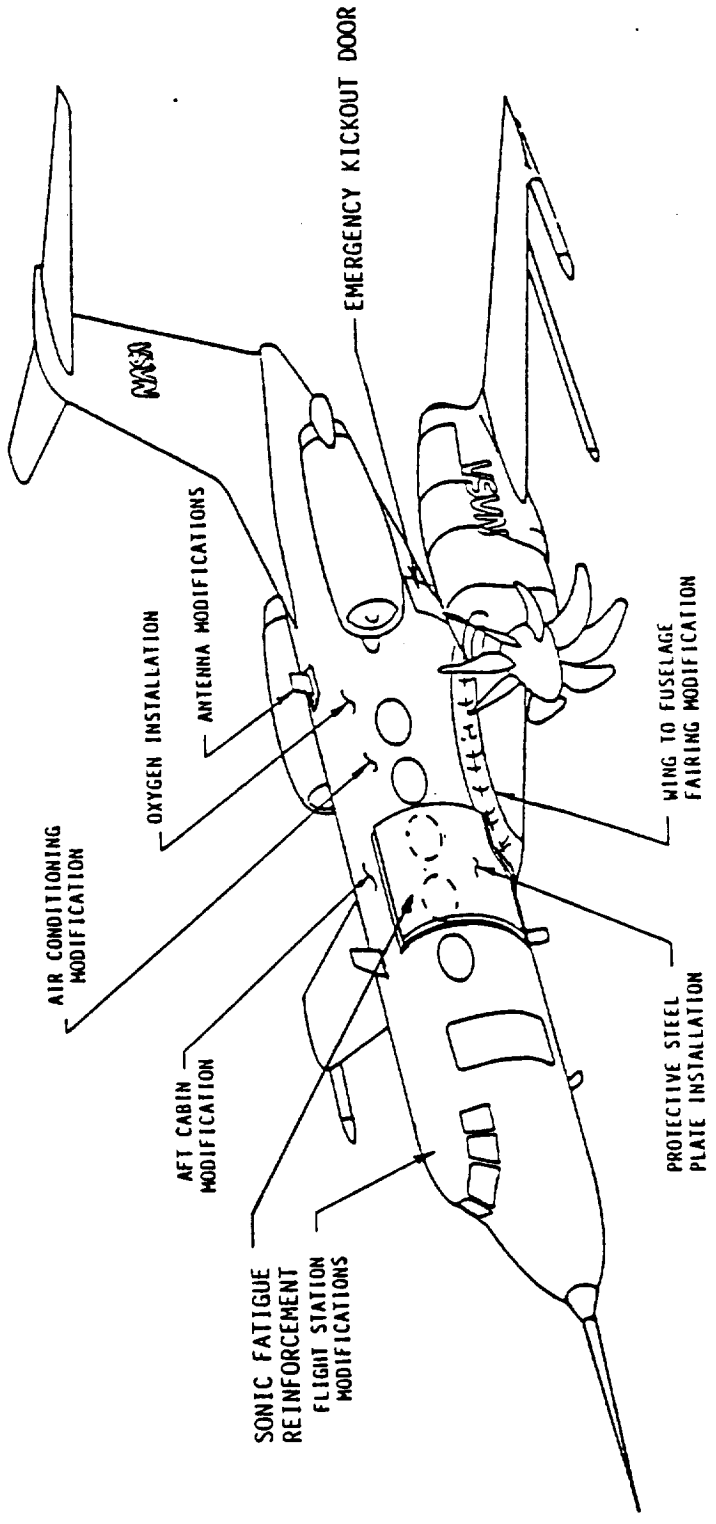


Figure 20. Fuselage Modifications

Antennae were added for the data telemetry system. The wing-to-fuselage fairing was modified to accommodate the wing surface doublers, and stiffeners were added to the fuselage skin in the vicinity of the propfan to increase resistance to sonic fatigue.

Floor panels over the wing were replaced with aluminum panels which provided penetrations for routing of instrumentation, electrical wiring, and tubing from the pressurized cabin to the wing/propfan system. The baggage compartment door was replaced with one designed to open even with a pressurized fuselage to provide an emergency escape for the flight crew.

A steel plate for fuselage protection in the event of blade loss was installed when the propfan was first operated to search for evidence of classical blade flutter. The 306 kg (675 lb) plate was designed to withstand the impact of a complete propfan blade without failure or penetration of the fuselage structure. It was removed following successful completion of the airworthiness portion of the test program.

3.2.2.2 Flight Station

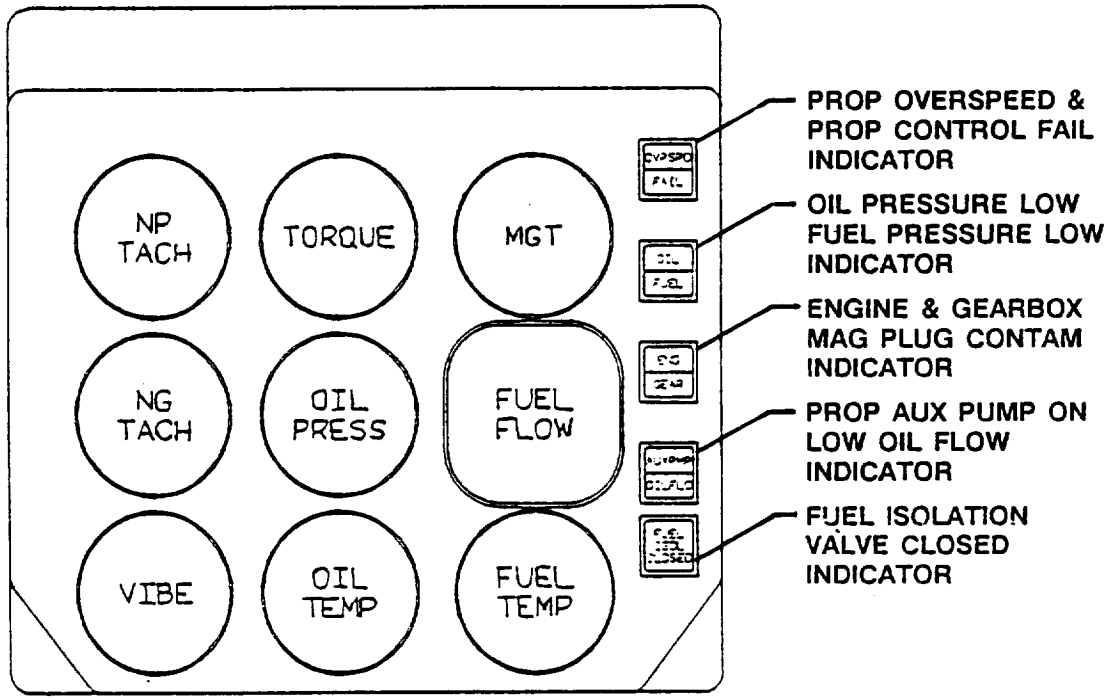
The flight station was modified by removal of the weather radar and installation of propfan controls and instrumentation plus a modified intercom system which accommodated all of the test crew.

In Figure 21, the drive system instruments are seen in a 3 x 3 cluster in the center of the panel, where both pilots and the flight engineer could read them. These instruments included:

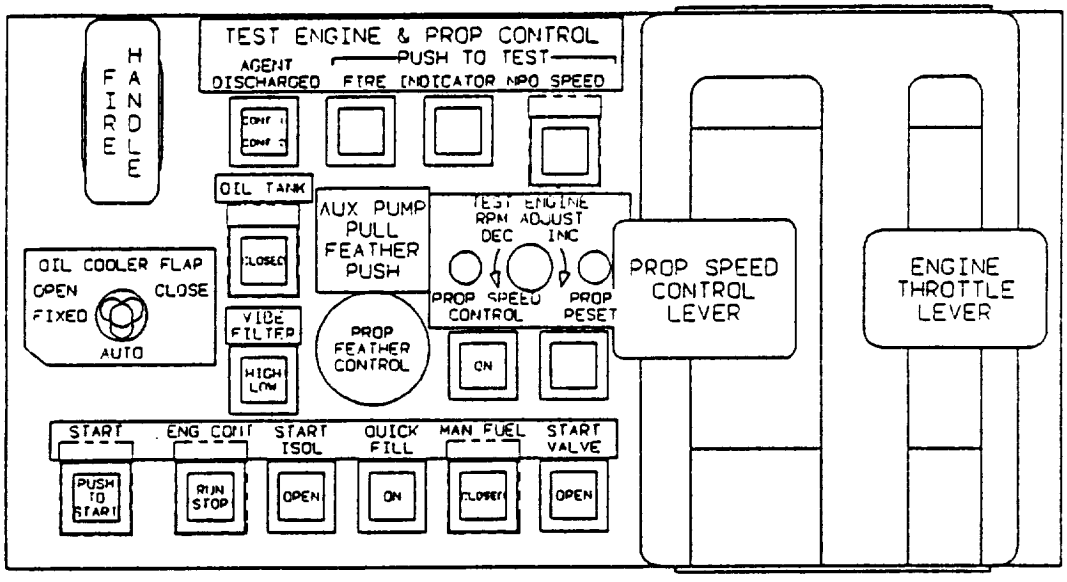
- N_P Tach - Propfan/power turbine speed (rpm)
- Torque - Engine output shaft torque
- TGT - Turbine gas temperature
- N_G Tach - Gas generator speed (rpm)
- Oil Pressure - Dual needle indication of gearbox and gas generator oil pressure
- Fuel Flow/o Vibe-Select Engine or Gearbox Vibration/o Oil Temp - Oil temperature at tank outlet
- Fuel Temp - Fuel pump inlet temperature
- Indicators - Warning light indicators were provided as noted on the right side of the figure

3.2.2.2 Test Engine and Prop Controls

The controls for the test engine and propfan were mounted in a panel that was qualified by use in the propulsion system static test program before installation in the testbed aircraft. It was located at the aft end of



(a) PROPFAN INSTRUMENT PANEL



(b) ENGINE AND PROPFAN CONTROLS

Figure 21. Flight Station Modifications

the center pedestal, accessible to both pilots and the flight engineer. The panel, also depicted in Figure 21, included the following:

- Oil Tank Shutoff Switch - To close the tank outlet valve
- Oil Cooler Flap Control Switch - To provide manual positioning of oil cooler air exit flap
- Engine Vibration Filter Select Switch - To select high or low band pass filter
- Engine Control Switch - To turn on power to the electronic engine control
- Prop Feather Control Push-Pull Switch - To feather or unfeather propfan
- Prop Speed Control Switch - To turn on/off power to the electronic speed control
- Prop Reset Switch - To align the command RVDT with the prop electromechanical actuator
- Prop Speed Control Lever - To control the speed (rpm) governing setting of the prop
- Engine Throttle - To control the engine output torque
- Fire Handle - This handle projected up from the control panel. When pulled, it armed the No. 1 and No. 2 fire bottles and closed the engine fuel control valves, the fuel isolation valve on the wing front beam, the air turbine starter air isolation valve, and the oil tank shutoff valve. A right or left twist of the handle fired the bottle discharge squib for the indicated bottle.
- Agent Discharge Indicator - This light indicated when a fire bottle had been discharged. A fire test switch was also provided to test the detection control circuitry continuity.
- Fuel Manifold Quick-Fill Switch - This switch provided power to the quick-fill valve.
- Manual Fuel Valve Switch - This switch opened the servo-operated fuel valve in the engine fuel control.

3.2.3 Nacelle Design

The PTA nacelle design was driven to a large degree by the requirement that the tilt angle of the propfan centerline be variable over a range large enough to provide the desired range of 1P excitation factor (2.0 to 4.5).

The 1P excitation of the propfan blades is determined by the relationship:

$$EF = \psi \times (V_E/348)^2$$

where: ψ = Mean inflow angle in degrees

V_E = Equivalent airspeed in knots

Figure 22 shows the variation of EF with altitude, Mach number, aircraft gross weight, and nacelle tilt angle. It can be seen in this figure that only the variation of nacelle tilt angle provides the range of excitation factor needed in the flight test program. Therefore, it was determined that the forward part (QEC portion) of the propfan nacelle would be designed to tilt through a range from 3 degrees below the fuselage reference plane to 5 degrees above.

3.2.3.1 Design Approach

The principal features of the PTA nacelle design were:

- The use of the quick engine change (QEC) concept in which all of the basic drive system is mounted in a detachable forward nacelle
- Provisions for tilting (in a vertical butt-line plane) of the forward nacelle
- The use of as much as possible of the primary structure from the Lockheed P-3 Orion nacelle

The resulting design is shown in Figure 23. The break between the QEC and the aft nacelle (which was permanently attached to the wing) is noted. The QEC was attached to the aft nacelle via four fittings, at the points noted, two of which were replaceable to allow for changing the tilt angle of the QEC. The QEC tilted about a line through the upper fittings, and the skin gap between QEC and aft nacelle was covered by replaceable fairings.

Obtaining a drag-optimized nacelle/wing design was not a PTA Program objective. It was recognized from earlier NASA work that installation drag could be minimized by appropriate contouring of the nacelle and the wing leading edges. For the PTA Program, however, it was determined that economics and schedules dictated the simplest design consistent with obtaining flight objectives. Therefore, as long as performance predictions indicated that the Mach 0.8 propfan design point could be obtained, no sophisticated nacelle/wing contouring was considered. An excess-drag-contingency plan was developed, however, that included in the scale model wind tunnel tests a leading edge extension, or LEX, for drag reduction if needed.

Aerodynamic design of the nacelle was also driven by the requirements for a certain range and harmonic content of the propfan dynamic loads. These requirements, as earlier noted, stated that 1P excitation factor should extend over the range from 2.0 to 4.0 and that higher order content should

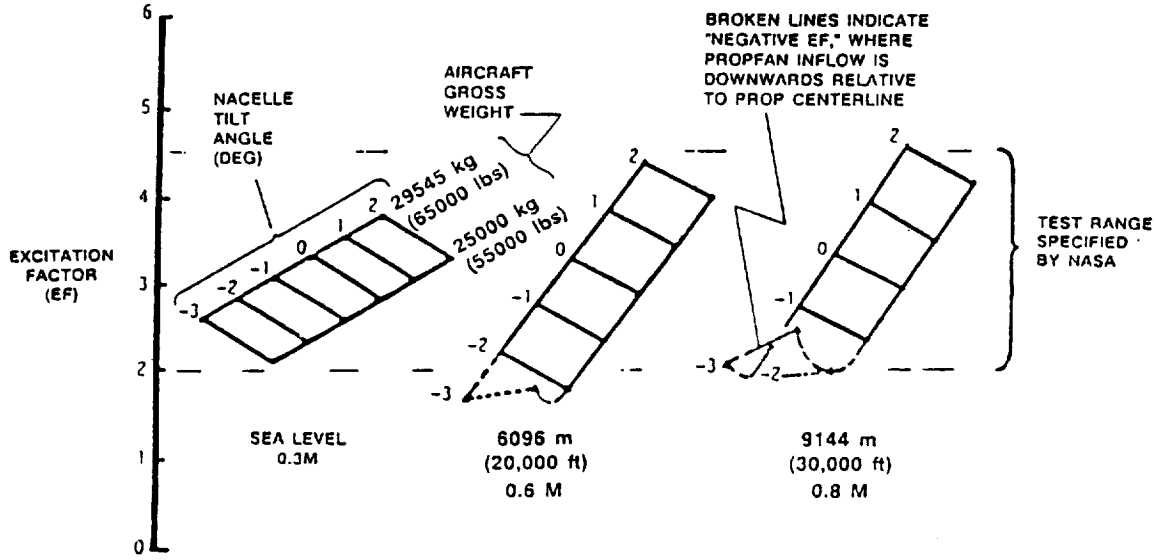


Figure 22. Predicted Propfan Excitation Factor

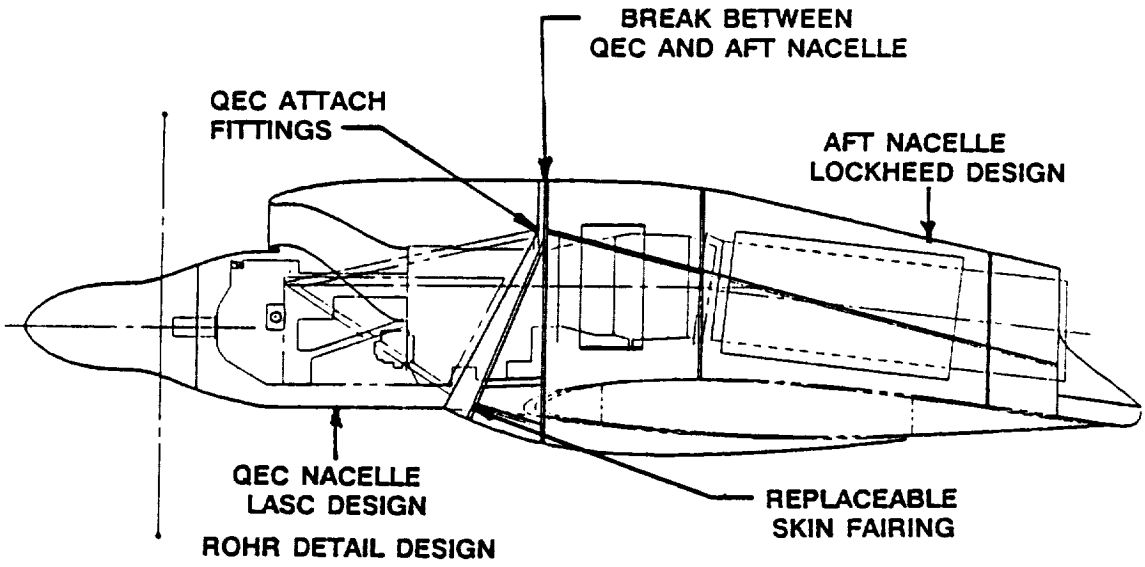


Figure 23. PTA Nacelle Features

comprise 12 to 30 percent of the total. The design approach to achieve the latter derived from small-scale tests (References 1 and 2) that showed the inlet location and size depicted in Figure 24 to yield a higher order content within the acceptable range. This is discussed in more detail in Section 5.1.1.

3.2.3.2 QEC Forward Nacelle

The general arrangement of the PTA nacelle is shown in Figure 25. The nacelle centerline was located at aircraft butt line, BL 165.3, a position that gave the desired 0.2 D_p clearance between the propfan blade tips and the fuselage surface. The engine inlet was located a distance behind the propfan rotor plane equal to 0.26 D_p, a dimension established by propfan blade dynamic loading requirements that will be further explained in Section 4.3.1.

The structural break between the QEC and the aft nacelle started on the top of the nacelle at the point where the wing leading edge intercepts BL 165.3, dropped vertically a short distance,. and then slanted forward to clear the wing leading edge on the inboard side of the nacelle. The primary structure of the QEC is shown in Figure 26. This figure shows the QEC built up from a V-brace system, two forward structural frames, upper and lower cowl panels, and an aft bulkhead. The secondary structure that completed the QEC is shown in Figure 27. Located at the aft ends of the V-braces were the fittings by which the QEC was attached to the aft nacelle.

A detailed view of one of the QEC upper attach fittings is shown in Figure 28. Together with replaceable fittings on the lower V-braces, this structure allowed the QEC to be detached from the aft nacelle and repositioned to a new tilt position with a minimum of effort. In the latter stages of the flight test program, proficiency in this change had progressed to the point where a tilt change could be made in less than two work shifts.

Figure 29 shows the range of QEC tilt angles designed into the nacelle structure. The baseline position was -1 degree--selected because analysis indicated this to provide vibratory loads in approximately the middle of the available range. The structure was then designed to allow the QEC to move 4 degrees from this position in either direction. As indicated, these angles were measured from the waterline plane, to which the fuselage reference plane was parallel.

The general arrangement of components and systems within the QEC is shown in Figure 30. It can be seen that the gearbox drive shaft extended forward through the spinner/QEC interface plane, and the propfan assembly was attached to that shaft. The gearbox and drive system are described in Section 3.3. The QEC also contained the engine starter, a fuel/oil heat exchanger for fuel preheat, the oil tank, and the air/oil heat exchanger system.

This arrangement of engine and gearbox lent itself most readily to the engine air inlet system shown where a single scoop inlet was located on

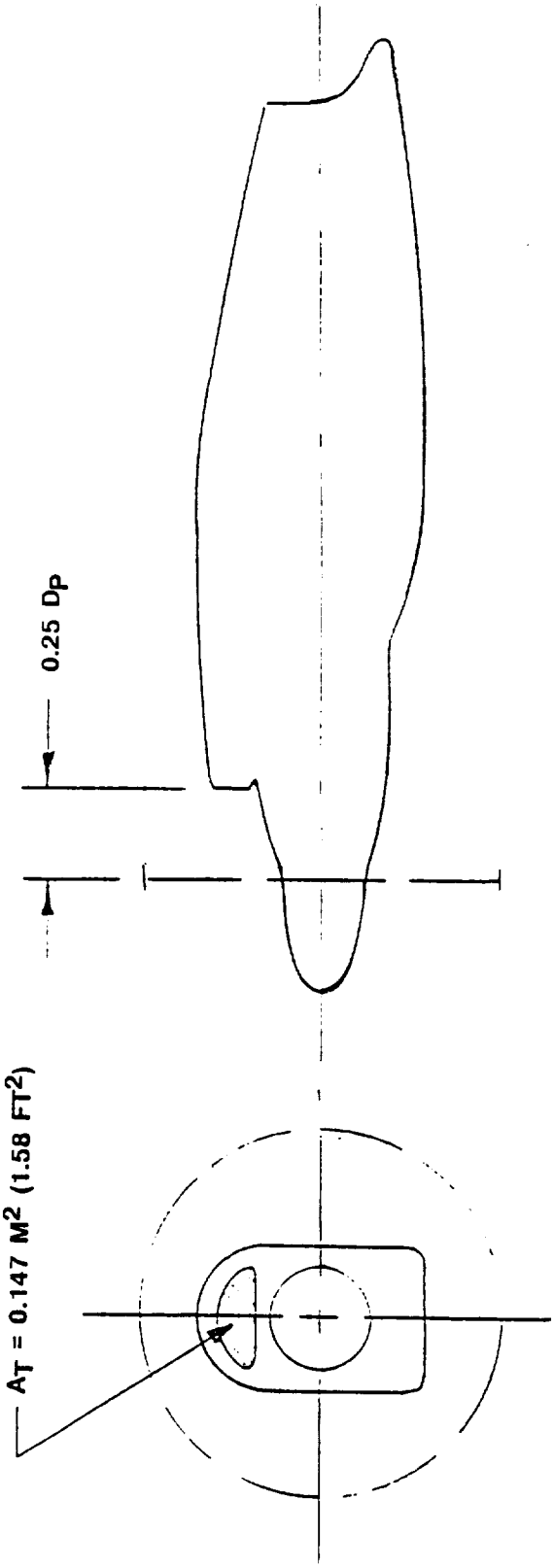


Figure 24. Size and Location of Engine Inlet

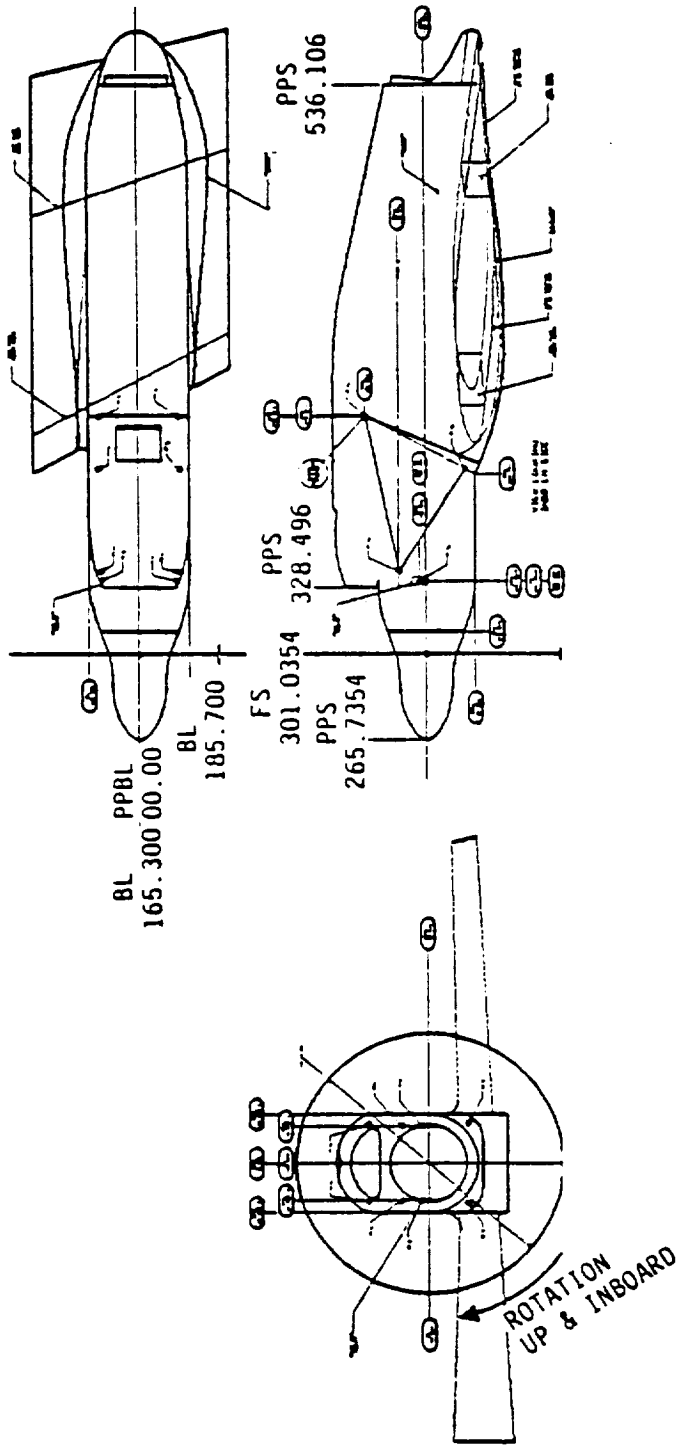


Figure 25. PTA Nacelle General Arrangement

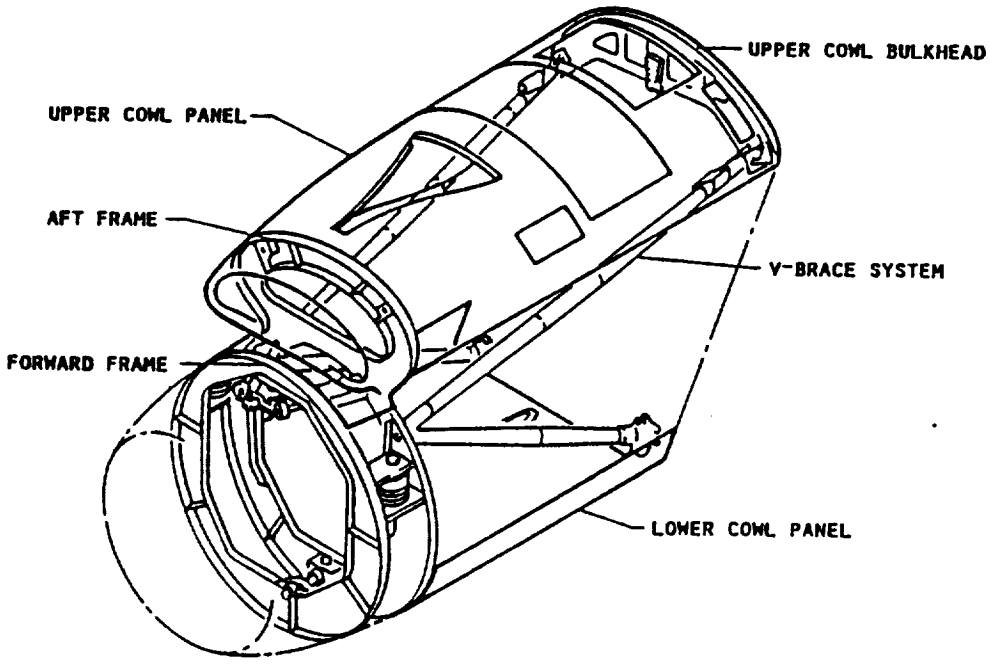


Figure 26. QEC Nacelle Primary Structure

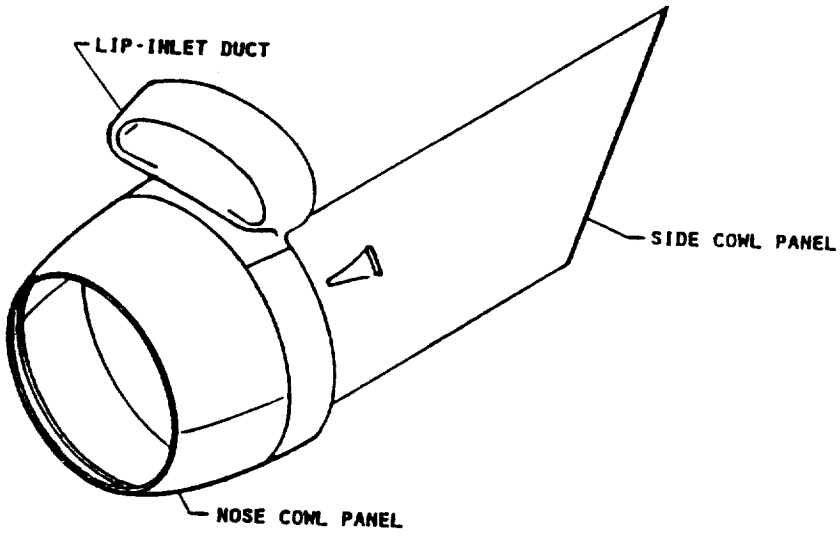


Figure 27. QEC Nacelle Secondary Structure

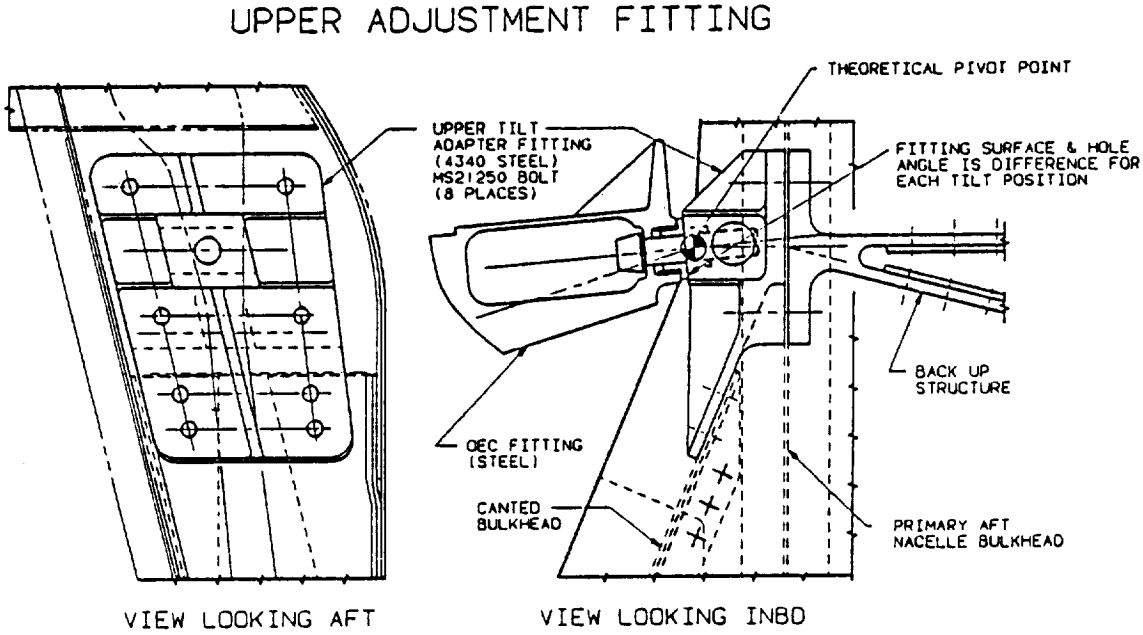
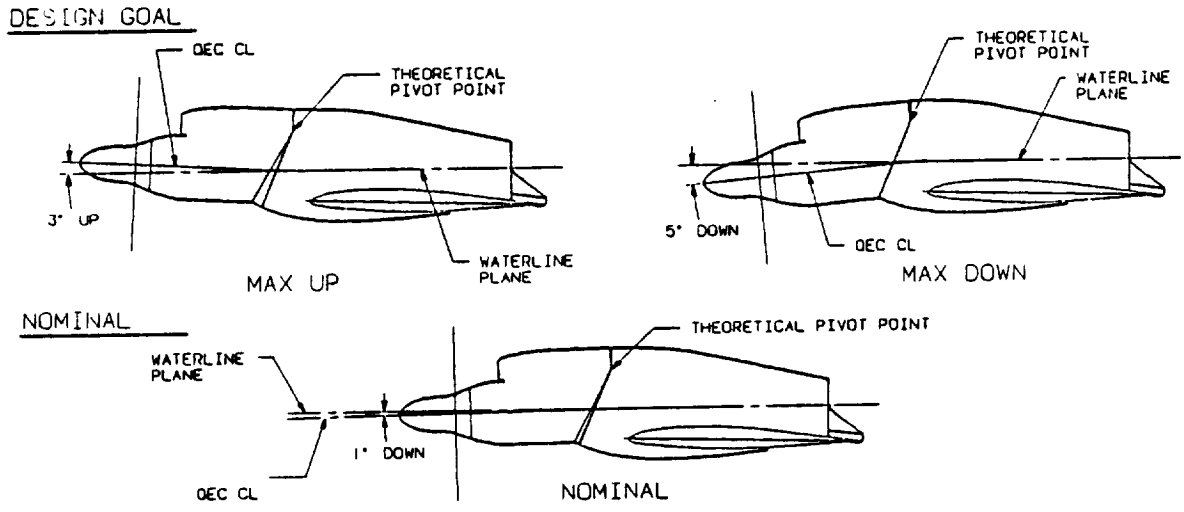


Figure 28. Nacelle Tilt Fitting



NOTE: ACTUAL TILT ANGLES FOR THE FULL SCALE MODEL WILL BE DETERMINED DURING THE SUB SCALE MODEL TESTS

Figure 29. Nacelle Tilt Range

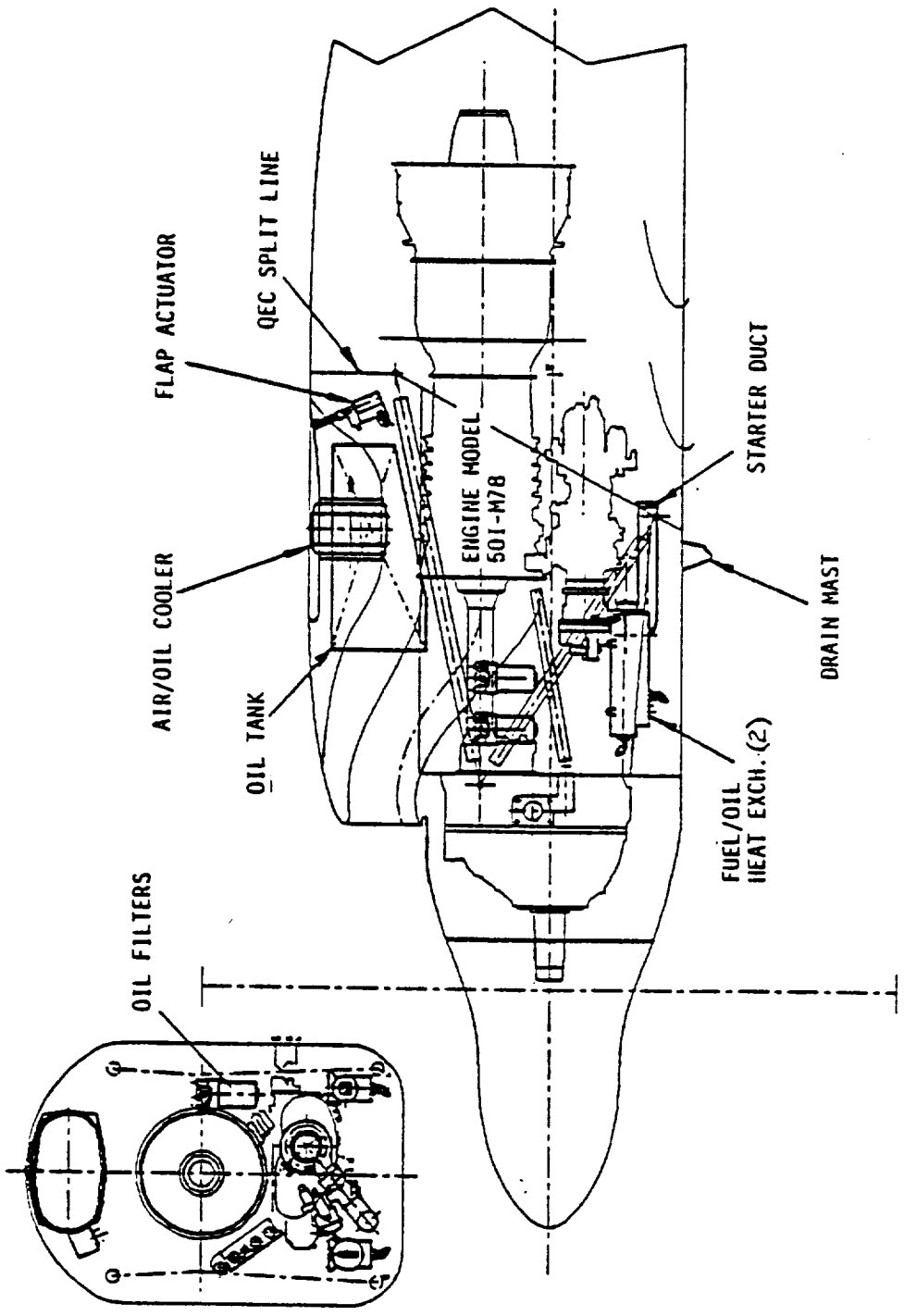


Figure 30. QEC Internal Arrangement

top of the nacelle and air was delivered from that inlet to the engine via an S-duct. It is possible with this drive system to use other air inlets and ducts, but the arrangement shown was selected as the best from consideration of inlet recovery, propfan blade excitation, and aerodynamic drag. This is discussed in more detail in Section 5.1.1.

The air inlet and outlet for the oil cooler can be seen in Figures 31 and 32. The air/oil heat exchanger was located at the top of the nacelle behind the engine inlet duct as shown in Figure 31. Air to the heat exchanger entered through a NACA submerged inlet with contoured ramp side walls and exited through an outlet with variable-position external flap. This flap, as shown in Figure 32, was positioned by an actuator that responded to oil cooler outlet temperature.

3.2.3.3 Aft Nacelle

Basic dimensions of the aft nacelle are shown in Figure 33. The aft nacelle was built onto the GII wing by Gulfstream as part of the wing modification, and in accord with Lockheed structural design. The interface between aft nacelle and wing structure has already been described in Section 3.2.1.1. A better view of aft nacelle details is given in Figure 34. As illustrated, the aft nacelle contained a vertical firewall just forward of the front spar of the wing and a horizontal firewall that separated the engine exhaust pipe from the wing structure.

A view of the exit region of the aft nacelle is shown in Figure 35. This view shows that portion of the wing spoiler system that had to be deactivated to accommodate the PTA nacelle installation.

The only element of the propfan propulsion system contained in the aft nacelle was the tailpipe, shown in Figure 36, which was supported from the aft nacelle structure. The tailpipe served two purposes--it ducted the turbine exhaust gasses and noises aft for discharge near the wing trailing edge, and it muffled the noise of the combustion processes. The muffler concept was designed by Lockheed and fabricated by Rohr. The entry adapter was a bell mouth that received the hot engine exhaust and was large enough to induce cooling air into the aft nacelle region by ejector pumping. An acoustic tailpipe lining was fabricated by Rohr and was the basic element in the tailpipe structure. This lining is discussed in more detail in Section 5.4.

3.2.3.4 Nacelle/Wing Fillets

The aerodynamic design goals in filleting were to: avoid adverse effects (like flow separation) in the flow interaction region of nacelle and wing surfaces, minimize disruption of the natural swept wing flow, and minimize The nacelle base area. The approach was to use the inviscid flow panel code QUADPAN (Reference 3) in an iterative fashion to maintain a smooth curve of the second derivative of surface pressure versus axial position. The filleted regions are shown by the shaded portions of Figure 37.

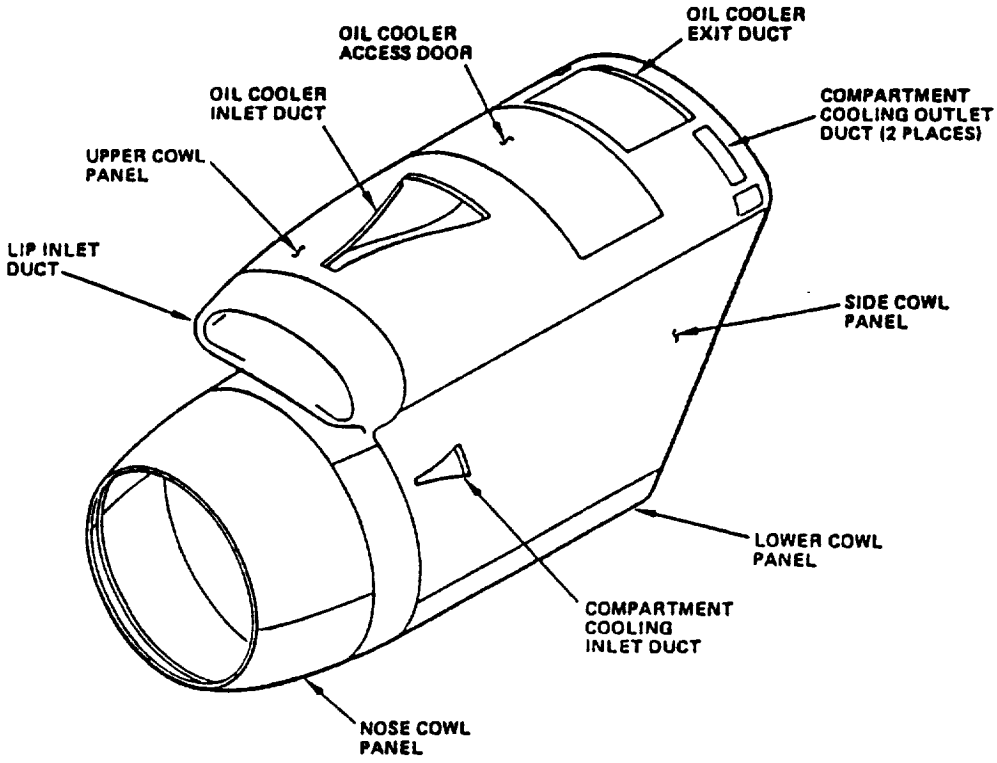


Figure 31. Air Inlet and Outlet for Oil Cooler

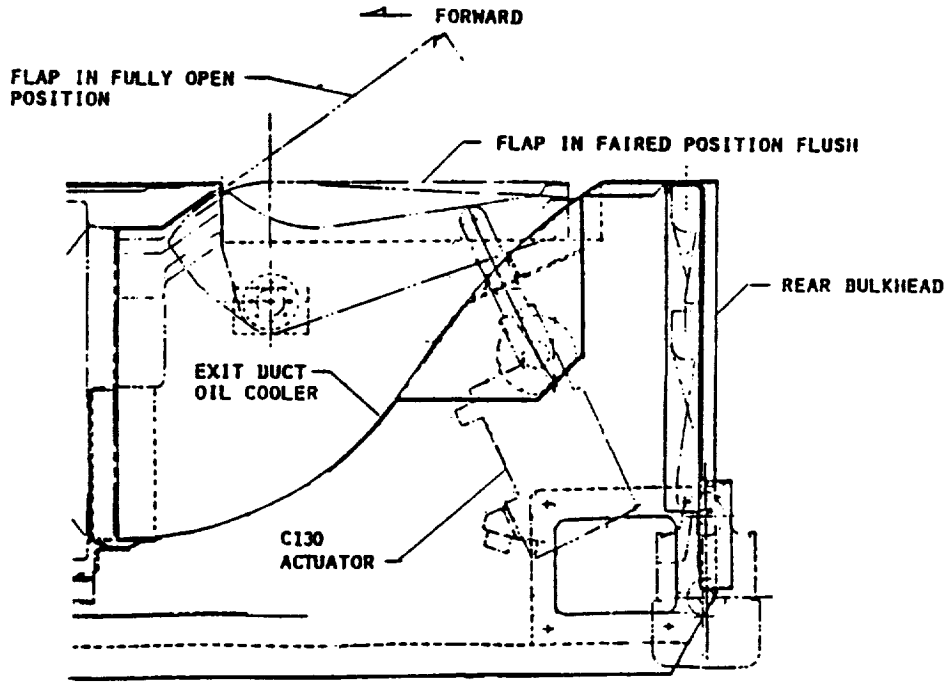


Figure 32. Oil Cooler Air Outlet Flap

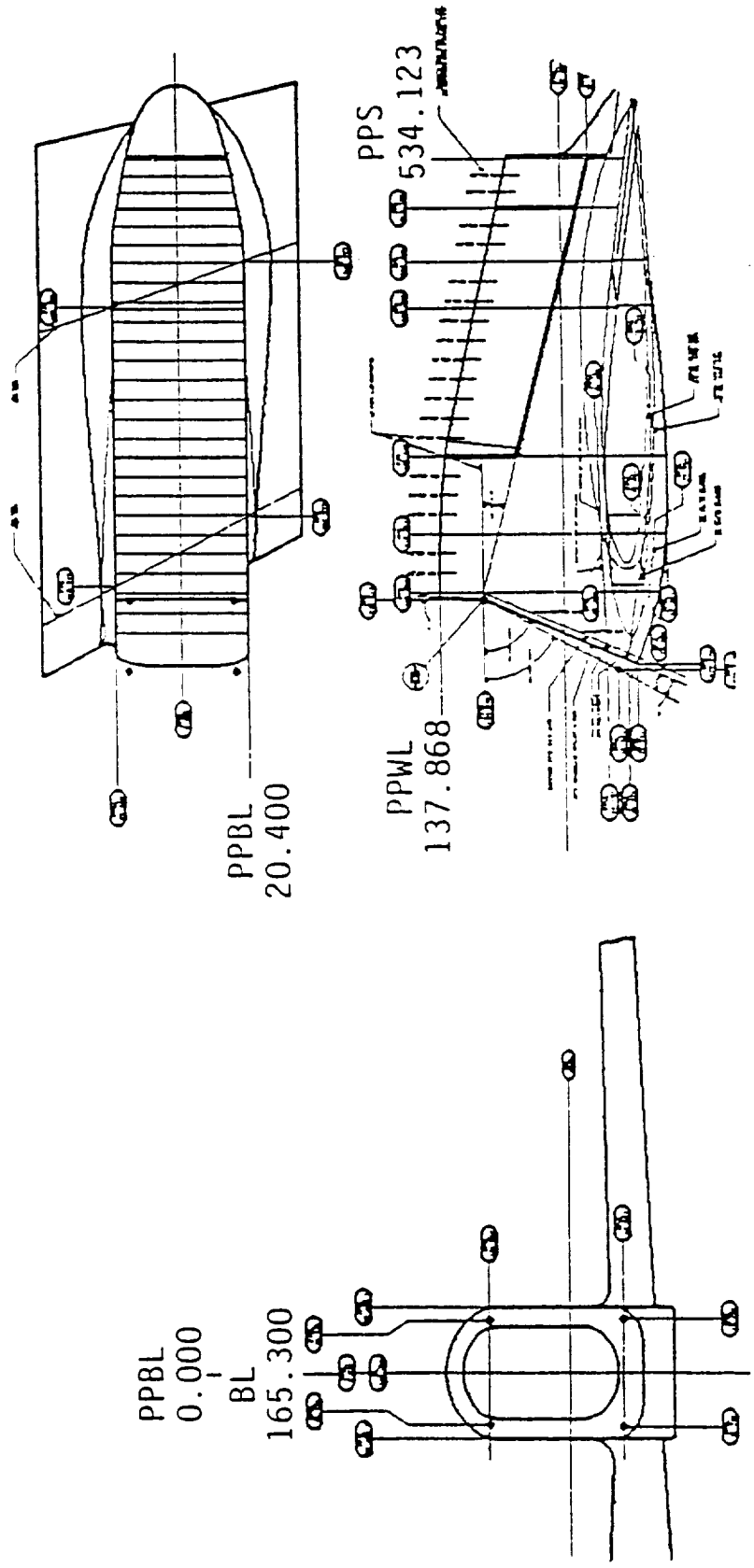


Figure 33. Aft Nacelle Basic Dimensions

ORIGINAL PAGE IS
OF POOR QUALITY

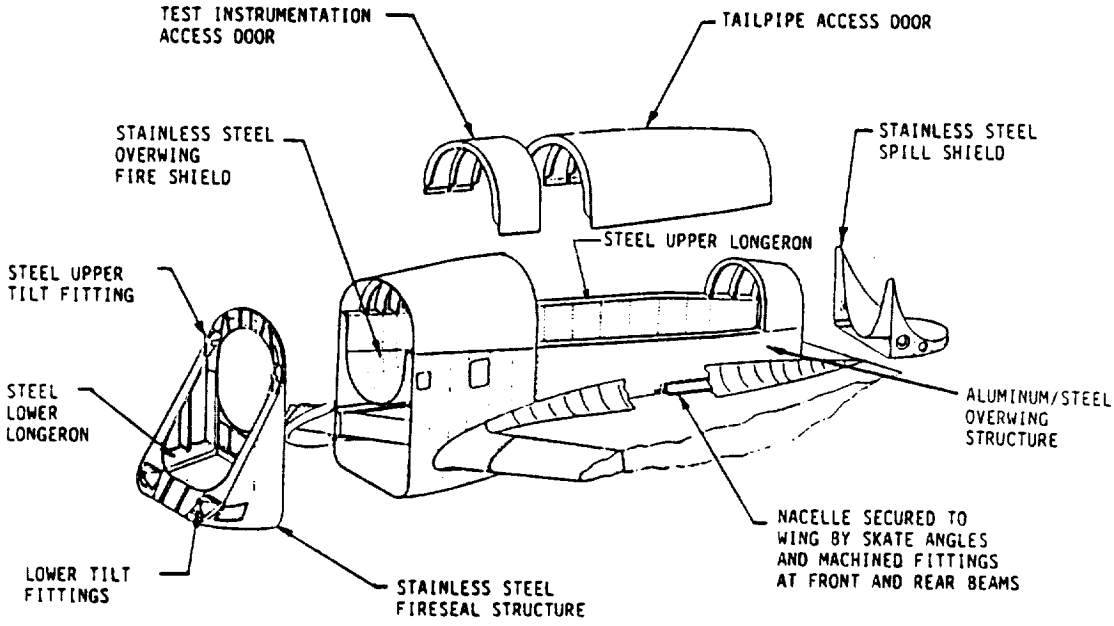


Figure 34. Aft Nacelle Structure

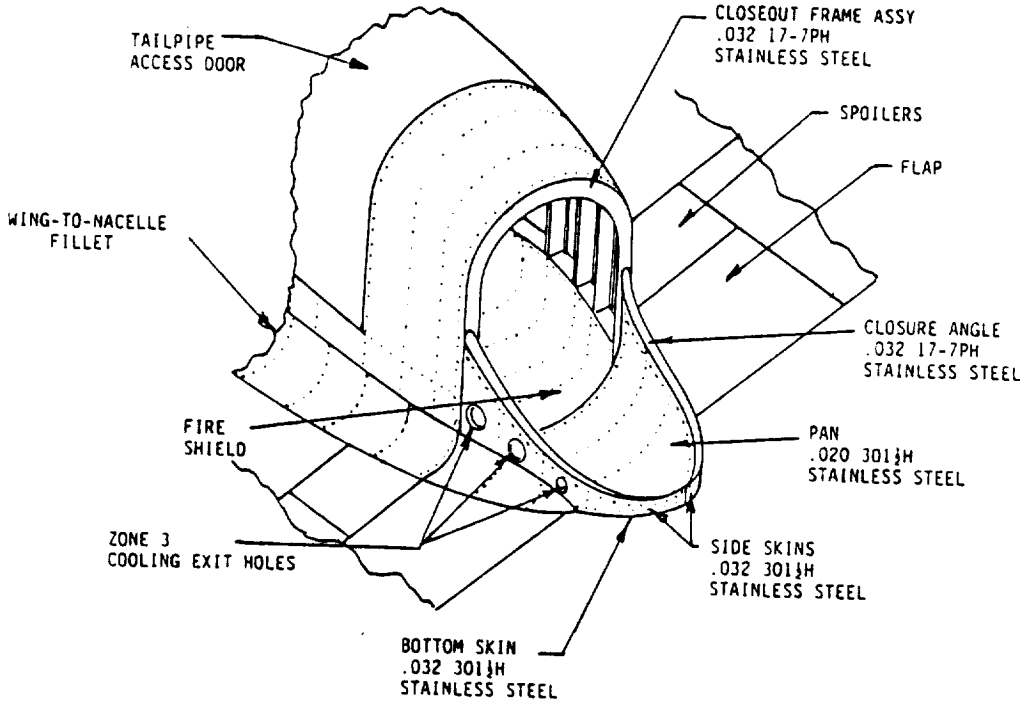


Figure 35. Aft Nacelle Exit Region

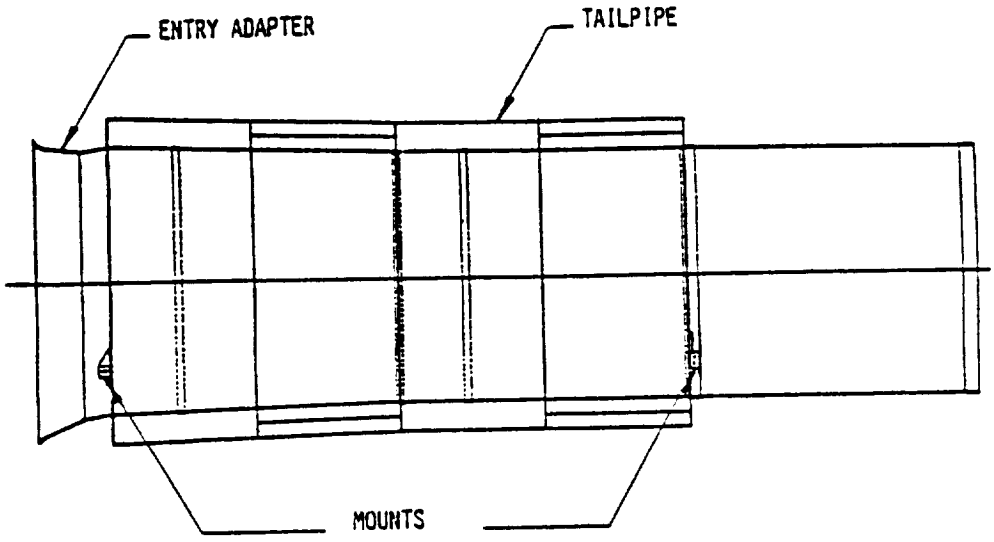


Figure 36. Acoustic Tailpipe Assembly

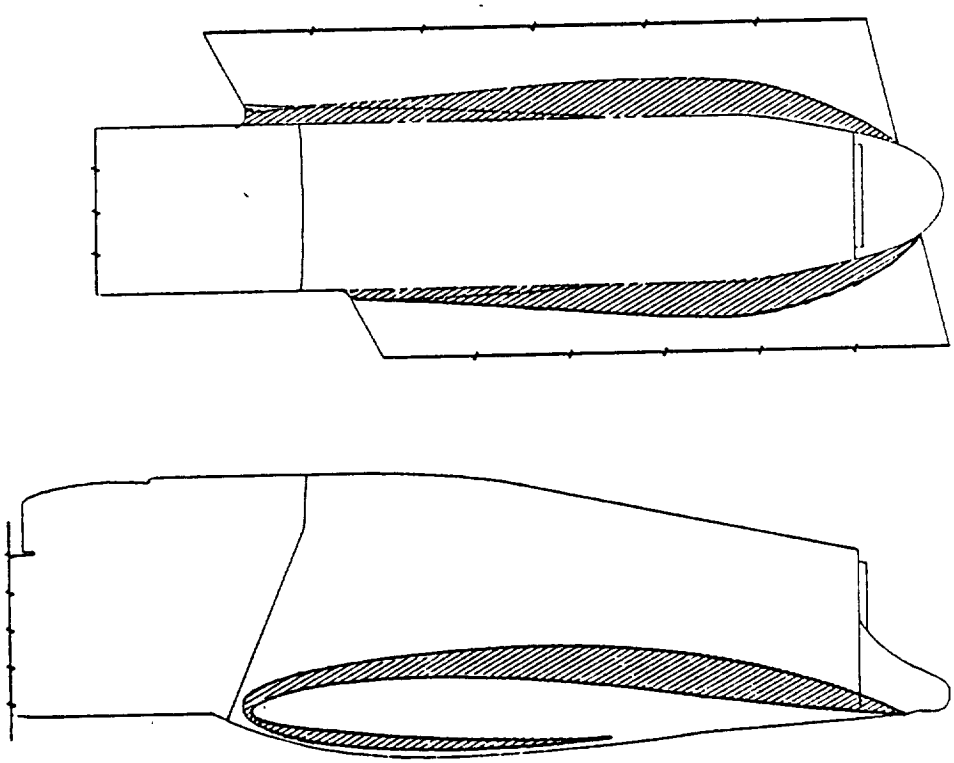


Figure 37. Nacelle/Wing Fillets

3.2.4 Aircraft Systems

3.2.4.1 Electrical System

The aircraft's electrical system was modified to account for the additional electrical loads of the testbed aircraft. Figure 38 shows a block diagram of the modified AC electrical power system with the modifications identified by the shaded areas. Minor modifications were also made to existing DC and AC electrical power distribution.

The AC electrical power system was modified to provide power to the propfan's auxiliary pump motor, power an additional inverter bus, and provide power from the existing aircraft busses.

The propfan's auxiliary pump motor required 115/200 VAC three-phase power at 400 Hz at approximately 4500 VA for 20 seconds. Since fixed-frequency, three-phase power was not available on the GII, ground tests were conducted to determine the effect of variable frequency power on the auxiliary pump motor. The tests indicated that the motor would work over the GII's AC frequency range if needed, but good engineering practice would dictate operating close to design frequency. This, then, became standard procedure for all except emergency conditions. The propfan's auxiliary pump motor was connected to the right alternator's monitor bus (from which all other loads were removed).

An additional inverter and the associated control components were added to provide additional fixed-frequency AC power to the Lockheed data system (LADS). Gulfstream had previously installed a similar configuration in certain GII derivative aircraft. During flight tests, however, it was determined that this additional inverter was not needed, so it was disabled and the LADS was transferred to the aircraft's secondary inverter bus.

The aircraft's main, pilot, and copilot circuit breaker panels were modified to accommodate the remaining PTA modification power requirements. Minor modifications were made to the pilot's circuit breaker panel to provide main inverter bus power for PTA modification AC fixed-frequency loads. Minor modifications were also made to the copilot's circuit breaker panel to provide secondary inverter bus power to the Lockheed data system and the Hamilton Standard data system. Modifications were made to the main circuit breaker to provide main DC power to the Lockheed data system and to the aircraft modifications. Essential DC bus power for other aircraft needs was also provided from the modified main circuit breaker panel.

The aircraft's two 20 KVA variable-frequency generators and its two 300A DC generators provided adequate power to the modified aircraft. The aircraft's 200/115 VAC, three-phase loads plus the PTA modification 200/115 VAC loads were less than 26,000 VA as summarized:

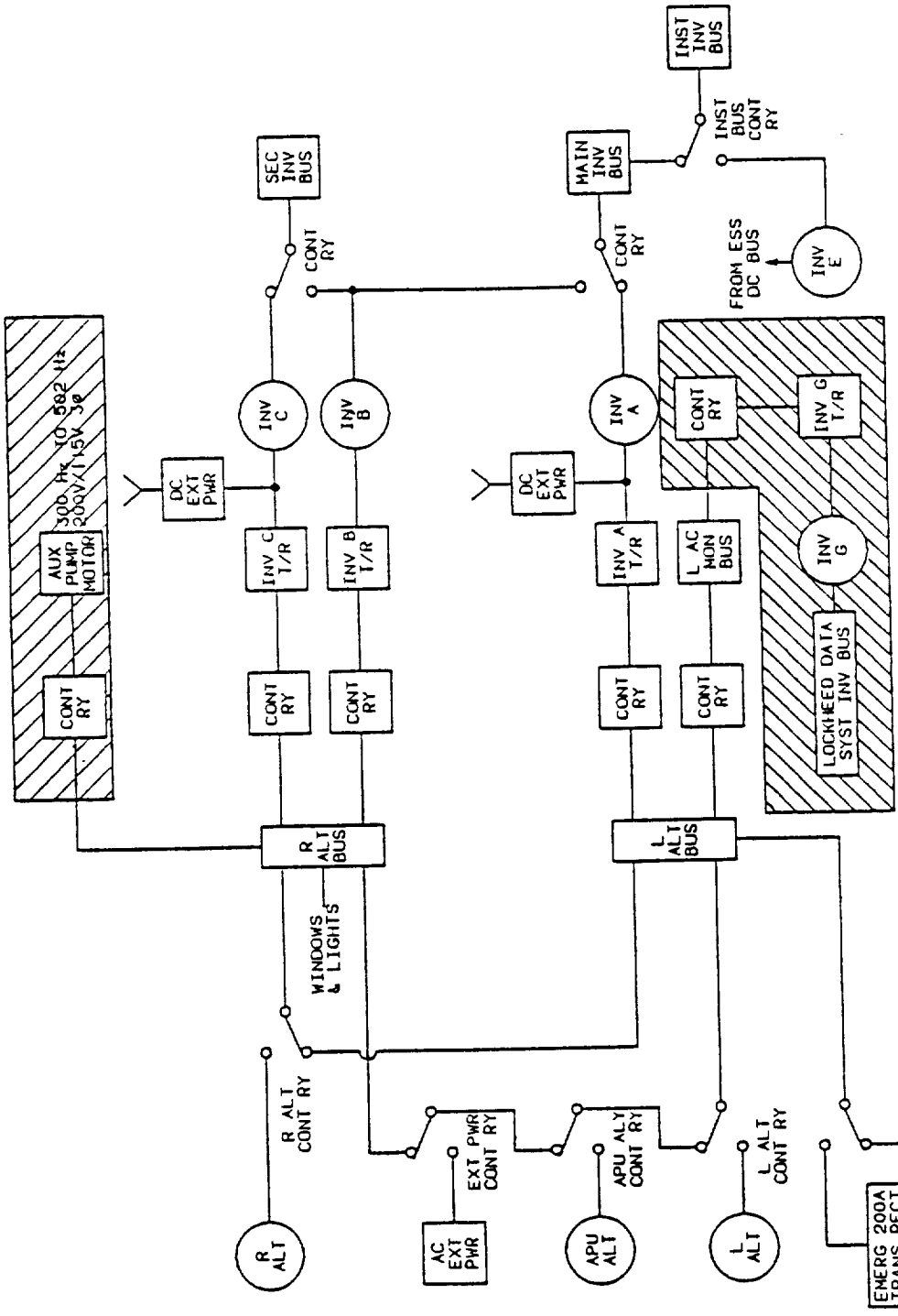


Figure 38. AC Electrical System Modification

	Operating Condition Cruise
GII Aircraft Loads	12,500 VA
Main Inverter T/R Load	4,229 VA
Secondary Inverter T/R Load	4,695 VA
*Auxiliary Pump Motor (6900 VA)	--
**Flight Test Inverter T/R Load	4,500 VA
Total Testbed Aircraft Load	25,924 VA

*Auxiliary pump motor load is not included because it is a momentary load; less than 25 seconds of operation for the flight condition.

**The flight test inverter system is currently disabled.

The two 20 KVA variable-frequency aircraft generators together were capable of producing 40,000 VA. In the event of the loss of one generator, the pilot had a switch to drop the Lockheed data system and the Hamilton Standard data system off the bus. Also, the auxiliary pump motor required a momentary load of only 12 seconds for each feather or unfeather operation so that the average load was very small. With these considerations, the average load was under 20 KVA, which meant that one AC generator could power the AC loads.

The two 300A DC power generators on the aircraft produced sufficient DC power to meet the GII aircraft loads plus the testbed modification loads, as shown by the following summary.

	Operating Conditions			
	Taxi (20 Min)		Day-Cruise	
GII Aircraft Loads	435A	6,936 Amp-Min	270A	15,695 Amp-Min
Testbed DC Bus Loads	89A	894 Amp-Min	89A	2,607 Amp-Min
Max Demand (Amps)	524A	---	360A	---
Total (Amp-Min)	--	7,831 Amp-Min	--	18,302 Amp-Min
Average Demand (Amps)	391A	---	305A	---

The two DC generators together were capable of producing 600A.

In the event of loss of power during test operation, critical PTA modification loads were powered by essential power busses or designed to fail in a safe manner.

PTA essential power loads located on the aircraft essential DC bus were:

- Feather control solenoid circuit

- Fire detector system
- Fire extinguishing system
- Fuel isolation valve
- Engine/gearbox oil shutoff valve
- Starter isolation valve

The propfan engine electronic control was on the main aircraft DC bus and was designed to fail "shutdown" if a power failure occurred. The propfan speed (rpm) control electromechanical actuator and control electronics were powered by the main AC inverter and main DC busses; power failure resulted in a failed-fixed speed command.

3.2.4.2 Subsystems

The following new subsystems were incorporated into the testbed aircraft:

- Torquemeter Indicator
- Fuel Flow Indicator
- Fuel Temperature Indicator
- Oil Temperature Indicator
- Oil Pressure Indicator
- NP and NG Speed Indicators
- Engine Vibration Indicator
- TGT Indicator
- Low Fuel Pressure Indicator
- MAG Plug Indicator
- Prop Oil Flow Indicator
- Oil Low Pressure Indicator
- Engine Start Control
- Prop Feather and Unfeather Control
- Prop Speed Control
- Oil Tank Shutoff Valve
- Fuel Isolation Valve
- Fire Detector
- Fire Extinguisher

The following GII electrical and electronic subsystems were modified:

- Electrical Power Distribution
- Intercom System
- Anti-Ice Valve

- o Fire Warning System
- o Cabin Lights
- o Compass Flux Valves

3.3 DRIVE SYSTEM DESIGN AND QUALIFICATION

3.3.1 Power Section

The power section was a slightly modified version of the Model 570 industrial engine, which earlier was derived from the Model XT701 turboshaft engine. Primary differences between the XT701 and the Model 570 were the elimination of compressor bleed and replacement of the titanium compressor case with a steel case. Certain mechanical and electronic features were also modified for increased durability and reduced cost for industrial application.

The power section core of the Model 570 was a Model 570KA engine with first stage gas generator turbine vanes reset. External modifications to the 570, shown in Figure 39, consisted of a T56 style drive coupling between the power section and reduction gearbox, a revised inlet housing casting to provide T56 mounting pads for the reduction gearbox support struts, and new rear engine mounts. Ten containment ring constraint blocks were mounted on the turbine case split lines to react impact loads in the event of an uncontained turbine failure. The end view in Figure 39 shows three of the configuration changes made to the 570 engine. At the 8 o'clock position, the rectangular box is the XT701 electronic fuel control and support raft. At 11 o'clock is the relocated XT701 compressor inlet temperature sensor with its element protruding into the flowpath. The third is the fire shield around the entire perimeter of the engine case just behind the fuel nozzles and ignitor plugs.

The changes from the Model 570 can be summarized:

- o XT701 features restored:
  - Fuel control system
  - Accessory raft
  - Compressor variable geometry fuel driven actuation systems
  - Center sump vent
- o PTA design changes:
  - Air inlet housing to accept gearbox support struts
  - Turbine vane changes
  - Combustor case drains
  - Fire shield attachment
  - Lubrication requirements

ORIGINAL PAGE IS
OF POOR QUALITY

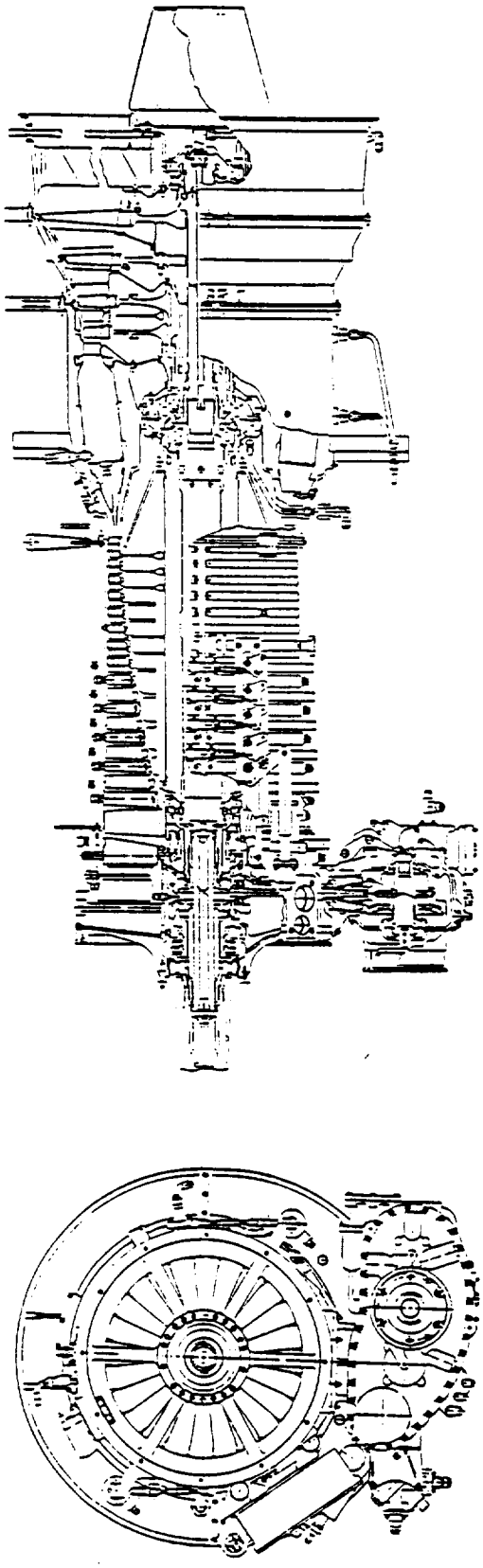


Figure 39. Model 501-M78 Power Section

3.3.1.1 Air Inlet Housing Assembly

The air inlet housing was made up of an outer ring and an inner hub connected by six radial struts. It supported the front of the compressor and provided mounting for the accessory gearbox. The front flange of the inlet housing mounted the adapter ring and torquemeter housing that transmitted mount loads from the reduction gearbox to the power section. The 501-M78 inlet housing was machined from a modified Model 570 casting to provide two T56 strut attachment pads and add stiffening ribs. Four threaded holes were added for the torquemeter flange, the inlet sensor probe was relocated from the lower left to the upper left quadrant, and external oil lines from the inlet housing to the accessory gearbox were relocated.

3.3.1.2 Lubrication and Vent System

The compressor variable-geometry actuation system was changed from oil to fuel, and the oil jet size was increased to lubricate the output spline, as shown in Figure 40. An external oil tank was sized to duplicate the capability of similar existing installation, and it was designed by building an engineering mockup which was finalized in the QEC forward nacelle mockup development. The vent system was changed by capping the rear bearing sump vent and two of the three center bearing sump vent lines, installing an orifice in the center remaining bearing sump vent, and rerouting the vent lines to the new oil tank. The resulting PTA lubrication system is depicted in Figure 41. Scavenge pump gear face clearances were reduced from the M570 tolerances in order to achieve the scavenge capability required for high altitude operation.

3.3.1.3 Compressor Assembly

The compressor assemblies for the 501-M78 and the Model 570 power sections were identical. The 13-stage axial flow compressor incorporated variable inlet guide vanes and 5 stages of variable stator vanes. The compressor variable geometry system (CVG) positioned the vanes for optimized performance and also provided adequate stall margin for start-ups.

3.3.1.4 Diffuser/Combustor Assembly

The diffuser/combustor assembly was identical to that of the Model 570 assembly except for the addition of two fuel drain valves to the bottom of the combustor case, provisions for attachment of the fire shield, and the capping-off of two of the three center bearing sump vents and addition of an orifice and line from the sump to the oil tank (XT701 configuration).

3.3.1.5 Turbine Assembly

This assembly comprised a two-stage axial flow gas generator turbine and, on a separate shaft, a two-stage axial flow power turbine. The gas generator turbine stage flow capacity was increased 1.5 percent from that of the Model 570 by opening the first stage vane area 3.0 percent through a 0.8-degree change in angle setting of the vane airfoil, as shown in Figure 42. The reset of the vanes was achieved by machining standard

ORIGINAL PAGE IS
OF POOR QUALITY

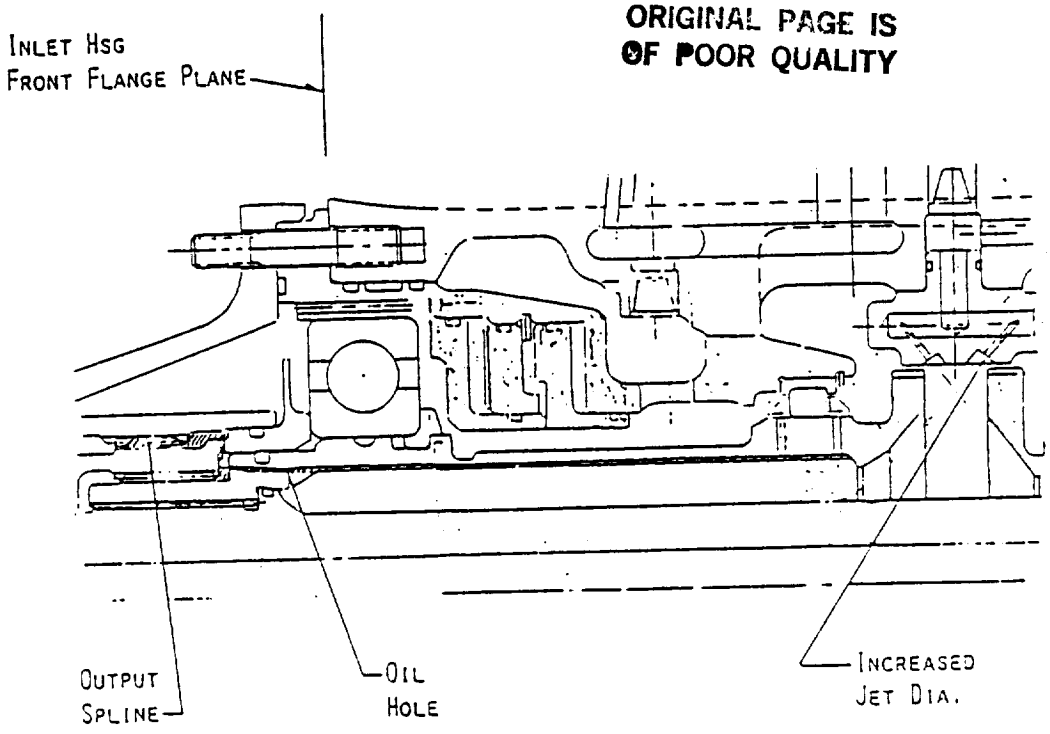


Figure 40. Power Section Lubrication System Change

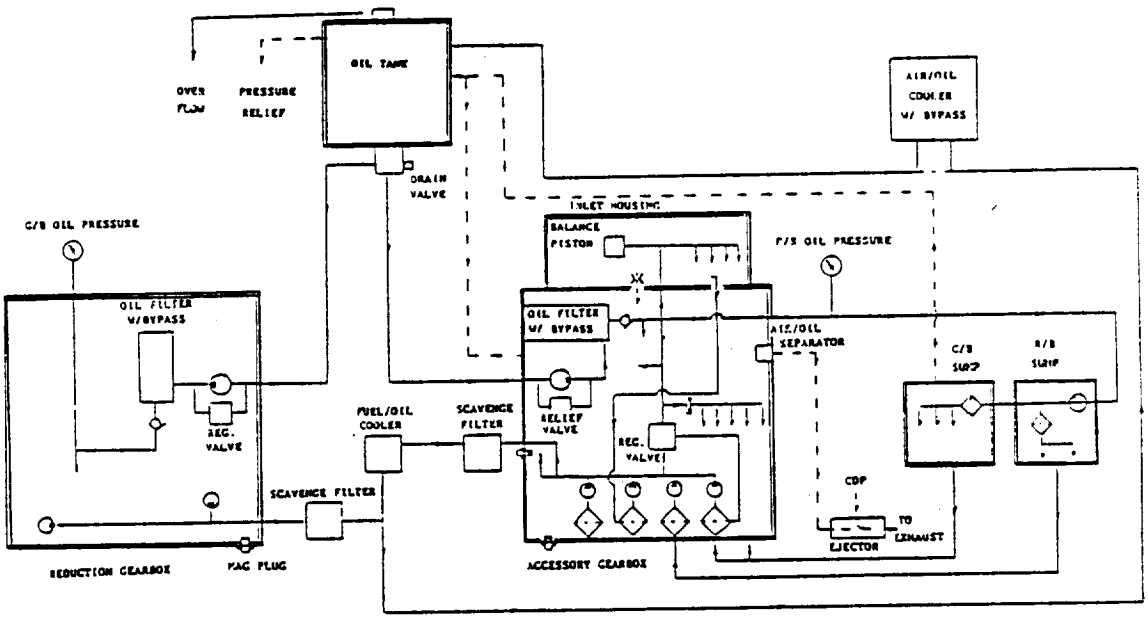


Figure 41. Lubrication and Vent System

castings at a 0.8-degree increased setting angle. The increased flow capacity provided compressor surge margin at limiting rpm (106.5 percent) at the Mach 0.8 design point that was comparable to the sea level static surge margin for the Model 570 engine.

The turbine case was designed to contain any single turbine blade failure. In the event of overspeed conditions, the failure order was as follows: turbine blades, wheel lugs, and wheel. Failure of blades would preclude further acceleration of the turbine, thus avoiding the risk of wheel failure due to failure of the control system to prevent overspeed.

In the event of turbine wheel failure due to some cause other than overspeed, a machined steel containment ring was mounted in the nacelle over the length of the turbine. Stand-off lugs were mounted on the turbine case flanges, as shown in Figure 43, to react the radial impact of the containment ring in such a case.

3.3.1.6 Accessory Gearbox

The accessory drive, mounted on the bottom of the air inlet housing was driven by the gas generator rotor system. It drove all the engine accessories, including the oil pump, centrifugal breather, and fuel pump. The starter drove the gas generator through this gearbox, which is unchanged from the Model 570 engine.

3.3.2 Gearbox

The Model 501-M78 two-stage reduction gearbox was adapted from the T56-A-14 (Figure 44) by making the changes shown in Figure 45. The first stage gear ratio was changed, reducing the overall gear ratio from 13.54 to 6.8, in order to provide 1692 rpm for the propfan. Because the output shaft of the Model 570 power section rotated in the opposite direction from that of the T56, an accessory gear train idler gear was added to restore the direction of rotation for existing oil pumps. A reworked nose scavenge pump mounting plate adapted the pump installation to the design changes. The prop brake was modified, and a T56 development oil pump, which has a 23 GPM capacity, was selected to obtain increased flow capacity for the range of variable speed operation (75 to 105 percent) for the PTA Program. The gearbox output shaft turned counterclockwise (viewed from the rear).

The T56 gearbox had four magnesium alloy castings which provided structural support for the two stages of reduction gearing and the accessory drive train. The structural members were the front case, bearing diaphragm, rear case, and rear case liner. Within the housing was the torquemeter shaft, which drove the input pinion. On each side of the rear case were large pads for attachment of the engine mounts, and eyebolts on the rear of the case provided for attachment of the tie struts to the power section air inlet housing. The rear case inner diaphragm, secured to the interior of the case, and the rear case provided the structural support for the accessory drive gear train. The rear housing was modified to accept the larger pinion gear and to accept the reversing idler gear for accessory drive. The internal oil nozzles were revised to accommodate the opposite rotation, and the oil supply to the pinion bearings was rerouted.

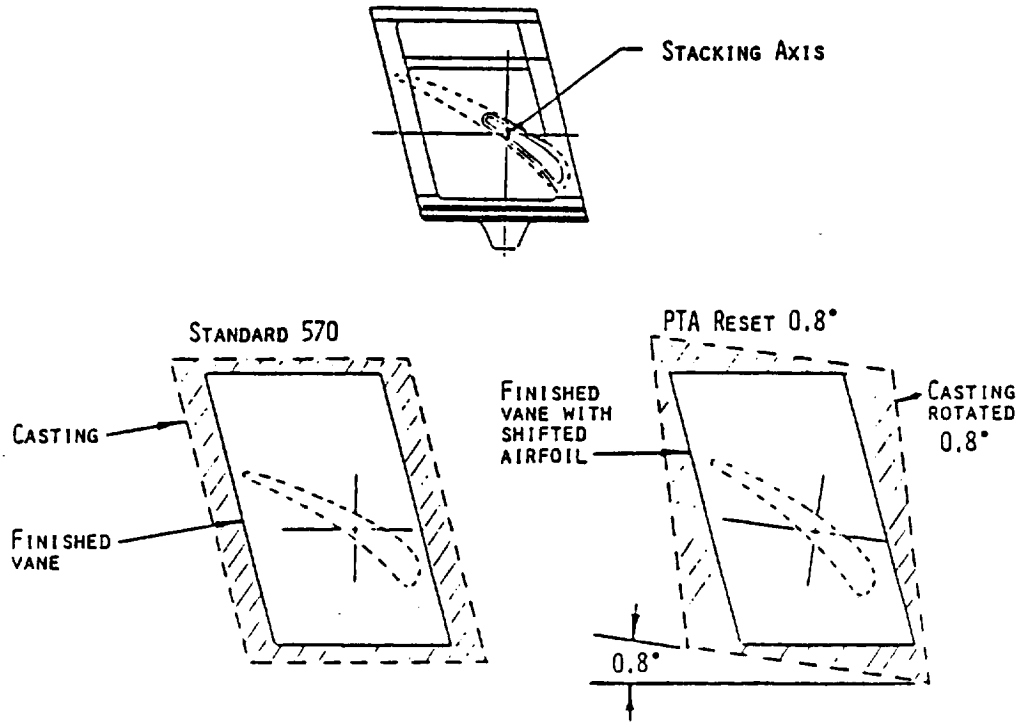


Figure 42. Power Section First Stage Vane Reset

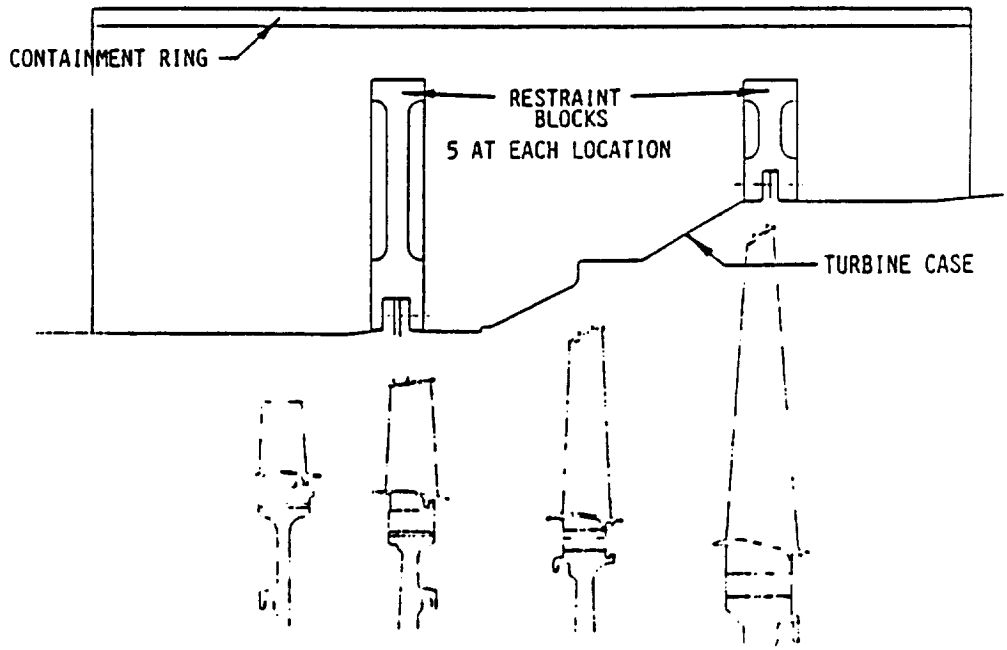


Figure 43. Power Section Containment Ring Restraint Blocks

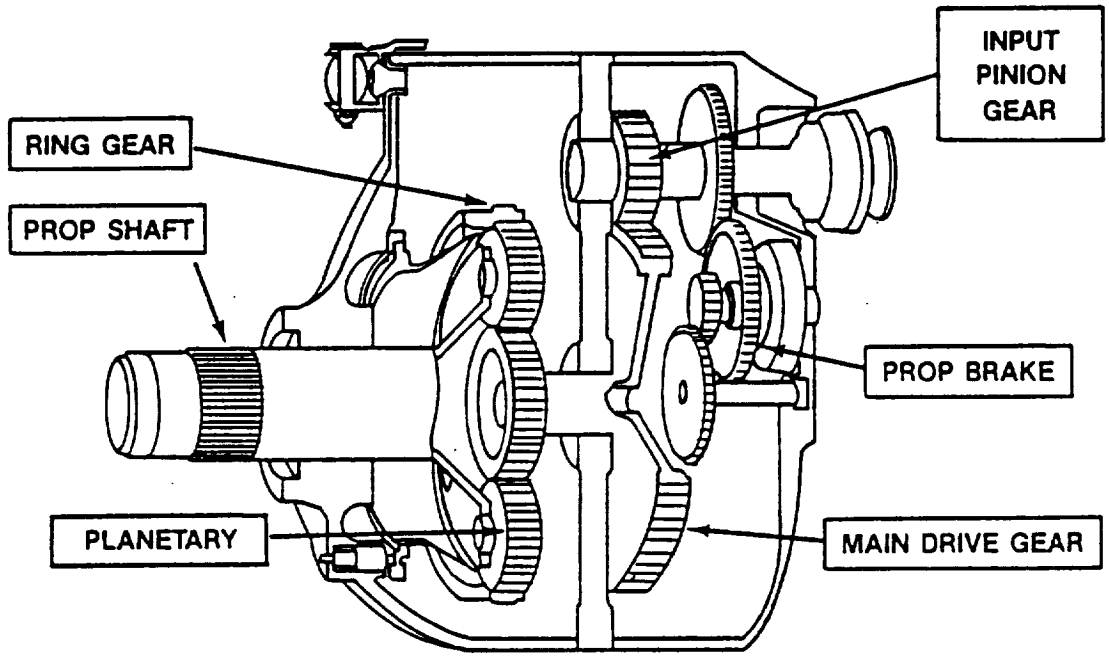


Figure 44. T56 Gearbox Features

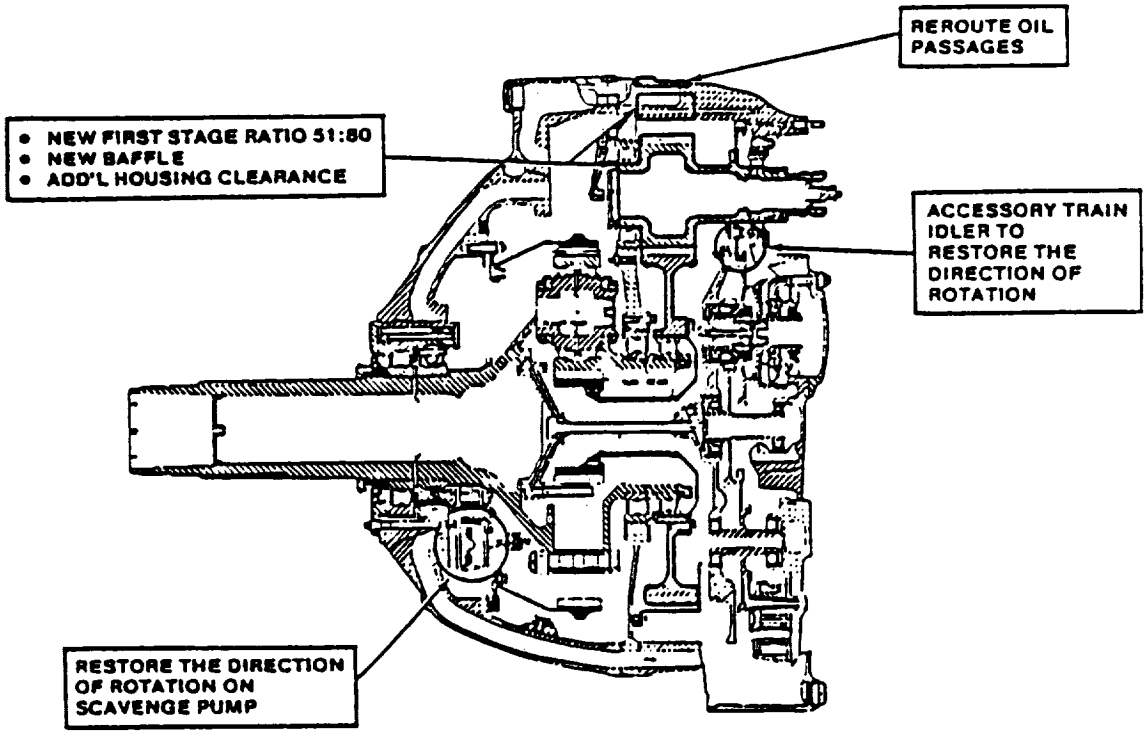


Figure 45. Model 501-M78 Gearbox Modifications

ORIGINAL PAGE IS
OF POOR QUALITY

The pinion gear that drove the main drive gear was enlarged from 32 teeth for the T56 to 51 teeth. The main drive gear was made smaller, from 100 to 80 teeth. Output from this first stage was delivered to the second stage reduction by the sun gear hub and a sun gear secured to the hub. The first stage reduction was 1.563:1, and the second stage reduction was 4.333:1, giving an overall reduction of 6.797:1. A reversing idler gear, depicted in Figure 46, was installed to restore the direction of rotation for the accessory gears that drove pressure and scavenge oil pumps.

Prior to completing the modification design, a 10-hour motoring test was conducted which rotated the planet gear system at 1730 rpm to establish that it would not be adversely affected by the "g" force increase on the separator side rails of the planet journal caused by the speed increase. No deleterious effect at the planet bearing separator/planet journal contact zone were found.

The modifications performed to convert the standard T56-A-14 gearbox into the 501-M78 configuration are summarized:

- New pinion gear (51 teeth)
- New main drive gear (80 teeth)
- New pressure pump assemblies
- Modified prop brake
- Additional accessory reversing idler gear
- Reworked front and rear housings
- Redirected oil supply to the pinion and sun gear teeth due to opposite rotation

The increase from 3728 kw (5000 shp) rating for the T56 to the 4474 kw (6000 shp) rating for the PTA Program and the reduction gear speed changes led to the estimate of cumulative life capability for the gearbox shown in Figure 47. This very conservative estimate was used as a guide for planning test operations.

The propeller brake was a friction-type brake, consisting of a stationary inner cone and a rotating outer member, located in the accessory drive train. When applied, it acted on the primary-stage reduction gearing. Reduction gear oil pressure held the brake disengaged, against a mechanical spring load, during normal drive system operation. When the propfan was not rotating, it resisted rotation in the normal (powered) direction with a torque of 247 N-m (182 ft-lb) and would withstand a maximum torque of 1532 N-m (1130 ft-lb) in the reverse direction. The helical splines of the prop brake were machined in the opposite direction from the T56 since powered rotation was opposite from the T56 application.

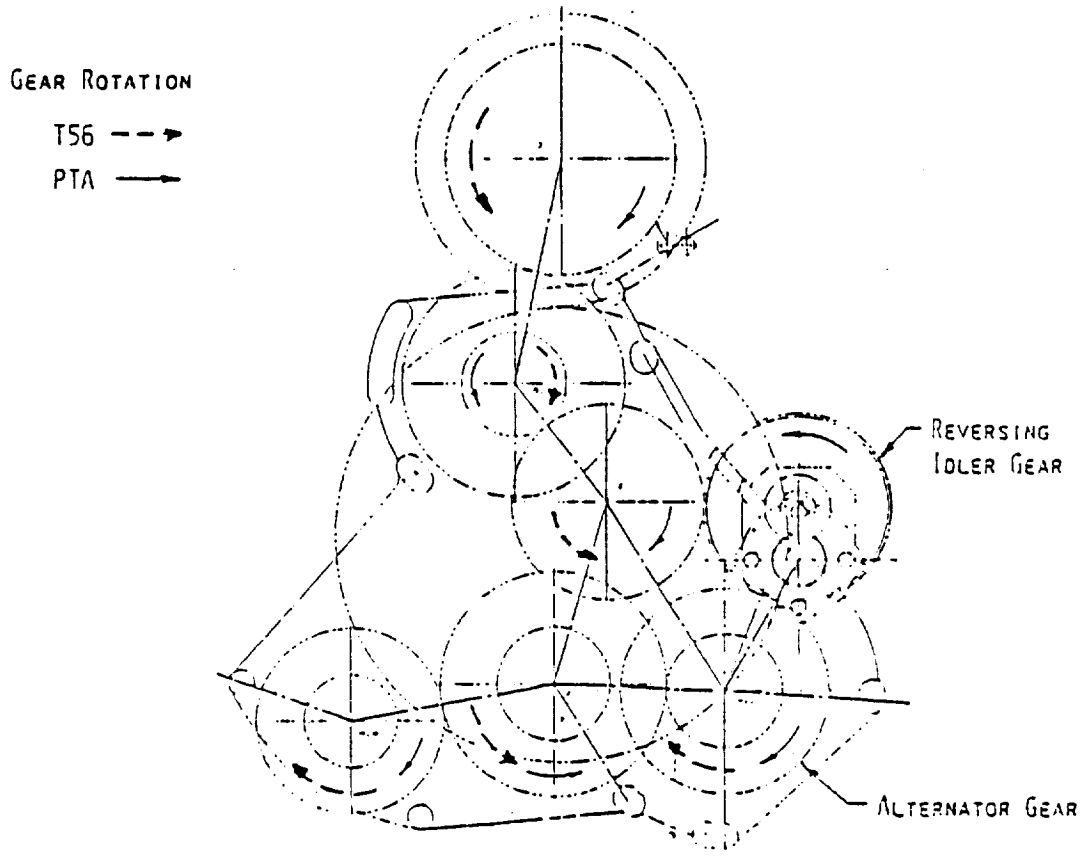


Figure 46. Reversing Accessory Drive Idler Gear

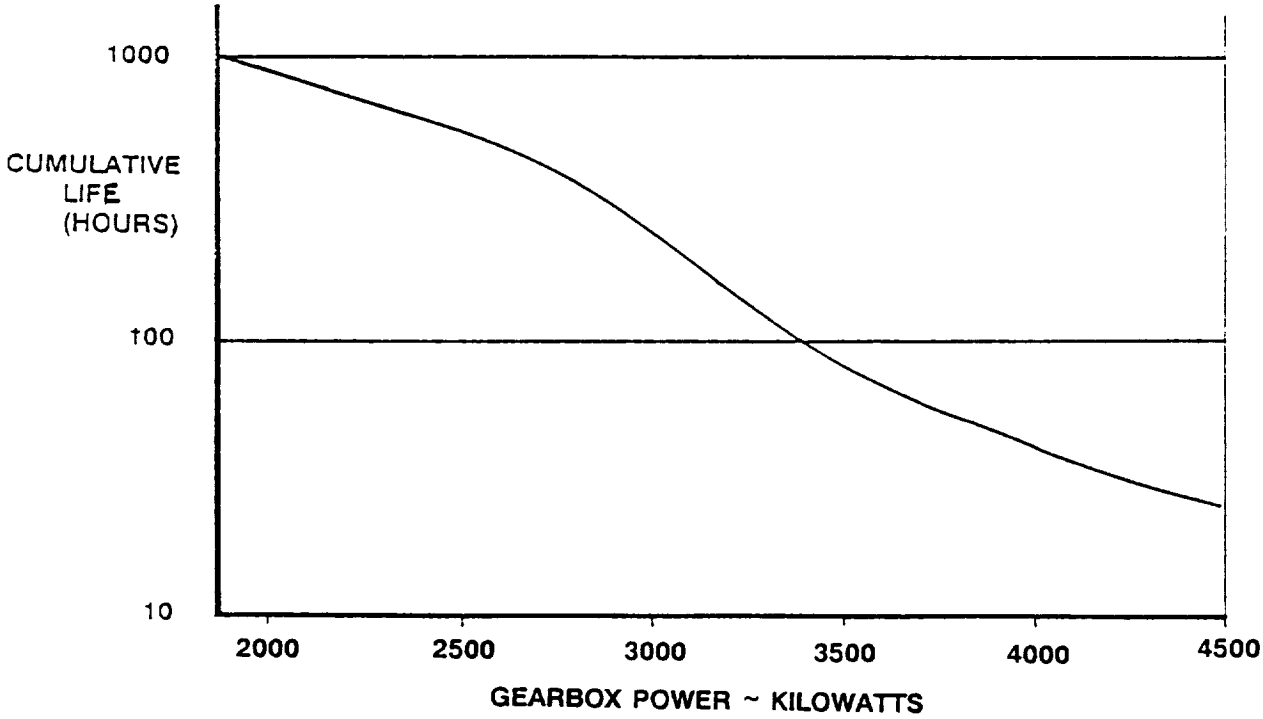


Figure 47. Gearbox Estimated Life Limit

3.3.3 Torquemeter

The torquemeter for the T56 power section was shown in Figure 10 and described in Section 3.1.3.3. The PTA torquemeter was identical to the T56-A-14 configuration except that the torquemeter tube was 1.27 cm (0.5 in.) shorter, and the support struts were 6.15 cm (2.42 in.) longer and 1.0 cm (0.394 in.) larger in outside diameter.

The torquemeter housing provided the structural connection between the power section front housing and the gearbox. It provided the mounting point for the torquemeter magnetic pickup assembly, the torquemeter mid-bearing outer race, and the bearing lock tube. The shaft assembly included two concentric shafts, two sleeve bearings, and the engine-to-torquemeter coupling. The outer shaft was connected to the inner torque shaft by a locating key at the aft end and provided a reference for measurement of the twist/torque reacted by the inner shaft. Both shafts rotated as a unit at power section output speed.

3.3.4 Controls, Subsystems, and Accessories

The drive system controls comprised the propfan control and the engine controls. The only subsystems for the 501-M78 were the starter, which was mounted to the accessory gearbox, and the oil tank, which was mounted in the nacelle.

3.3.4.1 Propeller Control

This system is shown schematically in Figure 48. It comprised the prop speed request system, which was mounted in the aircraft, and a rotary actuator, which was mounted to the modified prop control lever assembly. The prop speed control lever in the cockpit was connected to a rotary variable differential transformer (RVDT), which provided a command signal, through a slew transmitter and amplifier, to a rotary actuator mounted on the gearbox and connected to the prop control lever. The prop control lever assembly on the gearbox was modified to mount the rotary actuator, which was connected to a T56 prop control link. To set prop governing speed, the rotary actuator rotated the prop control lever assembly on command, moving the prop control link. The prop control link then rotated the prop input lever to set the propeller governing speed. This replaced the cable and lever control system used on T56-powered airplanes, as depicted in Figure 49.

3.3.4.2 Engine Control

The 501-M78 control system was based on the architecture for the XT701 engine and consisted of the following components:

- Hydromechanical fuel control unit - XT701 modified
- Compressor inlet temperature sensor assembly - XT701 recalibrated
- Main fuel pump - Model 570 modified
- Compressor variable guide vane (CVG) actuator - Model 570

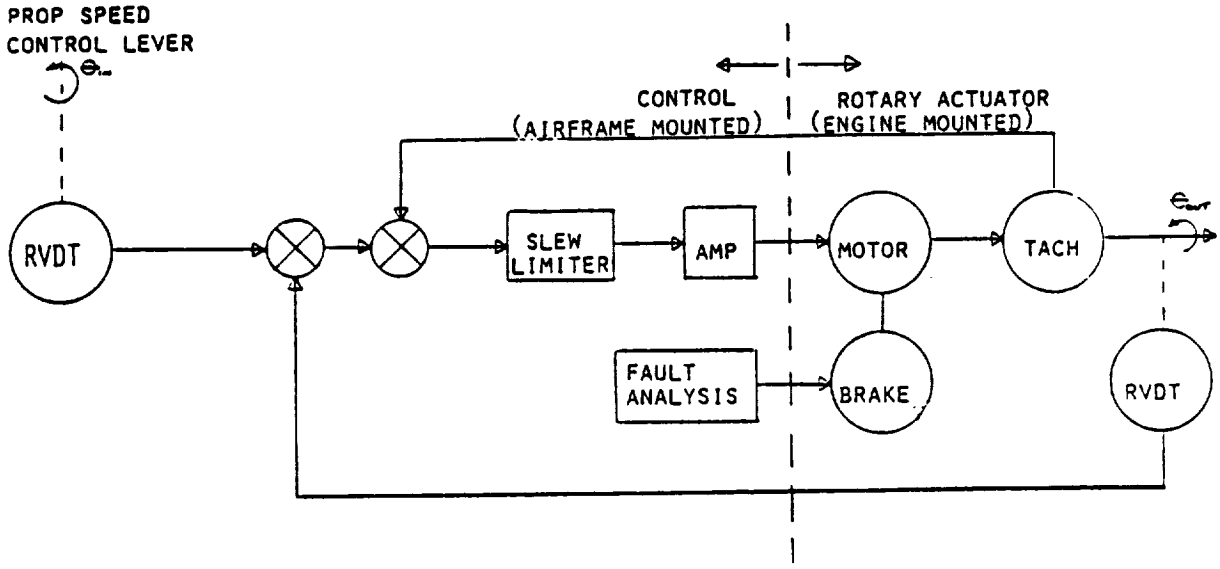


Figure 48. Propfan Speed Control Block Diagram

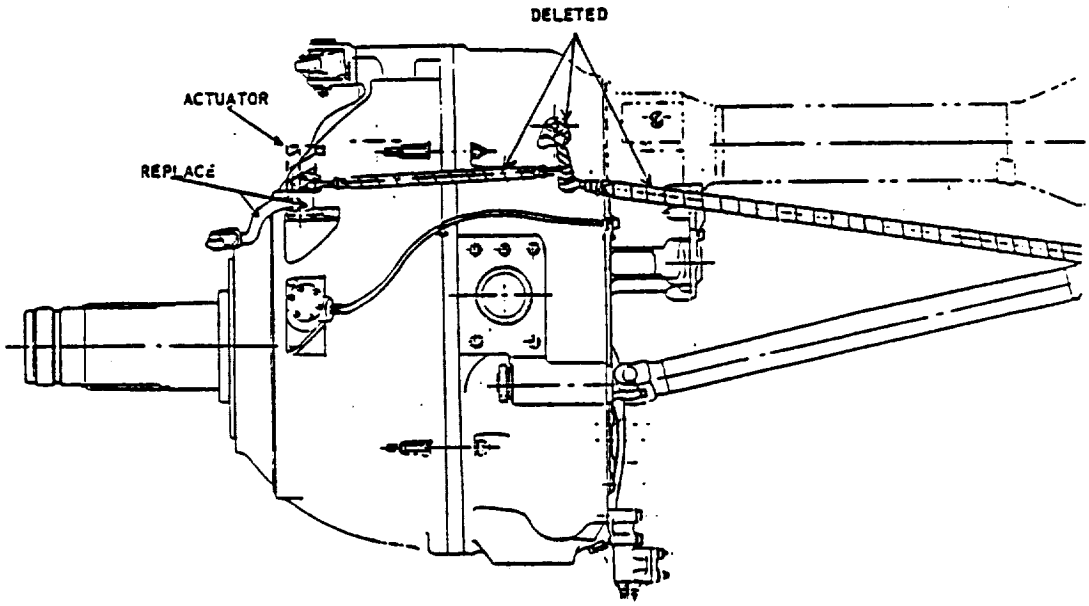


Figure 49. Propfan Speed Control ActuatorMounting Arrangement

- Engine electronic control unit (ECU) - XT701 modified
- Engine parameter transducers and pickups - Model 570
- Exciters/igniters - Model 570

A functional diagram of the system is shown in Figure 50. Figure 51 presents an input/output diagram which shows the required inputs and outputs for each control component and the interface between the control, engine, and cockpit. Because the XT701 was designed as a helicopter engine, the ECU system was modified for the PTA to delete selection of anti-ice, condition monitoring, the condition lever, magneto power supply, gas generator speed monitoring for collective pitch trim, and idle reset. Power turbine speed limiting at 109 percent and slew rate limiting at 20 degree/second were added. The gas generator speed limiting was changed to the new 100 percent limit, a manual fuel on/off signal and a power turbine overspeed test signal were added to the control function.

The hydromechanical fuel control was tandem mounted on the fuel pump, which was unchanged from the unit on the Model 570. It performed the following functions:

- Electrical power control
- Isochronous gas generator speed governing
- Start and transient fuel scheduling
- Dual electric fuel cut-off
- Manifold quick fill starting
- Idle governor selection

The torquemeter schedules were modified to change from fail-high (helicopter requirement) to fail-low and to change one torquemeter schedule. The gas generator overspeed limit was changed to 14,300 rpm from 15,000 rpm, and the speed request shaft position potentiometer was removed.

The relationship between power lever position and prop speed input position for normal operating conditions was as follows:

Condition	Power Lever Position	(Condition Lever) Prop Speed Input
Ground Start	Idle	Feather
Air Start	Idle	Feather
Minimum Governing	11,800 rpm	75% N_p
Max Power (Nominal)	13,900 rpm	105% N_p
Max Power (Extended)	14,500 rpm	105% N_p

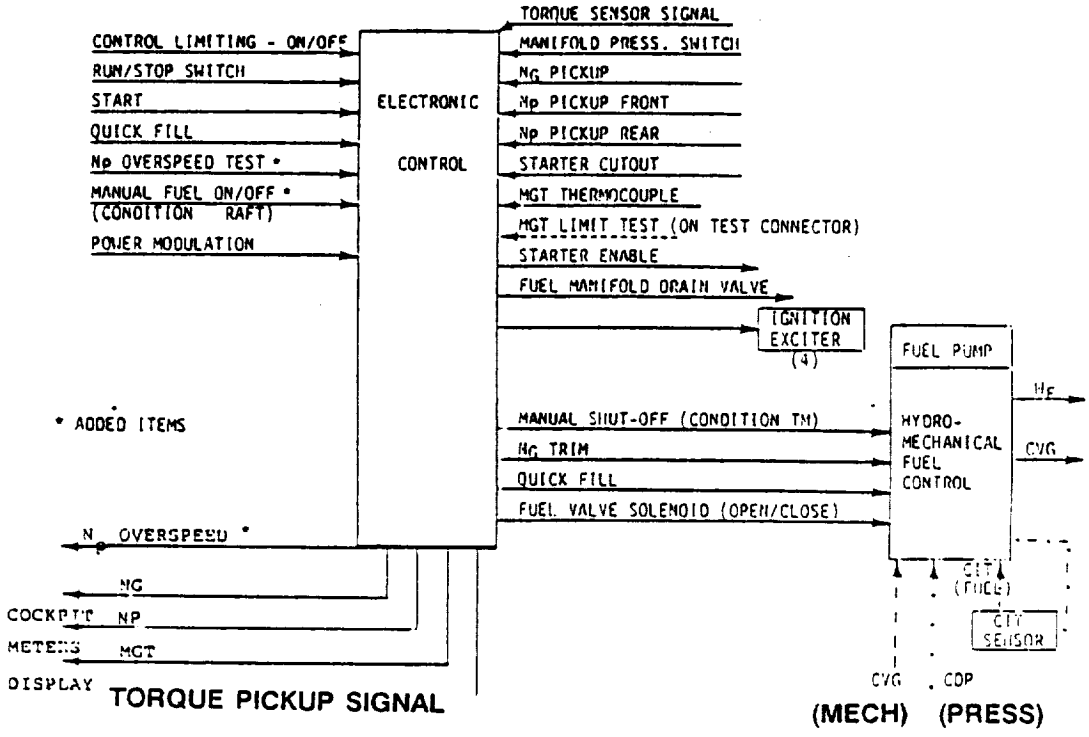


Figure 50. Functional Diagram of 501-M78 Control System

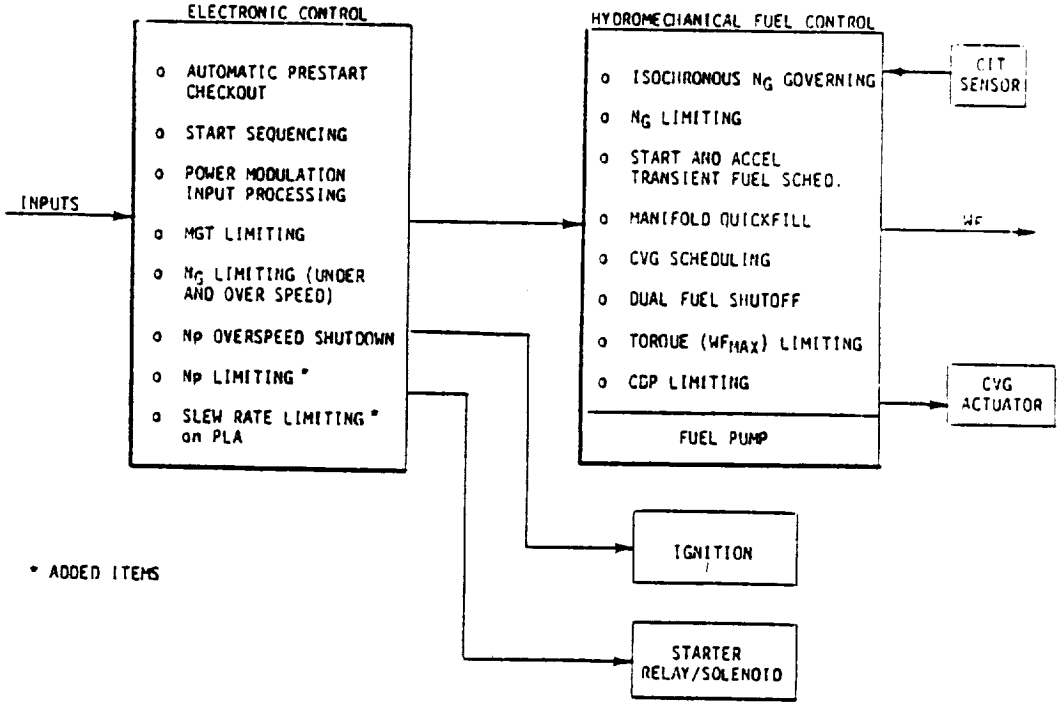


Figure 51. 501-M78 Control System Input/Outputs

There were three types of limits defined for flight operation: (1) limits imposed by the hydromechanical control, (2) limits imposed by the electronic control, and (3) operational limits imposed by the pilot. These are summarized:

- Hydromechanical control
  - N_G overspeed limit 15,230 rpm (106.5 percent)
  - Maximum fuel flow 1,814 kg (4,000 lb) per hour
  - Minimum fuel flow 113 kg (250 lb) per hour
- Electronic control
  - N_G overspeed limit 14,700 rpm (102.8 percent)
  - N_G underspeed limit 8,650 rpm (60.5 percent)
  - N_P overspeed limit 12,535 rpm (109 percent)
  - N_P overspeed shutdown 13,915 rpm (121 percent)
  - MGT (measured gas temperature) limit 874°C (1605°F)
- Operational limits
  - MGT starting 652°C (1205°F)
  - MGT max continuous 819°C (1505°F)
  - MGT takeoff 870°C (1598°F)
- Torque
  - 715,862 N-m (44,000 ft-lb)

When power turbine (N_P) overspeed was sensed, the control commanded the prop speed toward feather.

Start and/or stop initiation was commanded through a three-position, spring-centered switch. Momentary selection of the start position provided 28 VDC to the control for initiation of the automatic sequencing of the ignition, fuel shut-off (solenoid operated), and starter air control valve. A "manual" fuel shut-off was provided as a redundant means for engine shutdown. With 28 VDC applied, this valve closed and remained closed after engine coastdown, even in absence of the 28 VDC. With zero volts direct current applied, the valve remained open during starting and running. This valve in the fuel control assembly was differentiated from the airframe-mounted fuel isolation valve, which had a mechanical backup actuation mode, sometimes referred to as "manual fuel shut-off."

3.3.4.3 Starter

Allison defined the starter requirements which were met by a Garrett air turbine starter mounted to the accessory gearbox pad. The starter was powered by bleed air from the Spey engines. The air was delivered through an airframe-mounted pressure regulating valve with an opening rate of 28.12 kg/m²/sec (4 psi/sec). This controlled opening rate limited the impact torque for running engagements to 319 N-m (235 ft-lb), well below the limit of 441 N-m (325 ft-lb) established to permit engagement during flight windmilling and on the ground during shaft run-down.

3.3.4.4 Oil Tank

A requirement for 43.5 liter (11.5 gal) oil tank capacity was established based on anticipated flight durations and conservative oil consumption estimates. The vented tank was mounted in the nacelle above the drive system to provide a positive head and therefore avoid the need for boost pumps. The design made maximum utilization of existing tank hardware and was tailored to fit within the confines of the nacelle structure. The sump assembly and scavenge pickup from the P-3 and the filler assembly of the C-130 oil tanks were used. The splash return system (deaeration) was patterned from the successful P-3 design. The oil exited into the tank from a flat nozzle to spray across the top of the tank to maximize surface contact for deaeration. The sump incorporated dual outlets for the power section and gearbox, a shutoff valve, and a temperature bulb to monitor oil temperature out of the tank.

3.3.5 Mounts

The 501-M78 drive system was mounted from the propfan gearbox and power section in the same fashion as for the P-3 aircraft. The mount system incorporated redundant load reaction paths to provide safety from whirl-mode resonance and/or loss of the drive system in the event any of the mounts were damaged in flight.

The gearbox mounts are shown in Figure 52. All mounts were located from the front frame of the QEC/forward nacelle. The main mounts bolted to pads on the side of the gearbox and auxiliary mounts were located at the top and bottom of the gearbox.

The rear mounts were bolted to the rear flange of the compressor case. The upper mount was connected to the QEC/forward nacelle, and the side mount was connected by a link to the aft nacelle.

3.3.6 Installation

The 501-M78 drive system was designed for installation in the PTA QEC/forward nacelle in a fashion similar to that for the P-3 aircraft. The installation design features included:

- T56 type prop gearbox support
- P-3 type mounting of the drive system
- Design to meet the P-3 load envelope with subsequent review of PTA load envelope, to preserve long-lead design releases
- Flightworthy drain/vent systems
- Altitude performance to meet NASA propfan test requirements
- Installation interfaces
- Oil tank sizing and components based on successful aircraft experience

- o Aircraft proven starter system
- o Prop control actuator mounted on the propfan gearbox
- o Fireshield attachment
- o Inspection provisions for installed power section
- o Instrumentation routing to common airframe interface connectors

The PTA nacelle general arrangement drawing, Figure 25, defined the dimensions for the pertinent features of the nacelle and defined the interrelationship between aircraft, powerplant, and engine datum dimensioning systems. This figure depicts the nacelle in the untilted condition, as do all views of the aircraft/propulsion system unless otherwise noted.

As illustrated in Figure 25, the QEC (forward) nacelle and aft nacelle were equipped with adequate doors and removable panels to provide access to all line replaceable units (LRUs), test instrumentation, and service/adjustment points in the nacelle area.

3.3.6.1 Propfan Fuel Supply

The propfan fuel supply was taken from the left wing hopper near the wing root and routed behind the planes of rotation of the engine rotating compressors/turbine components to a shutoff valve that was mounted on the wing front beam outboard of the propfan installation. From the shutoff valve, the fuel line was routed inboard, pierced the side of the aft nacelle, and was connected to a quick-disconnect through the coated frame to the QEC/forward nacelle. All modified/added fuel lines were electrically bonded to the airframe structure.

A fuel supply emergency manual shutoff was provided for the flight engineer to use in case the electrical shutoff valve failed to close in an emergency. A "T"-handle end of a Teleflex control cable was mounted on the aft side of the bulkhead immediately behind the pilot, where it could be easily reached by the flight engineer or copilot. The control cable ran aft under the floor, pierced the FS 321 bulkhead, and traversed the wing front beam and on through the aft nacelle structure to the fuel shutoff/isolation valve. When the handle was pulled, the indicating arm of the shutoff valve was pulled into the closed position.

3.3.6.2 Air Starter System

The pneumatic anti-icing air supply duct was removed from the left wing and was replaced with a duct to supply high pressure air to the air turbine starter for the propfan engine. As shown in Figure 53, a crossover engine bleed air duct was removed between the main propulsion engines, and the exposed ends were capped. The anti-ice valve was recalibrated to serve as the isolation/pressure regulating valve for the propfan starter air supply. Aluminum ducts in the wing fillet and fuselage, with 90 degrees or greater bend angle, were replaced with steel ducts.

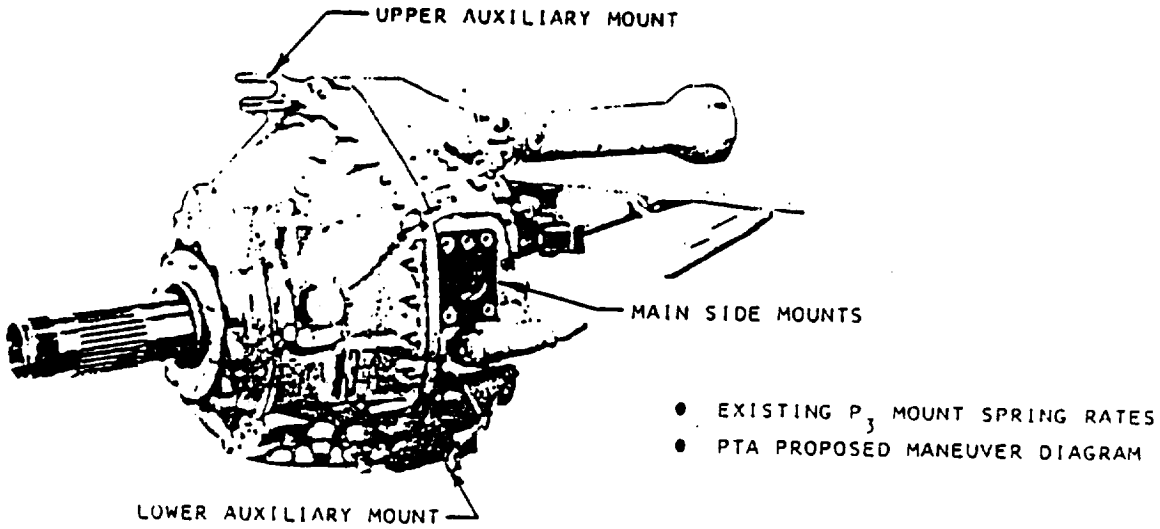


Figure 52. Gearbox Mounts

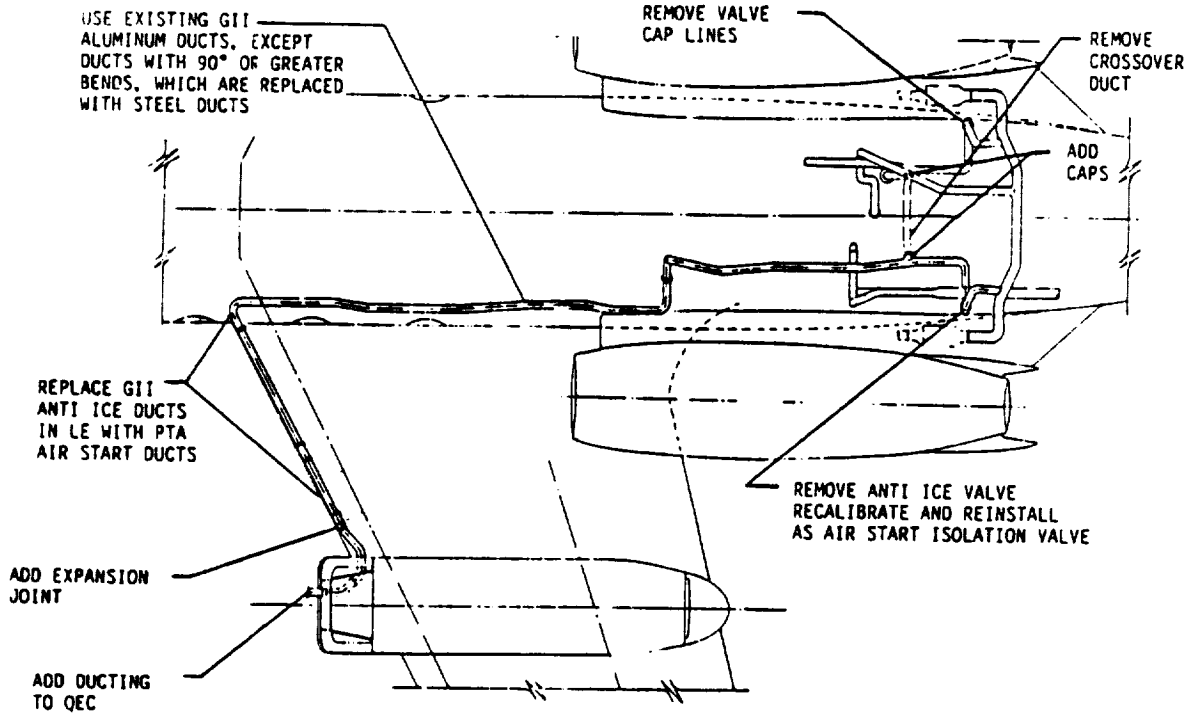


Figure 53. Bleed Air System Modification for Air Start

The controls for the air start system were located on the lower row of the test engine and prop control panel. These controls (engine start switch, air start isolation valve, starter valve open indicator) opened the bleed air isolation valve, pressurized the air start duct, and initiated the propfan engine start cycle. Duct pressurization was monitored on the pressure gage located on the flight engineer's overhead panel, and indicator lights were provided on the panel to annunciate valve "open" positions.

3.3.6.3 Engine Lubrication and Oil Cooling

Installation of the engine lubrication and oil cooling system is shown schematically in Figure 54. This system supplied oil to the engine and reduction gearbox, cooled and filtered engine/gearbox oil, and cooled the propeller hydraulic fluid.

The oil cooler was designed to fit on top of the nacelle behind the engine inlet duct as shown in Figure 31. The entire system was submerged in the upper nacelle contour for minimum high-speed drag. The air inlet was a modified NACA submerged inlet with curved diverging walls, a 12-degree ramp angle, and a width-to-depth ratio at the throat of 2.5. With a diffuser to the heat exchanger, pressure recovery was estimated to be greater than 65 percent of freestream dynamic pressure. The exit flap was estimated to produce a suction of more than 20 percent of dynamic pressure, so the total pressure head across the heat exchanger was estimated to be greater than 85 percent of freestream dynamic pressure. This exceeded predicted requirements by a comfortable margin.

Figure 55 summarizes the oil cooler system performance. There was no problem with continuous operation on a hot day except for the reverse flow static operation where such operation at 746 kw (1000 shp) was time limited. This, however, imposed no significant constraints on PTA operation.

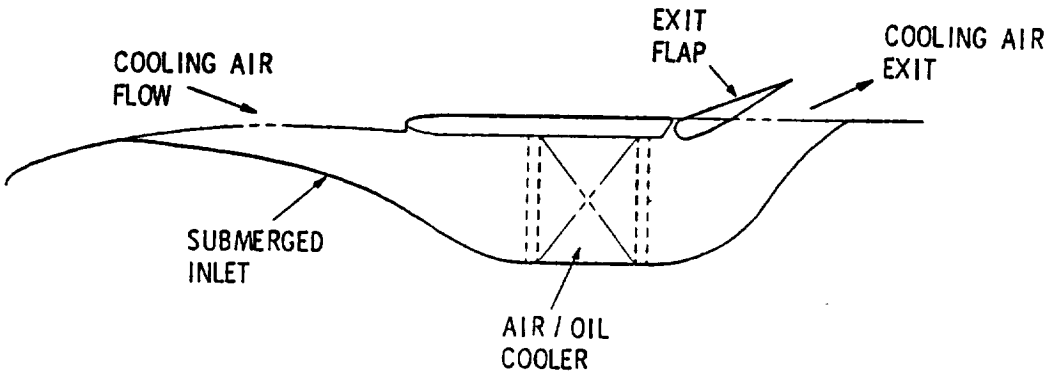
3.3.6.4 Fire Detection and Suppression

Fire detection in the QEC/forward nacelle was provided by a continuous element detector system, shown in Figure 56, connected in series to a similar element in the aft nacelle. The elements were routed through all anticipated high-temperature areas. There were two loops across the top, two loops under the engine, and two loops low and aft where ventilation air exits and spilled fuel may be expected to puddle.

The propfan nacelle fire suppression system consisted of two agent storage bottles which were installed in the fuselage and supplied a distribution manifold in the nacelle as shown in Figure 57.

3.3.6.5 Tailpipe Installation

A stub tailpipe, depicted in Figure 58, was bolted to the engine aft flange. It incorporated vanes to remove the swirl from the exhaust in order to facilitate entrainment of compartment ventilation exhaust flow into the tailpipe. A replaceable nozzle formed the aft end of the stub



OBJECTIVES: SATISFACTORY OIL COOLING
LOW CRUISE DRAG
MINIMUM PROPFAN BLADE EXCITATION

Figure 54. Oil Cooler Design

- 6,000 SHP STATIC OPERATION
  - TOTAL HEAT REJECTION = 3400 BTU/MIN
  - FUEL/OIL COOLER REMOVES 1030 BTU/MIN
  - AIR/OIL COOLER REMOVES 2370 BTU/MIN
  - PERMITS CONTINUOUS OPERATION ON HOT DAY (103°F)
- 3,500 SHP AT 50 KTS
  - TOTAL HEAT REJECTION = 2650 BTU/MIN
  - FUEL/OIL COOLER REMOVES 645 BTU/MIN
  - AIR/OIL COOLER REMOVES 2005 BTU/MIN
  - PERMITS CONTINUOUS OPERATION ON HOT DAY (103°F)
  - LIMITED DURATION OPERATION IN 120°F WIND TUNNEL
  - (OIL TEMP INCREASES APPROX 7°F/MIN)
- 1,000 SHP REVERSE STATIC OPERATION
  - TOTAL HEAT REJECTION = 1890 BTU/MIN
  - FUEL/OIL COOLER REMOVES 480 BTU/MIN
  - AIR/OIL COOLER REMOVES 1075 BTU/MIN
  - PERMITS CONTINUOUS OPERATION ON STANDARD DAY (59°F)
  - LIMITED DURATION OPERATION ON HOT DAY (103°F)
  - (OIL TEMP INCREASES APPROX 10°F/MIN)
- CONCLUSION
  - OFF-THE-SHELF SYSTEM COMPONENTS ADEQUATE

Figure 55. Oil Cooler System Performance

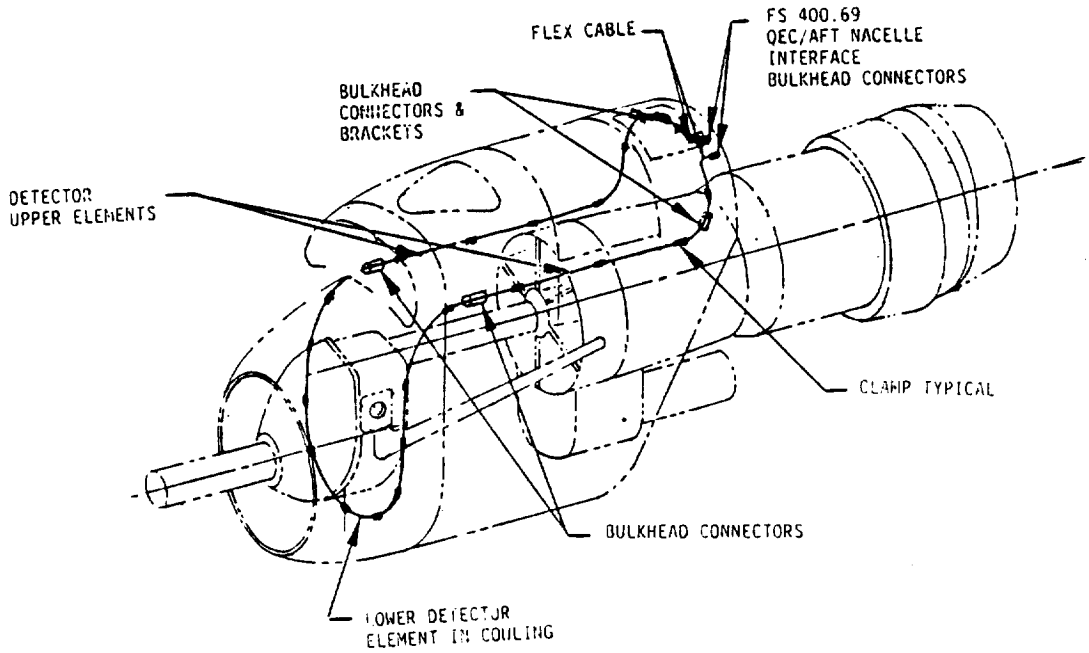


Figure 56. QEC Fire Detector Elements

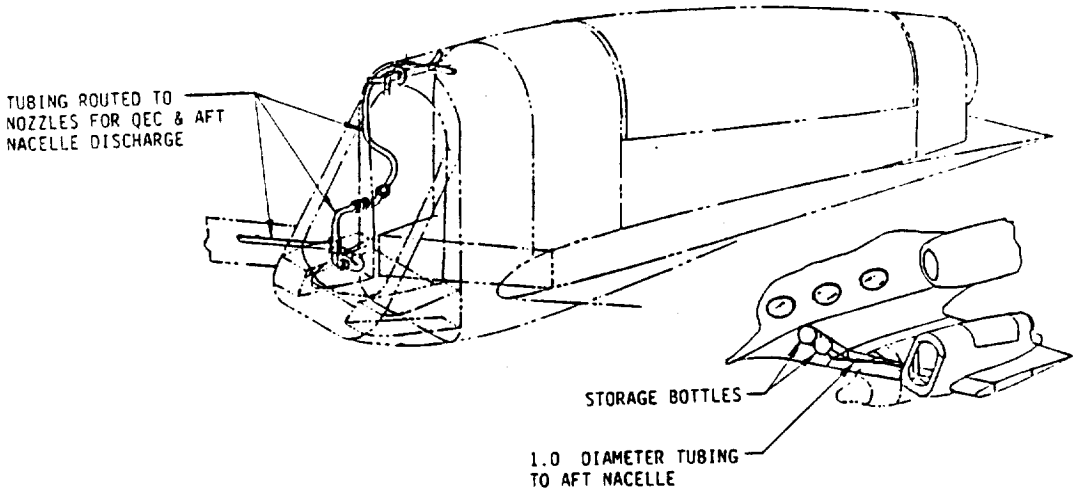


Figure 57. Propfan Fire Suppression System

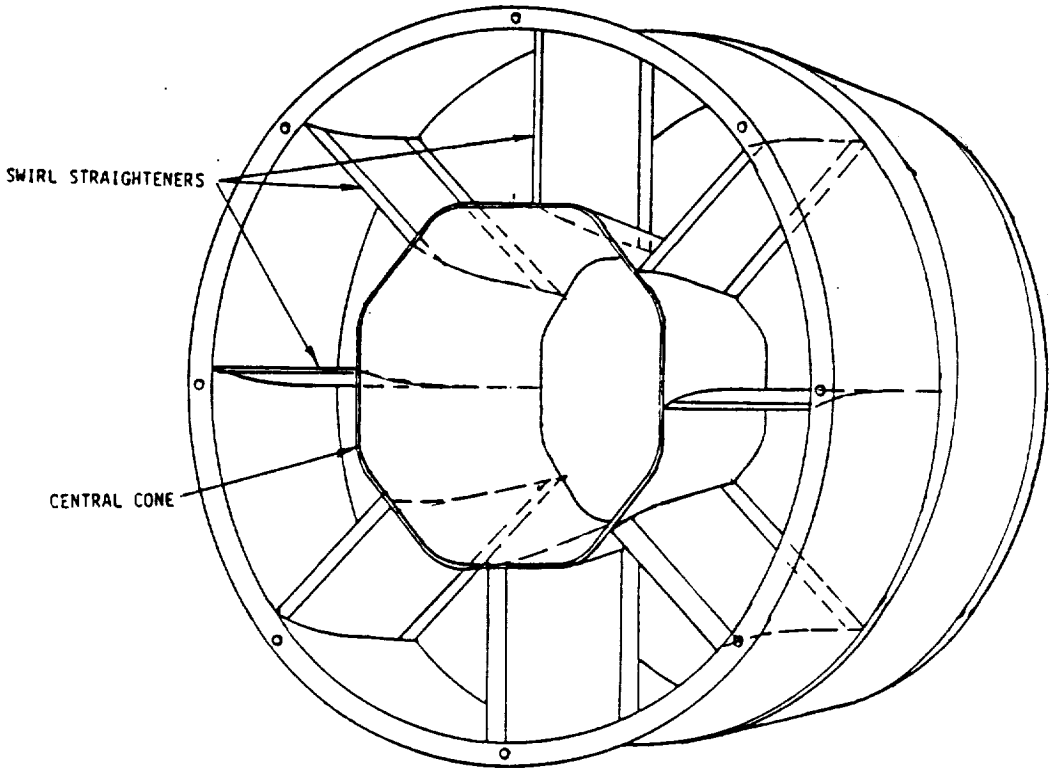


Figure 58. Stub Tailpipe

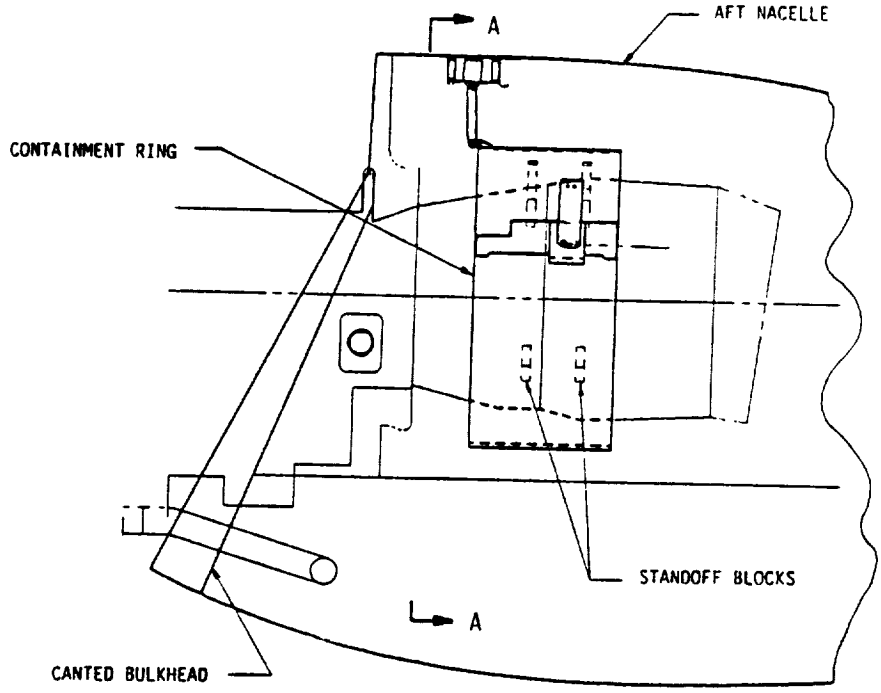


Figure 59. Turbine Containment Ring Installation

tailpipe and was oriented to align the engine exhaust flow with the tailpipe at each of the different nacelle tilt angles as shown schematically in Figue 23.

The tailpipe was pivoted near the exit and was raised or lowered to provide alignment with the stub tailpipe at each nacelle tilt angle. The aft portion of the engine and the tailpipes were wrapped with insulating blankets to protect the nacelle structure from radiated heat.

3.3.6.6 Turbine Containment Ring

The propfan engine turbine was located over a portion of the wing primary structure because it was not possible to increase the wing torsional strength sufficiently to permit location farther forward. In order to protect the wing structure in the event that the turbine suffered an uncontained failure, a machined-steel containment ring was installed as shown in Figure 59. It was bolted to the aft nacelle structure and relocated to align with the engine for each nacelle tilt angle. The standoff or restraint blocks, which are also shown in Figure 43, were designed to transfer failure momentum loads back into the engine casing.

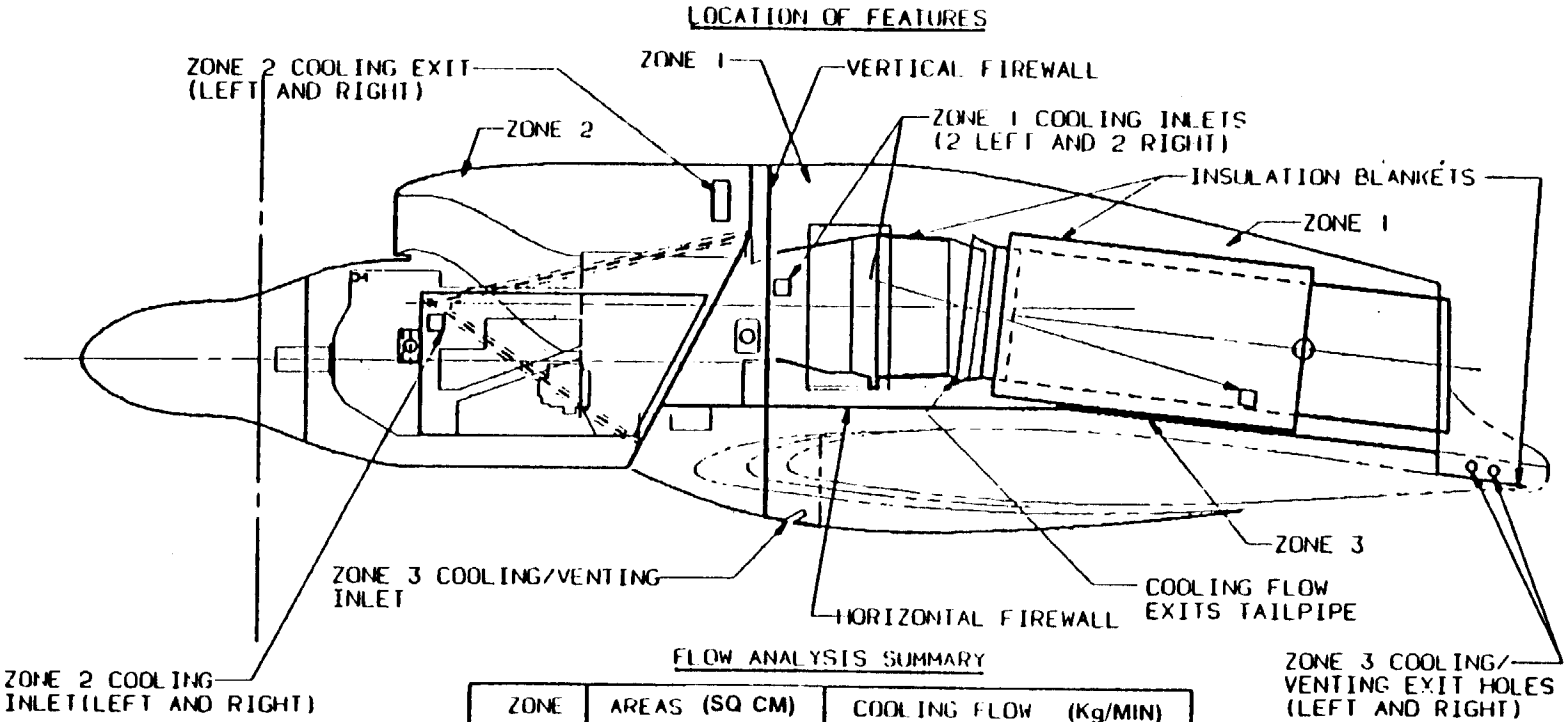
3.3.6.7 Nacelle Cooling

Figure 60 shows the several zones into which the nacelle was divided for fire containment and other safety considerations, and the cooling and ventilation provisions that were made. Zone 1 contained the hot section of the engine and the engine exhaust pipe. This section was isolated by vertical and horizontal firewalls. Zone 2 comprised the cool section of the nacelle forward of the horizontal firewall, and Zone 3 was an air barrier region between the firewalls and the wing structure. The table inset into Figure 60 shows design criteria for cooling and ventilation flow in the three regions and the inlet and exit areas estimated to provide this needed airflow. The locations of inlet and exit ports are also denoted in Figure 60.

The Zone 1 exit port was the open annulus separating the engine tailpipe from the surrounding nacelle structure. This was originally sized at 0.081 m^2 (125 $in.^2$). During flight checkout tests, however, an aft nacelle (Zone 1) heating problem was encountered at high Mach numbers that resulted from a combination of: the jet exhaust thrust being too low to carry hot exhaust gasses completely away from the exit region, a shock-induced flow separation on the aft nacelle that allowed a portion of the hot gasses to reverse flow direction and enter Zone 1, and the area of the cooling air exit annulus being too large. The problem was completely solved only by extending the length of the tailpipe, but in reaching a partial solution, the area of the Zone 1 exit annulus was reduced to approximately 0.026 m^2 (40 $in.^2$), and ram air scoops were added to the flush inlets of Zone 1.

3.3.7 Maintainability

The drive system maintenance plan included pre-flight and post-flight checks and consisted of routine preventive maintenance which involved



FLOW ANALYSIS SUMMARY

ZONE	AREAS (SQ CM) INLET	EXIT	COOLING FLOW (Kg/MIN) •DESIGN POINT	••MAX
1	12.9	806	13.6	68
3	12.9	38.7	1.36 (CHANGES PER MINUTE	

• SLS 39.40C MAX CONTINUOUS TIT
•• SEA LEVEL, 0.5 MACH NO (MAX FLT. EAS)

Figure 60. Nacelle Cooling and Venting

inspections, servicing, and adjustments that could be accomplished on the drive system while it was installed on the testbed aircraft. The checks are enumerated as follows:

PRE-FLIGHT	POST-FLIGHT
Inlet Area	Noise on Coastdown
Nacelle Area	Drains
Engine External	Filter Bypasses
Exhaust Area	Mag Plugs
Filter Bypasses	Engine Accessories
Oil Level	Engine External
Exhaust During Start	Oil Level
Drains During Start/Running	

3.3.8 Qualification

Two complete drive systems were qualified for flight testing through systematic testing of the power sections, gearboxes, control systems and subsystems, and accessories. A third gearbox was used as a slave unit in nose-to-nose gearbox testing at an Allison facility. Figure 61 shows an overview of the test plan for the major drive system assemblies: the gearbox and power section.

3.3.8.1 Controls

All control components were bench-acceptance tested prior to assignment to a power section build. In addition to the individual component tests, all control hardware was mounted on the power sections during power section testing. All components performed satisfactorily during the power section tests, demonstrating that the control system met the functional requirements of the PTA Program.

3.3.8.2 Power Section

Power section testing occurred in parallel with the gearbox component testing. Both 501-M78 power sections were used in the testing, which was conducted in a dynamometer test stand as depicted in Figure 62. The power section drive was input to a dynamometer which provided load absorbing capabilities within program requirements. An air inlet plenum and exhaust nozzle provided the capability to run conditioned air through the power section. The altitude performance envelope was limited by the capability of the test stand systems, necessitating analytical extrapolation of the performance results to the higher altitudes of the PTA flight envelope. The test durations are depicted in Figure 63, and the test envelope is shown in Figure 64.

Power section S/N 0085 became the prime unit. This unit successfully accomplished all its test objectives during 103 hours 23 minutes of operation. The testing included the following simulated inlet conditions.

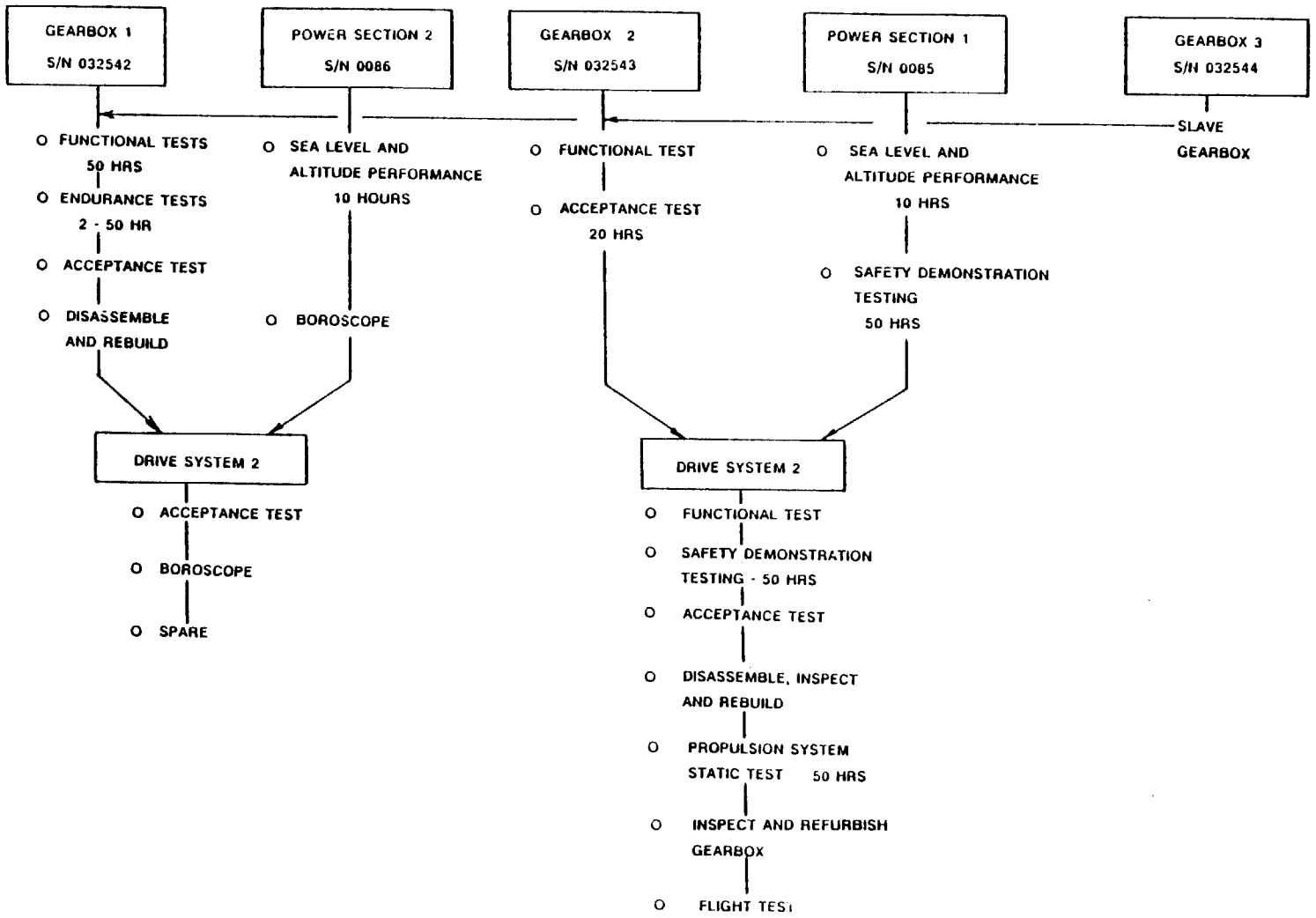


Figure 61. Drive System Test Plan Overview

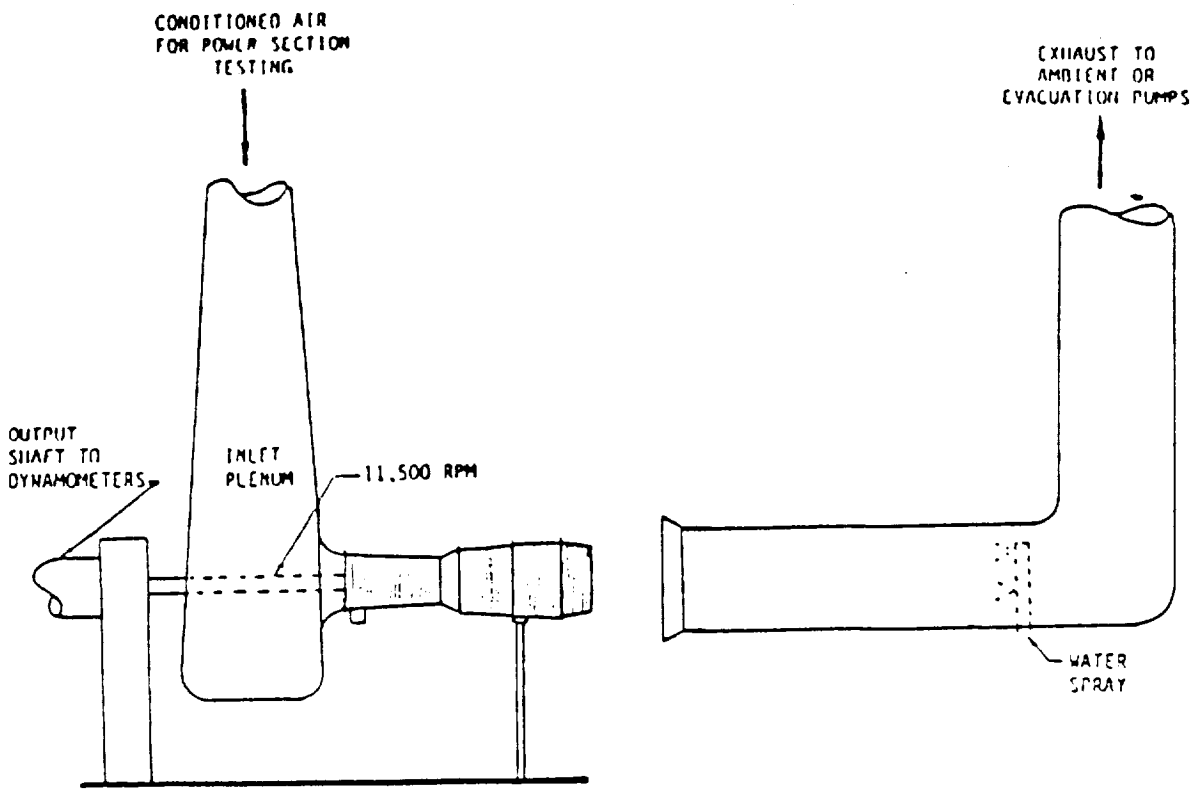


Figure 62. Schematic of Power Unit Test Setup

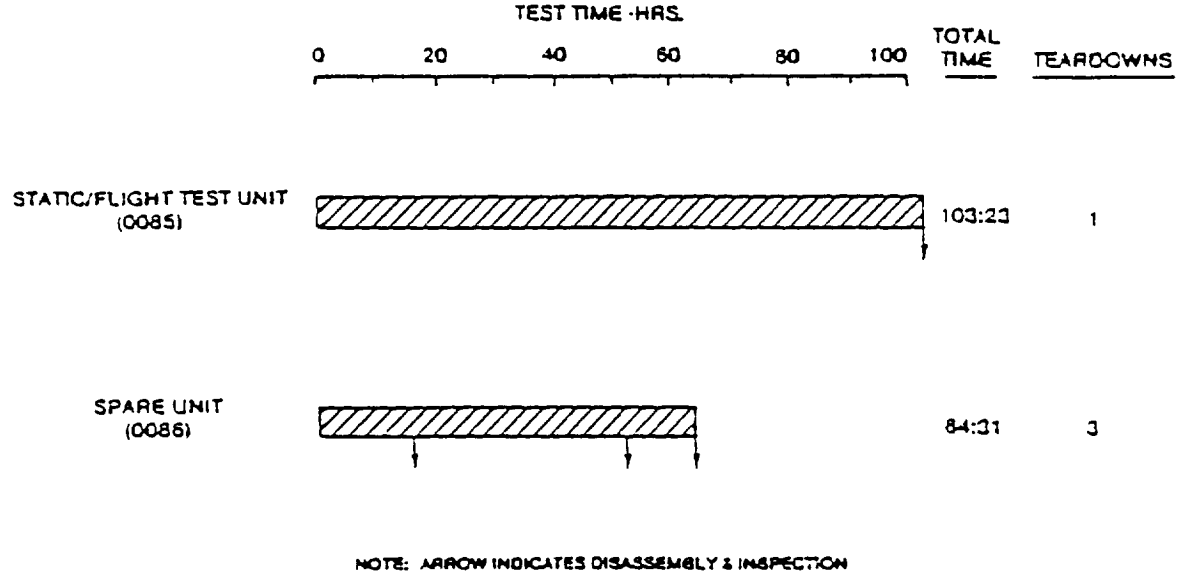


Figure 63. 501-M78 Power Section Component Tests

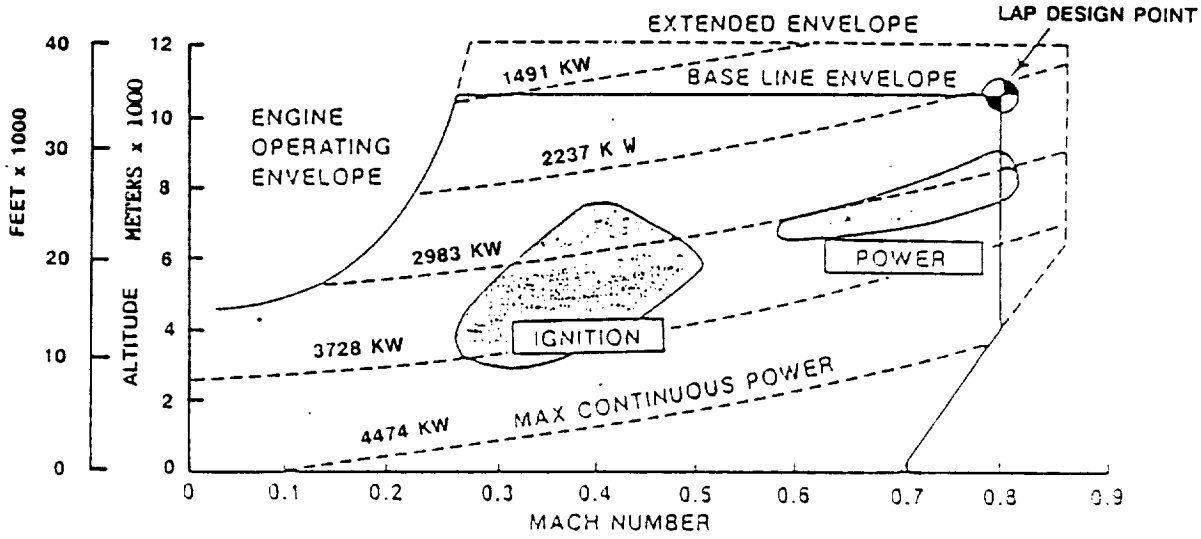


Figure 64. Power Section Altitude Test Envelope

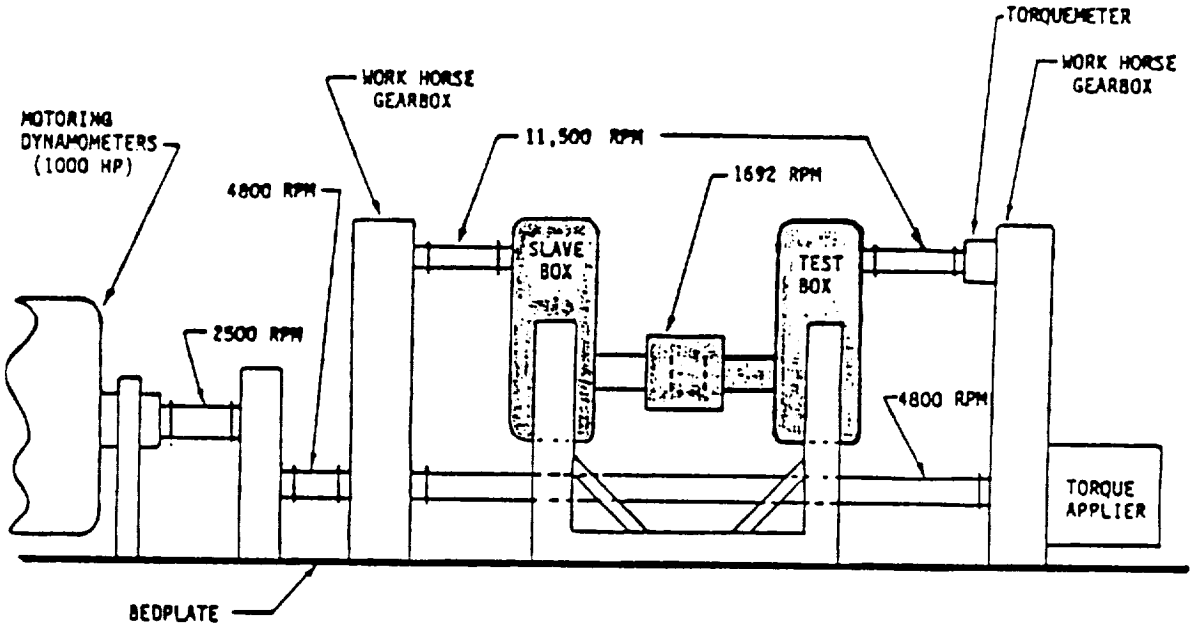


Figure 65. Allison Gearbox Test Arrangement

- o Sea level static performance
- o Altitude performance to 8.53 km (28,000 ft)
- o Altitude performance (as above) with total temperature reduced to that corresponding to 10.67 km
- o Altitude starts (simulated)
- o 60-hour safety demonstration test (SDT)
- o Repeat sea level performance

The 60-hour endurance test was conducted with the primary power section, S/N 0085, for verification of power section durability. The test was run, with ambient inlet and exhaust conditions, after completion of the altitude performance calibration. The following 20-hour schedule was completed three times.

DURABILITY TEST RUN SCHEDULE

	POWER TURBINE SPEED (RPM)			
POWER	8,625	10,062	11,500	12,075
KW (HP)	(75%)	(87.5%)	(100%)	(105%)
1491 (2000)	1:00	0:50	0:50	--
2237 (3000)	1:40	1:40	1:20	1:00
2983 (4000)	0:40	1:20	1:20	0:20
3728 (5000)	0:40	1:20	1:20	1:00
4474 (6000)	0:20	0:20	0:20	0:30

After completion of each 20-hour run, hot section components including the combustion liner, first stage vanes and blades, second stage vanes, and third stage vanes were boroscope inspected. Several fuel nozzles and gas temperature thermocouples were removed for inspection. No distortion, cracks, burning, or other distress was observed after completion of the test. The durability test run was completed with no discernible engine degradation, and the lubrication system verified acceptable operation of the PTA power section vent configuration. The net oil consumption was 0.257 liter (0.068 gal) per hour.

The second power section (S/N 0086) was designated as the spare and was tested for sea level and altitude (8.53 km/0.8 Mach) performance. During the tests, which accumulated 64 hours 31 minutes, the power section was boroscoped and process-inspected as appropriate. Lubrication system compatibility was also demonstrated on this power section. Testing initially showed a need for improved scavenging capability, which was accomplished by reworking the scavenge pump to reduce internal clearances. Prior to the last power section test, the scavenge pump was reworked to tighten gear tip and side clearances. The reworked pump worked well against back

pressure with nacelle components in the system and demonstrated satisfactory scavenge performance.

Demonstration of the altitude light-off characteristics for the PTA configuration power section was completed on S/N 0086. The power section lighted and reached stabilized idle on every attempt with simulated altitudes of 3,048m (10,000 ft) and below. Above that altitude, the power section did light-off but stagnated before reaching idle. The test results validated the PTA engine specification.

Light-off demonstrations up to 8.2 km (25,000 ft) and 0.5 Mach indicated that air starts would not be a problem, as confirmed in the flight test program. Altitude light-offs were successfully demonstrated at all inlet conditions attempted:

Altitude	Mach Number
Sea Level	0.2 and 0.5
1,524m (5,000 ft)	0.2 and 0.5
3,048m (10,000 ft)	0.2 and 0.5
4,572m (15,000 ft)	0.3
6,096m (20,000 ft)	0.4
7,620m (25,000 ft)	0.5

The performance of the PTA power sections with the Model 501-M78 specification is summarized below for 100 percent power turbine speed and standard inlet conditions for the indicated flight conditions:

	POWER SECTION 0085	POWER SECTION 0086	MODEL SPECIFICATION
dSea Level/Static			
Rated MGT, °C (°F)	808 (1486)	808 (1486)	808 (1486)
Rated Power, kw (hp)	4612 (6185)	4500 (6035)	4430 (5941)
8534m (28,000 ft), Mach 0.8			
Rated MGT, °C (°F)	804 (1479)	805 (1481)	808 (1486)
Rated Power, kw (hp)	3106 (4165)	3098 (4154)	2983 (4000)
10,668m (35,000 ft), Mach 0.8			
Rated MGT, °C (°F)	807 (1485)	809 (1488)	786 (1447)
Rated Power, kw (hp)	2307 (3094)	2344 (3143)	2215 (2970)
Power Design Point, kw (hp)			1933 (2592)

Both Model 501-M78 power sections satisfied the sea level static and altitude performance specification requirements. At sea level static, the demonstrated power margin above specification at maximum continuous rated

temperature of 808°C (1486°F) was 3.1 percent with S/N 0085 and 1.2 percent with S/N 0086. Similarly, the demonstrated power margin at 8534m (28,000 ft) and 0.8 Mach was 2.6 percent with S/N 0085 and 2.3 percent with S/N 0086.

3.3.8.3 Gearbox

Three T56-A-14 gearboxes were purchased for the PTA Program. Two were modified as described in Section 3.2.2 and identified as the static/flight test unit (S/N 032543) and the component test endurance unit (S/N 032542). The third unit (S/N 032544) was modified in a slightly different manner to allow reverse rotation for use as the slave unit in a nose-to-nose gearbox test configuration. The objectives of the test were threefold:

1. To prove acceptability of the 501-M78 gearbox design throughout the PTA speed and load range
2. To determine the operating characteristics of the gearbox including oil pressure, oil flow, heat rejection, and vibration levels throughout the operating range
3. To verify the integrity and durability of the hardware

The gearbox component testing revealed that the 501-M78 design was satisfactory throughout its specified operating range.

Two gearboxes were installed in a nose-to-nose configuration, as depicted in Figure 65. A hydraulic torque applier loaded up the continuous loop system through one of two workhorse gearboxes with a dynamometer absorbing this load. In Figure 66, Gearbox No. 1 (S/N 032542) and the slave gearbox are shown installed in the test cell. This arrangement provided a convenient means for evaluating the gearbox components over the intended speed and load range. The metoring dynamometer supplied only the power required to overcome system functional losses. The test rig consisted of the following items:

o Workhorse gearboxes (single stage reduction)	2 each
o Test gearbox (501-M78)	1 each
o Slave gearbox (501-M78, except that it used an external lubrication system and had no accessory gears)	1 each
o Torque applier (rotary, hydraulic)	1 each
o 2:1 speed increasing gearbox	1 each
o Motoring dynamometers	2 each

Over 700 hours of test time were accumulated among the three gearboxes, as summarized in Figure 67. Of the total, 132 hours were accumulated at



Figure 66. Nose-to-Nose Gearbox Test Rig

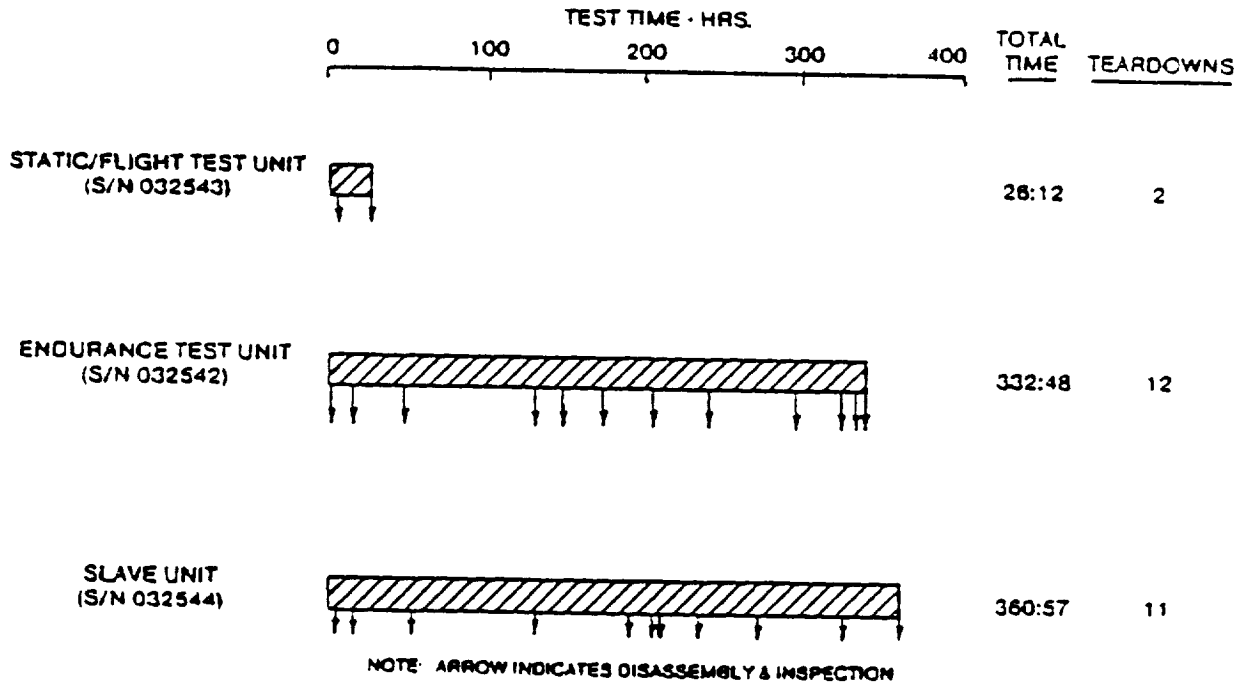


Figure 67. Gearbox Component Testing

ORIGINAL PAGE
BLACK AND WHITE PHOTOGRAPH

4474 kw (6000 hp). The static/flight test unit was subjected to operational and functional testing followed by a brief acceptance test. The endurance test unit accrued over 300 hours of operational, functional, mixed power endurance, and high power endurance prior to refurbishment and acceptance testing. The slave unit accumulated the sum of the times from these two gearboxes plus a small amount of time for torquemeter stand calibration. The distribution of test time among the three gearboxes is shown in Figure 68.

Following completion of the endurance test program, gearbox S/N 032542 was disassembled and inspected, critical parts which had consumed a large percentage of predicted life were replaced, the prop brake was installed (not compatible with nose-to-nose testing), and a 2-hour acceptance test was run to qualify it as a spare gearbox.

Operating characteristics for the PTA gearbox, including oil pressure, oil flow, heat rejection, and overall vibration levels, were recorded as functions of load and/or speed. Oil pressure, flow, and heat rejection data compared favorably with design expectations. Vibration levels were considered acceptable based on T56-A-14 gearbox test experience.

Following the static test, instrumentation and minor power section refurbishment activities were accomplished in preparation for flight test.

3.4 INSTRUMENTATION

3.4.1 Data System General Description

Research test requirements to monitor and record over 600 data parameters, and telemeter to a ground station over 100 of these parameters simultaneously, dictated unique design requirements for the PTA testbed data acquisition system. These recording/monitoring requirements are summarized as follows:

- 127 acoustic parameters
- 221 pressure pickups
- 100 vibration/acceleration channels
- 36 propfan load/strain parameters
- 59 aircraft operational parameters
- 56 propfan propulsion system parameters
- 14 wing strain channels
- 126 aircraft operational/flight acceleration channels

In order to satisfy these requirements, the data acquisition system was designed to use two primary multiplexing methods. A pulse code modulation (PCM) system and a constant bandwidth frequency modulation (CBFM) system were used to condition the data signals for recording on a 28-track, 1-inch magnetic tape. PCM was used for low frequency parameters such as vehicle operational, propfan propulsion system, and pressure scanning

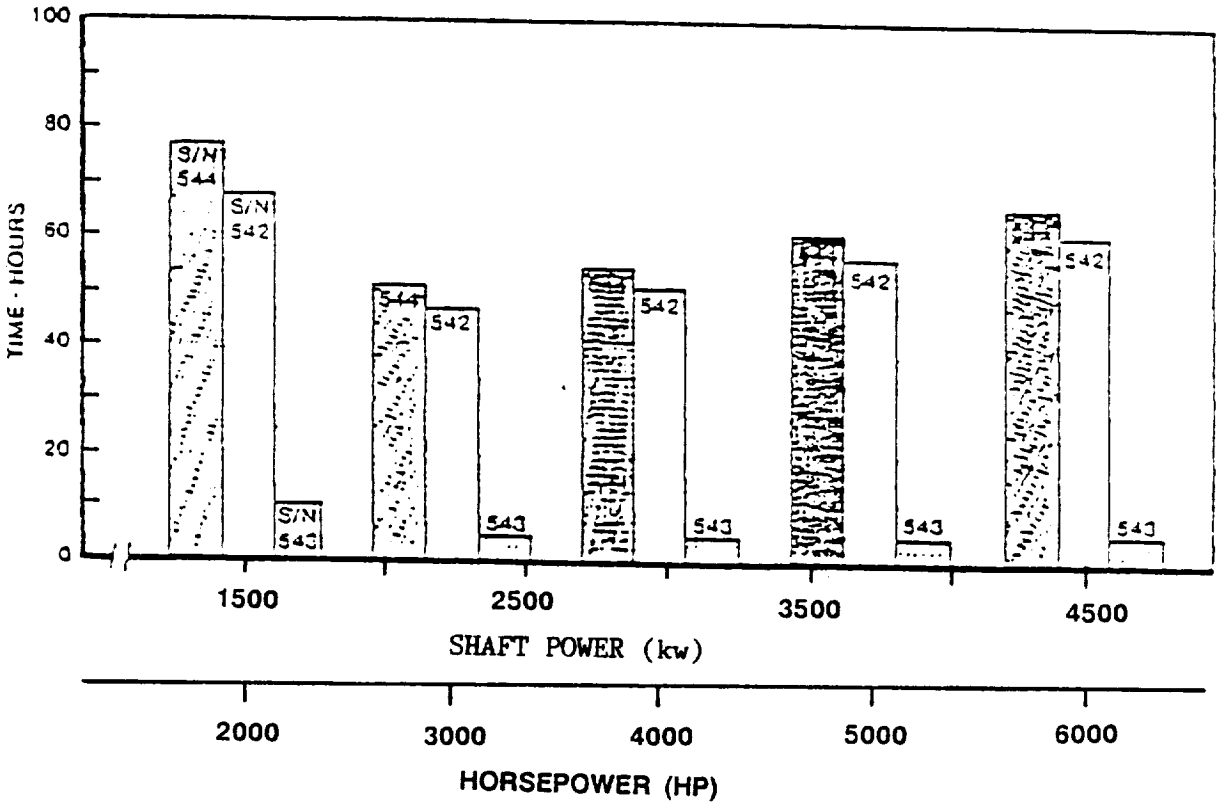


Figure 68. Gearbox Component Test Time Distribution

systems. CBFM was used to condition all dynamic data such as microphone and acceleration with frequency response requirements up to 2 kilohertz.

Hamilton Standard provided the data acquisition system for monitoring and recording the propfan load/strain parameters. All other data were recorded on the Lockheed system. A schematic of the Lockheed data acquisition system is presented in Figure 69, and, as shown in Figure 69, an airborne CRT data monitor was provided for monitoring in real time any PCM data channels in engineering units. Any channel could be selected from the keyboard and monitored continuously as a test progressed.

Constant bandwidth FM data could be examined in real time using an oscilloscope to display the switched output of the discriminator set for electrical noise content, adequate signal level, and signal clipping. This system was used throughout the acoustic data gathering phase to verify proper microphone signal level for subsequent analysis.

All PCM channels were telemetered to the ground for real time analysis primarily during flight airworthiness tests.

3.4.2 Aircraft Flight Instrumentation

The flight instrumentation consisted of aircraft condition parameters, wing/nacelle static pressures, and accelerometers for flight flutter use. All of these parameters, except the static pressures were a part of the PCM system that provided real-time monitoring capability on board the aircraft and the telemetry link for real-time analysis on the ground. A summary of the flight instrumentation is presented in Figures 70-85.

3.4.3 Drive System Instrumentation

The drive system instrumentation consisted of the following groups.

- QEC ambient air/structure temperatures
- Aft nacelle ambient air/structure temperatures
- Engine environment temperatures
- QEC subsystem temperatures
- Engine operational parameters
- Engine vibration pickups

With exception of the engine vibration, all the drive system instrumentation was processed through the data acquisition PCM system which provided real-time monitoring capability both on board the testbed and on the ground through the telemetry down link. The primary purpose of this instrumentation was for ground checkout and flight airworthiness tests of the propfan propulsion system. Figures 75 through 82 summarize the drive system instrumentation relative to location and type of measurement.

3.4.4 Acoustics Instrumentation

The microphones, accelerometers, and strain gages for acoustics and vibration measurements were purchased from commercial suppliers, as were the

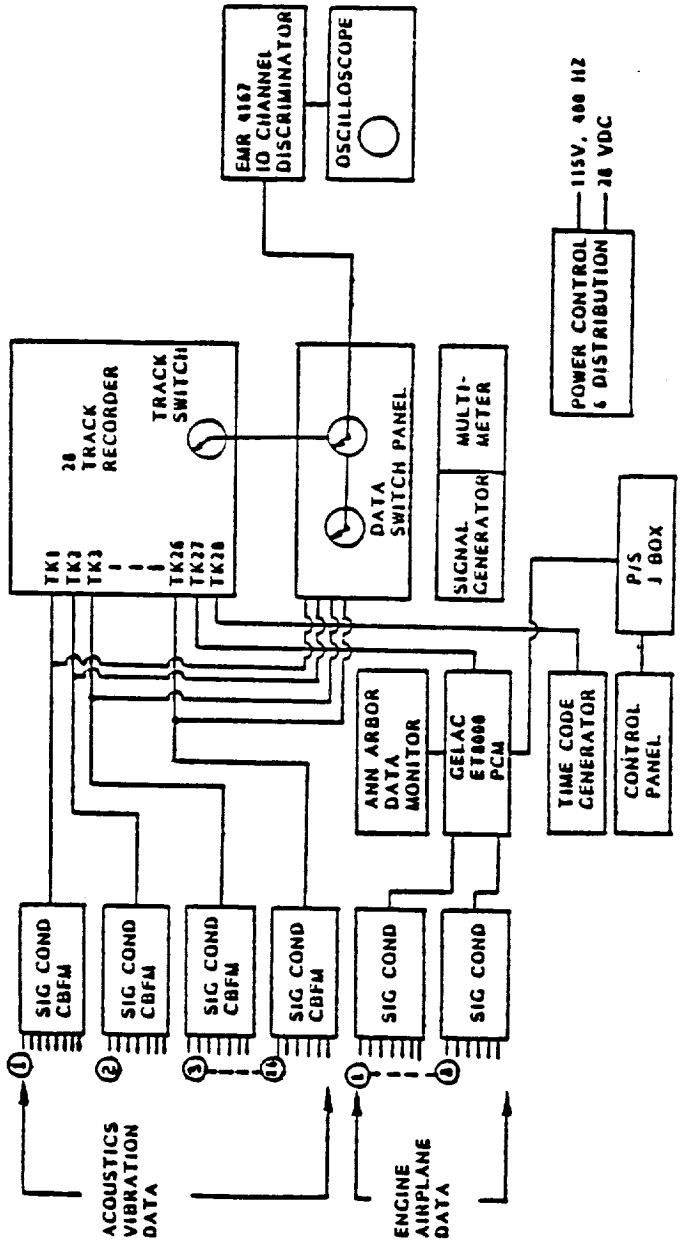


Figure 69. PTA Data System

28-channel, direct-record tape recorder and the two multiplexing systems. The static pressure porting devices; the 260 channels of dynamic signal conditioning hardware; the on-line signal selection, monitoring, and display hardware; and the special power supplies were Lockheed-designed and fabricated.

In general, the acoustic instrumentation was "current technology" and did not entail extensive development work. A few of the system design activities and technical features are worthy of note. A description of these follows.

High-speed flow tests were conducted to aid in the selection of microphones (pressure transducers) and accelerometers, and to evaluate surface mounting techniques. The primary motivation was to minimize the aerodynamic noise contamination and, in the case of the pressure transducers, to refine the static equilibrium vent.

As a result of these efforts and other considerations, the transducer selected for fuselage external surface and microphone boom sound pressure measurements was the Kulite Model XCS-92-093-2D. This is a piezoresistive D-C excited, Wheatstone bridge transducer with integral temperature compensation and a working-pressure range of ±2 psi differential. A typical installation arrangement of this cylindrical .093-inch diameter transducer is illustrated in Figure 83.

The transducer selected for the slipstream fluctuating pressure measurements on the wing was the Kulite Model LQ-IAL-200-2D. This is a similarly functioning device, but thin and rectangular in shape. These transducers were recessed into the wing surface as illustrated in Figure 84.

The microphone boom transducer type and arrangement was similar to the one in the fuselage. The transducers were installed in a plug which was inserted from the opposite side of the boom, as shown in Figure 85.

The comparatively controlled environment in the cabin permitted use of conventional laboratory microphones. The B&K Model 4176 condenser microphone and Model 2639 preamplifier were selected. The same combination was chosen for fixed locations on the wall and for the movable locations on the traverse.

An evaluation of the turbulence generated by the externally-mounted wing surface accelerometers led to the decision to locate all of these accelerometers on the lower surface (underside) of the wing. A miniature unit was selected for the wing and used universally in the fuselage, boom, and nacelle. This was the Endevco Model 2250A piezoelectric accelerometer with built-in charge amplifier.

To measure acoustically-induced dynamic strain in the wing spars, Micro Measurements Model CEA-250UW-350 strain gages were selected. These are constantan foil gages with a phenolic backing, bonded with epoxy cement. The strain gages were positioned on the upper and lower caps of the front and rear spars near the fuselage/wing juncture.

The specific locations for the various acoustic measurements and the final division of the 260 available data channels continued to be refined during the design phase. These specifics were finalized during the test planning and hardware fabrication/modification phase.

The acoustic instrumentation design effort included the design of hardware and procedures for in situ calibration of the microphones and accelerometers and for phase calibration of the transducers and the data acquisition system. Microphone phase accuracy was checked prior to installation, using a dual-transducer pressure stimulus device and cross spectrum analysis. Phase relation among the various channels of the acquisition and recording system was periodically determined by inserting and recording an AC signal through all 260 data channels simultaneously.

3.4.5 Propfan Blade Instrumentation

The propfan blade instrumentation was designed and installed by Hamilton Standard and is described in some detail in Section 6.4.1. It included up to 10 strain gages on each blade to measure vibratory strain and instrumentation to measure blade angle and propfan rotational speed.

Data from the blade instrumentation was recorded on a 14-track IRIG tape recorder. During tests, eight channels of data could be displayed and monitored simultaneously on two oscilloscopes in the aircraft cabin, and one channel could be displayed on a spectrum analyzer. This data system was manned by a Hamilton Standard engineer during all tests in which the propfan was operated.

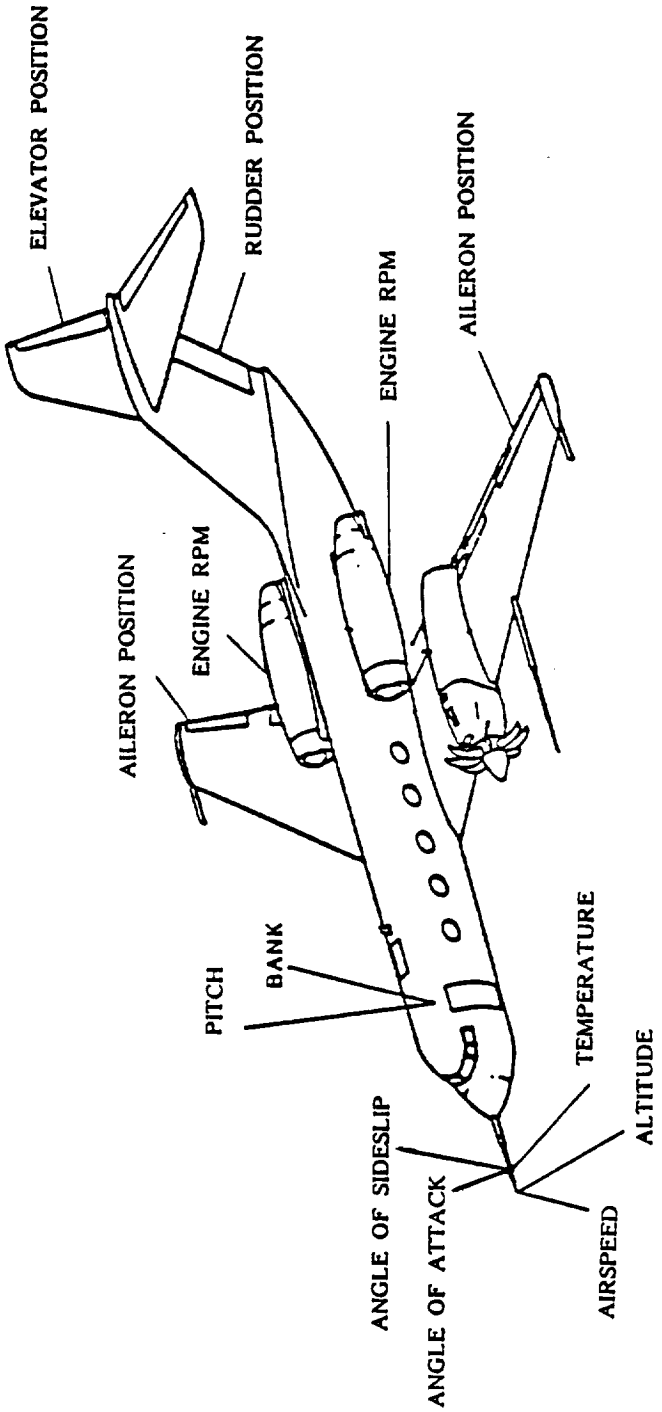


Figure 70. Aircraft Flight Instrumentation

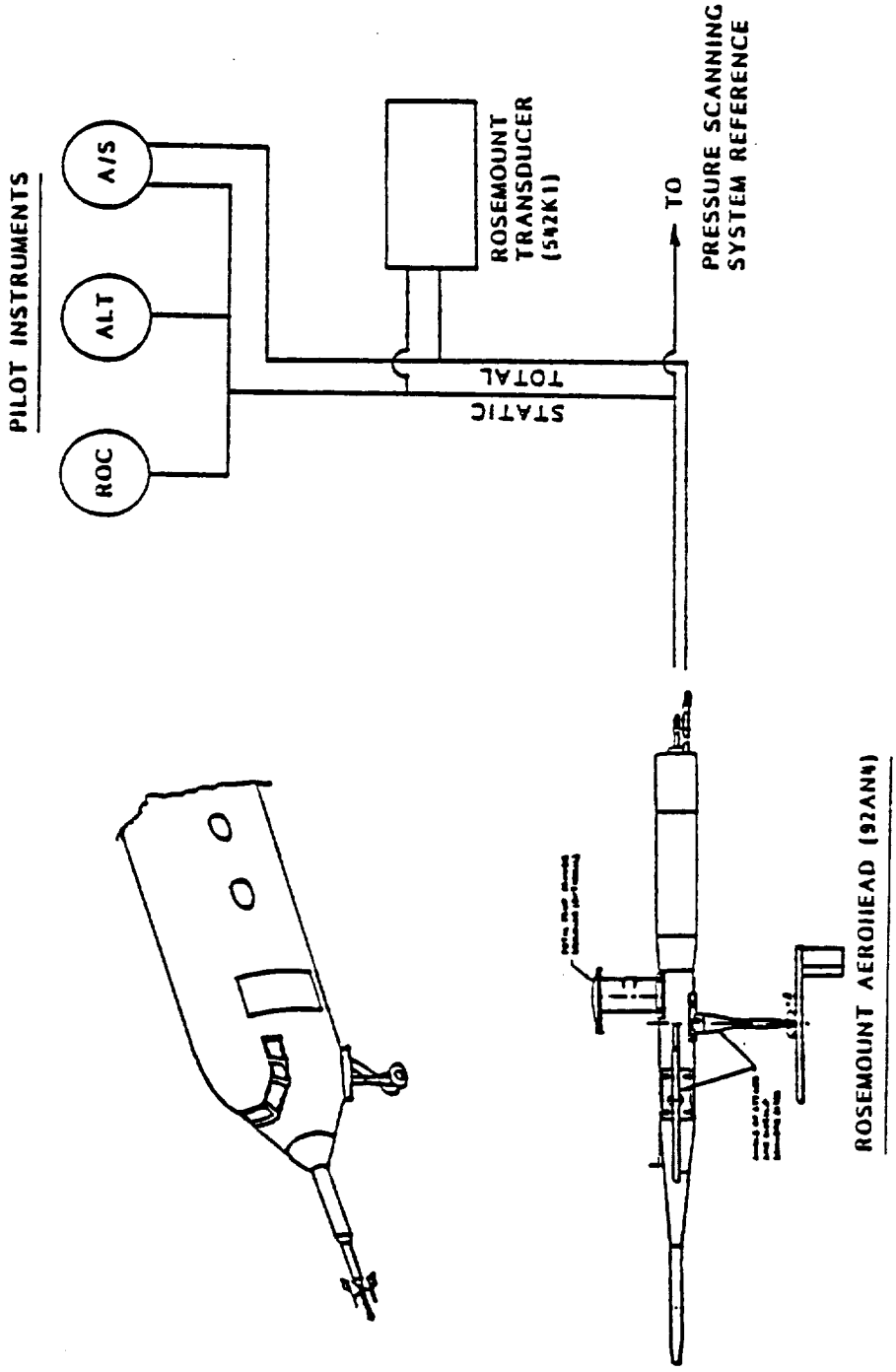


Figure 71. Aircraft Airspeed System

SUMMARY

WING (4), N_z, FRONT, AFT BEAM

ACOUSTIC BOOM (2), N_z, N_y

HORIZONTAL STABILIZER (3), N_z-RT, N_z & N_x-LT

TEST ENGINE (2) - N_z & N_y

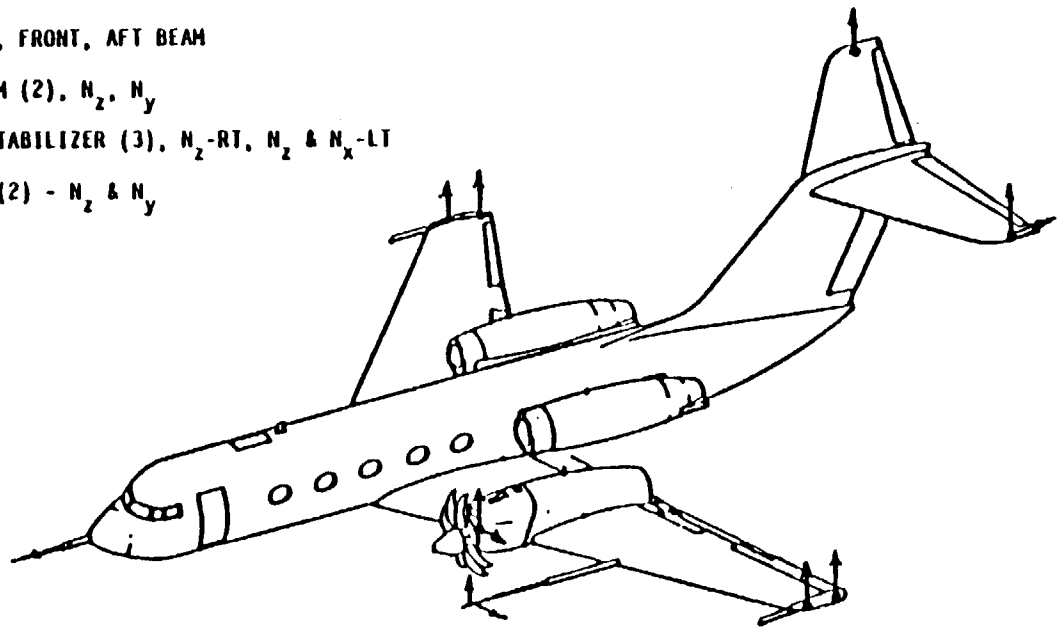


Figure 72. Flutter Accelerometer Locations

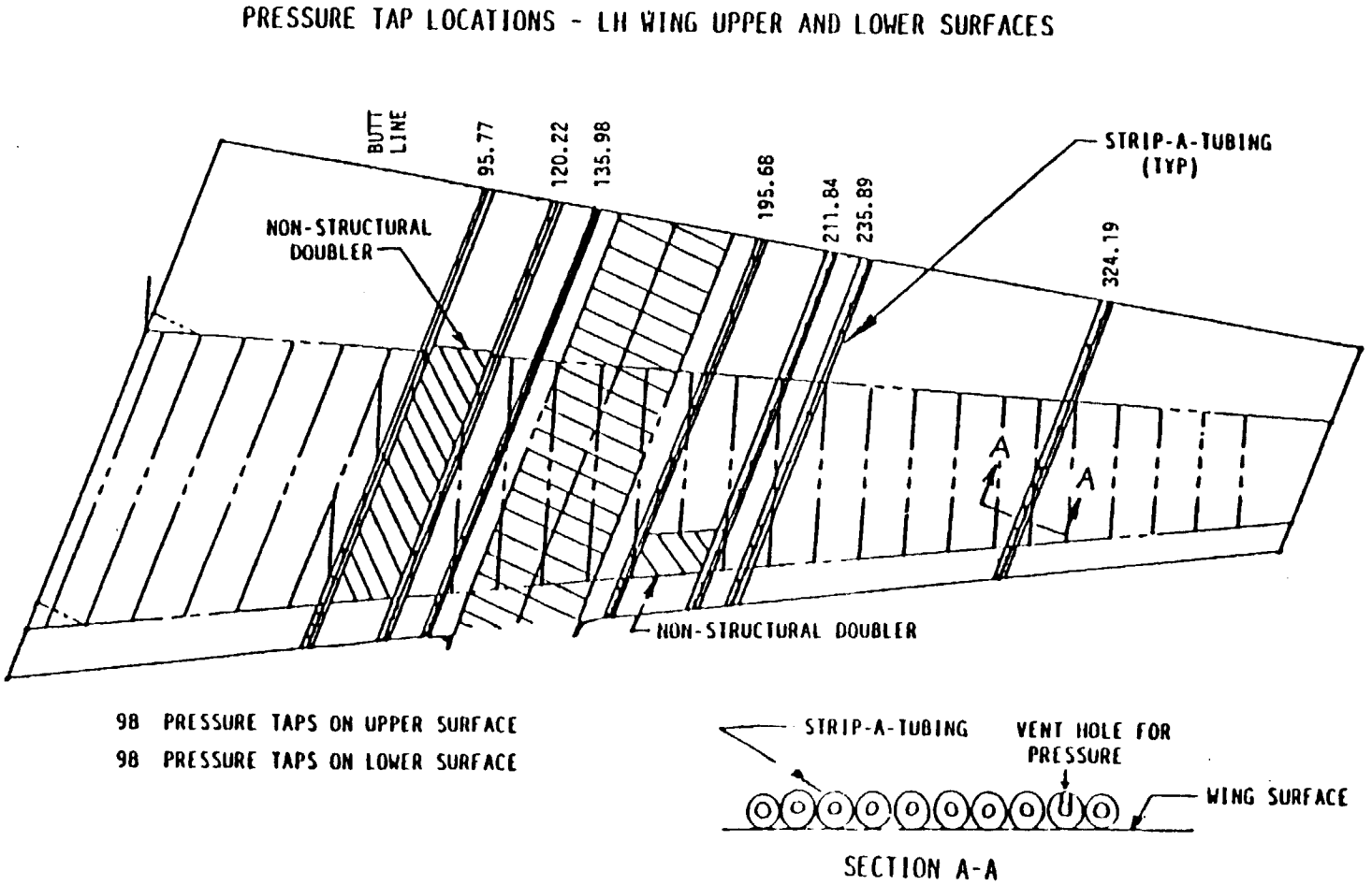


Figure 73. Wing Surface Static Pressures

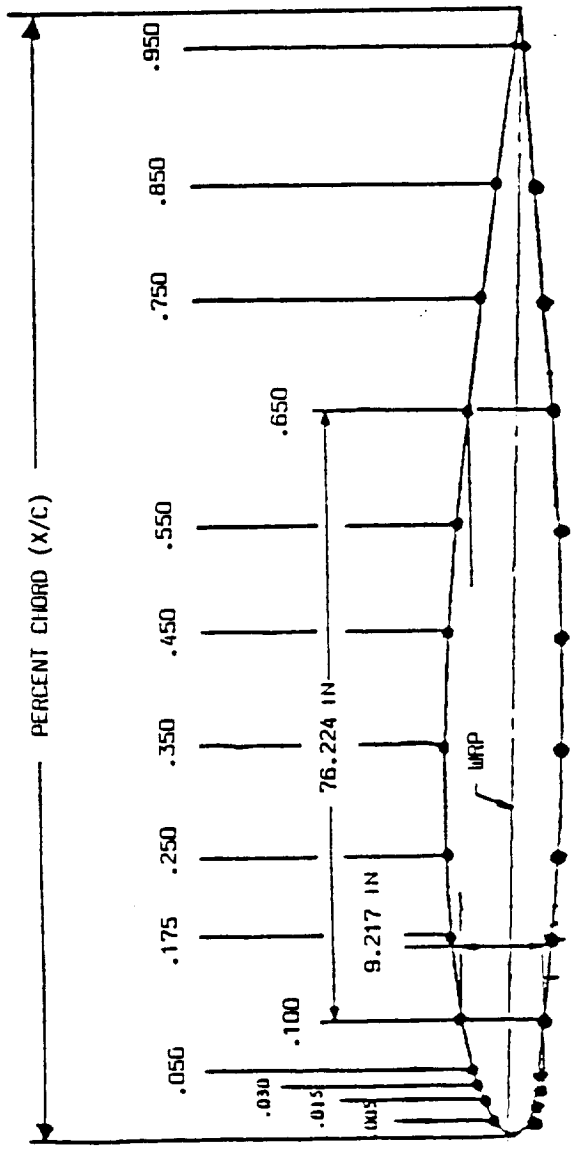


Figure 74. Typical Wing Pressure Tap Distribution

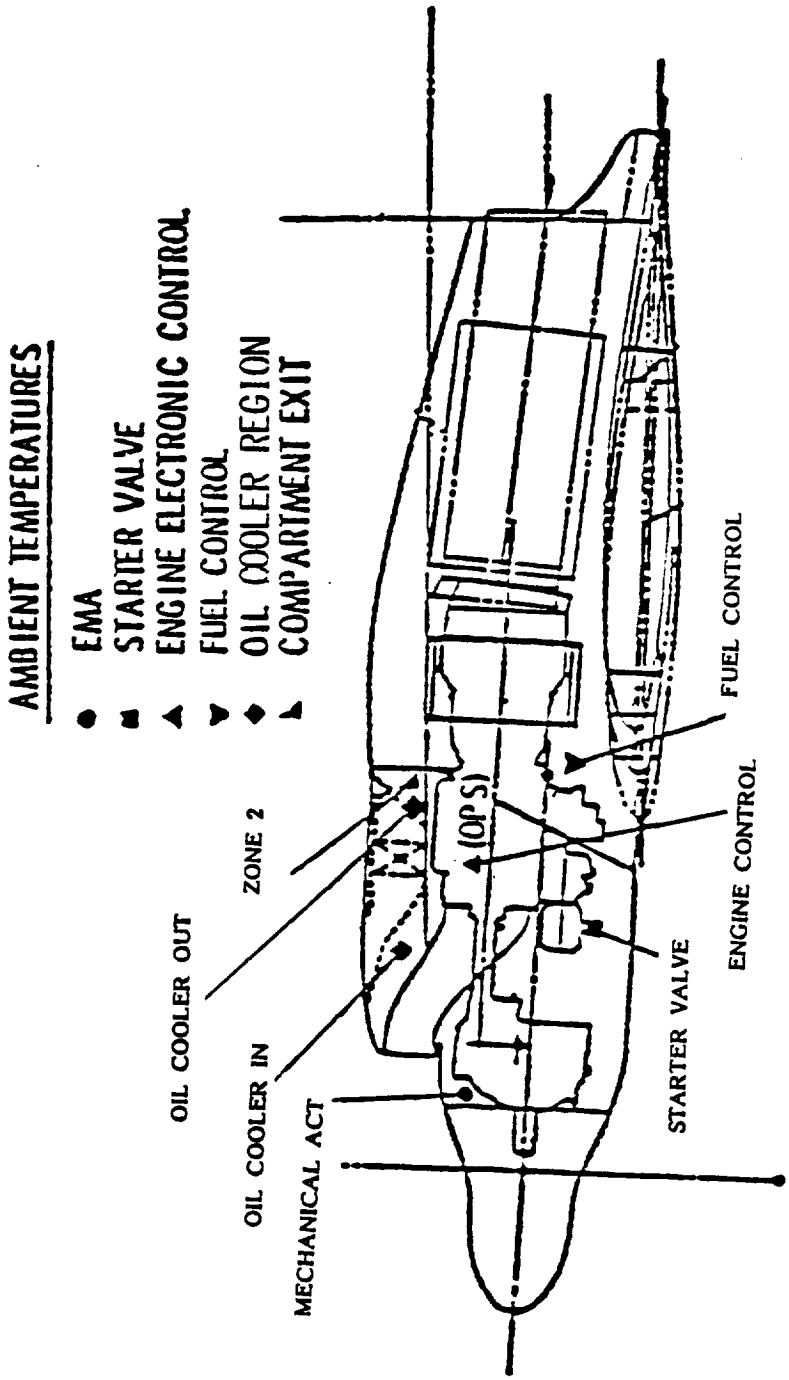


Figure 75. QEC Air Temperature Measurements

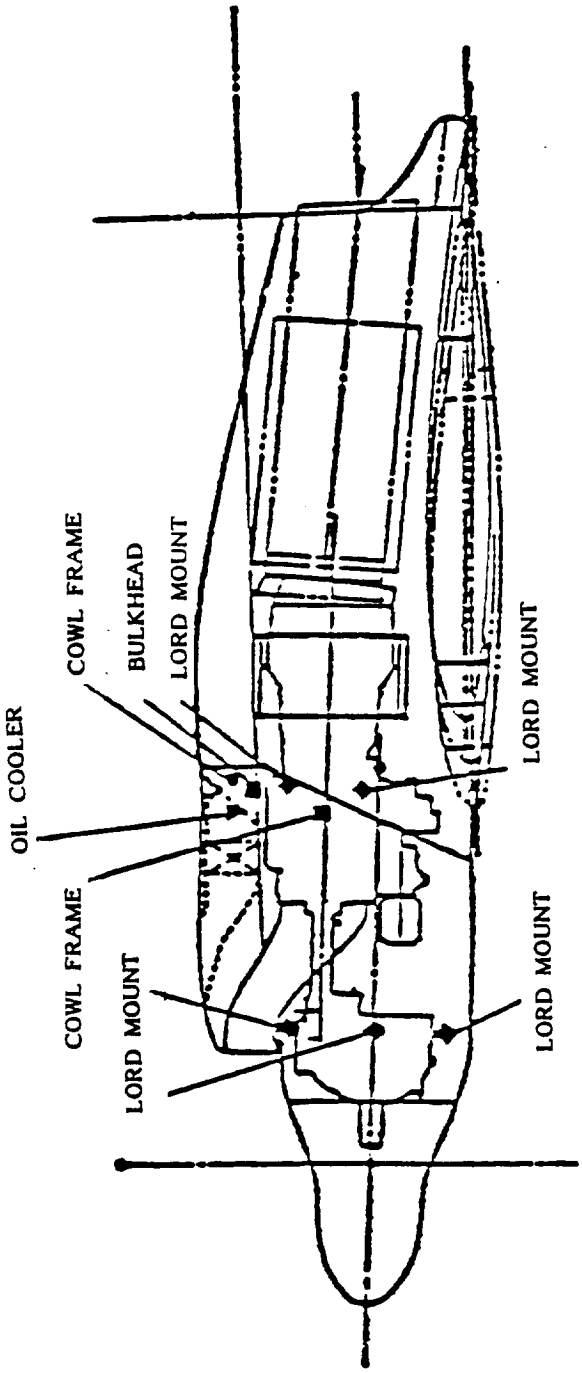


Figure 76 QEC Structural Temperature Measurements

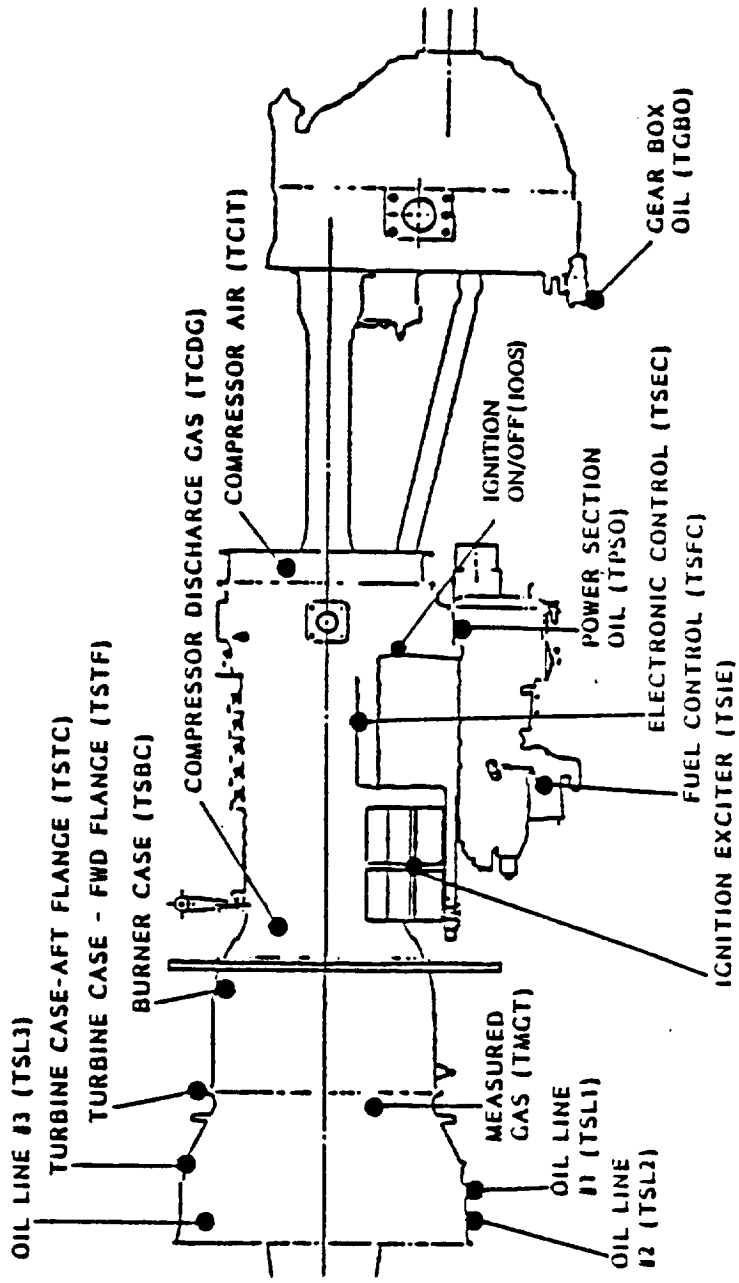


Figure 77. Drive System Air, Oil, and Surface Temperature Measurements

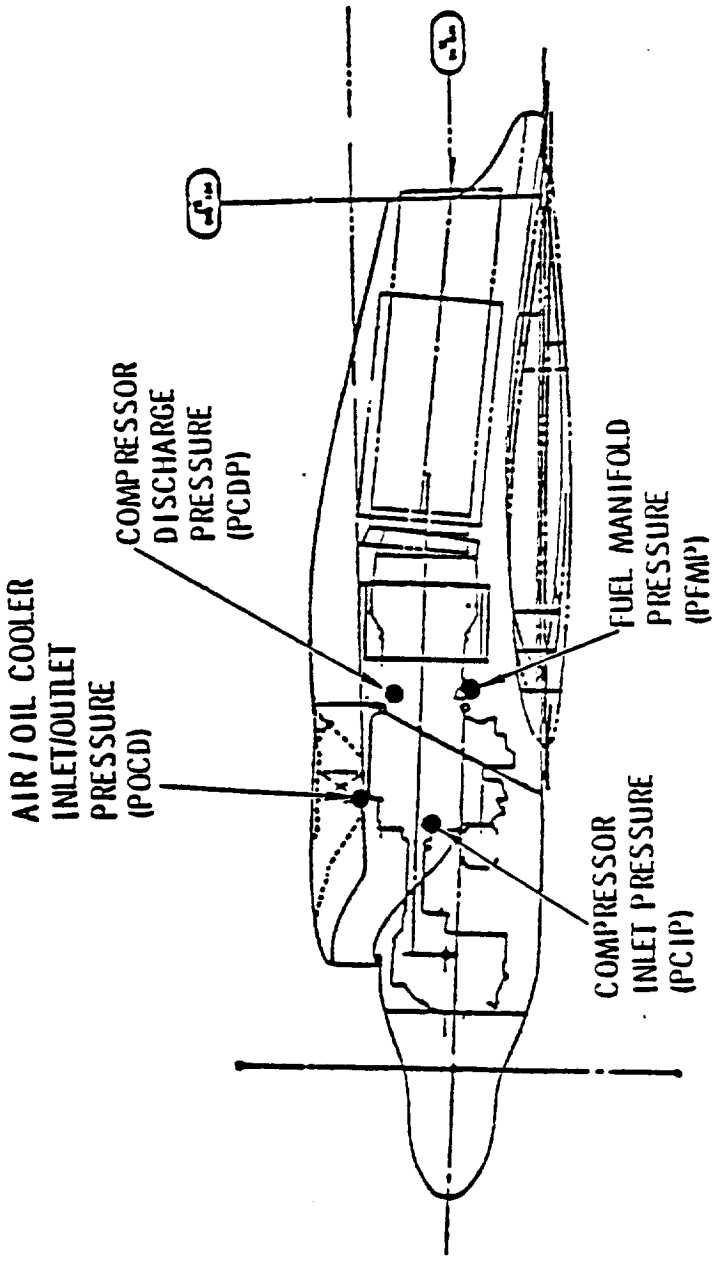


Figure 78. Subsystem and Engine Research Pressure Measurements

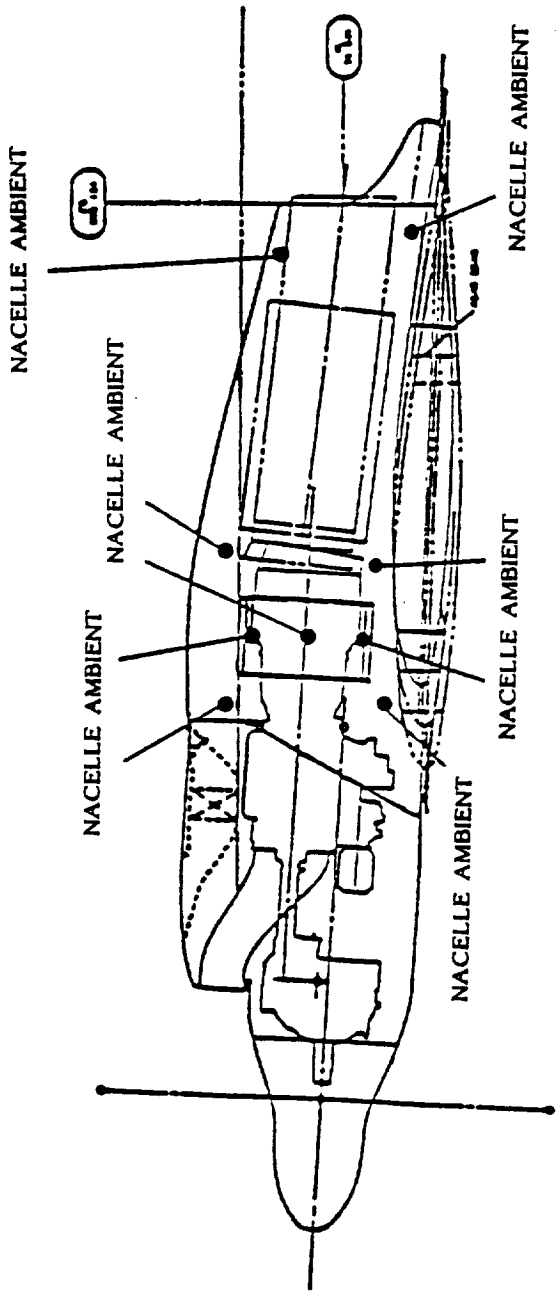


Figure 79. Aft Nacelle Ambient Temperature Measurements

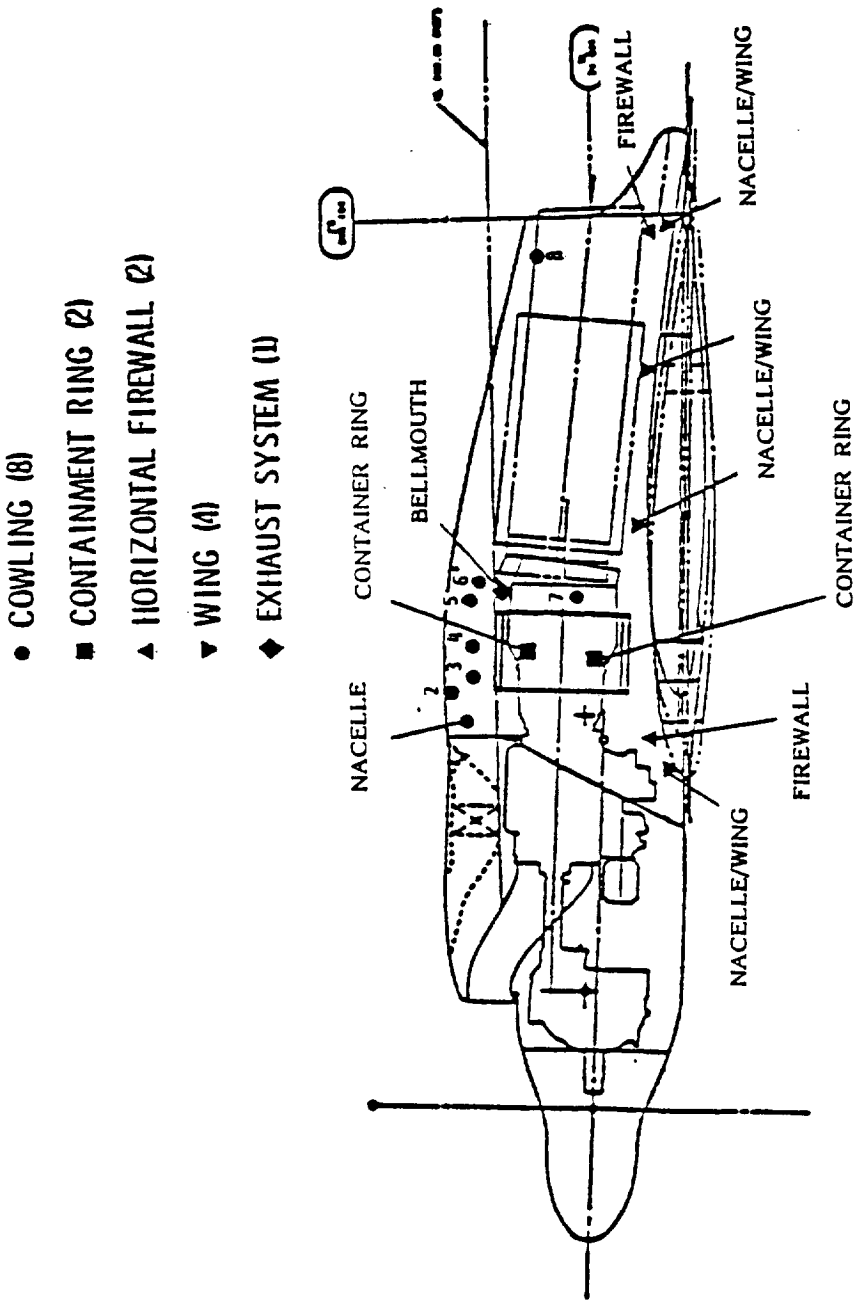


Figure 80. Aft Nacelle Structural Temperature Measurements

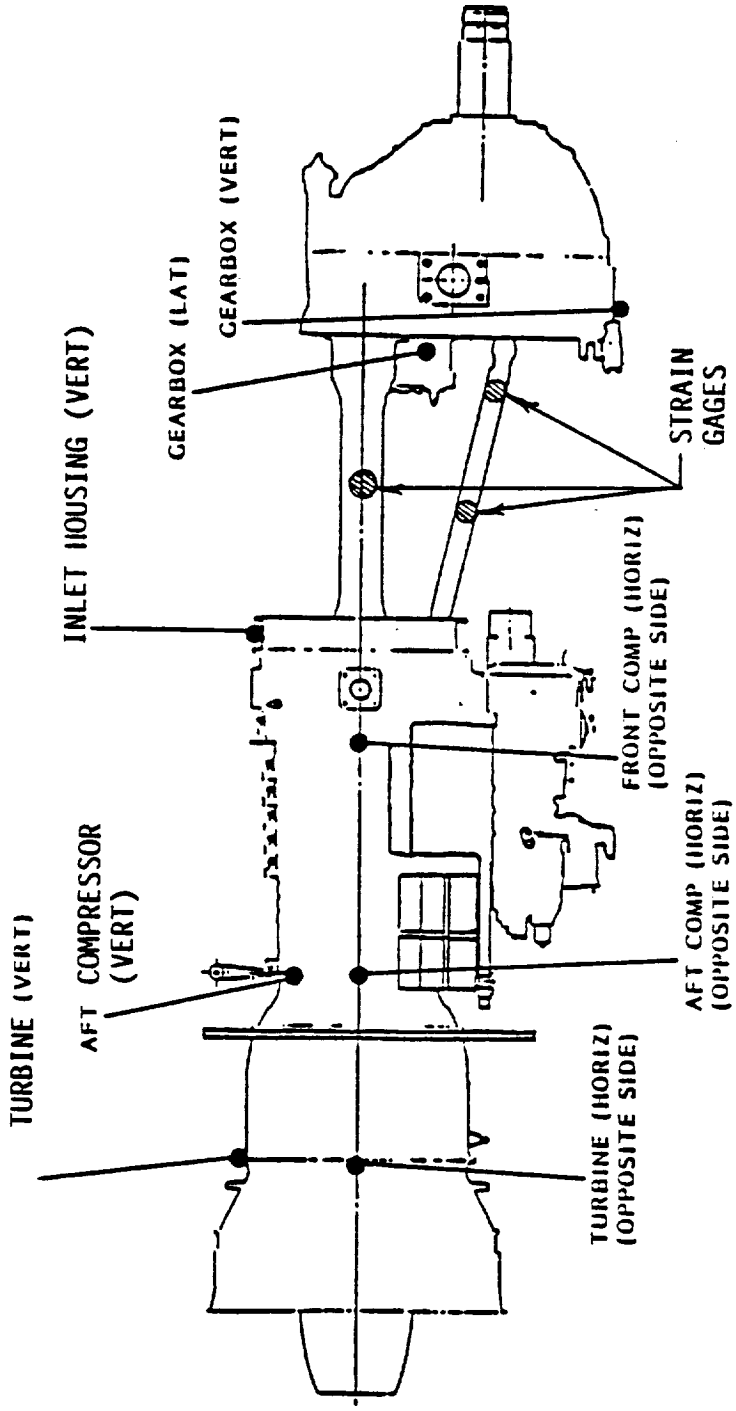


Figure 81. Drive System Vibration and Strain Gages

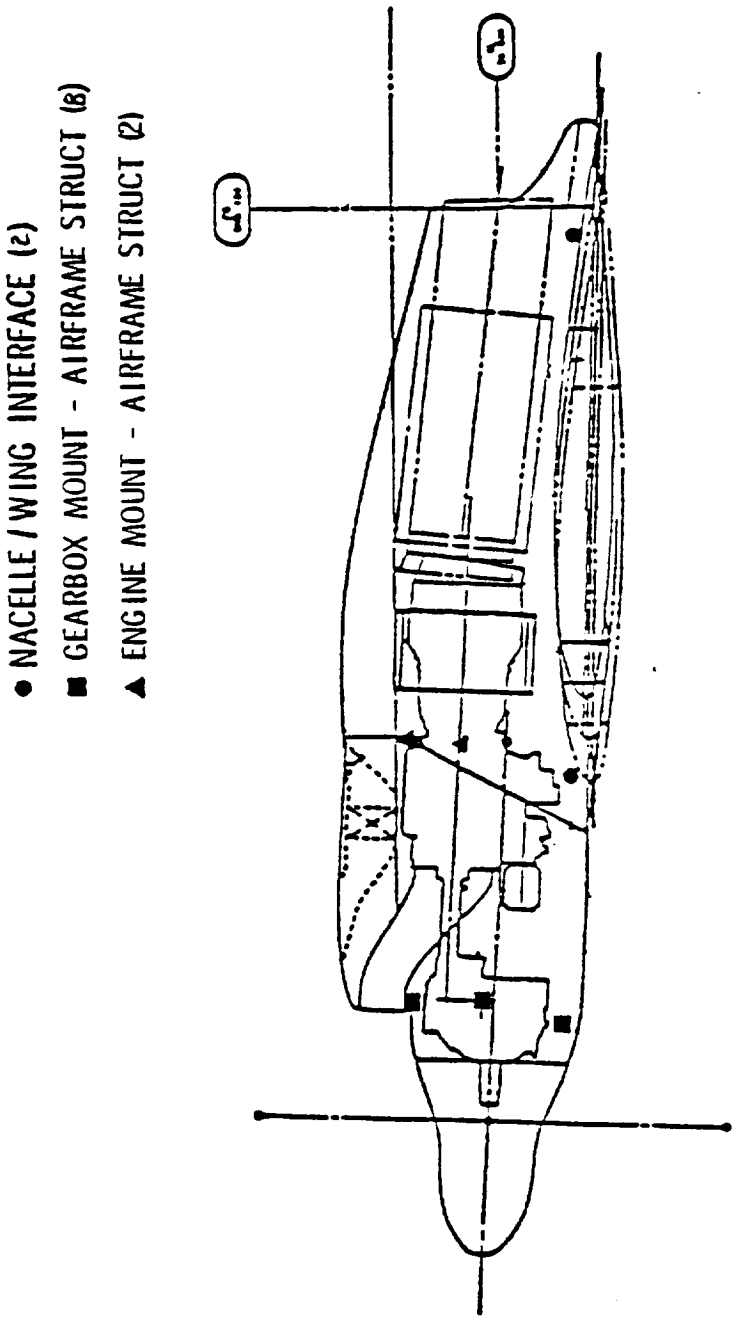


Figure 82. Vibration and Pickup Locations

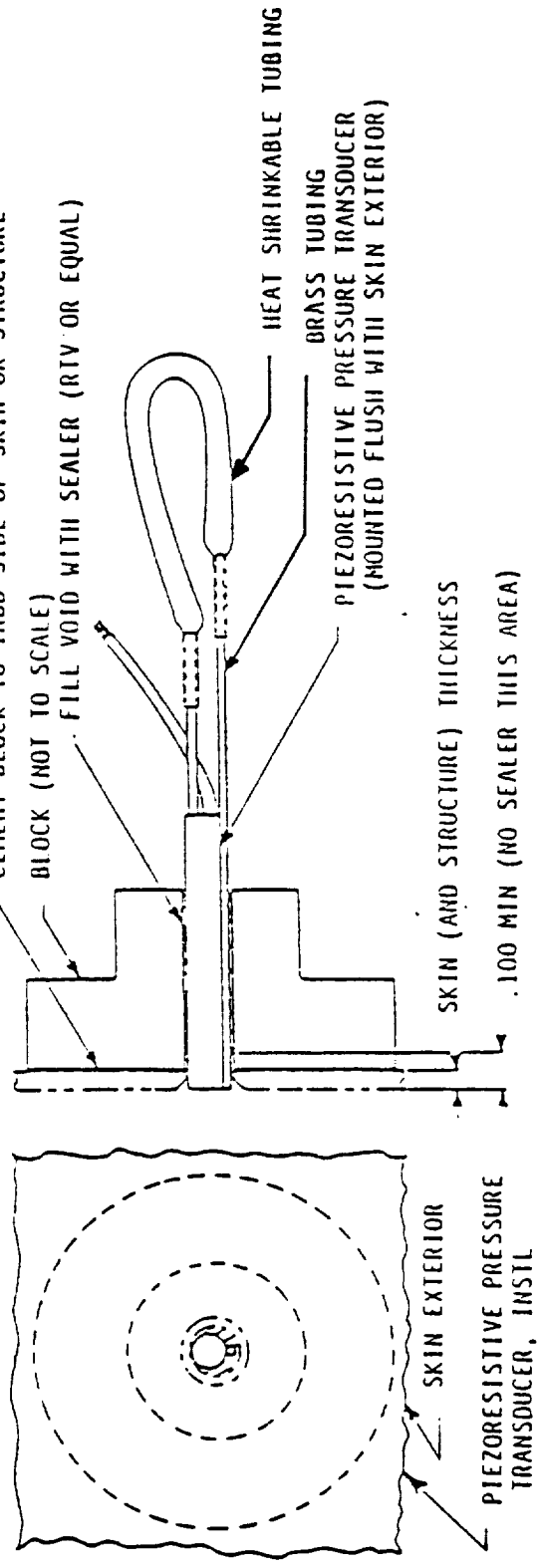


Figure 83. Typical Fuselage Microphone Installation

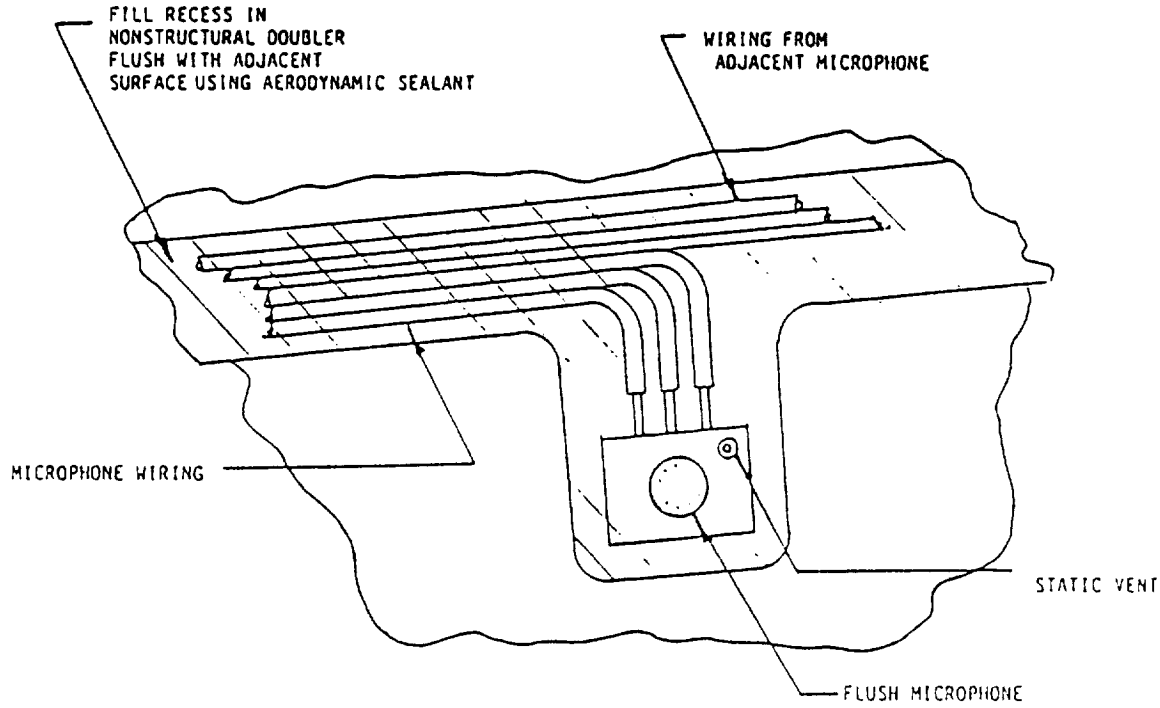


Figure 84. Typical Wing Microphone Installation

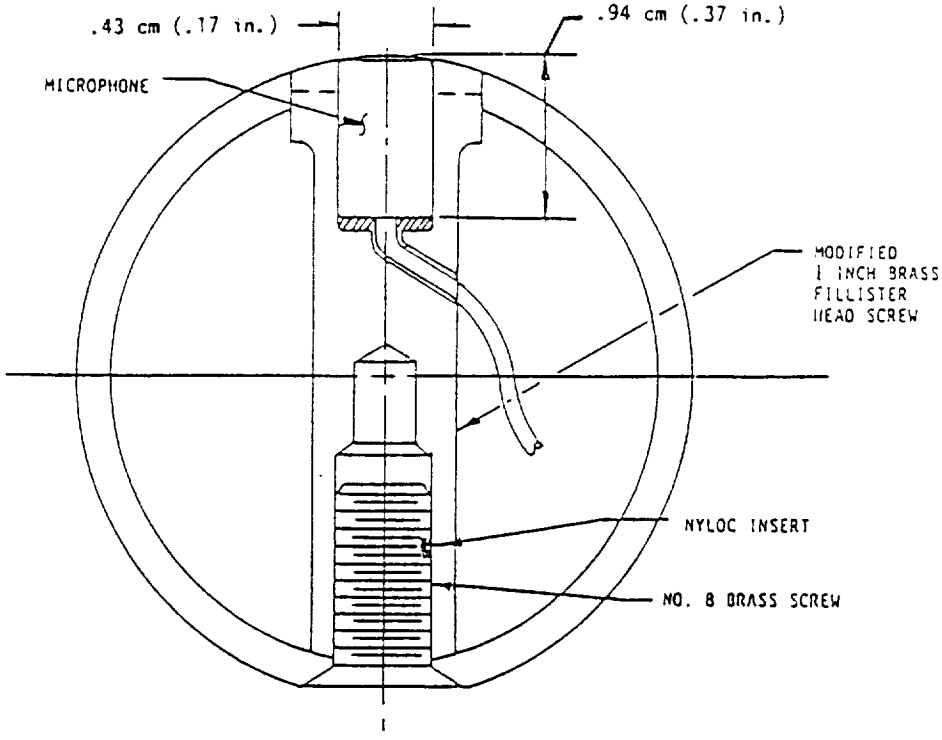


Figure 85. Typical Boom Microphone Installation

4.0 MODEL TESTS

Model tests were performed to provide data for full-scale design and to validate design procedures. These tests included:

- Powered propfan model tests in low- and high-speed wind tunnels to obtain aerodynamic and stability and control data
- Windmilling-propfan flutter model tests
- Static tests of the propfan engine inlet diffuser

These tests have been reported in detail in References 4 through 6. Highlights from these reports are provided in the following sections.

4.1 STABILITY AND CONTROL/PERFORMANCE/ACOUSTICS TESTBED MODEL TESTING

4.1.1 Objectives

In this phase of the PTA Program, dealing with wind tunnel model testing for stability and control, performance, and acoustics, the objectives were:

- To establish that the proposed PTA configuration would be a flightworthy vehicle
- To establish that the proposed PTA configuration would meet the performance objectives for the program
- To provide basic information about the effects of propfan rotation direction on aircraft acoustics
- To obtain flow field definition data to validate prediction codes

Because of difficulties with operation of the model-scale propfan rotors at speeds sufficiently high to get supersonic tip speeds, the acoustics objective was never achieved. The other objectives, however, were successfully attained.

The approach employed in these wind tunnel tests was to obtain data not only on the PTA configuration but also on the baseline GII configuration so that increments of aerodynamic forces and moments could be obtained. It was assumed that the full-scale increments would be the same as those measured at model scale. The model-scale increments were then added to GII flight data coefficients to obtain predicted aerodynamic characteristics for the PTA aircraft.

4.1.2 Models

It was decided early in the program that a single model would be used for both high- and low-speed wind tunnel tests and that the propfan rotor on the model would be powered. Model scale was set at one-ninth--primarily because of the size of the motors available to drive the propfan. The

PRECEDING PAGE BLANK NOT FILMED

PAGE 108 INTENTIONALLY BLANK

one-ninth scale established the propfan rotor diameter at 0.305m (1 ft). The major difference between the high- and low-speed models was that the low-speed model had provision for varying flap and spoiler angles.

The model propfan blades were fabricated of graphite fiber cloth. Because the edges were so thin, fabrication was a considerable challenge. At the highest rotational speeds, axial loads produced by the centrifugal forces were as high as 2600N (600 lb). Furthermore, the curved and twisted configuration of these blades at such loads produced extremely high root bending stresses.

The model blades were designed to match, as closely as possible, the loaded position of the full-scale blades. The degree to which this was accomplished was measured in tests of the propfan rotor on an isolated nacelle which permitted a comparison of the performance of the small-scale rotors with the predicted performance of the SR-7 full-scale hardware. This comparison showed that the rotor design objectives were met, and the swirling slipstream at model scale adequately simulated the full-scale slipstream. This work is reported in detail in Reference 7.

4.1.3 Test Facilities

The wind tunnel test facilities chosen are listed below.

Test	Facility
High-Speed Performance	NASA-Langley 16-Ft Transonic Wind Tunnel
Low-Speed Stability and Control	NASA-Langley 4M x 7M Subsonic Wind Tunnel
High-Speed Flow Surveys	NASA-Lewis 8-Ft x 6-Ft Supersonic Wind Tunnel

A photograph of a typical model installation is shown in Figure 86. The high-speed flow survey tests were made in the NASA-Lewis facility because the Langley 16-Ft Transonic Tunnel was not available at the appropriate time. This necessitated a reconfiguring of the model to a semispan configuration, and this installation is shown in Figure 87.

4.1.4 Instrumentation

Aerodynamic forces and moments were obtained with sting mounted six-component force balances for the performance and stability and control tests. Because the models included air-turbine-driven propellers, it was necessary to bridge high-pressure air across the force balances. In the low-speed wind tunnel this was no problem, but in the high-speed tunnel there was a continuing increase in tunnel air temperature with run time, and the flexible air lines bridging the balance were sensitive to temperature gradients in spite of design efforts to eliminate that sensitivity. Fortunately, the errors produced were limited to axial force measurements--lift, side force, and the various moments were unaffected.

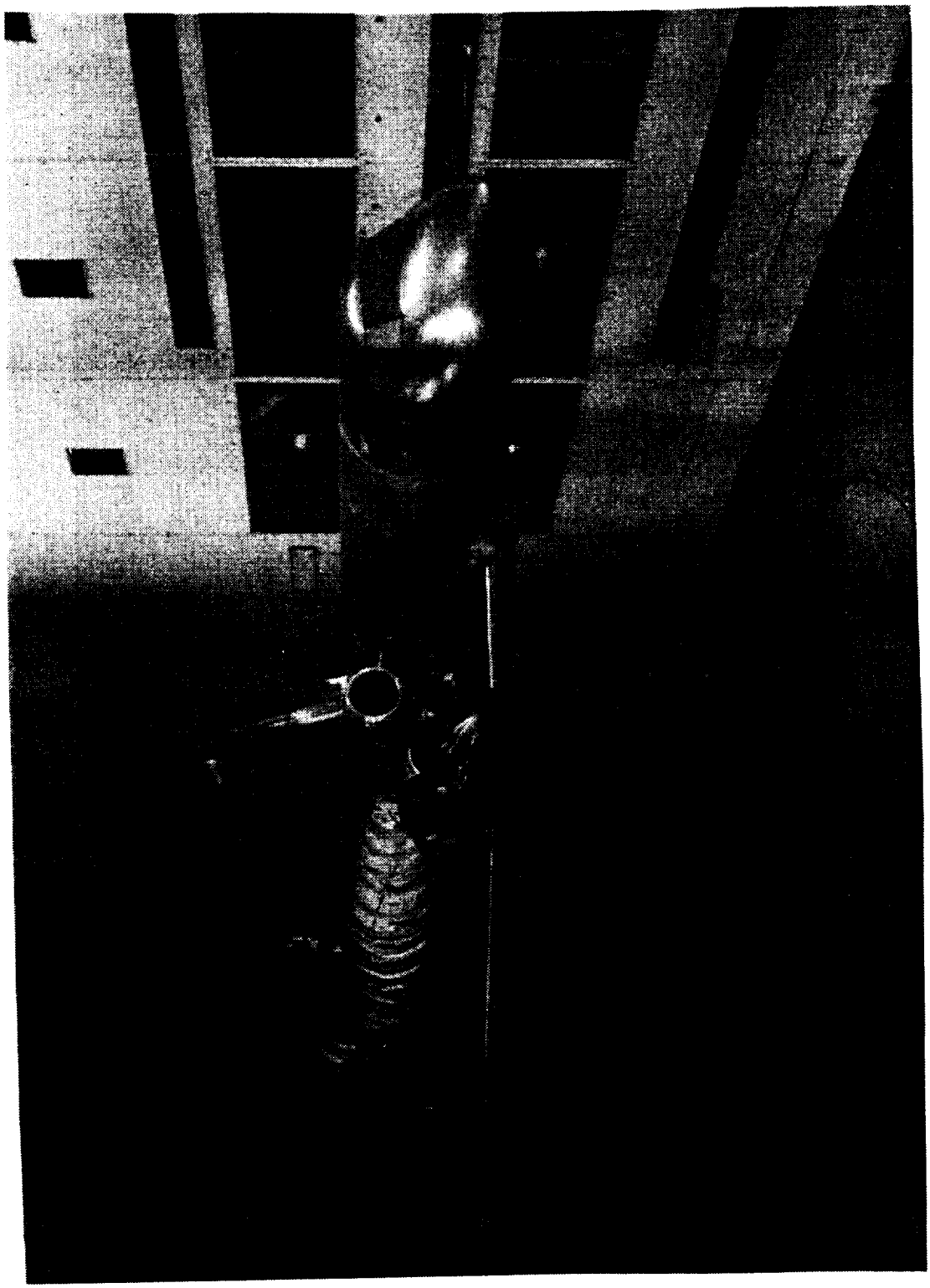


Figure 86. PTA Model in 4M x 7M Wind Tunnel

ORIGINAL PAGE
BLACK AND WHITE PHOTOGRAPH

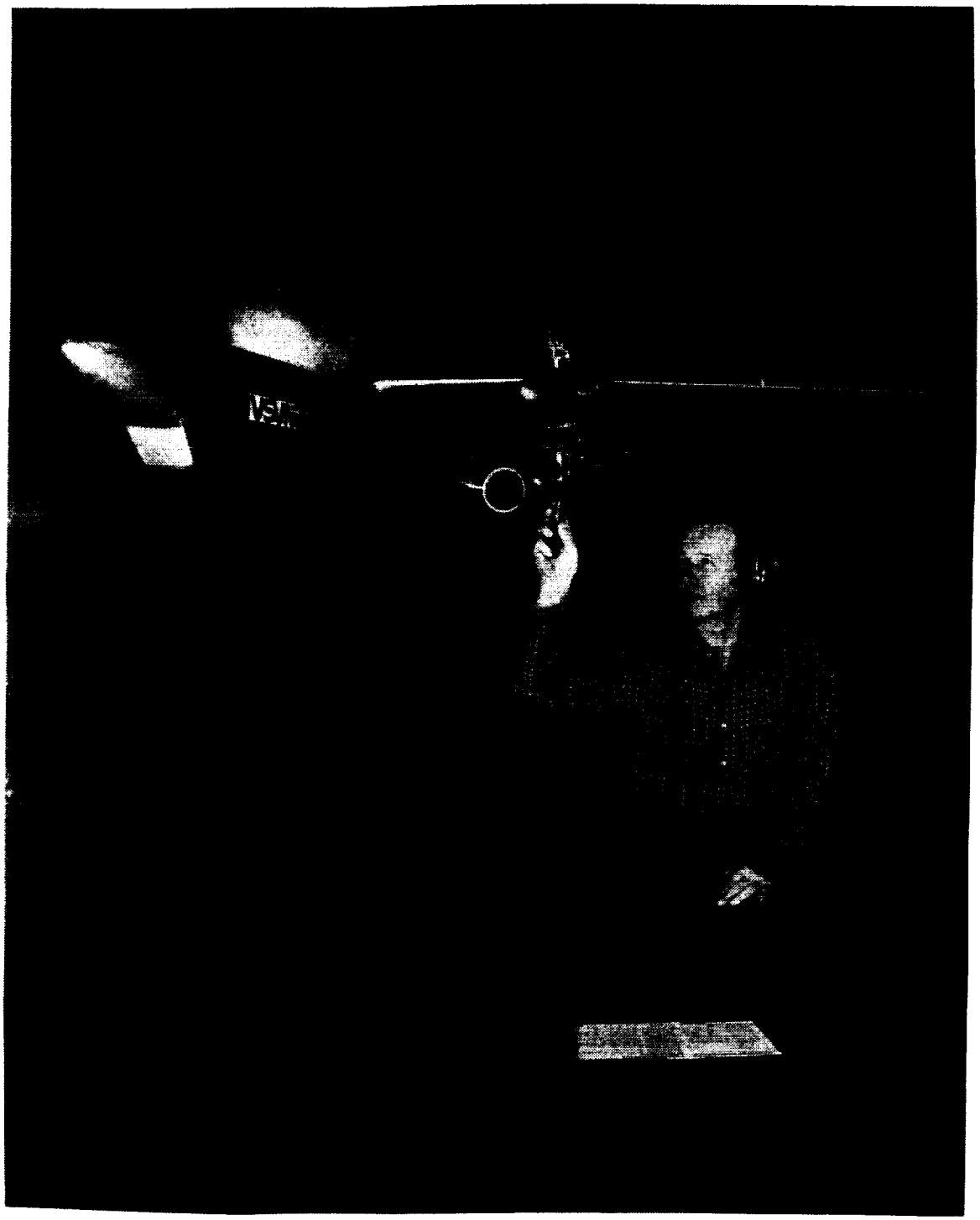


Figure 87. High-Speed Flow Field Model

Much of the high-speed drag data with the propfan powered, however, were subject to question because of these thermal effects and had to be examined very carefully.

Pressure taps were installed on the model wings--concentrating on the regions just inboard and outboard of the nacelle. More pressure taps were located on the nacelle surfaces so that diagnostic data might be obtained in the event of inordinate drag or other flow problems emanating from the nacelle installation.

For the flow survey tests, there was no interest in aerodynamic forces and moments so there were no force balances. Primary instrumentation consisted of flow survey rakes, each containing a number of 5-hole probes. These probes, when properly calibrated, provide data for three components of velocity. The calibration was performed in a subsonic-transonic wind tunnel at Mach numbers from 0.6 to 0.95. These rakes were mounted on a holder attached to the nacelle which positioned the probe tips in a plane just aft of the propeller plane. This instrumentation and the model are shown in Figure 88.

4.1.5 Supporting Analysis

The wind tunnel tests and the overall design of the PTA aircraft were greatly aided by a supporting analytical program which provided results to corroborate and extend the wind tunnel data. The basic tool in this methodology was the low-order panel code QUADPAN (Reference 3). A propeller performance code, PROPVRTX (Reference 8), was used to predict slipstream properties. PROPVRTX was interfaced with QUADPAN by restating surface boundary conditions to include velocity perturbations calculated with PROPVRTX, and then correcting surface pressures in the slipstream for the pressure rise across the propeller disc. This methodology is described in more detail in Reference 9.

4.1.6 Test Results

4.1.6.1 Performance

Figure 89 shows a comparison of lift and pitching moment coefficients from the wind tunnel tests with predicted values. There is excellent agreement of the $C_L - \alpha$ curves, but agreement was not quite so good for the pitching moment data. The latter implies that the neutral point for the QUADPAN predictions was slightly aft of that measured in the wind tunnel. Generally, however, the good agreement of these comparisons gave credibility to both analytical and experimental data.

The major impact of the PTA modifications on aircraft lift characteristics was due to the PTA nacelle. This can be seen in Figure 90, where it is shown that lift was increased slightly at low angles of attack and reduced slightly at angles of attack greater than 3 degrees. The lift generated by the nacelle offset, to a large degree, the weight of the nacelle and the other modifications to the left hand wing so that the aircraft required little lateral trim modification from the GII configuration. Figure 91 shows that these lift characteristics prevailed throughout the

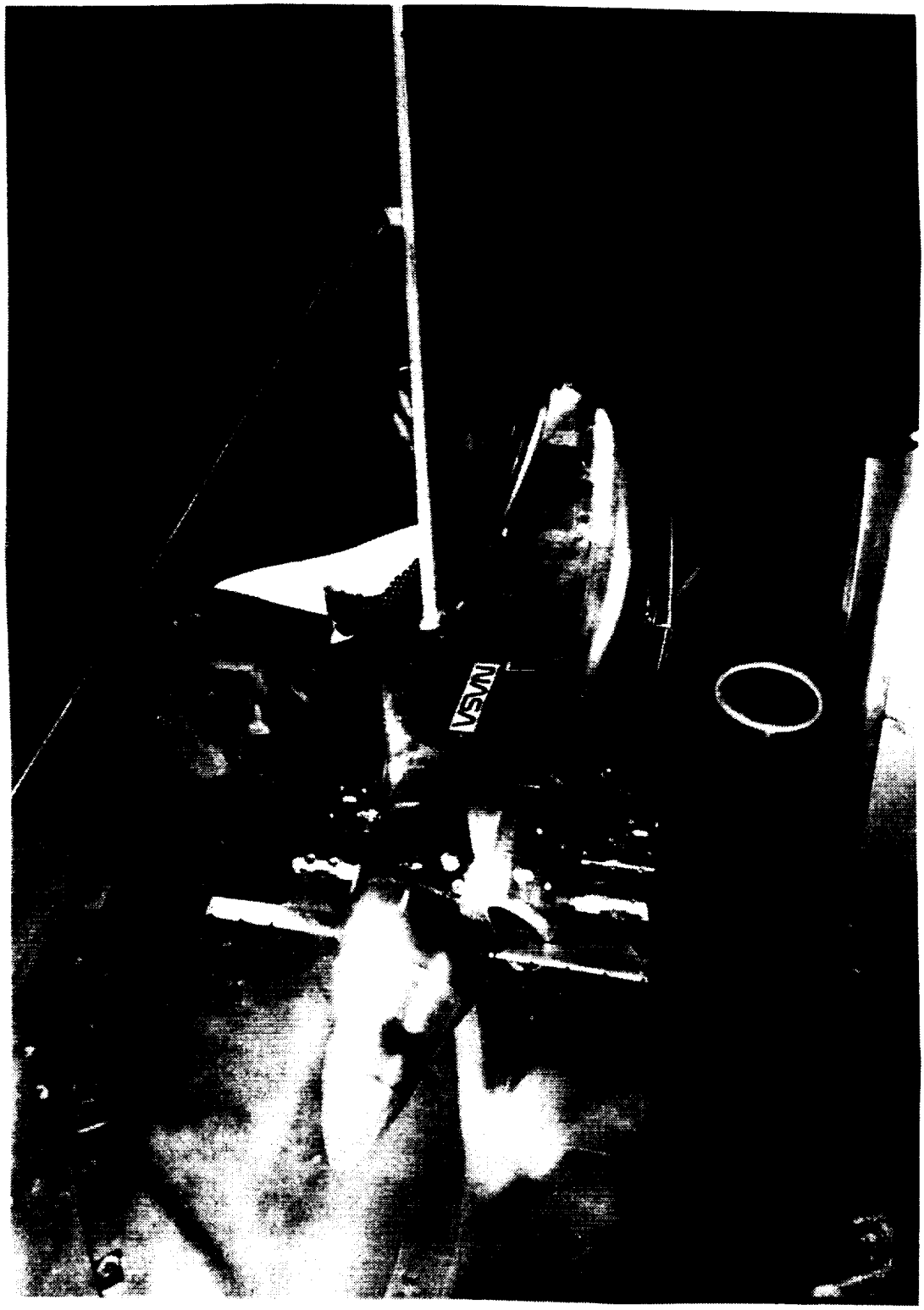


Figure 88. Flow Survey Rake

ORIGINAL PAGE
BLACK AND WHITE PHOTOGRAPH

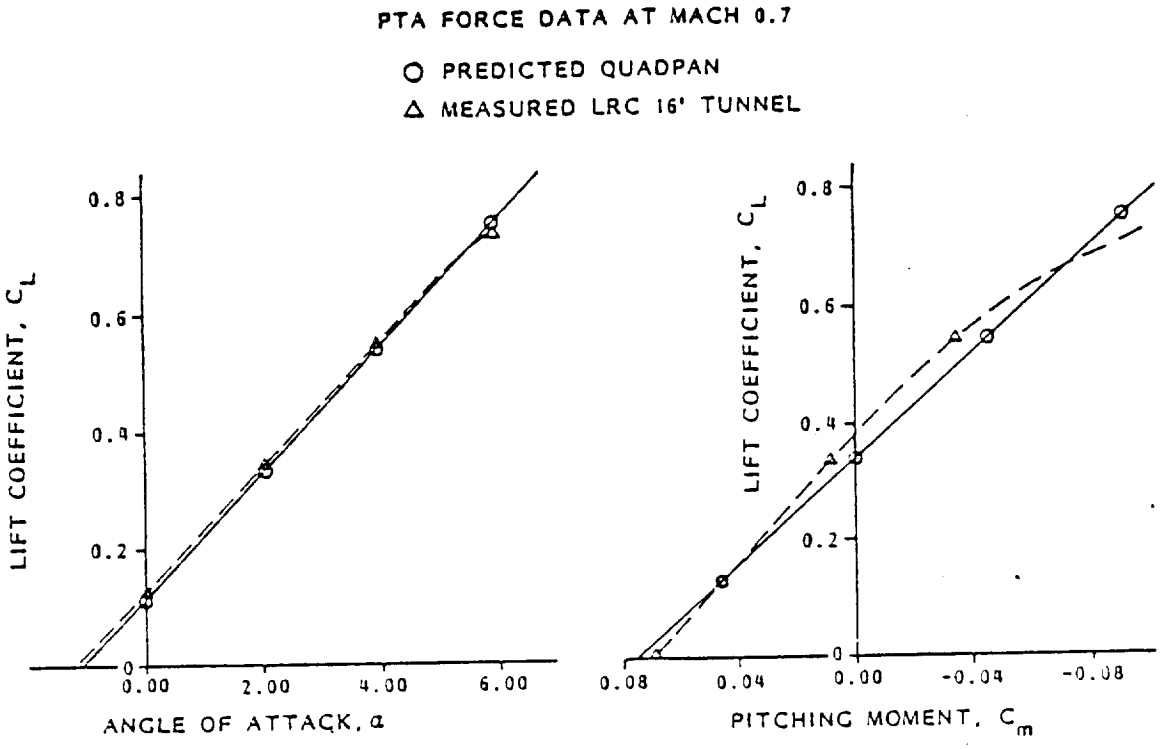


Figure 89. Lift/Pitching Moment Correlation with Theory

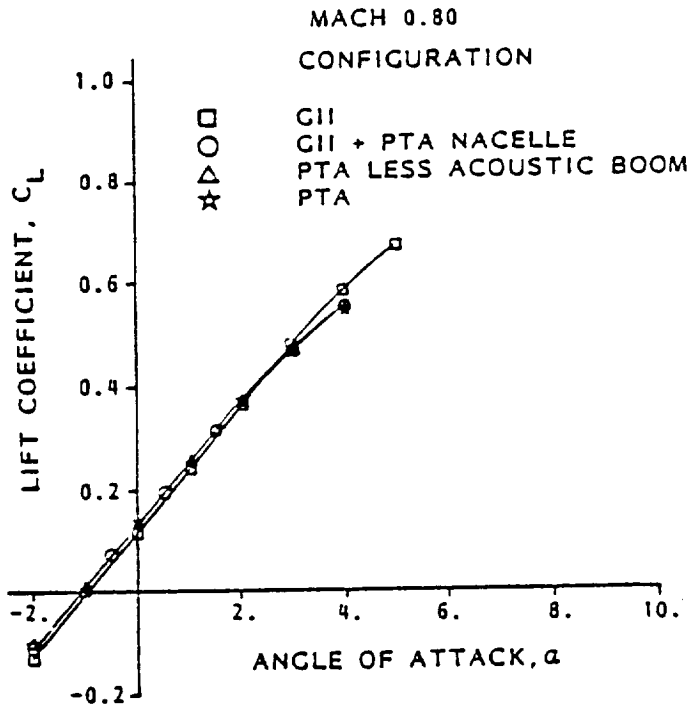


Figure 90. Lift Curves for PTA Buildup

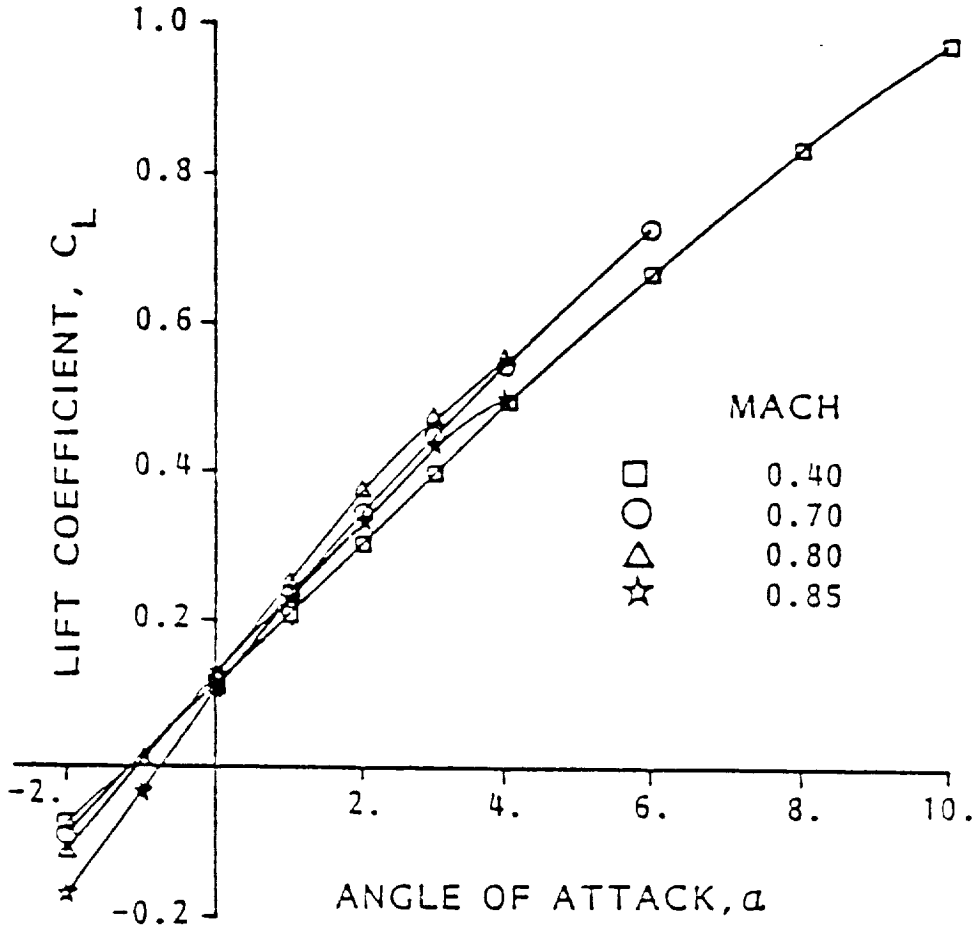


Figure 91. Effect of Mach Number on PTA Lift

range of flight Mach numbers. It also shows that the primary effect of Mach number on lift was to increase the slope of the $C_L-\alpha$ curve.

Drag polars for the GII and PTA models at low speeds are shown in Figure 92. Through most of the flight range, the PTA modifications added approximately 43 counts to the GII drag. At lift coefficients greater than 0.6, however, this increment increased rapidly. The effects of Mach number on PTA drag and a more detailed description of the drag buildup are shown in Figure 93. As in the case of lift, it can be seen that the largest effect was produced by the addition of the nacelle. Drag increments remained fairly constant with Mach number up to Mach 0.6, crept upwards gradually to Mach 0.7, and then rose rapidly at higher Mach number.

During the course of the design program for the PTA aircraft, there was some concern that transonic drag rise might preclude attainment of the Mach 0.8 design speed at 10,668m (35,000-ft) altitude. A contingency plan was therefore developed. This plan involved the design and subsequent wind tunnel test of a leading edge extension (LEX) to soften the impact of the slipstream swirl on the inboard wing leading edge. The swirl on this side of the nacelle tends to increase the effective angle of attack and, at high subsonic speeds, may cause a premature drag rise. The LEX, as shown in Figure 94, increased the camber of this part of the wing and pointed the leading edge into the upwash produced by the slipstream.

Figure 95 shows drag polars for the PTA model with and without the LEX in place. It can be seen that the LEX was quite effective--reducing drag at the design lift coefficient by 29 counts, or about 7 percent. This is believed to have significance for future design efforts because, if this fairly crude attempt to match wing contours to the swirling flow was effective, a more sophisticated contouring of nacelle and wing should result in a relatively low drag installation even at high subsonic speeds.

4.1.6.2 Pressure Measurements

Figure 96 shows pressure distributions on the upper wing surface adjacent to the nacelle and along the surface of the nacelle for a Mach number of 0.4. One of the major purposes of this figure is to show the excellent agreement of the wind tunnel data with the analytical predictions. However, the effects of the slipstream swirl on the wing flow can also be seen by comparing the pressure distributions at wing stations 2 and 6. As mentioned earlier, the slipstream effectively increased angle of attack on the inboard side of the nacelle and decreased angle of attack on the outboard side.

Figure 97, for a case without swirl included, shows that the subsonic flow code QUADPAN is not as accurate at Mach 0.7 where some supercritical flow occurs on the upper surface of the wing. Generally, however, QUADPAN was accurate enough, even at the higher subsonic Mach numbers, to give good indications of data trends.

Figure 98, which compares wing pressures with and without the nacelle, shows that even without the propfan swirl, installation of the nacelle

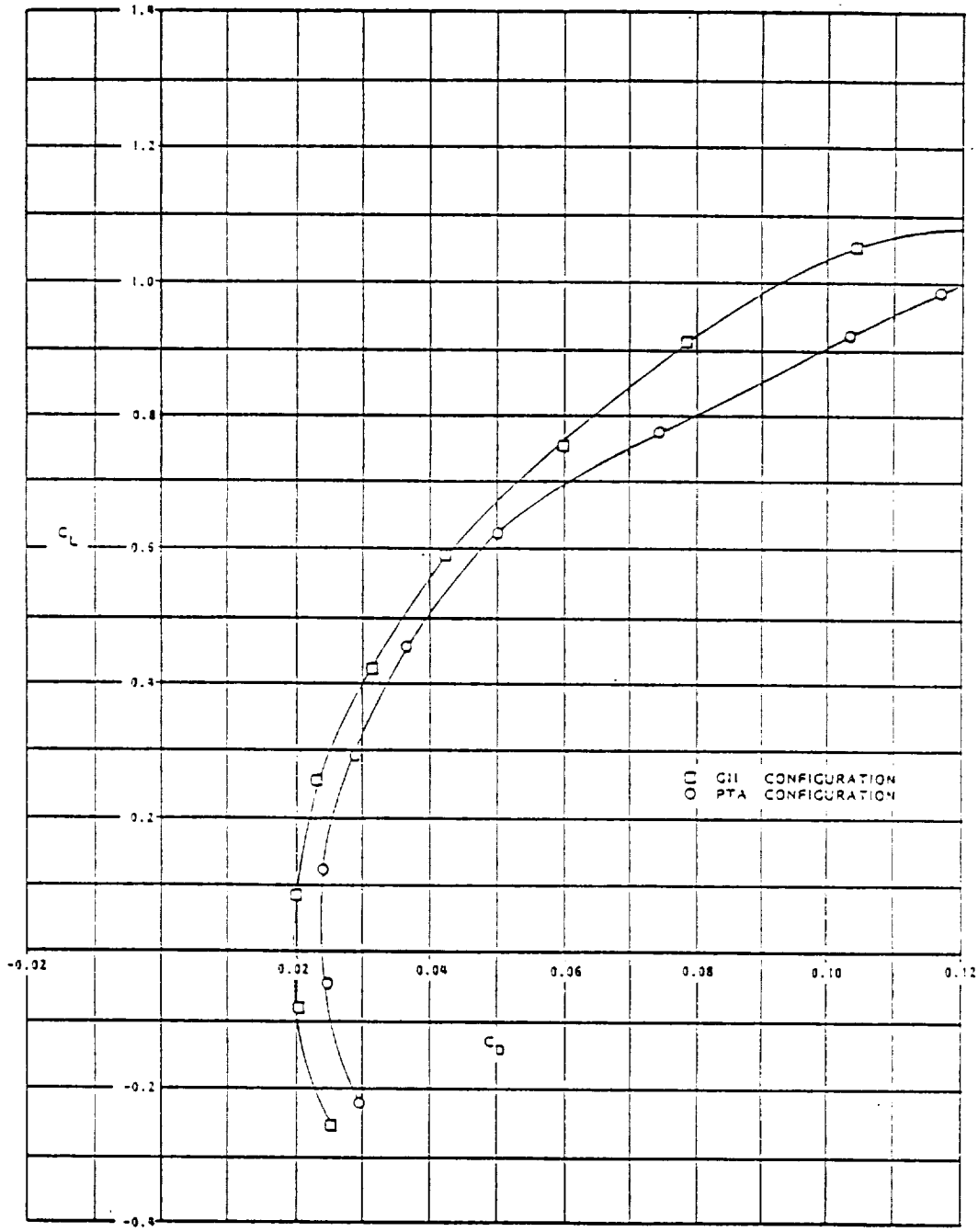


Figure 92. Drag Due to PTA Modifications

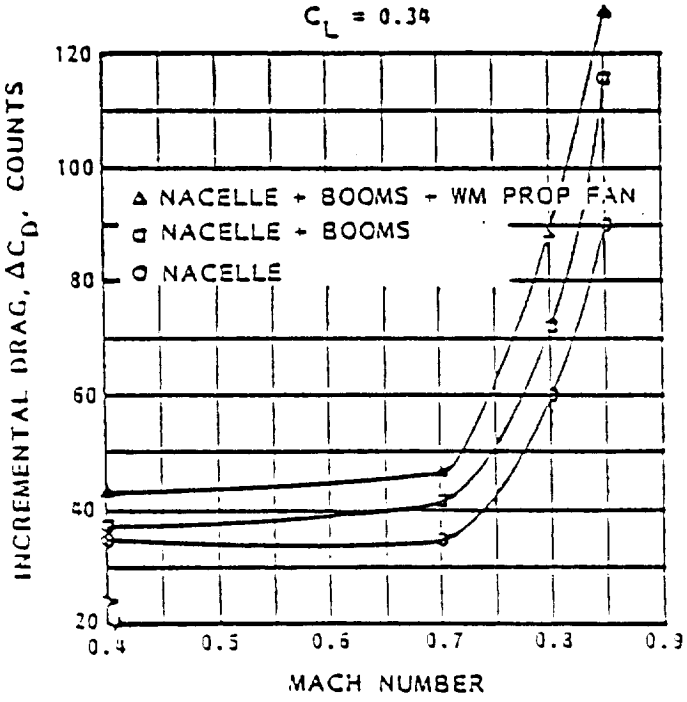


Figure 93. Drag of PTA Components at High Speed

LEX GEOMETRY - SECTION AT = 0.308

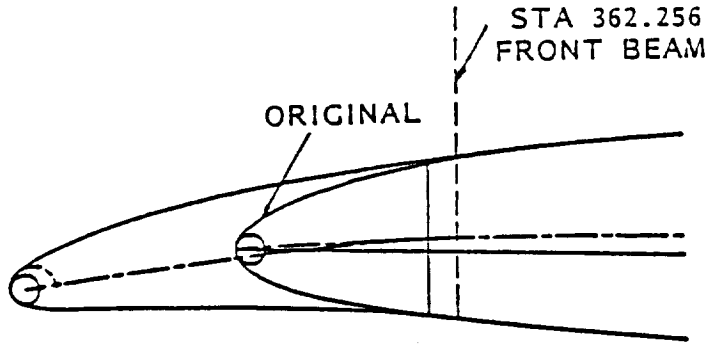


Figure 94. Airfoil Section Modification for LEX

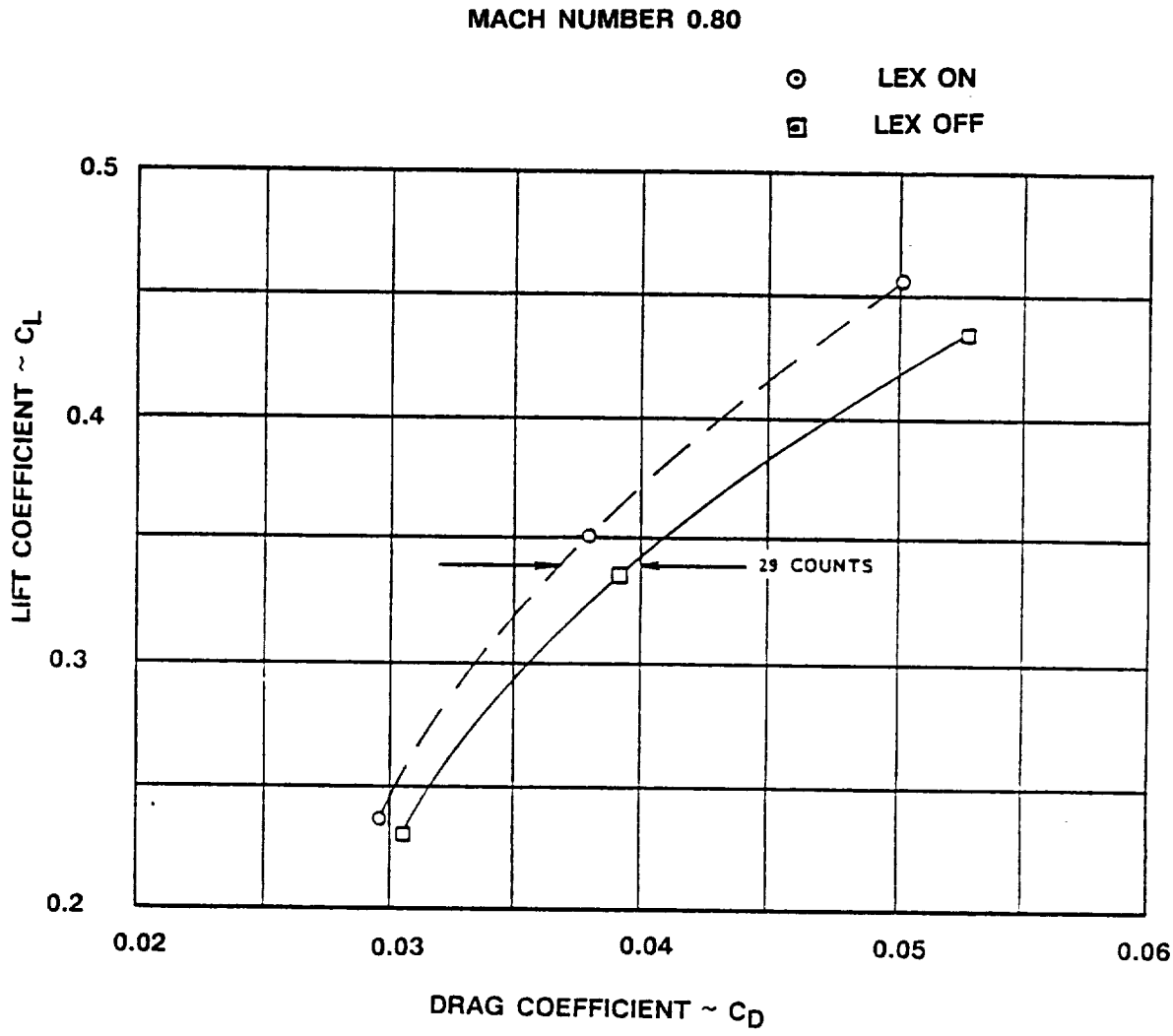


Figure 95. Effect of LEX on PTA Drag

ORIGINAL PAGE IS
OF POOR QUALITY

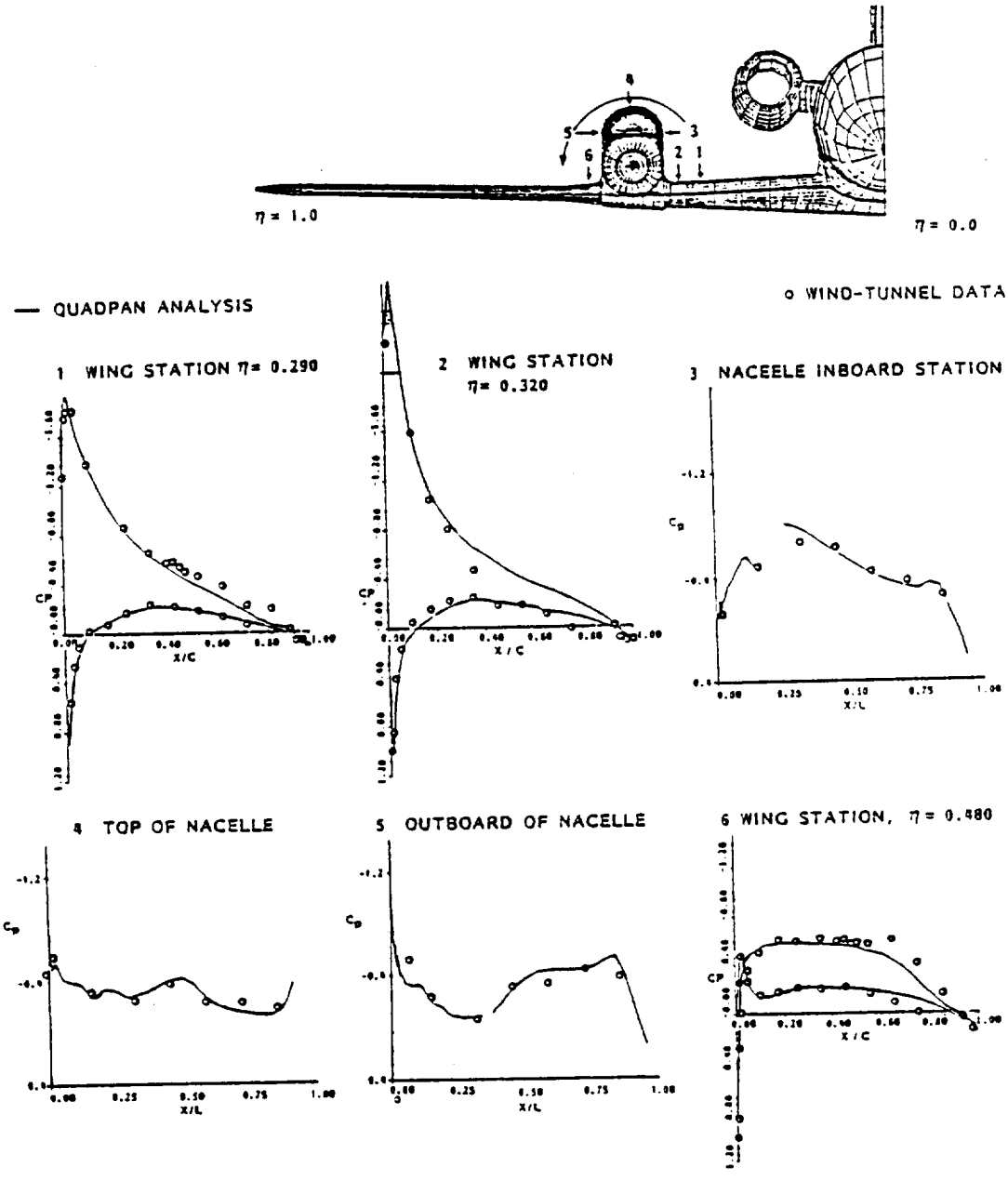


Figure 96. Wing Surface Pressure Distributions - Mach 0.4

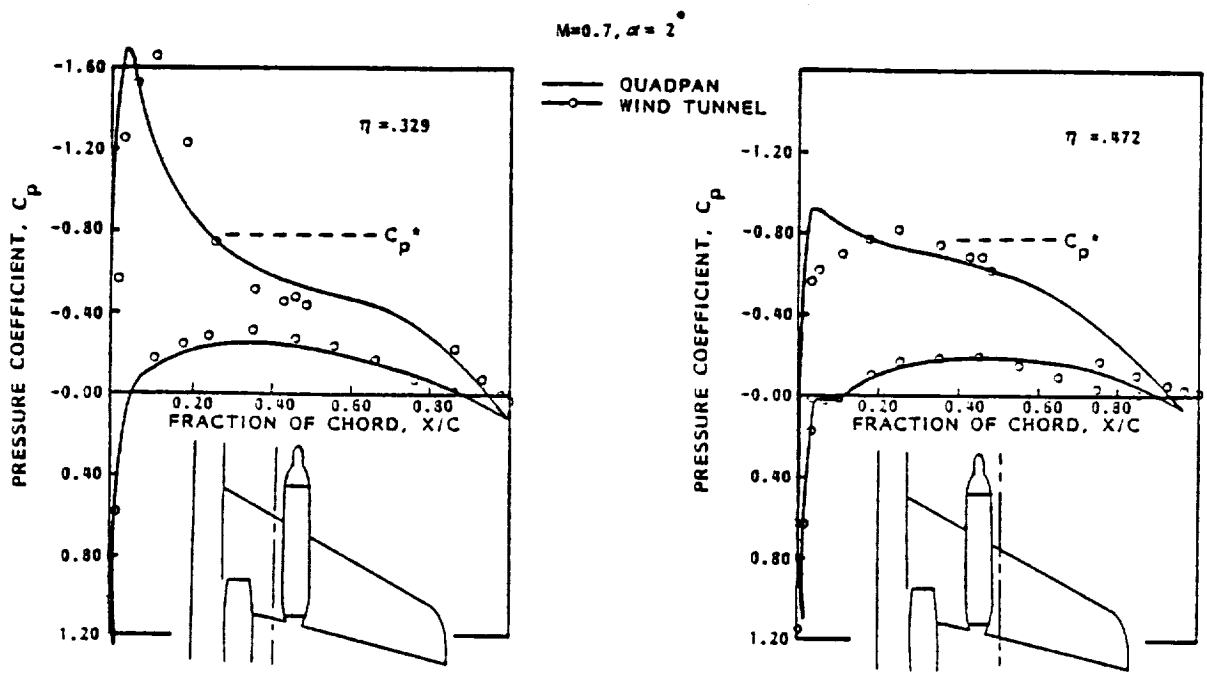


Figure 97. Wing Surface Pressure Distributions - Mach 0.7

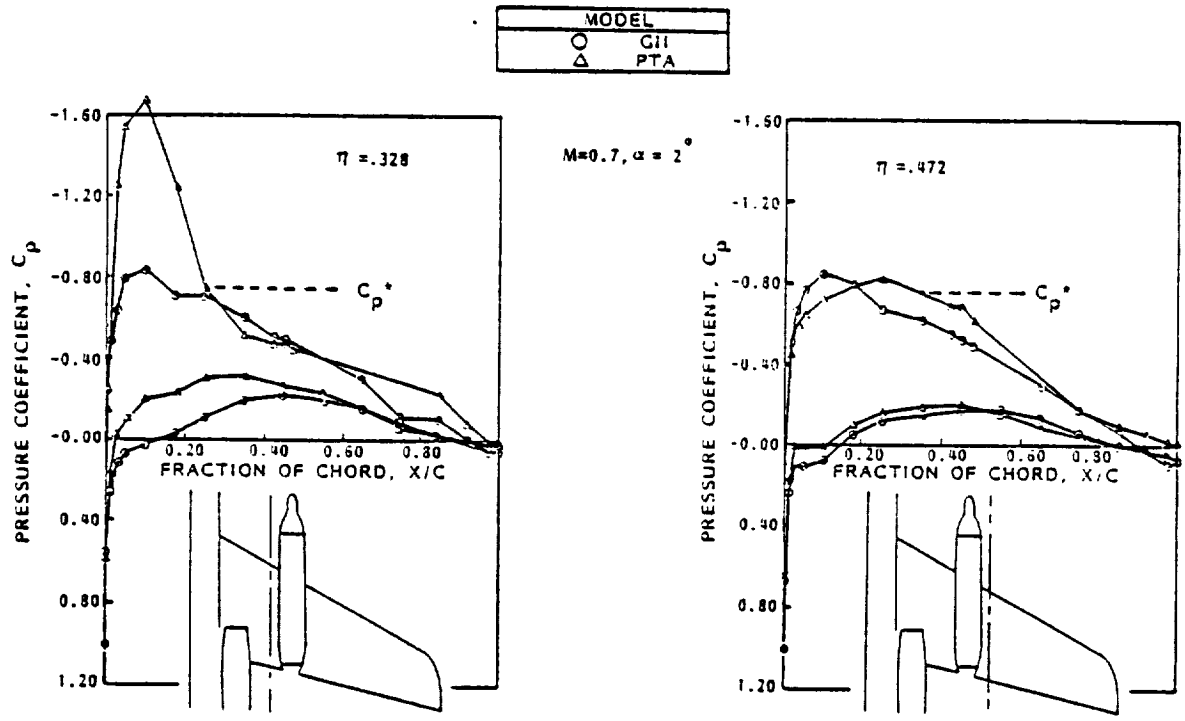


Figure 98. Effect of PTA Nacelle on Wing Pressures - Mach 0.7

caused an acceleration of flow on the inboard side (adjacent to the fuselage) that did not appear on the outboard side. This undoubtedly was caused by the flow "channeling" between the fuselage and the nacelle. This effect, together with the up-inboard rotation of the propeller and slipstream, made the inboard side of the nacelle a more critical region from the standpoint of transonic drag than the outboard side; and this in turn was the reason that the LEX was designed only for the inboard wing panel.

The susceptibility of the inboard wing region to the formation of pockets of supersonic flow and subsequent shock waves may also be seen in Figure 99 where the effects of increasing freestream Mach number on wing pressure distributions are shown. It can be seen that the flow inboard of the nacelle accelerated substantially more than on the outboard side of the nacelle with a tendency to the production of drag-producing shock waves.

4.1.6.3 Stability And Control

In the area of stability and controllability, the major concern was with the asymmetry of the aircraft and the effects of propfan power. It was decided early in the PTA Program that the aircraft would not be flown with flaps while the propfan was operating because the GII flaps were not designed to withstand the loads produced by the propeller slipstream. In the wind tunnel, therefore, tests with flaps were limited to the unpowered case.

Figure 100 shows the effects of the PTA modifications on lift and pitching moment coefficients with flaps in the takeoff (20-degree) and landing (40-degree) positions. Data are shown for: (a) the propfan removed, and (b) installed with the blades in the feathered position. (The aircraft was designed for ferry flights with the propfan blades replaced by stub blades of the same weight.)

The pitching moment data show no effect on C_{MO} but a significant destabilizing effect on dC_M/dC_L that is worse when the propeller is feathered. This destabilizing effect results from the lift of the nacelle which is generated forward of the wing center of gravity.

The reduced level of stability for the PTA configuration at all flap settings is almost exactly balanced by a forward shift in the center of gravity envelope relative to the GII. Thus the data predict that the static stability margin will remain the same as the GII at the design aft center of gravity. The impact of the reductions in maximum lift coefficients is a slight increase in minimum operational speeds relative to the GII.

The effects of propfan power on lift and pitching moment, flaps up, is shown in Figure 101. The lift increment due to power increased with angle of attack, and the maximum lift coefficient increased because of the propeller normal force and the slipstream effects on the wing and nacelle. At full scale the incremental effects of power on lift will be less than shown in these data because of Reynolds number effects, but the same

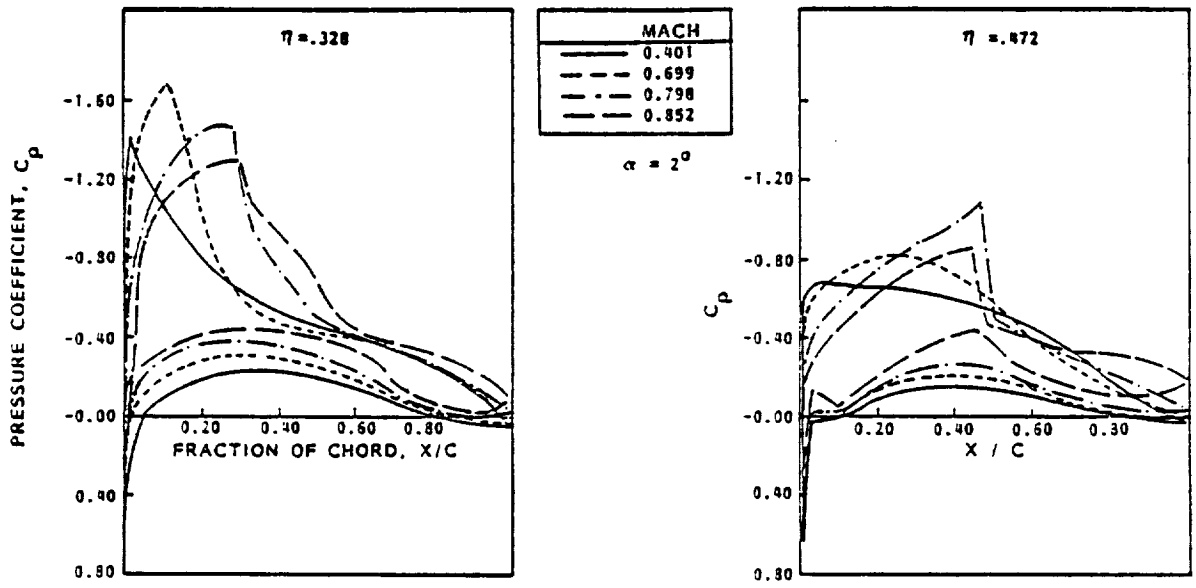


Figure 99. Effect of Mach Number on Wing Pressures

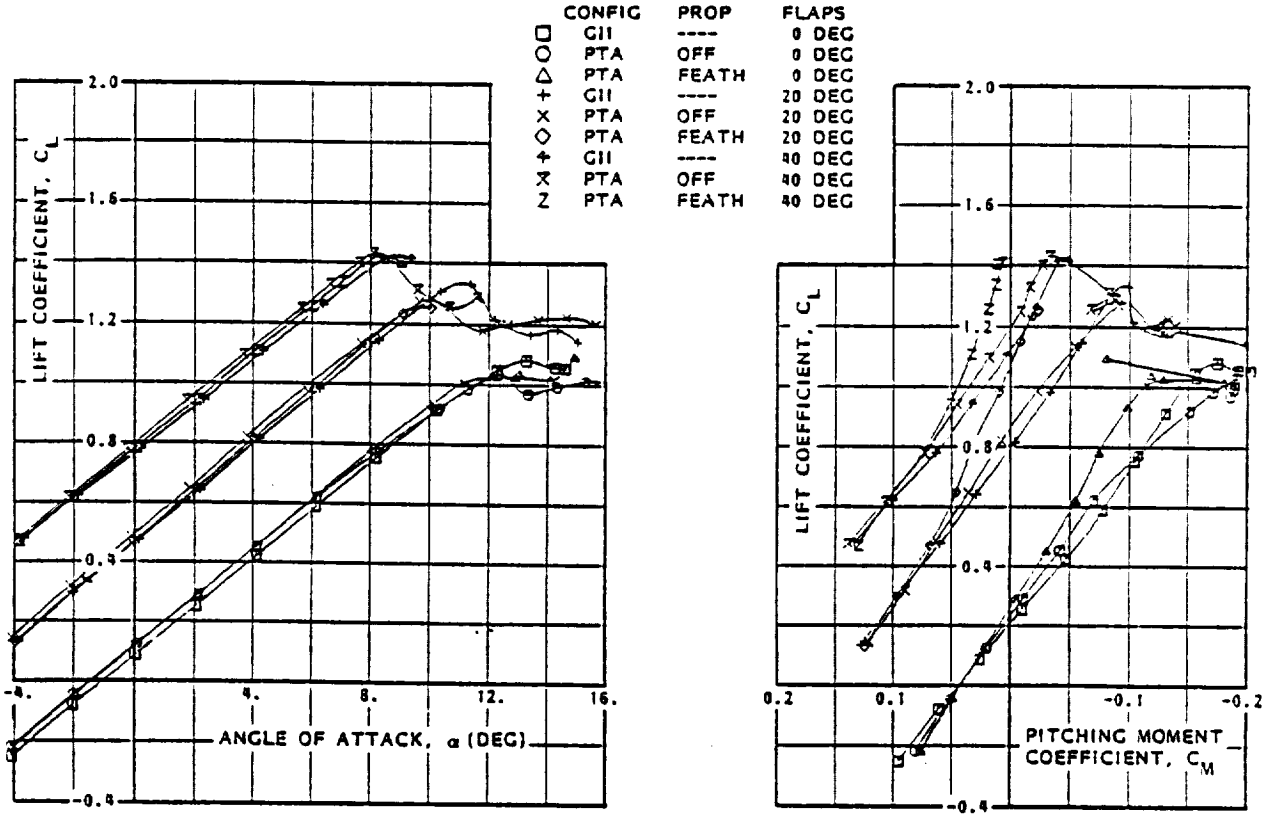


Figure 100. Effects of PTA Modifications on Lift and Pitching Moment

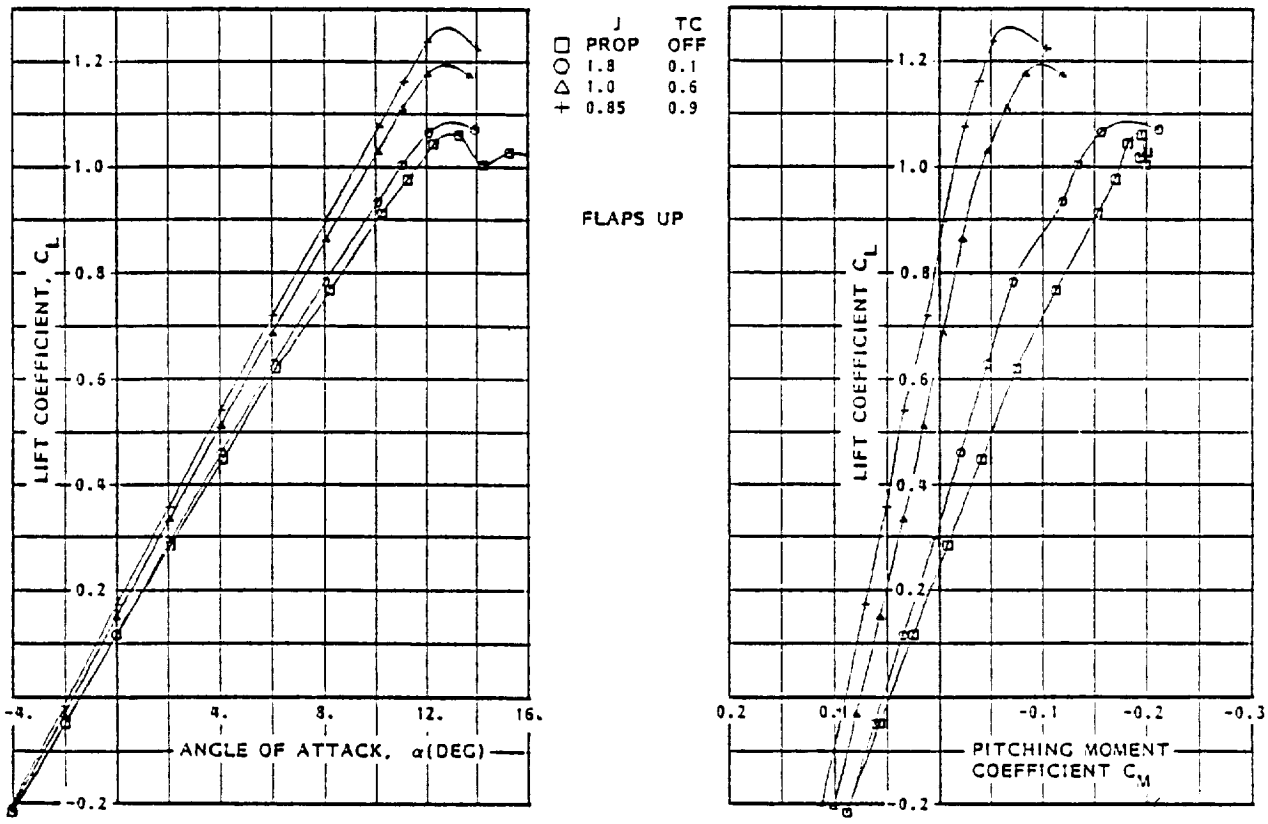


Figure 101. Effects of Propfan Power on Aerodynamic Characteristics in Pitch

trends will prevail--pitching moment becomes more positive with power and the stability level decreases. However, in summary, the wind tunnel data indicated no significant problems in longitudinal trim or flight characteristics for the PTA aircraft.

Side force, yawing moment, and rolling moment coefficients at zero sideslip are shown in Figure 102. The nacelle and booms of the PTA aircraft create a negative sideforce increment at angles of attack greater than zero. Yawing moment, however, was essentially zero at all operational angles of attack because the induced side loads on the fin offset the drag of the nacelle. The large yawing moments shown at high angles of attack were caused by low Reynolds number flow separation on the wing which is delayed to higher angles of attack at full scale Reynolds numbers. No rolling moments are indicated that cannot be easily balanced by available trim forces. The data for these coefficients with flaps deflected showed no additional significant effects.

Propfan power effects on side force, yaw, and rolling moments are shown in Figure 103. As expected, there is a strong effect of power on yawing moment, and in fact, the yawing moment shown at $T_C = 0.9$ is close to the maximum value available from the rudder and would limit minimum flight speed at full propfan power except that the rolling moment reaches limit at $T_C = 0.6$. For the PTA aircraft, the limiting condition for low-speed flight was based on the trim condition of no more than 50-percent wheel throw to balance roll.

The same kinds of data were obtained at sideslip angles other than zero and provided input to the equations that were used to predict aircraft flight characteristics. These equations also required tests to measure the effectiveness of elevator, rudder, and spoilers.

Since the PTA aircraft was designed to operate with several nacelle incidence angles, the effects of this variable were also evaluated in the wind tunnel tests. The trim changes associated with nacelle incidence variation were small and uniform.

In the operational range of angles of attack, increments in pitching moment between GII and PTA became smaller with increasing Mach number. Figure 104 presents a composite picture of compressibility effects on lift and pitching moment for the GII and PTA aircraft and utilizes data from both the low- and high-speed tests, corrected to the Reynolds number of the high-speed tests. Superimposed is a curve from GII flight test data showing the onset of high-speed buffet. Buffet onset is closely related to the angle of attack at which maximum lift occurs, and since this angle was reduced slightly for the PTA aircraft, it would be expected from these data that buffet onset would occur a little earlier for the PTA.

The effect of Mach number on a sideslip derivative was negligible except for a small reduction in roll due to sideslip at high angles of attack. This reduction tends to increase dutch roll stability and spiral instability, but is of little consequence with an operational yaw damper.

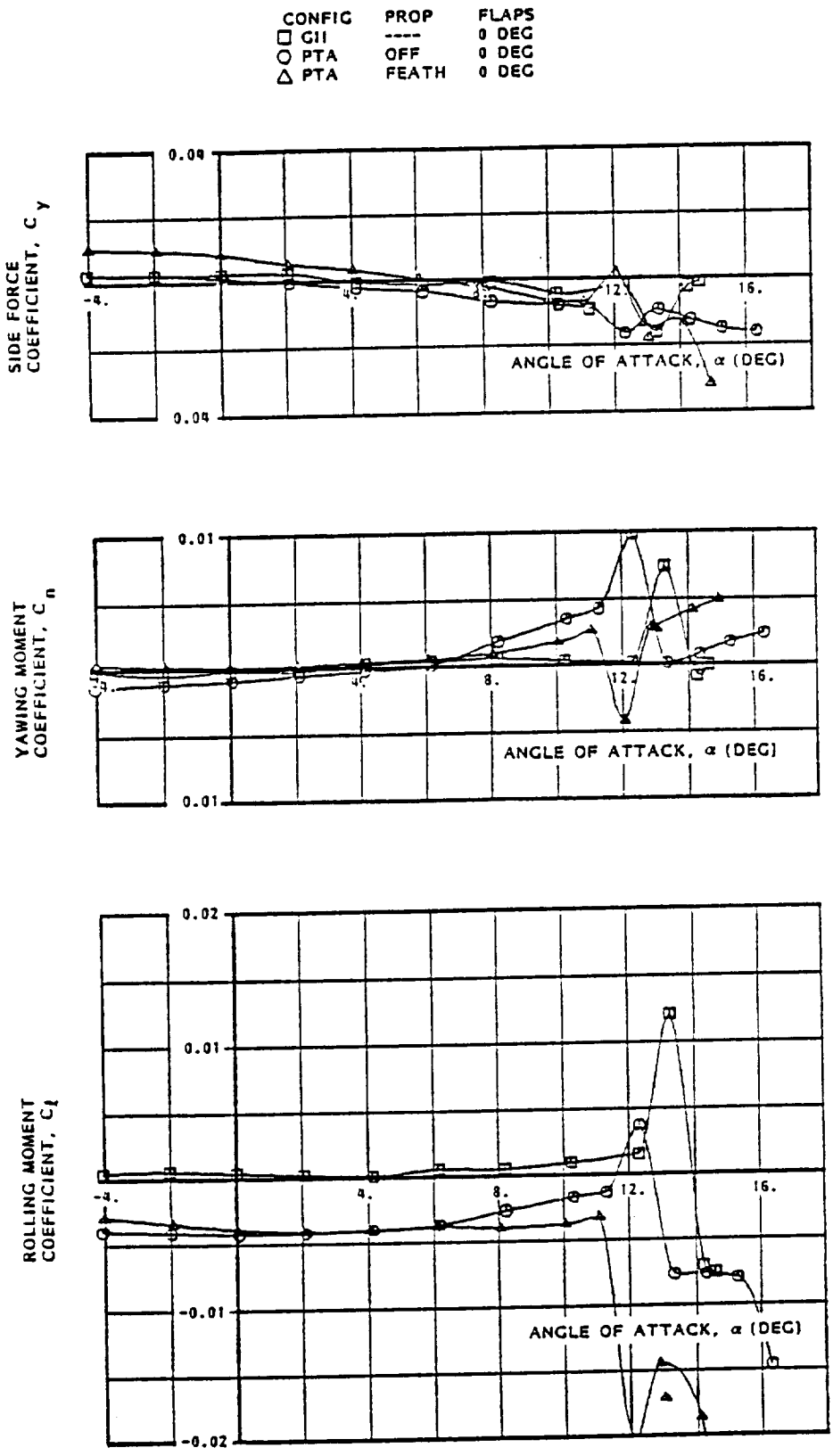


Figure 102. Effects of PTA Modifications on Side Force, Yawing Moment, and Rolling Moment

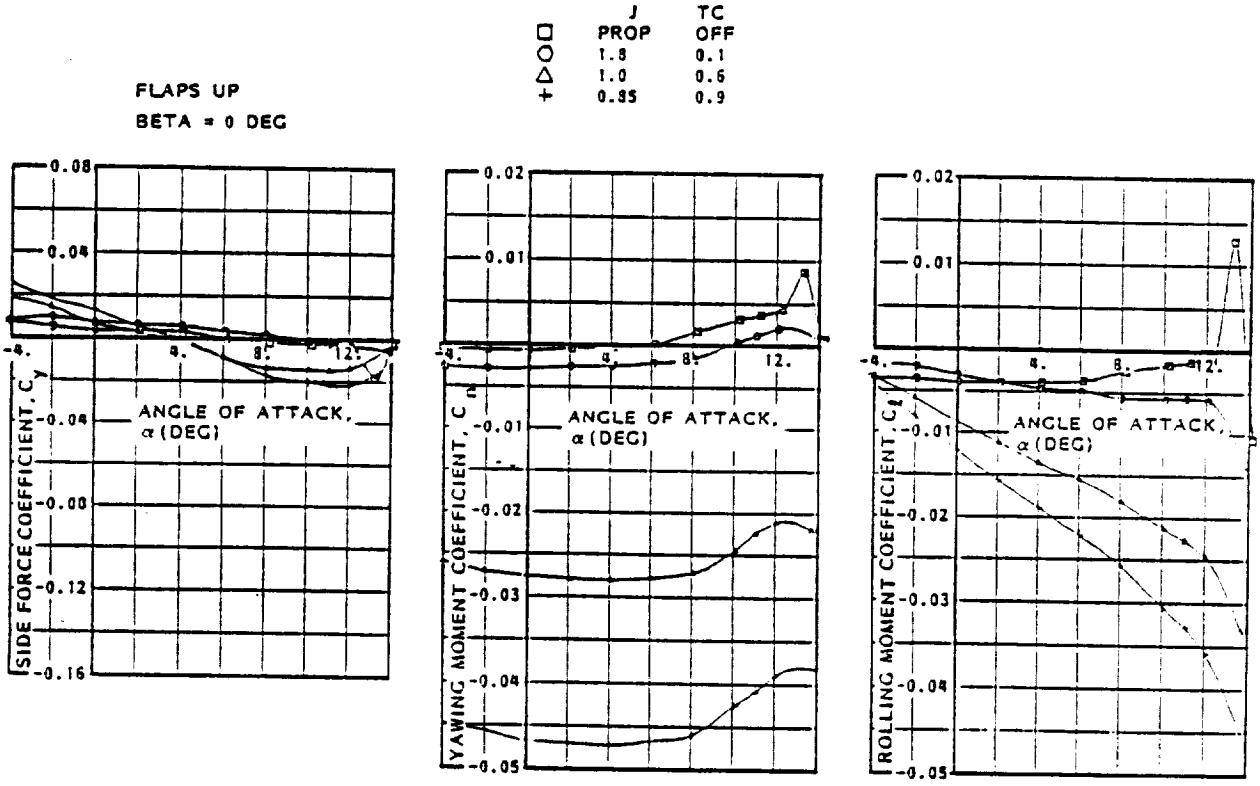


Figure 103. Effects of Power on Aerodynamic Characteristics in Pitch

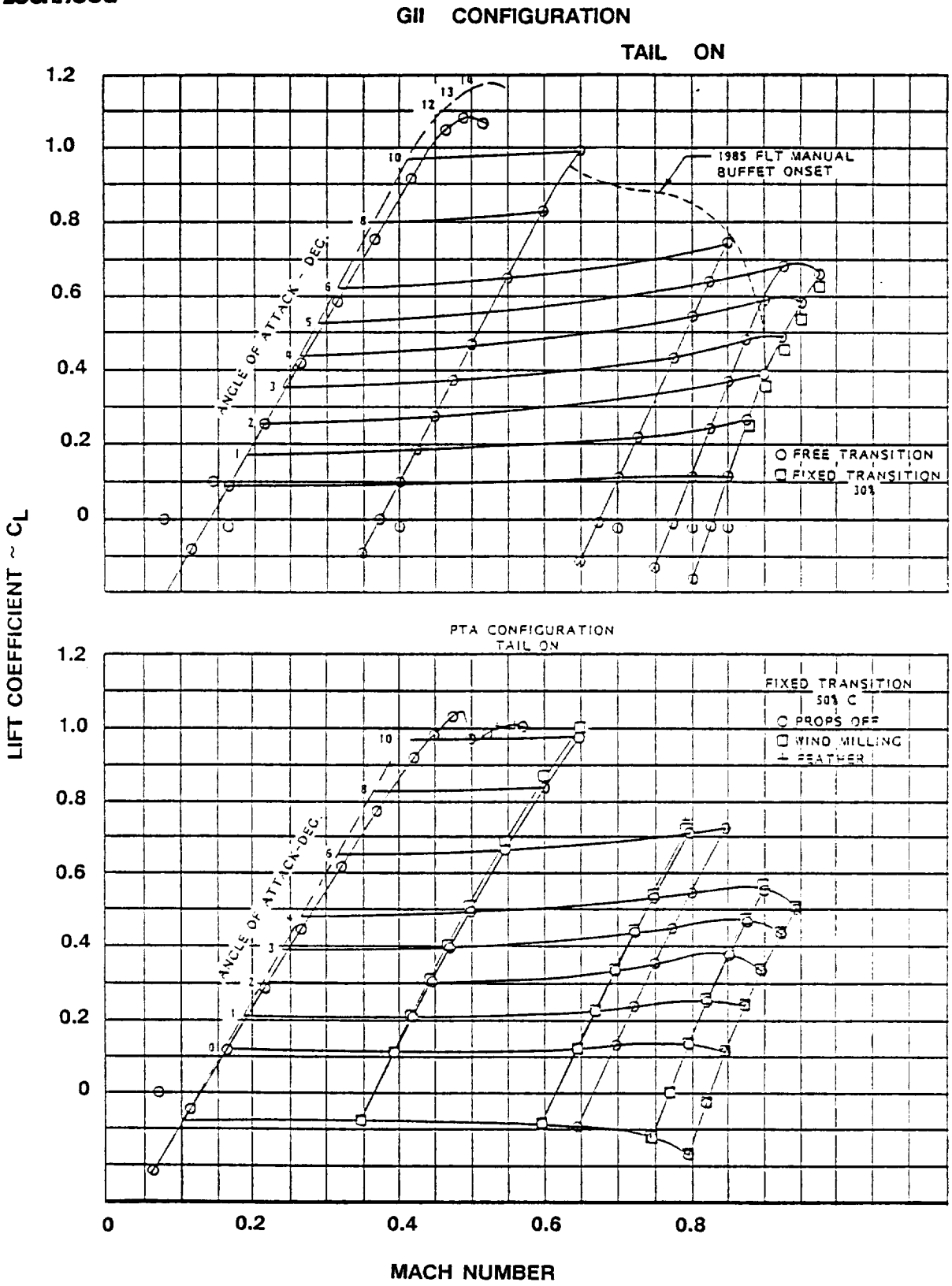


Figure 104. Mach Number Effects on Lift Characteristics

ORIGINAL PAGE IS
OF POOR QUALITY

Other tests were run to determine the effects of high-speed flow on rudder and aileron-spoiler effectiveness. Nothing was found that would have a significant impact on aircraft operation.

4.1.6.4 Flow Field Surveys

The flow field survey tests were made to validate the ability of the QUADPAN code to predict velocity components in the plane of the propeller in the range of flight test Mach numbers. There was particular interest in the question of whether or not that capability would diminish at the higher subsonic Mach numbers.

Some of the correlations of predicted and experimental data were disappointing, as shown in Figure 105, but it was felt that much of the lack of correlation could be blamed on: (a) difficulties in the QUADPAN predictions with modeling details of the rake support structure, and (b) differences between the calibrated and actual rake support structure. The data shown in Figure 105 for the axial velocity component are, however, the worst case. Agreement was much better for the lateral and vertical velocity components as can be seen in Figures 106 and 107.

Perhaps the most gratifying result of these tests was that there was no significant change in the correlations with increasing Mach number, so it was concluded that QUADPAN could reasonably be expected to predict the three-dimensional flow fields for the PTA flight tests.

4.1.6.5 Isolated Propeller Tests

The isolated propeller tests were run to assess propeller performance in the absence of installation effects. The tests were run at a Mach number of 0.4 in both the Langley 4M x 7M Subsonic Wind Tunnel and the 16-Ft Transonic Tunnel. Propeller blade pitch was set at 49 degrees, while angle of attack and advance ratio were variables. A hub balance permitted measurement of axial force, normal force, and pitching moment while torque and horsepower were obtained from the calibrated air motor.

Figures 108 and 109 show thrust and power coefficient data from these tests plotted against advance ratio. Also shown are curves from two predictions--one made with the Lockheed PROPVRTX code and the second made by Hamilton Standard for the full-scale propfan rotor. It can be seen that there is excellent agreement between experimental and predicted performance--implying that the small-scale rotor simulated the full-scale rotor quite well.

4.1.7 Results and Conclusions

Drag data from the wind tunnel tests showed that, as expected, the PTA modifications increased drag significantly. At the high-speed design point (Mach 0.8 at 10,668m (35,000 ft)), the tests indicated a drag increment relative to the GII of 88 counts. At low speeds with flaps extended, the increments were higher.

ORIGINAL PAGE IS
OF POOR QUALITY

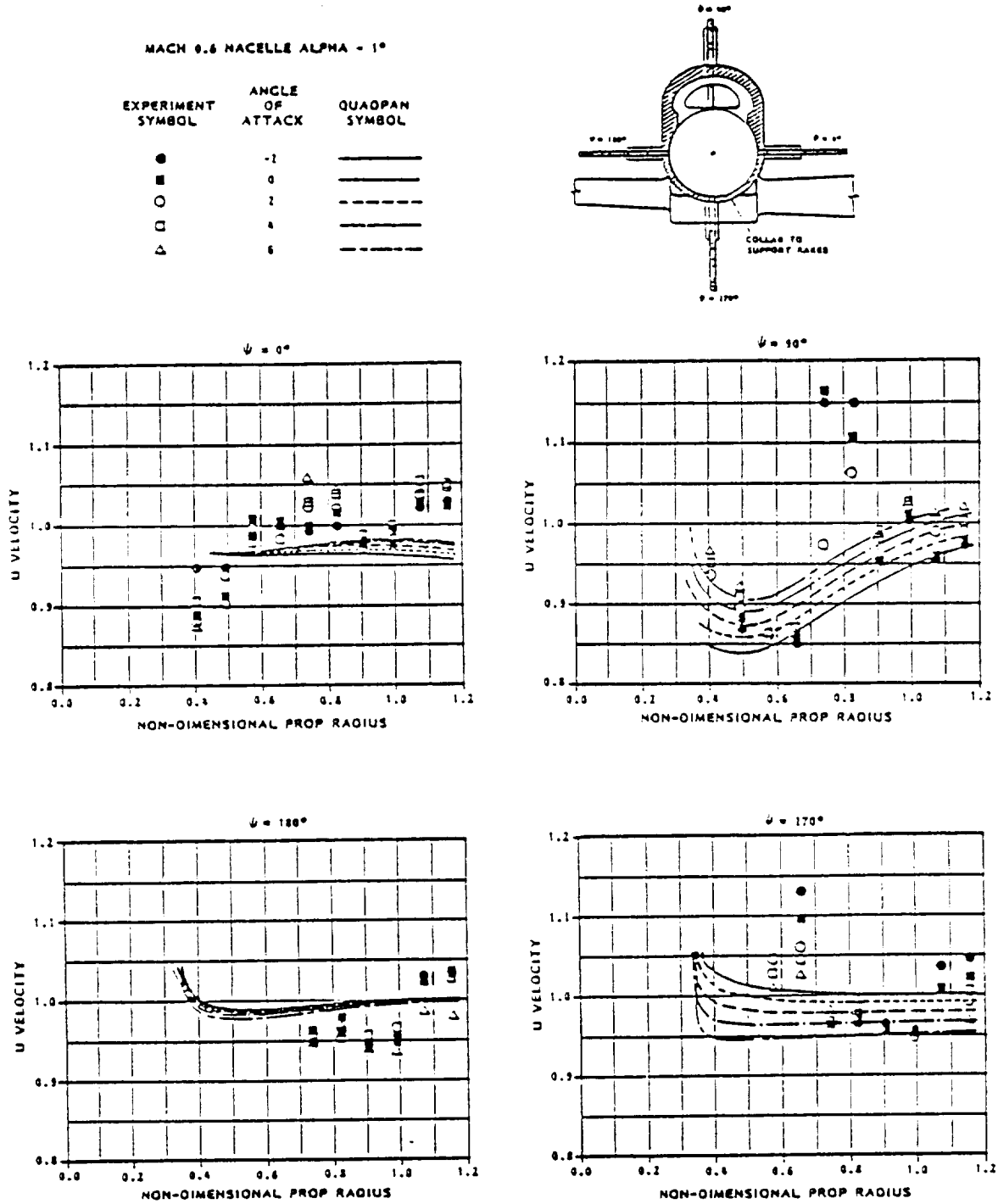


Figure 105. Axial Velocity Rake Data - Mach 0.6

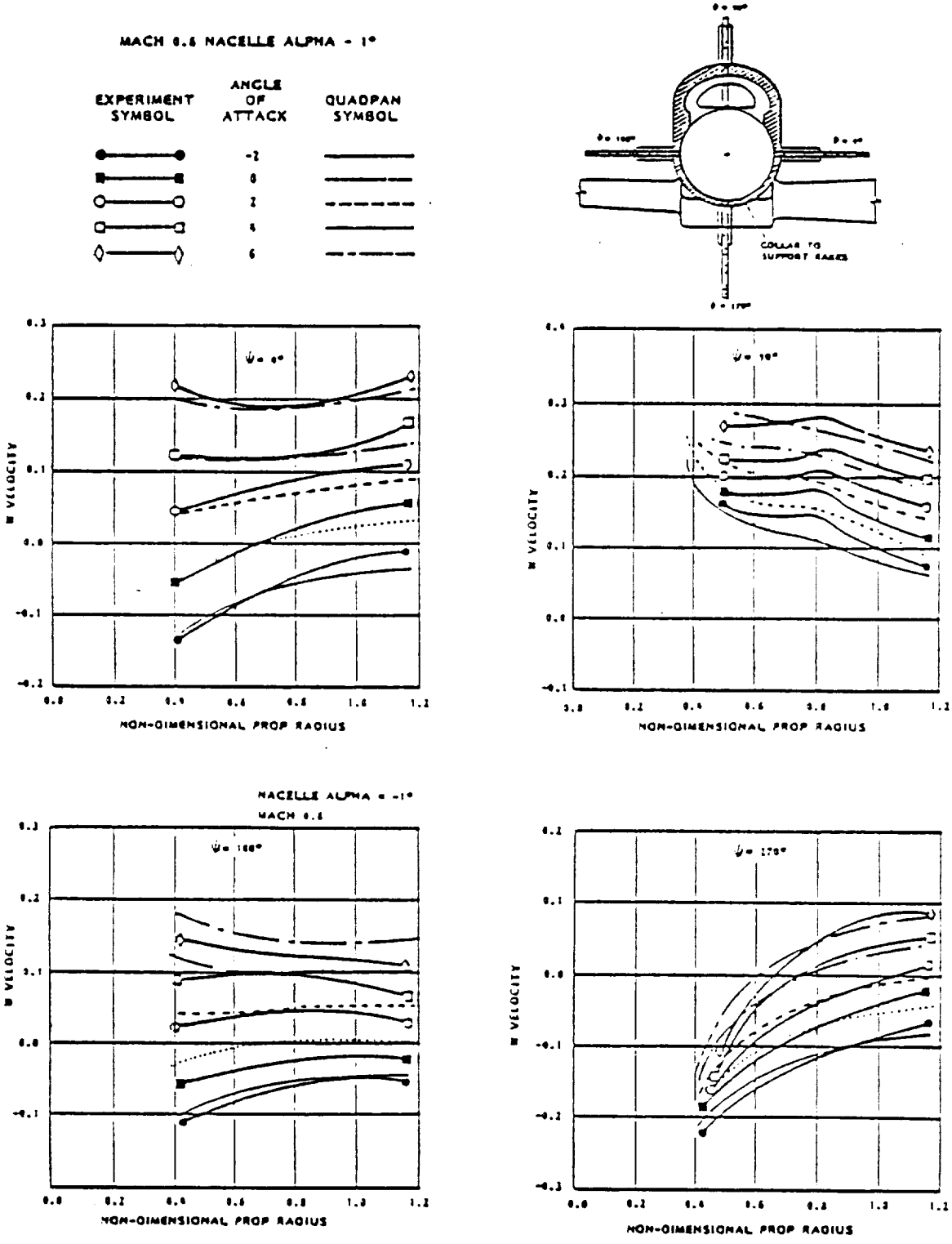


Figure 106. Vertical Velocity Rake Data - Mach 0.6

ORIGINAL PAGE IS OF POOR QUALITY

ORIGINAL PAGE IS
OF POOR QUALITY

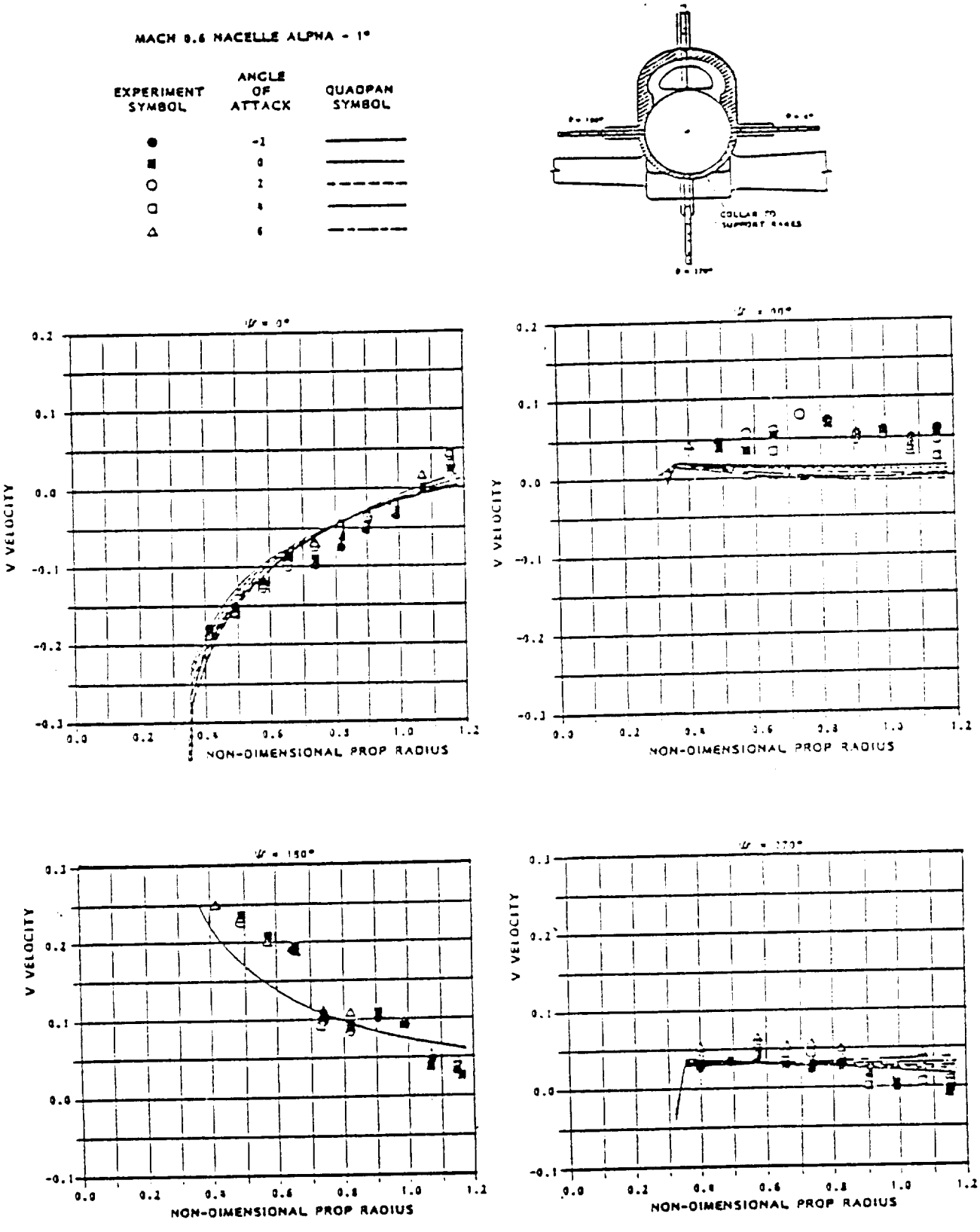


Figure 107. Lateral Velocity Rake Data - Mach 0.6

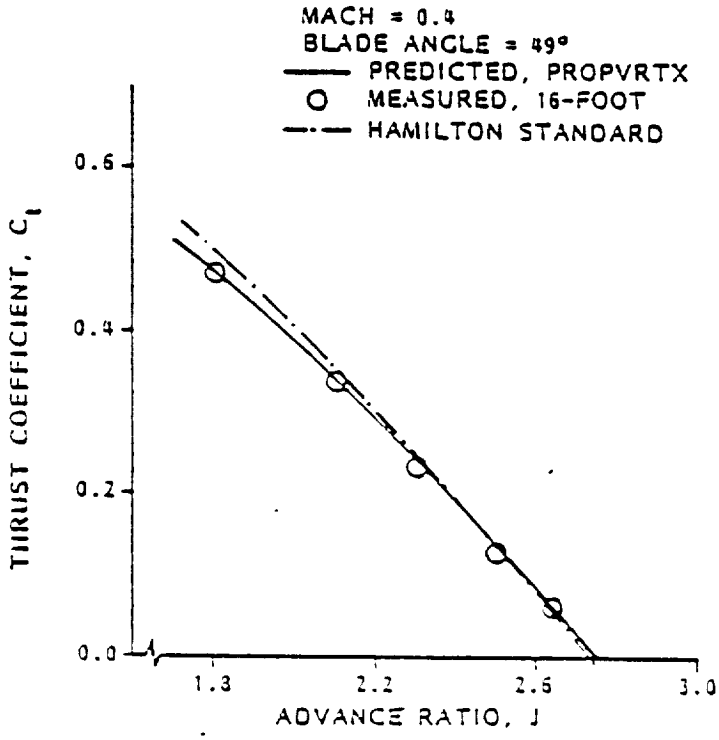


Figure 108. Thrust Coefficient Data - Mach 0.4

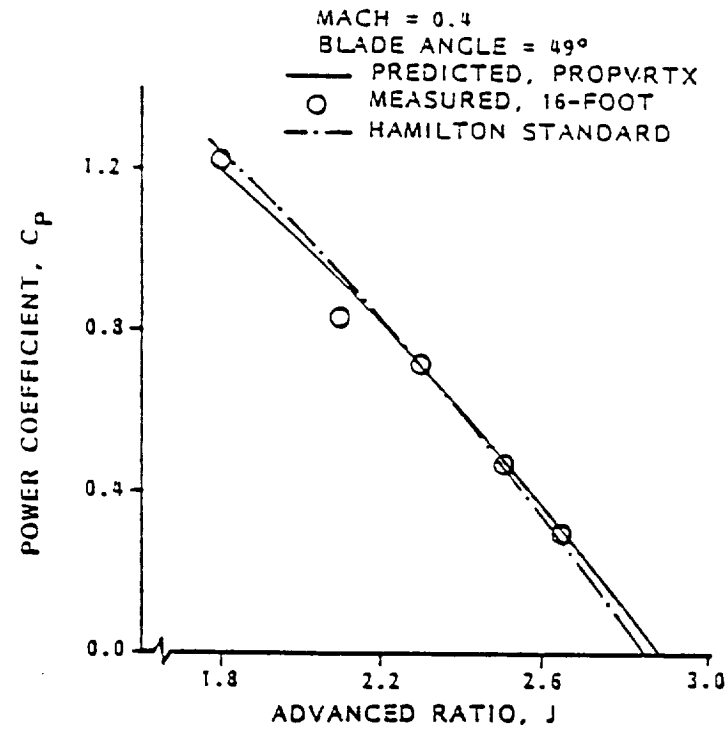


Figure 109. Power Coefficient Data - Mach 0.4

Installation of the PTA nacelle increased wing lift and nose-up pitching moment and slightly reduced pitch stability. Maximum lift coefficients were slightly decreased. Rudder and elevator effectiveness were only slightly affected, but roll control power was reduced--primarily because of the deactivation of inboard wing spoilers. As expected, the application of propfan power had a strong effect on yawing and rolling moments. In fact, the limiting condition for low speed flight was set by the requirement for adequate roll control margin.

Generally, the wind tunnel data were predicted with good accuracy by the analytical codes QUADPAN and PROPVRTX--validating that these codes could be used to fill gaps in the experimental data base.

The flow survey data showed reasonable agreement with QUADPAN predictions, and there was no significant degradation of this correlation with Mach number.

4.2 FLUTTER MODEL TESTS

4.2.1 Objectives

One objective of the high-speed flutter model test program was to substantiate the analytically predicted wing flutter safety of the single propfan testbed configuration and a similar design with propfan powerplants on both wings. A second objective was to obtain data with which to validate the flutter analysis methods proposed for aircraft final design.

4.2.2 Test Facilities and Procedures

Wind tunnel tests of the high-speed flutter model were conducted in the NASA-Langley Transonic Dynamics Tunnel (TDT). This tunnel uses Freon as the test gas so that model dynamic properties can be better simulated at representative test Mach numbers. The model was tested on a very compliant two-cable mount system which produced minimal effects on flutter stability. The model is shown in the wind tunnel in Figure 110.

The model test envelope, Figure 111, was established by applying the model scales to the testbed aircraft dynamic pressure at 1.2 V_D (where V_D is dive equivalent airspeed). The maximum model test Mach number was limited to 0.9 by the TDT facility safety requirements.

The test procedure consisted of speed buildups at several tunnel total pressures until flutter occurred or the test envelope limits (1.2 V_D, M = 0.90) were reached.

4.2.3 Model Description

The flutter models were designed to simulate the operation of the testbed aircraft throughout its flight test envelope and to demonstrate a 20-percent flutter speed safety margin above limit dive speed. A geometric scale of 1/9 was selected because it permitted the use of the same propfan blades used on the PTA stability and control model, and the resulting model size was compatible with the NASA TDT. The model design scales are shown in the table of Figure 112.

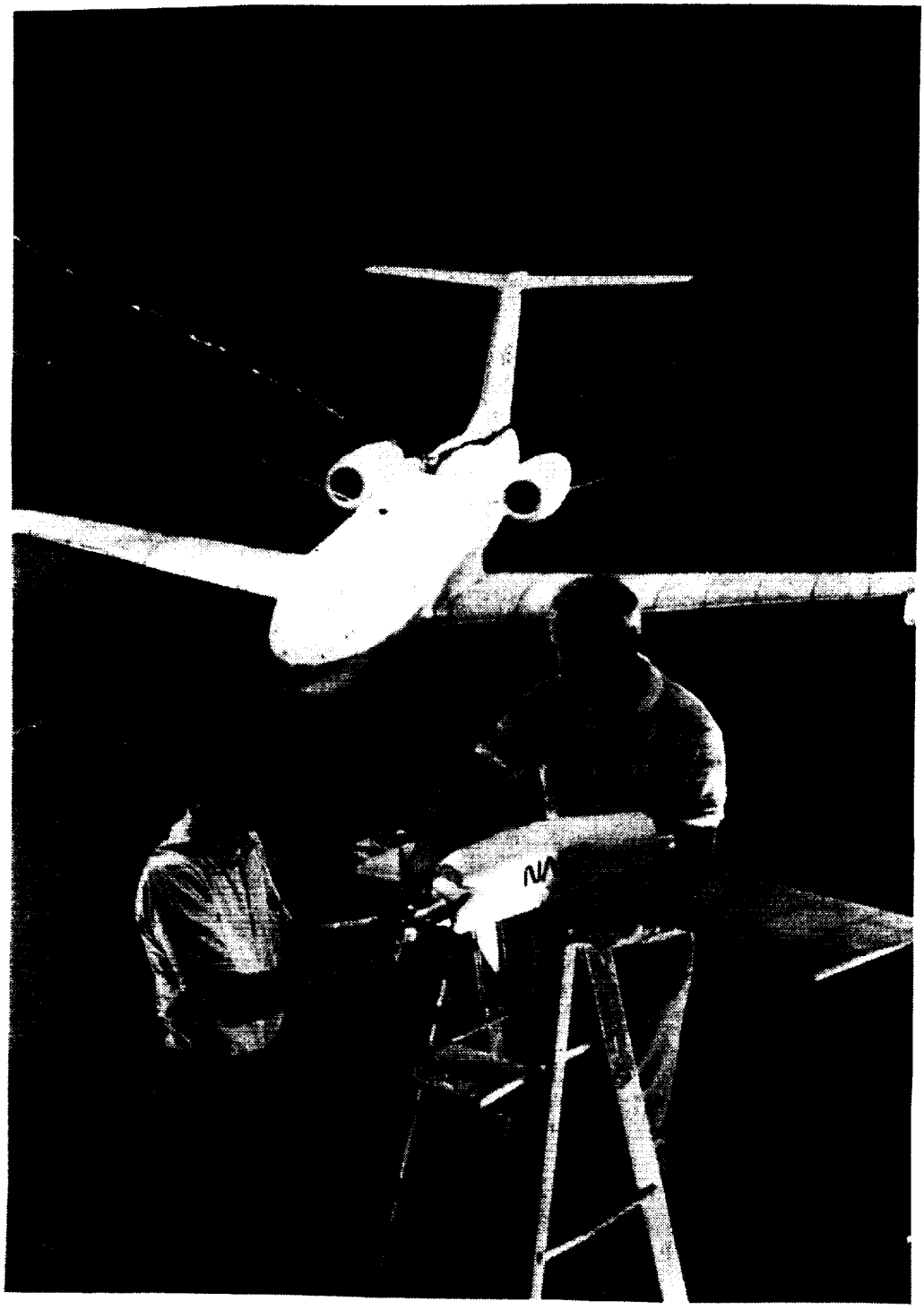


Figure 110. Flutter Model in Langley Transonic Dynamics Wind Tunnel

ORIGINAL PAGE
BLACK AND WHITE PHOTOGRAPH

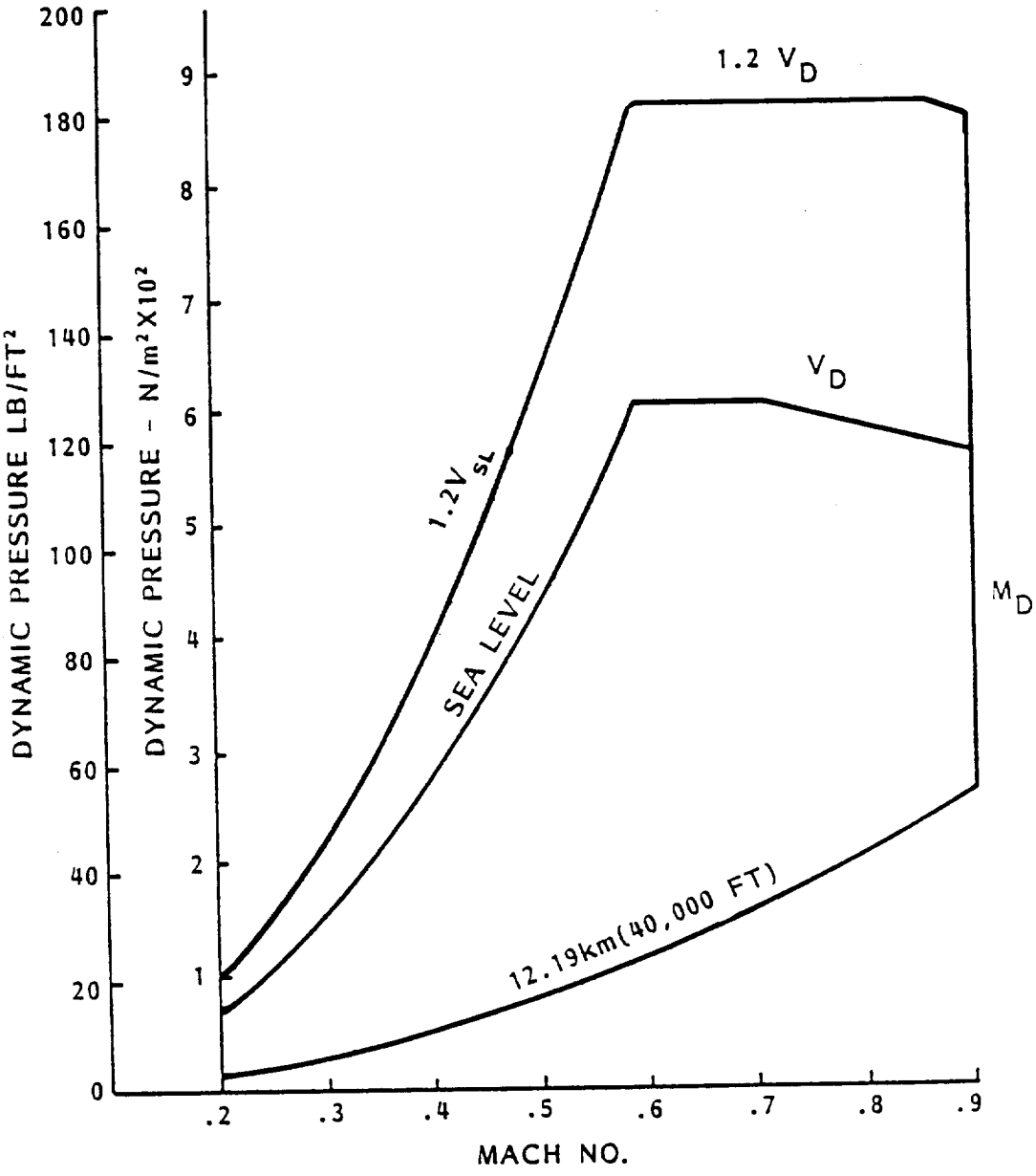


Figure 111. Flutter Model Test Envelope

QUANTITY	SCALE (1)
Geometry	1/9 (2)
Mach Number	1/1 (2)
Density	1/1 (2)
Velocity	1/2.02
Dynamic Pressure	1/4.08
Frequency	4.4554/1
Weight (Mass)	1/729
Mass Moment of Inertia	1/59.049
Stiffness (Beam)	1/26.772

NOTES: (1) Scale is for model-in-tunnel to aircraft-in-flight.

(2) When these model test quantities are established, the other scale factors result.

Figure 112. Model Design Scales

The three wing configurations tested were:

- o Bare wing
- o Twin propfan
- o Single propfan

The bare wing configuration represented an unmodified GII wing with 1134 kg (2500 lb) static balance booms on each tip. The twin propfan configuration represented the reinforced GII wing design with twin propfan powerplants and 136 kg (300 lb) flutter stabilizing booms on each side. The single propfan configuration represented the asymmetric PTA preliminary design with propfan powerplant and flutter boom on the left side and static balance boom on the right.

The model wings and fuselage were constructed with hollow aluminum spars and segmented, fiberglass-reinforced, wooden aerodynamic fairings attached to the spars. The propfan powerplants consisted of masses (representing the power section, gearbox, and propfan) which were supported by springs representing the engine mounts, and an aluminum truss representing the nacelle structure. The fin and stabilizer were unsegmented monocoque surfaces.

4.2.4 Instrumentation

The model was instrumented with a combination of strain gage bridges and miniature accelerometers to measure the loads and dynamic response. Hall-effect pulse transducers and frequency counters were used to monitor the propfan rotation speeds. Six to eight of the strain gage channels were calibrated and monitored to ensure that the model maximum design loads were not exceeded.

High-speed movie cameras were also used to record model responses. The wind tunnel parameters were obtained via the TDT facility data acquisition system.

4.2.5 Results

The tests that were conducted to substantiate the predicted flutter safety for the single and twin propfan testbed aircraft preliminary designs indicated that no flutter or near-flutter conditions occurred. The model test envelope and representative test points are shown in Figure 113. Tests with simulated severe failure conditions involving the powerplant-to-gearbox connections and loss of the flutter boom indicated no wing or whirl flutter.

Analysis validation tests were conducted with a destabilizing boom installed on each wing tip to induce flutter or near-flutter conditions near or within the test envelope. A near-flutter condition is indicated in Figure 114 for the single propfan configuration with destabilizing boom.

The wind tunnel model differed from the PTA aircraft in several respects. Firstly, the model wing could not be made light enough to accurately

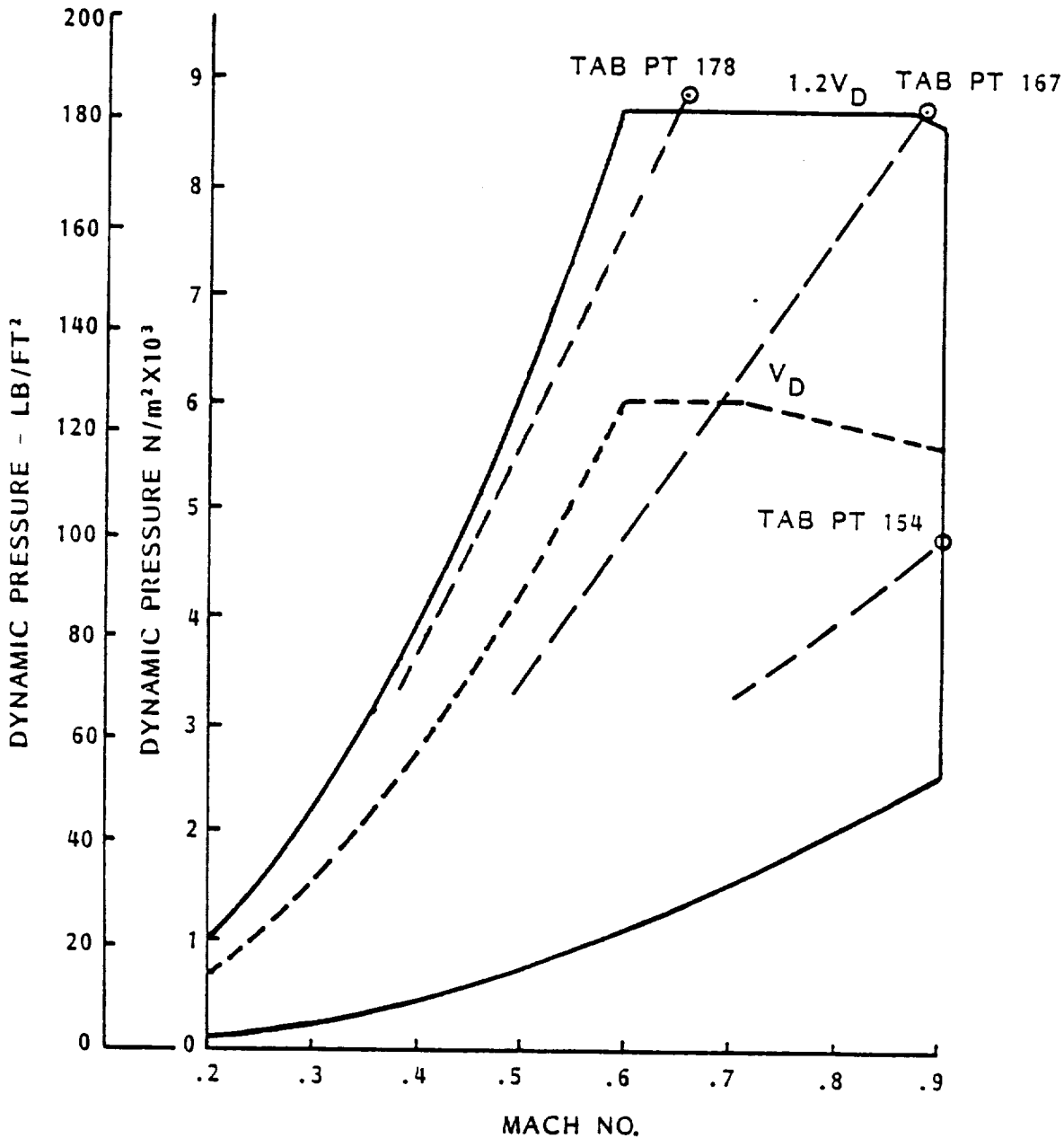


Figure 113. Flutter Test Envelope and Results

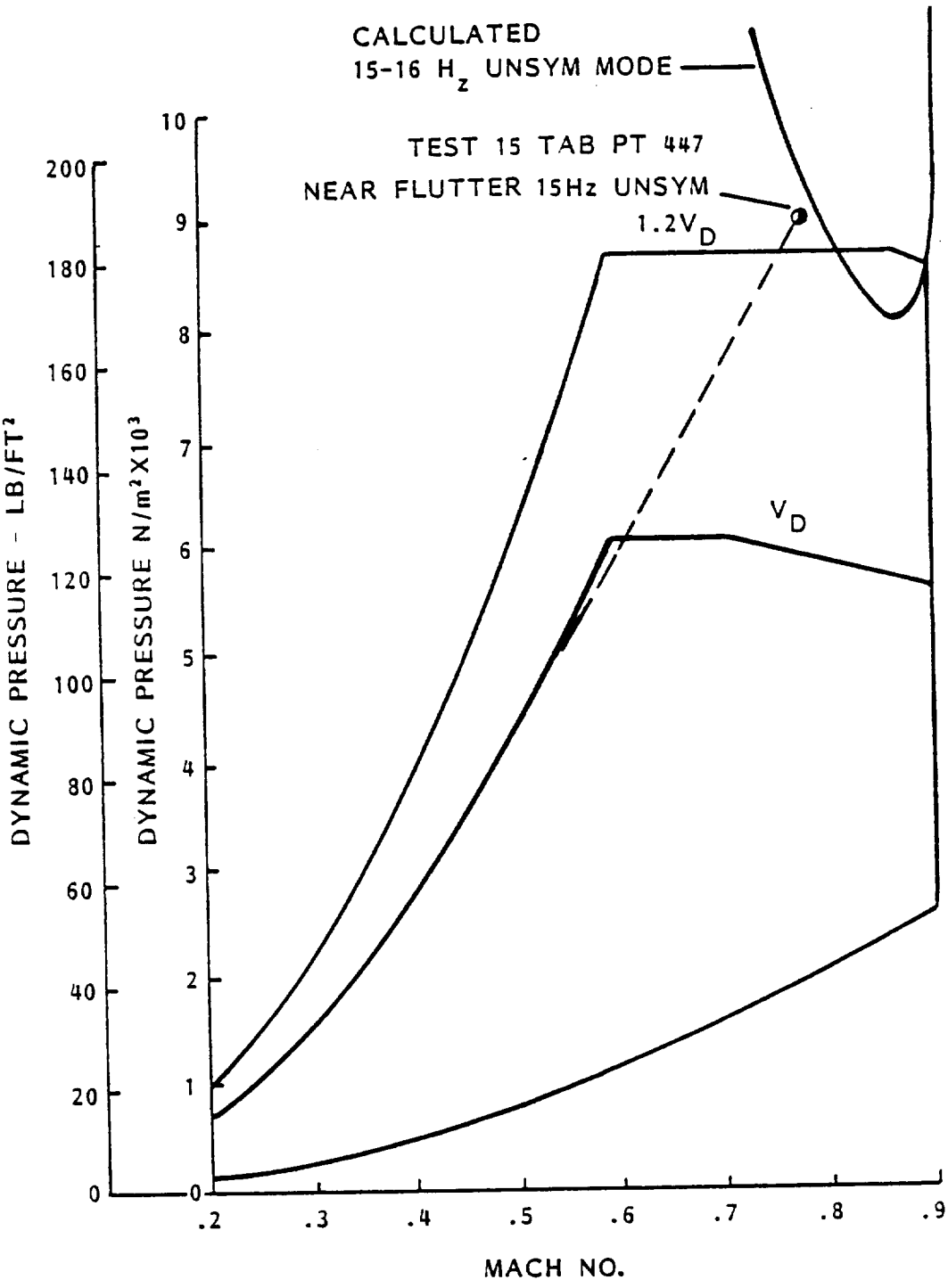


Figure 114. Calculated vs Measured Flutter Boundary - PTA Configuration with Destabilizing Boom

simulate empty fuel tanks in the outer wing - one of the most critical fuel conditions. Secondly, the model propfan nacelle flexibilities were greater than desired. Thirdly, for stability in the wind tunnel, it was necessary to add a nose ballast to the model that was equivalent to 3227 kg (7100 lbs) for the full-scale aircraft.

An analysis was performed to determine the net effect of these differences on the stability of the single propfan model without a flutter boom. The predicted flutter speed was well above 1.2 V_D, which was consistent with the test results but indicated that the model was more stable than the aircraft for this configuration. Therefore, the absence of flutter in the tests did not indicate that the flutter stabilizing boom was unnecessary for the testbed aircraft.

The test results alone could not be used to verify that the final aircraft design would have adequate flutter safety margins. They did indicate, however, that no serious flutter instablilities of the aircraft were overlooked in the analysis.

4.2.6 Conclusions

The results of the design verification tests generally confirmed the predicted wing and whirl flutter stability of the preliminary design configurations tested. No unexpected flutter instabilities were caused by the rotating propfan or the asymmetry of the single propfan testbed configuration. The flutter stability of the symmetrical twin propfan configuration was approximately the same as that of the asymmetric single propfan configuration. It was concluded from the correlation of model data with predictions that the flutter analysis methods proposed for aircraft design were capable of accurately predicting PTA wing flutter characteristics.

4.3 INLET MODEL TESTING

4.3.1 Objectives

Fabrication of the PTA forward nacelle was one of the first segments of the critical path leading to flight test. It was necessary at an early stage, therefore, to specify the size, shape, and location of the engine inlet, which is one of the dominant features of the nacelle. The design selected required the inlet duct to make a sharp "S" bend, and this aroused concern about the quality of flow from that duct into the engine inlet. A test was therefore planned to measure the performance of the inlet duct.

The larger objective of these tests was to validate that the duct would perform in a satisfactory way, or if that proved not to be the case, to provide diagnostic data that could be used to remedy deficiencies. The specific objectives were:

- To measure pressure loss through the duct
- To measure flow distortion at the exit of the duct

- To measure wall static pressure distributions
- To measure the efficacy of fairings around the propfan drive shaft that penetrated the duct
- To measure the impact of swirl at the inlet on duct performance

4.3.2 Test Apparatus

The inlet duct is shown in Figure 115, together with an inlet bell mouth that was part of the test hardware. This duct was designed as a one-third scale model of the full-scale hardware. Pertinent dimensional features of the duct are listed in the table of Figure 116.

The test duct was designed using the three-dimensional inviscid panel code QUADPAN. Figure 117 serves to illustrate the way that this inviscid code was used to design a duct that obviously was sensitive to viscous effects like boundary layer growth and separation. Part (a) of Figure 117 shows pressure distributions calculated by QUADPAN for an initial configuration of the duct; Part (b) shows pressure distributions after several iterations of changing local duct contours to soften strong pressure gradients. These were the predicted pressure distributions for the configuration that was tested.

The test setup is shown in Figure 118. The duct and inlet bell were attached to a cylindrical duct in which an axial flow compressor was installed. This compressor induced flow through the test duct. Instrumentation included the wall static pressure tubes that can be seen in Figure 118 and the duct exit total pressure rake that can be seen in Figure 119. Figure 119 also shows the simulated propfan drive shaft that penetrated the flow passage. Two fairings were designed to smooth the flow of air around the drive shaft and were included in the test program.

4.3.3 Test Results

Figure 120 shows measured wall static pressure distributions compared with those predicted. The agreement is, generally, quite good, but the best part is that the measured pressure distributions show none of the strong adverse pressure gradients that were to be avoided. These data imply that the design successfully avoided significant regions of flow separation.

Total pressure recovery at the duct exit is plotted against Mach number at the 0.36 compressor face in Figure 121. These total pressure values were obtained from six rakes at the duct exit with the readings area weighted. Pressure recovery for the basic duct (no drive shaft fairings) was very good. At the design value of compressor face Mach number (0.36), the pressure recovery was approximately 0.993. With fillet and hub fairings around the drive shaft, this was increased to about 0.996. With swirl simulation at the inlet, pressure recovery for the basic duct without fairings was about 0.990.

The rake data were also used to calculate flow distortion at the simulated engine compressor face. Distortion parameters used by the engine manufacturer are:

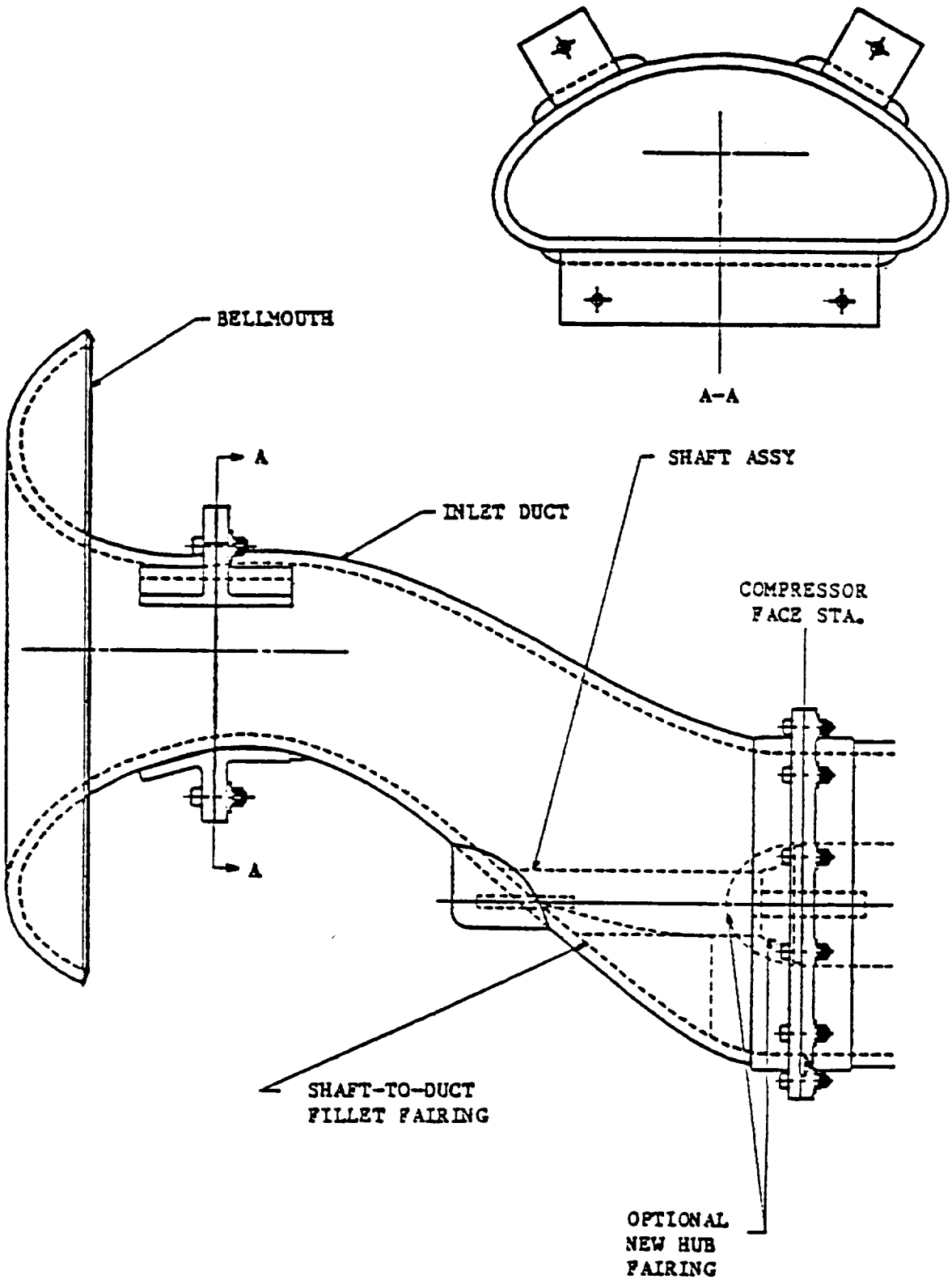


Figure 115. PTA Inlet Duct Test Hardware

PARAMETER	MODEL SCALE	FULL SCALE
LENGTH (TH. TO C.F.), CM	30.34	89.76
OFFSET, DELTA Y, CM	12.97	38.38
OFFSET RATIO, DY/DX	0.4275	0.4275
DIAM. OF COMPR. FACE, CM	15.8	46.74
DIAMETER OF HUB, CM	6.44	19.05
AREA, NET COMPR. FACE	163.4	1430
AREA RATIO, C.F./THROAT	0.975	0.975
WIDTH/HEIGHT AT THROAT	2.482	2.482
THROAT ASPECT RATIO (AREA/HEIGHT**2)	2.131	2.131
MAX FLOW TURNING ANGLE, DEG	29.0	29.0
DESIGN COMPR. FACE MACH NO.	0.36	0.36
PEAK LOCAL MACH NO.	0.46	0.46

Figure 116. PTA Inlet Duct - Major Dimensions and Design Parameters

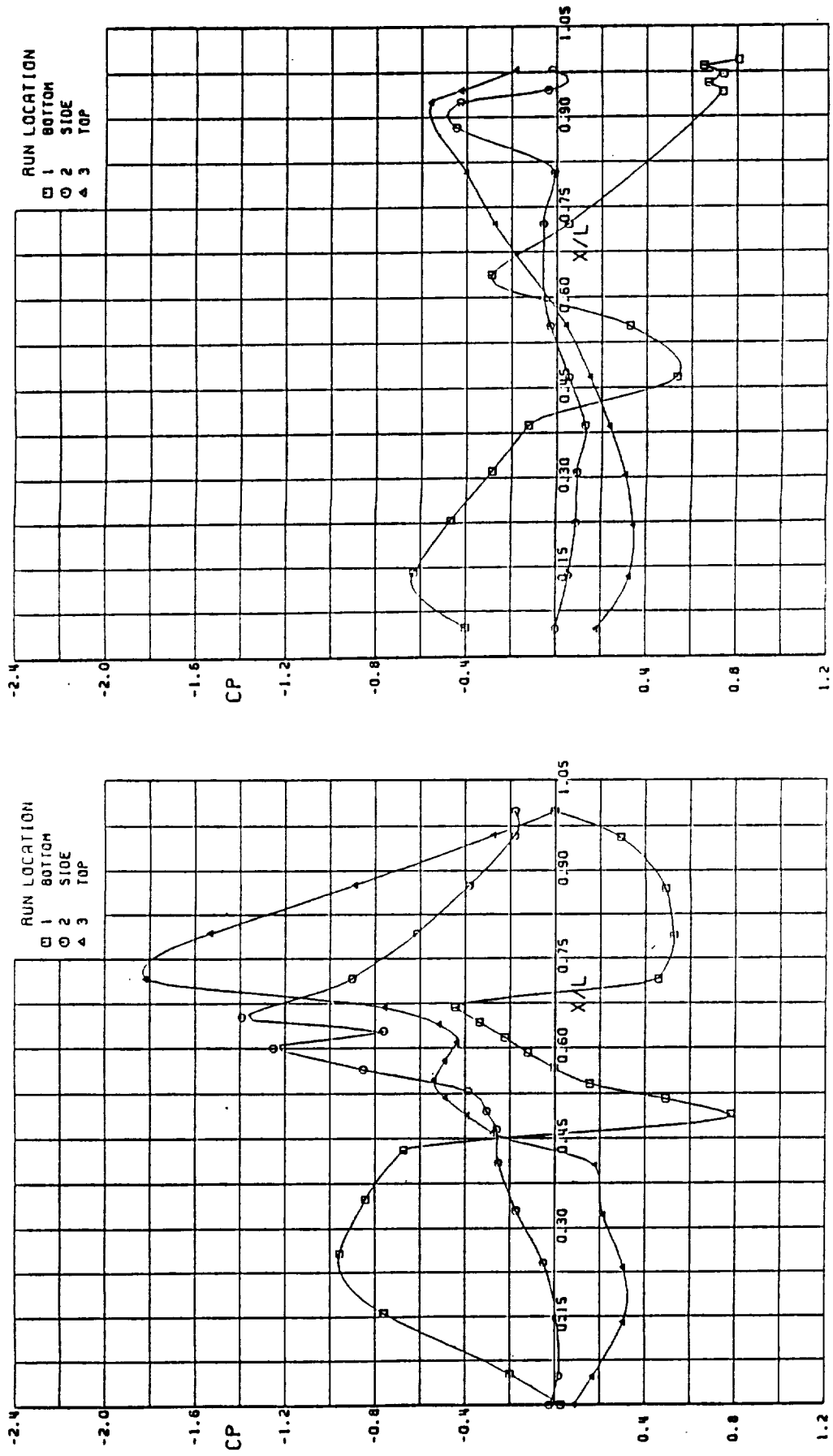
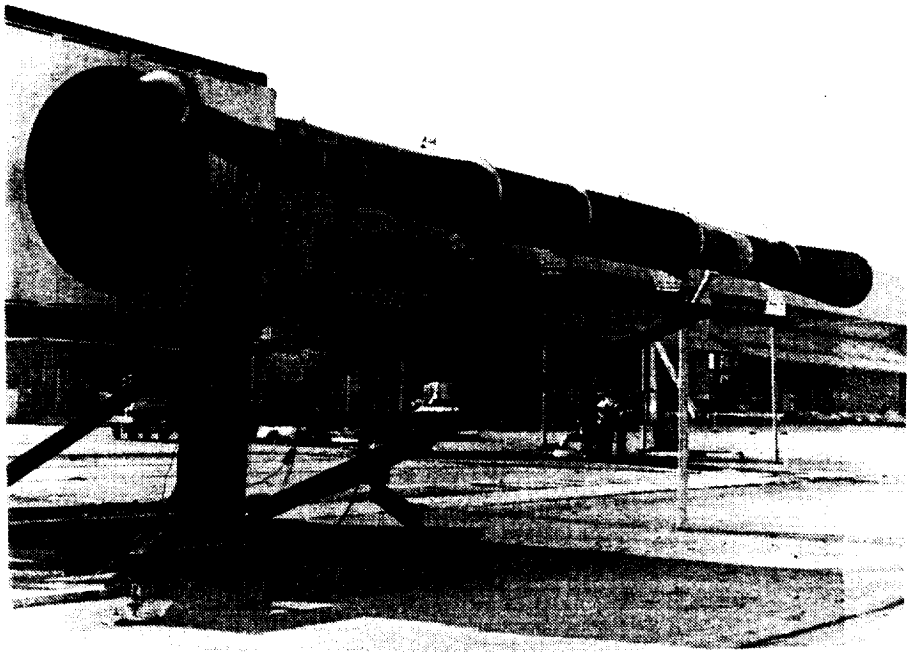
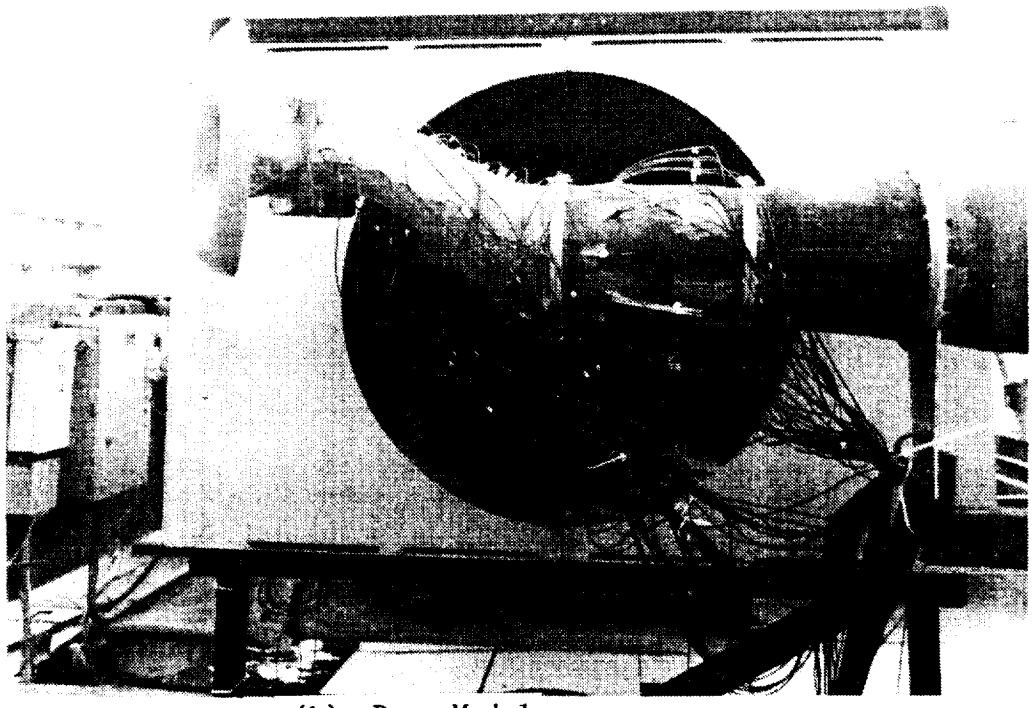


Figure 117. QUADPAN Pressure Distribution Predictions

ORIGINAL PAGE
BLACK AND WHITE PHOTOGRAPH



(a) Complete Test Rig with Model, Side View



(b) Duct Model

Figure 118. Inlet Duct Test Apparatus



Figure 119. View of Simulated Engine Compressor Face

ORIGINAL PAGE
BLACK AND WHITE PHOTOGRAPH

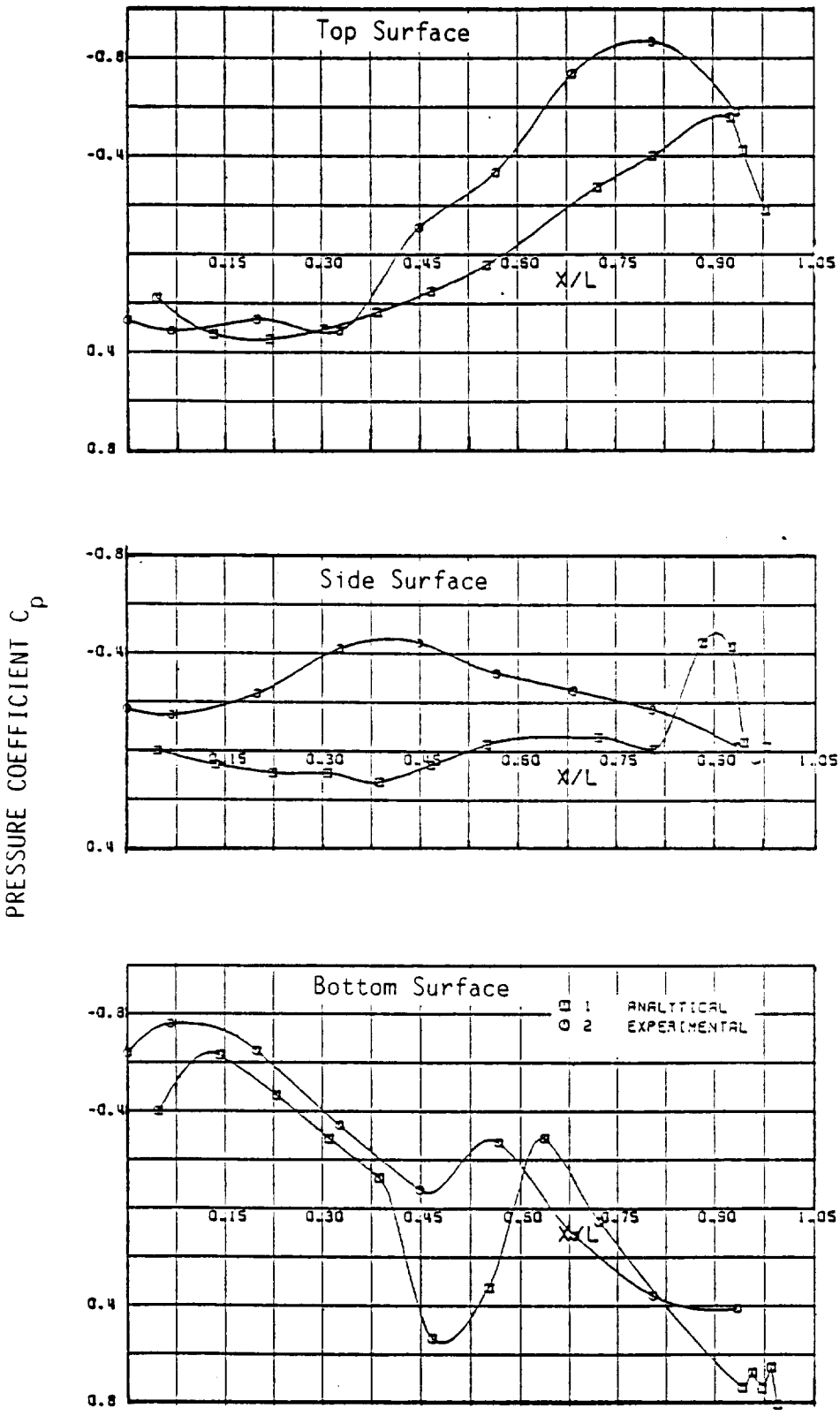


Figure 120. Predicted and Measured Static Pressure Distributions

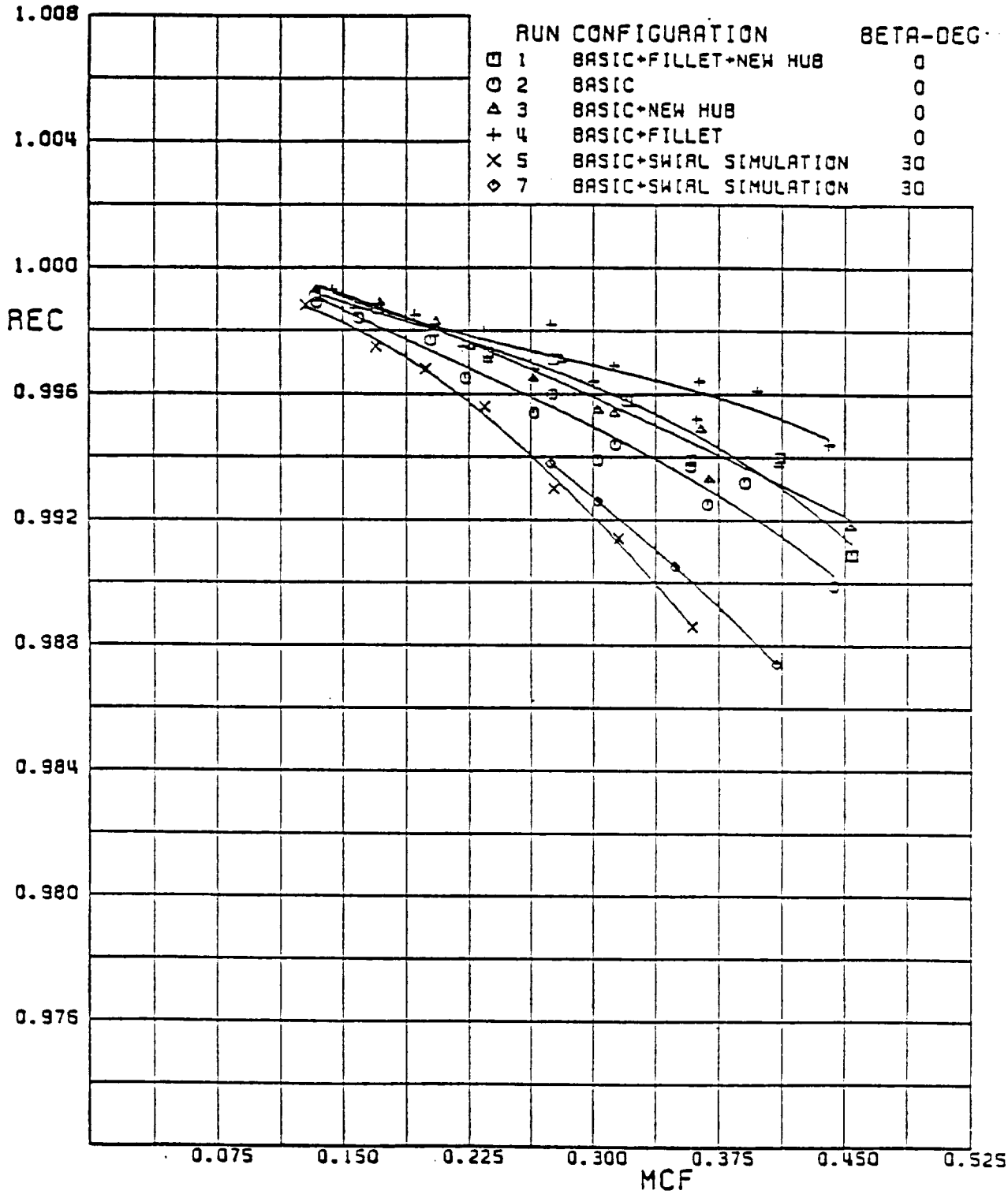


Figure 121. Total Pressure Recovery at the Compressor Face

- Circumferential Distortion (KTHETA) - average pressure for the highest 240-degree sector minus the average pressure for the remaining 120-degree sector and divided by the mean dynamic pressure

- Radial Distortion (KR) - average pressure in the inner annulus comprising 60 percent of the area minus the average pressure in the remaining 40 percent and divided by the mean dynamic pressure

Measured values of KR and KTHETA are plotted in Figure 122, together with an envelope of allowable distortion for the engine. It can be seen that there were no flow distortion problems for any of the duct configurations tested.

4.3.4 Conclusions

Based on the results of these tests, it was concluded that the basic duct designed with the QUADPAN analytic methodology was quite adequate for the PTA application and that no modifications in the form of shaft fairings, etc., were required. Performance, with total pressure recovery of approximately 0.99, was better than expected. The flow distortion margins were substantial and left room for some contingencies in the full-scale hardware.

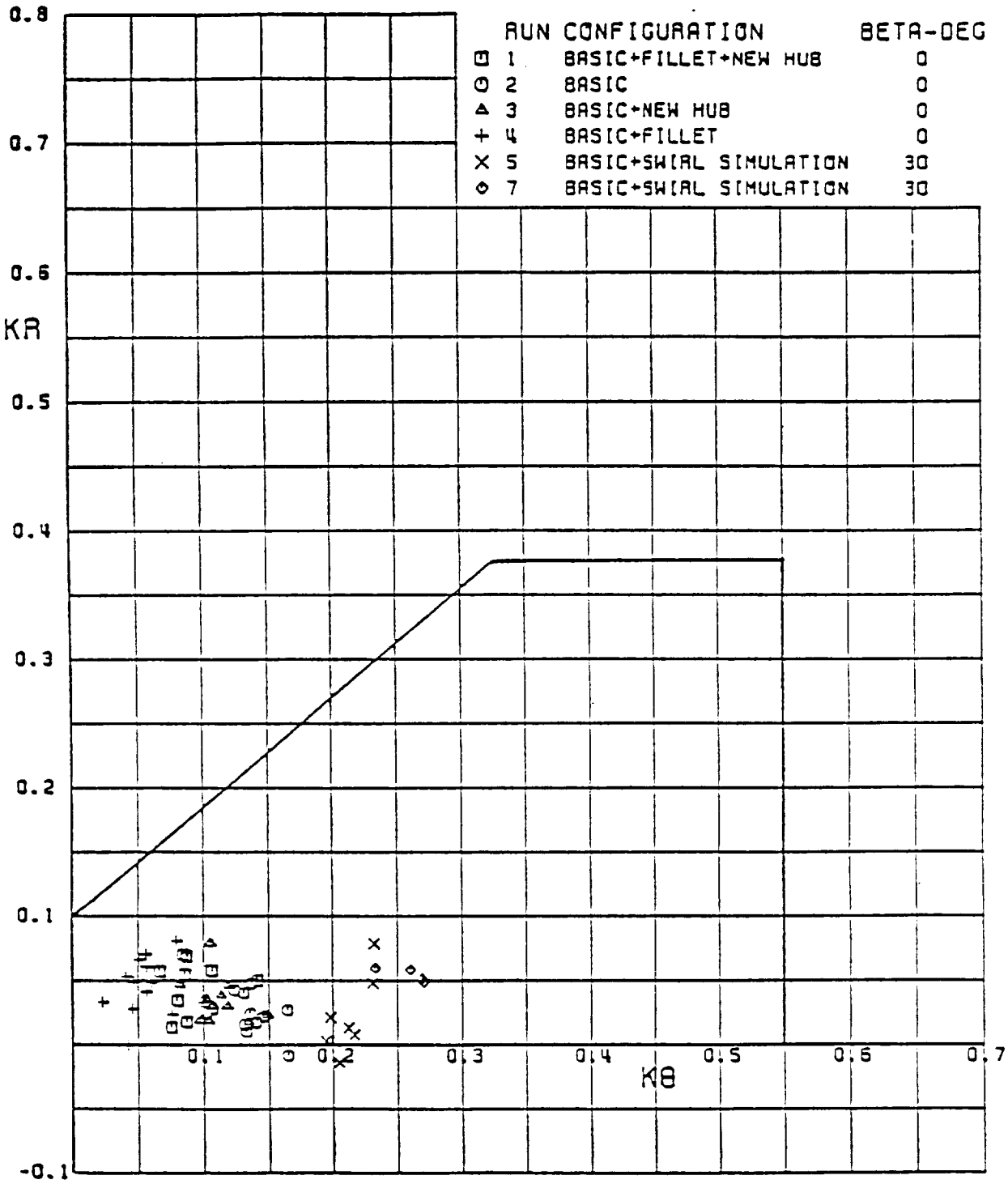


Figure 122. Flow Distortion Relative to Allison Envelope

5.0 ANALYSES

5.1 PROPFAN PERFORMANCE ANALYSES

5.1.1 Engine Inlet Design Analysis

Primary concerns with design of the forward region of the nacelle were:

- The impact of the engine inlet and other nacelle features on the propfan dynamic loads
- Pressure recovery at the engine inlet
- Height of the inlet off the nacelle surface and the shaping of the boundary layer diverter passage
- Pressure loss and flow distortion in the inlet diffuser

Valuable information to aid in the design of this region was obtained from small-scale tests reported in References 1 and 2. Relevant data from these tests are presented in Figure 123 and show that for a single-scoop inlet located close behind the propfan, the 1P and 2P blade stresses were approximately the same and the total was 3750 psi. For a twin-scoop inlet configuration in the same location, total blade stresses were somewhat reduced, but the 2P content was about 80 percent of the total. The single-scoop inlet moved downstream a distance equal to 9 percent of the propfan rotor diameter, however, produced more nearly the desired proportion of nP to 1P stress content, and furthermore, the total blade stress was the lowest of the three configurations tested. From the standpoint of propfan dynamic loading, therefore, the single scoop in the aft location was a good design.

Considering these results, the configuration shown in Figure 24 was developed. The aerodynamic code QUADPAN was used to predict flow field velocities in the plane of the propfan, and these flow field properties were then used by Hamilton Standard to predict blade stresses. These calculations confirmed that the higher order harmonic content was within the desired range (12 to 30 percent of total) and that the total blade vibratory stresses were within the allowable range from a structural design standpoint.

Placing the inlet plane in this aft position, however, had two negative impacts. The first was that the data from Reference 1 showed some degradation in pressure recovery at the inlet face as the inlet plane was moved downstream from the propfan. There was concern that total pressure loss, if it were too large, might prevent attaining the power needed for the flight research tests. Predictions based on Reference 1, however, indicated that even in the aft location a total pressure recovery of slightly greater than 1.04 times freestream total pressure would be obtained, and this was acceptable.

The second concern with the aft inlet location had to do with the impact on the inlet diffuser duct that connected the nacelle inlet with the

PROPFAN BLADE STRESS
GUN III TESTS; M = 0.8

STRESS COMPONENT \ INLET	11011 SINGLE-SCOOP MOST FORWARD LOCATION	11020 SINGLE-SCOOP INTERMEDIATE LOCATION	21011 TWIN-SCOOP MOST FORWARD LOCATION
1P	1950 PSI	1400 PSI	300 PSI
2P	1800	850	2500
TOTAL	3750	2250	2800

PRELIMINARY CHOICE

Figure 123. Propfan Blade Excitation for Several Inlet Configurations

PARAMETER	MEASURED	TARGET
RECOVERY	0.993	0.979
CIRCULAR DISTORTION	0.128	0.550
RADIAL DISTORTION	0.017	0.375
HARMONIC DISTORTION COMPONENTS	.12, .08 .04, .03	.16, .32 .20, .20

Figure 124. Inlet Diffuser Model Test Results

engine compressor face. The aft location made this duct shorter and made the "S" bends in the duct more severe than they would have been for a more forward location of the inlet. With these constraints, there were the risks of excessive inlet duct total pressure loss and flow field distortion in the air delivered to the engine compressor.

To insure that these factors did not become problems, the design was made conservative, and small-scale tests of the proposed design were conducted to verify that the quality of flow to the engine inlet was acceptable. The design was made conservative by electing to perform the diffusion or deceleration of flow from Mach 0.8 to the 0.36 compressor face Mach number external to the inlet. Thus the inlet duct area could be maintained practically constant. Results from the Reference 1 tests showed that this could be done with little or no spillage drag penalty as long as the cowl sections were carefully designed to avoid transonic drag.

Even with the non-diffusing duct, the "S" bends and penetration of the propeller drive shaft through the duct generated concern that unacceptable flow distortion might result. The duct, therefore, was carefully contoured using the flow code QUADPAN as an analytical tool, as discussed in Section 4.3.

Reviewing briefly, QUADPAN was used to predict the surface pressures through the duct along top and bottom centerlines and along the extreme side panels. Where these pressure distributions showed severe adverse pressure gradients, it was recognized that boundary layer separation would be likely to occur. In these regions, therefore, duct cross sections and surface contours were modified in the direction to relieve the perceived unfavorable flow environment. This procedure was followed through several iterations until the final configuration was developed.

The resulting duct design became the subject for the scale model tests reported in Section 4.3. The table of Figure 124 summarizes data from the diffuser tests and compares these data with performance targets. As it can be seen, the duct design was completely satisfactory.

Methods for cowl design were developed in the Reference 1 program and were validated by experimental data as described in Reference 10. These methods centered about the use of the QUADPAN code for the first stage of design and for examination of three-dimensional effects, and the use of PROPVRTX for power effects. Even though QUADPAN is a subsonic code, it provided good guidance for transonic design when used with foreknowledge of desirable pressure distribution characteristics. To verify that the cowl sections obtained with QUADPAN were valid for transonic flow, an axisymmetric transonic code FL049 was used to refine the cowl section at the vertical centerline of the nacelle. An example of the result is shown in Figure 125 where wind tunnel data show good agreement with predicted nacelle pressure distributions.

The remaining area of the inlet/cowl design was the boundary layer diverter trough between the inlet and the nacelle surface. It was determined in the Reference 1 tests that QUADPAN provided good predictions of flow tendencies in this region even though QUADPAN is an inviscid flow

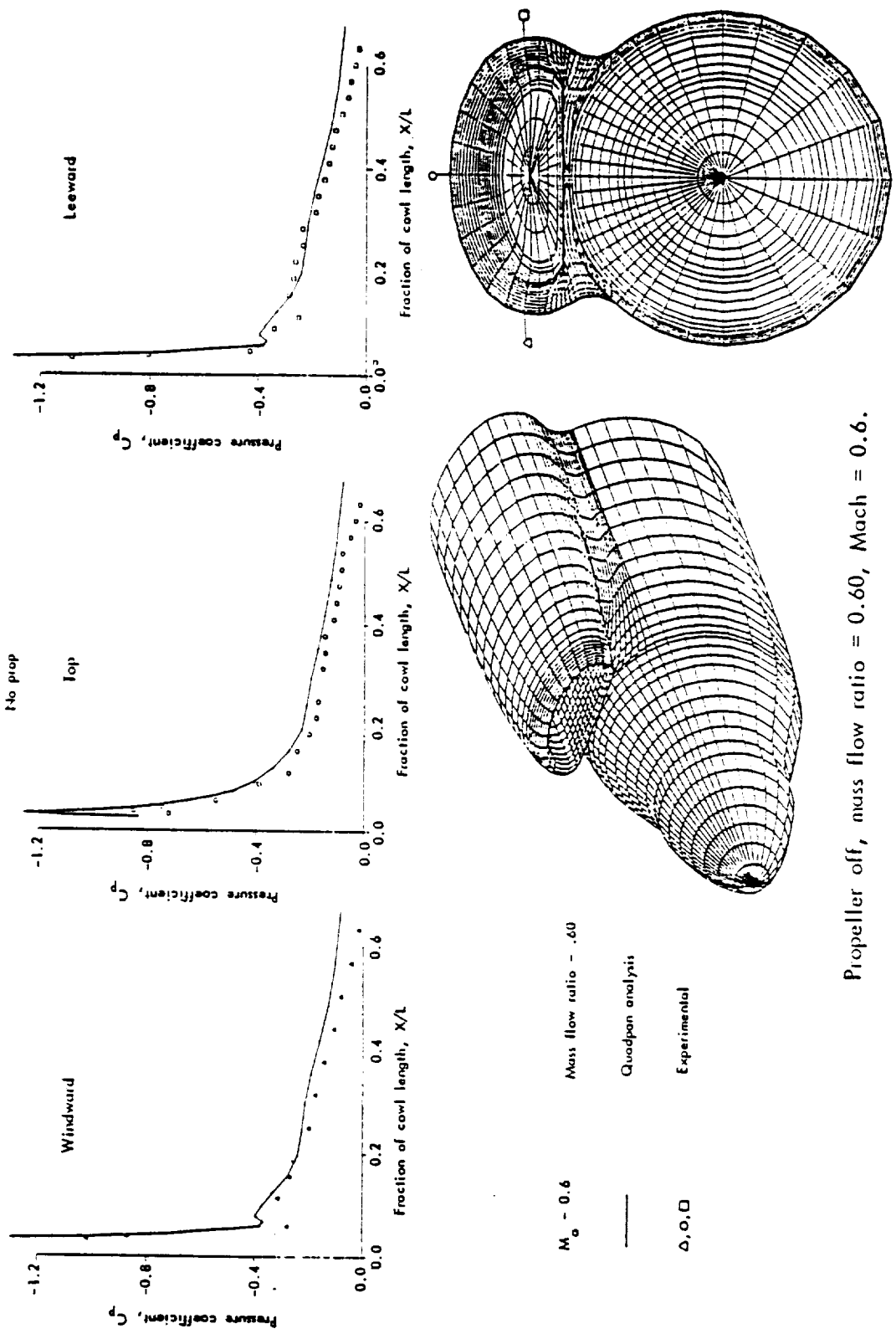


Figure 125. Predicted and Measured Cowl Pressures

ORIGINAL PAGE IS
OF POOR QUALITY

program. Therefore, QUADPAN became the tool for shaping the boundary layer diverter. The tests of Reference 1 also showed the inlet pressure recovery to be strongly related to the height of the inlet lower lip above the nacelle surface as shown in Figure 126. The PTA design point selected was a compromise that sacrificed a little total pressure recovery to avoid increasing the offset dimension of the S-duct.

5.1.2 Engine Exhaust Nozzle Sizing

Maximizing shaft horsepower was a primary consideration in sizing the exhaust nozzle of the PTA engine. Consequently, it was decided that the nozzle would be sized to operate at the Mach 0.8, 10,668m (35,000 ft) design point with only enough jet exhaust thrust to induce aft nacelle cooling flow. To aid in this sizing, Allison provided the estimated engine performance curves shown in Figure 127. The nozzle size for zero exhaust thrust was about .343 m^2 (530 $in.^2$). It can be seen that reducing nozzle size from this point soon approaches a "knee" in the shaft horsepower curve, but that nozzle area can be reduced to .291 m^2 (450 $in.^2$) without serious power degradation. At that nozzle size, thrust from the engine exhaust was estimated to be 222N (50 lb), and this was estimated to be enough for aft nacelle cooling. This then was the exhaust nozzle size selected for the PTA installation.

5.1.3 Predicted Drive System Performance

A major design goal for propfan performance was to attain a propeller disc loading of 300 kw/m^2 (37.5 hp/ft^2) at the Mach 0.8, 10,668m (35,000 ft) design point. This requires 2265 kw (3037 hp) shaft power and 2293 kw (3074 hp) from the power section. Data from Allison's simulated altitude tests indicated that this goal would be exceeded provided installation losses were not too high.

With the tailpipe sized at 0.291 m^2 (450 $in.^2$), as described in Section 5.1.2; with compressor face pressure recovery estimated at 104 percent of freestream total pressure, as described in Section 5.1.1; and for an estimated inlet total temperature rise of 5.5°C (10°F), drive system installed performance was predicted. The results are shown in Figure 128 for a range of altitudes and Mach numbers and a propfan tip speed of 244 mps (800 fps). Design requirements were exceeded in all cases.

Subsequent engine qualification tests and flight tests demonstrated that the drive system performance met or exceeded these predictions.

5.2 AIRCRAFT AERODYNAMICS

5.2.1 Aircraft Drag Prediction

The key element in prediction of aerodynamic performance for the PTA aircraft was the estimation of drag increments. These increments were then added to existing drag polars for the GII to obtain drag polars for the PTA configuration.

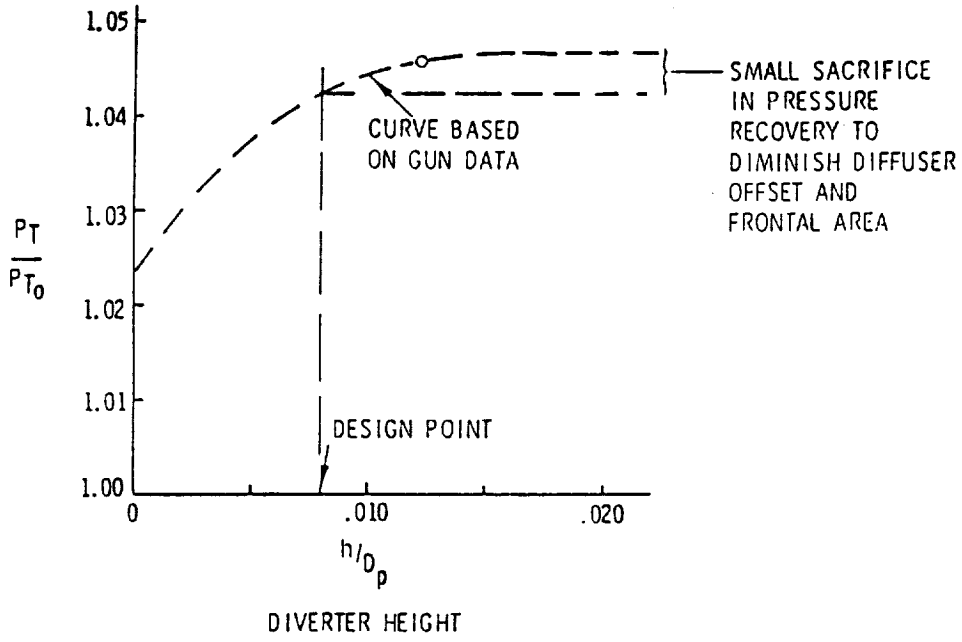
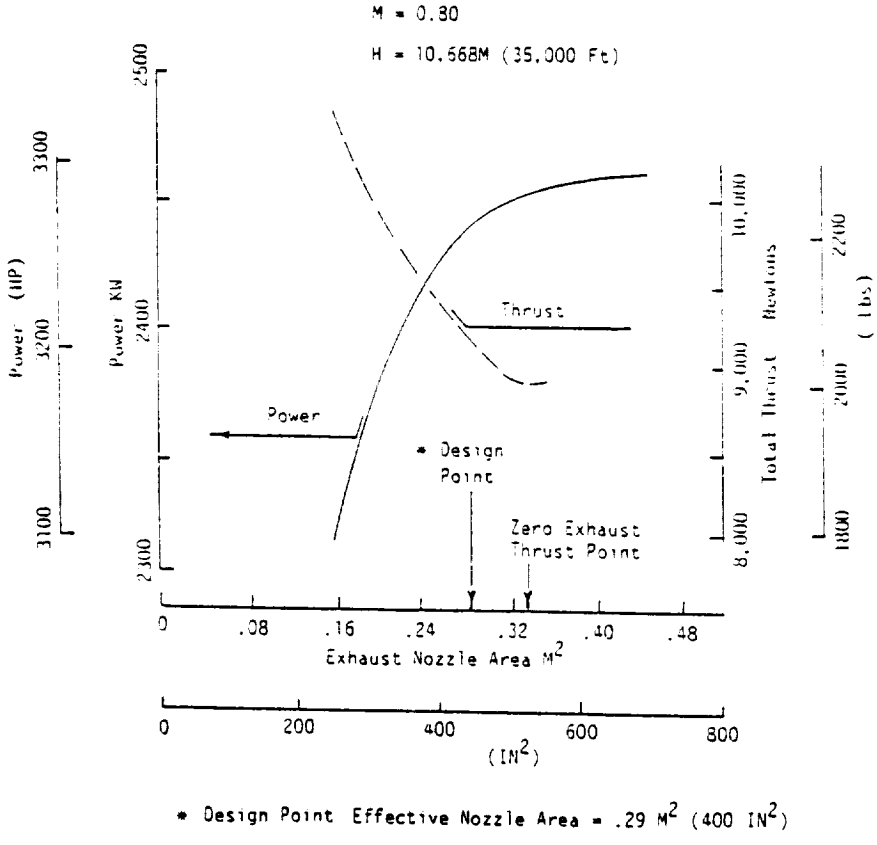


Figure 126. Impact of Boundary Layer Diverter Height on Inlet Pressure Recovery



* Design Point Effective Nozzle Area = .29 M^2 (400 IN^2)

Figure 127. Impact of Exhaust Nozzle Size on SHP and Thrust

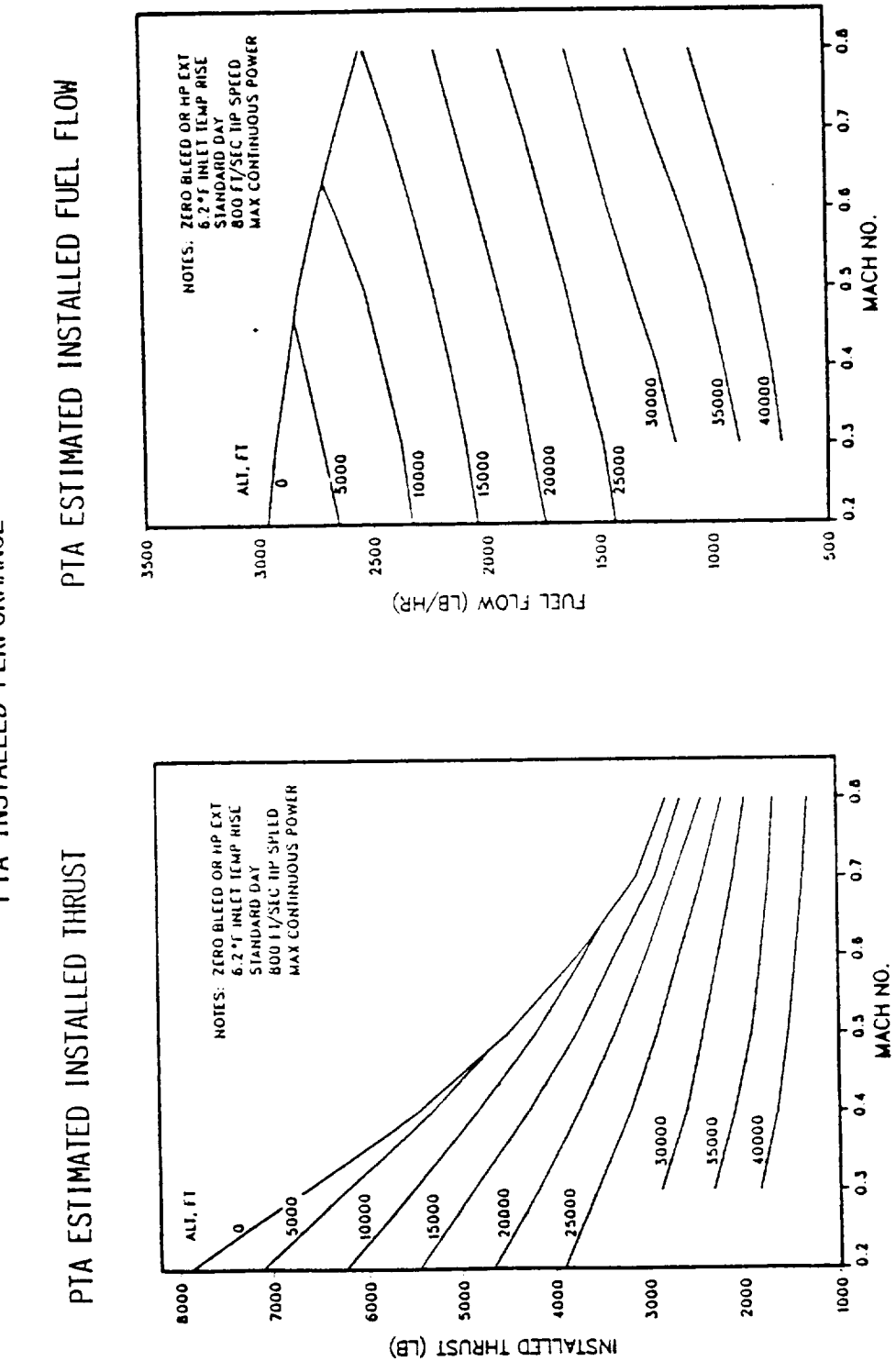


Figure 128. Predicted Drive System Performance

Untrimmed zero-lift drag for the nacelle was estimated by accounting for the following components:

- Friction drag
- Interference drag
- Pressure drag
- Compressibility drag
- Inlet boundary layer diverter drag
- Base drag
- Inlet spillage drag

These increments were estimated using conventional techniques as found in References 11 through 13.

Figure 129 shows plots of the nacelle incremental zero-lift drag for the conditions of propfan power on and off. The data point shown was obtained from Lockheed wind tunnel tests made prior to the PTA Program of a nacelle/wing assembly that was a prototype of the configuration used in the PTA design. The good agreement of the predicted drag with this data point gave confidence in the prediction methods.

To obtain drag for any flight condition, increments were added to account for:

- Drag due to power
- Drag due to lift
- Wing tip booms
- Propfan drag in both feathered and windmilling conditions
- Drag due to nacelle tilt
- Aircraft trim drag

This procedure led to the prediction of aircraft drag polars for Mach numbers ranging from 0.4 to 0.9. Typical results are shown in Figure 130 for Mach 0.4 and Figure 131 for Mach 0.8.

The estimated drag increments were also used to predict drag for the PTA wind tunnel model tests. For this purpose, it was assumed that the drag increments for the small-scale tests were the same as for flight. The increments, therefore, were added to available GII wind tunnel data results. Comparisons of these predictions with the wind tunnel data provided the basis for revision of the predictions, and the revised predictions were then used to update aircraft performance.

Agreement of wind tunnel data with drag predictions was generally good, so that there were no large revisions required. Figure 132 shows the revisions needed for drag predictions as a result of the wind tunnel tests.

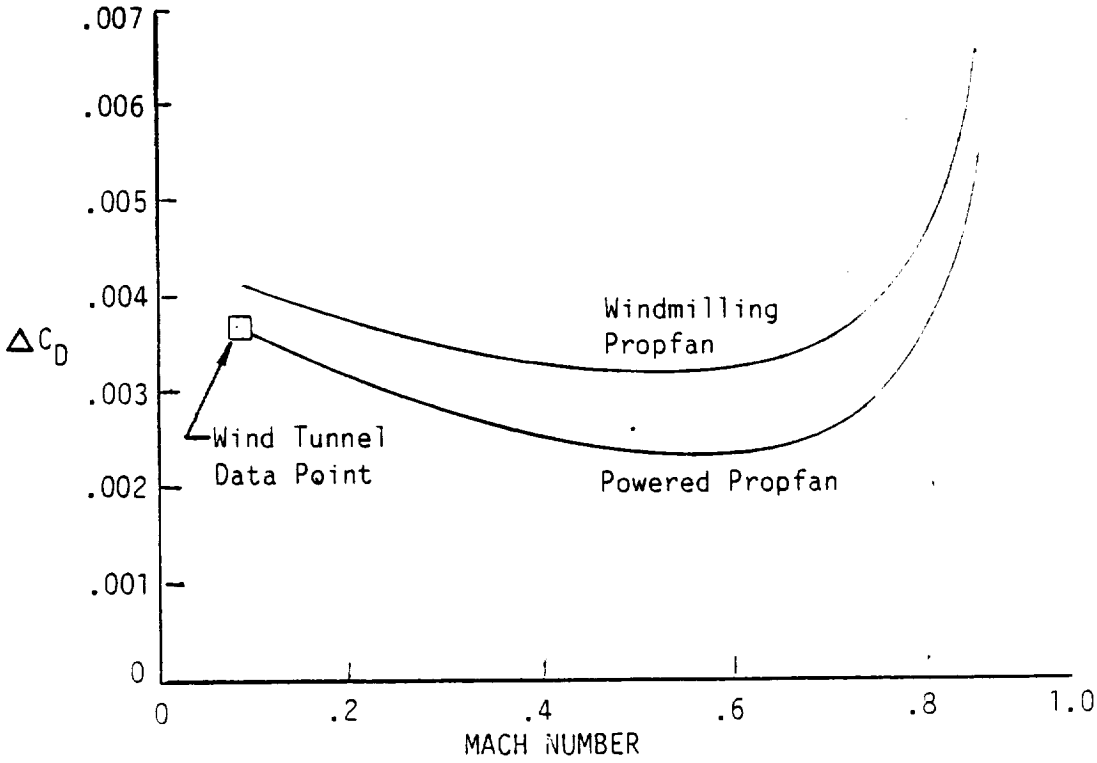


Figure 129. Estimated Nacelle Drag Increment

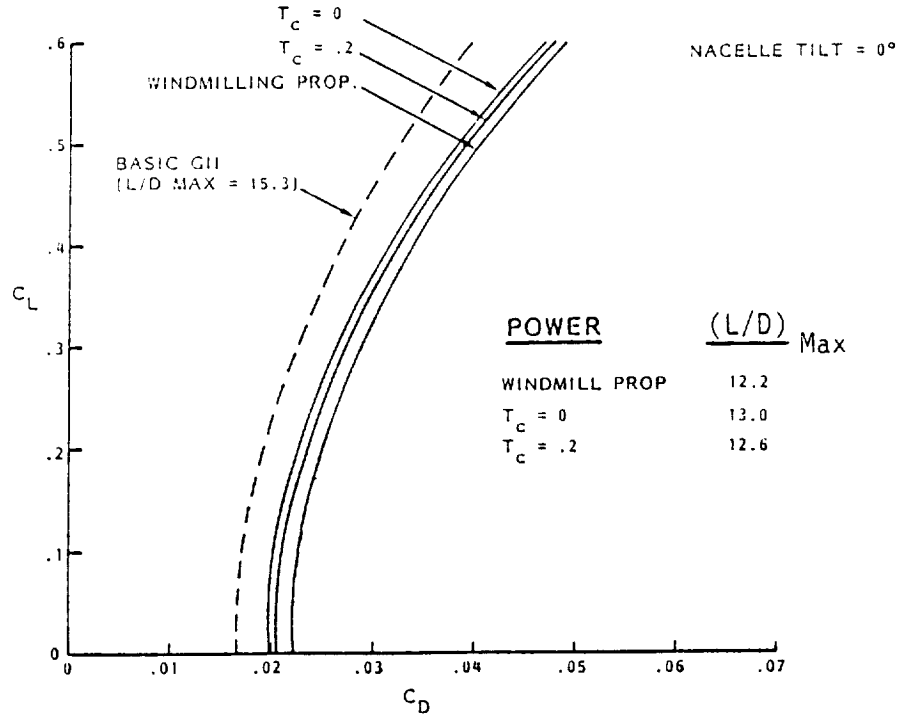


Figure 130. Estimated Drag Polars - Mach 0.4

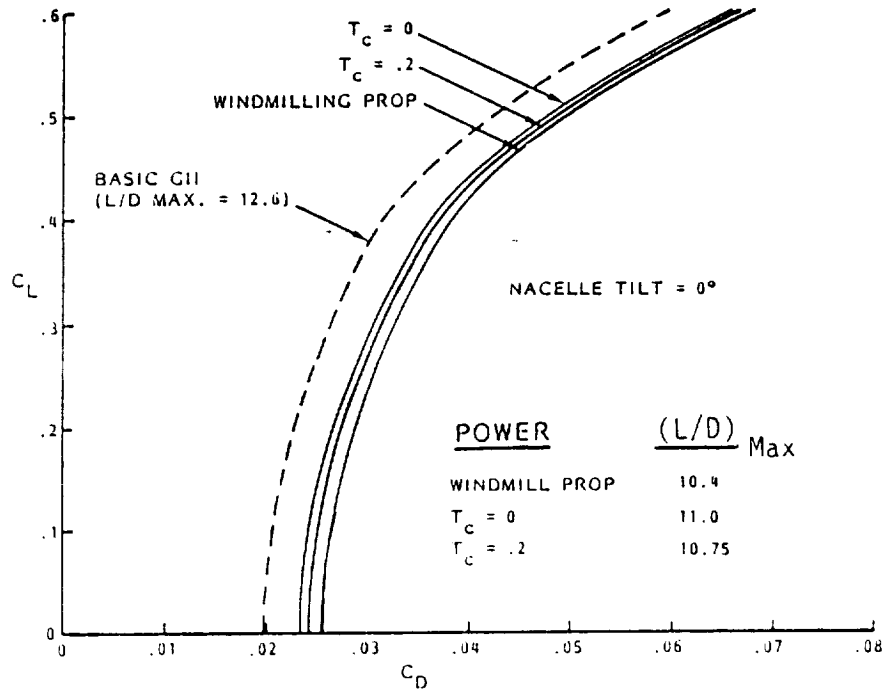


Figure 131. Estimated Drag Polars - Mach 0.8

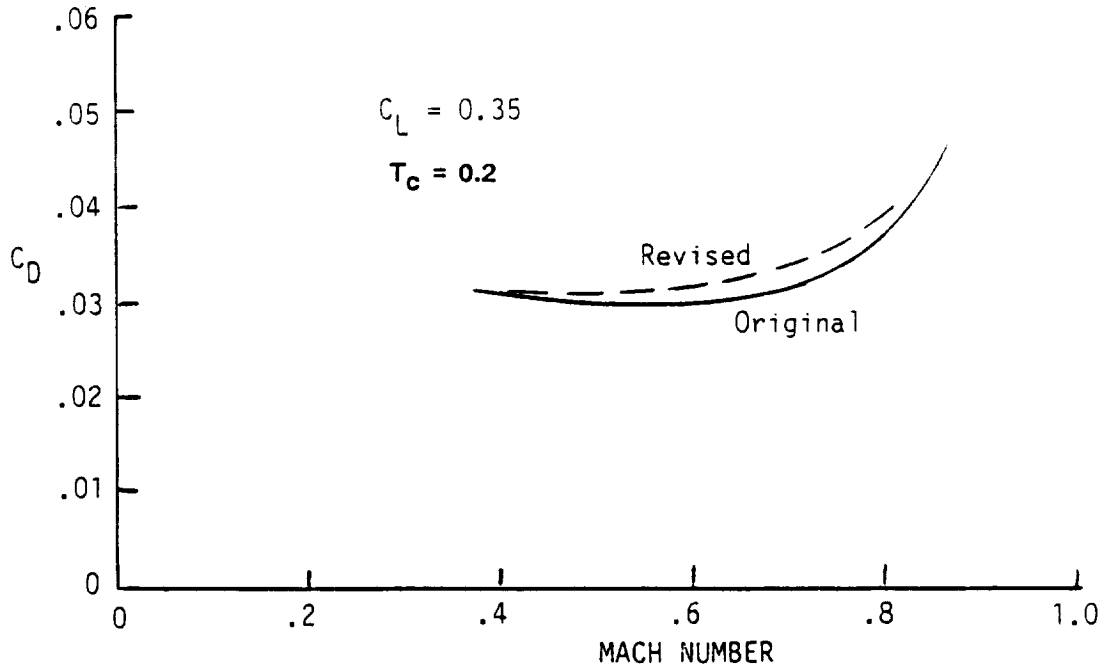


Figure 132. Original and Revised Aircraft Drag Predictions

5.2.2 Aircraft Performance

Aircraft lift and pitching moments were estimated using the QUADPAN code interfaced with the propeller slipstream prediction code PROPVRTX.

The combination of these aerodynamic prediction tools--empirical data for drag, an inviscid panel code coupled with a propeller slipstream code for surface pressures, and refinement of both with results from a wind tunnel test program--provided the basis for good estimates of aircraft performance.

Predicted PTA aircraft performance is summarized in Figures 133 through 138. Speed for best rate of climb is plotted in Figure 133; climb performance curves are given in Figure 134; long range cruise performance is plotted in Figure 135; estimated sea level loiter performance in Figure 136; and the predicted speed-altitude envelope is shown in Figure 137. Finally, these data are used to predict available test time as shown in Figure 138.

These predictions indicated that the PTA aircraft would meet or exceed all of the flight test performance objectives.

Prediction of airport performance for the PTA aircraft was based primarily on results of the low-speed wind tunnel tests where data were obtained for various combinations of flap and control deflections. These predictions are presented in Appendix D.

5.3 AIRCRAFT STABILITY AND CONTROL ANALYSIS

5.3.1 Basic Aerodynamic Characteristics

The first step in the prediction of stability and control characteristics of the PTA aircraft was the generation of an aerodynamic data file. The principal tool in this effort was again the aerodynamic code QUADPAN. To establish validity for QUADPAN, it was first used to predict the aerodynamic characteristics of the GII aircraft, and these predicted characteristics were compared with published GII data. An example of typical results is shown in Figure 139. The agreement of the C_L curves is excellent; the agreement for the pitching moment curves is not quite so good--probably because the neutral point for the QUADPAN predictions is slightly aft of that for the GII data.

After this validation of QUADPAN, the PTA modifications were added to the analytical code so that the characteristics of the PTA aircraft could be predicted. These, plus the drag characteristics that were predicted as described in Section 5.2.1, provided the basis for the aerodynamic data file.

A comparison of GII and PTA aerodynamic characteristics showed that the PTA modifications did not change elevator, rudder, or aileron effectiveness. Deactivation of the inboard spoilers, however, did reduce roll control power, and application of propfan power did affect roll and yaw moments. Changes in lift characteristics were very small, as were changes

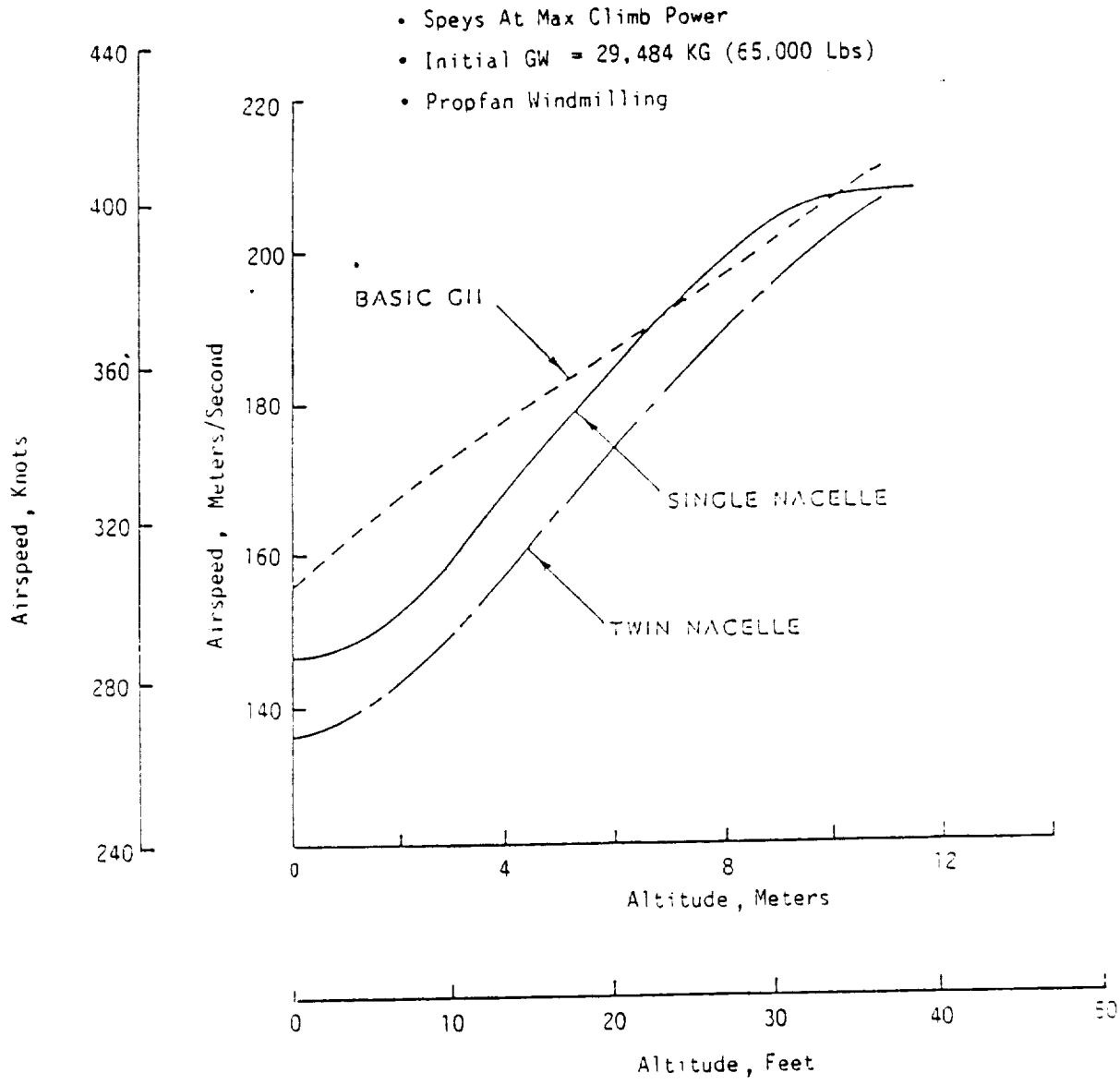


Figure 133. Predicted Speed for Best Rate of Climb

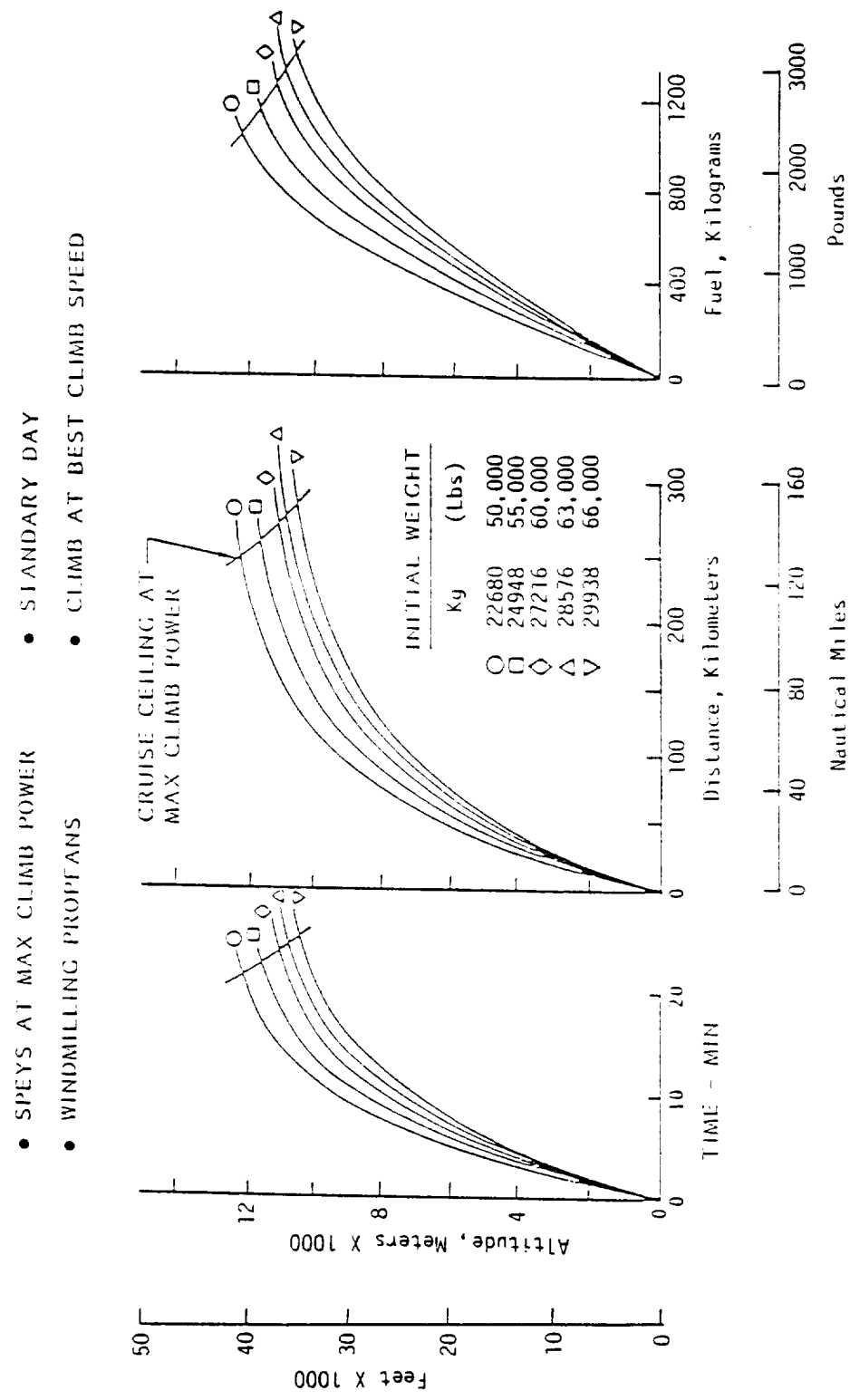


Figure 134. Predicted Climb Performance

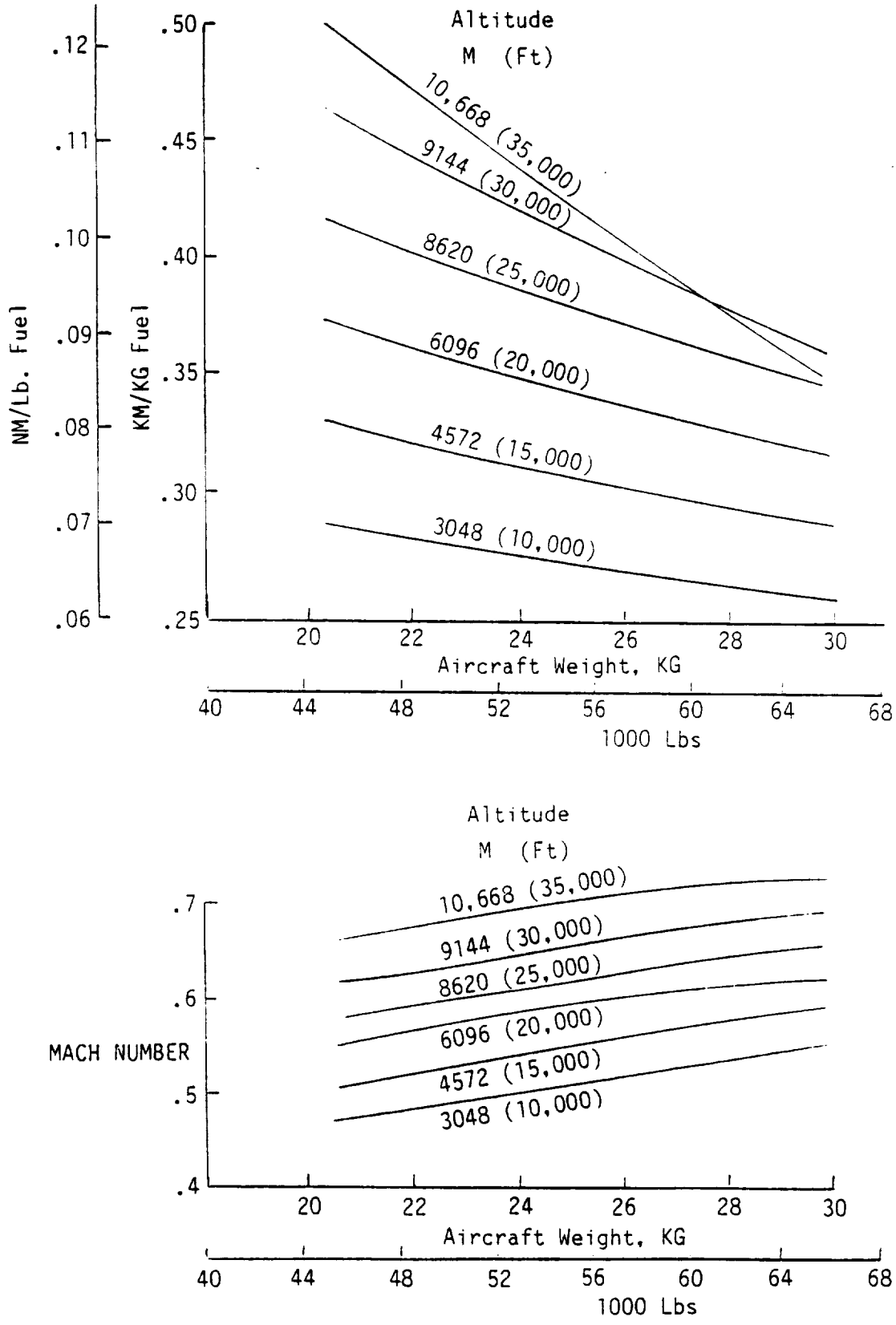
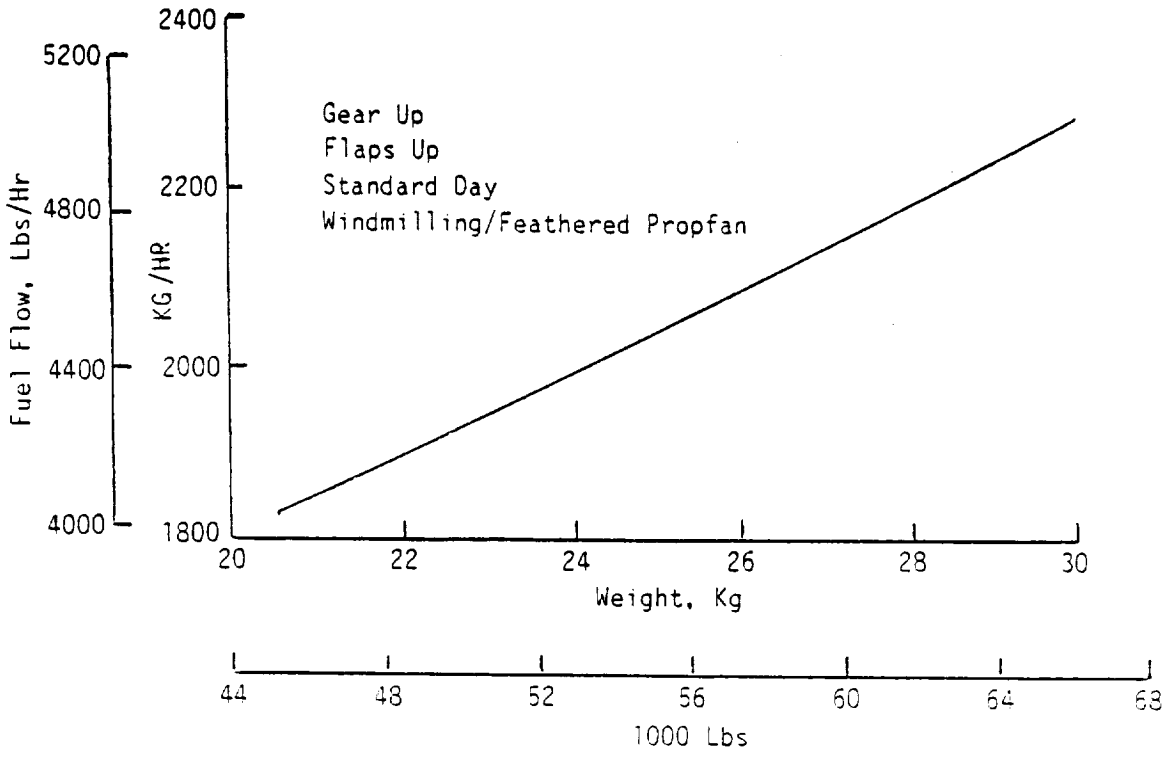


Figure 135. Predicted Long Range Cruise Performance



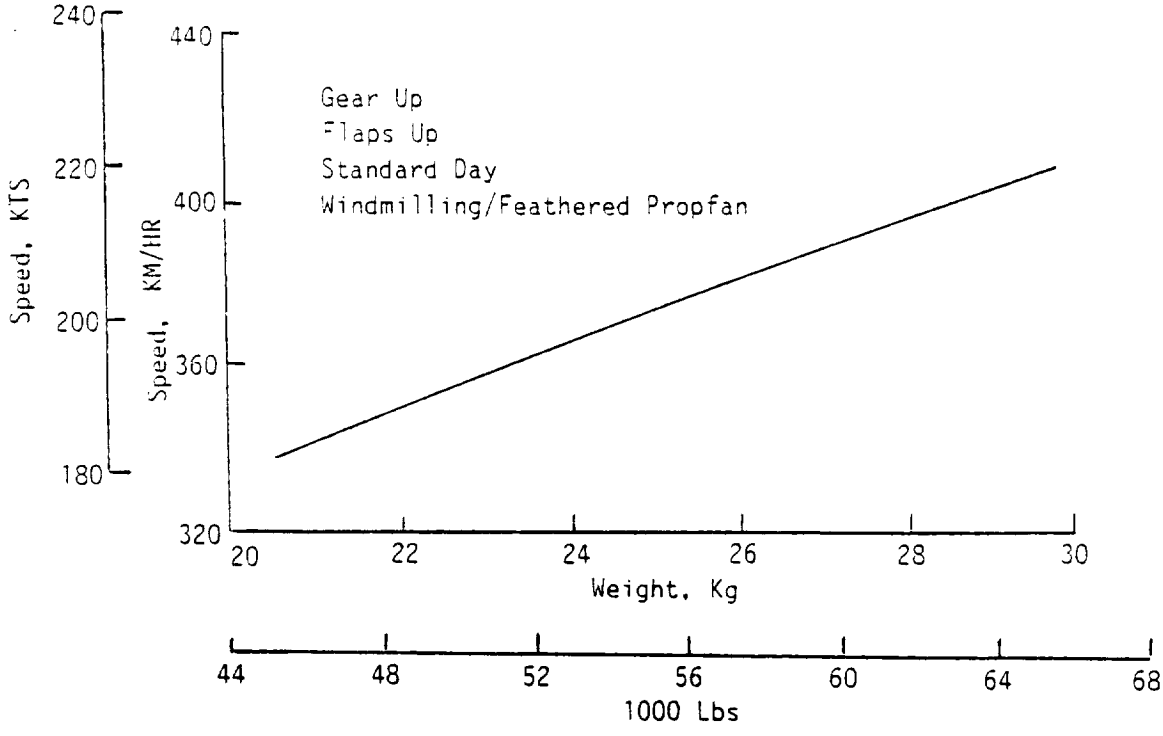


Figure 136. Predicted Sea Level Loiter Performance

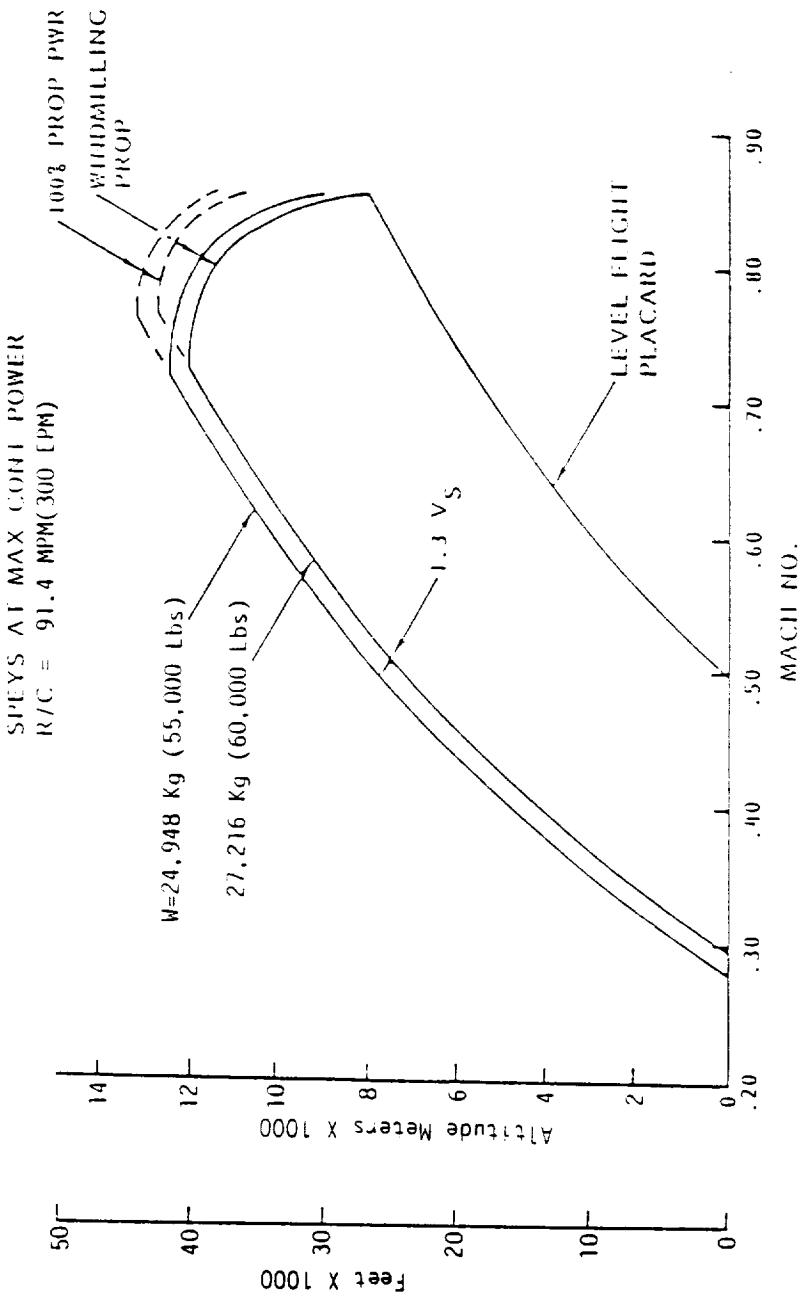


Figure 137. Predicted Speed-Altitude Envelope

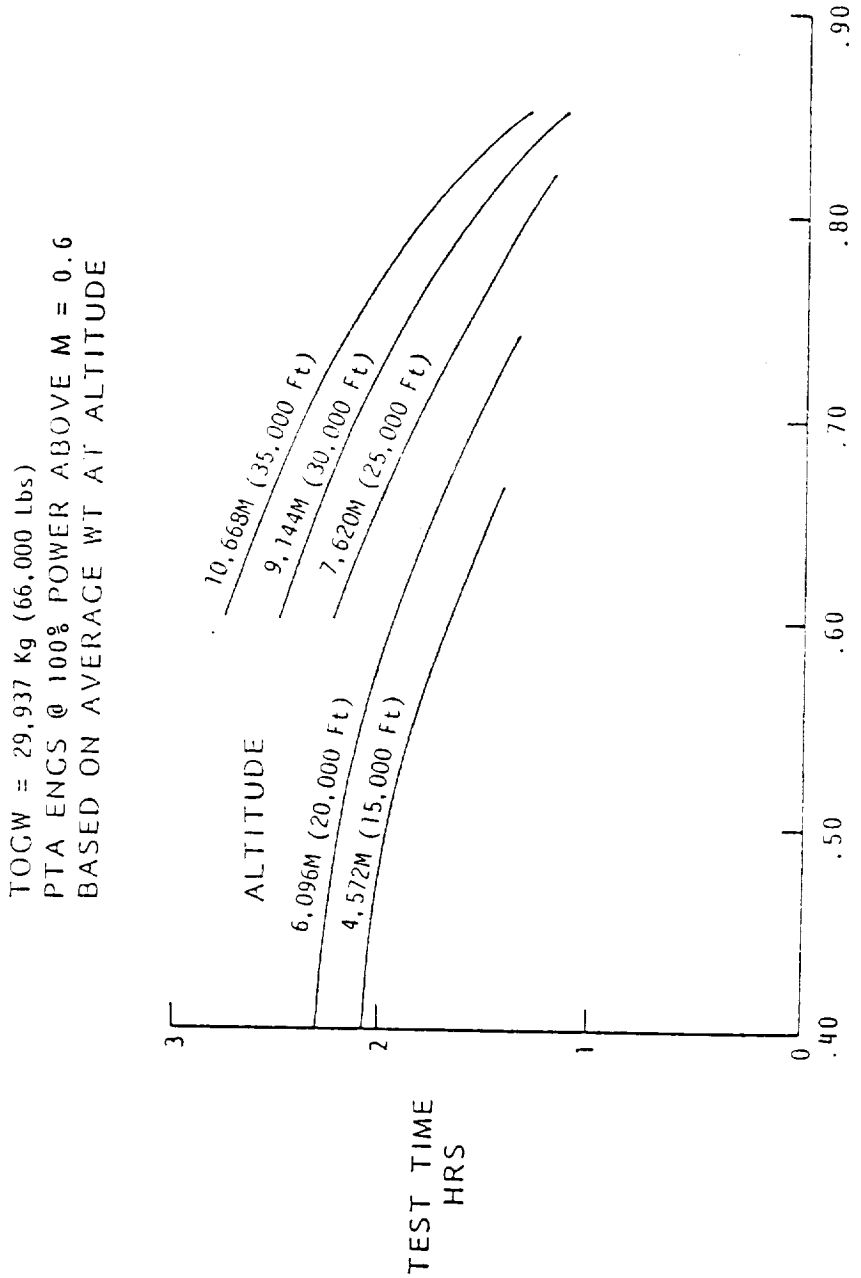


Figure 138. Predicted Test Times

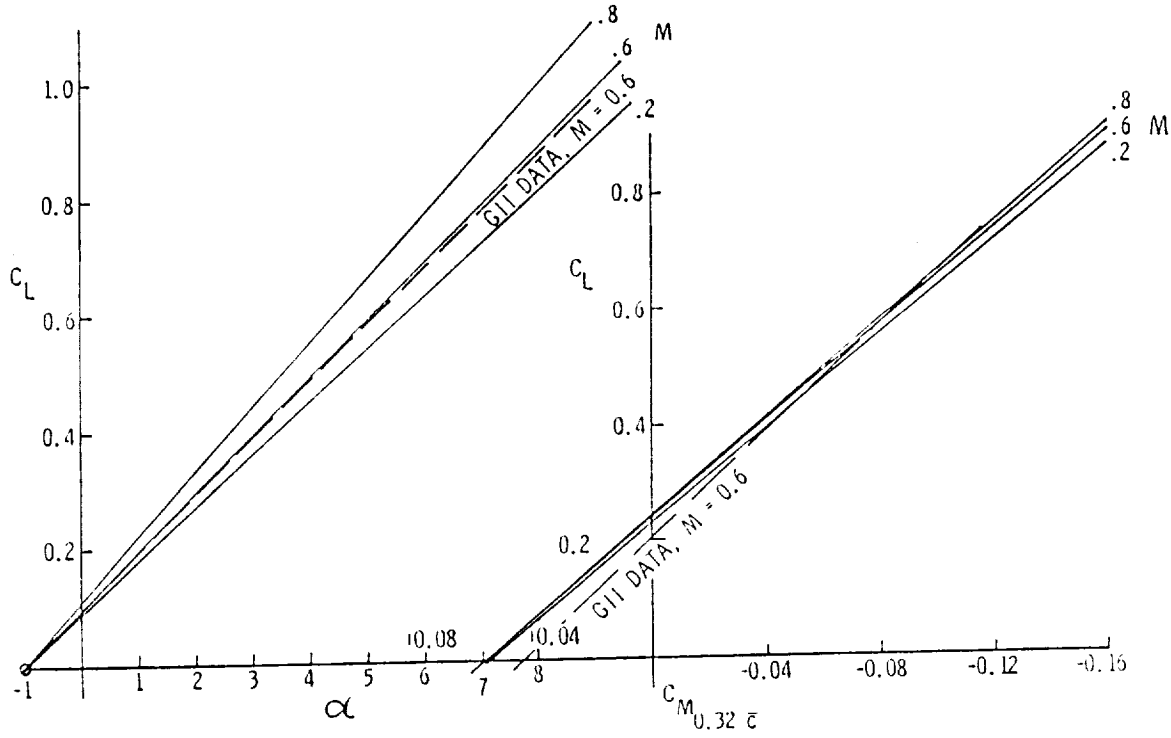


Figure 139. Comparison of QUADPAN Predictions with GII Data

in sideslip effects and changes in the dynamic stability derivatives. The major changes were in the pitching moment characteristics.

5.3.2 Stability and Control Evaluation

Estimated flying qualities for the GII aircraft are presented in Reference 14. These provided the baseline against which the PTA aircraft was compared. Flying qualities were predicted for flight within the speed-altitude envelope of Figure 140 and for the weight/center-of-gravity envelope of Figure 141.

Elevator and elevator tab angles required for trim are shown in Figures 142 through 145. Elevator trim was slightly less for the PTA than for the GII because of the forward location of the PTA neutral point; directional and lateral trim were considerably different. For directional trim with propfan power off, Figure 146 shows that only about one-half degree of rudder deflection was required to trim the aircraft at Mach 0.8 cruise, but at Mach 0.5, with the propfan at full power and symmetric power on the Spey engines, rudder deflection requirements ranged from about 20 percent full travel at 10,668m (35,000 ft) to about 50 percent at 3,048m (10,000 ft).

Lateral trim requirements, as shown in Figure 147, are small at high altitudes, but were more important at low altitudes and low speeds. Roll authority, at 50 percent wheel throw, was available for maneuvering at speeds down to 1.4 V_S. At 1.2 V_S and 100 percent power, roll authority was reduced to about 30 percent.

Results from the analysis of static longitudinal stability are shown in Figures 148 through 150. These figures show that speed stability is reduced by the PTA modifications but remains within acceptable limits. The center of gravity location for the PTA varies from about 31 percent to 28 percent with normal fuel burn-off, so that the variations of stick force with speed are reasonable.

Maneuvering stability characteristics for altitudes of 3,048m and 10,668m (10,000 ft and 35,000 ft) are shown in Figures 151 and 152. Elevator angle per "g" is slightly reduced by the PTA modifications, but a forward center of gravity movement offsets this reduction. Stick force per "g" remains within acceptable limits.

Longitudinal dynamic stability characteristics are shown in Figures 153 and 154. Figure 153 shows the short period frequency for both the baseline GII and the PTA configuration. The data points represent test conditions over the speed-altitude envelope and stay well within the specified limits for good handling.

Damping ratios for the short period and phugoid modes are presented in Figure 154. The short period damping ratio is increased by the PTA decrease in stability level and the phugoid damping ratio shows good characteristics in the 0.04 to 0.12 range for the entire speed-altitude envelope.

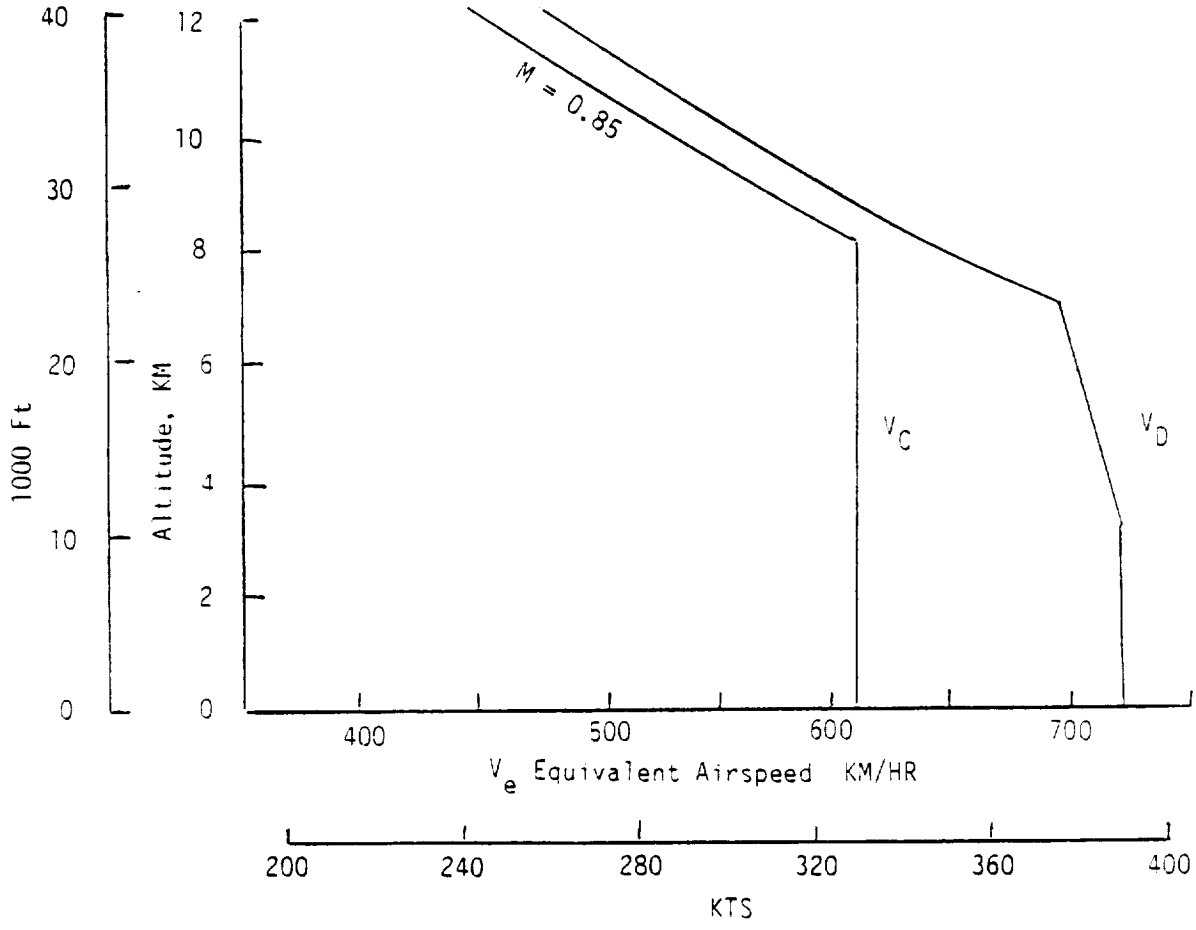
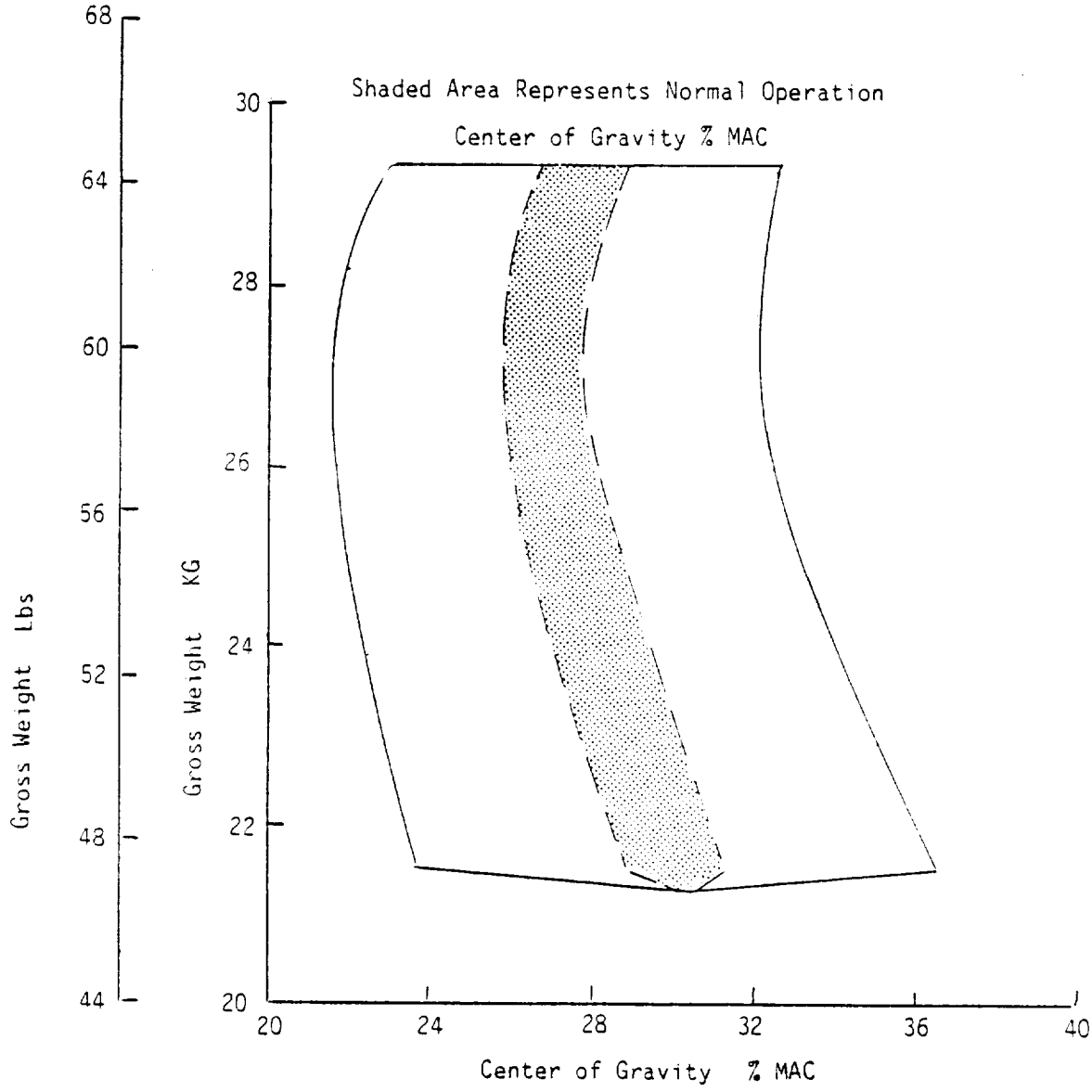
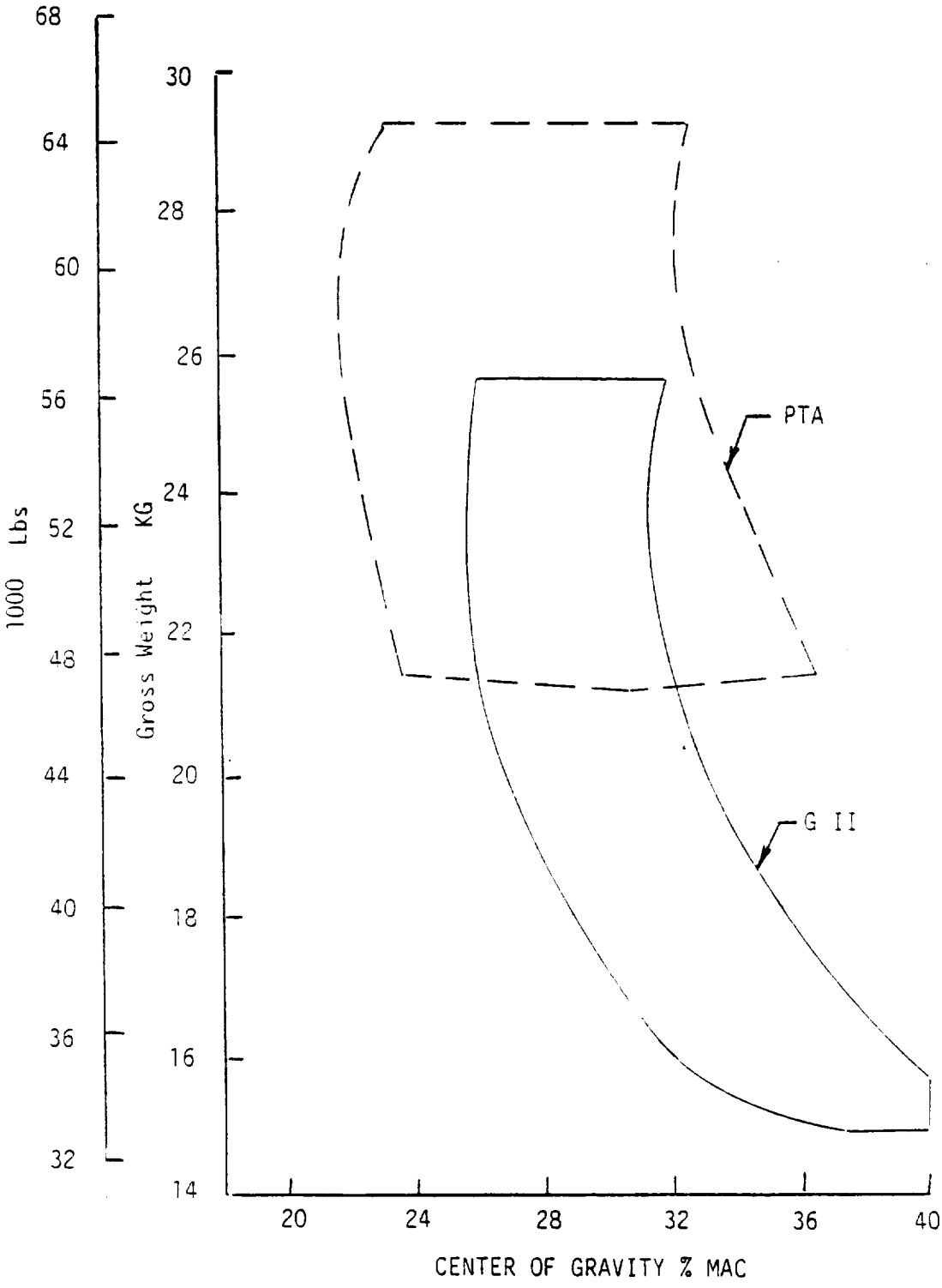


Figure 140. Speed-Altitude Envelope for S&C Evaluation



(a) Predicted PTA Envelope

Figure 141. Center of Gravity Envelope for S&C Evaluation



(b) Comparison of PTA and GII Envelopes

Figure 141. Center of Gravity Envelope for S&C Evaluation (Continued)

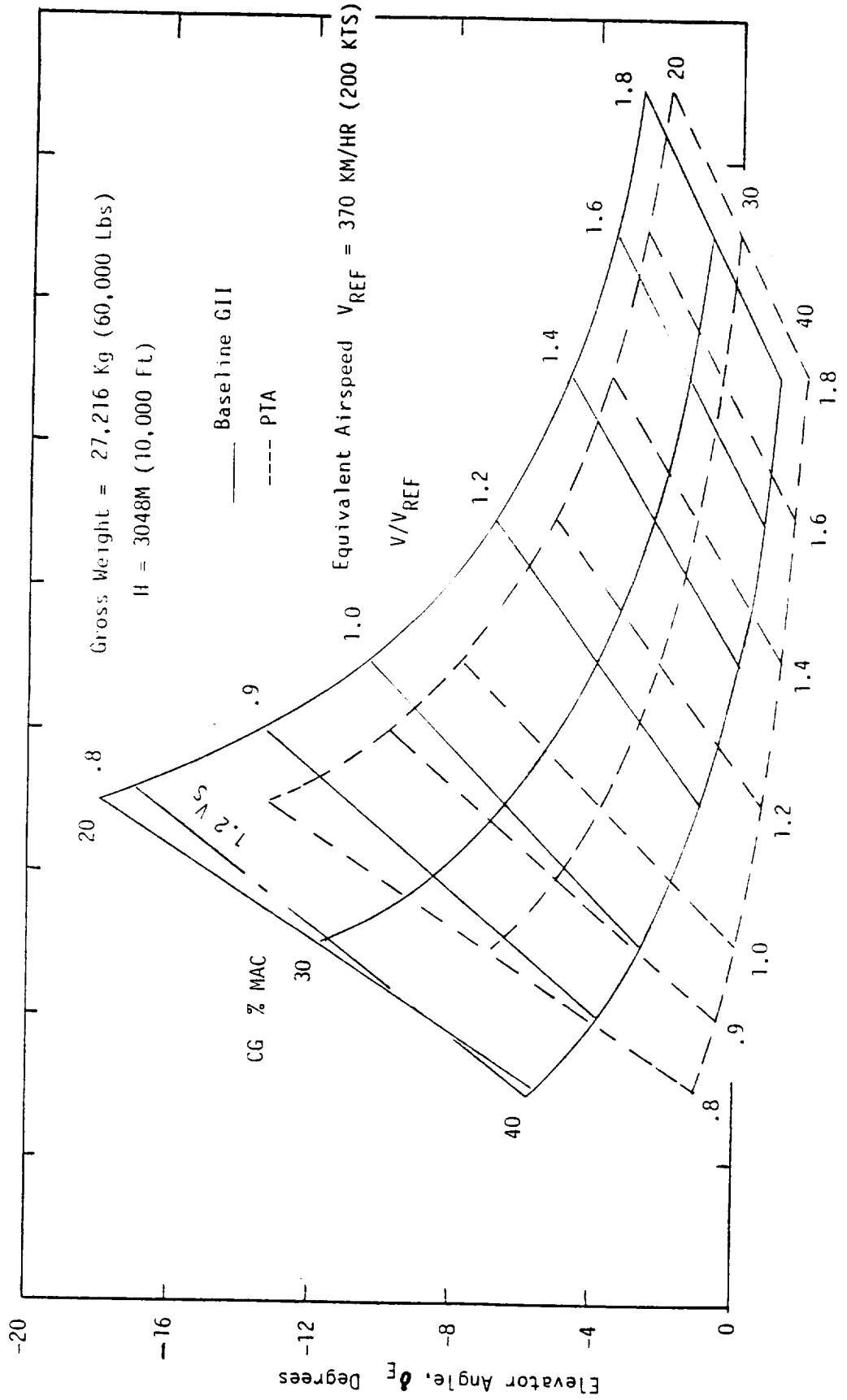


Figure 142. Elevator Angle Required for Trim - Low Altitude

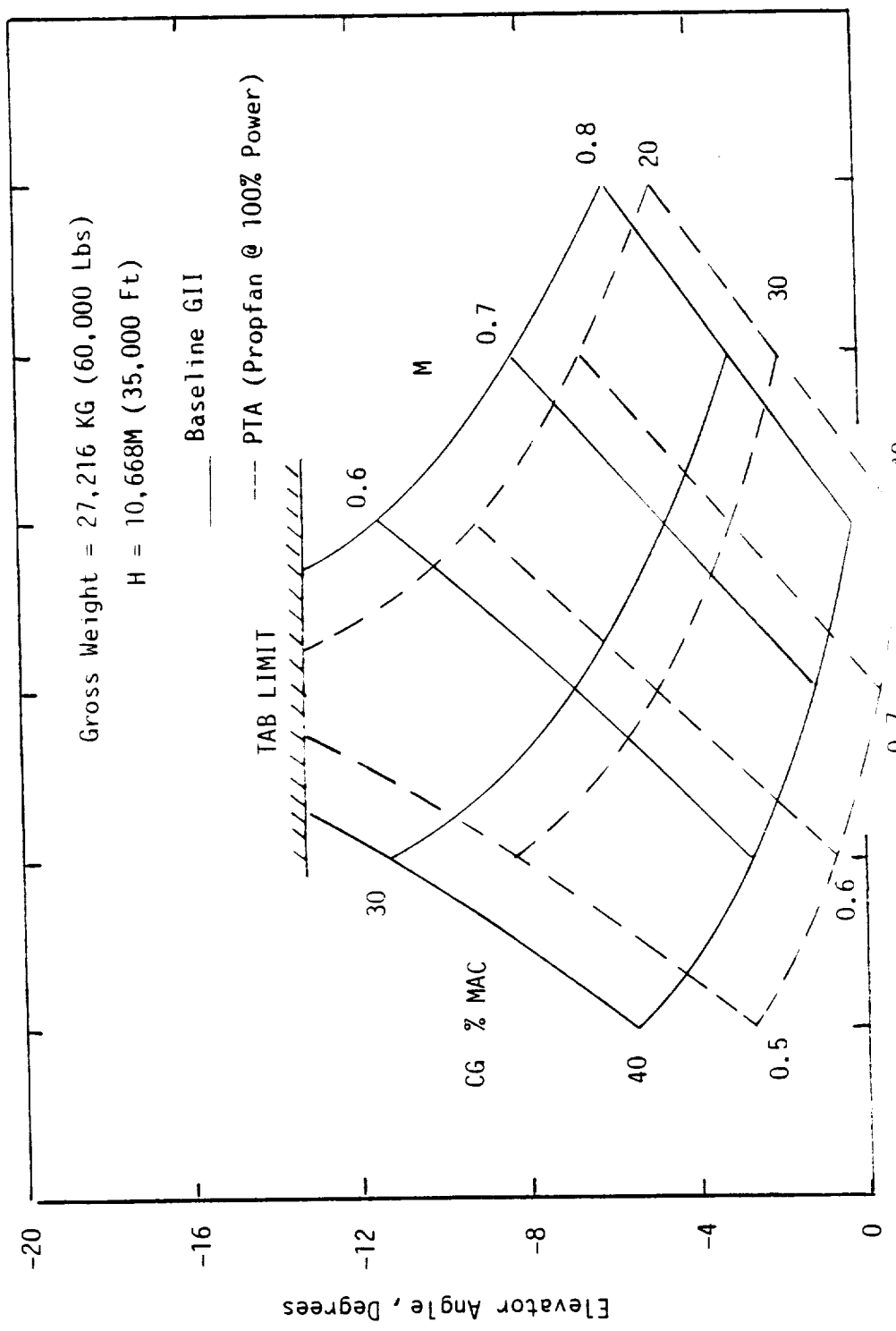


Figure 143. Elevator Angle Required for Trim - High Altitude

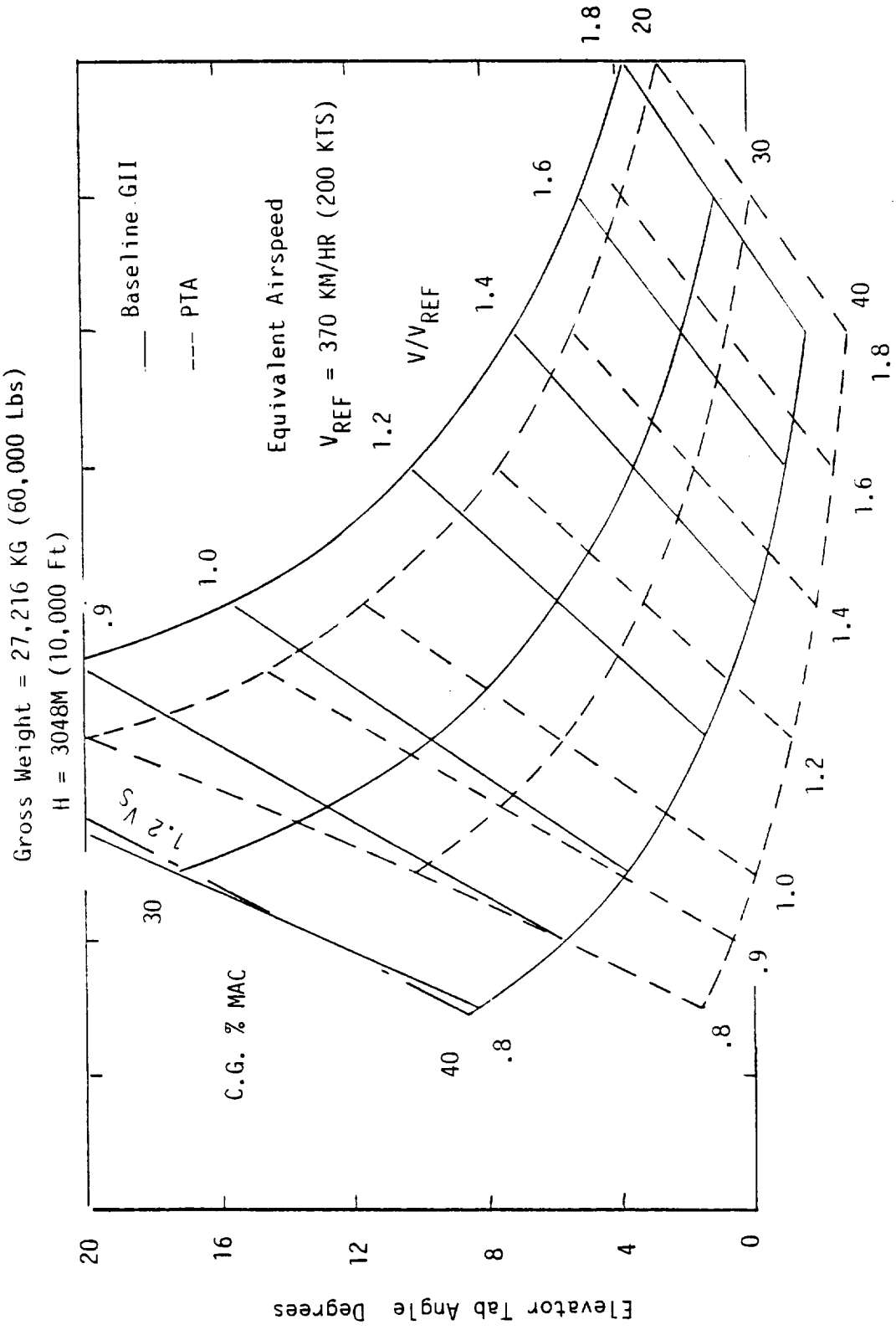


Figure 144. Elevator Tab Angle Required for Trim - Low Altitude

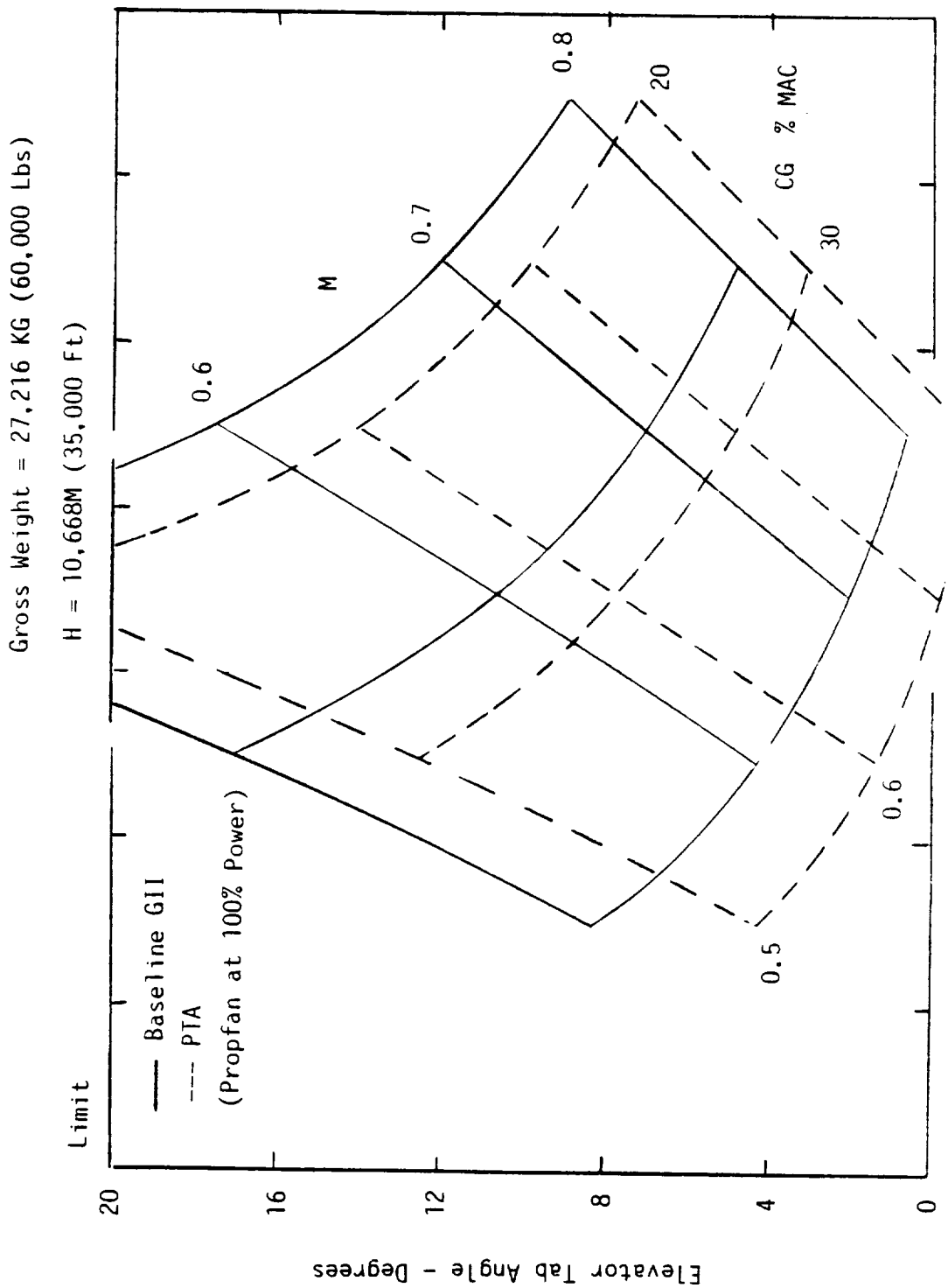


Figure 145. Elevator Tab Angle Required for Trim - High Altitude

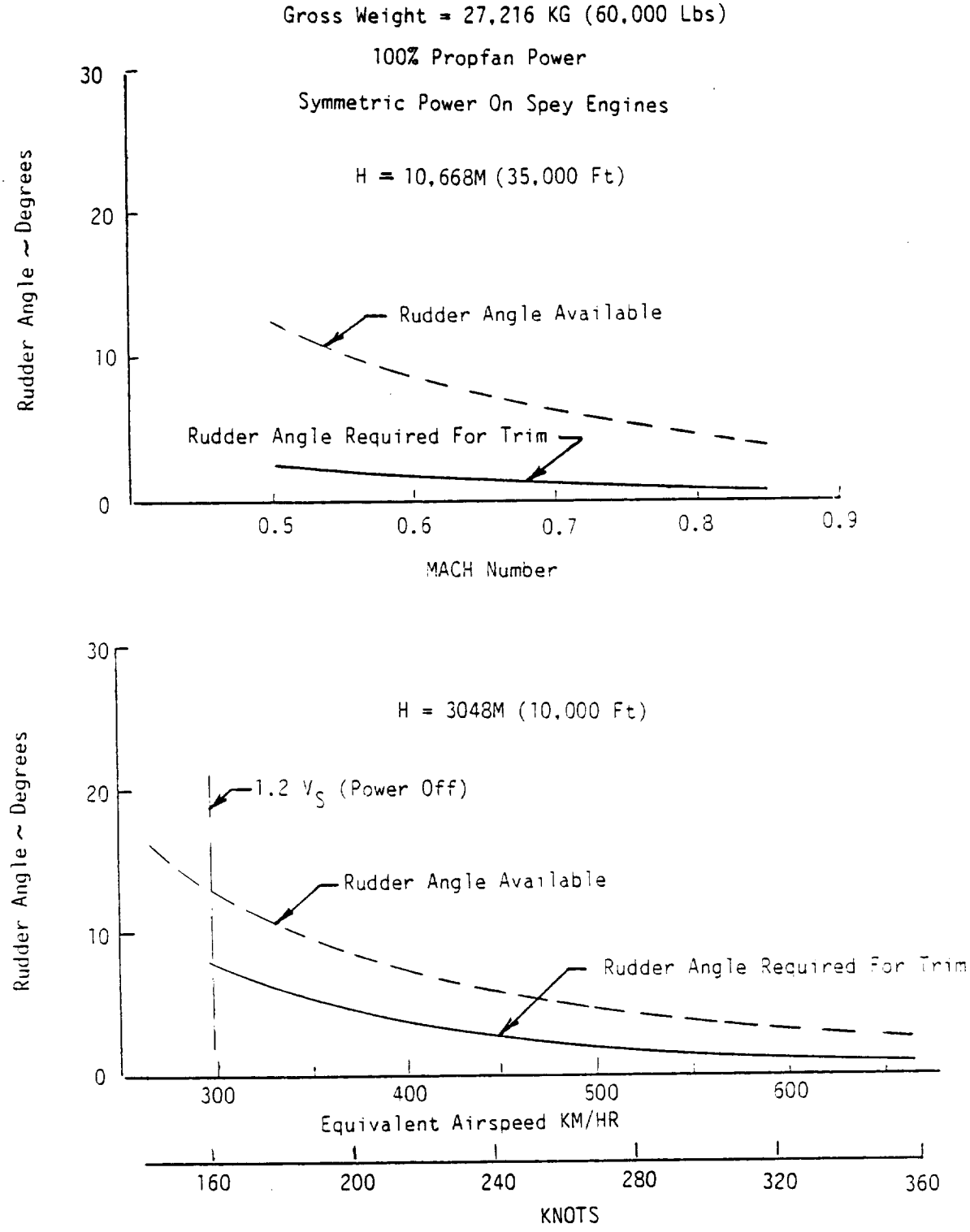


Figure 146. Directional Trim Requirements

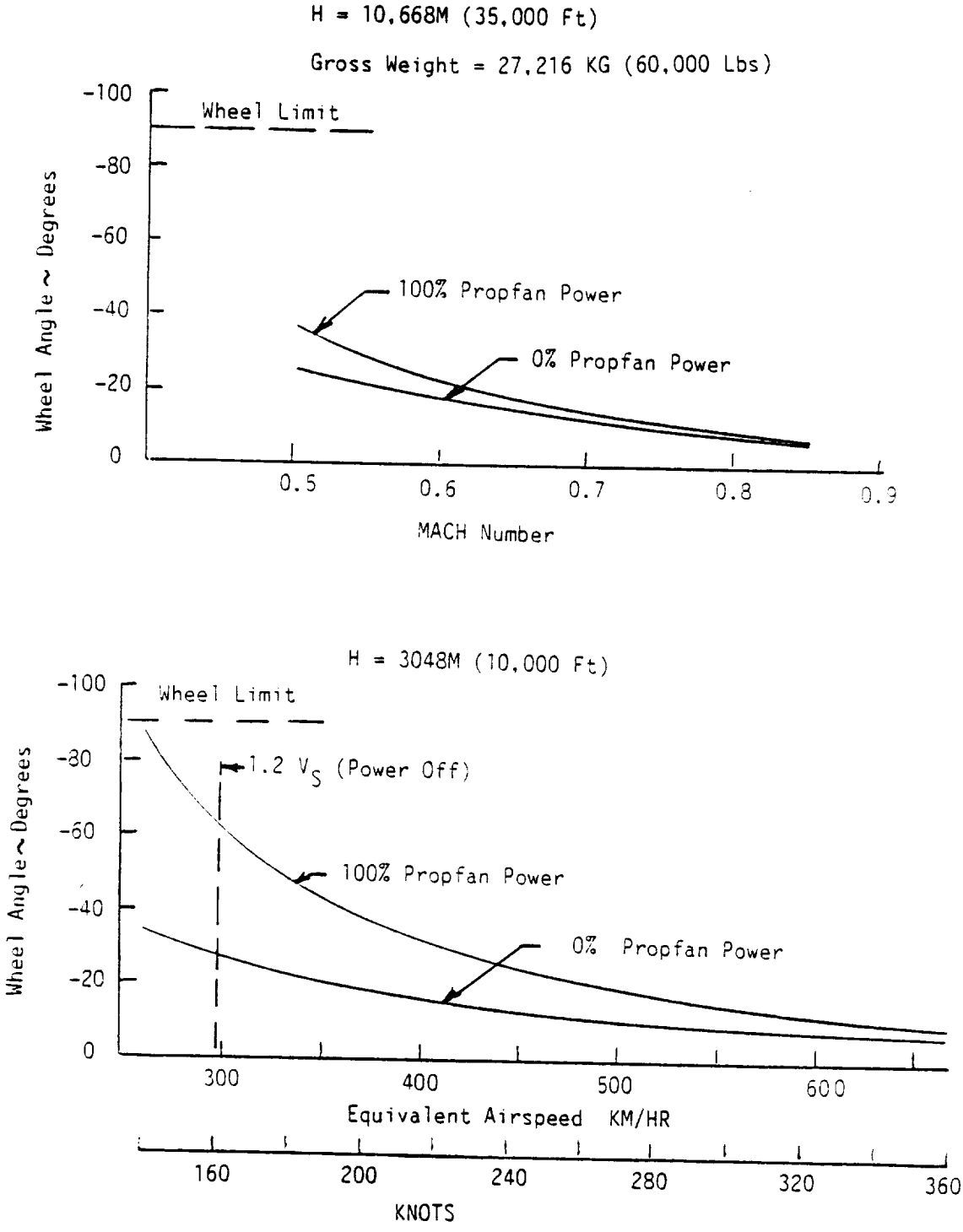
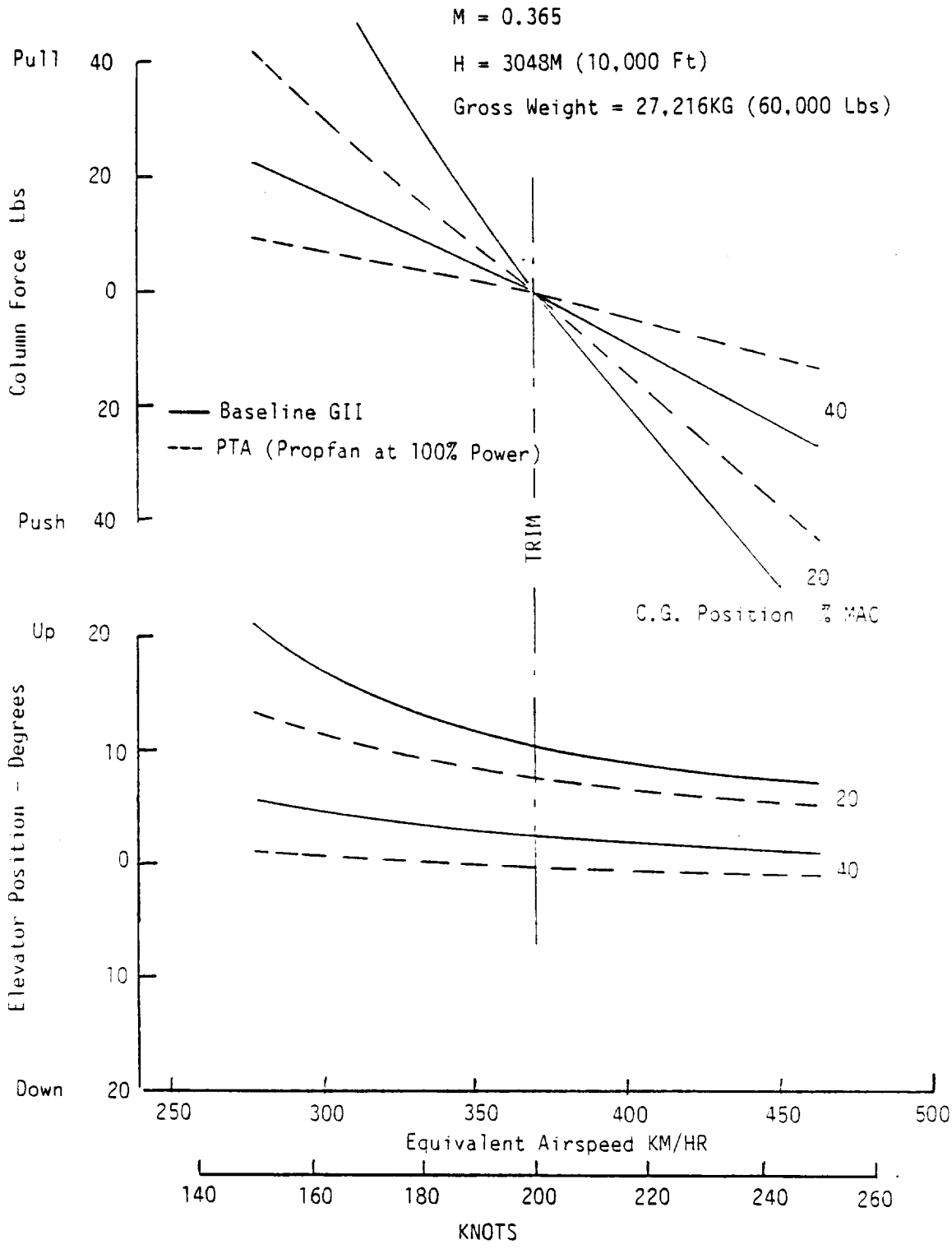
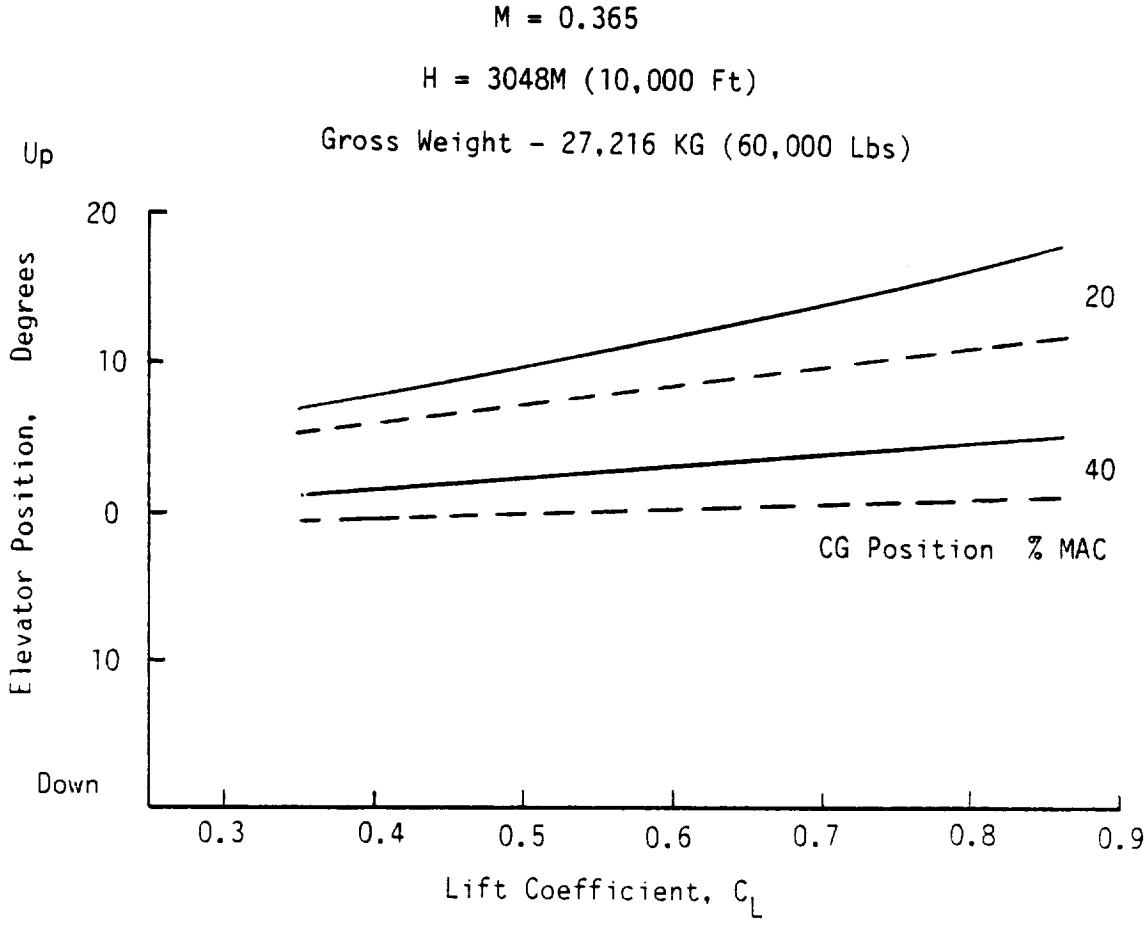


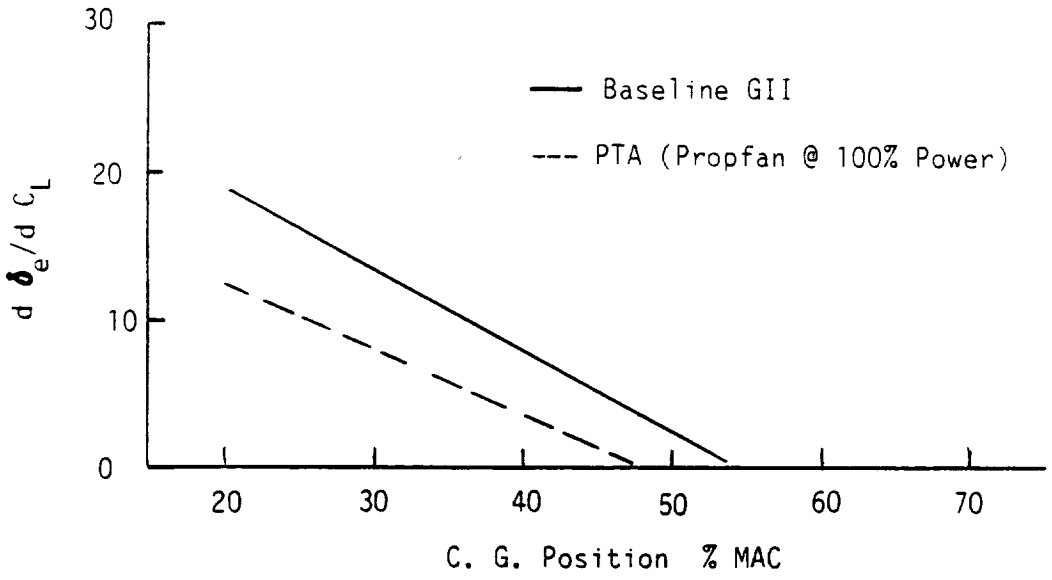
Figure 147. Lateral Trim Requirements



(a) Speed Stability

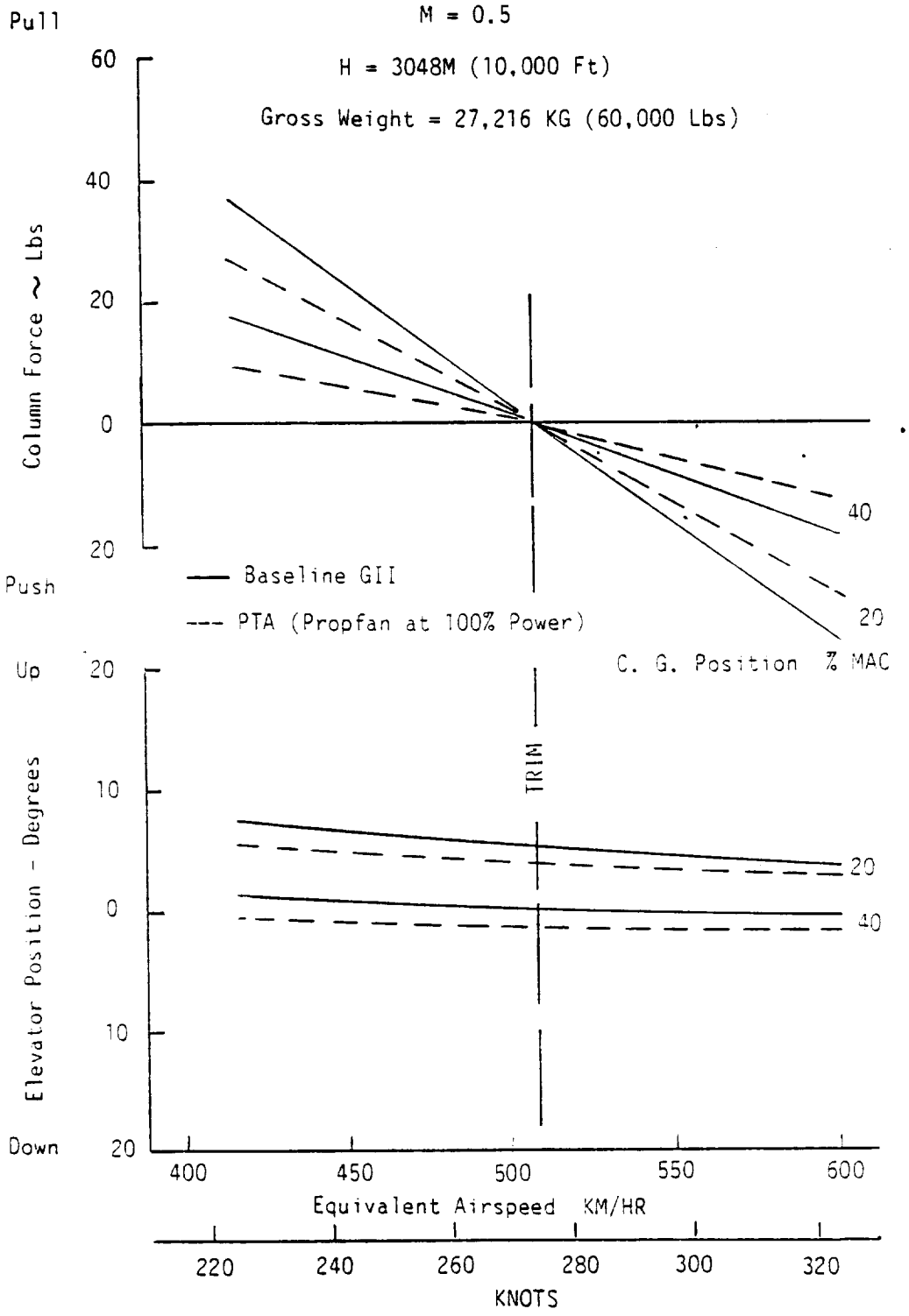
Figure 148. Static Longitudinal Stability





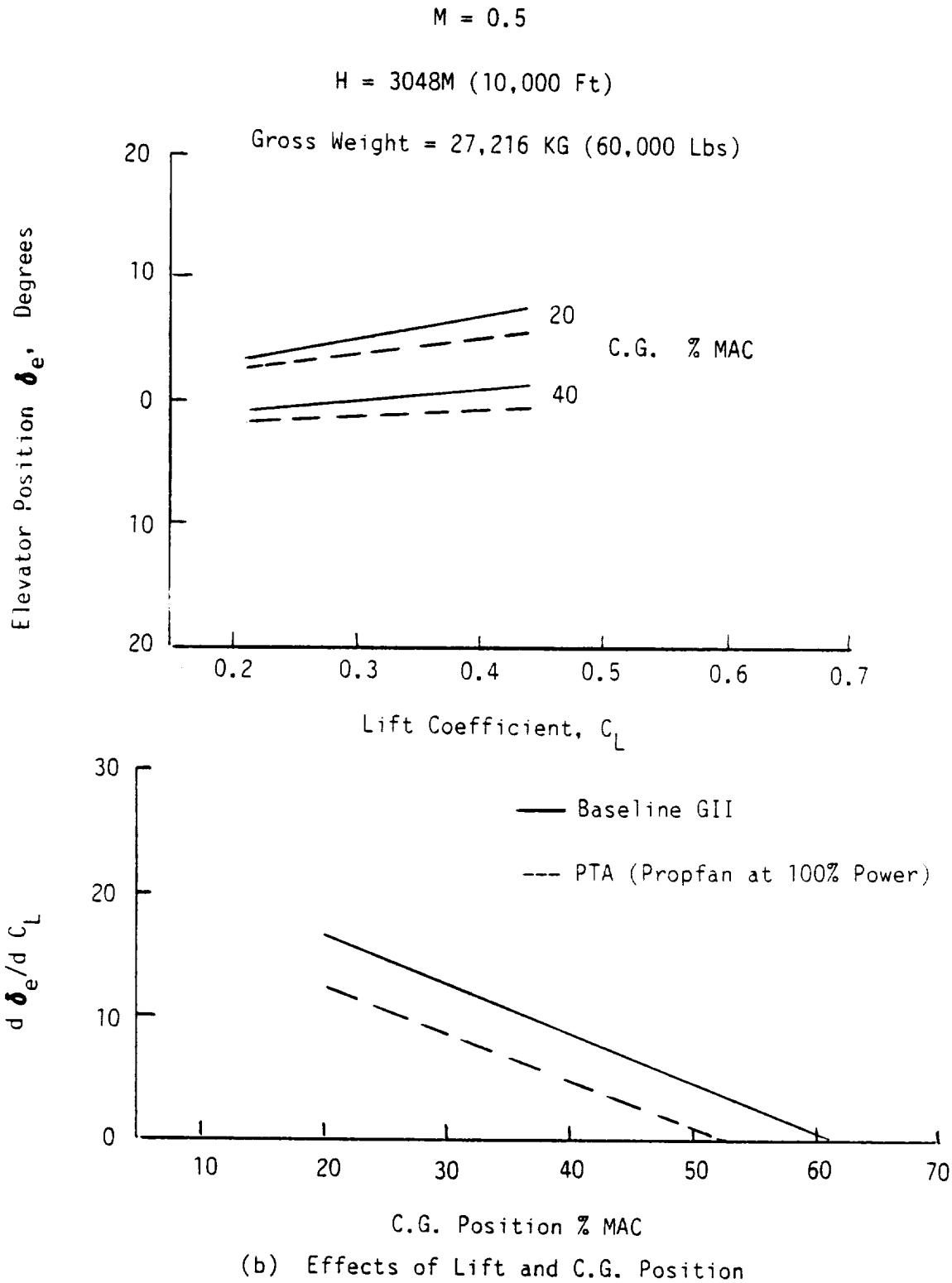
(b) Effects of Lift on C. G. Position

Figure 148. Static Longitudinal Stability (Continued)



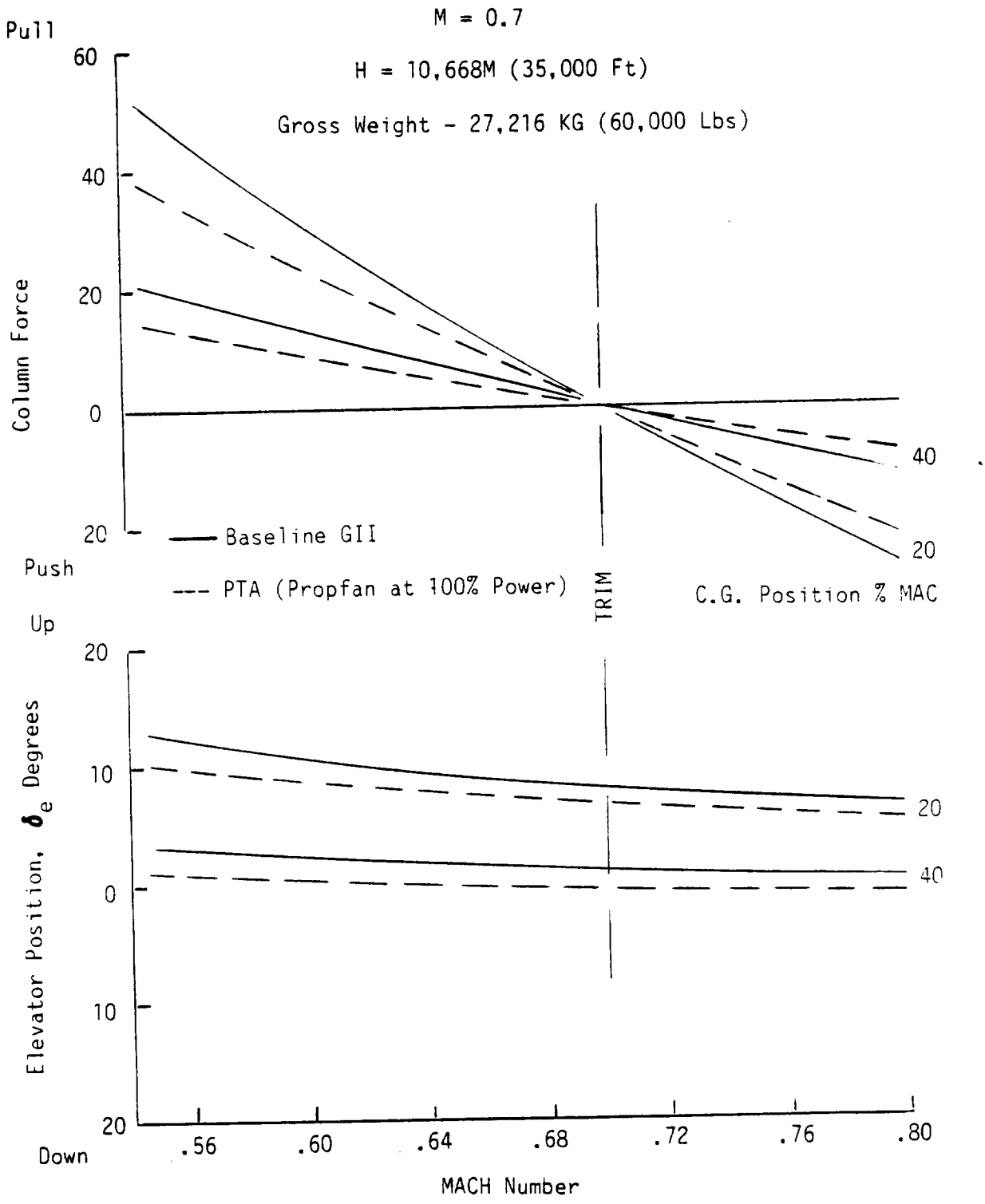
(a) Speed Stability

Figure 149. Static Longitudinal Stability - Mach 0.5



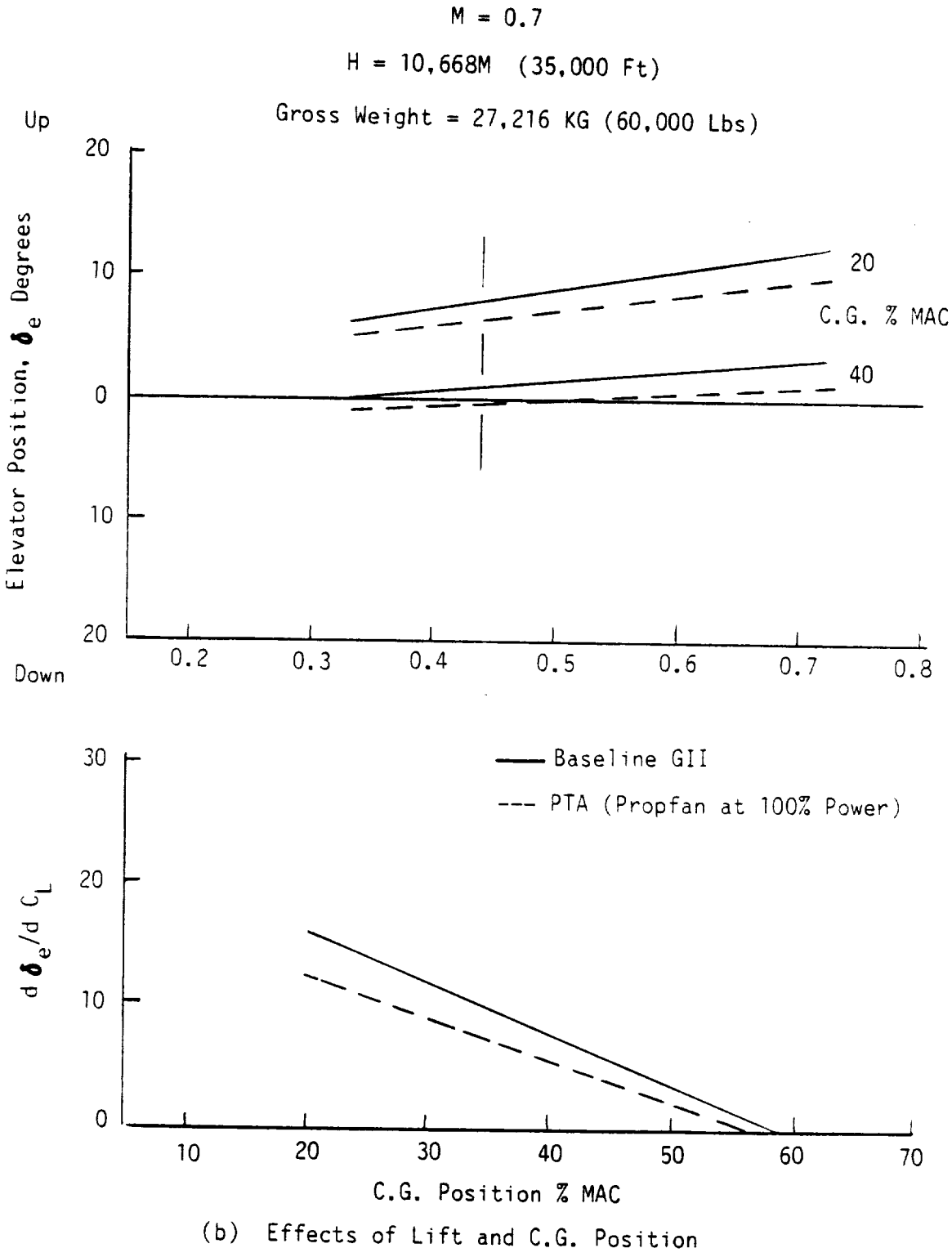
(b) Effects of Lift and C.G. Position

Figure 149. Static Longitudinal Stability - Mach 0.5 (Continued)



(a) Speed Stability

Figure 150. Static Longitudinal Stability - Mach 0.7



(b) Effects of Lift and C.G. Position

Figure 150. Static Longitudinal Stability - Mach 0.7 (Continued)

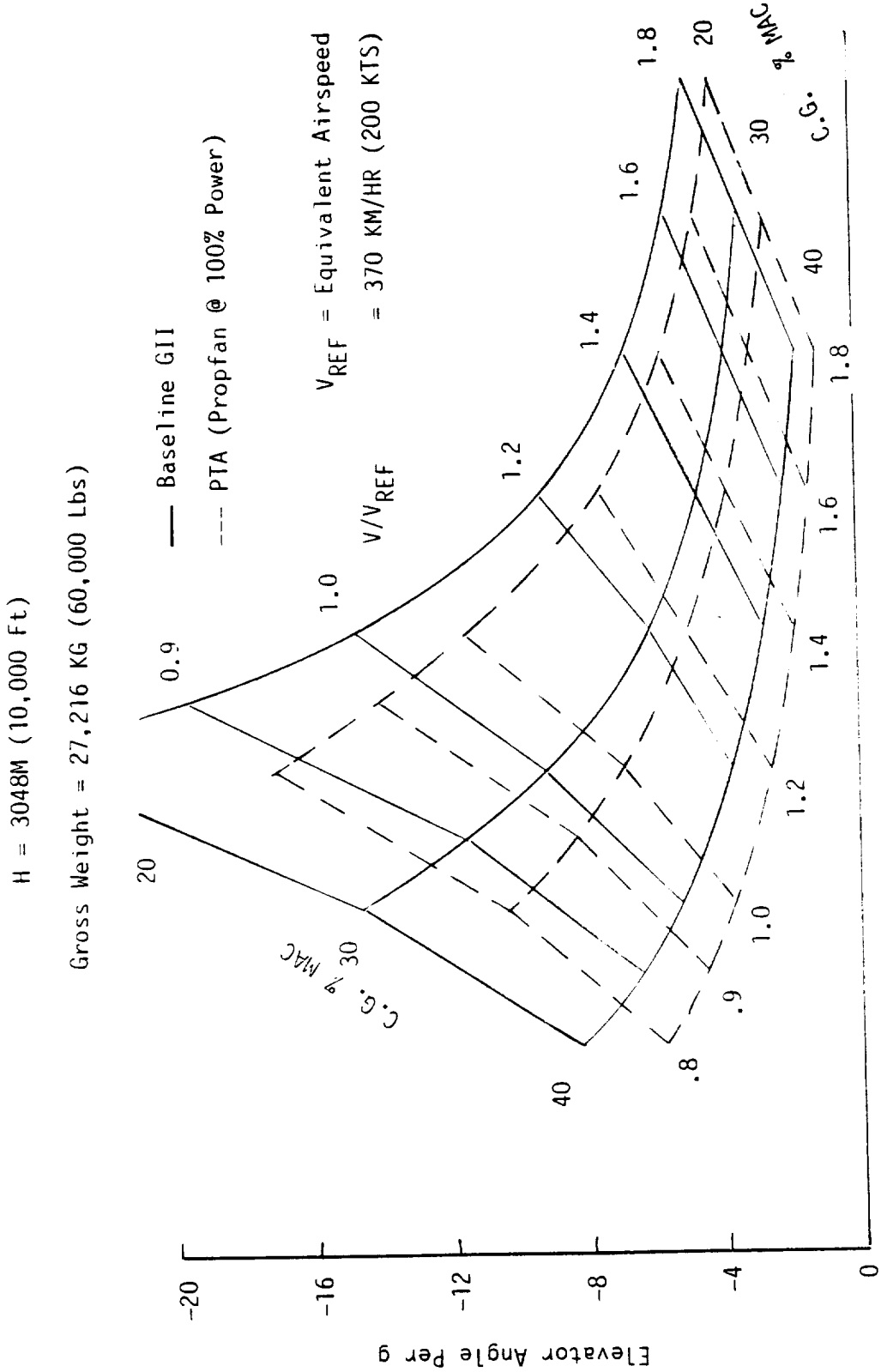


Figure 151. Low Altitude Maneuvering Stability - Elevator Gradient

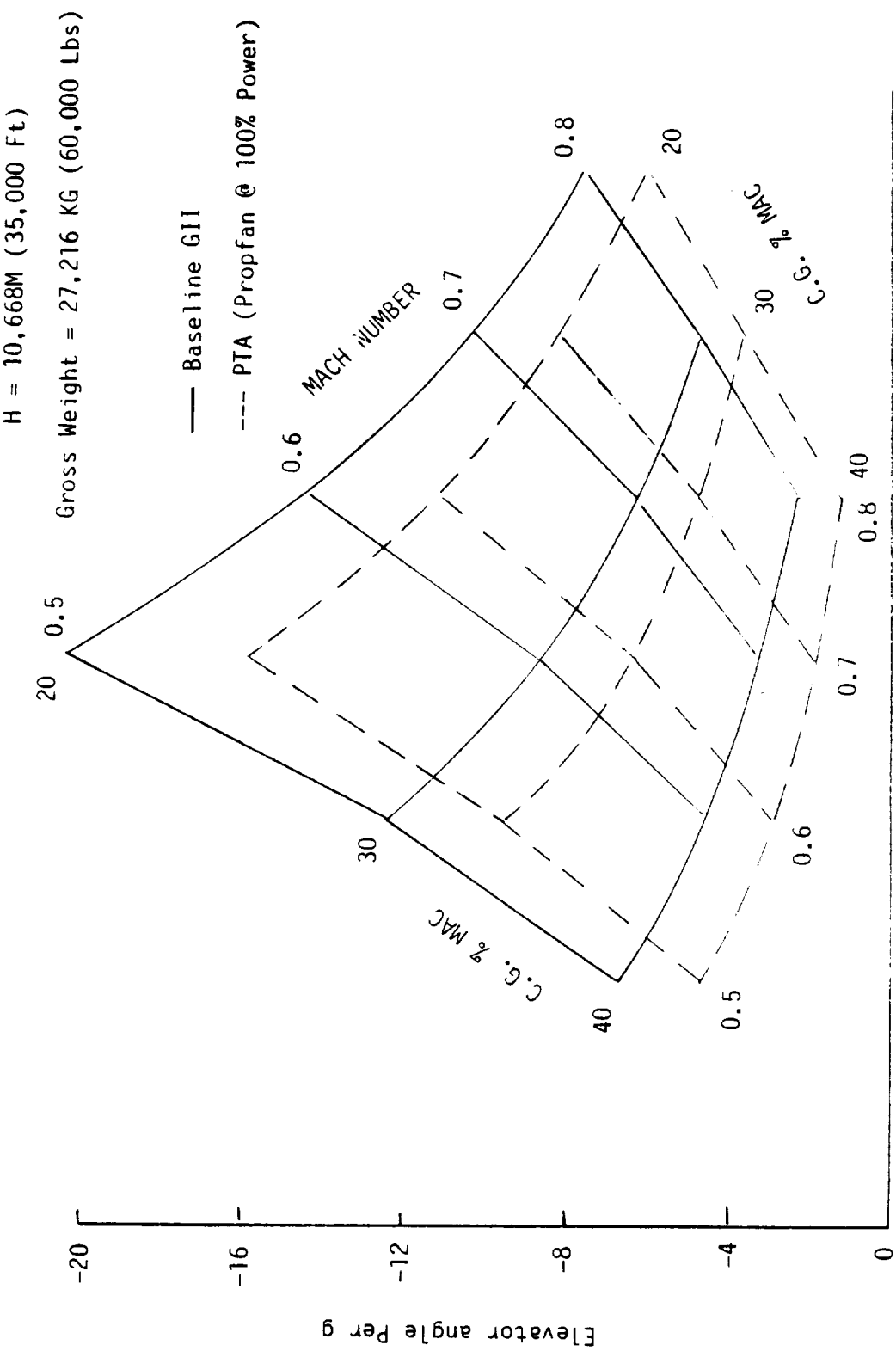


Figure 152. High Altitude Maneuvering Stability - Elevator Gradient

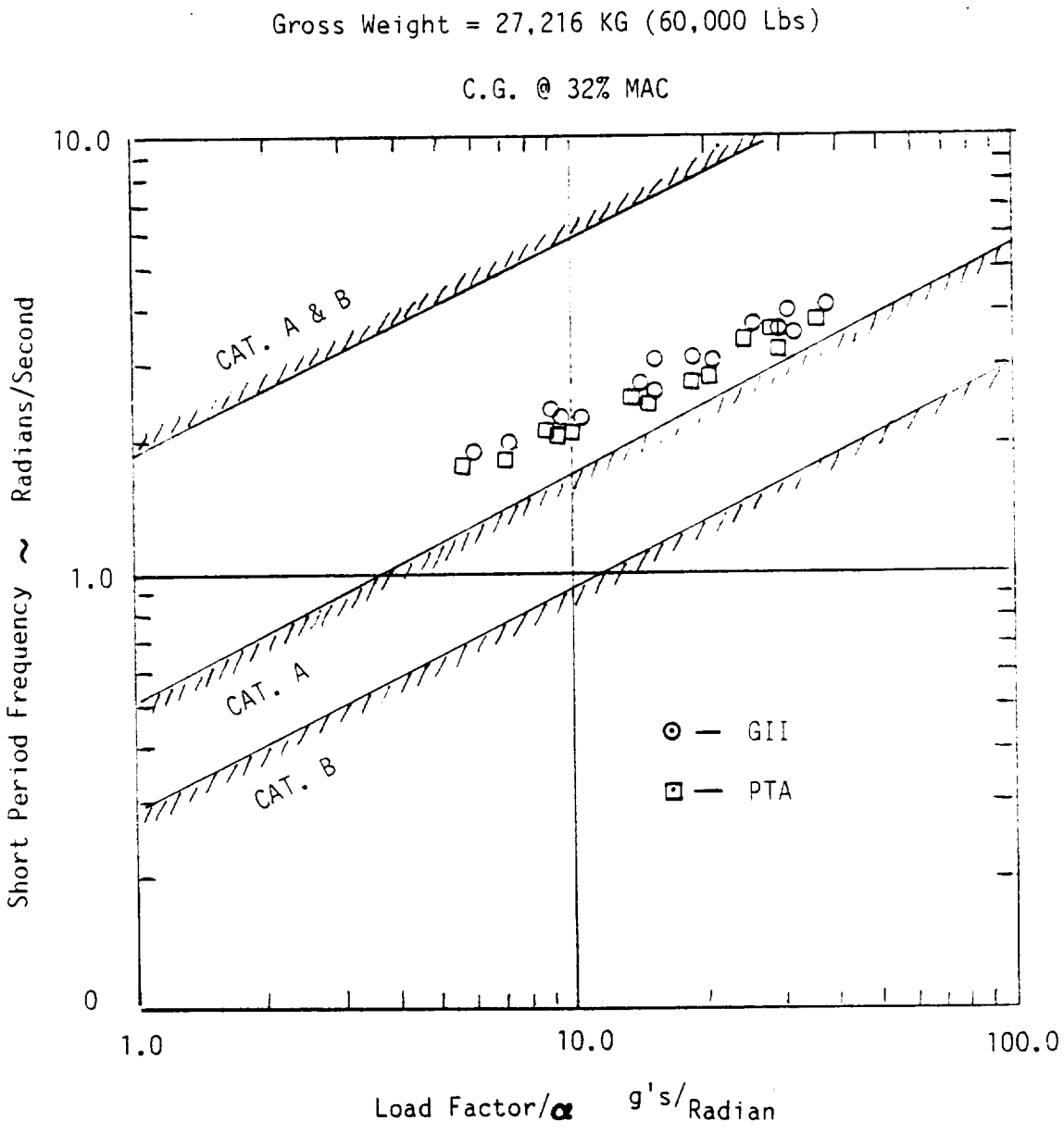


Figure 153. Longitudinal Dynamic Stability - Short Period Frequency

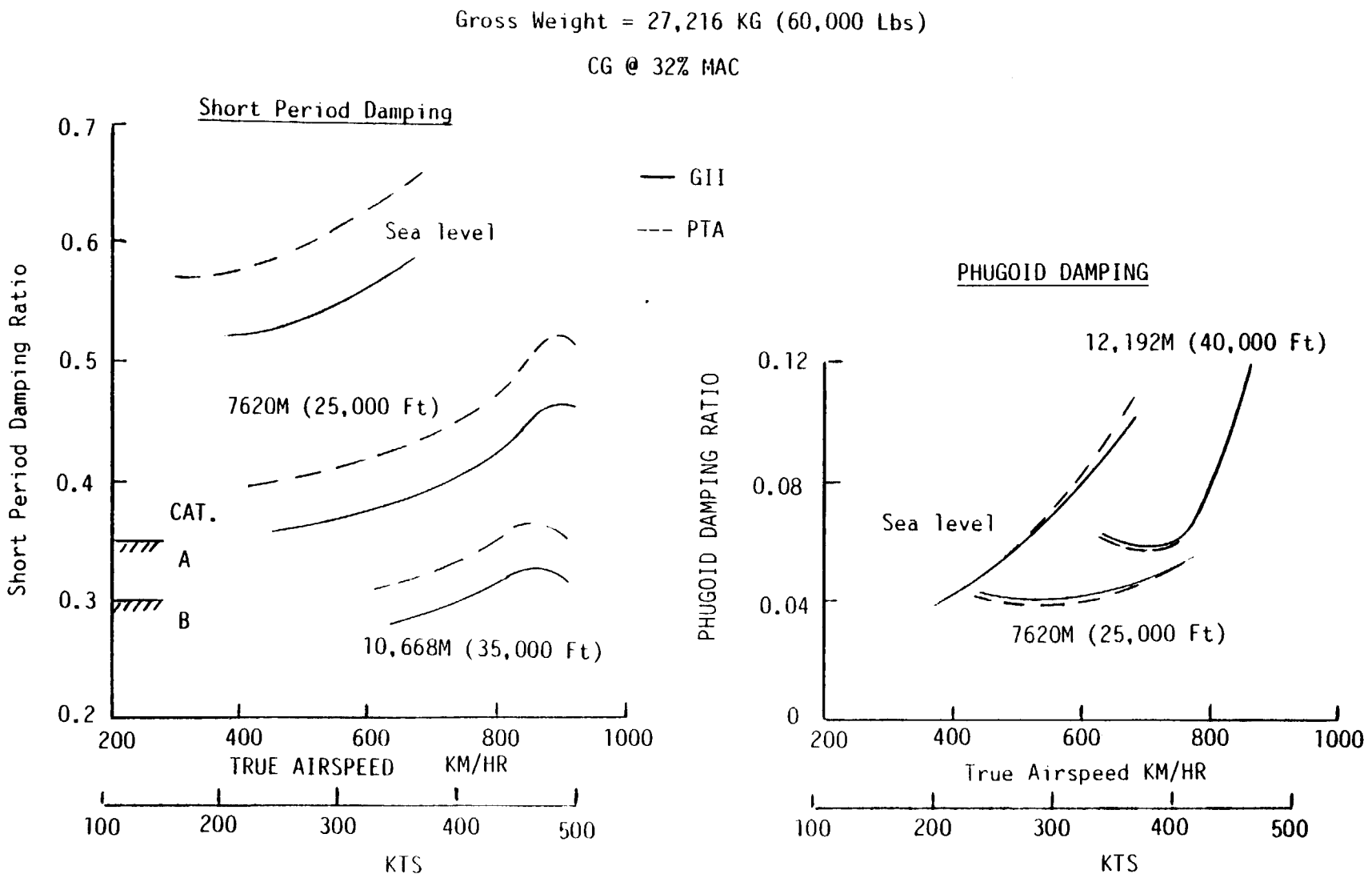


Figure 154. Longitudinal Dynamic Stability - Damping Ratios

Maximum level flight speed, M_H, is shown in Figure 155 for the PTA and GII configurations for a range of gross weights and altitudes. Dive speed, M_D, is presented in Figure 156. The dive speeds are attained by pushing over from M_H into a 7.5 degree dive for 20 seconds. Figure 157 shows that M_D limits can be set at M = 0.90 or 390 KCAS, whichever is less.

Calculations were made to determine the sensitivity of M_H and M_D to changes in drag or reductions in propfan thrust. For a 10-count drag increase on an 8-percent reduction in propfan power, the reductions in M_H and M_D were negligible.

Rudder deflection as a function of airspeed for flight with the left-hand side one Spey engine inoperative is shown in Figure 158. For the "normal" takeoff case, with flaps down 20 degrees and the propfan feathered or windmilling, the minimum control speed (V_{MC}) was essentially the same as for the baseline GII. The V_{MC} used in the GII flight manual was 102 KCAS. Since the PTA testbed aircraft was to operate in the 22,727 to 28,182 kg (50,000 to 62,000 lb) gross weight range, stall speed was the governing factor for takeoff and landing.

Figure 159 shows that the lateral-directional Dutch roll mode was altered very little by a combination of inertia changes and weathercock stability losses. These data are for the worst-case conditions simulating a failure of the GII yaw damper, which provides a series yaw rate feedback to the rudder control. The yaw damper provided Dutch roll damping that was essentially deadbeat with a single yaw damper gain value. The Dutch roll natural frequency lay between 1.0 and 2.6 over the required speed-altitude envelope for the PTA configuration. The Dutch roll time constant was low without the damper but acceptable with the damper operating.

The spiral mode, shown in Figure 160, was unstable at all speeds (damper off), except high speed at low altitude, but time to double amplitude was always much greater than the 20 seconds minimum requirement. The addition of the propfan propulsion system improved the spiral mode slightly and was of little consequence to handling qualities.

The roll mode time constant is shown in Figure 161. Roll response for the PTA configuration was decreased by the inertia increase and the lower spoiler effectiveness. Typical roll response data are shown in Figure 162 for sea level and for 12,216m (40,000 ft) altitude using 50 percent of the available wheel throw. Response is considered adequate for the required mission.

5.3.3 Conclusions

The stability and control analysis uncovered no areas of unsafe or objectionable handling qualities. Indeed, the handling qualities of the PTA aircraft were predicted to be generally the same as those of the GII. The small changes that appeared were predicted to be such that the pilot could absorb them with little or no conscious effort.

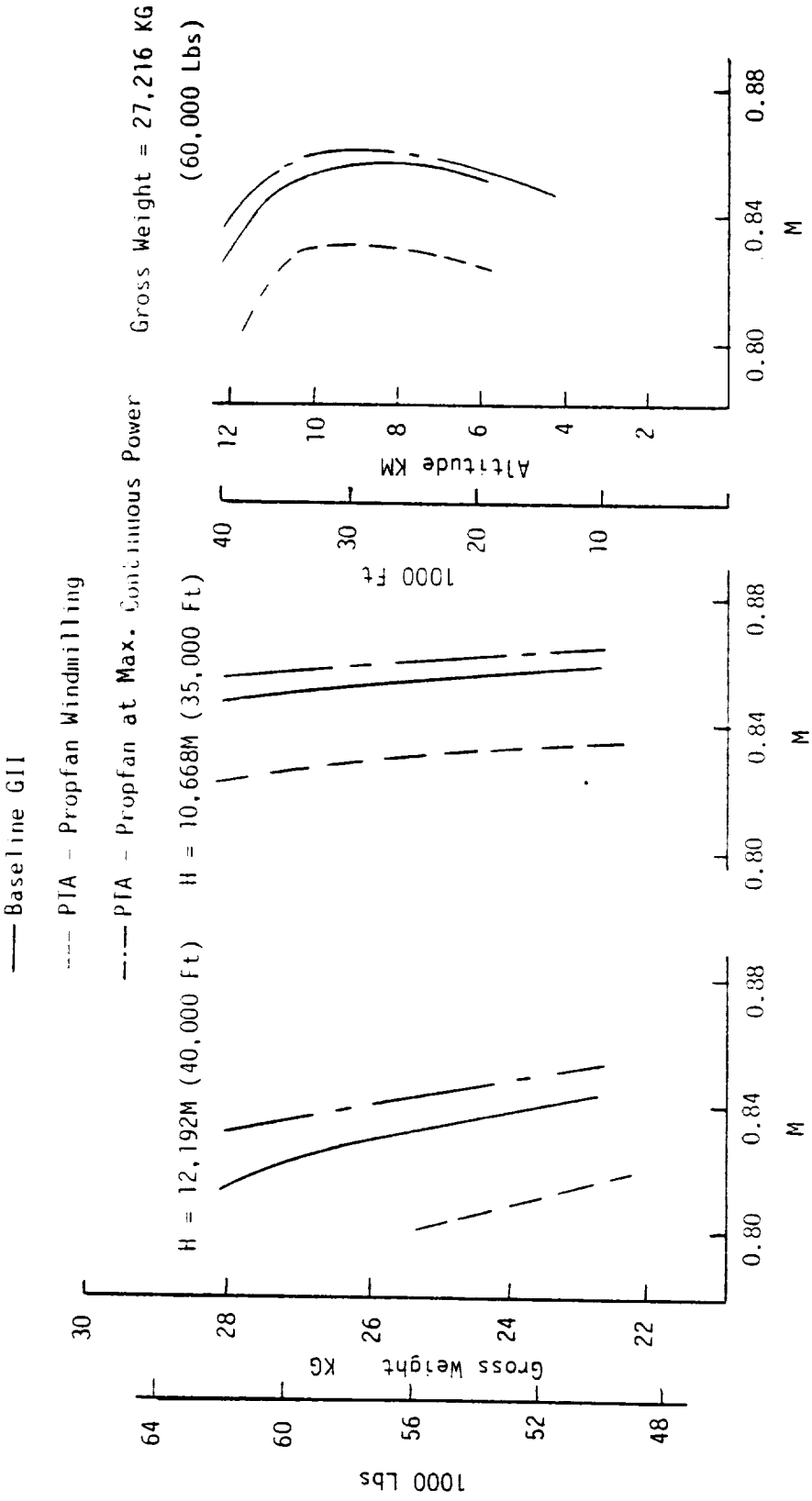


Figure 155. Maximum Level Flight Speeds

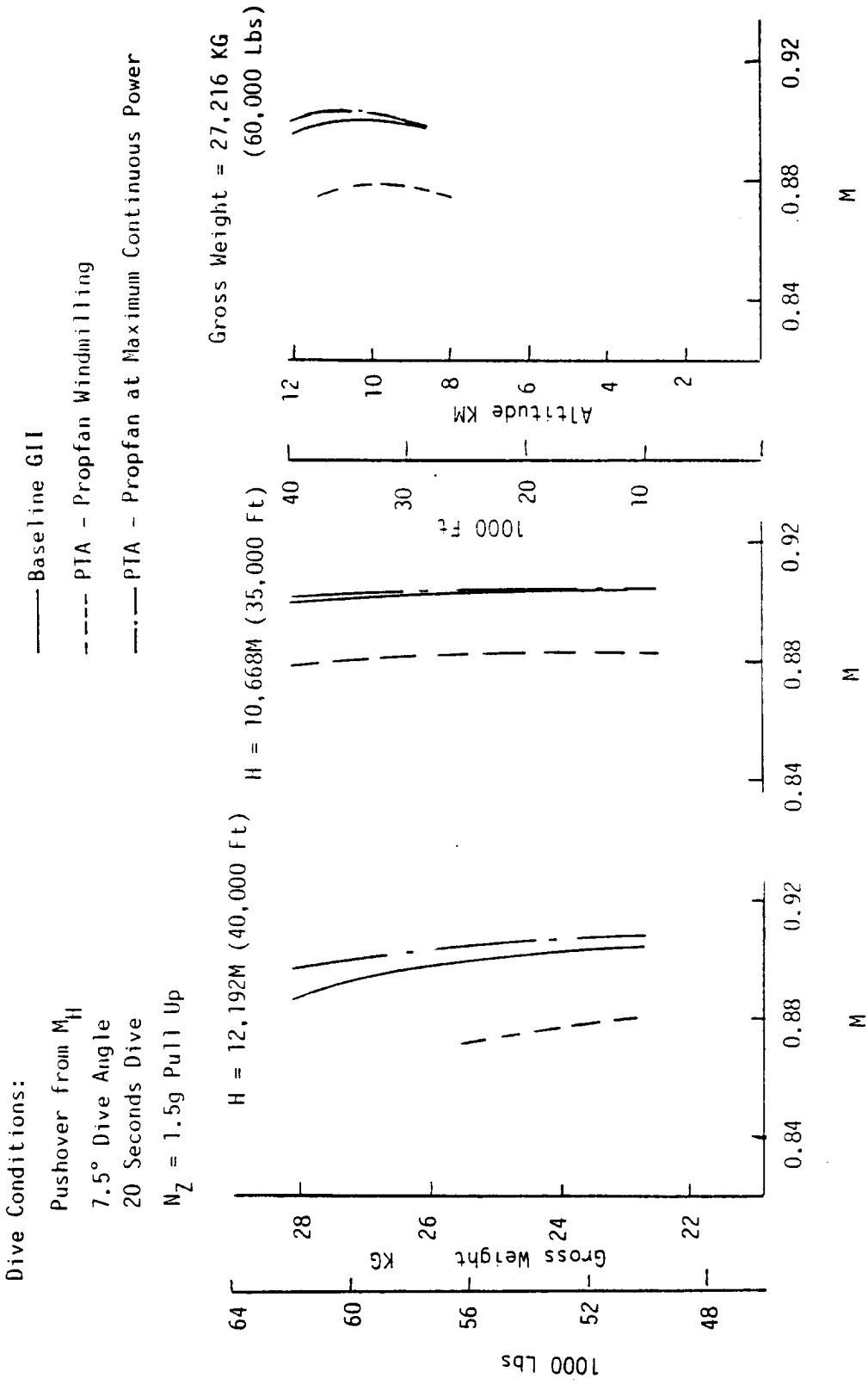


Figure 156. Dive Speeds

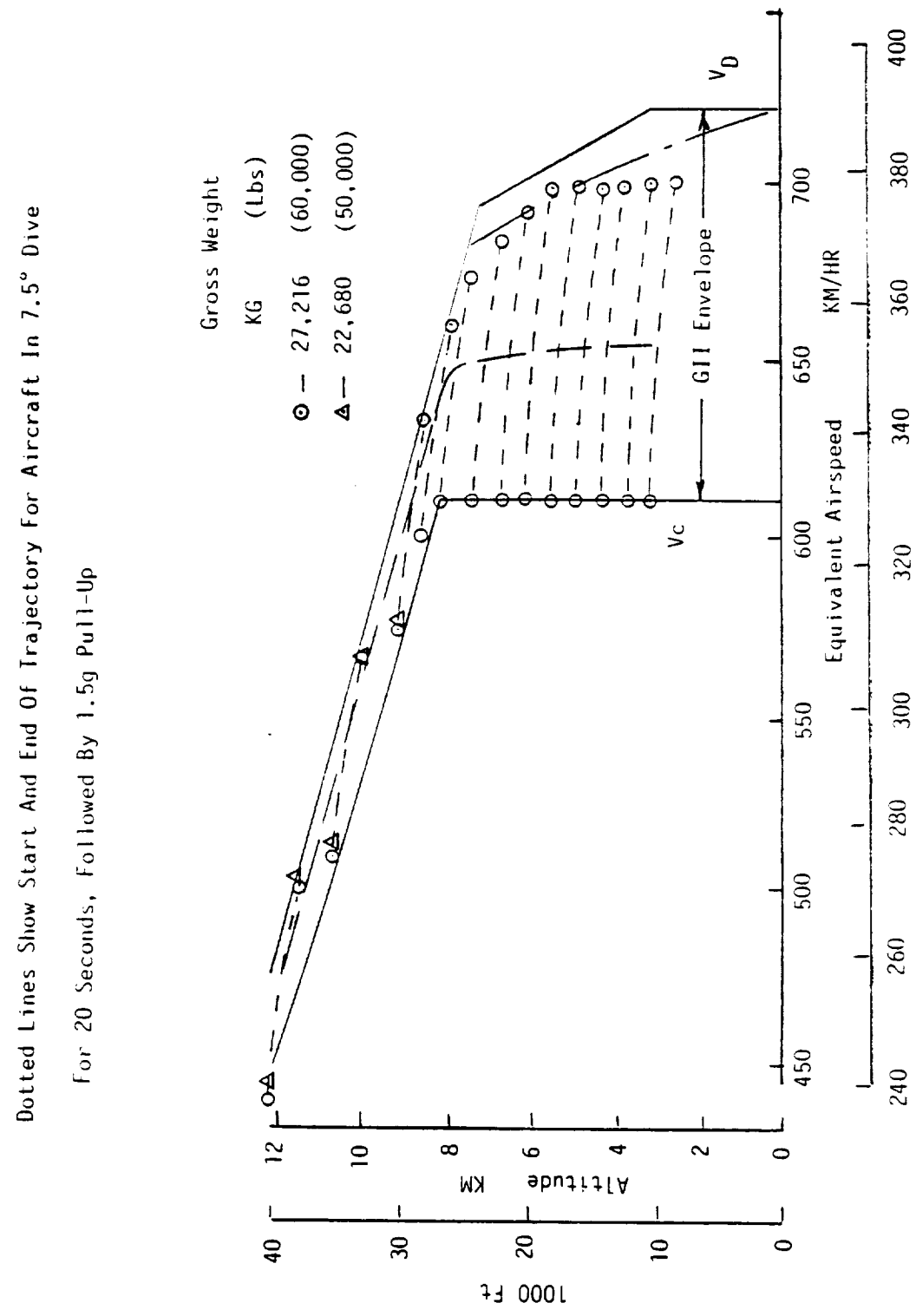


Figure 157. Upset Analysis for Determination of Dive Speed

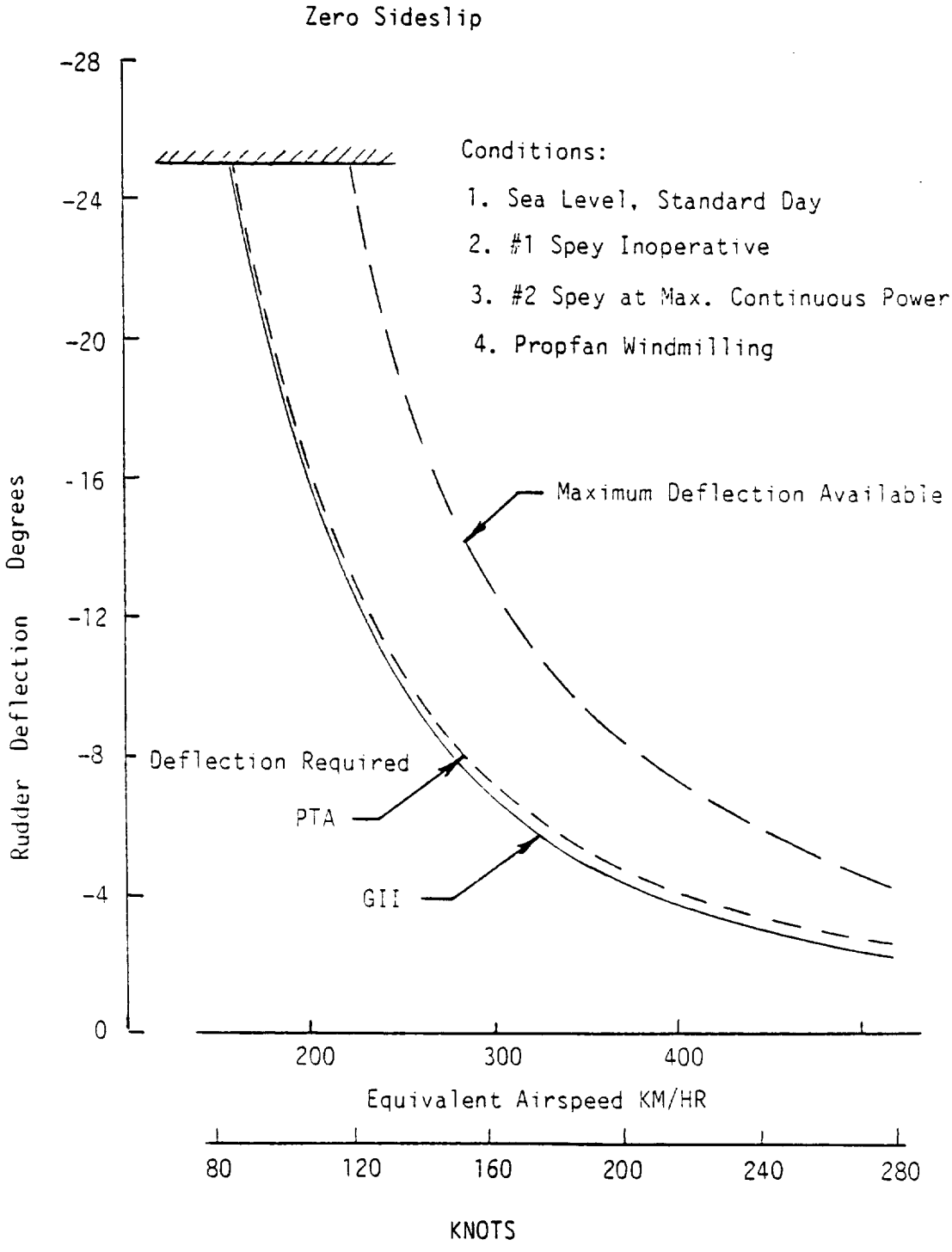


Figure 158. Single Engine Control

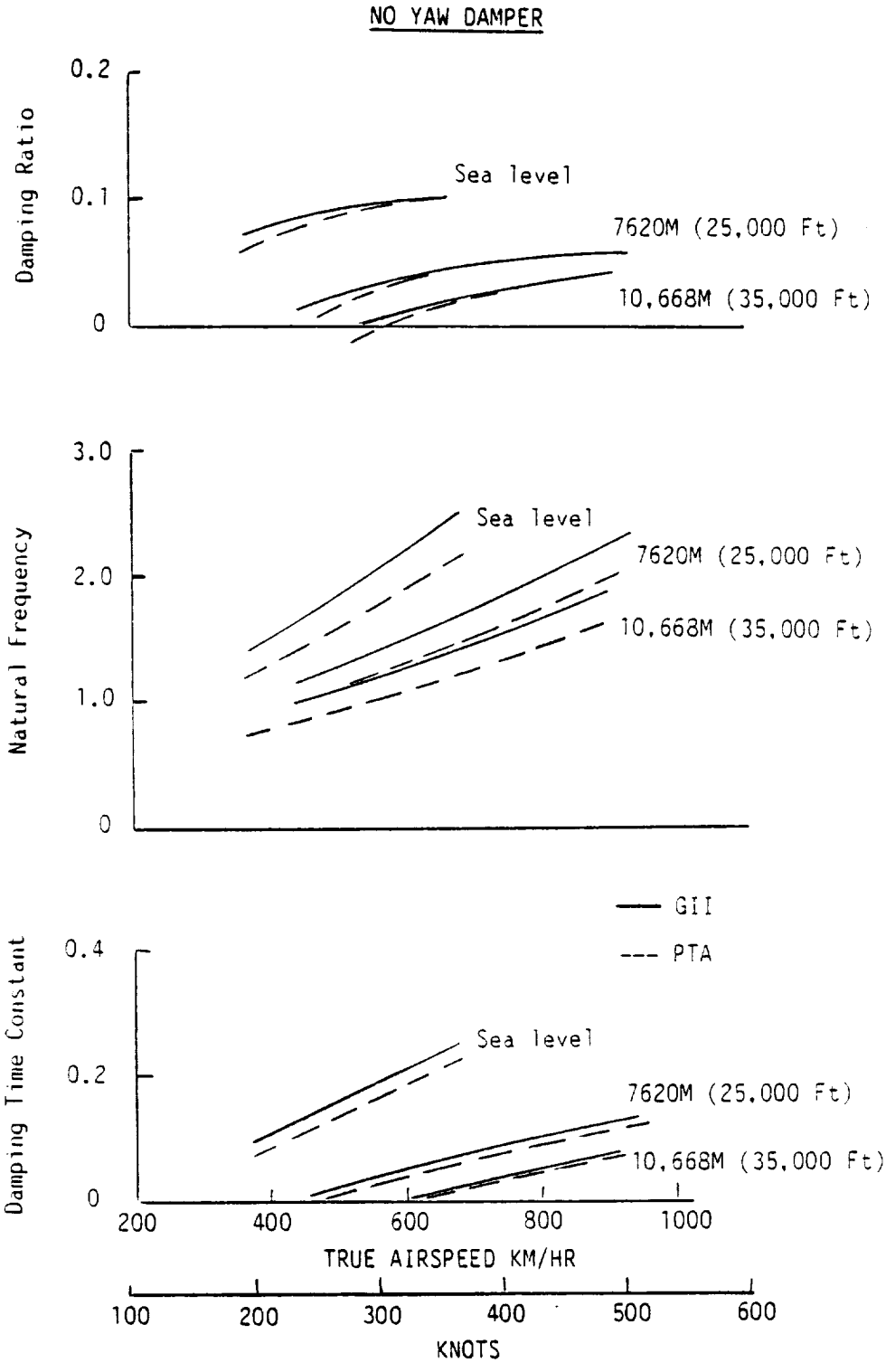


Figure 159. Lateral-Directional Dynamic Stability - Dutch Roll Mode

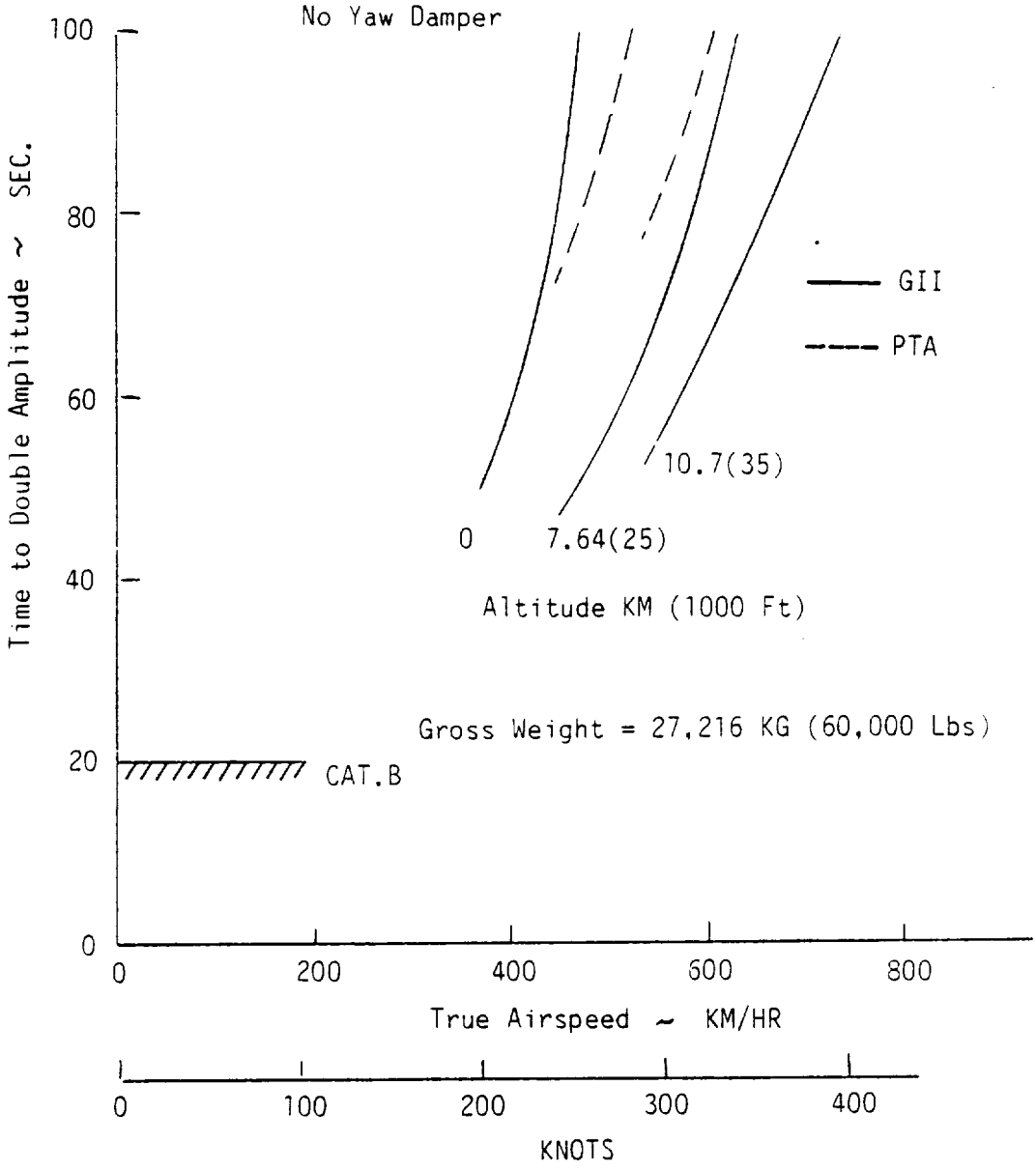


Figure 160. Lateral-Directional Dynamic Stability - Spiral Mode

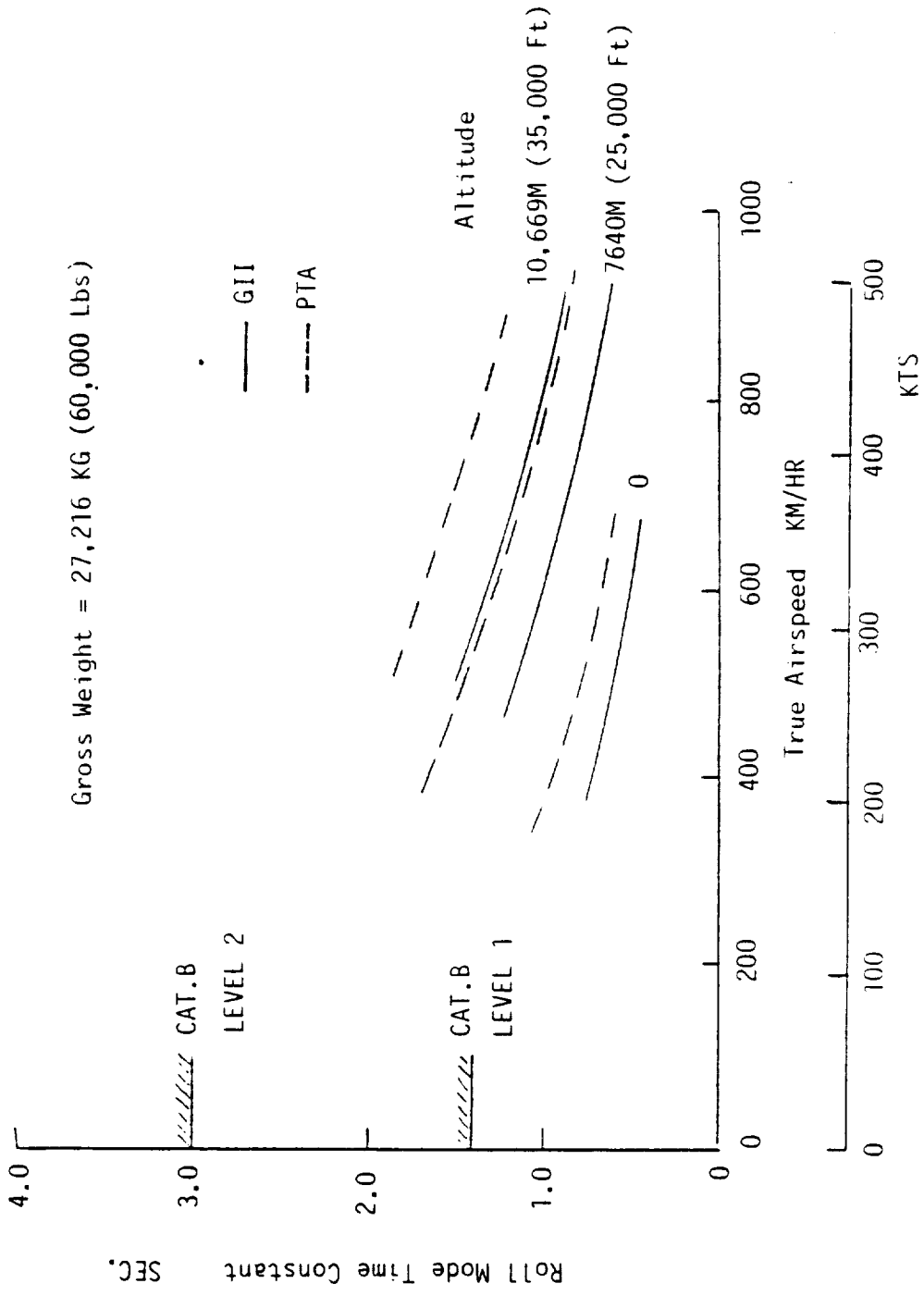


Figure 161. Lateral Dynamic Stability - Roll Mode

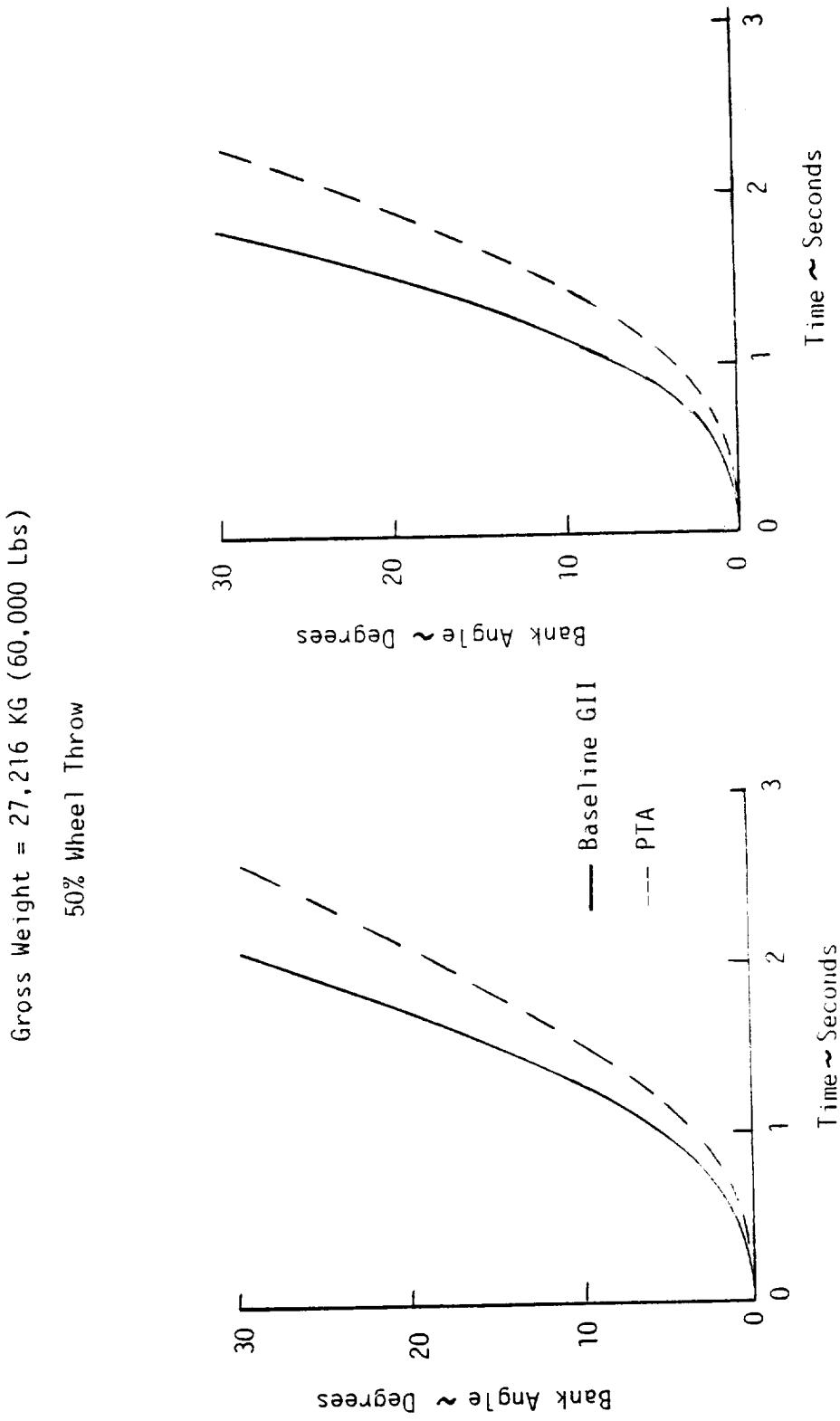


Figure 162. Roll Response to Lateral Control

5.4 ACOUSTIC ANALYSES

System design acoustic analyses were conducted to: (1) guide the initial planning of the near-field and far-field noise tests and quantify the acoustic environment that the airframe structure must be designed to endure, and (2) assess the aircraft capability to fly the conditions necessary to accomplish the acoustic test objectives.

5.4.1 Initial Test Planning

In the initial analyses for test planning, it was concluded that near-field and far-field noise data should be obtained for maximum and minimum contributions from each of the principal sources of propeller noise, i.e., blade thickness noise and steady and unsteady blade loading noise. This objective required analysis of the airplane and the propfan for operation over the widest possible ranges of propfan rotational and forward speed, shaft torque, inflow angle, and aircraft altitude. The analyses further led to the conclusion that, for many of the low-noise conditions, the noise from the unwanted sources (drive engine and Spey engines) could contaminate the propfan data, particularly in the far-field. To minimize these effects, acoustic analyses and aircraft stability and control analyses were made for flight with asymmetric Spey engine thrust and with one or both Spey engines at idle, and for baseline flights with the propfan blades removed.

5.4.1.1 Far-Field Noise

Since neither the testbed airplane or the propfan was designed for takeoff and landing with the propfan operating, the far-field noise tests were planned as a series of flyovers at constant airspeed, with flaps and gear fully retracted and Spey engines always at flight idle. The parameters selected to be varied were: propfan power (torque), tip speed (rpm), inflow angle (nacelle tilt and yaw), and distance/elevation angle (altitude).

The more important or fundamental far-field noise test criteria that were decided were as follows:

- Microphone placements, ground flush and 1.2m (4 feet) above ground at points directly under and also to the side of the flight path
- Shaft power test range, 1790 to 4475 kw (2400 to 6000 hp)
- Propfan tip speed test range, 183 to 256 mps (600 to 840 fps)
- Nacelle tilt range, -5 degrees down to +3 degrees (up)
- Yaw angle, ±5 degrees
- Altitude, 122 to 457m (400 to 1500 ft) above ground level

Specific values of these parameters, along with the many remaining detailed aspects of the far-field noise tests, were developed later during the flight research test planning.

Propfan performance maps were developed for the far-field noise test conditions as illustrated in Figure 163 to show the ranges of power coefficient, C_p, advance ratio, J, blade angle, β , shaft horsepower, shp, and propfan efficiency, η_p , for the nominal flight condition of 0.3 Mach at 305m (1000 ft). In Figure 163, it can be seen that the planned test cases adequately covered the upper segment of the performance map. The lower segment was not covered. However, this was considered to be acceptable since, for noise characterization purposes and for noise prediction methods evaluation purposes, most of the interest was expected to be focused on the higher-power operations.

Far-field noise preliminary estimates were made using rough engineering methods to assess the relative strengths of the various non-propfan sources and to assess the potential for these sources to contaminate the propfan test data. An example of the result is shown in Figure 164. These estimates indicated that at high power the propfan noise at the low-order blade-passage frequencies would be clearly evident above all other noises at the peak of the flyover signature. At frequencies beyond the second blade passage frequency, however, and in the latter half of the flyover signature, and at lower propfan power, the drive engine combustion noise was predicted to contaminate the propfan tone noise. Consequently, a drive engine exhaust noise suppressor was considered necessary to assure adequate measurement of propfan noise.

Subsequently, propfan noise levels were predicted by Hamilton Standard using more accurate theoretical methods that accounted for the non-axial inflow prevalent during low-speed flight. While these improved predictions showed slightly higher propfan tone noise levels, they did not alter the conclusion that an exhaust suppressor was needed. A muffler was, therefore, sized and configured to reduce combustion noise 15 dB over a broad frequency range. The design and fabrication of this hardware was described in Section 3.3.6.5.

5.4.1.2 Near-Field Noise

The near-field noise tests were planned as short-duration tape recordings of noise-related quantities during steady flight at predetermined fixed conditions. The quantities selected for recording included:

- Exterior sound pressures on either side of the propfan
- Fluctuating pressures in the propfan slipstream
- Vibratory accelerations on the drive system, nacelle structure, and wing structure
- Vibratory strains in the wing spars
- Vibratory accelerations on the fuselage structure

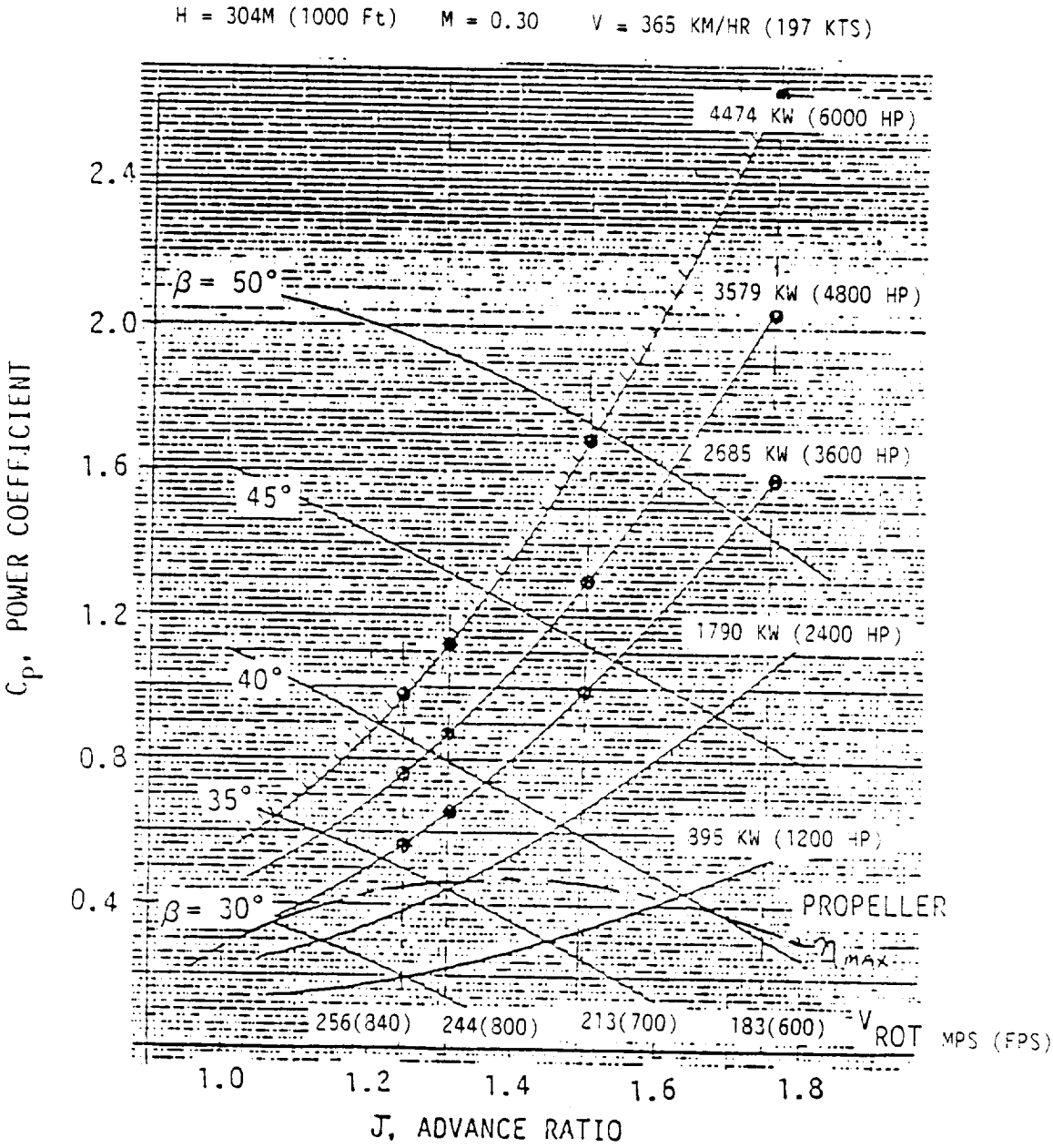


Figure 163. Propfan Performance Map for Far-Field Noise Tests

ORIGINAL PAGE IS
OF POOR QUALITY

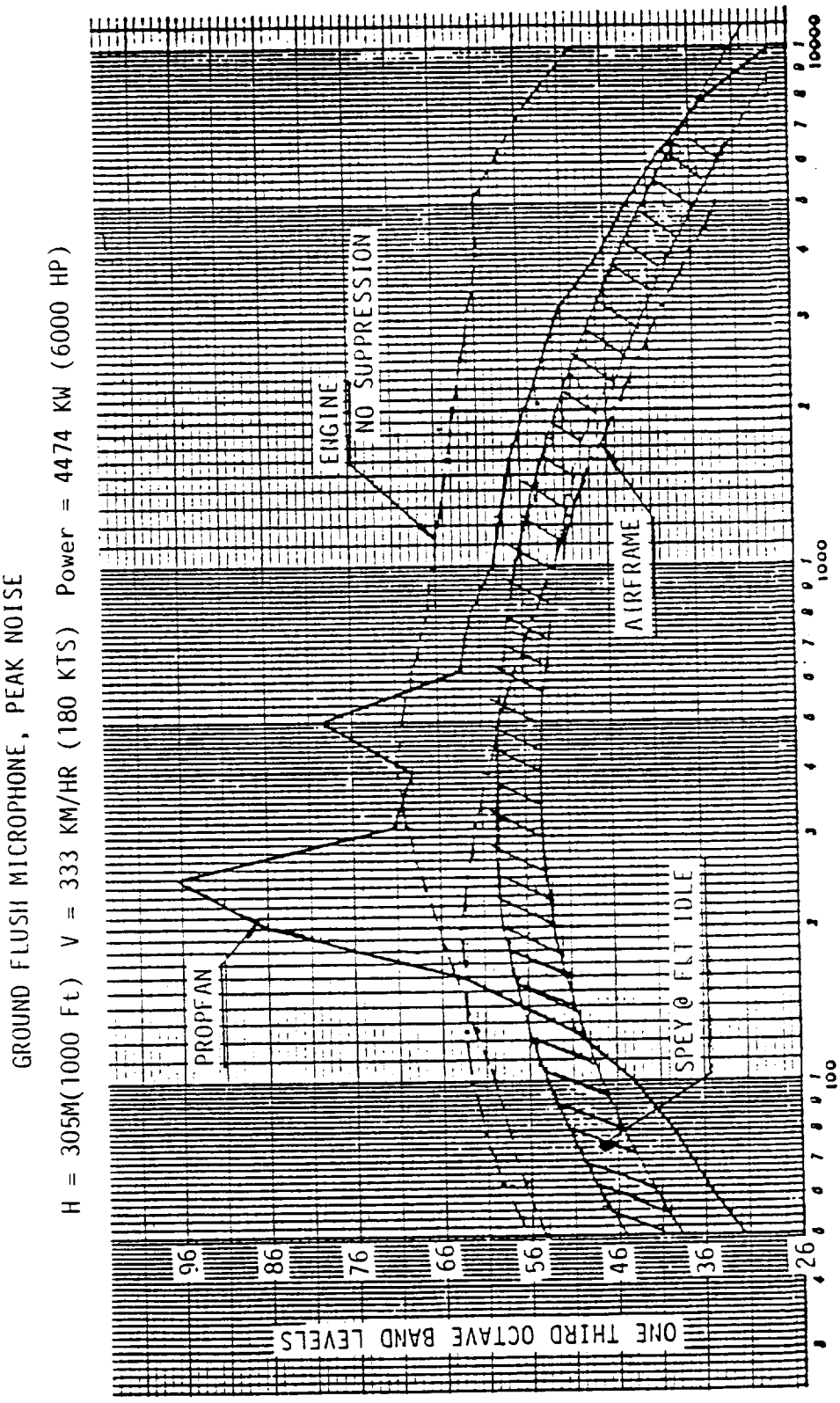


Figure 164. Predicted Peak Flyover Noise Spectra with Propfan at High Power

- o Cabin interior sound pressures
- o Approximately 30 relevant atmospheric airplane, propfan, and engine operational parameters

The test variables and range are given in the table below.

Test Variable	Range	
	Metric Units	English Units
Altitude	305 to 12,192m	1,000 to 40,000 ft
Airspeed	1.3 V_S to Max Cruise	1.3 V_S to Max Cruise
Propfan Tip Speed	183 to 256 mps	600 to 840 fps
Propfan Power	418 kw to Max Continuous	560 hp to Max Continuous
Nacelle Tilt	-5° to +3°	-5° to +3°
Yaw Angle	-5° to +5°	-5° to +5°
Cabin Pressurization	Sea Level to 3,658m	Sea Level to 12,000 ft

Specific values of the near-field noise test parameters, along with the many remaining detailed test criteria, were refined during the airplane performance evaluations and finally resolved during flight research test planning.

The basic configuration specifics that were settled during the system design acoustic analysis task were: a total of 260 data recording channels would be dedicated to the noise-related data; data would be obtained with and without the propfan installed; a wing-mounted microphone boom would be installed suitable for obtaining noise data on the outboard side of the propfan; the propfan would be geared to rotate up-inboard (clockwise looking aft); the cabin would be untrimmed and devoid of sound-proofing; a clear cabin area would be maintained forward and aft of the propfan plane; and a microphone traverse rig would be installed in the clear cabin area.

Propfan performance maps were developed for the near-field noise test conditions. An example is shown in Figure 165, which encompasses the propfan design point condition of 10,668m (35,000 ft), 0.80 Mach, 244 mps (800 fps) tip speed, and 1,933 kw (2,592 shp). This plot shows that at the high-power, low-tip-speed case, the required propfan blade angles were surprisingly large--nearly 70 degrees. Subsequent analyses with updated and improved propfan performance data produced essentially the same

ORIGINAL PAGE IS
OF POOR QUALITY

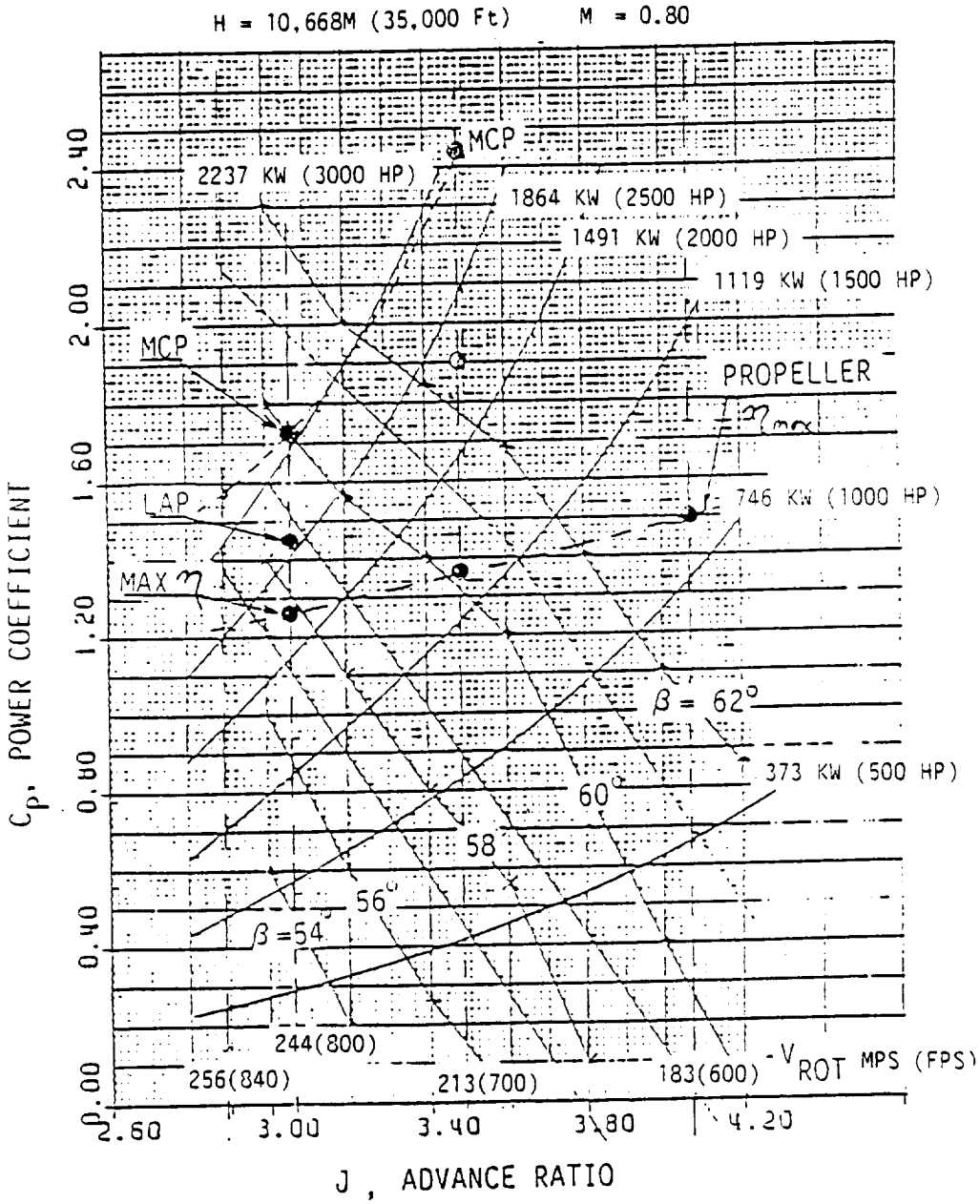


Figure 165. Propfan Performance Map for High-Altitude, Near-Field Noise Tests

results. The conclusion was that the high-power, low-tip-speed cases might be difficult to obtain, since they involve near-stall conditions on the blades and resultant high vibratory blade stress. It was clear that these cases would require reassessment during the detailed test planning.

Near-field and cabin noise levels were predicted to: (1) assess the difficulty of detecting propfan blade-order tone noise from among the Spey engine and boundary layer noises; (2) assess the near-field noise sensitivity to operating conditions, so the test conditions could be appropriately planned; (3) determine the level range, sensitivity, and frequency response capability required of the near-field and cabin acoustic test instrumentation; (4) determine the degree of ear protection required for the on-board test personnel; and (5) determine the noise exposure of the airframe structure. These predictions were first accomplished with rough engineering methods and subsequently with more theoretically refined methods. All of the intended applications of the predicted data were accomplished. The geometry and baseline cruise point conditions essential to the predictions are shown in Figure 166. Since the propfan was optimized in the LAP Program for cruise at 0.8 Mach at 10,668m (35,000 ft), 244 mps (800 fps) tip speed, 1,933 kw (2,592 shp), and axial inflow, those conditions were selected as the PTA baseline cruise test point. The nacelle tilt angle required for axial inflow at this condition was computed to be a down-tilt of -1 degree.

Figure 167 shows predicted free-field noise level variation with airspeed, power, and altitude for a single location in space. This prediction shows the somewhat different acoustic character of a high-speed propfan--namely, high noise at high dynamic pressures and tip helical speed rather than at high thrust or power. Predicted noise levels over the surface of the fuselage for the baseline cruise point are shown in Figure 168 where a substantial surface area is seen to be exposed to noise levels of 145 dB or more. Similar noise predictions were generated for higher orders of the propfan blade passage frequency and other flight conditions. The effects of tip speed, power, and inflow angle were also predicted.

Fluctuating pressure levels in the propfan slipstream were predicted to the same extent, so as to reveal operational parameter dependency as well as spatial variability.

From these predictions and related analyses, it was concluded that, on the whole, propfan tone noise would be measurable above the background noise at most locations and at most power conditions, if the data spectrum analysis bandwidth was sufficiently narrow and the data recording time was sufficiently long. Accordingly, data record length was set at nominally one minute; data frequency range was set at 10 to 2000 Hertz, and spectrum analysis bandwidth was set at nominally 5 Hertz. The sensitivity range of the fluctuating pressure transducers was set at 0 to 14 x 10^3 N/m^2 (2 psi).

Cabin noise levels were predicted for ground runup and for worst-cruise operations. For test personnel moving about the untreated aft cabin, it was concluded that their exposure to "A"-weighted noise level would occasionally exceed 120 dBA, and for ear protection and communication

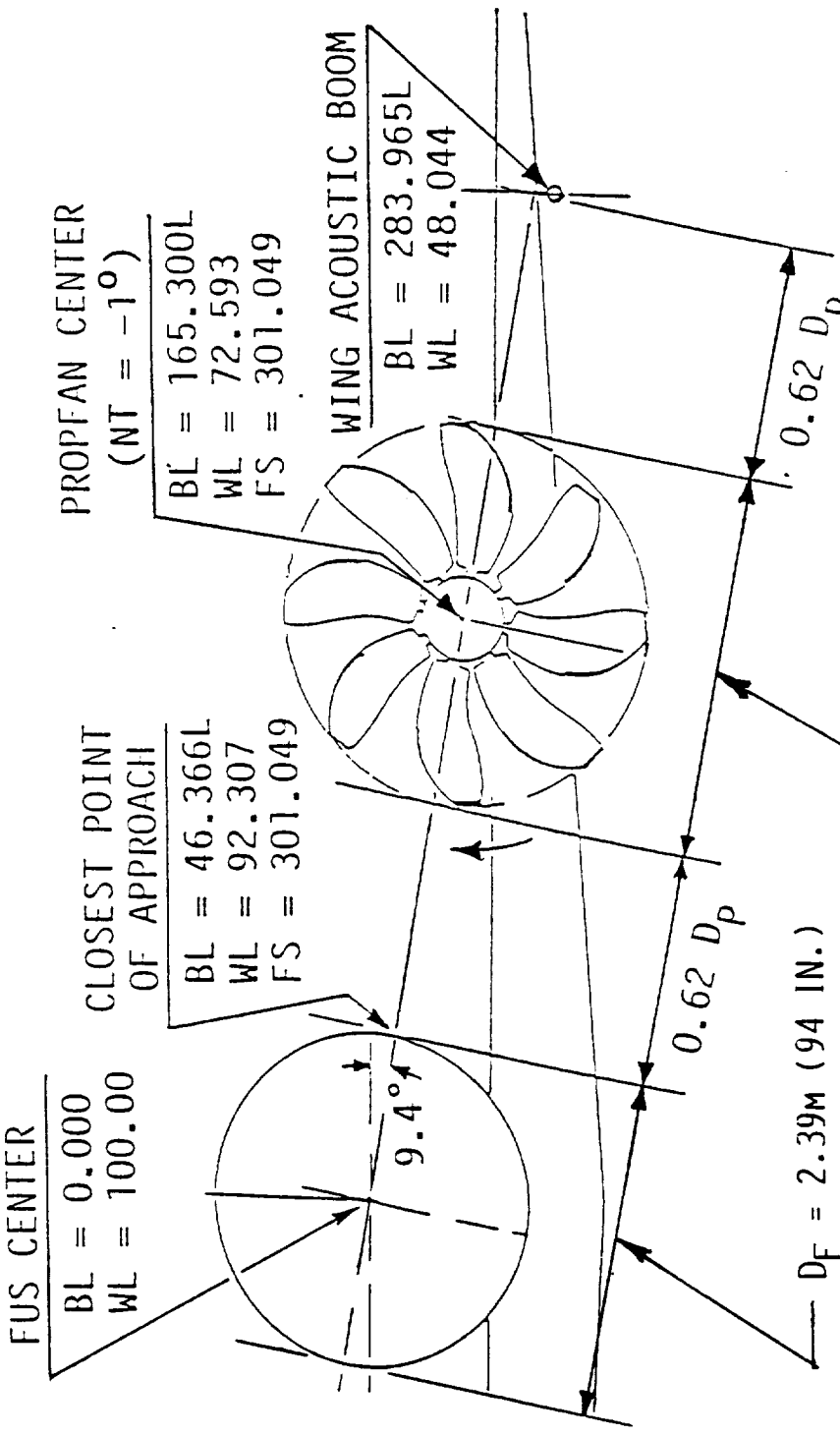


Figure 166. Acoustic Geometry and Baseline Cruise Conditions

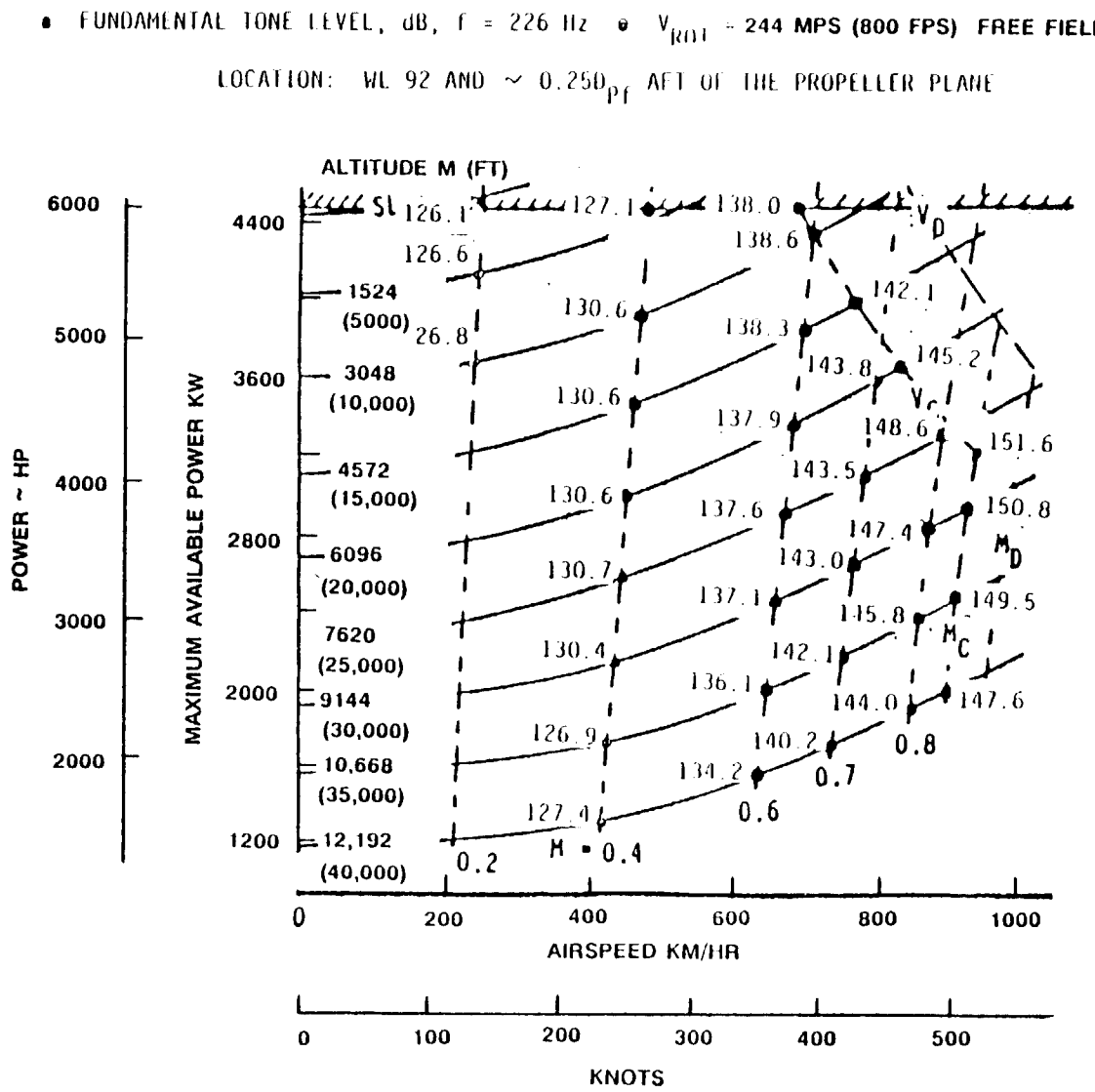


Figure 167. Operational Map of Predicted Near-Field, Free-Field Noise

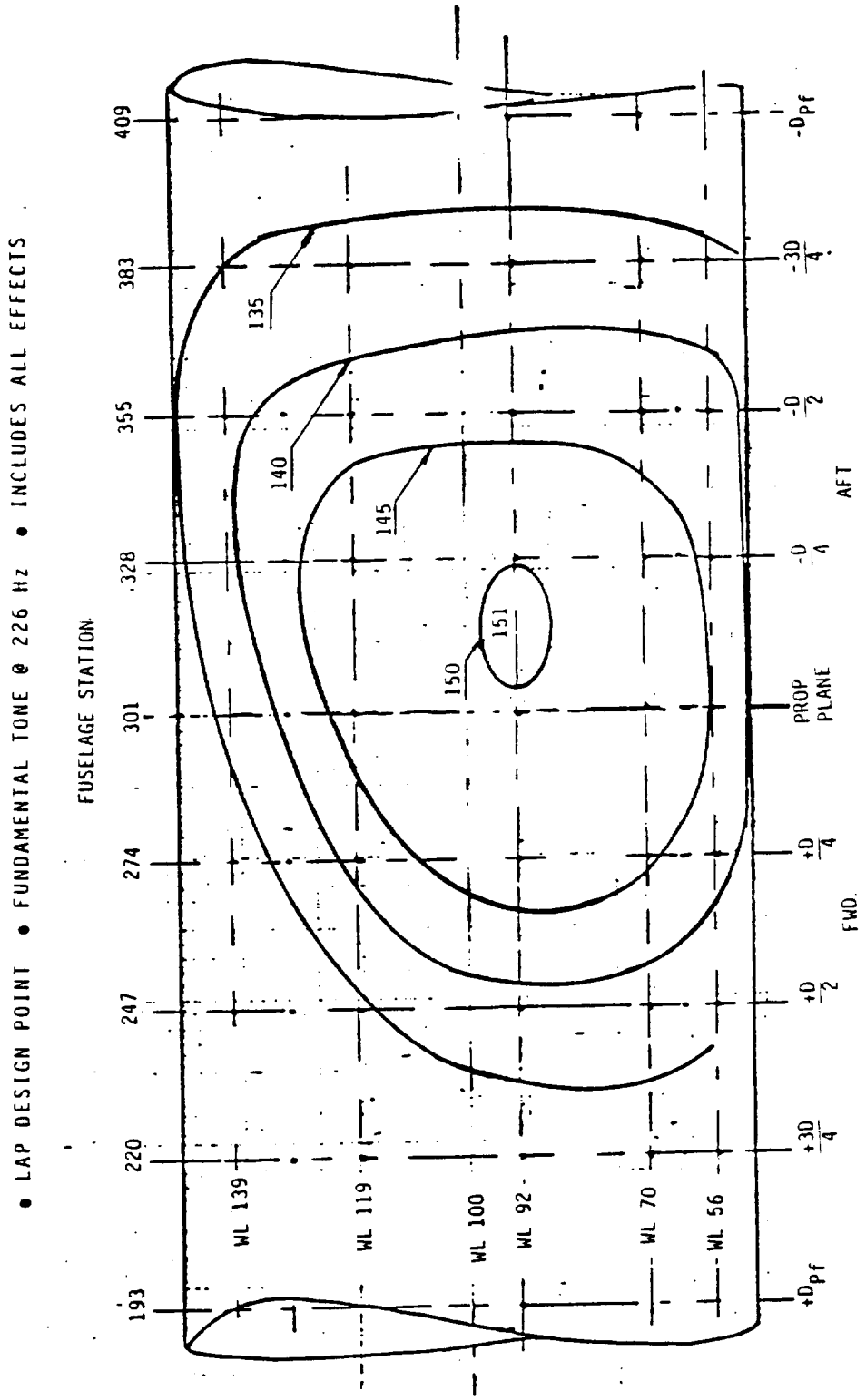


Figure 168. Fuselage Surface Predicted Noise Levels - Baseline Cruise

purposes, personally fitted helmets with integral muffs should be standard gear for all test operations.

As a result of the preliminary noise predictions and a review of the airframe structure design, certain structures were determined to require sonic fatigue and vibration analyses. They were the fuselage shell in the vicinity of propfan plane and the nacelle and wing structure immersed in the propfan slipstream. Noise levels for these areas were examined more closely for the worst-case conditions, which corresponded to highest power, highest tip speed, highest flight speed, and the intermediate altitude at which high dynamic pressures were encountered. For the fuselage, this worst case was identified, and the resulting noise levels are shown, in Figure 169. For the nacelle and wing area in the slipstream, the predicted worst-case noise levels occurred at a slightly lower altitude and speed where available power is slightly higher, as shown in Figure 170. Sonic fatigue analyses for new and for existing structures were based on these preliminary predictions, illustrated by Figures 167 through 170. The results of the sonic fatigue analyses are discussed under Structural Analysis, Section 5.5.

5.4.2 Acoustic Test Capability Assessment

Analyses were conducted to determine whether the testbed airplane could be flown in such a manner that the propfan could be operated at all of the conditions required to fully define its noise characteristics and to isolate the effects of various operational parameters.

5.4.2.1 Far-Field Noise

Evaluations of the Spey engine spool-up time led to the initial view that the minimum flyover altitude would be about 152m (500 ft) AGL. In subsequent, more detailed stability/control studies during the test planning task, the 152m (500-ft) minimum flyover altitude was increased to 229m (750 ft) AGL for aircraft safety.

The 229m (750 ft) minimum test altitude allowed time for crew reaction to a propulsion system failure and for sufficient recovery of thrust and speed to arrest the descent before reaching 152m (500 ft). The analyses were based on the premise that all propfan flyover noise testing would be done with the Spey engines at flight idle. A minimum test altitude of 229m (750 ft) was judged to be acceptable.

The flight speed available for the flyover noise tests was evaluated within the previously established criterion that all flying would be with flaps and gear retracted. Therefore, to allow for momentary yawing, rolling, and/or reduction in speed and lift in the event of a propulsion system failure, the flight speed was set at a 30-percent margin above the flaps-up stall speed, V_S. For a low flight-weight of approximately 25,000 kg (55,000 lb), 1.3 V_S was estimated to be about 340 km/hr (185 KEAS), and for high weight 29,500 kg (65,000 lb), about 380 km/hr (205 KEAS). Because speed variation among various flyovers was not wanted in these tests, a reasonable compromise single-speed for all flight weights was set at 370 km/hr (200 KEAS), which equates to 0.3 Mach for a sea-level

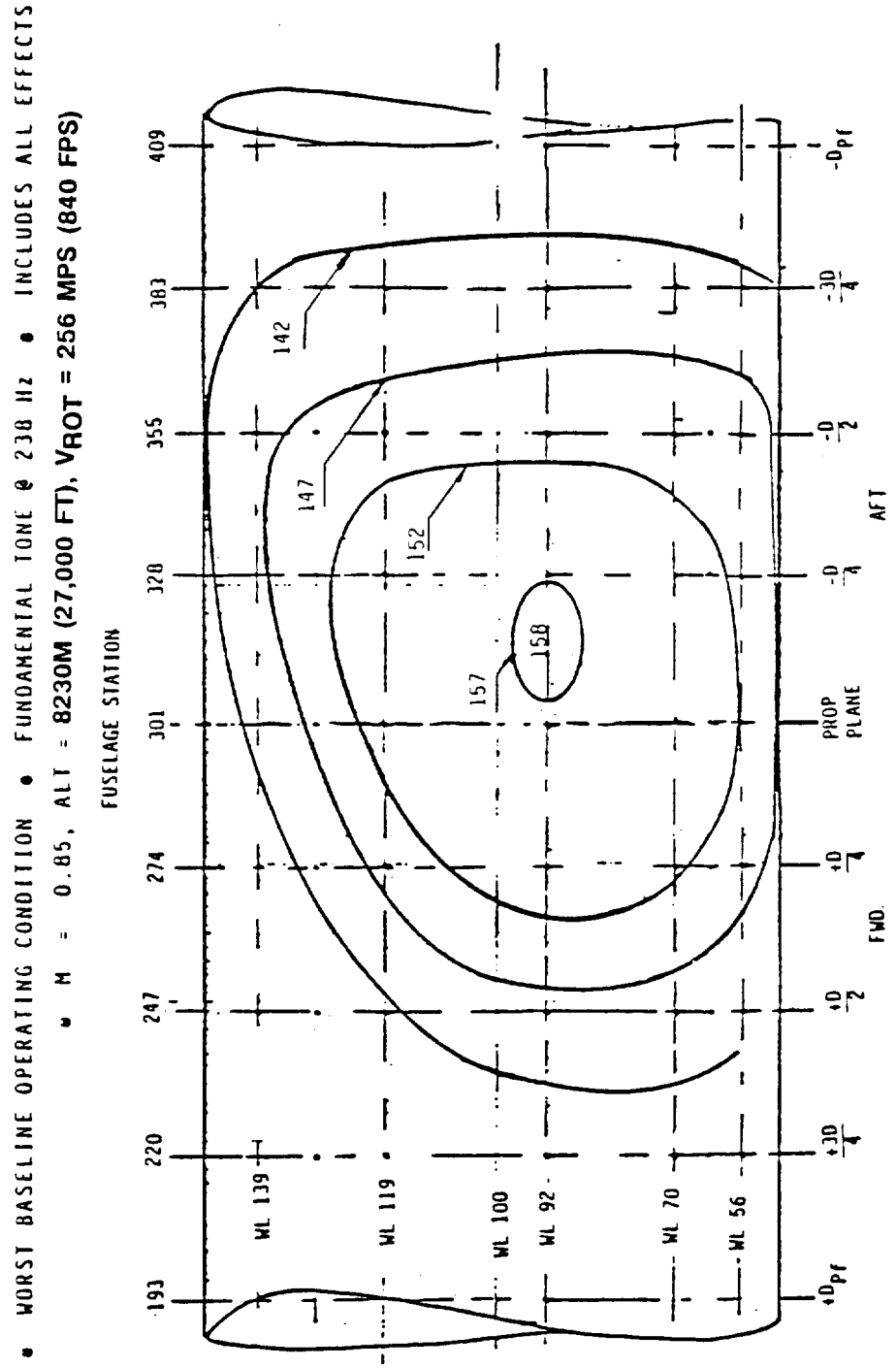


Figure 169. Fuselage Surface Predicted Noise Levels - Worst Case

H = 6096M (20,000 FT) M_o = 0.70; POWER = 3542 KW (4750 HP)

V_{ROT} = 256 MPS (840 FPS)

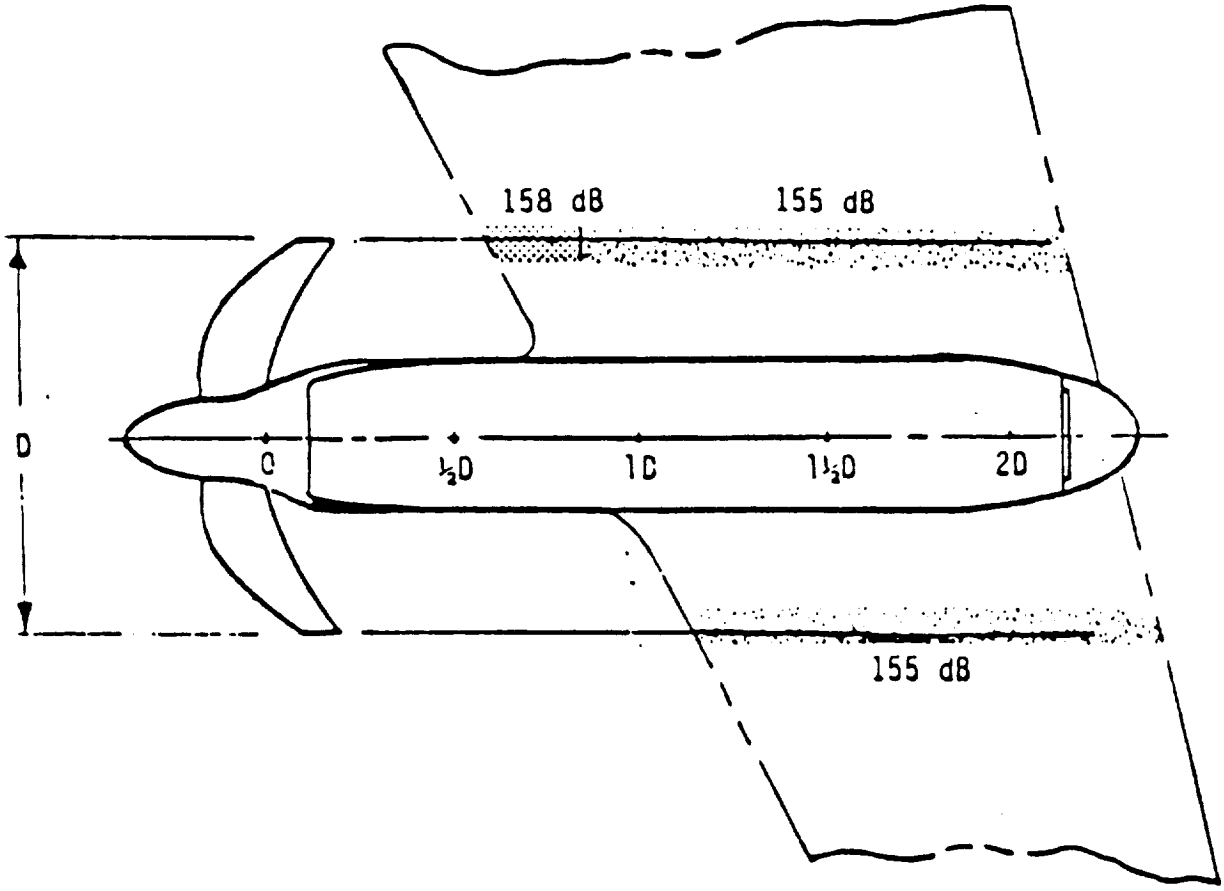


Figure 170. Fluctuating Pressure Levels on Wing and Nacelle - Worst Case

standard day. This is 15 to 20 percent faster than would be expected for a typical commercial propfan aircraft of similar weight and power, but was judged acceptable for flight research purposes.

The thrust required to maintain level flight at 0.3 Mach was estimated to be 24,465N (5,500 lb). This was with flaps and gear up, at a nominal altitude of 610m (2,000 ft) and weight of 27,300 kg (60,000 lb), and with controls set as required to counteract asymmetric thrust and lift. The Spey engines each produce about 1,000N (225 lb) thrust at flight idle. Therefore, for propfan power conditions producing less than 22,450N (5,050 lb) thrust, the aircraft would lose altitude; for conditions producing greater thrust, the airplane would gain altitude. Aircraft gradient, as a function of propfan system thrust, is shown in Figure 171. At maximum power, all propfan tip speeds are seen to produce a moderate climb gradient, less than 2 degrees. At minimum power (about 40 percent of max), moderate descent gradients resulted (3 degrees or less). These gradients were considered acceptable. It was concluded that it was feasible to conduct the acoustic flyovers with the Spey engines at flight idle. While the loss of altitude during a low-power flyover might sometimes require normalization for distance, this was considered less detrimental than the alternative, which was to increase Spey thrust (so as to maintain level flight) and risk contamination of the propfan noise data.

The control surface deflections were estimated for the large asymmetric thrust conditions, and the bank angles and attack angles were estimated for flight with intentional stabilized yaw. All were found to be acceptable, with the proviso that the yaw inflow tests might have to be conducted at reduced propfan power in order to reduce rudder loads and to increase the magnitude of the yaw angles.

In order to determine the extent to which the Spey engines and the aircraft contribute to the total noise present during the propfan tests, flyovers were planned for the same Spey power conditions used in propfan noise measurement tests but with the propfan removed. For this flight condition, total thrust from the Speys was not great enough to sustain level flight. The resulting gradient was determined to be about 5 degrees descending (as can be seen in Figure 171) when propfan thrust is zero. This descent rate was judged to be acceptable, particularly since these flyovers could be made at a slightly higher altitude if necessary.

5.4.2.2 Near-Field Noise

When measuring near-field propfan noise, it was desirable to operate the Spey engines at the lowest possible power to minimize contamination from those noise sources. Propfan thrust alone, however, was not sufficient to maintain level flight except at low altitudes and low speeds. This can be seen in Figure 172 where various level flight test conditions are represented by separate lines, and points along these lines denote the Spey thrust required when the propfan was operated at a given thrust. It can be seen that some Spey thrust was needed for all cases shown except Mach 0.35 at 914m (3000 ft) altitude when the propfan is operated at its higher power levels.

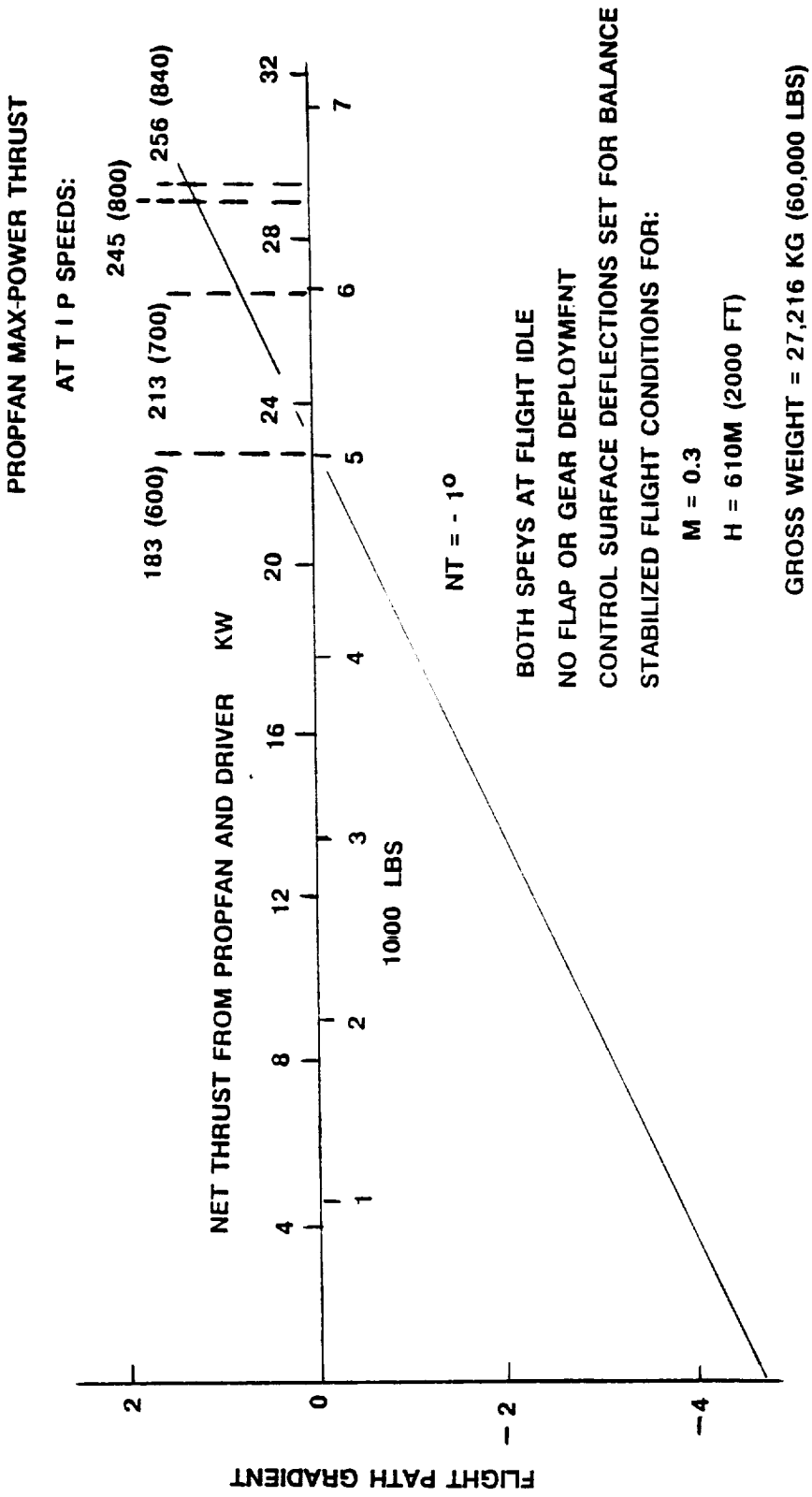


Figure 171. Flight Path Gradient with Spey Engines at Flight Idle

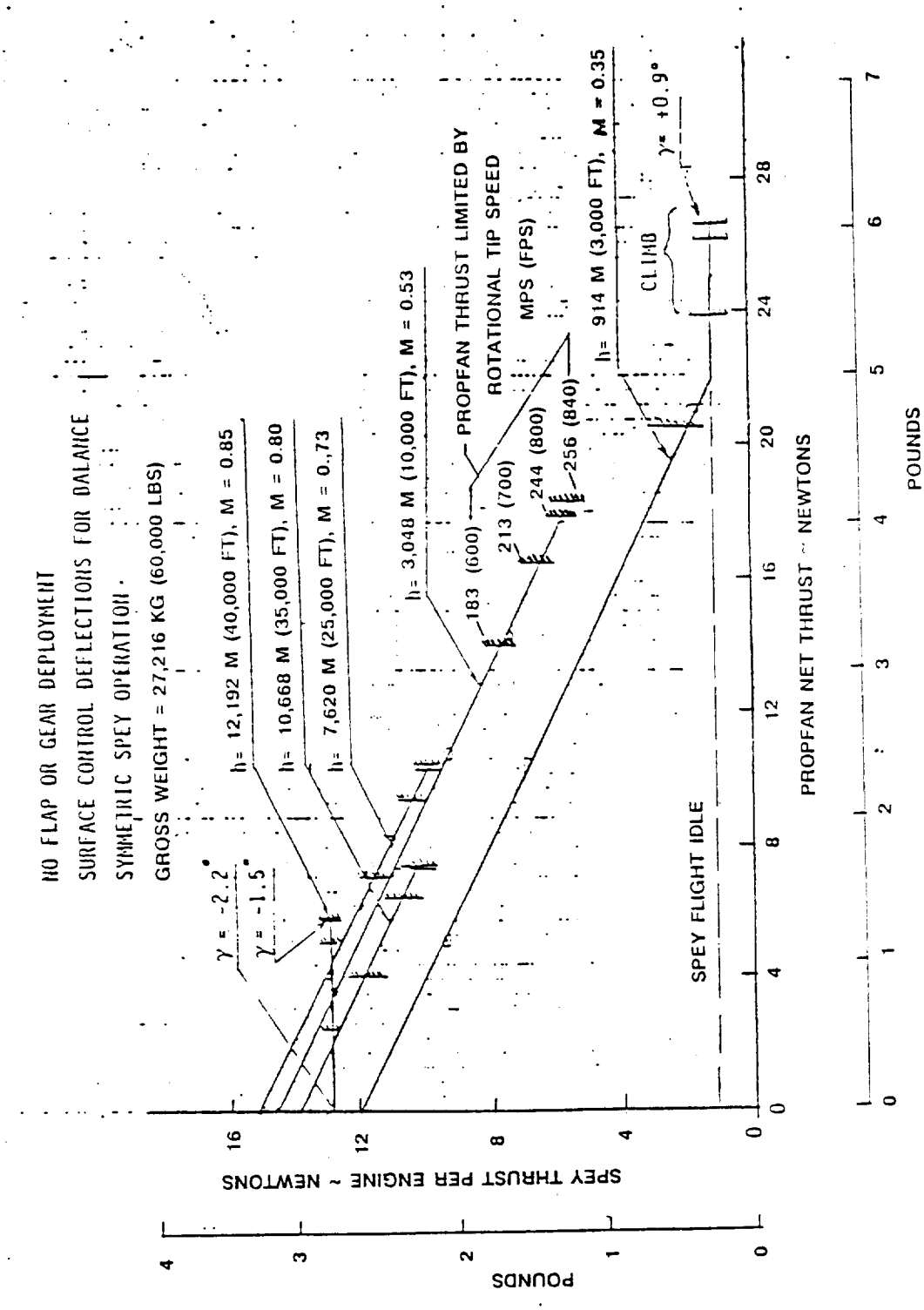


Figure 172. Thrust Trade-Offs for Level Flight

For the majority of test points, therefore, where it was necessary to use Spey engine thrust, the left hand Spey engine was not used as long as sufficient thrust could be produced by the single right hand engine. Only when that thrust was insufficient was the left hand engine powered.

Engineering estimates indicated that Spey noise contamination should not generally be a problem because the propfan noise was characterized by strong tonal characteristics at levels much higher than the broadband noise. Analyses like those resulting in Figure 172 were used to establish the most favorable operating conditions, and the data were closely monitored during testing to detect any contamination and permit use of alternative test techniques where necessary.

One alternative technique was to abandon the restriction of level flight and allow gliding flight with Spey engine power reduced. The baseline design point condition was examined more closely to determine the flight gradient that would result if both Spey engines had to be set at flight idle in order to measure uncontaminated propfan noise, particularly for low propfan tip speeds and thrusts. This analysis showed that for maximum propfan thrust with both Speys at flight idle, the gradient would be about 4½ degrees descending, and at zero propfan thrust, 6 degrees descending. This translates to descent rates of 18.3 mps (60 fps) to 24.4 mps (80 fps) and during a typical data record duration of about 45 seconds, it would result in about 975m (3,200 ft) of altitude variation on a mean of 10668m (35,000 ft). The noise changes from such altitude variations, though undesirable, were considered to be an acceptable tradeoff for reduced contamination. Therefore, the ability to obtain propfan noise with both Speys at flight idle was retained as an option, to be used only if unavoidable.

5.5 STRUCTURAL ANALYSIS

5.5.1 Airframe Structural Integrity

5.5.1.1 Criteria and Methodology

The GII aircraft was certified to the 1962 Civil Air Regulations for transport category aircraft, CAR-4b, and these regulations were used as structural design guidelines for the PTA aircraft modifications. Recognizing, however, that an across-the-board application of all CAR-4b requirements would dictate structural modifications beyond those necessary for PTA operations, each requirement was scrutinized for test program applicability, and accordingly, some of the CAR-4b requirements were adjusted. These adjustments are appropriately discussed in the paragraphs that follow. Safe achievement of the test program objectives was a priority consideration for the structural design.

Attention was given during structural design to the reinforcement necessary for the GII structure as well as to the design of the new components such as the propfan nacelle and the various booms. In other words, evaluation of the entire airframe from a strength standpoint was necessary to ensure structural integrity. Design substantiation was primarily analytical with testing directed primarily toward obtaining design data

and verification of analytical methods. A proof-load test was conducted, however, on the propfan nacelle after it was installed on the airplane, and this test is described in Section 8 of this report.

Evaluation of the wing, propfan nacelle, center fuselage, and the interfaces between these components was based on internal loads derived using the finite element model shown in Figure 173. Conventional analysis was used for the wing tip static balance boom, the wing tip dynamic balance boom, the microphone boom, and the fuselage protective plate installation. Integrity substantiation of other components was made by comparing PTA maximum external loads with the corresponding GII design loads.

The CAR-4b factor of safety value of 1.5 was used. This safety factor was applied to predicted limit loads (maximum loads anticipated) to obtain "Applied Load." New or modified structure was further required to have an ultimate margin of safety of at least 0.33, where MS is defined by:

$$MS = \frac{\text{Allowable Load}}{\text{Applied Load}} - 1$$

This provided additional conservatism to the design and compensated for minimum structural testing. A minimum margin of safety value of zero was considered acceptable for existing structure provided:

- Allowables were the same as used to calculate the GII basic component margin of safety
- No GII service failures of the component had occurred
- The component was, or was a part of, damage-tolerant structure

Damage tolerance was evaluated conservatively for fail-safe consideration by applying limit load with zero margin of safety.

Two methods were used to derive PTA configuration external loads. Loading conditions which were primarily static (cruise flight, normal maneuvering, nondynamic gust simulation, steady ground operations) were investigated by using a set of discrete element computer programs. Conditions requiring dynamic analysis (e.g., landing, taxiing, gust encounter) were examined using a lumped mass mathematical model representation wherein element masses were considered connected with beams having appropriate bending and torsional stiffness properties. Extensive programming and data modifications of existing computer programs were necessary to account for the asymmetry of the PTA configuration; mass distributions, stiffness distributions, aerodynamic loadings, and load condition parameters were affected.

Aerodynamic loading data were derived theoretically using the Lockheed QUADPAN flow analysis code, and then were adjusted as necessary to agree with total airplane forces and moments indicated by GII flight tests and high-speed wind tunnel tests. These data were supplemented within the static loads program by a three-dimensional, subsonic, vortex-lattice solution to provide the incremental loadings due to aeroelasticity. The aerodynamic representation consisted of 278 panels.

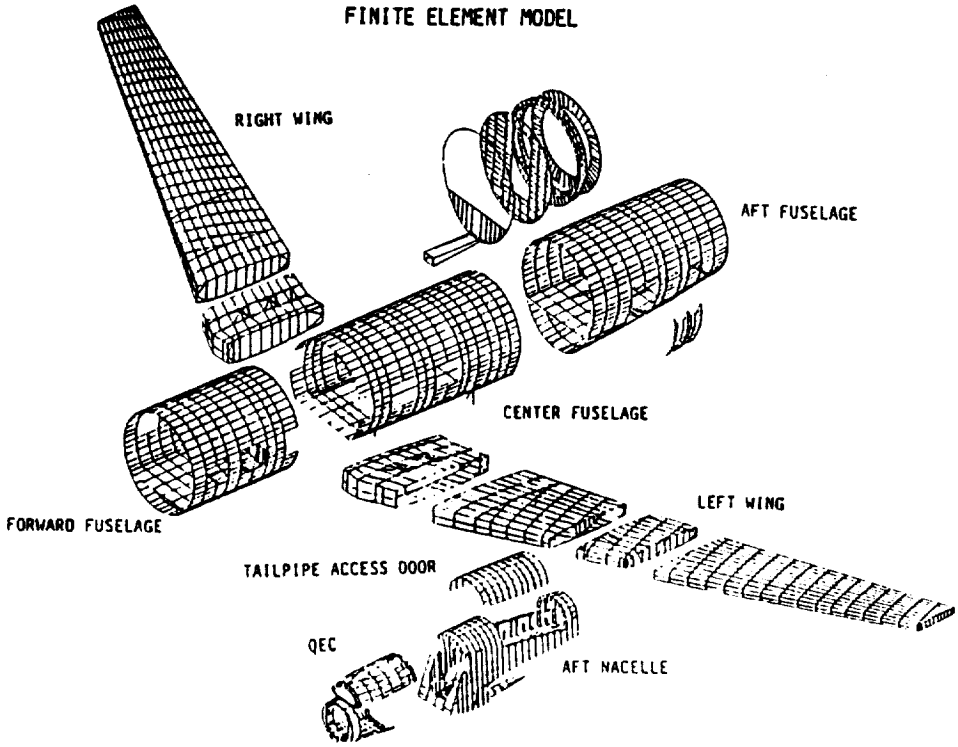


Figure 173. Finite Element Model for Structural Analysis

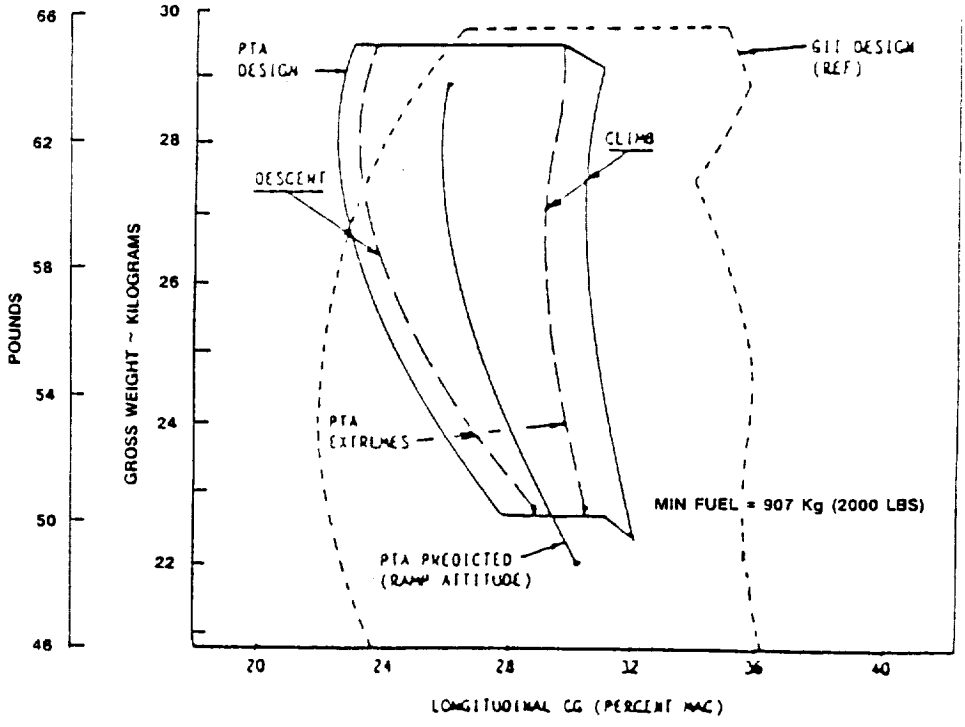


Figure 174. Weight-CG Envelope for Structural Analysis

ORIGINAL PAGE IS
OF POOR QUALITY

In addition to the aerodynamic panels, 344 grid points were used for distributing weight data, and 98 grid points were used for defining the flexibility matrix (122 elastic degrees of freedom for static deformations). The final matrix of external loads for each structural analysis condition consisted of 1573 nodes and 4755 degrees of freedom; this matrix was derived by expanding (spreading) the 484 node, 1227 degrees of freedom loads solution matrix to achieve compatibility with the internal loads analysis matrix.

Dynamic loading conditions were examined by using the first 30 complete airplane coupled modes. The solution accounted for the phasing of the external forces and the resulting structural deflections. Time varying lift build-up was accounted for by the Wagner and Kussner lift growth functions. Landing and taxi condition loads were obtained by mathematically representing the landing gear strut and tire characteristics as an energy absorbing and dissipating system acting between the ground and the airframe; mathematical model verification was by comparison with GII landing gear drop test results.

As with any airframe design/modification program, weight increases and decreases were monitored carefully. The maximum GII ramp gross weight of 30,000 kg (66,000 lb) with full external fuel formed the upper limit on gross weight. Likewise, the GII design landing gross weight of 26,590 kg (58,500 lb) was retained. During the design process the amount of static balance boom weight needed for lateral airplane balance continually increased. However, additional right wing reinforcing would have been required for boom weights exceeding 950 kg (2,100 lb), so as an alternative, a slight lateral static unbalance was accepted and the boom weight was restricted. The maximum allowable gross weight was reduced by 227 kg (500 lb) as an additional safeguard. As predicted from wind tunnel tests, the static lateral unbalance was counteracted by nacelle lift through most of the PTA flight spectrum and was not a significant problem.

The airplane center of gravity limits used for structural analysis are shown in Figure 174 as a function of gross weight. The extremes are produced by the fuel shifts associated with airplane attitude changes. Allowances were made for variations in equipment installations. The GII design envelope is shown for comparative purposes. Although the PTA forward limit was forward of the GII design limit at heavy gross weights, a forward shift of the stability neutral point for the PTA configuration kept the static stability margin within the GII design values. Hence, the more forward PTA center of gravity limits did not dictate any additional structural modifications.

Airspeed limits for structural design are illustrated in Figure 175. The cruising speed, V_C, was compatible with required PTA operations. The design dive speed, V_D, was derived in accordance with CAR-4b. These speeds were less than the corresponding maximum speeds of the unmodified GII. No value was selected for the speed for maximum gust intensity, and the GII flap limit speed was unchanged.

Two-dimensional envelopes of predicted external loads were used for selecting load conditions requiring detailed stress analysis. Component

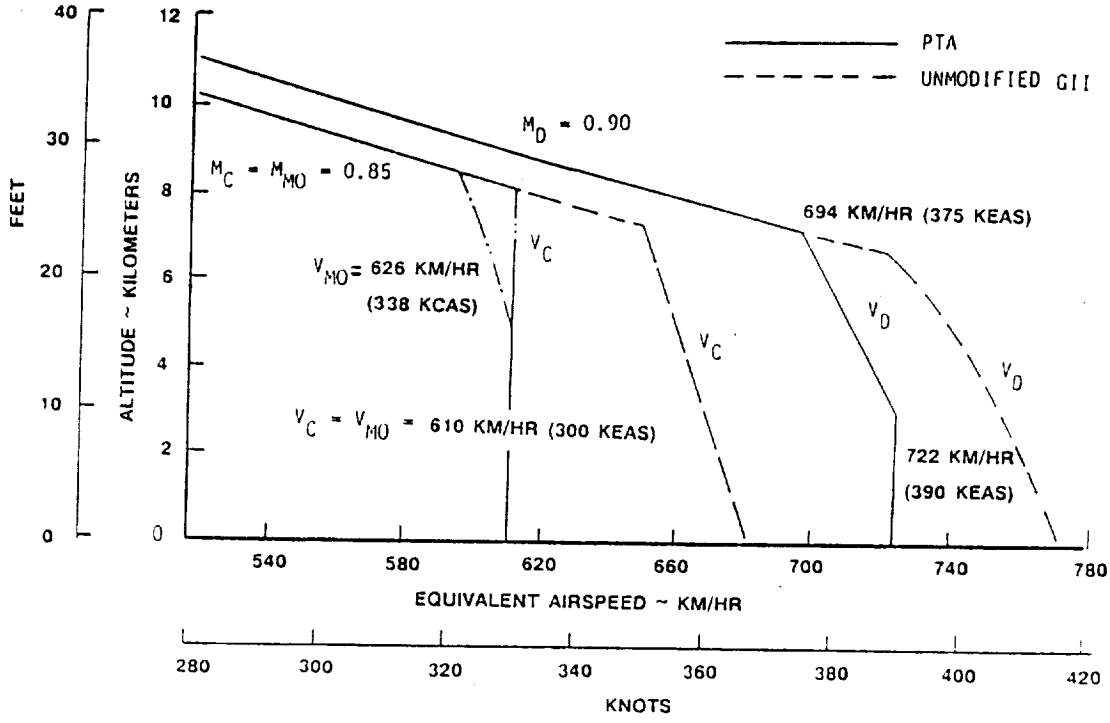


Figure 175. Maximum Airspeeds for Structural Design

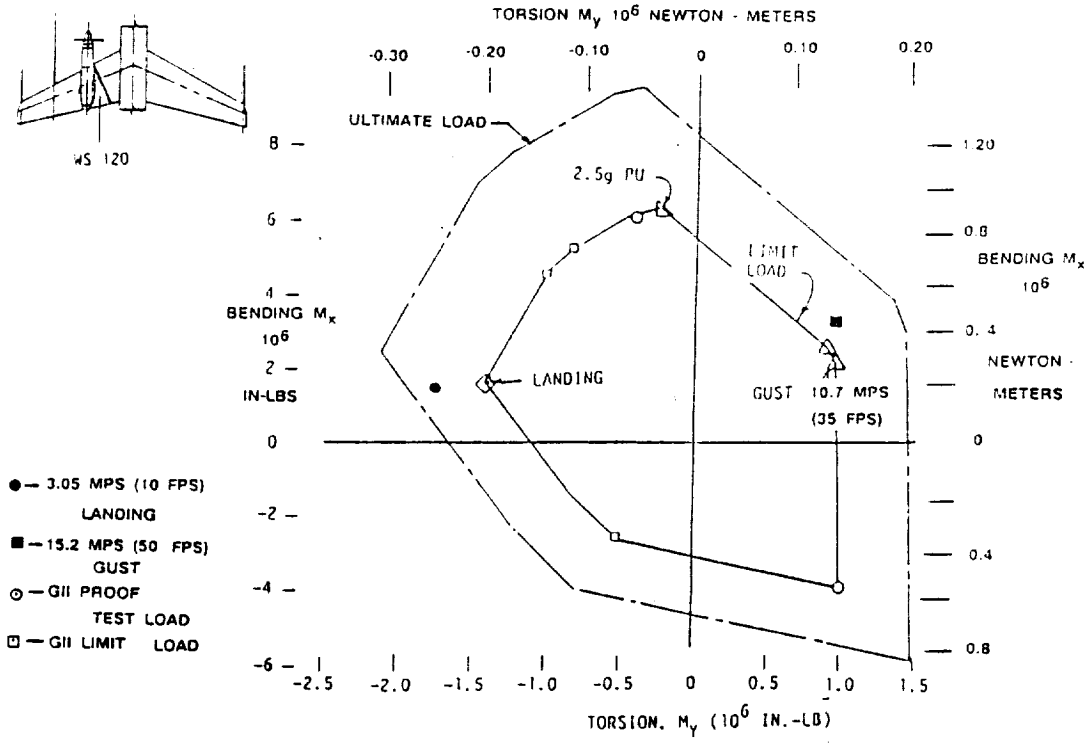


Figure 176. Wing Load Envelope - WS 120 Left

strength received primary emphasis; except for sonic fatigue, airframe durability analyses were unnecessary because of the testbed design limits of 1000 flights and 3000 flight hours.

5.5.1.2 Wing Strength

Loads on the left wing just inboard of the propfan nacelle are summarized by the bending moment versus torsion envelopes in Figure 176. Positive M_X is up-bending, and positive torsion, M_Y, tends to twist the leading edge up. The inner envelope is a composite of both PTA maximum limit loads and the GII design limit loads. The ultimate load envelope was 1.5 times the limit load envelope; the structure was required to withstand ultimate loads without failure. The maximum up-bending at this location occurred for a smooth 2.5g pull-up maneuver with propfan not operating. Maneuver load factor was reduced from 2.5 to 2.0 for propfan operating conditions because the tilt feature of the propfan nacelle allowed attainment of desired propfan inflows without extensive maneuvering; this minimized the effect of the propfan on the aerodynamic loading.

The envelope landing condition loads shown in Figure 176 are for a landing rate of sink equal to 2.3 mps (7.5 fps) at design landing gross weight rather than the CAR-4b specified value of 3.05 mps (10 fps). The loads for this higher rate of sink are also shown in the figure. According to GII design data, the maximum rate of sink expected statistically for civil transports in 1000 landings is 1.7 mps (5.5 fps). Thus the reduction to 2.3 mps (7.5 fps) posed no operational difficulty for the test program.

Also shown on the PTA envelope are the loads associated with turbulence. The unmodified GII wing structure was gust critical. The dynamic analysis approach used for GII design was also used for the PTA with the following exception: reduction factors which were applied to the GII dynamic response loads were not appropriate for use on the PTA. These factors were derived with continuous turbulence methodology for the GII design mission profiles.

For the PTA analysis, a less severe gust environment was assumed. Loads were determined analytically on the basis of one-minus-cosine shaped profiles of vertical gust velocity. For structural design, CAR-4b requires the maximum gust intensity at the design cruise speed to be 15.2 mps (50 fps), but this was reduced to 10.7 mps (35 fps) for PTA design.

When an evaluation of the effect of this change on PTA operations was made using continuous turbulence gust environment data, a restriction prohibiting flight in or near severe weather resulted. This 30-percent reduction in analytical gust severity, however, minimized structural reinforcement, and the weather restriction did not interfere with attainment of the program objectives.

Design load envelopes for the region outboard of the propfan nacelle are shown in Figure 177. PTA pull-up and push-down maneuvering conditions together with the GII loads formed the envelope. The CAR-4b 15.2 mps (50 fps) gust condition loads are shown for reference.

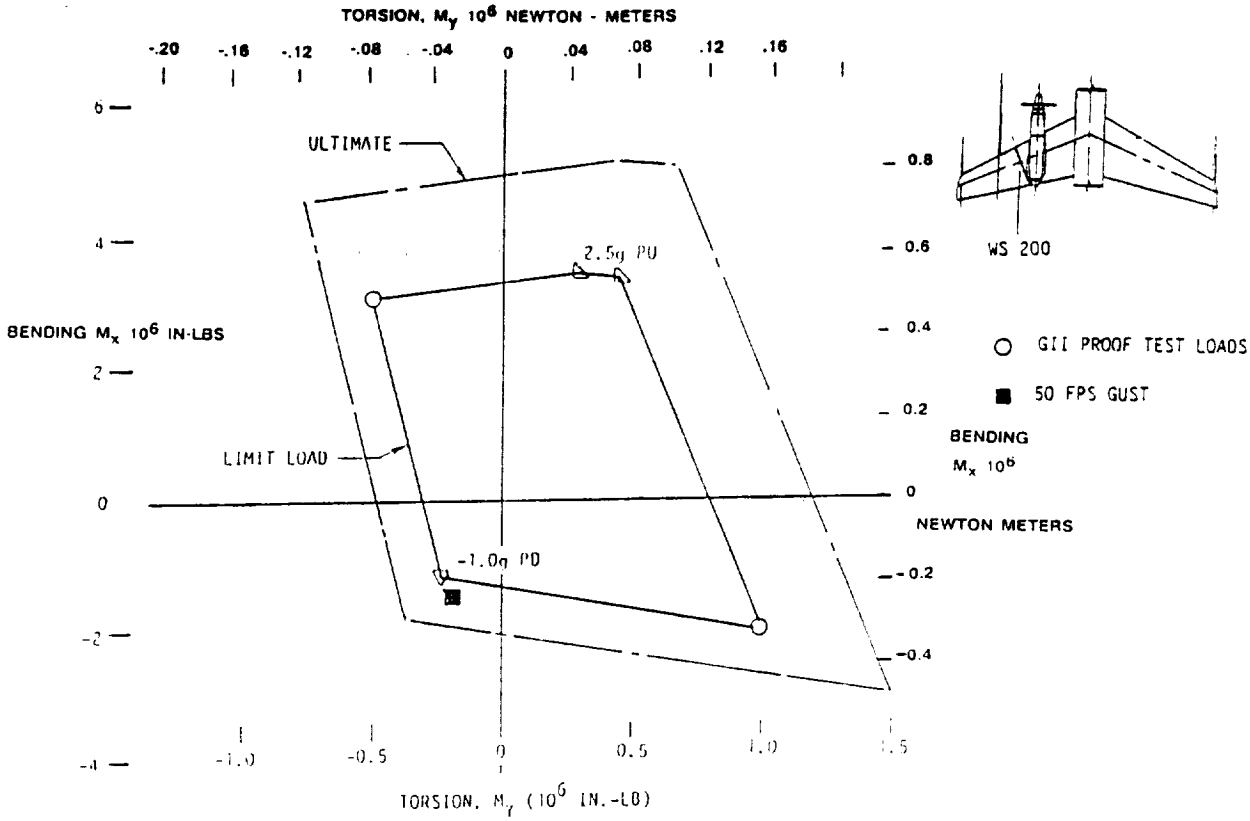


Figure 177. Wing Load Envelope - WS 200 Left

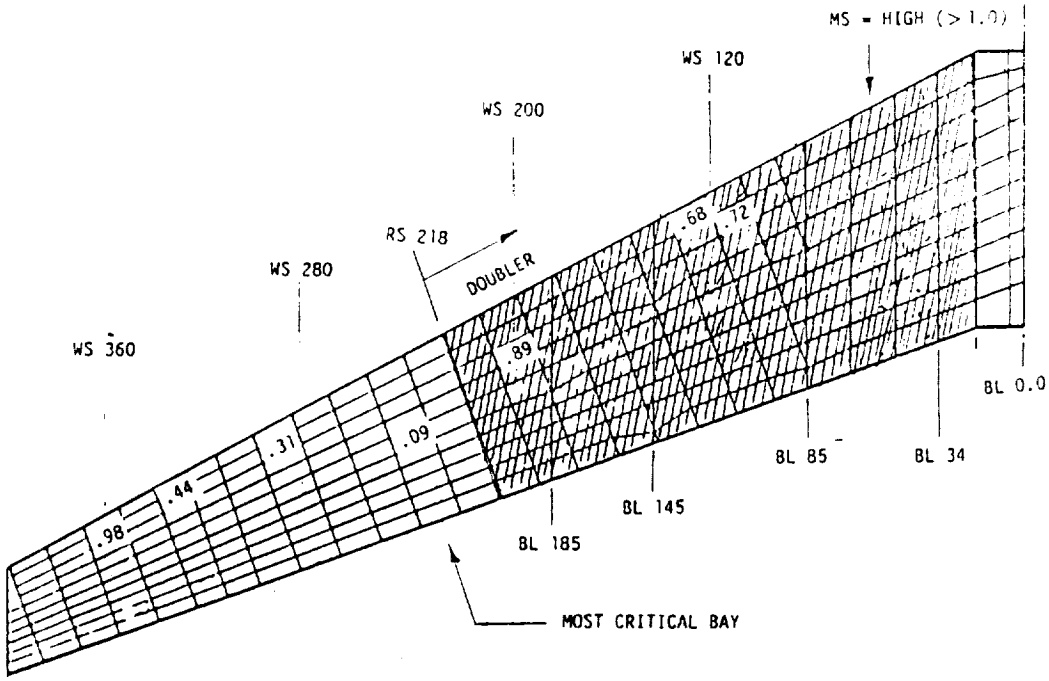


Figure 178. Margins of Safety - Left Wing Upper Cover

ORIGINAL PAGE IS
OF POOR QUALITY

Margins of safety for the left wing upper and lower covers are shown in Figures 178 and 179, respectively. The left wing upper and lower surface doublers were installed primarily to provide additional torsional stiffness necessary for flutter prevention. Secondarily, they provided strength margins of safety which were more than adequate.

Shear web doublers were installed on portions of the front and rear beam to react the interface loads from the propfan aft nacelle. The addition of these doublers furnished another degree of fail-safety, increased the web stability, and smoothed the stress discontinuities which would otherwise have occurred in the original web. The doublers increased web thicknesses by more than a factor of two; thus, the margins of safety were generally high.

The rib at Butt Line 145 was reinforced locally because of the loads introduced into the wing box by the aft nacelle structure. The installation of the new rib at Butt Line 185 provided an orderly transfer of nacelle load to the wing structure. Its design, being fashioned after the primary rib at Butt Line 145, resulted in high safety margins.

The acoustic (microphone) boom was lightweight, and its aerodynamic loading was minimal. The boom was designed structurally by the stiffness considerations required to provide a stable environment for acoustic microphones and by the need to avoid adverse coupling with wing modes. In order to evaluate the strength of the boom and its installation, an arbitrary 2g load of 182 kg (400 lb) was assumed to act at the forward tip of the boom. For this loading the most critical region was the forward 15 percent of the boom where the outer extremity was critical in bending compression with a margin of safety calculated to be 0.28. Even though this was new structure, this was deemed acceptable because of the arbitrary loading used and the boom's acceptable stiffness characteristics.

The wing tip dynamic boom installation is depicted in Figure 180. Attachment to the wing was through the GII wing tip fuel tank fittings. Inasmuch as the weight of the boom and its corresponding interface loads were so much less than those of the GII tip tank, only the boom itself required examination. Design was based on 10 g's acting downward at the boom center of gravity, and because the casing material was steel, margins were very high.

No other structural modifications were required for the left wing from a strength standpoint. However, to provide sonic fatigue protection for the flaps and the fixed trailing edge, new skins, stiffeners, and flap ribs were added. To avoid reinforcing the GII flaps and supporting structure to withstand propeller slipstream loads, propfan testing was restricted to flaps-up operations.

The static balance boom was installed beneath the right wing tip as shown in Figure 181. Modification design loads are shown in Figure 182 along with those which would be required to satisfy CAR-4b loading requirements. Positive shear is up. The GII tip tank forward and aft attachment fittings were changed from aluminum to steel to ensure safe-life margins in the absence of multiple load paths. Examination of the margins of safety

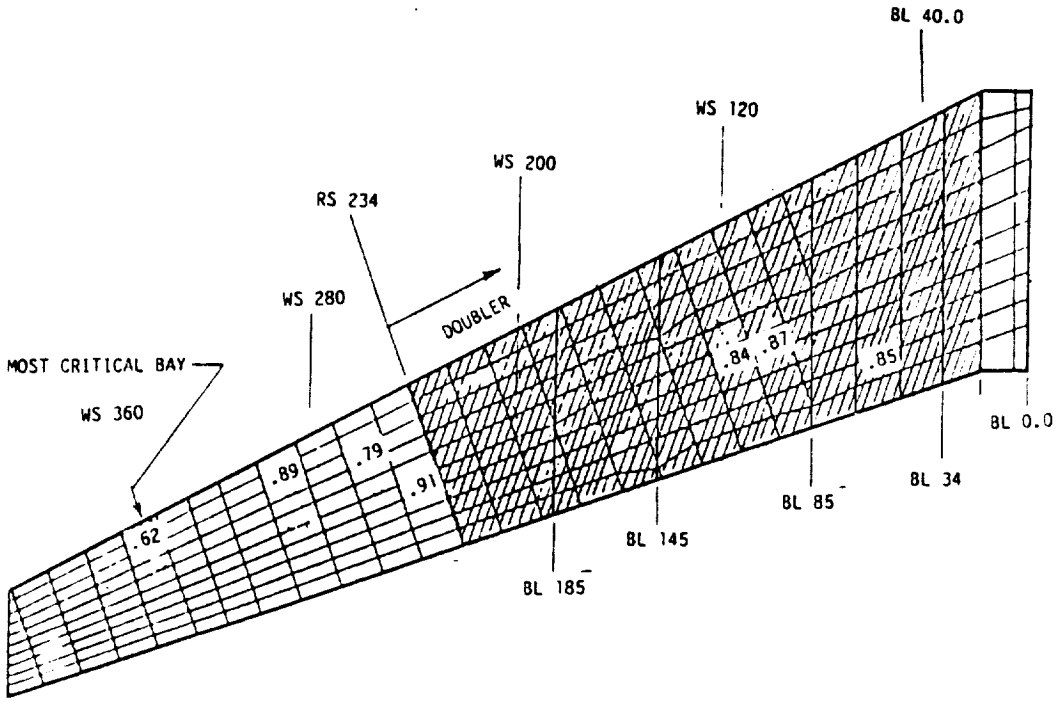


Figure 179. Margins of Safety - Left Wing Lower Cover

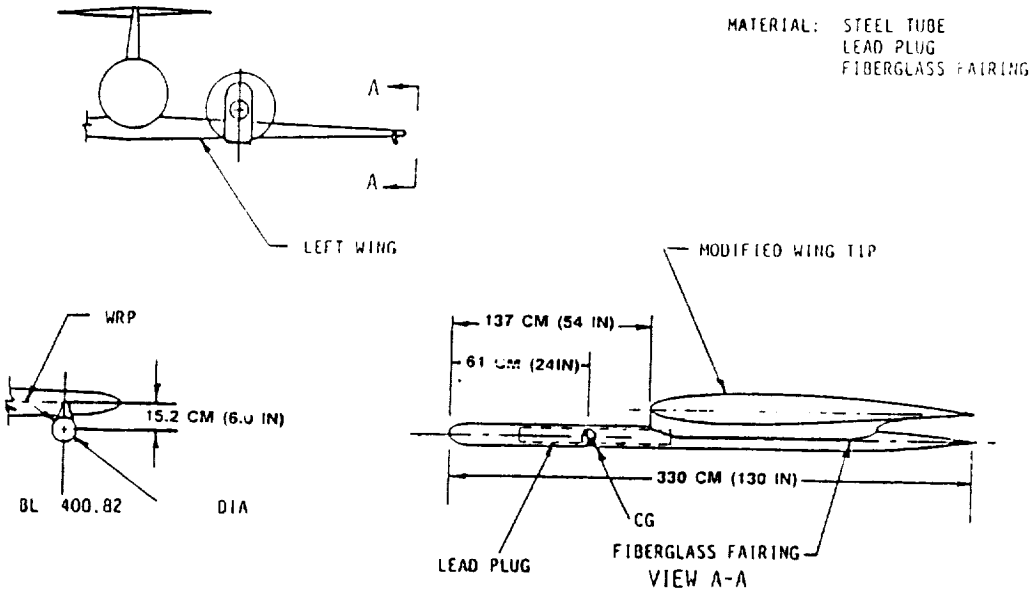


Figure 180. Dynamic Balance Boom

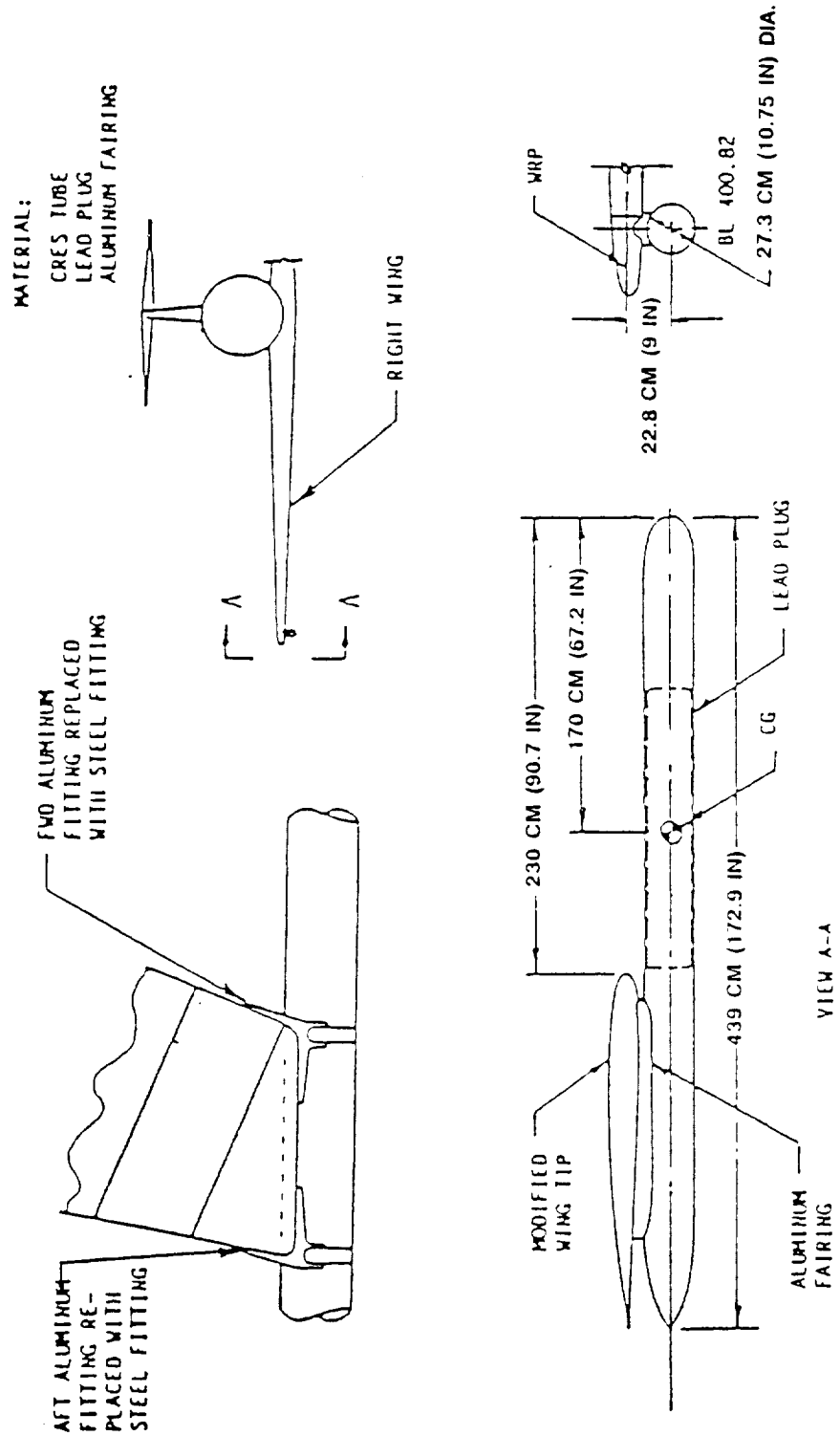


Figure 181. Static Balance Boom

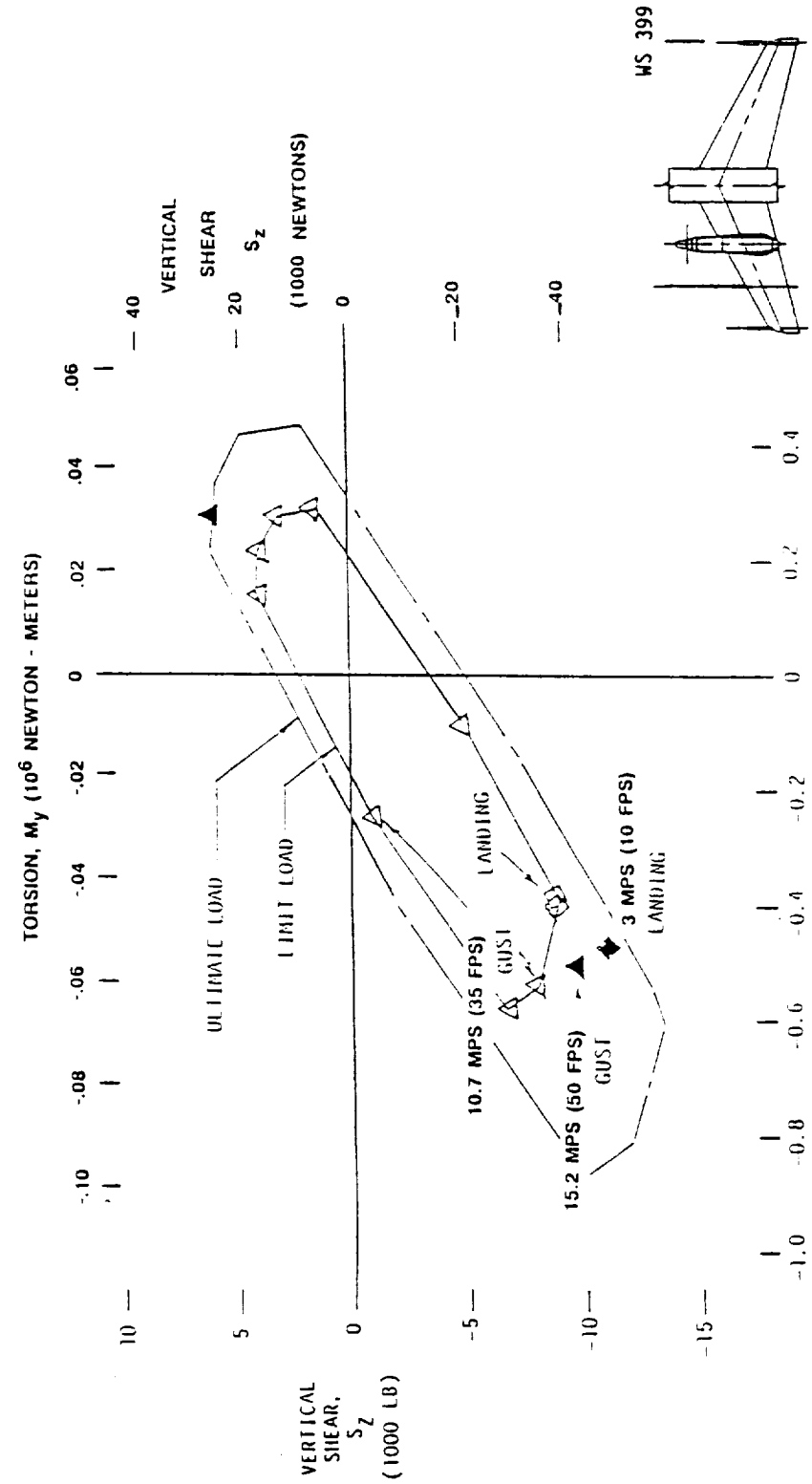


Figure 182. Wing Load Envelope - WS 399 Right

calculated for the structure associated with the boom showed that the minimum value was 0.34. The most critical component was the torque fitting on the inboard side of the attachment rib.

The outer span of the right wing was affected by the inertial loadings of the wing tip boom. This is demonstrated in Figure 183 by the types of conditions which define the load envelope for Wing Station 280. Margins of safety are shown for the upper and lower covers, including the doublers, in Figures 184 and 185, respectively. It was the analysis of the taxi condition which led to the necessity of reducing the static balance boom weight.

The right wing tip boom weight required for lateral balance of the aircraft after other modifications was almost 1320 kg (2900 lb). Analysis of taxi loads showed, however, that additional strengthening of the right wing would be required for this boom weight and the dynamic load criteria used for GII design. As an alternative, it was decided:

- To reduce boom weight to 954 kg (2100 lb) and tolerate the static imbalance
- To moderate the dynamic load criteria of the GII to more practical levels for the PTA aircraft
- To reduce aircraft gross weight by 340 kg (750 lb) (about 113 kg (250 lb) below the allowable)

As stated previously, the static imbalance was not an operational problem. As a verification of the adequacy of the wing structure for taxiing with these changes, five discrete roughness profiles were generated randomly, each having a power spectral density matching the most severe level described by military design specifications for paved airfields. Wing response time histories for these profiles showed that peak wing loads never exceeded 70 percent of the GII design limit values.

5.5.1.3 Empennage Strength

The empennage evaluation included the horizontal tail, the vertical fin, and the pivot point/pitch trim actuator area. The elevator and rudder surfaces were omitted from the strength analysis because the PTA airspeeds were less than the GII limit airspeeds, and the changes in aerodynamic loading on these surfaces due to PTA modifications were insignificant.

PTA horizontal tail maximum loads were less than the GII design limit loads. These loads are shown relative to the GII loads in Figure 186. Because of the lateral offset of the airplane center of gravity, the skewing of the airplane principal axes and the effects of the propfan on the distribution of airloads, the side-to-side distribution factors required by CAR-4b were not used. Rather, the derived aerodynamic data, along with the computed maneuver and gust response parameters, were used with no other arbitrary factors applied. The aforementioned tailoring of the

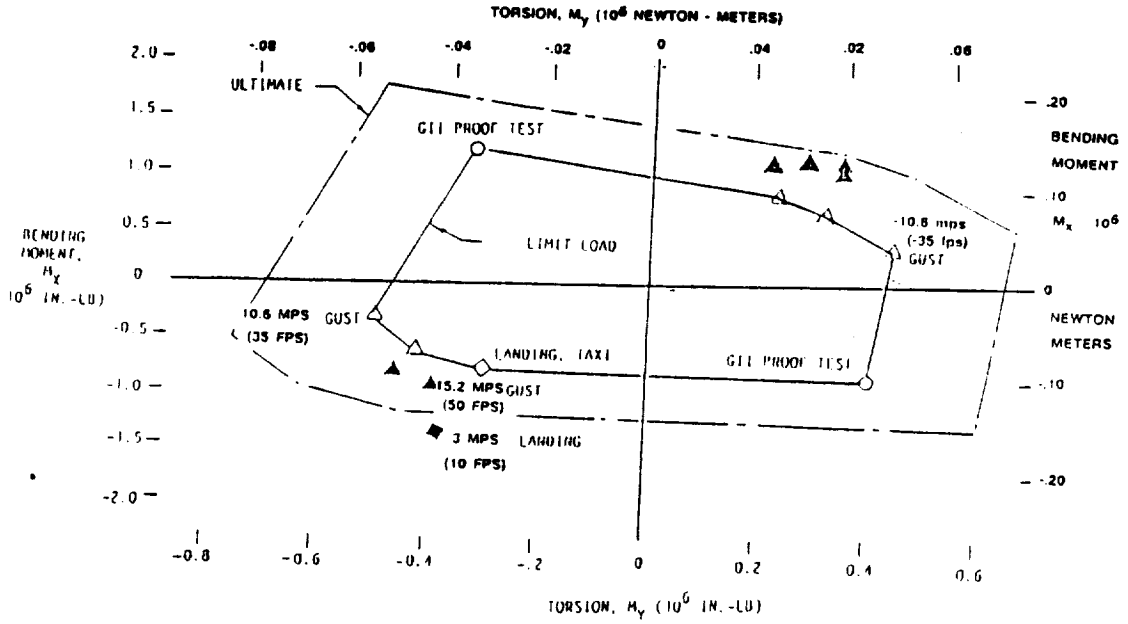


Figure 183. Wing Load Envelope - WS 280 Right

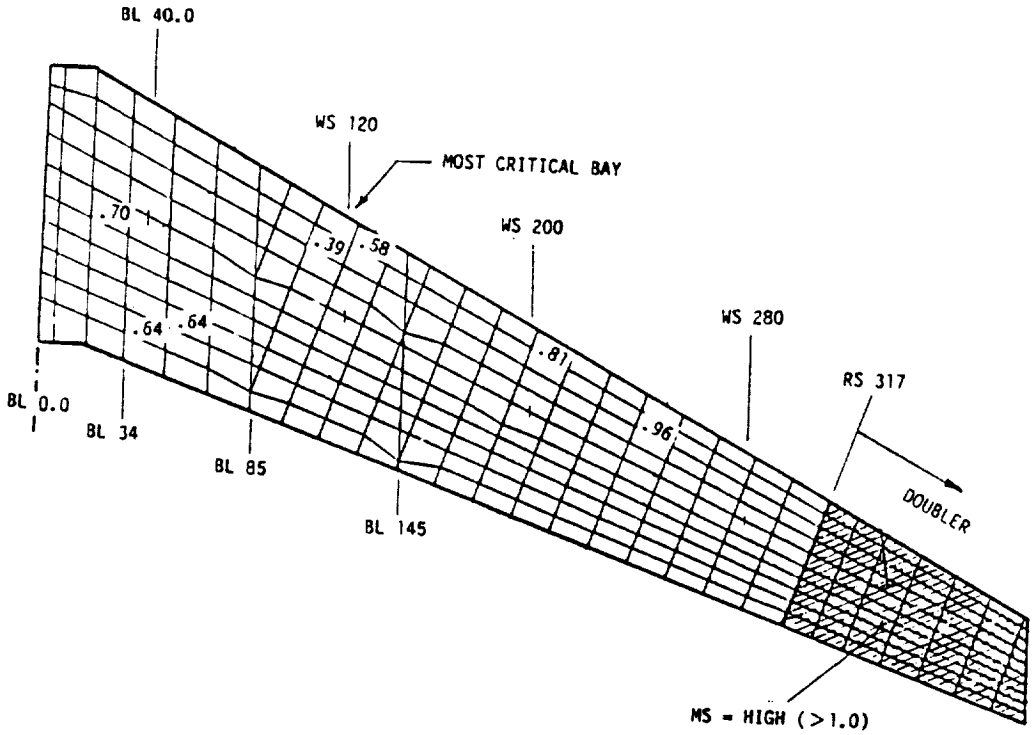


Figure 184. Margins of Safety - Right Wing Upper Cover

ORIGINAL PAGE IS
OF POOR QUALITY

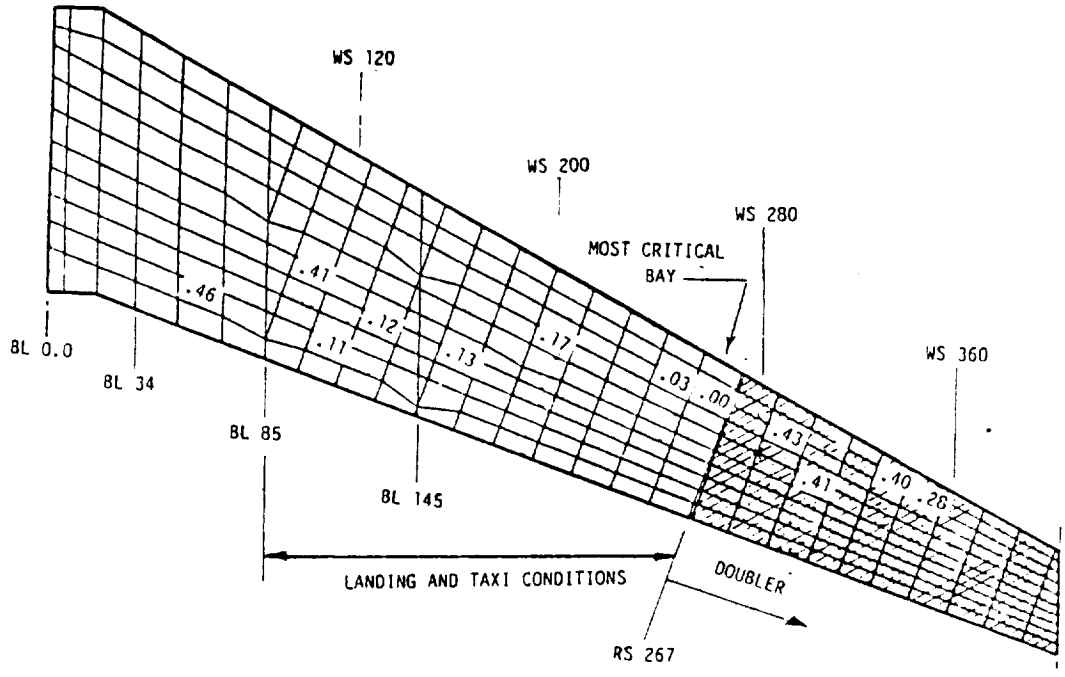


Figure 185. Margins of Safety - Right Wing Lower Cover

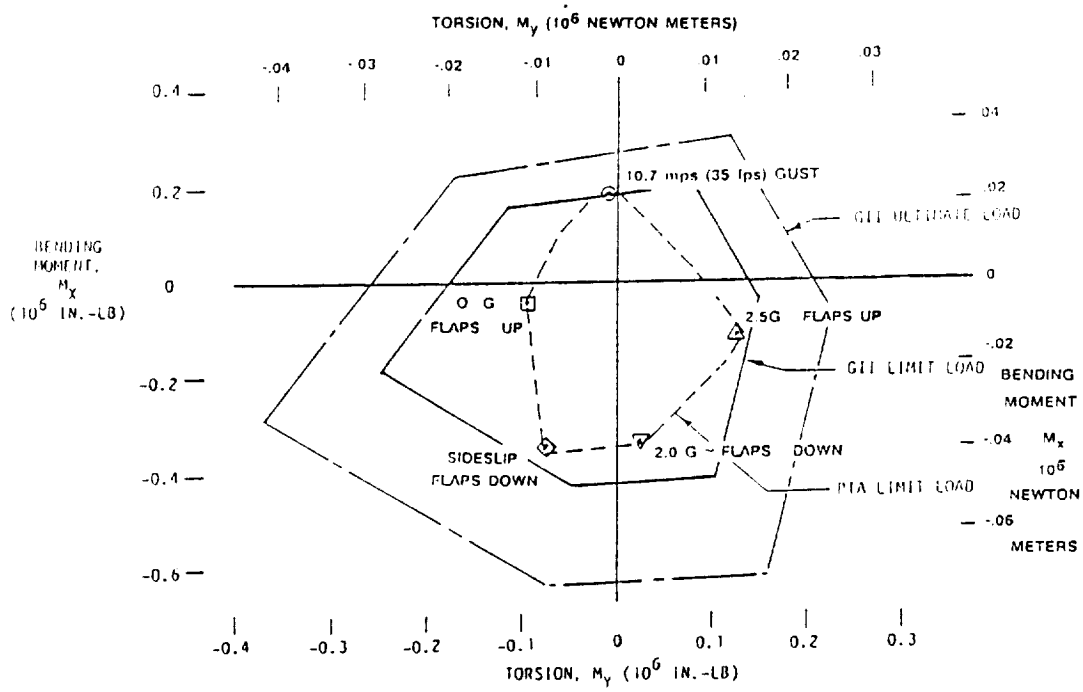


Figure 186. Horizontal Tail Load Envelope - BL 32

maneuver and gust loading requirements assured that no changes to the horizontal tail structure were necessary.

Figure 187 summarizes the vertical tail evaluation. The side load on the vertical tail necessary for trimming out the yawing moment inherent to the asymmetry of the configuration added directly to the vertical tail loading produced by maneuvering or caused by turbulence; this was especially significant during propfan operation. The 15.2 mps (50 fps) lateral gust, with propfan operating, produced loads which exceeded GII design limit loads, so a 30-percent reduction in gust velocity was required in order to stay within the limit load capability. Also, during propfan operation, rudder maneuvering conditions had to be limited to nonabrupt rudder inputs. Capability did exist, however, for classical steady sideslips and abrupt control applications immediately following the sudden failure of an engine. The loads calculated for maneuvering and engine failure conditions were based on time history response parameters from a solution of the aircraft equations of motion in six degrees of freedom.

Horizontal tail loads were transferred to the vertical tail through the pitch-trim actuator, two pivot lugs (one left and one right), and two rubbing pads which, along with the lugs, reacted side loads. The loads for these members were determined for PTA conditions from the horizontal tail net loads acting at the tip of the vertical tail. Maximum PTA loads were computed to be approximately 90 percent of the GII design limit loads.

5.5.1.4 Fuselage Strength

To evaluate the effects of the modified wing loads on the center fuselage, a center fuselage module was included in the finite element analysis. This is illustrated in Figure 173. Forward and aft fuselage stiffness modeling was also included for the purpose of providing the proper boundary considerations for the center section analysis.

The fuselage was evaluated for the external loads calculated for the conditions examined for the wing and empennage. Emphasis was placed on determining local loadings for fuselage structure most affected by the propfan installation, or specifically, the wing/fuselage interface. Evaluations were made by comparing PTA loads to GII design limit loads: internal loads for the interface areas and external loads for all others. Interface items were:

- The wing-to-fuselage drag shear web (BL 34.0) and the fuselage bending continuity links (BL 6.0)
- The front spar wing-to-fuselage attachment at FS 345.875
- The aft spar wing-to-fuselage attachment at FS 452.5
- The floor-to-wing pressure posts (20 places)

The internal loads for the drag shear web and links are summarized in Figure 188. Web shear flows were found to be within the capability of the

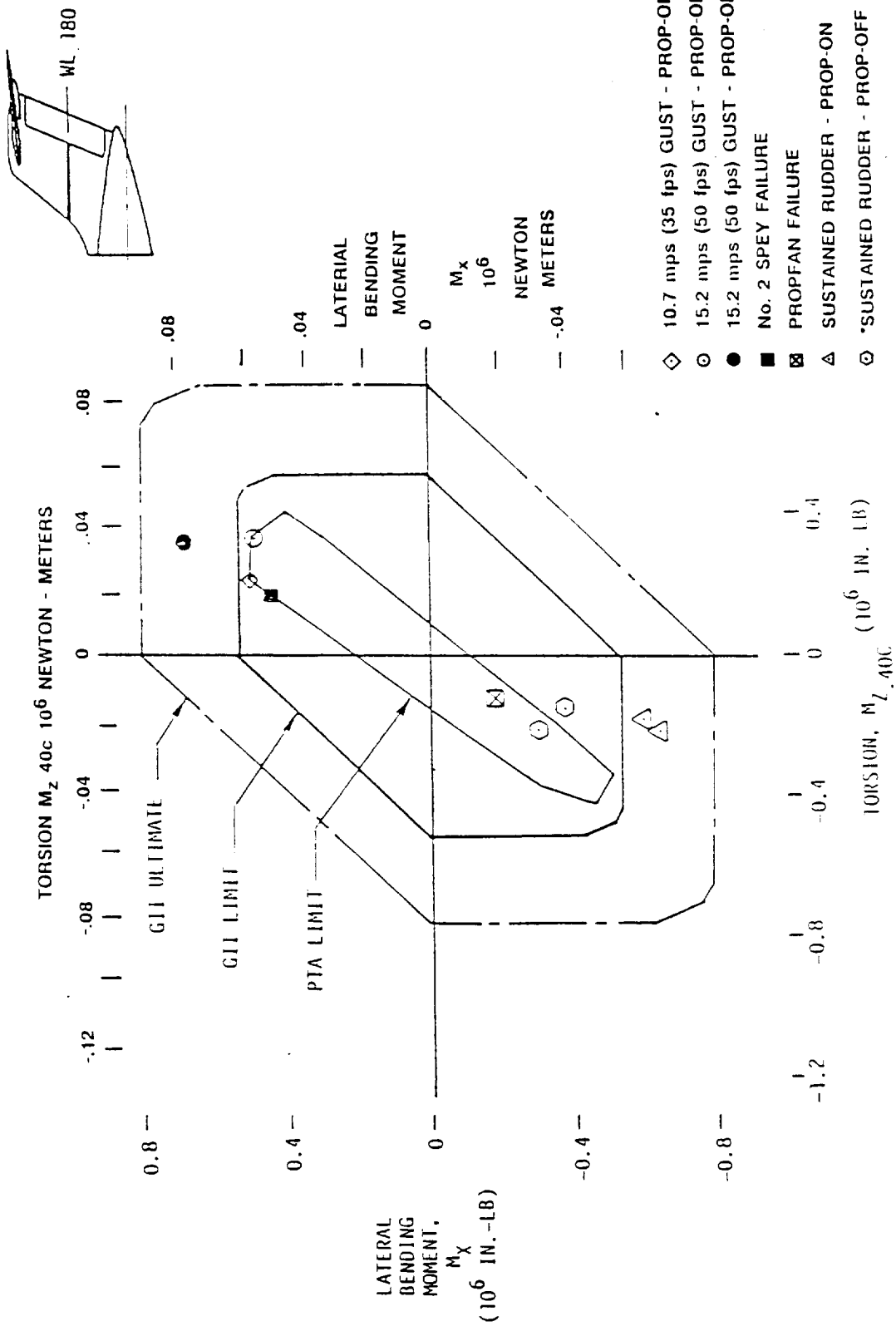


Figure 187. Vertical Tail Load Envelope - WL 180.

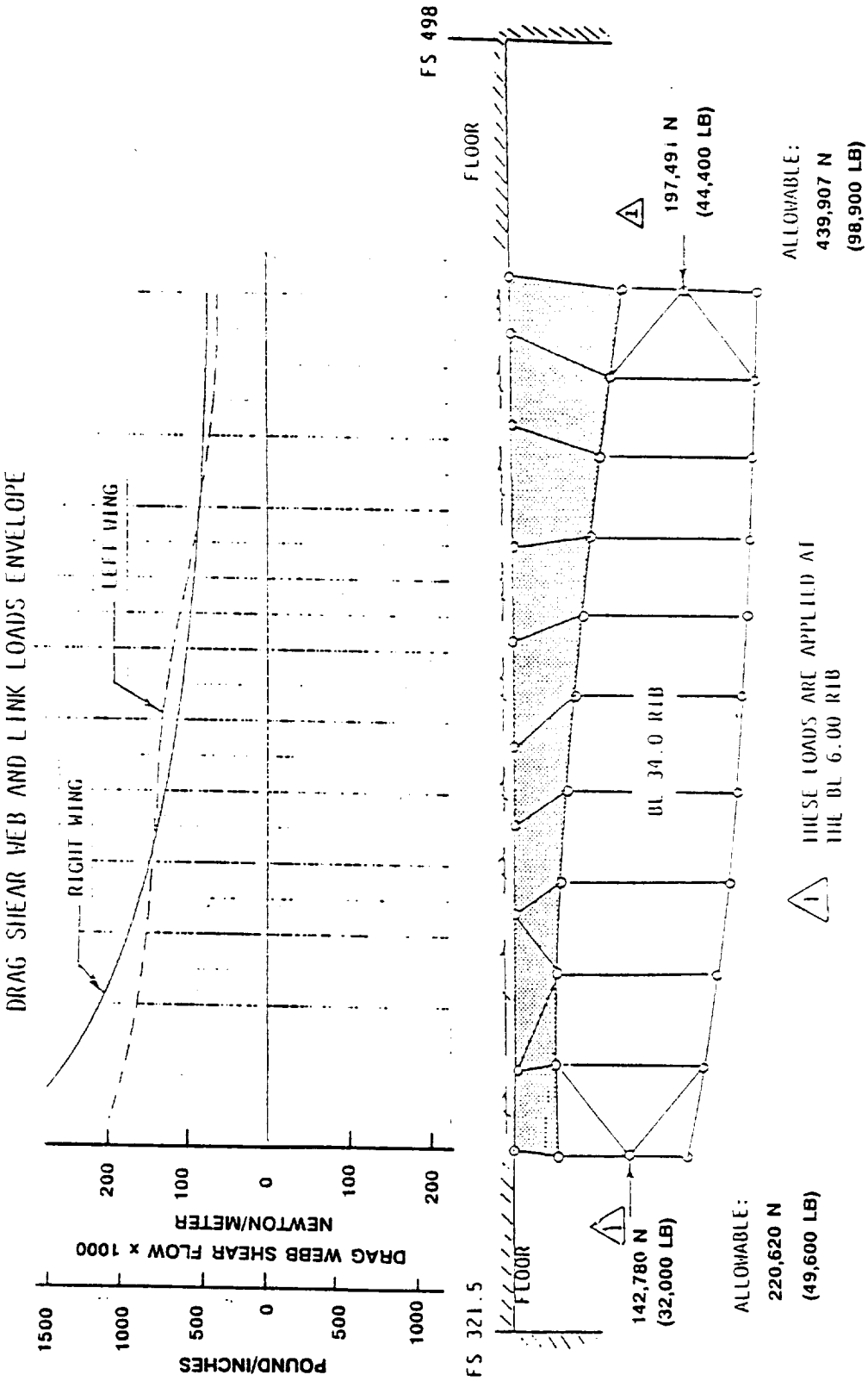


Figure 188. Drag Shear Web and Link Loads Envelope

GII web; however, web-to-wing attachment fasteners were changed to allow for rework provisions. The maximum loads in fuselage/wing links at Butt Line 6.0, which maintain bending continuity of the fuselage across the wing intersection and wheel well, were well within allowable values.

The front spar wing-to-fuselage attachment loads are shown in Figure 189. The PTA loads were within the corresponding GII loads with the exception of Case 2122; however, analysis of this case using a fitting factor of 1.15 showed the margin of safety to be 1.22. The loads acting at the similar attachment at the aft spar were less than the GII loads.

The floor-to-wing pressure posts transmitted loads from the floor to the hard points on the wing upper surface at BL 6.0, BL 19.9, and BL 30.5. These were designed by cabin pressure, which was unchanged for the PTA configuration; therefore, additional analysis was unnecessary.

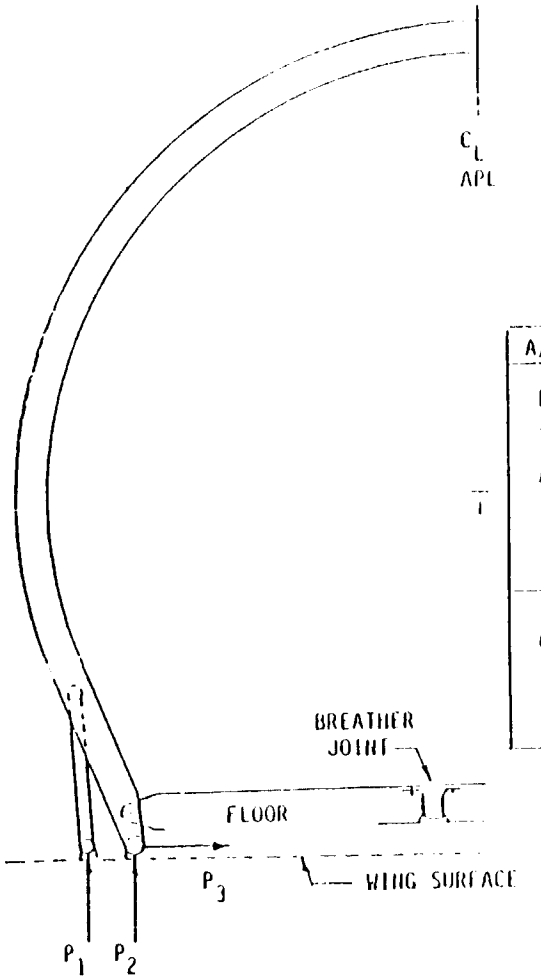
The structural design analysis of the forward section of the GII fuselage determined that the highest forebody loads occurred for pressurization, gust, and landing; certain ground handling conditions also affected the structure in the immediate vicinity of the nose landing gear. The relationship of the PTA loads to the design loads at Fuselage Station 288 is shown in Figure 190. The PTA loads were less than the GII design values because of the landing and turbulence limitations.

Aft of the wing rear spar, the PTA fuselage loads were less than GII design values because the empennage loads were less, the structure inertia was unchanged, and the maneuver and gust accelerations were the same or less. The load envelope comparison made in Figure 191 is typical for the aftbody.

To provide protection for the fuselage in the event of propeller blade failure or loss, a steel plate was added to the left side of the fuselage for the propfan structural integrity portion of the program. Installation is shown in Figure 192. The plate and its installation were evaluated for in-flight pressures, in-flight accelerations, and CAR-4b emergency landing accelerations. Modifications consisted mainly of reinforcing the cap sections of existing fuselage frames and adding clips and brackets to transfer loads from the plate support fittings into the fuselage frames and skin. Structurally, the intent of these particular changes was to provide strength equivalent to premodification values. Modifications necessary for sonic fatigue kept other reinforcement to a minimum. In fact, these modifications actually reduced stress values by at least 12 percent. By virtue of being steel, the plate itself was not critical, but determination of temperature effects due to material dissimilarity was necessary for fastening design.

With the exceptions of providing support for the protective steel plate and adding skin reinforcement for sonic fatigue resistance in the vicinity of the propeller plane of rotation, no strength related changes were necessary for the fuselage structure.

Bulkheads, floor sections, and support ribs affected by the installation of personnel seats, test equipment consoles, and the like, were evaluated



A/C	C O N D I T I O N	ultimate load N (lbs) ⚠1 P_1	P_2	P_3
P T A	1039 (DPG 349 .600)	57,690 (12970)		
	2009 (SPU27, 2.5 G)	-88,000 (-19780)		
	1121 (SRR 317 STEADY RL.)		43,500 (9780)	-30,400 (-6840)
	2122 (SRR 318, STEADY ROLL) t_p		-157,000 (-35260)	126,500 (28439)
G II	POSITIVE GUST	106,000 (23810)		
	2 PT. LANDING	-161,000 (-36266)		
	ABRUPT RUDDER MAN.		63,760 (14334)	-31,800 (-7160)
	CABIN PRESSURE (18.4 PSI)	-32,000 (-7200)	135,000 (-30400)	134,700 (30300)

⚠1 LOADS DUE 9.2 PSI CABIN PRESSURE INCLUDED WITH FLIGHT LOADS WHERE ADDITIVE

Figure 189. Wing-Fuselage Attachment Loads - Front Spar (FS 345.875)

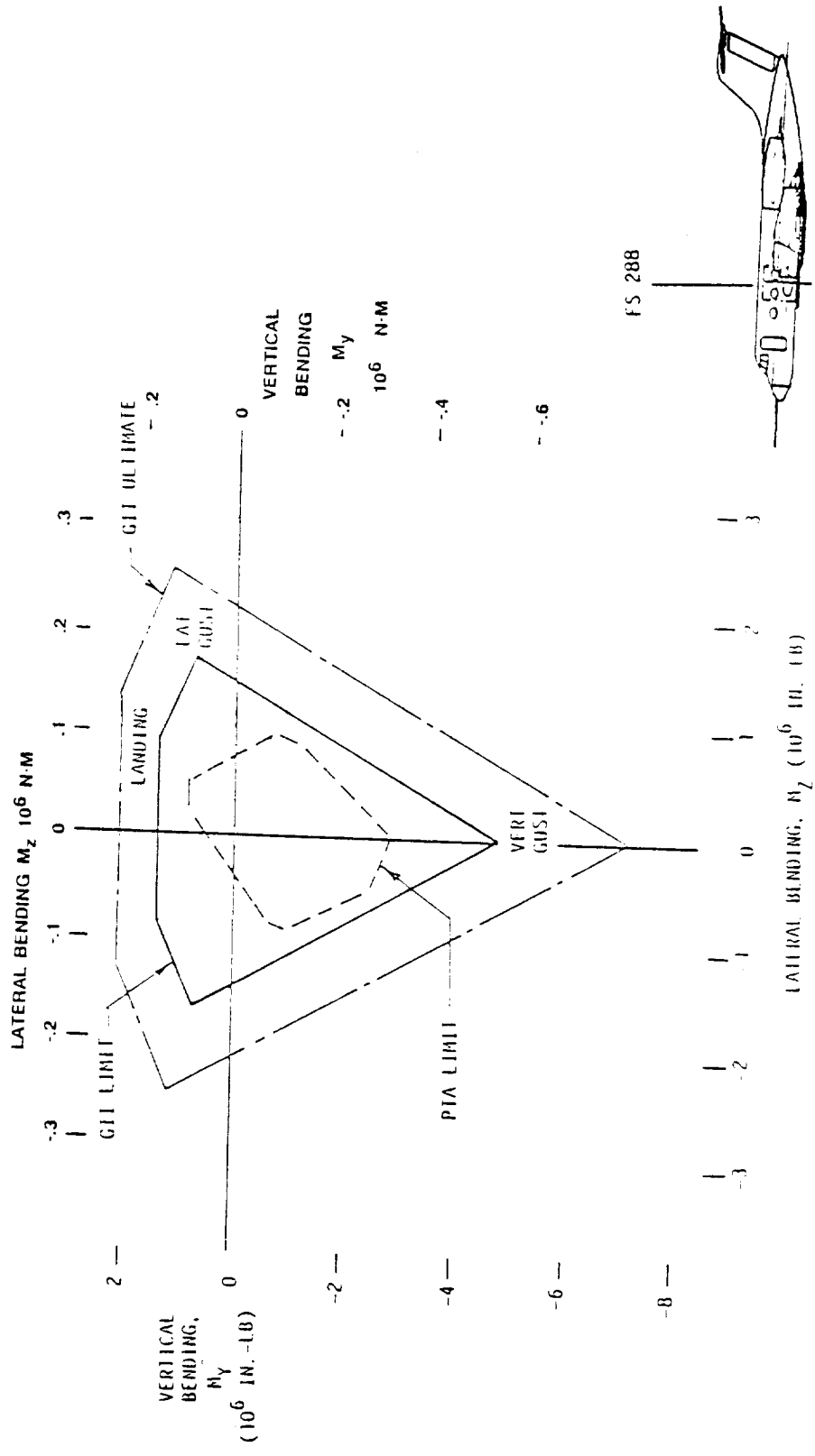


Figure 190. Forward Fuselage Load Envelope - FS 288

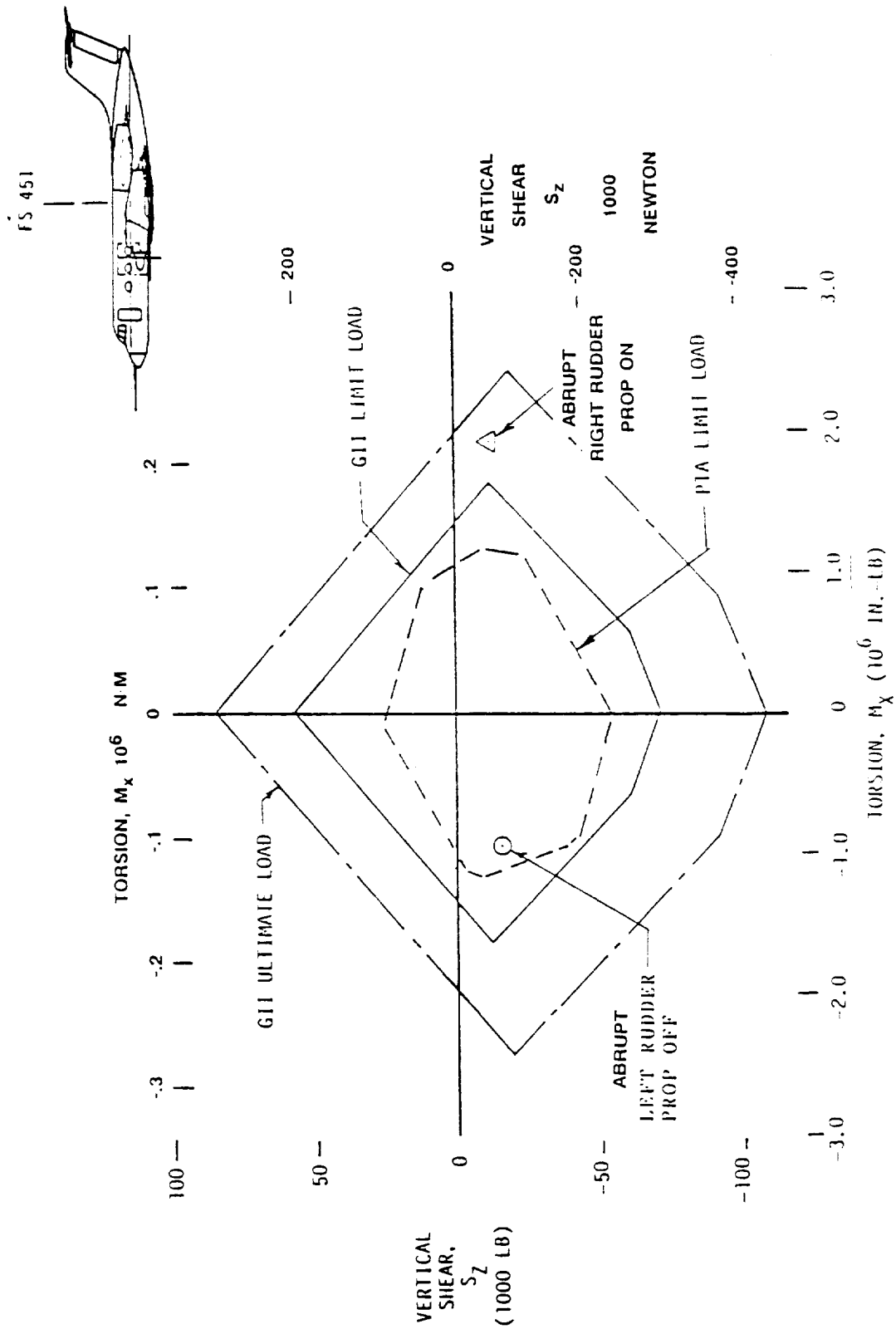


Figure 191. Aft Fuselage Load Envelope - FS 451

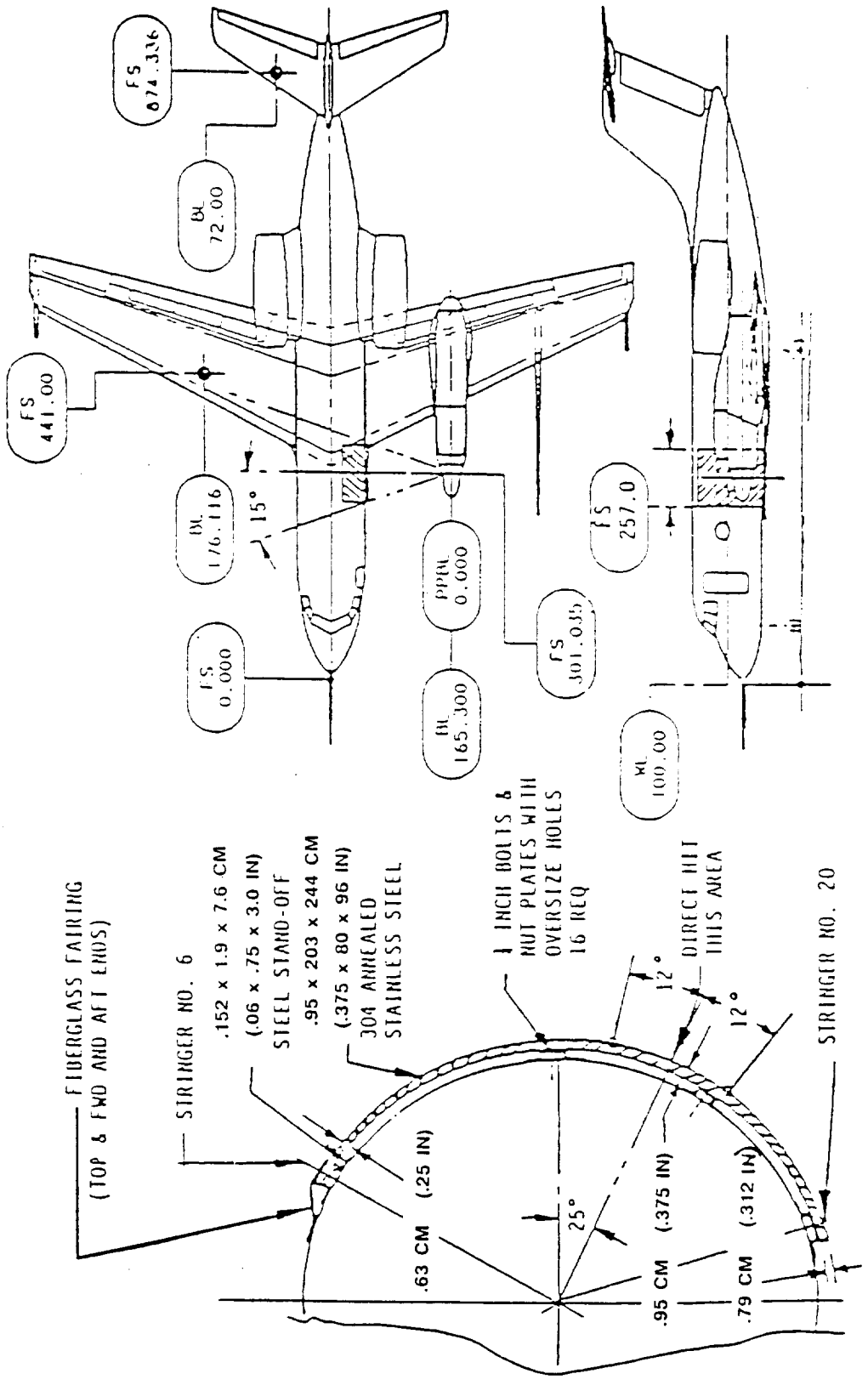


Figure 192. Fuselage Protection - Steel Plate Installation

for flight accelerations and CAR-4b emergency landing accelerations, and some local modifications were made accordingly.

5.5.1.5 Landing Gears and Landing Gear Support Structure

For a given loading condition, the loads for the main and nose landing gears and their associated back-up structure were increased by the PTA airframe modifications; however, the differences between the modified airframe loads and the GII design loads were not of sufficient magnitude to warrant structural changes. The lateral offset of the aircraft center of gravity slightly increased the left main gear static reactions. Aside from landing impact loads, which were reduced substantially by the sink rate restriction, the critical conditions were jacking, braking, and turning.

The GII design limit load for jacking was determined by multiplying the landing gear static reaction at the established jacking gross weight, 28,636 kg (63,000 lb), by an arbitrary jacking factor, 1.33. At a PTA jacking weight of 29,200 kg (64,200 lb) (maximum gross weight less crew), the main gear allowable jacking load was exceeded by 2 percent. The arbitrary jacking factor was reduced to 1.30 to avoid exceeding the allowable jacking load. Alternately, the allowable weight could have been reduced to 28,400 kg (62,500 lb).

In a similar fashion, braking and turning design loads incorporated static reaction factors in terms of braking coefficient and lateral accelerations, respectively. Prudent taxiing procedures, such as minimizing ground speed on taxiways, were sufficient for dispositioning the otherwise slight increase in these loads.

5.5.1.6 Flutter Analysis

The overall program used to verify freedom of the airframe from classical and whirl flutter is diagrammed in Figure 193. The analytical methods were validated by successfully predicting the flutter boundaries of a 1/9-scale flutter model of the PTA configuration. These tests are described in Section 4.2 of this report. Airframe dynamic characteristics were confirmed with ground vibration tests as described in Section 8 of this report.

The flutter analysis used the same analytical model that was used for determining modal characteristics in the dynamic loading studies. Development of the model began with the basic GII airframe, and adjustments were made so that predicted vibration modes agreed with ground vibration test results. The model was then adapted to the propfan configuration. The propfan nacelle flexibilities were calculated from a finite element model and coupled to the airplane by modal synthesis. Unsteady aerodynamic forces on the wing, aileron, and empennage were calculated by the doublet lattice method. Propfan aerodynamic forces were calculated from quasi-steady derivatives developed by Hamilton Standard.

Initial analyses identified a flutter instability caused by classical wing bending and torsion coupling. This instability was sensitive to the

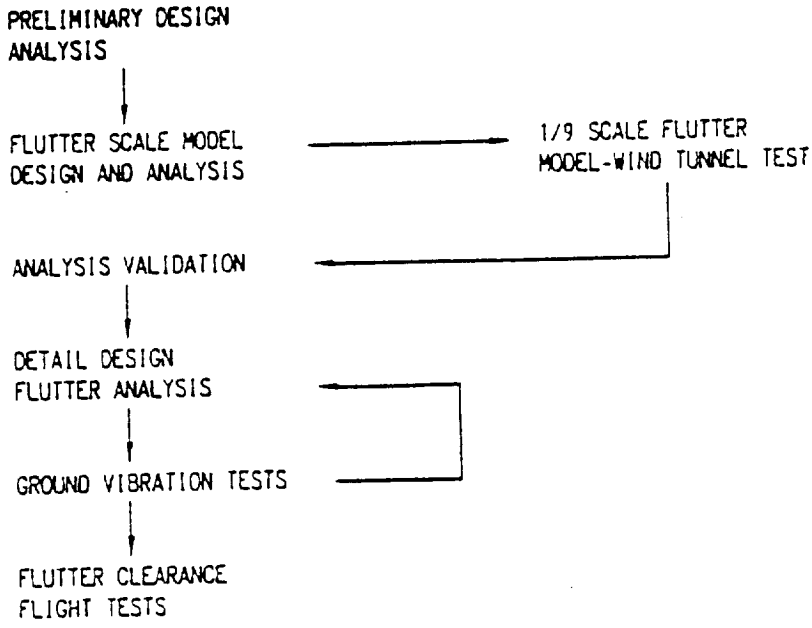


Figure 193. Flutter Clearance Program

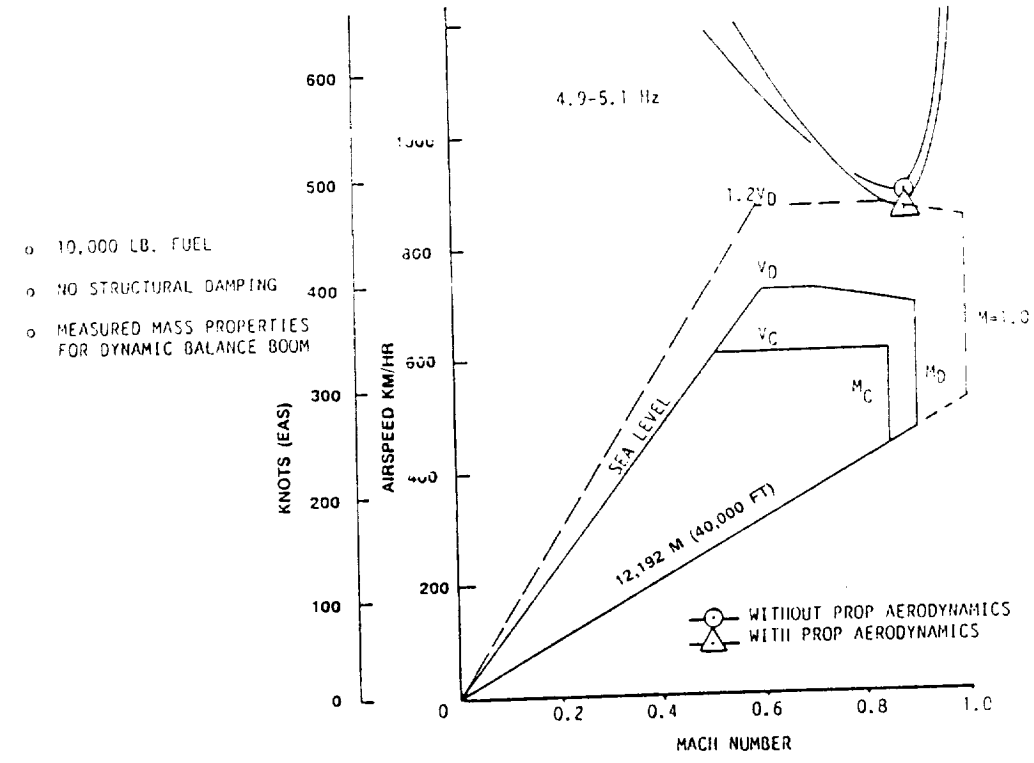


Figure 194. Predicted Flutter Boundaries

propfan propulsion system location (both spanwise and longitudinally), wing torsional stiffness, and the propfan propulsion system stiffness. Analysis showed that the instability could be eliminated by: (a) locating the propfan system as far inboard as possible, (b) increasing the wing torsional stiffness just inboard of the propfan nacelle (2.23 mm (0.09 in.) doubler required), and (c) adding a 136 kg (300 lb) boom to the left wing tip.

From a criteria standpoint, the minimum airspeed permissible for airframe flutter occurrence was selected to be 1.2 times the structural design dive speed; additionally, after the failure of a single structural element, freedom from flutter must exist at all speeds up to the structural design dive speed. Parameter variations investigated included fuel loadings, QEC-nacelle stiffnesses, propfan hub stiffnesses, fuselage loadings, and weight and fore/aft location of the static and dynamic balance booms. Failures considered included propfan mount failures, propfan gearbox-powerplant interconnecting structure failure, loss of the static balance boom, and loss of the dynamic balance boom.

Three fuel loadings were analyzed: 0; 4,540 kg (10,000 lb); and 7,730 kg (17,000 lb). For the most critical, 4,540 kg (10,000 lb), flutter boundaries are shown in Figure 194. These boundaries were calculated conservatively assuming no structural damping.

Variations in fuselage loading were found to have a negligible effect on the flutter boundaries, and no evidence of any instability involving aileron rotation was detected for any of the conditions analyzed. The static and dynamic balance booms were designed to possess primary modal frequencies in excess of 15 Hz to preclude adverse coupling with the basic wing instability.

Flutter boundaries resulting from a massive multiple failure of the gearbox and powerplant interconnecting structure are shown in Figure 195. The failure of any one propfan supporting mount negligibly affected the flutter stability because of the redundant design of the mounting system.

Addition of the static balance boom lowered the flutter speed of the right wing. Static boom loss, therefore, improves the overall flutter stability. Large variations in boom mass did not significantly affect the airframe flutter characteristics as long as the center of gravity of the boom assembly was forward of FS 505.

Loss of the dynamic balance boom would result in the boundary presented in Figure 196. Although these results indicate instabilities within the flight envelope, less than 2 percent structural damping is required to raise these boundaries to airspeeds beyond the outer envelope. In any event, the GII wing tip tank installation was designed to withstand loads well in excess of those predicted for the dynamic balance boom, so the probability of occurrence for this failure was low.

Throughout the analyses, no evidence of whirl flutter was found.

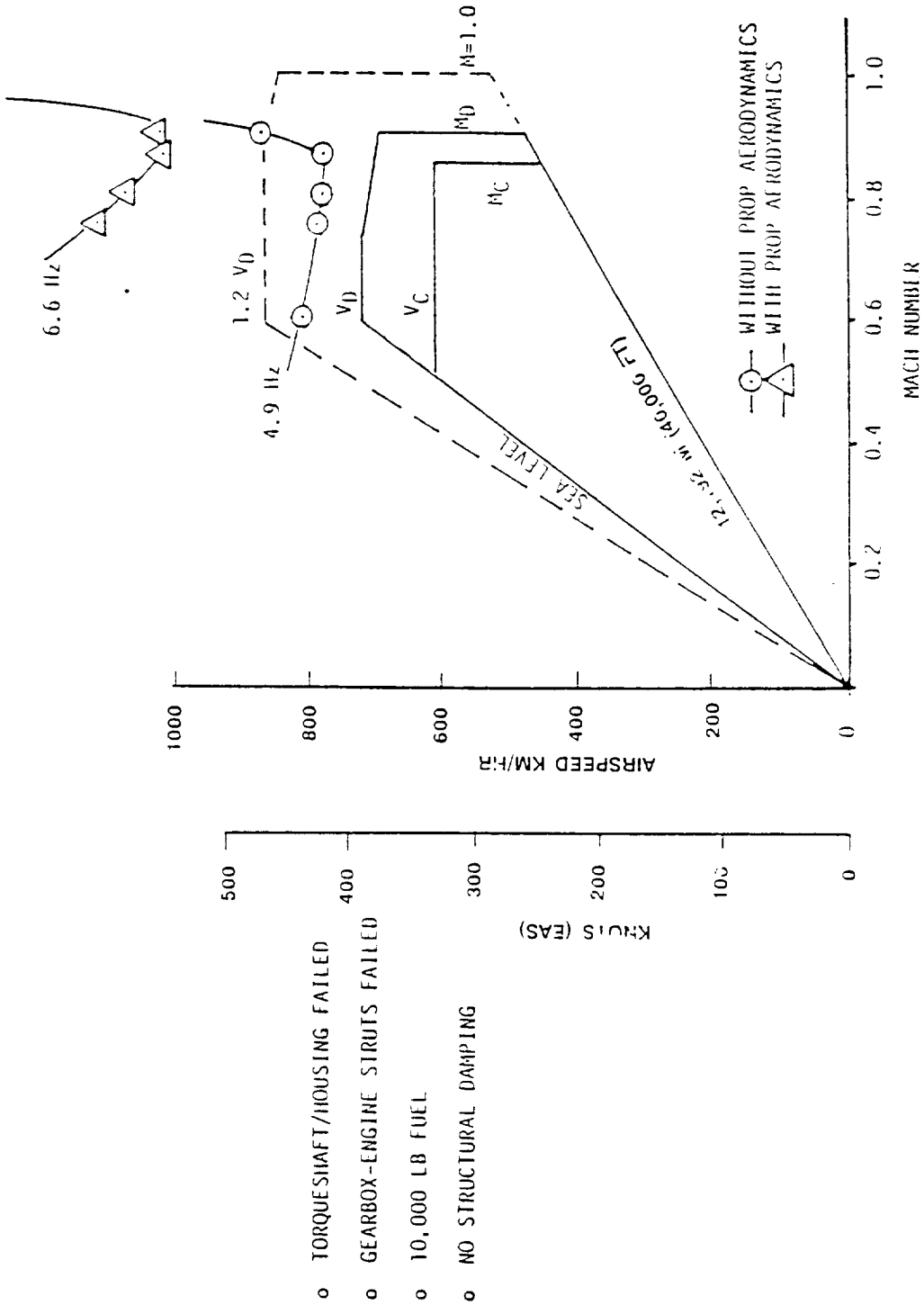


Figure 195. Predicted Flutter Boundaries with Drive System Failures

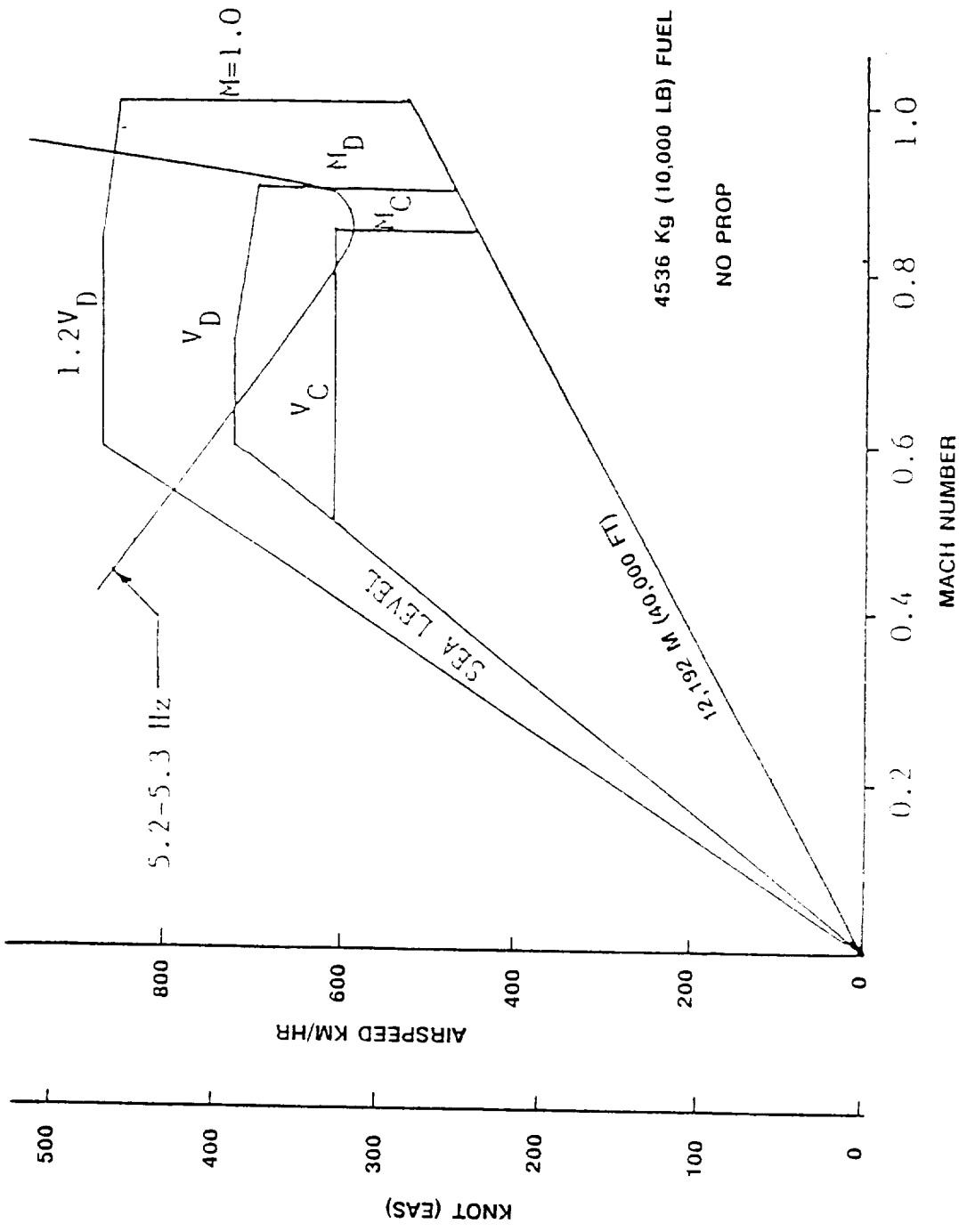


Figure 196. Predicted Flutter Boundaries with Loss of Dynamic Balance Boom

5.5.1.7 Sonic Fatigue Considerations

The following GII structural components were analyzed with regard to their tolerance of the propfan acoustic environment:

- Fuselage skins
- Wing-fuselage fairings
- Wing leading edge
- Wing upper surface trailing edge
- Spoilers
- Trailing edge flaps

In addition to these components, analysis was also required for the propfan nacelle, wing-nacelle fairings, and the wing upper and lower surface modifications in the vicinity of the propfan. The nacelle analyses are described in Sections 5.5.2 and 5.5.3.

The design life criteria which were used for the sonic fatigue analyses are summarized in Figure 197. For an average 3-hour flight, a propfan operating time of two hours was assumed. Fatigue damage was assumed to accumulate at local resonant frequencies, and these were assumed to be the same as the propeller blade passage frequencies. The analysis also assumed that the structure should be capable of withstanding the highest operating noise level at the worst location in a particular area.

The procedures used to assess the structure were taken from Reference 15 and based on structural vibratory response in one degree of freedom. Transient response (tap) tests were made on actual GII aircraft structure to verify the conservatism of the analysis assumptions and to locate areas which would be sensitive acoustically. Response spectra were developed from these tap tests to obtain the resonant characteristics of structure likely to be damaged by the propfan acoustic environment.

The analysis of the widest skin bay of the flap is illustrated in Figure 198; this particular example pertains to the analysis performed after it was determined that reinforcement in this area was necessary. The sonic fatigue margin of environment for the premodified flap structure was -19.7 dB; as shown in the figure, the margin is positive for the reinforced flap. Similar calculations were made for other sensitive areas. The following minimum environment margins were determined for unmodified structure:

Fuselage skin (in plane of prop rotation)	- 4.7 dB
Flaps	-19.7 dB
Wing leading edge (inboard)	+ 1.2 dB
Wing/fuselage fairing	- 7.9 dB
Outer wing panel	+ 0.07 dB
Wing upper trailing edge	-19.1 dB
Ground spoiler	-13.3 dB
Outboard spoiler	- 2.1 dB

AIRFRAME DESIGN SERVICE LIFE ---------- 3000 HRS
(TOTAL - ALL OPERATIONS)

PROPFAN OPERATING TIME ---------- 67%
(2 HOURS RUNNING DURING 3 HOURS AVG FLT)

PROPFAN OPERATING TIME COINCIDENT WITH STRUCTURAL ---------- 25%
RESONANCE (RESONANCES AT ANY 1 OF 4 RPMs)

PROPFAN OPERATING TIME AT WORST NOISE CONDITION (WITHIN 3 dB) -------- 30%

DESIGN SCATTER FACTORS ---------- METALS -- 2; NON-METALS -- 4

DESIGN LIFE - METALS (3000 HRS x .67 x .25 x .30 x 2) ---------- 300 HRS

DESIGN LIFE - NON-METALS (3000 HRS x .67 x .25 x .30 x 4) ------ 600 HRS

Figure 197. Airframe Structure Design Life

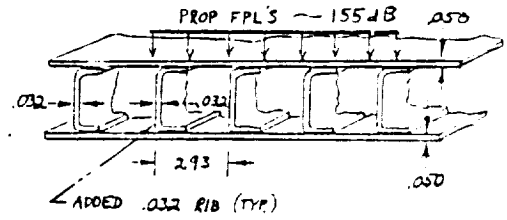
UPPER SKINS - 2024-T3, .050 INCH
LOWER SKINS - 2024-T3, .050 INCH
RIBS (EXISTING AND ADDED) - 2024-T3, .032 INCH

- RESONANT RESPONSE ASSUMED
  $\therefore Q = 25$
- UNIT STRESS $\sigma_o = K_o \left(\frac{b}{t}\right)^2$

  $b = 2.93$ INCH $t = .050$ INCH

  $a/b > 2$ $K_o = .38$ (AVG OF CLAMPED AND SUPPORTED EDGES)

  $\sigma_o = 1305$ PSI/PSI



- DYNAMIC STRESS $\sigma_{RMS} = \sigma_o \; Q \; P$

  MAX FPL = 155 dB AT 238 Hz $P = .1634$ PSI_{RMS}

  $\sigma_{RMS} = 5331$ PSI_{RMS}

- $\sigma_{ALLOW} = 6000$ PSI_{RMS} (ALONG FASTENER ROW)
- M.E. $= 20 \log_{10} \left(\frac{6000}{5331}\right) = +1.0$ dB

Figure 198. Flap Sonic Fatigue Analysis

Of the areas having negative margins, the following were reinforced:

- o Flaps
- o Fuselage shell
- o Wing upper trailing edge

A sonic fatigue inspection schedule was established for all acoustically sensitive components including the spoilers and the wing-to-fuselage fairing. Inspection intervals were specified as a function of propfan operating time beginning with intervals of 2, 3, and 5 hours between the first three inspections; thereafter, the required interval was set to be twice the previous one. Early detection and repair, if necessary, was selected as a viable alternative to making additional modifications to the structure.

5.5.2 Forward Nacelle Structural Analysis

5.5.2.1 Design Loads

Structural requirements for the forward nacelle, or QEC, were established early to allow sufficient lead time for its detail design and manufacture. As with the airframe, CAR-4b was used as a guideline for structural design criteria. Although the configuration was adapted from the Lockheed P3V powerplant installations, all QEC structure was new except for P3V engine mounts and P3V "Vee" braces.

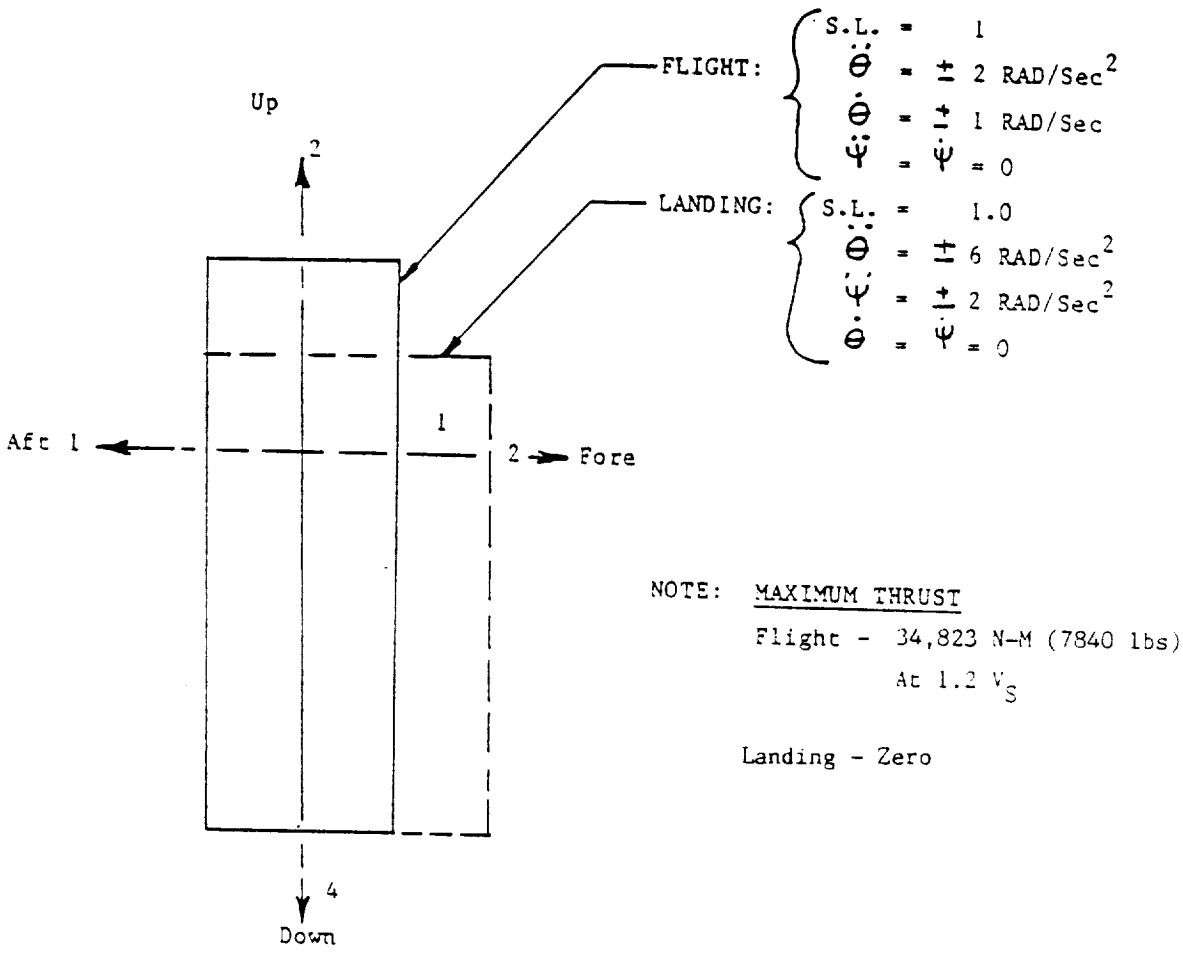
The applied loads for nacelle design comprised the most severe loadings anticipated during flight and ground operations of the testbed aircraft. The following contributed to QEC design loads:

- o Propeller loads, including thrust and torque
- o Gyroscopic moments
- o Inertia loads
- o Spinner airloads
- o Nacelle cowling external airloads
- o Nacelle internal pressures

Loads were also defined for the compressor inlet duct, the oil cooler duct and door, handling and transportability hard points, and the various accessories.

At the outset of design, values of QEC inertial loads were needed for evaluating the engine mounts of the modified gearbox and for initial sizing of nacelle-related structural members. Inasmuch as acceleration response characteristics for maneuver, gust, and ground operations were yet to be determined, envelopes of inertial loads were developed from those of similar wing-mounted powerplant installations making allowances for the PTA environment. The loads shown in Figure 199 were used in lieu of the more conservative loading requirements of the general engine specification, MIL-E-8593(ASG). Values slightly exceeding these envelopes

I. FLIGHT AND LANDING-LIMIT LOADS



II. Precession Moment($\dot{\Psi}$) = ± 1.75 RAD/Sec.

III. Side Load Condition = ± 1.33 g

IV. EMERGENCY LANDING-ULTIMATE LOADS

3g Forward	Acting Separately
1.5 Aft	
1.5 Side	
4.5 Down	
2.0 Up	

Figure 199. Inertia Forces for Nacelle Design

were derived from the subsequent design dynamic gust analysis (15.2 mps (50 fps)), but later incorporation of these data did not necessitate any change to the design configuration. (Note: Because of airframe limitation, the gust intensity for design was subsequently reduced by 30 percent. Reduced loads were prepared for the nacelle, but not used.)

Based on propeller aerodynamic characteristics, Hamilton Standard specified propeller loadings due to inflow as a function of power coefficient, advance ratio, and Mach number. Inflow at the propfan plane of rotation was estimated using the QUADPAN code. Thrust and torque loadings were determined from the drive system capabilities.

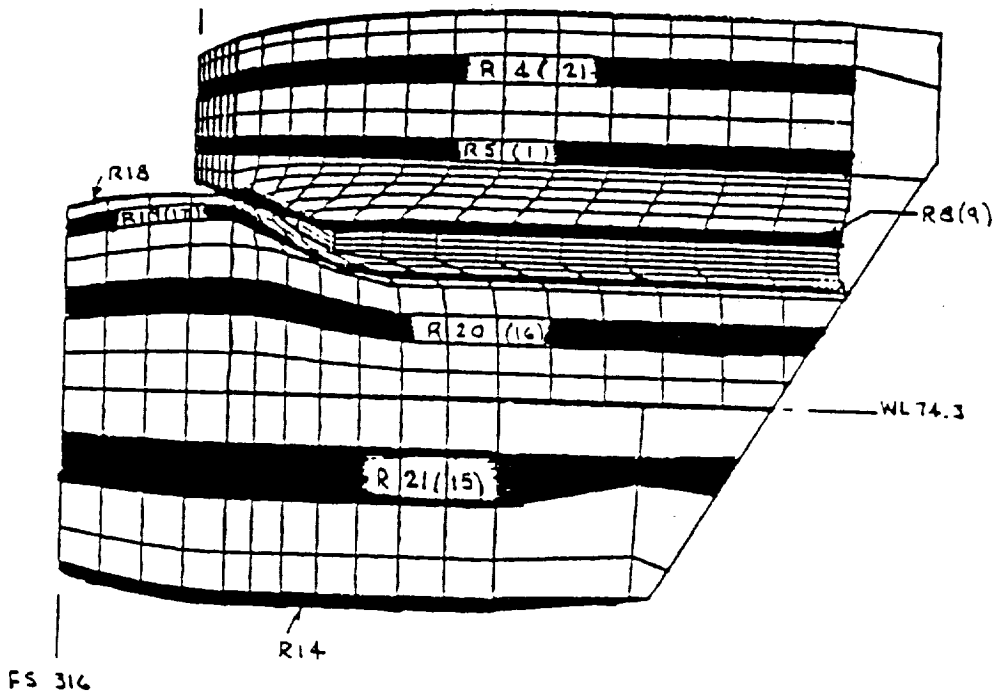
External airloads were based on pressure distributions derived by QUADPAN. Surface pressure coefficients were determined for variations of Mach number, thrust coefficient, nacelle incidence, and the airplane angles of attack and sideslip. These coefficient data were defined for points along the 15 selected strips illustrated in Figure 200; values for other cowling regions were then obtained by interpolation/extrapolation. For analyzing a particular condition, airloads were used in two formats: integrated values of aerodynamic forces and moments for the entire QEC were used for identifying conditions appearing to be critical to the design; panel pressures also provided data necessary for the compartmental ventilation analysis and corresponding internal pressures.

Applied QEC loads were computed for the following ranges of variables:

- Nacelle incidence, -5.0 to +3.0 degrees
- Prop tip speed, 183 to 256 mps (600 to 840 fps)
- Power, 0 to 4,475 kw (6,000 shp)
- Gross weight, 22,000 to 29,800 kg (48,000 to 65,500 lb)
- Angles of attack corresponding to load factors of -1.0 to 2.5 with propfan not operating and 0.0 to 2.0 with the propfan operating, as limited by maximum lift
- Sideslip angles, GII overswing yaw with prop not operating and GII steady sideslip with prop operating
- Vertical, horizontal, and unsymmetric gusts, -15.2 to +15.2 mps (-50 to +50 fps)

Loads for overtorque, or torque surge, were limited to the P3V design limit value of 1,994 N-m (568,000 in.-lb). This limiting torque was 1.91 times the torque for 4,475 (6,000 shp) at 183 mps (600 fps) tip speed, and was only slightly shy of the factor of 2.0 required by CAR-4b.

External loads were determined for 352 conditions in addition to the loads of Figure 199. These conditions excluded the dynamic loads for landing impact and gust. The nacelle portion of the airplane dynamic response analysis model consisted of three interconnected masses: the prop/gearbox



Note: Outboard Side Shown; Corresponding Inboard Region Strip Numbers Shown in Parentheses.

Figure 200. QUADPAN Paneling for Nacelle Loads

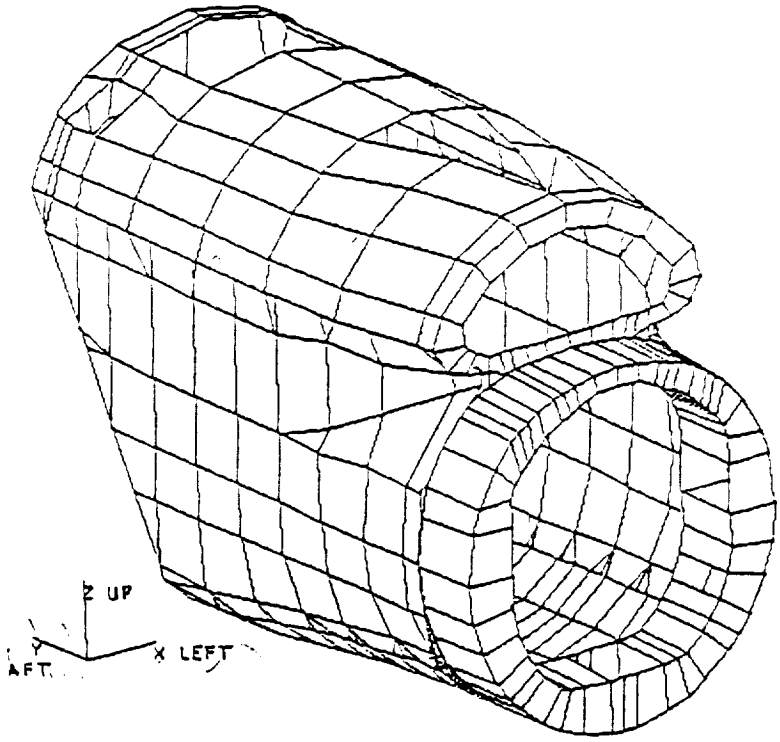


Figure 201. QEC Finite Element Model

assembly, the engine/torquemeter assembly, and the nacelle structure (including the aft nacelle). Analysis flexibility coefficients were derived from a structural finite element model having engine mount and drive system characteristics included. Specifically examined for dynamic loadings were landing impacts at 2.3 mps (7.5 fps) and vertical gusts; wavelengths of the gust forcing functions were varied from 10 to 40 wing chords to assure coverage of the wing/nacelle fundamental frequencies. The landing loads were within the limit loads of the initial cases; the gust analysis, however, yielded an additional 92 cases for internal loads evaluation.

5.5.2.2 Forward Nacelle Strength Analysis

Nacelle strength design was based on a safety factor of 1.5, a minimum margin of safety of 0.33 for all new structure, and fail-safe capability for design limit load. (These criteria were discussed in Section 5.5.1.1.) The minimum margin of safety for failure conditions was zero. Single failures were assumed for:

- Upper gearbox mount
- Outboard gearbox mount
- Left vee brace forward attachment
- Right vee brace forward attachment
- Upper engine mount attachment
- Aft upper left interface attachment
- Aft lower left interface attachment
- Aft upper right interface attachment
- Aft lower right interface attachment
- Engine-to-gearbox torque shaft housing
- Starter duct rupture

Metallic material allowables were taken from MIL-HDBK-5D while graphite/epoxy allowables were derived by Rohr using FAA-approved procedures. Thermal effects were taken into consideration for the GII design climatic extremes -54 to +71°C (-65° to +160°F) at sea level and local temperatures as determined from the nacelle thermal analysis.

Primary components of the QEC nacelle structure were illustrated in Figure 26. The basic support structure consisted of two connected bulkhead type frames which supported the main gearbox mounts. The frames were supported in the axial and vertical directions by two vee braces. The apexes connected to the machined frames, and the bases to the four aft nacelle interface points. Side shear was transmitted from the frames to the aft nacelle attachment points via the composite upper and lower panels. The removable composite side panels were attached structurally to increase the nacelle torsional stiffness. For strength analysis, QEC structural components were represented by the finite element model illustrated in Figure 201. The model includes element representations of all

mounts, cowl panels, frames, and braces. In addition to providing the internal loads for stress analysis, this model was used to obtain stiffness matrices for flutter analysis, forward nacelle/aft nacelle interface loads, and engine mount loads.

Minimum margins of safety for nonfailure conditions were found to be greater than 0.33 for all new elements of the QEC with the exception of the oil cooler flapper door. Because the analysis was conservative and the door contributes nothing to the structural integrity of the load bearing structure, the flapper door margin of safety of +0.13 was deemed acceptable.

For failure conditions, all margins of safety were positive. The three lowest values were:

- MS = +0.08, aft engine support frame; Failure (9); torque surge
- MS = +0.33, aft machined frame; Failure (1); torque surge
- MS = +0.08, forward lower engine mount support; Failure (1); torque surge

Three structural subelement strength tests were performed to supplement the analytical results. These tests were conducted on the upper longeron aft joint, the lower longeron aft joint, and the side cowl frame; test results validated the predicted margins of safety.

Structural integrity of the forward nacelle was further substantiated by the propfan nacelle proof load test described in Section 8.1.1.

5.5.3 Aft Nacelle

5.5.3.1 Design Loads

The aft nacelle structure was illustrated in Figure 34. Design loading requirements took into consideration the loads at the aft nacelle/forward nacelle interface, the external aerodynamic pressures, the interior compartmental pressures, the inertial loads, and loadings induced at the nacelle/wing interface.

Aft nacelle structural requirement criteria were the same as those used for the forward nacelle. Therefore, the forward nacelle conditions which produced the greatest loads at the QEC interface fittings were flagged for aft nacelle strength analysis. Twenty-seven cases were thus identified, excluding the gust conditions of the dynamic response analysis. All 92 dynamic gust cases considered for the QEC were used in the aft nacelle analysis.

External pressures were determined from the pressure coefficients computed by QUADPAN. Dependent variables were Mach number, airspeed, propfan thrust, airplane angle of attack, and angle of sideslip. Pressures for a representative operating condition are shown in Figure 202.

BASIS: QUADPAN ANALYSIS PRESSURE COEFFICIENTS

$C_p = f(MACH, T_C, \alpha, \beta)$

$\Delta P = C_p \times q$

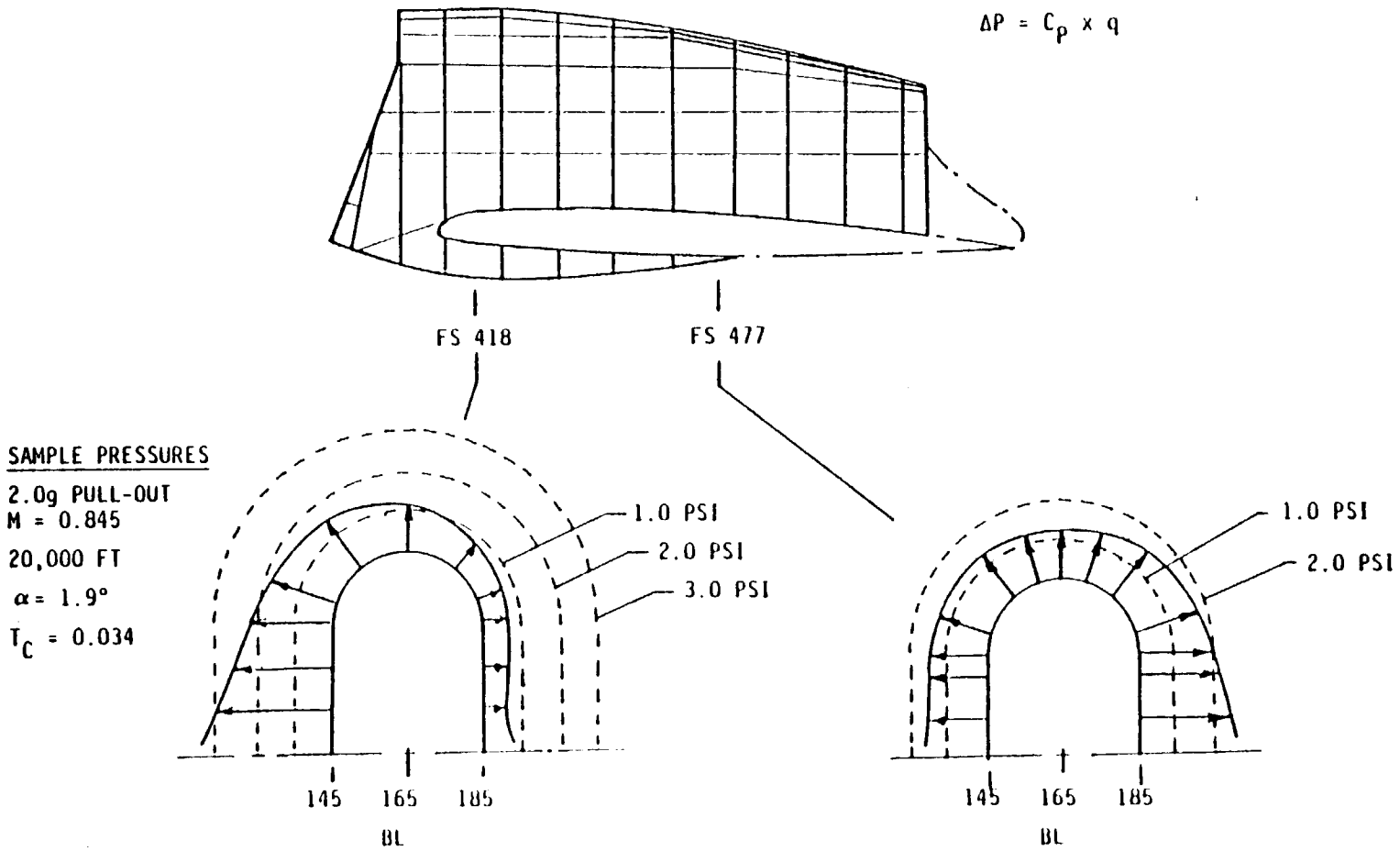


Figure 202. Aft Nacelle External Aerodynamic Pressures

Internal pressures were determined from an analysis of the compartment ventilation flow characteristics. Structural design values are shown in Figure 203.

The net pressure forces acting on each nacelle panel were summed for each operating condition. This was done for the entire aft nacelle, including the large upper access door, and also for the access door alone. A survey of 106 flight conditions for maximum pressure loads produced 15 potentially critical strength cases. These were in addition to the cases identified with the forward nacelle interface.

In all, there were 134 sets of aft nacelle panel loads. Component strength was established for these loads acting together with the corresponding interface loads.

5.5.3.2 Aft Nacelle Strength Analysis

Aft nacelle design strength criteria were the same as the criteria used for the forward nacelle. Attention was given to fail-safety by:

- Using multi-element design for all major frames, longerons, and supporting substructures
- Providing strength capability to withstand design limit load with any one of the QEC interface fittings failed

The finite element model used to generate internal loads for the aft nacelle and left wing interface structure is illustrated in Figure 204. Not shown, but included in the analysis, is the QEC stiffness matrix which supplied necessary boundary conditions. The aft nacelle interface module included the new rib at WS 185, the reinforcement of the WS 145 rib, front and rear beam reinforcements, and portions of the wing doublers. The wing inboard module included surface doublers and front beam reinforcement.

The maximum and minimum QEC-to-aft nacelle interface loads are listed in Figure 205. The predominant conditions were dynamic gust, unsymmetric gust, landing impact, and torque surge. The first digit of the 4-digit case numbers in Figure 205 indicates QEC tilt position (1 is 3 degrees up; 2 is 5 degrees down). The second digit indicates the condition being represented (0 or 1 is used for a basic QEC condition; 2 denotes an aft nacelle pressure condition; 3 is used for dynamic gust analysis cases; and 4 to 7 indicate fail-safe cases). The remaining two digits are sequential subcase numbers for a given condition.

Critical wing/aft nacelle interface loads along the wing surface at WS 145 and WS 185 were obtained from the finite element analysis. Wing spar reactions at WS 145 were generally greater than those at WS 185 because the wing sweep angle placed the WS 145 reaction point closer to the nacelle center of gravity.

Internal loads were also determined for the nacelle frames and the upper and lower longerons. Stiffness requirements were instrumental in the design of the canted QEC-to-aft nacelle interface frame.

ENGINE COMPARTMENT

FLIGHT AND LANDING:	$\Delta P = -0.2q_o$ TO $0.6\delta + 0.2q_o$	POWER ON
	$\Delta P = -0.2q_o$ TO $+ 0.2q_o$	POWER OFF
SEA LEVEL STATIC:	$\Delta P = -0.15$ TO $+ 0.20$	

WING ISOLATION COMPARTMENT

FLIGHT AND LANDING:	$\Delta P = 0$ TO $0.6q_o$	POWER ON OR POWER OFF
SEA LEVEL STATIC:	$\Delta P = 0$	

NOTE: $\Delta P = P - P_{AMB}$, PSI

δ = STATIC PRESSURE RATIO

q_o = INCOMPRESSIBLE DYNAMIC PRESSURE, PSI

Figure 203. Predicted Aft Nacelle Internal Pressures

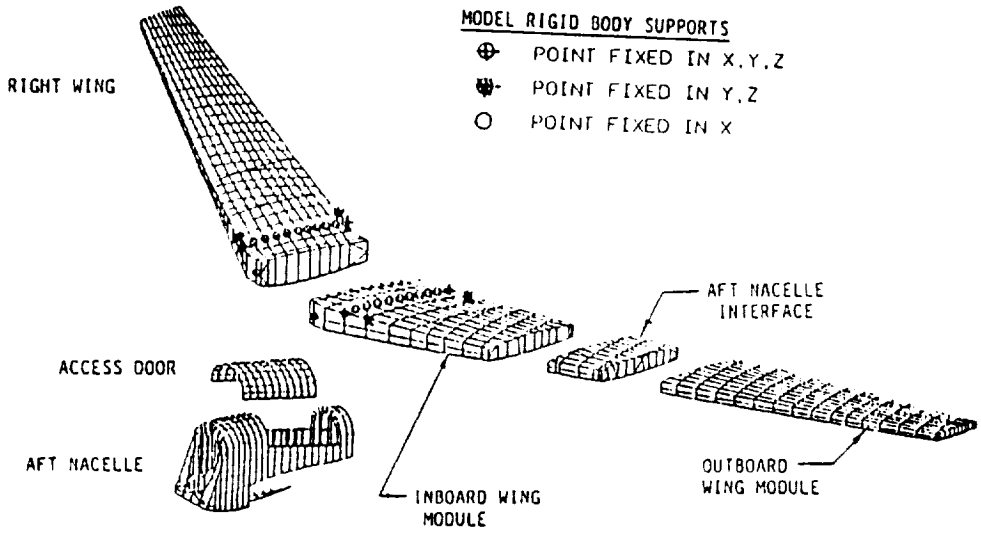
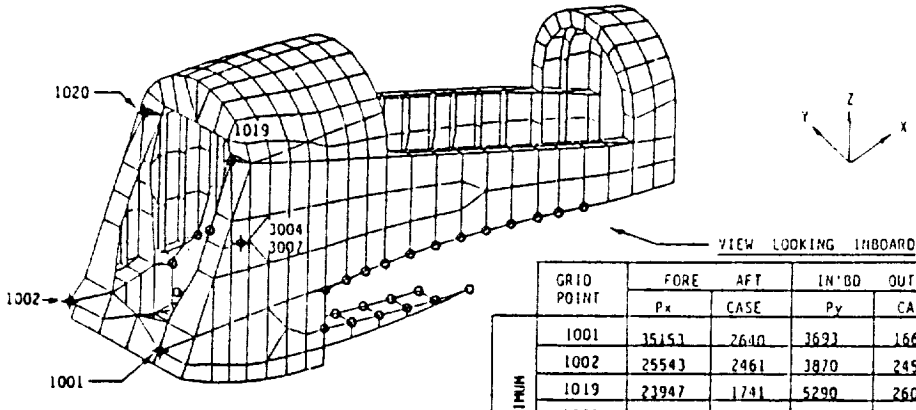


Figure 204. Aft Nacelle Finite Element Model



CRITICAL BASIC CONDITIONS:

- DYNAMIC GUST
- UNSYMMETRIC GUST
- LANDING
- TORQUE SURGE

	GRID POINT	FORE	AFT	IN'BD	OUT'BD	VERTICAL	
		Px	CASE	Py	CASE	Pz	CASE
MAXIMUM	1001	35153	2640	3693	1666	7800	1638
	1002	25543	2461	3870	2454	7741	1538
	1019	23947	1741	5290	2602	3981	2501
	1020	28624	1566	5226	1105	3052	1438
	3004	---	---	3997	1311	---	---
	3007	---	---	5058	2311	---	---
MINIMUM	1001	-27393	1666	-8195	2702	-9753	2704
	1002	-25883	1311	-8044	1504	-10259	1120
	1019	-28824	2634	-2956	2731	-4468	2605
	1020	-35994	2540	-3885	2540	-6089	2119
	3004	---	---	-3092	1319	---	---

Figure 205. QEC/Aft Nacelle Interface Loads

Critical side panel shear stresses for the inboard side of the nacelle are shown in Figures 206 and 207 for various load conditions. Outboard side skin stresses were less.

Unlike the graphite-epoxy and aluminum structure of the forward nacelle, the aft nacelle was made primarily of stainless steel and aluminum as shown in Figure 208. These materials were compatible with the operating temperatures estimated by the ventilation flow analysis. This analysis was summarized in Section 3.3.6.7, and design operating temperatures are shown in Figure 209.

Aft nacelle minimum margins of safety are identified in Figure 210. Margins denoted as "high" were greater than +1.0. These margins indicate strength conservatism in some areas because of requirements for stiffness and sonic fatigue resistance.

5.5.4 Nacelle Sonic Fatigue

Sonic fatigue design life criteria for the nacelle were:

- QEC cowling; 600 hours
- Aft nacelle cowling; 300 hours
- Inlet and exhaust components; 8000 hours

Design provisions were made for the following acoustic environments:

- QEC cowling; 154 dB top and 143 dB sides
- Aft nacelle cowling; 150 dB top and 138 dB sides
- Inlet; 114 dB at 250 Hz and 145 dB at 3150 Hz
- Exhaust; 129 dB at 250 Hz and 132 dB at 500 Hz

Sonic fatigue substantiation for the QEC inlet is described in Figure 211. Substantiation of the QEC upper and side cowling panels is made in Figures 212 and 213, respectively. Panels were also subjected to random fatigue shaker tests; these are described in Figures 214 and 215.

The predicted life of each aft nacelle component was shown analytically to exceed its design sonic fatigue life. Resonance response was assumed to occur in skin panels because their natural frequencies coincided with blade passage frequencies; response characteristics of a typical skin panel are shown in Figure 216. An analysis example is given in Figure 217; the allowable stress in this example included the effects of a 6 ksi shear stress, conservatively assumed to be in the direction of the maximum dynamic stress. Aft nacelle acoustic environmental margins are listed in Figure 218. These margins are the design pressure level increases which could be tolerated without causing the predicted life to fall short of the sonic fatigue design life.

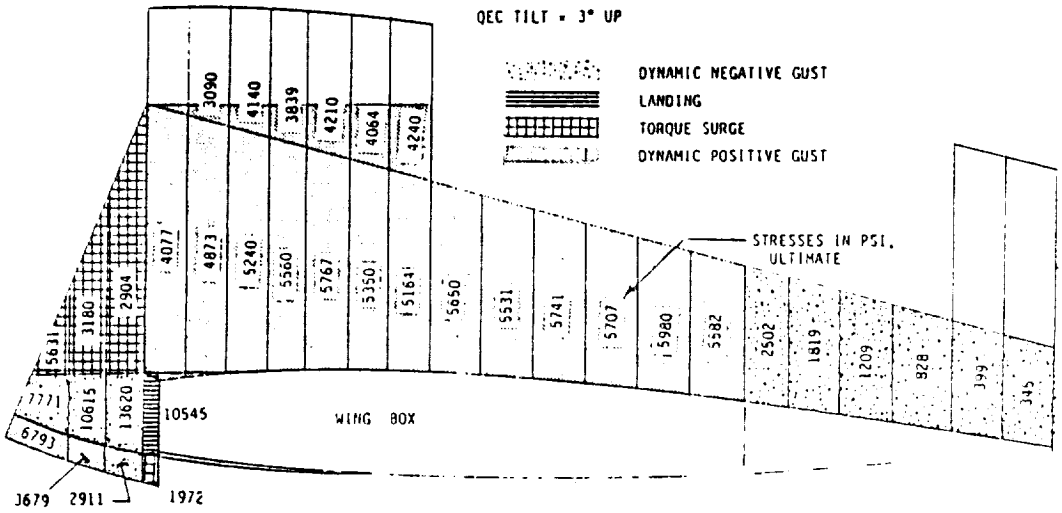


Figure 206. Inboard Skin Stresses - WS 145, NT = +3°

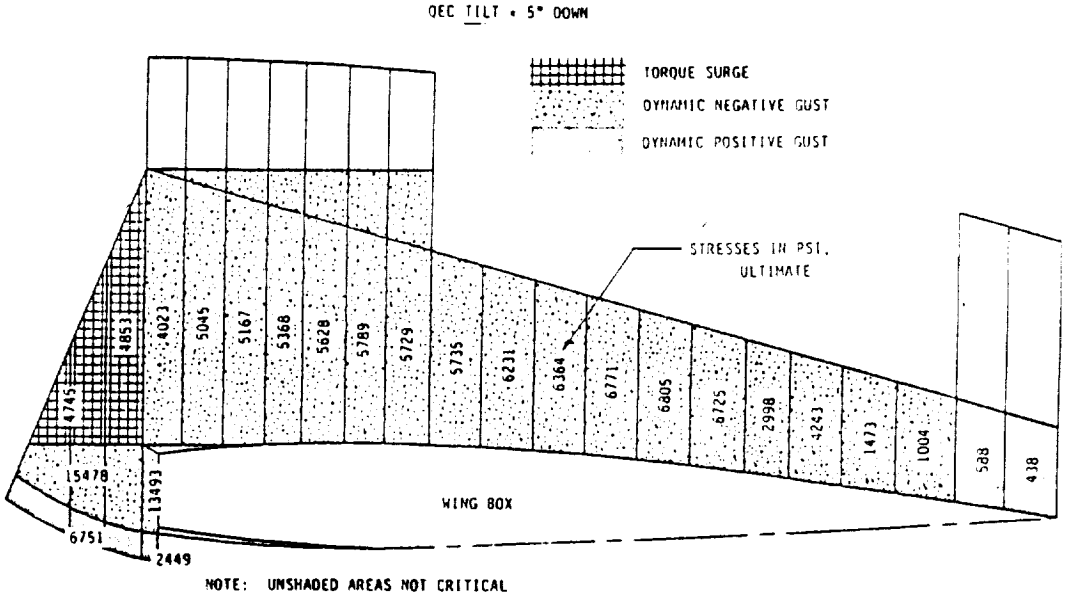


Figure 207. Inboard Skin Stresses - WS 145, NT = -5°

ORIGINAL PAGE IS
OF POOR QUALITY

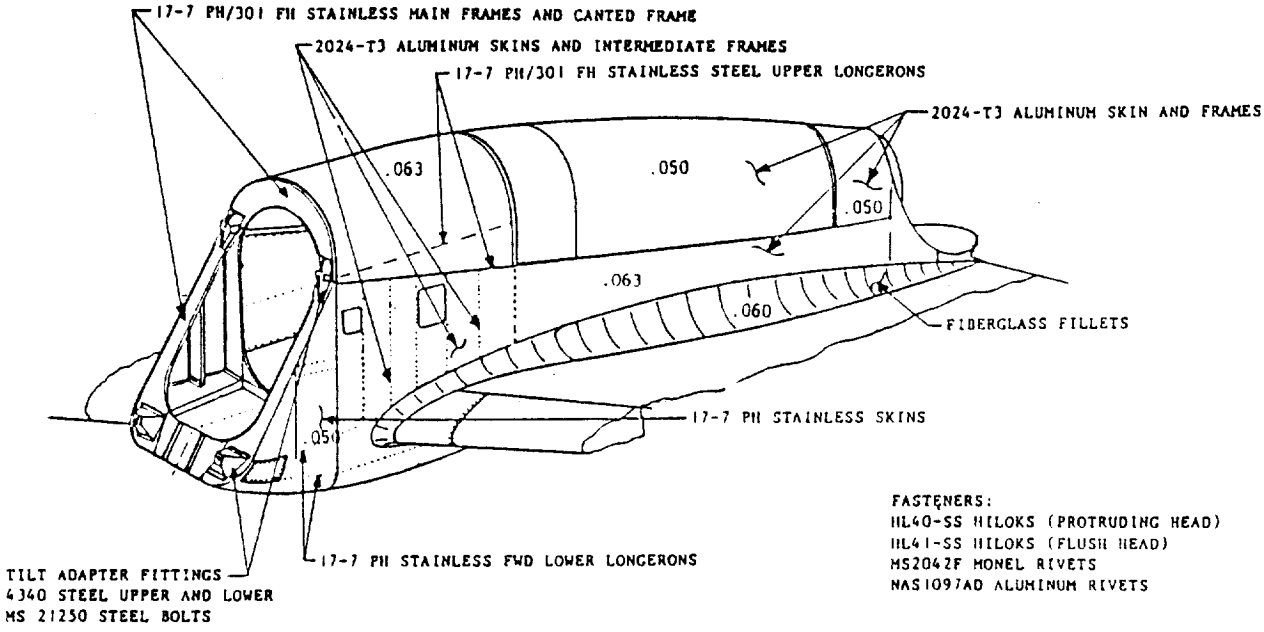


Figure 208. Aft Nacelle Materials and Fasteners

	°C	(°F)
ALUMINUM SKIN AND FRAMES	121	(250)
STEEL STRUCTURE	204	(400)
CONTAINMENT RING	260	(500)
NACELLE/WING FIRE BARRIER	165	(330)
SPILL SHIELD	538	(1000)
WING SURFACE UNDER PYLON	93	(200)
ZONE 1 AIR	204	(400)
ZONE 3 AIR	93	(200)

Figure 209. Aft Nacelle Maximum Operating Temperatures

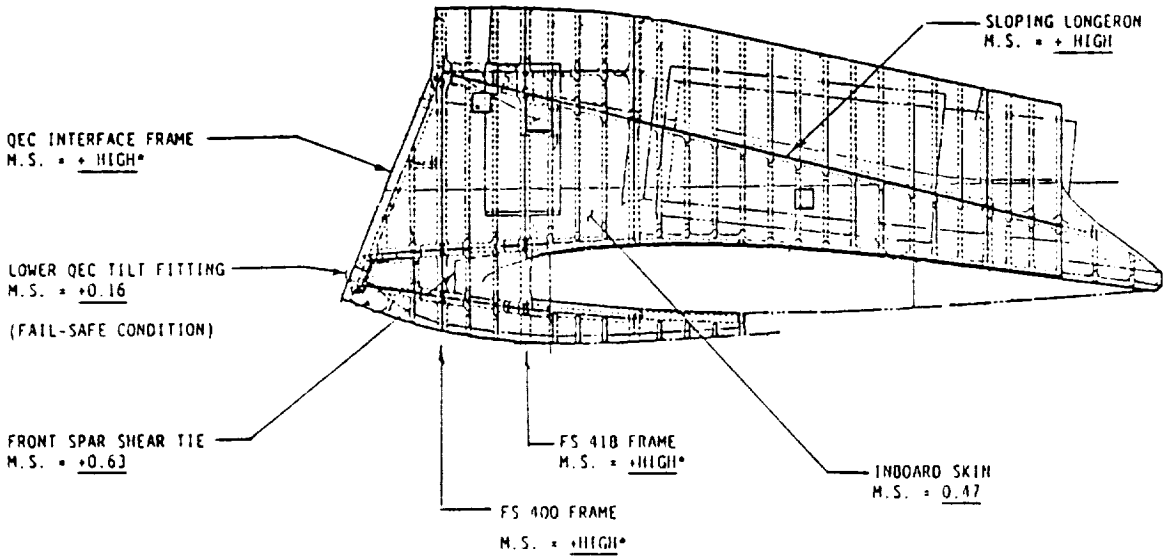


Figure 210. Summary of Aft Nacelle Safety Margins

- STRUCTURAL CONFIGURATION:
  - 2 PLY GRAPHITE/EPOXY FACE SHEETS, 0.028 IN. THICK
  - SYNTACTIC CORE, 0.04 IN. DEEP
  - CRITICAL AREA - 14 IN. BY 24 IN. FLAT SECTION

- DESIGN SUBSTANTIATION:
  - SONIC FATIGUE TESTS ON SYNTACTIC CORE SANDWICH PANELS PERFORMED BY LOCKHEED BURBANK - NADC CONTRACT, REF. NADC-78169-60 FEBRUARY 1982.
    - PANELS TESTED AT 167 dB OVERALL SOUND PRESSURE LEVEL (SPECTRUM LEVEL = 140)
    - RESULTING FATIGUE LIFE = 3 TO 6 MILLION CYCLES
  - COMPARE ESTIMATED RESPONSE LEVELS OF LOCKHEED PANEL & PTA INLET PANEL, FOR A GIVEN ACOUSTIC LOAD, TO ACCOUNT FOR CONFIGURATION DIFFERENCES. EXTRAPOLATION BASED ON ALUMINUM HONEYCOMB DESIGN METHOD - REF. AFFDL-TR-74-42.
    - PTA INLET PANEL STRESS = 2.4 TIMES LOCKHEED PANEL FOR SAME ACOUSTIC LOAD.
  - LOCKHEED PANELS TESTED AT ACOUSTIC SPECTRUM LEVEL 37 dB HIGHER THAN MAXIMUM INLET SPECTRUM LEVEL. 37 dB = x 72 STRESS FACTOR.
  - STRESS RATIO TO INCREASE RANDOM FATIGUE LIFE FROM 3×10^6 CYCLES TO ENDURANCE LEVEL = x 0.8.
  - COMBINED STRESS FACTOR FOR CONFIGURATION DIFFERENCES AND FATIGUE LIFE REQUIREMENT = 3.0. STRESS RATIO OF 3.0 EQUIVALENT TO 10 dB.
  - DESIGN EXCEEDS 8000 HOUR DESIGN LIFE REQUIREMENT, WITH 27 dB MARGIN.
  - RANDOM FATIGUE SHAKER TESTS TO SUBSTANTIATE INLET PANEL MATERIALS.

Figure 211. Sonic Fatigue Substantiation of Inlet

- STRUCTURAL CONFIGURATION:
  - 3 PLY GRAPHITE/EPOXY FACE SHEETS, 0.042 IN. THICK
  - NOMEX HONEYCOMB CORE, 1/2 IN. THICK, 1/8 IN. CELL SIZE
  - PANEL SIZE - 44 IN. BY 63 IN., 23 IN RADIUS

- DESIGN SUBSTANTIATION:
  - SONIC FATIGUE TESTS PERFORMED BY ROHR ON FLAT HONEYCOMB SANDWICH PANELS WITH GRAPHITE FACE SHEETS. (ROHR REPORT RHR 81-015)
    - PANELS TESTED AT 165 dB FOR 5 MILLION CYCLES WITHOUT FAILURE, PLUS 10 MILLION CYCLES AT 166 dB, ONE-OCTAVE BAND WIDTH, WITHOUT FAILURE; EQUIVALENT TO 172 dB OVERALL SOUND PRESSURE LEVEL.
    - MAXIMUM TEST ACOUSTIC SPECTRUM LEVEL = 147 dB/HZ (RANDOM)
  - COMPARE ESTIMATED RESPONSE LEVELS OF ROHR TEST PANELS AND PTA COWL PANEL, FOR A GIVEN ACOUSTIC LOAD, TO ACCOUNT FOR CONFIGURATION DIFFERENCES, INC. CURVATURE.EXTRAPOLATION BASED ON AFFDL-TR-74-156 (AND ROHR TEST PANEL DATA) AND AFFDL-TR-80-3019 (REVISED VERSION - IN PREPARATION)
    - PTA COWL PANEL STRESS = 0.16 TIMES ROHR TEST PANEL FOR SAME ACOUSTIC LOAD.
    - EQUIVALENT TO 16 dB INCREASED ACOUSTIC LOAD CAPABILITY.
  - MAXIMUM PTA COWL PANEL ACOUSTIC SPECTRUM LEVEL IS 6 dB HIGHER THAN ROHR TEST LEVEL.
  - DESIGN EXCEEDS 600 HOUR DESIGN LIFE REQUIREMENT WITH 10 dB MARGIN.
  - NO TEST SUBSTANTIATION REQUIRED.

Figure 212. Sonic Fatigue Substantiation of Upper Cowling Panels

- STRUCTURAL CONFIGURATION:
  - 5 PLY GRAPHITE/EPOXY SKINS, 0.070 IN. THICK
  - STIFFENERS SPACED AT 7 IN.
  - LENGTH OF FLAT PANEL PORTION $\triangleq$ 34 IN.

- DESIGN SUBSTANTIATION:
  - SONIC FATIGUE DESIGN METHOD FOR GRAPHITE/EPOXY STIFFENED - SKIN PANELS (REFERENCE *).
  - CALCULATED OVERALL RMS STRAIN FOR OVERALL SOUND PRESSURE LEVEL OF 148 dB = 78 $\mu\varepsilon$.
  - RANDOM FATIGUE ENDURANCE LEVEL (REFERENCE *) = 440 $\mu\varepsilon$.
  - DESIGN EXCEEDS DESIGN LIFE REQUIREMENT OF 600 HOURS WITH 15 dB MARGIN.
  - RANDOM FATIGUE SHAKER TESTS TO SUBSTANTIATE MATERIAL & PROCESS DIFFERENCES FROM DESIGN ANALYSIS REFERENCE*.

* REFERENCE: "SONIC FATIGUE DESIGN TECHNIQUES FOR ADVANCED COMPOSITE AIRCRAFT STRUCTURES", I. HOLEHOUSE, UNIVERSITY OF SOUTHAMPTON Ph.D. THESIS, 1983.

Figure 213. Sonic Fatigue Substantiation of Side Cowling Panels

- 0 INLET PANELS & SIDE COWLING PANELS
  - SUBSTANTIATION OF MATERIAL & PROCESS DIFFERENCES BETWEEN PTA STRUCTURES AND EMPIRICAL DATA BASIS OF ANALYTICAL METHODS USED.
- 0 TEST DESCRIPTION (SAME FOR INLET & COWL PANELS)
  - o CUT 12 (TWELVE) 9 IN. X 3 IN. SPECIMENS FROM 36 IN. X 9 IN. PANEL OF EACH STRUCTURE.
    - WITH STIFFENERS ALONG THE CENTERLINE, TRANSVERSE TO THE 9 IN. DIRECTION
  - o INSTALL 10 STRAIN GAUGES AND 2 ACCELEROMETERS ON ONE SPECIMEN OF EACH TYPE.
    - 4 STRAIN GAUGES ON EACH OF REMAINING 22 SPECIMENS
  - o MOUNT ON SHAKER TABLE - AS SHOWN IN THE FIGURE BELOW.
  - o TEST SEQUENCE:
    1. SINE SWEEP TO DETERMINE FUNDAMENTAL IN-PHASE RESONANCE.
    2. ATTACH BALANCE WEIGHTS TO ENSURE SYMMETRIC RESPONSE.
    3. ENDURANCE TESTS WITH 1/3 OCTAVE EXCITATION, CENTERED AROUND RESONANT FREQUENCY (GAUSSIAN).
       - INCREMENTAL LOADING TO PRODUCE OVERALL RMS RESPONSE STRAINS OF 400, 600, 800 and 1000 MICRO-STRAIN.
       - TEST FOR 10^7 CYCLES AND PROCEED TO NEXT LOAD LEVEL, IF NO FAILURE OCCURS.
    4. STRAIN GAUGE AND ACCELEROMETER OUTPUTS RECORDED ON MAGNETIC TAPE.
    5. GENERATE FREQUENCY SPECTRA AND PEAK LEVELS.
  - o PLOT RANDOM FATIGUE CURVES USING BOTH RMS AND PEAK VALUES.
  - o COMPARE RESULTS WITH ANALYSIS DATA BASE.

Figure 214. Random Fatigue Shaker Testing

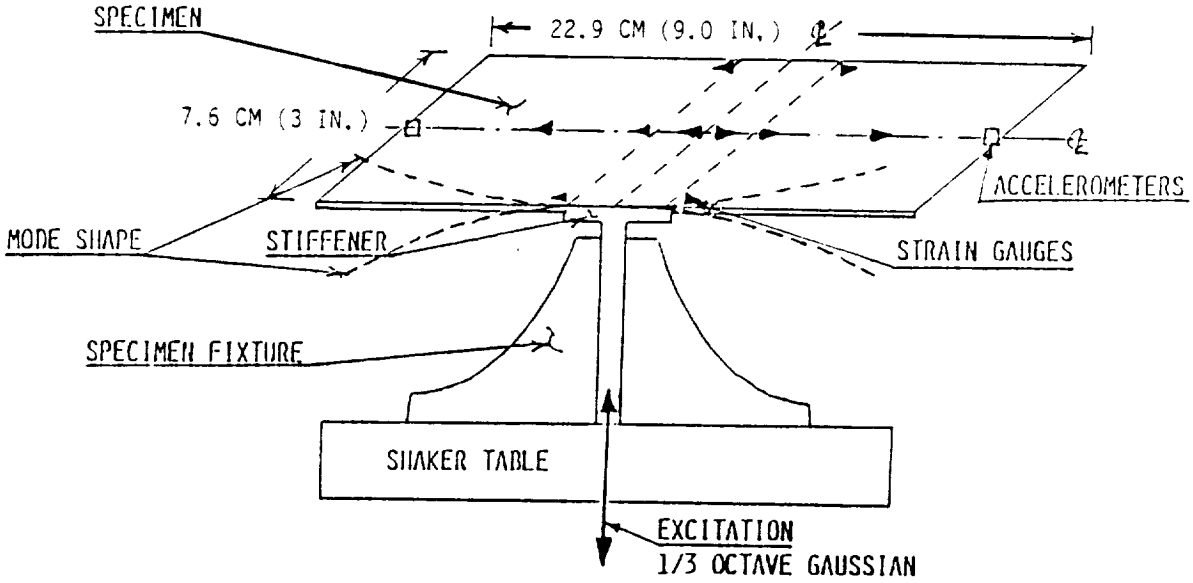
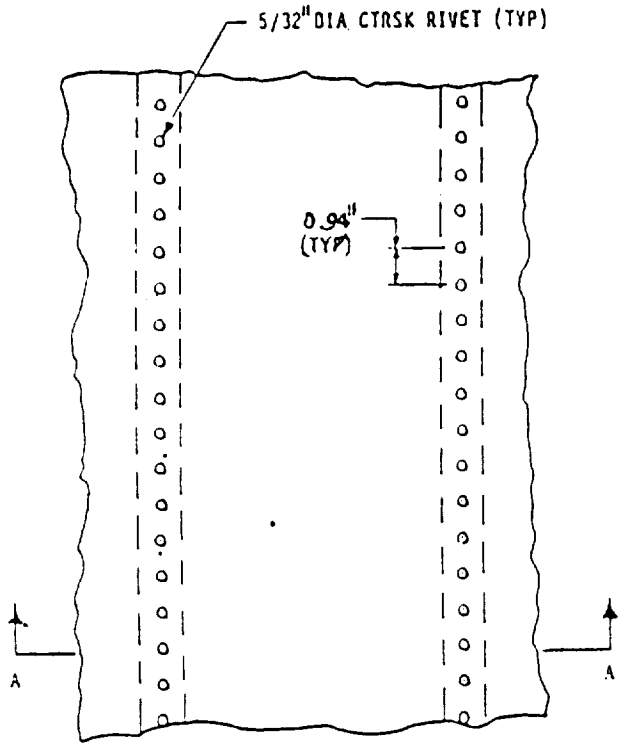
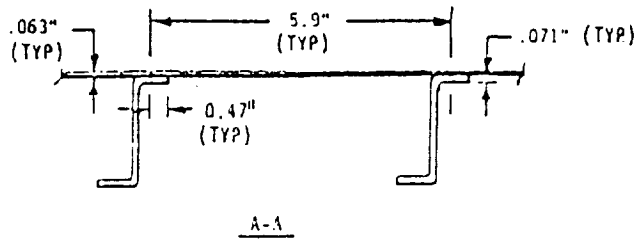


Figure 215. Test Specimen and Instrumentation

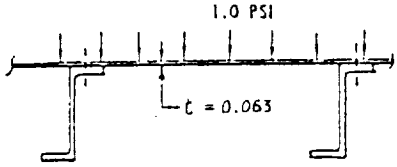
C - 4





- o FLAT ALUMINUM PANEL - 2024
- o ASSUME CLAMPED EDGES
- o $E = 10^7$ PSI, $I = 2.18 \times 10^{-5}$ IN.^{4}
- o $M = 1.63 \times 10^{-5}$ LBS-SEC^2/IN., $L = 5.9$ IN.
- o $f_n = \frac{22.4}{2\pi}\sqrt{\frac{EI}{ML^4}} = 374$ Hz
- o PROP 2ND ORDER BLADE-PASSAGE RANGE - 340 Hz to 475 Hz
- o CONCLUSION - STRUCTURAL RESONANCE AND FREQUENCIES CAN COINCIDE

Figure 216. Typical Large-Bay Skin Panel



UNIT STRESS

$\sigma_o = K_o\left(\frac{b}{t}\right)^2$ (FROM AFFDL-TR-74-112)

$K_o = .5$ (ASPECT RATIO > 2)

$b = 5.9$ IN. $t = .063$ IN.

$\sigma_o = 4385 \frac{PSI}{PSI}$

ACOUSTIC ENVIRONMENT

SPL = 136 dB $P = 0.01834$ PSI_{RMS}

DYNAMIC AMPLIFICATION

(RESONANT RESPONSE ASSUMED)

$Q = \frac{1}{2C/C_c} = \frac{1}{2(.02)} = 25$

DYNAMIC STRESS

$\sigma_{RMS} = \sigma_o \; Q \; P$

$\sigma_{RMS} = 2011$ PSI_{RMS}

ALLOWABLE STRESS

STATIC SHEAR STRESS IN SKIN IS 6KSI (MAX) AND ASSUMED TO BE IN DIRECTION OF MAX DYNAMIC STRESS, WHEREBY

$\sigma_{ALLOW\ @\ 6KSI} = 4000$ PSI_{RMS}

MARGIN

$M.S. = 20 \log_{10}\left(\frac{\sigma\ ALLOW}{\sigma\ ACTUAL}\right)$

M.S. = +6.0 dB

Figure 217. Skin Panel Sonic Fatigue Analysis Example

STRUCTURE	MARGIN
FWD SIDE PANELS	+8.6dB
FWD TOP PANEL	+3.2dB
MID/AFT SIDE PANELS	+8.6dB
TAILPIPE ACCESS DOOR	+1.1dB
LOWER FWD ACCESS DOOR	+0.7dB
SPILL SHIELD	+3.8dB
HEAT SHIELD	+0.2dB

Figure 218. Aft Nacelle Sonic Fatigue Analysis Conclusions

5.6 SAFETY ANALYSES

Product and system safety was "life-cycle" from the proposal to delivery of the PTA testbed aircraft to NASA-LeRC. System safety functions included:

- o Establishing safety criteria
- o Identifying program safety hazards
- o Assessing safety risks
- o Recommending cost-effective courses of action
- o Tracking results

5.6.1 Failure Modes and Effects Analysis

The failure mode, effects, and criticality analysis (FMECA) is one of three key reliability tasks which contributed to the achievement of PTA program objectives, namely: FMECA on PTA-unique and GII modified items; use of a closed-loop failure reporting, analysis, and corrective action system (FRACAS); and qualitative establishment of reliability through analysis and testing. The FRACAS and reliability tracking were incorporated into the PTA Program by adopting a company procedure which is used to collect information, analyze, and report on failures occurring during PTA testing. The testing program was designed, in part, to acquire experience to evaluate the reliability in areas where risks were identified.

A single FMECA analysis was conducted for both the aircraft design modifications and the propfan propulsion system. The analysis included a systematic evaluation of possible failures on a case-by-case basis, the ways that an item can fail, the causes for each failure mode, the effects of each failure, and the criticality of each effect on system safety and program objectives. The primary objective of the PTA FMECA was to identify the critical single point failure areas associated with the propfan propulsion system and aircraft modification designs. The FMECA includes:

- o Part description
- o Failure modes and causes
- o Failure detection
- o Failure effect on system
- o Failure criticality
- o Pertinent remarks

The criticality definitions used for the PTA Program were as follows:

Category	Personnel	Property And/Or System	Flight Test Program Objectives
I (Catastrophic)	Death	System Loss	Jeopardize Achievement
II (Critical)	Severe Injury	Major Damage	Major Schedule Delay
III (Marginal)	Minor Injury	Minor Damage	Minor Delay
IV (Minor)	None	None	Unscheduled Maintenance or Repair

Of a total of 370 failure modes that were postulated, 8 were Category I failures and 23 were Category II failures. Six of the Category I failures resulted from instant decoupling of the propfan from the power turbine at high rpm/power. The turbine was assumed to overspeed to failure, with the fourth stage airfoils failing at 178% rpm, although predictions indicate that the governor system could cut off fuel in time to prevent overspeed to failure. The PTA nacelle containment ring would contain all failures except a one-third disc at well above the maximum governed rpm. Two Category I failures involved loss/separation of the propfan resulting from the loss of propfan blade, although the blade construction was such that only a portion of a blade would probably be lost in any operational incident.

5.6.2 Safety Analysis

System safety was integrated into the management, design, review, and test tasks of the program. Real-time safety input allowed for determination of optimized courses of action, which led to an accident-free program. The safety analysis was documented in three contractual reports (References 16 through 18).

In addition, non-hazard assessments were conducted for:

- Flight test formation flying requirements
- Fuselage shield requirements
- Cockpit/radio functional switches
- Emergency egress requirements

Of the 556 potential safety hazards identified, all were closed with a "medium" or lower risk level, using the severity-versus-probability risk assessment matrix shown in Figure 219 as a guide. Overall program safety risk was evaluated as "medium-low." A sample of a computerized safety tracking log which facilitated real-time review of status for each hazard is shown in Appendix E.

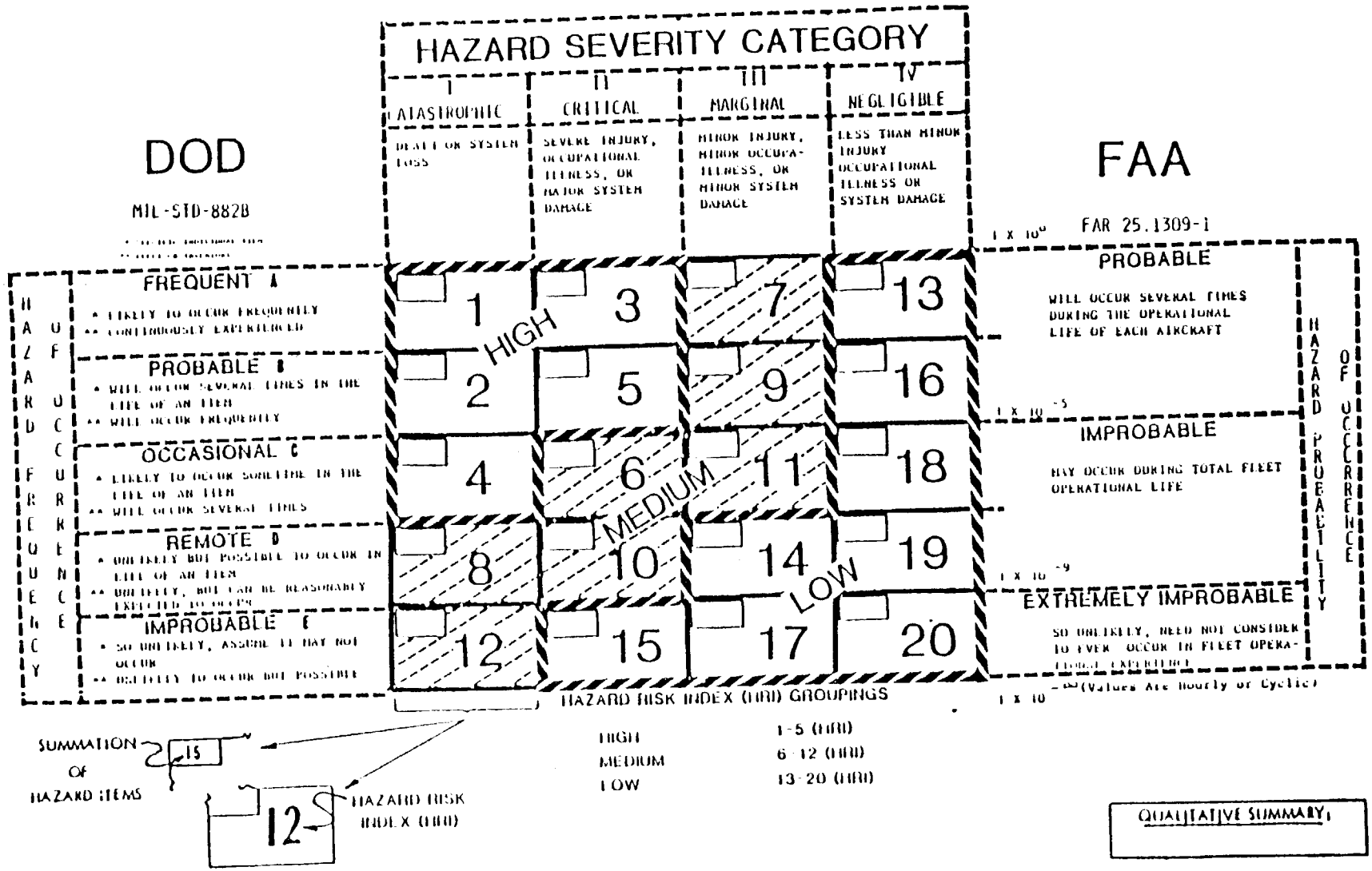


Figure 219. Risk Assessment Matrix

ORIGINAL PAGE IS
OF POOR QUALITY

A System Safety Integration Group (SSIG), chaired by Lockheed, provided for integration of all safety-related data for all sources into the program Hazard Analysis series of reports. Systems safety specialists assisted in preparation for, and participated in, all preliminary and detail design reviews, test readiness reviews, yearly reviews, and NASA and Lockheed reviews prior to first flight.

Product and System Safety personnel participated in each PTA test flight, including pre- and post-flight briefings. Flight test failure events were investigated, coordinated, and reported by Product and System Safety personnel. All such events were categorized as "NASA Incident" damage or lower.

6.0 PROPFAN PROPULSION SYSTEM STATIC TEST

The Propfan Propulsion System Static Tests are described in detail in Reference 21. Highlights from these tests are presented herein.

6.1 TEST OBJECTIVES

The goals of the propfan propulsion system static test were to qualify and obtain baseline data for the propulsion system, including its related subsystems, under static conditions prior to the start of the Propfan Test Assessment (PTA) flight test program. In order to fulfill these goals, the specific objectives of the propulsion system static test program were to:

- Functionally check out the propfan propulsion system
- Substantiate the structural integrity of the propfan
- Verify safe and stable operation of the propfan propulsion system
- Functionally check out operational and research instrumentation
- Define propfan and drive system static noise characteristics
- Obtain drive system baseline vibration data
- Verify drive system sea level performance
- Evaluate modified propfan blade seal
- Verify system endurance capability at static conditions by completing simulated flight cycles

6.2 TEST HARDWARE AND FACILITY DESCRIPTION

6.2.1 Test Assembly

The test assembly (Figure 220) consisted of the Hamilton Standard SR-7L propfan, the Allison Model 501-M78B drive system, the Rohr quick engine change (QEC) nacelle, and related subsystems. The aft nacelle was not installed for the static tests.

The acoustically treated engine tailpipe was designed to be installed into and mated with the attachment fittings in the aft nacelle, but since the aft nacelle was not used during static test, the tailpipe was attached directly to the test stand. The tailpipe was designed to provide for 15 dB exhaust system noise suppression throughout the engine combustor frequency spectrum.

6.2.2 Control System

The propulsion system functions for the static test were controlled and monitored at the same control console and instrument panel (Figure 21) that would later be used in the aircraft flight station.

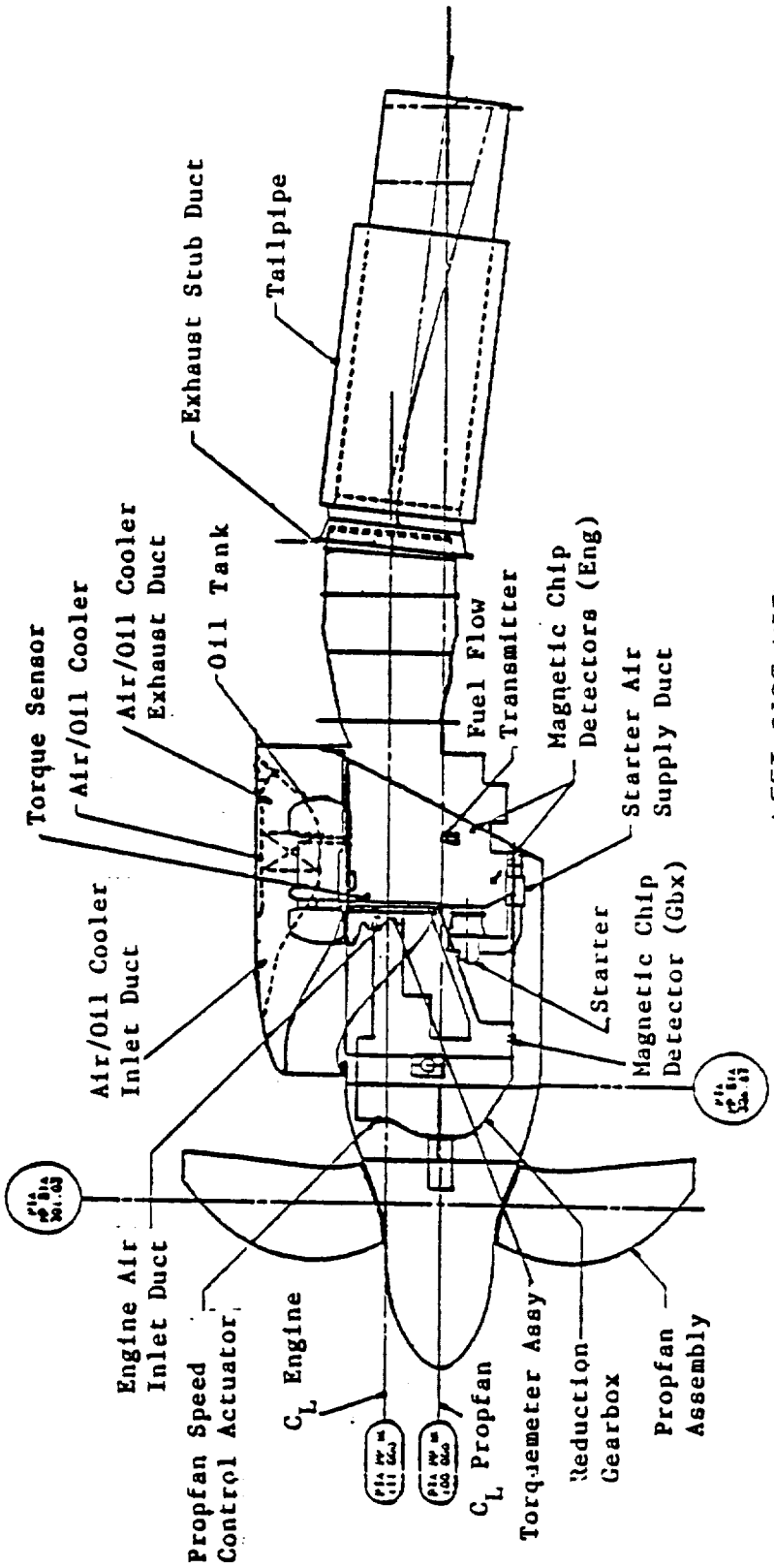


Figure 220. Propfan Propulsion System Static Test Assembly

The control console contained the switches and levers for engine starting and normal shutdown, emergency shutdown, engine power, prop speed, and prop feather and unfeather. The results of the actions taken on the control console were displayed as performance or engine health parameters on the instrument panel.

Power, which is a function of power turbine (prop) speed (N_p) and torque, was controlled by both the prop speed control lever and the power control lever and monitored on the N_p and torque indicators.

6.2.3 Test Limits

6.2.3.1 Engine Limits

During the static test, the engine was operated within the limits specified in the Allison 501-M78B Model Specification. These limits are summarized in the following table:

501-M78B ENGINE MAXIMUM LIMITS

	Maximum Continuous		Transient	
Speed, rpm (%)				
Gas Generator	14,300	(100)	14,700	(102.8)
Power Turbine	12,075	(105)	12,535	(109)
Gearbox	1,777	(105)	1,844	(109)
Temperature, °C (°F)				
Compressor Inlet	39	(103)	39	(103)
Power Turbine Inlet (Starting)	677	(1250)	677	(1250)
Power Turbine Inlet (Operating)	808	(1486)	846	(1555)
Torque, N-m (ft-lb)	4,972	(3667)	4,972	(3667)
Vibration, cm/sec (in./sec)				
15-40 Hertz	2.54	(1.00)	3.81	(1.5)
150-250 Hertz	1.91	(0.75)	3.05	(1.2)
Power, kw (shp)	3,729	(5000)	4,474	(6000)
Oil Inlet Temperature, °C (°F)				
Above Flight Idle	85	(185)	100	(212)
Flight Idle or Below (30 Minute Limit)	100	(212)		

In addition to the above limits, an effort was made to avoid operation below 475 N-m (350 ft-lb) torque, which was the approximate torque load required to prevent the reduction gearbox main drive gear roller bearing from skidding. Low power turbine speed running (below approximately 50-percent N_p) was also avoided, since that condition could have resulted in lower than recommended gearbox oil pressures.

6.2.3.2 Propfan Limits

Due to stall buffet conditions discovered in LAP static rotor testing at Wright-Patterson AFB, during endurance tests, propulsion system limitations were established as shown in Figure 221. The operating envelope high-and-low torque limits at any rotational speed are established by the onset of buffet and the occurence of low pressure stall respectively.

6.2.3.3 Temperature Limits

During static testing, thermocouples were applied to the engine surfaces and QEC nacelle structure to monitor surface and ambient temperatures and insure that limits were not exceeded. The maximum allowable air temperature surrounding the engine forward of the vertical firewall was 121°C (250°F) while the engine was running and 135°C (275°F) while the engine was not operating. Aft of the vertical firewall, the limit was 371°C (700°F) whether the engine was operating or not. The limit temperatures for components are shown below:

LIMITING COMPONENT SURFACE TEMPERATURES, °C (°F)

Component	Minimum	Maximum
Hydromechanical Fuel Control	-55 (-67)	120 (248)
Fuel Pump	-54 (-67)	121 (250)
Electronic Engine Control	-55 (-67)	125 (257)
Ignition Exciters	-54 (-67)	121 (250)
Prop Speed Control Actuator	-54 (-67)	121 (250)

6.3 TEST FACILITY

The test site facility, as shown in Figure 222, consisted of a 30,350 m² (7-1/2 acre) fenced area situated within a 42,500 m² (10.5 acre) plot located at Brown Field Airport in Chula Vista, California. The prevailing wind conditions (speed and direction), mild temperatures, and near sea level elevation of the site provided a high percentage of run windows with minimal data corrections. The test site was located in an area that was virtually flat with no obstructions for at least 1.6 km (1 mile) in any direction, thus making the site ideally suited for acquiring engine noise data.

Test stand operation was controlled and monitored from a soundproof control building equipped with an engine control station. The control room was environmentally conditioned to provide temperature and humidity stability for instrumentation systems, thus ensuring satisfactory data accuracies and instrument reliability.

The PTA propulsion system was mounted on the B-60 test stand which provided an overhead structure mounting arrangement as shown in Figure 223. The single component thrust system measured operating performance of

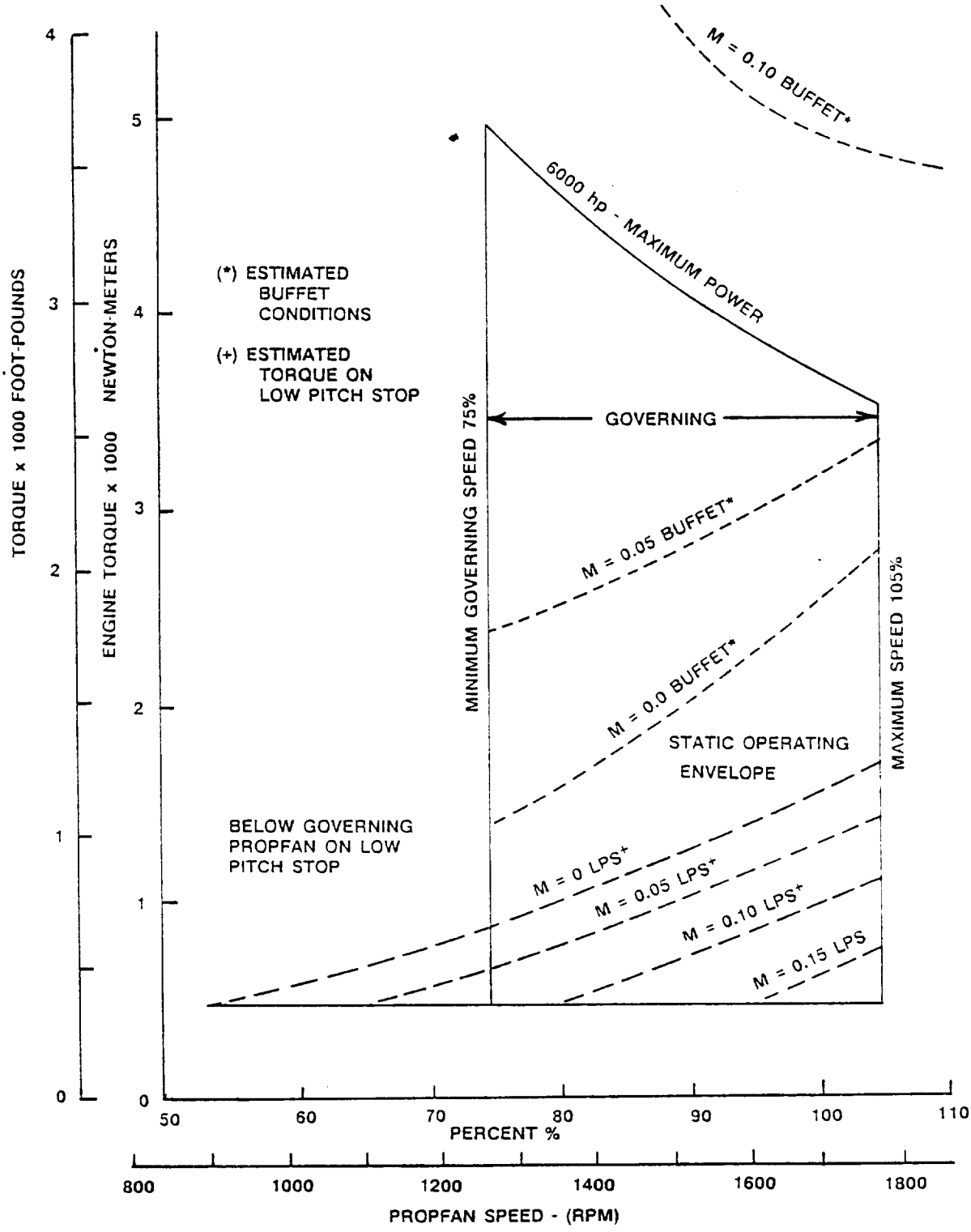


Figure 221 Propfan Operating Limits

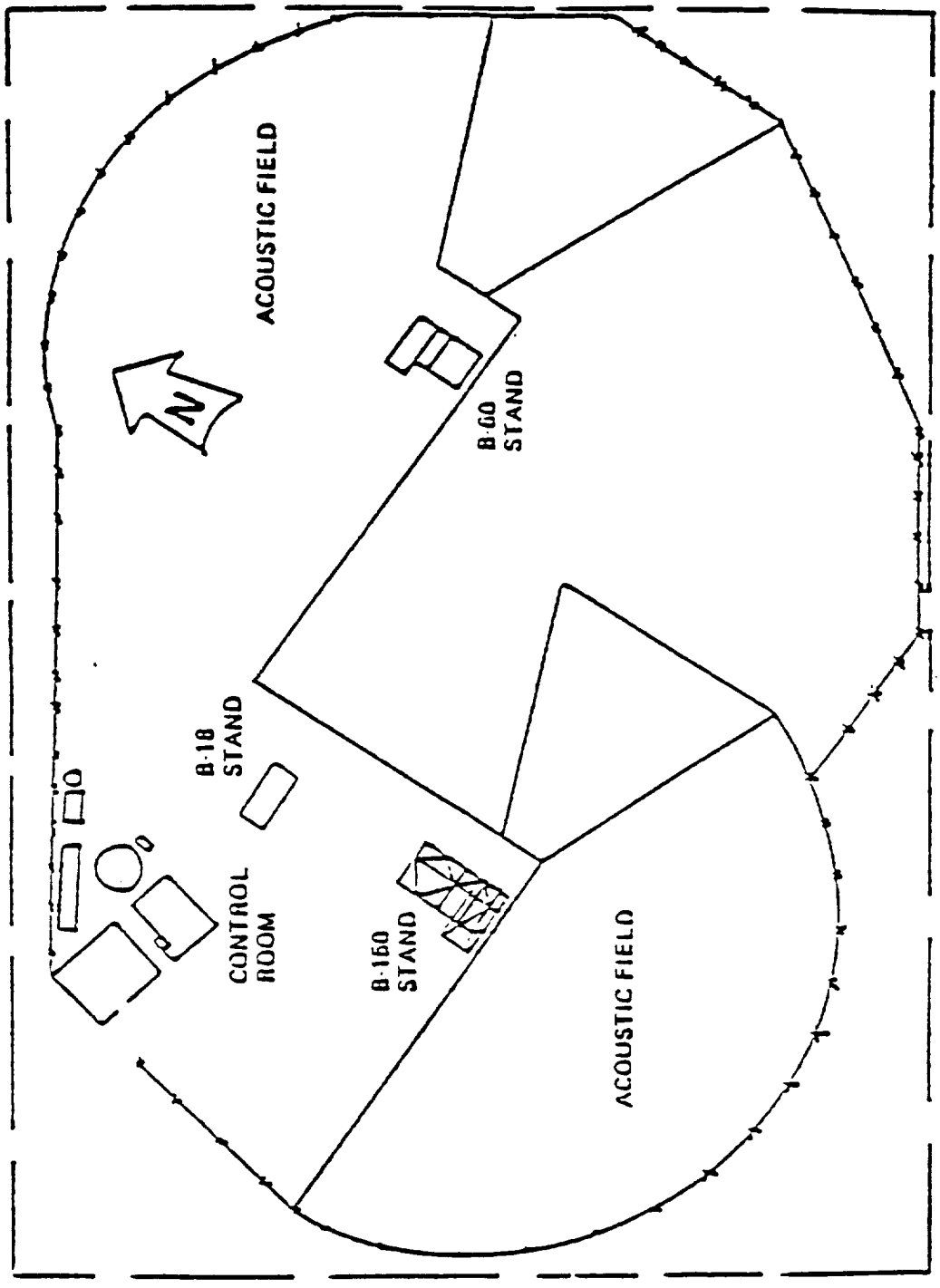


Figure 222. Rohr Brown Field Test Facility

ORIGINAL PAGE
BLACK AND WHITE PHOTOGRAPH



Figure 223. PTA Propulsion System on Rohr Test Stand

aircraft turbine engines rated up to and including 267 kN (60,000 lb) thrust. The thrust bed was designed to provide systems accuracies of ±0.1 percent of the rated capacity of the installed thrust load measurement string over the temperature range of 21°C ±17°C (70°F ±30°F).

Acoustic data were gathered in a smooth concrete sound measurement field on and to the right of the propfan propulsion system centerline as shown Figure 224. The field was defined by a 180-degree arc of 45.3m (150 ft) radius about the microphone reference point. This reference point was a defined location on the ground below the engine centerline approximately 2.74m (9 ft) aft of the propfan disc.

Some of the acoustic data were obtained with an acoustic barrier erected alongside the propulsion system in order to separate propulsion system noise from propfan noise. Barrier positions are shown in Figures 225 and 226.

Microphones were positioned at 19 locations in the far field and 7 locations in the near field. Figure 224 defines the locations according to azimuth angle and distance from the microphone reference point.

All 7 near-field and 18 of the far-field microphones (Number 19 was removed) were in place during acoustic testing without the acoustic barrier. During testing with the acoustic barrier in position, the near-field microphones and poles were removed. When the barrier was placed in the forward position, the microphones at 70 degrees through 110 degrees sensed discharge noise while propfan noise was partially blocked. With the barrier in the aft position, the microphones at 100 degrees through 130 degrees sensed propfan noise while discharge noise was partially blocked.

6.4 INSTRUMENTATION

6.4.1 Propfan

Transducers installed on the propfan included strain gages to measure vibratory strain in the blade structure, pressure transducers to measure the actuator high and low pitch pressures, a potentiometer to measure the blade pitch angle, and a 1P sensor for measuring the propfan rotational speed. A flow switch was also located in the stationary propfan pitch control to warn if a hydraulic pump failure occurred.

The instrumentation system allowed for up to 10 strain gages to be installed on each blade, though a maximum of 30 gages were active at any one time. Sixteen active gages could be selected from Blades 1 through 4, and an additional 16 could be selected from Blades 5 through 8. Selection of the desired combination of strain gages was accomplished using eight programmable connectors mounted on the propfan hub. Programming of the connectors required jumper wires to connect the sockets of patch boards in the connectors. The gage locations are shown in Figure 227, and the active gages are indicated. The inactive gages were positioned to be used as backups in the event of primary gage failure. The strain gage pairs on

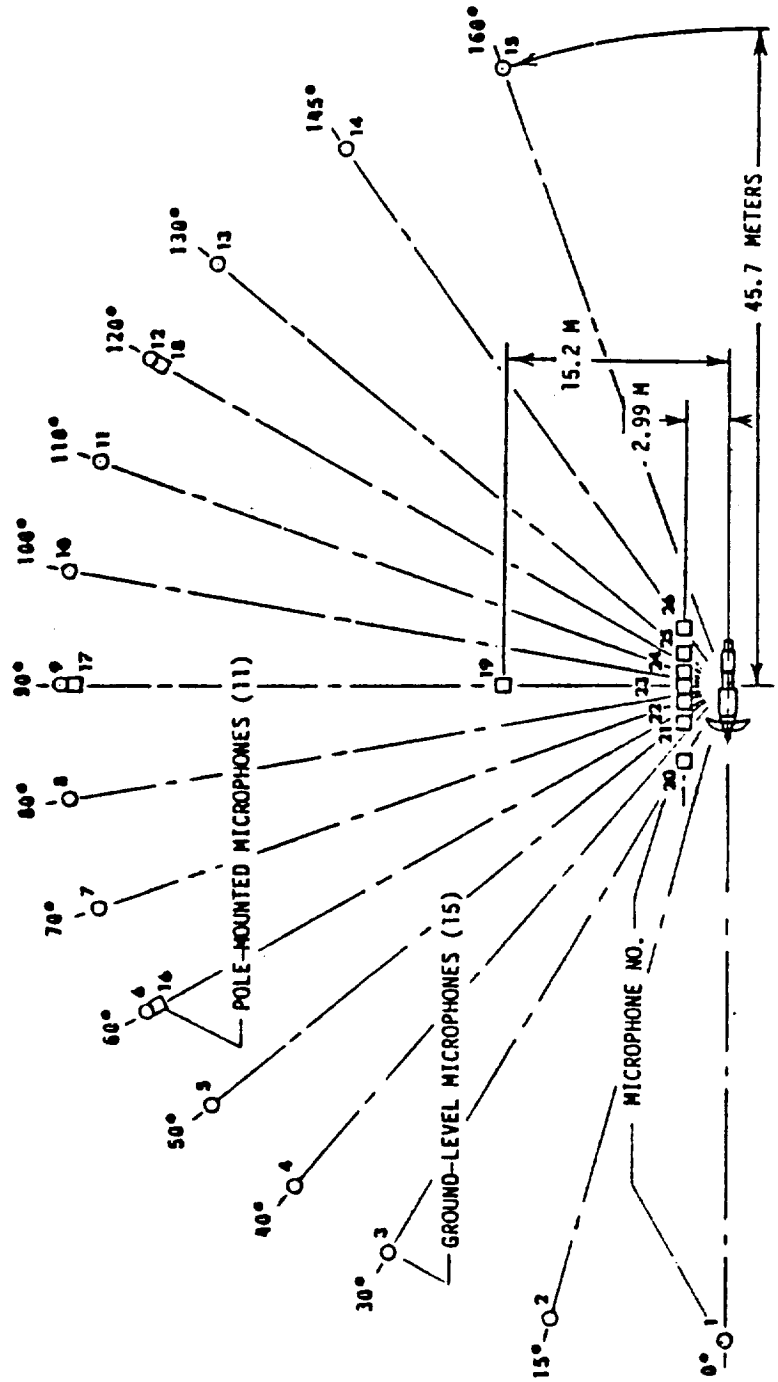


Figure 224. Acoustic Data Field

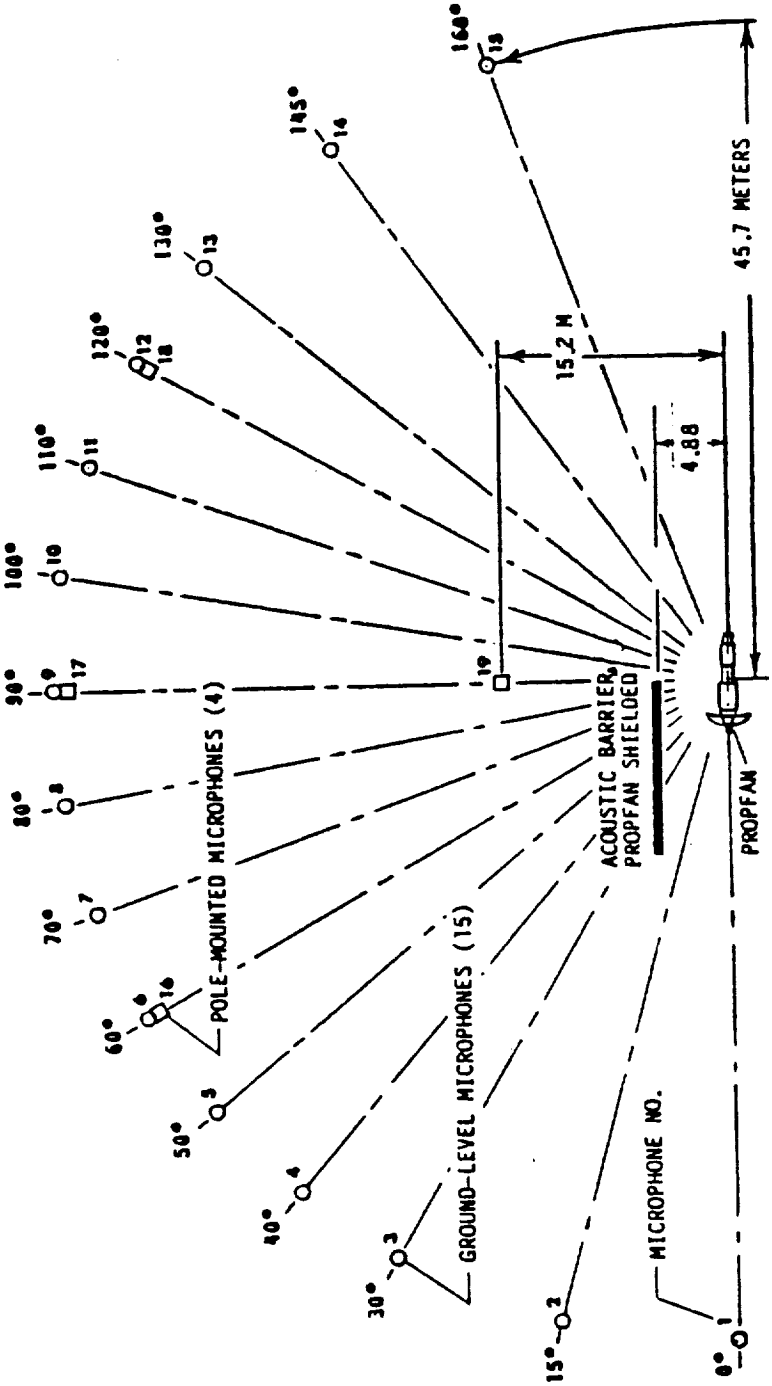


Figure 225. Acoustic Data Field with Barrier in Forward Position

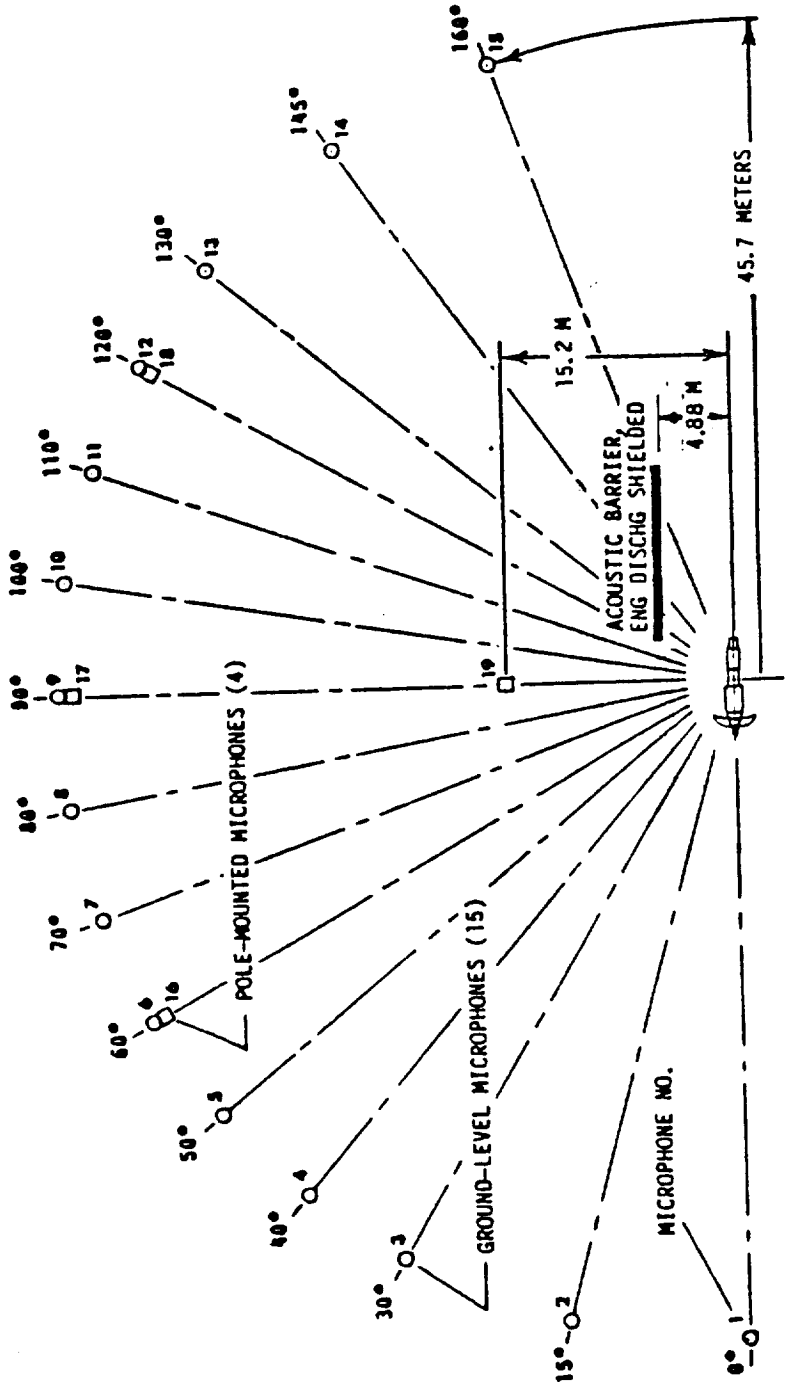
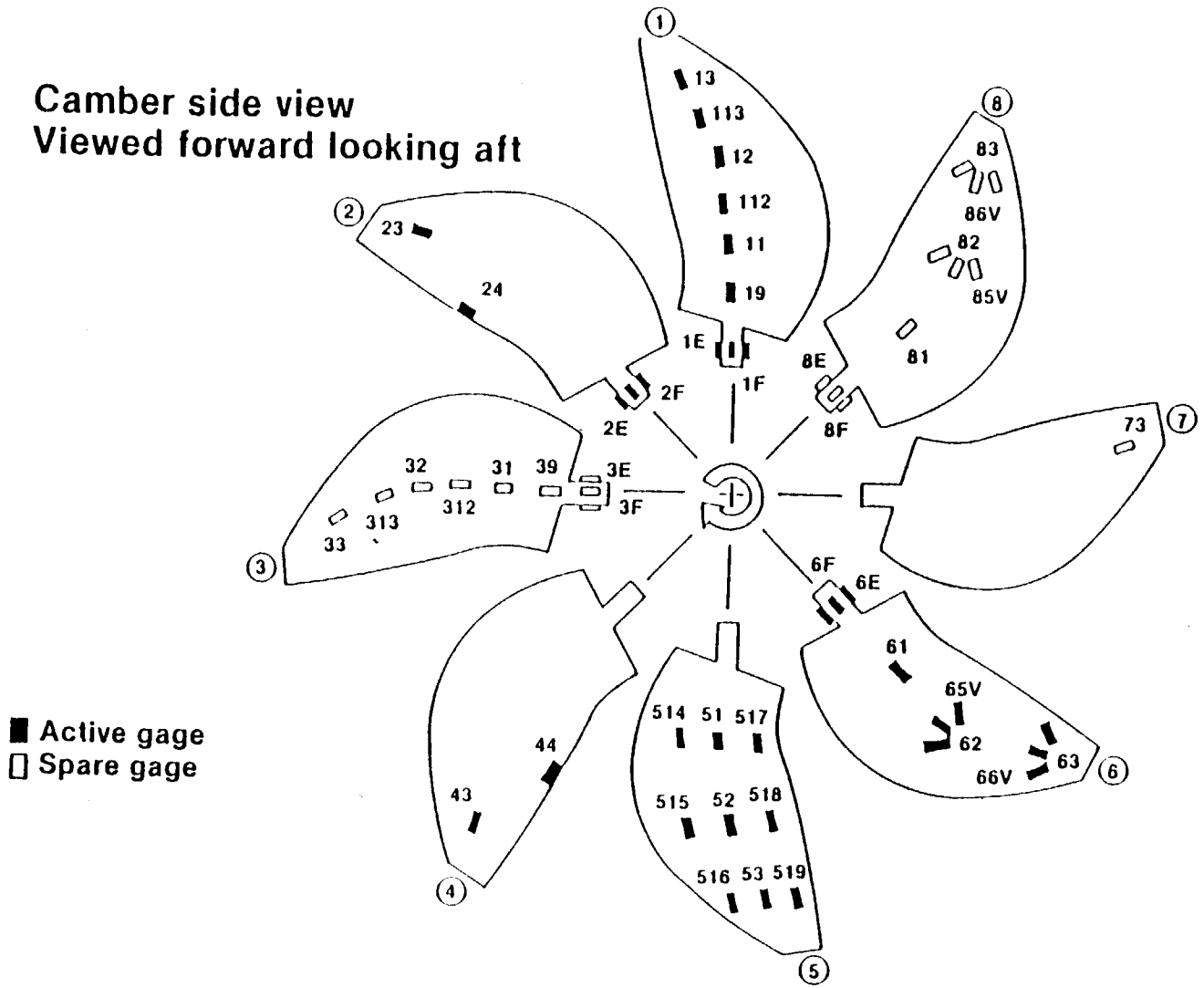
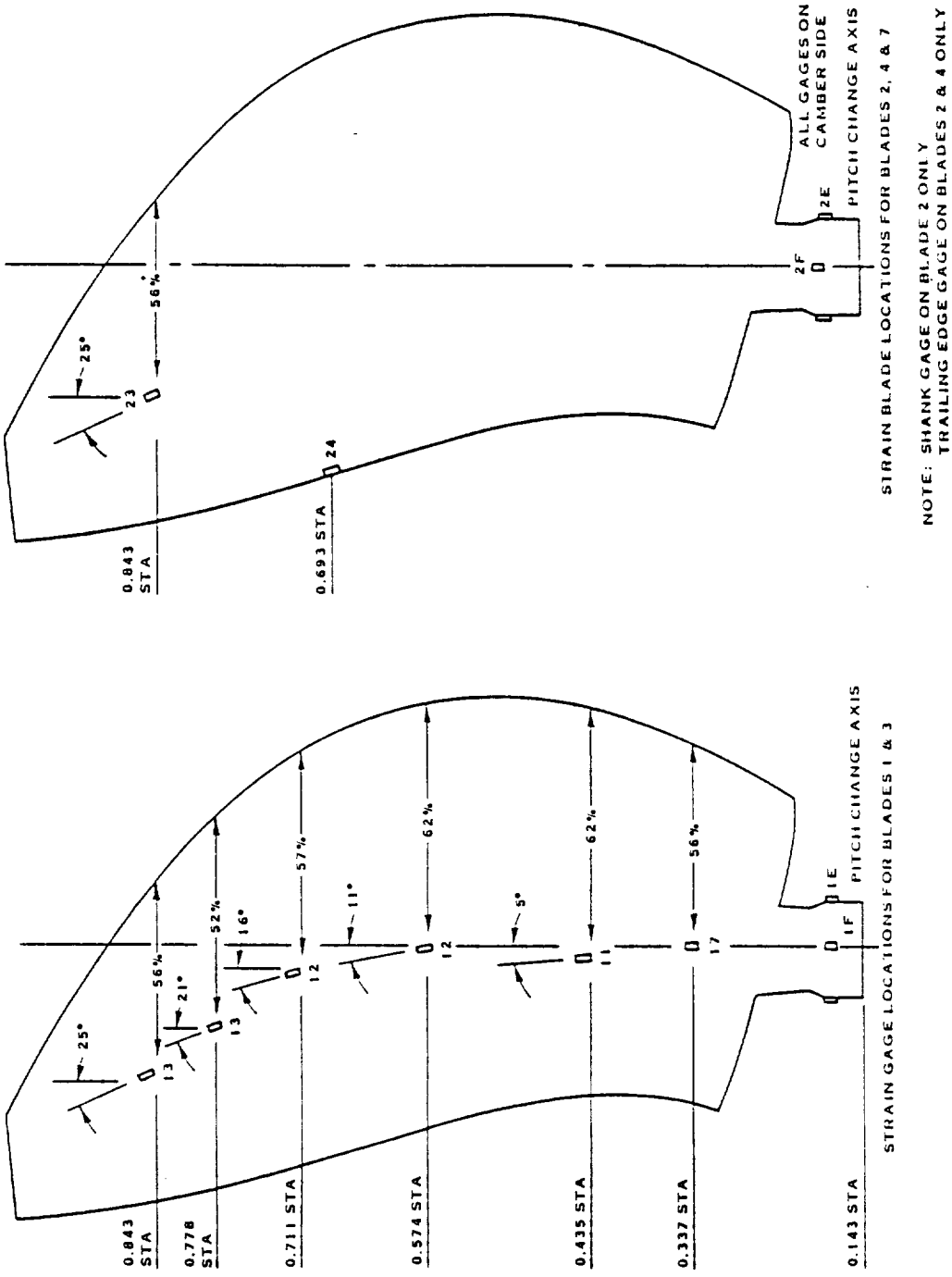


Figure 226. Acoustic Data Field with Barrier in Aft Position



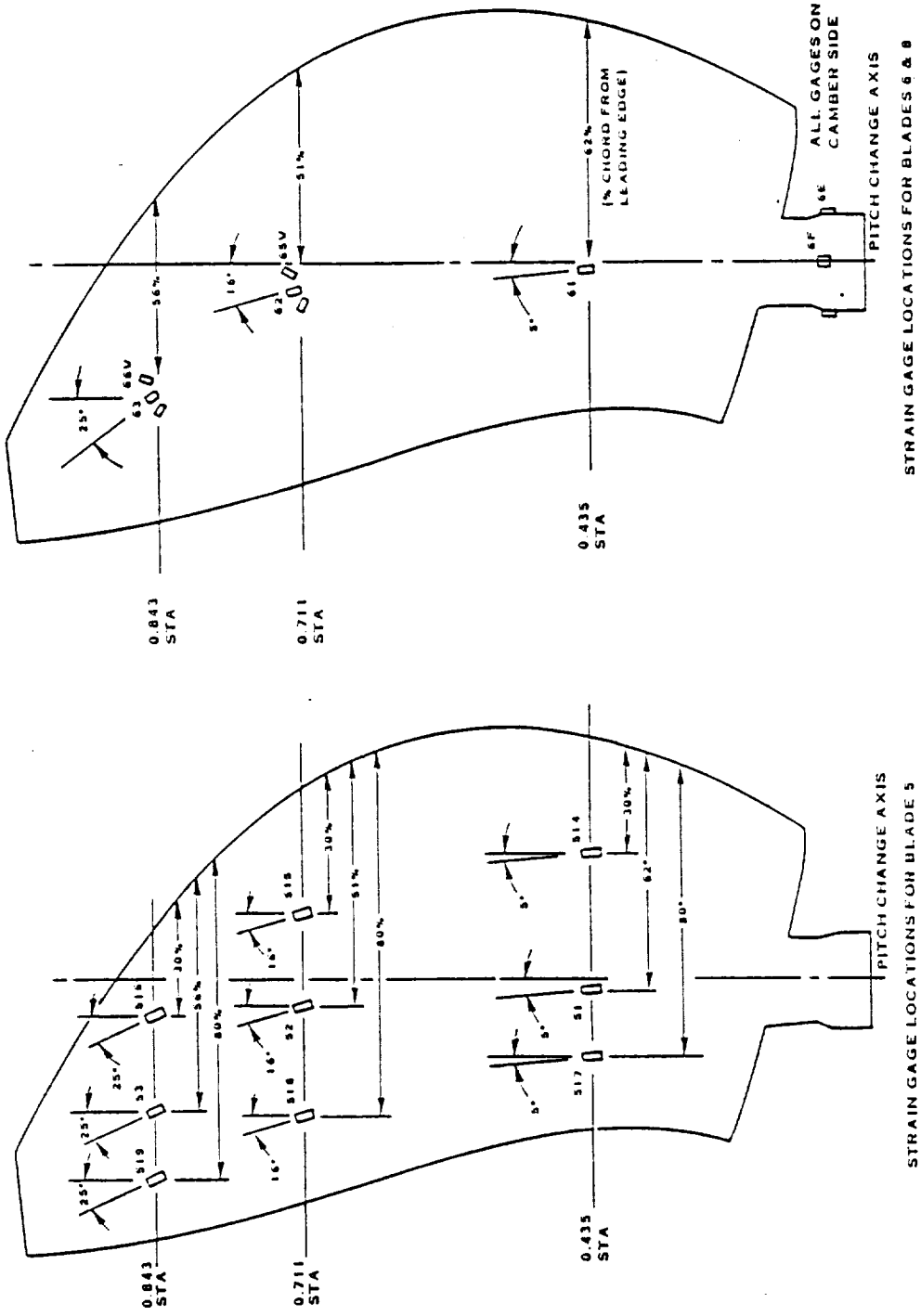
(a) INSTRUMENTATION DISTRIBUTION ON ROTOR

Figure 227. Propfan Blade Strain Gages



(b) STRAIN GAGE LOCATIONS ON BLADES 1, 2, 3, 4, & 7

Figure 227. Propfan Blade Strain Gages (Continued)



(c) STRAIN GAGE LOCATIONS ON BLADES 5, 6 & 8

Figure 227. Propfan Blade Strain Gages (Continued)

the blade shanks and vee shear pairs on the blade aerodynamic surfaces were wired to act as one gage.

Data from the propfan instrumentation was recorded on a 14-track IRIG tape recorder. Real time monitoring of data was accomplished using two, 4-channel oscilloscopes and a spectrum analyzer. The oscilloscope provided a time domain display of eight channels simultaneously. The spectrum analyzer provided a frequency domain display of one channel at a time.

6.4.2 Drive System and Nacelle

The data parameters measured on the drive system during static testing were divided into two groups: operational and research instrumentation. Operational instrumentation parameters were those which related directly to drive system health or were required by the engine operator to set a specific test point. Research instrumentation consisted of those parameters which were used for eventual processing and analysis of test results.

6.4.3 Acoustics

The principal elements of the acoustic test instrumentation were the microphones, the amplifiers, and the tape recorder. The 26 microphones, located at the angles and positions illustrated in Figure 224, were 1.27 cm (1/2 in.) diameter condenser microphones with companion preamplifiers. The microphone signals were routed into 26 acoustic amplifiers having selectable fixed-gain settings covering a 60 dB range. The conditioned signals were then routed to a 28-track FM tape recorder.

The propfan speed/phase signal (1P) was also recorded on the acoustic data tape.

6.4.4 Ambient Conditions and Facility Data

The Brown Field Test Facility had the capability of measuring ambient conditions, such as ambient pressure and temperature, relative humidity, and wind speed and direction, as well as some engine performance parameters such as gross thrust, fuel flow, fuel inlet temperature, and specific gravity.

The measurement of gross thrust was accomplished by a dual bridge strain gage type load cell located on the thrust bed of the engine.

6.5 TEST PROCEDURES AND RESULTS

During static testing at Rohr, the propfan propulsion system was operated for over 50 hours in 45 test runs. The first 27 runs were primarily devoted to propfan balancing, checkout, and demonstration. The next 17 runs were primarily endurance and acoustics runs, and a reverse thrust test was completed on the last run.

The choice of test points for the static test was constrained by operating limitations of the propfan, the gas turbine engine, and the reduction gearbox. The operating envelope for the endurance test phase is illustrated in Figure 228. The lower limit of the operating envelope is determined by a minimum 475 N-m (350 ft-lb) engine torque to prevent skidding of the reduction gearbox main drive bearing. A minimum power turbine/propfan rpm of 53 percent of design speed was required to provide sufficient oil flow to the reduction gear surfaces for continuous operation. A maximum power turbine/propfan speed of 105 percent was determined by the propfan governing range. The power turbine/propfan 100-percent speed is defined as 11,500 power turbine rpm, or 1692 propfan rpm. The upper boundary of the operating envelope was based on blade vibratory stress restrictions determined during the propfan stress survey.

6.5.1 Functional Checkout

The engine dry motor functional check was conducted by following the normal engine start procedure except that the test stand fuel valve remained closed and the fuel pump remained off. The wet motor was performed with the fuel supply on, but the circuit breaker to the engine ignitors was pulled. The engine was then started and run at idle to check the engine/propfan compatibility.

The engine air turbine starter performed satisfactorily, with recorded start times in the 15- to 25-second range. These start times compare favorably with the estimated time of 20 seconds for a 21°C (70°F) day. No hot starts (transient MGT exceeding limit) or "hung" starts (failure to accelerate to idle) were encountered during the static test phase. The engine progressed through its pre-fire acceleration, ignition, and post-light acceleration events to idle as predicted.

Five different shutdown checks were performed.

- Normal shutdown (run/stop switch)
- Manual fuel shutdown
- Simulated engine overspeed shutdown
- Loss of electrical power shutdown
- Fire handle shutdown

All were satisfactory.

6.5.2 Propfan Balancing

Dynamic balancing of the propfan and specialized rotating instrumentation were required to attain acceptable vibration levels over the entire operating speed range. Balancing was conducted using data collected from the gearbox horizontal (V_5) and vertical (V_1) accelerometers. Data from accelerometers located on the gas turbine were also recorded during balancing procedure. The unfiltered signals from the gearbox accelerometers were analyzed by a trim balancer, which determined the 1P amplitude and phase of the vibratory response. Vibration data were collected at

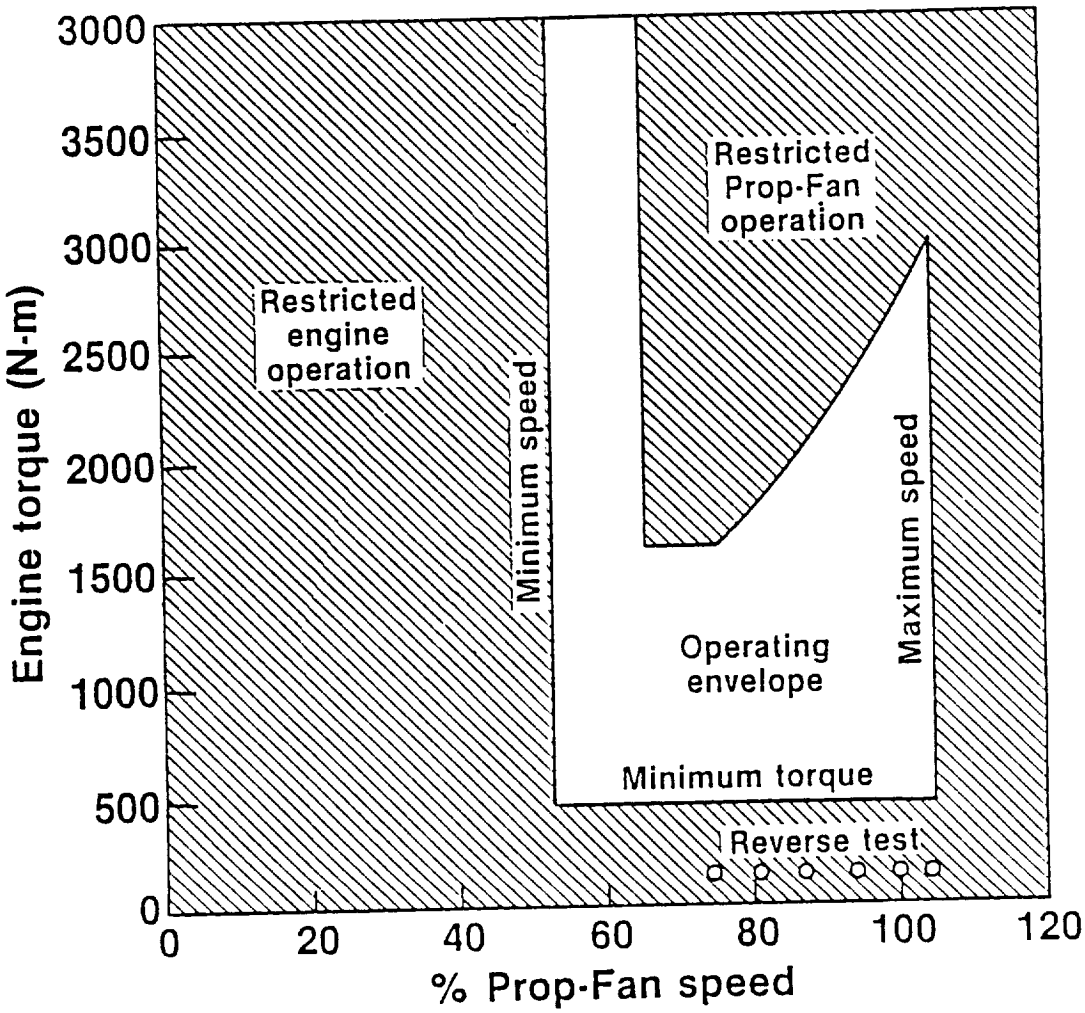


Figure 228. Static Engine Test Operating Limits

55 percent, 75 percent, 81 percent, 88 percent, and 94 percent speed for the base propfan, and with a trial weight of 74 grams added to the forward balance ring at a radius of 20.87 cm (8.125 in.). The change in 1P amplitude and phase angle caused by the trial weight were noted for each rotational speed. The mass and orientation of the weight required to balance the propfan was determined using a single plane balancing calculation.

Balancing of the propfan was accomplished by the addition of 147 grams to the forward balance ring at a 20.87 cm (8.125 in.) blade radius. Once balancing was accomplished, vibration levels were independent of blade angle for a constant rpm. No additional balancing of the propfan was required throughout the duration of static tests. Replacement of components on the rotating portion of the propfan and changing the low pitch stop setting did not adversely affect the balance.

6.5.3 Low Power Governing Check

The low power governing test consisted of selecting set point speeds of 75 percent, 87.5 percent, 100 percent, and 105 percent on the propfan speed control lever, then slowly increasing power until the propfan began to govern. Governing was indicated by the blade pitch angle lifting off the low pitch stop and rpm remaining constant with increasing power. The low pitch stop was set at 20 degrees for these runs. If governing did not commence at the set point speed, the control speed trim adjustment on the propfan was employed to fix the governing speed at the correct value. Speed trim adjustment continued until the desired governing range of 75 percent to 105 percent of the design speed was achieved.

During the low power governing check, the preload of the servo governor speeder spring was altered using the speed trim adjustment to achieve the desired governing range of 75 percent to 105 percent of the propfan design speed. Three engine runs were required to adjust the servo governor to obtain this range. These tests verified that the desired governing range could be attained with the available travel on the propfan speed control input lever.

6.5.4 Stress Survey

The stress survey was conducted with the blade angle set by the low pitch stop and also with the propfan operating in a governing mode. Low pitch stop settings of 20 degrees and 35 degrees were employed during the stress survey. Below the minimum governing speed, the propfan operated on the low pitch stop setting. The 35-degree setting permitted high power test points to be run at rotational speeds below the minimum governing rpm. Testing on the low pitch stop was accomplished by setting the propfan speed control lever to 105 percent so that rotational speed was controlled by the application of engine power. During the governing portion of the stress survey, rotational speed was controlled with the propfan speed control lever, and power was controlled with the engine power lever. The blade angle was greater than the low pitch stop position during governing.

From the stress survey, 32 key conditions were selected for data analysis in terms of vibratory mean and infrequently repeating peak (IRP) strain. The mean vibratory strain is the average peak amplitude of a sample of strain gage data, while the IRP vibratory strain is a statistical value representing the mean strain plus two standard deviations of the data sample. The IRP vibratory strain is used to define the boundaries of the blade continuous operating envelope. Figure 229 shows the test conditions selected for analysis.

The SR-7L exhibited high blade tip vibratory response that limited torque at constant speed conditions as shown in Figure 230. For constant speed operation, the blade strain was relatively low until a critical torque condition was attained and the blade strain increased rapidly with increases in torque as occurred during earlier static tests of the LAP Program. The only difference between the PTA test results and the LAP test results was that higher torque could be absorbed at a given strain level as seen in Figure 230.

The relationship between strain and torque becomes apparent when blade angle is introduced as the key variable. Figure 231 shows that torque increased with increasing blade angle and that the rate of torque increase with blade angle changed in the 25- to 30-degree range. Also included in Figure 231 is a comparison of measured torque and blade angle for the LAP and PTA tests. In all cases higher torque was measured during PTA tests than during LAP tests for a given blade angle. The higher blade angles required during LAP tests account for the increased blade strain noted in Figure 230.

Using blade angle as the key parameter affecting blade strain, the data in Figure 230 and 231 is replotted versus blade angle in Figure 232. The strain increased rapidly when the blade angle was increased above 25 degrees for all torques and rotational speeds plotted. This relationship with blade angle was also found during LAP tests. One factor that Figure 232 does not show is that a relationship existed between blade strain and rotational speed. For low rotational speeds, below 59-percent N_p (1000 rpm), the blade vibratory tip strain was low.

At the 34.2-degree low pitch stop blade angle, the blade strain increased from a low level at low rotational speed to high levels at 83-percent N_p (1407 rpm) that prevented further increases in rotational speed. Increasing rotational speed at a constant blade angle had two effects that altered blade response. One was an increase in aerodynamic loads due to increased dynamic pressure and the second was a decrease in the local section reduced frequency. Both of these factors adversely affected blade response.

Figure 233 shows the relationship between rotational speed and blade strain at a high blade angle and the distribution of strain along the blade radius. Although the blade angle measurement system indicated the low pitch stop blade angle to be 34.2 degrees, the system had approximately a ±2-degree error. The low pitch stop was set at 35 degrees blade angle.

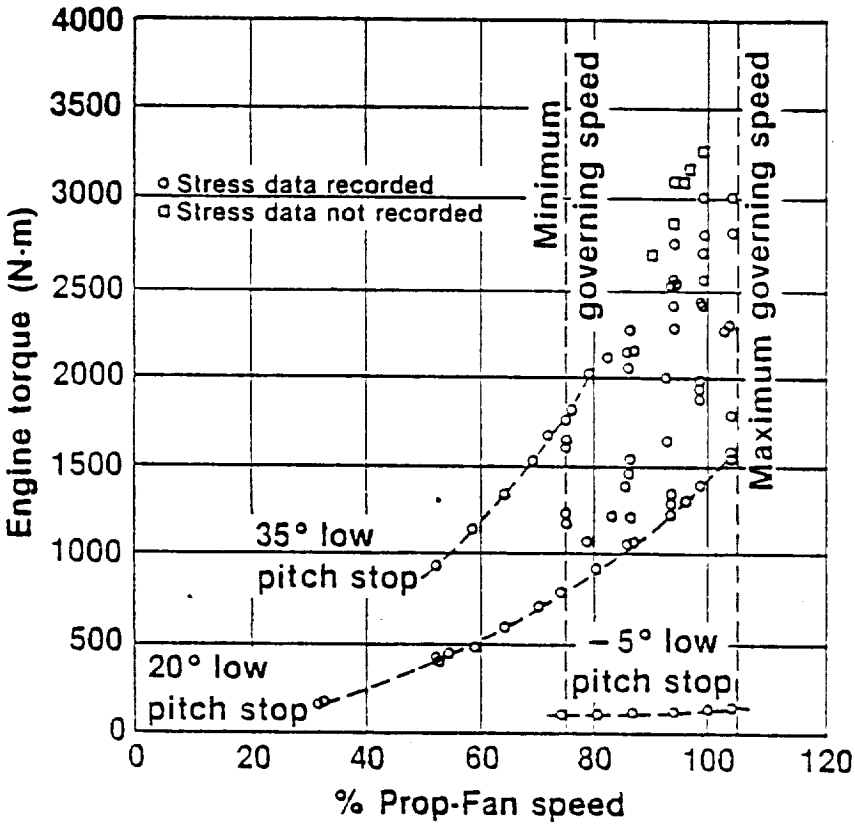


Figure 229. Stress Survey Conditions Selected for Data Analysis

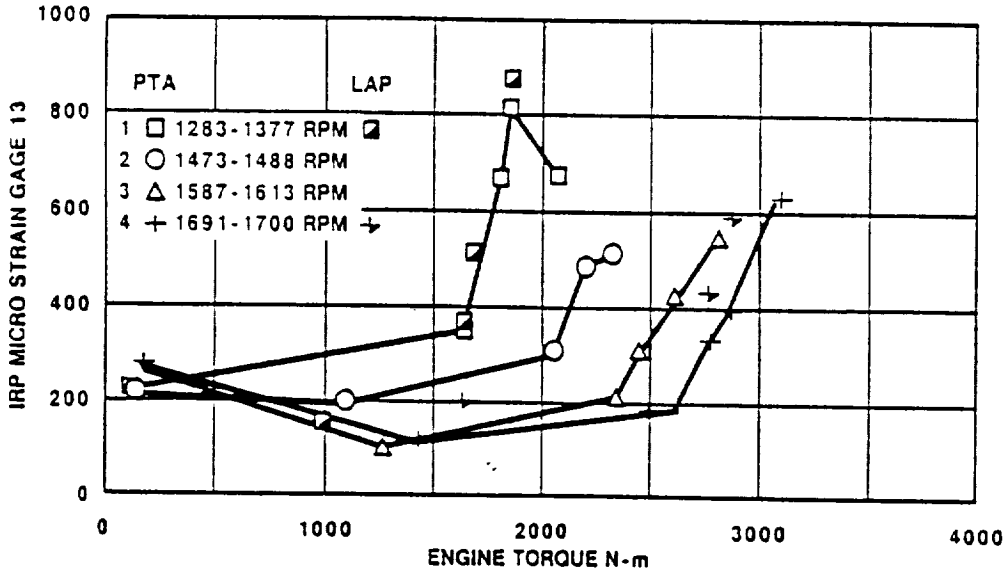


Figure 230. Tip Bending Strain Variation with Torque

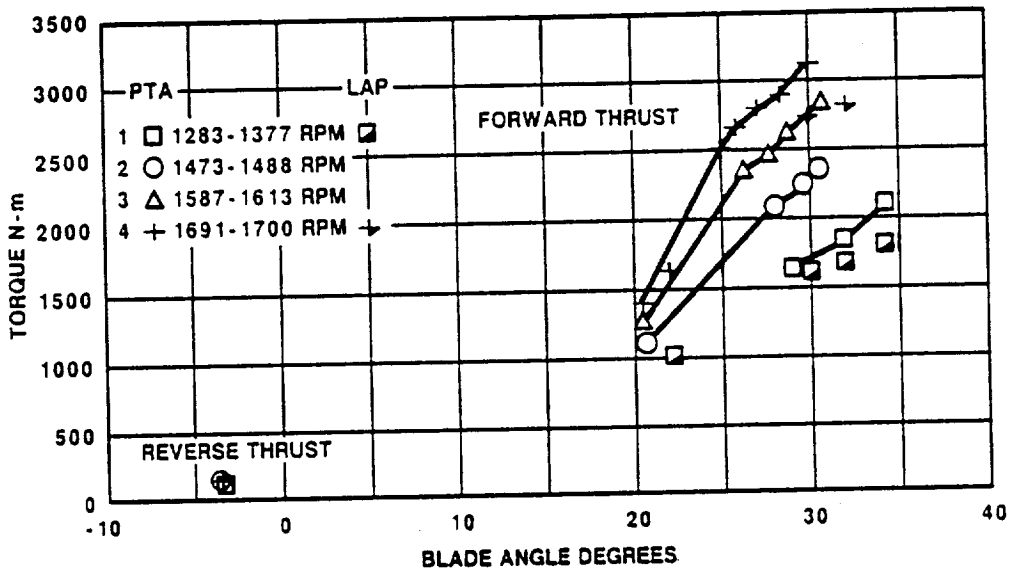


Figure 231. SR-7L Torque Change with Blade Angle

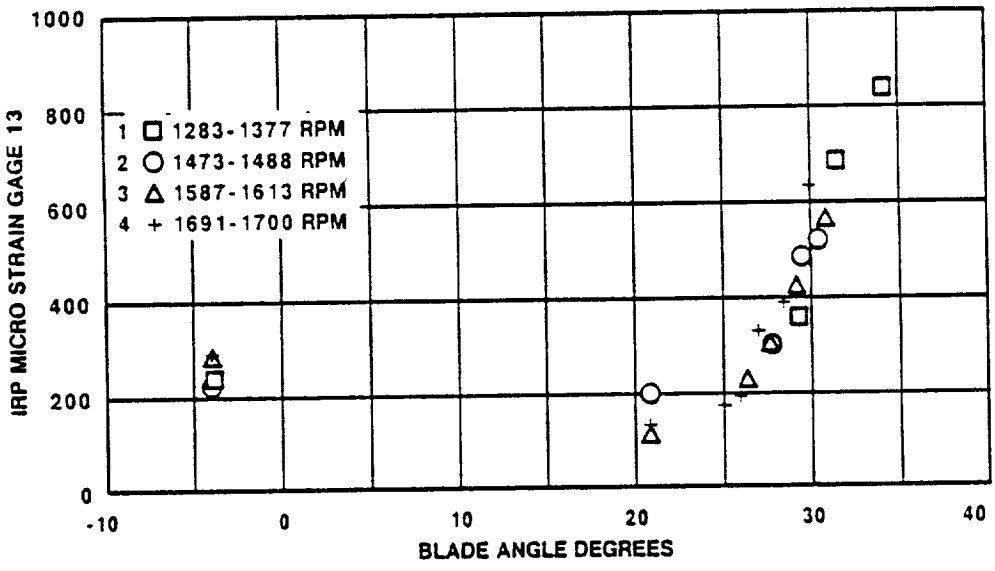


Figure 232. Tip Bending Gage Strain Variation with Blade Angle

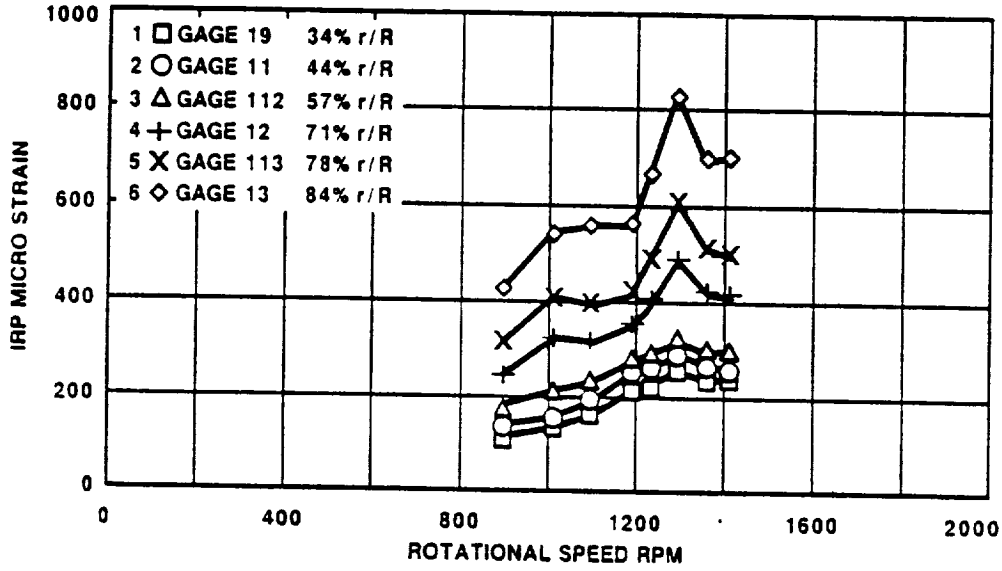


Figure 233. Vibratory Strain Distribution

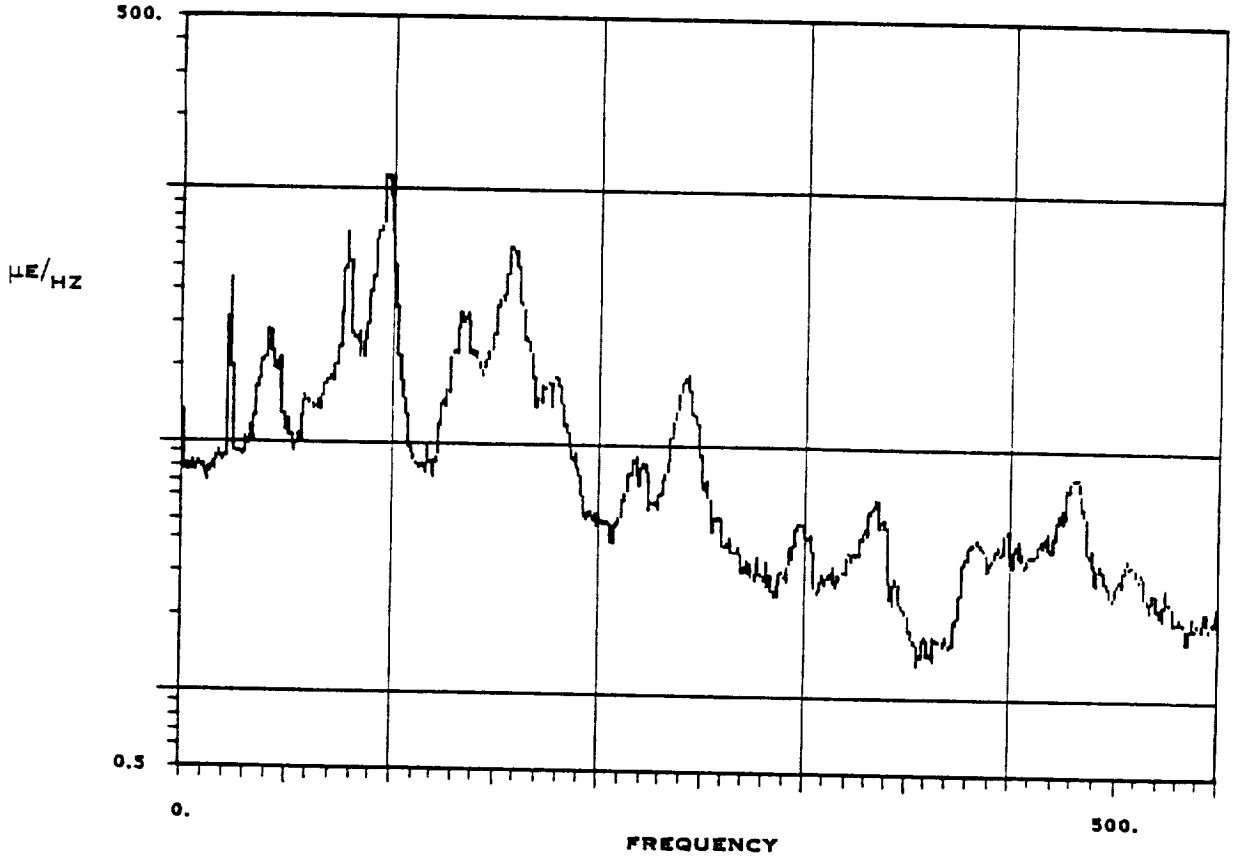


Figure 234. Frequency Content of the Tip Bending Gage 13

As stated previously, the blade vibratory response was dominated by activity on the tip bending gage as shown in Figure 233. The reason for the high tip bending response is evident from the examination of the frequency content of the strain gage signals. Spectral analysis of Gage 13 at 1407 rpm and 34.2 degrees blade angle shows that the primary blade response was at 95 Hz which corresponds to the second flatwise blade vibratory mode. The blade response was characterized during LAP static rotor tests as buffeting response, dominated by the second flatwise mode. However, substantial response existed at frequencies other than 95 Hz as shown in Figure 234.

To establish the blade natural frequencies and response frequencies, spectral analyses were performed on 18 test conditions. The blade natural frequencies compared very well with the measured frequencies from the LAP static rotor tests. The pre-test predictions were in good agreement for the flatwise modes. The edgewise mode was higher than predicted because the blade retention was found to be stiffer than predicted. The torsion mode was lower than predicted, and no reason is apparent for the lower than predicted result. The measured blade natural frequencies are shown in Figure 235.

Blade-to-blade strain variations are summarized in Figures 236 through 238 for the inboard, mid-blade, and tip bending strain gages. Differences were on the order of 12.6 percent for the highly strained tip bending gage and 7 percent for the mid-blade bending gage. The blade-to-blade differences on the inboard bending gage were 20 percent, which is high because the strain amplitudes were low. Independent of strain level or gage location, the blade-to-blade variation was on the order of 75 microstrain.

6.5.5 Transient Tests

The purpose of the transient tests was to evaluate the dynamic response of the propfan propulsion system to time dependent variations in engine power and speed set point. The blade vibratory response to these transients was also monitored. The transients were initiated by manually actuating either the engine power lever or the propfan speed control lever. The severity of the transients was altered by varying the rate at which the power or speed levers were moved. Conducting the transient test in this manner resulted in the system response being affected by the dynamics of the turbine engine fuel control and the propfan control input lever actuator. These devices had features which limited the maximum rate at which engine power or propfan speed set point could be changed no matter how quickly the control levers were moved. A slow transient and fast transient were run in both directions along each operating curve. Engine power lever position, propfan speed lever position, propfan rpm, engine torque, and propfan blade pitch angle were recorded and plotted as functions of time for each transient. Acoustic tailpipe static and dynamic strains and temperatures also were recorded during the power lever transient to full power and for a prescribed time at power. Dynamic strain data also were recorded during the fast speed lever transient.

Figures 239 and 240 show the conditions at which propfan speed and power transient tests were run. Plots of the propfan and engine control dynamic

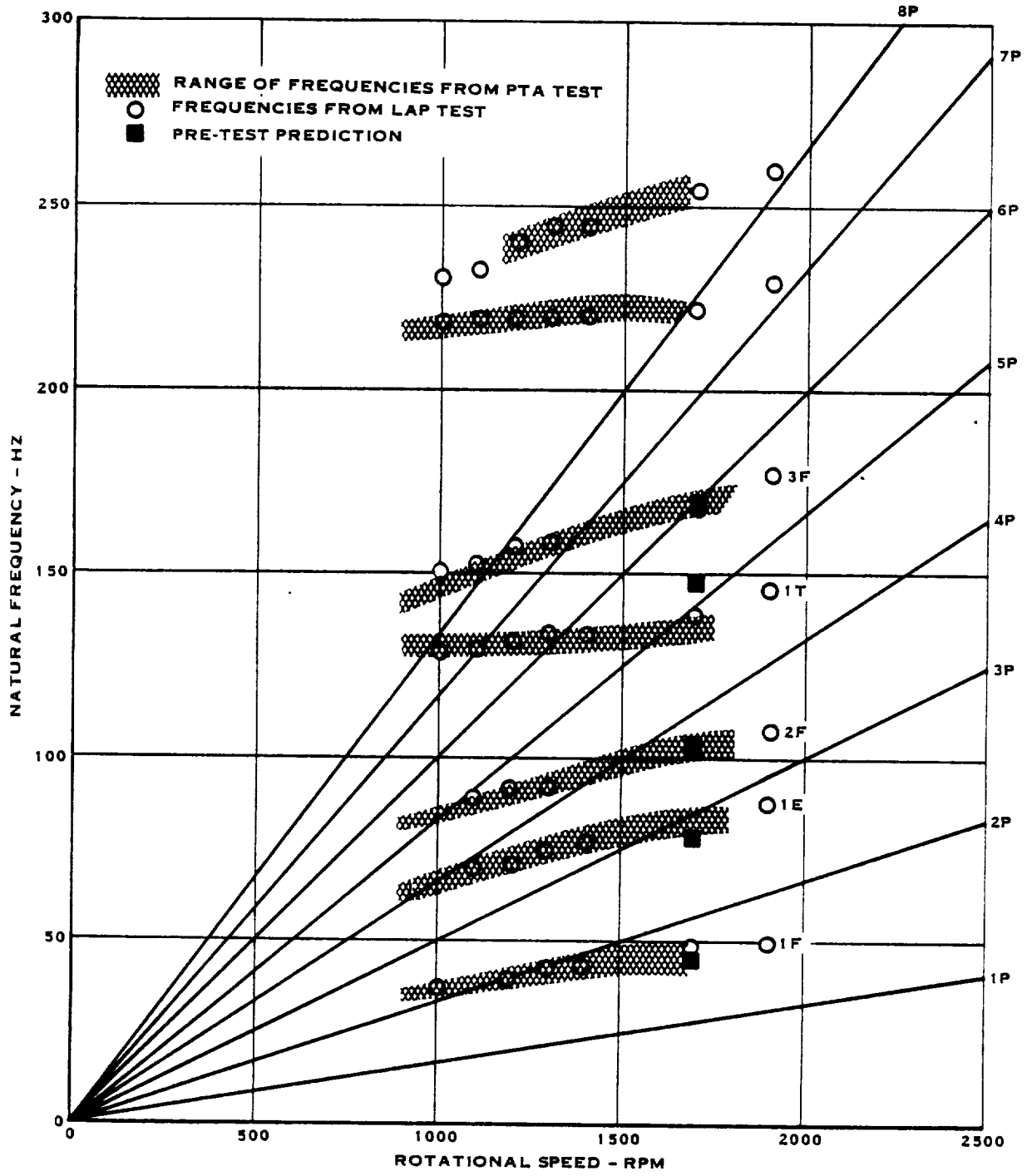


Figure 235. Predicted and Measured Blade Natural Frequencies

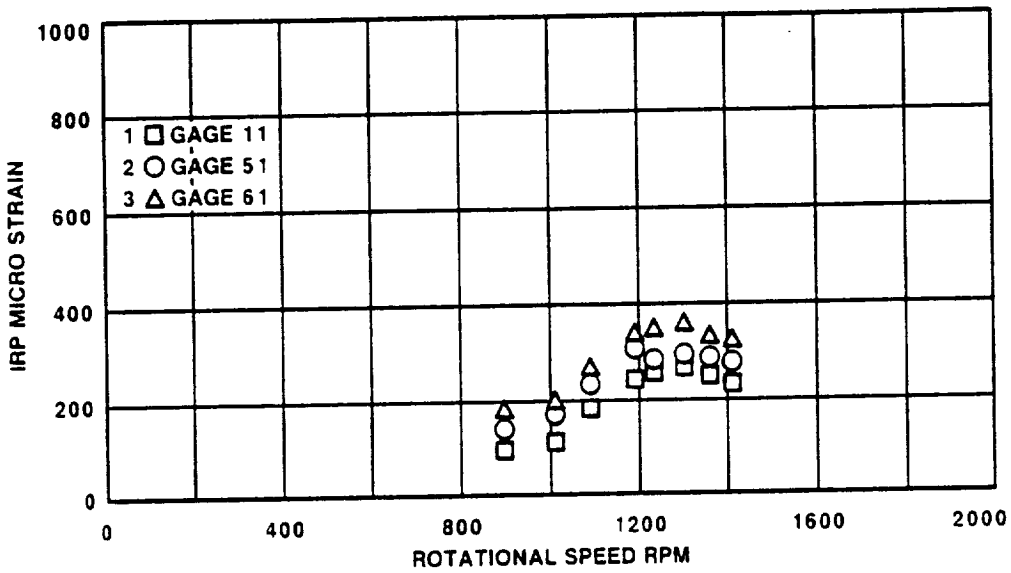


Figure 236. Inboard Bending Vibratory Strain

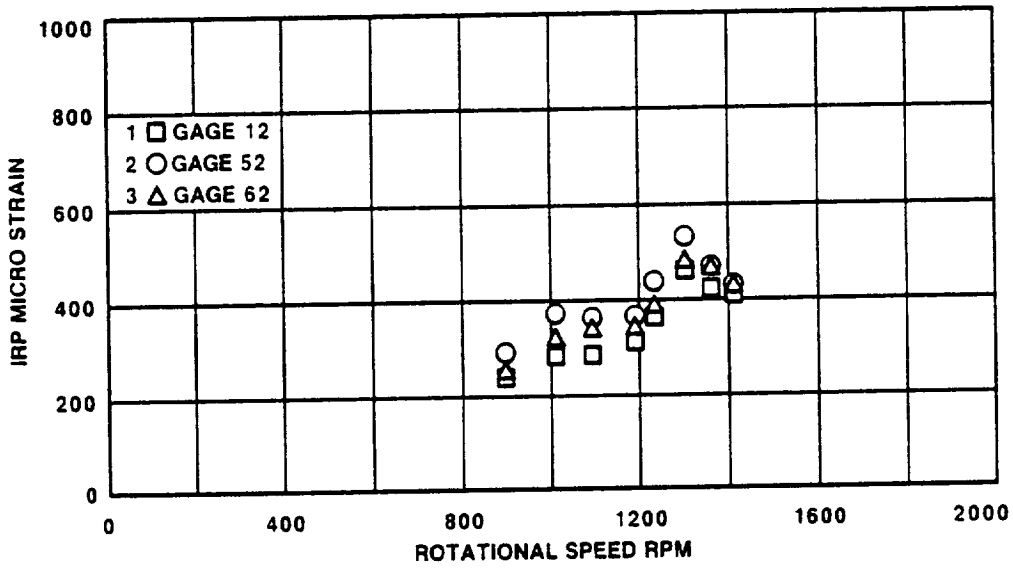


Figure 237. Mid-Board Bending Vibratory Strain

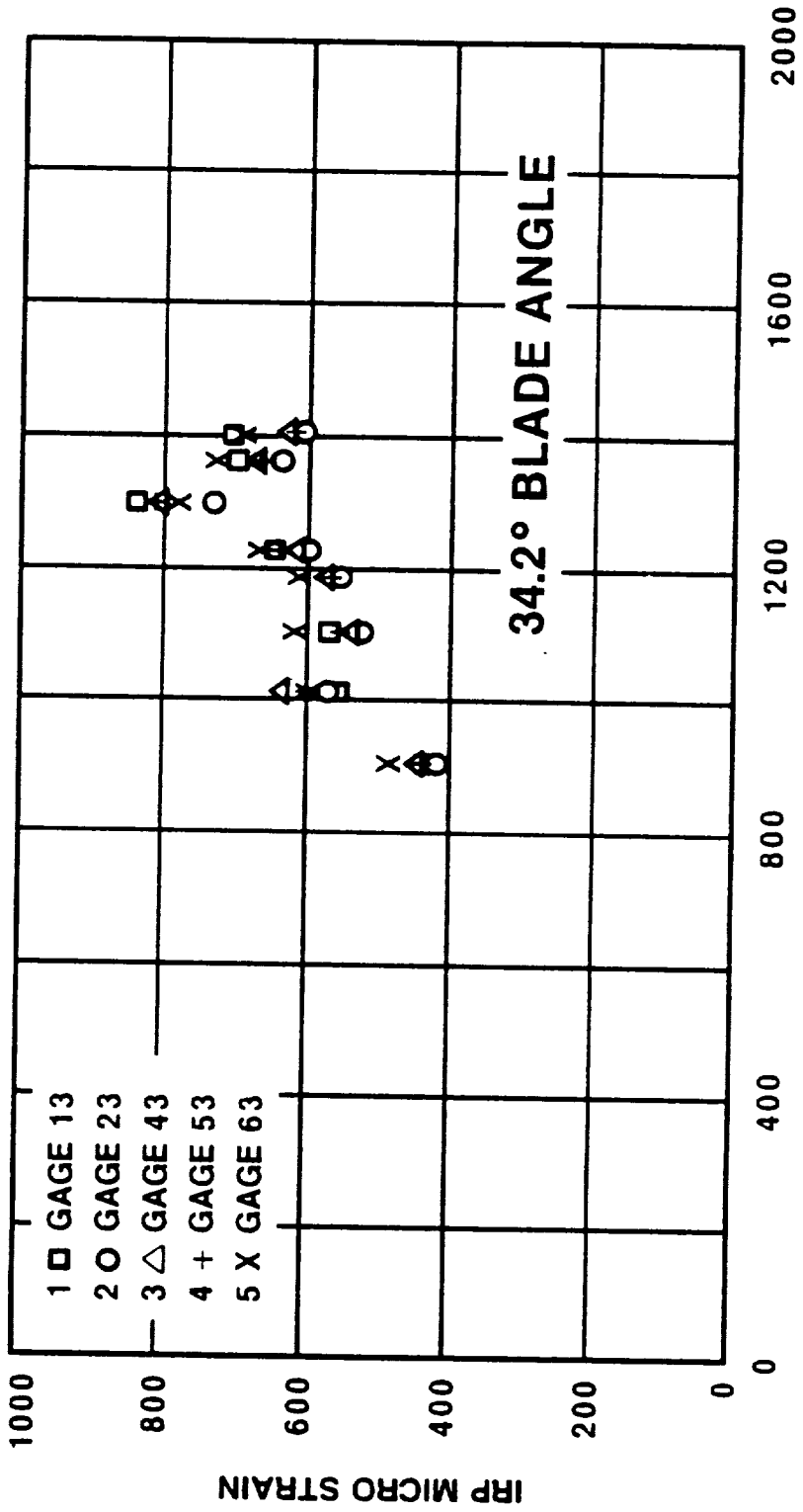


Figure 238. Tip Bending Vibratory Strain

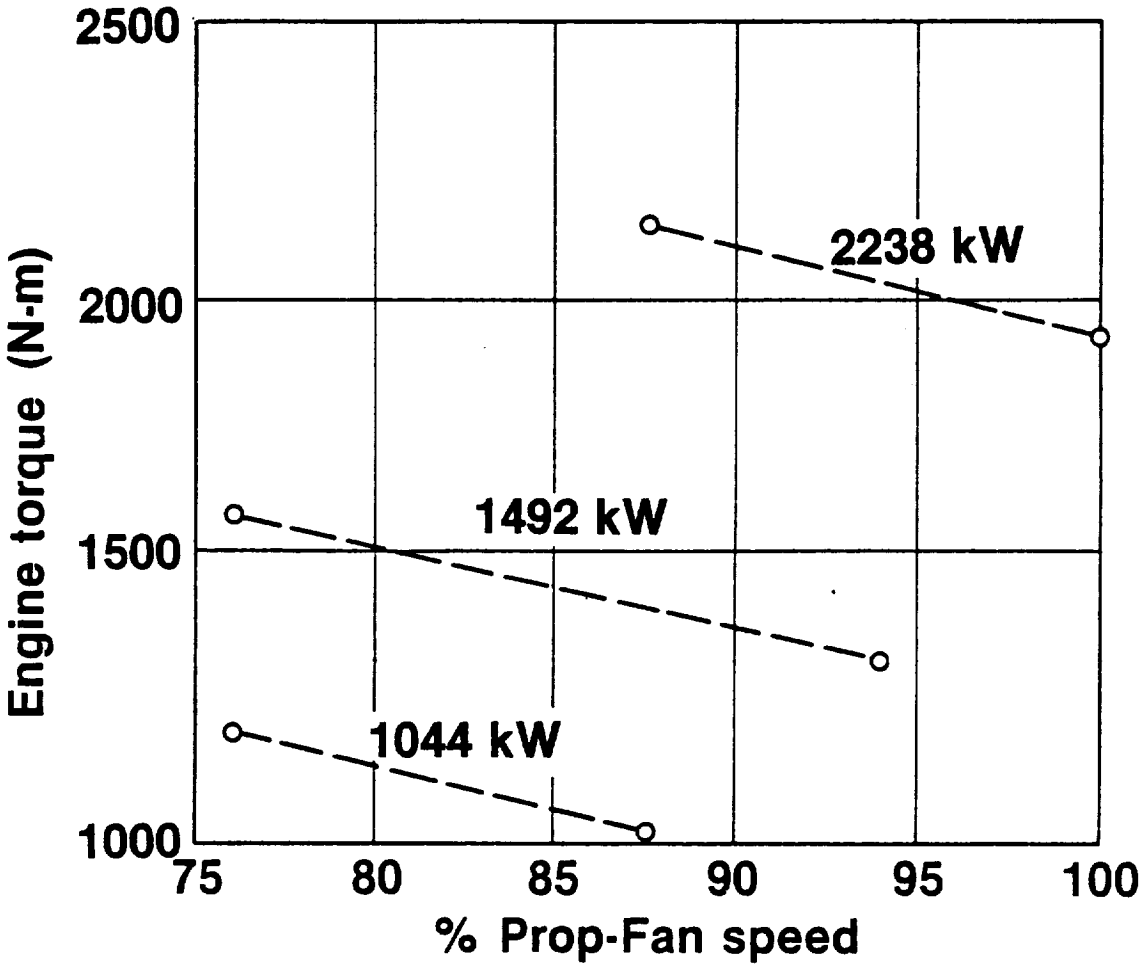


Figure 239. Speed Transient Conditions

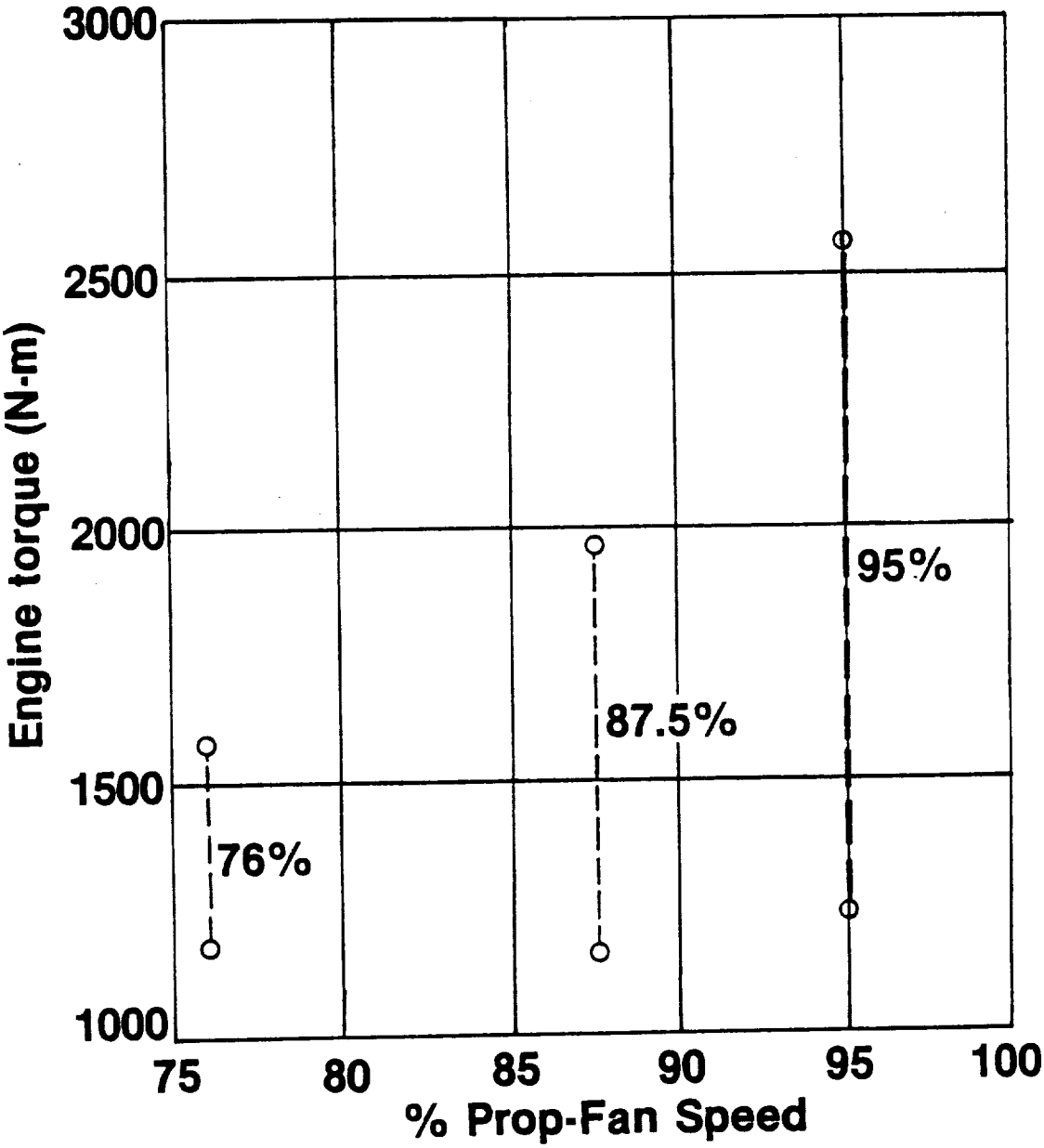


Figure 240. Power Transient Conditions

response to speed and power lever transients are presented in Figures 241 through 248. Figures 241 and 242 show the response to ramp changes in the speed set point between 87.5-percent and 100-percent propfan speed. The time intervals to traverse this set point range were four seconds and two seconds, respectively. Figures 243 and 244 show the responses to essentially step changes in power lever position between 1268 kw (1700 shp) and 2089 kw (2800 shp) at 87.5-percent propfan speed. Figures 245 and 246 show the responses to more severe transients, step changes in power lever position between 1350 kw (1810 shp) and 2700 kw (3620 shp) at 95-percent speed. Propfan blade peak vibratory strain response to a fast speed transient from 87.5-percent to 100-percent and back to 87.5-percent propfan speed at a constant 2240 kw (3000 shp) power setting is shown in Figure 247. Peak vibratory strain response to a fast power transient at 95-percent speed is shown in Figure 248. These data indicate that while there is an increase in propfan blade stressing as the blade angle approaches the buffet boundary (defined in Paragraph 6.2.3.2), there is no relationship between rate of change of the speed or power lever settings and blade stressing. This is indicated by the absence of any significant measurable spike in blade stressing during the transient.

During propfan speed transients, the propfan speed governor held power turbine overshoots within approximately 3 percent. Gas generator speed was unaffected since the power lever was not changed.

Results also show that gas generator speed is linear with power lever position during power lever transient tests, and the propfan speed control held over- and under-speeds to a minimum. The transient response of the propfan propulsion system verified stable, predictable performance during speed lever or power lever transients.

6.5.6 Endurance Test

The endurance portion of the static test consisted of 12 repetitions of a simulated three-hour flight cycle plus pre- and post-endurance calibrations. Acoustic data were recorded for three configurations during these tests.

The pre-endurance calibration consisted of two parts: a seven-point calibration and a three-point calibration. The seven-point calibration involved setting the propfan rotational speed at 100 percent and varying engine power between 1640 and 3280 kw (2200 and 4400 shp). Data were taken at seven steady state conditions between the low- and high-power settings. The three point calibration was performed by setting the propulsion system at three set points and taking data when steady state conditions were reached. The system was set at 76-percent N_p speed and 1340 kw (1800 shp), 87.5-percent N_p and 2160 kw (2900 shp), and 105-percent N_p and 3580 kw (4800 shp) for the three-point calibration.

Twelve repetitions of a three-hour simulated flight cycle were performed to determine if any excessive wear might occur in either the propfan assembly or the drive system, especially the reduction gearbox. Of primary concern in the propfan assembly were the propfan actuator and the blade retention hardware.

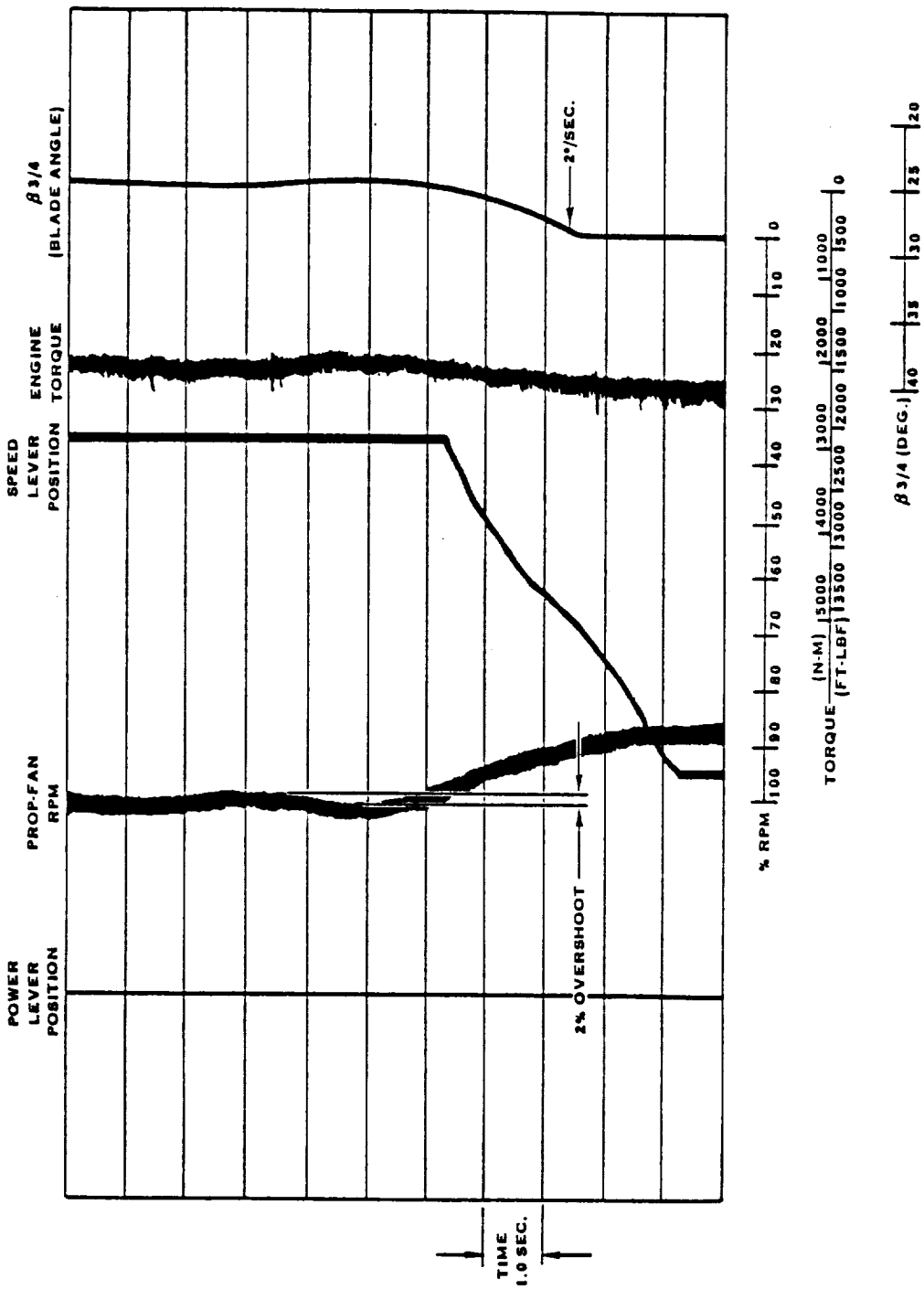


Figure 241. Response to 4-Second Speed Lever Traverse - 87.5 to 100% N_p; 2238 kw (3000 hp)

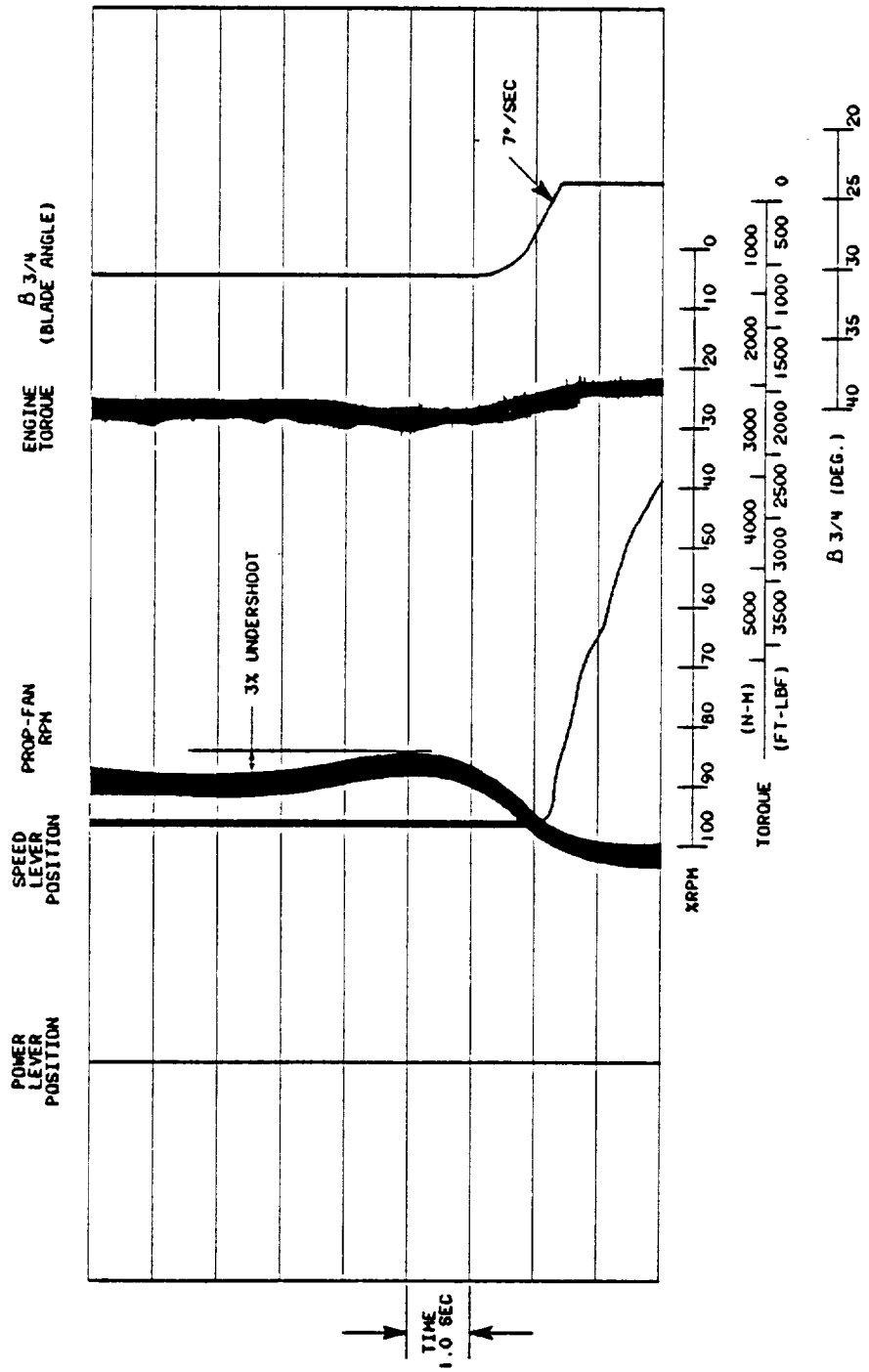


Figure 242. Response to 2-Second Speed Lever Traverse - 87.5 to 100% N_p; 2238 kw (3000 hp)

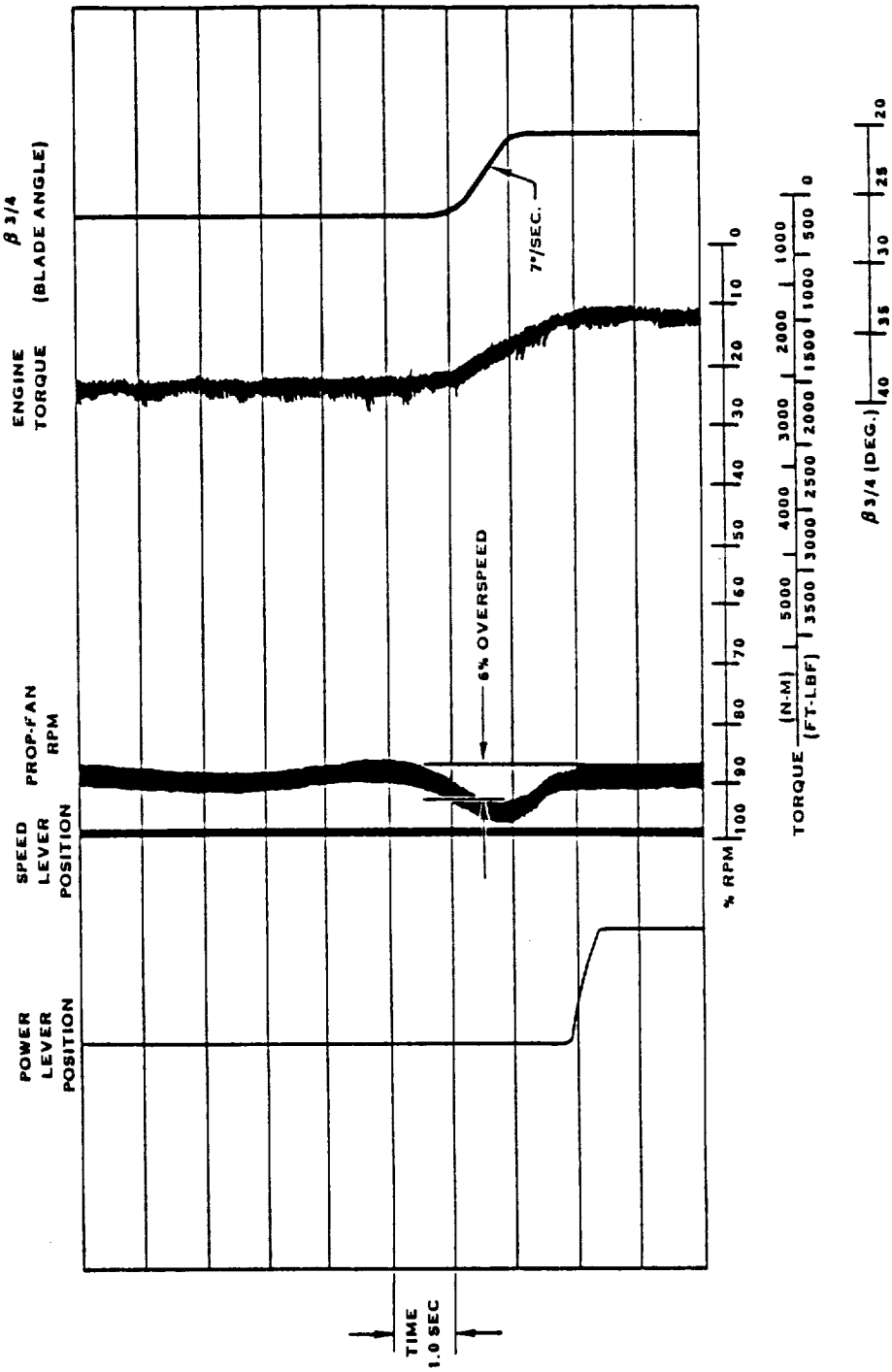


Figure 243. Response to Step Increase in Power - 1268 kw to 2089 kw (1700 to 2800 hp), 87.5% N_P

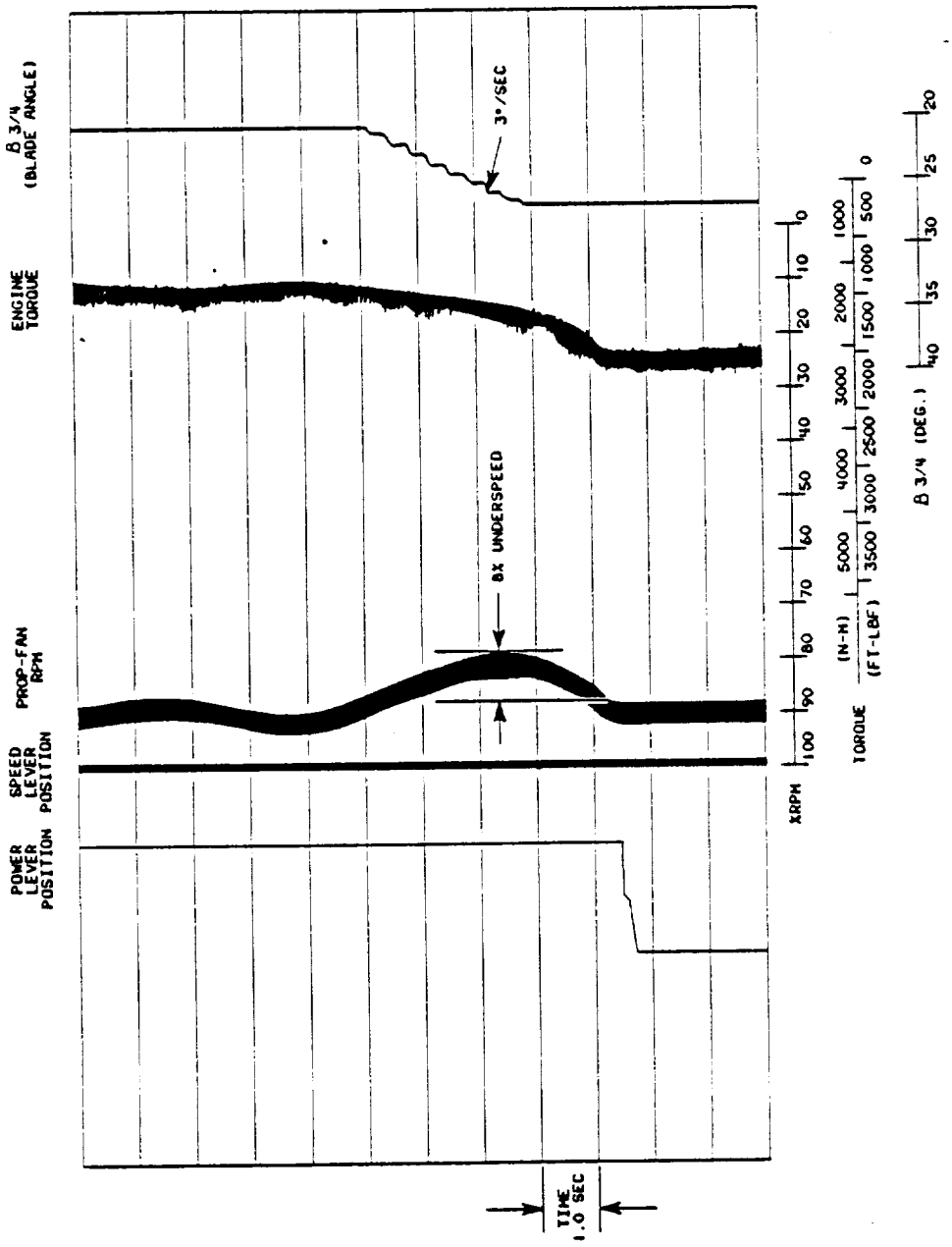


Figure 244. Response to Step Reduction in Power - 2089 kw to 1268 kw (2800 to 1700 hp), 87.5% N_p

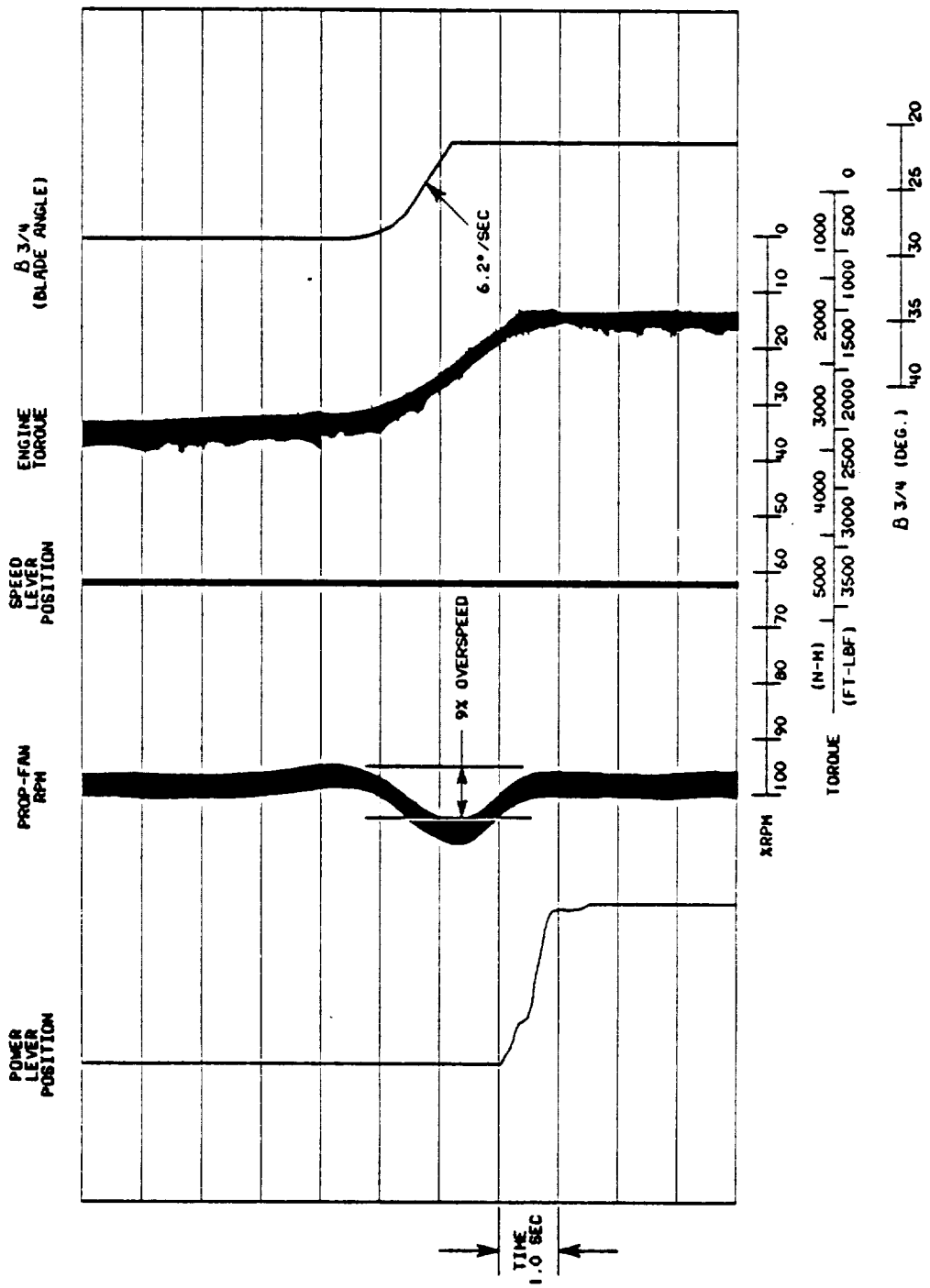


Figure 245. Response to Step Increase in Power - 1350 kw to 2700 kw (1810 to 3620 hp), 95% N_p

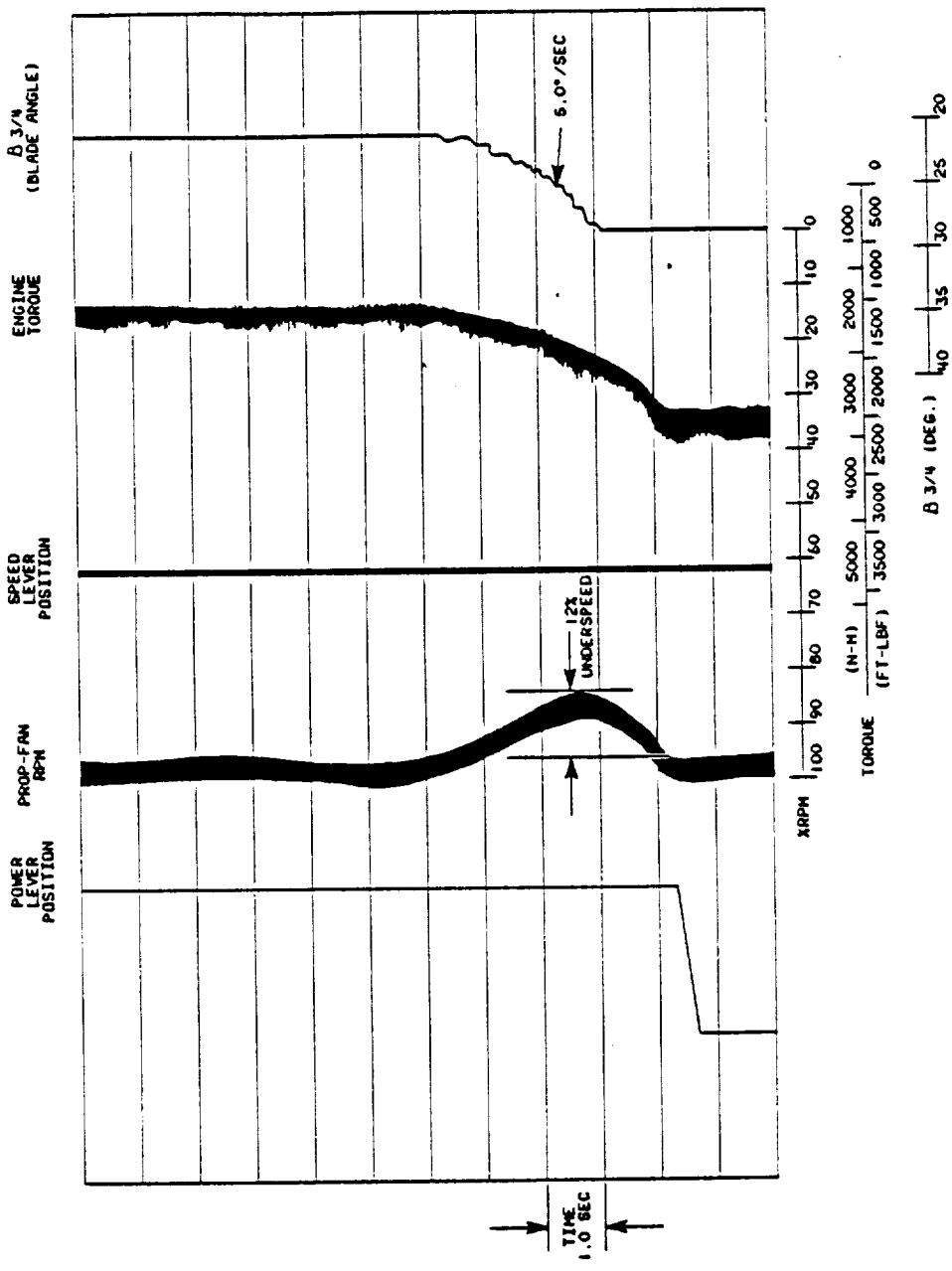


Figure 246. Response to Step Reduction in Power - 2700 kw to 1350 kw (3620 to 1810 hp), 95% N_p

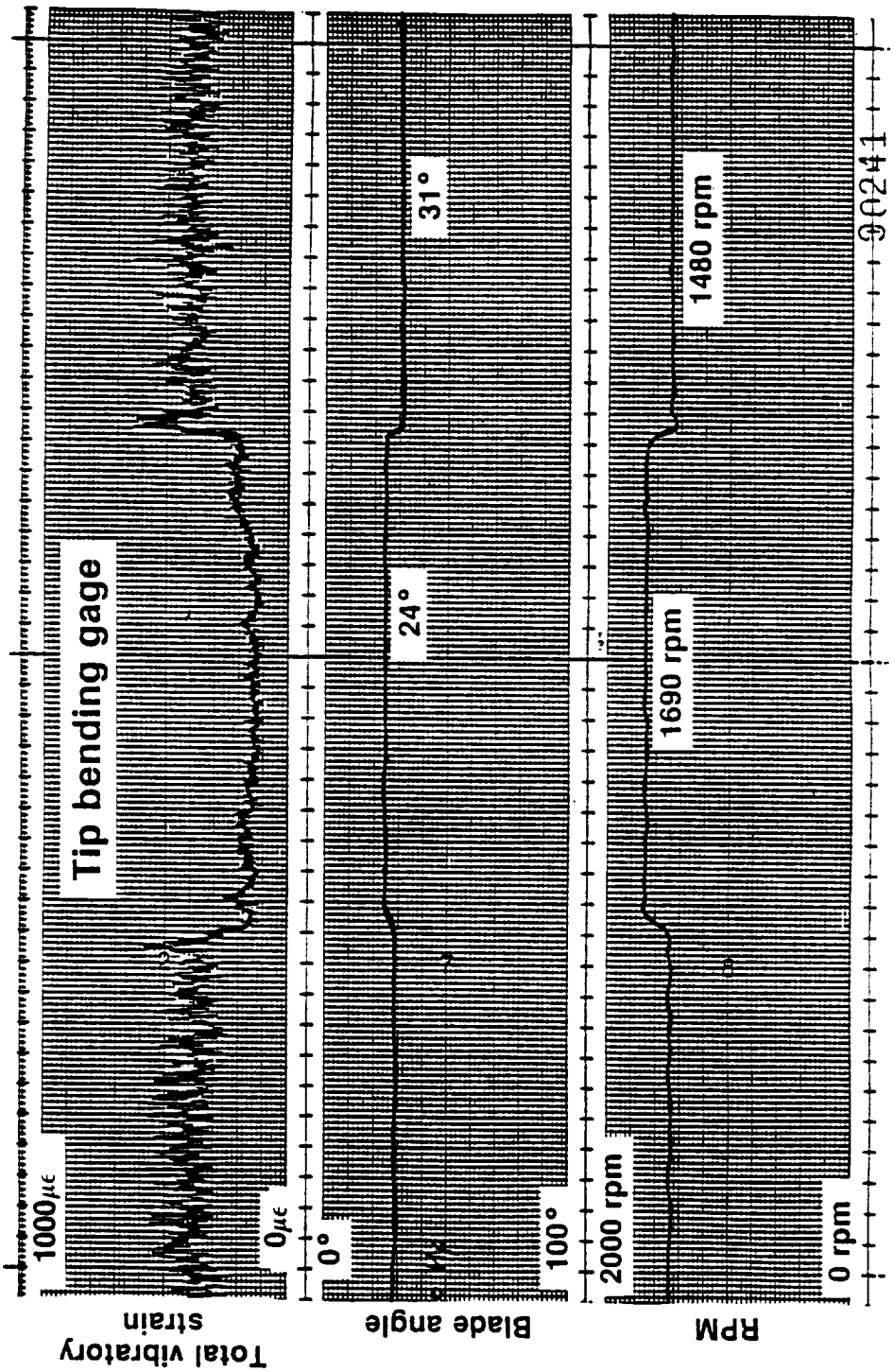


Figure 247. Fast Speed Lever Transient - 2240 kw (3000 hp)

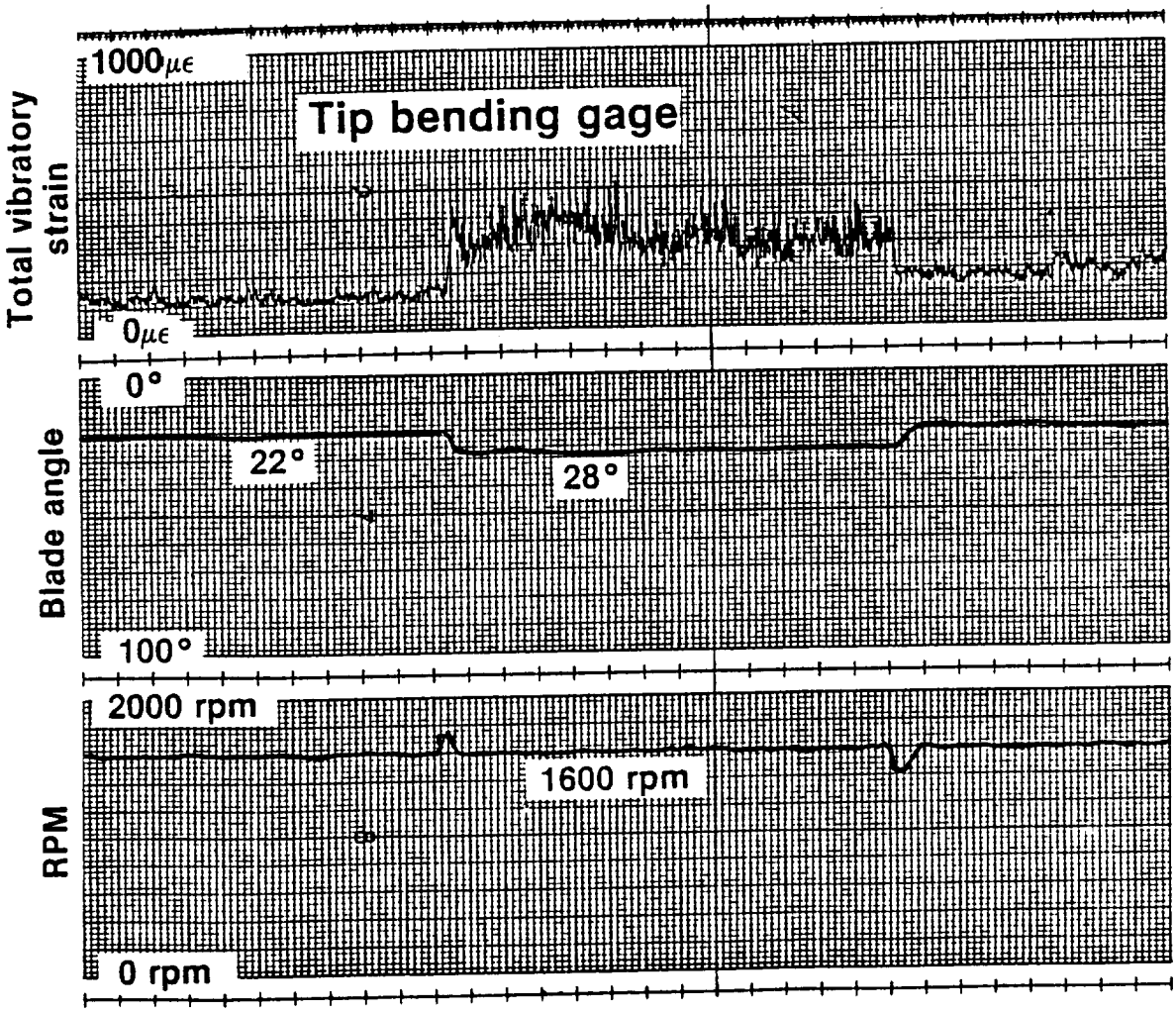


Figure 248. Fast Power Lever Transient - 95% N_p

Each endurance cycle consisted of setting the propfan propulsion system on 12 different set points and recording engine and propfan performance data at each steady state point. Data were recorded more than once for some set points so that 17 sets of data were obtained for each cycle. Propfan rotational speed ranged from 77 percent to 105 percent, and engine power from 1940 to 3430 kw (2600 to 4600 shp) over the course of a cycle.

After completion of the 12 endurance cycles, the pre-endurance calibrations were repeated to determine any engine performance degradation which may have occurred during endurance tests.

Results from the pre- and post-endurance performance calibrations corrected to sea level static and unity ram conditions are presented in Figures 249 through 251. Comparison of the two calibration runs indicated that engine performance degraded slightly during the 36-hour endurance test. Considerable dirt and propfan hydraulic fluid buildup was evident on the inlet duct and engine inlet guide vanes.

The post-endurance calibration shows an increase of approximately 2.5 percent in fuel flow (Figure 251) and a resultant MGT increase of 8°C (15°F) at the maximum power condition. The performance results are indicative of a loss in compressor efficiency. After completion of all scheduled testing, the engine flow path was chemically cleaned for removal of propfan oil and dust deposits.

6.5.7 Reverse Thrust Test

Testing was conducted to verify safe and stable operation of the propfan propulsion system while producing reverse thrust. The reverse thrust test was accomplished with the blade angle set at -5 degrees by the adjustable low pitch stop. The propfan speed control lever was set at 105 percent, and the test was conducted with the propfan on the low pitch stop so that propfan speed would be controlled by the engine power lever. Data were recorded at six power settings corresponding to 75 percent, 81 percent, 87 percent, 94 percent, 100 percent, and 103 percent propfan speeds. Power was then reduced, and a slow power transient which changed propfan speed from 75 percent to 103 percent was performed.

The propfan propulsion system performed satisfactorily during these reverse thrust tests. Blade stresses were low, and the propfan reached approximately 103 percent design speed. The set points for which data were recorded are shown on the -5.0 degree low pitch stop line in Figure 229.

6.5.8 Propfan Auxiliary Pump Motor Test

The propfan auxiliary pump motor was a 3.7 kw (5 hp) three-phase electric motor designed to supply power to the propfan auxiliary pump which provides hydraulic pressure for blade angle changes when the propfan is not rotating. This motor was rated for 400 Hz supply power. However, the frequency of the power supplied on the GII testbed aircraft was a function of GII main engine speed and varied between 350 Hz and 500 Hz.

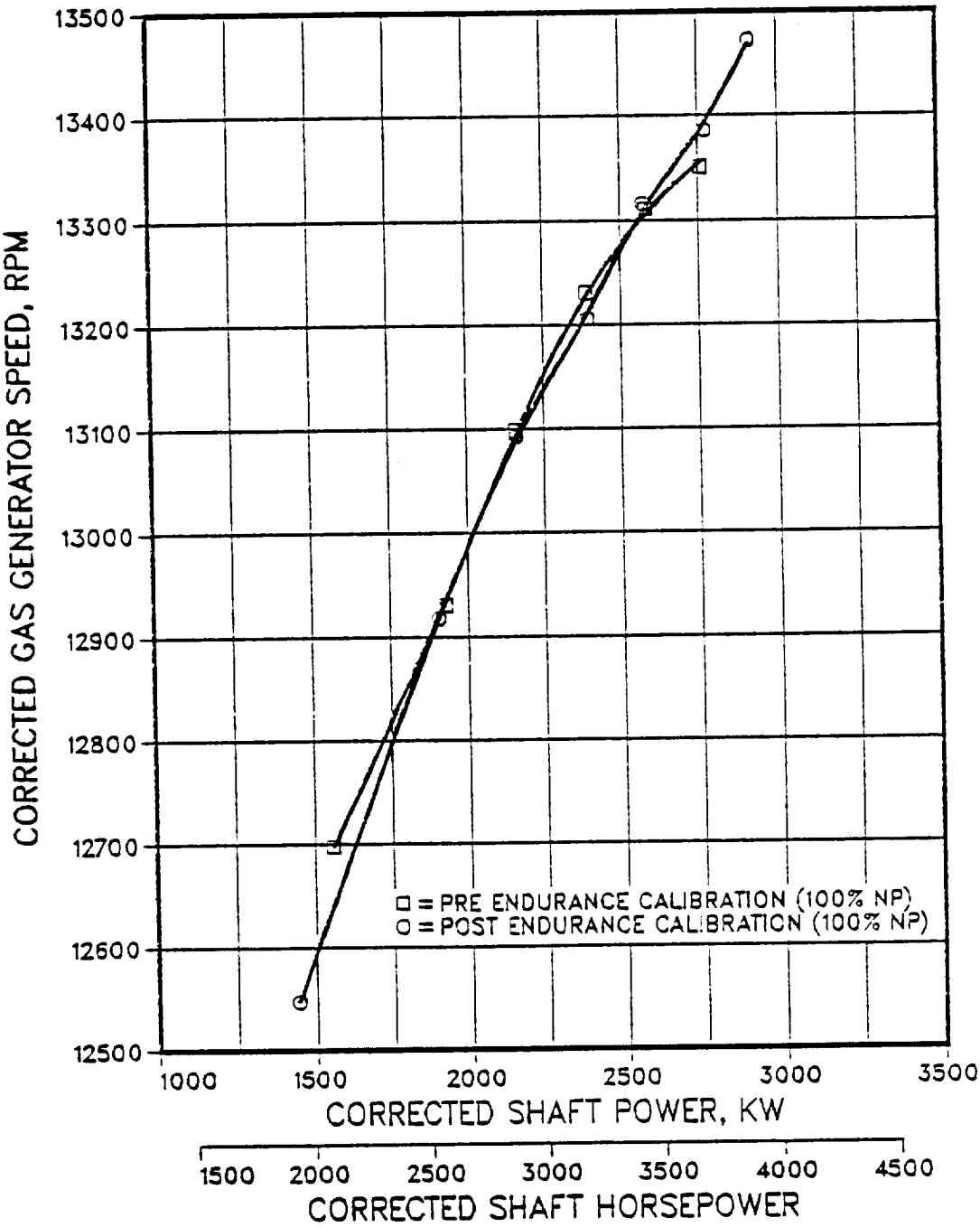


Figure 249. Effects of Endurance Test on Gas Generator Speed

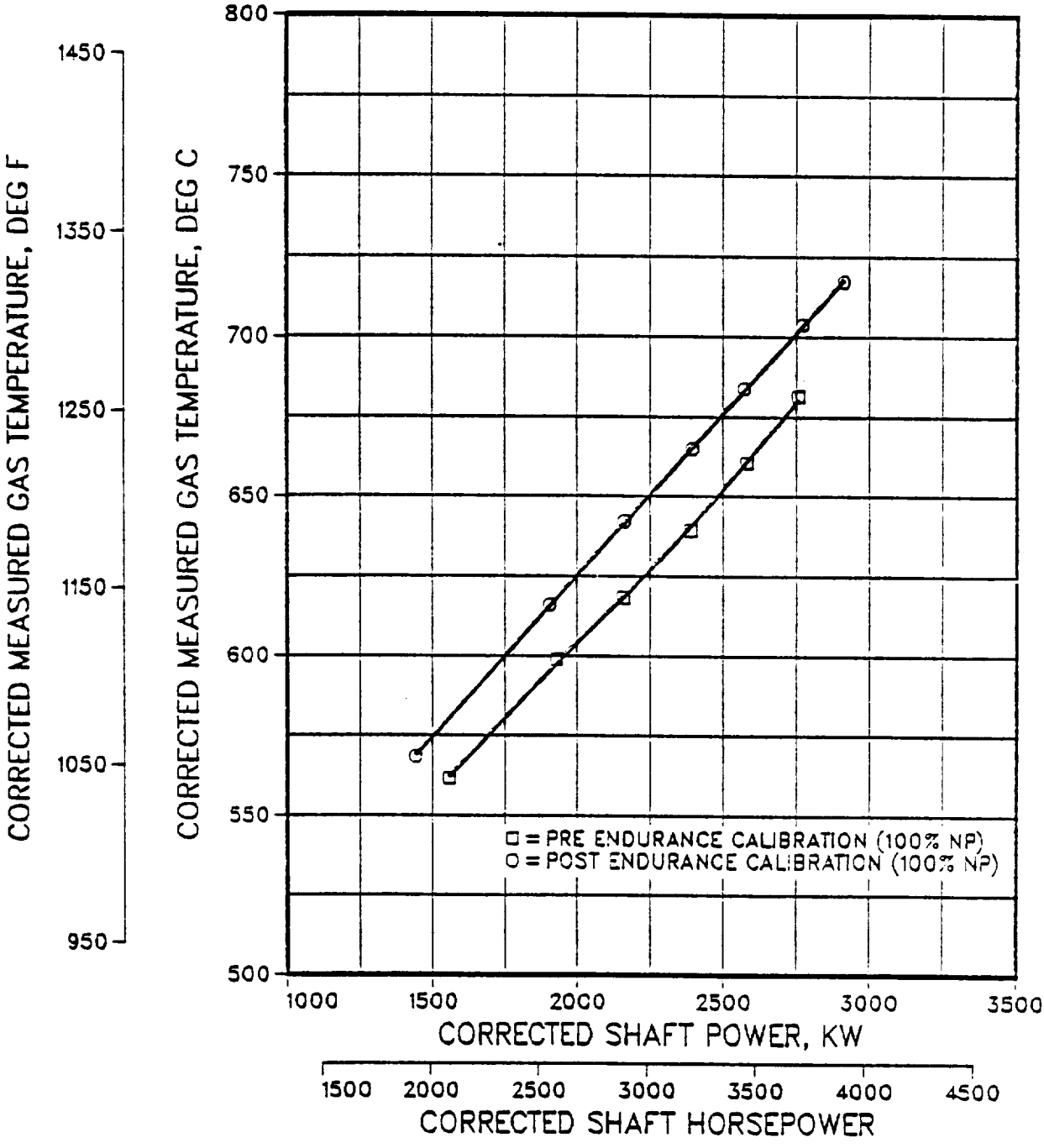


Figure 250. Effects of Endurance Test on Correct MGT

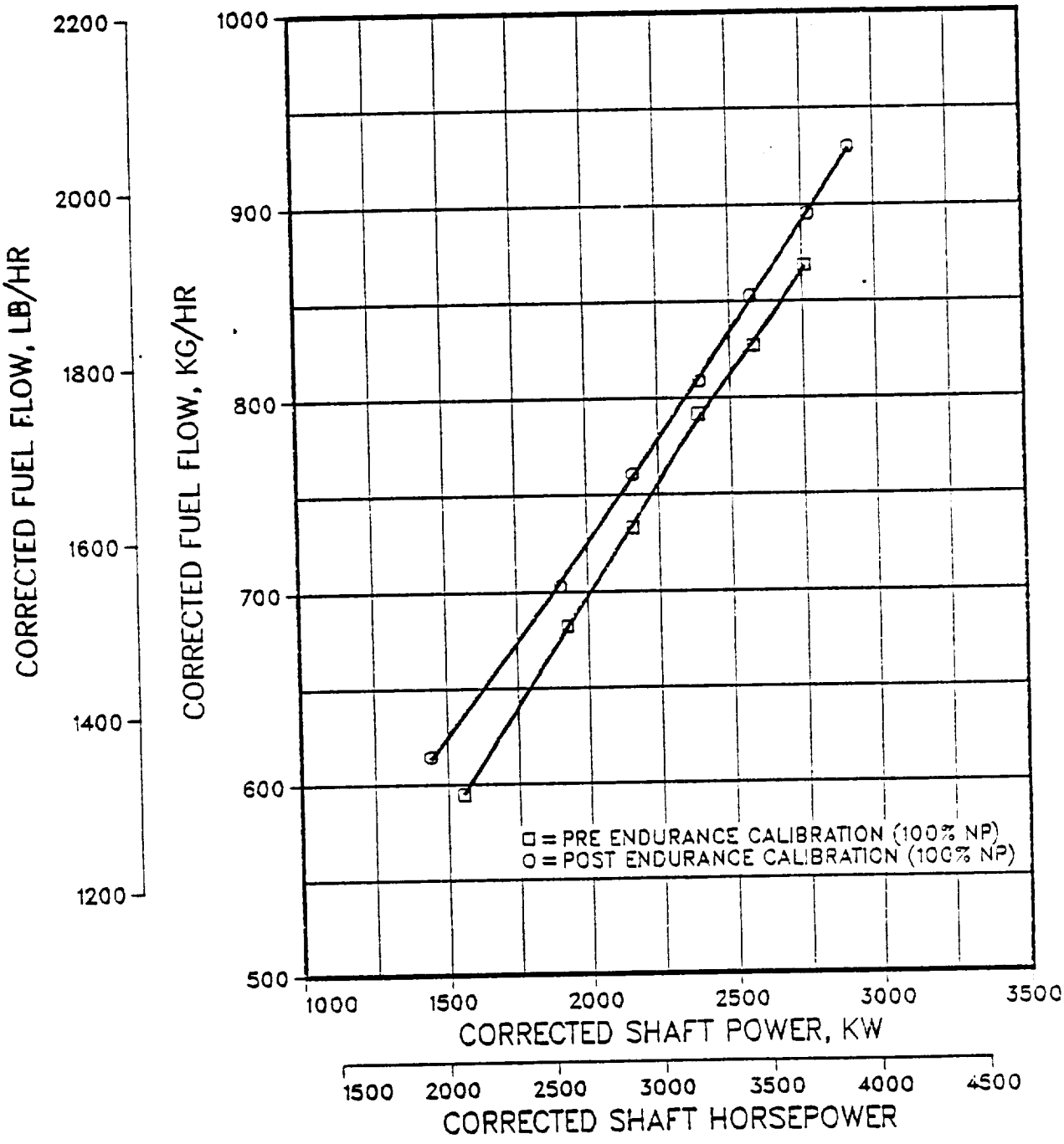


Figure 251. Effects of Endurance Test on Fuel Flow

A test was conducted with the propfan propulsion system shut down to determine the performance of the propfan auxiliary pump motor at supply frequencies other than 400 Hz. A variable frequency, three-phase power source was used to provide between 300 Hz and 500 Hz to the auxiliary pump motor, and supply current and voltage were recorded while the motor was started and run. Strip chart data were recorded for supply frequencies of 300, 350, 400, 450, and 500 Hz. Results showed that the motor produced the power needed to feather and unfeather the propfan blades at all frequencies evaluated.

6.5.9 Acoustics Tests

The acoustics data were recorded during and immediately after the endurance tests. Both far-field and near-field acoustic data were obtained for a range of tip speeds and horsepowers.

These acoustic data were machine processed to convert the electrical analog records into engineering units of noise level measurement--sound pressure in psi and sound pressure level in decibels--and are presented in three forms: sound pressure time histories, narrow band constant bandwidth sound pressure level spectra, and 1/3-octave sound pressure level spectra.

6.5.9.1 Far-Field Noise Spectrum Content

Figure 252 shows features of the far-field sound pressure level spectrum at 30 degrees azimuth for a moderate power of 1732 kw (2323 shp) and 100 percent tip speed.

The first few orders of propfan blade noise were distinct at multiples of 220 Hertz. Other tones were evident near 4000 Hertz. One of these tones (though often not the strongest) always occurred at the compressor first-order blade frequency, while the rest occurred at sums of or differences between the compressor and the propeller blade frequencies. Broadband random noise was evident throughout the audible range. It was strongest in the comparatively low frequency range of 500 to 1500 Hertz.

The level of the first-order propfan blade tone shown in Figure 252 was 98 dB; the second-order tone was 92; the third was 88. The third, fourth, and fifth order tones were contaminated by the random noise, and higher orders were totally masked.

The tone frequencies were determined more accurately by high resolution spectrum analysis, wherein the analysis frequency range and bandwidth were reduced by a factor of 10, the display resolution was increased to 8000 lines, and 50 averages were obtained. In so doing, the cursor indication was accurate to within ±0.62 Hertz. Figure 253 shows the results of such an analysis for the same microphone and power conditions as Figure 252.

The peaks adjacent to the compressor fundamental peak in Figure 253 are seen to be at exact multiples of 220 Hz (the propfan fundamental) above or below the 4052.5 Hz compressor tone. These tones in the vicinity of

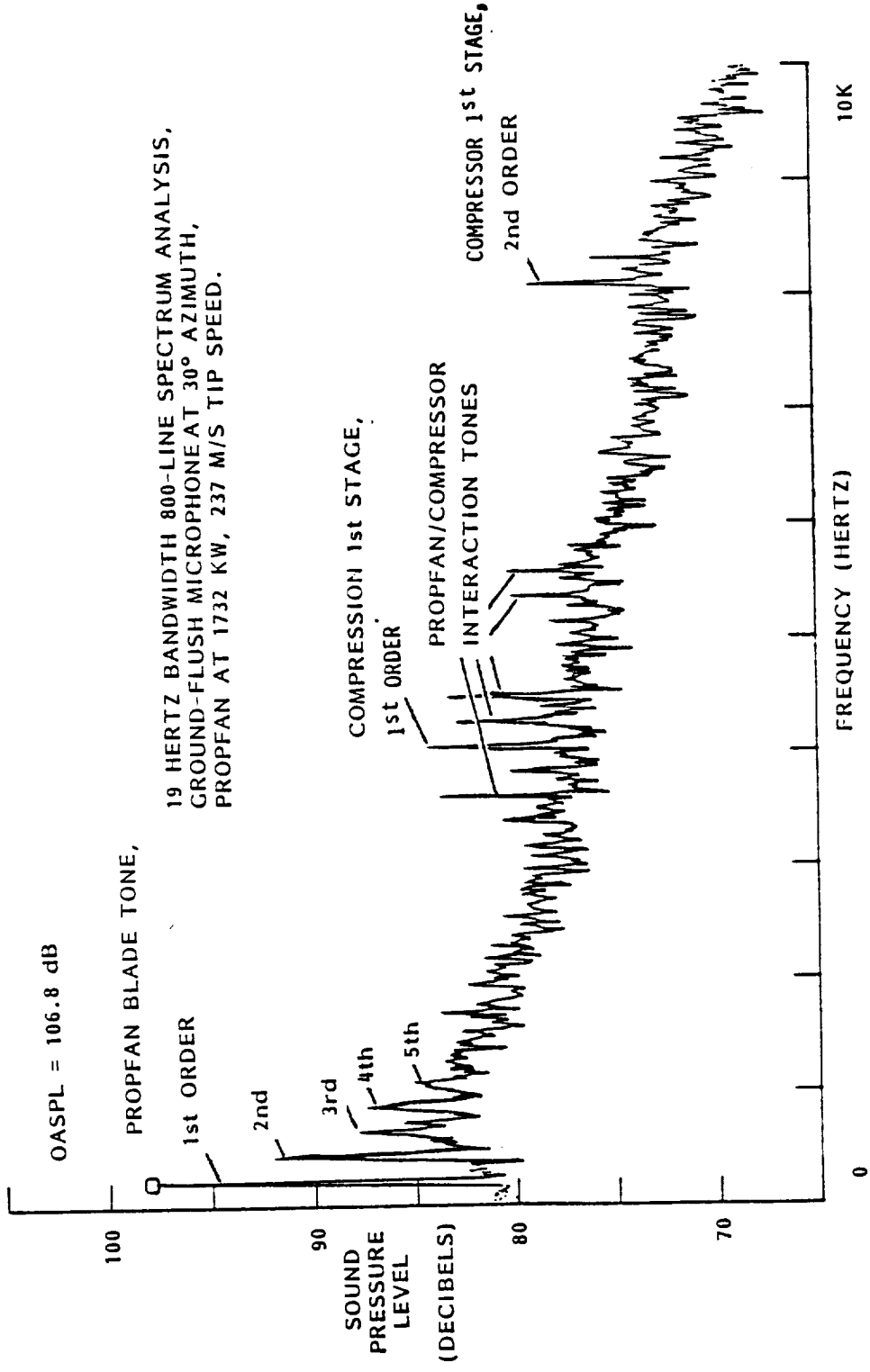


Figure 252. Ground Level Noise Spectrum

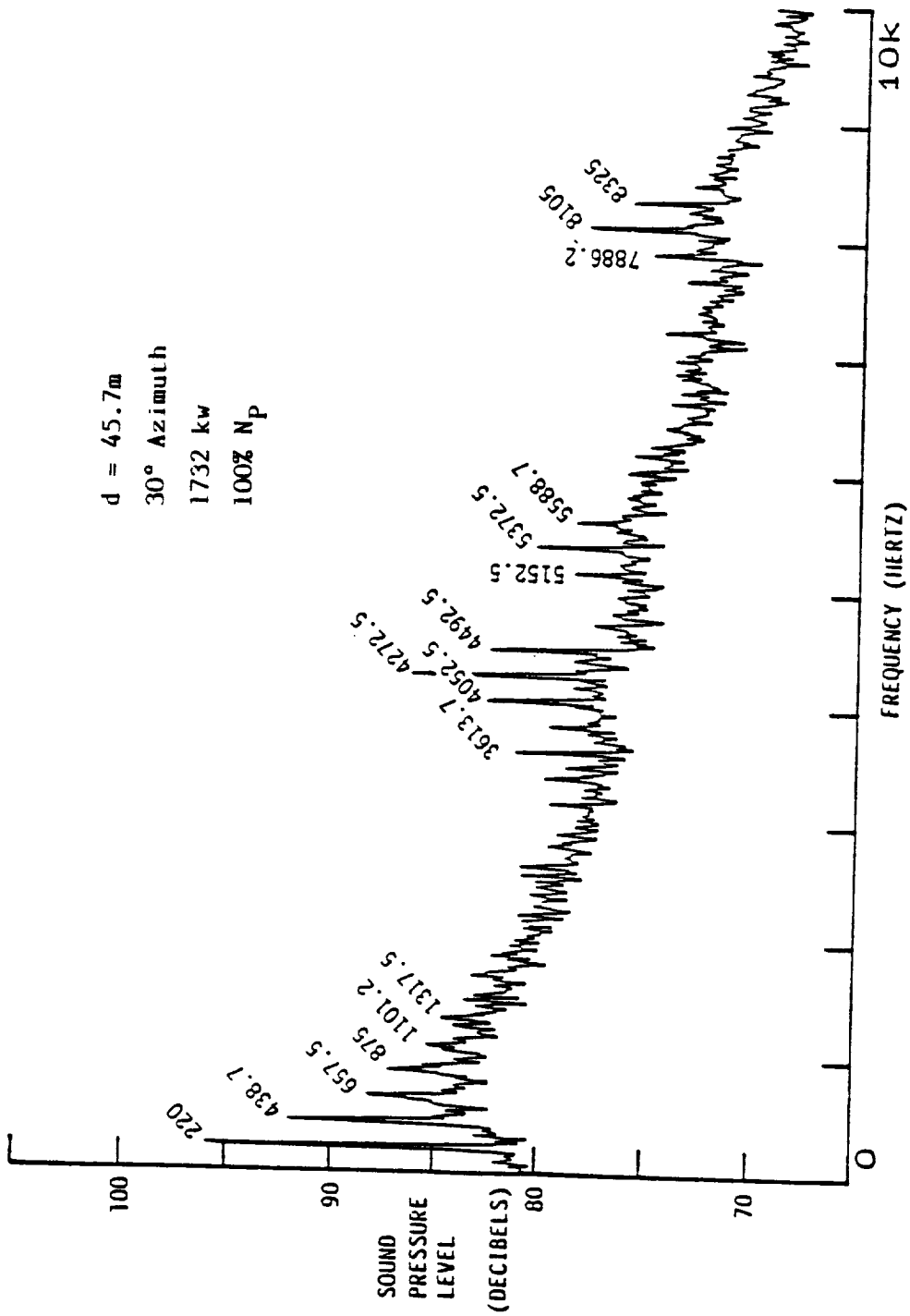


Figure 253. Ground Level Noise Spectrum with High Resolution (10x) Frequency Analysis

4000 Hertz are not the 18th, 19th, 20th, etc., order of propfan noise alone, but appear to be the result of an interaction between the compressor and propfan wake. The noise frequency was seen to track compressor rotation speed when power was changed; directivity of the tone noise was seen to agree with inlet rather than propfan noise directivity; and the level of these tones remained constant at conditions where propfan tone levels changed.

The broadband random noise shown in Figure 252 maximized near 800 Hertz, at a level of about 84 dB. This level is deceptively low because of the comparatively narrow (19 Hertz) analysis bandwidth used. In fact, the random noise governed the overall sound pressure level, OASPL, which at 107 dB was 9 dB above the highest tone level. The importance of this low frequency random noise was also visible in 1/3-octave analyses.

The low frequency random noise was attributed to stall on the propfan blades and/or possible inflow turbulence since the random noise behavior was consistent with the blade stress behavior. As flow separation increased, the random noise typically increased throughout the audible spectrum, but the increase in the low frequency portion of the noise spectrum was always more pronounced. For that reason, the random noise discussion and illustrations hereafter will refer to the "crest" of the low-frequency portion of the random noise spectrum.

The three spectrum components discussed above (propfan tone noise, compressor-related noise, and low frequency random noise) took on varying significance, depending on direction and power.

6.5.9.2 Directivity Effects on Spectrum Content

At an azimuthal location of 60 degrees, the propfan tone noise was lower, the compressor/propfan interaction tone noise was higher, and the random noise crest was at a higher frequency than at 30 degrees.

At 90 degrees azimuth, the propfan first-order tone level increased from the level at 60 degrees, the compressor/propfan interaction noise decreased, and the random noise level was slightly lower.

At 120 degrees azimuth, the propfan first-order tone noise decreased from the level at 90 degrees, while the higher-order propfan tones increased slightly. The compressor-related noise also showed preference to higher orders, and the level of the random noise crest increased.

6.5.9.3 Power Effects on Spectrum Content

At 60 degrees azimuth, increasing the power from 1732 kw (2323 shp) to 3007 kw (4032 shp), increased the propfan first-order tone 7 dB while the random noise crest increased 13 dB. Most of the random noise increase occurred in the 500 to 1500 Hz range.

A 1/3-octave analysis of the noise at 60 degrees azimuth, 1732 kw (2323 shp), is shown in Figure 254. This analysis illustrated the greater significance of the random noise relative to the propfan tones. The

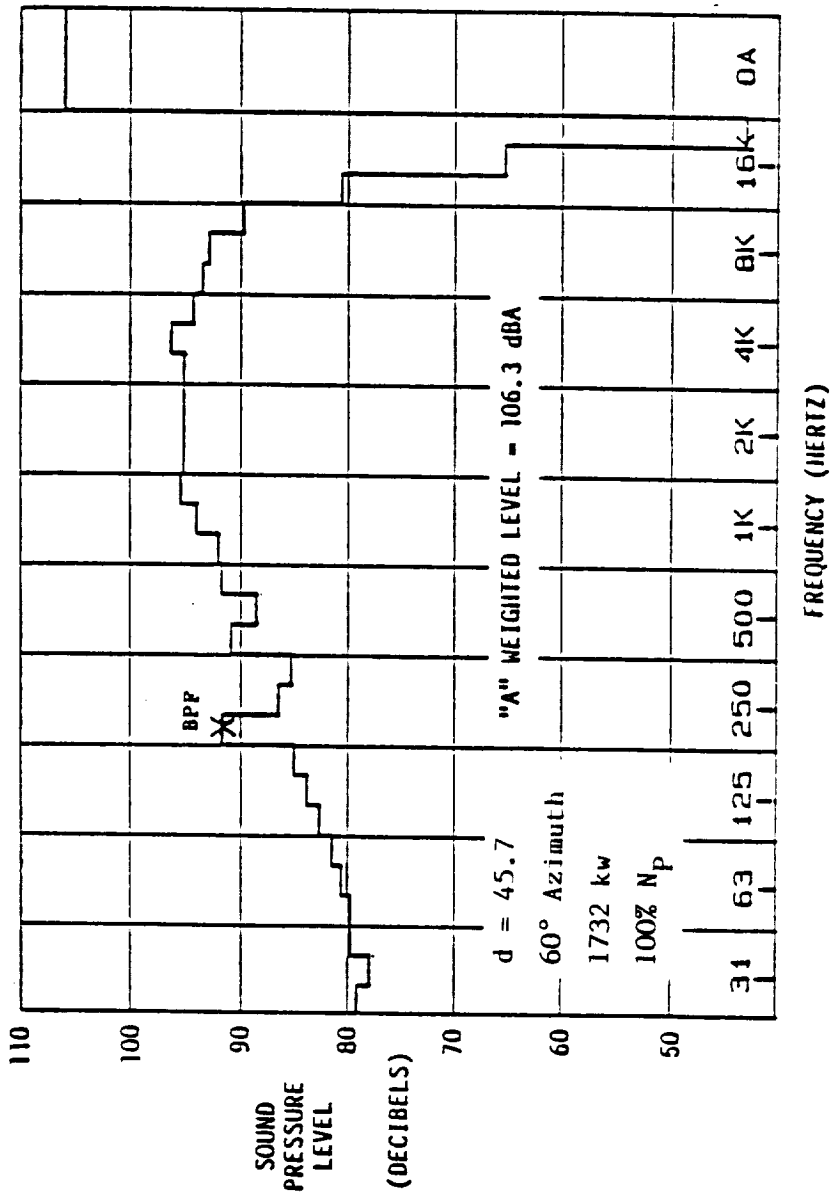


Figure 254. Ground Level One-Third Octave Noise Spectrum

random noise maximized in the 1600 Hertz band, where it was 4 dB above the propfan fundamental. The highest noise level occurred in the band containing the compressor/propfan interaction tones and random noise combined.

The 1/3-octave spectrum for the same 60 degrees azimuth and 3007 kw (4032 shp) maximized in the band containing the crest of the random noise, as seen in Figure 255.

At 90 degrees azimuth, increasing propfan power increased the propfan tone noise by 3 dB and increased the random noise by 15 dB.

At 120 degrees, increasing the propfan shaft power increased propfan tone noise about 4 dB and increased the random noise crest about 15 dB.

6.5.9.4 Far-Field Noise Directivity

Directivity was different for each of the major contributors to total noise. First order blade passage SPL for the propfan tended to peak at 115 dB from 90 degrees to 110 degrees. Random noise had approximately equal lobes at 0 degrees to 15 degrees and 130 degrees. The strongest compressor tone peaked at about 15 degrees with a secondary peak at about 50 degrees.

Subjective annoyance levels of the total noise spectrum, however, were surprisingly uniform in the range from straight ahead to ϕ = 145 degrees. This can be seen in Figures 256 and 257 where directivity curves are plotted for different tip speeds and different power levels.

6.5.9.5 Effects of Operational Parameters

The first-order blade noise at 100 degrees azimuth is shown as a function of shaft power in Figure 258. The noise levels were tip speed dependent as well as power dependent. Similar plots were made for power coefficient C_p, measured thrust, and thrust coefficient C_T. The better descriptor of first-order blade noise was thrust. The relationship is shown in Figure 259. It suggests "lift" noise as the source, since thrust relates to the forward component of blade lift.

The low-frequency random noise at 130 degrees azimuth is shown as a function of shaft power in Figure 260. At the higher tip speeds where there were sufficient data to show the trend, noise level was seen to increase roughly linearly with shaft power. At a given power, the random noise level decreased as tip speed increased. The relationship of random noise to blade lift (measured thrust) is presented in Figure 261. At a given tip speed, random noise increased nonlinearly with thrust, while at a given thrust, random noise decreased as tip speed increased. Blade vibratory stress behaved in a similar fashion. All of these trends indicate that random noise was strongly related to blade stall. This random noise would be expected to be substantially lower in flight, where flow through the propeller disc is clean and blade stall is absent.

The random noise data are correlated with thrust coefficient C_T in Figure 262 where the data are seen to converge toward a single nonlinear

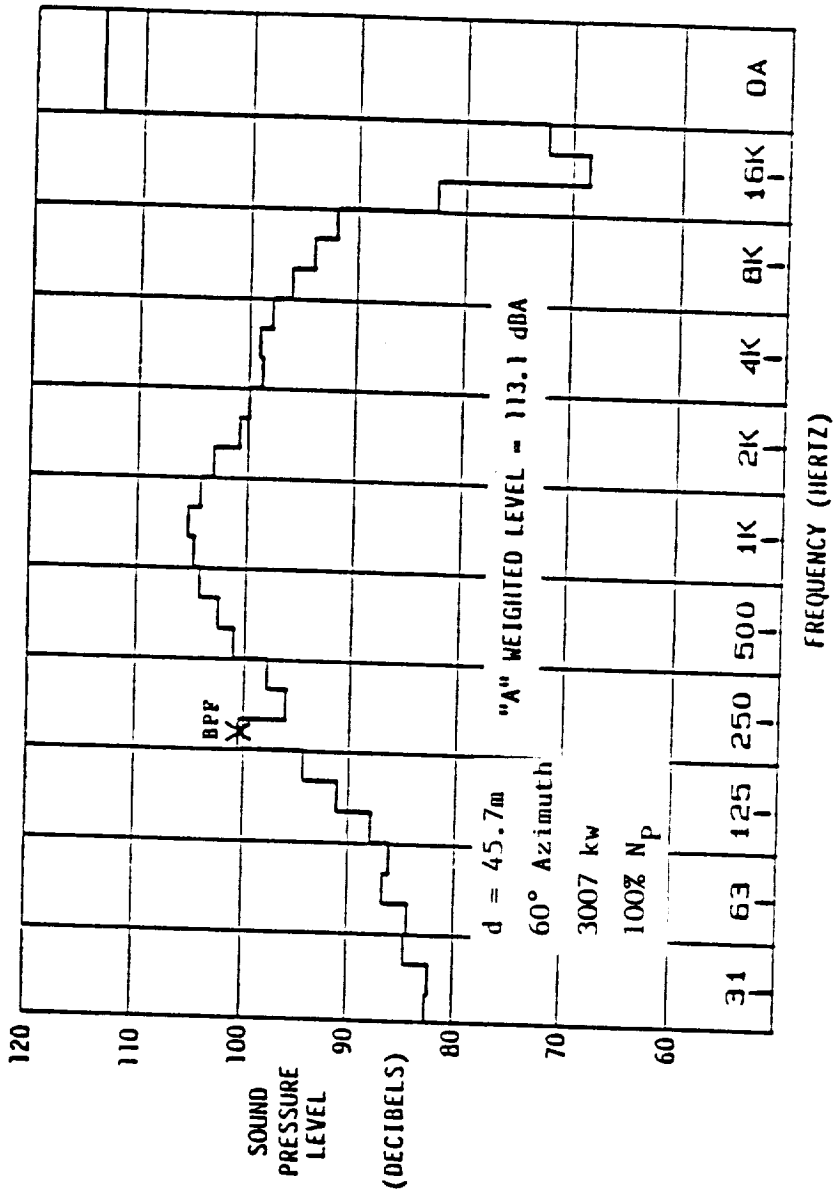


Figure 255. Ground Level One-Third Octave Noise Spectrum

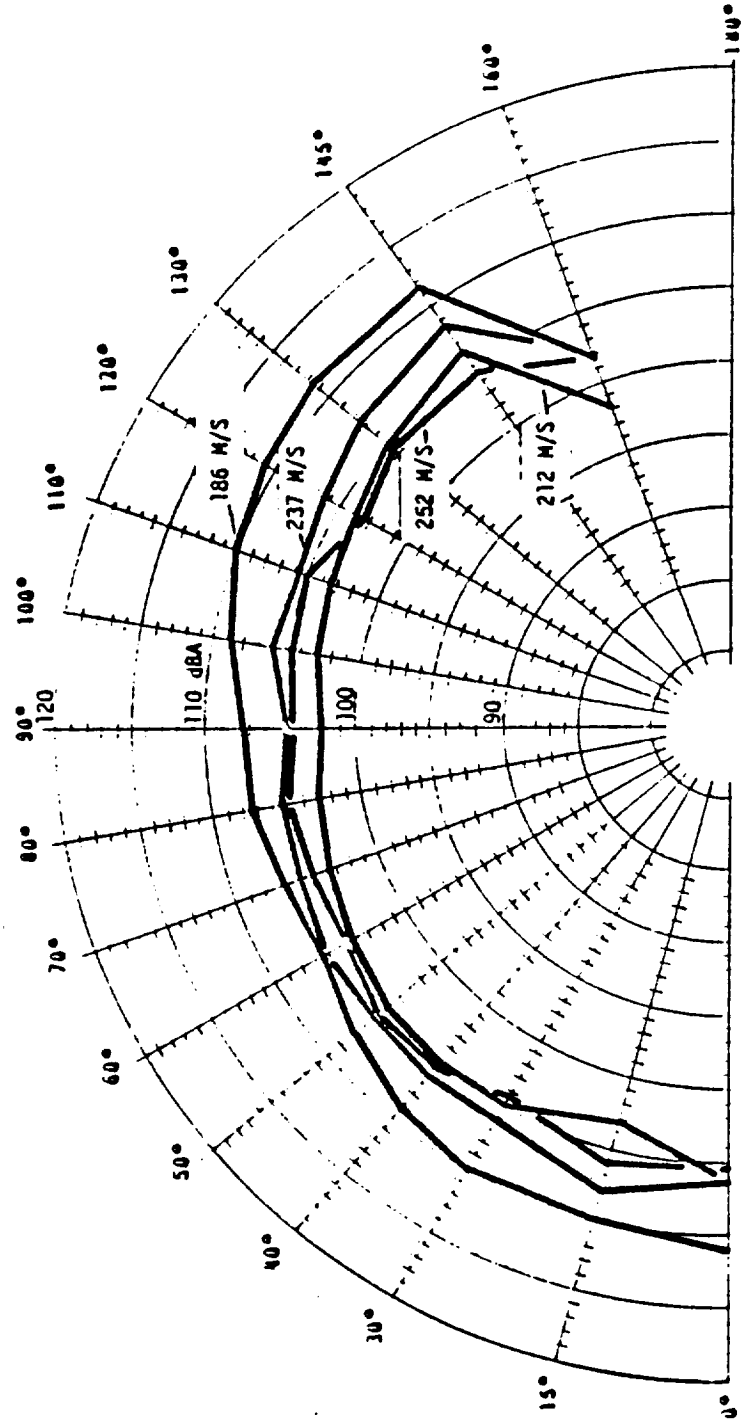


Figure 256. Ground Level Subjective Noise Level - Minimum Test Powers

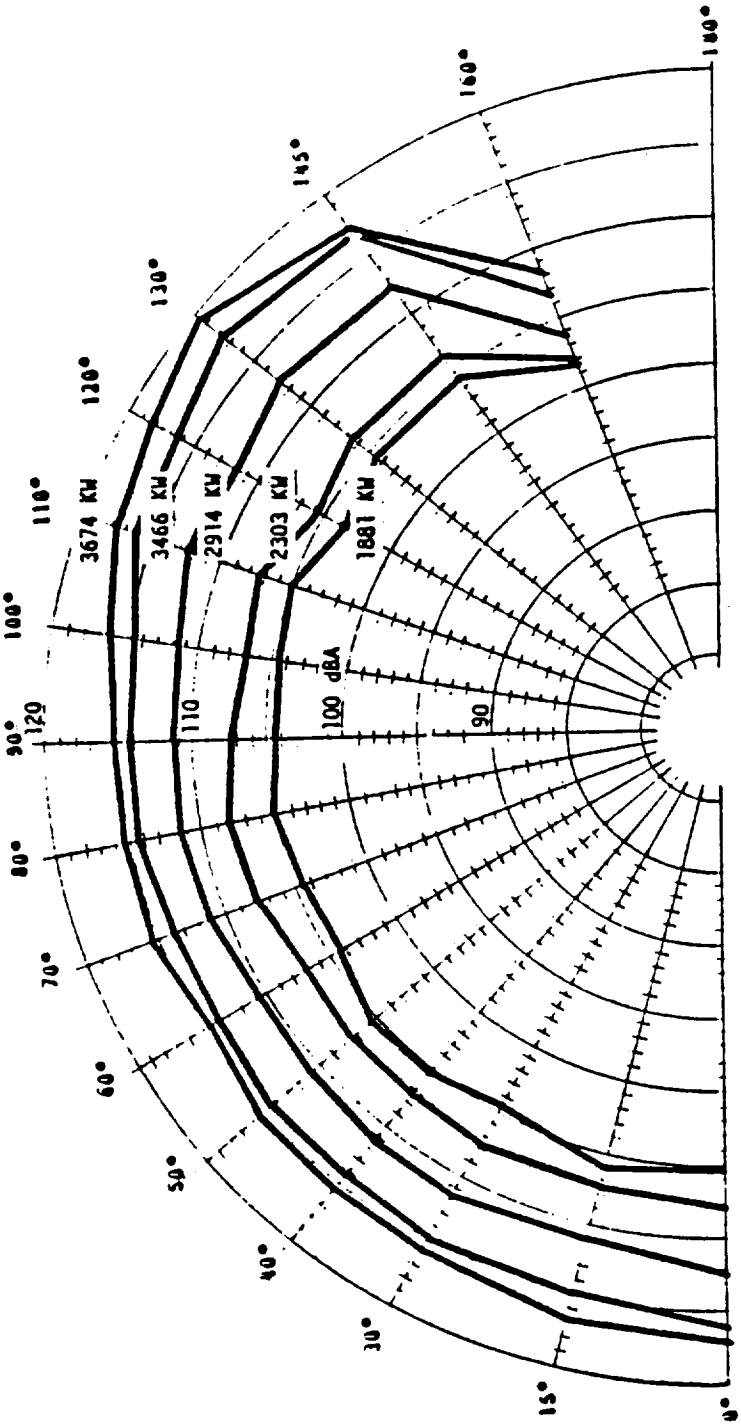


Figure 257. Ground Level Subjective Noise Level - 105% N_p

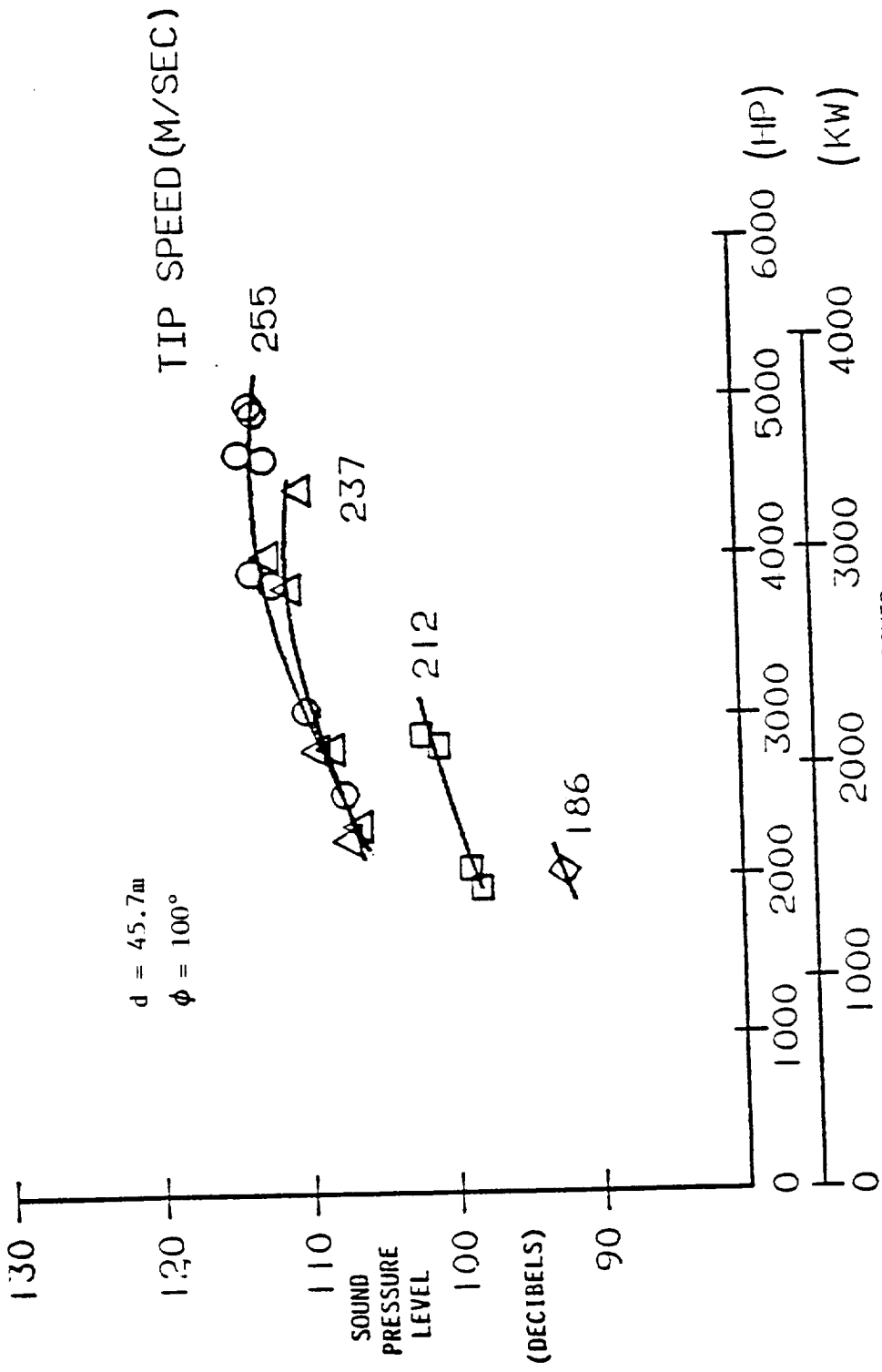


Figure 258. Ground Level First Order Blade Noise Dependence on Power

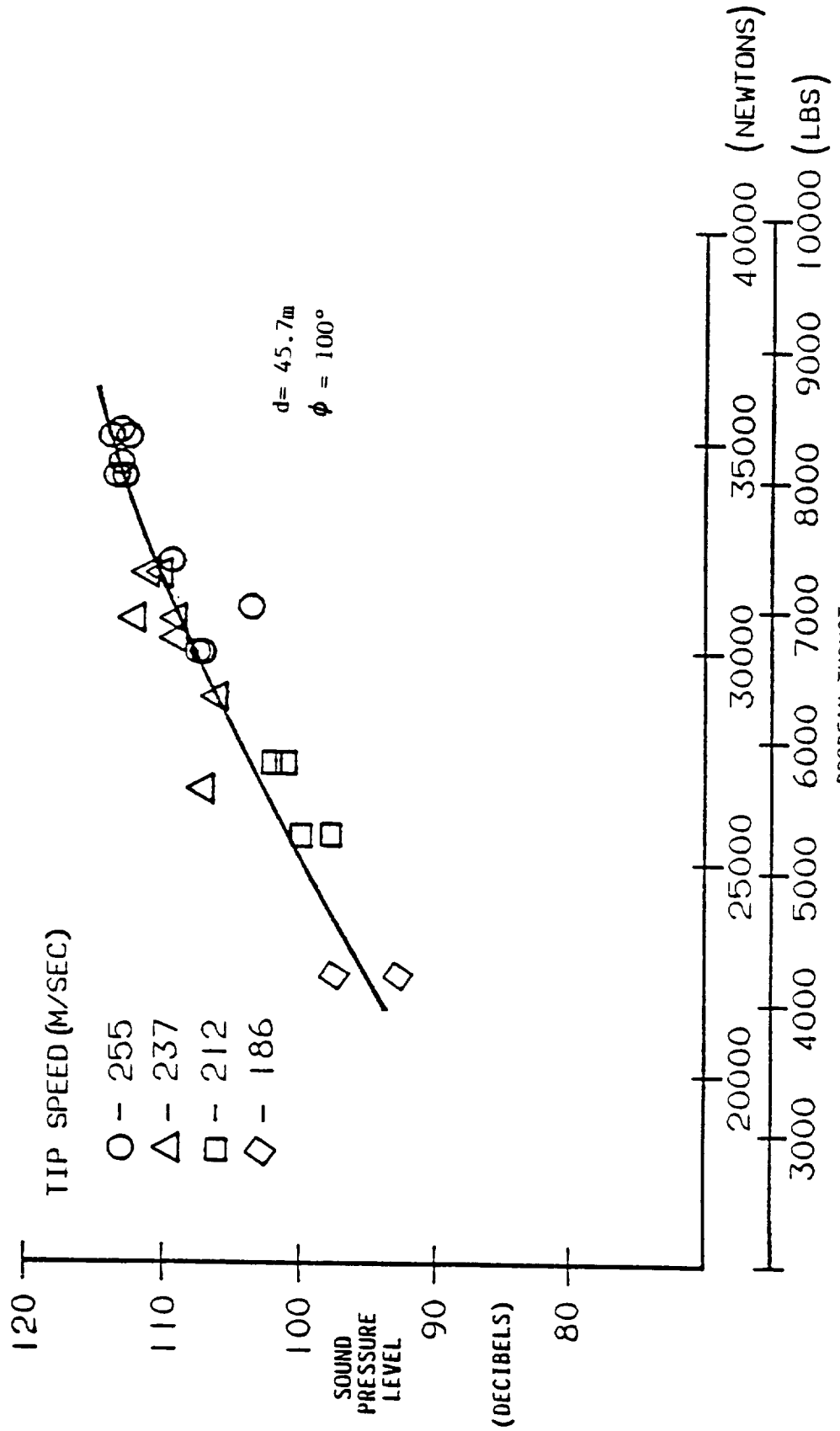


Figure 259. Ground Level First Order Blade Noise Dependence on Thrust

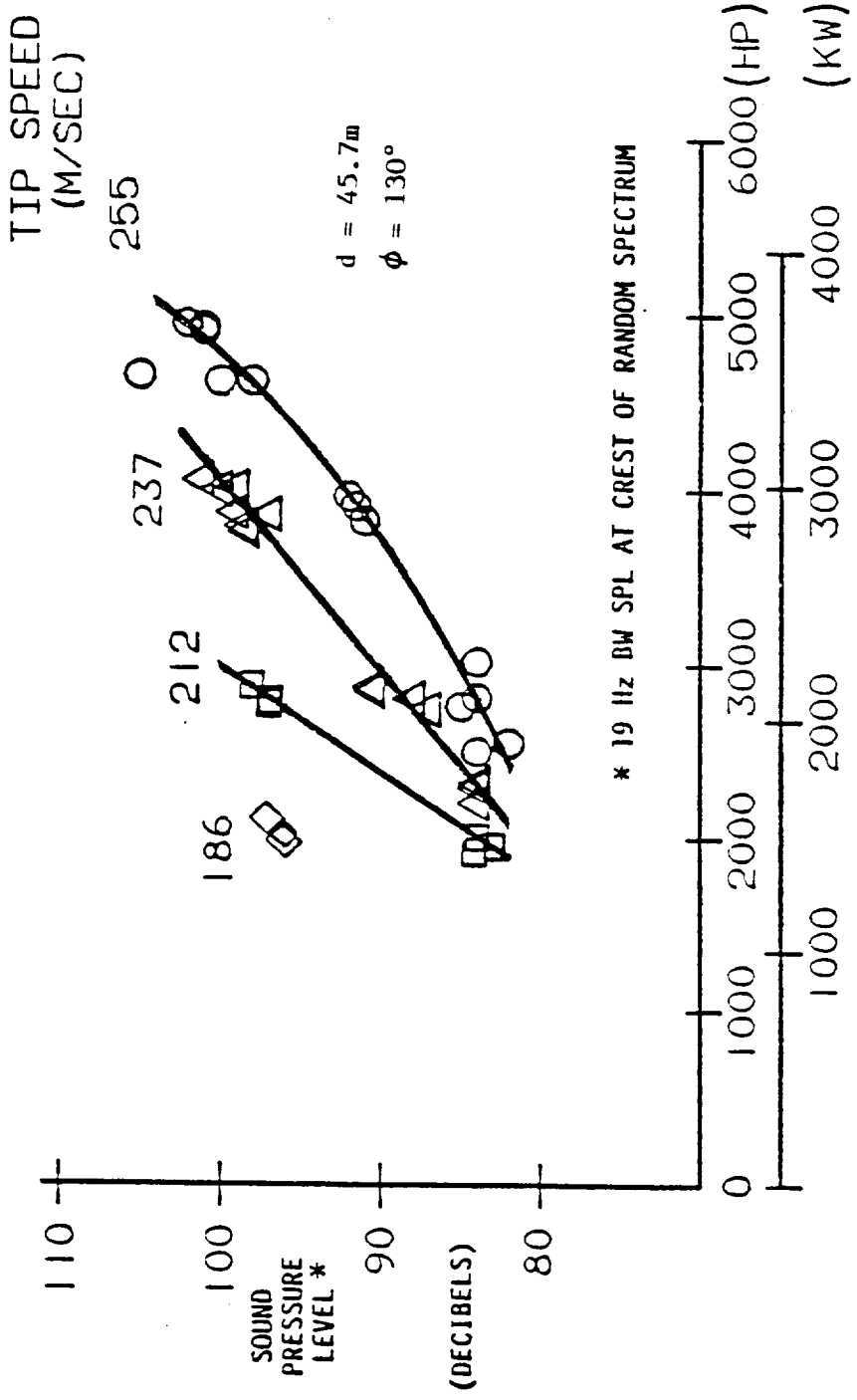


Figure 260. Ground Level Random Noise Dependence on Power

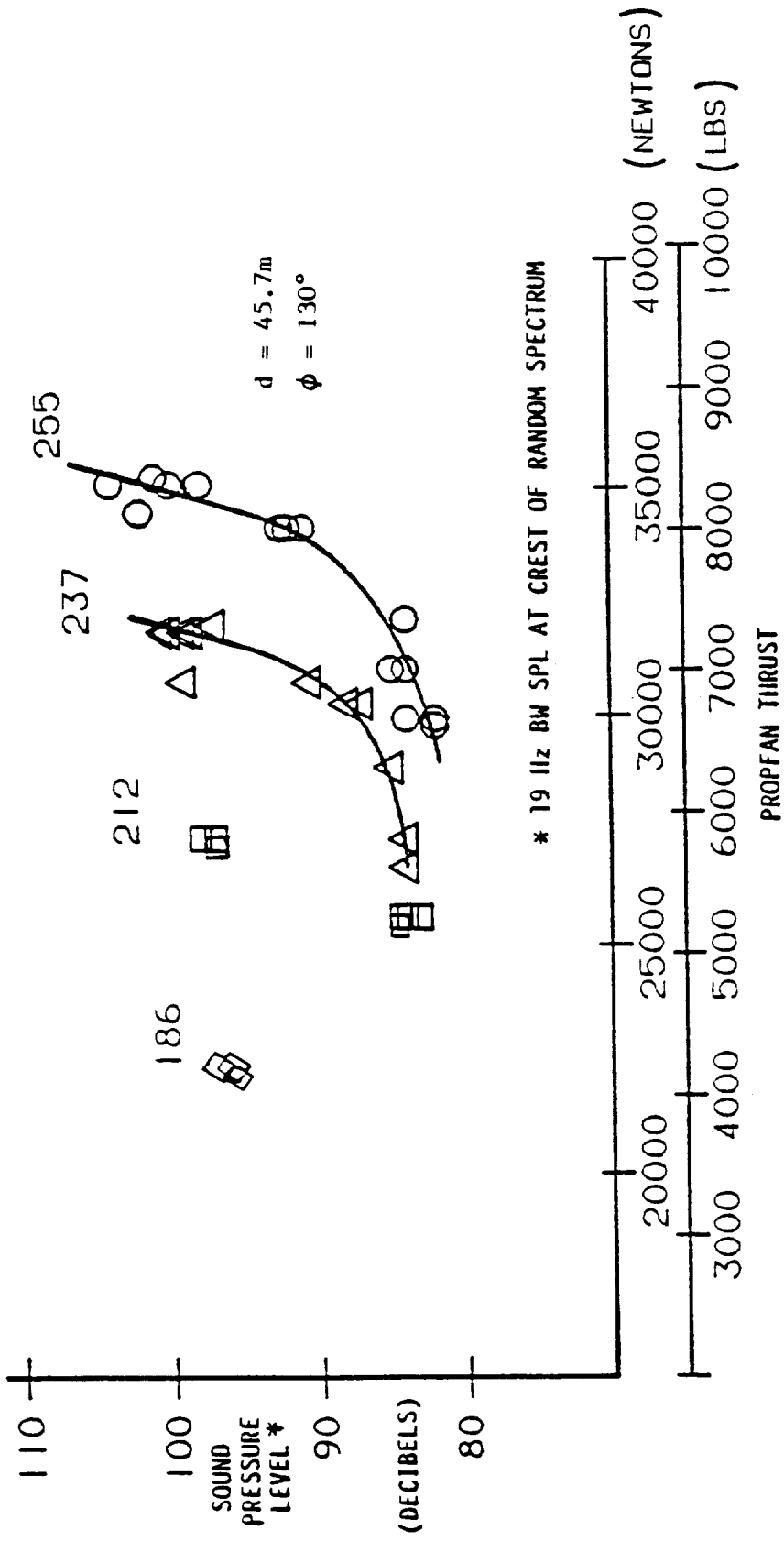


Figure 261. Ground Level Random Noise Dependence on Thrust

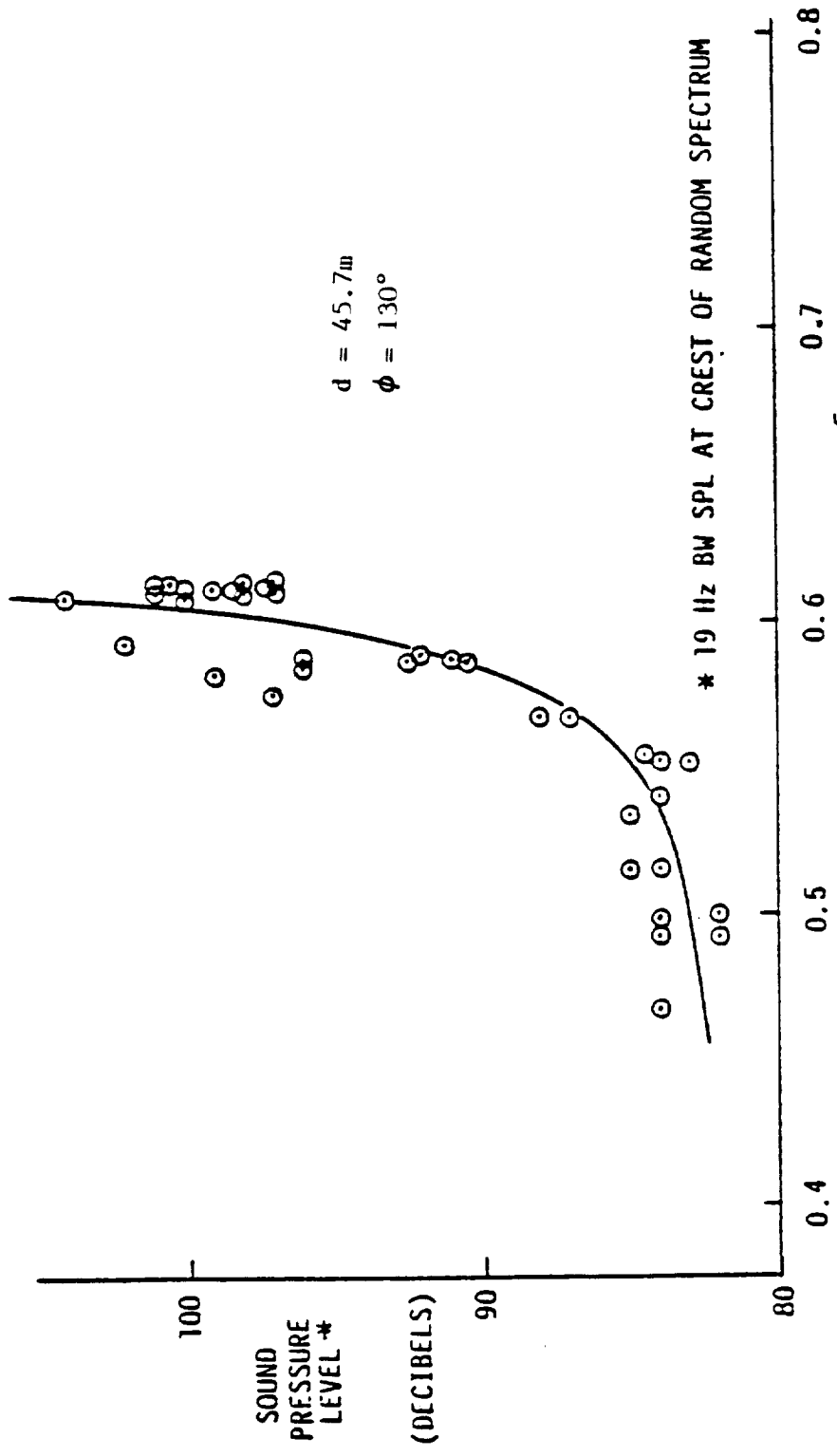


Figure 262. Ground Level Random Noise Relationship to Thrust Coefficient

curve. A better describer of the random noise level was found to be power coefficient, C_p. As shown in Figure 263, when plotted against C_p, the noise data for all tip speeds converged toward a single slightly nonlinear curve.

The compressor/propfan multiple-tone interaction noise at 50 degrees azimuth is shown as a function of shaft power in Figure 264. In this figure, the ordinate is the sound pressure level of the strongest interaction tone, regardless of the tone frequency. The strongest interaction tone frequency was always in the range of 4000 to 5500 Hertz. The tone level data followed a linear power relationship with rather flat slope, indicating only a mild sensitivity to power. The tone-level sensitivity to thrust was very similar. At the higher shaft power conditions, the compressor/propfan interaction noise was masked by the random noise. Frequency-wise, the compressor related tones were well removed from the propfan tones and did not contaminate the propfan tone measurement.

Data with the acoustic barrier in place led to the conclusion that this low frequency random noise originated at the propfan and was not combustion noise.

6.5.9.6 Near-Field Noise Analyses

Near-field noise was recorded at seven sideline microphone locations that relate to positions on the PTA aircraft fuselage as shown in Figure 265.

Spectra from data recorded at these locations showed the same characteristic propfan tones, random noise, and compressor tones that were observed in the far-field data.

Propfan first-order blade passage sound pressure levels at the seven equivalent fuselage stations are shown in Figure 266 for the nominal tip speed of 237 mps (800 fps). These data show the tone level maximized at equivalent FS 322, which was slightly aft of 90 degrees from the propfan. While the spacing of the microphones was too great to pinpoint the location of the maximum level, the microphone at equivalent FS 322 was within the directivity lobe of high levels observed in the far field and should be within a few dB of the maximum.

The noise level peaked at an intermediate horsepower rather than the highest power. This behavior also resembled that observed for the far-field data. It was probably because directivity changed with power, and the single microphone at equivalent FS 322 missed the maximum.

First-order blade noise distributions as a function of tip speed, for roughly equal, moderate, shaft power conditions, are shown in Figure 267. In the region of the maxima, the noise level increased systematically with tip speed. Aft of the maxima the noise levels were less dependent on tip speed.

For fuselage sonic fatigue design purposes, the near-field noise was the highest at the high tip speeds and high powers, where worst case levels reached 141 dB. This was still well below the levels expected during

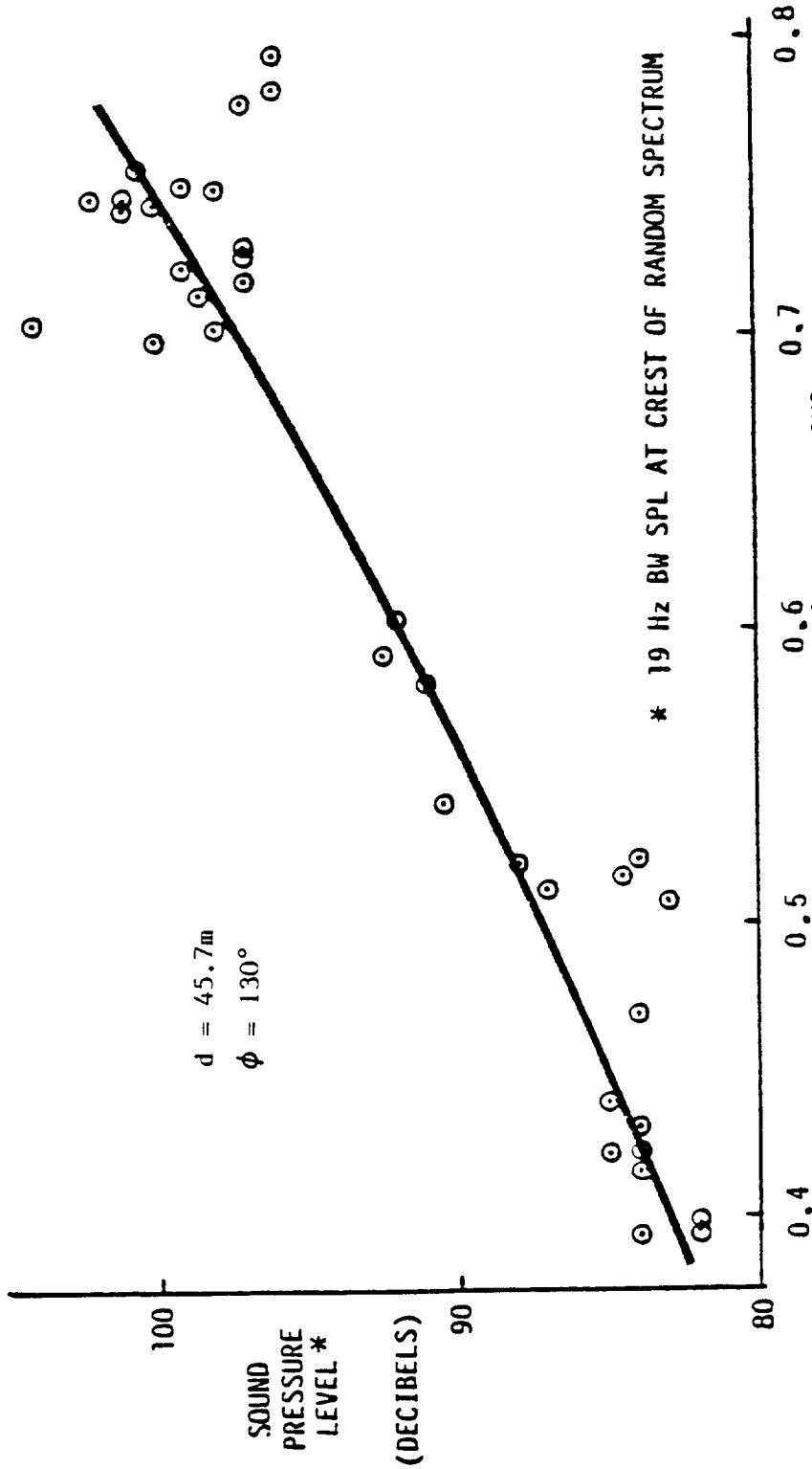


Figure 263. Ground Level Random Noise Relationship to Power Coefficient

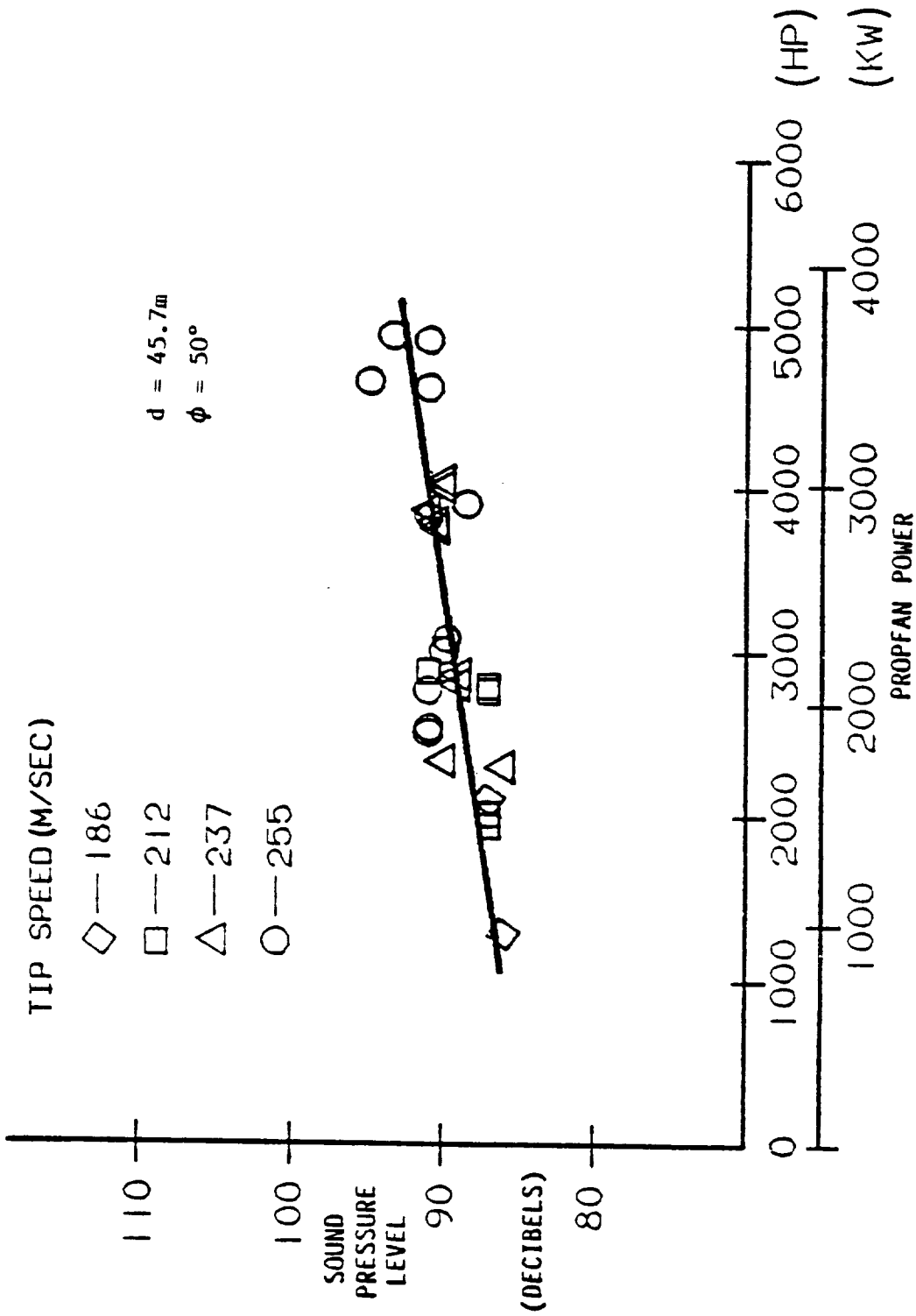


Figure 264. Ground Level Compressor/Propfan Interaction Tone Noise Dependence on Power

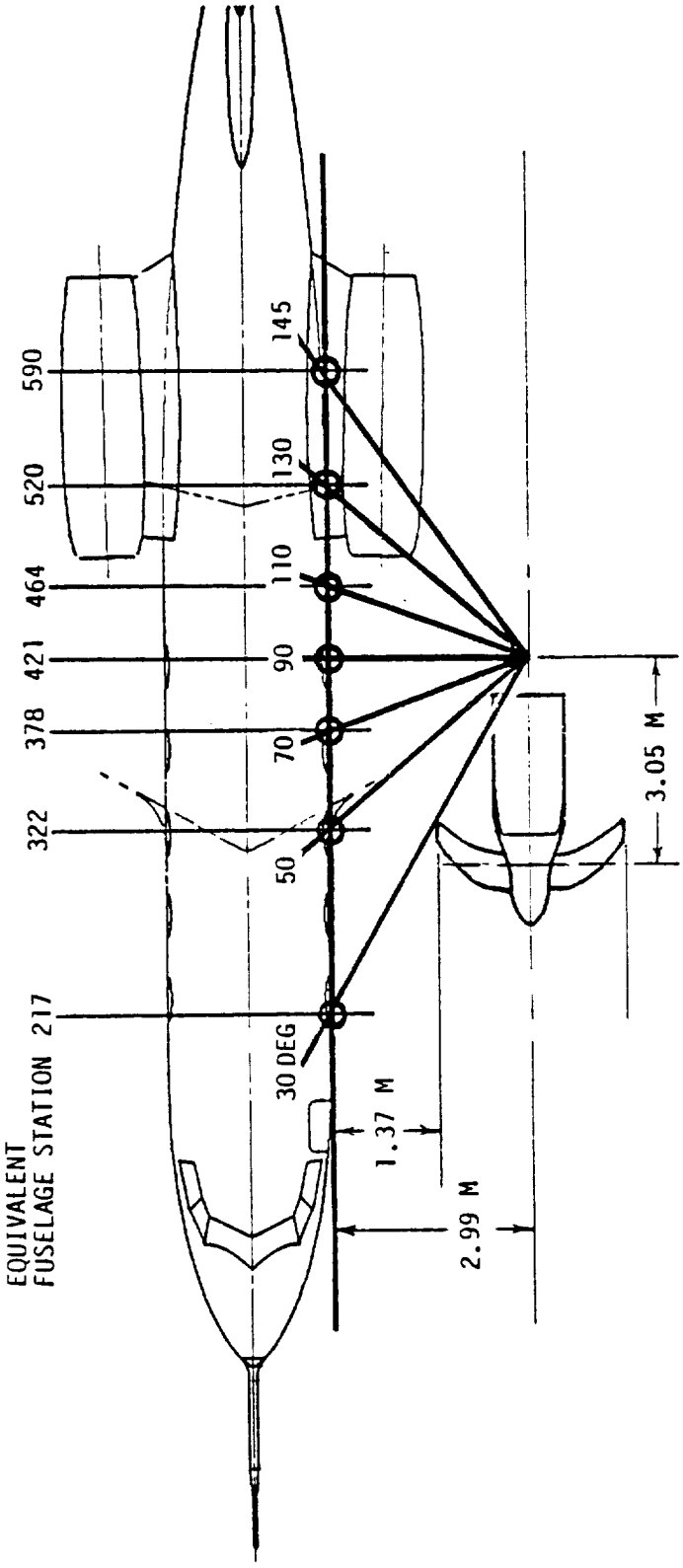


Figure 265. Near-Field Microphone Locations Relative to Aircraft Fuselage

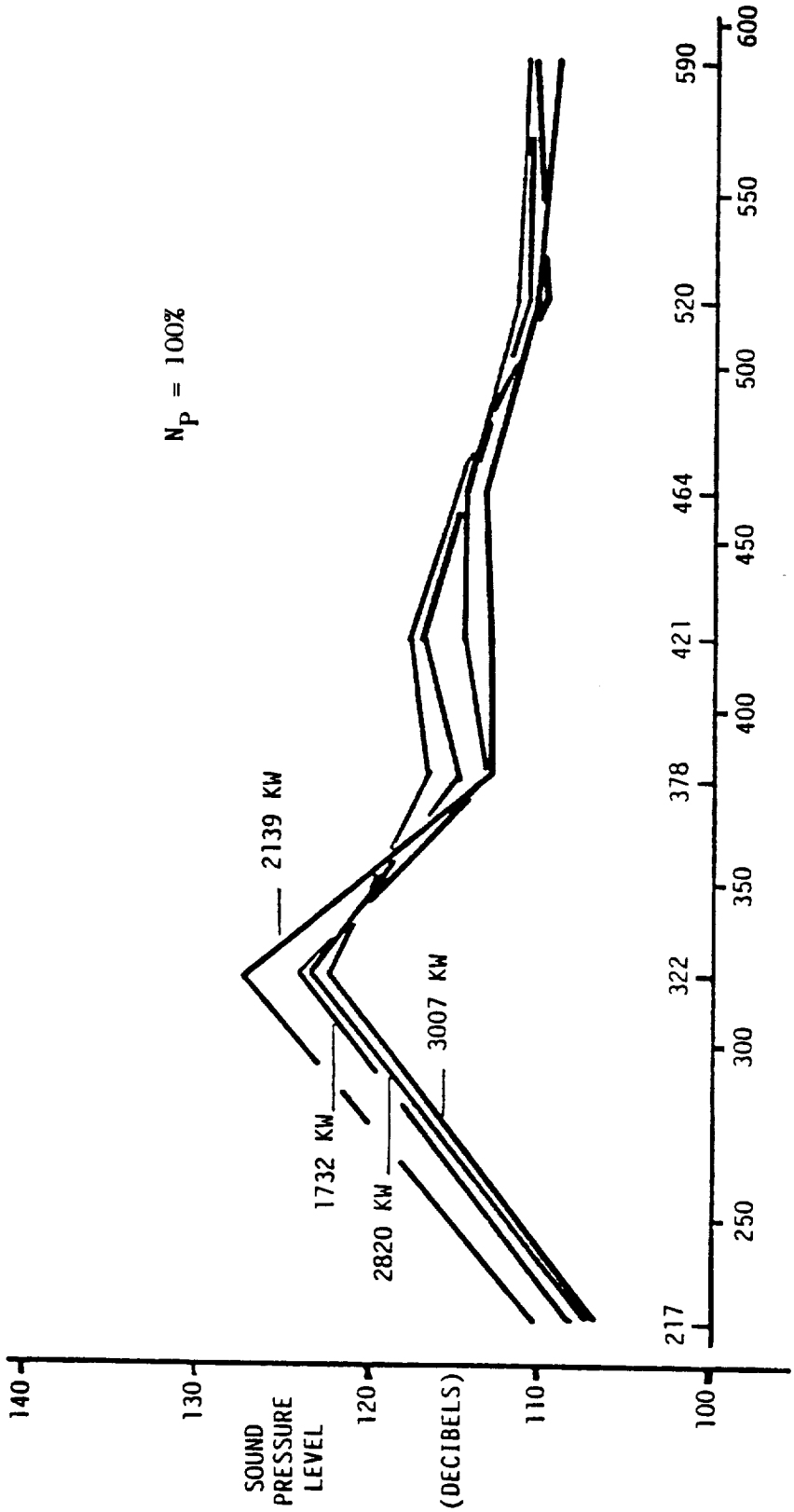


Figure 266. Near-Field BPF1 Noise Levels at Equivalent Fuselage Stations for Different Powers

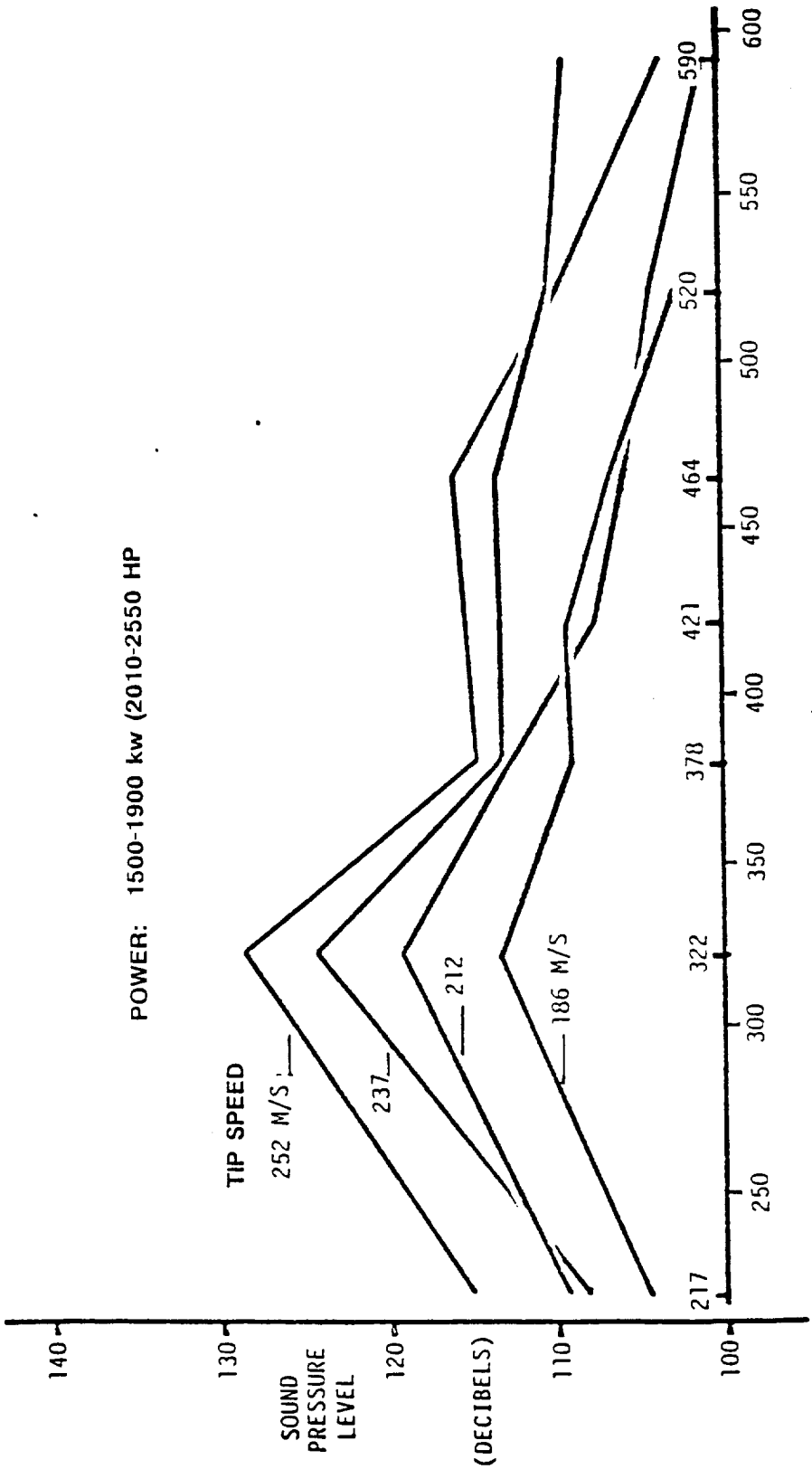


Figure 267. Near-Field BPF1 Noise Levels at Equivalent Fuselage Stations for Different Tip Speeds

high-speed cruise. Since the testbed fuselage shell was reinforced to tolerate the cruise case, it should not be unduly affected by ground running.

Cabin noise levels that result from exterior surface noise being transmitted to the interior will be substantially higher in flight because of the higher exterior noise during that condition. Crew ear protection provisions that are suitable for the flight case should therefore be adequate for ground running.

Instantaneous and time-averaged sound pressure signatures were obtained for selected conditions to reveal the nature of the pressure loading on the structure and to determine the non-uniformity, if any, of the pressure waves from the propfan blades.

Examples of a typical instantaneous and an average of 50 pressure wave samples of 200 milliseconds duration (about 5.5 propfan revolutions, or 44 blade passes) are shown in Figure 268 for equivalent Fuselage Station 322. The averaged wave shows the same characteristics as the far-field data, i.e., certain blade signatures were consistently weaker (indicated by "W"), and others consistently stronger (indicated by "S"). Typically, the strongest and the weakest pressure signatures deviated from the average by about 10 percent.

A typical instantaneous and an average of 50 pressure wave samples of 8 milliseconds duration is shown in Figure 269 for the same equivalent Fuselage Station 322. The instantaneous wave illustrates the complex nature of the instantaneous pressure loading on the structure. Because random pressures coexisted with the discrete phase-correlated pressures, the instantaneous pressure loading varied a great deal between samples. In the time-averaged pressure wave, the randomly phased pressures averaged to near zero, leaving only the discrete phase-correlated pressure. The first-order wavelength was seen to dominate at the location and condition shown. The pressure distribution was slightly saw-toothed, but essentially sinusoidal.

6.5.10 Propfan Performance

6.5.10.1 Aerodynamic Performance

Propfan aerodynamic performance data gathered during the stress survey and the endurance test are presented in Figures 270 and 271. The data were corrected for ambient temperature and pressure, nondimensionalized, and compared with analytical predictions and the results of the LAP static rotor test. The large amount of scatter in the power coefficient versus blade angle data was the result of significant hysteresis and dead band in the blade angle instrumentation. However, the same data trends that were observed in the LAP test data were discernible in the PTA test data. The power coefficient began to fall short of predictions at blade angles above 30 degrees. The plot of thrust coefficient versus power coefficient shows that the thrust measured during the PTA test seemed to be slightly lower than thrust measured during the LAP test in the lower blade angle range. However, the same maximum thrust coefficient was obtained for both tests.

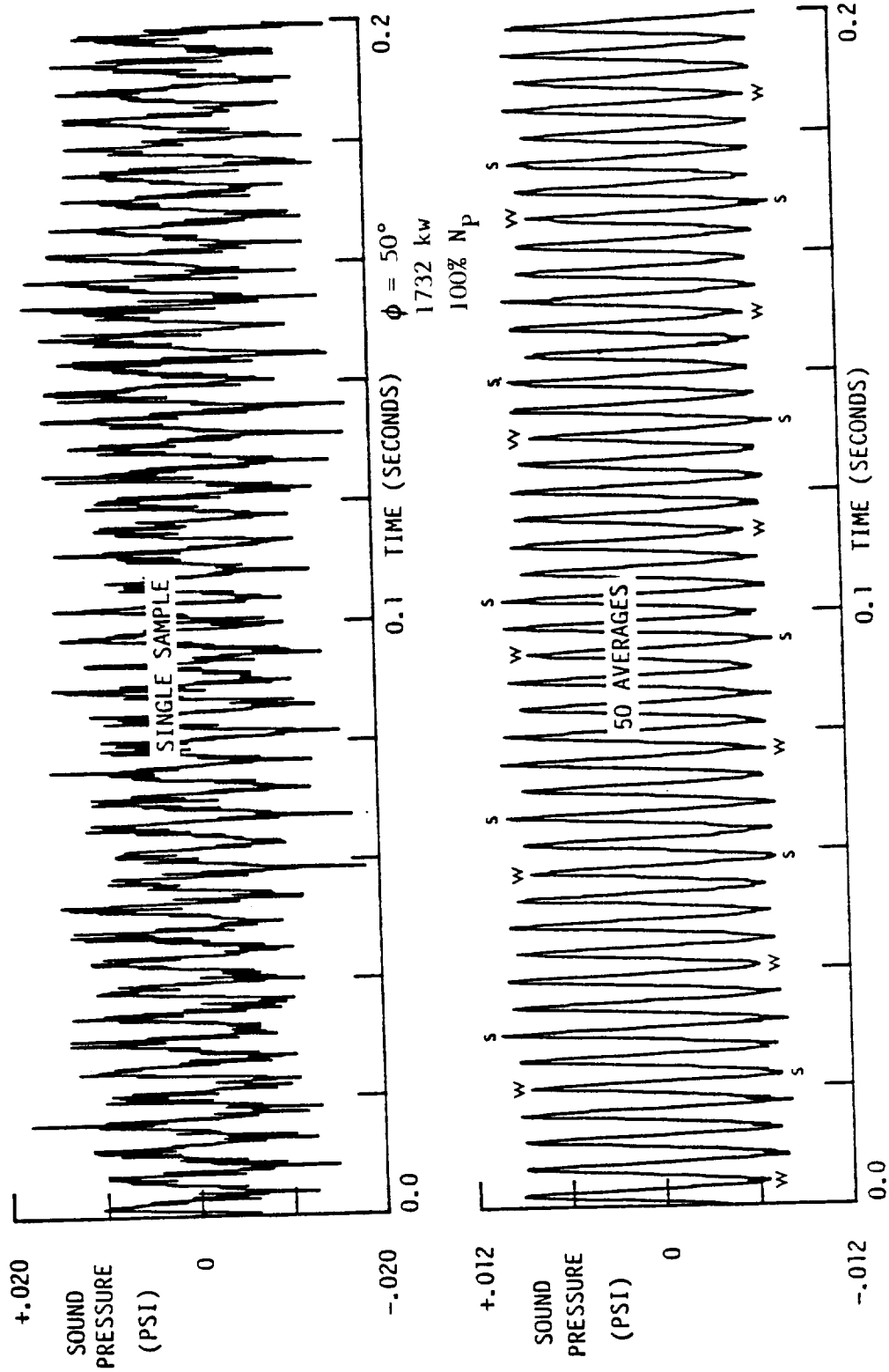


Figure 268. Near-Field Sound Pressure Time Histories Centerline Height Sound Pressures

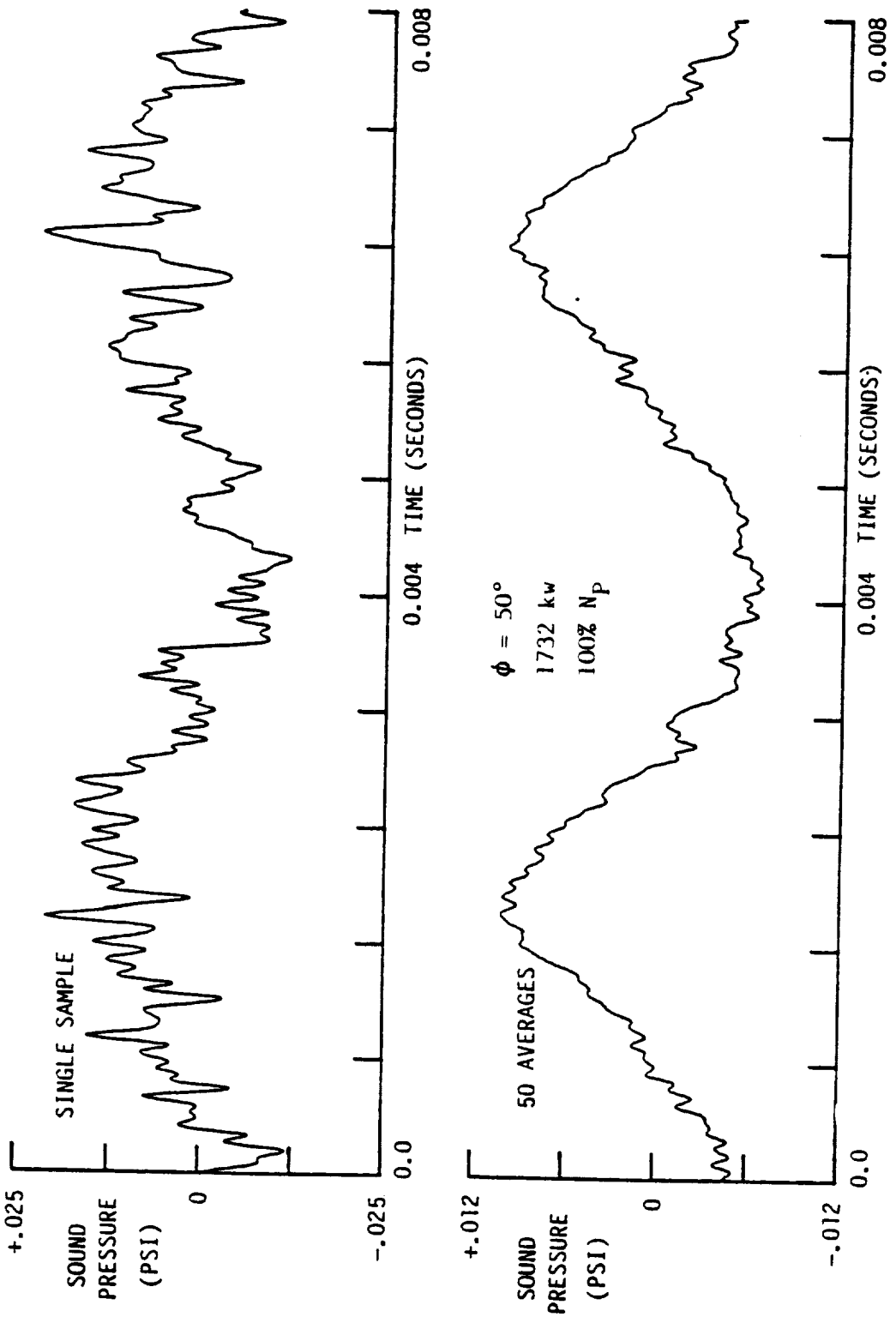


Figure 269. Instantaneous and Average Pressure Wave Samples

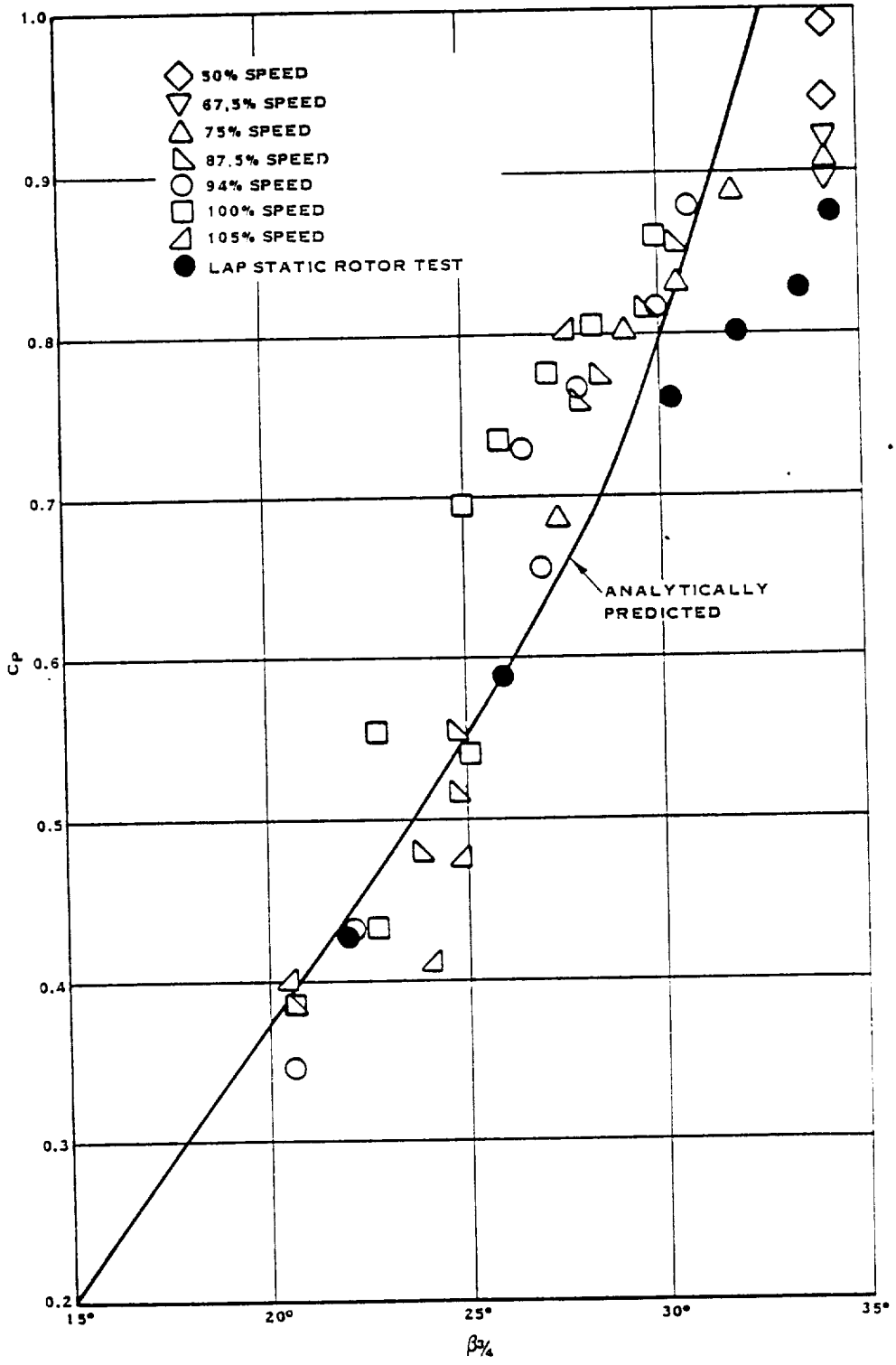


Figure 270. Propfan Power Coefficient vs Blade Angle

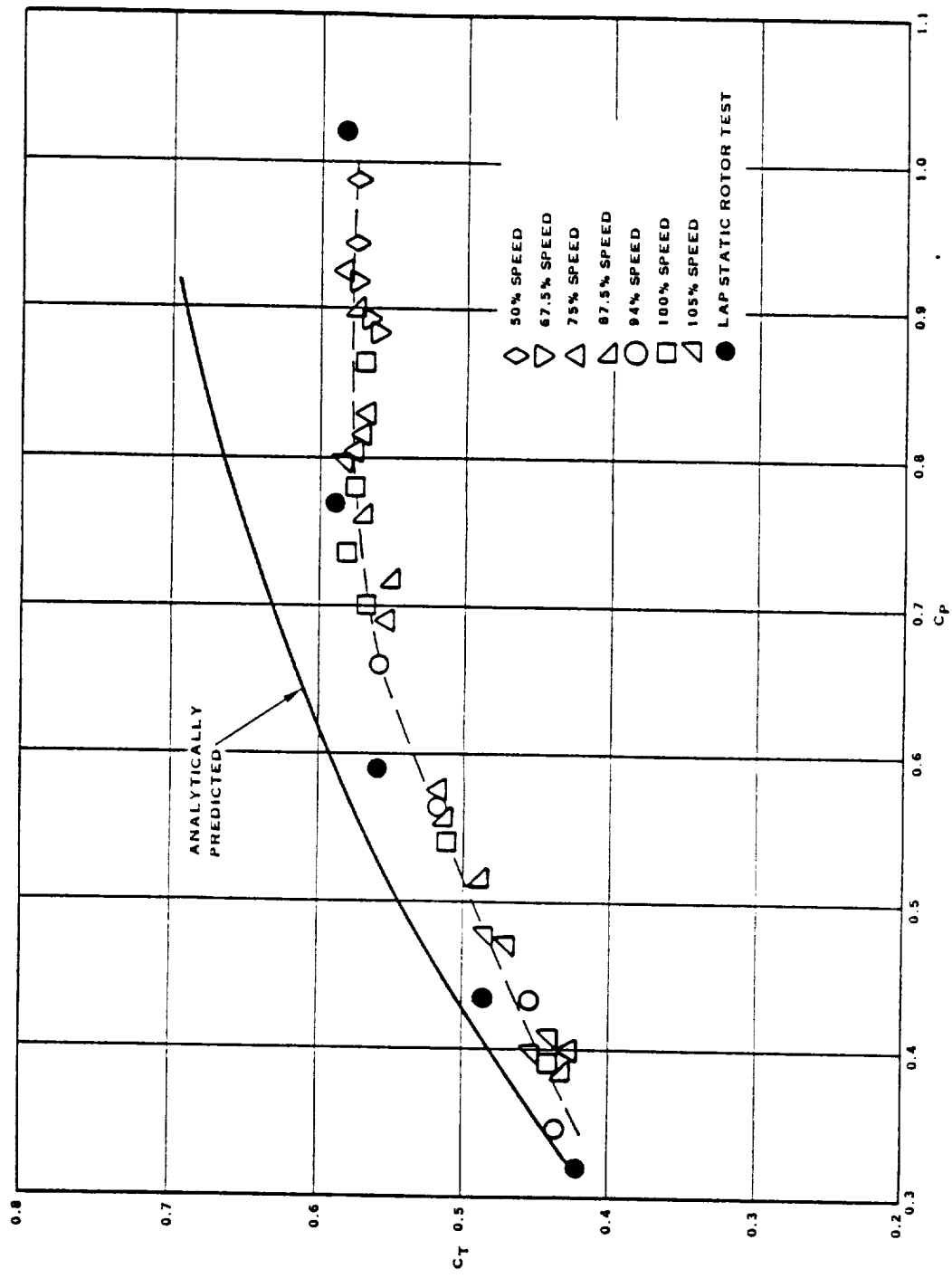


Figure 271. Propfan Thrust Coefficient vs Power Coefficient

The reason for the lower PTA thrust at the lower blade angles may be related to the 4.5 mps (8 mph) headwind that was present throughout most of the test. The effect of a headwind was to reduce the angle of attack seen by the blades for a given blade pitch angle.

6.5.10.2 Mechanical Performance

During the course of testing, oil leakage was observed from the rear lip seal area of the propfan control. Upon completion of testing, the leakage was eliminated by bonding a new seal into the retainer.

During the test program, the blade strain continuous operating limits were slightly exceeded due to variations in wind speed and direction when operating near limit conditions. As a result of these tests, the static operating limits were revised as shown in Figure 272.

6.5.11 Drive System

Allison supplied a performance program to calculate engine performance data. This program was developed based on the engine and test stand instrumentation available during the static test. In order to compare the test results with the results obtained during power section and gearbox testing at Allison, this performance program corrected the data to sea level unity ram conditions. In the correction process, however, several assumptions were necessary. For example, since the engine exhaust static pressure was not instrumented, the ram pressure ratio across the engine had to be estimated. Also, the effect on engine performance of inlet pressure and temperature distortion due to the inlet duct could not properly be accounted for with only the single compressor inlet pressure/temperature probe.

6.5.11.1 Steady State Performance

The 501-M78B drive system provided necessary power for all requirements of the static test while operating within engine specification limits. A maximum disc loading factor of 503.3 kw/m^2 (62.7 shp/D_p^2) was provided with a comfortable measured gas temperature (MGT) margin of 56°C (100°F) below the maximum continuous rating. Oil consumption was virtually non-existent with a final oil loss (which included not only oil consumption and leaks, but also losses due to magnetic plug inspections) of approximately 3.8×10^{-4} m^3 (0.1 gal.) per operating hour. Stable operation was demonstrated at every required point during the test.

6.5.11.2 Sea Level, Unity Ram Performance

Figures 273 through 275 reflect performance comparisons from propulsion system testing at Rohr and power section testing at Allison. The static test data were taken from the pre-endurance performance calibration. The Allison data consisted of the final ambient performance calibration conducted on engine Serial Number 0085. Both sets of data were corrected to unity ram, allowing a comparison to validate instrumentation, correction factor accuracy, and engine health. Figure 273 shows that corrected gas generator speeds versus power section power were nearly identical for the

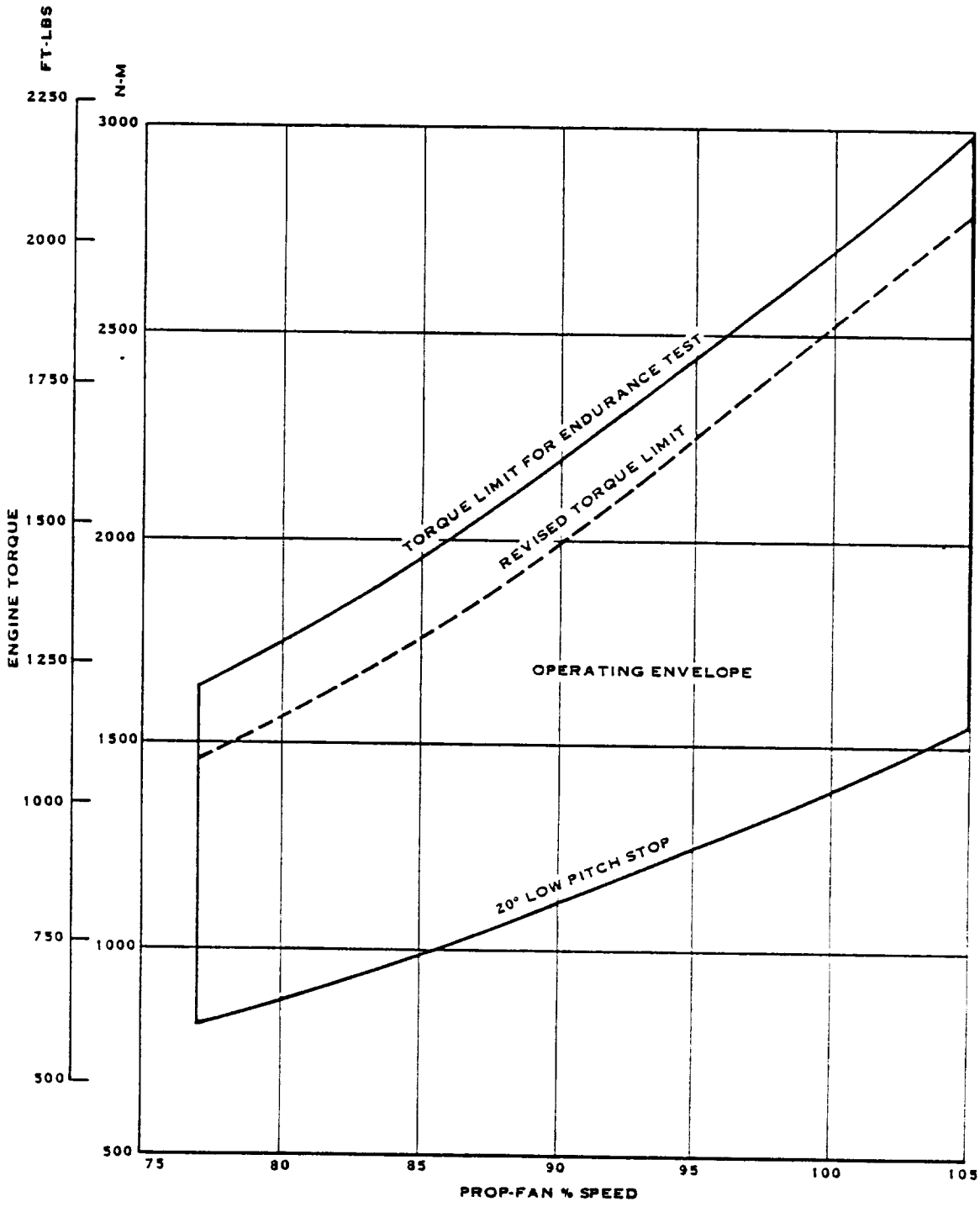


Figure 272. Revised Static Operating Envelope

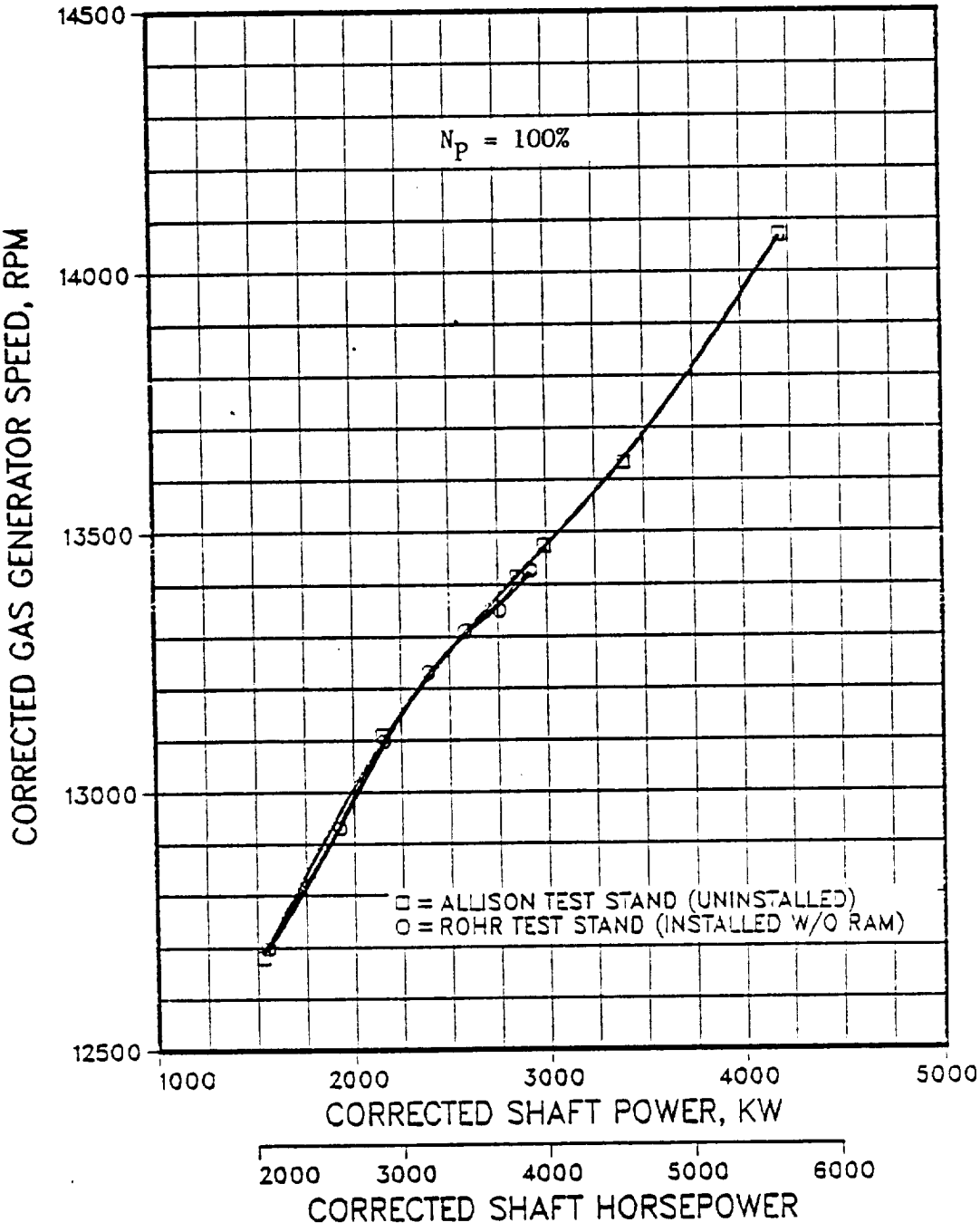


Figure 273. Installation Effects on Unity Ram Gas Generator Speed

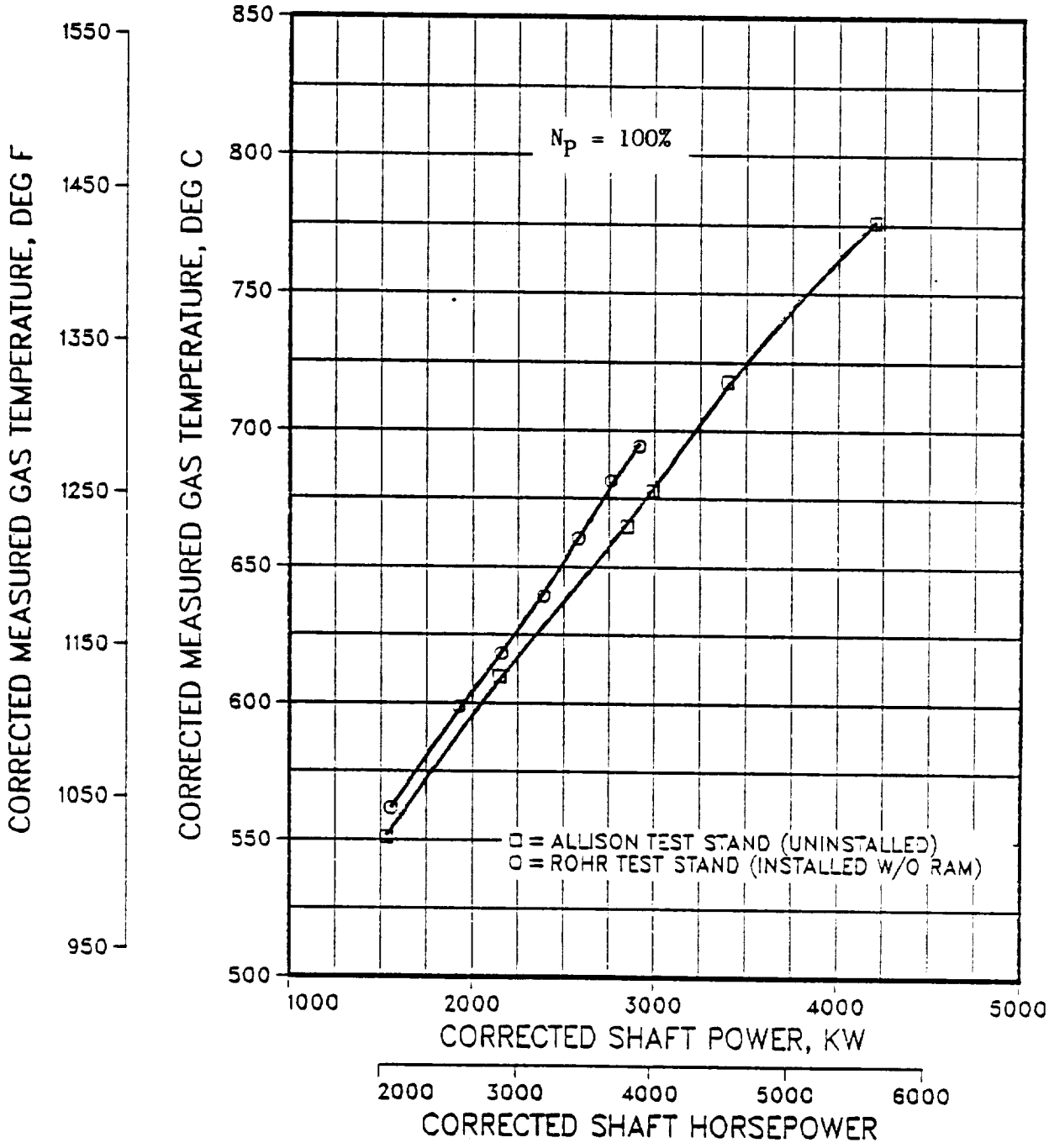


Figure 274. Installation Effects on Unity Ram MGT

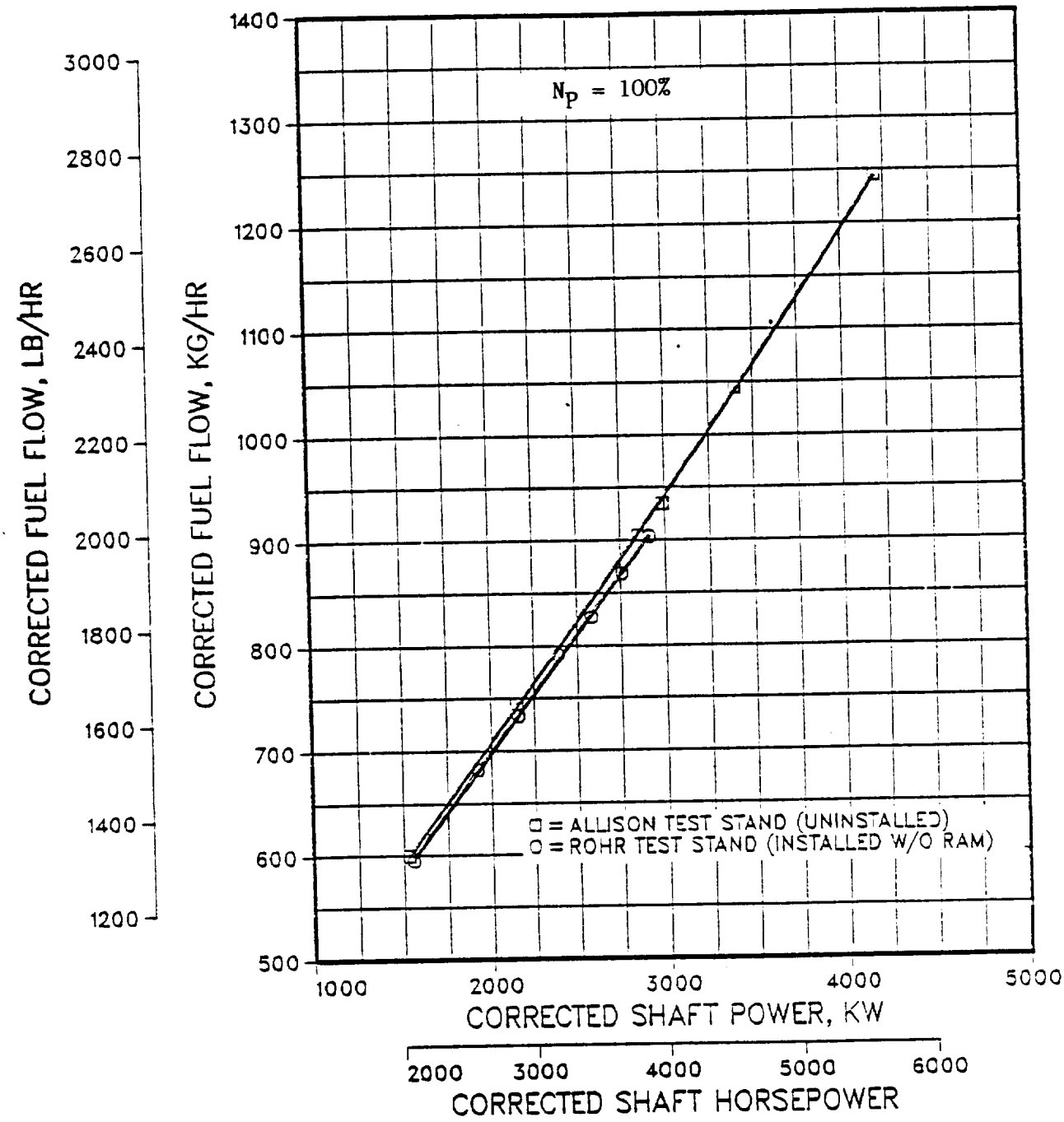


Figure 275. Installation Effects on Unity Ram Fuel Flow

two runs. This helped to verify the accuracy of engine instrumentation such as the torquemeter, rotor speeds, and the compressor inlet temperature and pressure probes. Figure 274 shows that corrected MGT data from the static test were slightly higher than the MGT measured on the Allison power section test stand. Installed static test MGT was within 1.5 percent of the power section uninstalled test data. Corrected fuel flow rates, shown in Figure 275, agree within 2.5 percent between the two test stands.

6.5.11.3 Ram Effects

Figures 276 through 278 compare the installed power section performance, which included the ram effect of the propfan, to unity-ram results obtained at Allison. The data presented in these figures reflect the improvement in drive system performance due to the ram assist from the propfan. At the maximum corrected MGT run in the pre-endurance calibration at Rohr, 7 percent more power was produced by the power section than was produced under unity-ram conditions on the isolated power section test at Allison. Extrapolation to the maximum continuous MGT rating shows that the power section could be expected to produce a 10-percent power margin above specification requirements.

6.5.12 Subsystems Performance

Propulsion subsystem characteristics were measured and recorded concurrent with propfan and drive system performance during static testing.

6.5.12.1 Propfan Oil Cooling

The propfan fluid cooling system maintained the hydraulic fluid temperature at or below 87°C (188°F) throughout the endurance test cycles. Fluid cooling is dependent upon not only the heat rejection rate from the propfan, but also on the fuel flow rate. Therefore, the more critical periods with respect to propfan fluid cooling occurred at high propfan speed and relatively low engine power. Prolonged operation under these conditions resulted in relatively high prop fluid temperatures as well as high engine fuel pump inlet temperatures. As shown in Figure 279, the maximum prop fluid temperatures occurred during endurance testing at the 105-percent propfan design speed, 1865 kw (2500 shp) test condition. These maximum temperatures occurred at test stand supplied fuel temperatures of approximately 27°C (80°F), which were considerably higher than the estimates of 10 to 16°C (50 to 60°F) for the stored fuel.

Both propfan fluid temperature and fuel engine inlet temperature increased rapidly during the reverse thrust test. Propfan hydraulic fluid reached 114°C (237°F) within approximately 15 minutes after starting the engine. Fuel inlet temperature exceeded 100°C (212°F) at shutdown.

6.5.12.2 Engine Oil Cooling

The power section and gearbox oil cooling system provided sufficient cooling throughout the static test to maintain the oil temperature within the engine specification limits. Figure 280 shows drive system oil

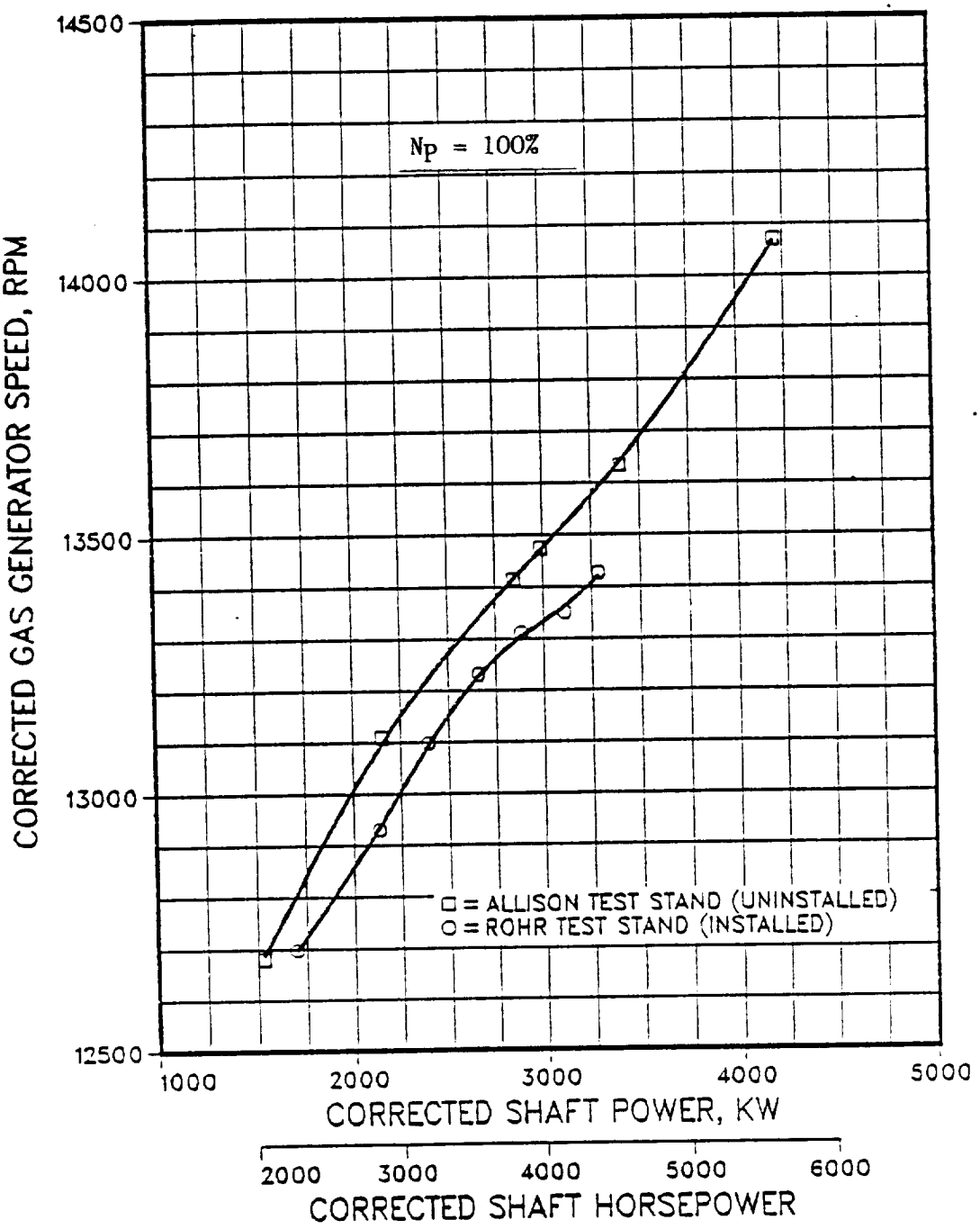


Figure 276. Installation Effects on Corrected Gas Generator Speed

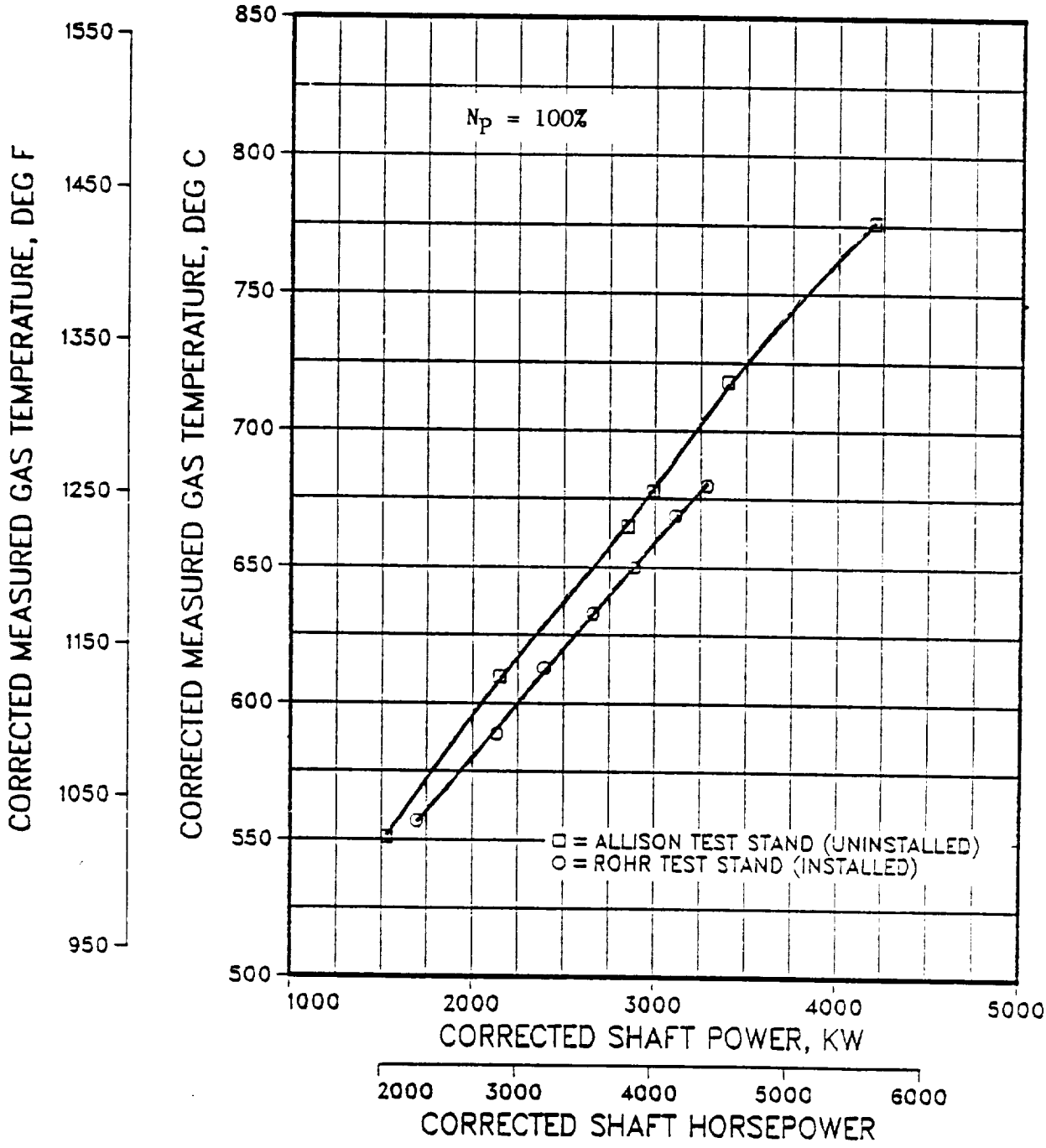


Figure 277. Installation Effects on Corrected MGT

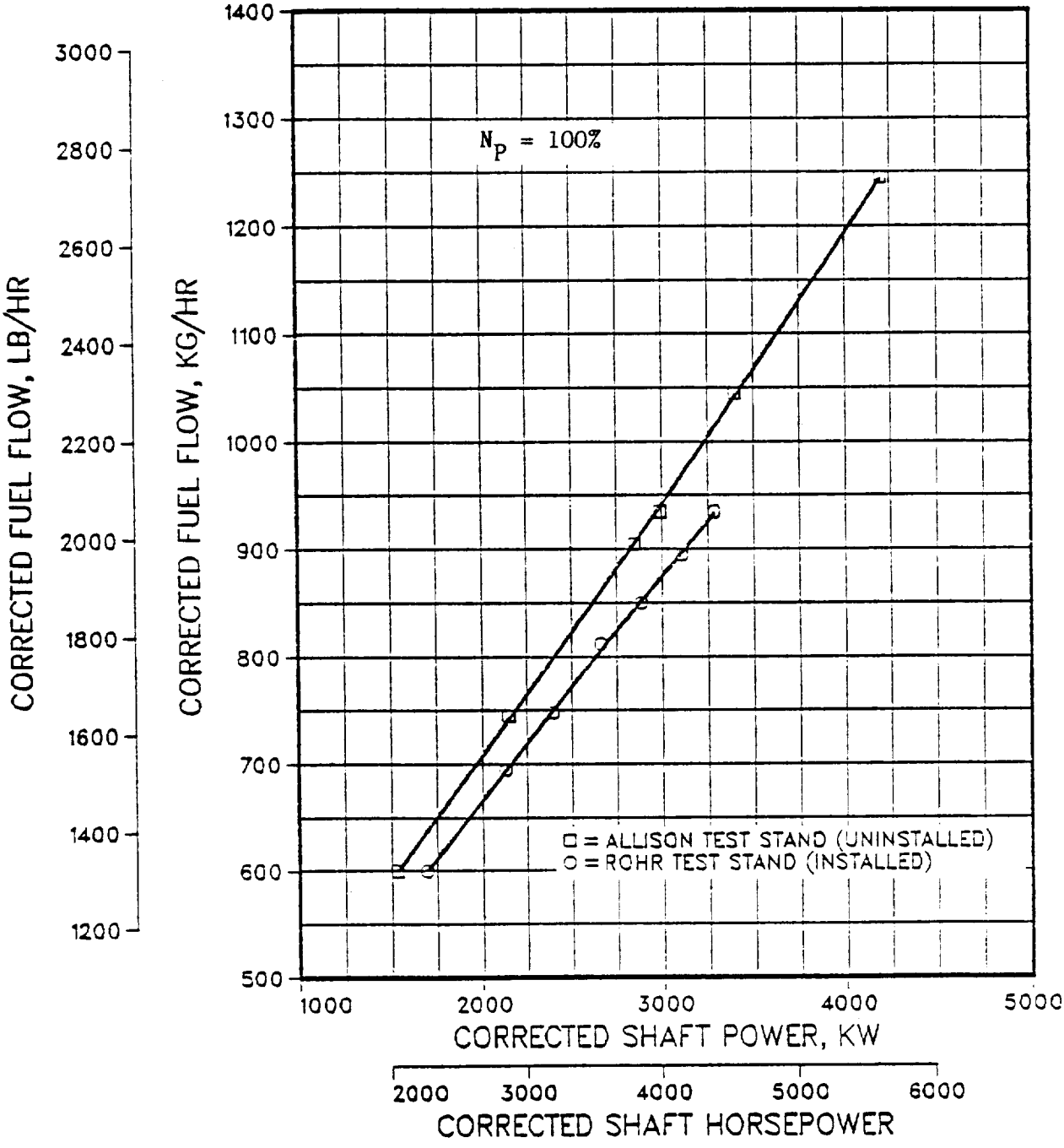


Figure 278. Installation Effects on Corrected Fuel Flow

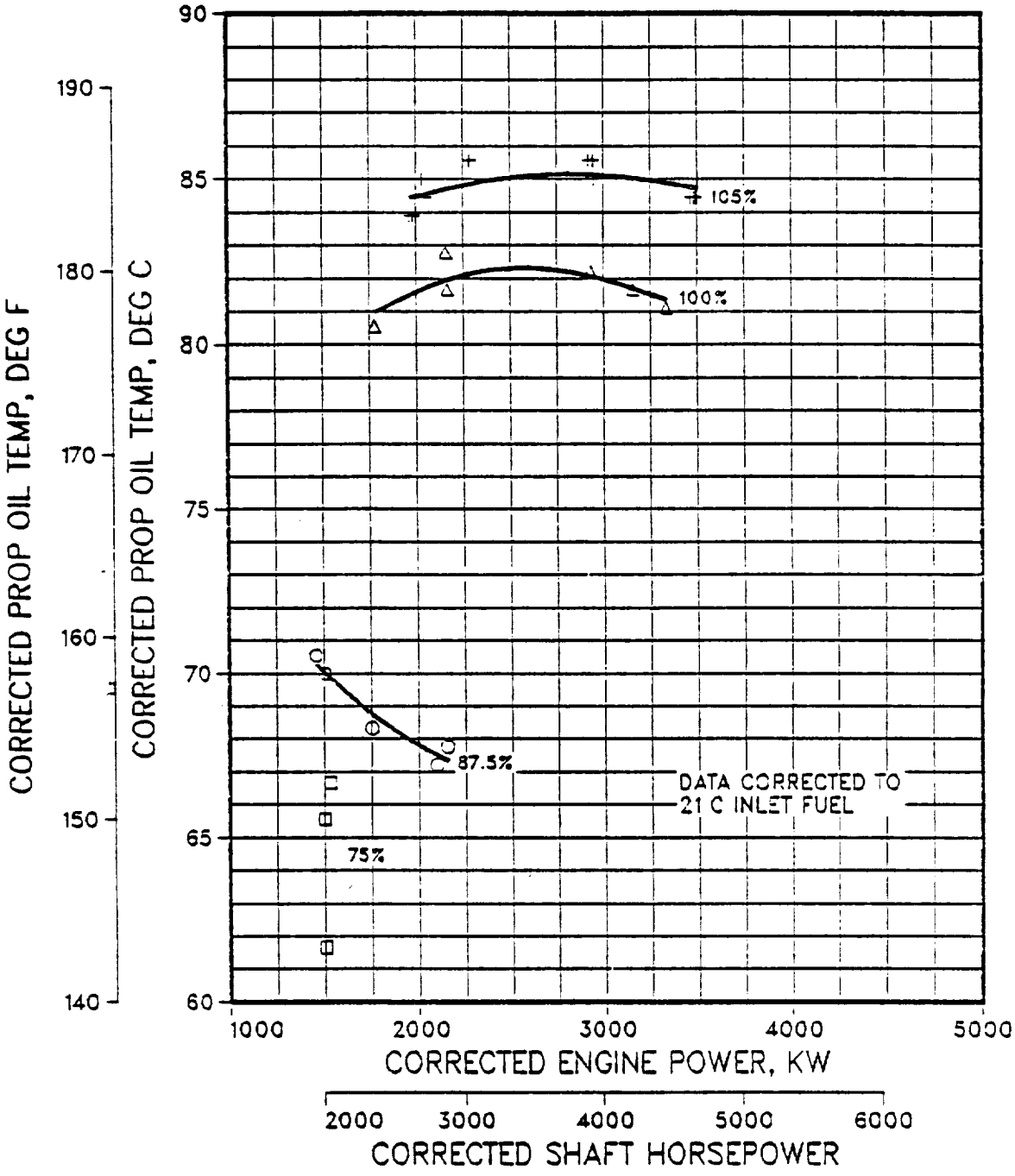


Figure 279. PTA Static Test Propfan Fluid Temperature

temperature as a function of engine output power and propfan speed. Extrapolating these data show that the drive system oil cooling system can maintain the engine oil temperature at or below 100°C (212°F) at maximum power static conditions for hot day (39°C or 103°F) operation. A 100°C oil temperature is considered the maximum transient (five-minute) limit by Allison.

Reverse thrust operation was the most severe condition for lubrication oil cooling. During the reverse thrust test, engine/gearbox oil temperature reached a maximum of 85°C (183°F) within 15 minutes of engine startup. The primary reason that oil temperatures did not increase beyond this value is that the low power input to the propfan resulted in low drive system heat rejection to the lubricating oil.

6.5.12.3 Nacelle Cooling

QEC surface and internal air temperatures measured during the static tests indicated satisfactory temperature, but it should be noted that these tests were conducted without the aft nacelle.

Maximum surface and air temperatures consistently occurred after engine shutdown following an endurance operating cycle. The maximum recorded air temperature inside the QEC, which occurred near the fuel control, was 66°C (150°F). Corrected to hot day conditions (39°C or 103°F), this is equivalent to 84°C (183°F), well below the limit of 120°C (248°F).

Typical maximum recorded surface temperatures are shown below:

Component	Recorded Temperature	Corrected to Hot Day 39°C
Fuel Control	71°C (159°F)	89°C (192°F)
Electronic Engine Control	41°C (106°F)	59°C (139°F)
Ignition Exciters	74°C (165°F)	92°C (198°F)
Prop Speed Control Actuator	36°C (96°F)	54°C (129°F)

QEC cowl frame, cowl skin, bulkhead, and engine mount surface temperatures were monitored throughout the conduct of the static tests to verify that limit temperatures were not exceeded and that sufficient cooling air was available for static operation.

6.5.12.4 Acoustic Tailpipe Stress and Temperatures

The strains and temperatures measured in all areas of the acoustic tailpipe were lower than those assumed by a theoretical analysis performed prior to the static test program. The analysis showed an expected fatigue life of 15,000 thermal cycles, based on an estimated 300 engine hours for both the static and flight test programs. The analysis estimated an outer skin maximum stress of 487×10^6 N/m² (70,700 psi), much greater than the 83.4×10^6 N/m² (12,100 psi) measured.

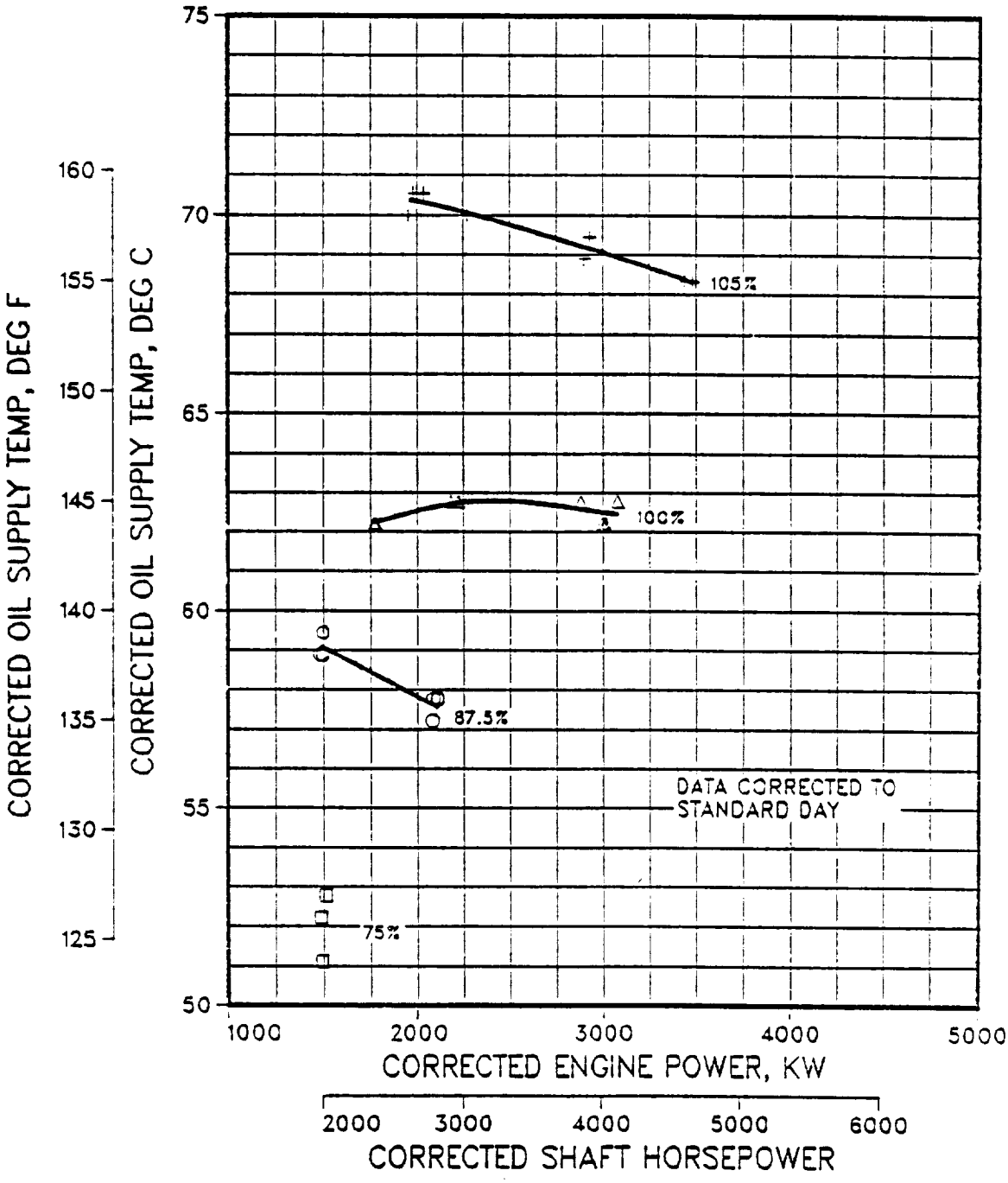


Figure 280. PTA Static Test Drive System Oil Temperature

Although tailpipe temperatures were lower than predicted, e.g., 471°C (880°F) versus 649°C (1200°F) for the inner skin, the maximum differential temperature between the inner and outer skins was greater than predicted. The analysis used a value of 167°C (300°F) while the measured value was 226°C (407°F). This implied that yielding might occur earlier than expected, but the tailpipe should possess the same fatigue life that was predicted.

6.5.12.5 Propfan Speed Control

During the system checkout phase of the static tests, it was discovered that the gearbox-mounted electromechanical prop control actuator would not rotate the prop control input lever to the feather position. Bench test confirmed that the available torque of 7.91 N-m (70 in.-lb) was marginal for the mechanical feather input torque requirement. Therefore, the actuator specification stall torque was increased to 13.6 N-m (120 in.-lb), with a control voltage of 26 VDC. Except for this, the actuator system functioned satisfactorily throughout the prop speed control range.

6.5.13 System Vibration Characteristics

Propulsion system vibration was monitored by accelerometers in eight locations. Although only two locations were used by the engine operator for health indication, all eight were displayed and recorded on the data acquisition system.

A critical speed was found near 94-percent propfan design speed during the balancing procedure. Prior to balancing, the vibratory response was magnified 8.25 times at the critical speed as shown in Figure 281. The mode shape defined by data acquired from accelerometers V_1, V_2, and V_4 was determined to be vertical bending as illustrated in Figure 282. The mode shape indicates that the major source of flexibility is in the structure connecting the engine to the gearbox. Once balancing was accomplished, the propfan propulsion system could be operated at the critical speed without exceeding vibration limits. This critical speed was expected to exist in the flight structure, but it was not expected to pose any problem with the propfan balance.

Although the recorded values (30-second averages) of the various vibration sensors remained within limits after the propfan was balanced, the overall signal from a given unfiltered accelerometer occasionally exceeded the established limits. When these signals were reviewed either in real time on a spectrum analyzer, or after the test from a spectrum analysis plot, the amplitudes of the vibrations within the bandwidths of concern did not exceed limits. Vibration limits were defined for two bandwidths: 15 to 40 Hz (900 to 2400 rpm), which enclosed the normal range of the propfan rotational speed, and 150 to 250 Hz (9,000 to 15,000 rpm), which is approximately the range of the gas generator and power turbine normal rotational speeds.

Based on the data recorded during static testing, accelerometer position V_5 (reduction gearbox lateral) appeared to be an acceptable choice as a

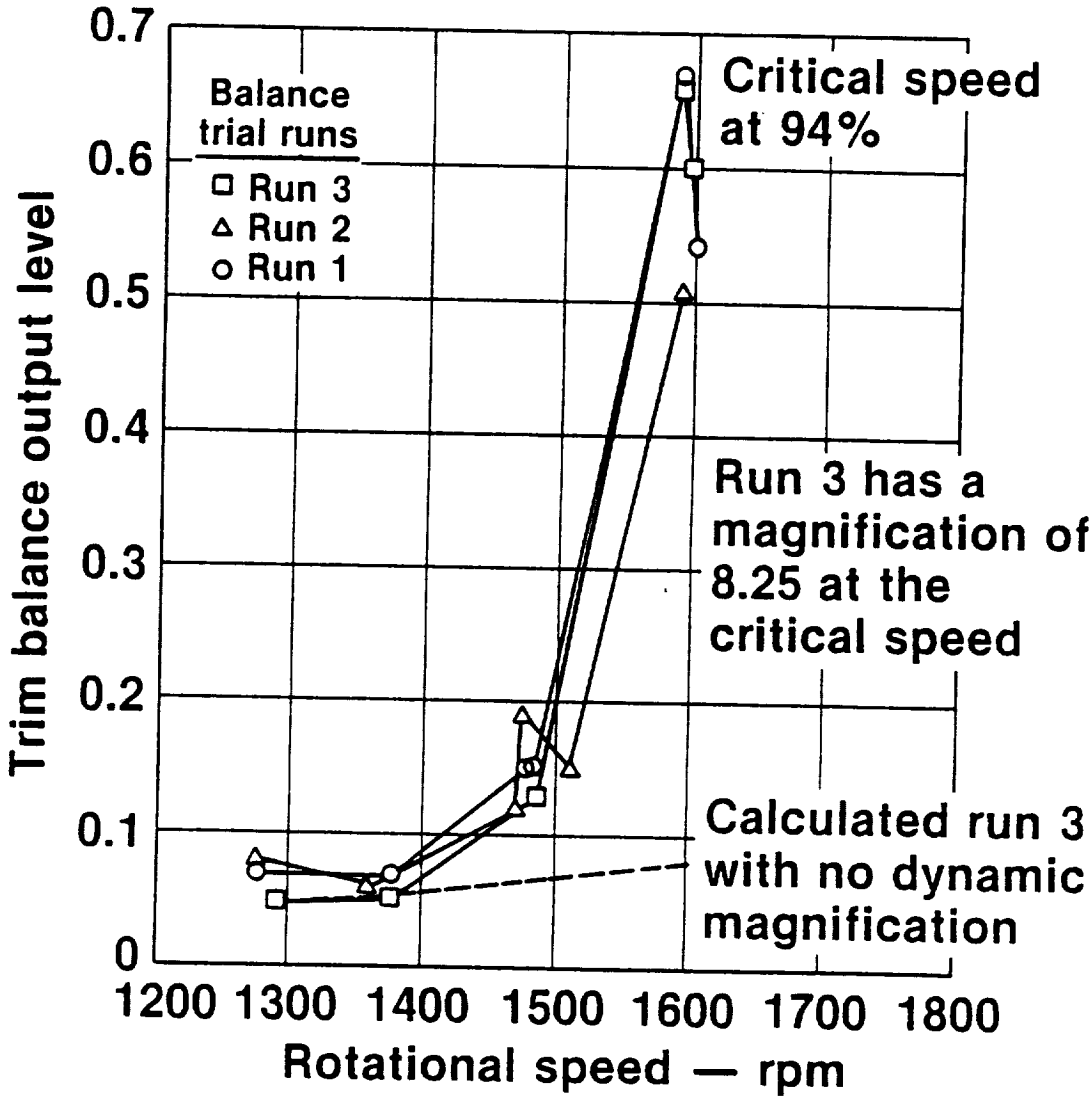


Figure 281. Propfan Relative Vertical Acceleration on the Static Test Stand Prior to Balancing

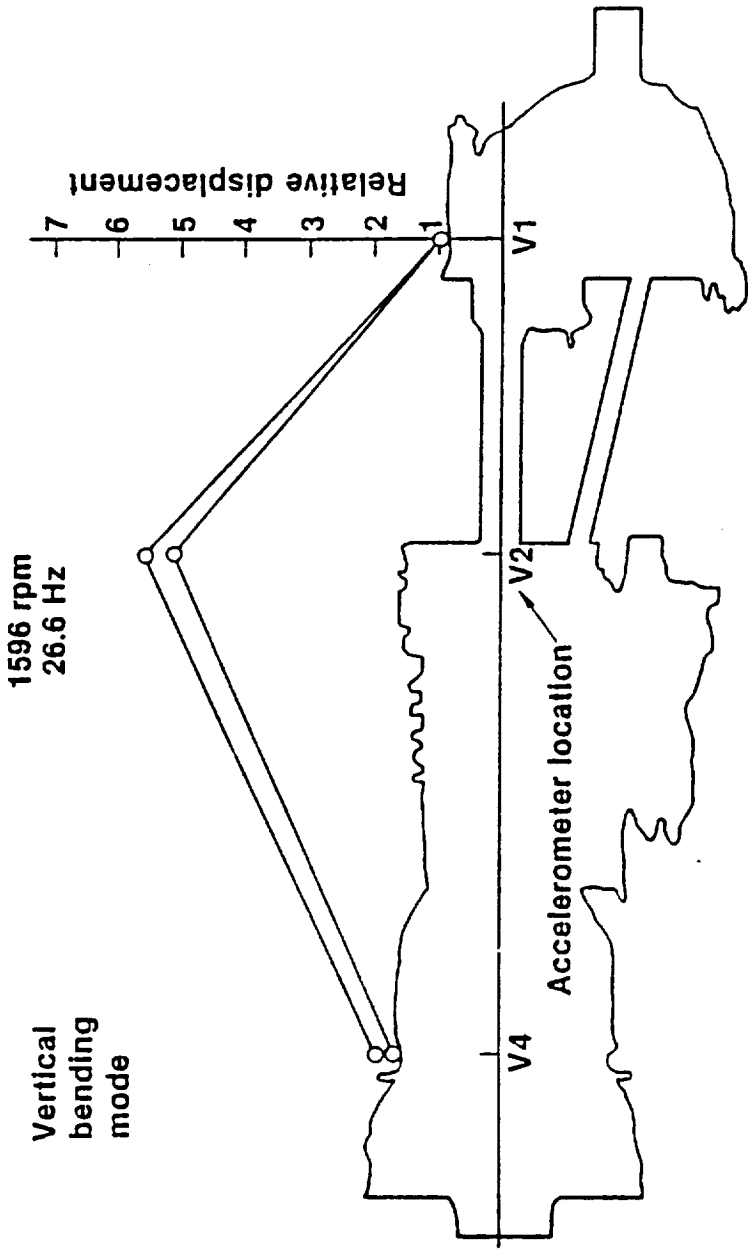


Figure 282. Propulsion System Vibration Mode Shape at N_p = 94%

location for monitoring propulsion system health. The V_3 (compressor rear frame vertical) position was also used during the static test for monitoring by the engine operator. Based on spectrum analyses of signals from all eight accelerometer locations on the drive system, it appeared that the V_7 (compressor front frame lateral) location would provide a more appropriate indication. Throughout the static test, V_7 appeared to be somewhat more sensitive to compressor unbalance and considerably more sensitive to propfan unbalance than V_3.

6.6 CONCLUSIONS

All of the major objectives for the static test program were achieved. The propulsion system and its related subsystems operated as they were intended to operate. Control inputs to the propfan and drive system provided stable, predictable responses. Instrumentation outputs were accurate. Fluid cooling was adequate, with fluid temperatures remaining within specification limits during normal running conditions. Compartment temperatures indicated that the nacelle cooling provisions permitted a suitable environment for propulsion system operation. Operation in reverse thrust, however, was time-limited due to inadequate fluid cooling and insufficient propfan power absorption to prevent reduction gearbox main drive bearing skidding.

Propfan blade stresses were lower than those encountered at similar operating conditions during the LAP static rotor test. No adverse stressing was encountered during transient testing. Blade strain limits were occasionally exceeded during the endurance testing, and a revised torque limit was defined for static operation.

The propfan control dynamic response was very stable but slightly slower than predicted. Overspeed or underspeed conditions could occur if power changes were introduced too rapidly. The propfan balanced well, and vibration levels were independent of blade angle. Replacement of components on the rotating portion of the propfan and changing the low pitch stop setting did not adversely affect the balance.

Drive system instrumentation provided accurate, readable displays to the engine operator. Research instrumentation outputs were also consistent and accurate. The performance of the Hamilton Standard blade stress instrumentation was satisfactory with the strain gage signals reliable and free of noise.

Engine speed stability and propfan 1P signal quality were satisfactory for time domain averaging of acoustic pressures and for high resolution frequency domain analyses. The far- and near-field noise spectra contained three components whose significance depended on power, tip speed, and direction. The components were propfan blade tones, propfan random noise, and compressor/propfan interaction noise. No significant turbine noise or combustion noise was evident. The combined noise of all sources, on an "A" weighted basis, was uniformly directional over an azimuthal range of 0 to 145 degrees. The static near-field noise levels were well below the worst case cruise noise levels used for fuselage sonic fatigue

analyses, and the fuselage structure should not be unduly affected by ground running.

The drive system provided necessary power for all portions of the static test program while operating within the engine specification limits. The pre-endurance calibration data agreed with Allison predictions of drive system performance. The engine inlet duct performed better than predicted, with a large beneficial effect on drive system performance. Measured gas temperature exhibited a 56°C (100°F) margin below the maximum continuous limit. The 1- to 2-percent degradation observed between the pre- and post-endurance calibrations was probably due to compressor contamination by hydraulic fluid and dirt.

The modified propfan blade seal significantly reduced hydraulic fluid leakage. Although the propfan assembly leaked a significant amount of fluid, the majority of the leakage occurred past the prop control rear lip seal.

7.0 AIRCRAFT PROCUREMENT AND MODIFICATION

Only a little more than two years were required to procure all the various parts of the PTA assembly and produce the final flight-ready test aircraft. Procurement started in September 1984, almost immediately after contract go-ahead with the ordering from Allison of the two Model 570 power sections and the three T56 gearboxes that would be used in the program.

Almost simultaneously, design work started at Rohr on the QEC, so that when Allison delivered a drive system mockup to Rohr in February 1985, work was started on building a QEC mockup around the mockup of the drive system. This activity is illustrated in Figure 283.

Gulfstream had several GII wing sets on hand at the start of the PTA Program that had been traded in by aircraft owners desiring to upgrade to a more modern wing design. This availability of GII wings was one of the attractive features favoring the use of the GII aircraft because it permitted a large part of the aircraft modification work to be done prior to purchase of a complete aircraft. It also permitted a relatively inexpensive retrofit to the original aircraft condition after the PTA Program was completed.

The wing set from GII Serial Number 245 (S/N 245), shown in Figure 284, had only a little more than 1600 total flight hours and 715 landings, so after inspection it was selected for the PTA modification.

By mid-1985, all of the instrumentation and data system equipment was on order, and some parts had been delivered.

Wing modification work was started in September 1985. Preliminary structural design indicated that it would be necessary to strengthen some of the internal structure of the wing--requiring that the wing covers be removed. Special jigs were constructed for this work, as shown in Figure 285, so that the structure needed to sustain the loads produced by the drive system installation could be added.

After the internal strengthening, the wing skins were replaced and doublers were added to the outer skins for the needed torsional strengthening. This restored the wings to the configuration shown in Figure 286.

Also shown in Figure 286 is the jig structure in which the aft nacelle was built up. This structure is shown again in Figure 287 where it can be seen being fitted to the modified left-hand wing.

Meanwhile, at Rohr, work was continuing on fabrication of the QEC using the drive system mockup, and at Allison, the drive system was being assembled and tested. And in the last quarter of 1985, another team was working on selection of the GII aircraft to be procured for the PTA Program.

PRECEDING PAGE BLANK NOT FILMED

PAGE 350 INTENTIONALLY BLANK

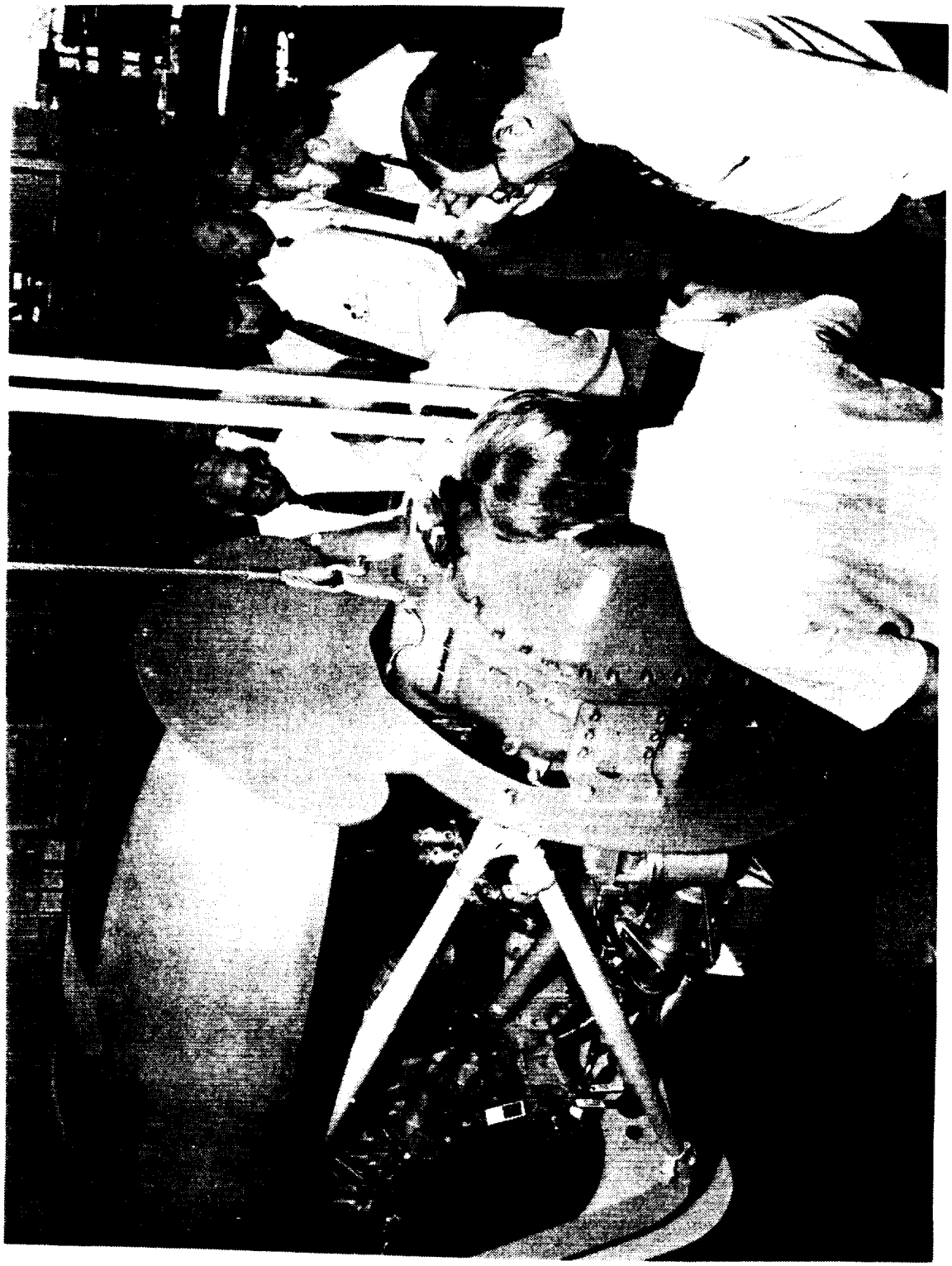


Figure 283. QEC Mockup and Drive System Mockup

ORIGINAL PAGE
BLACK AND WHITE PHOTOGRAPH

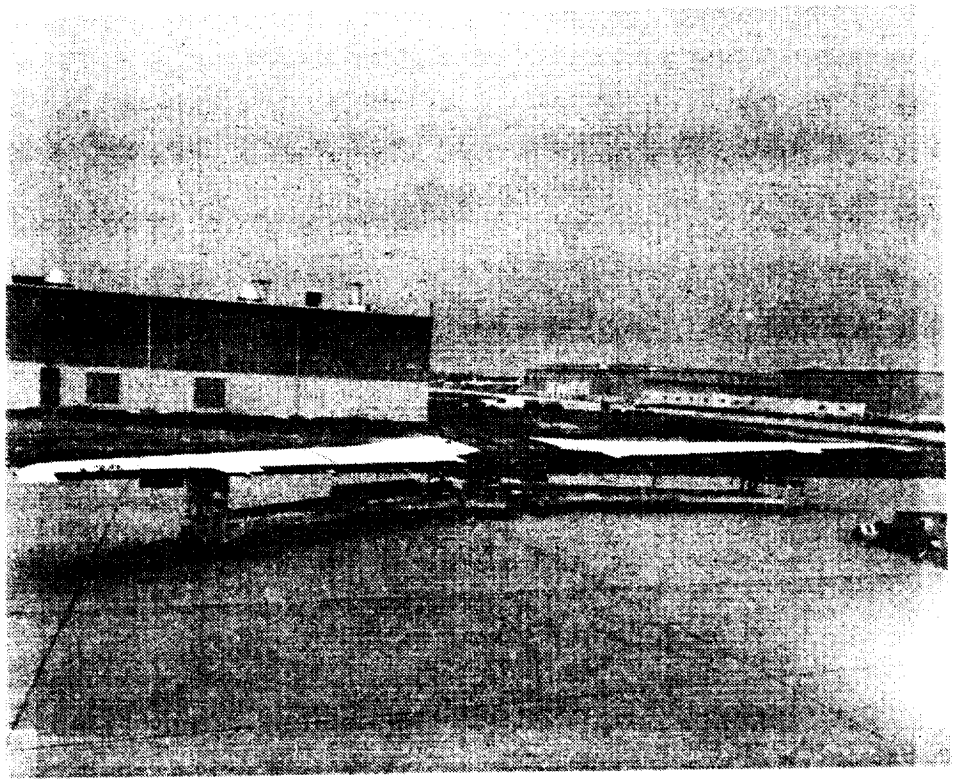


Figure 284. Wing from GII S/N 245

ORIGINAL PAGE
BLACK AND WHITE PHOTOGRAPH

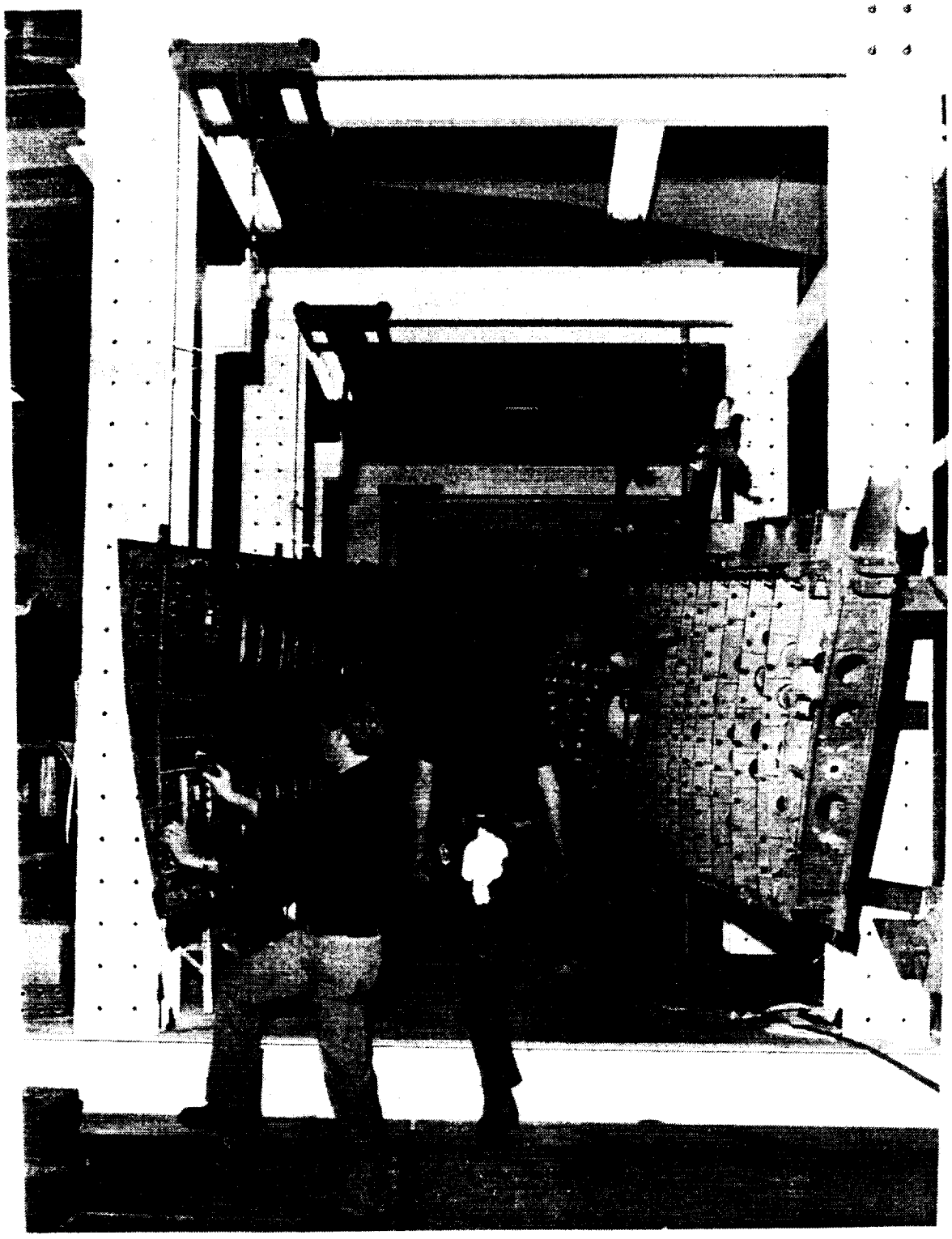


Figure 285. Wing Structural Modification

ORIGINAL PAGE
BLACK AND WHITE PHOTOGRAPH

ORIGINAL PAGE
BLACK AND WHITE PHOTOGRAPH

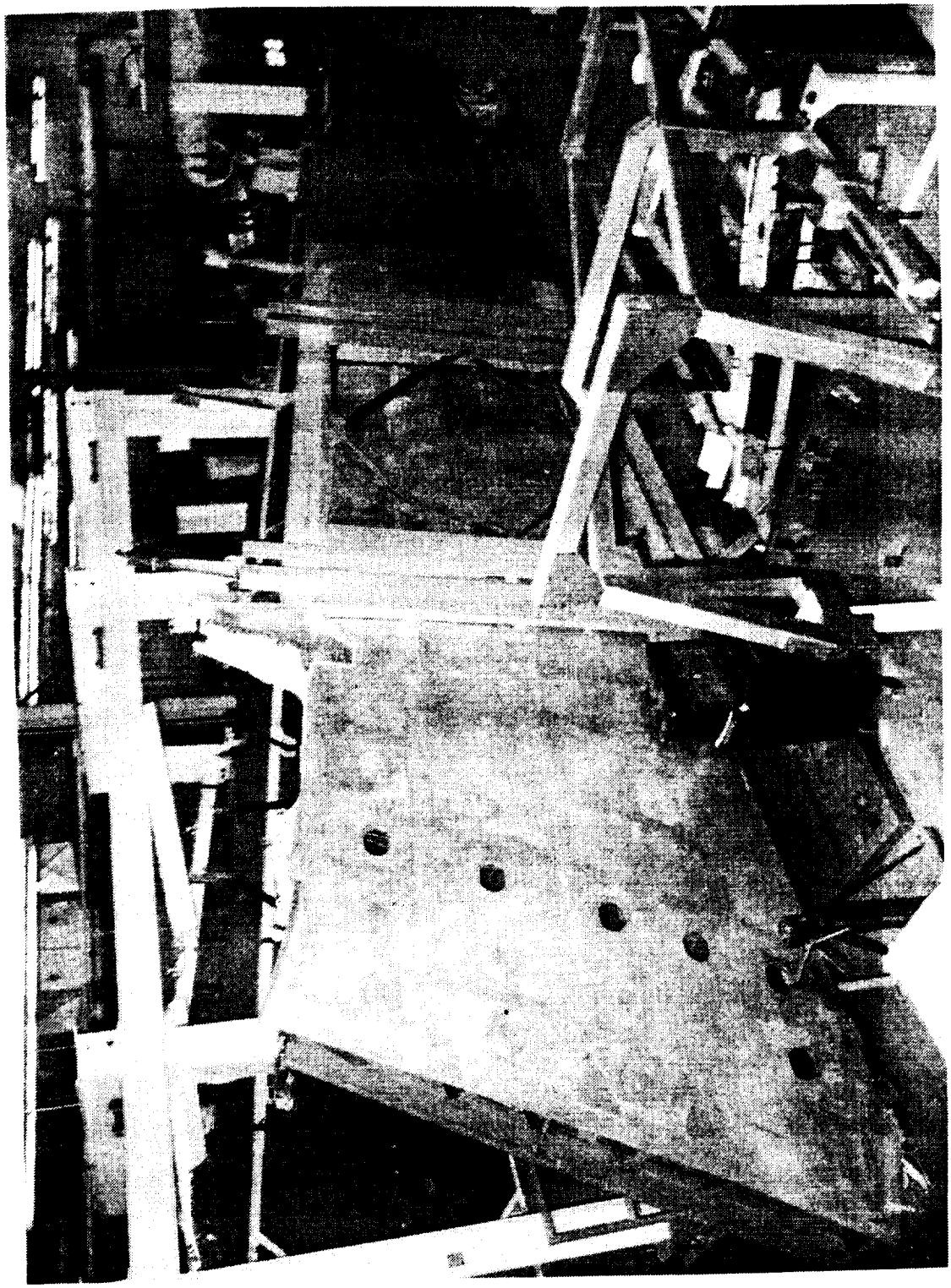


Figure 286. Wing After Primary Modification

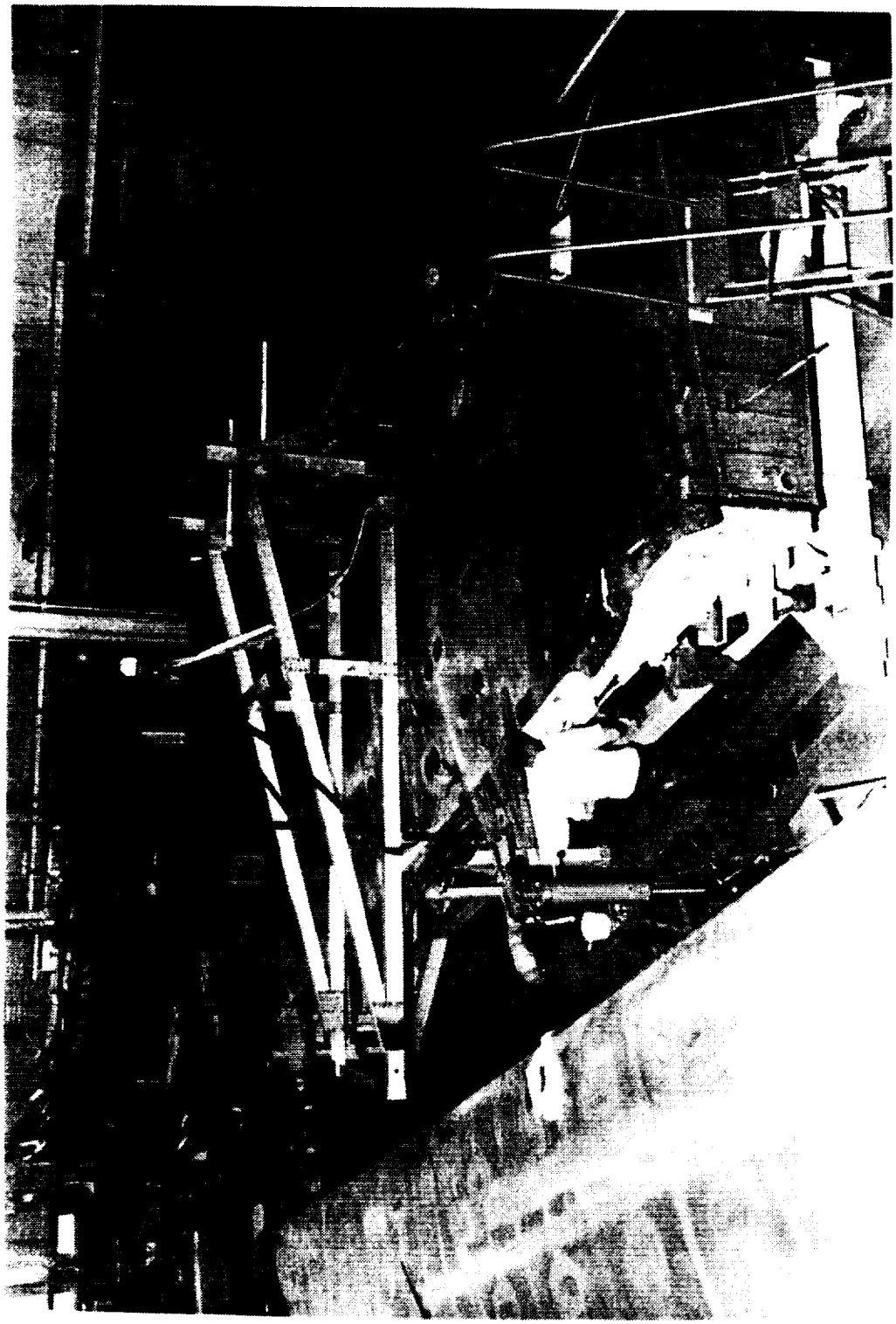


Figure 287. Modified Wing with Aft Nacelle Buildup Jig

ORIGINAL PAGE
BLACK AND WHITE PHOTOGRAPH

The criteria for aircraft selection were:

- Ramp weight capability of 29,620 kg (65,300 lb)
- Remaining service life of 3,000 flight hours, including 1,000 takeoff and landing cycles without major repair or refurbishment to the airframe or propulsion system
- Price not to exceed $\$5 \times 10^6$
- Capability for installation of jump seat with shoulder harness and protection against nose gear drag brake penetration
- Compliance with structural inspection requirements
- Major airframe and engine inspections accomplished
- Sufficient avionics equipment to comply with test requirements

Using these criteria, four candidate aircraft were selected for evaluation on the basis of estimated two-year operating costs. Results are shown in Figure 288. On the basis of these comparisons and a careful review of aircraft and engine records, Aircraft S/N 118 was selected for more detailed evaluation.

Ground tests and flight tests were performed: the ground tests consisted of systems evaluations and engine runs; and the flight tests concentrated on handling characteristics, climb performance, level flight performance, buffet boundaries, and stall characteristics. Flight test results indicated a general conformance with the GII Flight Manual and the GII Cruise Control Manual.

Based on the overall results of these aircraft evaluation tests, the test team recommended procurement of the S/N 118 aircraft, and an Aircraft Selection Review Package (DRD 233) was forwarded to NASA.

Allison delivered a complete drive system to Rohr in January 1986, and the QEC, as pictured in Figure 289, was completed in March 1986. Hamilton Standard delivered the LAP assembly to Rohr in April 1986, and preparation was started for static tests of the entire propulsion system. Another part of the Rohr activity was fabrication of the acoustic tailpipe, as pictured in Figure 290, which was designed to reduce noise from the drive system jet exhaust.

Gulfstream GII S/N 118 was delivered to Gulfstream for modification in May 1986. Its wing was removed and stored, and the modified wing from Aircraft S/N 245 was mated to the aircraft fuselage as shown in Figure 291. Work then began on build-up of the aft nacelle on the wing as shown in Figures 292 and 293. At the same time, all of the interior trim was stripped from the aircraft cabin, and it was modified to the test configuration shown in Figure 294. In Figure 294, the data system consoles can be seen in the background, and the support for the traversing microphones

AIRCRAFT S/N	085	113	110	140
AIRCRAFT ASKING PRICE	$3,300,000	$5,300,000	$4,700,000	$3,650,000
ASC INCORPORATION				
NO. 256 65,300 LB GW	139,253	139,253	139,253	139,253
NO. 226 NOSE GEAR PENETRATION	C/W	C/W	C/W	55,100
NO. 241 SHOULDER HARNESS	C/W	C/W	C/W	6,840
No. 81 62,500 GW	274,251	C/W	C/W	C/W
ENGINE O/H AND MAINTENANCE	250,000	0	0	500,000
THRUST REVERSER O/H AND MAINTENANCE	430,000	215,000	0	430,000
A/C MAINTENANCE & INSPECTION	168,761	95,060	93,133	279,125
TOTAL	$4,562,265	$5,750,113	$4,932,386	$5,060,318

Figure 288. Estimated Two-Year Operating Costs of Candidate Aircraft

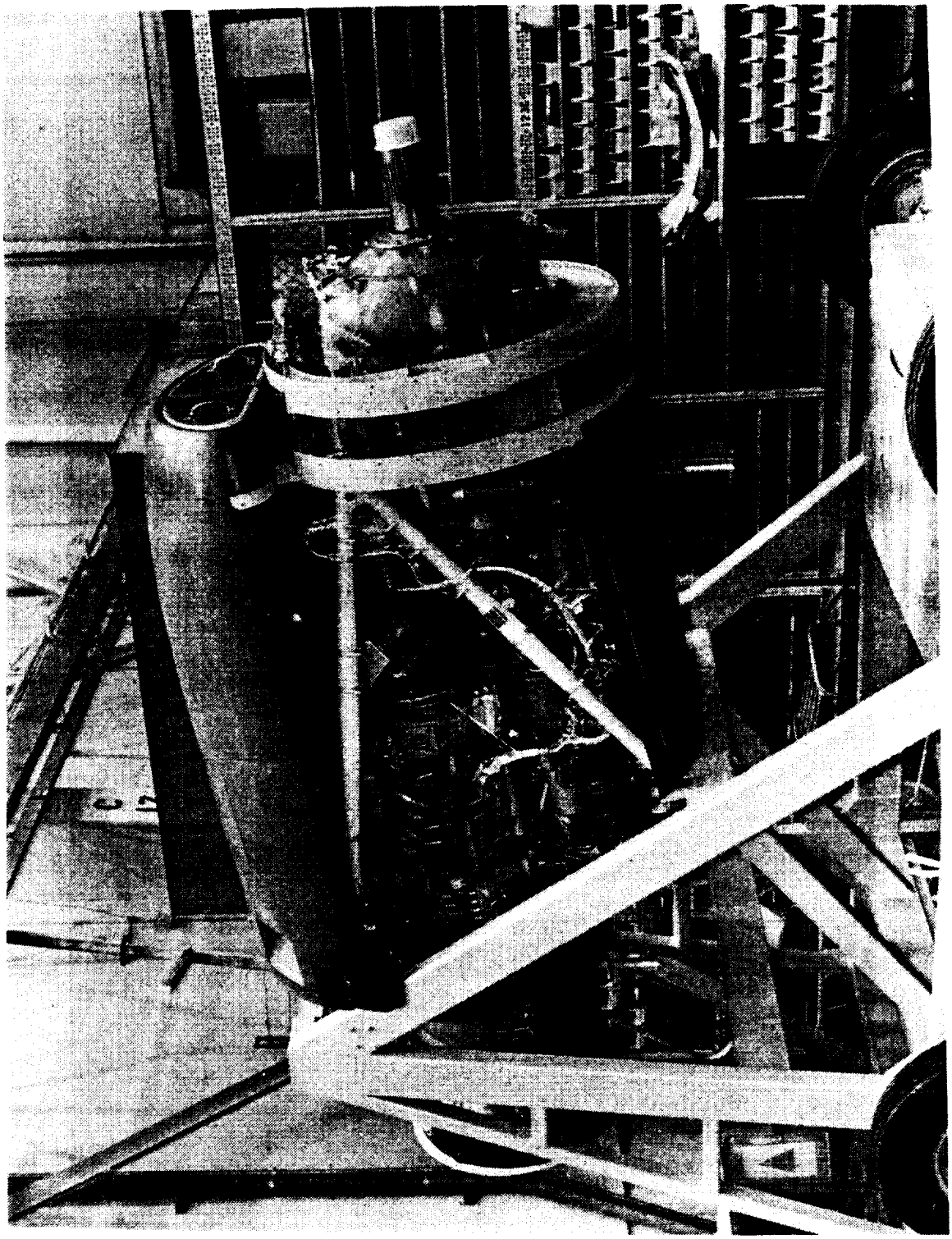


Figure 289. Completed QEC/Drive System Assembly

ORIGINAL PAGE
BLACK AND WHITE PHOTOGRAPH

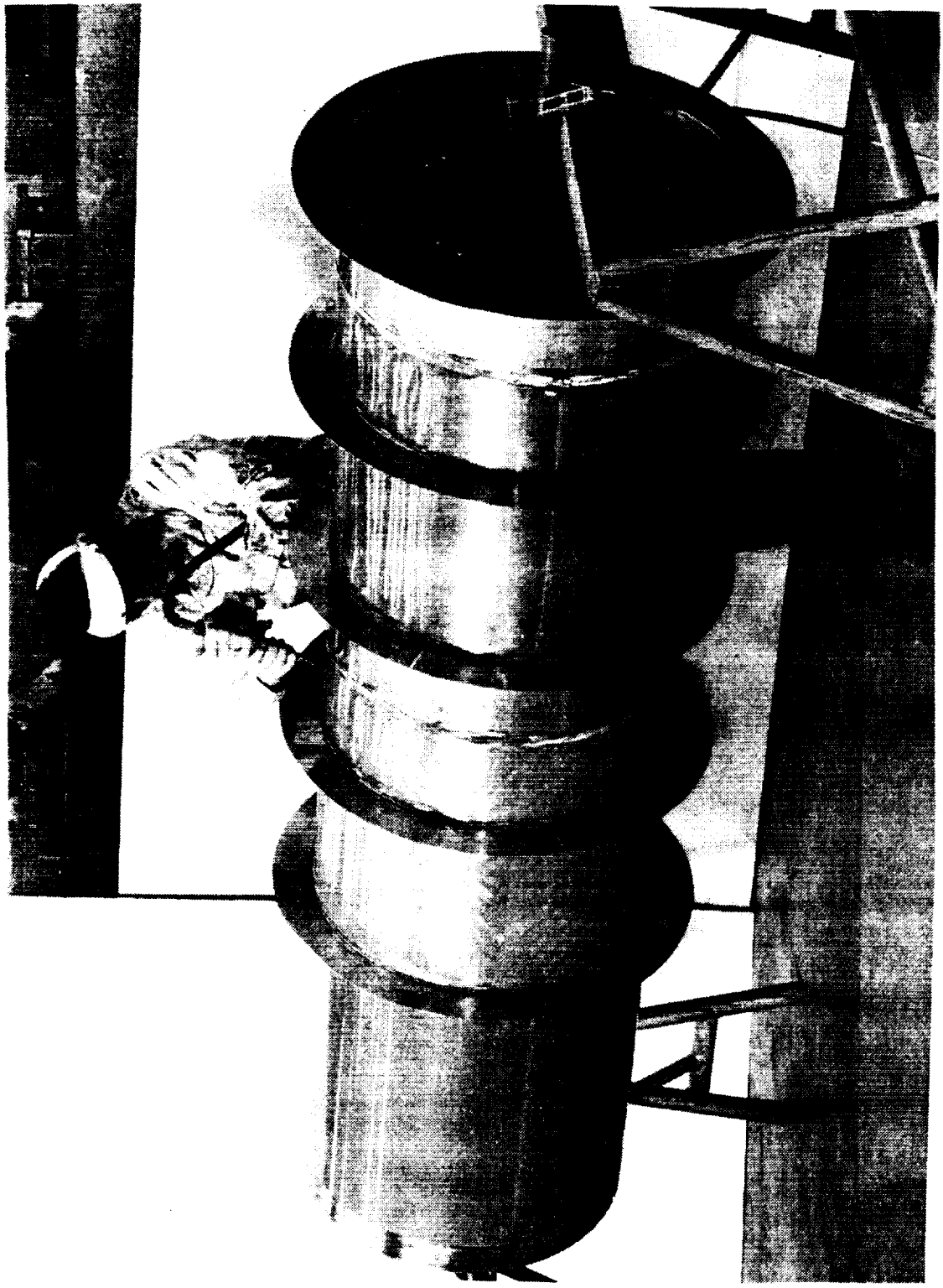


Figure 290. Fabrication of Acoustic Tailpipe at Rohr

ORIGINAL PAGE
BLACK AND WHITE PHOTOGRAPH

ORIGINAL PAGE
BLACK AND WHITE PHOTOGRAPH

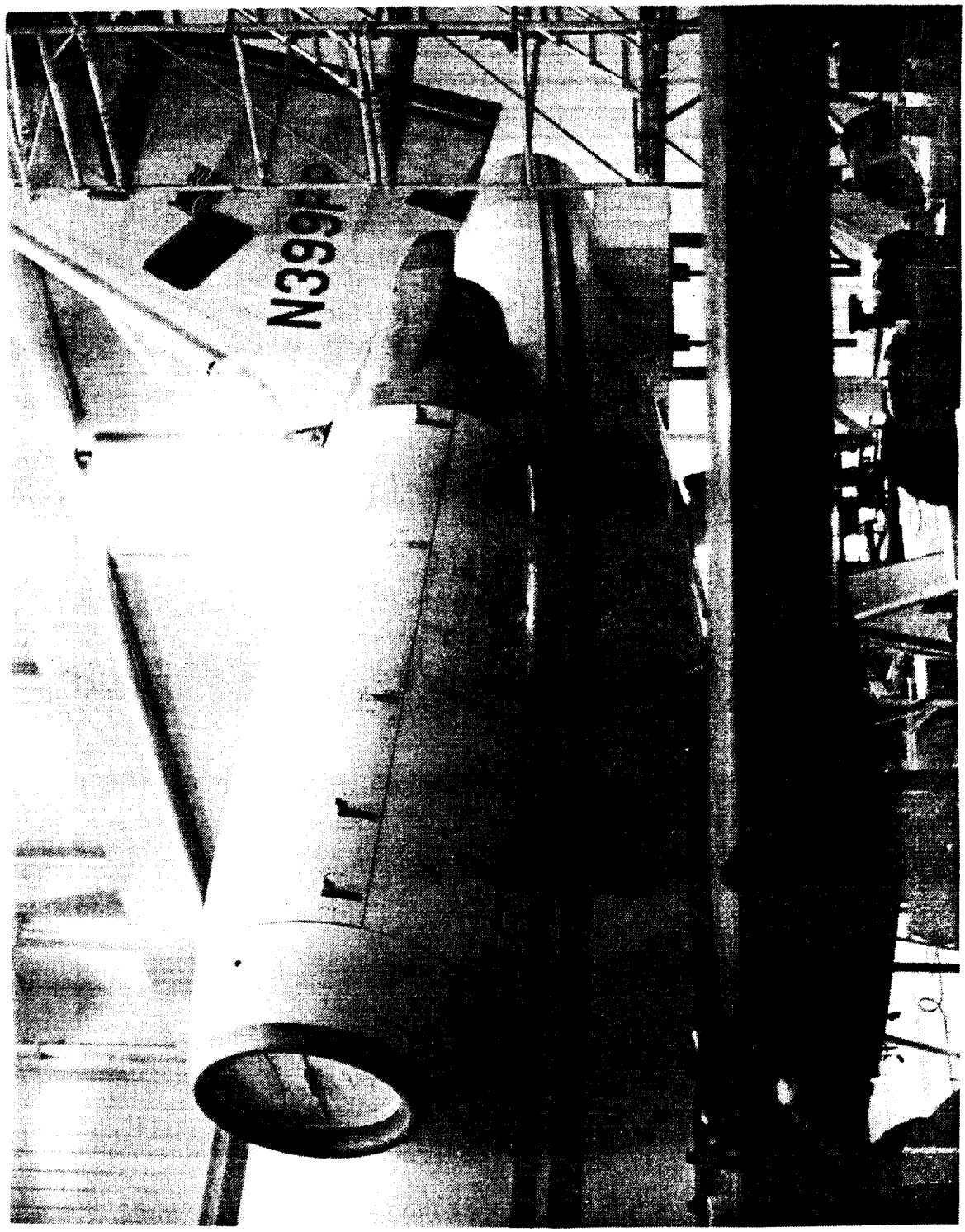


Figure 291. Mating of S/N 245 Wing with S/N 118 Aircraft



Figure 292. Buildup of Aft Nacelle on Wing

ORIGINAL PAGE
BLACK AND WHITE PHOTOGRAPH

ORIGINAL PAGE
BLACK AND WHITE PHOTOGRAPH

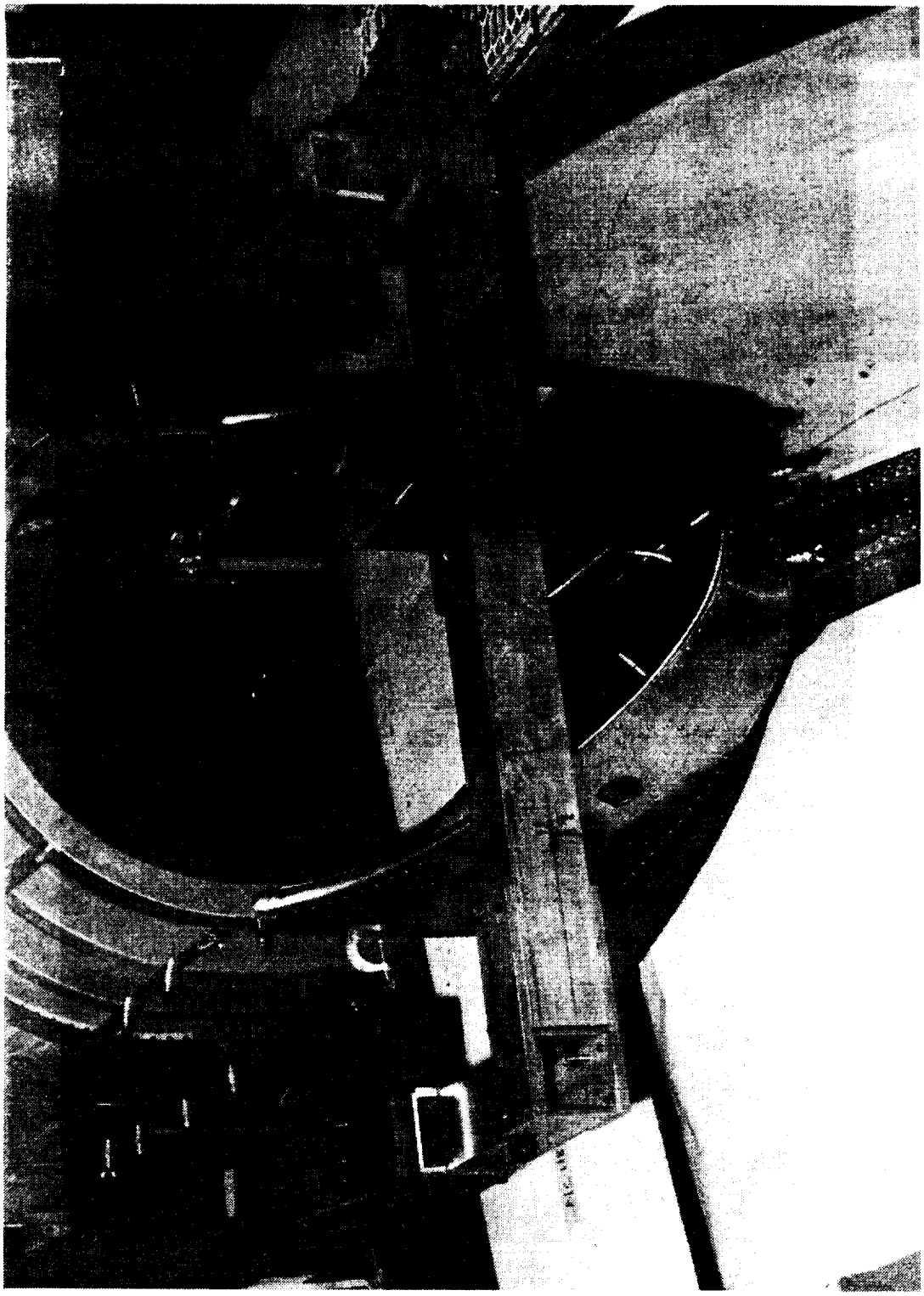


Figure 293. Rear View of Aft Nacelle Buildup

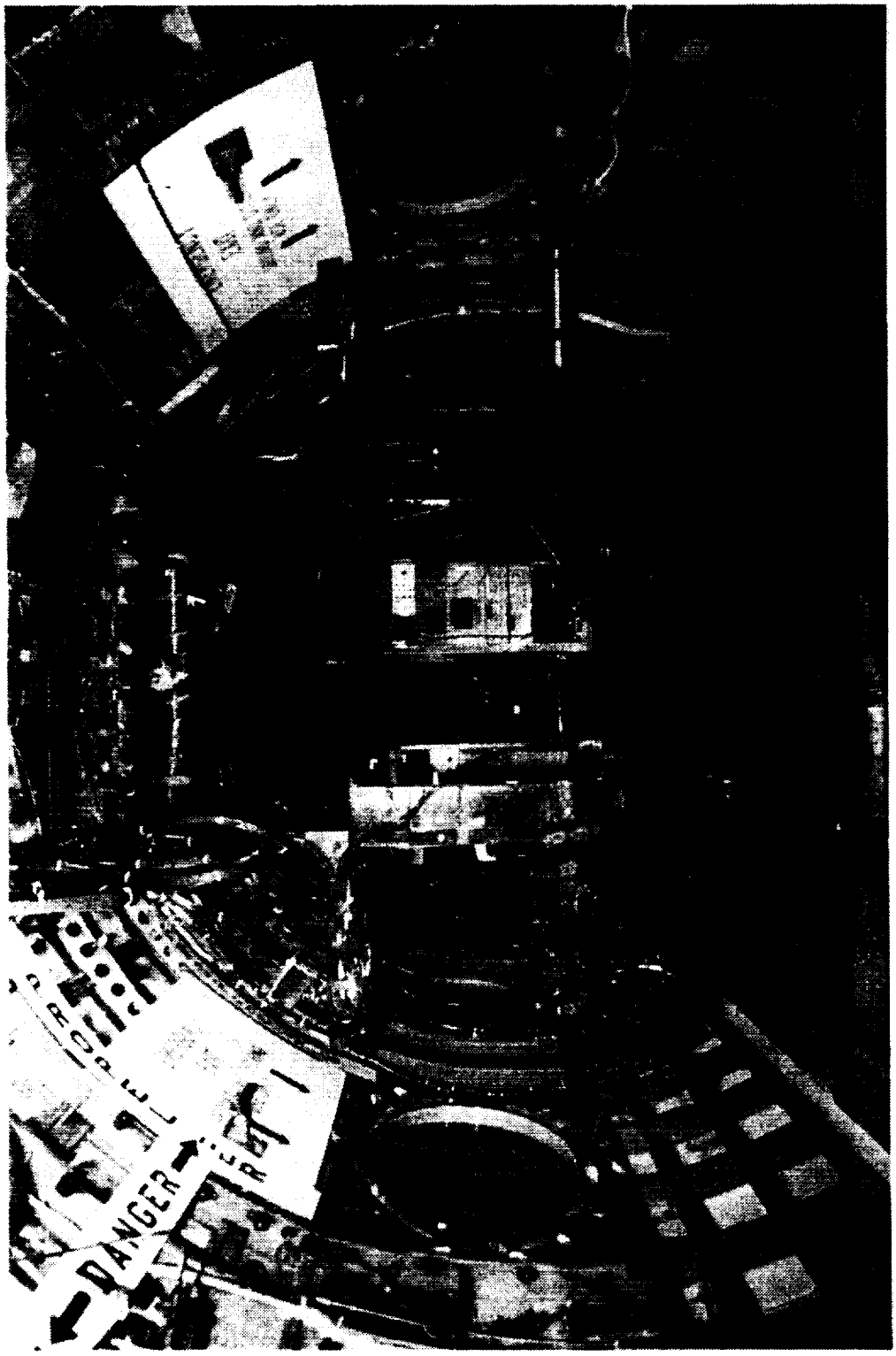


Figure 294. Aircraft Cabin Modified to Test Configuration

ORIGINAL PAGE
BLACK AND WHITE PHOTOGRAPH

can be seen in the foreground. Cockpit modification for the propfan controls was also done at this time.

There was, of course, a good bit of "secondary" modification to the aircraft ongoing in the form of new ducting for starter systems, and wiring and pressure tubes for the various instrumentation systems. Figure 295 shows some of the pressure tubing on the wing and the routing of much of the abovementioned tubing and wiring through the leading edge region of the wing.

Figures 296 and 297, respectively, show modifications to the wing to attach the acoustic boom and one of the wing tip booms.

After completion of the propulsion system static tests at Rohr's Brown Field Facility, the QEC and drive system assembly was delivered to Gulfstream in July 1986 .for mating with the wing and aft nacelle, as pictured in Figure 298. The LAP assembly, with stub blades installed in place of the propfan blades, was shipped to Gulfstream in October 1986, thus bringing together at Gulfstream all the major components of the PTA system.

Modification of the aircraft was essentially completed in the final quarter of 1986, and after completion of proof tests, ground vibration tests, and other checkout tests, the PTA aircraft made its first flight on 6 March 1987. The completed PTA drive system installation is shown in Figure 299.



Figure 295. PTA Modifications in Wing Leading Edge

ORIGINAL PAGE
BLACK AND WHITE PHOTOGRAPH

ORIGINAL PAGE
BLACK AND WHITE PHOTOGRAPH

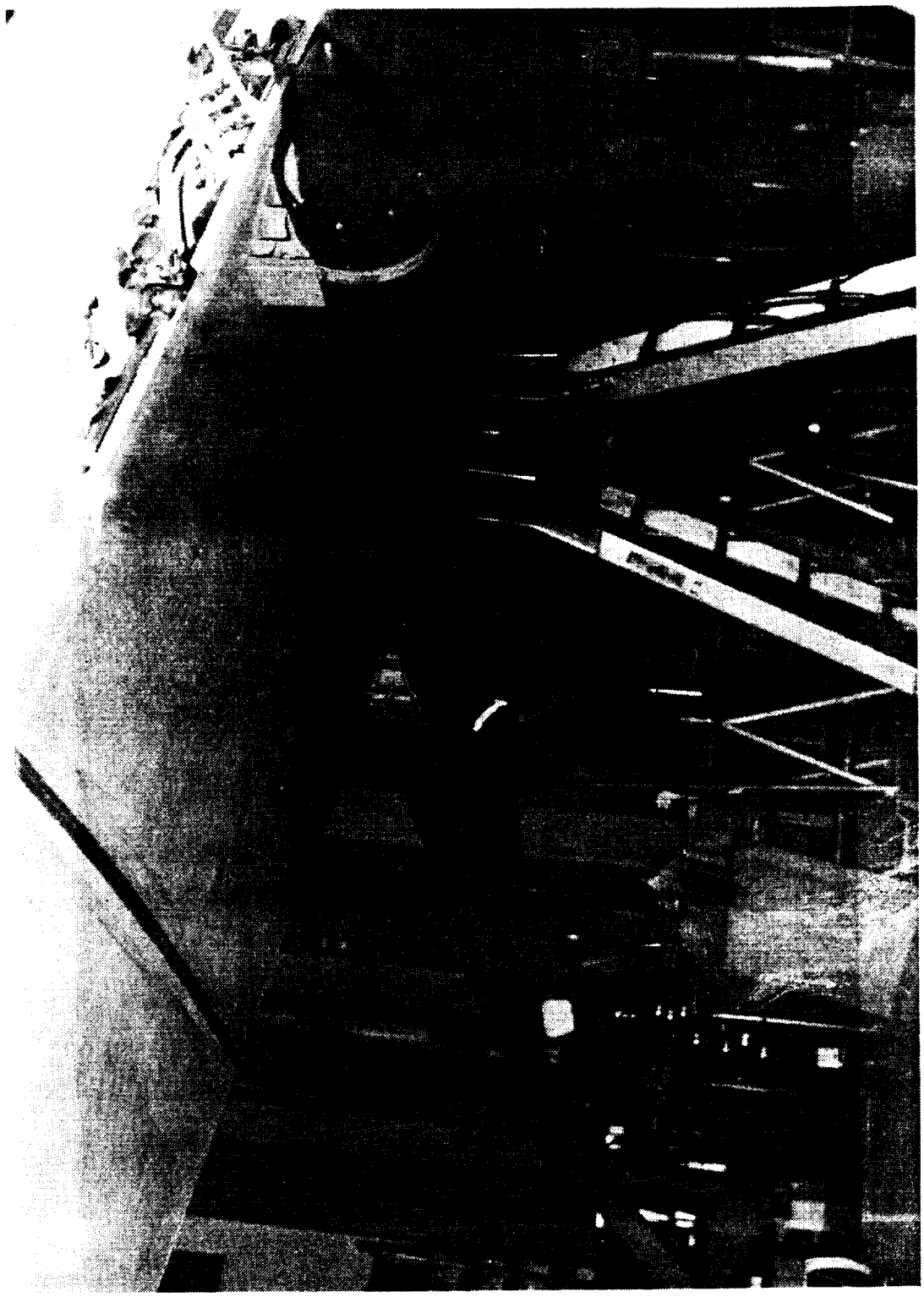


Figure 296. Mounting of Acoustic Boom on Wing

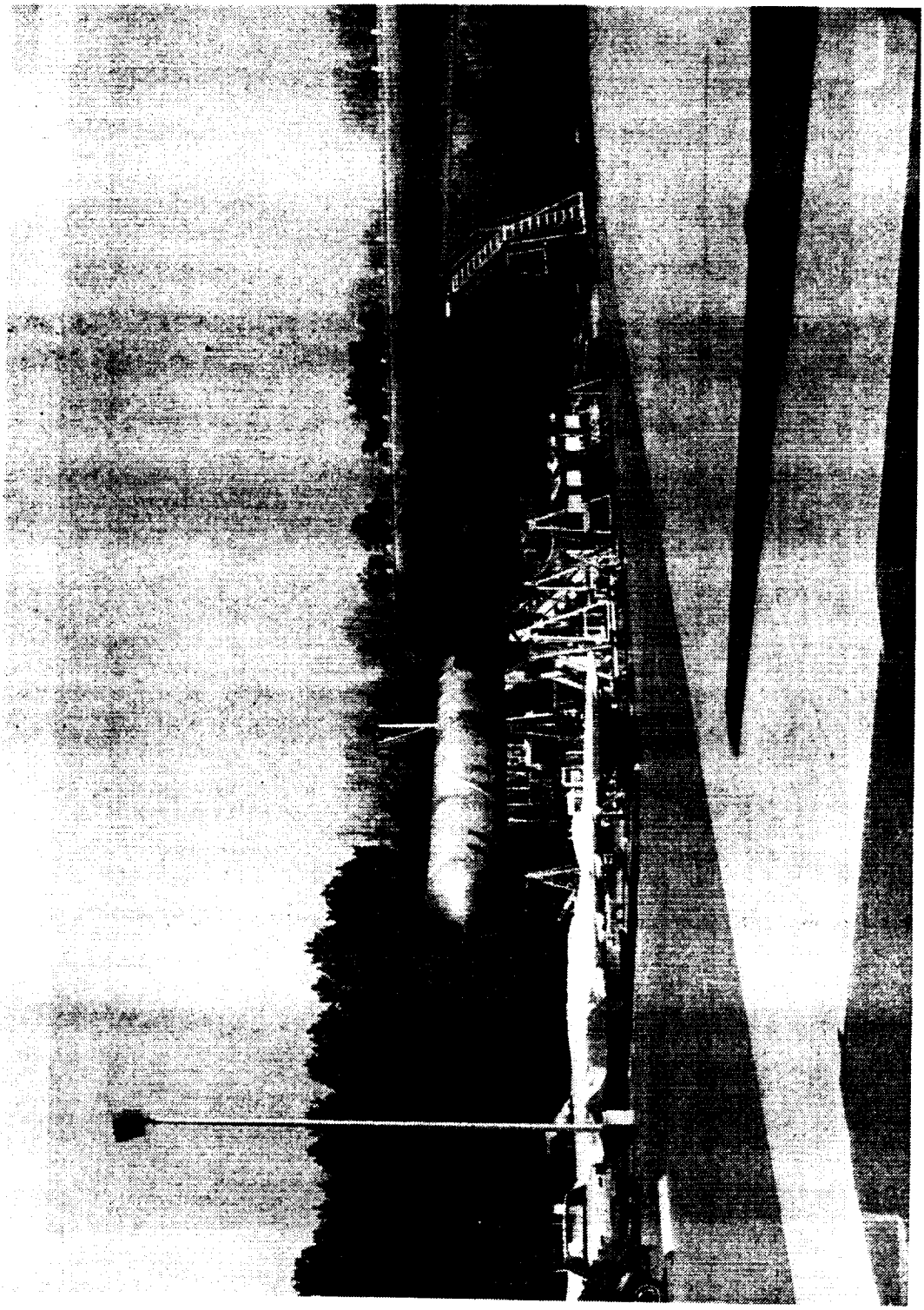


Figure 297. Mounting of Wing Tip Boom

ORIGINAL PAGE
BLACK AND WHITE PHOTOGRAPH

ORIGINAL PAGE
BLACK AND WHITE PHOTOGRAPH



Figure 298. Mating of QEC with Wing and Aft Nacelle

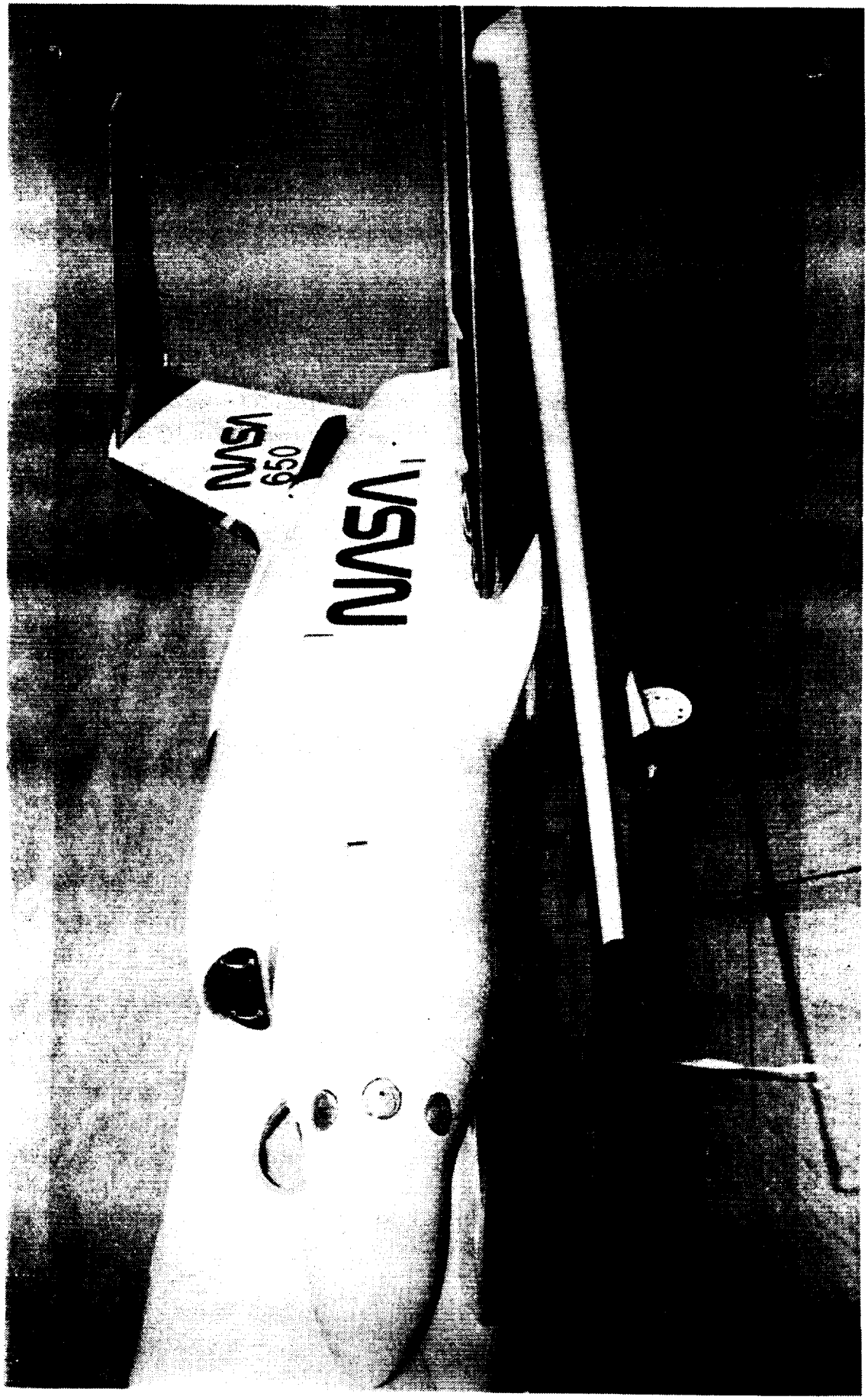


Figure 299. Completed Propfan Drive System Installation

ORIGINAL PAGE
BLACK AND WHITE PHOTOGRAPH

8.0 AIRCRAFT CHECKOUT TESTS

A number of checkout tests were performed after the PTA aircraft was assembled and prior to the flight research tests. These were planned to methodically check the aircraft, the propfan and its propulsion system, and all subsystems. They also included tests to examine propfan blade stresses during ground run and taxi conditions.

A special set of ground tests was performed to obtain baseline acoustics and vibration data that would later be used in interpretation of flight cabin noise data.

In flight, there were other checkout tests--first without installation of the propfan blades and then with the blades. Again, all systems were checked, and tests were performed to clear the aircraft and the propfan for operation throughout the flight research envelope. These tests are described in the following sections.

8.1 GROUND TESTS

8.1.1 Nacelle/Wing Proof Tests

Nacelle/wing proof tests were conducted to substantiate the structural integrity of the QEC, the aft nacelle, and the wing interface structure. The nacelle was proof tested to the limit design load conditions for the nacelle primary structure and the attachment of the nacelle to the modified wing. The test conditions represented the maximum upbending and downbending of the nacelle and the maximum propfan/drive system torque and thrust loads.

8.1.1.1 Test Article

The test article comprised the structurally complete modified GII aircraft with the QEC nacelle installed on the left wing in the -1 degree tilt position. A dummy powerplant and propfan were installed in the nacelle as equivalent structure for applying thrust and torque loads.

The tests were conducted in the structural test hangar at the Gulfstream facility in Savannah, Georgia. The aircraft was positioned in the hangar above floor tracks that were used as part of the load application and reaction fixtures.

The test loads were applied by hydraulic actuators linked through load transducers to the dummy propfan or dummy powerplant except for the dynamic positive-gust test where the low-magnitude loads were difficult to apply with the servo/hydraulic system. Consequently, this test was accomplished using a cable running forward of the propfan and over a pulley to a weight. The weight of the dummy powerplant and dummy propfan was counterbalanced by an equal and opposite vertical load acting through the center of gravity. This counterbalance load was held constant during each test.

8.1.1.2 Instrumentation

Instrumentation was provided to measure the strain and deflections at critical locations in each test area as well as the applied test loads. Electrical resistance strain gages were bonded to the aft nacelle, wing, and QEC structure. Deflection transducers were installed to measure deflection of the structure relative to the hangar floor. For each of the QEC and aft nacelle, 22 strain gages and 2 deflection gages were used; and for the wing/nacelle interface, 6 strain and 10 deflection gages were used.

8.1.1.3 Test Conditions

The four conditions selected for the proof tests were:

- Dynamic positive gust (DPG028 .80A)
- Dynamic negative gust (DNG028 .80B)
- Torque surge (TS 600 14A)
- Torque surge (TS 840 00A)

The test sequence and loads for these conditions are shown in Figure 300.

8.1.1.4 Test Procedures and Results

Proof test loads were applied incrementally with the exception of the thrust load for the dynamic positive gust condition which was applied at the beginning of the test and held constant. For the other tests, the loads were applied incrementally at 10, 20, 40, 60, 80, and 100 percent of limit loads. After the data were recorded for load conditions above 40 percent, the loads were reduced to 40 percent for data review prior to proceeding to the next load point.

Following completion of each of the four proof tests, the nacelle structure was inspected for indications of yielding or permanent set. Results showed no signs of permanent deformation.

Results of the proof tests compared favorably with predicted data and substantiated the structural integrity of the QEC, aft nacelle, and wing interface.

8.1.2 Ground Vibration Test

The objective of this test was to measure the primary airframe modal frequencies and shapes. These data were used to validate the results of airplane vibration and flutter analyses.

8.1.2.1 Test Article

The test article consisted of the complete, flight-ready PTA testbed airplane with the following exceptions: stub blades were installed in lieu of the propfan blades, the inboard QEC access panel was removed to allow access to rotate the powerplant, and various fuselage instruments

Test Sequence	Condition	P_X		P_Z		M_X			
		Newton	(Lbs)	Newton	(LBS)	Newton-Meters	(IN-LBS)	PPS	PPWL
1	DNG028.80B	-21323	-4794	-63580	-14294	2008	17771	302.1	100.0
2	TS60014A	-20283	-4560	-6525	-1467	64179	568000	302.1	100.0
3	TS84000A	-48928	-11000	-16391	-3685	48003	424840	302.1	100.0
4	DPG028.80A	-1939	-436	-43968	-9885	21555	180763	296.3	100.0

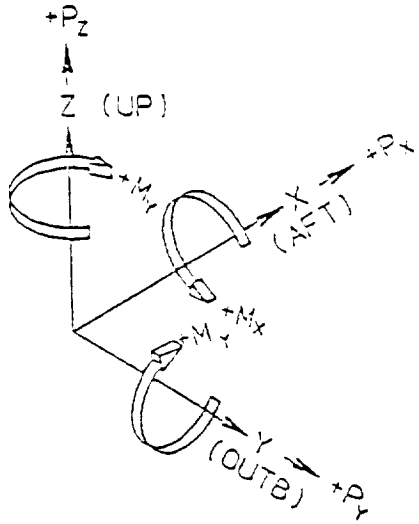


Figure 300. Proof Test Loads

and wiring were either missing or incomplete. Aircraft weight immediately prior to the ground vibration test was 20,514 kg (45,225 lb) with a center of gravity at FS 455.12.

The airplane, for test purposes, was configured as follows:

- Empty fuel
- QEC-nacelle installed in the baseline -1 degree position
- All flaps and spoilers were retracted
- Stub propfan blades were shimmed to prevent vibration within the hub
- Ailerons, elevators, and rudder were clamped to their parent surfaces

As initially planned, the airplane was to be supported at its jack points on vibration isolators. These isolators were designed specifically for use in ground vibration testing the Gulfstream IV airplane and were readily adaptable to the PTA airplane.

Unfortunately, during the test setup, the bladder in the right main isolator ruptured rendering this isolator unusable. The decision was made to support the airplane on the remaining isolators and the right main gear with tire deflated from normal operating pressure of 1172×10^3 N/m² (170 psi) to 448×10^3 N/m² (65 psi). This produced an asymmetric suspension system but was considered better than supporting the airplane entirely on its landing gear.

8.1.2.2 Test Procedures

The test article was excited by electromechanical shakers at various locations on the airplane. Due to the asymmetric configuration of the test article, only one shaker was used at any one time. The shaker was attached to the airplane structure with metal brackets, and when this was not practicable, with an adhesive wax. Response versus frequency plots were made at each shaker location and at several reference accelerometer locations using slow sine sweep excitation. These plots and the analytical mode shapes were then used to determine the optimum combination of shaker and reference accelerometer locations for each mode surveyed.

The sine dwell method was used to map vibratory mode shapes of the airframe. The primary bending modal frequency of each boom and the rotational frequency of each control surface were measured by a Fast Fourier Transform (FFT) analyzer using impulse excitation. The structural damping of each mode was measured by the quick stop-decay method.

8.1.2.3 Test Results

The asymmetric configuration of the test article significantly complicated the process of gathering modal data during the ground vibration test. The necessary single-point excitation caused problems in obtaining an adequate

amount of energy to excite the total airplane. The asymmetric configuration also caused the test article to be more sensitive to shaker location than is usually experienced with a symmetric test article. Measurable variations in mode shapes and modal frequencies, in excess of normal expectations, were encountered with different shaker locations. Therefore, data were gathered only where clean, well-behaved modal peaks were encountered with emphasis on obtaining the most important modes.

Boom Modes - The frequencies of the primary bending mode of each boom are presented in the table of Figure 301. It was determined during the preliminary design phase of the PTA Program that the flexibility of the wing mounted booms need not be included in the analytical model if the primary bending modal frequencies of these booms were greater than 10 Hz. The results presented in Figure 301 verify that this condition was attained. It should be noted that the elimination of these degrees of freedom in analysis is slightly conservative since a small increase in stabilizing unbalance is obtained due to dynamic amplification in the flexible booms.

Control Surface Rotational Modes - The rotational modal frequencies of the control surfaces are presented in Figure 302. These results compare well with the results of previous Gulfstream II ground vibration tests.

Airframe Modes - The response versus frequency plots used to identify the airframe modes to be surveyed were generated by an FFT analyzer and contained some inherent frequency shift errors due to sweep rate, sampling rate, and bandwidth. Therefore, these plots were used only as a guide to the general location of a mode. The actual frequency of each mode surveyed was determined by carefully adjusting the frequency to obtain the maximum structural response.

Comparisons between the measured modes and the analytical modes are presented in Figure 303. The description of each mode is based on the components contributing the principal amounts of strain energy to the overall mode as indicated by the analysis. Analyses conducted after the ground vibration test indicated the first seven modes could easily be brought into close agreement by adjusting the rigid body modes to represent the actual suspension system stiffnesses that were encountered during the test.

During the final design phase, the analysis was frozen prior to a final decision on the actual extent of the structural modifications to the right outboard wing. The inclusion of this additional stiffness in the analysis brought Mode 10 into excellent agreement with the test results. The measured results for Modes 15, 17, 18, and 19 indicated the airplane was stiffer than the analysis predicted. These differences were caused by combinations of increased left wing torsional stiffness and increased stiffness in the propfan QEC-nacelle structure in both the vertical and lateral directions. A definitive modification to the analysis would require extensive additional analyses that were beyond the scope of this investigation. The remaining measured modes are in good agreement with the predicted results.

ITEM	VERTICAL EXCITATION Hz	LATERAL EXCITATION Hz
DYNAMIC BOOM	*	13.0 Hz
STATIC BOOM	*	12.125 Hz
AIRSPEED BOOM	8.5 Hz	8.25 Hz
ACOUSTIC BOOM	11.0 Hz	11.5 Hz

*Unable to separate from wing modes

Figure 301. Measured Boom Frequencies

ITEM	PTA RESULTS Hz	GII RESULTS Hz
AILERON	10.76	11.25
ELEVATOR	8.04	7.90
RUDDER	6.56	6.65

Figure 302. Control Surface Rotation Frequencies

MODE	CALCULATED FREQUENCY (Hz)	MEASURED FREQUENCY (Hz)	DESCRIPTION
1	0.45	**	A/C Lateral Translation & Yaw
2	0.50	**	A/C Fore & Aft Translation
3	0.57	0.48	A/C Yaw & Lateral Translation
4	0.94	1.46	A/C Roll & Right Wing Bending
5	1.07	0.68	A/C Pitch & Vertical Translation
6	1.42	1.80	A/C Vertical Translation & Pitch
7	2.47	2.89	Right & Left Wing Bending, Aft Fuselage Torsion & Fin Bending, A/C Vertical Translation
8	3.27	3.12	Aft Fuselage Torsion & Fin Bending, Right & Left Wing Bending
9	4.33	4.46	Left Wing Bending
10	4.66	5.47	Right Wing Torsion
11	5.26	**	Fin Torsion
12	5.47	5.76	Spey Engine Vertical Translation & Left Wing Torsion
13	6.49	6.63	Fuselage Vertical Translation
14	6.91	7.32	Right Wing Fore & Aft Bending
15	7.25	8.26	Left Wing Torsion
16	7.77	7.90	Fuselage Lateral Bending
17	8.46	9.08	Propfan QEC-Nacelle Lateral Translation/Yaw

(a) Modes 1-17

Figure 303. Summary of Measured Modes

MODE	CALCULATED FREQUENCY* (Hz)	MEASURED FREQUENCY (Hz)	DESCRIPTION
18	8.65	9.46	Left Wing Torsion, Spey Engine Vertical Translation
19	8.77	10.02	Left Wing Torsion & Propfan Pitch
20	10.17	**	Propfan Powerplant Yaw/Lateral Translation
21	10.74	10.28	Stabilizer Bending
22	11.14	**	Spey Engine Yaw
23	11.43	**	Spey Engine Yaw, Higher Order Aft Fuselage and Fin
24	12.30	**	Spey Engine Yaw (Out of Phase)
25	12.57	12.71	Left Wing Fore & Aft Bending
26	13.18	14.09	Right Wing 2nd Bending
27	14.25	**	Right Wing 2nd Bending, Spey Engine Yaw
28	15.58	**	Propfan Powerplant Lateral Translation
29	16.40	16.40	Left Wing 2nd Bending
30	17.23	**	Spey Engine Pitch

* Reference 1, Pre-Ground Vibration Test Analysis

** Not Measured

(b) Modes 18-30

Figure 303. Summary of Measured Modes (Continued)

8.1.3 Acoustic and Vibration Tests

A series of ground tests were conducted to (1) diagnose sound transmission into the cabin, (2) investigate the cabin volume resonant response to acoustic excitation, and (3) determine the degree of surface pressure doubling on the wing microphone boom. During these tests, the PTA airplane rested on its landing gear in a hangar. No propulsion systems were operated; all acoustic and vibratory excitations were produced with laboratory test equipment.

8.1.3.1 Test Description

Figures 304 and 305 are block diagrams of the vibration and the acoustic input measurement systems. These systems were used to enable the differentiation of the sources of the cabin sound pressure levels.

Two source signals were prerecorded on a Nagra IV SJ reel-to-reel, ¼-in. tape recorder operating at 7.5 in./sec. The first signal consisted of the first three propeller harmonics at cruise conditions: 226, 452, and 678 Hz. The second signal consisted of band-limited white noise at 150 to 900 Hz. The taped signals were conditioned and equalized with a Marantz preamplifier.

The vibration system included a 200-lb Unholtz-Dickie Exciter (UD-4C) and Power Amplifier (TA-250-6-4C). An Endevco Force Transducer (2104-1000) was attached to a plate placed at the wing bottom and in series with the shaker tubular drive rod and shaker. The transducer output was used to set the input levels. The force was monitored with a digital voltmeter and an Ono-Sokki Dual-Channel FFT Analyzer (CF-900). The selected force levels were 10, 20, 40, and 80 lb peak for the harmonic signal and 40 lb rms for the random signal. The pre-amplifier equalizer was used to reduce the high-frequency roll-off of the force signal.

The shaker input plate was mounted at three different wing locations to simulate a variety of input positions. The first location was inboard of the engine on the front wing spar. The other two locations were outboard of the engine on the front wing spar and inboard of the engine on the rear wing spar.

The acoustic system consisted of the same source signal and pre-amplifier conditioning as described in the force tests above. A 500-watt Crown power amplifier (PS-400) drove an Emilar 150 Hz horn and electrodynamic driver system. The horn and driver were supported against the lower wing surface for one test and against the fuselage sidewall in the propeller plane for a second test. The horn was closed by the aircraft surface; a ¼-in. thick foam gasket was used to seal the two surfaces. The mouth of the horn covered an area of 36.8 cm by 63.5 cm (14.5 in. by 25 in.).

The lower wing surface microphone (ML15) was inside the horn mouth and acted as the control microphone for the first acoustic test. The acoustic tests were run at 2.75 V_{rms} (136 dB SPL) measured at the power amplifier output. In addition, data were taken at -6, -12, and -18 dB relative to the original source level. The fuselage sidewall microphone (M303) was

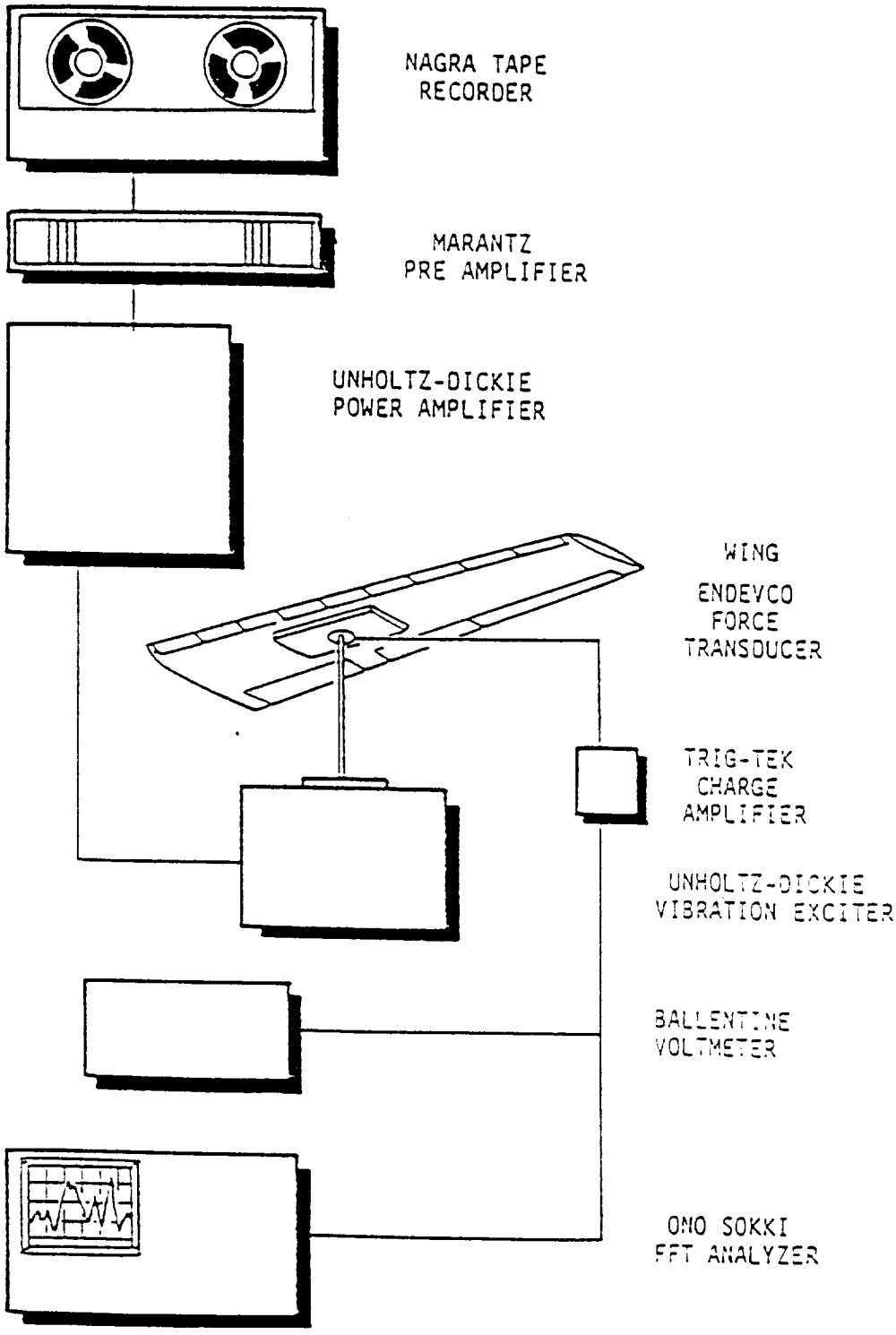


Figure 304. Block Diagram of the Vibration Excitation System

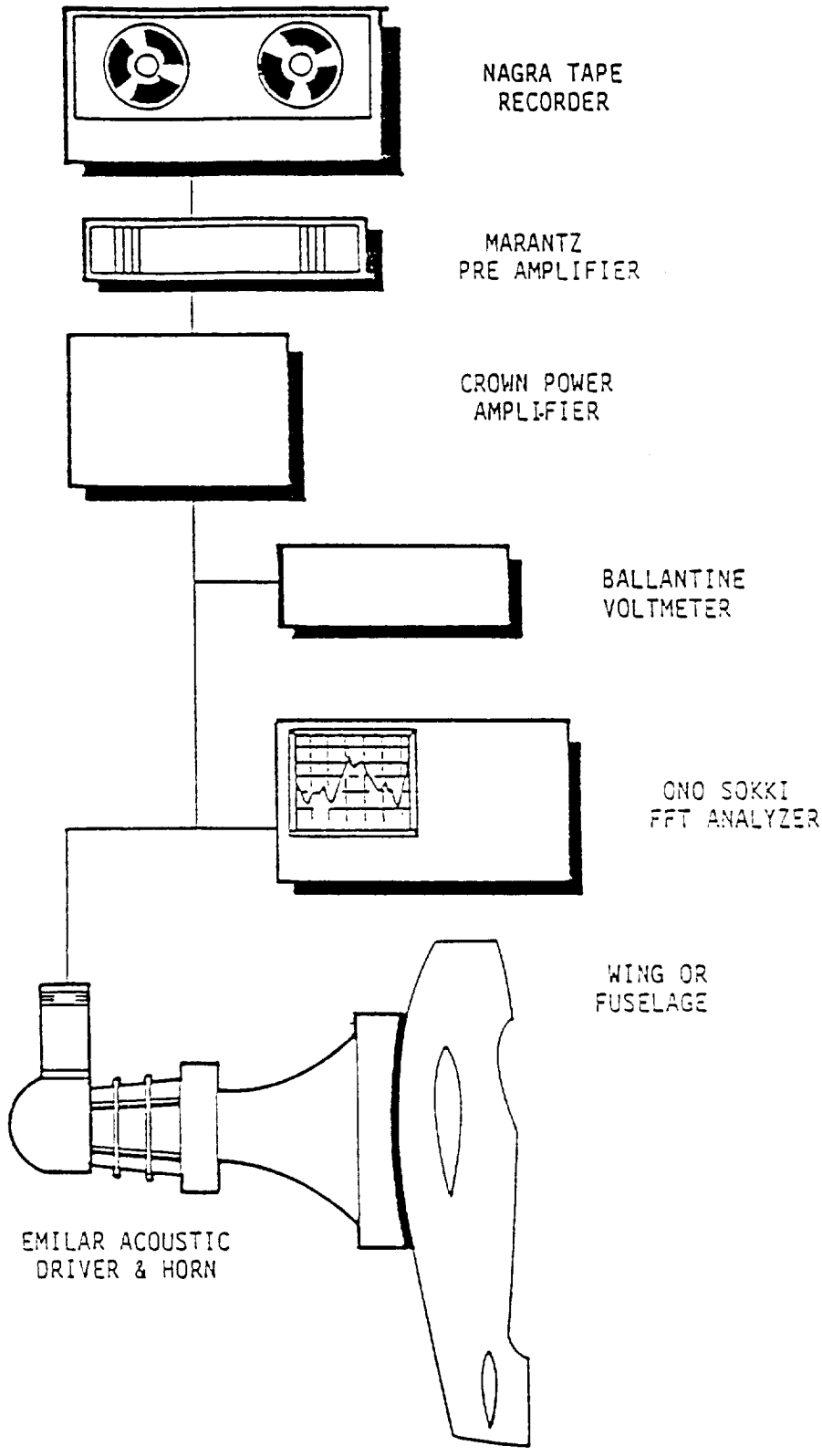


Figure 305. Block Diagram of the Acoustic Excitation System

inside the horn mouth and acted as the control microphone for the second acoustic test. The same levels were used as in the first acoustic test.

8.1.3.2 Test Results and Discussion

Test results showed that a nominal vibratory force of 5.5N (40 lb) (rms overall) normal to the wing front spar lower surface produced cabin noise levels of 90 dB overall. A 140 dB overall acoustic excitation on the cabin exterior in the plane of the propfan plane produced cabin noise levels of 110 dB overall. The results suggest that for flight conditions involving high fluctuating pressures on the wing and low sound pressures on the fuselage, the cabin noise data at some locations may be influenced by structureborne noise.

Cabin volume resonance frequencies were surveyed, and response mode shapes were determined for selected resonances. The first-order axial mode occurred at 13.1 Hertz; the second order at 22.3 Hertz; the third at 30.5 Hertz. Higher order axial modes were separated by about 8 Hertz. The first-order radial mode occurred at 96 Hertz; the second at 168 Hertz. The first-order tangential mode occurred at 83 Hertz; the second at 156 Hertz.

Many cabin volume resonances were found in the frequency range of the propfan first-order blade passage noise, most of which were complex modes. This has the effect of reducing the degree of noise level variation with changing spatial location, and with changing propfan rpm.

8.1.4 Systems Functional

The systems functional tests were accomplished in two phases. The first phase consisted of tests to check out the basic GII systems unaffected by the PTA modifications. For these tests, the Gulfstream Computerized Maintenance Program procedures were followed. The second phase checked those systems altered to some degree by the PTA modification process. For these tests, there were no specific research instrumentation requirements. Cockpit instruments were utilized where appropriate.

8.1.4.1 Basic GII System

The following GII systems were checked.

- Hydraulic systems
- Flight control systems
- Fuel systems
- Electrical systems
- Engine systems
- Environmental systems
- Subsystems

All systems were found to operate normally.

8.1.4.2 Modified GII Systems

The GII systems, altered to some extent by the PTA modification, were functionally checked using the procedures defined in Reference 19.

All systems listed below were satisfactorily checked-out prior to first flight.

- Electrical power system
- Fuel system
- Fire detection system
- Fire suppression system
- Propfan propulsion system starter duct
- Propfan propulsion system oil cooler flap
- Propfan propulsion system dry motor
- Interphone system
- Interior lights
- Testbed airspeed system

8.1.5 Propfan Structural Integrity

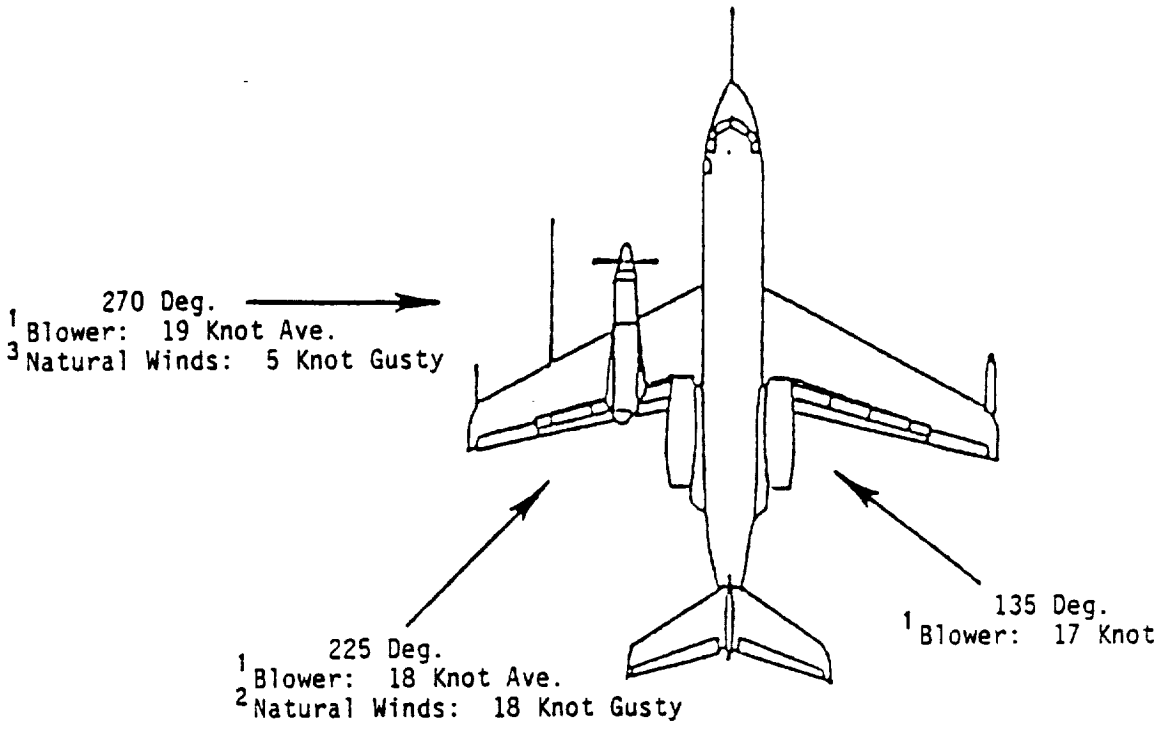
8.1.5.1 Test Description

Following completion of the propfan propulsion system functional checkout, a series of ground tests were conducted to substantiate the structural integrity of the Hamilton Standard SR-7L propfan.

The first portion of the structural integrity assessment involved evaluating blade vibratory stress levels during governing and power lever traverses for calm wind and steady crosswind conditions.

Initial natural crosswind testing was unsuccessful due to unacceptable levels of fluctuations in ambient wind speed and direction. Subsequently, crosswind testing was completed successfully by employing a C-130 as a blower aircraft. Figures 306 and 307 illustrate the three crosswind test conditions and the position of the PTA aircraft relative to the blower aircraft for one of the three crosswind conditions.

The power lever traverse test was performed with the blades against the low pitch stop, which was set at 20 degrees (low power/nongoverning operation), and provided the opportunity to search for and define any propfan/drive system critical frequencies. The test was conducted by setting the speed lever to 105 percent and adjusting the power lever accordingly to ascend from high idle speed (53 percent) to 105 percent in 3-percent increments. Repeatability of the test data collected was confirmed by descending in rpm from 105 percent to high idle speed (53 percent), in 3-percent increments. Strain gage data were collected for 30 seconds at each interim point.



Note:

1. Wind speed adjusted to prevent high blade stress.
2. Natural Cross-wind Testing at NASA Wallops Flight Facility.
3. Calm wind testing.

Figure 306. Crosswind Test Conditions

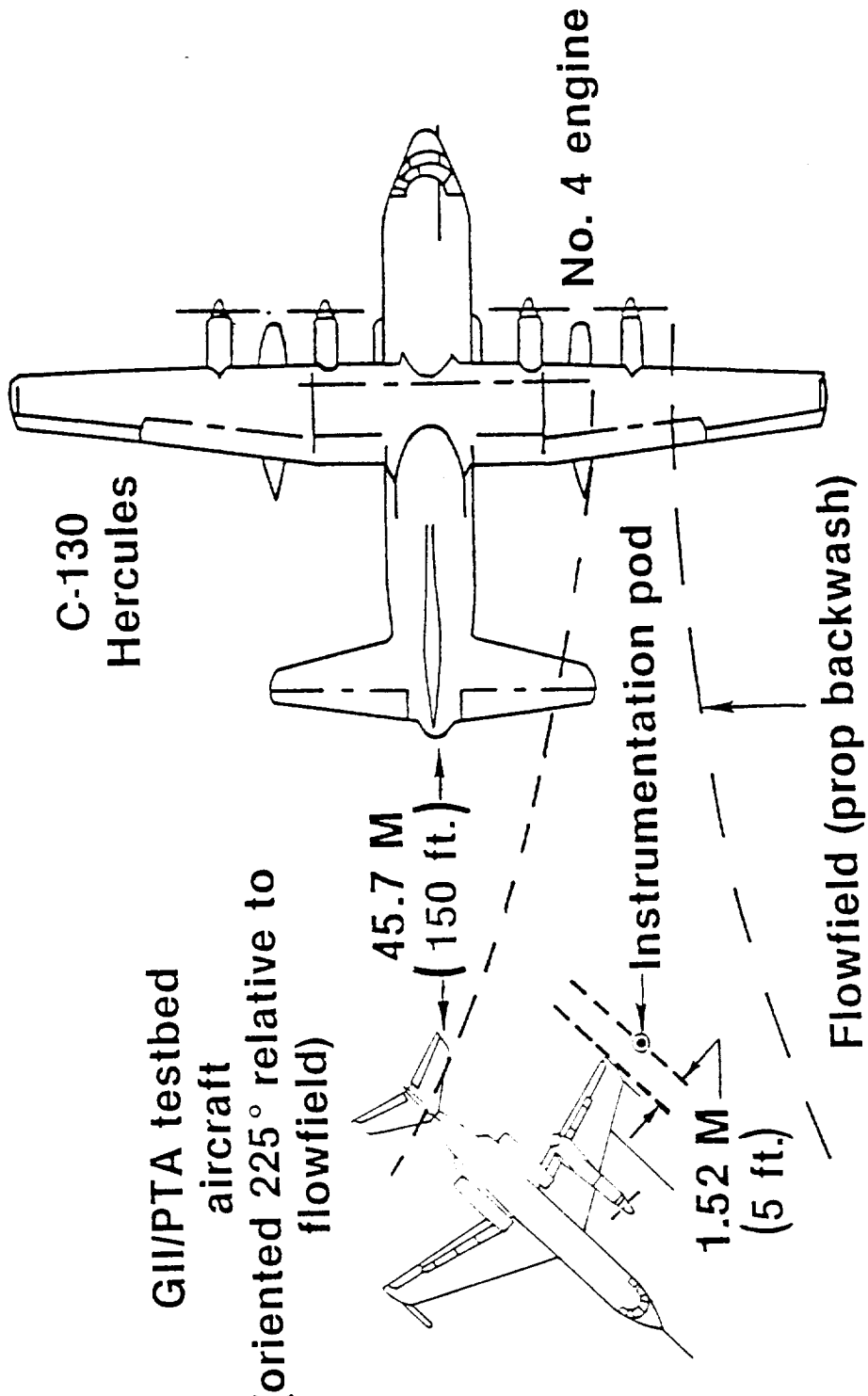


Figure 307. Crosswind Testing Using a C-130 as a "Blower" Aircraft

The stress survey (governing) test was performed to establish the operational limits for high power static conditions. Data were collected over a range of stabilized torque conditions for propfan speeds ranging from 75 percent to 105 percent, in 5-percent increments. As with the power lever traverse test, strain gage data were collected for 30 seconds at each test point.

The final portion of the structural integrity assessment was the taxi test to determine the effect of forward velocity on the blade buffet boundary found during static operation. Initial plans called for a feather test, a low-speed buffet boundary exploration, and constant torque tests. However, because of aircraft handling problems encountered during high-speed taxi testing, portions of the buffet boundary exploration and the constant torque test were deleted from the test matrix. The feather test was conducted by accelerating the aircraft from 0 to 68 mps (0.2 MN) and decelerating back to 0 with the propfan feathered. The buffet boundary was established at taxi speeds of 10 mps (20 KCAS) and 21 mps (40 KCAS) for a propfan speed setting of 78 percent, with a series of slow power lever transients up to the maximum torque permissible without exceeding blade stress limits. Data was recorded continuously during the taxi test.

8.1.5.2 Test Results

The test data were analyzed in terms of data sample average (DSA) and infrequently repeating peak (IRP) stress for all steady state conditions. The DSA strain is the average peak vibratory amplitude of a sample of strain gage data while the IRP vibratory strain is a statistical value representing the mean vibratory strain plus two standard deviations of the data sample. The IRP vibratory strain is used to define the boundaries of the blade continuous operating envelope and to plot all relevant total vibratory response data for the structural integrity tests. In addition to total vibratory response data, selected strain gage channels were harmonically analyzed to establish the frequency content of the blade response.

Calm Wind Tests - The calm wind static tests were performed in two parts. First, a power lever traverse along the fixed blade angle of the low pitch stop was accomplished, followed by governing points which were obtained at conditions where the system maintained constant rotational speed by changing blade angle to absorb increasing power. Figures 308 and 309 show the test conditions obtained during the power lever traverse and governing portions of the static tests in a calm wind. For these tests, calm winds are defined as less than 3 mps (5 knots) crosswind or 5 mps (10 knots) head wind. The calm wind tests were actually run with a 3 mps (5 knot) gusting, 270 degree crosswind as shown earlier in Figure 306.

As was the case for both the WPAFB and Rohr Brown Field tests, the SR-7L propfan exhibited high blade tip vibratory response that limited torque at constant speed conditions as shown in Figure 310. The data show that stress levels remained at moderate levels during constant speed conditions until a critical torque level was reached, above which, stress levels increased rapidly with torque. The only exception to this was a high strain point at 85-percent propfan speed at low torque. The stray point

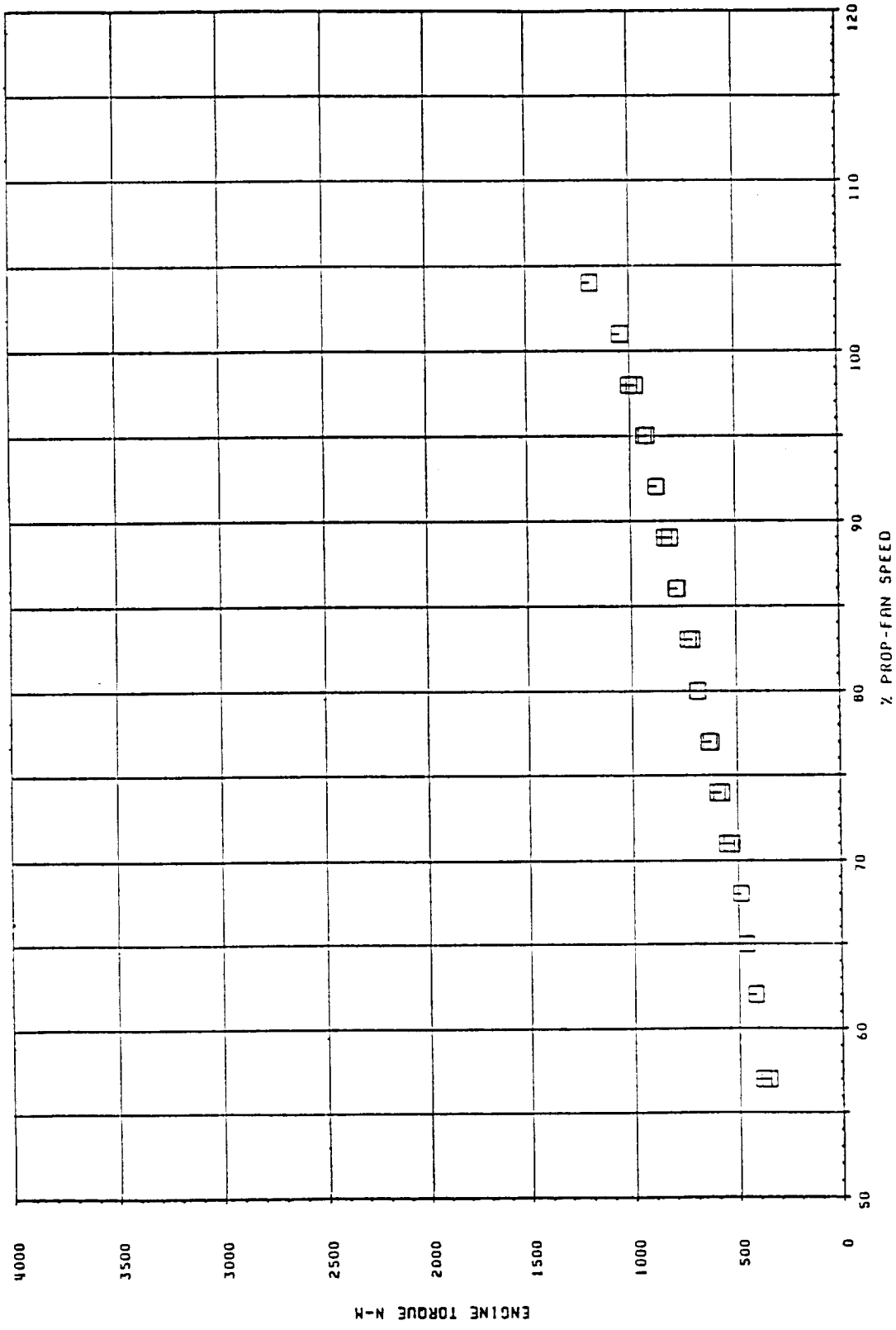


Figure 308. Power Lever Traverse During Calm Wind Conditions

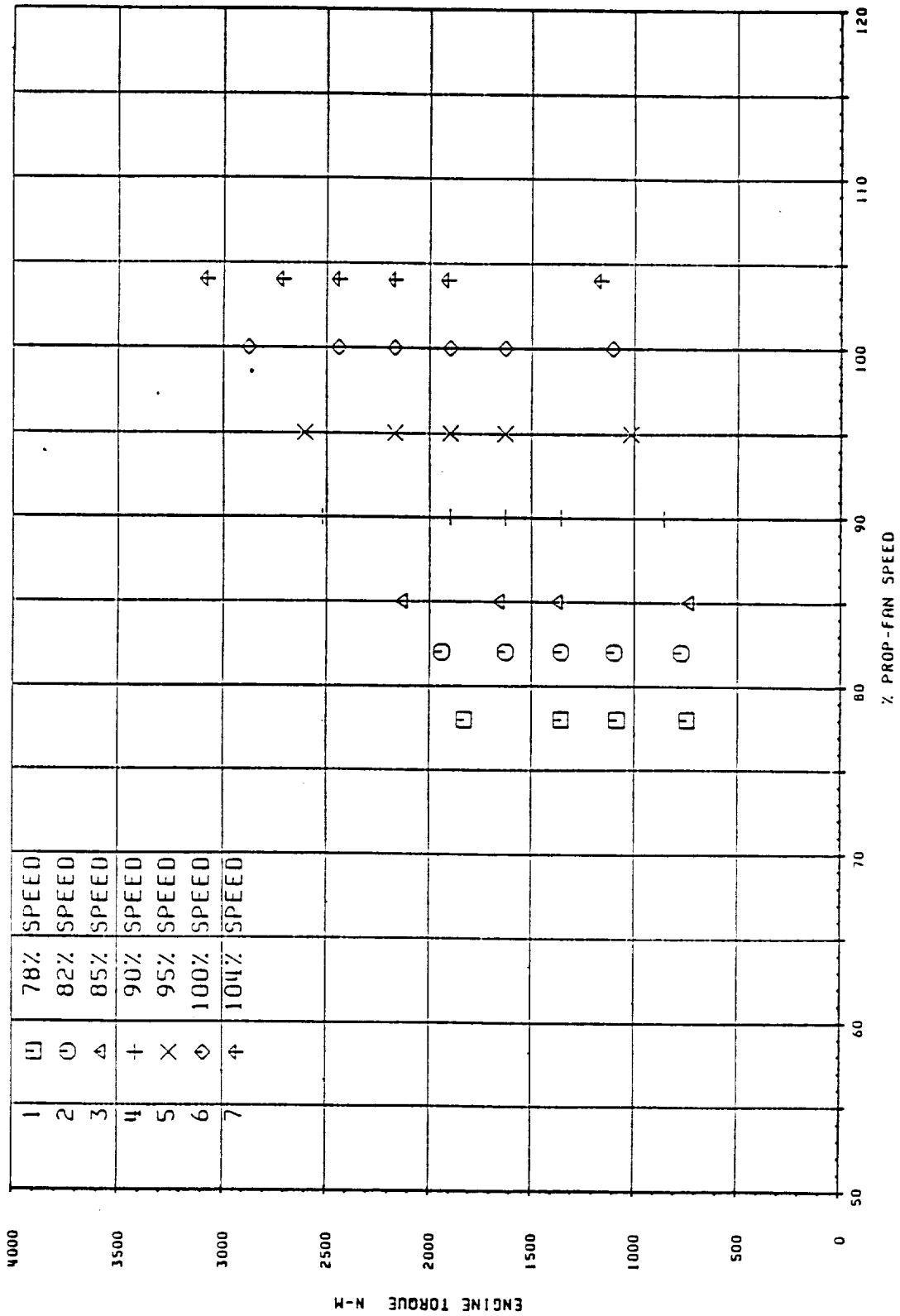


Figure 309. Calm Wind Governing Tests

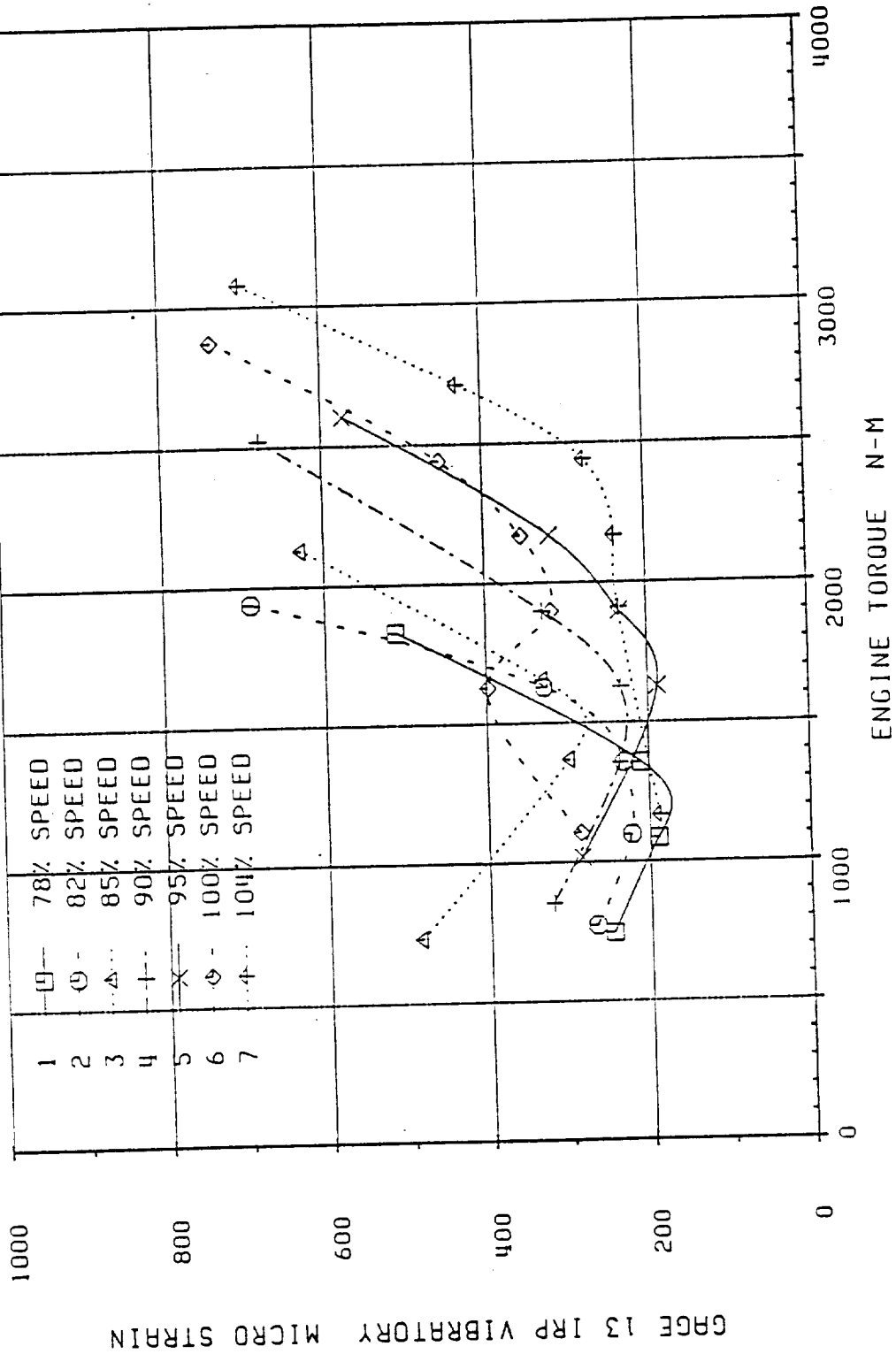


Figure 310. Variation of Tip Bending Strain with Torque

is most likely due to the variability of the winds during testing. The role of crosswinds is discussed in more detail later.

The trends of vibratory stress during static operation in calm wind conditions were similar to those experienced during previous static testing on the engine test stand at Rohr and on the whirl rig at WPAFB. The primary difference between the aircraft tests and the other tests was due to aircraft environment. This environment contributed to higher P-order response. Figure 311 shows that at 78-percent speed all three static tests showed the same results, but at 100-percent speed the blade stressing was greater for the aircraft installation due to increased P-order response near the 3P first edgewise mode critical speed (See Figure 235.). Another difference between the three static tests was the environmental wind conditions. The engine test stand had 5 to 7 mps (10 to 14 knots) head winds which reduced the stresses, while the aircraft environment had a 3 mps (5 knot) gusting crosswind which would have the effect of raising blade stresses. The whirl rig tests were conducted in an indoor facility and, therefore, had no winds.

Figure 312 presents a comparison between amplitude response spectra from the aircraft ground test and from the static engine test at 100-percent rotational speed. This comparison highlights the effects of the different environments. The 3P excitation at 100-percent speed is near the first edgewise critical speed so the 3P response is magnified. During the engine test, the blade buffeting in the 3F and 2F blade modes dominated the response, but during the aircraft ground test near the 3P/1E critical speed, the 3P response dominated the blade vibration. It should be noted that buffeting response in the 3F and 2F modes was not significantly affected by the difference in test environments, while the P-order response was significantly affected.

When results from the SR-7L and the SR-7A (small-scale aeroelastic model) are examined in terms of power loading (power per disk area) and tip speed, a comparison of static operating boundaries can be made. This comparison is shown in Figure 313 for all three SR-7L tests and for the SR-7A test in the NASA-LeRC 9-Ft x 15-Ft Wind Tunnel. The SR-7L tests and the SR-7A test show similar results.

The increase in tip strain with torque as shown earlier in Figure 310 is actually a blade angle effect. The relationship between torque and blade angle is shown in Figure 314. Torque increased with a constant slope up to approximately 25 degrees blade angle; above 25 degrees blade angle, the torque sensitivity to blade angle began to decrease. This result was also observed during the Rohr Brown Field and WPAFB static tests of the SR-7L blades. The change in slope at 25 degrees is related to flow separation at the blade tip which causes a local reduction in section lift and an increase in blade tip vibratory response. The stress data of Figure 310 were plotted versus blade angle in Figure 315. Stress increased substantially at blade angles above 25 degrees independent of torque and rotational speed. This relationship between stress and blade angle was also observed during the static rotor tests at WPAFB and the static engine tests at Rohr's Brown Field.

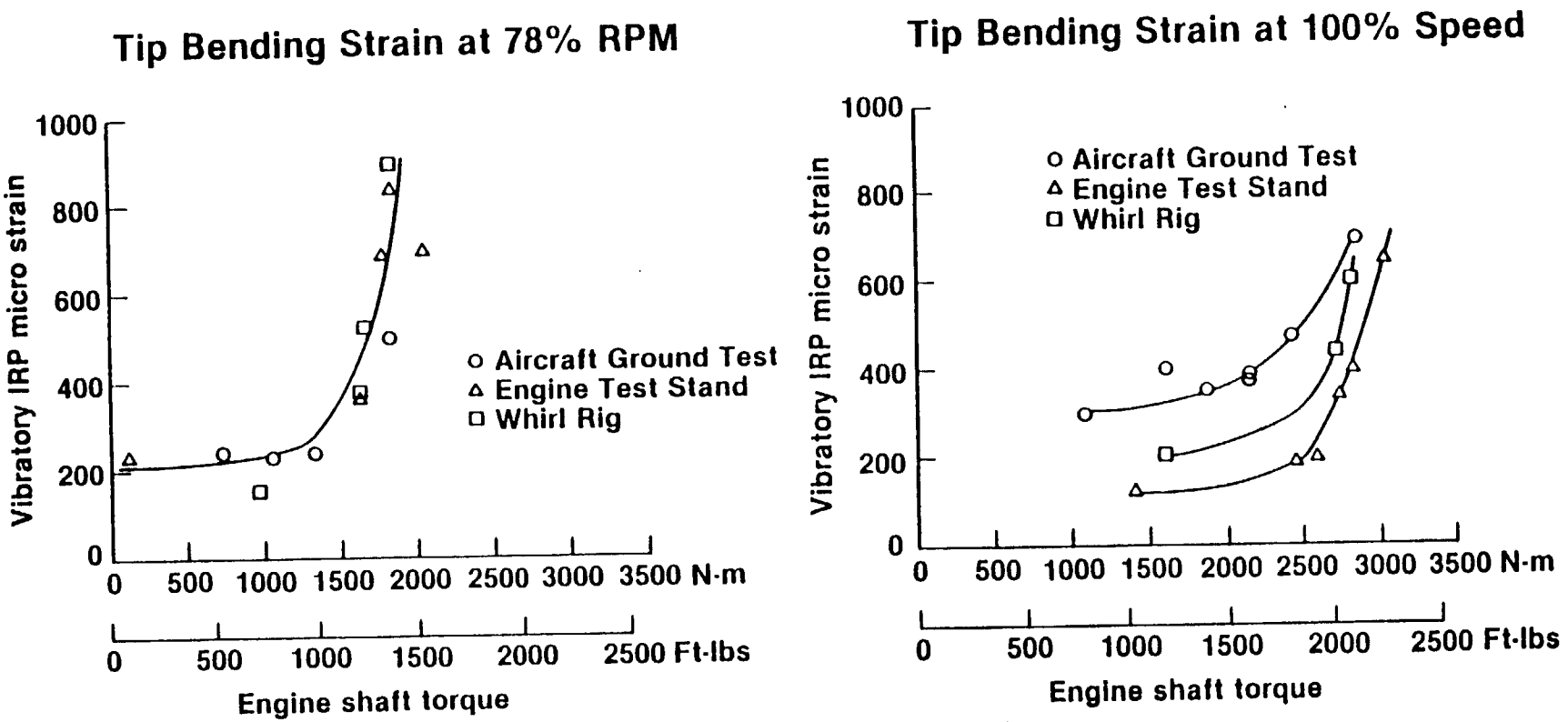


Figure 311. Tip Bending Strain During Static Operation

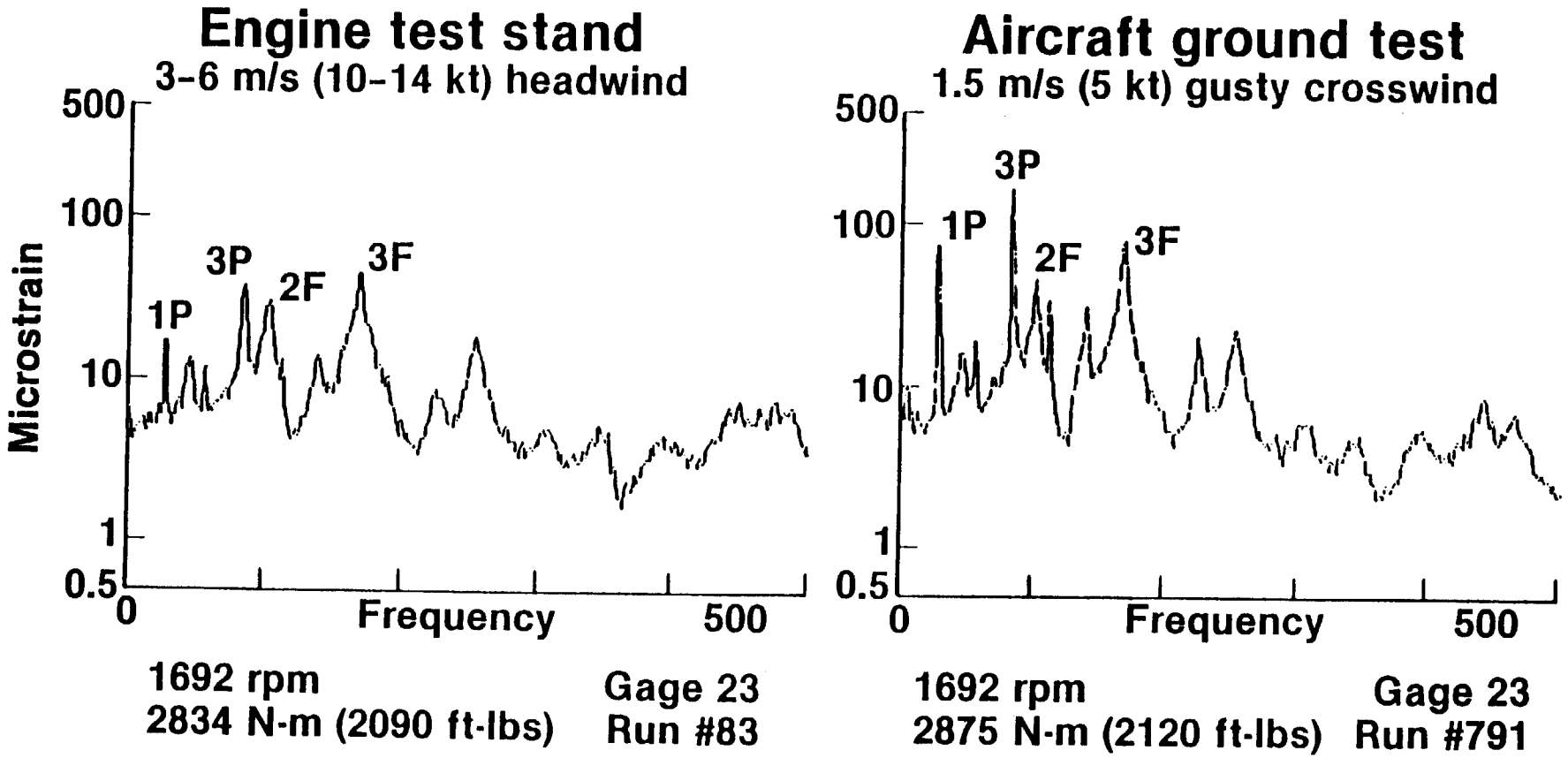


Figure 312. Tip Bending Gage Response Spectra at 100% N_p

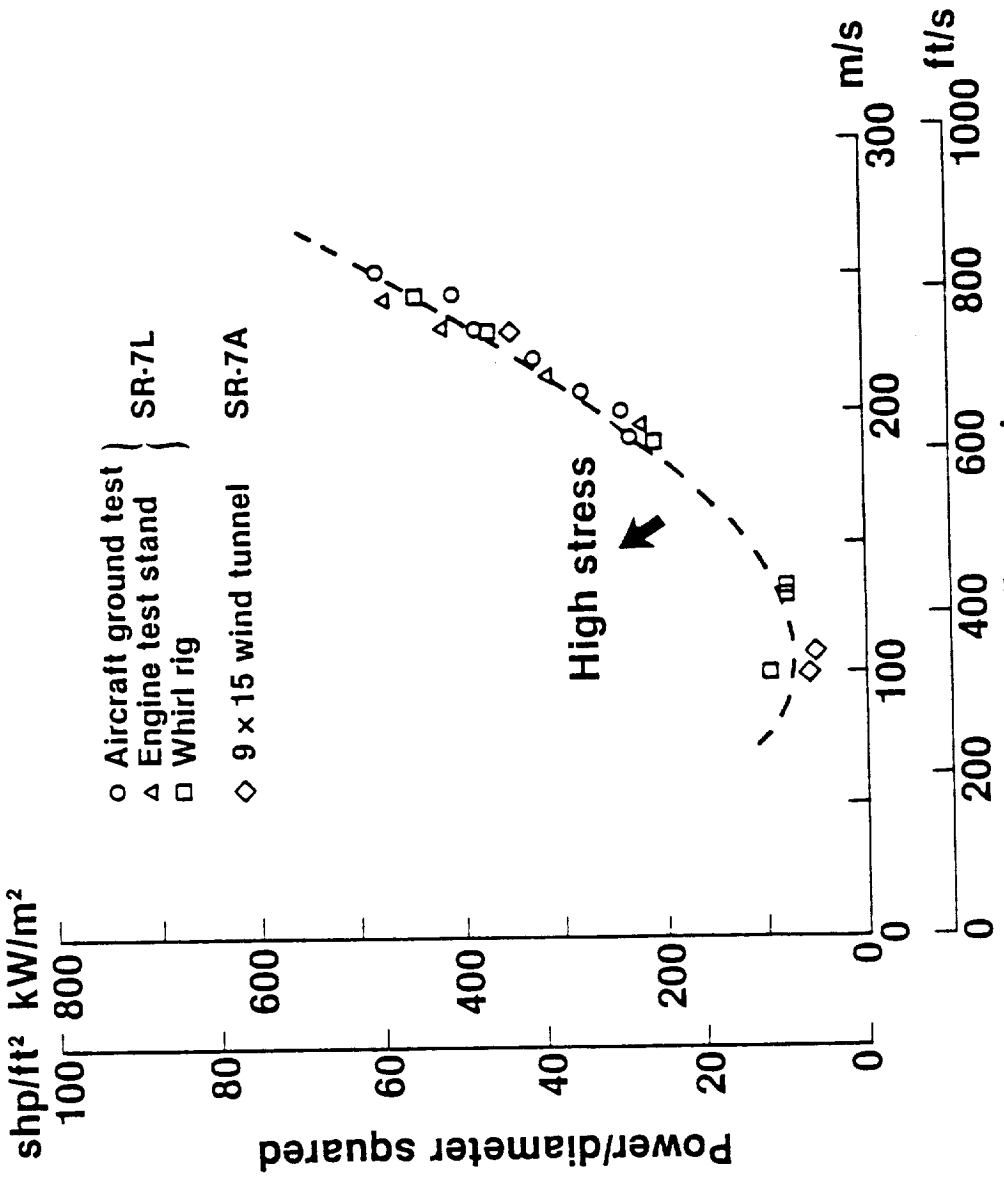


Figure 313. Comparison of Static Boundaries for SR-7L and SR-7A

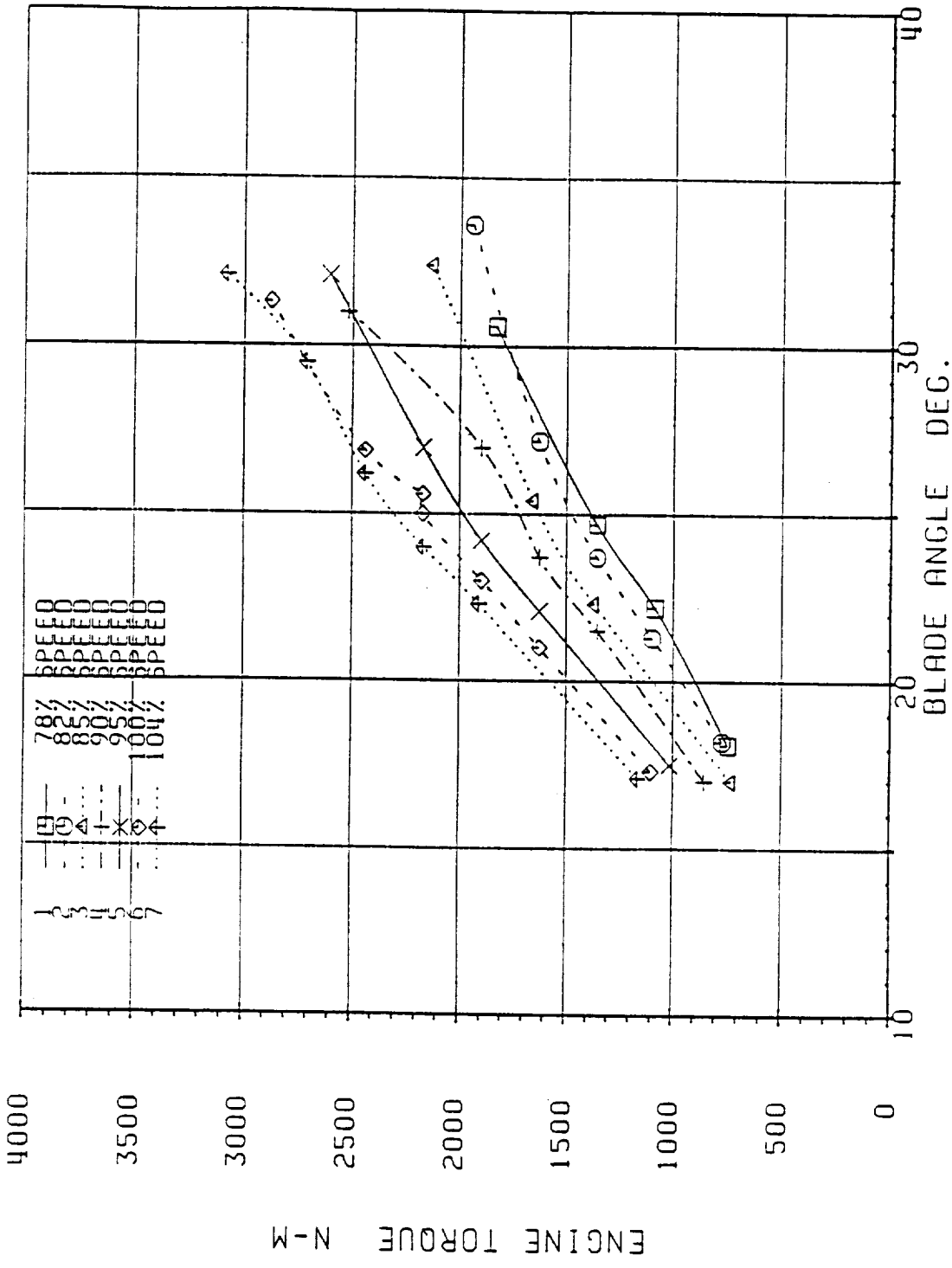


Figure 314. Torque Variation With Blade Angle While Governing

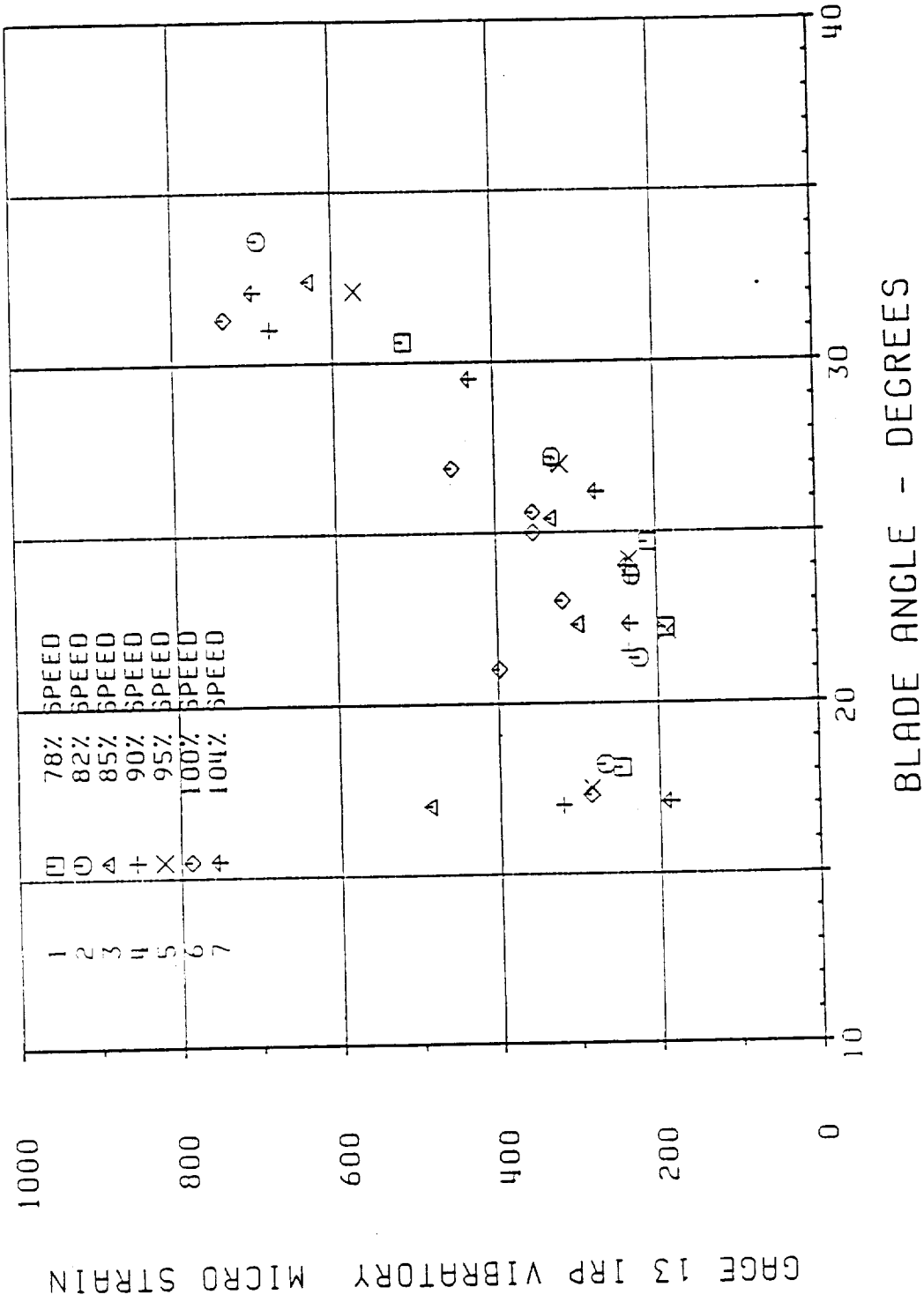


Figure 315. Tip Bending Strain Variation with Blade Angle

The data presentation thus far has concentrated on the blade tip bending gages. To show the response of inboard gages, the radial strain distribution is plotted for both high and low torque conditions in Figure 316. The strain distribution is seen to be level to about the 70-percent span where it increases to a maximum at the blade tip.

Figure 317 shows typical raw strain gage signals for the maximum torque of 2874 N-m (2120 ft-lb) obtained while operating at 100-percent rpm. The top curve, the edgewise shank moment gage 2E, shows a 3P harmonic vibratory moment because of the 3P/first edgewise critical speed. The flatwise shank gage 2F exhibited much lower amplitudes at the 3P frequency and showed traces of high frequency noise. Gages 23 and 24 are the tip bending and tip trailing edge gages, respectively. These gage signals show the effect of the flow separation resulting from static operation at blade angles above 25 degrees. The flow separation and reattachment phenomena excites blade natural modes that add to the base 3P vibratory signals. Gage 61, the inboard bending gage, shows a low amplitude signal with a 1P harmonic and high frequency noise component. Gage 62, the mid-blade bending gage, shows less severe signs of the buffeting that was observed at the tip.

The frequency content of the tip bending Gage 23 for the same operating conditions of Figure 317 is shown in the vibratory stress amplitude spectrum of Figure 318. The primary response was at the 3P/first edgewise critical speed at 85 Hz. There was a substantial response at the frequency of 170 Hz which corresponds to the fifth natural mode (3F) of the SR-7L blade. Other natural blade modes responded at moderate levels, including the first, third, fourth, sixth, and seventh modes as shown in Figure 318. Figure 319 shows an amplitude spectrum for gage 23 while operating at 85-percent speed and the maximum torque at that speed of 2129 N-m (1570 ft-lb). The primary response at those conditions was at the third natural frequency of 96 Hz which is characterized as the second flatwise mode. Although for this case the buffeting response was dominated by the second flatwise mode, response at other natural frequencies was present, as shown by Figure 319. These results are similar to the static test results at WPAFB and static engine testing at Rohr Brown field except that the aircraft environment induced higher 3P excitations. The additional 3P could be the result of the intermittent 3 mps (5 knot) gusting crosswind and/or the proximity of the ground plane, aircraft wing, or fuselage.

Spectral analysis was performed on 16 test conditions to establish the SR-7L blade natural frequencies and response frequencies. The measured blade natural frequencies are plotted on Figure 320. This data agrees well with spectral data obtained from the WPAFB and Rohr static tests which showed good agreement with predicted blade natural frequencies.

As part of the ground stress survey, a power lever traverse was recorded to obtain a fine grid of rpm conditions to locate blade critical speeds as a function of propfan speed. The procedure for this portion of the ground stress survey was to set the speed lever at the 105-percent position and increase the propfan speed from 57 percent to 104 percent in 3-percent increments with the power lever. Torque versus propfan speed for the test

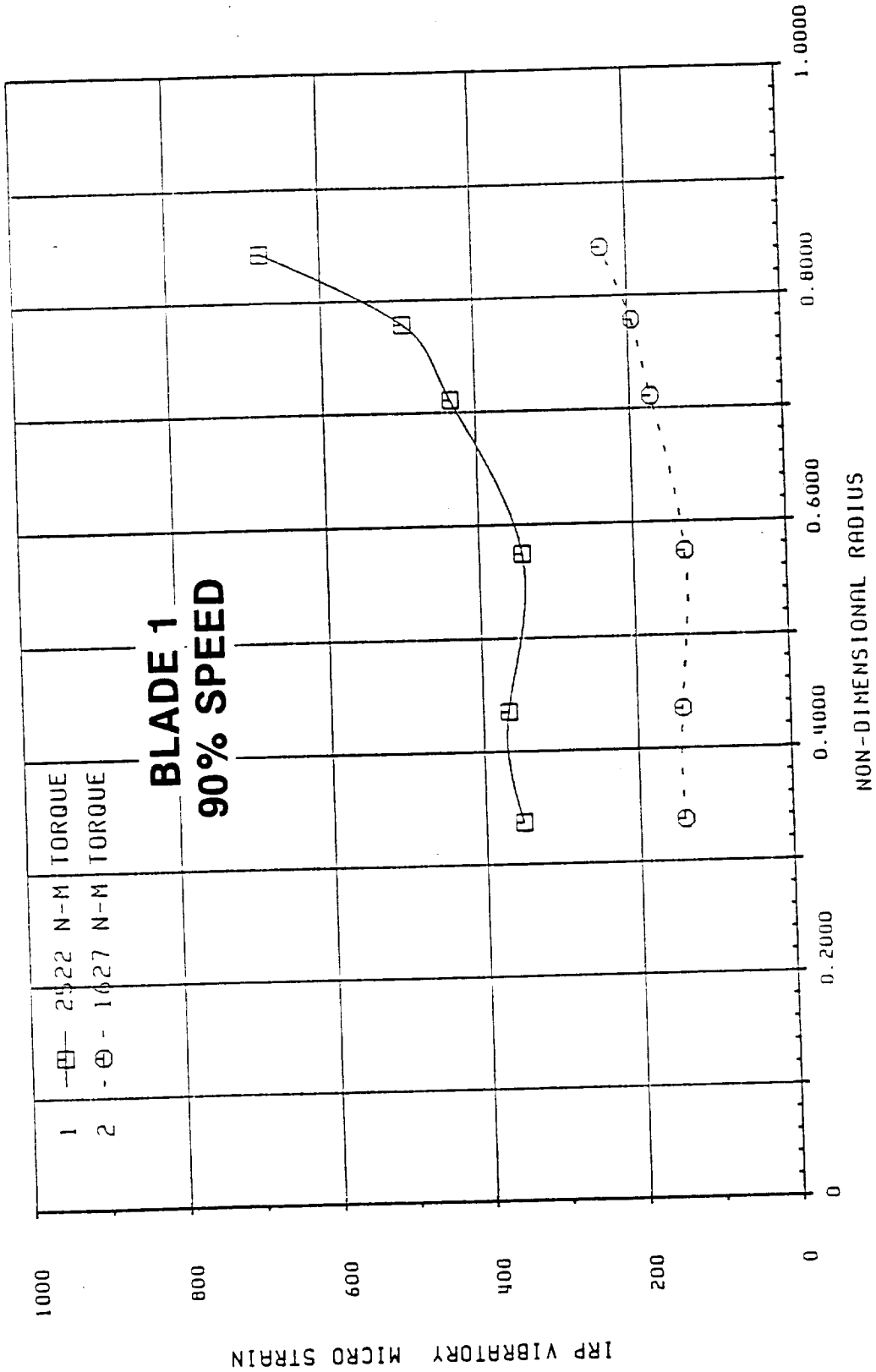


Figure 316. Radial Strain Distribution for Two Torque Values

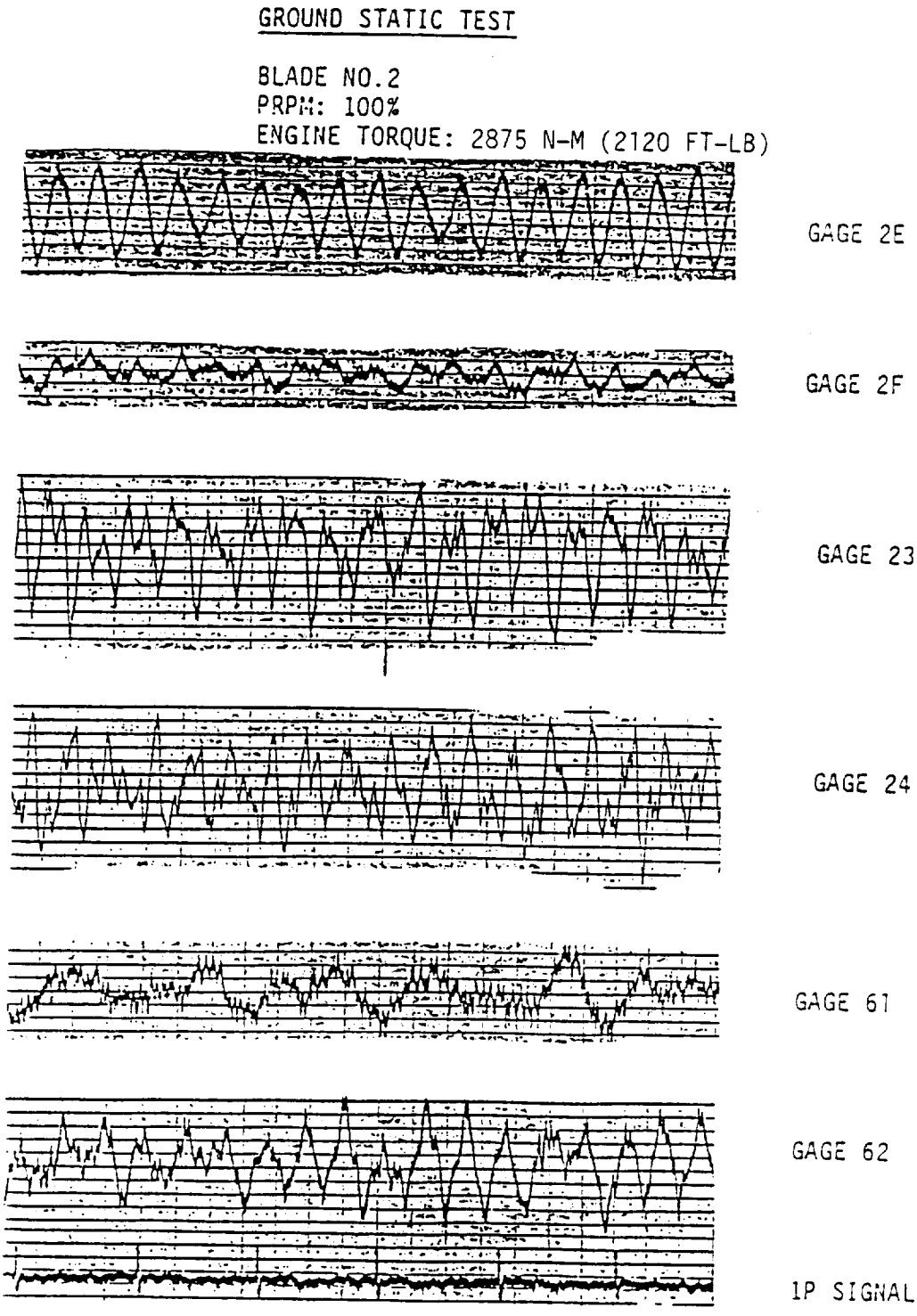
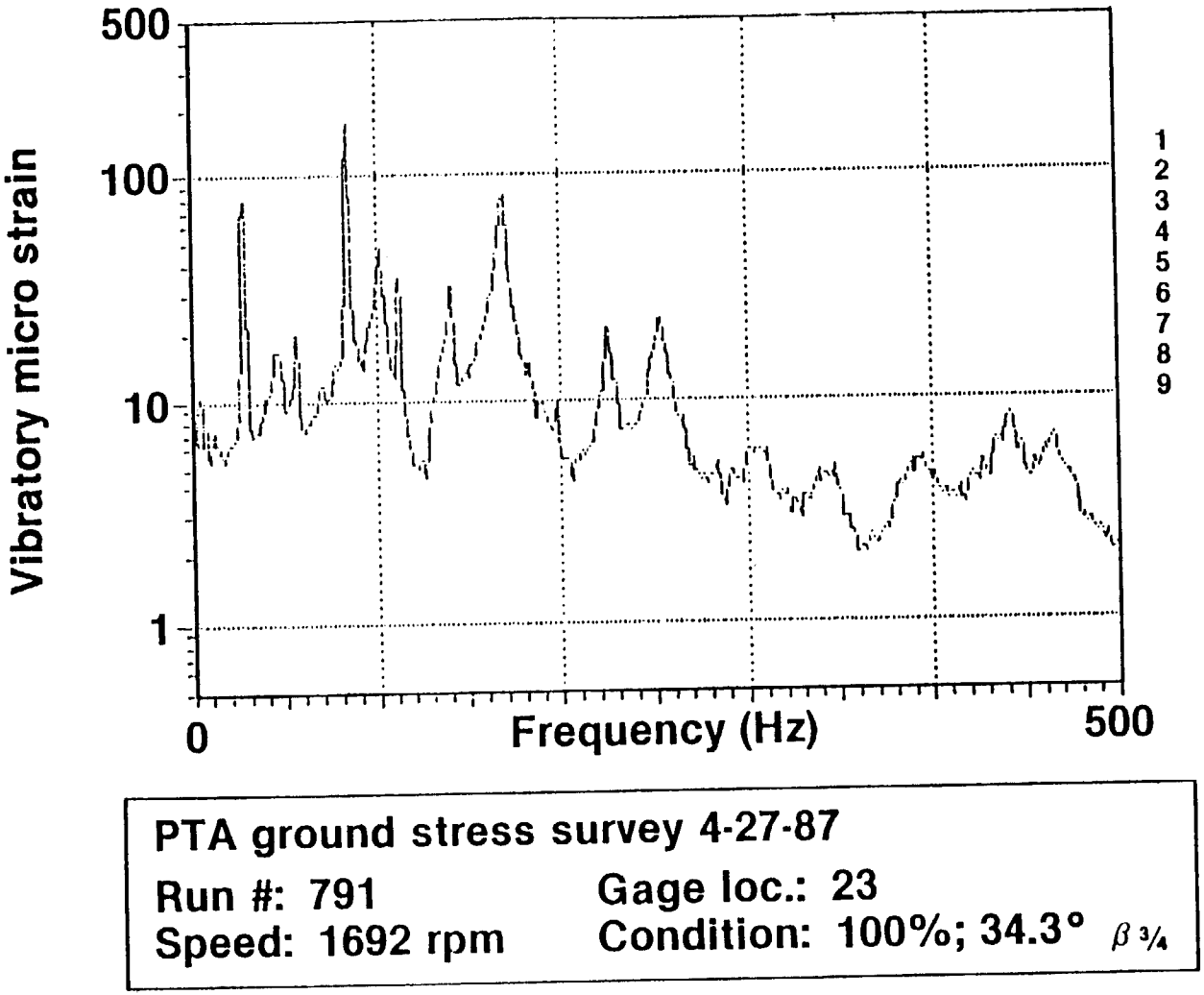
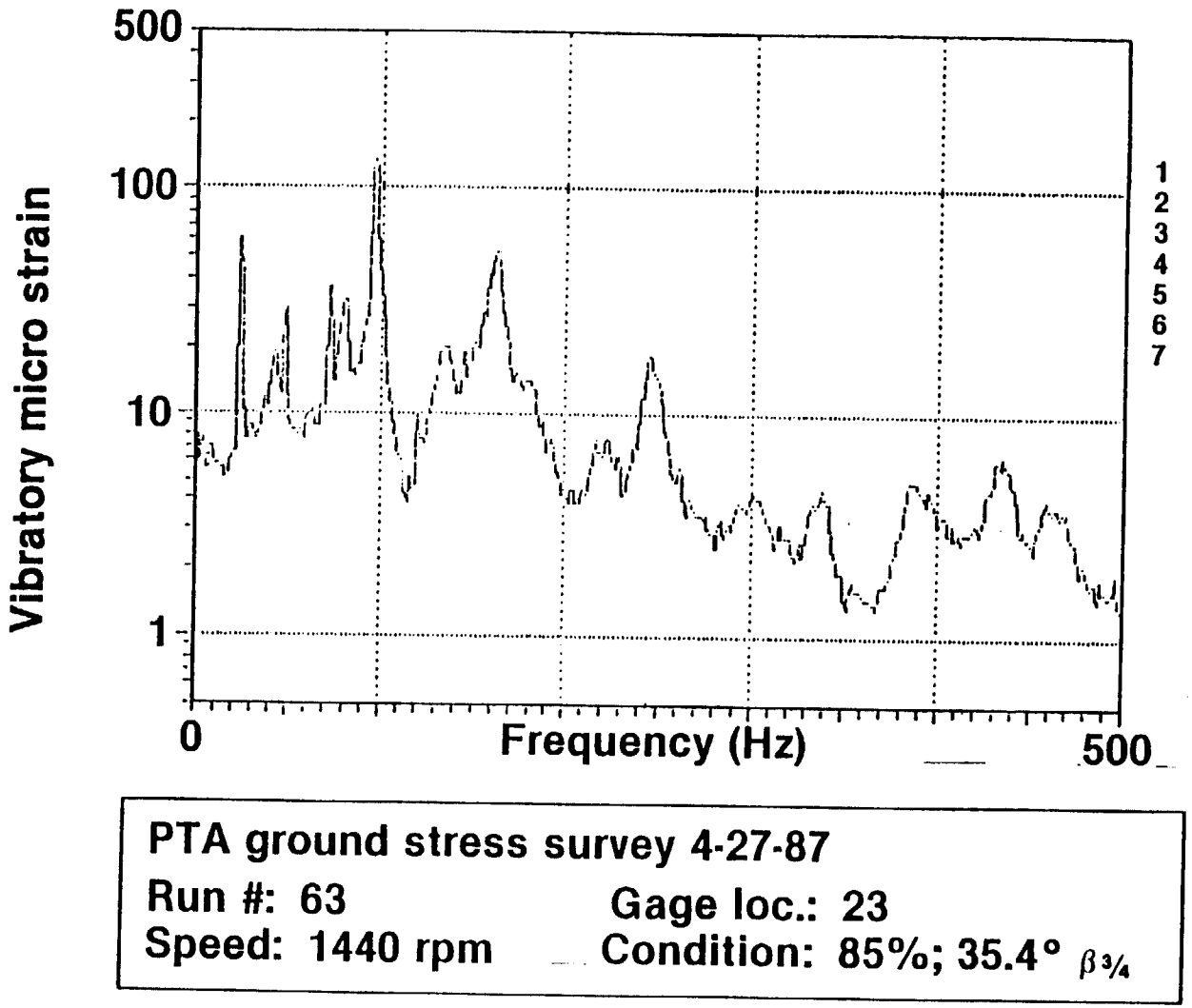


Figure 317. Visicorder Plots of Strain Gage Signals



	Frequency (Hz)	Amplitude (μ Strain)
1	28.75	77.8
2	56.25	20.1
3	85.00	174.3
4	102.50	49.0
5	112.50	36.5
6	141.25	31.5
7	170.00	82.0
8	226.25	20.9
9	253.75	22.8

Figure 318. Blade Strain Amplitude Spectrum - 100% N_p



	Frequency (Hz)	Amplitude (μ Strain)
1	23.75	60.2
2	48.75	29.8
3	72.50	37.9
4	96.25	132.9
5	135.00	19.8
6	162.50	52.3
7	245.00	18.4

Figure 319. Blade Strain Amplitude Spectrum - 85% N_P

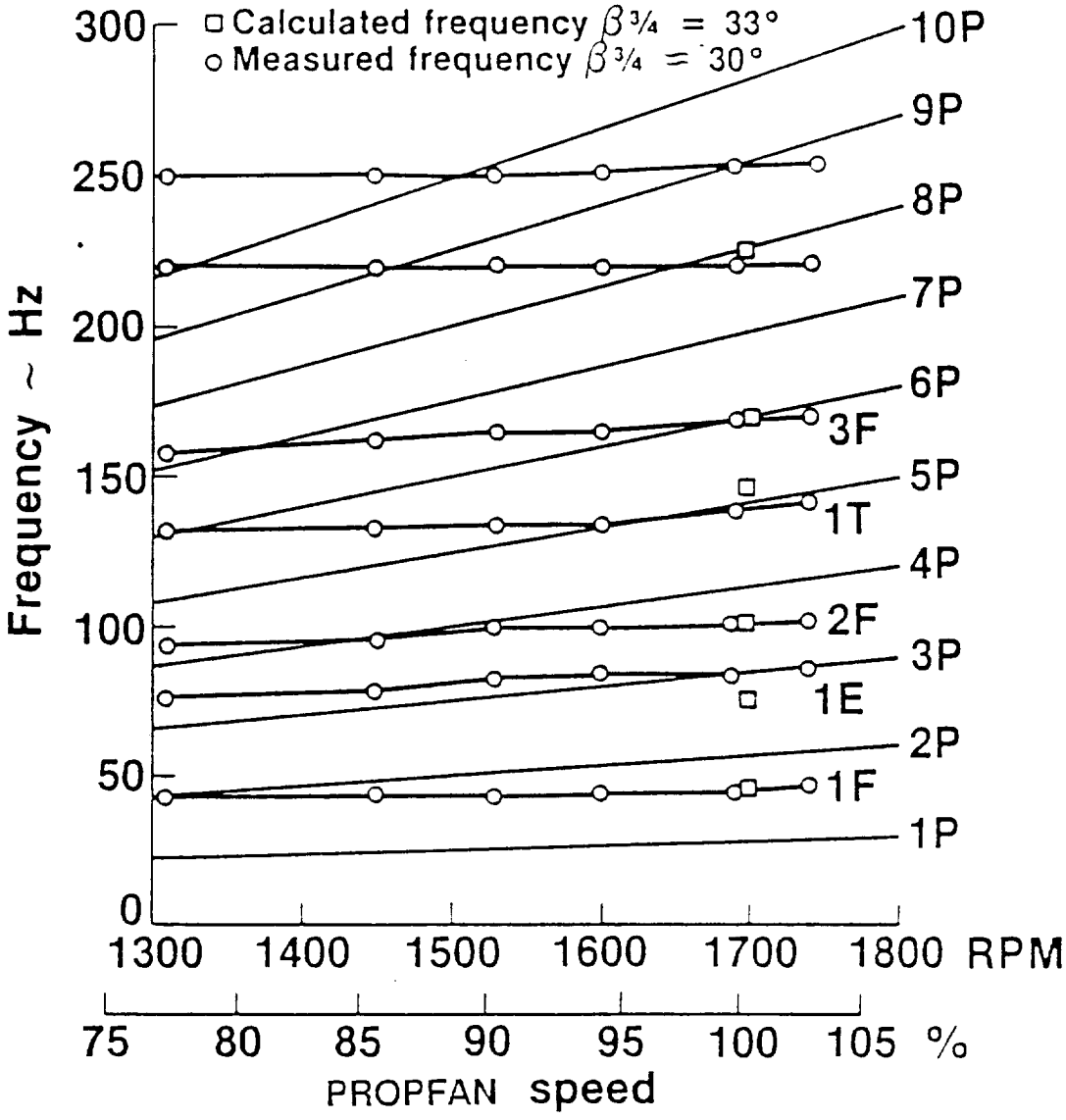


Figure 320. Blade Natural Frequencies from PTA Ground Tests

conditions recorded during the power lever traverse is plotted, as discussed earlier, in Figure 308.

Figures 321 through 325 summarize the blade response during this calm wind power lever traverse. The plots show relevant critical speeds of the propfan blades. The tip bending strain plotted in Figure 321 and the mid-blade strain plotted in Figure 322 show evidence of a 4P/2F flatwise critical speed at 86-percent propfan speed. The inboard bending gage plot shown in Figure 323 and the shank flatwise moment plot in Figure 324 illustrate the 2P/1F critical speed at 74-percent speed. The only critical speed of significance is displayed in Figure 325 which is a plot of the vibratory shank edgewise moment. There is a strong 3P/1E critical speed at 98-percent speed for static ground running on the aircraft.

Crosswind Tests - As discussed earlier, the crosswind tests involved the same power lever traverse and governing conditions as the calm wind tests, with the additional component of a crosswind which was applied in three directions: 135 degrees, 225 degrees, and 270 degrees (Figures 306 and 307). Crosswind static operation has traditionally been a concern during propeller ground operation because this type of environmental condition results in unsteady, highly turbulent flow coming into the propeller. The turbulent flow of a crosswind excites propeller natural response frequencies at resonant P-order critical speeds. The resulting P-order response may be substantial enough to result in ground operational restrictions.

One problem with propellers with more than three blades is that the critical speeds tend to be most severe in reactionless natural propeller modes of vibration. A reactionless mode of propeller vibration is one in which all vibratory loads experienced by the blades are cancelled at the hub and therefore no vibratory loads are transmitted into the aircraft structure. When no blade vibratory loads are transmitted to the aircraft, the pilot cannot feel that the propeller blades may be experiencing high vibration in the crosswind environment.

Therefore, as part of the structural integrity checkout of the SR-7L propfan, static crosswind tests were performed at three aircraft positions shown previously in Figure 306. A C-130 aircraft was employed, as shown in Figure 307, and the No. 4 propeller used as a blower to obtain steady winds at the desired angles. Wind speeds varied from 3 mps (6 knots) to 12 mps (23 knots) during testing with the majority of runs falling in the 8 mps (16 knots) to 11 mps (21 knots) range. Figures 326 through 331 contain the data points that were obtained and reduced for analysis in terms of torque and propfan speed for the 225-degree, 270-degree, and 135-degree crosswind power lever traverse and governing survey tests.

It should be stressed at this point that crosswind test conditions are quite variable, even when a blower aircraft is employed. Figure 332 shows a sample time history of the recorded wind speed and direction during testing. In addition to the variability of the ambient wind during "steady state conditions," the strength of the C-130 propeller slipstream was varied to prevent severe overstressing of the propfan blades. Figures 333 through 335 show the average wind speed for the recorded test points and illustrate the high variability of the test conditions.

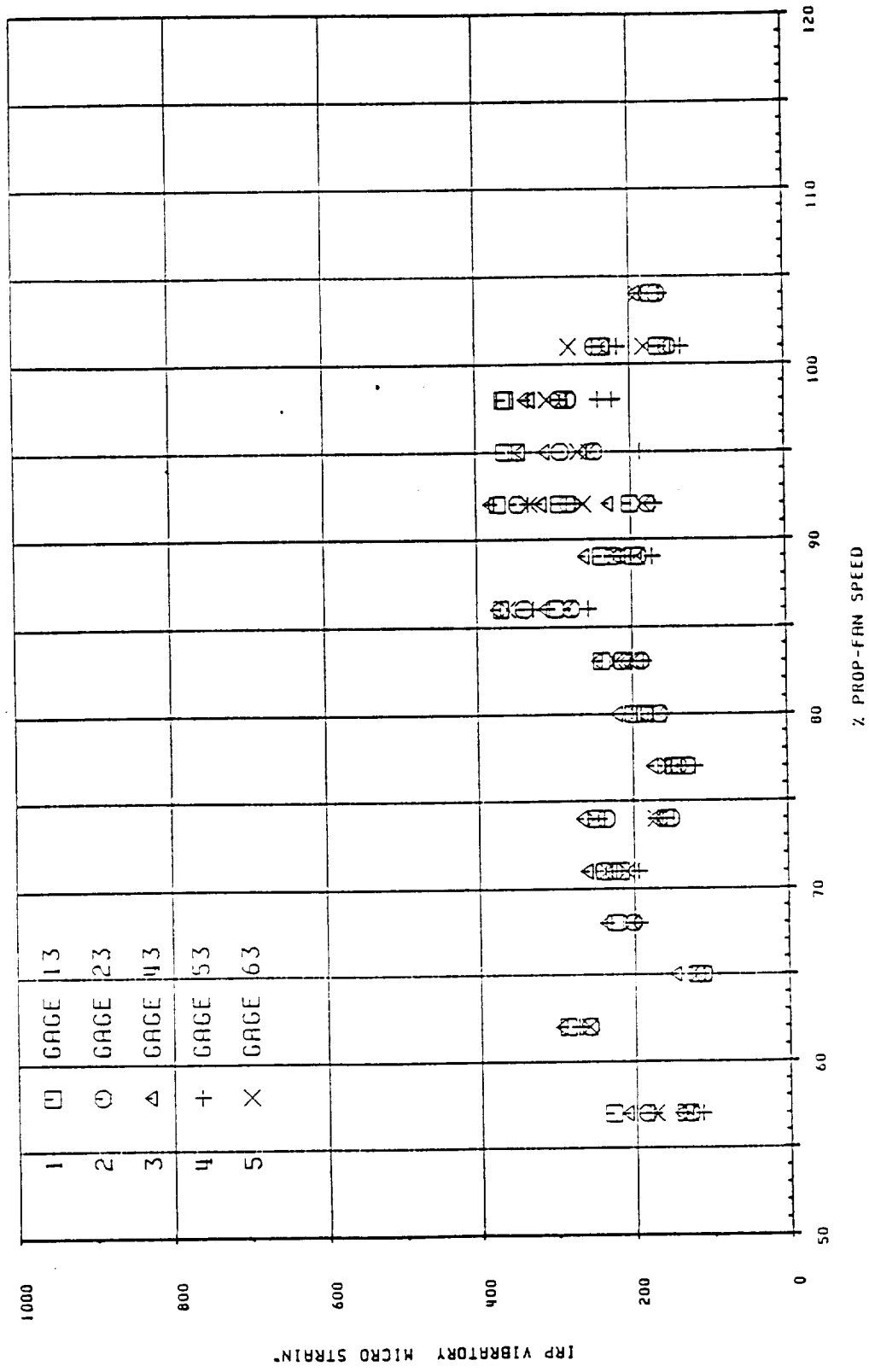


Figure 321. Tip Bending Strain During Calm Wind Power Lever Traverse

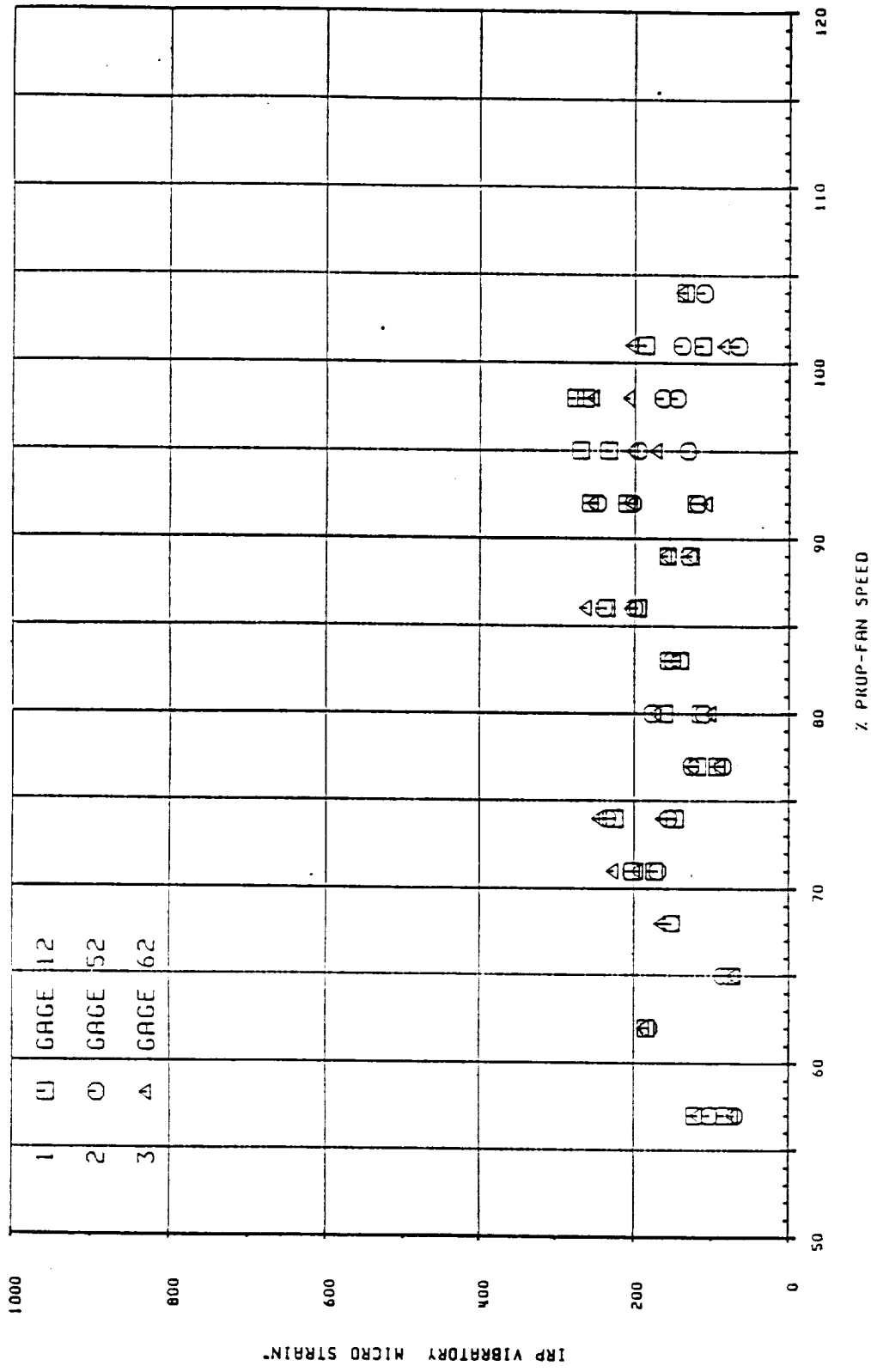


Figure 322. Mid-Blade Bending Strain During Calm Wind Power Lever Traverse

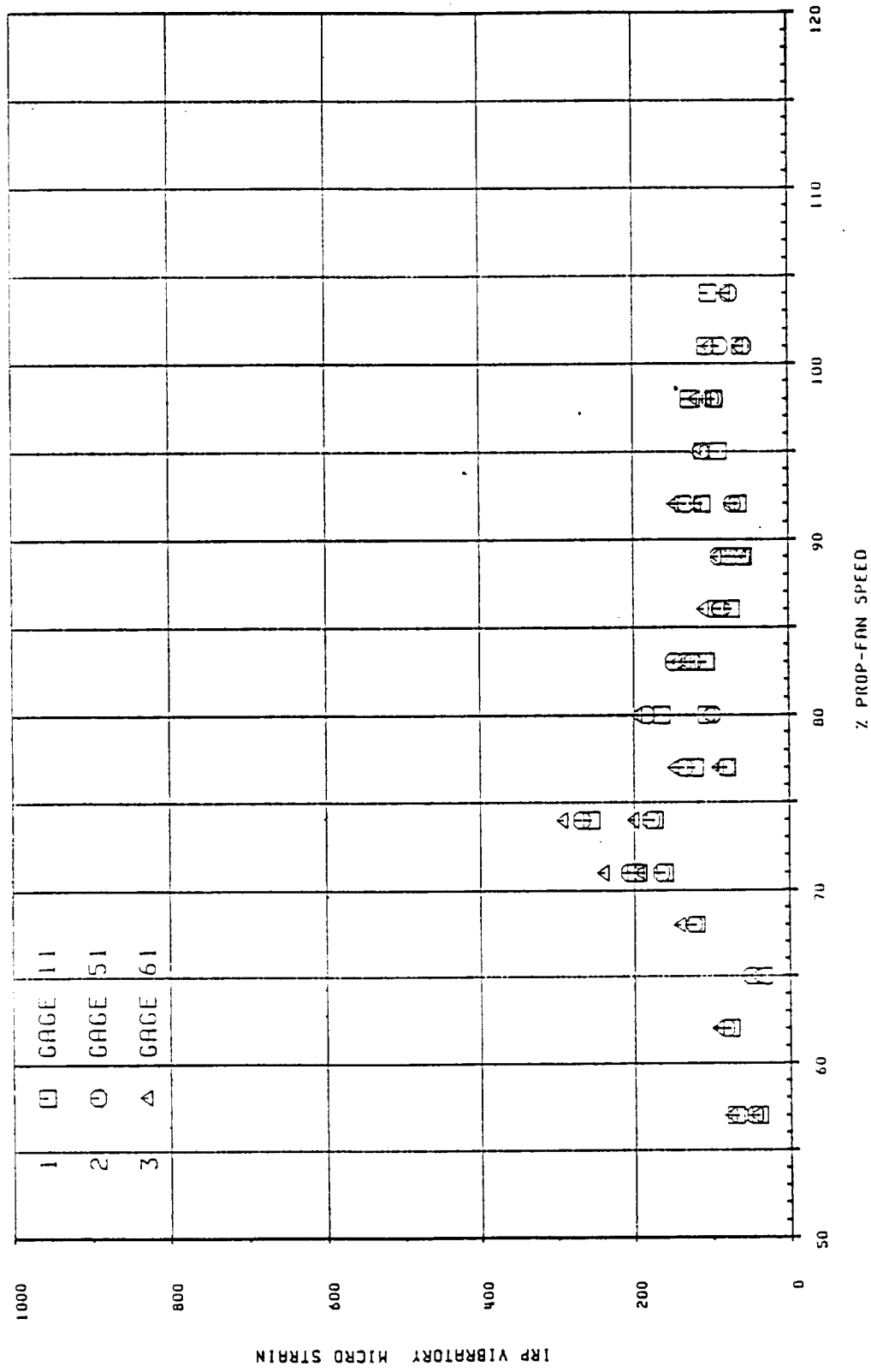


Figure 323. Inboard Bending Strain During Calm Wind Power Lever Traverse

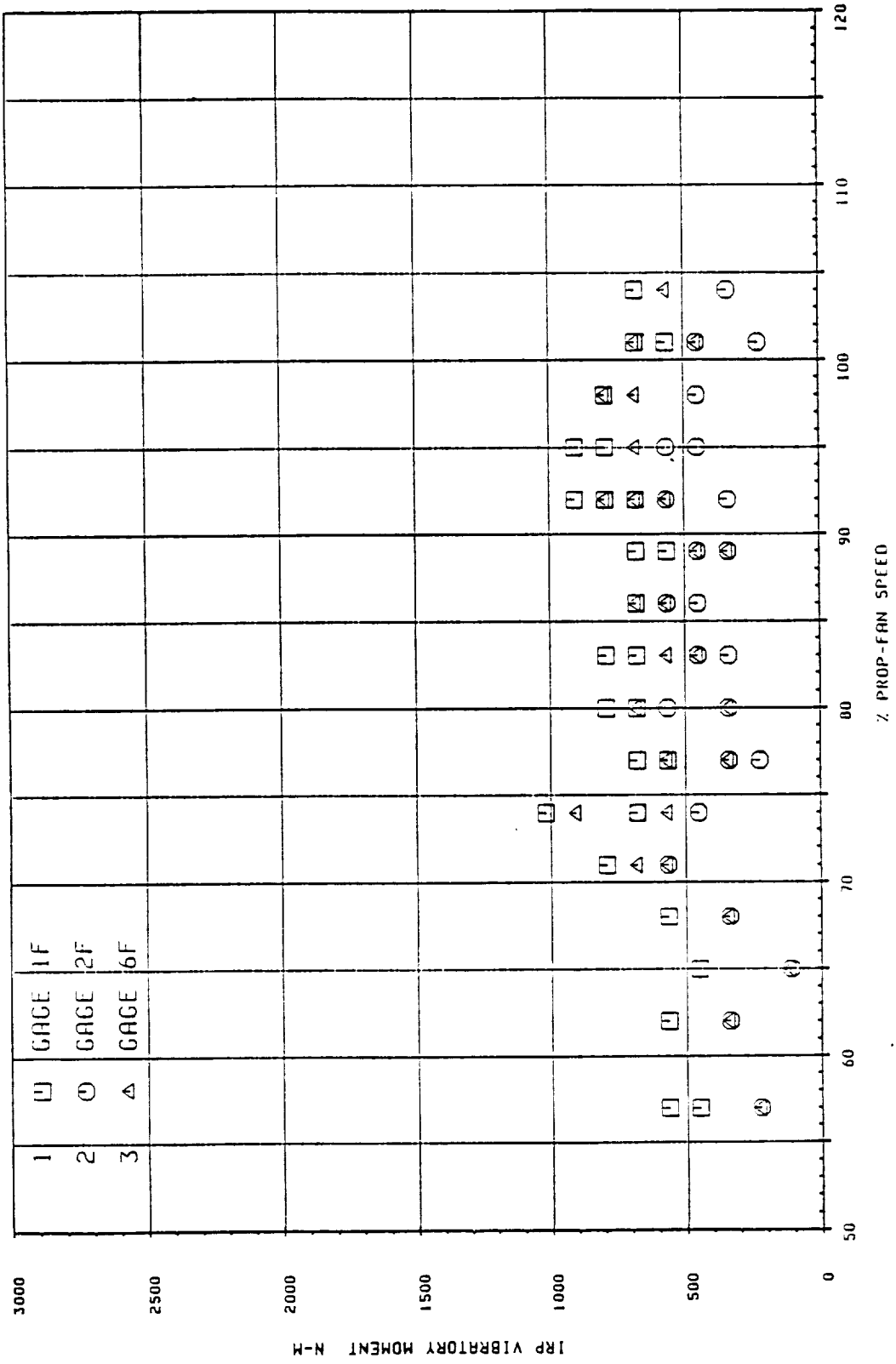


Figure 324. Shank Flatwise Moment During Calm Wind Power Lever Traverse

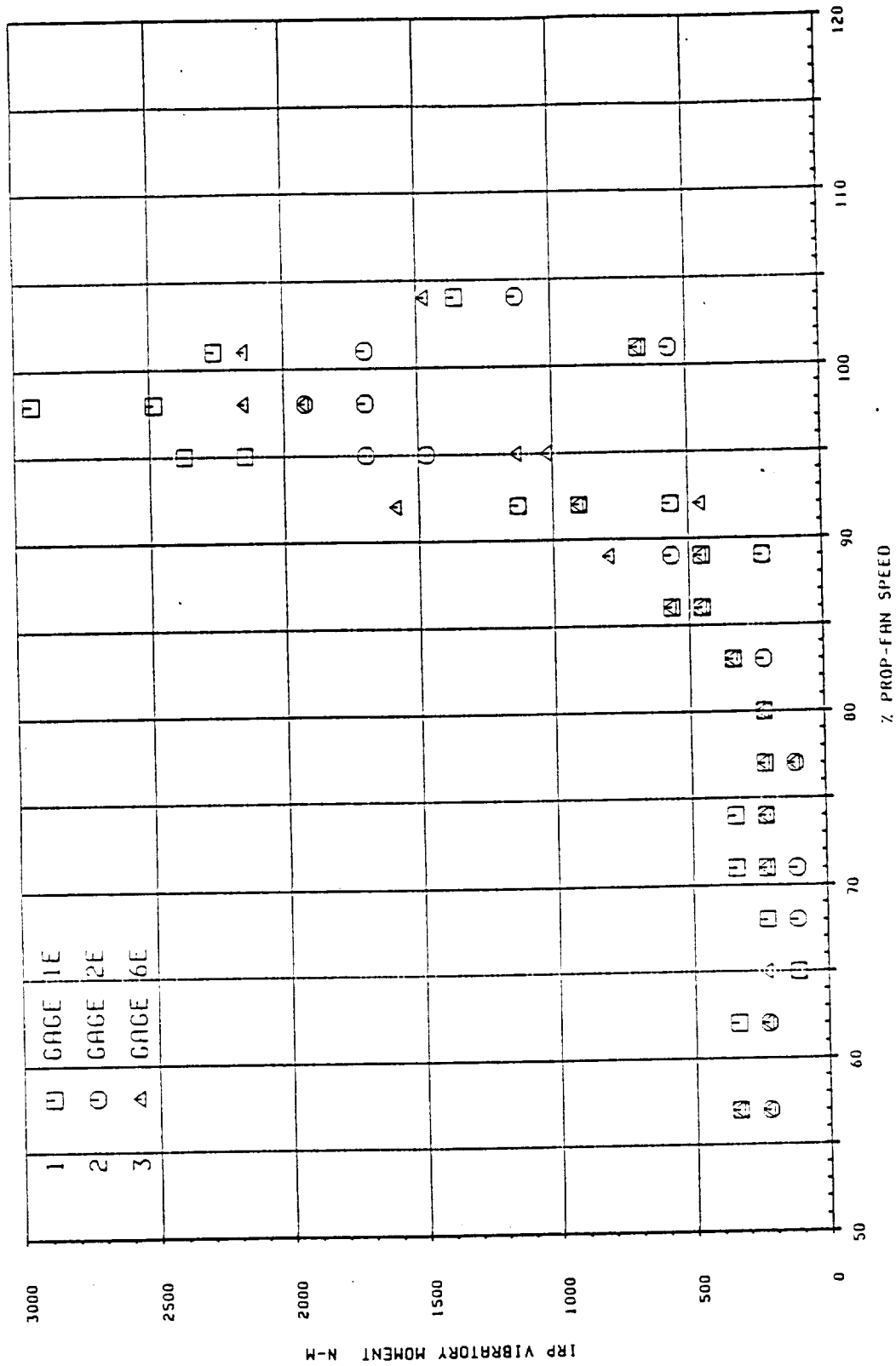


Figure 325. Shank Edgewise Moment During Calm Wind Power Lever Traverse

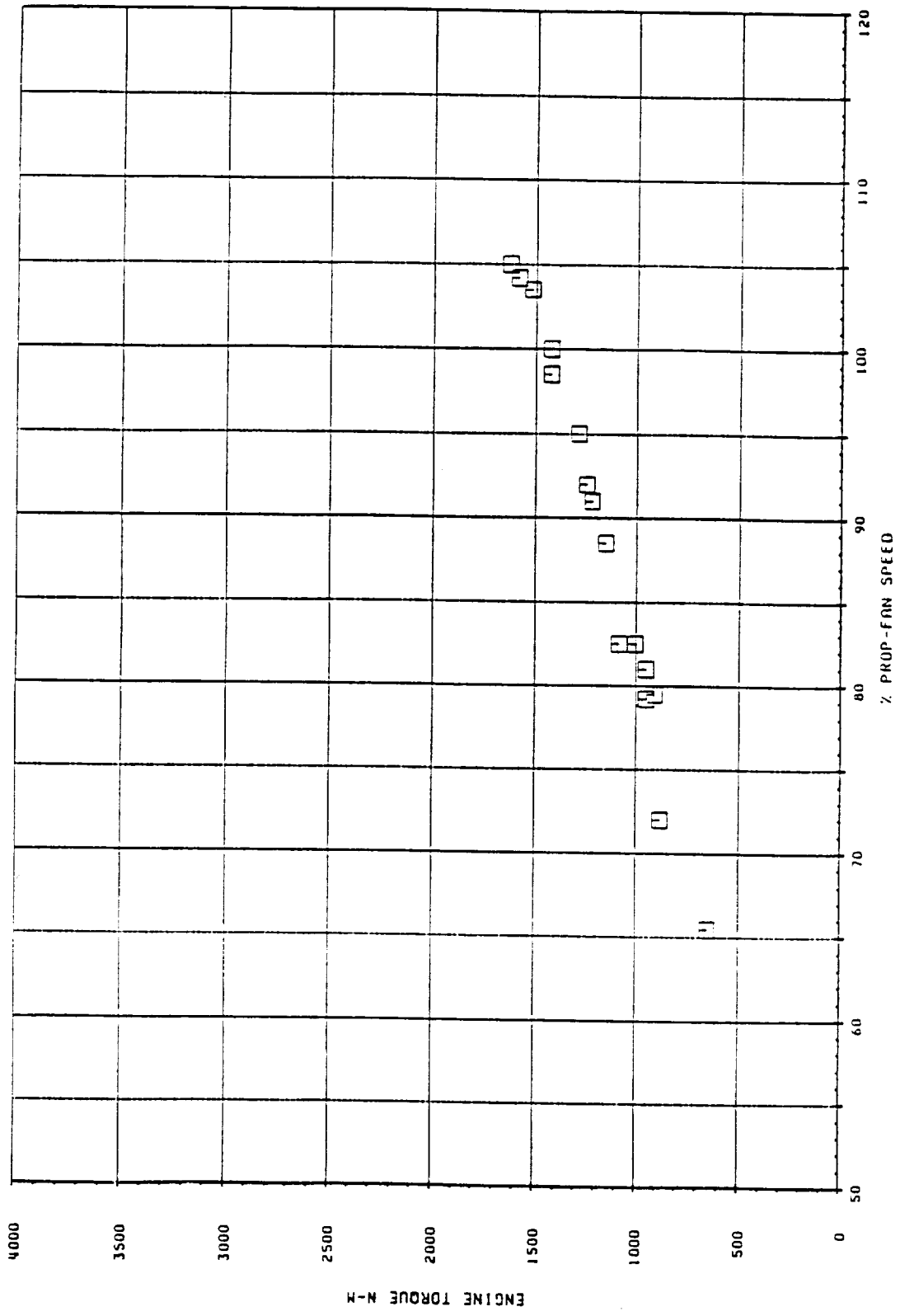


Figure 326. Power Lever Traverse During 225° Crosswind Tests

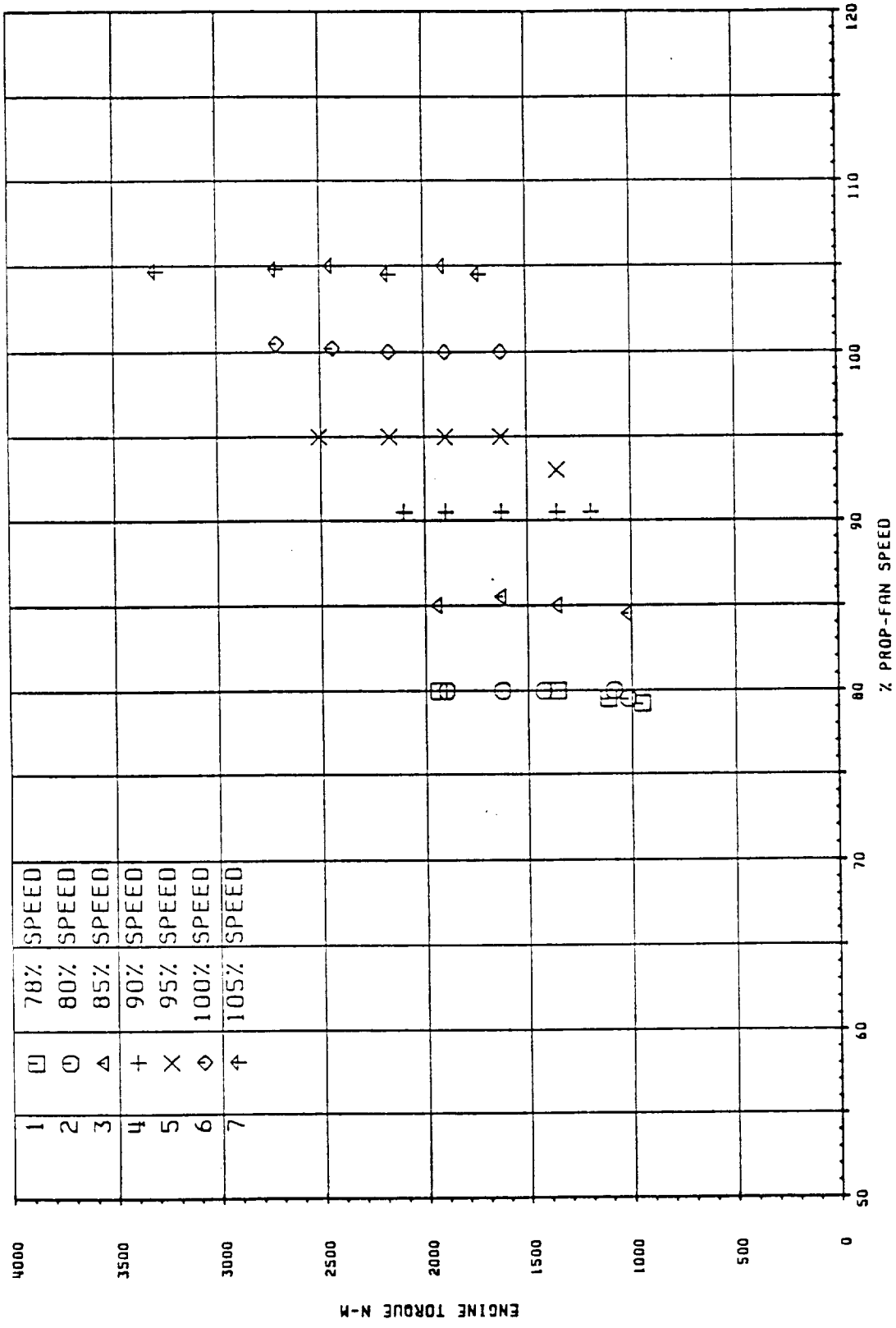


Figure 327. Governing Conditions During 225° Crosswind Tests

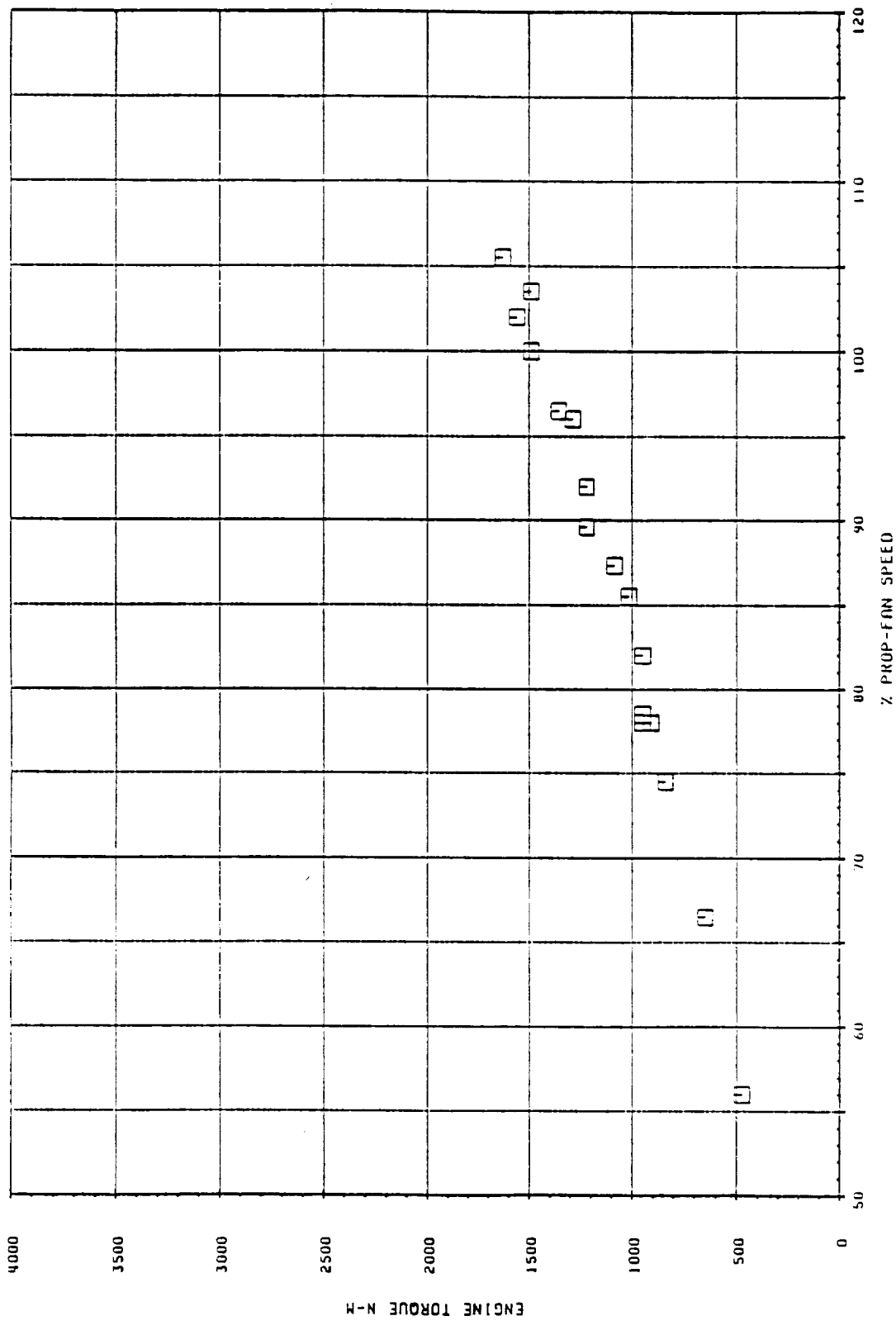


Figure 328. Power Lever Traverse During 270° Crosswind Tests

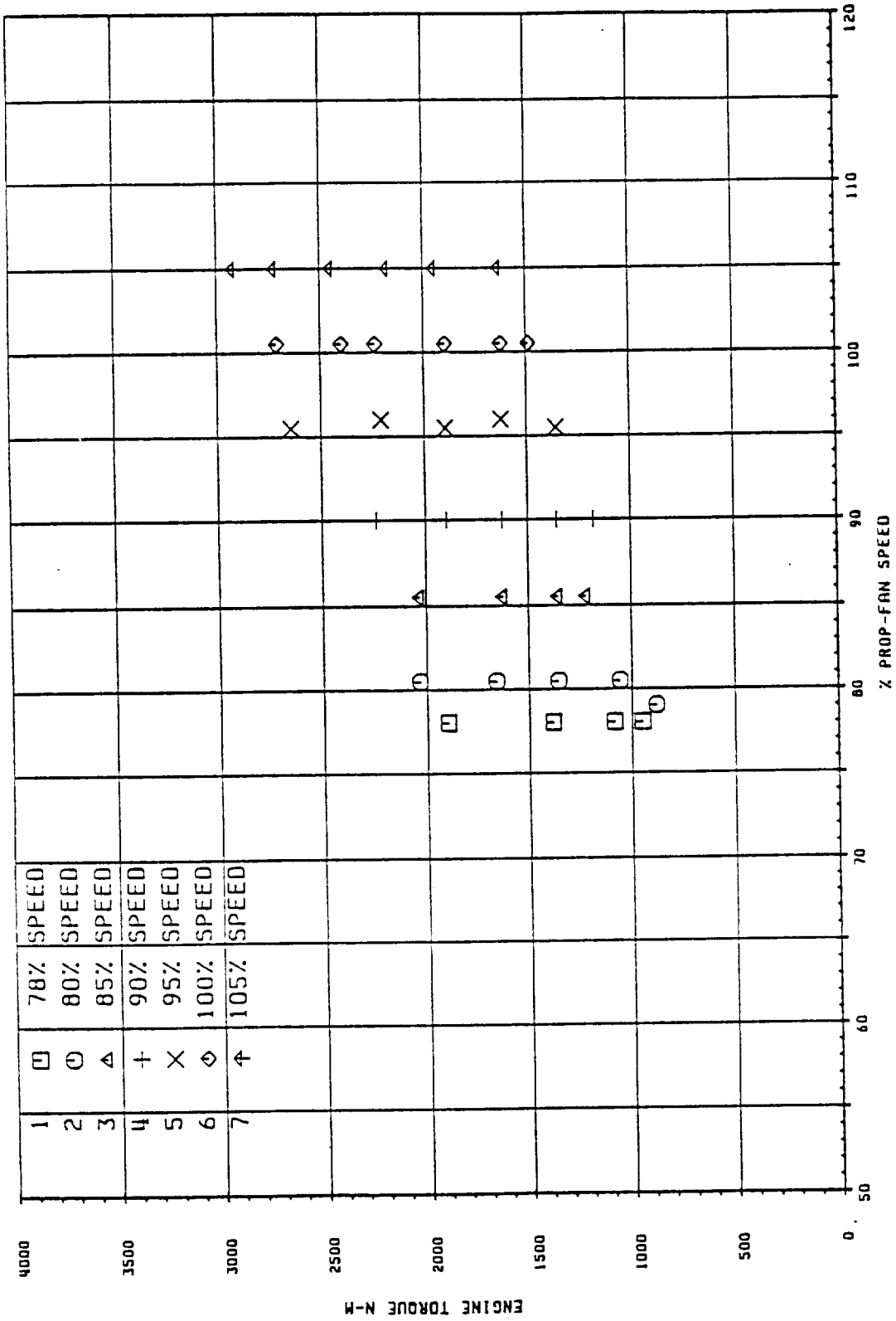


Figure 329. Governing Conditions During 270° Crosswind Tests

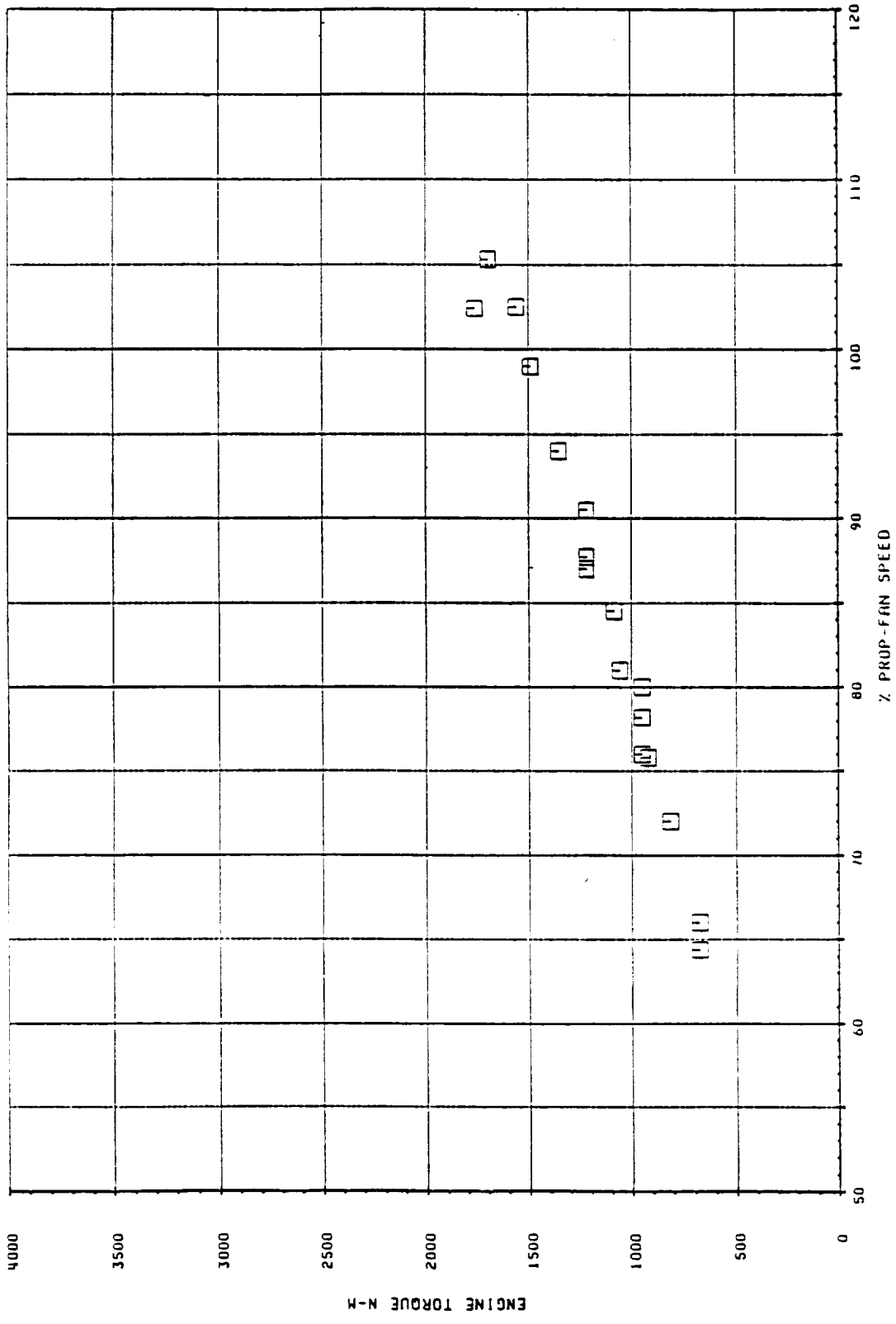


Figure 330. Power Lever Traverse During 135° Crosswind Tests

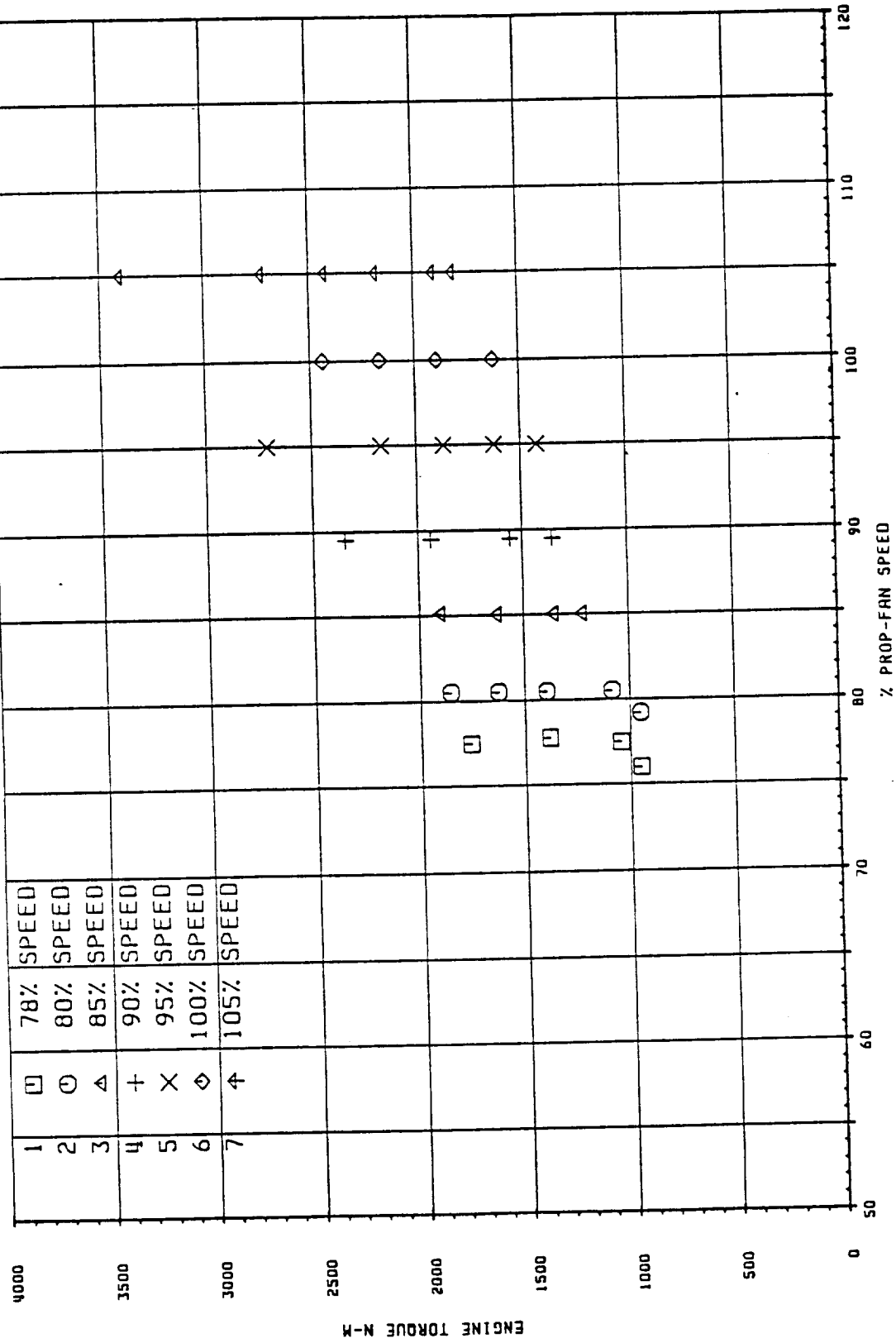


Figure 331. Governing Conditions During 135° Crosswind Tests

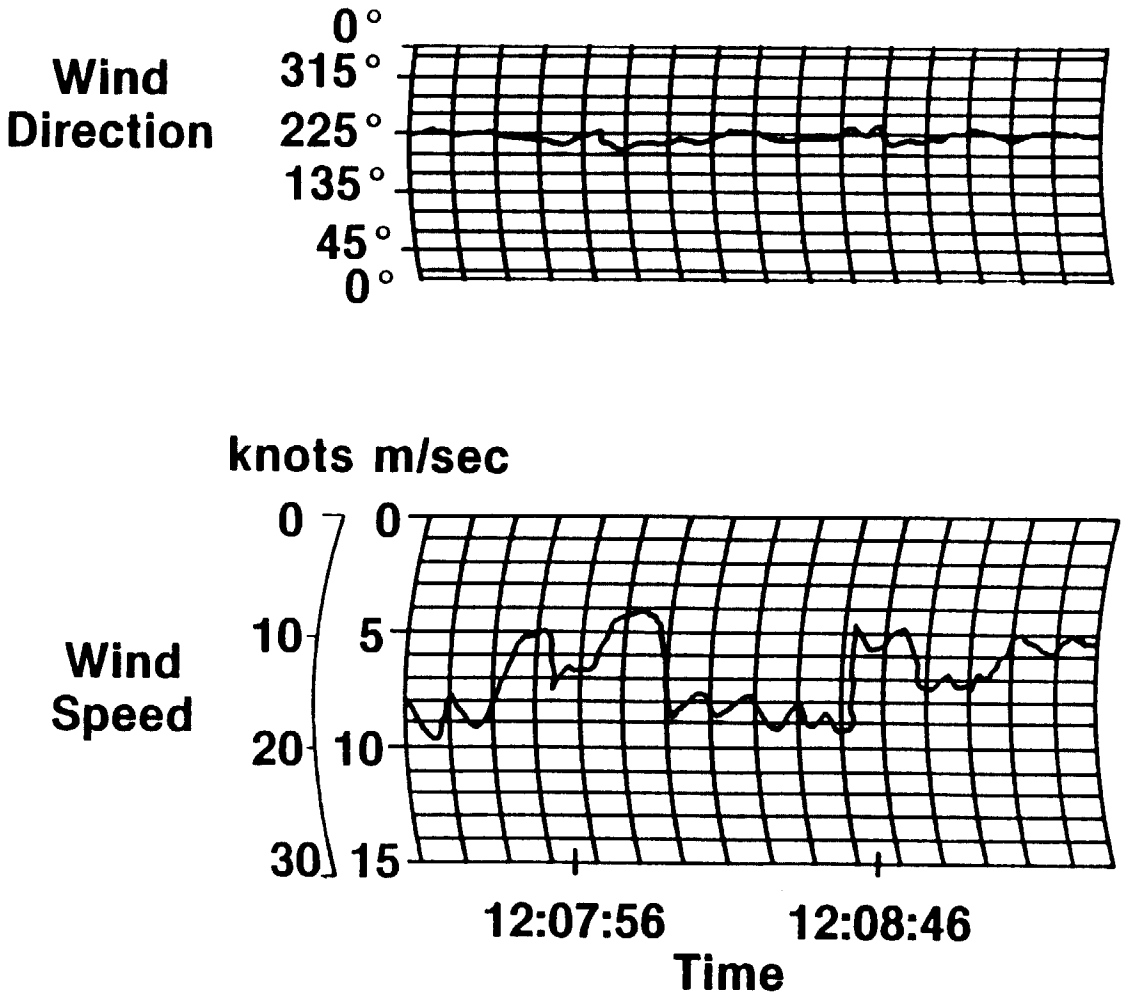


Figure 332. Wind Direction and Speed Recorded During 225° Crosswind Tests

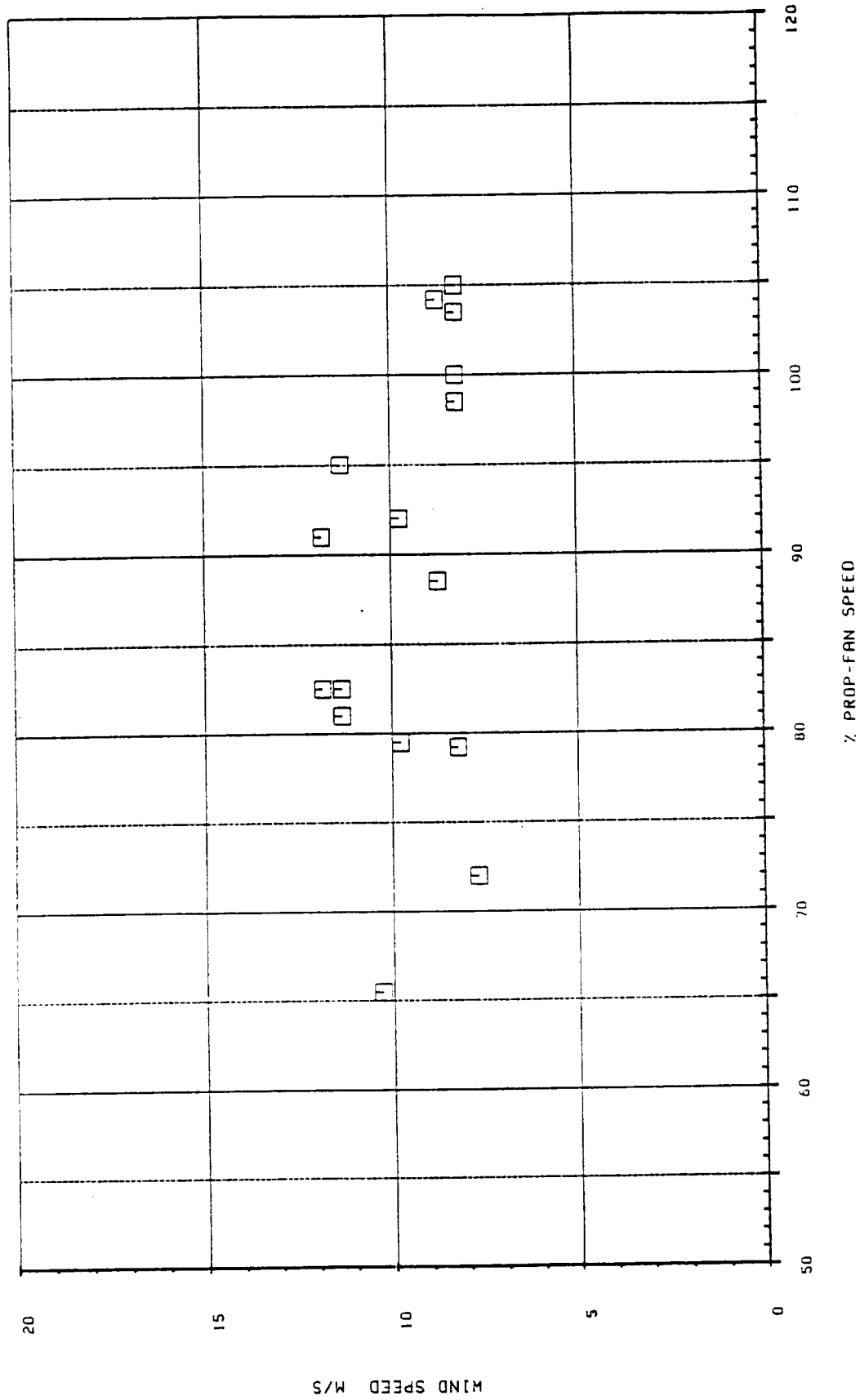


Figure 333. Wind Speed During the 225° Power Lever Traverse

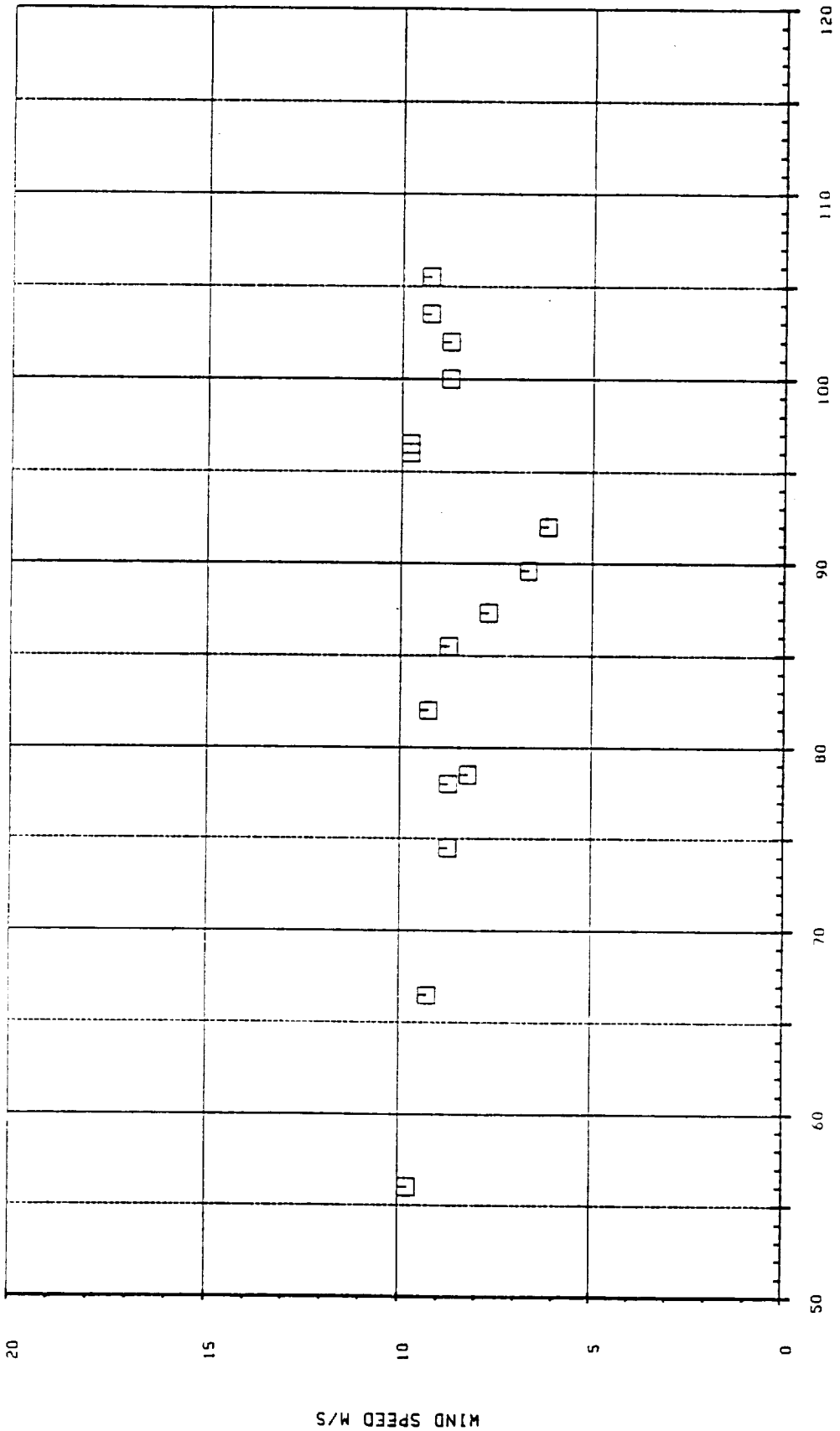


Figure 334. Wind Speed During the 270° Power Lever Traverse

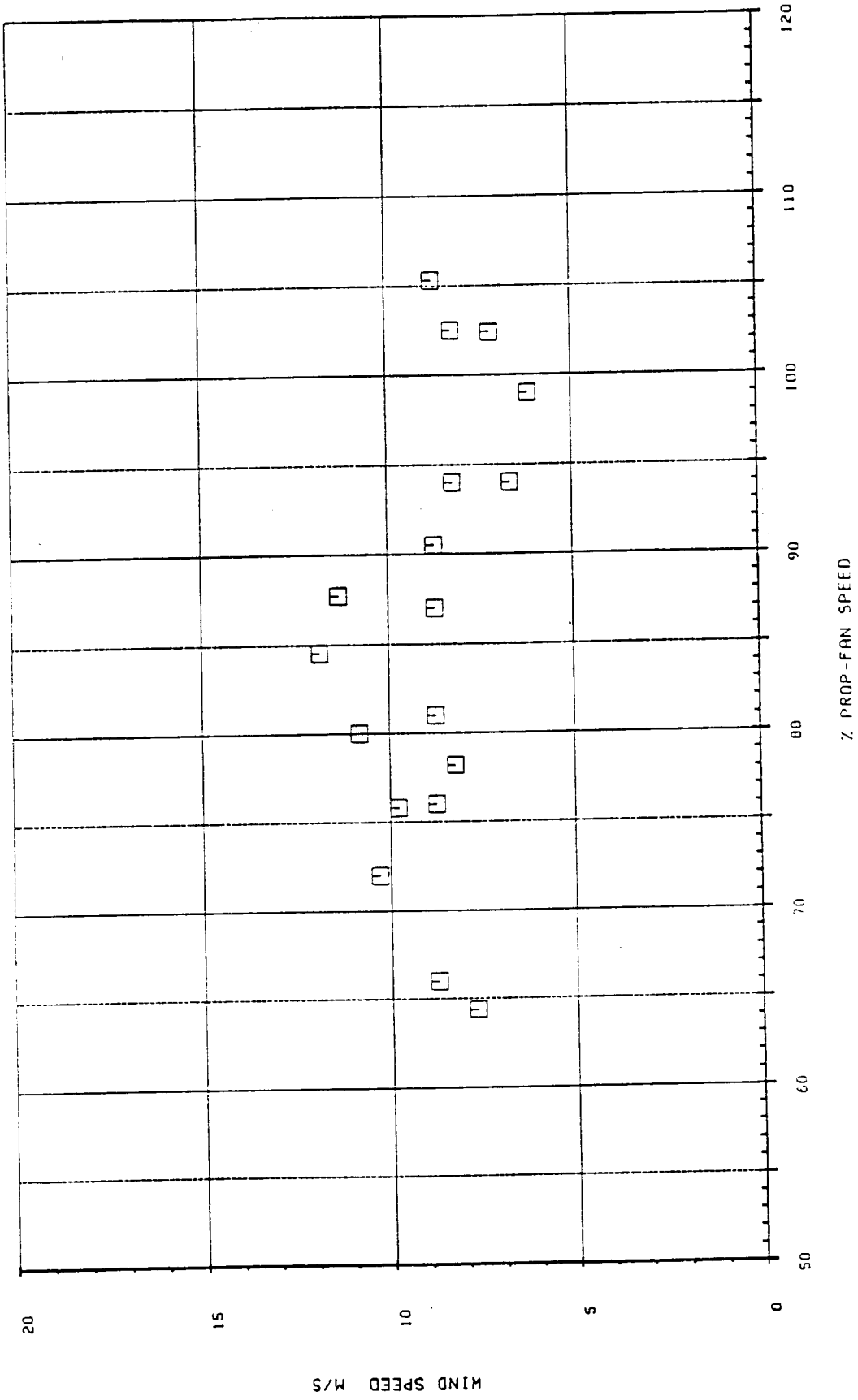


Figure 335. Wind Speed During the 135° Crosswind Power Lever Traverse

A power lever traverse was recorded for each crosswind direction using the same procedure as the calm wind tests. Figure 336 shows the operating torque versus propfan speed for the three crosswind directions at a 20-degree low pitch stop setting. Figure 337 shows a plot of the tip bending (Gage 13) strain versus propfan speed for the three directions with the calm head wind data included. All three crosswind directions had significantly higher amplitudes than the calm head wind data. The 135-degree direction had the highest strain amplitudes in the 64-percent to 87-percent speed range. The highest tip response at 86-percent speed is a result of the 4P/2F flatwise critical speed. At speeds from 88 percent to 105 percent, the 225- and 270-degree positions had the dominant amplitudes.

Figure 338 shows a comparison of the crosswind data with the calm head wind data for the 2E shank moment gage location. The crosswind data had higher amplitudes when compared to the calm head wind result, but differences were not as large as the tip bending results discussed previously. At propfan speeds below 95 percent, all moment levels remained at moderate levels. At speeds between 95 and 105 percent, the moments were high because of the response of the edgewise gage to the 3P/1E critical speed at 100-percent speed.

Figure 339 compares the 2F shank moment gage location crosswind to the calm head wind power lever traverse data. There is a large increase in flatwise moment amplitude at speeds below 90 percent. This is from the response of the 2F shank gage location to the 2P/1F critical speed which occurs at 77-percent propfan speed and the 4P/2F critical speed at 86-percent propfan speed. The 135-degree direction had higher amplitudes in this range compared to the 225- and 270-degree directions. This was also observed in Figure 337 where the 135-degree direction had the greatest tip strain amplitude at speeds below 87 percent.

Figures 340, 341, and 342 contain IRP strain data for the tip bending gage (Gage 13) versus blade angle for the 225-degree, 270-degree, and 135-degree directions, respectively. As was the case for the calm head wind static governing tests, the tip bending gages had the highest response of any location on the blade. Because the low pitch stop was set at approximately 20 degrees, there is no blade angle data below that setting. Comparing these plots to the calm head wind plot of Figure 315, there is more scatter in the data and the strain amplitude is higher for all three crosswind directions in the 20-degree to 25-degree blade angle range. Crosswind data points that were above 30-degree blade angle had strain levels that were equivalent to the calm head wind data at similar conditions. The 135-degree wind direction produced the highest strain levels at blade angles less than 25 degrees.

Taxi Tests - The taxi tests consisted of a high-speed feather run and two buffet boundary exploration runs. The high-speed feather test showed no prop rotation during the taxi run indicating that the feather angle was correct to prevent rotation during feathered flight.

As illustrated in Figure 343, the buffet boundary exploration showed that increasing taxi speed improved the blade buffet response to a greater

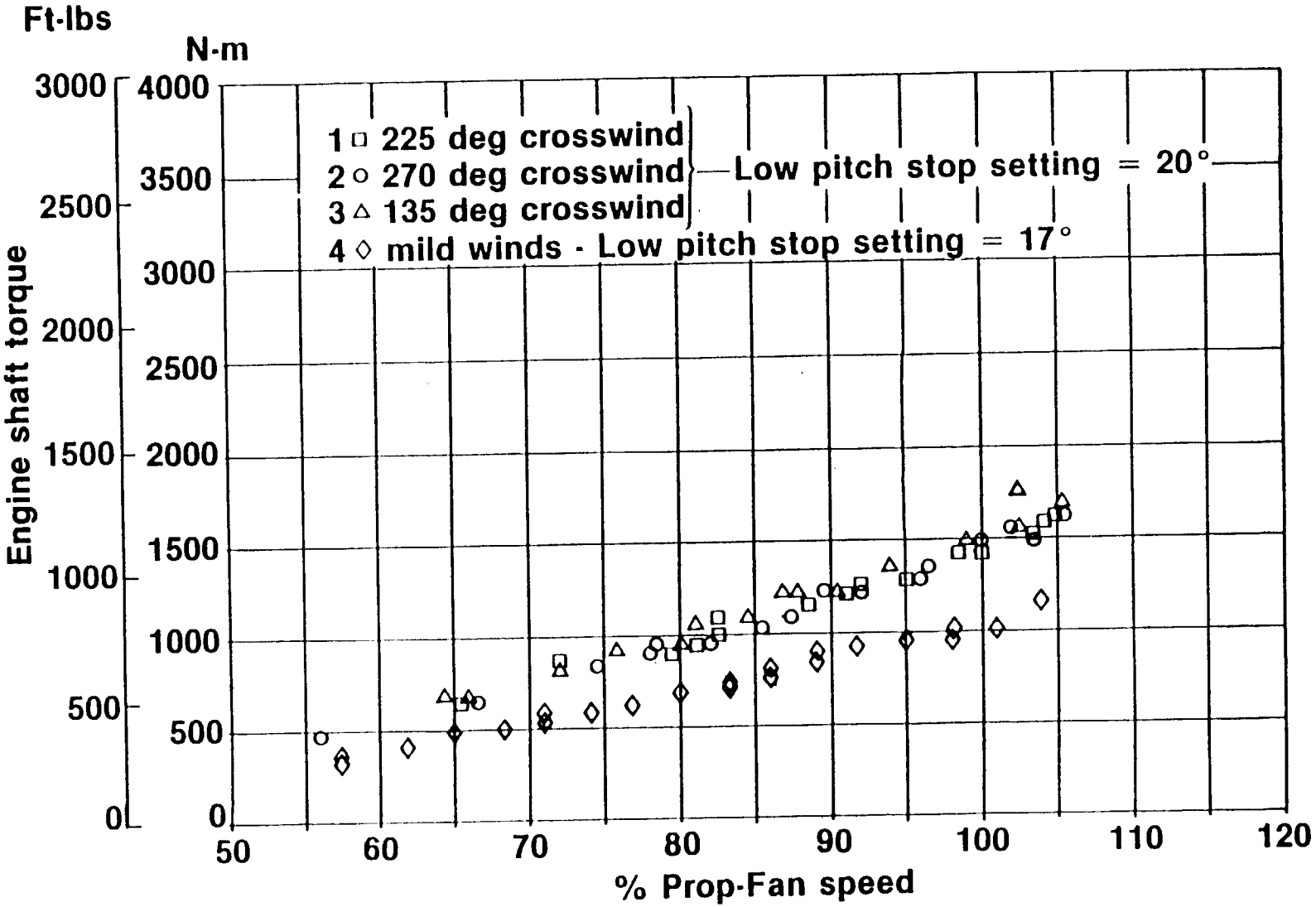


Figure 336. Power Lever Traverse During Crosswind Conditions

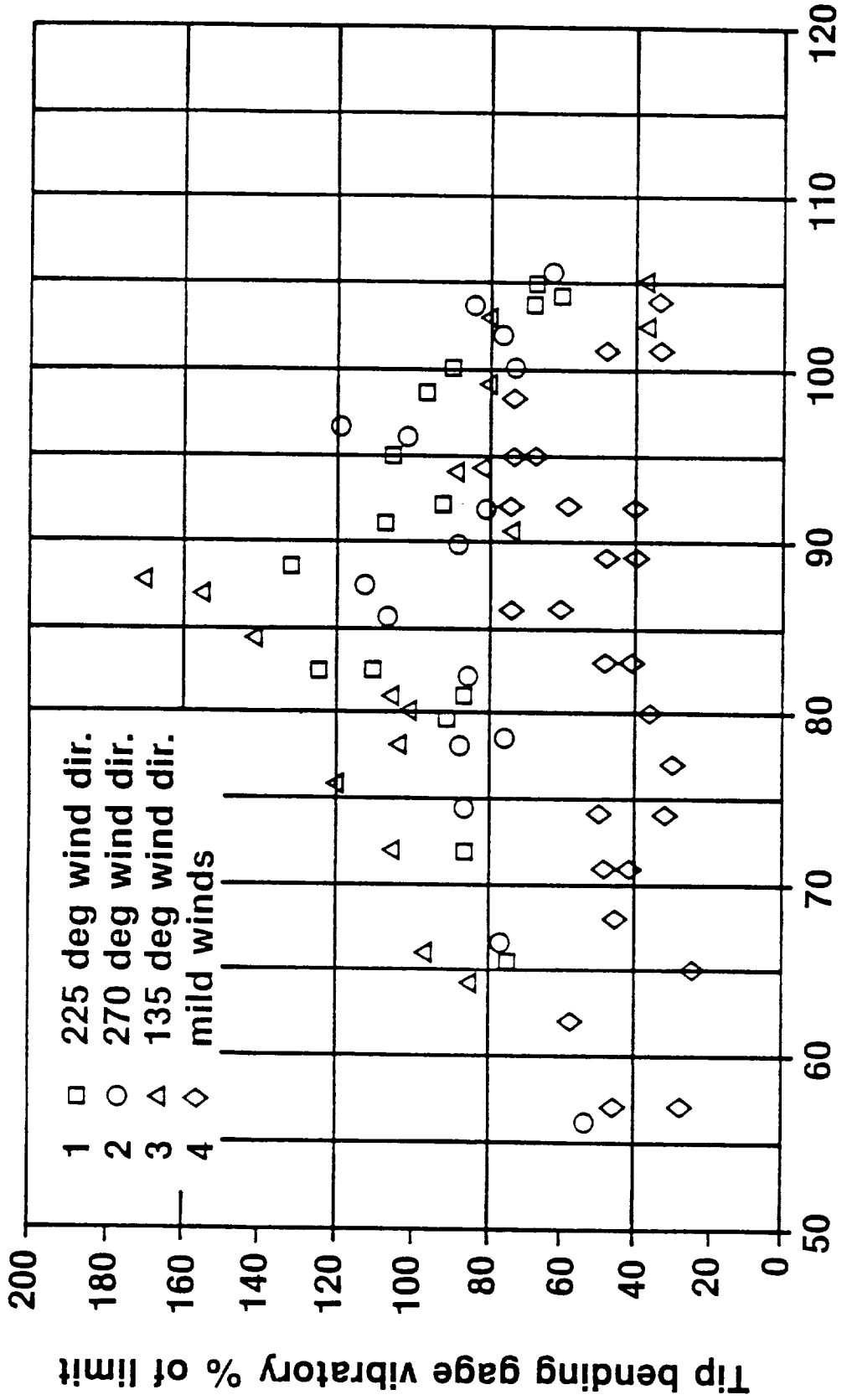


Figure 337. Tip Vibratory Response In a Crosswind Environment

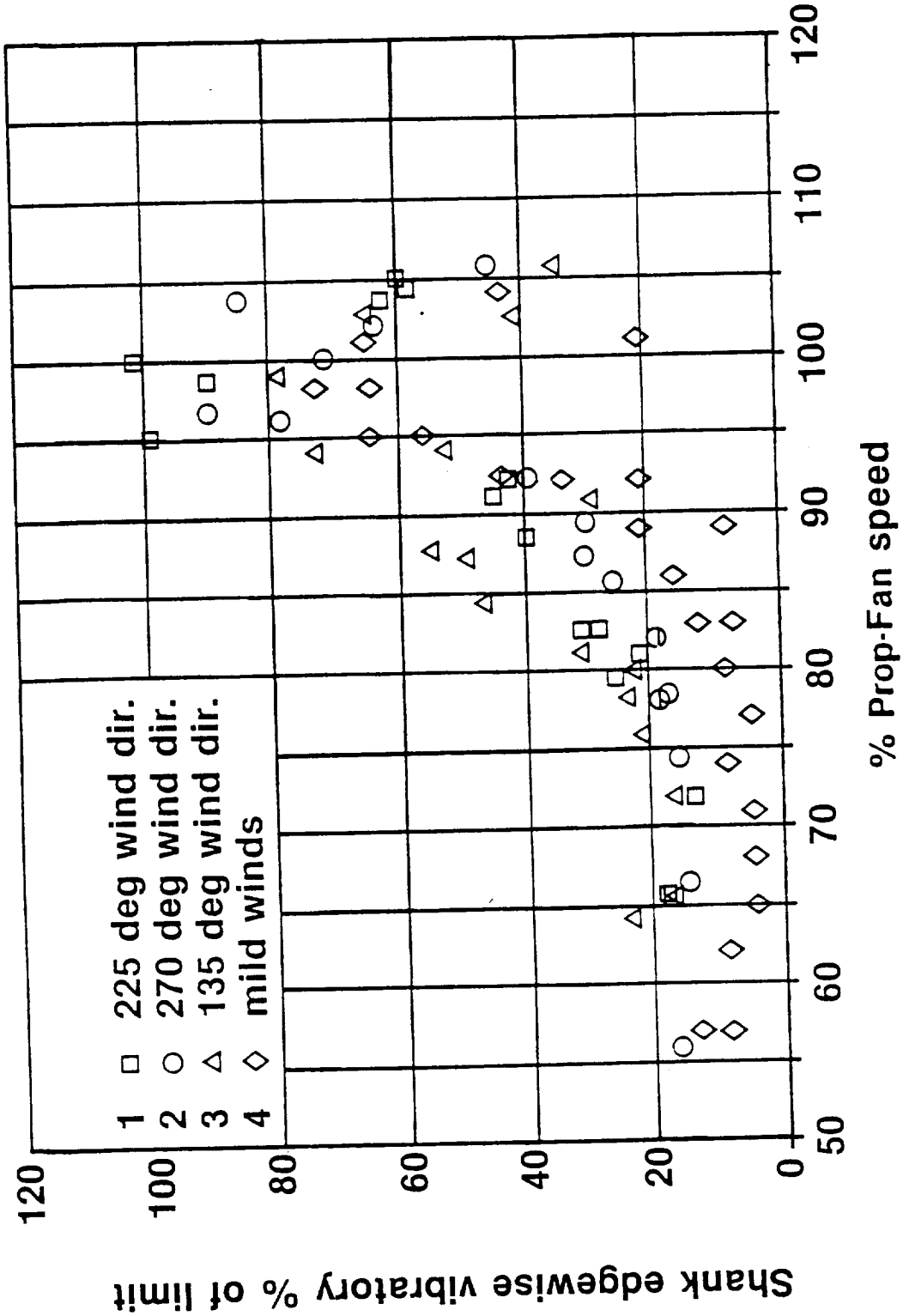


Figure 338. Shank Edgewise Response in a Crosswind Environment

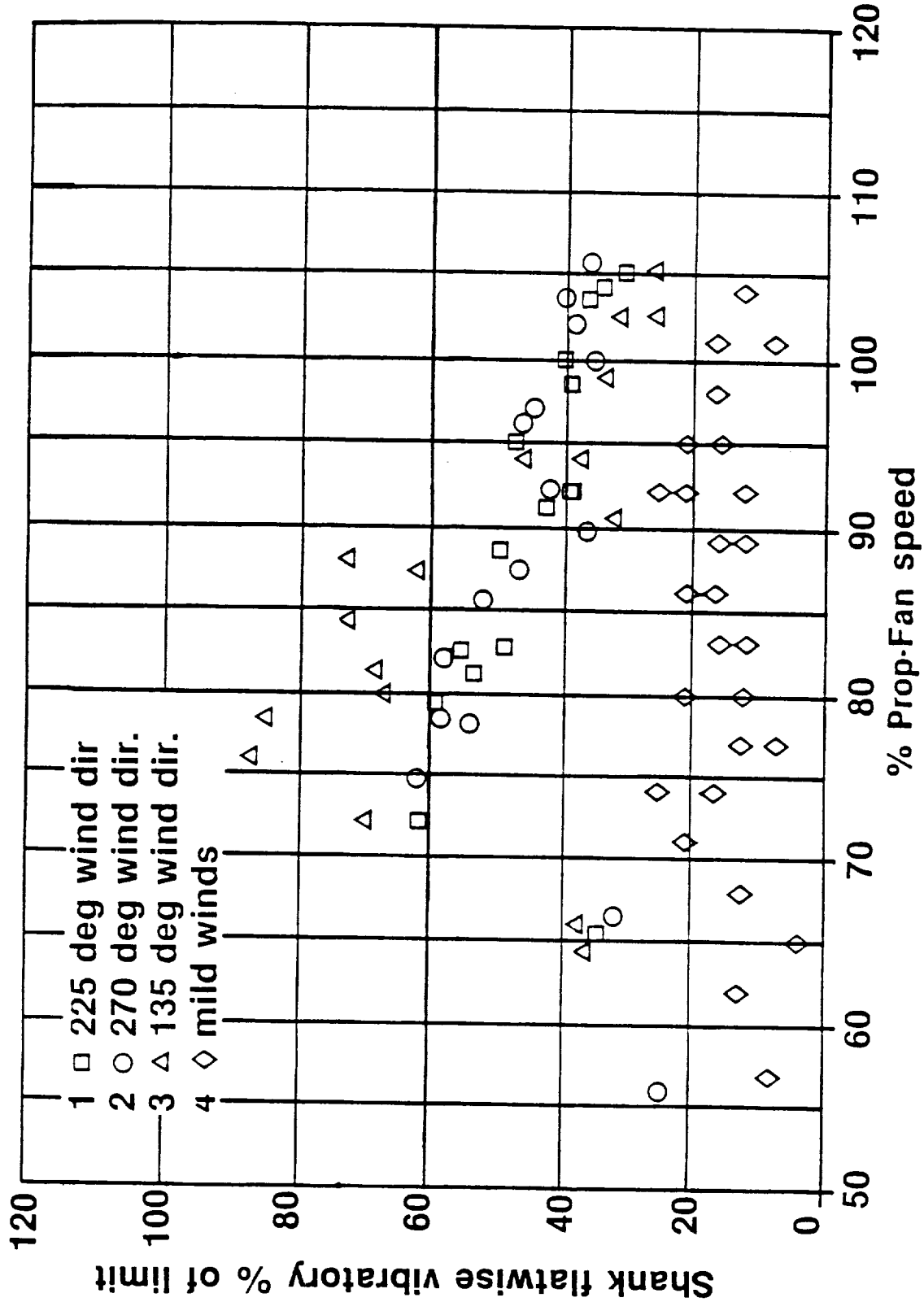


Figure 339. Shank Flatwise Response in a Crosswind Environment

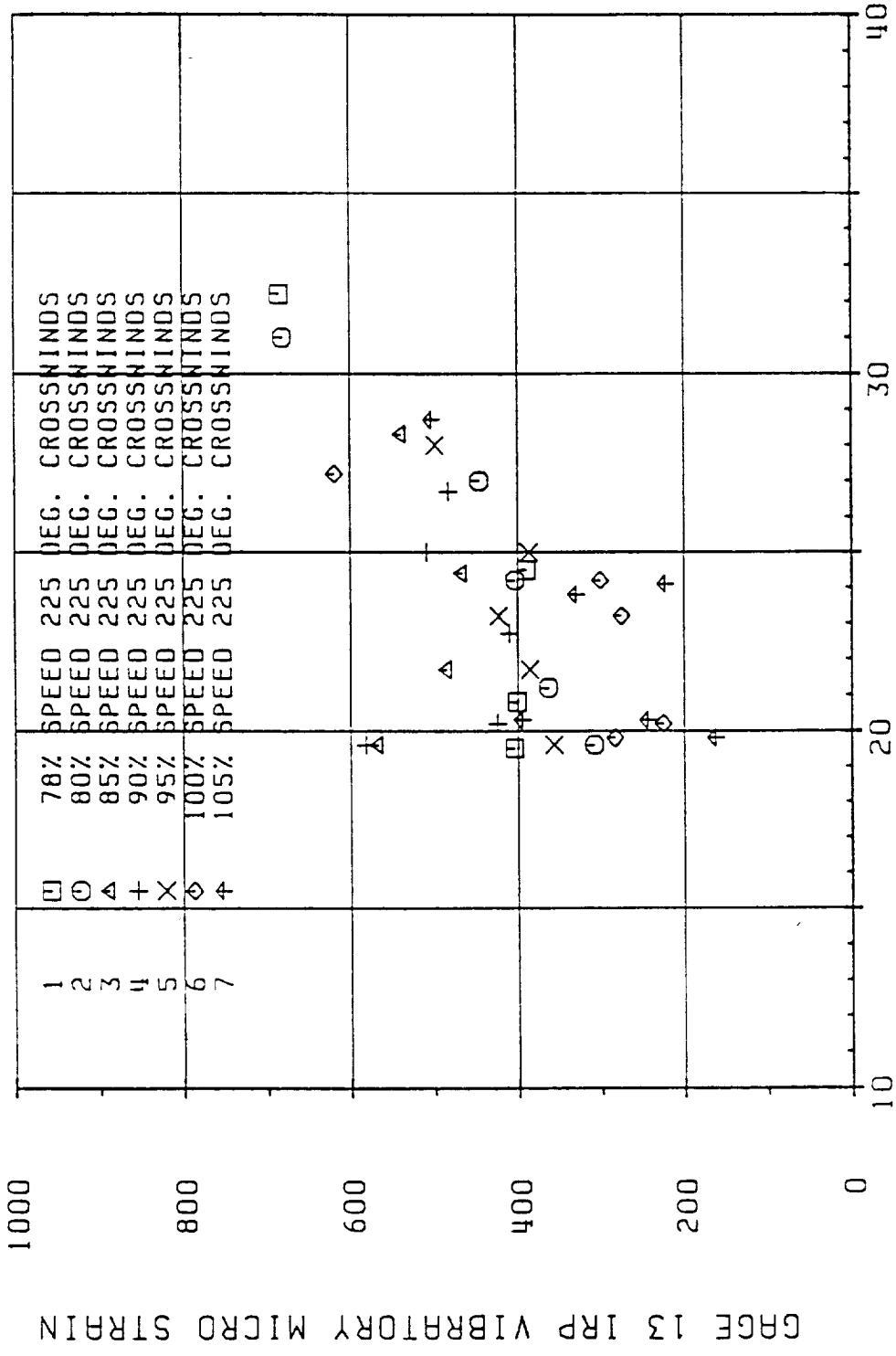


Figure 340. Tip Bending Strain Variation with Blade Angle - 225° Crosswind

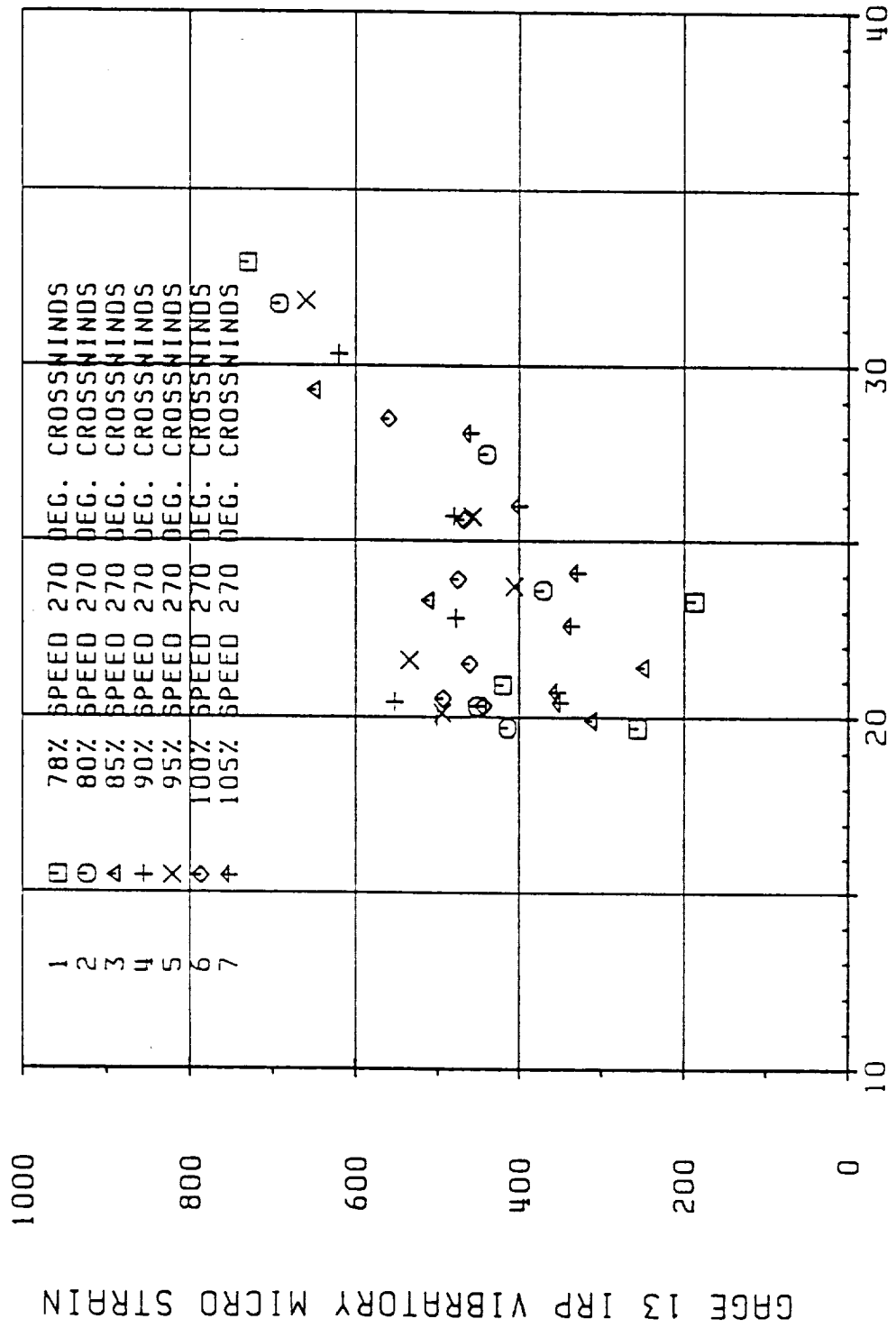


Figure 341. Tip Bending Strain Variation with Blade Angle - 270° Crosswind

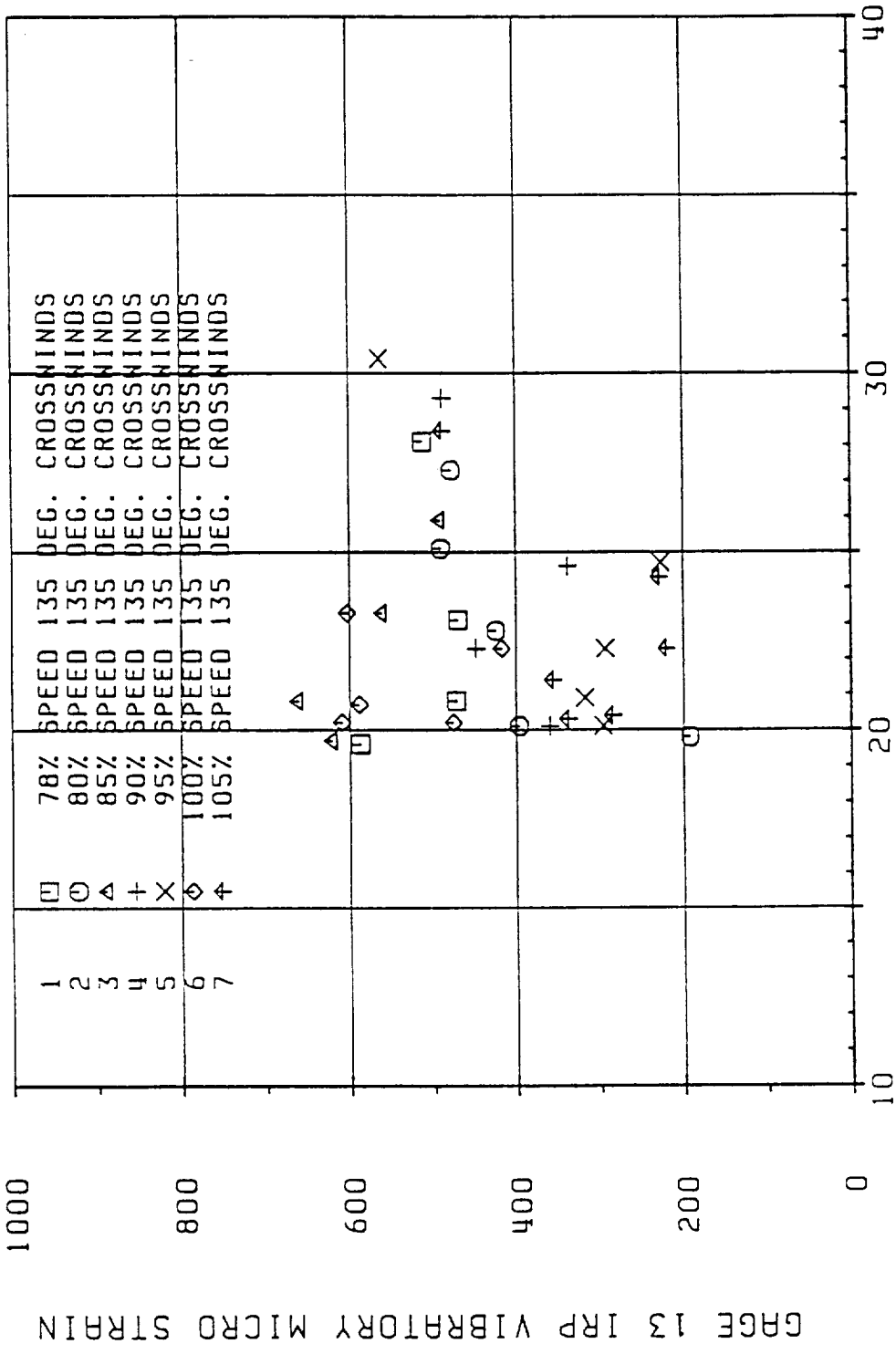


Figure 342. Tip Bending Strain Variation with Blade Angle - 135° Crosswind

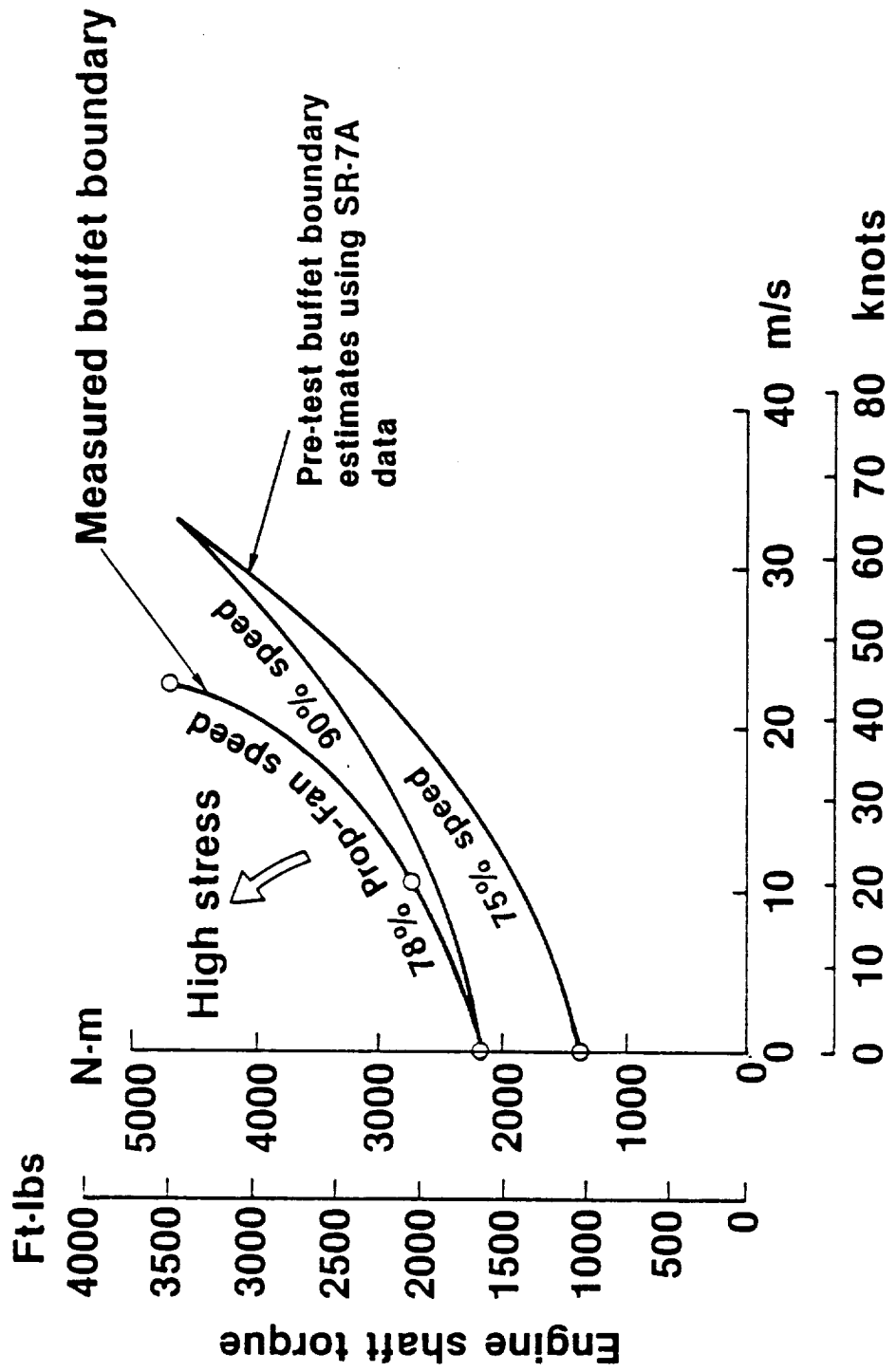


Figure 343. Effect of Taxi Speed on the Buffet Boundary

extent than indicated by SR-7A aeroelastic model tests. However, aircraft handling problems due to asymmetric thrust during these low-speed, high-power taxi tests prevented further exploration of the buffet response.

8.2 FLIGHT CHECKOUT TESTS

8.2.1 Propfan Off

Flight airworthiness tests were conducted on the PTA testbed without the propfan blades installed to evaluate the effects of the PTA modifications on the basic GII characteristics and to clear the operational envelope at speeds up to V_{DF}/M_{DF}.

8.2.1.1 Systems Functional Tests

Following completion of the taxi tests on 5 March 1987, first flight was accomplished on 6 March 1987 at the Gulfstream Aerospace facility in Savannah, Georgia. Systems functional tests were accomplished at speeds up to 123 mps (240 KIAS) and altitudes of 4,572m (15,000 ft) and 7,010m (23,000 ft). All normal systems checks were accomplished including shutdowns and airstarts of each Spey engine. On 13 March 1987 additional systems functional checks were accomplished during the ferry flight from Savannah to Dobbins AFB. All systems operated normally within the allowable speed-altitude range of 129 mps (250 KIAS)/Mach 0.54 and 7,620m (25,000 ft).

8.2.1.2 Flight Flutter Tests

The initial flight flutter tests were conducted with the propfan blades removed to evaluate the effects of the PTA modifications on the basic GII aeroelastic response characteristics and to clear the PTA testbed at speeds up to 186 mps (362 KCAS)/Mach 0.89 (V_{DF}/M_{DF}).

As shown in the table below, seven speed conditions were accomplished at approximately 4,877m (16,000 ft) and six were accomplished at 8,534m (28,000 ft). At each speed condition, aileron, rudder, and elevator control pulses were performed to excite the various structural modes. Accelerometers, strategically placed throughout the aircraft structure, measured aircraft response and provided information for engineers in the telemetry ground station to establish aircraft frequency and damping characteristics. These data showed that the PTA testbed, without the propfan blades installed, was flutter-free throughout the speed/altitude envelope up to V_{DF}/M_{DF}.

FLUTTER TEST CONDITIONS

ALTITUDE METERS (FT)	AIRSPEED MPS (KEAS)	MACH NUMBER M
4,877 (16,000)	129 (250)	0.513
4,877 (16,000)	139 (270)	0.554
4,877 (16,000)	149 (290)	0.596
4,877 (16,000)	159 (310)	0.636
4,877 (16,000)	170 (330)	0.678
4,724 (15,500)	176 (342)	0.695
4,572 (15,000)	182 (353)	0.710
8,534 (28,000)	134 (260)	0.690
8,534 (28,000)	144 (280)	0.738
8,534 (28,000)	154 (300)	0.798
8,534 (28,000)	165 (320)	0.850
8,382 (27,500)	170 (330)	0.865
8,230 (27,000)	176 (342)	0.890

8.2.1.3 Handling Characteristics

Concurrent with the conduct of flight flutter tests, handling characteristics of the PTA testbed were appraised with the propfan blades removed. Following clearance from monitors in the telemetry ground station, at each of the flutter speed conditions, the following handling characteristics tests were accomplished.

- Longitudinal trim
- Directional trim
- Lateral trim
- Dynamic longitudinal stability
- Dynamic lateral-directional stability

Results of the tests showed that the effects of the PTA modifications on the basic GII handling characteristics were negligible in all areas except lateral trim. As predicted from wind tunnel data, the left wing was heavy at speeds below 103 mps (200 KCAS), and the right wing was slightly heavy at higher speeds. This reversed again, however, at Mach numbers higher than about 0.85 due to transonic flow effects.

8.2.1.4 Test Airspeed System Calibration

The test airspeed system was calibrated, concurrent with the initial flight flutter tests, using a NASA-owned T-38 chase airplane as a reference. Tests were conducted at 4,877m (16,000 ft) for airspeeds ranging

from 129 mps (250 KIAS) to 180 mps (350 KIAS) and at 8,534m (28,000 ft) for airspeeds up to Mach 0.79. Prior to each test flight, ground block records were obtained on the PTA and chase aircraft to determine any initial altimeter differences which must be accounted for in the reduction of the test results.

Results of the calibration tests are presented in Figure 344 in the form of a pressure coefficient correction ($\Delta p/q$) versus indicated Mach number. The broken line represents the predicted position error correction based on data obtained by Gulfstream on their GIV flight test airplane with a similar nose boom configuration. These data were used in the conduct of all subsequent test flights and were also used in the reduction of flight test results.

8.2.2 Flight Airworthiness - With Propfan Blades

Flight checkout tests were conducted on the PTA testbed with the propfan blades installed to clear the flight envelope at speeds up to 186 mps (362 KCAS)/Mach 0.89 (V_{DF}/M_{DF}). The tests consisted of a functional checkout of the propfan propulsion system, flight flutter clearance, airplane handling characteristics, and structural integrity of the LAP.

8.2.2.1 Propfan Propulsion System Functional Checkout

Ground Tests - The entire propfan propulsion system was thoroughly checked-out on the ground prior to flight tests. The objective of these ground tests was to functionally check all systems associated with the propfan propulsion system operation. Tests included:

- The satisfactory performance of the starter and associated electronic controls
- Verifications of the ability of the propfan and drive system control system to govern or maintain constant speed steady state power conditions
- Verification of satisfactory transient response characteristics
- Functional checkout of the instrumentation, recording, monitoring, and display systems

In preparation for these tests, the PTA engine underwent a dry-motor water wash to clean the preserving oil from the compressor and turbine prior to the initial wet motor of the engine. The wet motor check was then conducted, verifying the integrity of the oil and fuel system plumbing. After the wet motor check had been completed, the engine was started and run at idle; the following shutdowns were accomplished:

- Normal
- Manual fuel
- Mechanical fire handle
- Fire T-handle
- Simulated overspeed

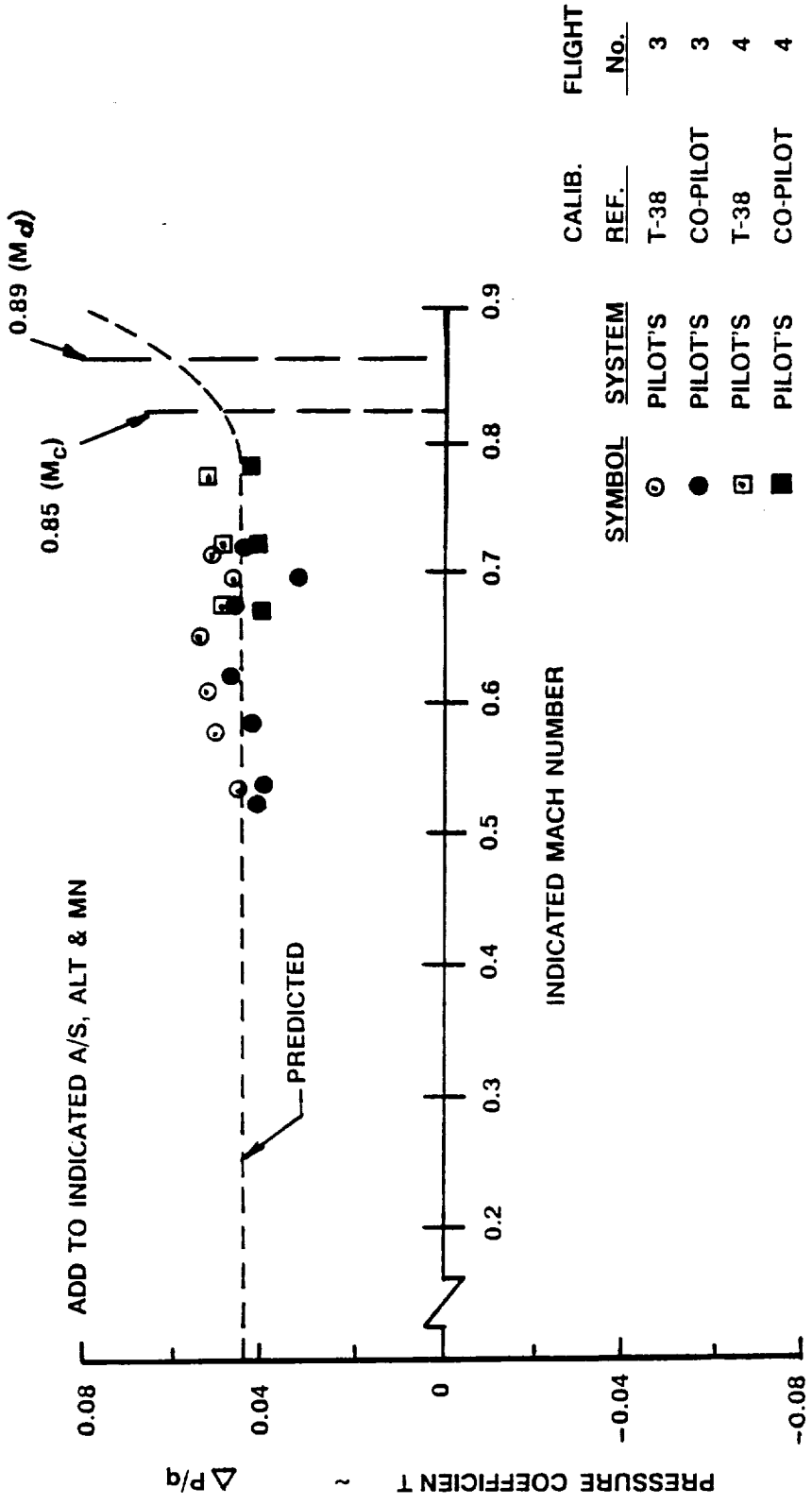


Figure 344. Nose Boom Position Error Correction

During the initial checkout, all systems functioned as intended. Minor problems discovered in the Brown Field tests were shown to have been corrected.

Starting - Satisfactory starting was accomplished utilizing the Spey engines as the pneumatic bleed source.

Propfan Balance - The propfan was installed on the propulsion system in the same configuration, including balance weights, that existed for the Brown Field tests. After the initial balance run, it was determined that no additional propfan balancing was required.

Low Power Governing Check - The low power governing check indicated that the propfan governor and blade low pitch stop required adjustment. The low pitch stop was adjusted to 20 degrees, and the governor was adjusted in order to reach 105 percent N_p. Both were verified on subsequent runs.

Transient Response - Both rapid and slow throttle and prop speed control lever inputs were made. Slow movement of both the throttle lever and prop control lever produced, as expected, a benign system response. The prop speed lever 2-second traverse, which was the maximum input rate capability of the electromechanical actuator, resulted in approximately a 3-percent N_p overshoot, but quickly stabilized. A rapid throttle input of about 1 second resulted in approximately the maximum torque rate change of 2 to 3 seconds permitted by the electronic engine control. The maximum overspeed observed was 8-percent N_p. The system functioned essentially as it had during the Brown Field tests.

Test Results Summary - The PTA propulsion system functioned normally during the checkout tests. Propfan blade stress remained within limits up to a maximum power of 3855 kw (5170 shp).

During transient testing, a power turbine overshoot of 8 percent was experienced which occurred using a step increase in power lever. This was not, however, considered to be a significant problem. The transient response to prop control lever was excellent. In general, transient response testing verified stable, predictable response of the engine power and propfan speed control.

Fluid cooling, both propfan hydraulic fluid and engine oil, were satisfactory. Nacelle cooling and ventilation were satisfactory.

All systems functioned in the same manner as experienced at Rohr during static testing, with much better performance from the propfan electromechanical actuator and linearity of the power lever potentiometer. Installed power estimates showed that sufficient power was available to provide the required disk loading of 257 kw/m^2 (32 shp/D_p^2) at 10,668m (35,000 ft), Mach 0.8.

8.2.2.2 Envelope Clearance Flights

The PTA propfan propulsion system was started in flight for the first time at an airspeed of 103 mps (200 KIAS) and at a pressure altitude of 1646m

(5400 ft). The start was normal, and the maximum measured gas temperature (MGT) was 520°C (968°F). After the engine stabilized at 80 percent Ng, it was shut down to verify proper systems operations and cockpit procedures. The shut-down was normal including propfan feather operation.

The engine was restarted at the same flight conditions, and all engine parameters indicated normal operation. However, during climb through 3,048m (10,000 ft), while propfan governing checks were being accomplished, the PTA fire warning system activated. The PTA propulsion system was immediately shut down using the fire handle. All emergency shutdown systems functioned properly. No smoke or fire was observed by the chase plane, and the fire warning light went out.

Analyses of aft nacelle temperature data indicated that the aft compartment temperatures had exceeded the set point limit of the fire detector system (approximately 430°C (806°F). Examination of additional data showed that, while there was no fire, temperatures in the compartment had reached values higher than allowable. Post-flight visual inspection also revealed evidence of soot around the inlet of the cooling air scoop for the aft nacelle compartment implying a back flow through the air scoops.

Since this problem only occurred in the high Mach number part of the flight test envelope, the decision was made to continue flight tests at the lower Mach numbers with careful monitoring of temperatures while various "fixes" for the overheat problem were tried. Ram air scoops were added to the flush inlets of the aft nacelle, but this did not completely eliminate the problem.

After several flights, it was determined that the problem stemmed from the tendency of hot gasses from the engine exhaust to "puddle" in separated flow regions around the nacelle base and thence find their way back into the aft nacelle compartment. This puddling resulted because, in the initial design of the propfan propulsion system, the decision was made to size the engine tailpipe area for near-maximum shaft power. Thus the jet exhaust had little axial momentum to carry the hot gasses completely away from the nacelle base. Following a strategy of evaluating "fixes" of progressive complexity, a barrier to the hot gas backflow was introduced by attaching sheet metal sections to the nacelle base to reduce the annular area around the tailpipe. This was helpful but did not completely solve the overheat problem. An effective fix was ultimately developed by fabricating a short extension to the tailpipe (shown in Figure 345). The extended tailpipe was used in subsequent high Mach number flights, and nacelle compartment temperatures stayed well within the allowable range. The engine oil cooling system functioned as expected with the system automatically maintaining the oil temperature within the desired operating range of 75°C to 85°C (167°F to 185°F). The propfan fluid cooling system, although fuel flow dependent, maintained the fluid well within the 85°C (185°F) continuous operating temperature limit.

8.2.2.3 Flight Flutter

Flight flutter tests with the propfan propulsion system operating were conducted using the same test procedures and at the same flight conditions

ORIGINAL PAGE
BLACK AND WHITE PHOTOGRAPH

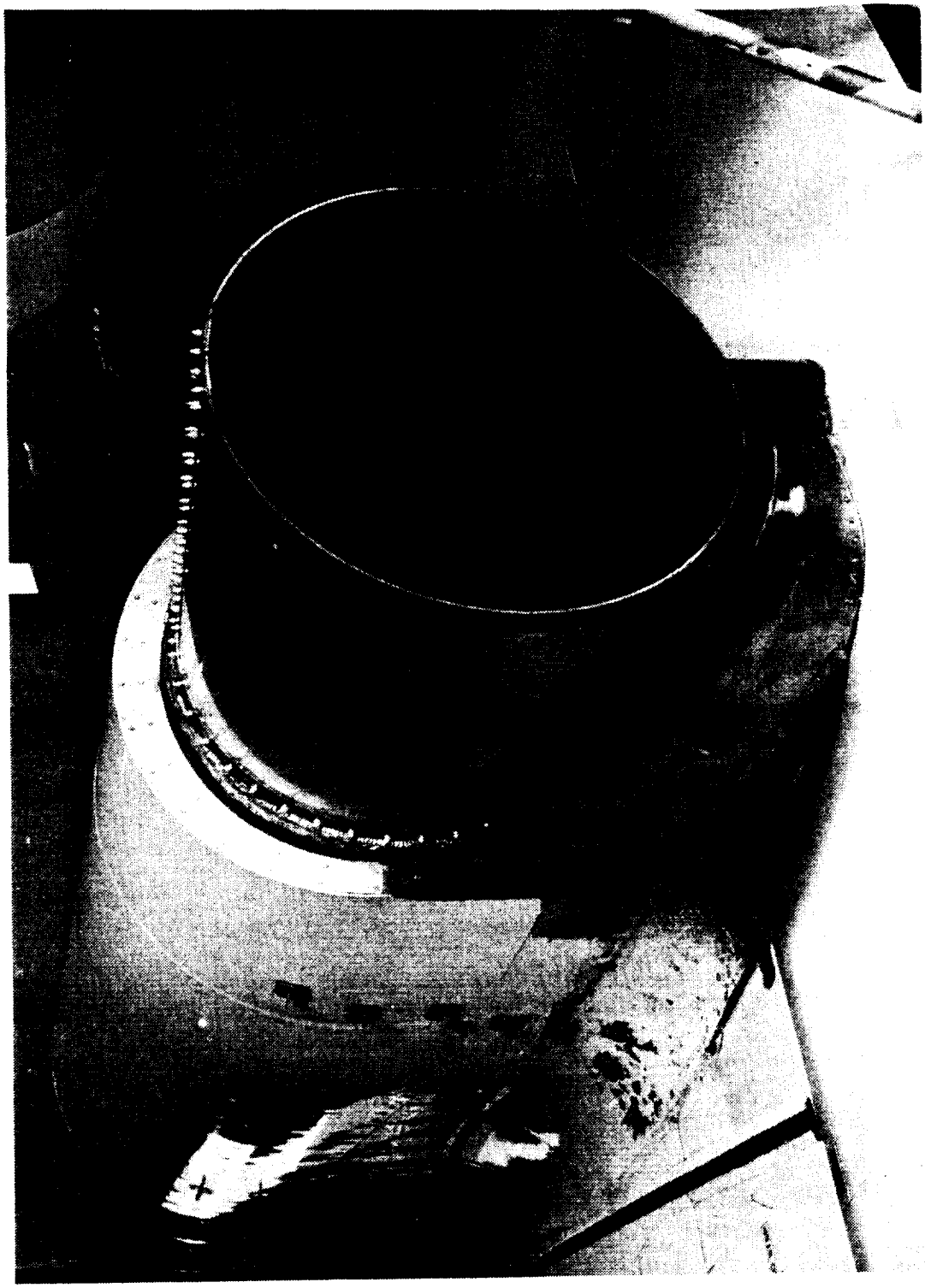


Figure 345. Engine Tailpipe Extension

as the blades-off flutter tests (Section 8.2.1.2). For these tests, the propfan was operated at 100 percent N_p and Maximum Continuous power. The tests were accomplished without incident throughout the speed range from 129 mps (250 KCAS) up to V_{DF}/M_{DF}. The fuel load was maintained between 3,628 kg and 5,897 kg (8,000 and 13,000 lb) which was the most critical from a structural damping standpoint.

Accelerometer transducer outputs were monitored in the telemetry ground station by flutter engineers. Each speed point was analyzed prior to granting approval to proceed to the next higher speed.

Results of the tests showed that the PTA testbed with the propfan propulsion system operating was flutter free at all operational speeds up to V_{DF}/M_{DF}.

8.2.2.4 Handling Characteristics

Like the flight flutter tests, the aircraft handling characteristics tests with the propfan installed used the same techniques and procedures as the blades-off tests described in Section 8.2.1.3.

Test results of the handling characteristics agreed very well with predictions from wind tunnel data and those based on Gulfstream GII data. There were no flight restrictions as a result of handling characteristics tests.

A summary of results is presented as follows:

- Static longitudinal stability was essentially the same as the basic GII.
- Dynamic longitudinal characteristics were well damped. However, there was a tendency for the PTA testbed to roll during pitching maneuvers due to the lateral offset of the center of gravity.
- Like the GII, the PTA testbed experienced a "Mach tuck" (undesirable reversal of stick force/velocity characteristics in high speed flight) at approximately 0.82 Mach number.
- Dynamic lateral-directional characteristics substantiated predictions and were very similar to basic GII damping data. The yaw damper was a requirement for operations above 10,668m (35,000 ft) with a Spey engine inoperative.
- Results of lateral trim tests were very similar to those obtained with the propfan blades removed. At speeds below 103 mps (200 KCAS), the left wing was heavy; at speeds above 103 mps (200 KCAS) the right wing was heavy; and at speeds above about 0.86 Mach number, the left wing became heavy again.

8.2.2.5 Envelope Clearance for Propfan Blade Stresses

Test Description - Throughout the propfan functional tests, flight flutter tests, and handling characteristics tests, a Hamilton Standard flight

analyst on board the test aircraft monitored propfan blade stresses and substantiated that stresses did not exceed allowable limits.

Aeroelastic clearance of the propfan for the PTA operating envelope was established using the matrix of 21 steady state test points shown in Figure 346. All of the test points with the exception of one--the Mach 0.89, 8,534m (28,000 ft) point--were run at maximum continuous power and 100-percent propfan rpm. In addition, a traverse of the propfan rpm operating range was conducted at a Mach 0.675, 8,534m (28,000 ft) altitude flight condition in order to search for any critical speed response. The rpm traverse was conducted at two engine torque settings, 475 N-m (350 ft-lb) and 2061 N-m (1520 ft-lb).

In order to evaluate the aerodynamic stability of the PTA aircraft with the propfan installed and producing thrust, a series of aircraft transient response tests were performed at selected flight operating conditions. These tests consisted of observing and recording the aircraft response to maneuvers such as elevator and rudder doublets, right and left 30-degree banked turns, pull-ups, push-overs, and nose right and left sideslips. These maneuvers also resulted in time-dependent changes of the aerodynamic inflow conditions at the propfan rotor. The aerodynamic variation experienced by the propfan during these maneuvers resulted in increased vibratory response of the blades in some instances. Therefore, blade strain gage data was acquired during these aircraft transients and was analyzed to ensure that the increases in vibratory stress were the result of forced response and not aeroelastic instability.

A simulated PTA engine failure was performed by a step change in the power lever position which resulted in a reduction of engine torque from 2983 N-m (2200 ft-lb) to the minimum level of 1225 N-m (350 ft-lb). A 14-percent underspeed resulted; however, propfan speed recovered to within 2 percent of the setpoint within 2 seconds, and the transient damped out quickly thereafter. This was the most severe transient to which the propfan was subjected. The blade angle rate of change measured during this transient was approximately 8 degrees/second which compares very favorably to the design slew rate of 9 degrees/second.

Test Results - Reduction of the vibratory stress data acquired during the flight envelope clearance portion of the flight checkout testing included generation of brush charts of the peak stresses, spectral plots and visicorder plots of the total strain signal.

The infrequently repeating peak (IRP) vibratory stress was estimated from the brush charts for each test point. Experience has shown that the IRP value is a good measure of the maximum amplitude of a given data sample and is the value which is compared to vibratory strain limits. Brush charts of the peak stress were generated for all of the 21 operating points depicted in Figure 346. The brush charts depict the stresses measured at gage locations 1E, 1F, 11, 13, 19, 2E, 2F, 23, 24, 43, 44, 6E, 6F, 61, 62, 63, 65V, and 66V. These gage locations were deemed sufficient to completely define the vibratory stress distribution for the blade at any operating condition. The IRP values of the 1P components of the shank moments were also determined for all of the operating points of

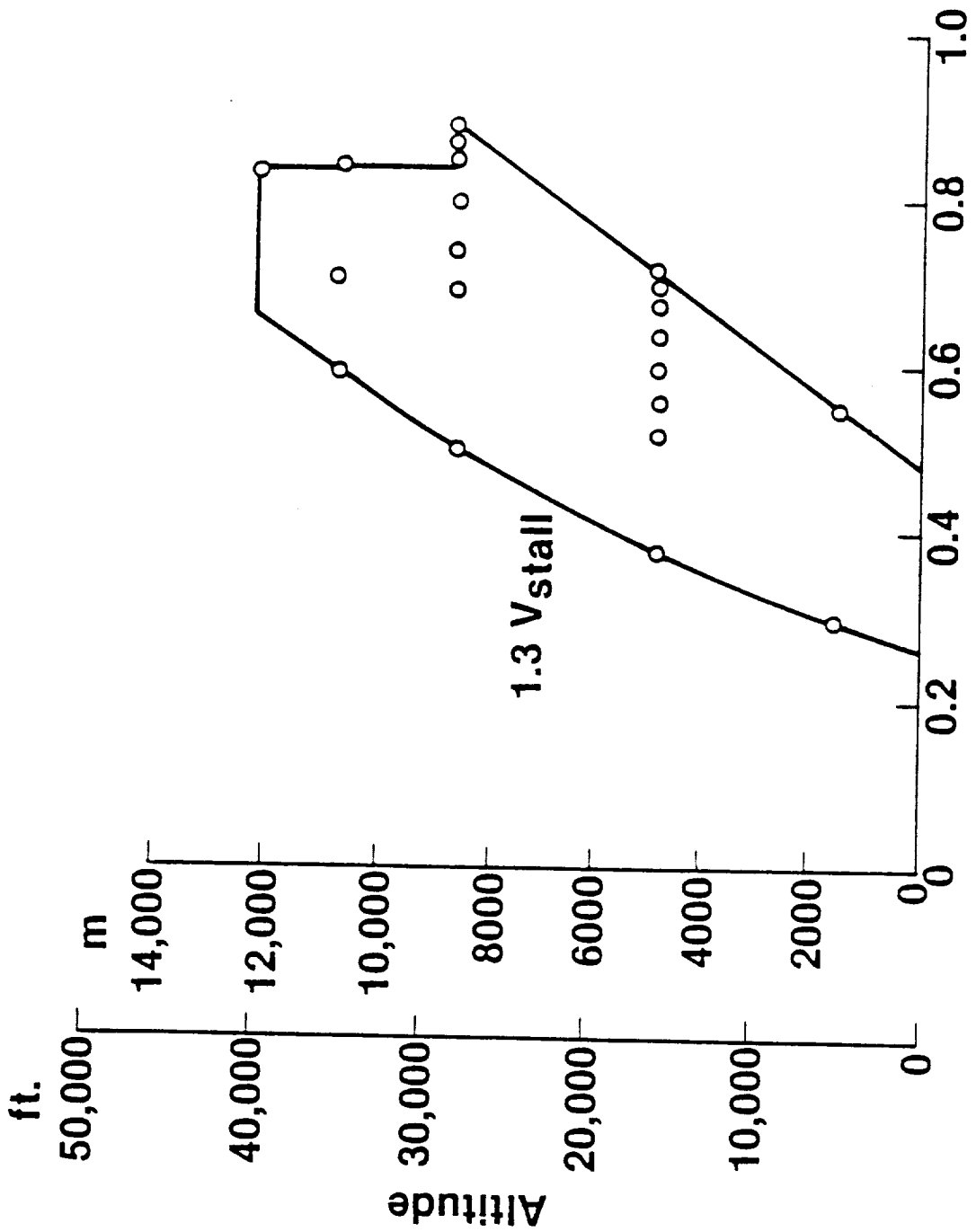


Figure 346. Flight Envelope Clearance Points for Blade Stress

Figure 346. This was accomplished by first filtering the total strain signal from gages 1E, 1F, 6E, and 6F, using a 35 Hz low pass filter, prior to determining the IRP stress.

Data gathered during the test points of Figure 346 allowed the distribution of IRP stress in the blade structure to be plotted as functions of indicated airspeed. These plots are presented in Figures 347 through 349. The trend in the variation of IRP stress with airspeed illustrated by these plots is that the maximum stress at a given gage location occurred at the minimum and maximum airspeeds in the range and reached a minimum at 129 mps (250 KIAS) to 155 mps (300 KIAS). This trend can be explained by the 1P excitation that occurs during flight. The magnitude of the 1P excitation is proportional to the inflow angle and the square of the equivalent airspeed. At low airspeeds, the high angle of attack needed to maintain level flight causes a large excitation. At high airspeeds, the angle of attack is reduced, but the velocity squared term keeps the excitation high.

The variation of the 1P component of the blade shank moment as a function of airspeed is compared to the variation of the total vibratory blade shank moment with airspeed in Figure 350. The shank moments are seen to be predominantly 1P at low airspeed. However, higher order components are more significant at higher speeds as seen by the differential between the 1P and total vibratory moments at the high speed end of the curves. Since the 1P components of the shank moments were determined for the flight envelope clearance points, extensive spectral analysis of the data taken was not considered necessary. A large number of spectral plots were generated for data taken during the flight research portion of the testing.

The variation of the IRP vibratory stresses and shank moments with torque and altitude are shown in Figure 351. As the aircraft altitude increased from 1,524m (5,000 ft) to 10,668m (35,000 ft) at the $1.3V_S$ airspeeds, the maximum continuous torque the PTA engine was capable of producing decreased by almost 50 percent. The large changes in torque and altitude had a minor effect on vibratory stress levels because the $1.3V_S$ speeds represent an operating line of constant dynamic pressure and angle of attack. Therefore, the 1P excitation remained almost constant.

The effect of an rpm traverse on the vibratory stresses and shank moments is shown in Figure 352. With decreasing speed, there was a rise in vibratory stress level at low rpm as the rotational speed approached the 2P/1F critical speed, which occurred at approximately 77 percent propfan rpm. At rotational speeds above 90 percent, there was little change in vibratory stress levels with rpm.

The blade shank vibratory bending moment response to a sideslip maneuver is illustrated in Figure 353. The edgewise shank gage did not respond, while the flatwise gage amplitude nearly doubled. The response of the flatwise shank gage is a result of the increased 1P excitation which is related to the inflow angle of the air with respect to the propfan plane of rotation. The left and right sideslips did not increase the flatwise response equally because of the asymmetric effects the PTA nacelle and Gulfstream fuselage had on the propfan flow field. The frequency spectrum

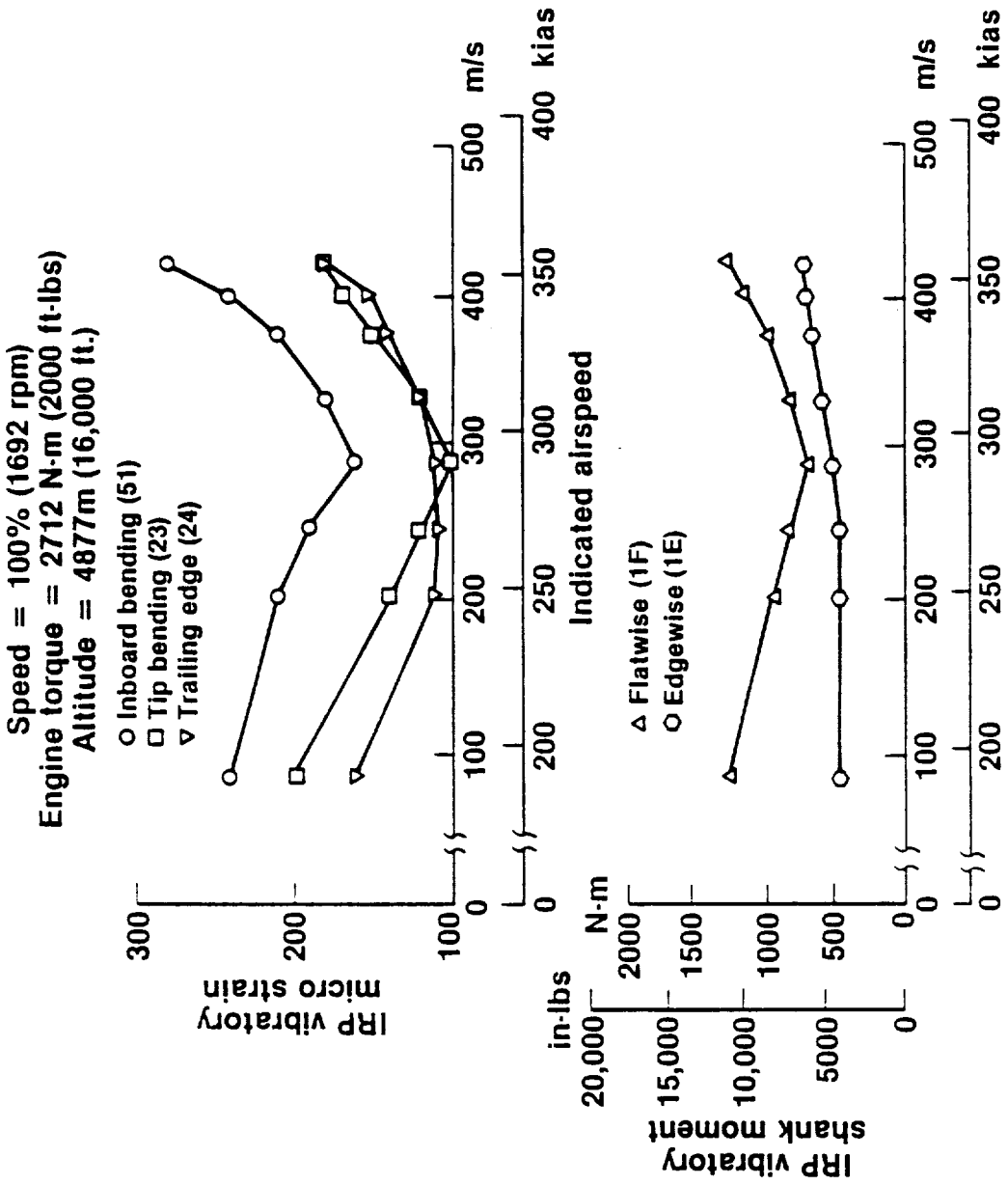


Figure 347. Effect of Airspeed on Vibratory Loads in Stabilized Flight

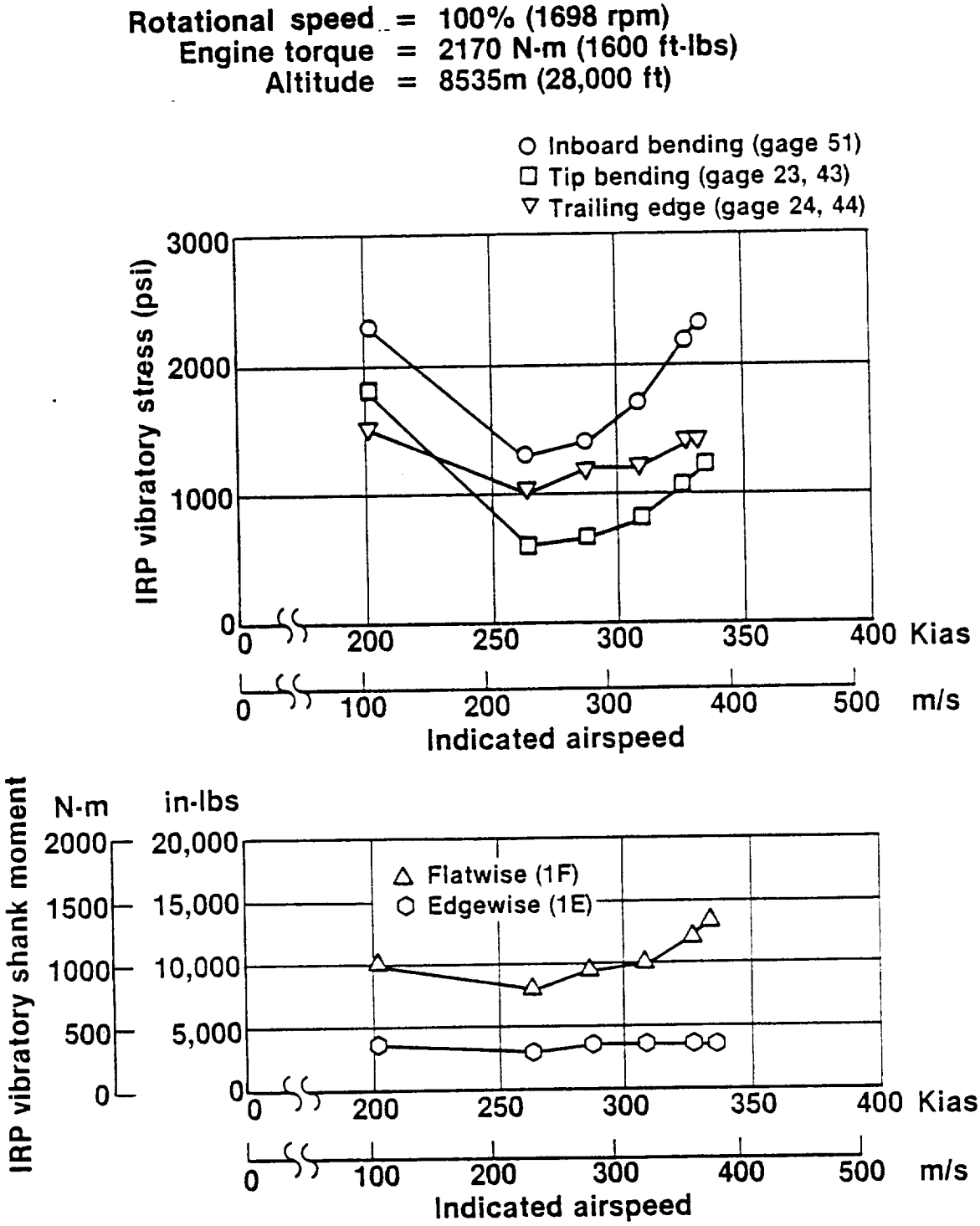


Figure 348. Blade Vibratory Load vs Indicated Airspeed

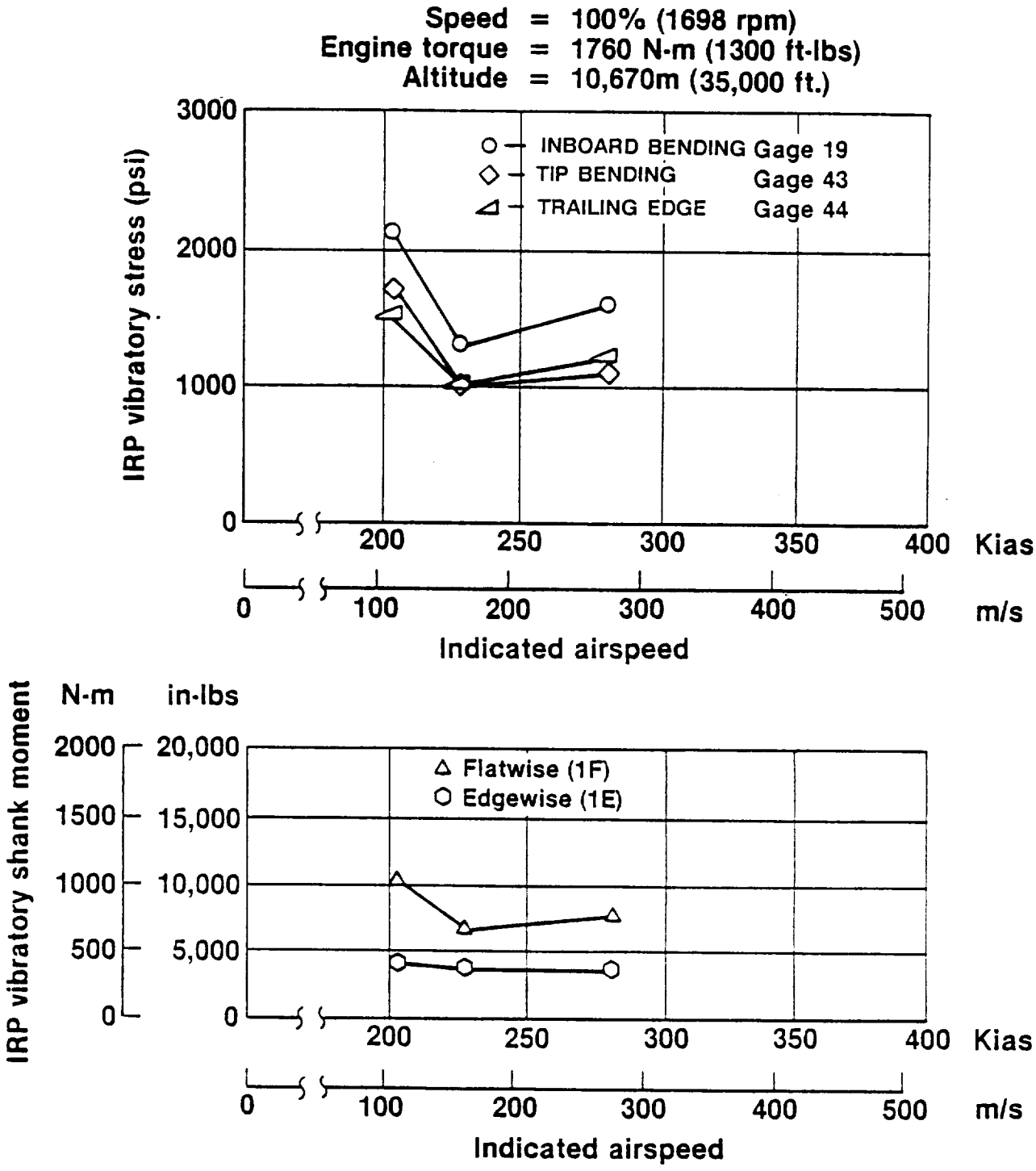


Figure 349. Blade Vibratory Loading vs Indicated Airspeed

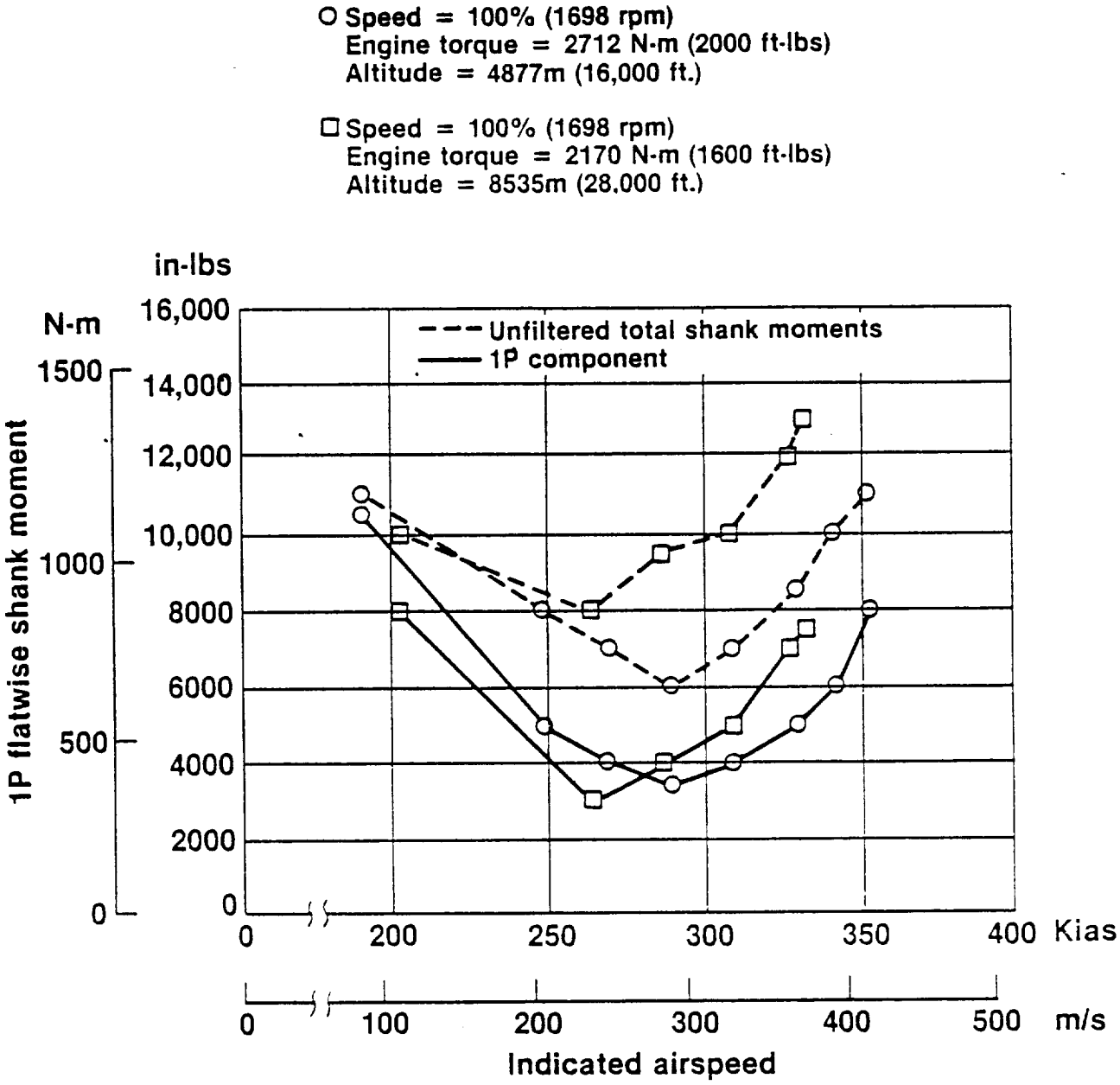


Figure 350. Comparison of the 1P Component and Total IRP Shank Moment

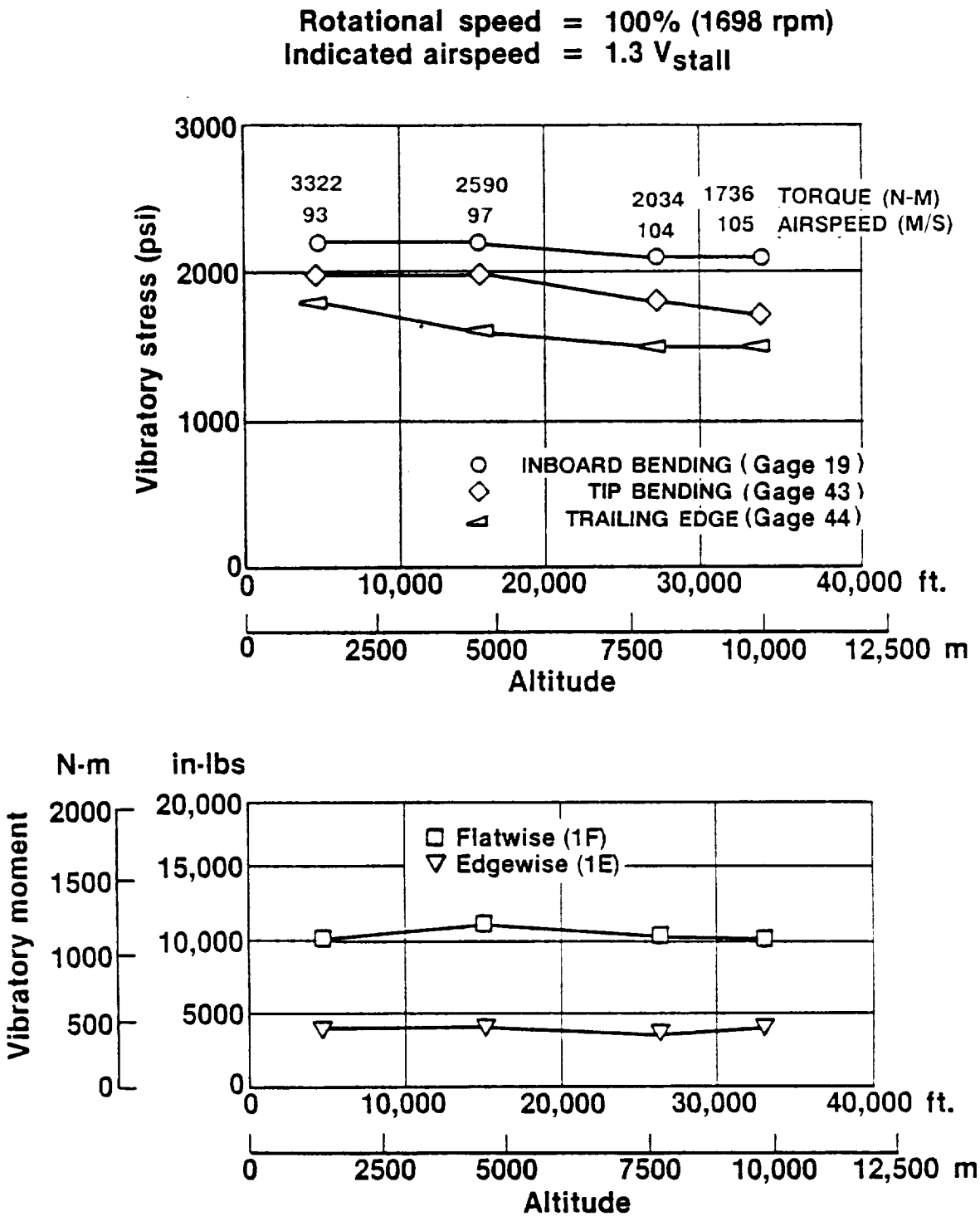


Figure 351. Vibratory Loading vs Altitude (Maximum Continuous Torque)

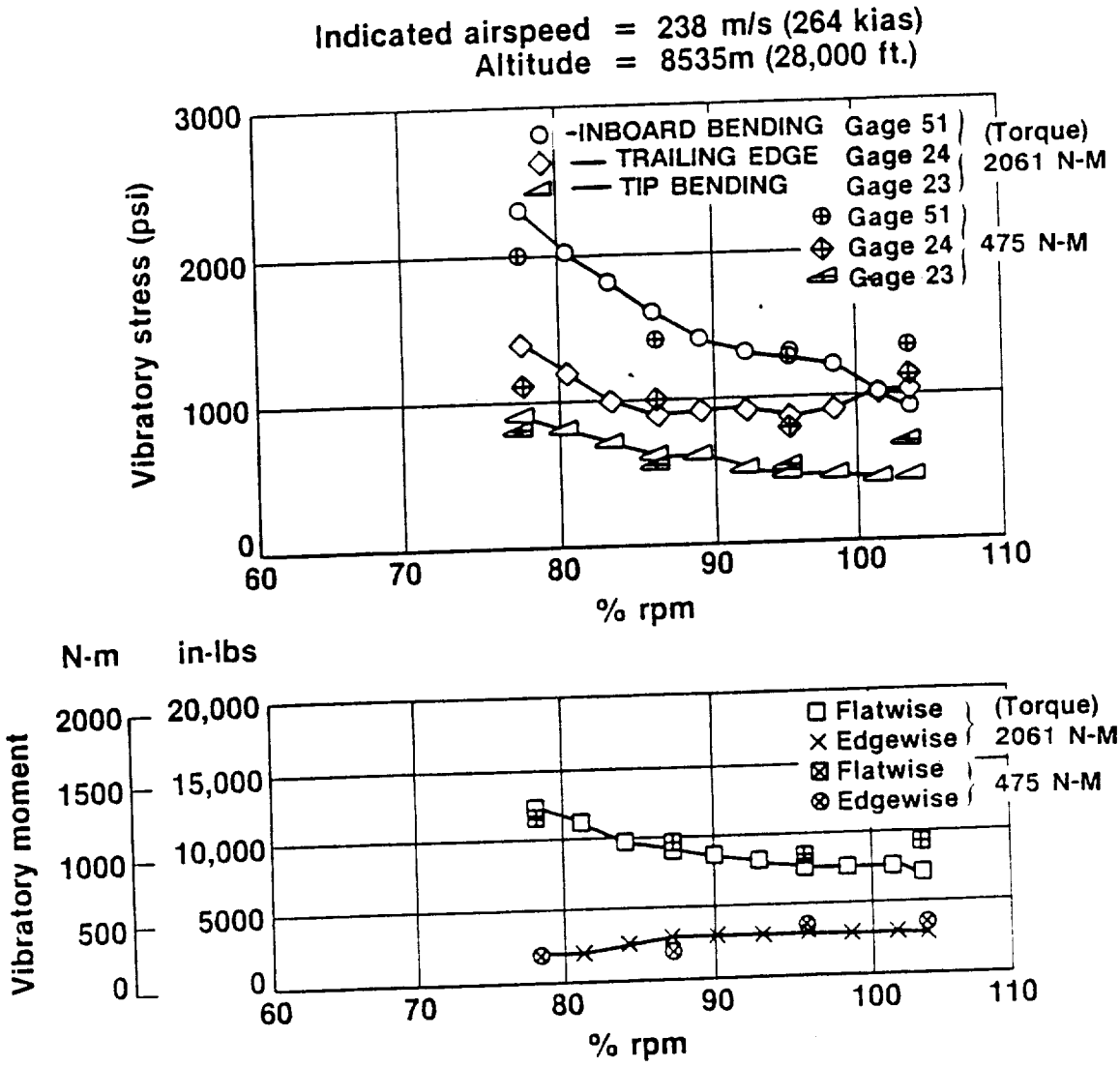


Figure 352. Vibratory Loading vs RPM (Constant Torque)

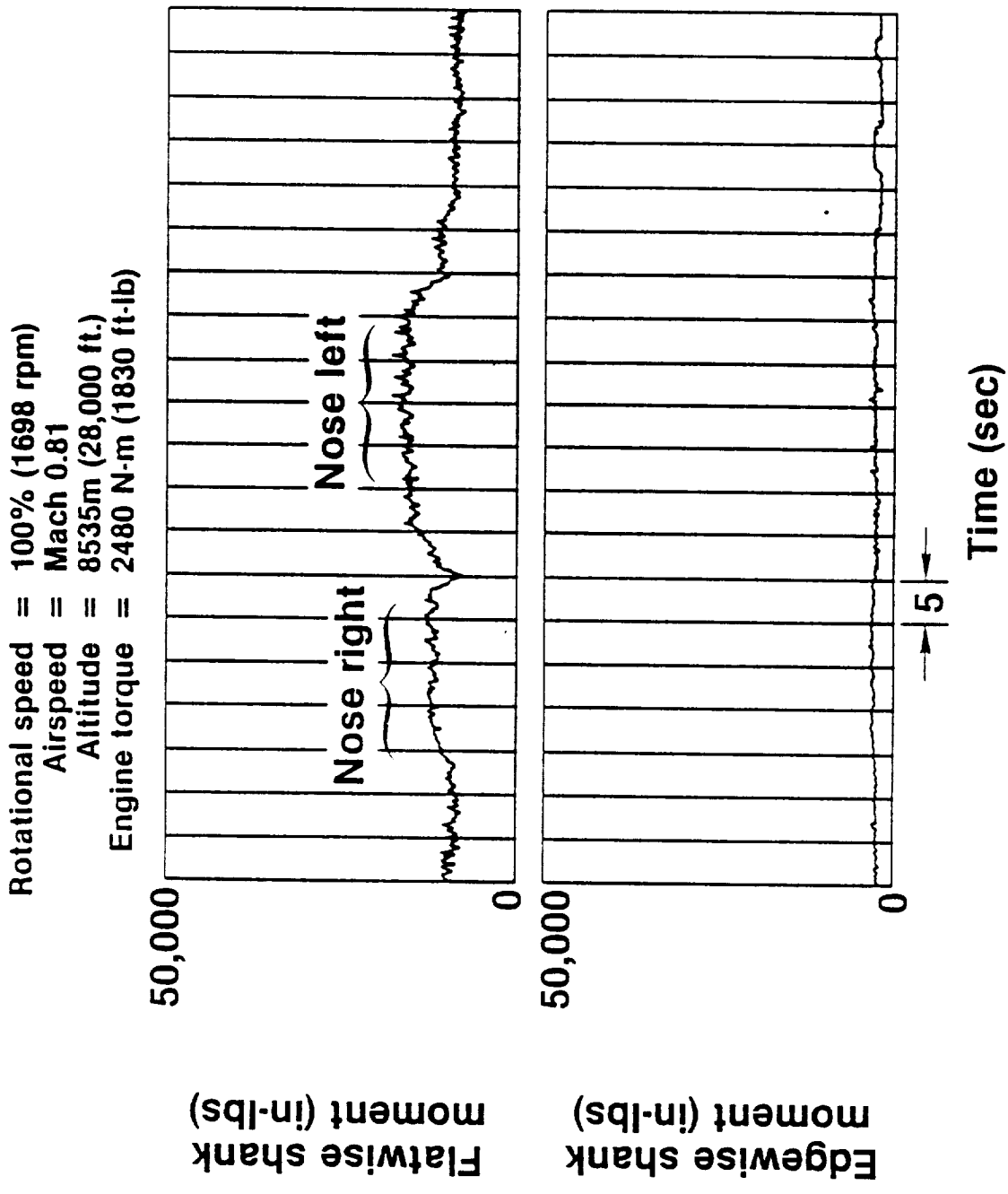


Figure 353. Vibratory Loads in a Sideslip Maneuver

of Figure 354 for the nose-left portion of the sideslip maneuver shows that the main vibratory component was 1P or first harmonic of rotation. All higher frequency components were nearly an order of magnitude lower in amplitude.

Figure 355 shows the flatwise and edgewise bending response to an elevator doublet maneuver. Again, the flatwise gage showed a significant response, but the edgewise gage did not respond to the 1P excitation. The spectrum plot of Figure 356 showed that the response was again predominantly 1P with no significant higher harmonics.

Figure 357 illustrates the response to a shutdown that occurred, due to an engine compressor stall at 12,192m (40,000 ft) as the aircraft was being decelerated to $1.3V_S$. As the blade angle increased to feather, the vibratory stress increased from 5,516 x 10^3 N/m² to 20,685 x 10^3 N/m² (800 to 3,000 psi); then decreased; then peaked again at 15,169 x 10^3 N/m² (2,200 psi). Visicorder plots of the first and second stress peaks of Figure 357 are shown on Figures 358 and 359, respectively. The first peak of Figure 357 responded at the 2P/1F critical speed as the propfan speed passed through 1050 rpm. The 2P response is apparent in the visicorder plots of Figure 358. The visicorder plots of the second stress spike on Figure 359 show a critical speed response at the 3P/1F mode crossover as the propfan speed decelerated through 600 rpm.

None of the test points in the matrix of Figure 346 resulted in IRP stress greater than the allowable maximum continuous vibratory stress levels for the SR-7L. Analysis of the flight maneuver transient cases revealed normal forced response activity. No aeroelastic instability was detected. This constituted clearance of the flight envelope.

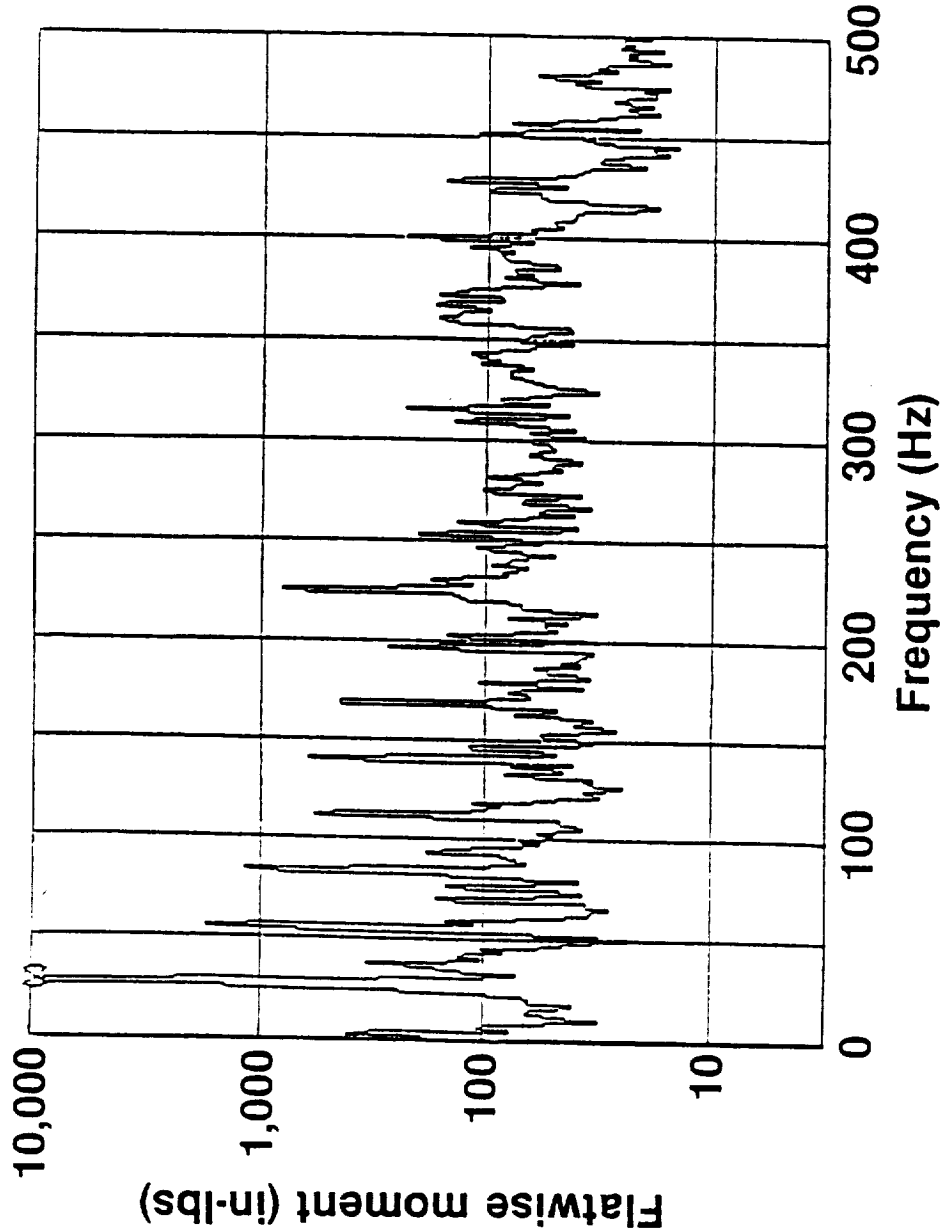


Figure 354. Spectral Plot, Blade Shank Flatwise Vibratory Bending Moment, Sideslip Maneuver

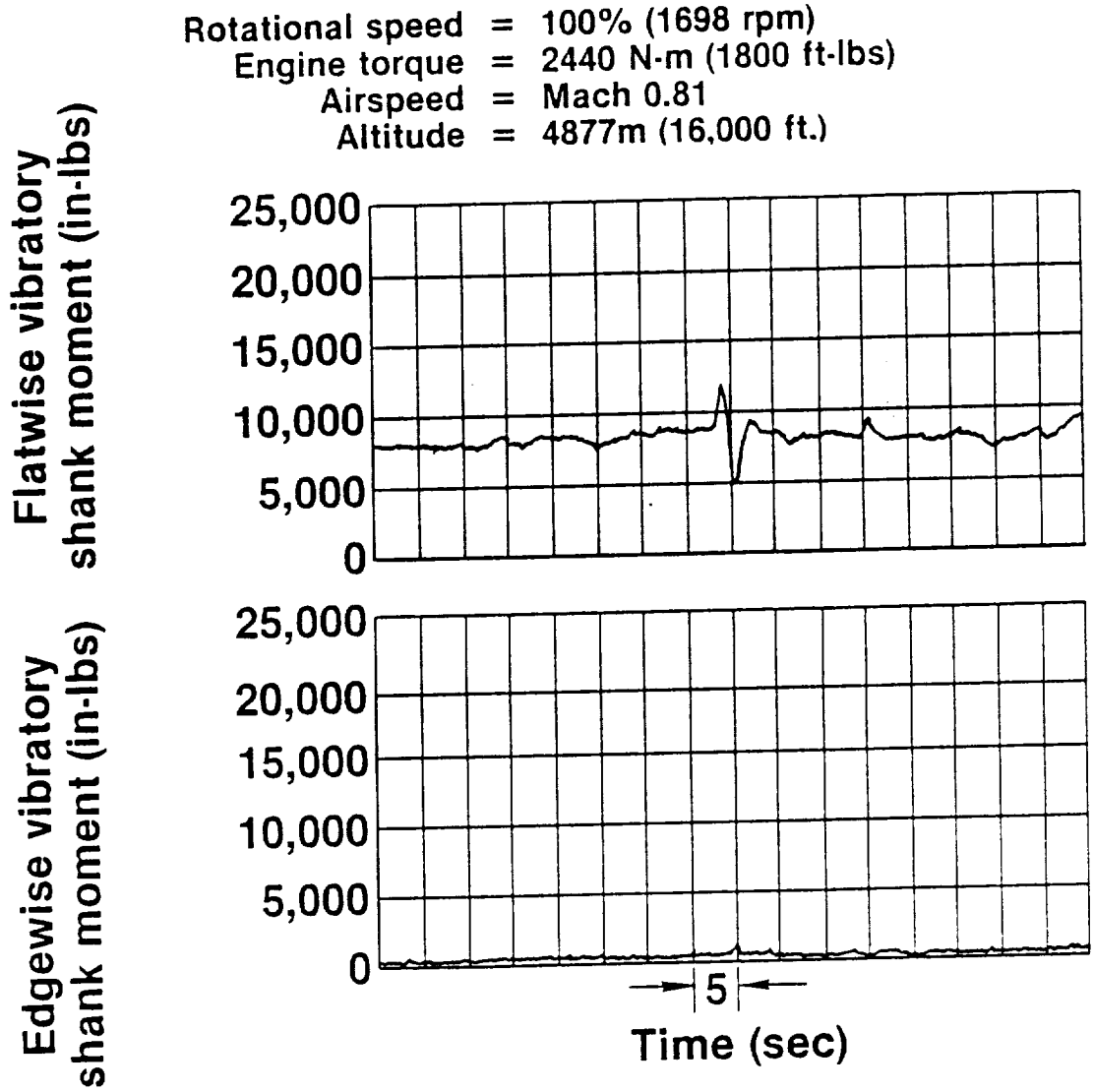


Figure 355. Vibratory Response to an Elevator Doublet

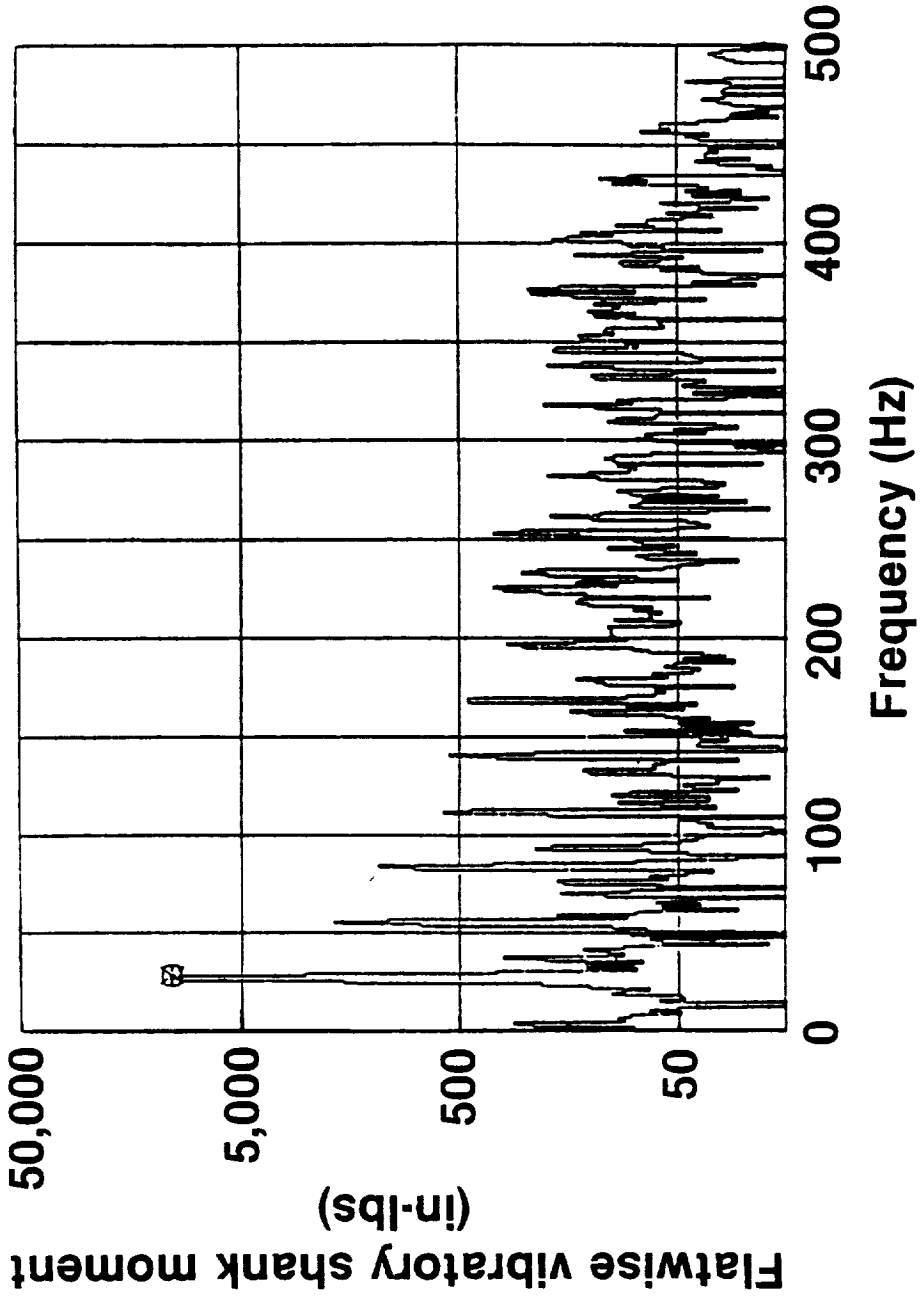


Figure 356. Spectral Plot, Blade Shank Flatwise Vibratory Bending Moment Elevator Doublet

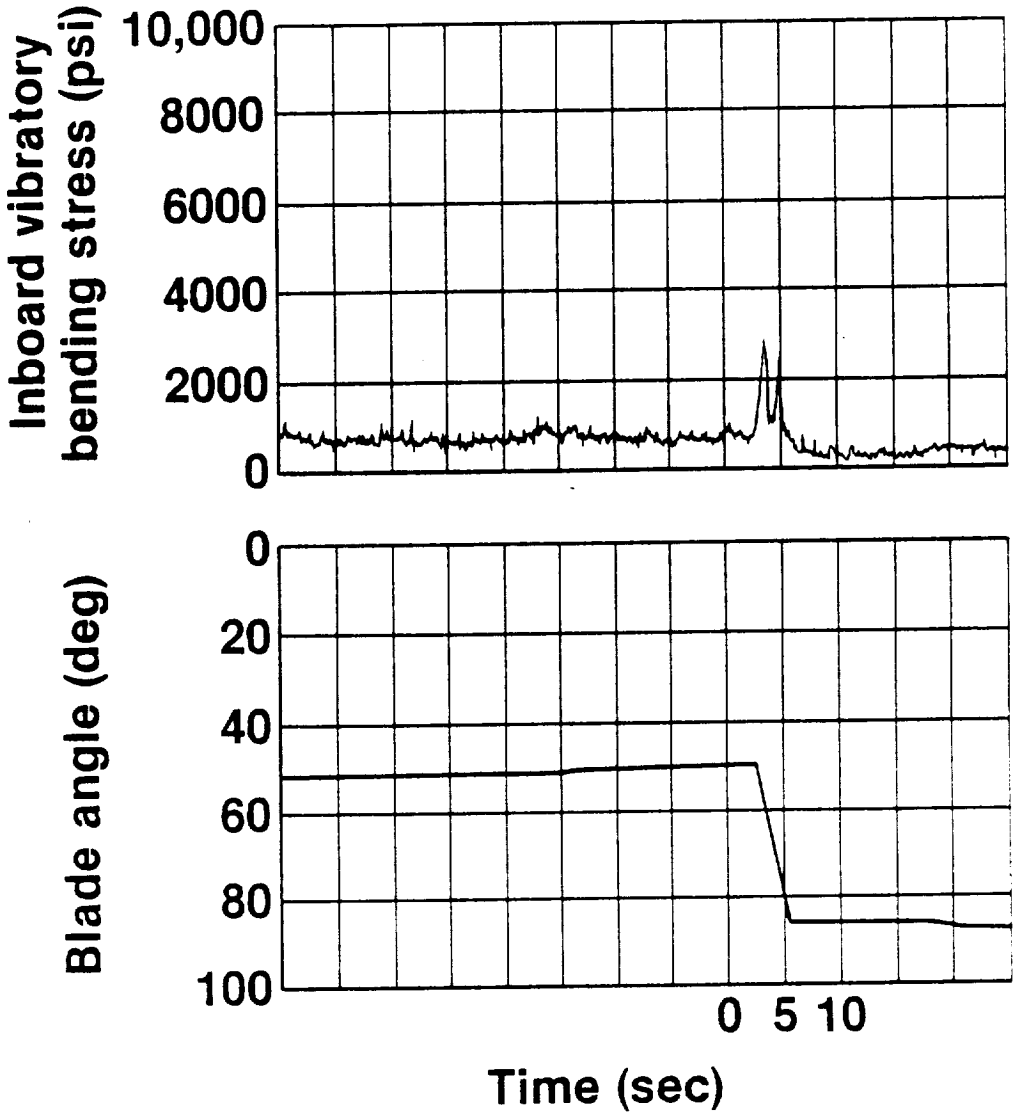


Figure 357. Vibratory Loading During Feathering and Shutdown

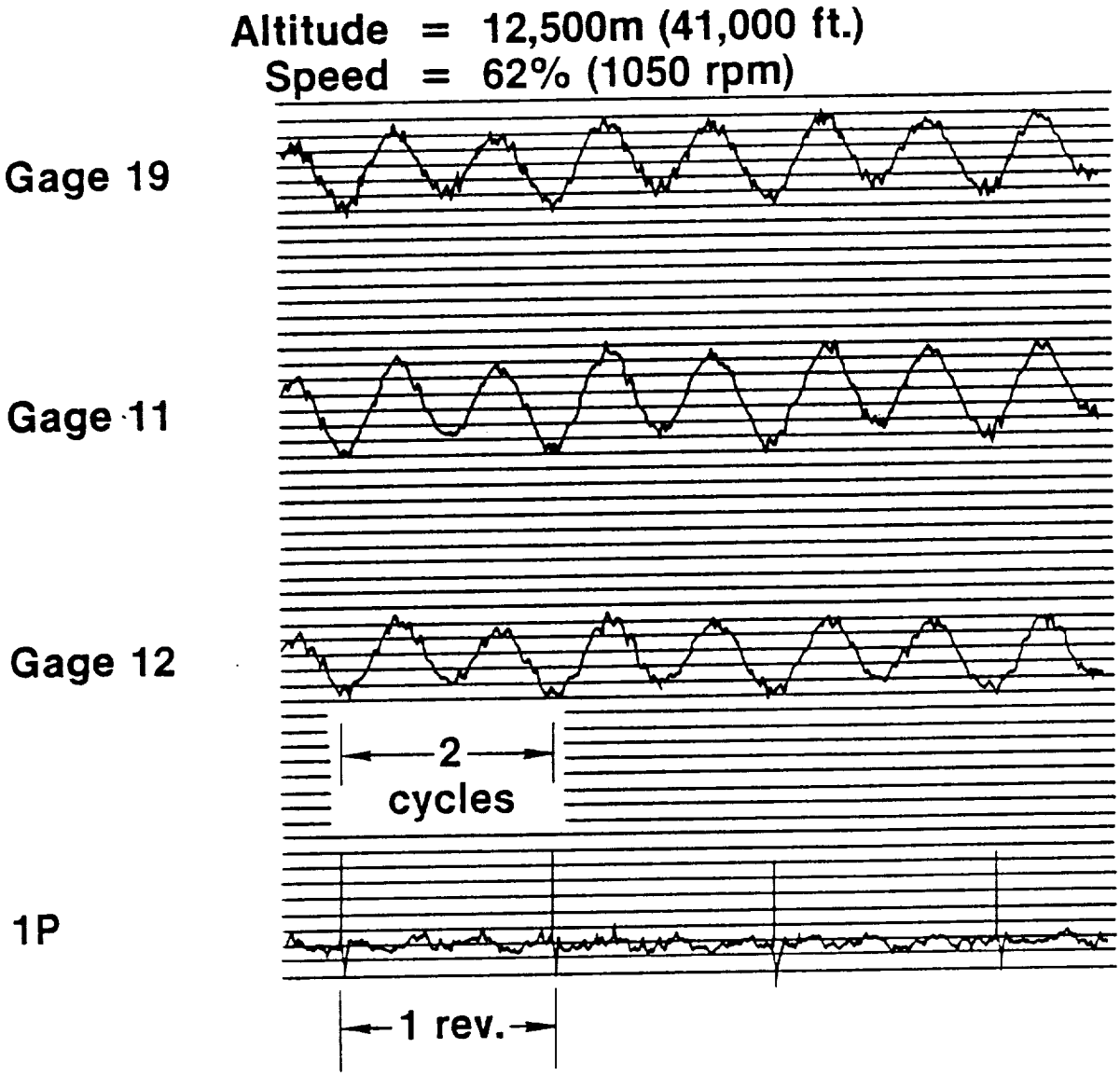


Figure 358. Visicorder Traces During Shutdown and Feathering

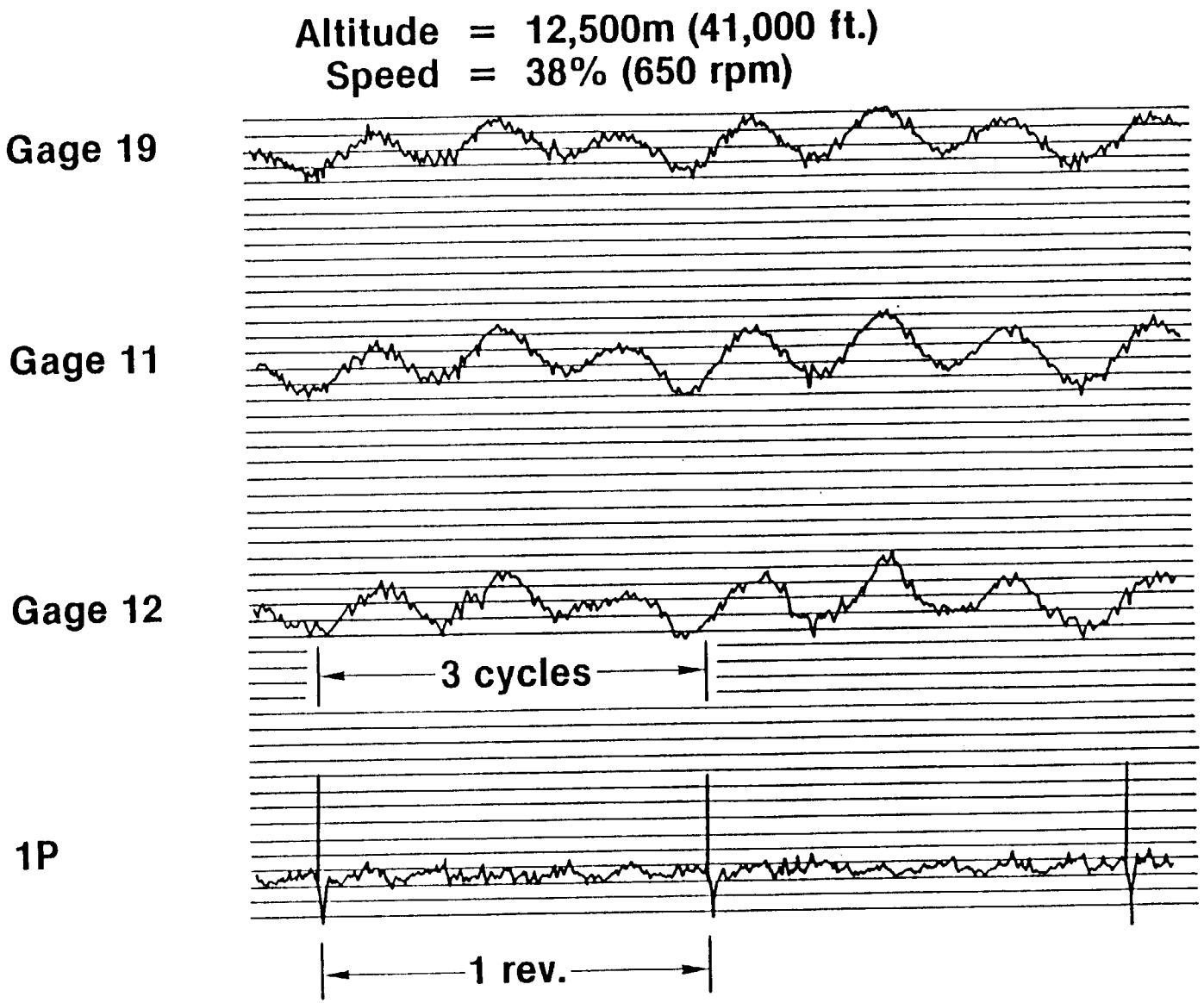


Figure 359. Second Peak Visicorder Traces During Shutdown and Feathering

9.0 FLIGHT RESEARCH TESTS

The flight research test program was subdivided in four phases:

- o High altitude tests
- o Low altitude tests
- o En route noise tests
- o Cabin interior acoustic treatment tests

In each phase there were different test emphases as pointed out in the following paragraphs.

High Altitude Tests - These were the basic tests for propfan blade stress measurements, but they also were a major part of the acoustics tests. They covered a speed-altitude envelope typical of that experienced by commercial transport aircraft in climb-out and cruise operation. Altitudes ranged from 1,524m (5,000 ft) to 12,192m (40,000 ft) and Mach numbers from 1.3 times stall speed to Mach 0.85. Propfan power and speed matrix variations were performed at a large number of flight conditions within this flight envelope. Nacelle tilt angle was also a primary variable. Near-field noise measurements were made concurrent with the blade stress measurements. These included measurements of sound pressure levels on aircraft surfaces and fluctuating pressure levels on surfaces in the propfan slipstream.

Low Altitude Tests - These tests were made primarily to measure the FAR 36 type noise characteristics of the propfan. Ground microphones were arrayed to measure flyover and sideline noise for several flight altitudes, several nacelle tilt angles, and a matrix of propfan power and rotational speeds. Propfan blade vibratory stresses were also recorded.

En Route Noise Tests - Tests were performed in cooperation with the FAA to measure ground noise for flyovers at altitudes of 6,096m (20,000 ft) and 10,668m (35,000 ft). The primary purpose of these flights was to evaluate an analytical model for atmospheric absorption of noise. In order to define source noise not yet affected by the atmosphere, NASA flew an instrumented Learjet in formation with the PTA aircraft at separation distances of approximately 152m (500 ft). All ground data were recorded by the FAA and will be reported by that agency.

Cabin Interior Acoustic Treatment Tests - Under a separate NASA contract, the California Division of the Lockheed Aeronautical Systems Company developed an advanced cabin wall treatment system employing the tuned resonator concept for noise reduction. An enclosure was built, using this wall treatment, that was small enough to fit snugly inside the PTA fuselage. Flight tests were then flown to measure the effectiveness of this treatment. All tests were flown at simulated cruise conditions.

The flight research tests were reported in detail in Reference 10(a). Highlights of the results will be discussed in the sections that follow.

PRECEDING PAGE BLANK NOT FILMED

PAGE 452 INTENTIONALLY BLANK

9.1 PROPFAN BLADE STRUCTURAL EVALUATION TESTS

9.1.1 Objectives and Scope

The objectives of the propfan blade structural evaluation tests were to measure propfan blade structural data within the PTA operational envelope to assess the effects on blade stressing of:

- o Airspeed
- o Altitude
- o Torque
- o Rotational speed
- o Nacelle tilt

The flight test envelope and test points obtained are shown in Figures 360 through 362. Blade stress data were obtained for all the points shown. The letters identifying each point and the inset tables show the matrices of power and rotational speeds obtained for these points.

9.1.2 Test Procedures

All of the high altitude tests were flown from the Lockheed flight test facilities at Dobbins Air Force Base, Marietta, Georgia. The general test technique was to measure blade stress and acoustics data concurrently at each test point. Data were recorded for approximately 60 seconds after the aircraft was stabilized on a test point. The Spey engine on the left side of the aircraft was always operated at the lowest power setting needed to maintain level flight so that the propfan noise signal would be as strong as possible relative to the background noise.

9.1.3 Results and Discussion

9.1.3.1 Blade Stress

Data from strain gages on the propfan blades were reduced to obtain "data sample averages" (DSAs) of the total vibratory strain at a stabilized flight condition. Figures 363 through 365 show DSA values measured over the entire flight envelope for the three nacelle tilt values. It can be seen that nacelle tilt had a large effect on the vibratory response of the propfan blades.

Figure 366 shows the typical frequency content of the measured vibratory response of the blade inboard bending strain gage during flight. The figure shows that the response is dominated by response at integer multiples of the rotational speed and that the first harmonic (1P) dominates the response. A comparison of measured and calculated mid-chord strain for the above and other conditions will establish the relative importance of the strain gage locations and the harmonic content of their response.

A

N_p / POWER	77%	105%
MAX CONT	X	X
MINIMUM	X	X

E

N_p / POWER	100%
MAX CONT	X

P

N_p / POWER	77%	100%
MAX CONT	X	X
MINIMUM	X	X

B

N_p / POWER	77%	87.5%	100%	105%
MAX CONT	X	X	X	X
80%			X	
50%			X	
MINIMUM			X	

	$\%N_p$	%MCP
F	87.0	100.0
G	78.6	81.0
H	105.0	50.5
I	94.8	40.1
J	105.0	100.0
K	94.8	78.4
L	81.0	100.0
M	77.2	93.1
N	105.0	100.0
O	100.1	90.7

◇B

N_p / POWER	77%	87.5%	100%	105%
MAX CONT	X	X	X	X

C

N_p / POWER	77%	78.1%	81.3%	84.4%	87.5%	90.6%	93.8%	96.9%	100%	102.5%	105%
MAX CONT	X	X	X	X	X	X	X	X	X	X	X
80%									X		
50%									X		
MINIMUM									X		

◇D

N_p / POWER	77%	81.3%	87.5%	93.5%	100%	105%
MAX CONT	X	X	X	X	X	X
80%	X	X	X	X	X	X
50%	X	X	X	X	X	X
MINIMUM	X	X	X	X	X	X

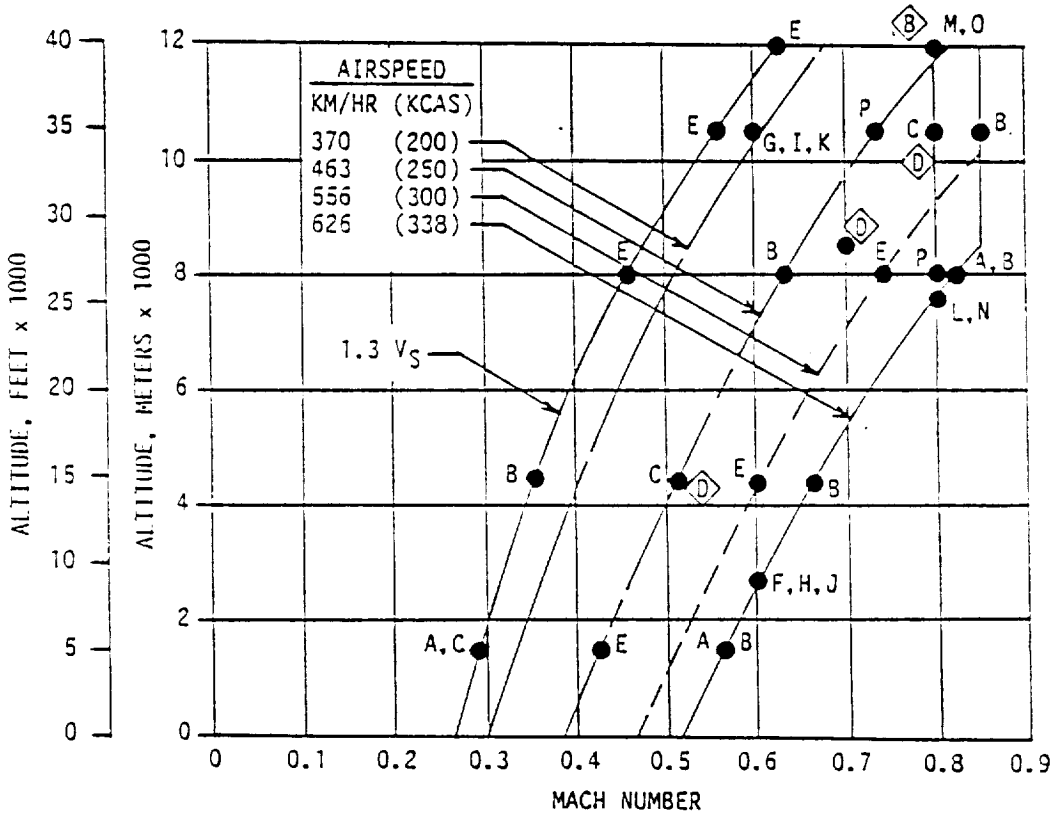


Figure 360. High-Altitude Flight Test Envelope, NT = -1°

A

N_p / POWER	77%	105%
MAX CONT	X	X
MINIMUM		X

B

N_p / POWER	77%	87.5%	100%	105%
MAX CONT	X	X	X	X
50%			X	

C

N_p / POWER	77%	78.1%	81.3%	84.4%	87.5%	90.6%	93.8%	96.9%	100%	102.5%	105%
MAX CONT	X	X	X	X	X	X	X	X	X	X	X
50%									X		

D

N_p / POWER	100%
MAX CONT	X

E

N_p / POWER	87.5%	100%
MAX CONT	X	X
80%	X	X
50%	X	X
MINIMUM	X	X

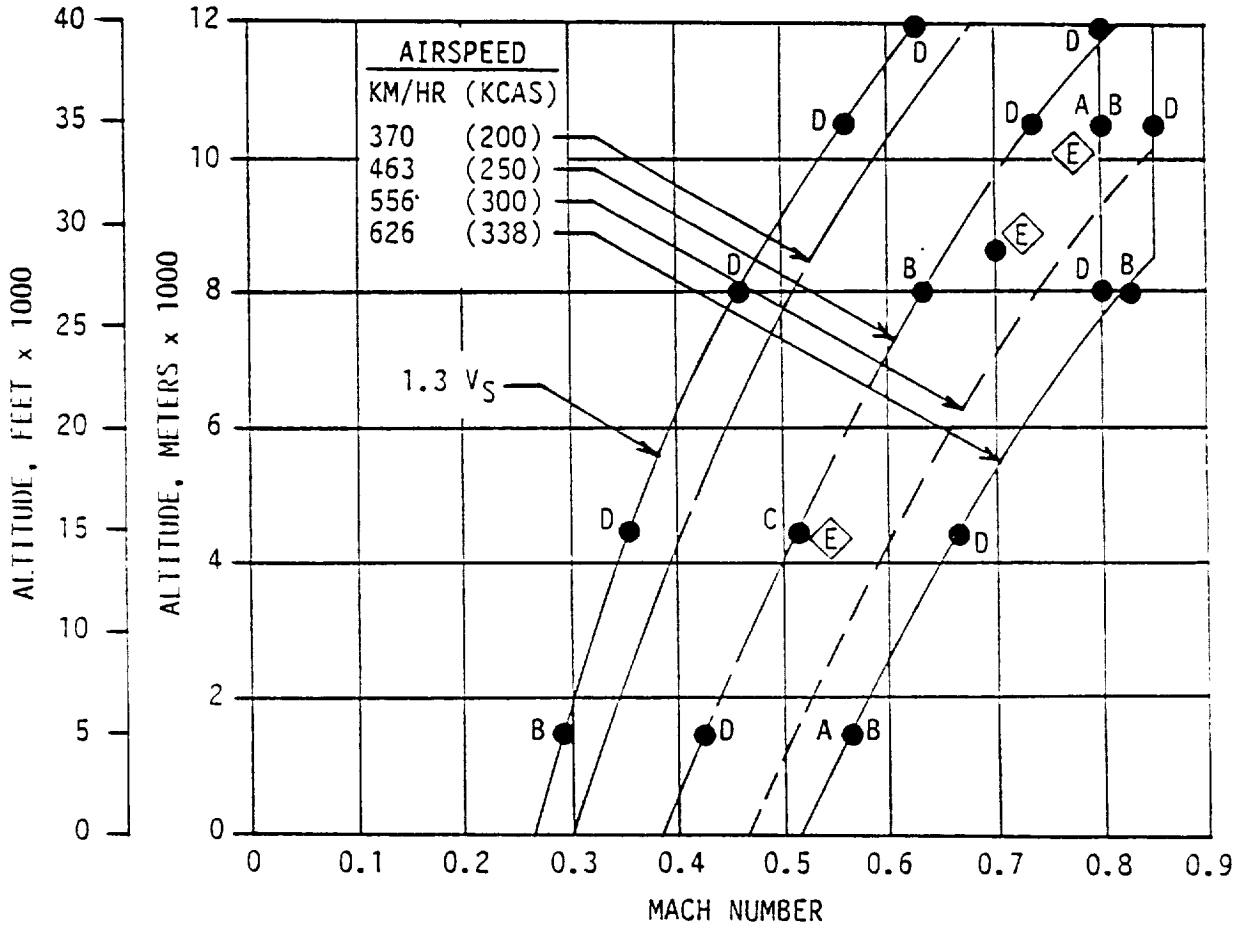


Figure 361. High-Altitude Flight Test Envelope, NT = -3°, +2°

C - 6

POWER \ N_p	77%	105%
MAX CONT	X	X
MINIMUM		X

A

NACELLE TILT = -1°

YAW ANGLE = +TBD° & -TBD°

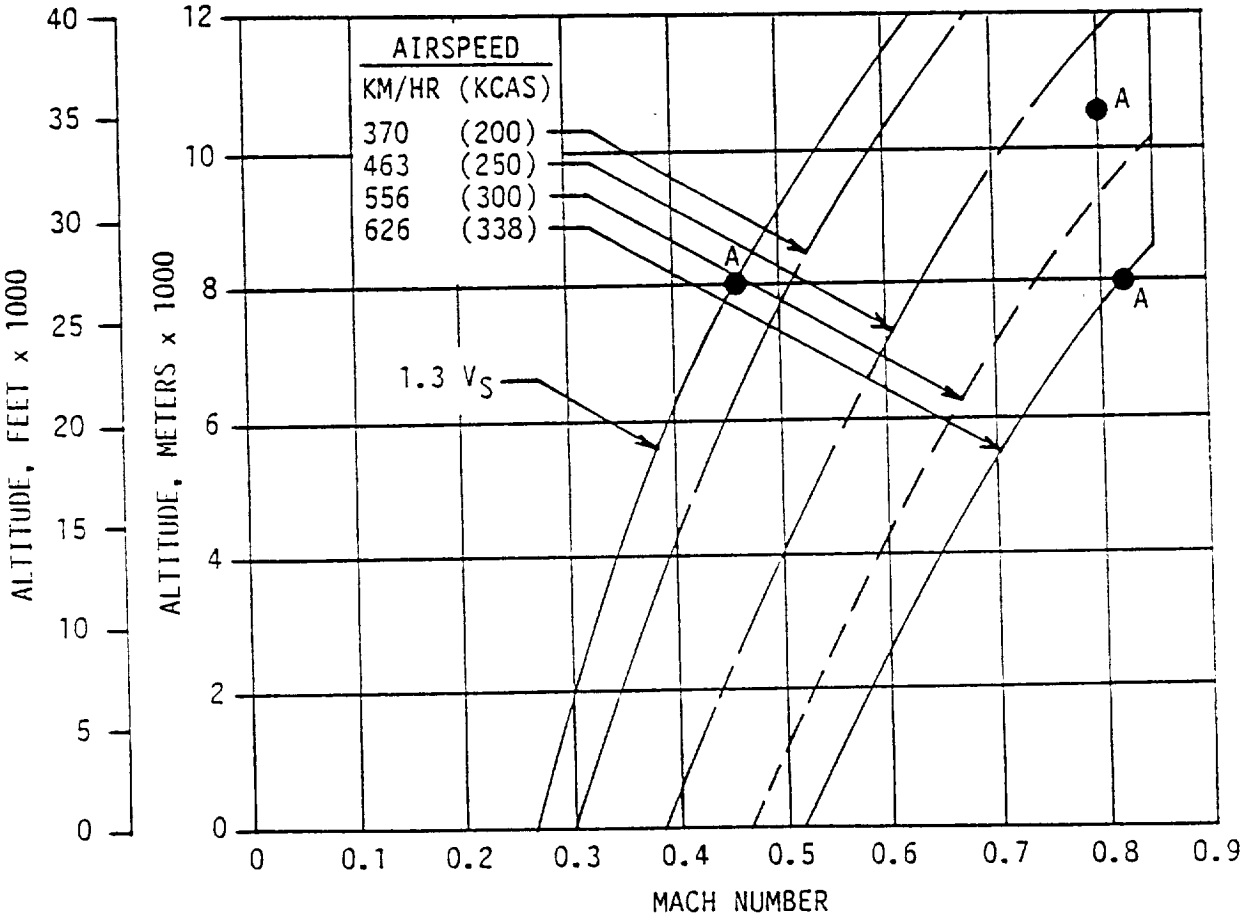


Figure 362. High-Altitude Flight Test Envelope, Yaw Conditions

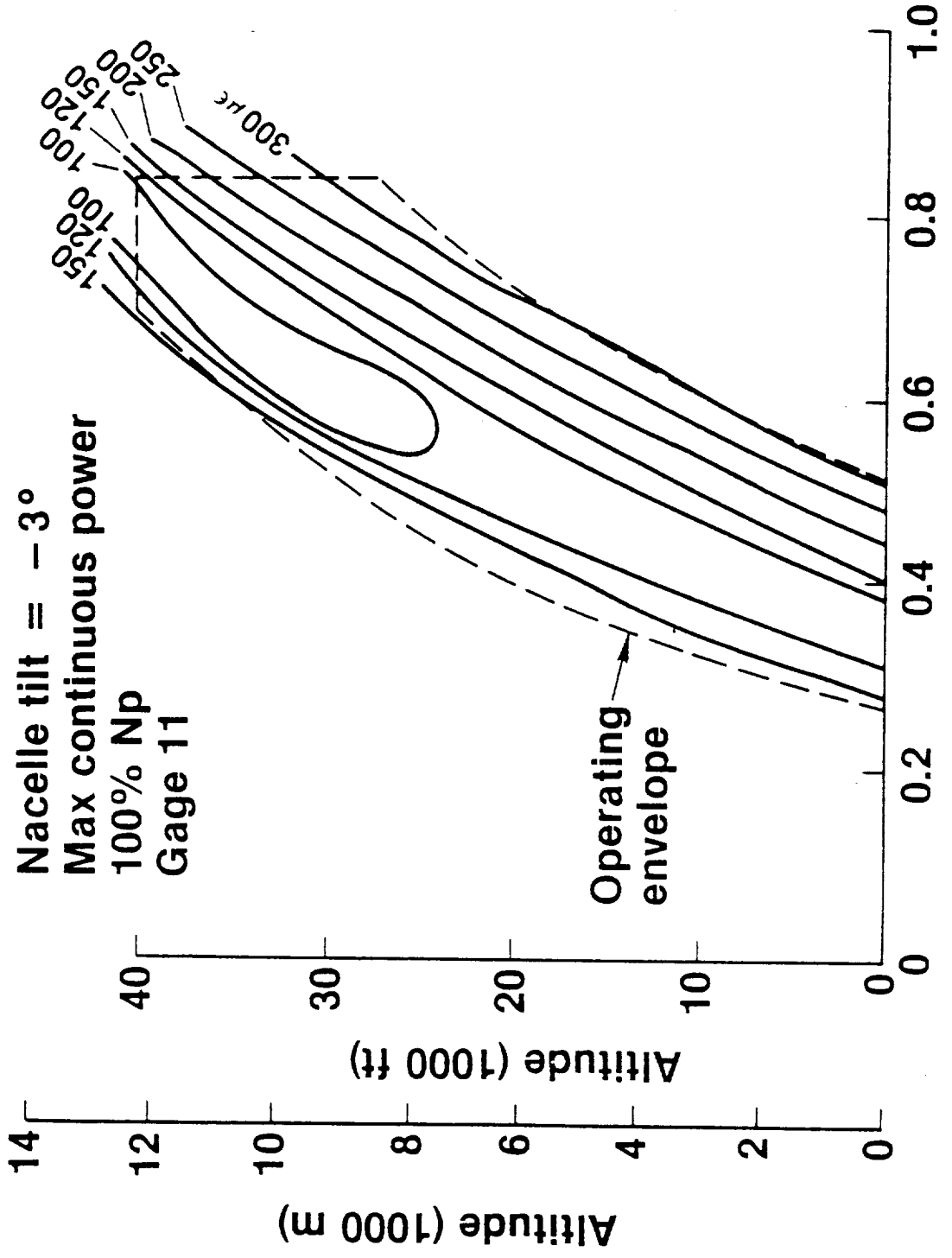


Figure 363. Inboard Bending Vibratory Strain, NT = -3°

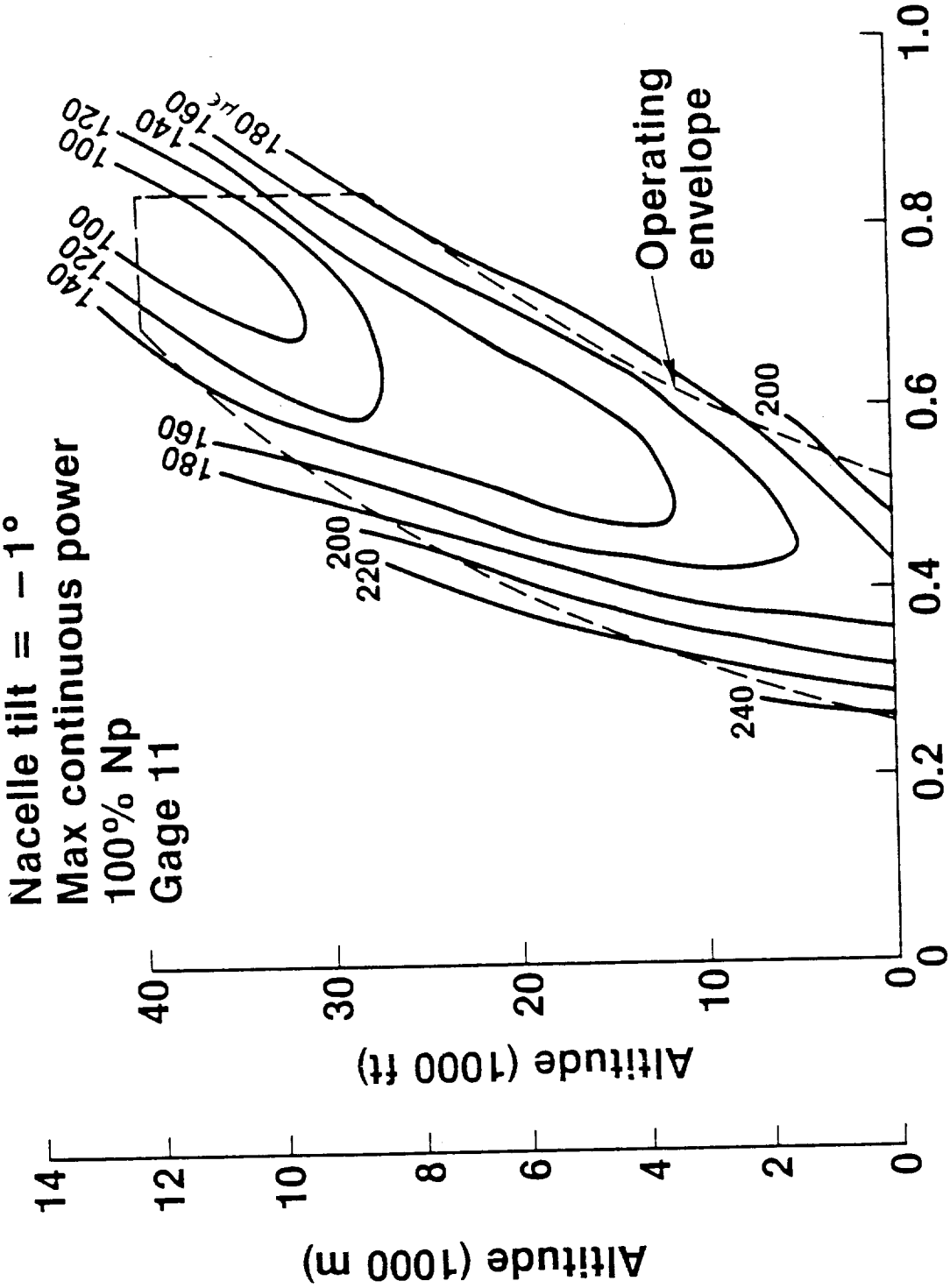


Figure 364. Inboard Bending Vibratory Strain, NT = -1°

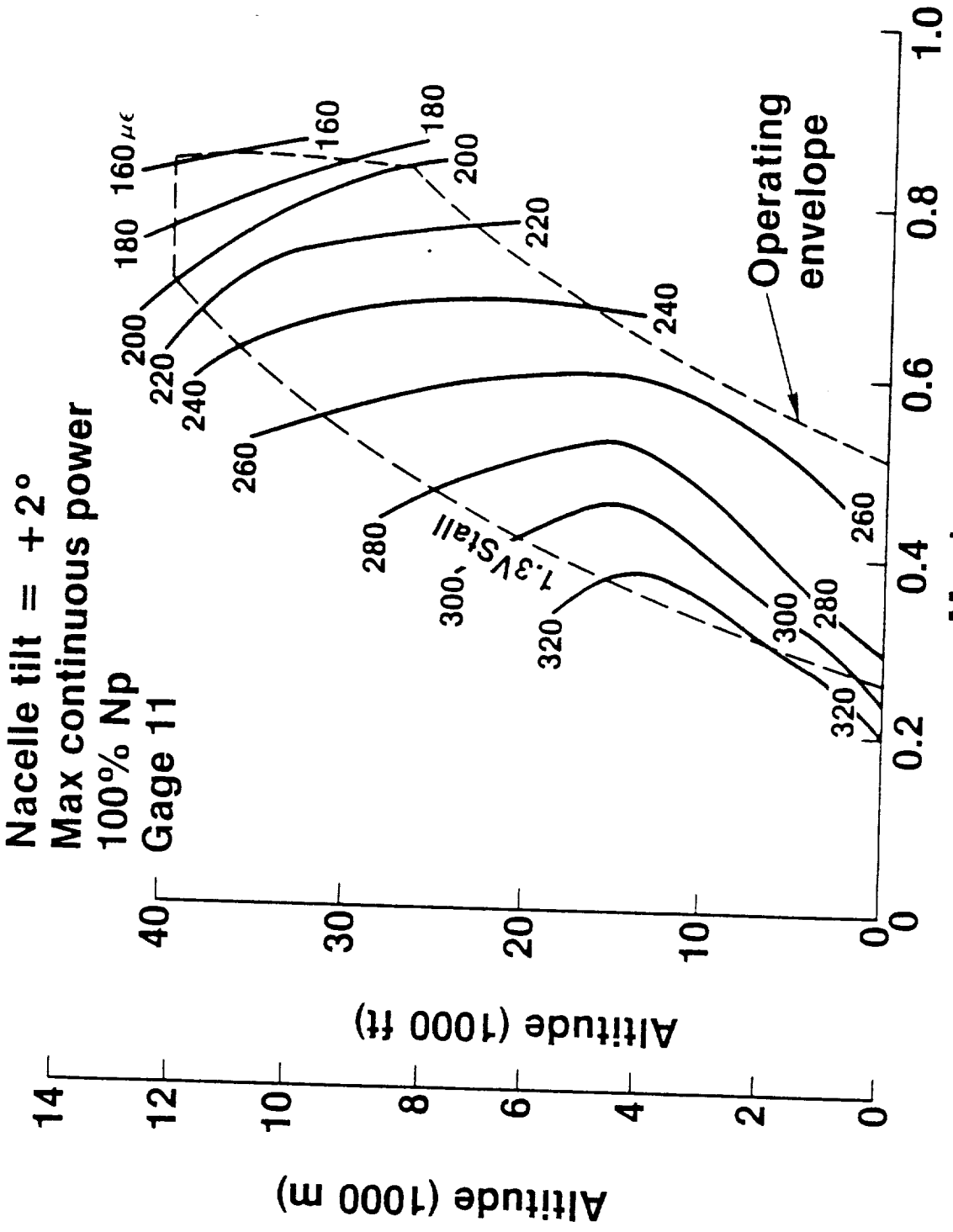


Figure 365. Inboard Bending Vibratory Strain, NT = +2°

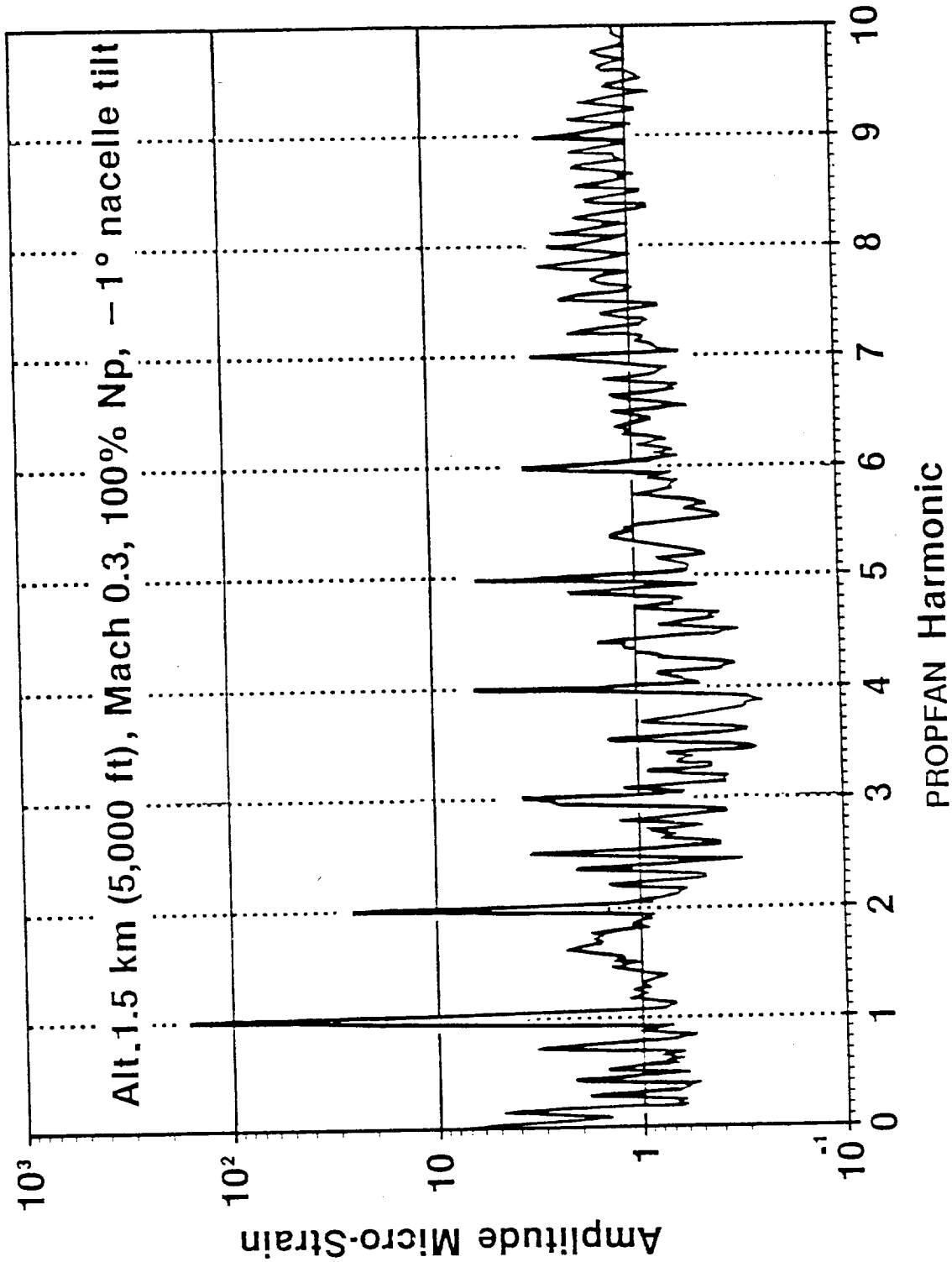


Figure 366. Typical Frequency Spectrum for an Inboard Bending Strain Gage

Figures 367, 368, and 369 show calculated and test 1P and 2P vibratory strain plotted versus nondimensional blade radius for nacelle tilt angles of -3, -1, and +2 degrees, respectively. These data are for the Mach 0.3, 1500m (5000 ft) flight condition. As can be seen on all three figures, the measured 1P strain distribution exhibits a peak near the 42-percent radial station, and the strain decreases toward the blade tip until the outermost strain gage shows a slight upward trend in measured strain. The calculated strain follows a similar distribution but at a 15-percent higher level inboard on the blade tapering to 5-percent higher in the mid-blade region and showing lower strain at the blade tip. The calculation does not show the strain rise at the blade tip, indicating that the local tip loading is higher than predicted. This is possibly due to some three-dimensional and/or vortex action as evidenced in previous tests that is not included in the current aerodynamic methodology.

The 2P correlation was good for the -3 degree and -1 degree nacelle tilt angles and underpredicted in the tip region of the blade at the +2 degree nacelle tilt angle. The +2 degree nacelle angle 2P results are trivial because of the low amplitude response of the 2P harmonic at that condition.

Figure 370 shows curves of the test and calculated 3P and 4P vibratory strain versus nondimensional radius for nacelle tilt of -1 degree at the same flight conditions. The strain scale of Figure 370 has been reduced to 100 micro-strain because of the low amplitude response of the third and fourth harmonics. The 3P harmonic is overpredicted, and the 4P harmonic underpredicted. The majority of the predicted test points gave similar results for the 4P harmonic; both calculated and measured amplitudes were at negligible levels.

The Campbell plot, Figure 320, obtained from PTA ground testing, shows a 3P/first edgewise critical speed at 100-percent propfan speed. All of the test points chosen for predictions are at 100-percent propfan speed with the exception of the points selected to analyze the effect of propfan speed. As shown by Figure 370, the 3P predictions at 100-percent speed overpredict the strain values because of this critical speed. This overprediction arises from the lack of damping in the structural and aerodynamic model of the SR-7L blade used in the prediction code. The exact location of the 3P critical speed changes with each unique operating condition, and as a result the degree of error at the 100-percent speed condition changed greatly from case to case. Since the test data shows that the primary vibratory blade strain is at the 1P frequency and that the highest strain occurs on the inboard portion of the blade, the remaining flight test discussion will focus on 1P inboard blade and shank response trends.

The reason for the 1P propfan vibration is as follows. When a propfan is operating in a uniform flow perpendicular to the disc, each blade is subjected to the same relative velocity at the same angle of attack, and therefore, no vibratory loads are generated. When the flow enters the propfan disk at an angle, the blades now encounter relative velocities at angles of attack that are a function of azimuth. The angularity of flow is caused by yawing or pitching of the propfan shaft with respect to the

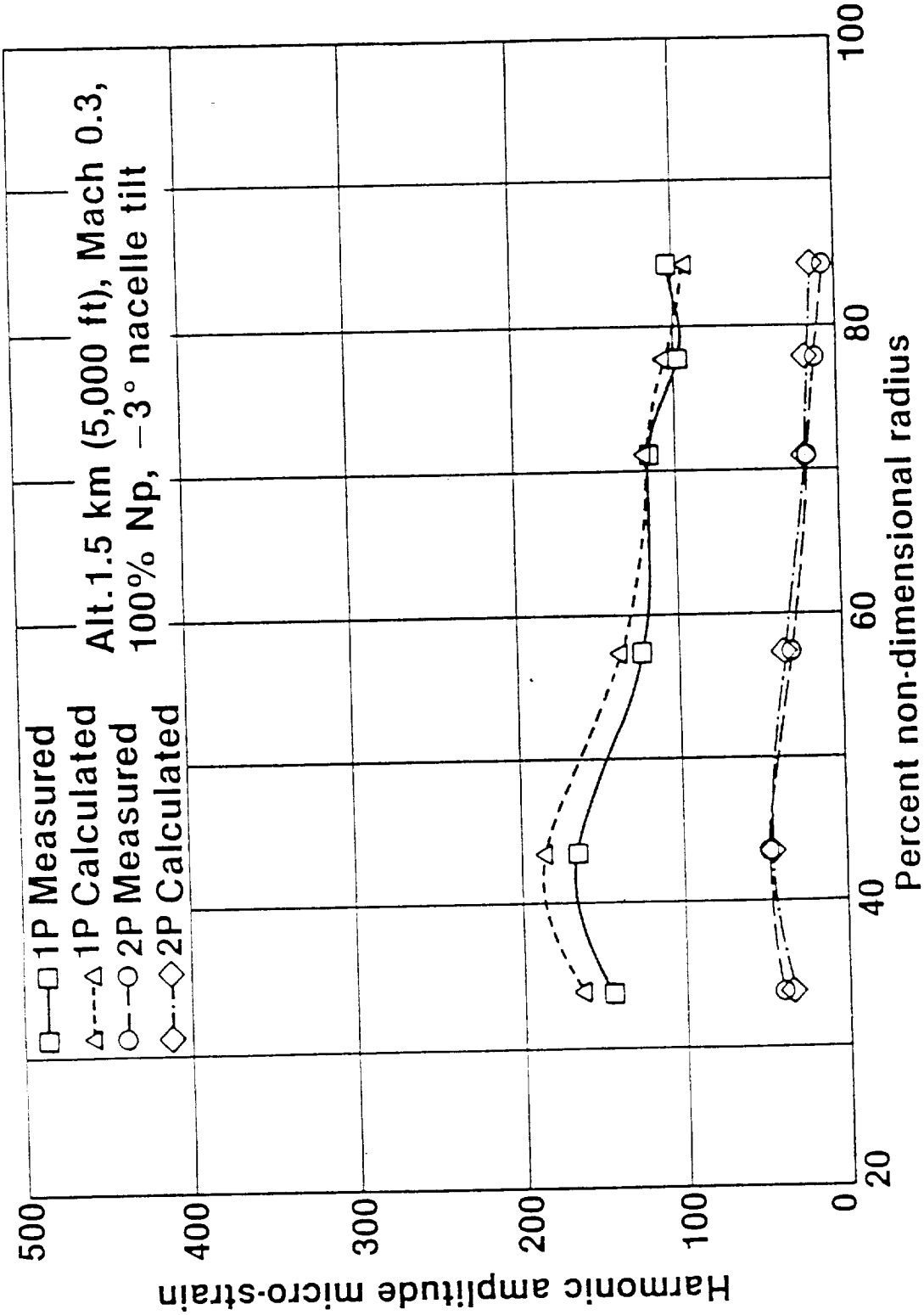


Figure 367. Radial Distribution of 1P and 2P Strain, NT = −3°

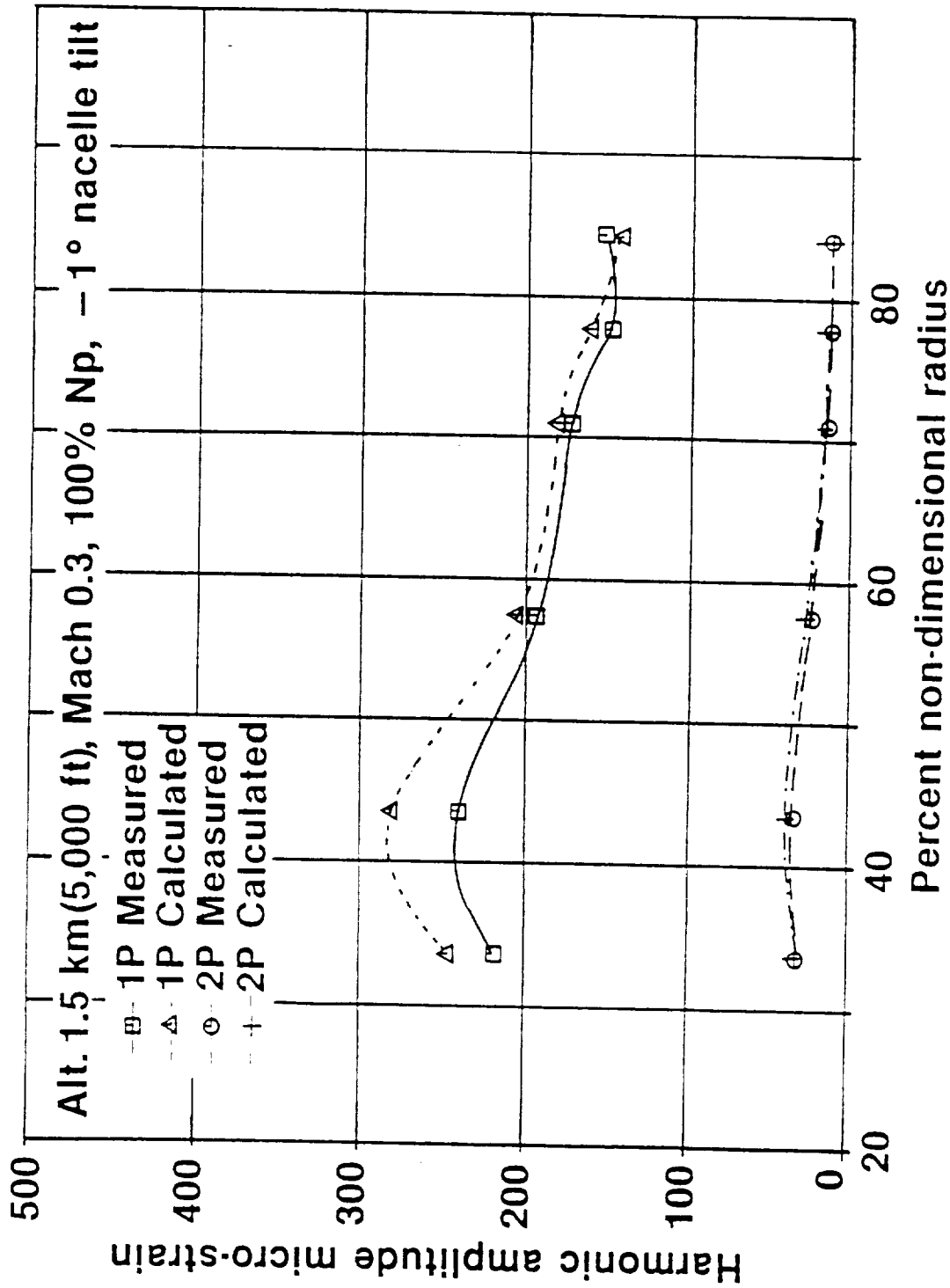


Figure 368. Radial Distribution of 1P and 2P Strain, NT = -1°

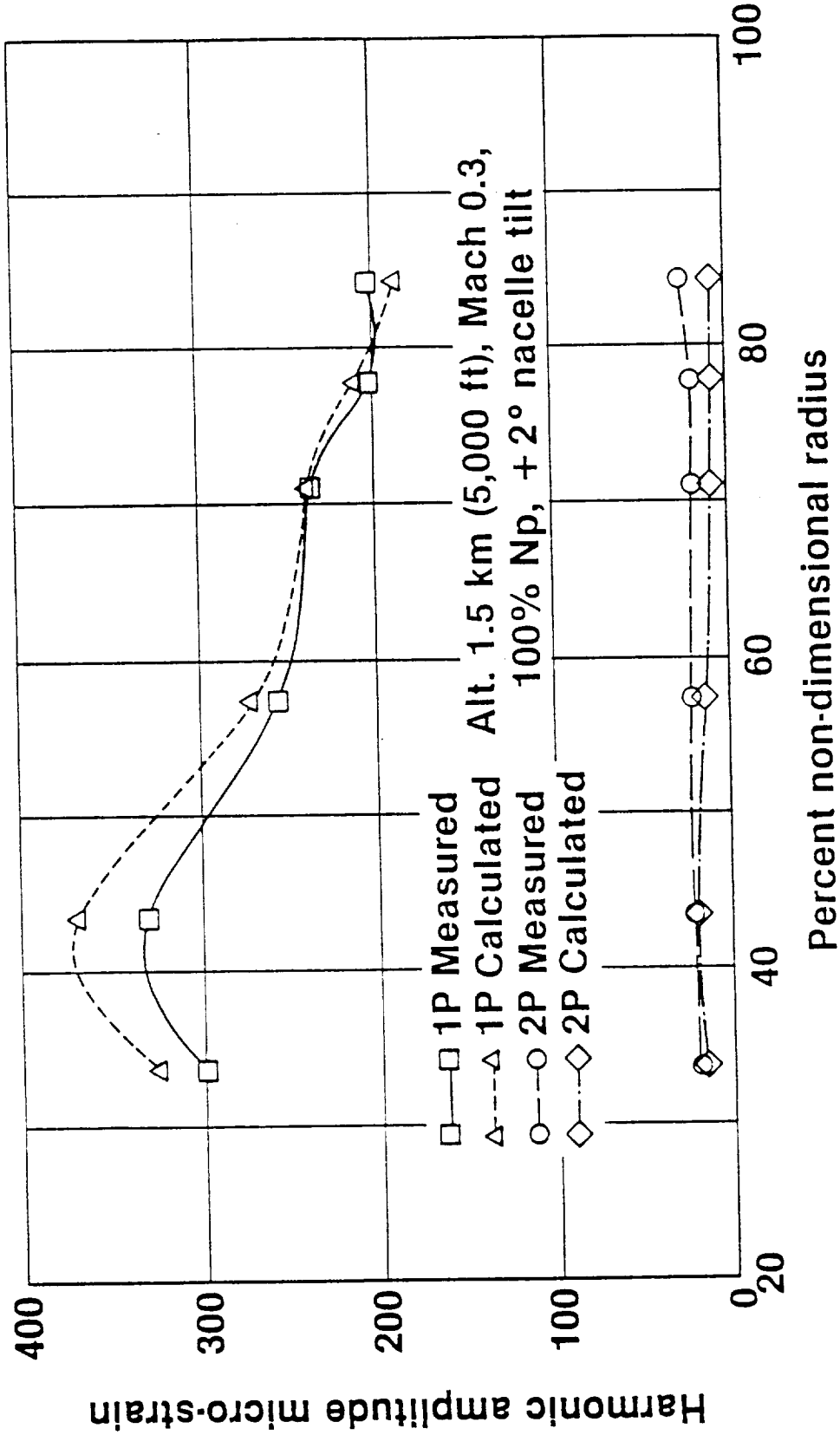


Figure 369. Radial Distribution of 1P and 2P Strain, NT = +2°

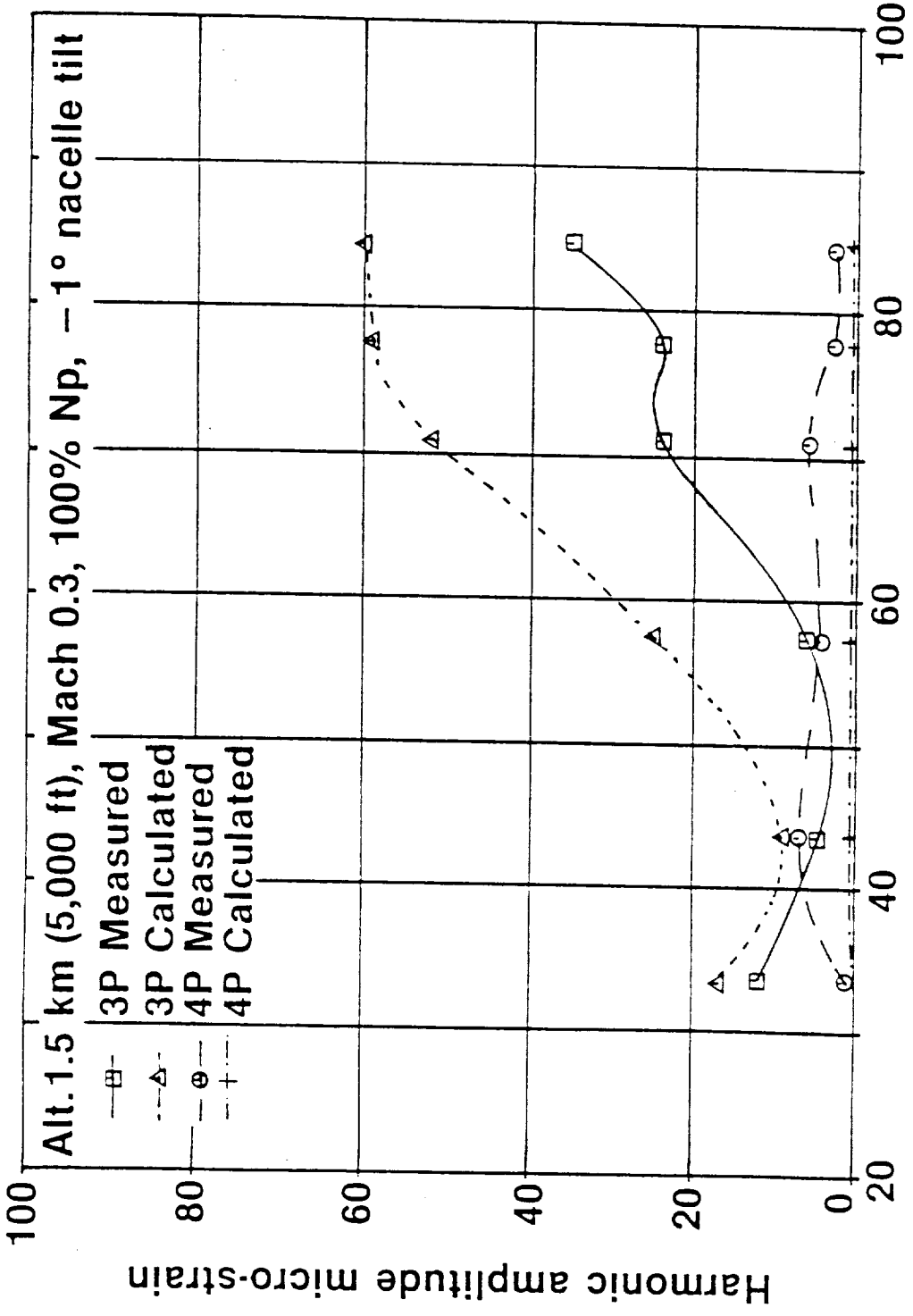


Figure 370. Radial Distribution of 3P and 4P Strain, NT = -1°

air. For each revolution, the local blade section lift varies sinusoidally, reaching a maximum and minimum for each half revolution. This vibratory load results in 1P vibration. The 1P loading on the propfan is directly related to the freestream dynamic pressure and the inflow angle into the propfan, giving rise to the definition of excitation factor:

$$EF = \Psi \times (V_{KEAS}/348)^2$$

Where:

Ψ = Inflow angle
V_{KEAS} = Equivalent airspeed in knots

EF is used as an indicator of the severity of the 1P flow environment. The SR-7L was designed for an EF of 4.5.

As illustrated by the definition of EF, the key parameters that influence blade 1P response are equivalent airspeed and nacelle tilt (inflow angle). Other secondary parameters are power, Mach number (compressibility), and rotational speed. The effect that equivalent airspeed and nacelle tilt have on the blade response is shown in Figures 371 and 372 for low altitude climb condition and a high altitude cruise condition. The general shape of the response curves with equivalent airspeed is similar for both altitudes. For the -3 degree tilt angle, the strain level initially decreases with airspeed and then begins to increase rapidly as airspeed increases, while the -1 degree tilt curves show relatively flat response with a slight decrease in strain at an intermediate airspeed. The +2 degree tilt angle shows a steady decrease in strain over the entire airspeed range. The importance of nacelle tilt is brought out when the design cruise condition of 134 mps (Mach 0.8, 35,000 ft) is examined in Figure 372. A 2 degree decrease in tilt from -1 degree to -3 degrees nearly doubles the blade response. Proper choice of tilt angle significantly affects the overall design of an installation.

To further clarify the relationship between excitation factor and blade response, the relative excitation factor for the three nacelle tilt angles, in pitch only, is illustrated in Figure 373. Changes in the magnitude of vibratory response correspond to the absolute value of the excitation factor. The blade response reaches a minimum when the EF passes through zero. The -3 degree nacelle tilt EF passes through zero at the lowest airspeed while the +2 degree nacelle tilt EF never passes through zero. Comparing Figure 373 to Figures 371 and 372 leads to the conclusion that the trend of propfan response to changes in nacelle tilt angle is as expected.

The sensitivity of blade response to nacelle tilt is shown in Figures 374 and 375 along with a comparison to predicted values of strain. Figure 374 shows the 1P and 2P response variation with nacelle tilt for an initial climb condition of maximum continuous power at Mach 0.3, 1.5 km (5000 ft). The 1P strain increases with increasing tilt angle at a rate of approximately 25 micro-strain per degree of tilt.

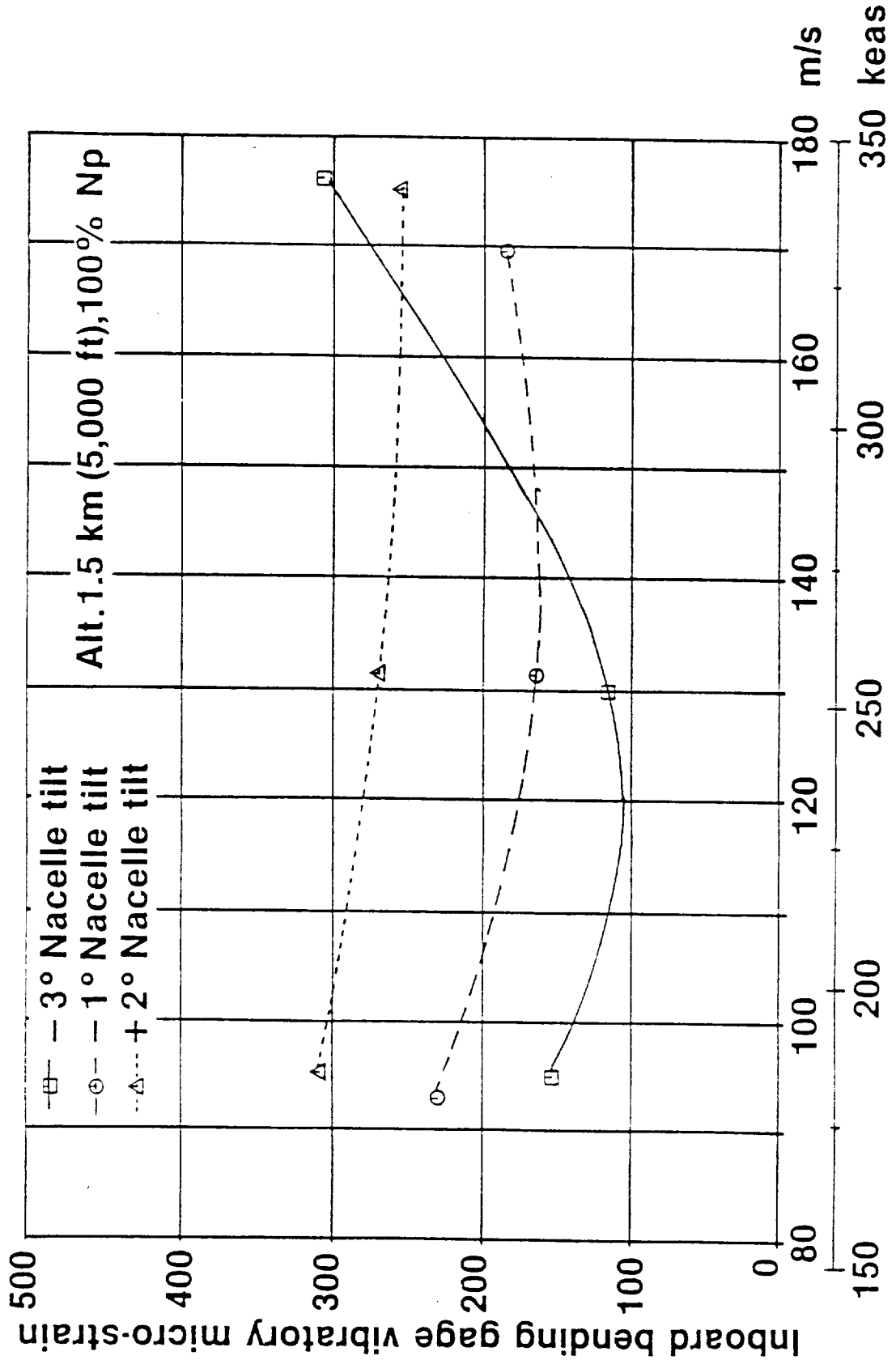


Figure 371. Effect of Airspeed on Blade Response at Low Altitude

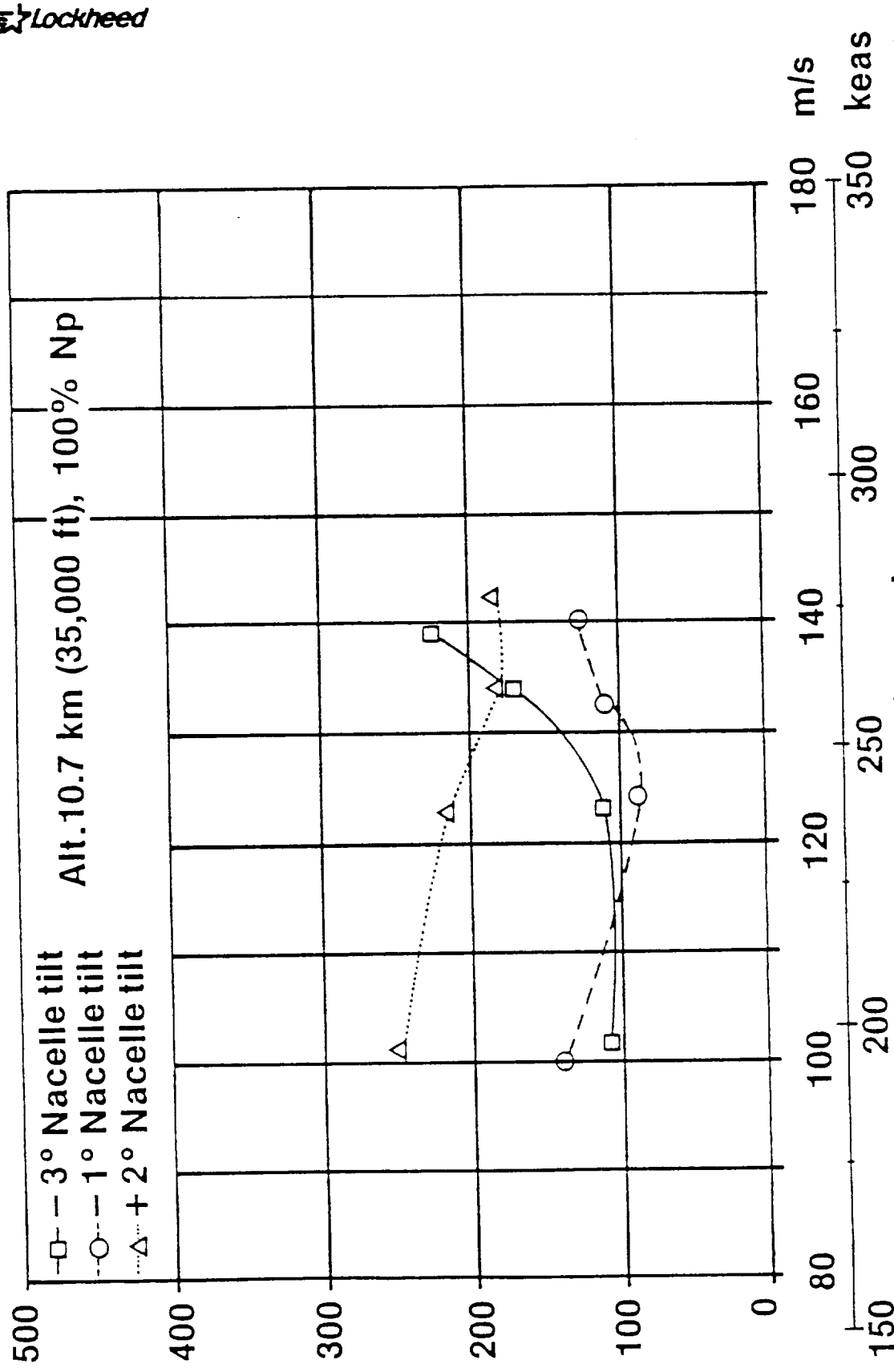


Figure 372. Effect of Airspeed on Blade Response at High Altitude

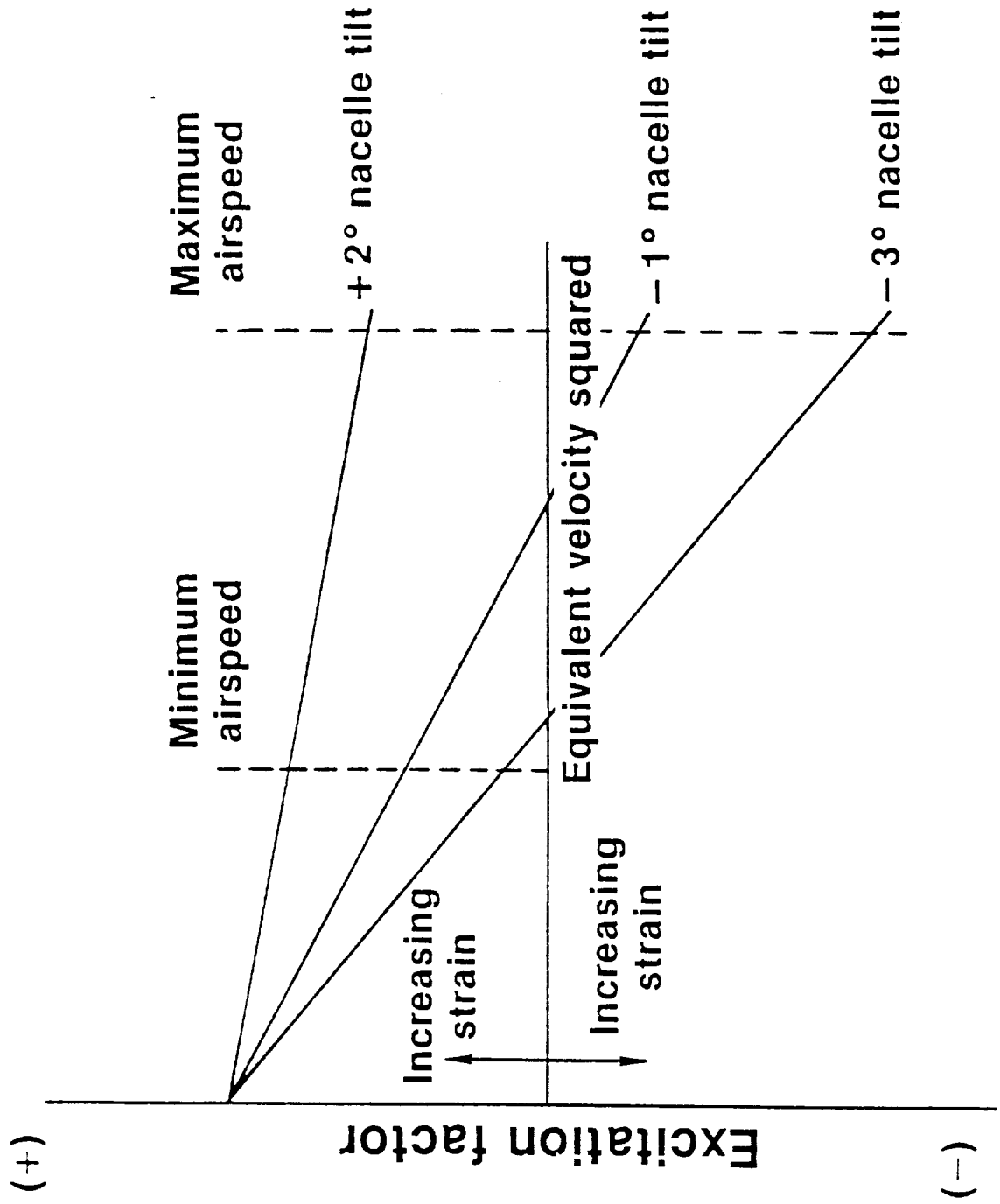


Figure 373. Propfan Relative Excitation Factor

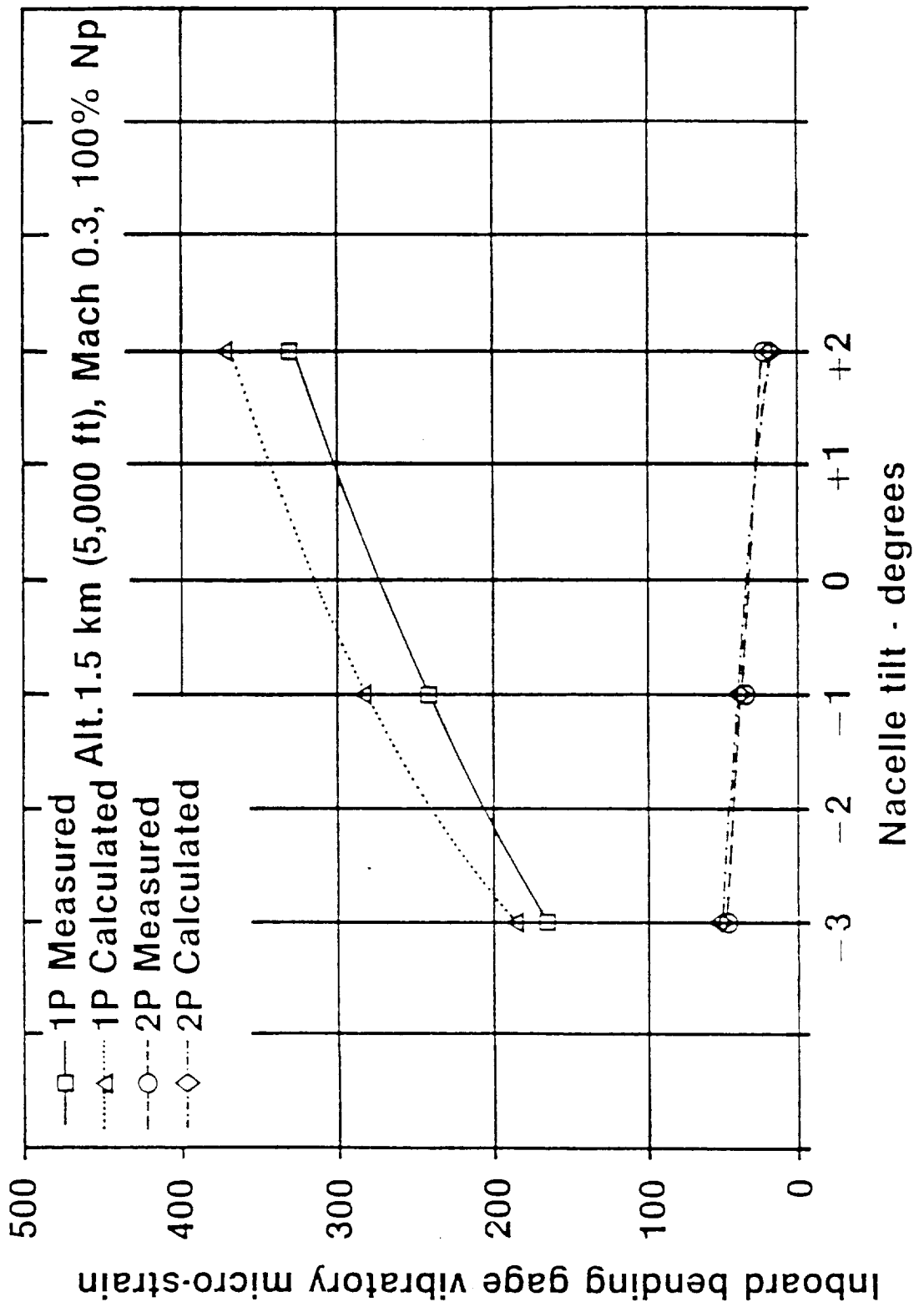


Figure 374. Effect of Nacelle Tilt on Blade Response at Low Speed

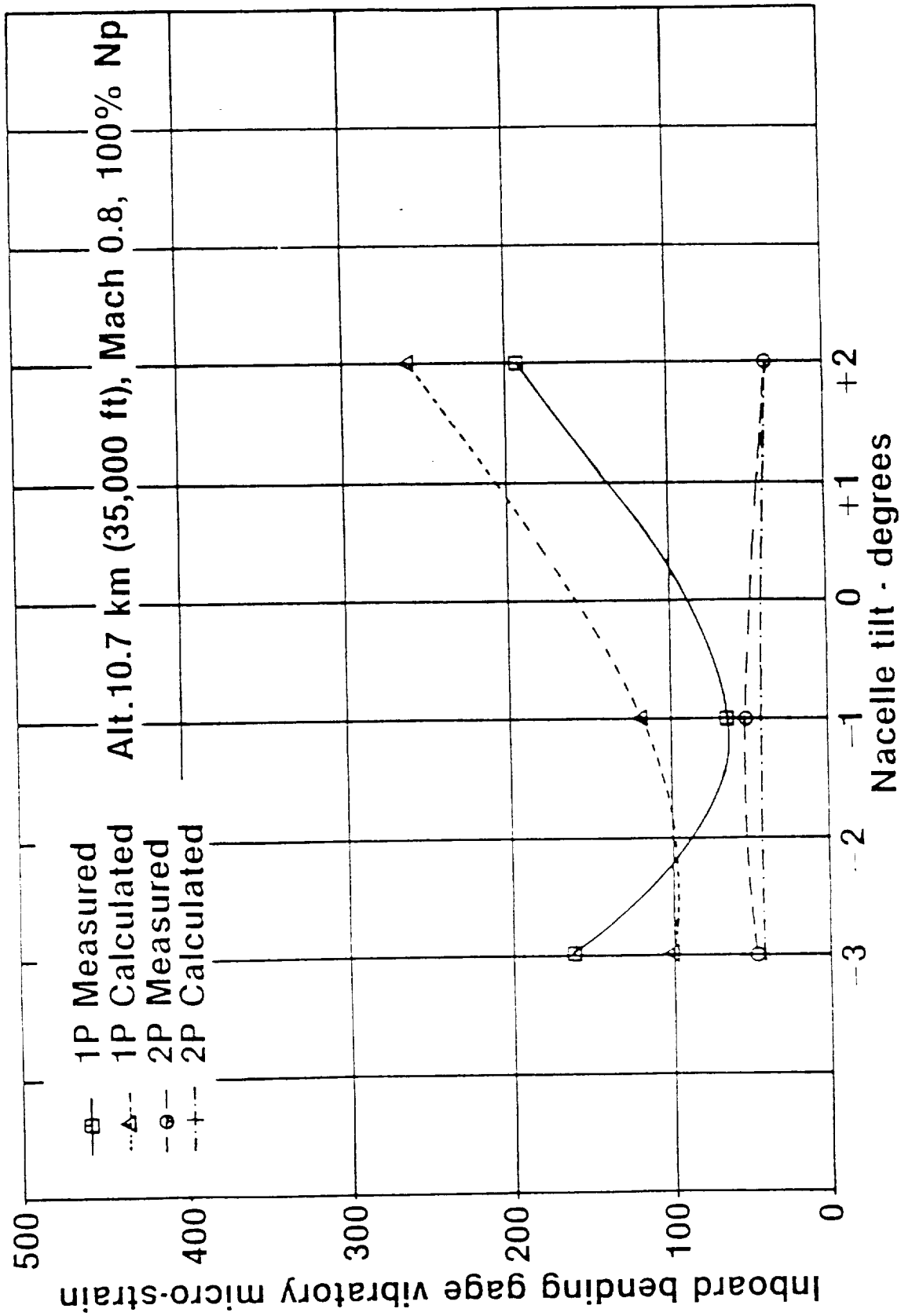


Figure 375. Effect of Nacelle Tilt on Blade Response at High Speed

Figure 375 shows the 1P and 2P response variation with nacelle tilt for a cruise condition of Mach 0.8, 10.7 km (35,000 ft). In this figure, the measured 1P strain forms a parabola around the -1 degree tilt angle with a strain increase of approximately 60 micro-strain per degree of tilt on either side of the minimum. The increased sensitivity at high speed is due to the high dynamic pressure at these conditions and can be related back to the EF which shows a linear increase with tilt but a quadratic increase with equivalent airspeed. In both figures, the 2P strain is low and relatively unaffected by the large nacelle tilt changes.

The correlation of predicted and measured 1P strain is better at the low-speed conditions in Figure 374 than at the high-speed conditions in Figure 375. To get a better understanding of why the measured and predicted values differ, the excitation factors resulting from the calculations were examined for a number of operating conditions. The computed excitation factors show that for the calculations to better correlate with measurements, the assumed down tilt would have to be increased. This suggests two areas in need of improvement that would ultimately improve the correlation. One is that the nacelle tilt used in the calculation of the flowfields could be improved, and secondly, the measurement of aircraft pitch and yaw angles could be improved. It should be noted that the aircraft pitch and yaw measurements have an accuracy of ±0.5 degree, and these values are used directly to compute the flowfields needed for the 1P calculations. In terms of accuracy of the predictions, this puts an error band of ±15 micro-strain around the 1.5 km (5000 ft) calculations in Figure 374 and an error band of ±30 micro-strain around the 10.7 km (35,000 ft) calculations in Figure 375.

After equivalent airspeed and nacelle tilt, power has the greatest effect on blade 1P response. Power is a factor because the cyclic loads are influenced by the propfan induced flow. As power is raised, the induced flow increases causing the 1P loads to increase. At low-speed climb conditions, the loads increase approximately with the square root of the power ratio. As flight speed increases, induced flow becomes less important, and the rate of increase with power falls off. Figure 376 shows the effect that engine torque, which at constant rotational speed is synonymous with power, has on the low-speed and high-speed 1P response of the propfan. As shown, at low speed the strain increases at approximately the square root of the power ratio, but at high speed power has very little effect on the response. Calculations were performed at the low-speed conditions. The calculations show a similar, but not as strong, effect as displayed by the test data. The differences between test and analysis become substantial at low power where the propfan is almost windmilling.

To gain an understanding of the importance of a calculation scheme that assumes consistent blade deflection and loads, the maximum camber values were plotted versus nondimensional blade radius for the above torque conditions on Figure 377. There was a substantial increase in camber as torque was increased, especially at span locations below 75 percent. Since camber is a function of the chordwise curvature, it is directly related to the chordwise bending deflections. This figure illustrates the importance of the calculation of the steady state blade deflected position

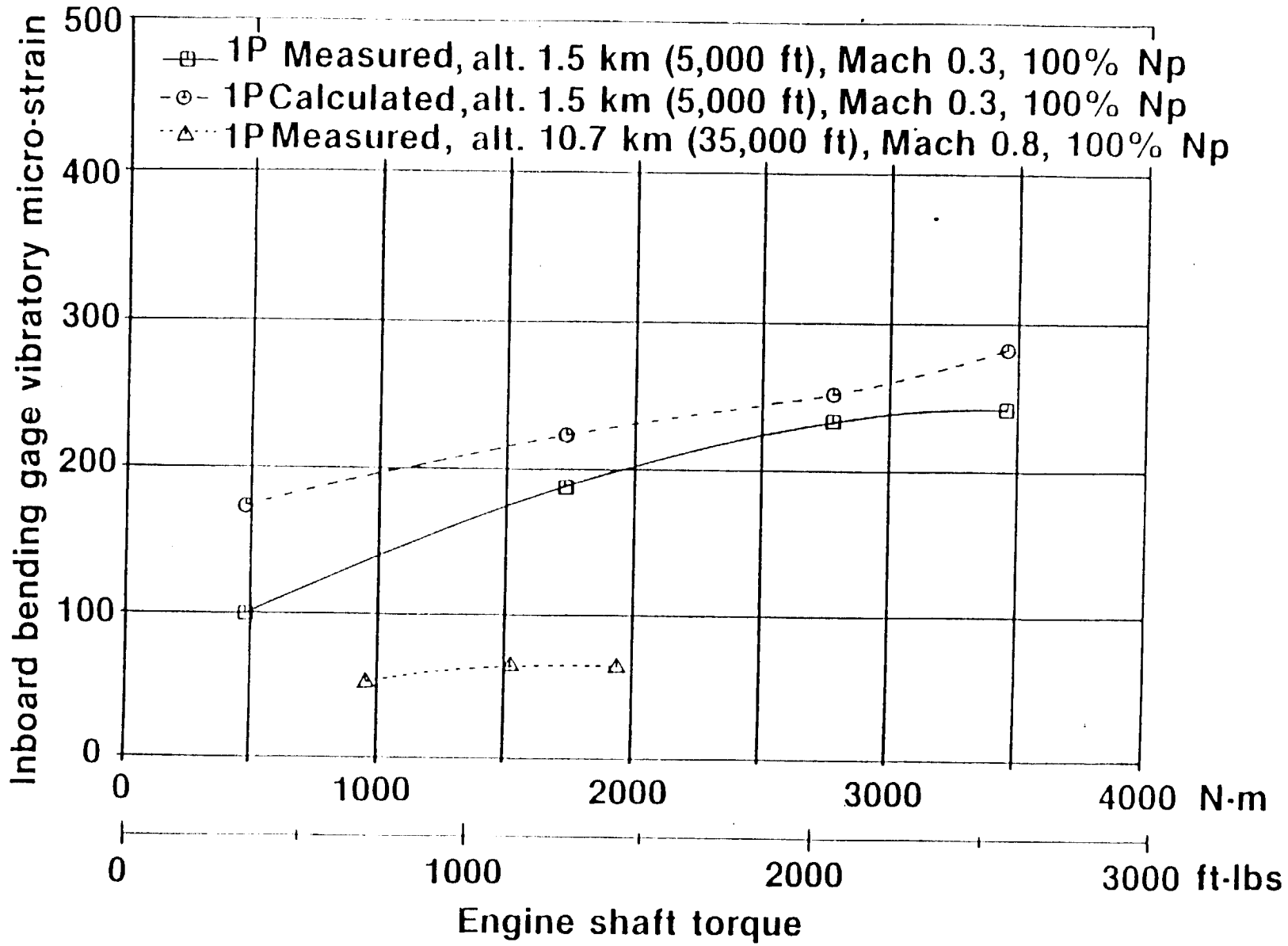


Figure 376. Effect of Torque on Blade Response

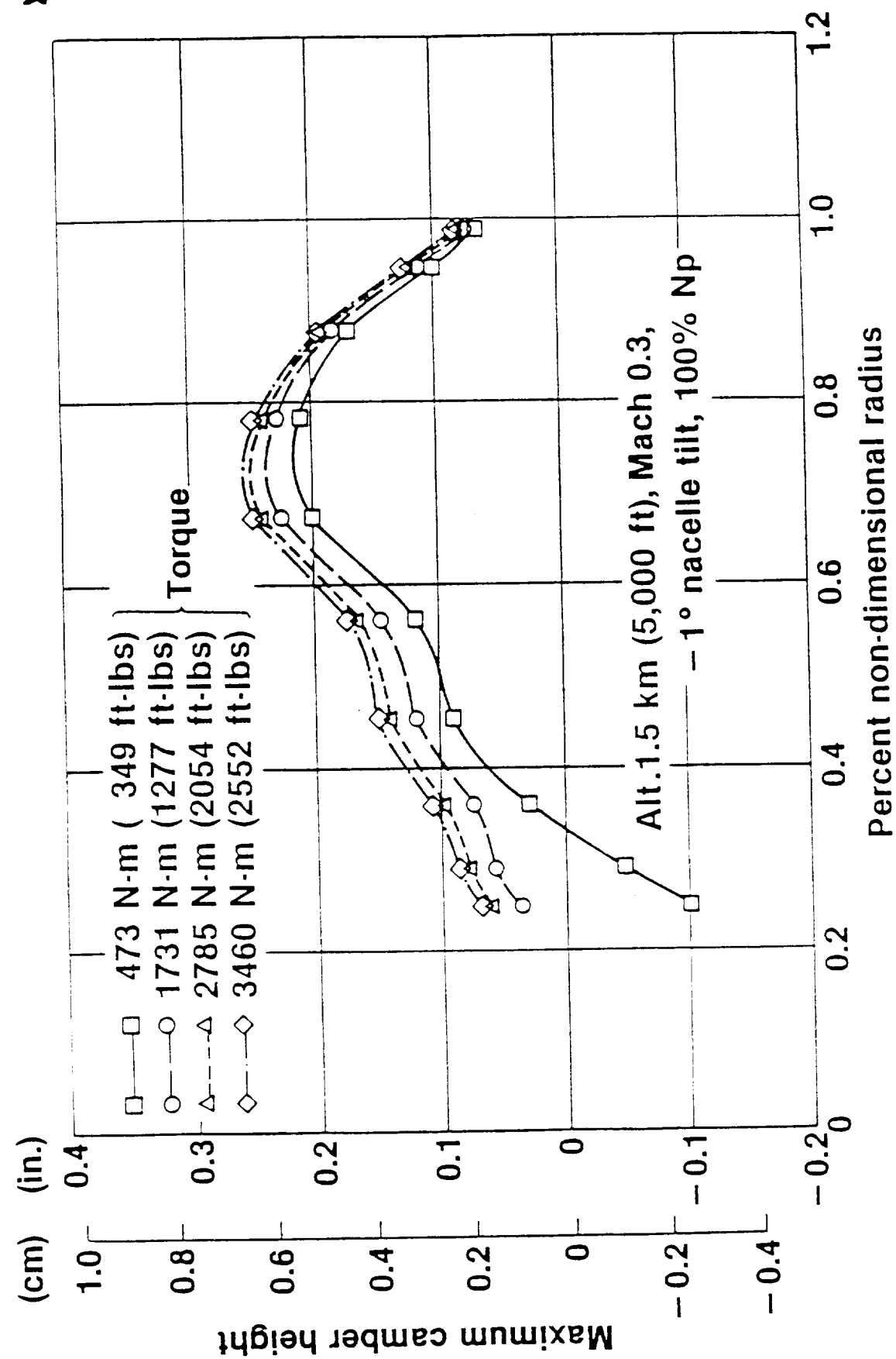


Figure 377. Calculated Camber Change with Torque

because of the impact the deflections have on camber and therefore aerodynamic loading.

The 1P and 2P calculated flatwise shank moment amplitudes are plotted in Figure 378 along with test data versus percent propfan speed at Mach 0.3, 1.5 km, and maximum continuous power. Both test results and calculations show that rotational speed has little effect on the 1P response. Through some analytical steps it can be shown that the change in 1P loading for a propfan blade is not directly related to the relative blade section velocity, which contains both freestream and rotational speed components, but is directly related to the freestream velocity as implied by the excitation factor and shown in the data.

The comparison in Figure 378 of 2P test data to calculated values correlates well at propfan speeds above 88 percent. At 78-percent speed, the calculated amplitude was substantially overpredicted. This result is due to the fact that the structural model of the SR-7L blade had no damping properties, and operating at 78-percent speed, the blades are near the 2P/1F critical speed. The 2P test data did not show a large increase in amplitude as the propfan speed was decreased to 78-percent speed. The calculated 2P curve peak location suggests that the calculated 2P/1F frequency is too high.

Figure 379 shows the 1P, 2P, and 3P flatwise shank moment test data plotted versus percent propfan speed at the design cruise point and maximum continuous power. The high-speed conditions show similar amounts of 1P and 2P excitations for the -1 degree tilt angle and negligible 3P excitation.

Figure 380 shows curves of 3P and 4P edgewise shank moment variation with propfan speed for the Mach 0.3, 1.5 km condition discussed above. The 3P amplitude is overpredicted at the 3P/1E critical speed near 100-percent propfan speed and correlated well at speeds up to 94 percent. Again, as was the case with the 2P critical speed, the calculated 3P amplitudes are much higher than test values at resonance (critical speed) because of the lack of damping in the blade model. It also appears that the calculated 3P/1E resonant frequency is too low, considering where the 3P amplitude peak is located by the test data.

The 4P calculations shown in Figure 380 are in reasonable agreement with test data although the amplitude levels are low compared to the first two harmonics of propfan speed.

The lack of influence of compressibility on 1P response is shown in Figure 381 where blade strain is plotted against Mach number for the same equivalent airspeed. The test and analysis conditions used to create this plot are all at 100-percent rotational speed, constant equivalent airspeed of 129 mps (250 KEAS), but at different altitudes so that the speed of sound changed. The only factor that could not be held constant, although it would have been desirable, was power, which was decreasing with Mach number. The 2P amplitude decreased as the Mach number increased and torque decreased. At the equivalent airspeed of 126 mps and the -3 degree nacelle tilt angle, the 1P excitation is near the minimum value

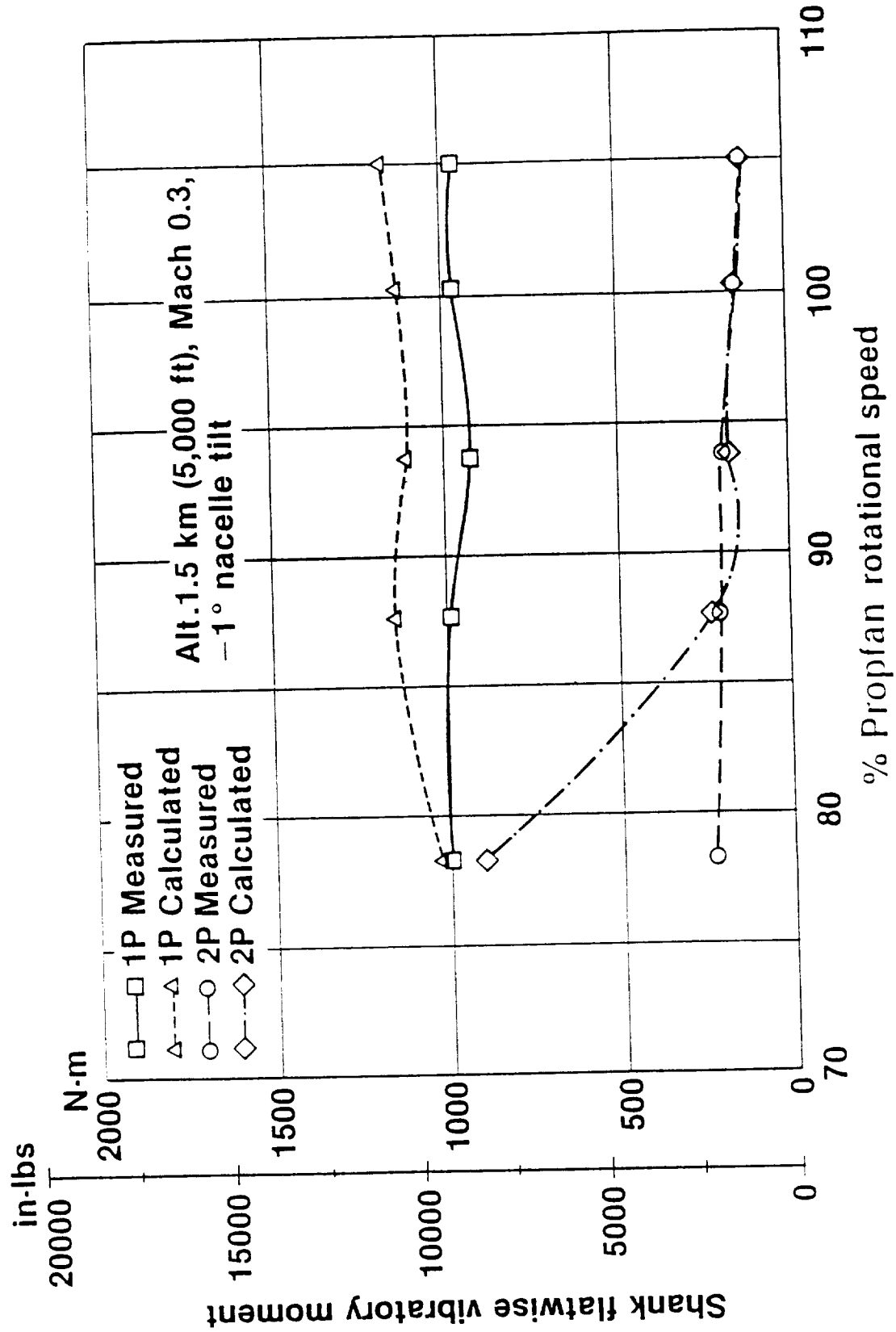


Figure 378. Effect of Rotational Speed on Blade 1P and 2P Response at Low Speed

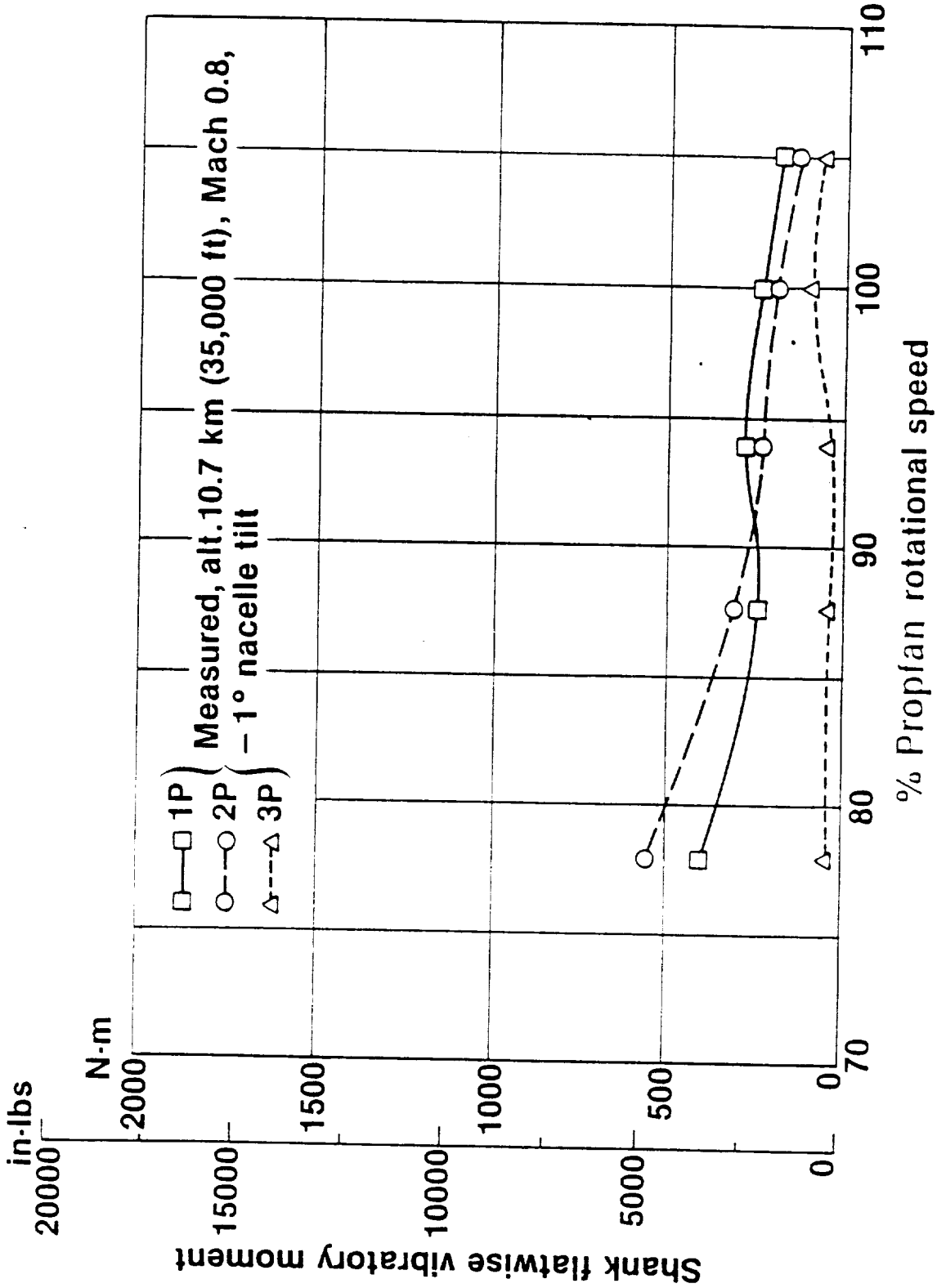


Figure 379. Effect of Rotational Speed on Blade 1P, 2P, and 3P Response at High Speeds

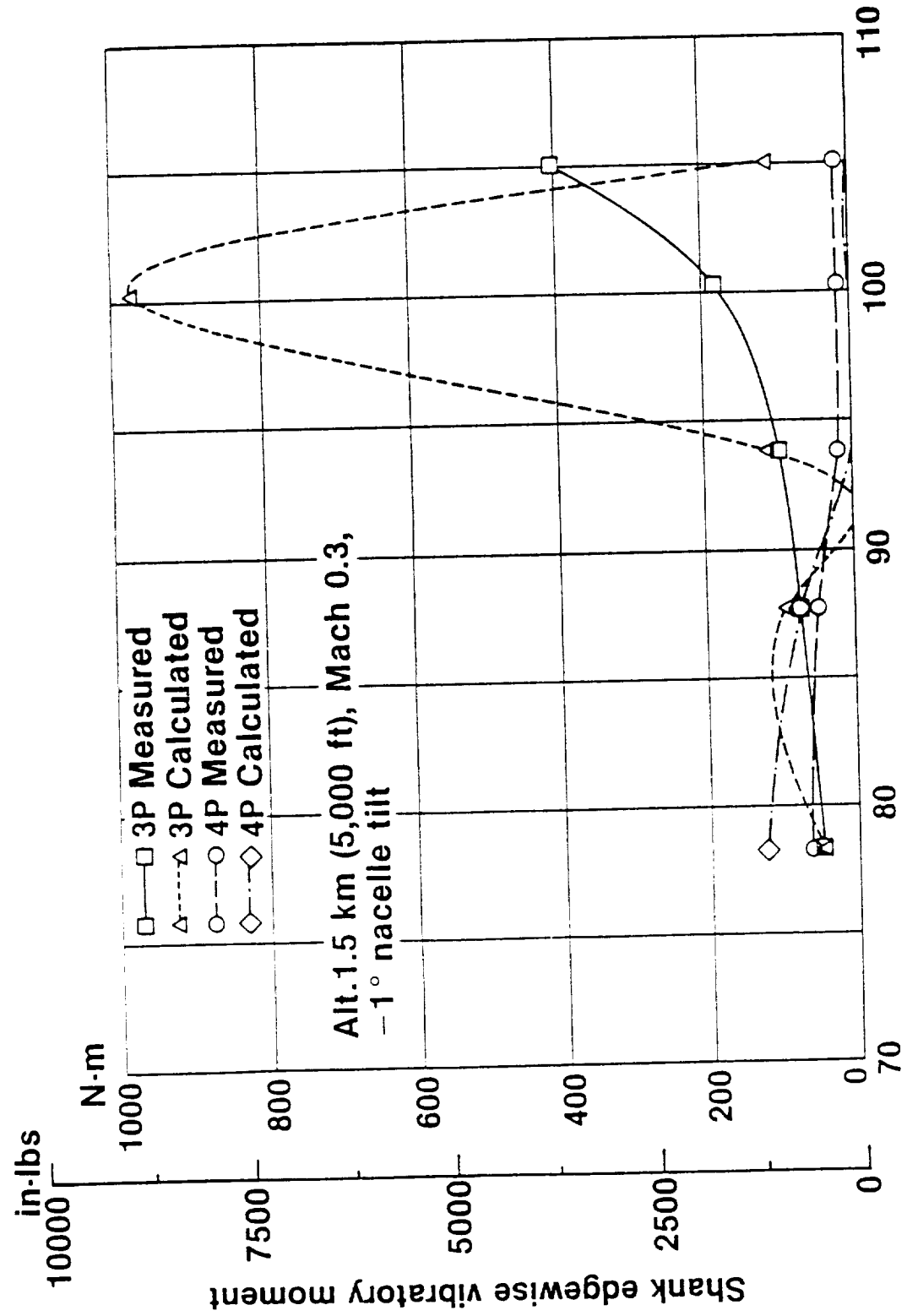


Figure 380. Effect of Rotational Speed on Blade 3P and 4P Shank Edgewise Response

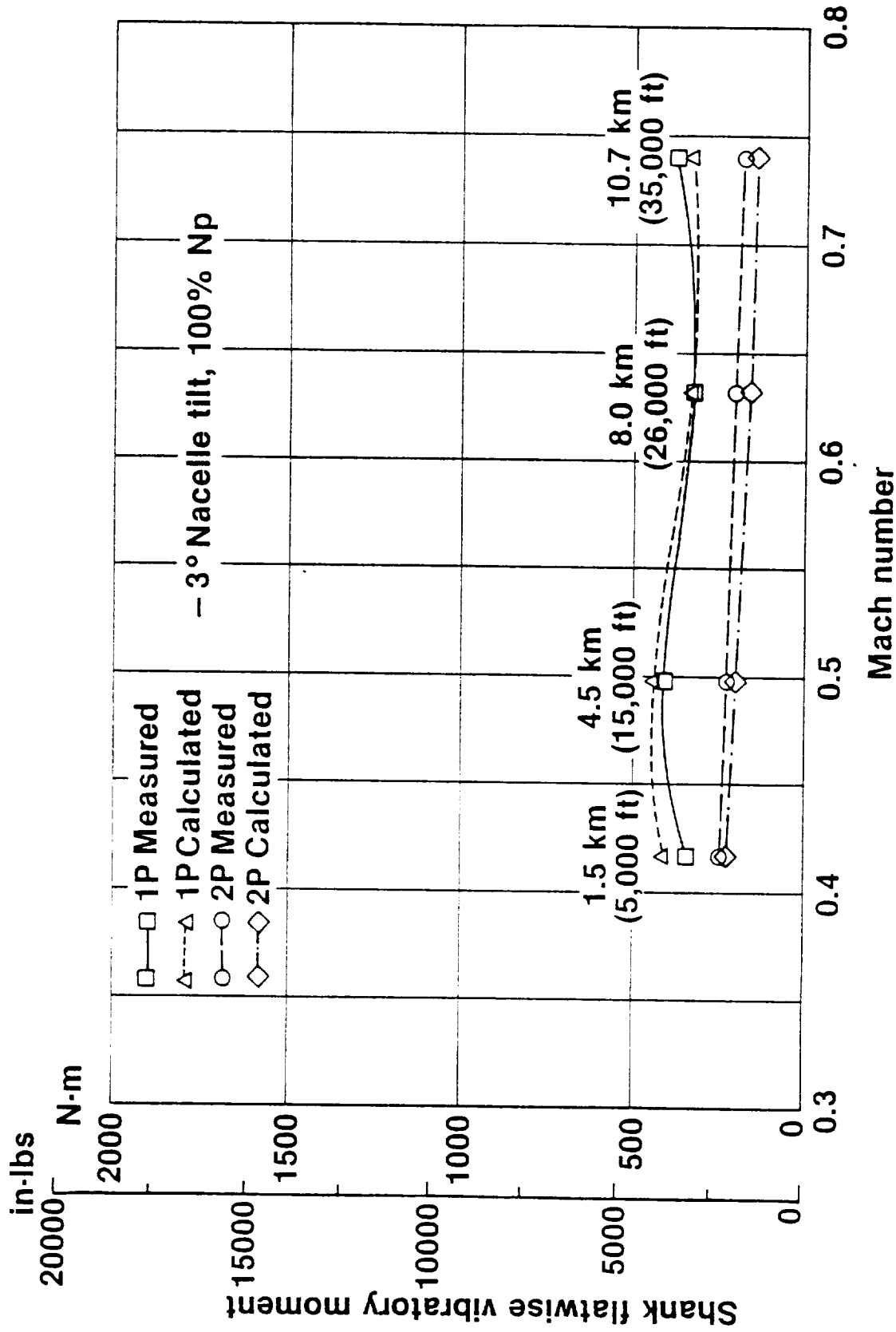


Figure 381. Effect of Mach Number on Blade Response at Constant Equivalent Airspeed

at the tested altitudes. This low excitation factor results in low 1P amplitudes over the wide Mach number range tested.

9.1.3.2 Aerodynamic Performance

Power coefficients derived from data taken during Flight Numbers 13, 15, and 19 are presented as a function of blade angle and are compared to predictions in Figures 382, 383, and 384. A smooth variation of power coefficient with blade angle was observed. The discrepancy between the measured and predicted power coefficient distribution is attributed to inaccuracies in the measurement of blade angle and the measured parameters; torque, rpm, airspeed, and density ratio; which are used to compute power coefficient and advance ratio. Periodic checks of the blade angle calibration, which were conducted during the course of the test, indicated up to a ±1 degree potential error in measured blade angle. A system accuracy analysis, which considered the individual errors in each of the measured quantities, indicated that a possible overall error of ±.09 was possible in power coefficient. In addition, the effect of blade deflections were neglected in the aerodynamic performance calculations for these off-design operating cases.

9.2 NEAR-FIELD NOISE TESTS

9.2.1 Objectives and Scope

The objectives of the high-altitude, near-field noise tests were to measure acoustic data on the surfaces of the wing and fuselage, on the wing acoustic boom, and in the cabin, in enough detail to define:

- Source noise characteristics
- Source pressure levels on the fuselage surface
- Fluctuating pressure levels on surfaces in the propfan wake
- The relative importance of airborne and structureborne noise

The basic flight test envelope and test points obtained were shown in Figures 360 through 362. The letters identifying each point and the inset tables show the matrices of power and rotational speeds obtained for those points.

Figure 385 shows another set of test points obtained for flights with the propfan blades removed. These tests were performed to evaluate background noise and provide a basis for removing this background noise so that noise for the propfan alone could be obtained. Finally, Figure 386 shows test points at which cabin noise surveys were made with the TRAM.

9.2.2 Test Procedures

Test procedures were the same as those for the high-altitude blade structural evaluation tests.

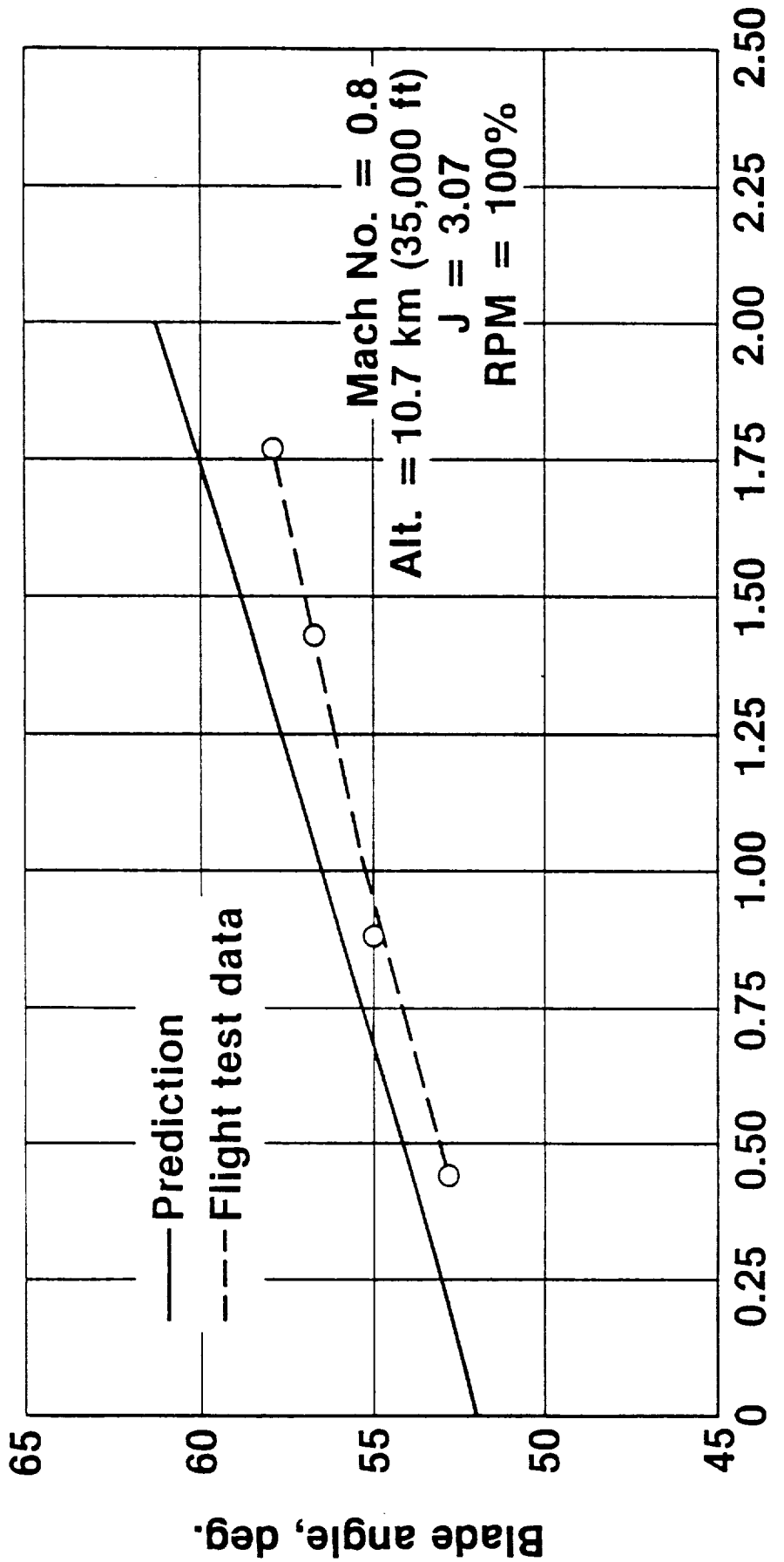


Figure 382. Comparison of Measured and Predicted Propfan Performance, Mach 0.8, J = 3.07

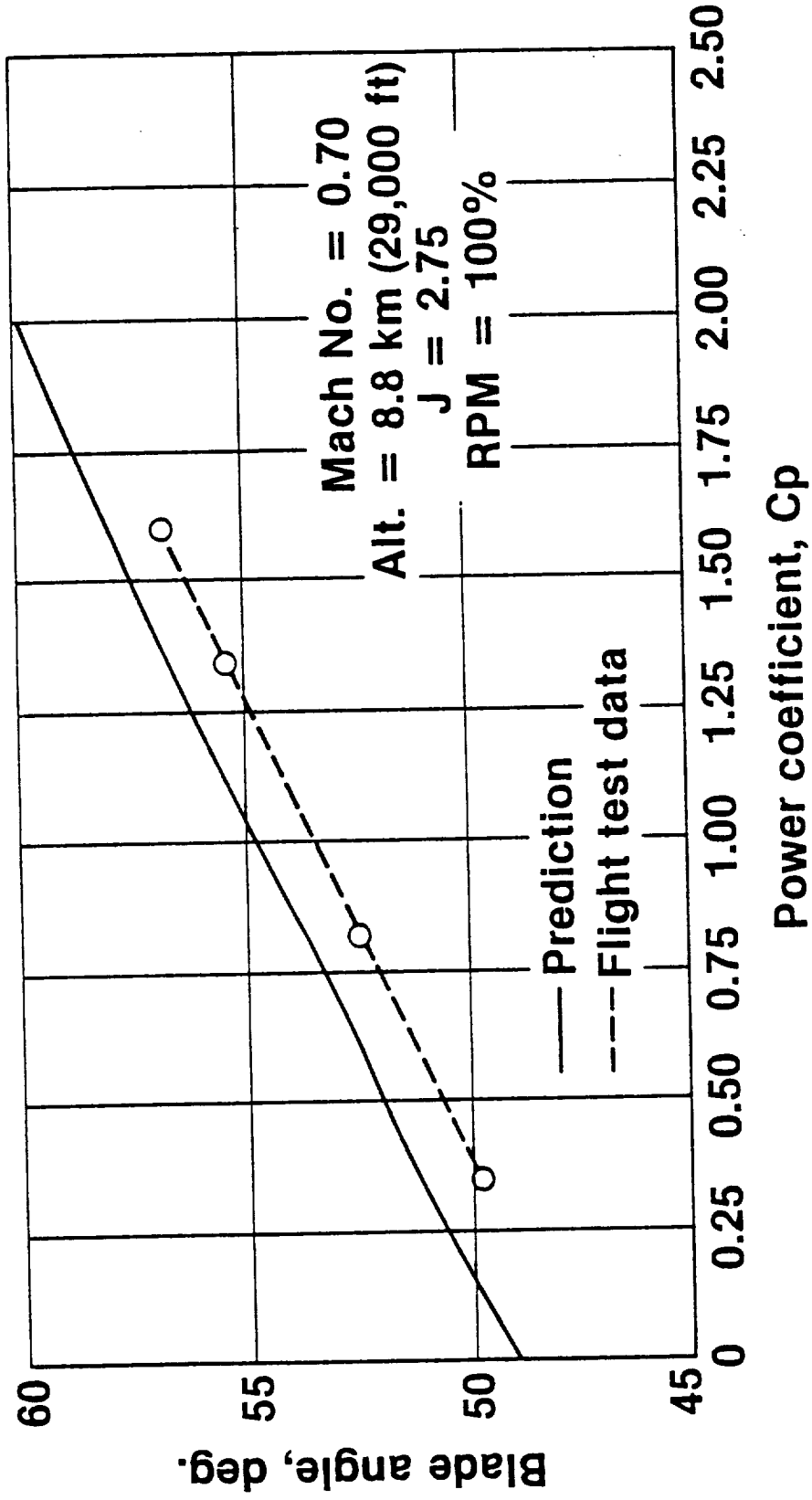


Figure 383. Comparison of Measured and Predicted Propfan Performance, Mach 0.7, J = 2.75

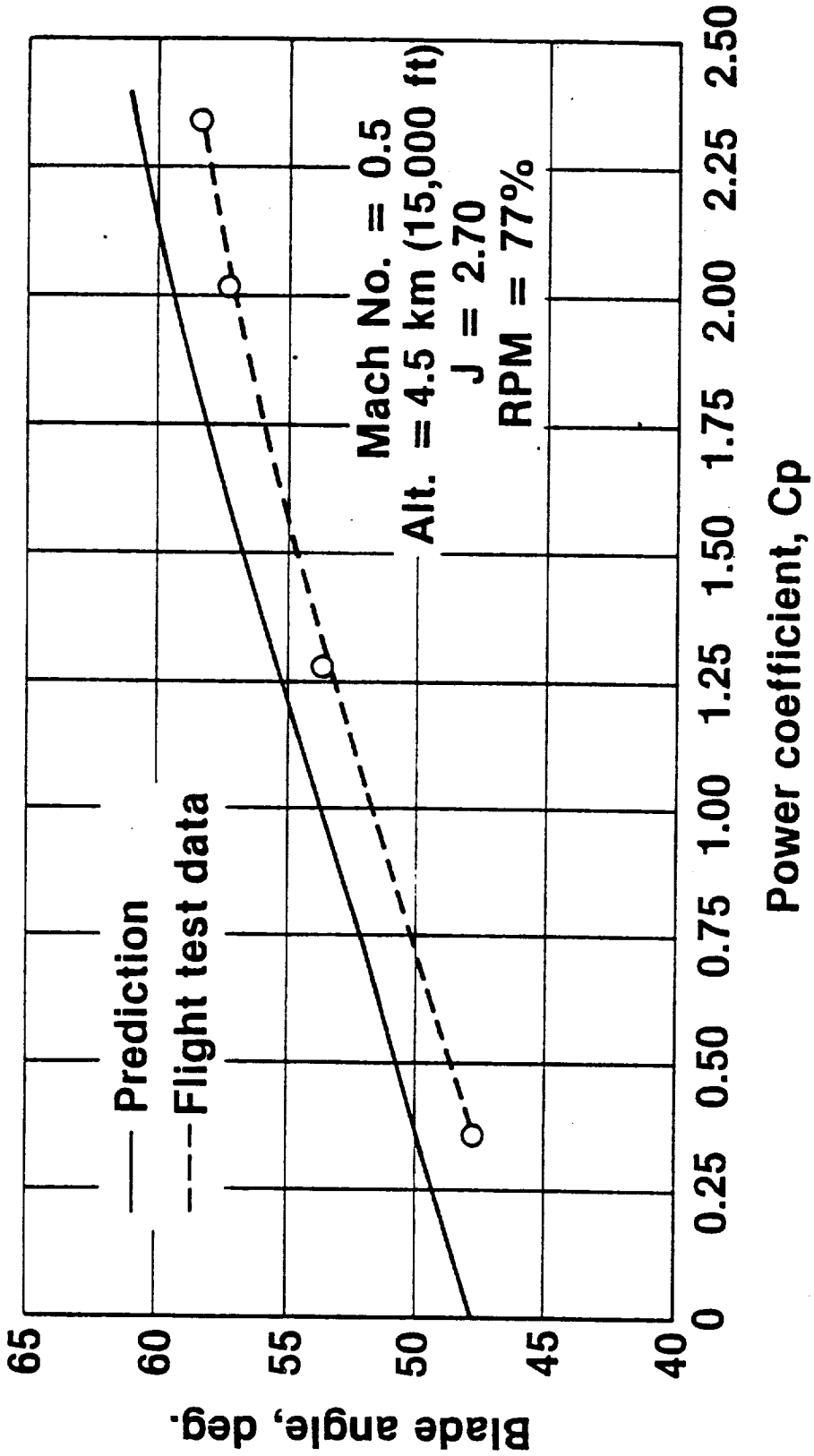


Figure 384. Comparison of Measured and Predicted Propfan Performance, Mach 0.5, J = 2.70

A

SPEY ENGINE THRUST	
NO. 1	NO. 2
FLT IDLE	MAX CRUISE
FLT IDLE	70%
FLT IDLE	40%
FLT IDLE	10%

B

SPEY ENGINE THRUST	
NO. 1	NO. 2
MAX CRUISE	MAX CRUISE
70%	MAX CRUISE
40%	MAX CRUISE
FLT IDLE	MAX CRUISE

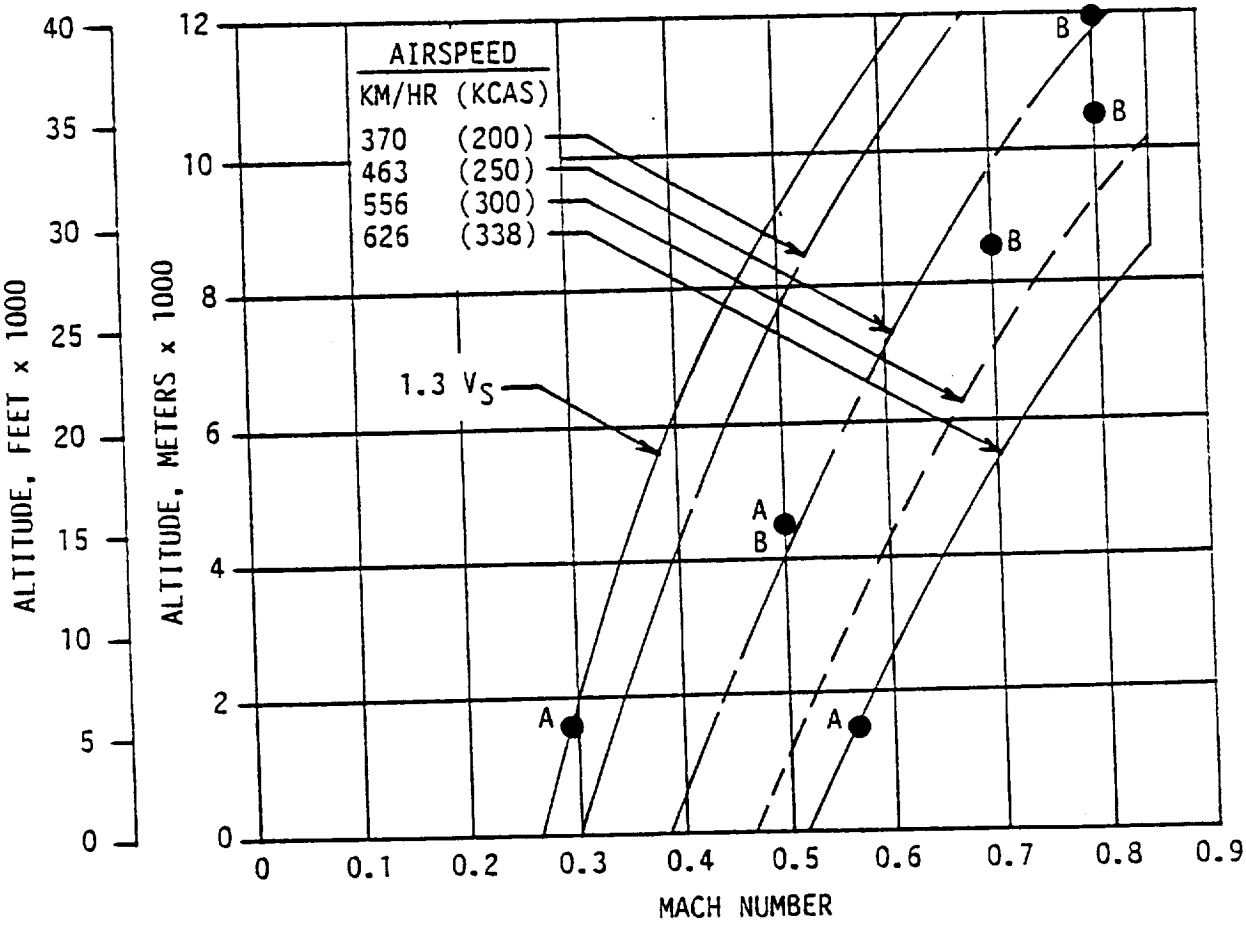


Figure 385. High-Altitude Flight Test Envelope - Propfan Off

A & B

POWER / N_p	77%	87.5%	100%	105%
MAX CONT	X	X	X	X

SET SPEY ENGINES EQUALLY AT THRUST REQUIRED FOR LEVEL FLIGHT

FOR EACH "A" TEST CONDITION SHOWN, POSITION TRAM AT 18 DISCRETE POSITIONS SPACED AT 10.25-INCH INTERVALS BETWEEN FS 250 AND FS 440

FOR EACH "B" CONDITION SHOWN, POSITION TRAM AT FS 301 AND RECORD DATA WITH FUSELAGE UNPRESSURIZED AND WITH MAXIMUM APPROVED CABIN PRESSURE SETTING

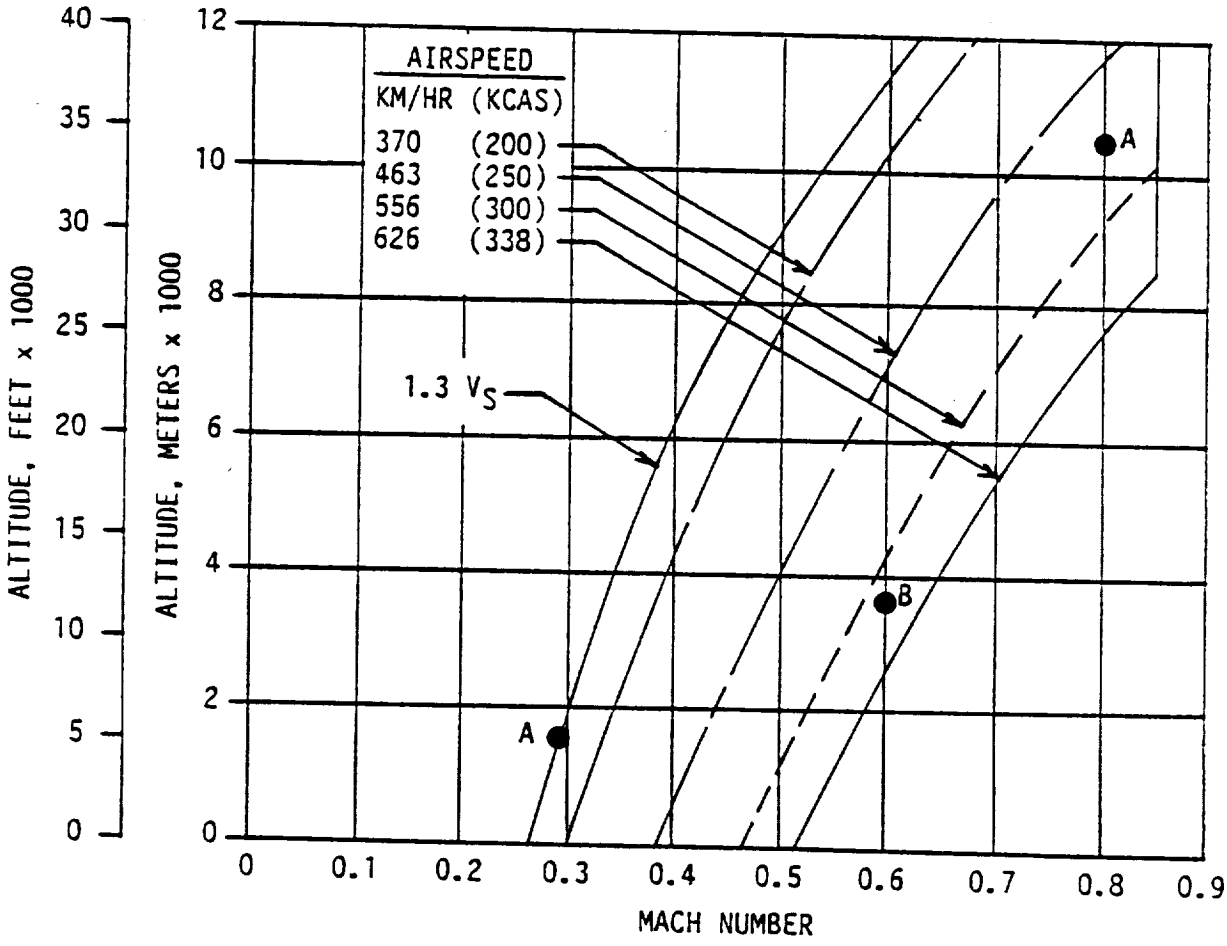


Figure 386. High-Altitude Flight Test Envelope for Cabin Noise Surveys

9.2.3 Results and Discussion

9.2.3.1 Sound Pressure Levels

The sound pressure levels (SPLs) measured on the fuselage and acoustic boom included contributions from the propfan, the propfan drive system, the Spey engines, surface boundary layer, and miscellaneous other sources.

Figure 387 shows a typical fuselage SPL measured in the propeller plane with the propfan powered, and Figure 388 shows data from the same transducer for a propfan-off test. Spey engine power was the same in both cases. The discrete tones produced by the propfan at blade passage frequency (BPF) and higher orders of BPF can be clearly seen in Figure 387. Figure 388 shows no such tones but does show a high noise level at frequencies less than 300 Hz that was not measured with the propfan on. This might have been a cavity noise from the windmilling propfan engine inlet, but appears to have little significance since it was only measured in the propfan-off cases.

The more important observation from a comparison of Figures 387 and 388 is that broadband noise levels at frequencies greater than about 500 Hz are about the same with propfan on and off. This says that propfan broadband noise was buried in the background noise and would be difficult, if not impossible, to extract from the background noise; but it also says that propfan broadband noise is at most no greater than the level indicated in Figure 388, and that propfan noise was clearly dominated by the tone noise shown in Figure 387.

Figure 389 shows a comparison of spectra from microphones on the wing boom and on the fuselage for the design cruise condition. Major differences between the two are the levels of the tone noise signals and the levels of the broadband noise. The higher tone noise levels on the fuselage are attributable to pressure doubling effects; the higher broadband noise is attributed to the thicker boundary layer on the fuselage.

Because propfan noise was dominated by tone noise, most of the discussion that follows is based on observations and analyses of tone noise levels. Furthermore, in analyzing the effects of power, tip speed, etc., the noise levels selected were generally the maximum values measured in a given region of the aircraft.

The distribution of SPL at BPF over the surface of the fuselage facing the propfan is shown in Figure 390. The maximum SPL was 147.1 aft of the propfan plane, a distance equivalent to approximately $D_p/4$, and near but slightly below the waterline of closest approach. The region where SPLs were greater than 140 dB approximated a circle with diameter equal to D_p.

Circumferential distribution of SPLs around the fuselage in the propfan plane is shown in Figure 391. Here the maximum noise near the point of closest approach is evident, together with the rapid diminution of noise levels in the regions facing the propfan less directly.

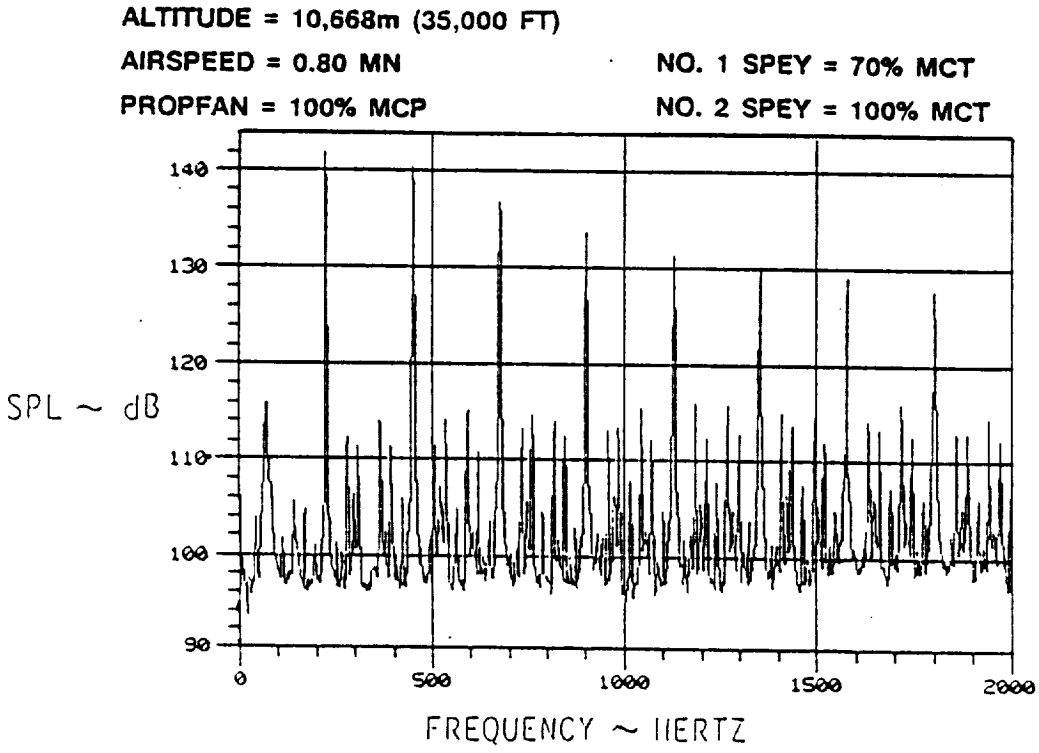


Figure 387. Effects of Near Side Spey Engine on Fuselage Noise - Prop On

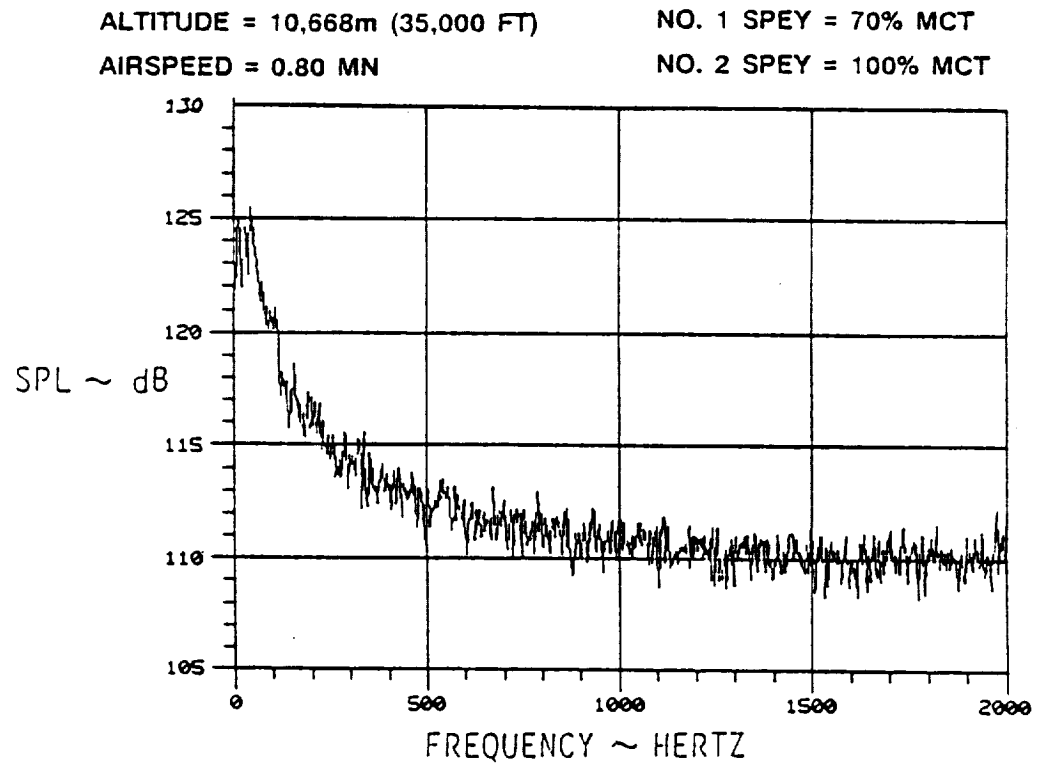


Figure 388. Effects of Near Side Spey Engine on Fuselage Noise - Prop Off

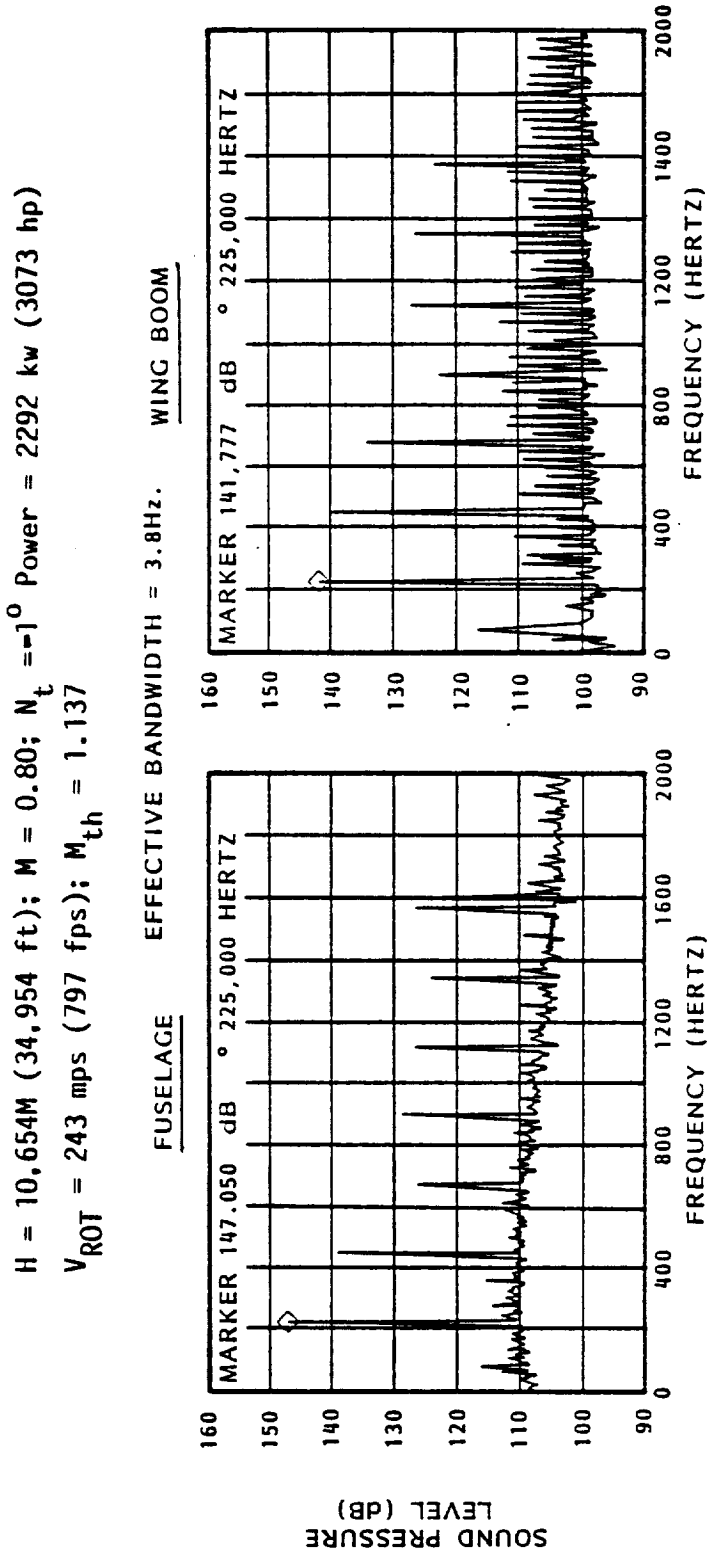


Figure 389. Sound Pressure Spectra on Fuselage and Acoustic Boom

FIRST ORDER OF BPF (226 Hz)
NACELLE TILT = -1°
ALTITUDE = 10,654m (34,954 FT)
AIRSPEED = 0.80 MN

V_{ROT} = 243 MPS (797 FPS)
POWER = 2292 KW (3073 HP)
M_{TH} = 1.137

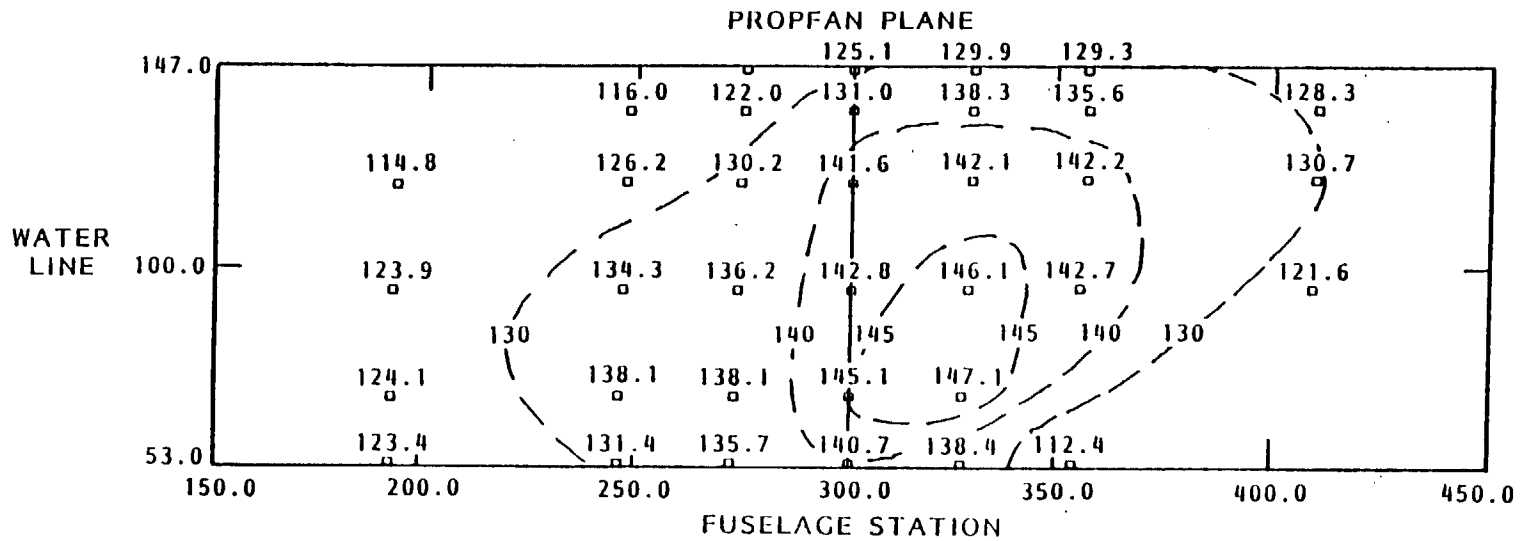


Figure 390. Sound Pressure Distribution on Fuselage

FIRST ORDER OF BPF (226 Hz)
NACELLE TILT = -1°
ALTITUDE = 10,654m (34,954 FT)
AIRSPEED = 0.80 MN

V_{ROT} = 243 MPS (797 FPS)
POWER = 2292 KW (3073 HP)
M_{TH} = 1.137

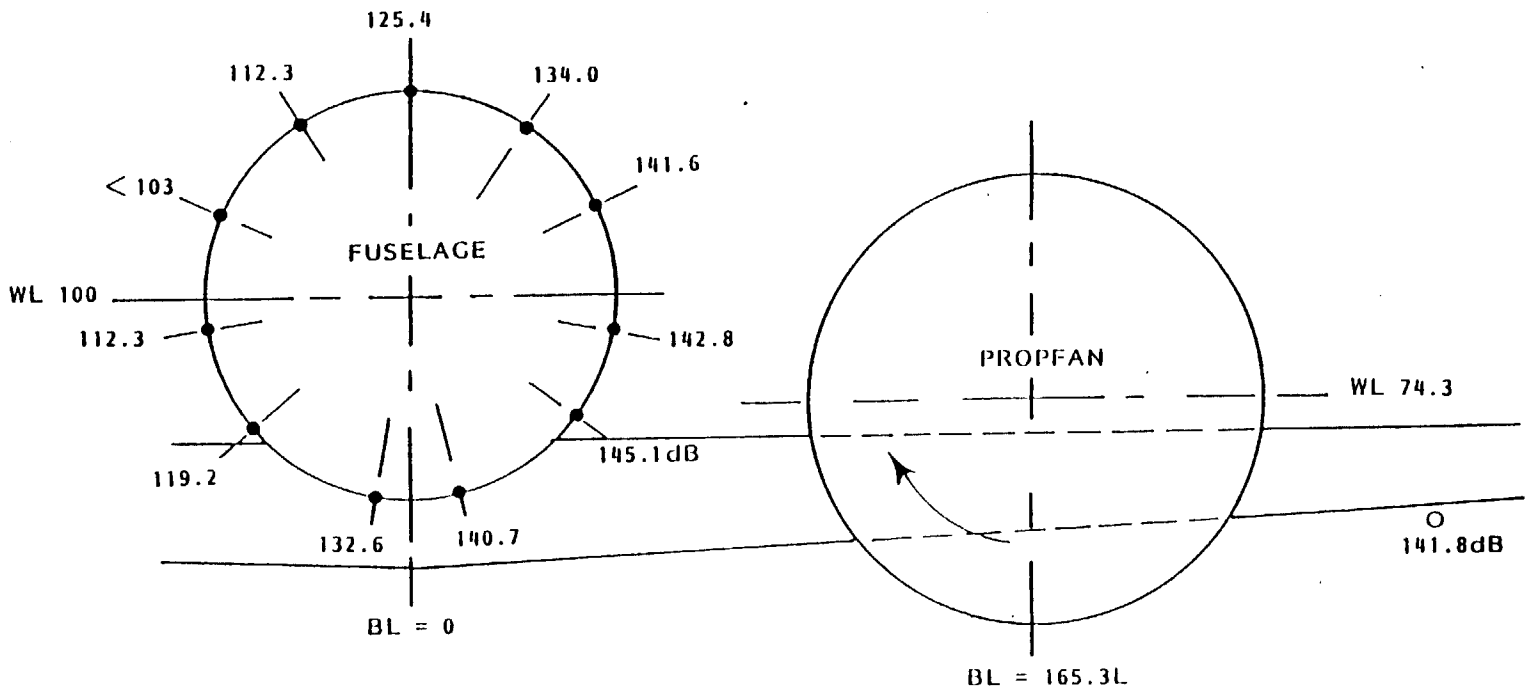


Figure 391. Circumferential Distribution of SPL on Fuselage

The variation of fundamental tone SPL on the fuselage with propfan power is shown in Figure 392 for several constant rotational speeds. These plots are for the design cruise condition where the helical tip Mach number ranged from 1.02 to 1.16.

The noise signals presented in these plots are made up of contributions due to blade loading and blade thickness. As power is increased, it is expected that loading noise would increase, and vice versa. If blade loading is decreased and noise levels do not diminish, there is the implication that some other noise mechanism is beginning to control. This is the case for the two highest tip speeds shown in Figure 392 where there appears to be a noise "floor." This suggests that for high tip speeds and lower powers, thickness noise dominated in these results. For the other conditions represented in Figure 392, loading noise appears to be the dominant mechanism.

In Figure 393, fuselage noise data are plotted against propfan thrust for several constant rotational speeds. Generally, the attainment of higher thrust was accompanied by an increase in noise. At the highest thrust levels, however, the highest noise level was measured at the rotational speed of 243 mps (797 fps) with slightly lower noise levels on either side of that point.

Noise levels are displayed as functions of propfan power coefficient, advance ratio, and blade angle in the carpet plot of Figure 394. The SPLs for the propfan fundamental tone increased in level in an orderly manner with decreasing advance ratio and increasing power coefficient. There was no optimum design combination for minimum noise.

Values of area maximum SPL at BPF are shown in Figure 395 in terms of where they occurred in the flight test envelope. The data trends are orderly in that SPL increased with flight Mach number at a given altitude and increased slightly with altitude at constant Mach number--at least up to about 10,668m (30,000 ft). Thus SPL was maximum at the design cruise condition and lower for climb-out. The same trends were followed for the higher order tone levels.

A similar presentation is shown in Figure 396 but this time to show the reduction in levels from first to second order tone. Generally, the second order tone levels were about 5 to 7 dB lower than the first order levels.

The variation of SPL with helical tip Mach number is shown in Figure 397. Increasing tip Mach number produced a steady rise in noise levels for all flight conditions, and the rate of increase is approximately the same for all conditions. There is no difference between the rate of increase for subsonic and for supersonic cases.

Test cases were planned to produce data that would enable an evaluation of the parameter ρc^2 for altitude scaling of acoustic pressures. The tables of Figure 398 show five pairs of test points--two for supersonic tip speeds and three for subsonic. In each of these five cases, data were

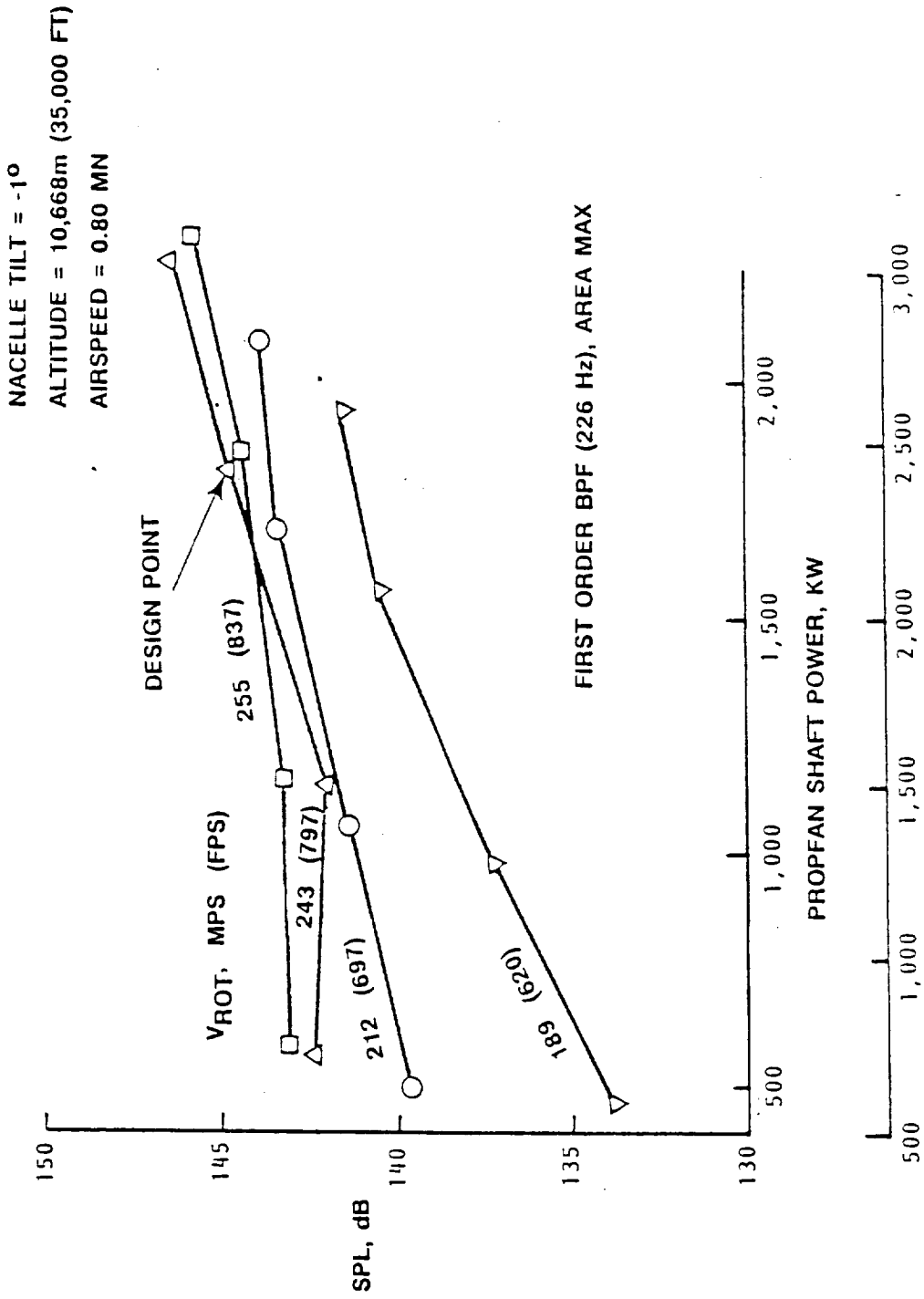


Figure 392. Effects of Power Variation at Constant Tip Speed on Fuselage SPL

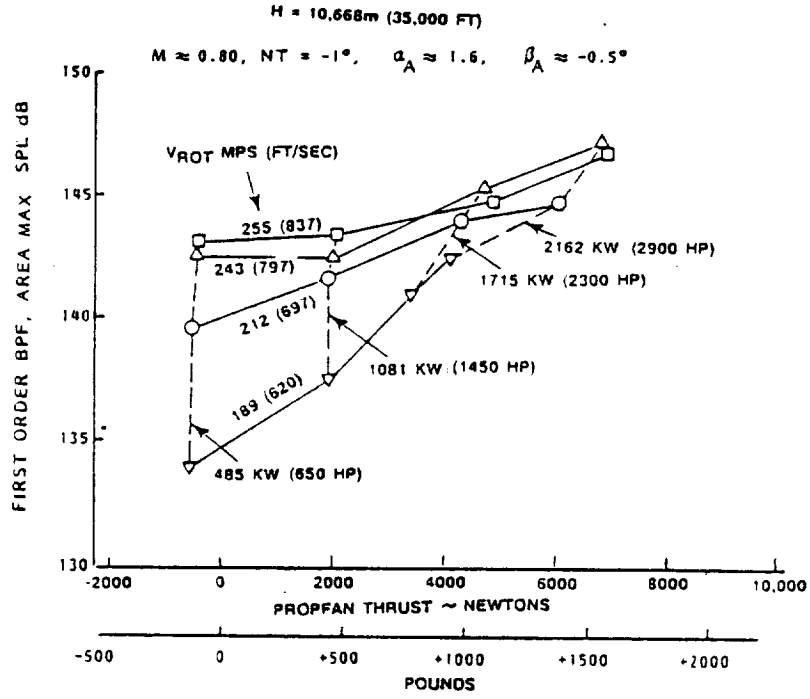


Figure 393. Effects of Propfan Thrust and Tip Speed on Fuselage SPL Measurements

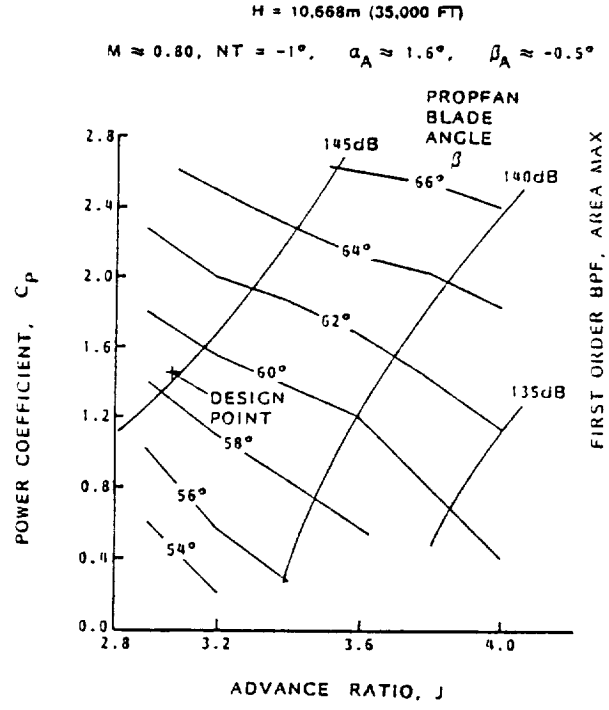


Figure 394. Effects of C_p and J on Fuselage SPL Measurements

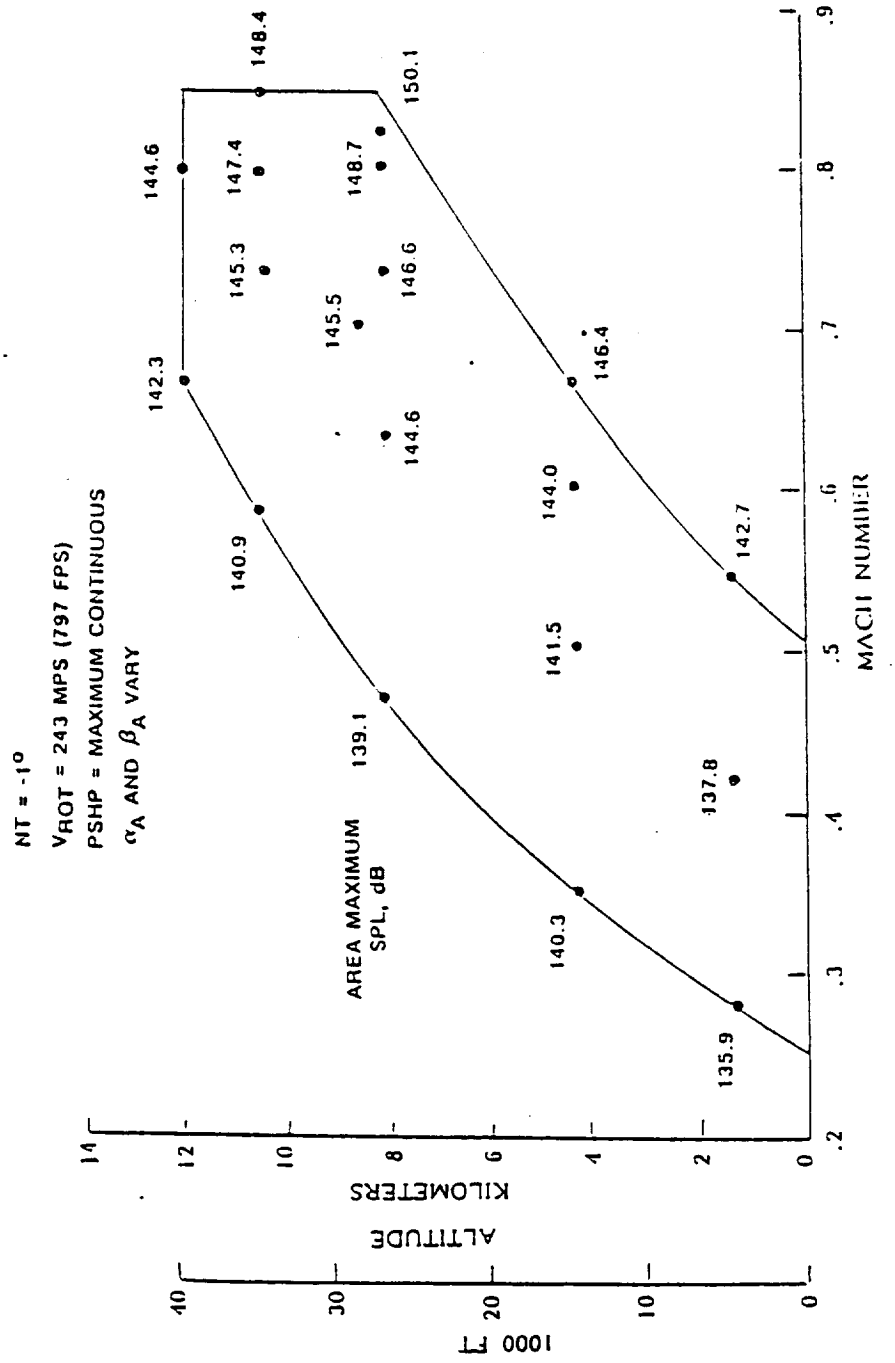


Figure 395. Variation of SPL on Fuselage over Flight Envelope

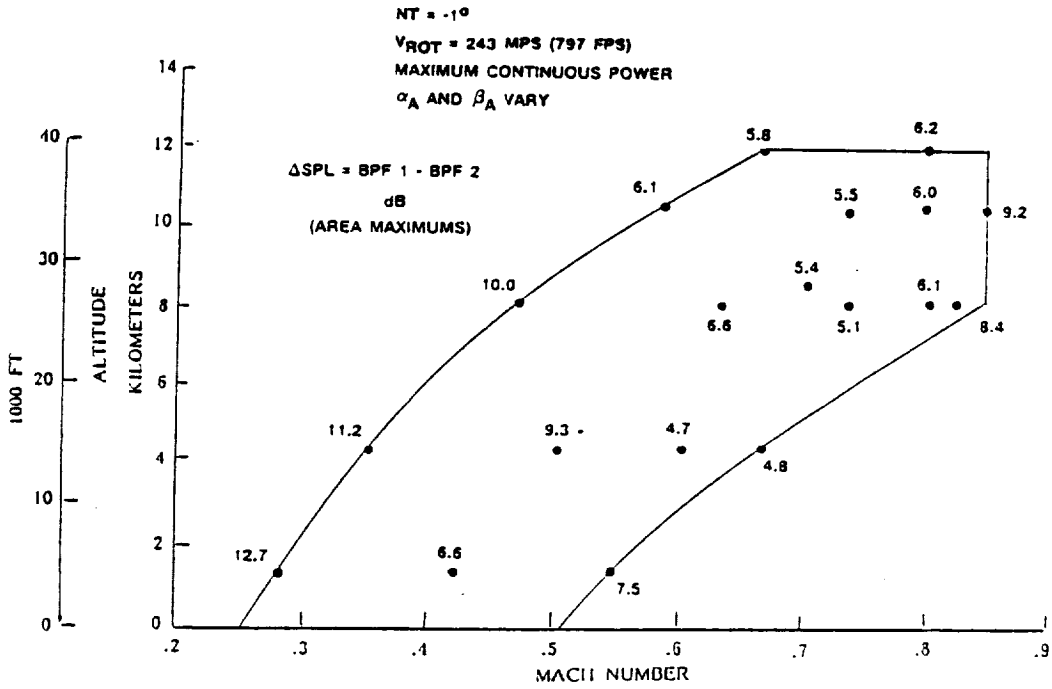


Figure 396. Differences Between Fuselage SPLs at BPF1 and BPF2

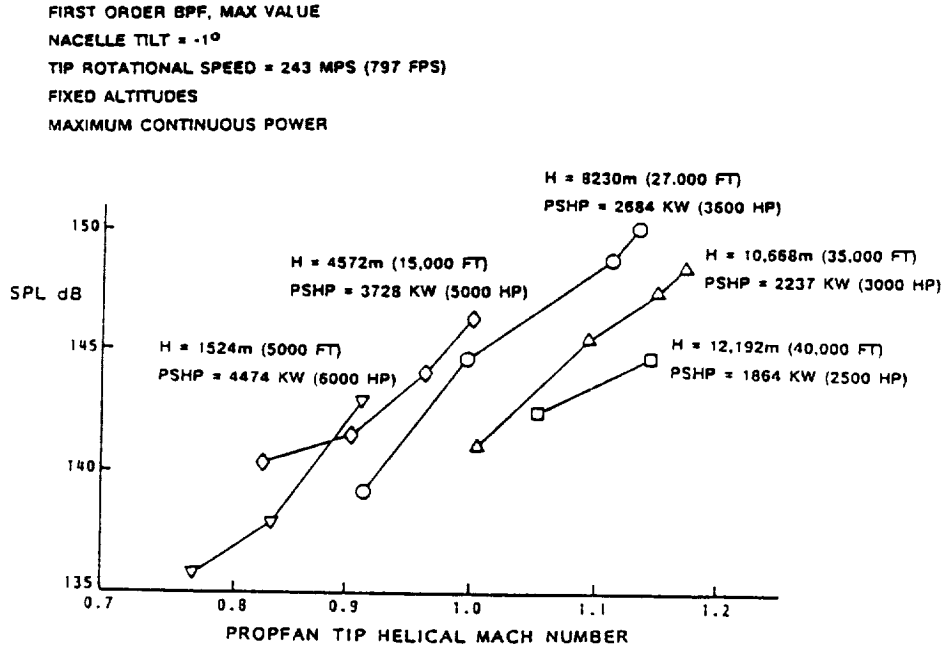


Figure 397. Effect of Propfan Helical Tip Mach Number on Fuselage SPL

SUPERSONIC PROP TIPS

H = 7620m (25,000 FT) AND 12,192m (40,000 FT)
M = 0.8

	CASE 1	CASE 2
M_{TH}	1.02	1.14
C_p	2.859	1.526
J	3.974	3.108
BPF 1 ΔdB	5.6	5.0
BPF 2 ΔdB	4.2	5.1

- Δ dB BASED ON FUSELAGE MAXIMUM SPLs
- Δ dB CORRECTED FOR Δα

SUBSONIC PROP TIPS

H = 3048m (10,000 FT) AND 10,668m (35,000 FT)
M = 0.6

	CASE 3	CASE 4	CASE 5
M_{TH}	0.87	0.97	0.97
C_p	1.981	0.628	1.225
J	3.002	2.484	2.492
BPF 1 ΔdB	7.5	6.5	7.5
BPF 2 ΔdB	8.8	6.4	6.4

Figure 398. Test Conditions for Altitude Scaling Validation

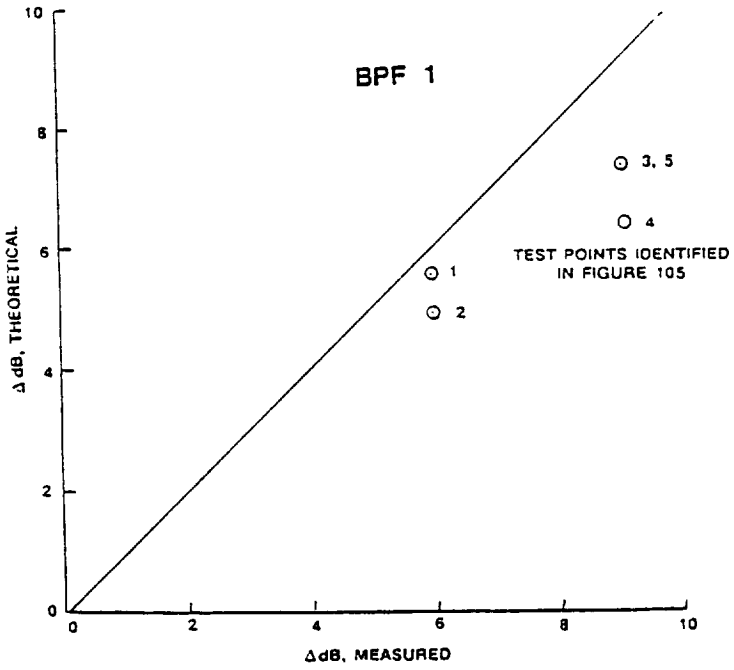


Figure 399. Results from Altitude Scaling Validation Tests

obtained for two altitudes at common C_p and J values. The tables list for each case the difference in SPL measured at the two altitudes.

The scaling theory uses the relationship:

$$\Delta dB = 20 \log \frac{\rho_2 c_2^2}{\rho_1 c_1^2}$$

to define theoretical differences in SPL for different altitudes. This relationship was used to calculate the differences in SPL for the five pairs of test conditions shown in Figure 398. Figure 399 shows the measured SPL differences plotted against the theoretical values. These data indicate that the scaling parameter is moderately accurate--giving results within about 2 dB of measured values. The fact that better agreement of the theory was obtained for Cases 1 and 2 than for Cases 3 through 5 is probably more a function of the magnitude of altitude differences than of a subsonic-versus-supersonic relationship.

All of the results so far discussed have been for the baseline nacelle tilt angle of -1 degree. The PTA tests revealed, however, that propfan noise is strongly affected by nacelle tilt. This follows from the results already discussed that showed blade loading noise to be a strong contributor to total blade noise. Recognizing that, Figure 400 shows how radiated noise inboard and outboard of the propfan may be affected by changes in nacelle tilt angle.

With the blades moving upwards on the inboard side of the propfan axis, an increase in nacelle tilt decreases the blade angle of attack and diminishes loading noise. On the outboard side of the propfan, an increase in nacelle tilt angle increases the blade angle of attack and increases loading noise. The data shown in Figure 401 for SPL on the fuselage and on the acoustic boom show these hypotheses to be correct. It can be seen that SPL was a strong function of nacelle tilt angle, and the curve slopes were reversed from inboard to outboard sides.

It is obvious from these results that inflow angle is a strong consideration in new configuration design if propfan noise is to be minimized.

After the near-field noise tests were completed, 46 points were selected for comparison with theoretical predictions. The aircraft and engine flight condition data were used as input, and Hamilton Standard used state of the art prediction methods to calculate propfan noise. The prediction technique is outlined in Figure 402.

A summary of results for all the calculated cases is shown in Figure 403. Generally, the theory tended to overpredict noise for the design cruise case where the noise levels were highest and underpredict for the low speed climb cases where the noise was lower. This tendency is displayed more graphically in Figure 404 where differences between predicted and measured SPLs are shown for all the test points in the flight envelope.

Figure 405 shows a comparison between predicted SPL along the side of the fuselage and that measured for the BPF tone and the second harmonic. Generally, the theory did a good job of predicting the location of maximum

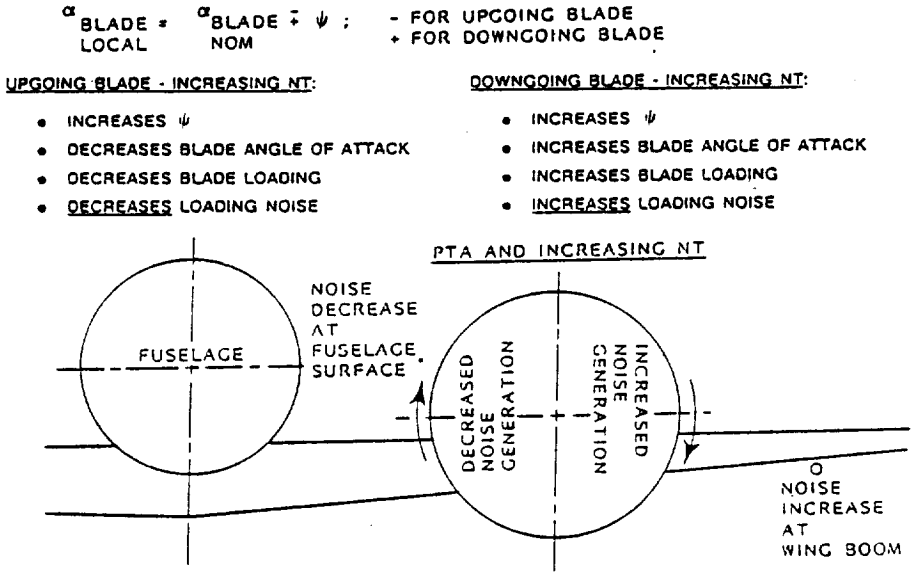


Figure 400. Expected Influence on Near-Field Noise of Propfan Inflow Angle and Direction of Rotation

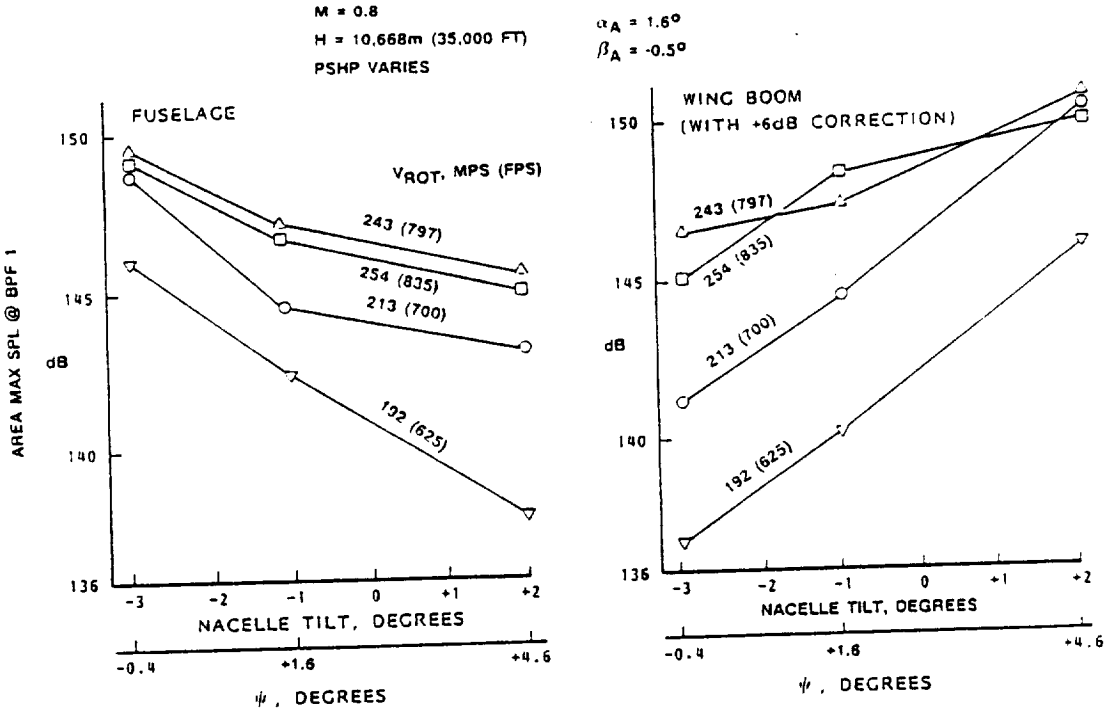


Figure 401. Effect of Nacelle Tilt on Fuselage and Boom SPLs

- HAMILTON STANDARD (HANSON) FREQUENCY DOMAIN PROPELLER NOISE RADIATION THEORY
- SOURCES
  - THICKNESS NOISE (MONOPOLE SOURCE)
    - BASED ON BLADE CHORD, THICKNESS, AIRFOIL SECTION, AND SWEEP DISTRIBUTIONS
  - STEADY LOADING NOISE (DIPOLE SOURCE)
    - BASED ON BLADE AERODYNAMIC LOADING DISTRIBUTION
    - SPANWISE PRESSURE DISTRIBUTION DERIVED FROM 2D LIFTING LINE METHODS
    - CHORDWISE PRESSURE DISTRIBUTION DERIVED FROM TRANSONIC AIRFOIL CODES
  - UNSTEADY LOADING NOISE (DIPOLE SOURCE)
    - BASED ON QUASI-STEADY AERODYNAMIC LOADING DISTRIBUTION
    - LASC SUPPLIED FLOW-FIELD INFORMATION
  - NON-LINEAR NOISE (QUADRUPOLE SOURCE)
    - BASED ON ACOUSTIC SHEAR TENSOR
- PROPAGATION
  - FUSELAGE PREDICTIONS INCLUDE BOUNDARY LAYER REFRACTION AND FUSELAGE SCATTERING EFFECTS
  - WING BOOM PREDICTIONS ARE FREE-FIELD
- PREDICTION
  - DISCRETE TONES AT BPF
  - AMPLITUDE AND RELATIVE PHASE OF PROPFAN TOTAL NOISE
- PREDICTION METHODOLOGY DOES NOT INCLUDE:
  - EFFECT OF LEADING EDGE AND TIP EDGE VORTICES ON LOADING DISTRIBUTIONS (LIFTING SURFACE)
  - REFLECTIONS FROM FUSELAGE, WING, AND NACELLE
  - ANY EMPIRICAL ADJUSTMENTS

Figure 402. Propfan Near-Field Acoustic Prediction Methodology

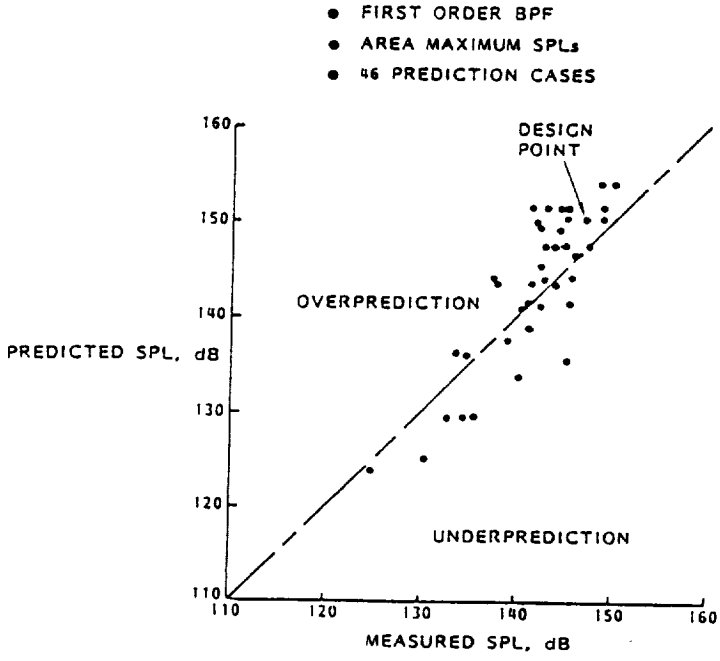


Figure 403. Summary of Fuselage Predicted and Measured SPLs

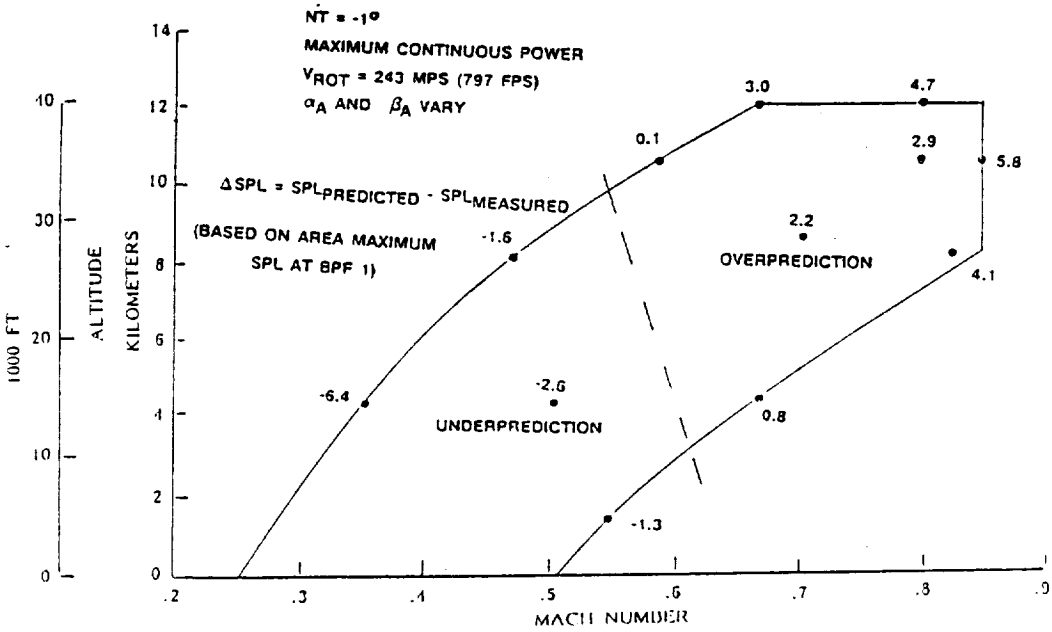


Figure 404. Summary of SPL Prediction Accuracy

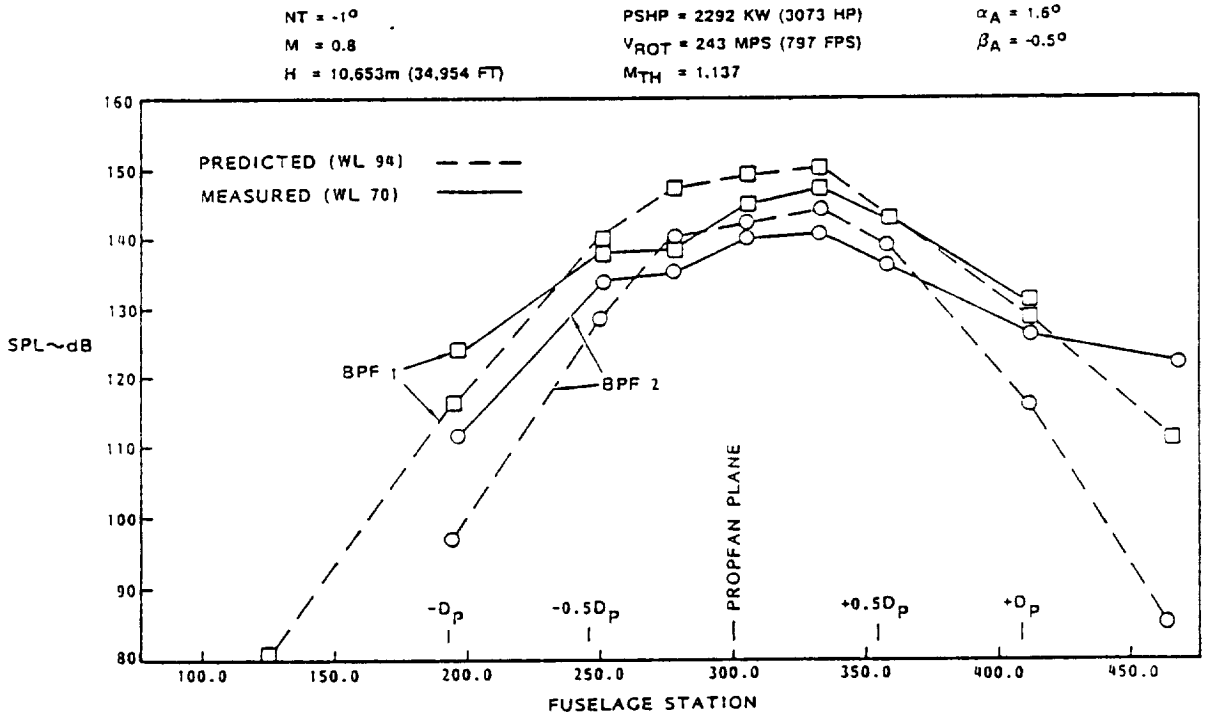


Figure 405. Fuselage Axial Distribution of SPL

SPL, but predicted a more rapid fall-off fore and aft than shown by the data. Figure 406 shows that the theory predicted the shape of the spectra well even though the SPL level was off.

The comparison of predicted and measured power effects on fuselage SPLs shows a general failure of the theory to adequately predict power effects and suggests (following the line of reasoning used in the discussion of Figure 392) that the theory is overly dominated by thickness noise. Figure 407 shows that the theory does a better job of predicting the increase in noise with increasing rotational speed, but fails to predict the reversal of this trend at higher rotational speeds that is shown by the data.

Another area in which the theory was inadequate was in the prediction of the effects of inflow angle on noise. This is shown in Figure 408. In the worst case, the data show a 9 dB reduction in SPL for the 5 degrees of change in nacelle tilt, whereas the theory predicts less than 1 dB change.

9.2.3.2 Fluctuating Pressure Levels

The most significant acoustic impact of the propfan on the aircraft other than the sound pressure levels produced on the fuselage was the production of fluctuating pressure in the region where the propfan slipstream impinged on the wing. The slipstream contains blade trailing edge wakes and blade tip vortices--both of which produce oscillating surface pressures.

The character of the oscillating pressure on the wing is more complex than that on the side of the fuselage. The fuselage oscillating pressures result from airborne sound pressures, while the wake-impacted oscillating pressures are more nearly hydrodynamic in nature.

Fluctuating pressures were measured with 44 transducers mounted on the wing upper and lower surfaces. They were arrayed, inboard and outboard of the nacelle, from leading to trailing edge of the wing in the region near the edge of the propfan slipstream.

As was the case with SPLs, the FPL signals were characterized by a strong fundamental tone at BPF and higher order harmonics as shown in Figure 409. These tones exceeded the noise floor level by at least 20 dB, so attention in the analysis was concentrated on these tone signals.

The noise levels varied from quadrant to quadrant in the four regions of slipstream influence as may be seen in Figure 410. The highest FPL levels were measured on the wing lower surface on the inboard side of the nacelle. Distribution of FPL values over the wing lower surface is shown in Figure 411. For the design cruise condition shown, the highest FPL was 148.2 dB near the wing leading edge. The comparable distribution over the wing upper surface is shown in Figure 412, with a maximum value of 140.6 dB.

Chordwise distributions of FPL over the wing in the regions inboard of the nacelle are shown in Figure 413. For the signal at BPF, both upper and

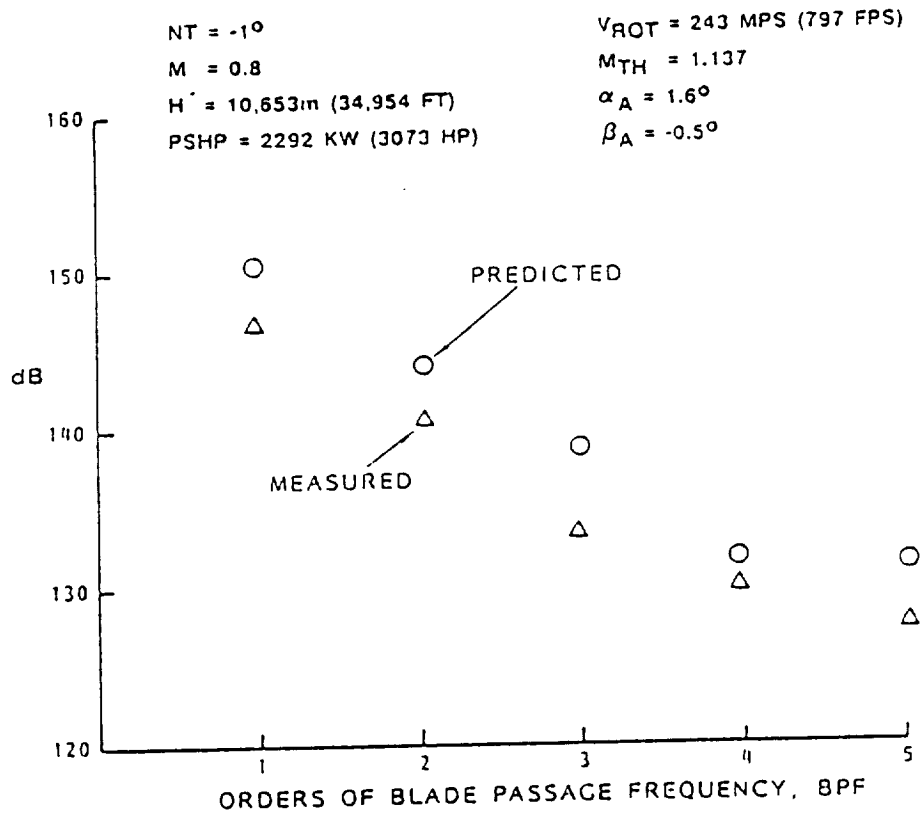


Figure 406. Comparison of Predicted and Measured SPL Spectra on Fuselage

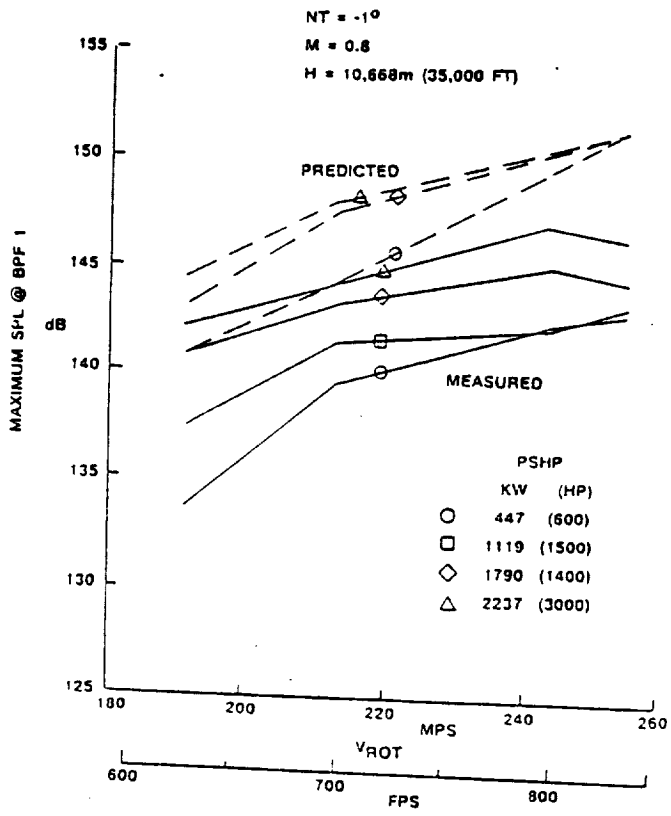


Figure 407. Effects of Rotational Speed on Fuselage SPL

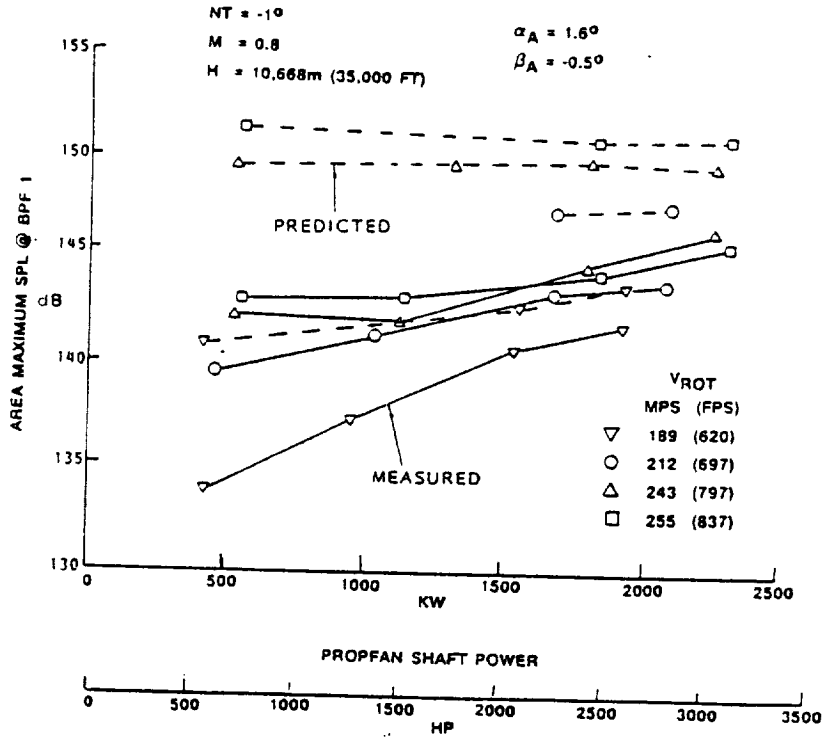


Figure 408. Effect of Nacelle Tilt on Fuselage SPL

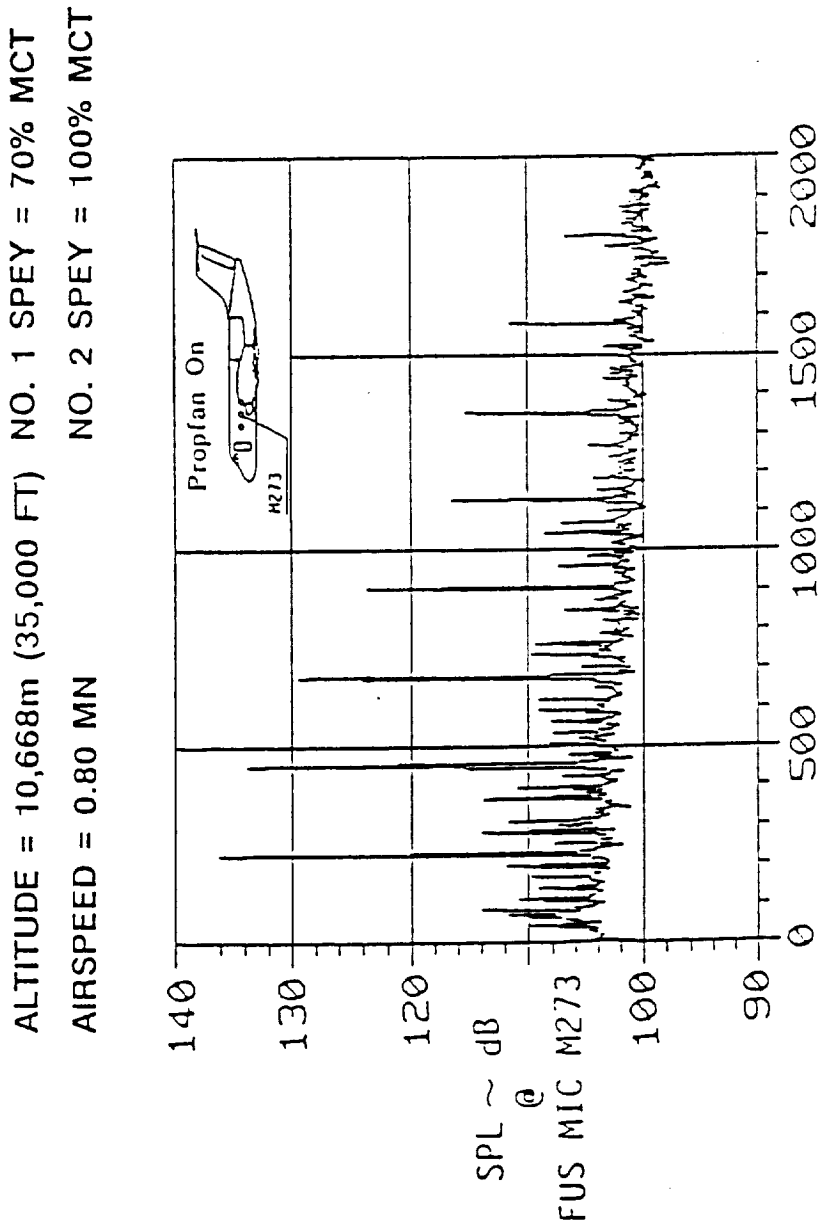


Figure 409. Spectrum of Fluctuating Pressure on Wing Lower Surface

NT = -1°

M = 0.8

H = 10,653m (34,954 FT)

PSHP = 2292 KW (3073 HP)

V_{ROT} = 243 MPS (797 FPS)

M_{TH} = 1.137

α_A = 1.6°, β_A = -0.5°

SPECTRA FROM WING LEADING EDGE TRANSDUCERS WHERE MAXIMUM FPL @ BPF1 OCCURS

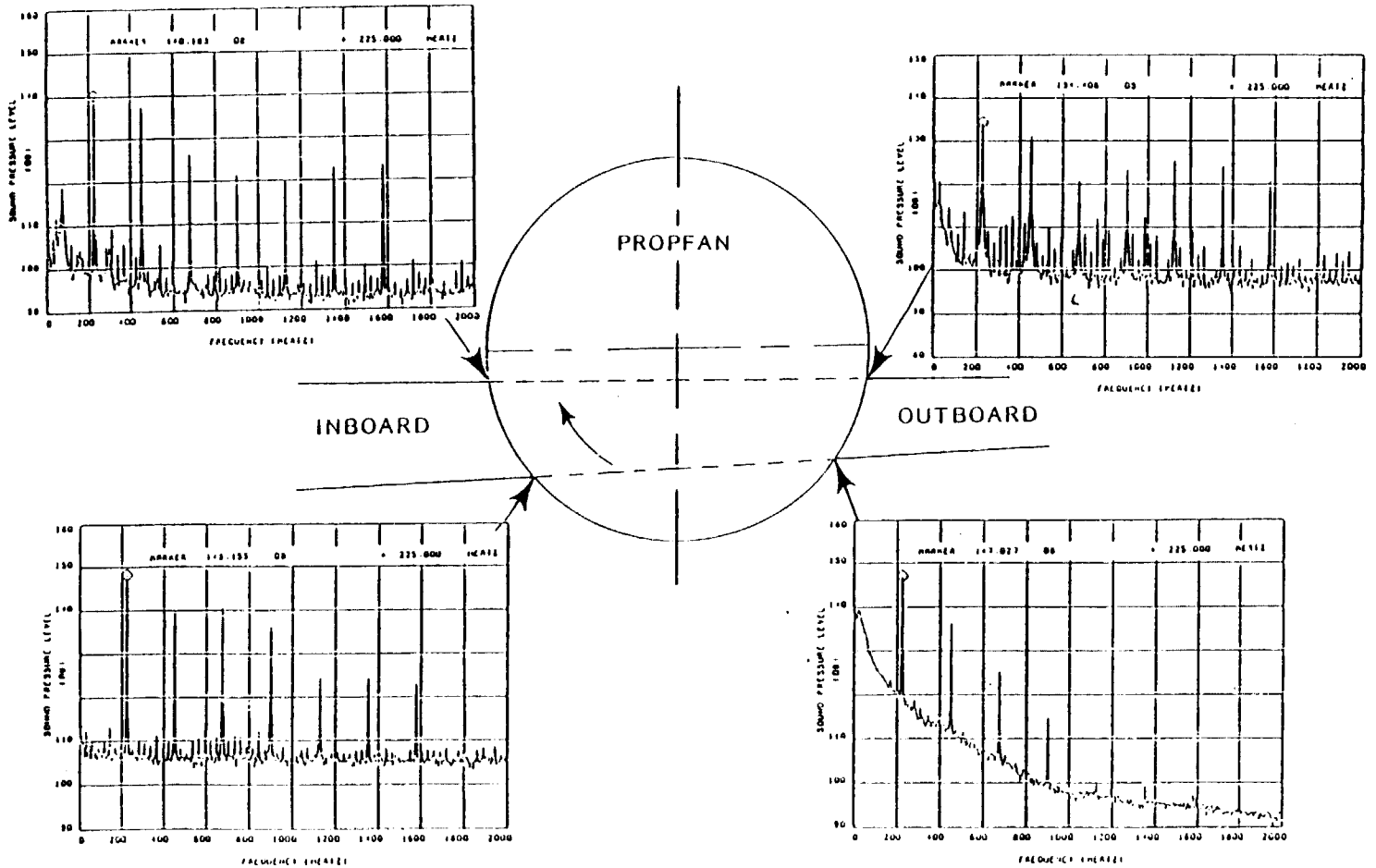


Figure 410. Spectra of Wing FPL in Four Quadrants

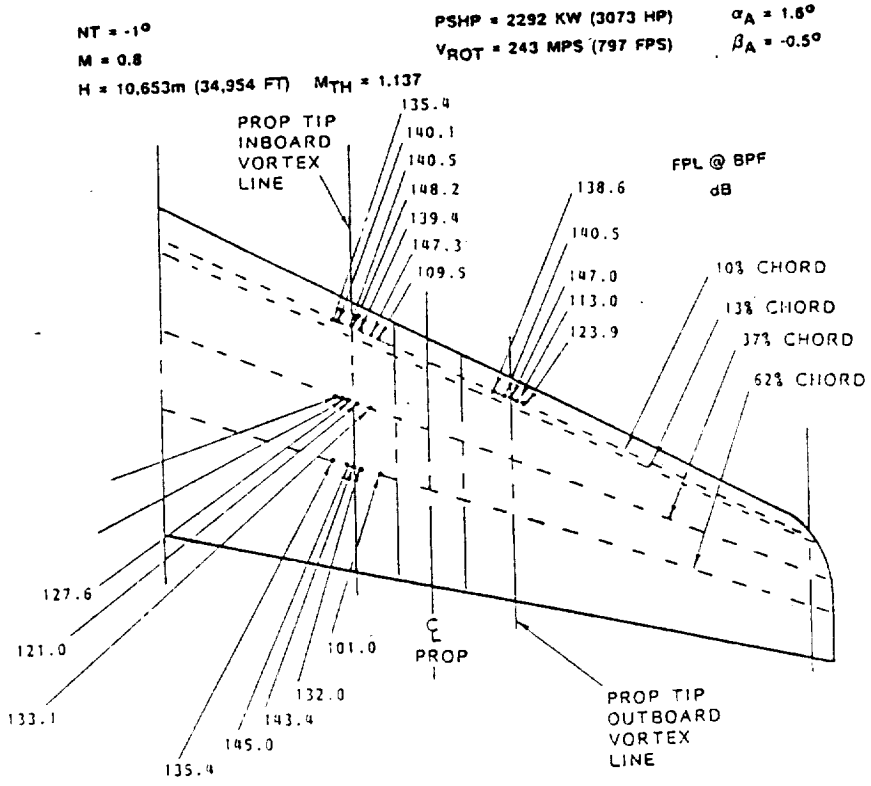


Figure 411. Distribution of FPL on Wing Lower Surface

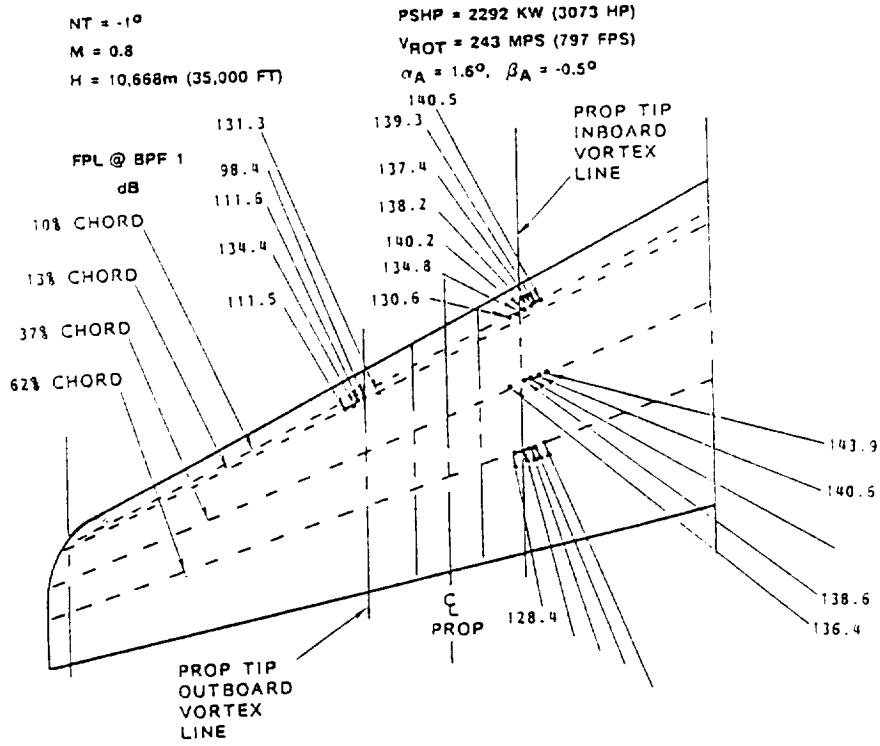


Figure 412. Distribution of FPL on Wing Upper Surface

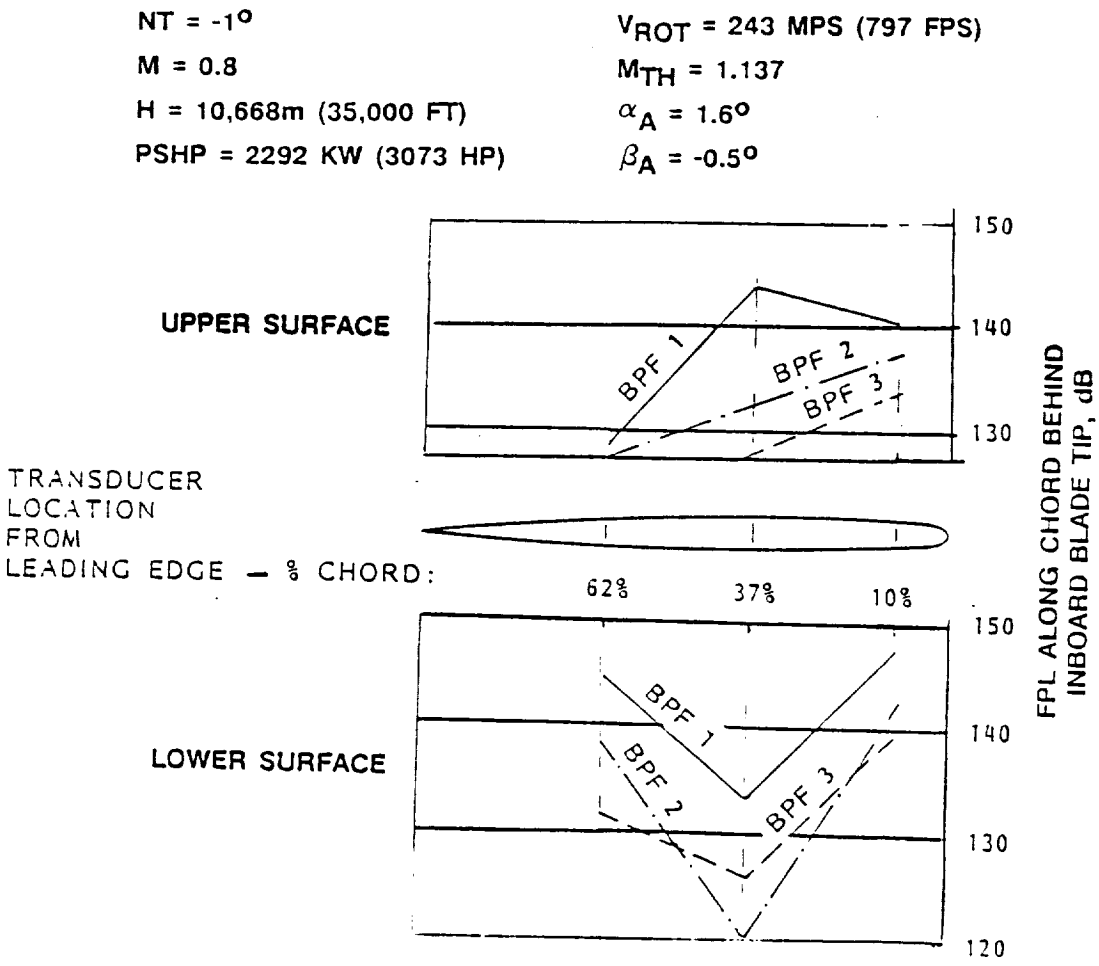


Figure 413. Chordwise Distribution of Wing FPL

lower surfaces show FPL values greater than 140 dB over a considerable portion of the wing.

The effects of propfan power and tip speed on FPL levels are shown in Figures 414 and 415 for inboard and outboard sides of the nacelle respectively. On the inboard side, levels increase with power as in the case of sound pressure levels, but are almost independent of rotational speed. On the outboard side, there are stronger effects of both power and speed. One of the reasons for the different levels of excitation inboard and outboard is that, because of wing sweep, the propfan tip vortices that cause much of the excitation must travel further on the outboard side to reach the wing leading edge.

The variation over the flight envelope of FPLM at BPF for the wing lower inboard quadrant is shown in Figure 416. For this 19-point data set, propfan tip speed was held constant, and power was held at the maximum attainable. Some of the levels shown on this figure are low and out of pattern, but for most of the points, the FPL is about 150 ±3 dB. The same data are used to show the differences between FPL and SPL in Figure 417. Fluctuating pressure levels on the wing ranged higher than sound pressure levels on the fuselage by about 17 dB at the lowest speeds and altitudes and were of the same order of magnitude as the sound pressure levels at the higher speeds and altitudes.

The effect of nacelle tilt on FPL in the four quadrants is shown in Figure 418. There is considerable inconsistency in the data, but generally a tendency for FPL to decrease slightly with increasing nacelle tilt angle on the inboard side, and perhaps increase slightly on the outboard side. These same trends were more pronounced in the SPL data.

Fluctuating pressure levels were also predicted for the same set of data used in the SPL predictions. An outline of the prediction methodology is shown in Figure 419. An overall comparison of the correlation between predicted and measured points is shown in Figure 420. It can be seen that the theory considerably underpredicted FPL.

Figure 421 shows, on the other hand, that the theory predicts quite well the effects of power on FPL even though absolute levels are missed. It is conjectured that the main reason for the significant underprediction of FPL is the failure of the theory to account for the intense localized loading produced by the tip vortices from the propfan blades.

9.3 LOW ALTITUDE TESTS

9.3.1 Objectives and Scope

The major objective of the low-altitude research tests was to obtain far-field noise data of the type needed for aircraft certification to FAR 36. This involved ground measurements directly below the flight path and at sideline distances of 450m (1476 ft). Other measurements were made at sideline distances out to 2469m (8100 ft) for the purpose of studying the lateral attenuation of noise.

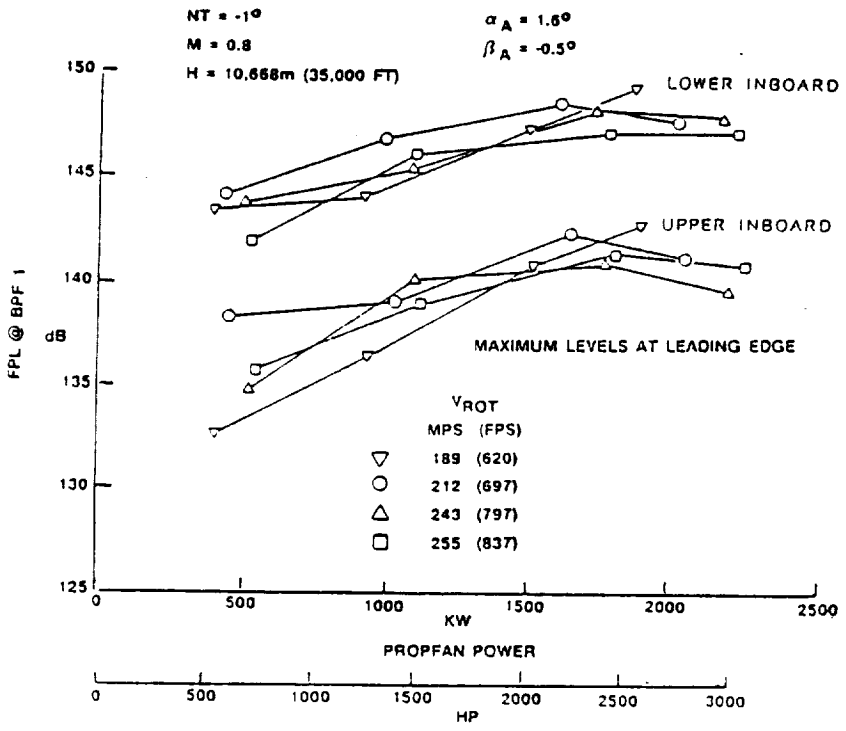


Figure 414. Effects of Propfan Rotational Speed and Power on Wing Inboard FPLs

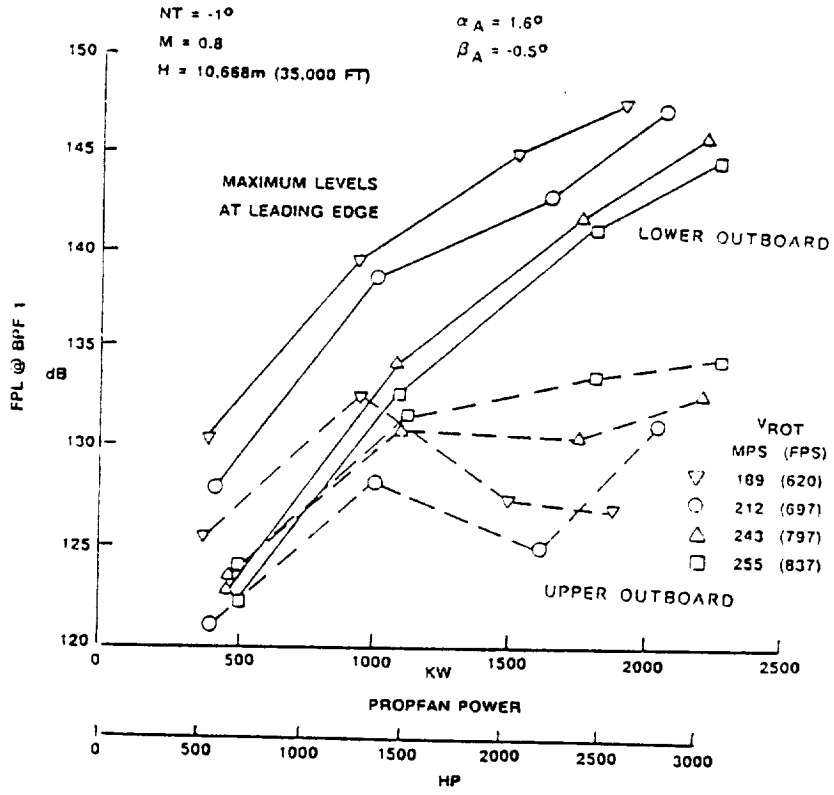


Figure 415. Effects of Propfan Rotational Speed and Power on Wing Outboard FPLs

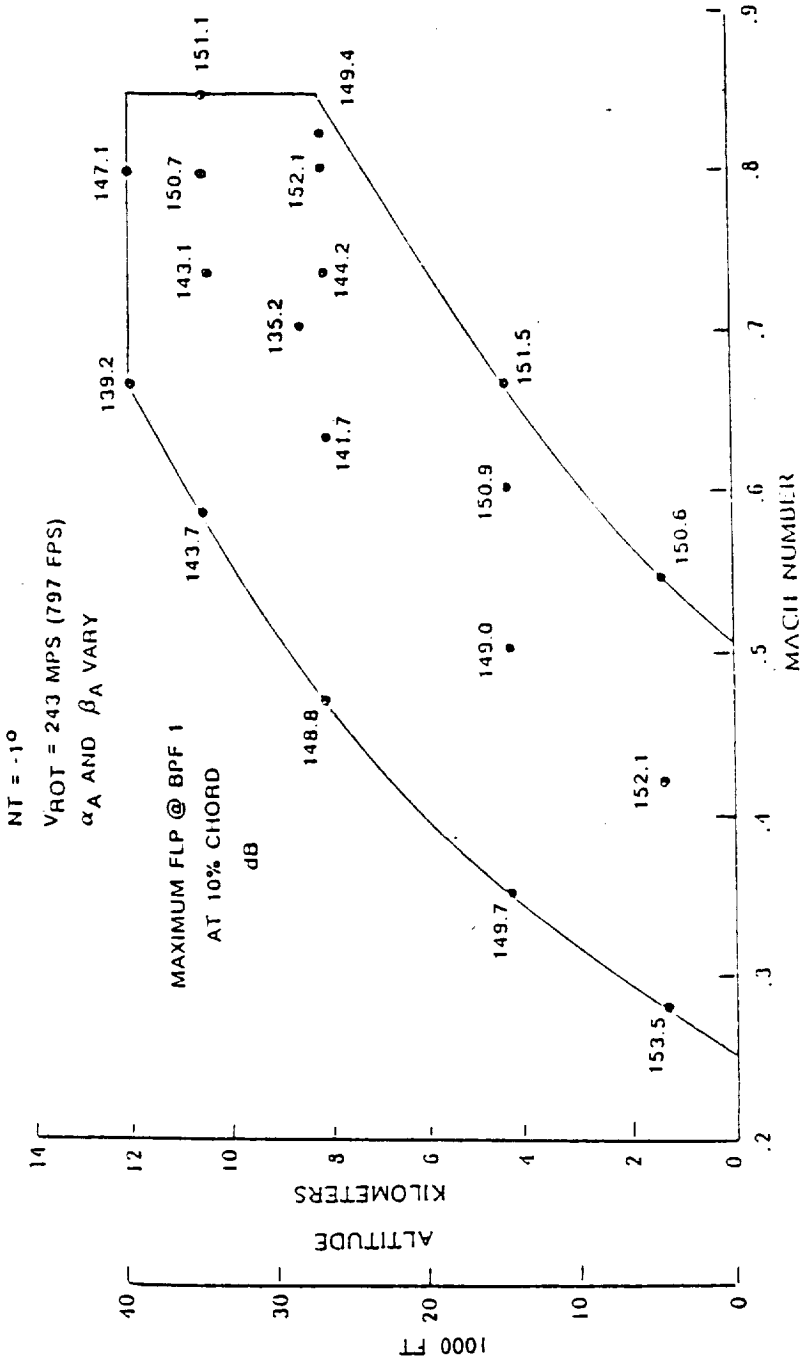


Figure 416. Variation of FPLM over Flight Envelope

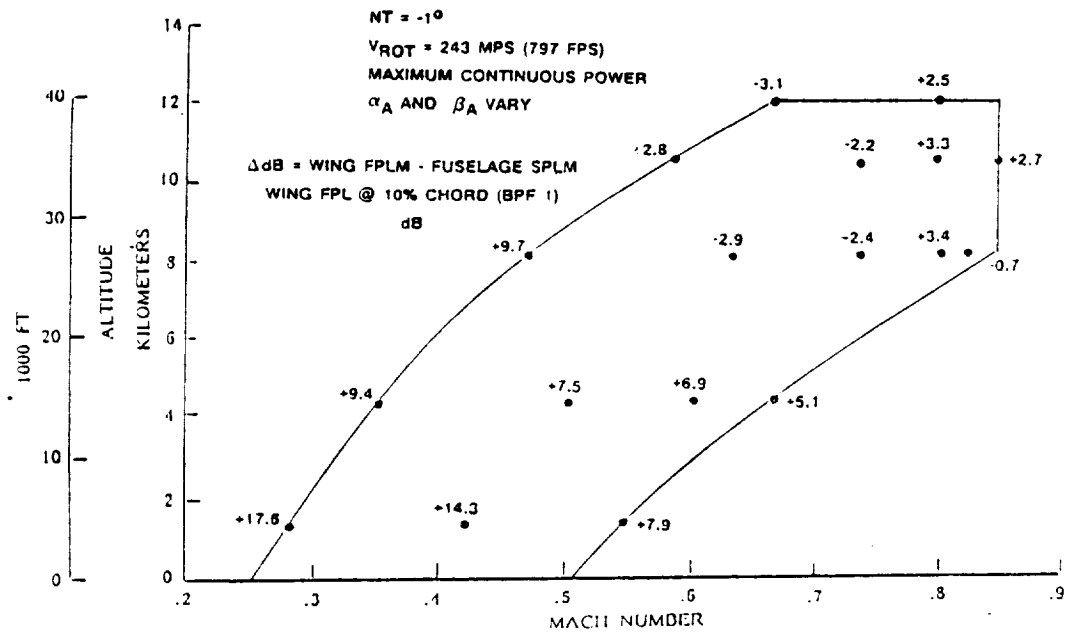


Figure 417. Relation Between Wing FPLM and Fuselage SPLM

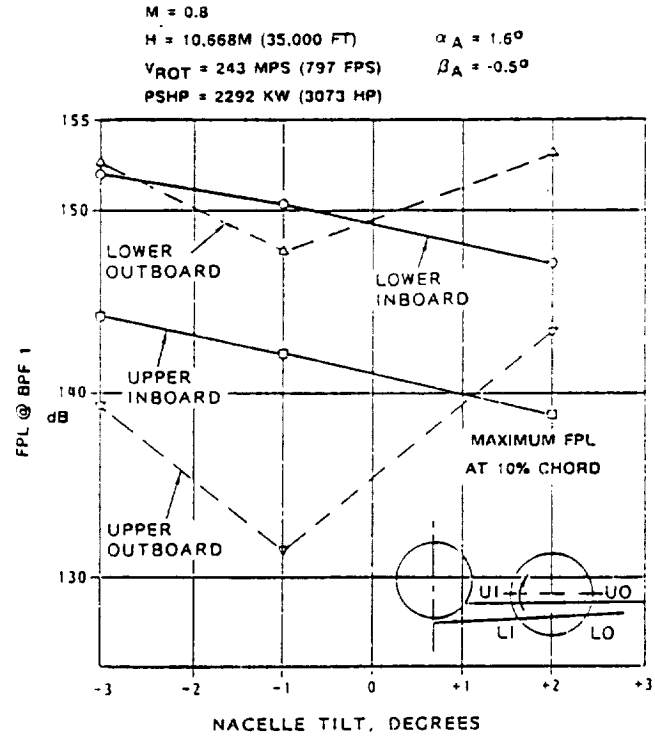


Figure 418. Effect of Nacelle Tilt on Wing FPLs in Four Quadrants

- HAMILTON STANDARD PROCEDURE
- CALCULATE PROPFAN WAKE CHARACTERISTICS
  - POTENTIAL WAKES (BASED ON LIFTING-LINE AERODYNAMICS FOR SPANWISE LOADING DISTRIBUTION)
  - VISCOUS WAKES (SILVERSTEIN WAKE MODEL BASED ON BLADE SECTION DRAG
  - OBTAIN DISTURBANCE COMPONENT PERPENDICULAR TO THE WING SURFACES
- DETERMINE DISTURBANCE MAGNITUDE AS A FUNCTION OF WAVE NUMBER
  - FOURIER TRANSFORM
- DERIVE FPL ACROSS THE AIRFOIL SURFACE USING AIRFOIL LIFT RESPONSE METHOD
  - INFINITE SPAN, THIN, CONSTANT CHORD, SWEPT WING
  - CALCULATES DIFFERENTIAL PRESSURE (PRESSURE TOP AND BOTTOM OF WING ASSUMED TO BE OF EQUAL AMPLITUDE AND OPPOSITE PHASE)
  - PROPFAN AXIS IS ASSUMED TO LIE IN THE PLANE OF THE WING SURFACE
- PREDICTION
  - DISCRETE TONES AT BPF
  - AMPLITUDE AND RELATIVE PHASE OF FPL
- PREDICTION METHODOLOGY DOES NOT INCLUDE
  - LEADING EDGE OR TIP EDGE VORTEX LIFT
  - UNSTEADY BLADE LOADS DUE TO INFLOW ANGLE-OF-ATTACK EFFECTS
  - ROLL-UP OF BLADE VORTEX SHEET IN TIP REGION
  - WING LOADING EFFECTS ON LIFT RESPONSE
  - ANY EMPIRICAL ADJUSTMENTS

Figure 419. Fluctuating Pressure Prediction Methodology

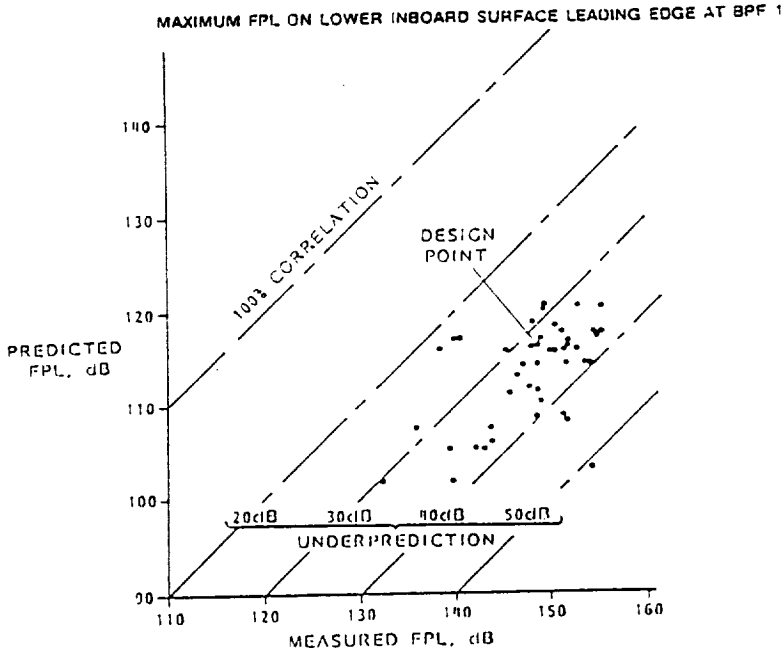


Figure 420. Summary of Predicted Wing FPLs

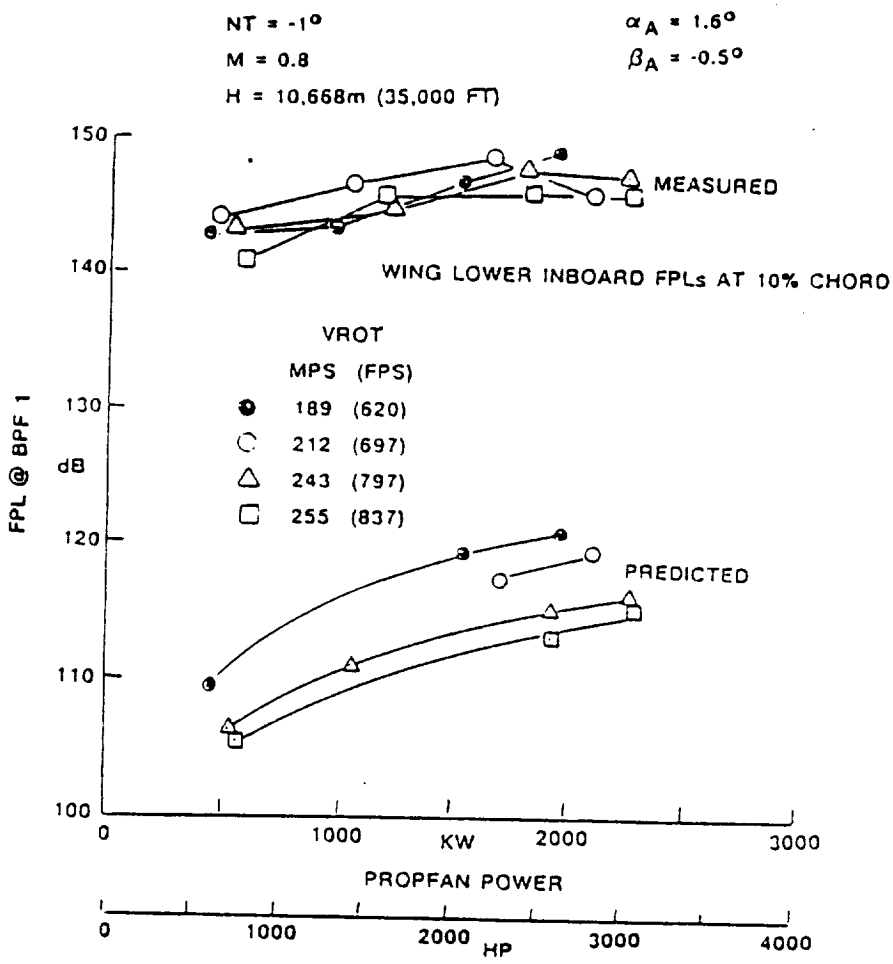


Figure 421. Effects of Propfan Power and Tip Speed on Wing FPLs

The test conditions planned for these tests are shown in Figure 422. Test variables included flyover altitude, nacelle tilt, propfan power, and propfan tip speed. These tests were flown from NASA's Wallops Flight Test Center, Wallop's Island, Virginia.

9.3.2 Test Procedures

As in the case of the high-altitude tests, all test flights were made with the left hand Spey engine set at minimum power to maintain level flight. Tests were normally flown north-to-south over long the west end of an east-west runway. The sideline instrumentation was arrayed along that runway. Some flights were also made in the south-to-north direction to obtain data on the opposite side of the aircraft and assess lateral directivity effects.

Obtaining propfan-power-off data required a special technique. The objective was to get data with the Spey engines set at the same levels used when the propfan was on and powered. At those Spey engine power settings, but without the propfan thrust, the aircraft could not maintain level flight. In order to get these propfan-off data, therefore, it was necessary to take data as the aircraft glided through the stations where data points were needed. Since these stations were located along the flight path for a considerable distance, it was necessary to fly a number of short glides to get a complete set of prop-off data for a single flyover altitude. This technique is depicted in Figure 423.

Other procedures were the same as for the high altitude tests.

9.3.3 Results and Discussions

9.3.3.1 Far-Field Noise

Typical data samples from the far-field noise tests are shown in the time histories of Figure 424 and the 1/3-octave spectra of Figure 425. These results show that peak noise was measured close to the aircraft-overhead position at the time of sound emission. The spectra show that the propfan blade-passing-frequency (BPF) tone was clearly distinguishable from other noise sources, and that in many cases the first harmonic was also distinguishable.

To compare the total aircraft acoustic data with the data from flights with the propfan blades removed, the data were normalized to 305m (1000 ft) radius as free-field lossless data. This was achieved by determining the emission angle, the emission time, and the corresponding airplane coordinates from radar data. The sound propagation distance was calculated using the emission coordinates, and atmospheric corrections were applied. To minimize the ground reflection effects as functions of frequency and incidence angle, only inverted ground microphone data were used. Ground reflections were assumed to be 6 dB and independent of frequency and incidence angle. Contamination of the noise signals from extraneous sources limited the useful propfan data to that at frequencies below 1000 Hz.

AIRSPEED: 361 KM/HR (195 KCAS)

CONDITIONS TO BE FLOWN ARE INDICATED BY A (✓). UNLESS INDICATED OTHERWISE, ONE FLYOVER WILL BE FLOWN FOR EACH TEST CONDITION.

	SHAFT POWER KW	(SHP)	259 m (850 ft) AGL TIP SPEED M/S & (FT/SEC) 183 (600)	213 (700)	244 (800)	256 (840)	305 m (1000 ft) AGL TIP SPEED M/S & (FT/SEC) 183 (600)	213 (700)	244 (800)	256 (840)	396 m (1300 ft) AGL TIP SPEED M/S & (FT/SEC) 183 (600)	213 (700)	244 (800)	256 (840)	488 m (1600 ft) AGL TIP SPEED M/S & (FT/SEC) 183 (600)	213 (700)	244 (800)	256 (840)	TBD FT AGL TIP SPEED M/S & (FT/SEC) 183 (600)	213 (700)	244 (800)	256 (840)
-1°NT, 0° ψ̇	1790	(2400)							✓													
	2685	(3600)					✓	✓	✓	✓												
	3579	(4800)						✓	✓													
	4474*	(6000)*		✓(3)		✓(3)	✓	✓(1)(2)	✓	✓(1)(2)		✓(3)		✓(3)		✓		✓	✓	✓(1)	✓	✓(1)
-1°NT, +TBD ψ̇	1790	(2400)																				
	2685	(3600)																				
	3579	(4800)						✓														
	4474*	(6000)*																				
-1°NT, -TBD ψ̇	1790	(2400)																				
	2685	(3600)																				
	3579	(4800)						✓														
	4474*	(6000)*																				
+2°NT, 0° ψ̇	1790	(2400)																				
	2685	(3600)					✓	✓		✓												
	3579	(4800)						✓														
	4474*	(6000)*					✓	✓	✓	✓												
-3°NT, 0° ψ̇	1790	(2400)																				
	2685	(3600)					✓	✓		✓												
	3579	(4800)						✓														
	4474*	(6000)*					✓	✓(3)	✓	✓(3)												

* OR MAX OPERABLE

(1) FLY 2 ADDITIONAL PASSES IN THE SAME DIRECTION FOR A TOTAL OF 3 NORTH-TO-SOUTH PASSES

(2) FLY 3 ADDITIONAL PASSES IN THE OPPOSITE DIRECTION FOR A TOTAL OF 3 SOUTH-TO-NORTH PASSES

(3) FLY 1 ADDITIONAL PASS IN THE OPPOSITE DIRECTION

Figure 422. Low-Altitude Flight Test Conditions

ORIGINAL PAGE IS OF POOR QUALITY

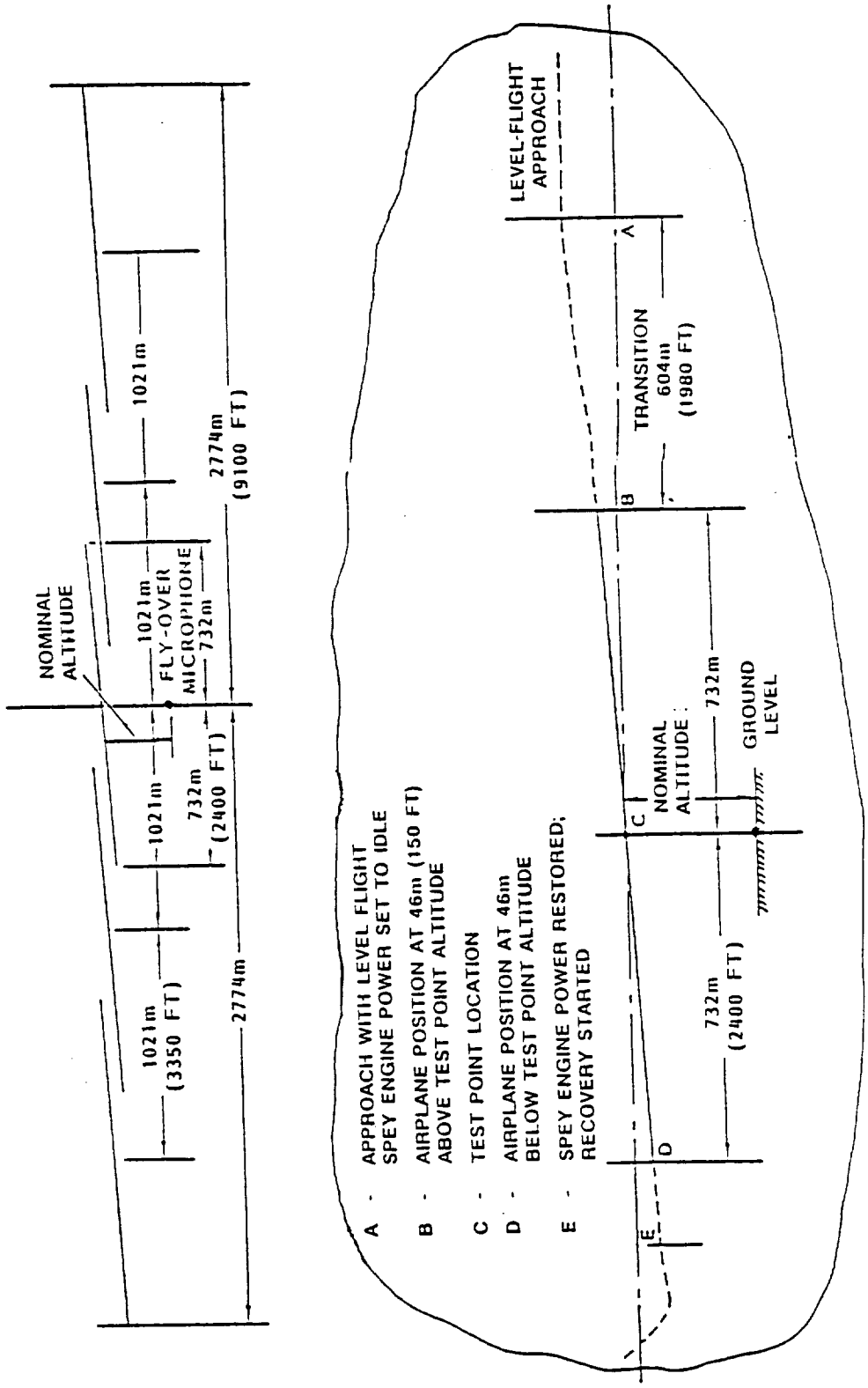


Figure 423. Low-Altitude Test Procedure with Propfan Blades Removed

M = 0.303; H= 314M(1030 ft); Power = 4389 kw (5886 hp)
M_{th} = 0.726; N_t = -1°; α = 4.7°; β = 2.35°

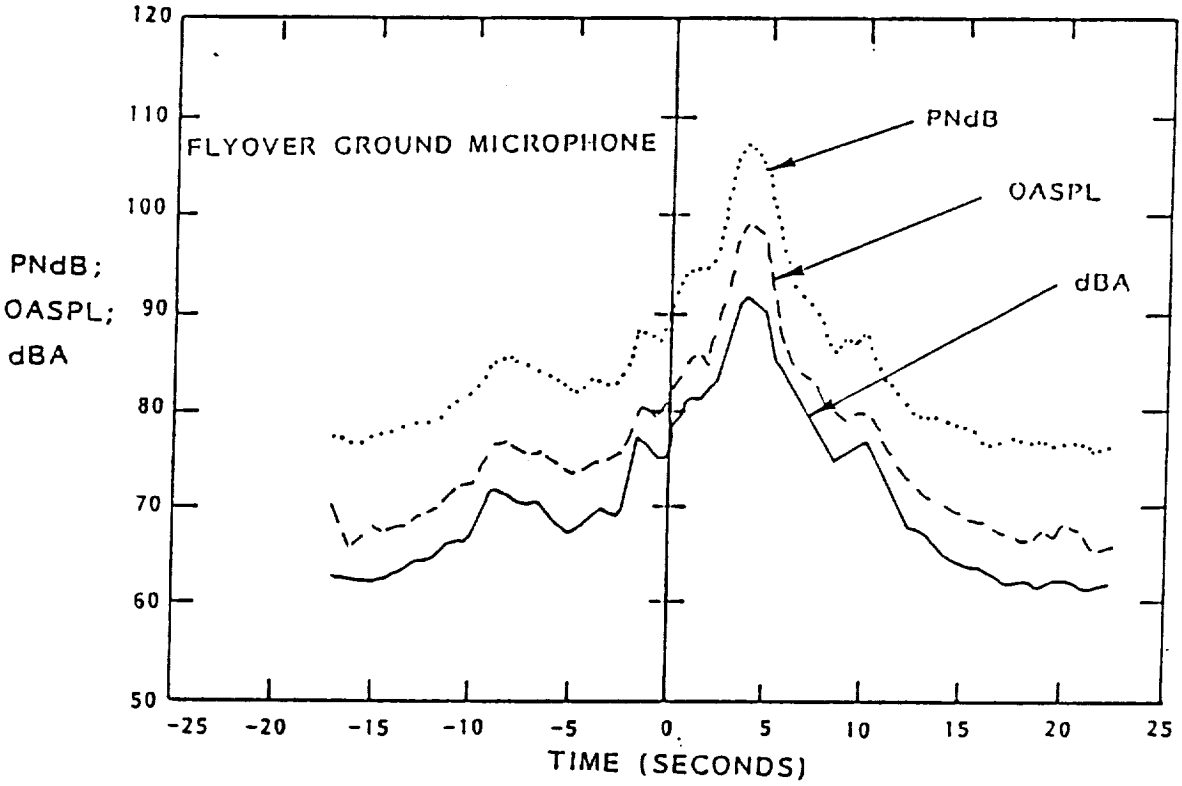
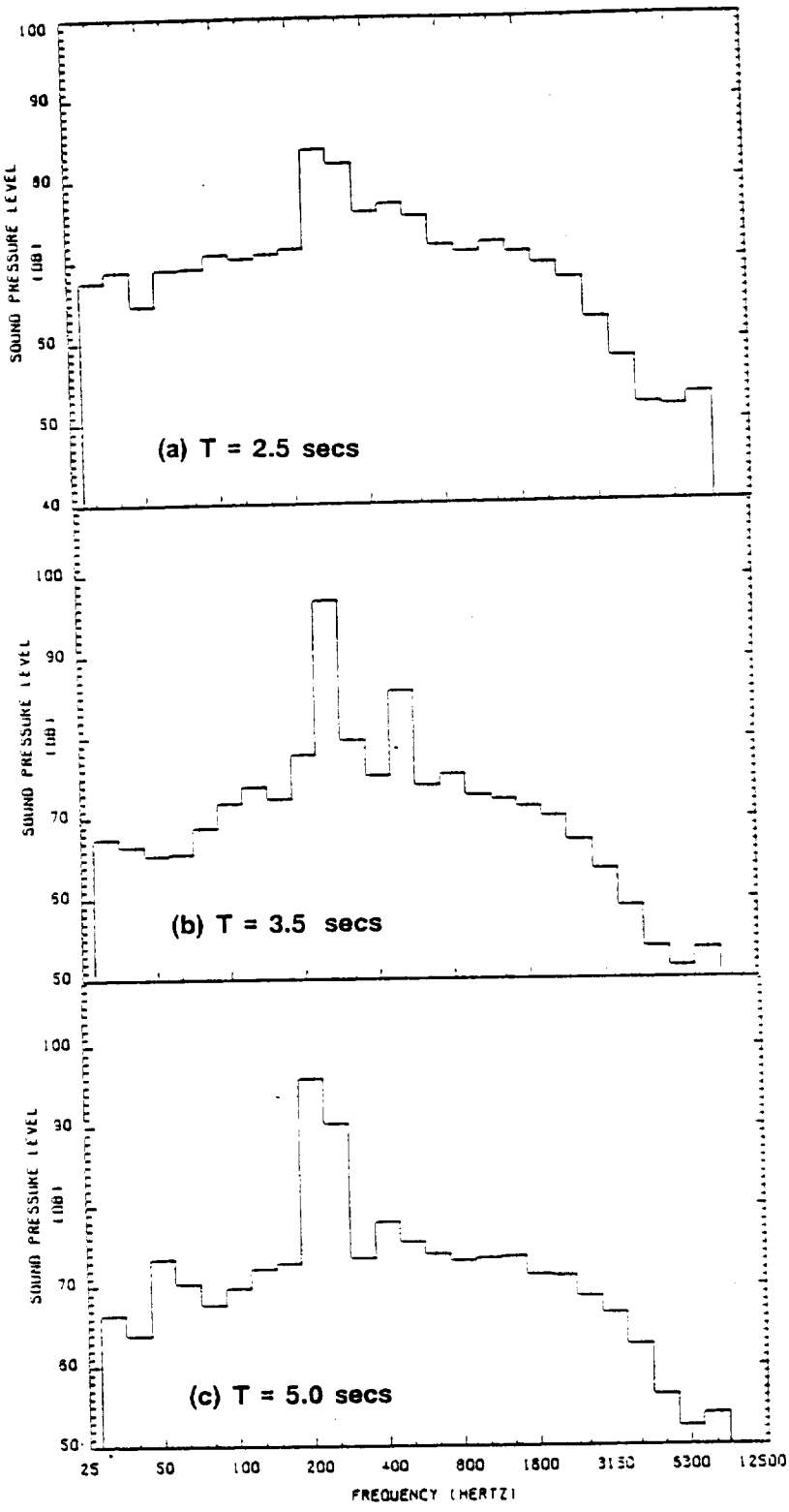


Figure 424 Typical Far-Field Noise Time History



M = 0.3
314m (1030 ft)
4389 kw (5886 hp)
M_{ROT} = .726
M_{TH} = .787
NT = 1°
α = 4.7°
β = -2.35°

Figure 425. Typical 1/3-Octave Band Spectra

Other analyses were performed, as reported in Reference 10(a), to extract propfan noise from the total noise signals recorded. These led to the determination that overall sound pressure level (OASPL) of total aircraft noise was a suitable parameter by which to evaluate the propfan far-field noise.

Noise directivity in the azimuthal plane was derived using the data from inverted microphones at seven ground stations at the time of peak OASPL in the time histories. These data are plotted in Figure 426. Some of the scatter at least may be attributed to the fact that the data came from several different flyovers. The curve shown is a least squares fit through the data points. It can be seen that noise was several dB higher on the side of the aircraft away from the propfan. It is believed that this directivity results from the fact that there is some net inflow angle to the propfan. At the conditions flown, this angle in the vertical plane was approximately 5 degrees.

Noise levels are plotted in the polar plane (for an azimuthal angle of 90 degrees) in Figure 427. A strong directivity is apparent with SPL peaking at about $\theta = 86^{\circ}$ and falling off rapidly fore and aft. The effects of operating parameters on far-field noise was studied using linear regression curve fits through large quantities of data obtained within narrow bands of flight and propfan operating parameters. Figures 428(a) through (e) show the effects of propfan power and tip speed on peak OASPL values for five different ground microphones. Generally, increasing propfan power from 1715 kw (2300 hp) to 4400 kw (5900 hp) at constant tip speed caused OASPL to increase by about 13 dB. For constant power, an increase in tip Mach number from 0.63 to 0.81 caused OASPL to increase about 10 dB.

Figures 429(a) through (d) show the effects of nacelle tilt angle on peak OASPL for four ground microphone positions. Increasing nacelle tilt from -3 to +2 degrees increased OASPL about 3 to 4 dB. Since angle of attack for the aircraft during these tests was approximately 5 degrees, there was always a positive upwash angle into the propfan even at nacelle tilt of -3 degrees.

Sound pressure levels were predicted by Hamilton Standard using a method that included steady and unsteady loading, thickness, and broadband noise components. Atmospheric effects were computed using the measured temperature and relative humidity, and corrections for ground reflections were applied.

Overall comparisons of predicted and measured data are presented in Figure 430 with a linear regression curve fit through the data points. The peak OASPL plotted is the maximum value in the OASPL time history and represents the tone level at blade passage frequency. It can be seen that the sound pressure levels were generally underpredicted by 6 to 10 dB.

A predicted OASPL time history is compared with the measured time history in Figure 431. It can be seen that the theory predicted the shape of the time history well even though the level of the peak was missed. The plots of Figure 432 show a comparison of the predicted and measured 1/3-octave

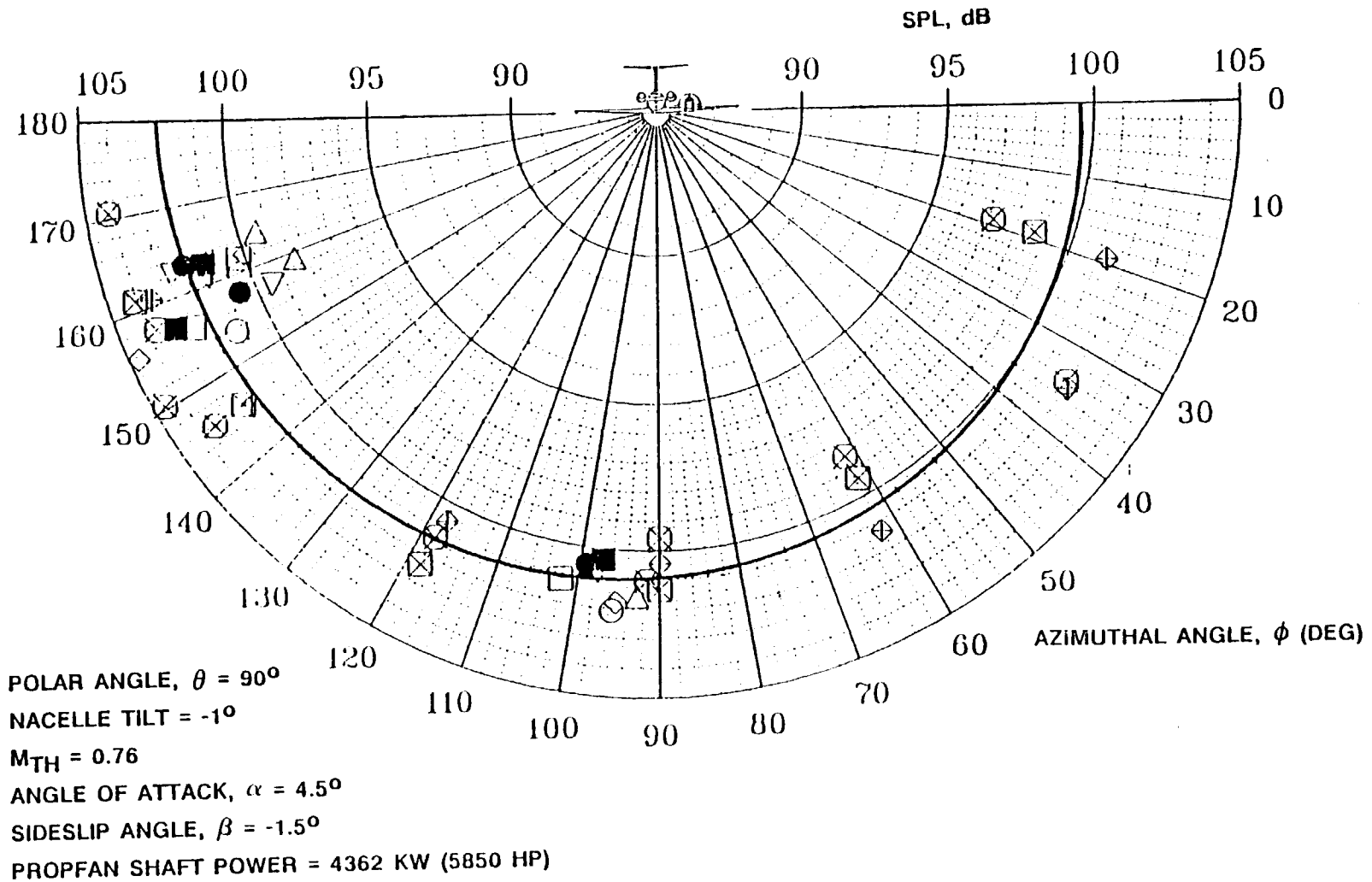


Figure 426. Azimuthal Noise Directivity at Blade Passage Frequency - Data Normalized to 305m (1000 ft) Radius

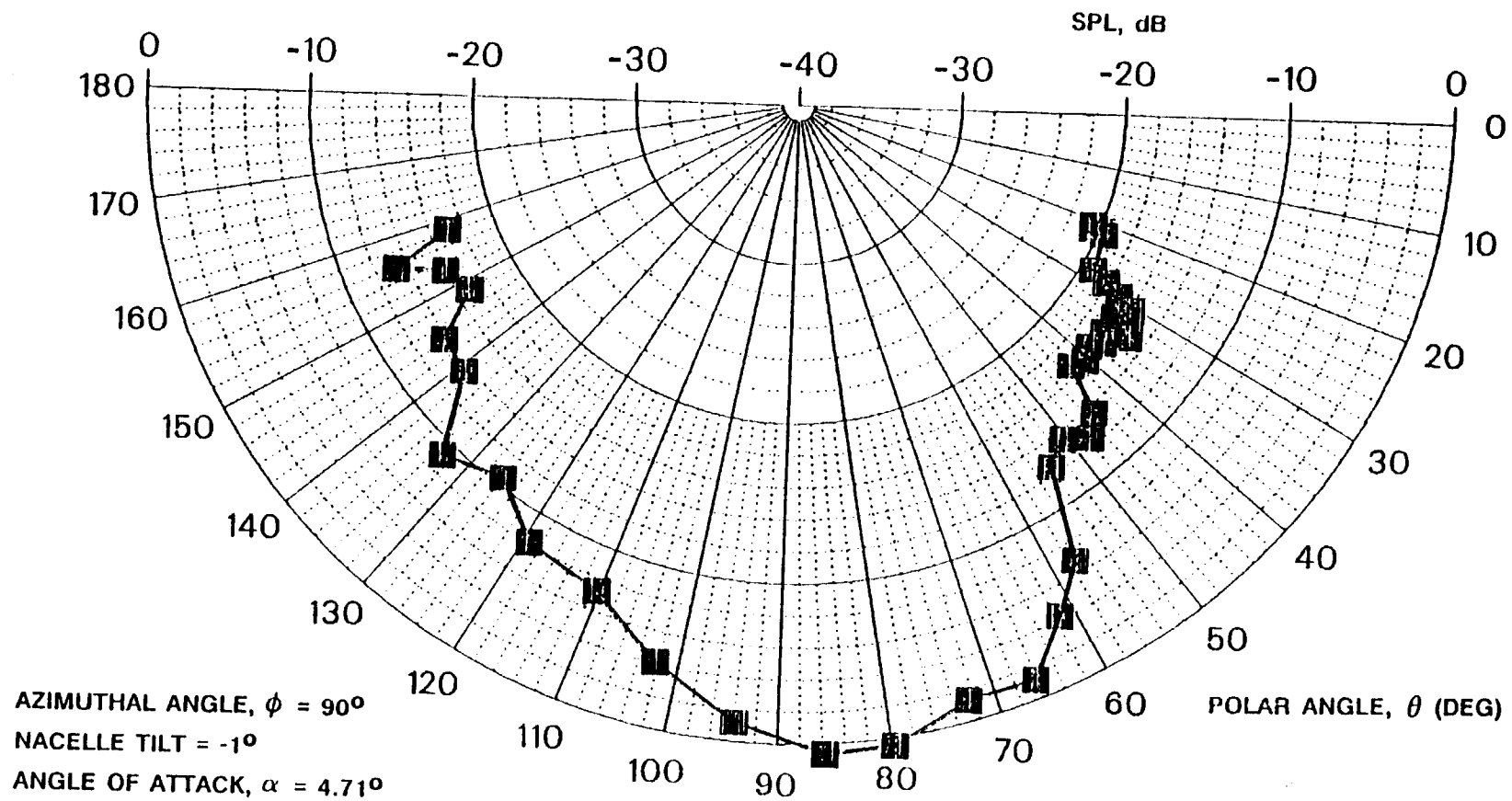


Figure 427. Polar Noise Directivity at Blade Passage Frequency - Data Normalized to 305m (1000 ft) Radius

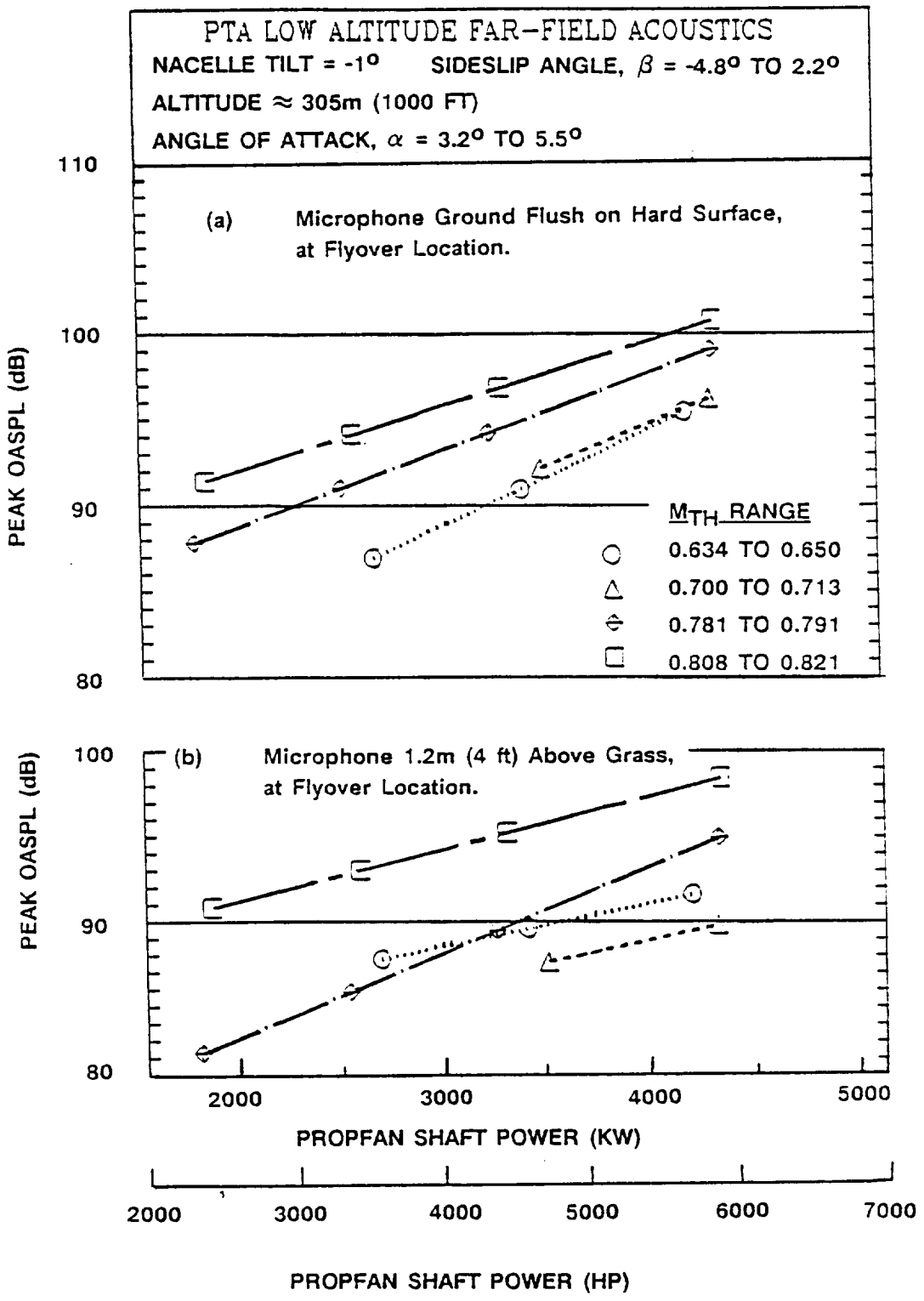


Figure 428. Effects of Power and Helical Tip Mach Number on OASPL

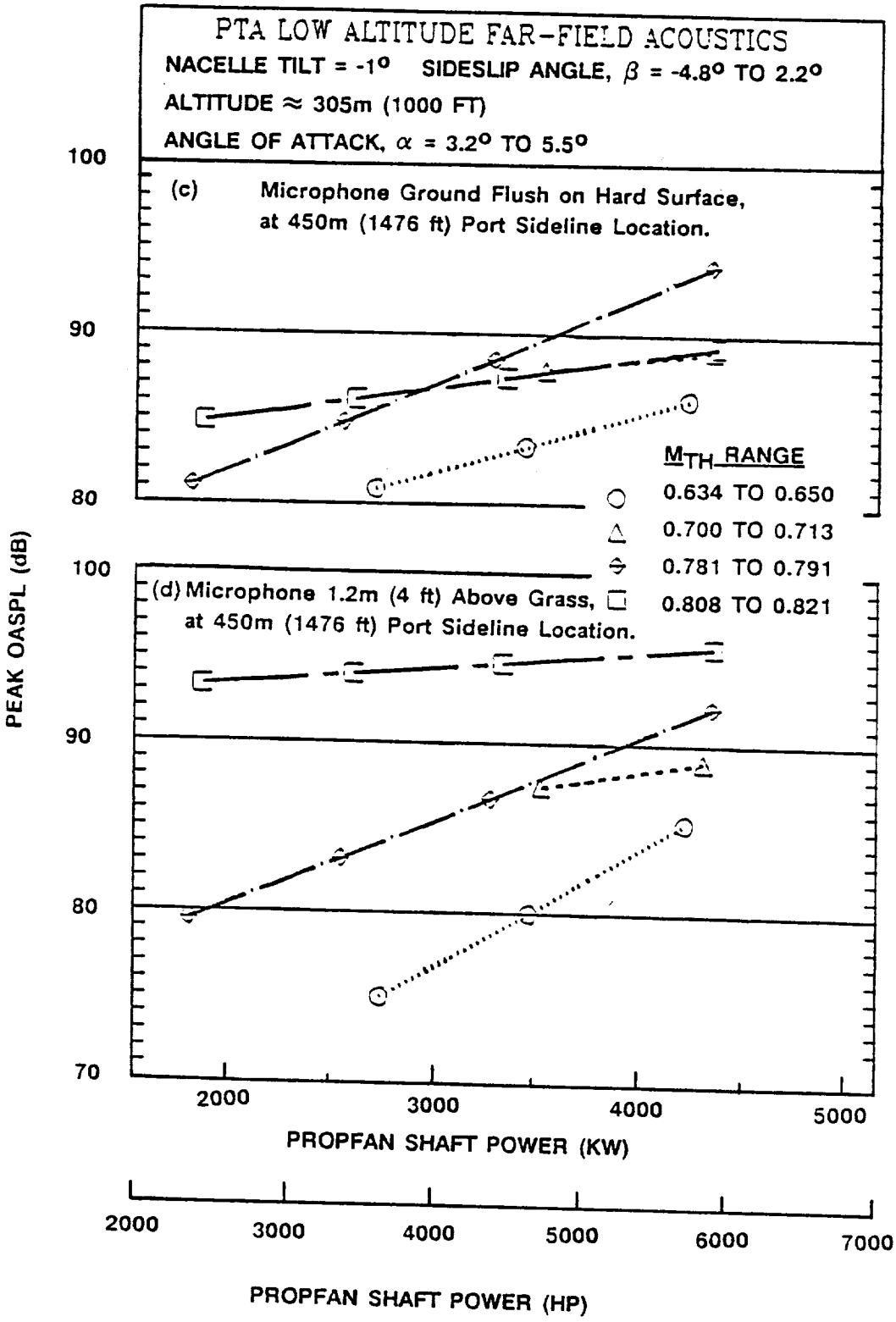


Figure 428. Effect of Power and Helical Tip Mach Number on Peak OASPL (Continued)

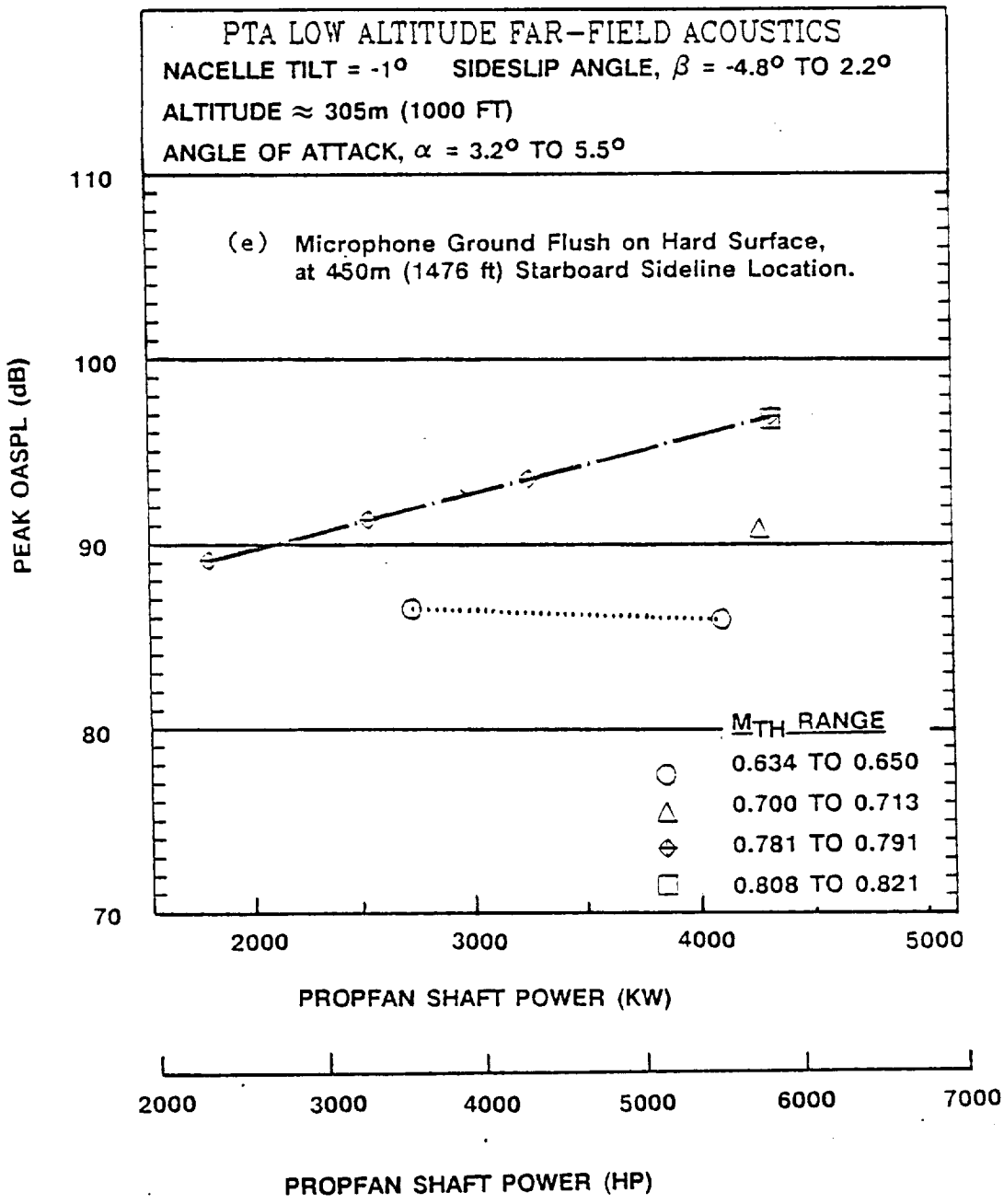


Figure 428. Effect of Power and Helical Tip Mach Number on Peak OASPL (Continued)

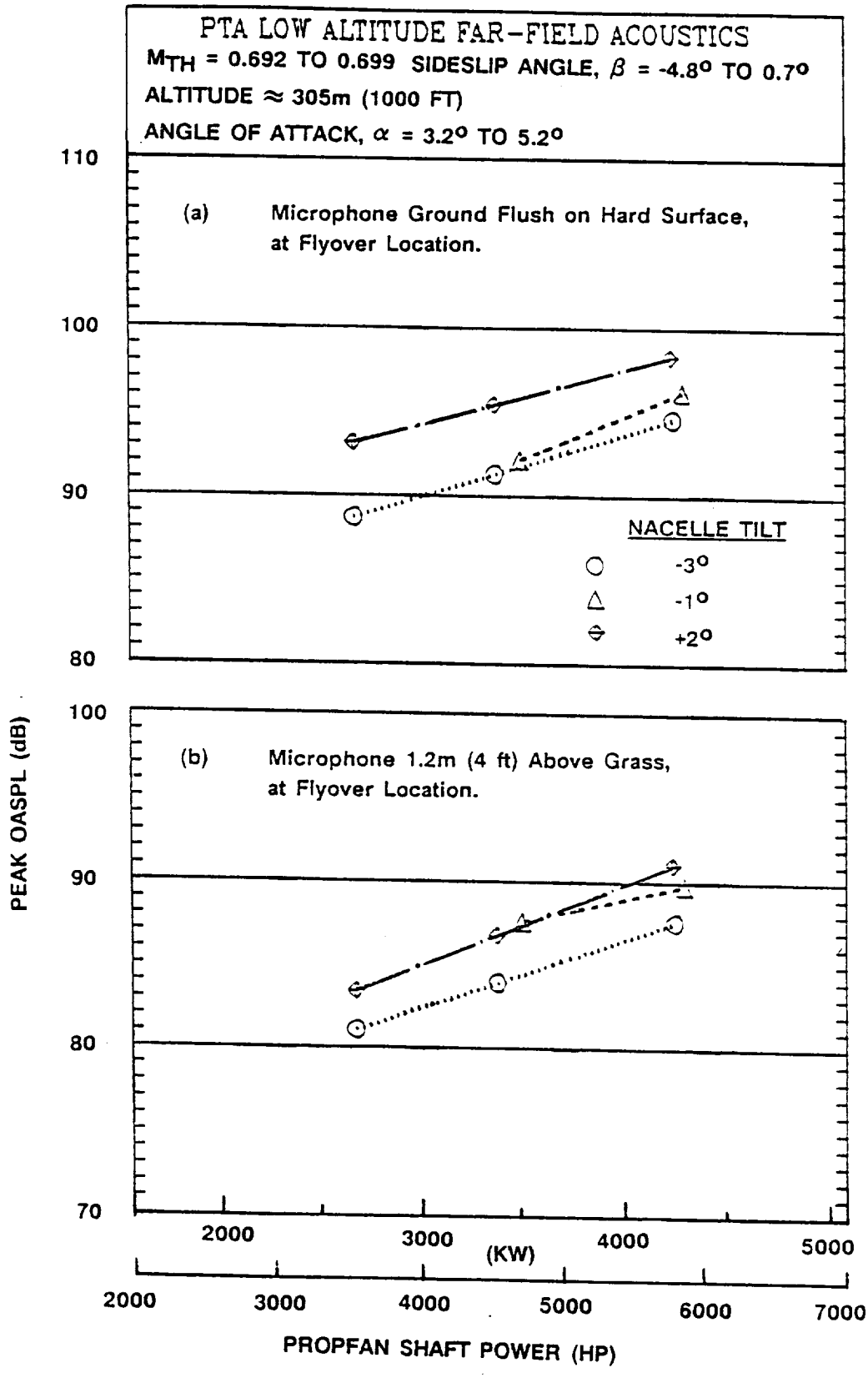


Figure 429. Effects of Power and Nacelle Tilt on Peak OASPL

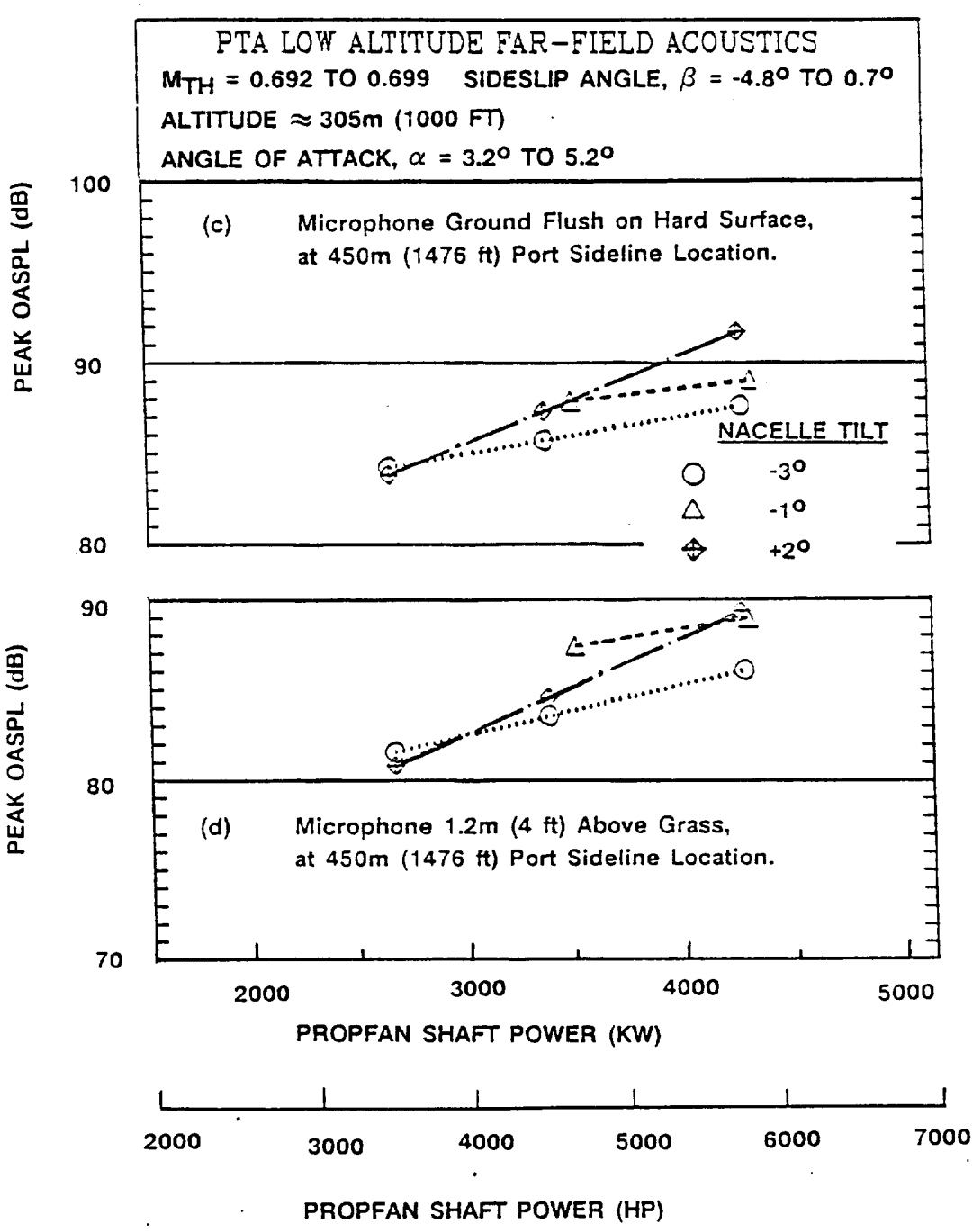


Figure 429. Effects of Power and Nacelle Tilt on Peak OASPL (Continued)

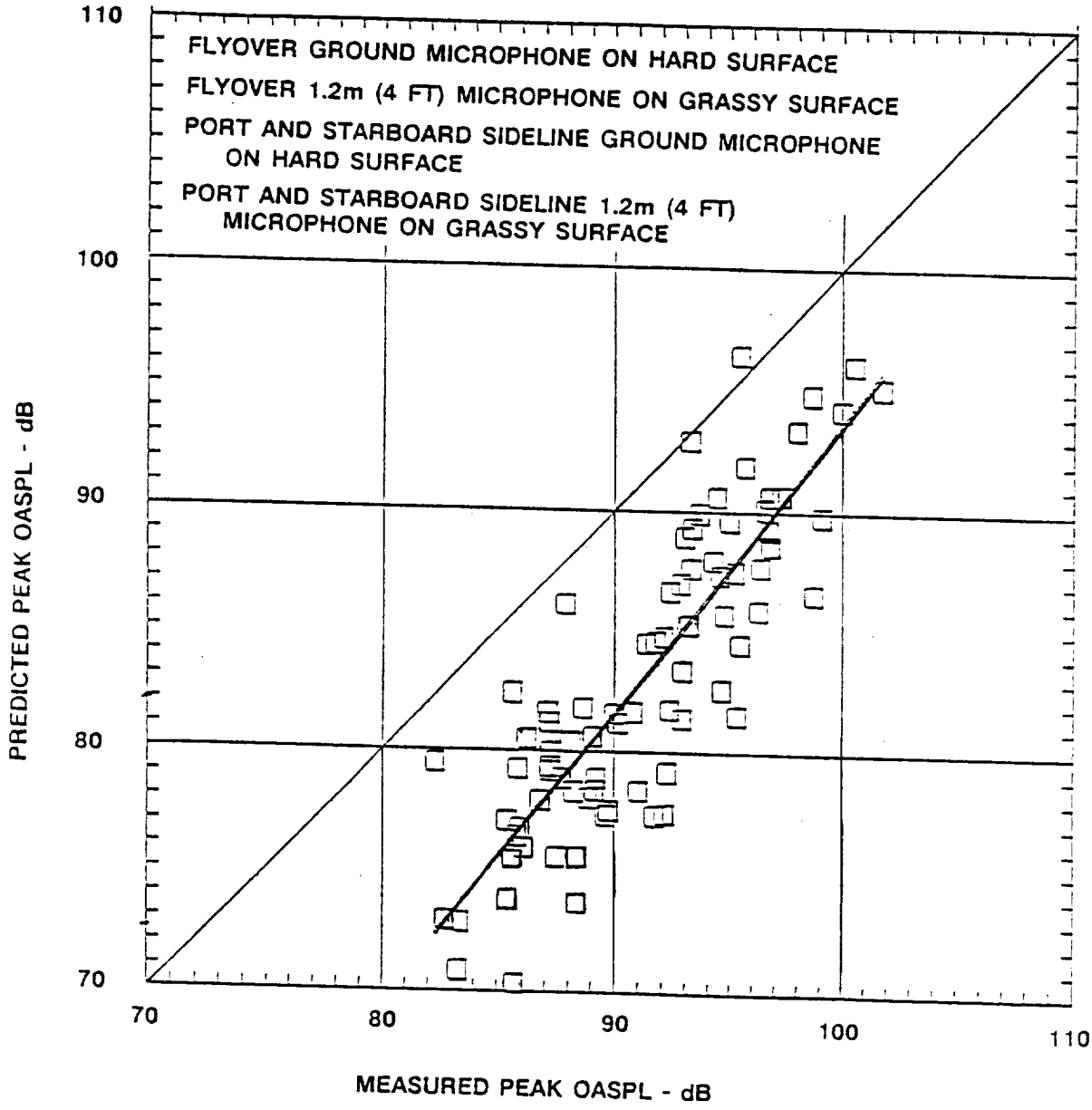


Figure 430. Comparison of Predicted and Measured Peak OASPL

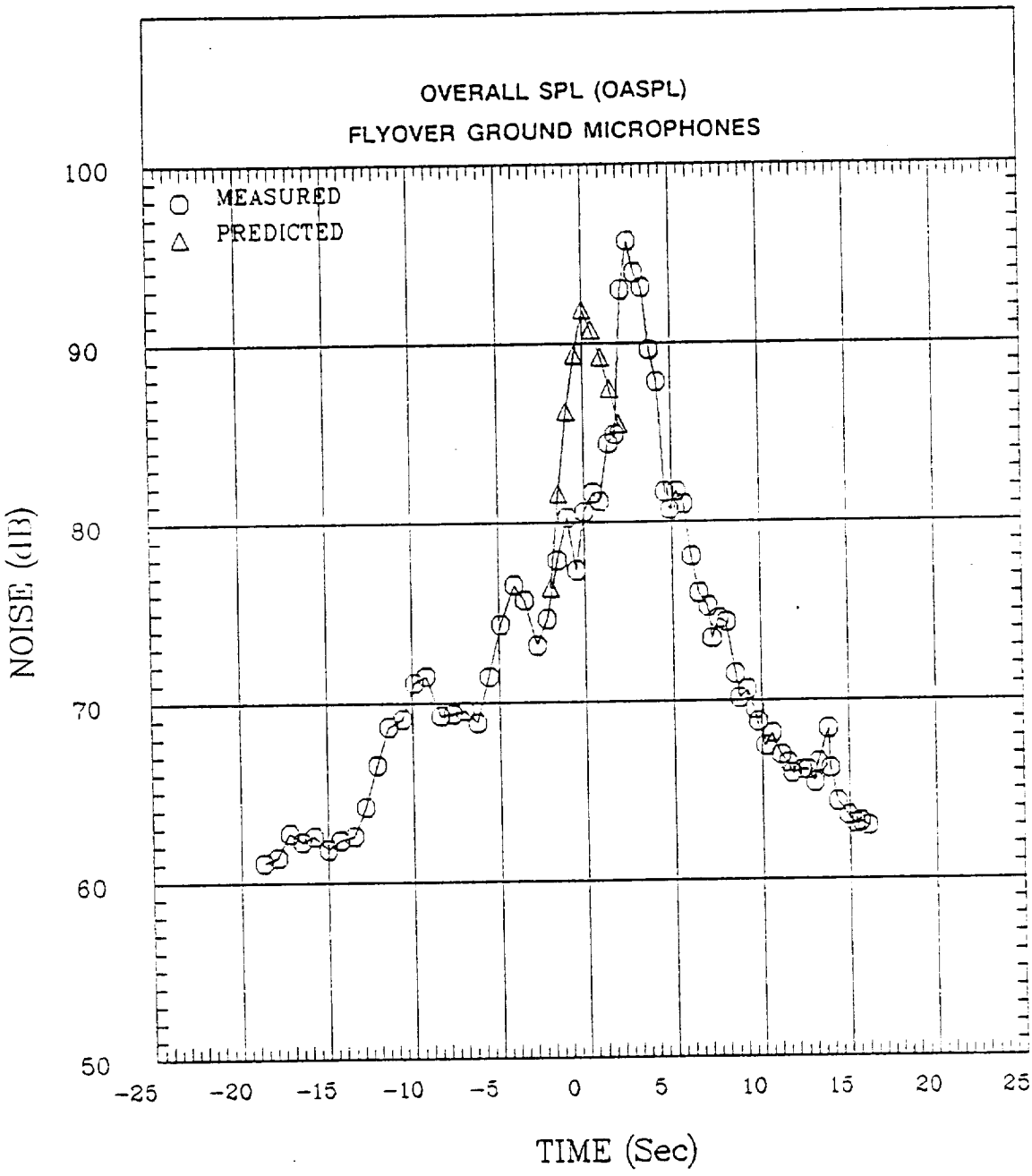


Figure 431. Comparison of Predicted and Measured Time Histories

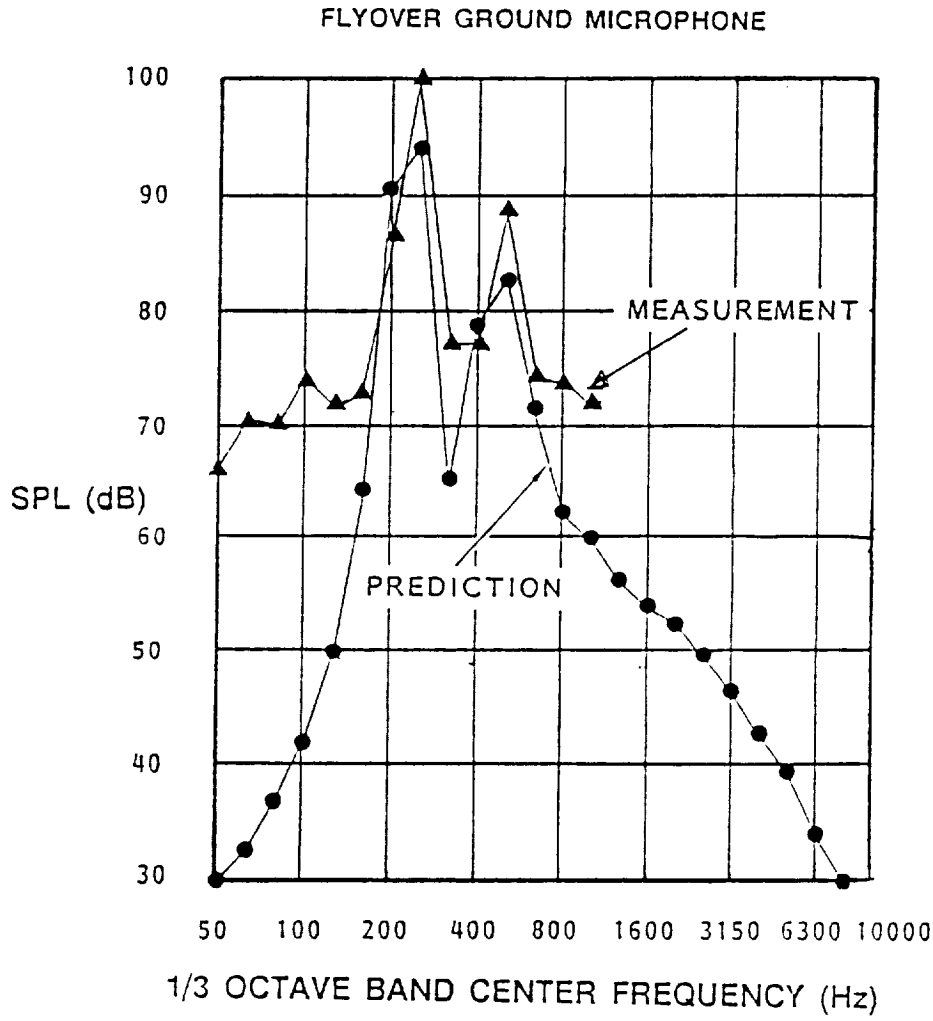


Figure 432. Comparison of Predicted and Measured Noise Spectra

band spectra. Since the theory predicted only propfan noise, it would not be expected to match the data except in the regions near the tone and harmonics.

Figures 433(a) through (d) show that the trends of power effects on OASPL are reasonably predicted even though the levels are missed. Figures 434(a) through (d) show a similar result for prediction of tip Mach number effects. Figure 435, however, shows that as was the case for other noise parameters, the theory was inadequate in prediction of nacelle tilt angle effects.

9.3.3.2 Lateral Noise Attenuation

Lateral noise attenuation is that attenuation of sideline noise that cannot be accounted for by known factors. As illustrated in Figure 436, lateral attenuation is defined for the purposes of this discussion as the difference between sound pressure levels under the flight path and the sound pressure levels for the same propagation distance at some azimuthal angle to the side of the aircraft.

The lateral attenuation was calculated by using the sound pressure levels from flyover and sideline inverted ground microphones at the time corresponding to peak OASPL in the time history. Only the inverted ground microphone data were used so that the differences in ground reflections were minimized. The calculations were made only for the first blade passing frequency tone.

Since the propfan rotational speed changed from one flight to the other, BPF varied within the range of four 1/3-octave bands. The sum of the sound pressure in those four bands represents the BPF tone since the BPF tone level is higher than the other three bands by about 10 dB. Therefore, the total sound pressure levels (sum in the four bands) were used to derive the lateral attenuation of BPF tone. The measured flyover sound pressure levels were extrapolated to the same propagation distances as that of the sideline microphone (both corresponding to the emission time). The emission coordinates and the extrapolations were derived using the measured radar, forward speed, and ambient condition data.

Figures 437 and 438 show for port and starboard sides of the aircraft, respectively, the lateral attenuation data thus derived. It can be seen that there is considerable scatter in the data, but this is typical for such data since they came from many different flights at different altitudes and different propfan operational parameters. Curves faired through these data with least squares methods do, however, show systematic trends. This can be seen in Figure 439 where all of the faired data are shown.

As shown in Figure 439, on the port side of the aircraft, or side nearest the propfan, there was positive attenuation (noise was reduced with elevation angle) while on the side away from the propfan, the noise attenuation was negative. Increasing the nacelle tilt angle increased noise attenuation.

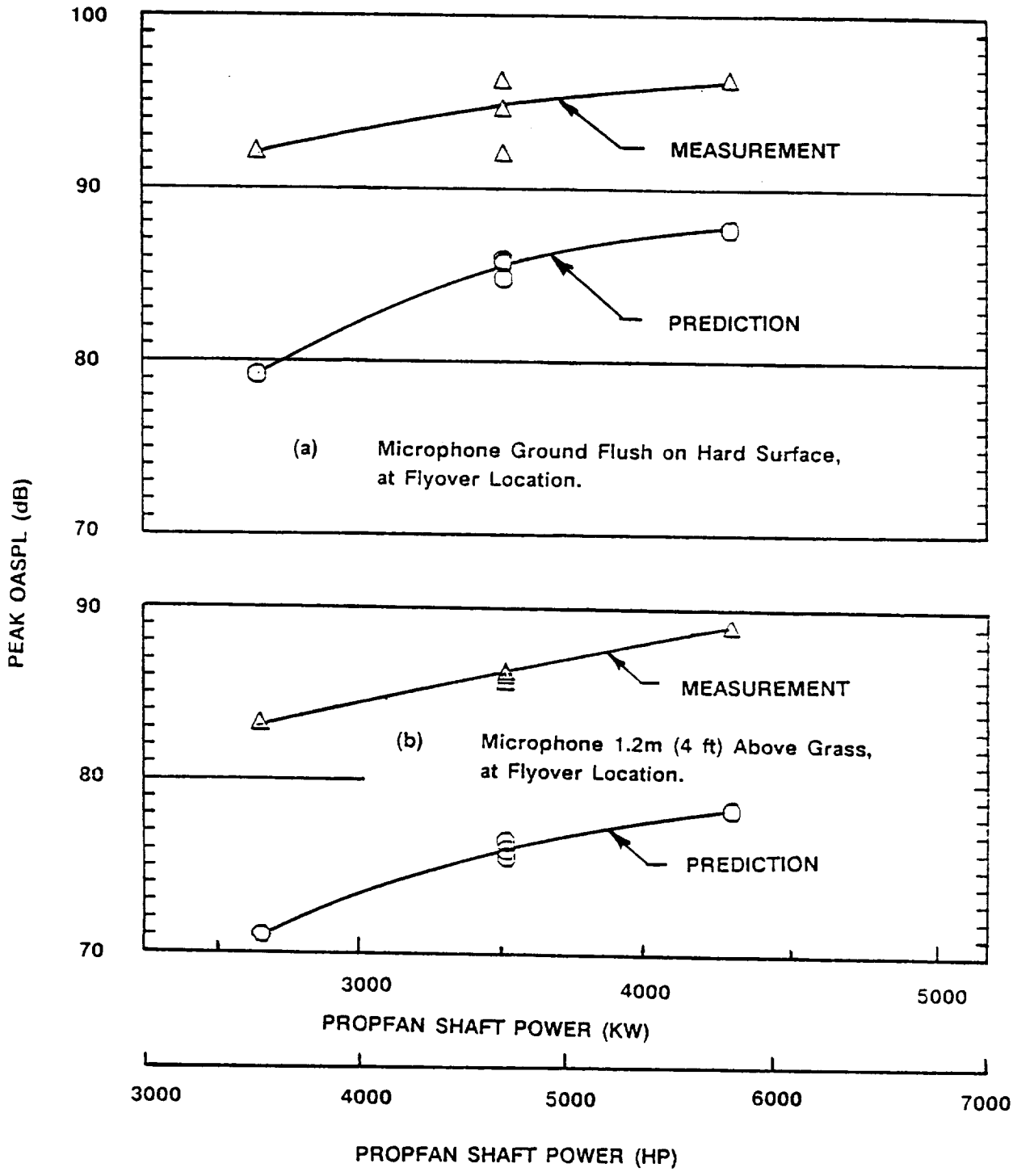


Figure 433. Effects of Shaft Horsepower on Predicted and Measured Noise at the Nominal Conditions of: Altitude = 305 m (1000 ft); V_{ROT} = 213 m/s (700 fps); M_{TH} = 0.7; NT = -1°; Angle of Attack = 4.3°; Sideslip Angle = -1°.

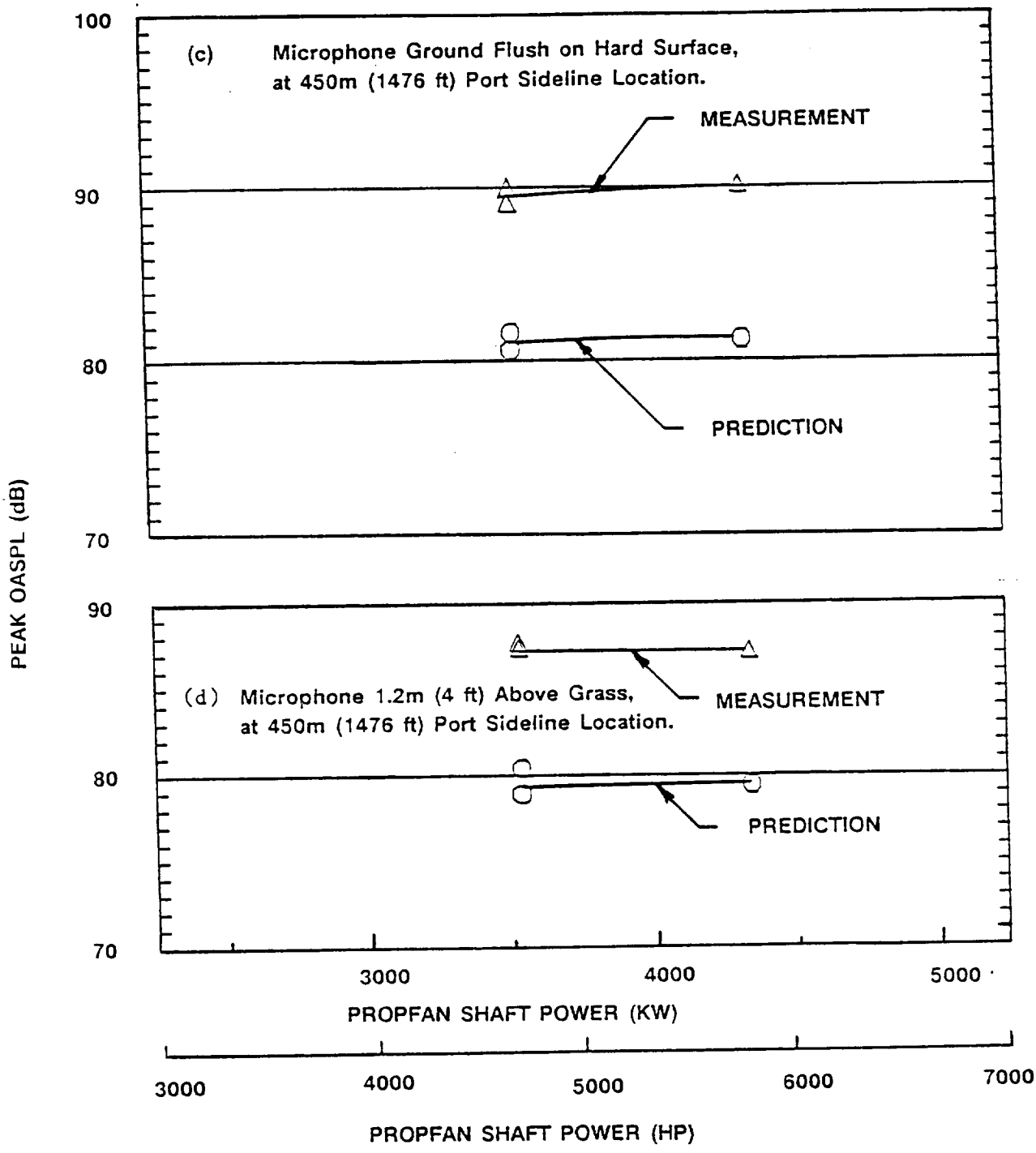


Figure 433. Effect of Shaft Horsepower (Continued)

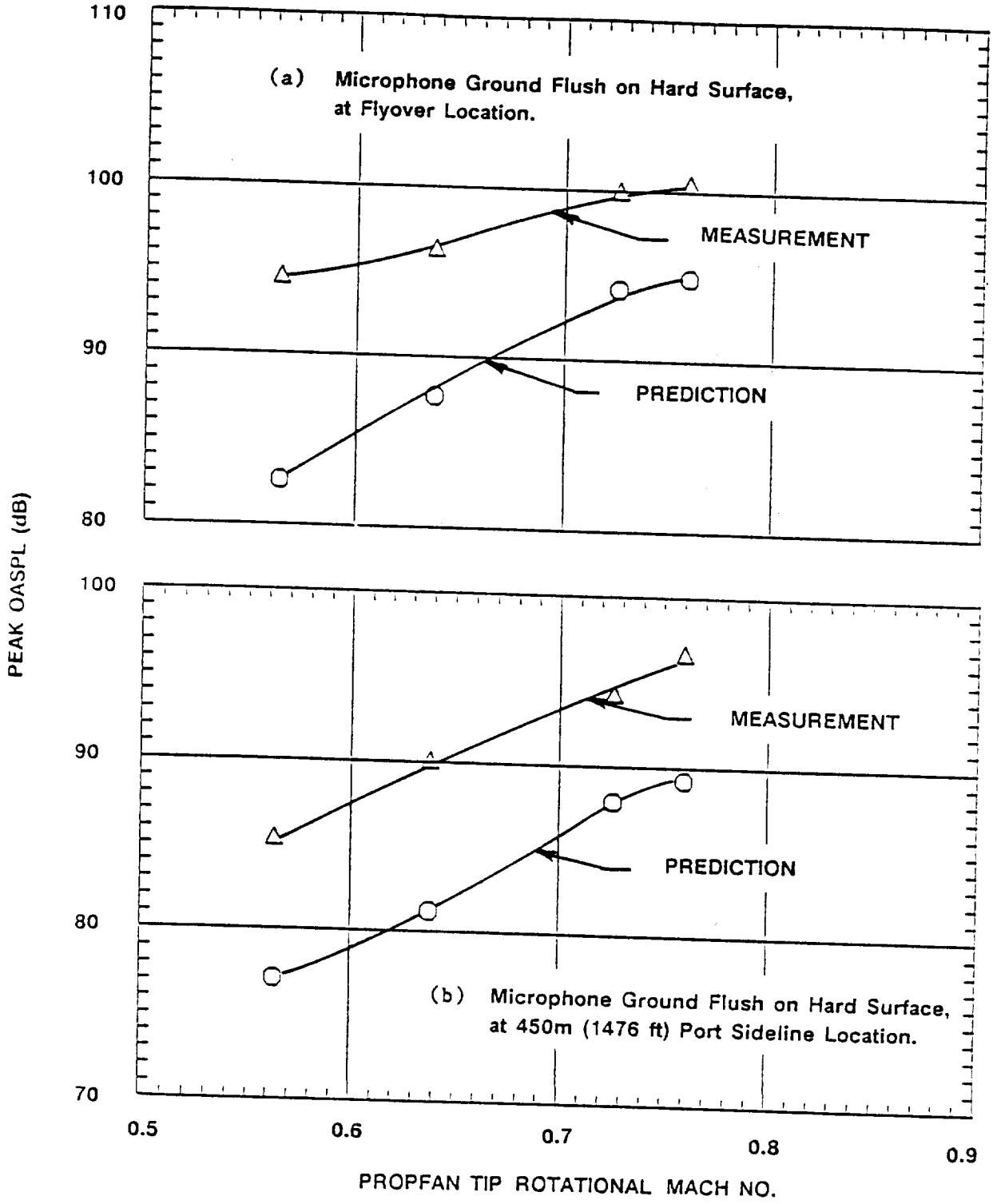


Figure 434. Effects of Tip Speed on Predicted and Measured Noise at the Nominal Conditions of: Altitude = 305 m (1000 ft); Power = 4320 kw (5790 PSHP); NT = -1°; Angle of Attack = 4.3°; Sideslip Angle = -1°.

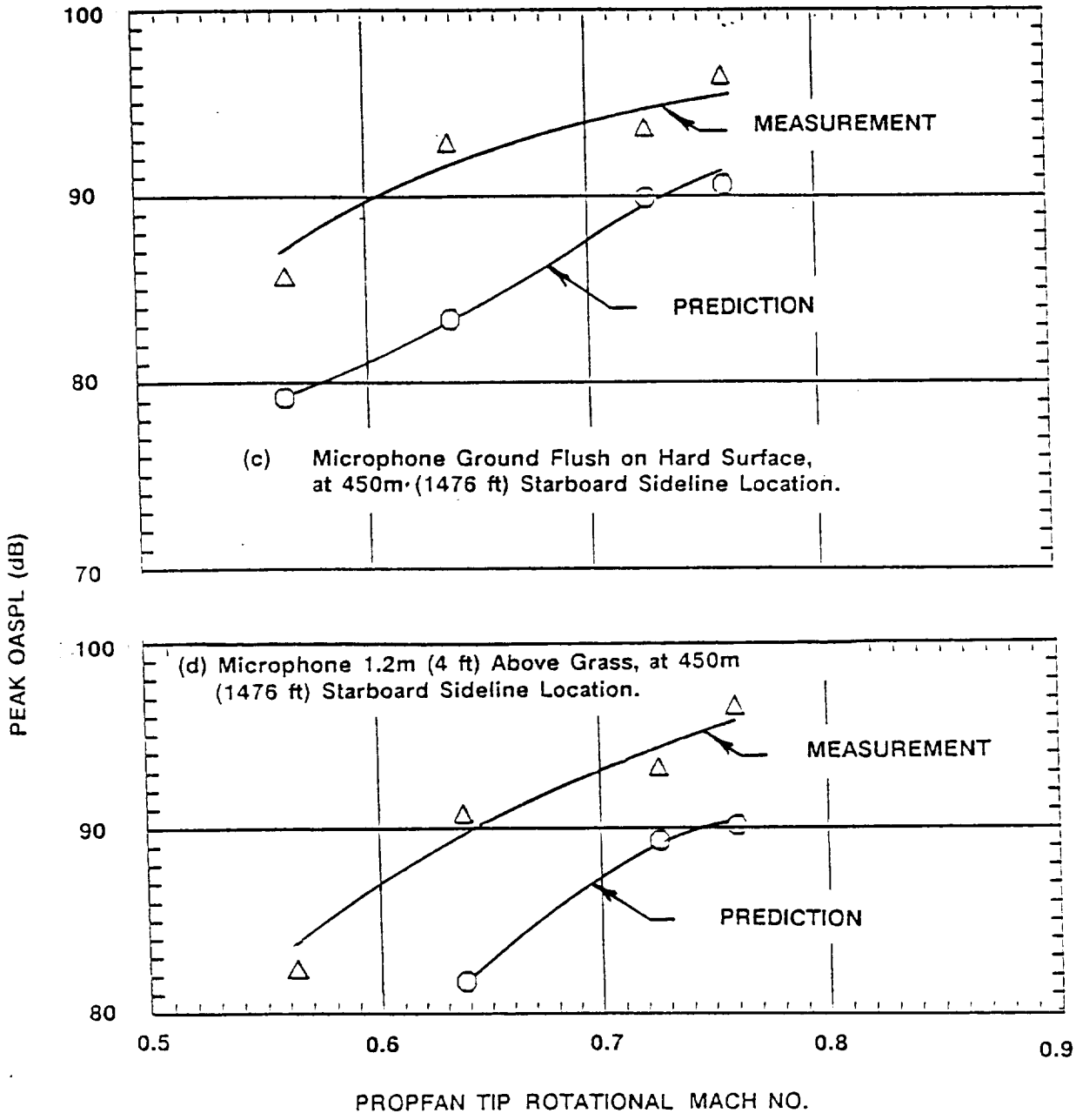


Figure 434. Effect of Propfan Tip Mach Number (Continued)

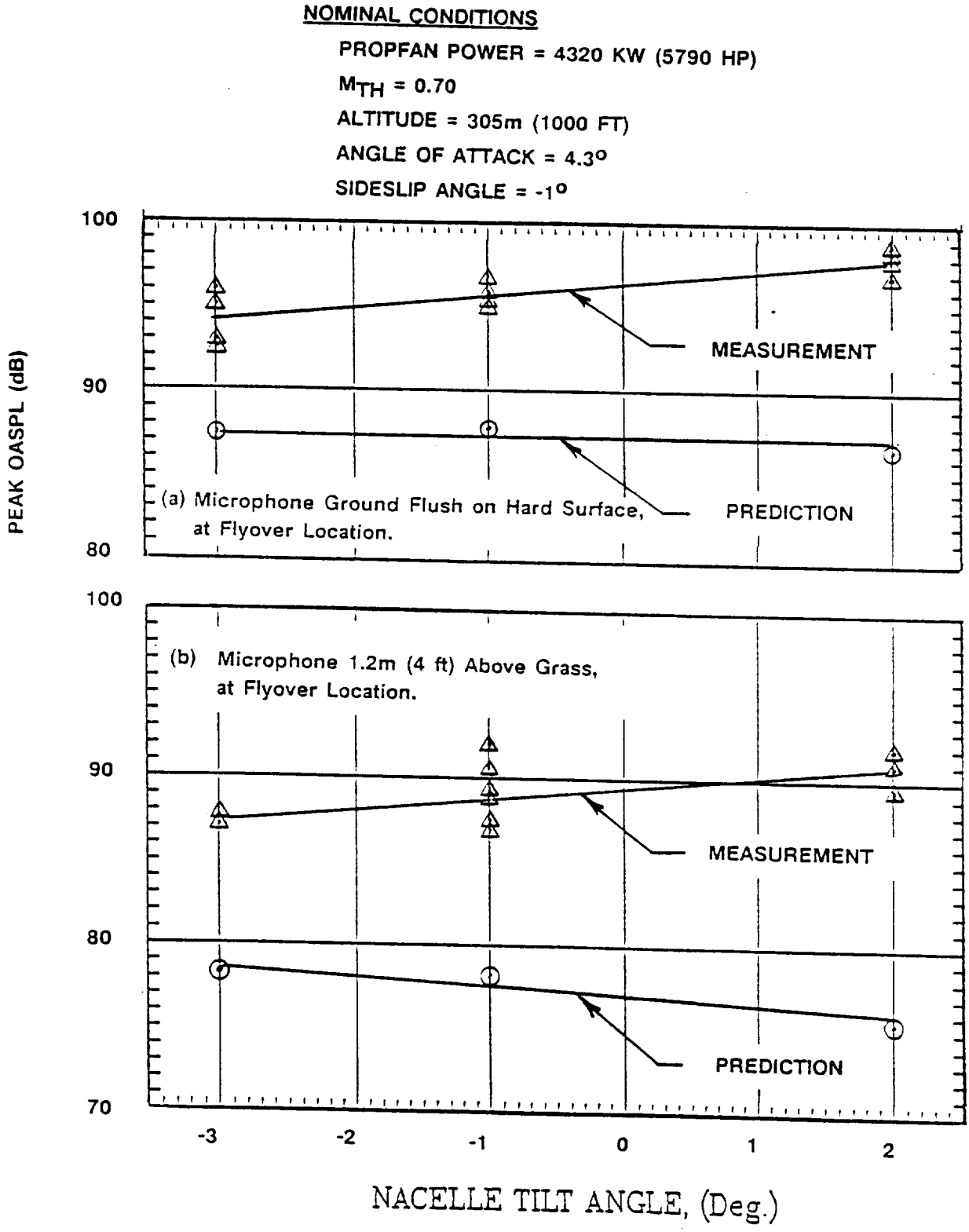


Figure 435. Effect of Nacelle Tilt on Far-Field Noise

LATERAL NOISE ATTENUATION:

$$LNA_{\phi} = SPL'_2 - SPL_1$$

$$SPL'_2 = SPL_2 - \Delta SPL$$

ΔSPL = CORRECTION FOR DISTANCE, (R - H)

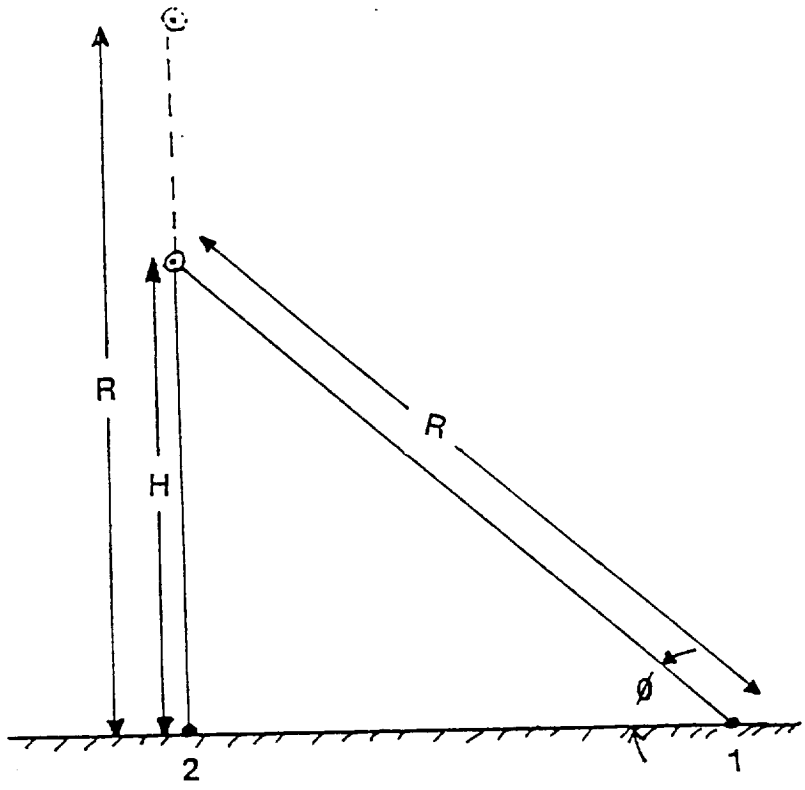


Figure 436. Calculation Procedure for Lateral Noise Attenuation

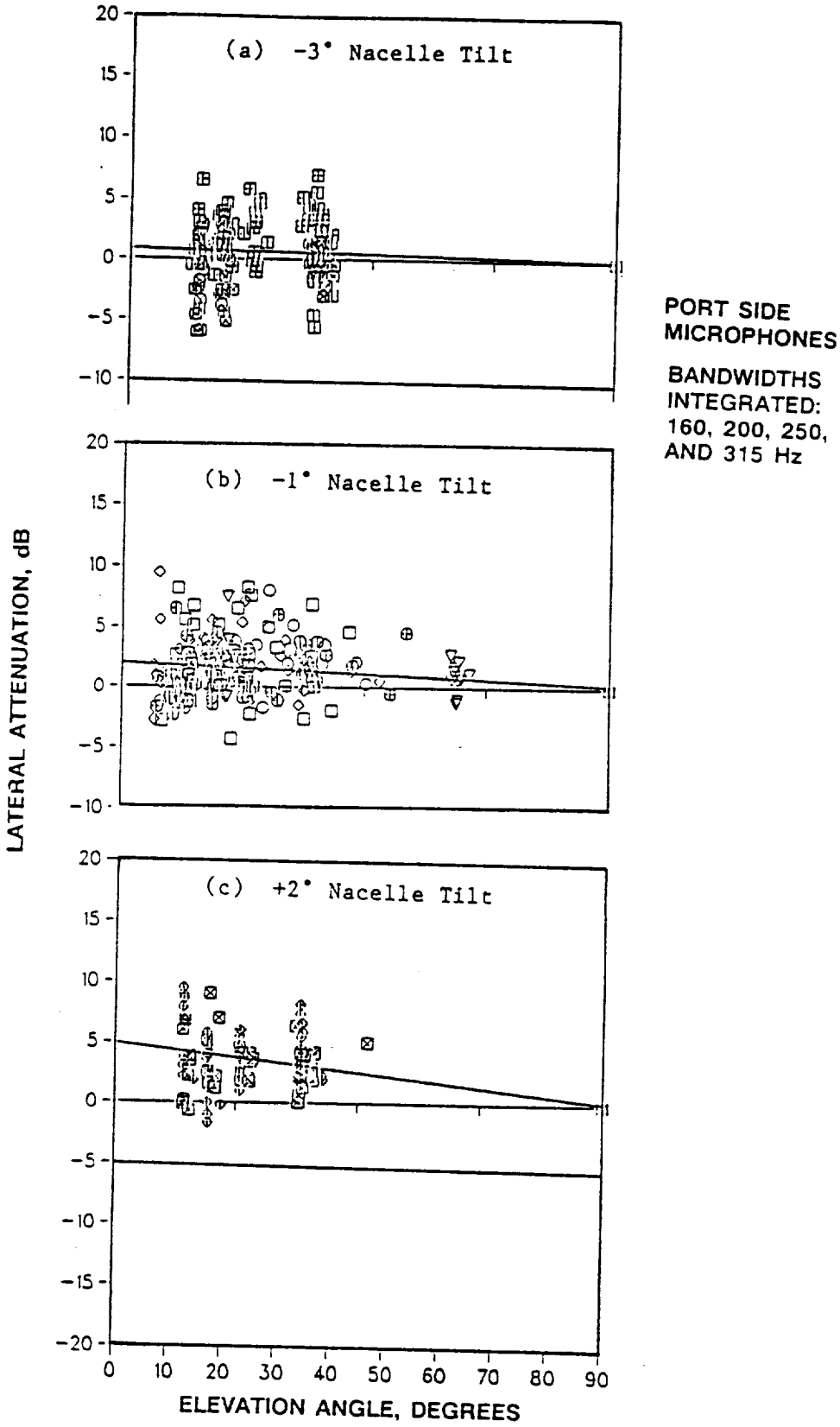


Figure 437. Lateral Attenuation as a Function of Elevation Angle - Port Side

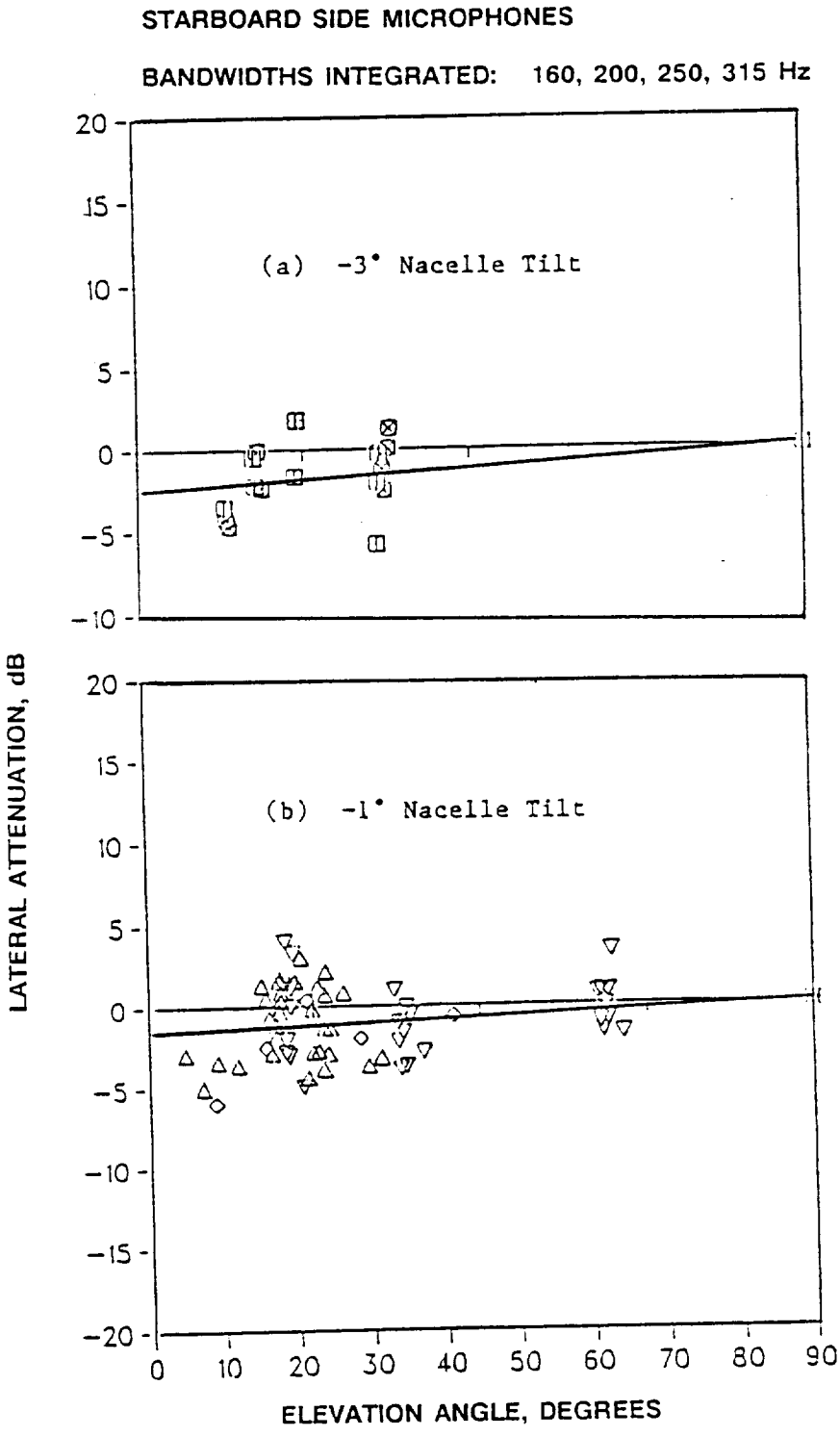


Figure 438. Lateral Attenuation as a Function of Elevation Angle - Starboard Side

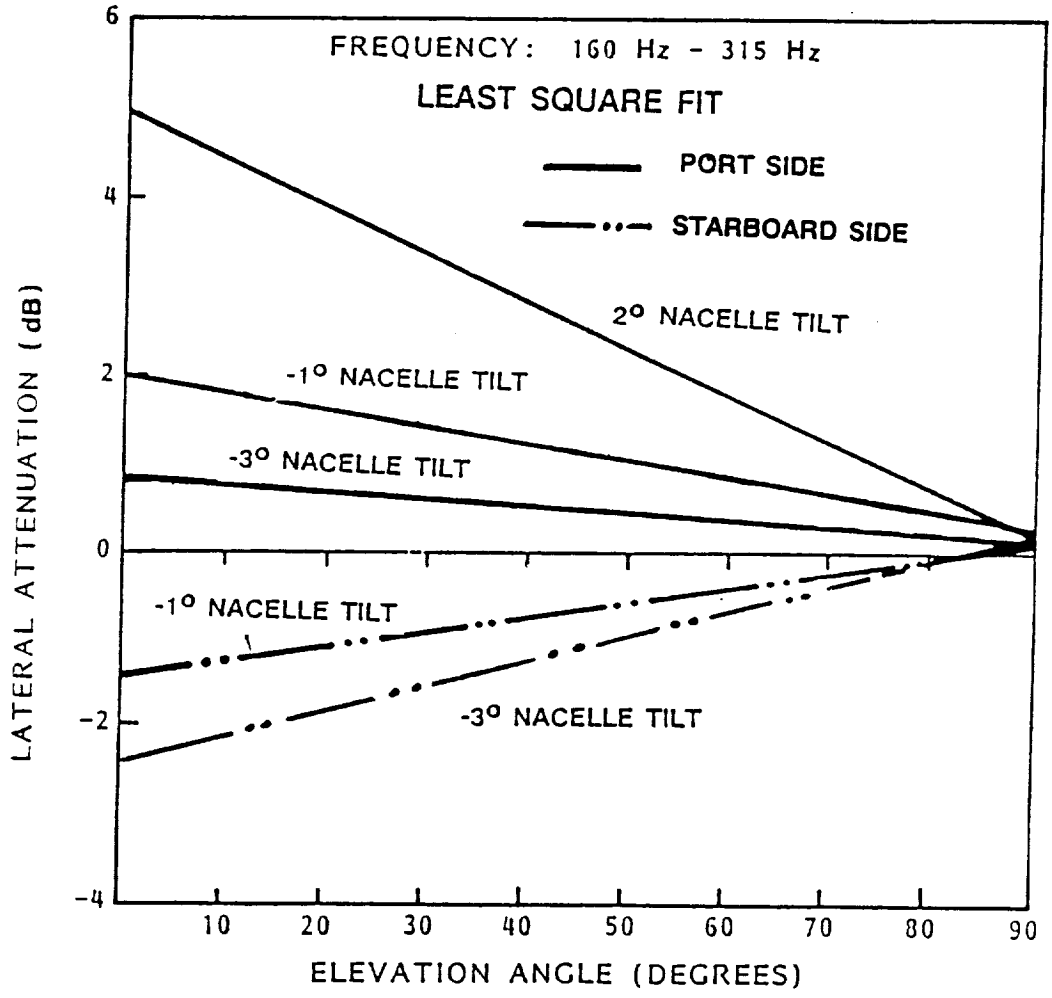


Figure 439. Summary of Lateral Attenuation Results

9.4 CABIN NOISE TESTS

9.4.1 Objectives and Scope

The cabin noise tests were performed to determine levels and spatial distributions of noise in the untreated-wall cabin of the PTA aircraft. In conjunction with the ground acoustics and vibration tests, these tests also provided information about noise paths and the relative importance of airborne and structureborne noise.

9.4.2 Test Procedures

The cabin area of interest for the cabin noise tests is shown in Figure 440. The cabin was clear of all personnel and equipment for a space approximately 1.5m (5 ft) forward of the prop plane to 3m (10 ft) aft of the prop plane. The cabin walls were essentially untreated throughout this region, and windows were production model hardware. Cabin air temperatures were maintained within a constant range for all tests.

Cabin noise data were obtained concurrently with the other high altitude test data. In addition, however, tests for some flight conditions were made with a movable TRAM inside the cabin to obtain spatial surveys of noise distribution. The flight test envelope for these tests was shown in Figure 386. For two of the flight conditions shown in Figure 386, the TRAM (with an array of microphones as shown in Figure 441) was positioned at 18 points along the fuselage axis spaced approximately 26 cm (10.25 in.) apart. Data were then recorded for variations of rotational speed at maximum continuous power. At one TRAM position and one flight condition, the effects of cabin pressurization were measured.

All data were obtained with the aircraft in level flight and the Spey engine on the propfan side operating at minimum power needed to maintain level flight.

9.4.3 Results and Discussion

The time histories of sound pressures inside the cabin were similar to those measured on the exterior surface of the fuselage with multiple tones standing well above a random noise floor as shown in Figure 442. The level of the first-order tone inside the cabin was lower than expected--indicating a noise reduction ranging from 30 to 35 dB at the low-order tones to 40 to 45 dB at the high orders. These data are for a position corresponding to that where the highest exterior noise levels were measured.

Spectra for a lateral array and a longitudinal array of microphones at seated head height are plotted in Figure 443. At any given blade order frequency, it can be seen that there is a variation of 10 to 25 dB from one position to another. Highest levels did not necessarily occur nearest the propfan, nor did the lowest levels occur farthest from the propfan. Noise level contours in the plane of the propfan at blade passage frequency are shown in Figure 444. The levels were clearly influenced by the

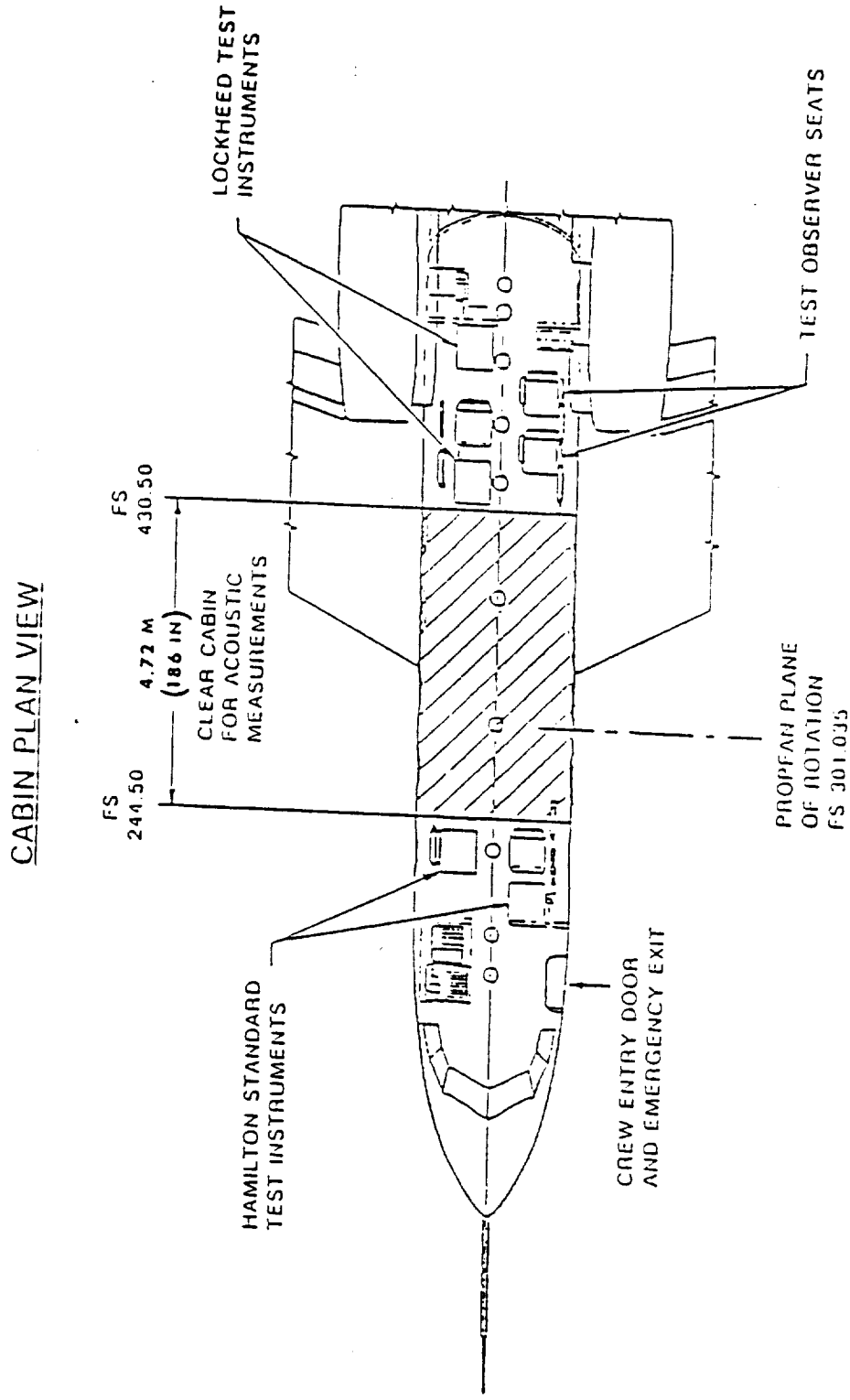


Figure 440. Cabin Acoustic Measurement Area

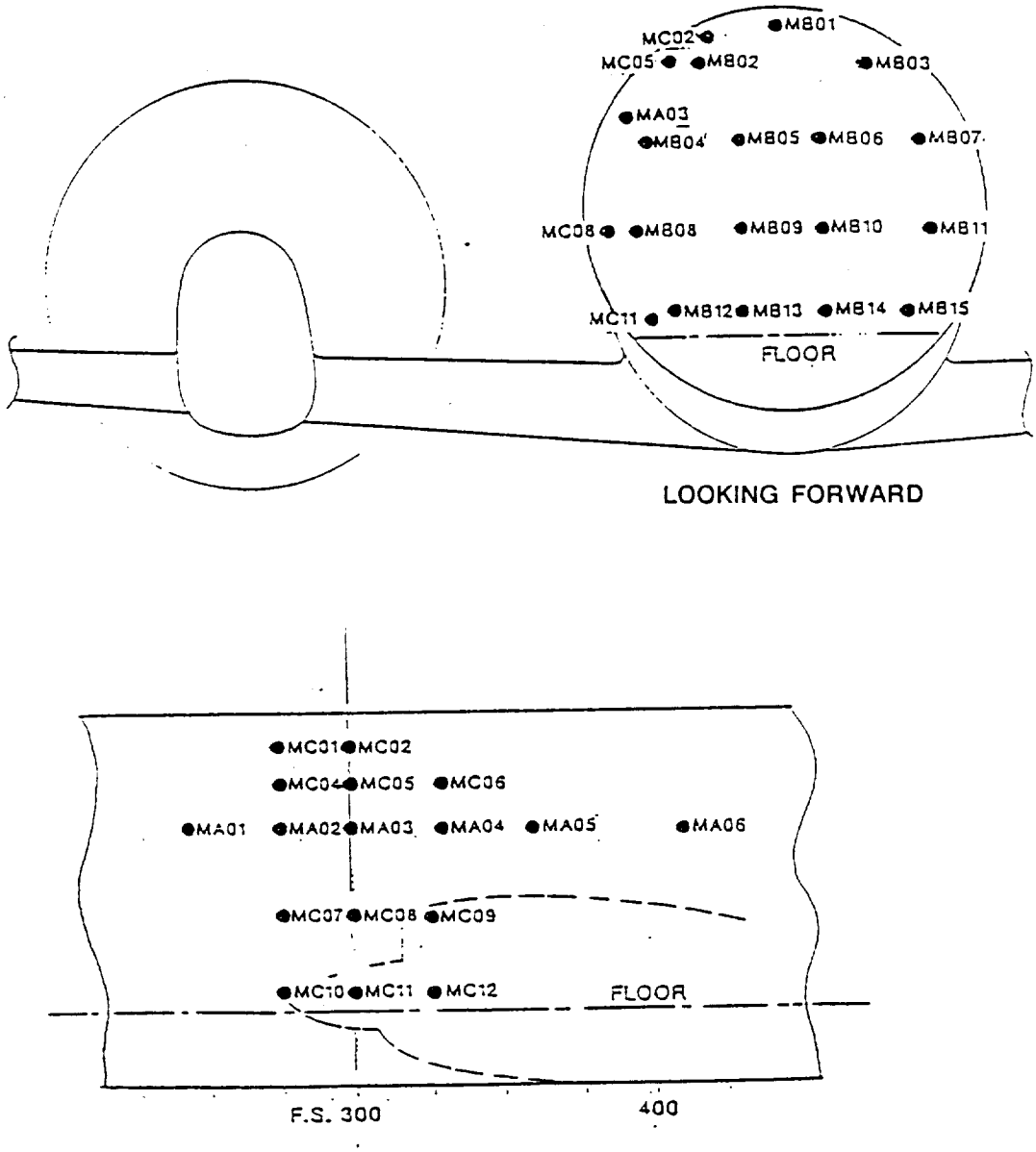
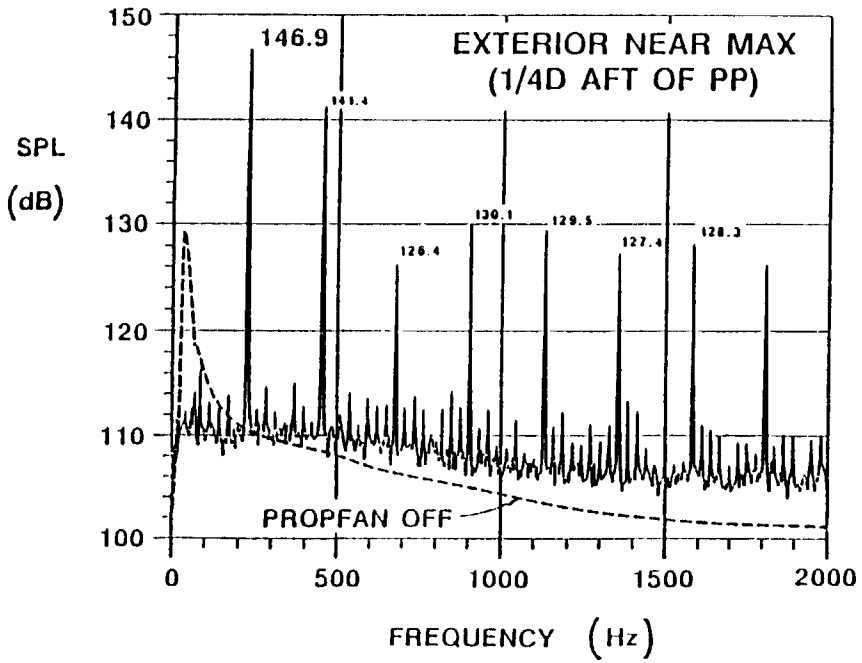


Figure 441. Identification and Location of Cabin Figure Microphones

NT = -1°
M = 0.8
H = 10,668m (35,000 FT)

V_{ROT} = 243 MPS (797 FPS)
PSHP = 2259 KW (3029 HP)



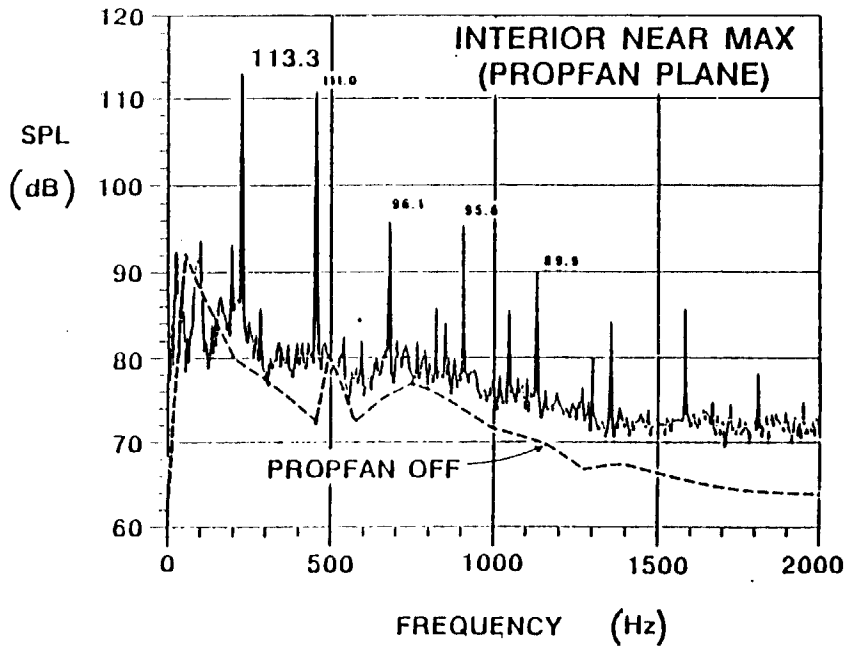


Figure 442. Comparison of Interior and Exterior Cabin Noise Spectra

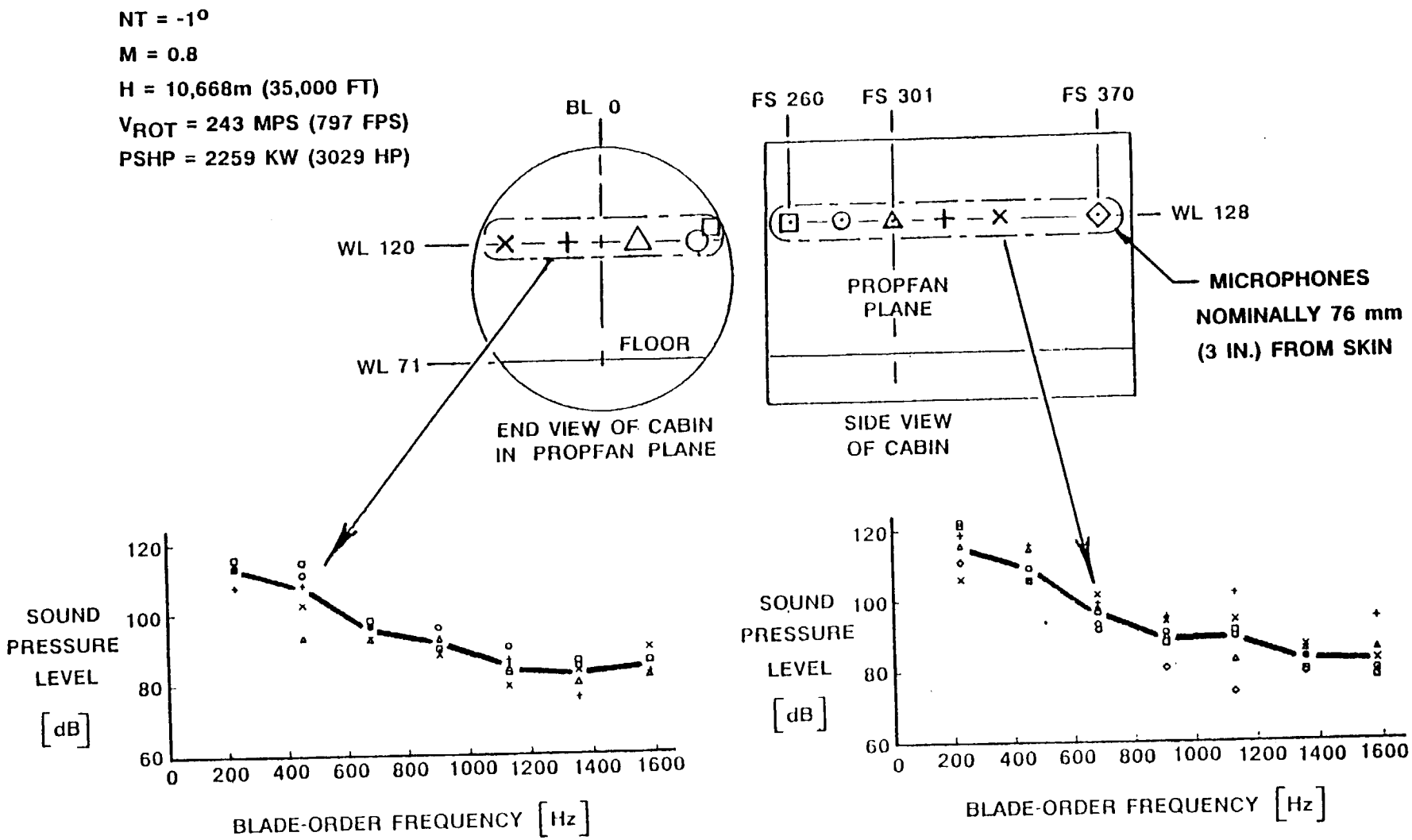
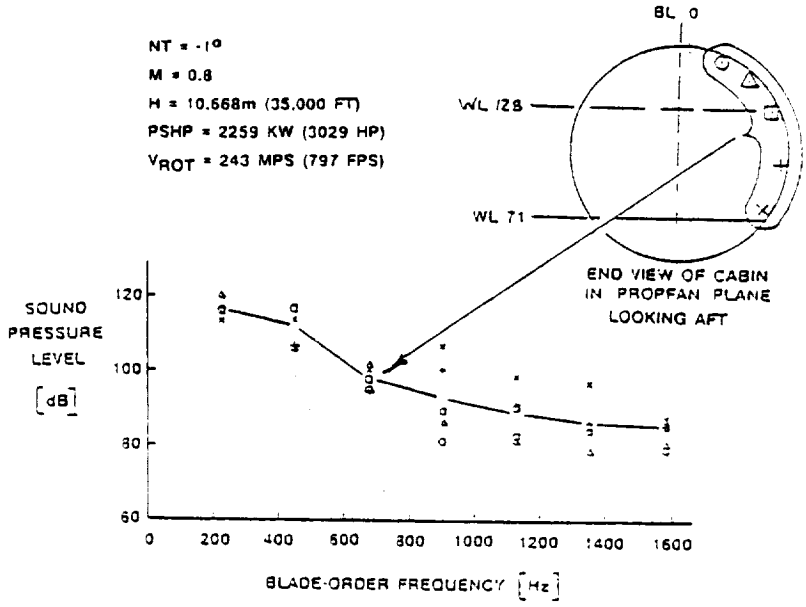


Figure 443. Lateral and Axial Distribution of Cabin Noise



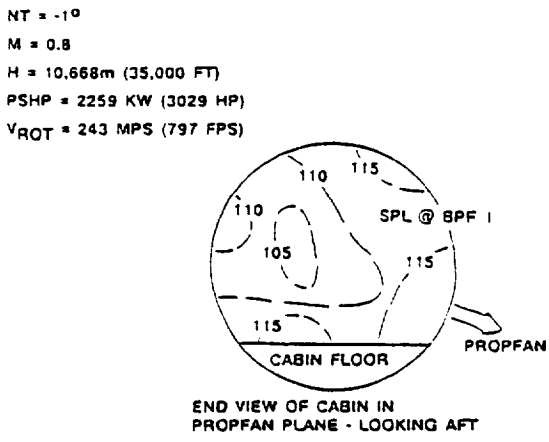


Figure 444. Spatial Variation of Cabin Noise in the Propfan Plane

dynamics of the shell structure and by the acoustic response of the cabin volume.

For the cases presented in Figures 443 and 444, propfan tip speed was 243 mps (797 fps), which corresponds to a blade passage frequency of 226 Hz. At other blade passage frequencies, the noise level spatial variation was similar, but highest levels occurred at other locations--again as a result of shell dynamics and cabin volume modal response.

The lines faired through the frequency spectra peaks in Figures 443 and 444 are average values for the arrays represented. Such averages will be used hereafter in the discussions of the effects of the various flight and propfan power parameters on noise. Thus the effect of propfan tip speed is displayed in Figure 445 for two conditions of cabin pressurization.

It can be seen that average cabin noise level was 1 to 5 dB higher when the cabin was pressurized. This is attributed to a stiffening of the shell when the cabin was pressurized and to the effects of the higher air density. Theoretically, the effect of the latter is expected to account for a noise increase of about 3 dB, so the effects of shell stiffening and resonance change appear to be insignificant.

Data analysis showed that cabin noise varied with aircraft and propulsion system operating parameters in the same manner as did exterior noise. This can be seen in Figure 446 where cabin average and fuselage average SPLs are plotted for four different speed/altitude conditions. The highest noise levels in both cases is for the design cruise condition, while lowest noise levels were measured in the low-speed climb condition.

The difference between the two sets of curves in Figure 446 represents the average noise reduction--approximately 25 dB for all conditions and all tones. The same kind of result is shown in Figure 447 where interior and exterior noise is shown for different propfan powers.

In order to assess the relative importance of structureborne noise, ground tests were performed, as described earlier, in which the structure of the aircraft was excited with shakers and acoustic horns. Certain reference accelerometers were used to define the level of excitation, and the cabin noise level was recorded as a function of these reference readings. The same reference instruments were then used in the flight tests to estimate the level of cabin noise caused by wing structural vibration.

Cabin structureborne noise predicted by this empirical technique was generally found to be significantly lower than measured cabin noise. This is illustrated in Figure 448 where predicted cabin noise for several values of wing vibration are compared with the values measured in flight. These results indicate that structureborne noise probably did not contribute to cabin noise except perhaps at the low-altitude, low-speed condition, and then only at the third-order blade passage frequency.

Other analysis techniques were also used to search for evidence of significant structureborne noise, but nothing was found to change the conclusion that the primary noise path in the PTA tests was airborne.

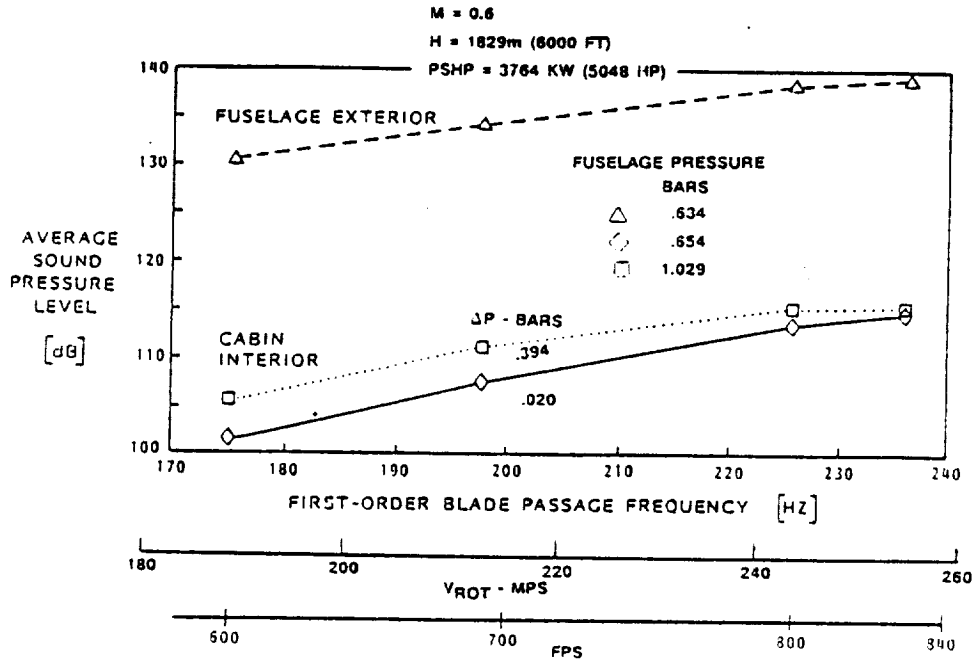


Figure 445. Effect of Fuselage Pressurization on Cabin Noise

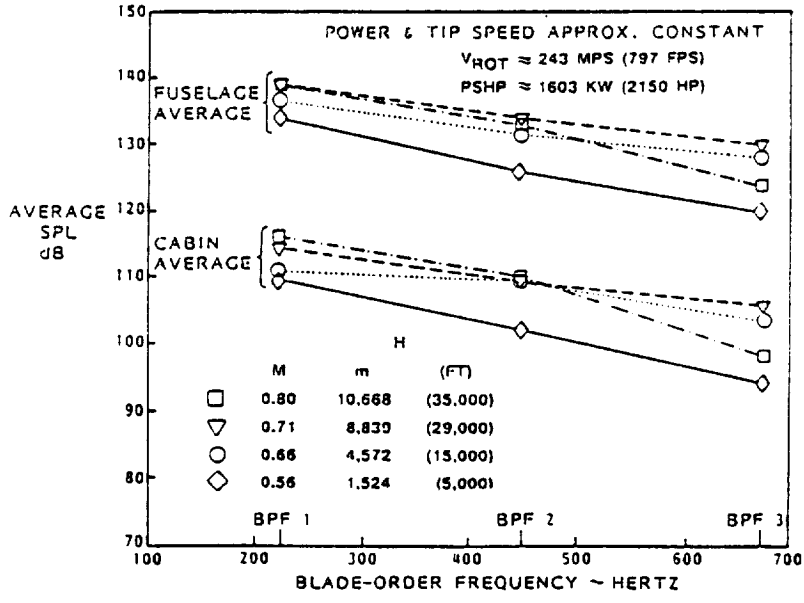


Figure 446. Effects of Flight Conditions on Cabin Noise

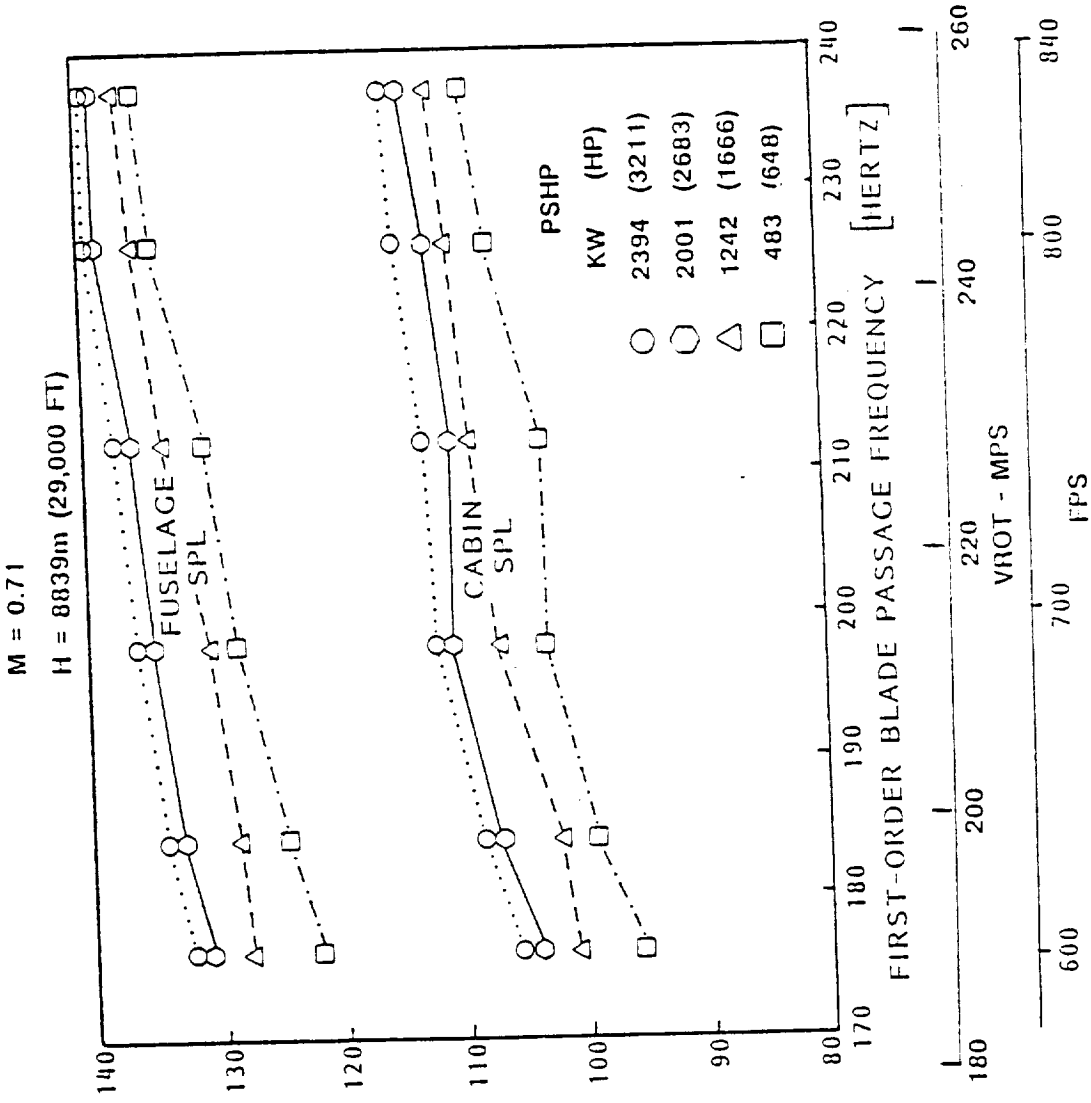


Figure 447. Effects of Propfan Power and Tip Speed on Cabin Noise

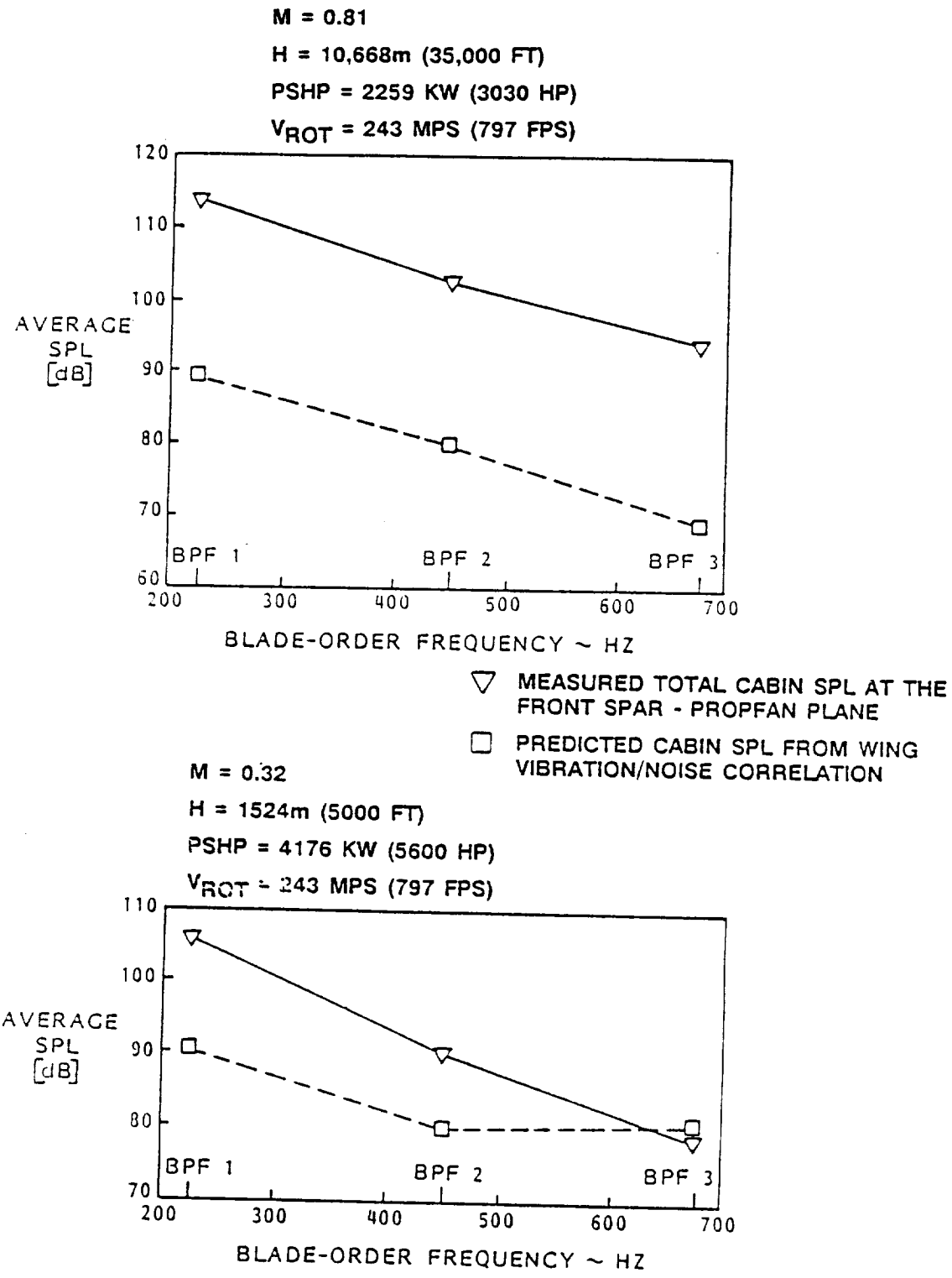


Figure 448. Predicted Structureborne Noise and Measured Cabin Total Noise

At the design cruise condition of the PTA propfan, the "A-weighted" sound levels of the cabin ranged from 106 dBA to 86 dBA over the first seven blade orders, as shown in Figure 449. These levels sum to an overall level of 110 dBA, whereas a reasonable cabin noise target might be about 80 dBA. For practical design, an addition cabin noise reduction of about 40 dB may be required, and this added to the noise reduction of 25 dB attained in the PTA cabin shell structure would require a noise suppression goal for a new propfan cabin wall of about 65 dB. This would be a significant design challenge, but noise control research now in progress indicates that such a goal is attainable.

9.5 CABIN ACOUSTIC TREATMENT TEST

Development of an advanced cabin wall acoustic treatment concept was funded by NASA-Langley Research Center under the contract of Reference 20. This treatment took advantage of the fact that propfan noise is dominated by tones at discrete frequencies and used acoustic resonators that were tuned to the blade passage frequency. Small-scale tests indicated that such resonators could reduce this dominant tone noise by 60 dB or more.

To test this concept, a compartment was built that would fit inside the PTA cabin. The walls of this compartment contained an array of Helmholtz resonators that were tuned to the blade passage frequency at 100-percent Np. Assembly of this acoustic enclosure is depicted in Figure 450. The end walls of the enclosure were acoustically sealed.

Three PTA flights were made to test the acoustic enclosure. In one, the resonator openings were sealed off, so that their effectiveness could be evaluated. All in all, the results were somewhat inconclusive. The predicted large transmission loss into the enclosure was not achieved, but there was evidence of enough effectiveness to warrant further study. There was some suspicion that the effort to acoustically seal the end walls was insufficient and that noise may have entered the enclosure via that route. The evaluation of these results and further study of this concept is continuing under another contract.

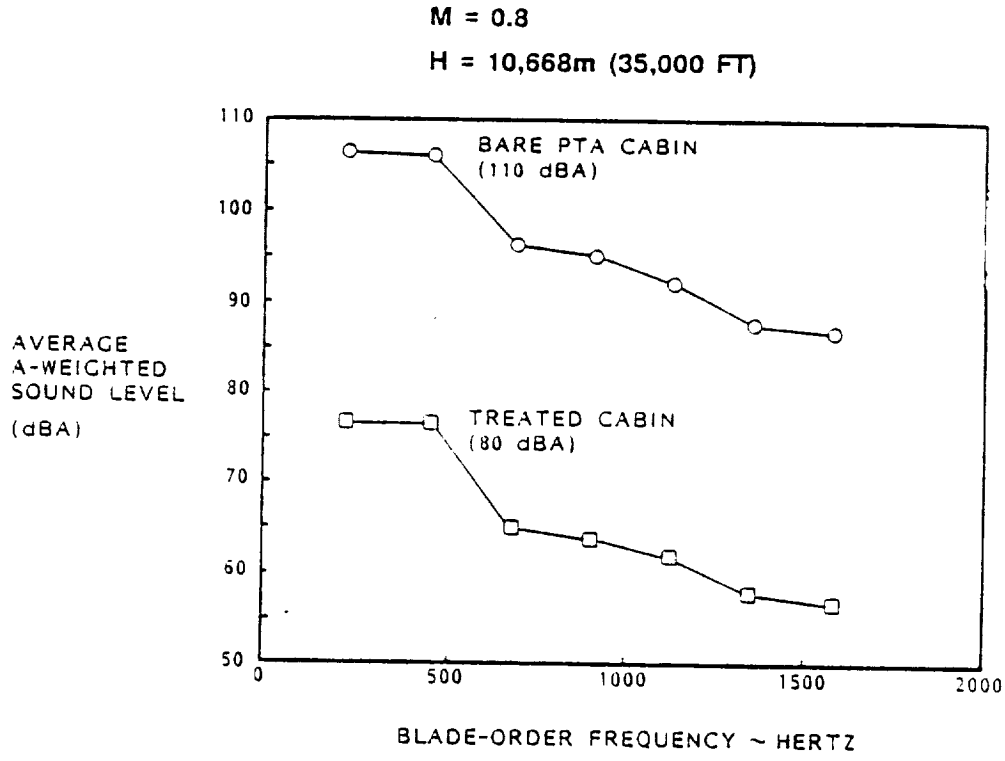


Figure 449. Noise Reduction Required at BPF to Achieve 80 dBA in Cabin

ORIGINAL PAGE--
BLACK AND WHITE PHOTOGRAPH

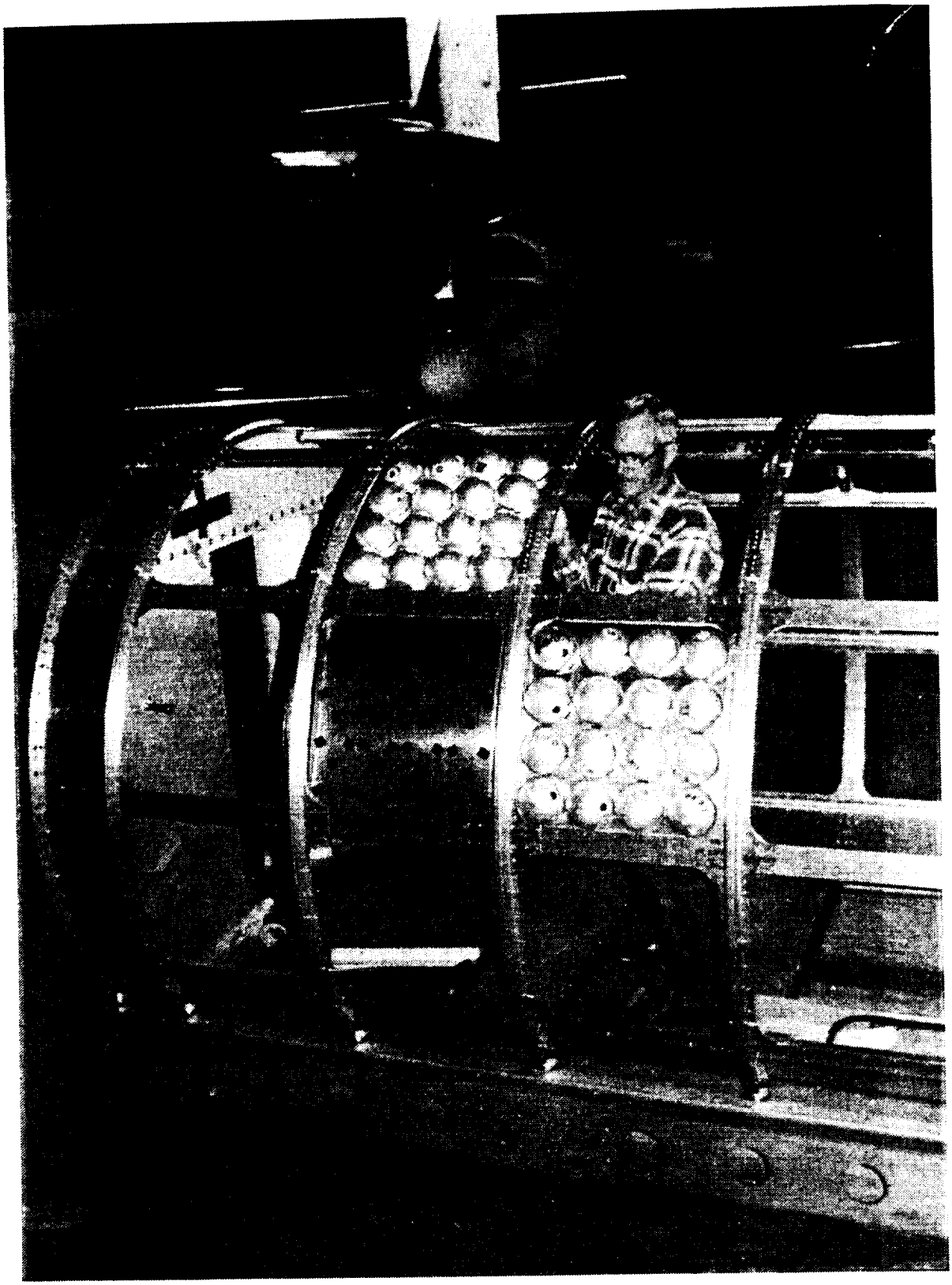


Figure 450. Assembly of the Advanced-Acoustic-Wall Cabin Enclosure for PTA Flight Tests

C-7

10.0 CONCLUDING REMARKS

The Propfan Test Assessment Program resulted in the collection of a large array of systematic flight test data on the structural dynamics and acoustics of high-speed propfans. All objectives were met or exceeded on schedule and under budget. The test envelopes covered all the various flight environments of propfan-powered commercial transport aircraft, and obtained near-field noise and vibratory blade stress data over a wide range of power and rotational speeds. Far-field noise data were obtained in low-altitude flyover tests to simulate FAR 36 test conditions.

Cabin noise data were obtained for bare cabin walls and for a new-technology wall configuration built around the use of Helmholtz resonators tuned to the blade passage frequency of the propfan.

In cooperation with the FAA, tests were performed to measure ground noise for flyovers at 7,620m (25,000 ft) and 10,668m (35,000 ft).

An important feature of the test hardware was the provision to change the tilt angle of the propfan centerline. This feature allowed propfan inflow angle to be an independent variable in these tests and provided much valuable new data on the effects of this variable.

The major portion of the flight research test program was performed during a four-month period during which 472 test runs were obtained in 33 aircraft flights. Seventeen more flights were required to obtain data for the cabin enclosure and flyover noise tests. The results of these latter tests are to be reported by other agencies and are not dealt with in detail in this report.

With regards to blade stress results, there were no significant deviations from predicted behavior. The highest test Mach number was 0.89, and within the flight regime to this extreme, results showed that vibratory loads were well within the limits for infinite fatigue life.

The near-field noise tests showed the propfan noise to be dominated by blade-order tones--with the fundamental tone rarely exceeded by the higher orders. Maximum sound pressures on the fuselage were generally over-predicted in the cruise conditions and underpredicted for the low-speed climb conditions. Inflow angle to the propfan had a strong effect on both near-field and far-field noise.

The bare cabin wall resulted in noise transmission loss of approximately 25 dB, and the inconclusive results of the cabin enclosure tests still showed promise that advanced wall treatments can provide cabin environments in the range of 80 dB.

Far-field ground noise measurements for low altitude flyovers were higher than predicted by enough to warrant further studies of airport noise for propfan-powered aircraft. These data show far-field noise to be affected by a number of design variables and provide a good basis for aircraft system trade studies. The PTA data also provided an evaluation of lateral

noise attenuation--showing significant dependence of lateral attenuation on elevation angle and negligible dependence on slant range.

Fluctuating pressure levels on the wing in the wake of the propfan slipstream were approximately equal to sound pressure levels on the fuselage at high-speed cruise, but were 10 to 20 dB higher at climb conditions. These fluctuating pressures were considerably underpredicted by existing theory.

The acoustic analyses within the scope of the PTA Program did not exhaust the potential value of the research data. In fact, as in most research programs, the analyses produced a good many questions as well as answers. These data are available at NASA-Lewis Research Center and are recommended to other researchers as a rich source of information on the characteristics of high-speed propeller noise.

REFERENCES

1. DeGeorge, C. L. "Large-Scale Advanced Propfan (LAP) Final Report" NASA CR 182112 (prepared by Hamilton Standard Division, United Technologies).

2. Hancock, J. P., V. Lyman, and A. P. Pennock, "Analysis of Results from Wind Tunnel Tests of Inlets for an Advanced Turboprop Nacelle Installation," NASA CR 174937 (prepared by Lockheed Aeronautical Systems Company and issued as LG85ER0105), June 1986.

3. Bansal, Prem N., "Experimental and Analytical Evaluation of the Effects of Simulated Engine Inlets on the Blade Vibratory Stresses of the SR-3 Model Propfan," NASA CR 174959, September 1985.

4. Youngren, H. H., et al, "Comparison of Panel Method Formulations and Its Influence on the Development of QUADPAN, an Advance Low Order Method," AIAA 83-1827, July 1983.

5. Little, B. H., et al, "Propfan Test Assessment Testbed Aircraft Stability and Control/Performance 1/9 Scale Wind Tunnel Tests," NASA CR 182121 (prepared by Lockheed Aeronautical Systems Company and issued as LG88ER0056), May 1988.

6. Jenness, C.M.J., "Propfan Test Assessment Testbed Aircraft Flutter Model Test Report," NASA CR 179458 (prepared by Lockheed Aeronautical Systems Company and issued as LG85ER0187), June 1986.

7. Hancock, J. P., "PTA Testbed Aircraft Engine Inlet Model Report," NASA CR 174845 (prepared by Lockheed Aeronautical Systems Company and issued as LG85ER0012), May 1985.

8 Aljabri, A. S., and B. H. Little, "High Speed Wind Tunnel Tests of the PTA Aircraft," SAE Preprint 861744, October 1986.

9. Aljabri, A. S. "Prediction of Propeller Slipstream Characteristics," Lockheed Aeronautical Systems Company, LG79ER0120, 1979.

10. Aljabri, A. S., V. Lyman, and R. J. Parker, "Evaluation of Propeller/ Nacelle Interactions in the PTA Program," AIAA Preprint 86-1552, June 1986.

11. Lyman, V., and J. P. Hancock, "Correlation of Theory and Experiment for Propfan Inlets," AIAA Preprint 86-1628, June 1986.

12. Little, B. H., et al, "Propfan Test Assessment (PTA) Flight Test Report," NASA CR 182278 (prepared by Lockheed Aeronautical Systems Company and issued as LG89ER0026), July 1989.

13. S. F. Hoerner, Fluid-Dynamic Drag, Hoerner Fluid Dynamics, Brick Town, N.J., 1965.

14. "USAF Stability and Control DATCOM," Project 8219, Task No. 821901, Flight Control Division, Air Force Flight Dynamics Laboratory, Wright-Patterson Air Force Base, Dayton, Ohio, October 1960.

15. Perkins, C. D., and R. E. Hage, Airplane Performance Stability and Control, John Wiley and Sons, New York, N.Y., 1949.

16. "Gulfstream GII Estimated Flying Qualities," Grumman Aircraft Engineering Corporation, Report XA1159-B-5.4, September 1966.

17. "Sonic Design Handbook for Military Aircraft," Air Force Flight Dynamics Laboratory, AFFDL-TR-74-112, 1974.

18. Lotze, H. E., and J. W. Kuehl, "Propfan Test Assessment Hazard Analysis Series, Volume 1, Preliminary Hazard Analysis," Lockheed Aeronautical Systems Company, LG85SER0004, April 1985.

19. Lotze, H. E., "Propfan Test Assessment Hazard Analysis Series, Volume 2, Subsystem Hazard Analysis and System Hazard Analysis," Lockheed Aeronautical Systems Company, LG85SER0012, November 1985.

20. Lotze, H. E., "Propfan Test Assessment Hazard Analysis Series, Volume 3, Operating and Support Hazard Analysis No. 1, (Propfan Propulsion System Static Test)," Lockheed Aeronautical Systems Company, LG86SER0001, April 1986.

21. Lotze, H. E., "Propfan Test Assessment Hazard Analysis Series, Volume 4, Operating and Support Hazard Analysis (Flight Test)," Lockheed Aeronautical Systems Company, LG86SER0005, December 1986.

22. O'Rourke, D. M. "Propfan Test Assessment, Propfan Propulsion System Static Test Report" NASA CR 179613 (Prepared by Lockheed Aeronautical Systems Company and issued as LG86ER0173), September 1987.

23. Riggs, D. F., "Propfan Test Assessment Ground Test Plans (Vol. 3 Systems Functional)," Lockheed Aeronautical Systems Company, LG86ER0134, December 1986.

24. Gatineau, R. J., "Informal Report on Flight Test Program of Acoustic Treatment in PTA Testbed Aircraft," Lockheed Aeronautical Systems Company, LR 31449, 28 June 1988.

Lockheed

APPENDIX A
ACOUSTIC REFLECTION CONTAMINATION TESTS IN THE NASA-LANGLEY 16-FT TRANSONIC TUNNEL

List of Figures

Figure	Title	Page
A-1	Typical Time History Showing Direct and Reflected Signals	A-3
A-2	Scale Drawing of the Source Installed in the Tunnel	A-4
A-3	Time History from a Fuselage Transducer Illustrating Decay of Tunnel Reverberant Field	A-6
A-4	Typical Time Domain-Averaged Time History from a Fuselage Transducer at M = 0	A-6
A-5	Time-Domain Averaged Time Histories at M = 0 for All Fuselage Transducers Monitored	A-8
A-6	Time-Domain Averaged Time Histories at M = 0 for All Wing and Boom Transducers Monitored	A-9
A-7	Time-Domain Averaged Time Histories for Fuselage Transducer F54 at All Mach Numbers Tested	A-10
A-8	Time History and Direct and Reflected Signal Spectra at M = 0 for the Unshielded Fuselage Transducer F54	A-11
A-9	Time History and Direct and Reflected Signal Spectra at M = 0 for the Unshielded Fuselage Transducer F34	A-12
A-10	Time History and Direct and Reflected Signal Spectra at M = 0 for the Unshielded Fuselage Transducer F57	A-13
A-11	Time History and Direct and Reflected Signal Spectra at M = 0 for the Unshielded Lower Surface Wing Transducer LIA1	A-14
A-12	Effect of Mach Number on Direct and Reflected Signals Measured at Fuselage Transducer F54	A-15

APPENDIX A
ACOUSTIC REFLECTION CONTAMINATION TESTS IN THE NASA-LANGLEY 16-FT TRANSONIC TUNNEL

Introduction

The original PTA work plan called for near-field acoustics measurements on the 1/9-scale model in the Langley 16-Ft Transonic Tunnel. The test section of that tunnel, however, was hard-wall. It was, therefore, not known to what extent the propfan sound waves reaching the various acoustic transducers might be contaminated by sound reflections from the walls. These concerns prompted a study to determine the degree of contamination. The method and the apparatus used for this study, and the results, are described briefly herein. Detailed descriptions are available in Reference A-1.

The method used was the "impulse technique" which is described in Reference A-2. In the PTA application, a series of very sharp acoustic pulses were propagated into the wind tunnel test section flow. By ensuring that the pulse rate and width were such that reflected pulses were adequately separated (in time) from the direct pulses and from each other, it was possible to isolate the direct incident wave from the reflected waves.

An example is presented in Figure A-1 in which the direct signal (denoted by D) and the reflected signals (denoted by R_1 and R_2) can easily be distinguished and quantified in the frequency domain by performing a Fourier transform on each individual pulse component. In the presence of high velocity flow, it becomes increasingly difficult to isolate the pulses from the tunnel broadband flow noise, so time domain signal averaging was used to overcome this problem.

Test Apparatus

A high intensity impulsive noise source was developed and installed in the wind tunnel in such a way that its noise would be radiated from the region where the propfan would normally be located. The source was supported so that it would remain in place and steady when subjected to the loads imposed by the high velocity wind tunnel flow. A sketch of the arrangement is shown in Figure A-2.

Figure A-2 also shows the relative position of the 1/9-scale model which was instrumented with 108 miniature microphones. Forty-three of the transducers were installed on the fuselage, five were installed on an acoustic boom located diametrically opposite the propfan from five of the fuselage microphones, and the rest were installed on the upper and lower surfaces of the wing.

Twelve transducers were selected for monitoring during the reflection contamination tests. They were chosen to give information representative of the total instrumented area of the model.

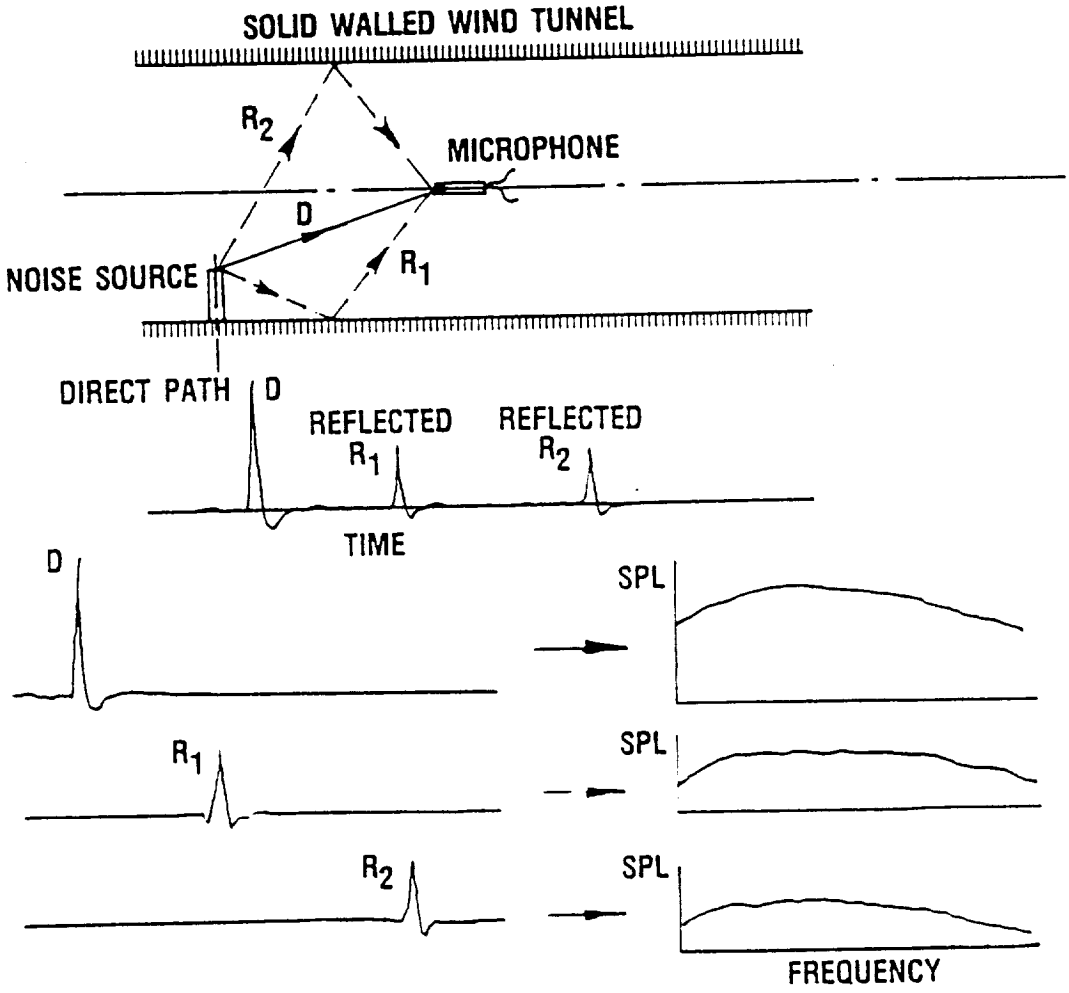


Figure A-1. Typical Time History Showing Direct and Reflected Signals

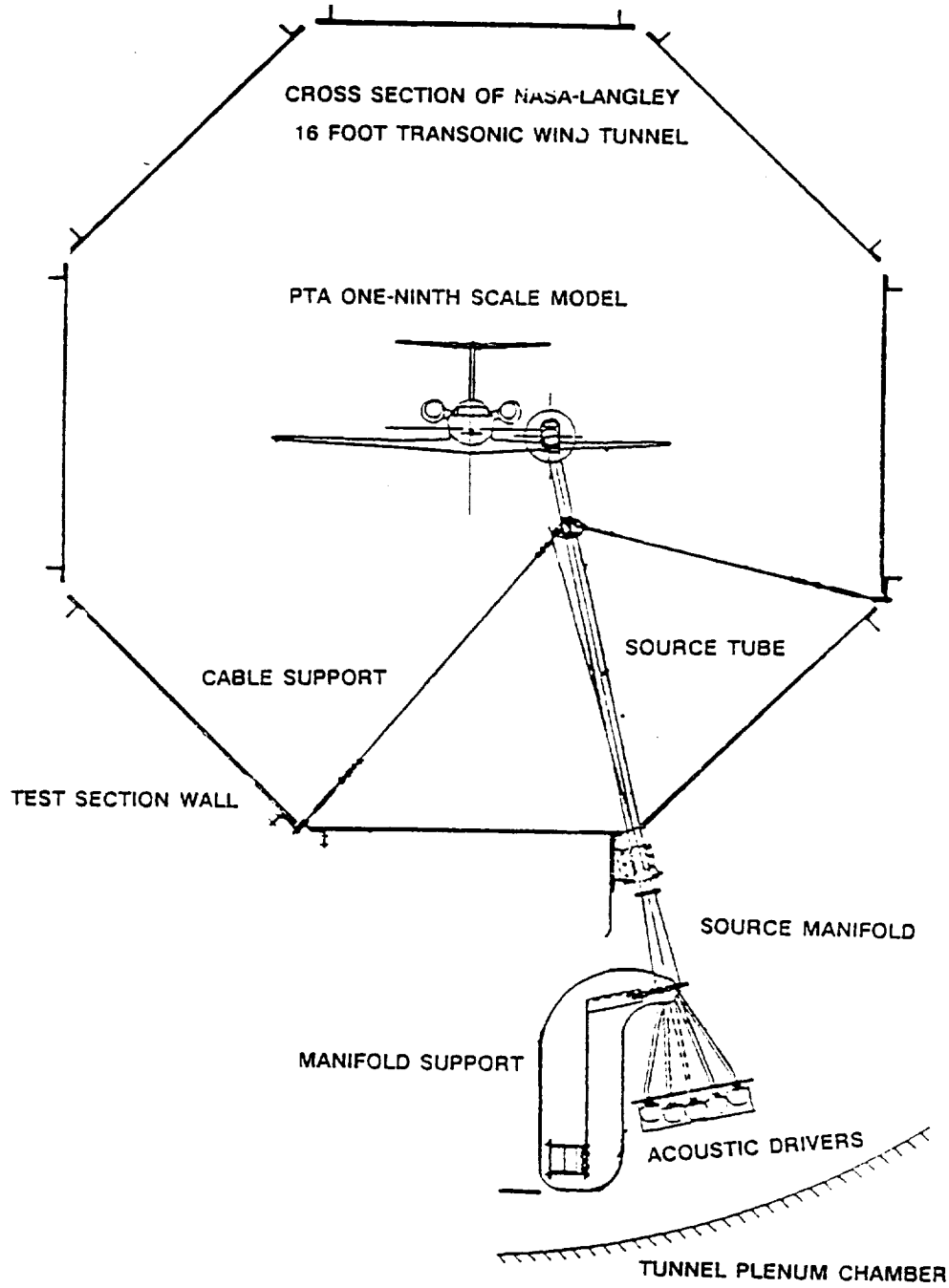


Figure A-2. Scale Drawing of the Source Installed in the Tunnel

A dual-channel pulse generator was used to drive the power amplifiers for the acoustic drivers and to generate a slightly delayed trigger signal which was recorded on the data tape for later time domain averaging. The response of the 12 transducers was also simultaneously recorded on the tape recorder.

Tests

The effect of pulse peak voltage, pulse width, and pulse rate on the acoustic source output were first investigated in Lockheed's Acoustics Laboratory, and subsequently in the 16-Ft Tunnel. Based on these results, all tests were performed using a pulse width of 300 microseconds. The pulse rate was selected on the basis of the tunnel reverberation characteristics by operating the acoustic source at different pulse rates starting with a very low value. The pulse rate was gradually increased until a maximum tolerable level of residual signal existed, before the arrival of the next pulse. The chosen rate was ten per second, and the time history from a fuselage transducer for this case is shown in Figure A-3. Clearly, the reverberation had decayed to a very low level, compared with the initial direct pulse, by the arrival time of the next pulse.

The signal recording time was governed by the number of averages necessary to extract the required signal from the tunnel flow noise--the higher the background noise, the longer the recording time.

The directivity of the pulse source was, of course, quite different from that of the model propfan. The impact of this difference was examined in Reference A-1 and found to not significantly affect the results. The effects of structural shielding of the direct acoustic wave (but not the reflected wave) were examined in the wind tunnel. These two effects were studied so that appropriate corrections could be made in the event that reflection contaminations were found to be significant. Corrections were not necessary, however, because the reflections were insignificant for all important configurations and locations.

Having established the noise source operation conditions, and the length of record required, the tests were then conducted at tunnel Mach numbers ranging from zero to 0.8, in one-tenth steps, with the model at an angle of attack of 2 degrees. This angle was representative of the majority of the test configurations planned for the acoustic measurement program.

Results

The data were reduced using a digital signal processor, which was capable of performing up to 4096 averages in the time-averaging mode. This maximum number was used to analyze data for Mach numbers above 0.6. Fewer averages were needed for the lower Mach number data. A typical averaged time history from a fuselage transducer at M = 0 is shown in Figure A-4.

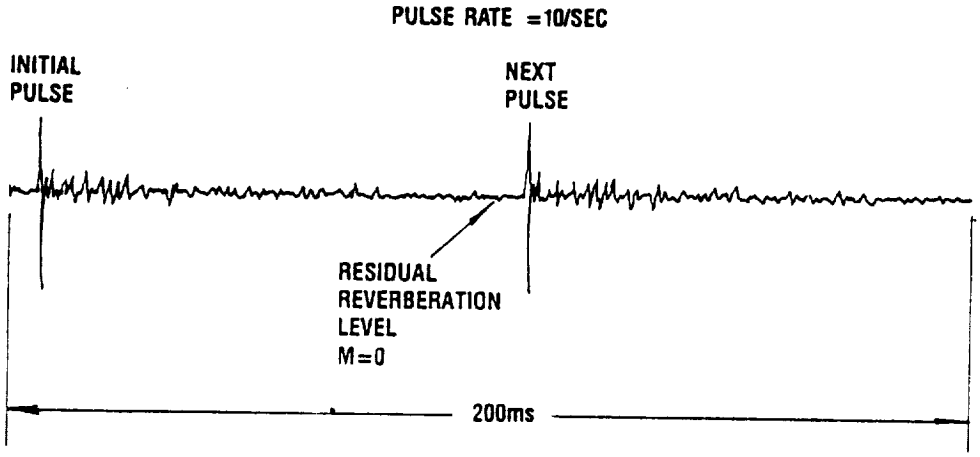


Figure A-3. Time History from a Fuselage Transducer Illustrating Decay of Tunnel Reverberant Field

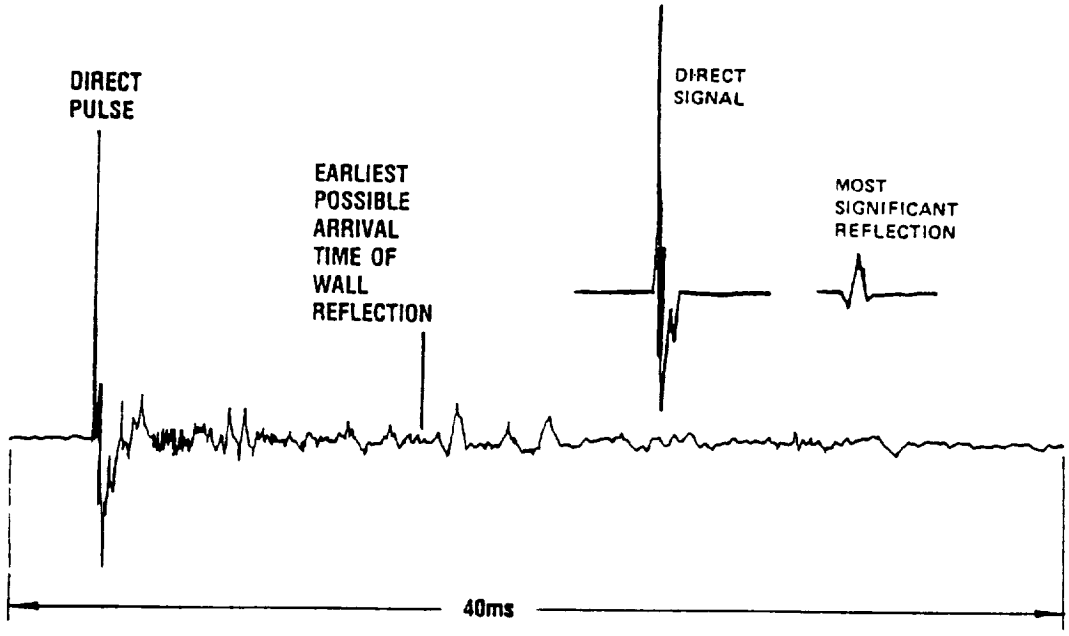


Figure A-4. Typical Time Domain-Averaged Time History from a Fuselage Transducer at M = 0

In Figure A-5, to the left of the model schematic, are shown the time histories recorded at each of four transducers along the fuselage side facing the source. As would be expected, the maximum pulse peak value occurred at the transducer located in the plane of the source. The relatively small magnitude of the peak at Fuselage Station 9, which in terms of propagation distance should be similar in magnitude to that at Fuselage Station 1, was due to the shielding effect of the wing. The reflections shown at approximately 1 millisecond and 1.5 milliseconds after the direct pulse originate from the propfan spinner/nacelle and the wing leading edge.

To the right of the schematic in Figure A-5 are shown the time histories measured at the transducers around the fuselage in the plane of the source. Once again, the effect of shielding is evident from the time histories of transducers F51 and F5A.

Figure A-6 shows the time histories for the wing and boom transducers.

Figure A-7 shows the time histories measured at the transducer on the fuselage side at the propfan plane for all tunnel Mach numbers tested. The full 40 milliseconds time period is shown in each case. As the Mach number increased, the pulse source efficiency deteriorated, and the pulse became increasingly broad. In addition, the wall reflections became increasingly more difficult to identify, and by the time $M = 0.8$ was reached, identification of the wall reflections was practically impossible.

Spectrum analyses of the direct and reflected pulses are shown in Figure A-8 for a fuselage microphone in the propfan plane. It is clear that the most significant reflection spectrum was more than 30 dB below that of the direct signal. This confirms that measurements of propfan noise made at this point on the model would not be contaminated by tunnel wall reflections. This was confirmed again at fuselage transducers F34 and F57 in Figures A-9 and A-10, respectively, where the margin was of the order of 20 to 30 dB. Data from the wing lower surface transducer, LIA1, are shown in Figure A-11. In this case, the margin was again greater than 20 dB at frequencies corresponding to the first three blade-passage tones.

At higher Mach numbers, the results for transducer F54, at Mach numbers of 0.2, 0.4, and 0.7, are shown in Figures A-12(a), (b), and (c), respectively. Once again, the margin was better than 30 dB for the first three blade-passage tones.

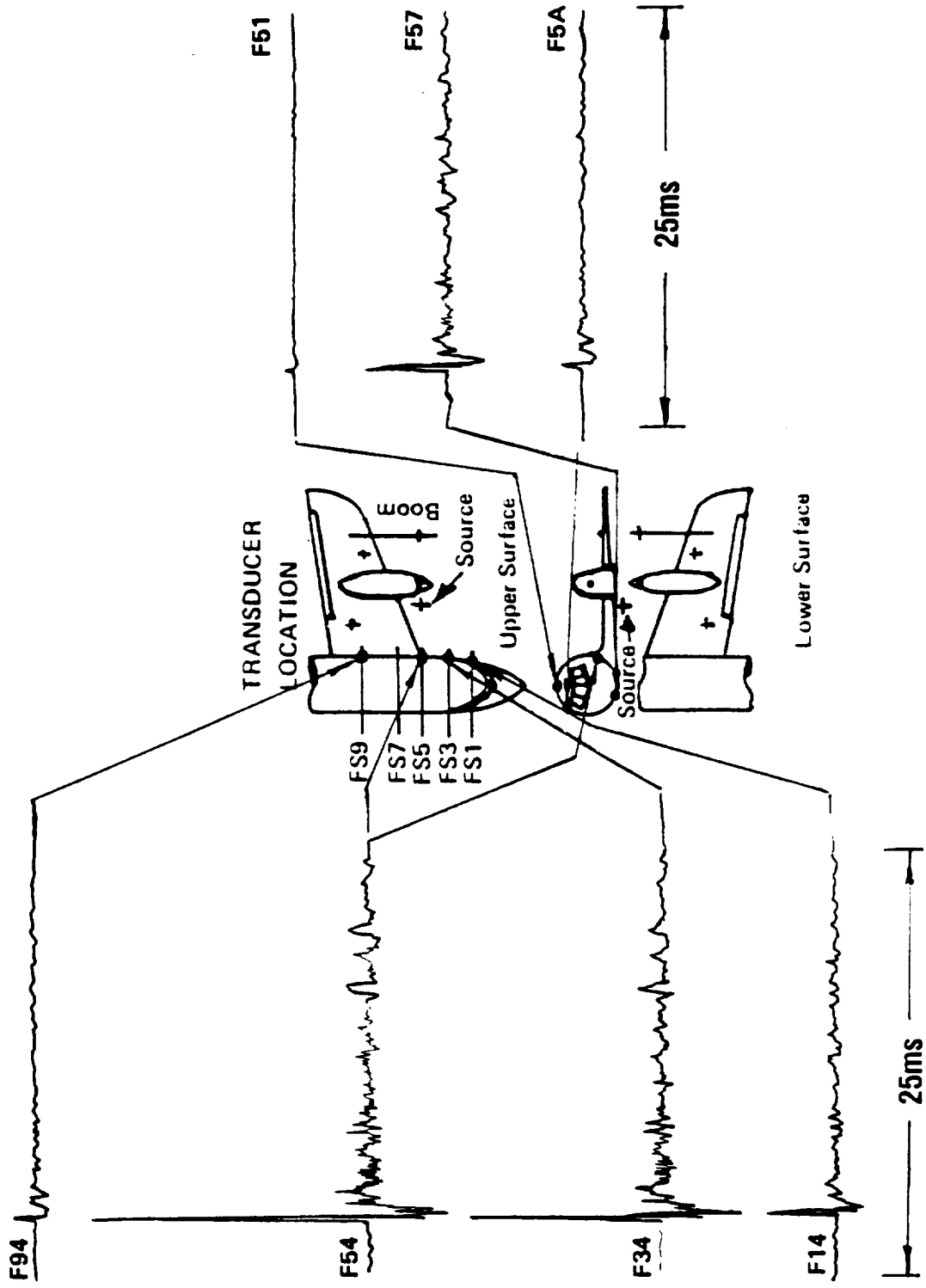


Figure A-5. Time-Domain Averaged Time Histories at M = 0 for All Fuselage Transducers Monitored

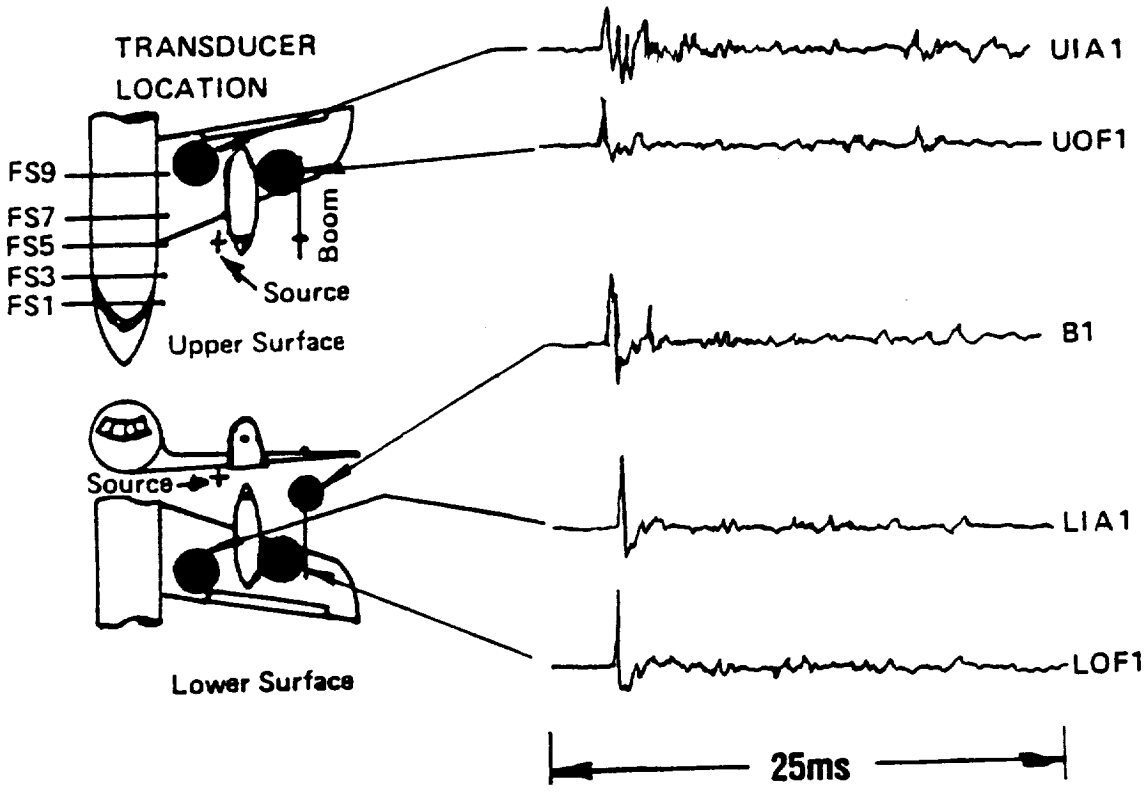


Figure A-6. Time-Domain Averaged Time Histories at M = 0 for All Wing and Boom Transducers Monitored

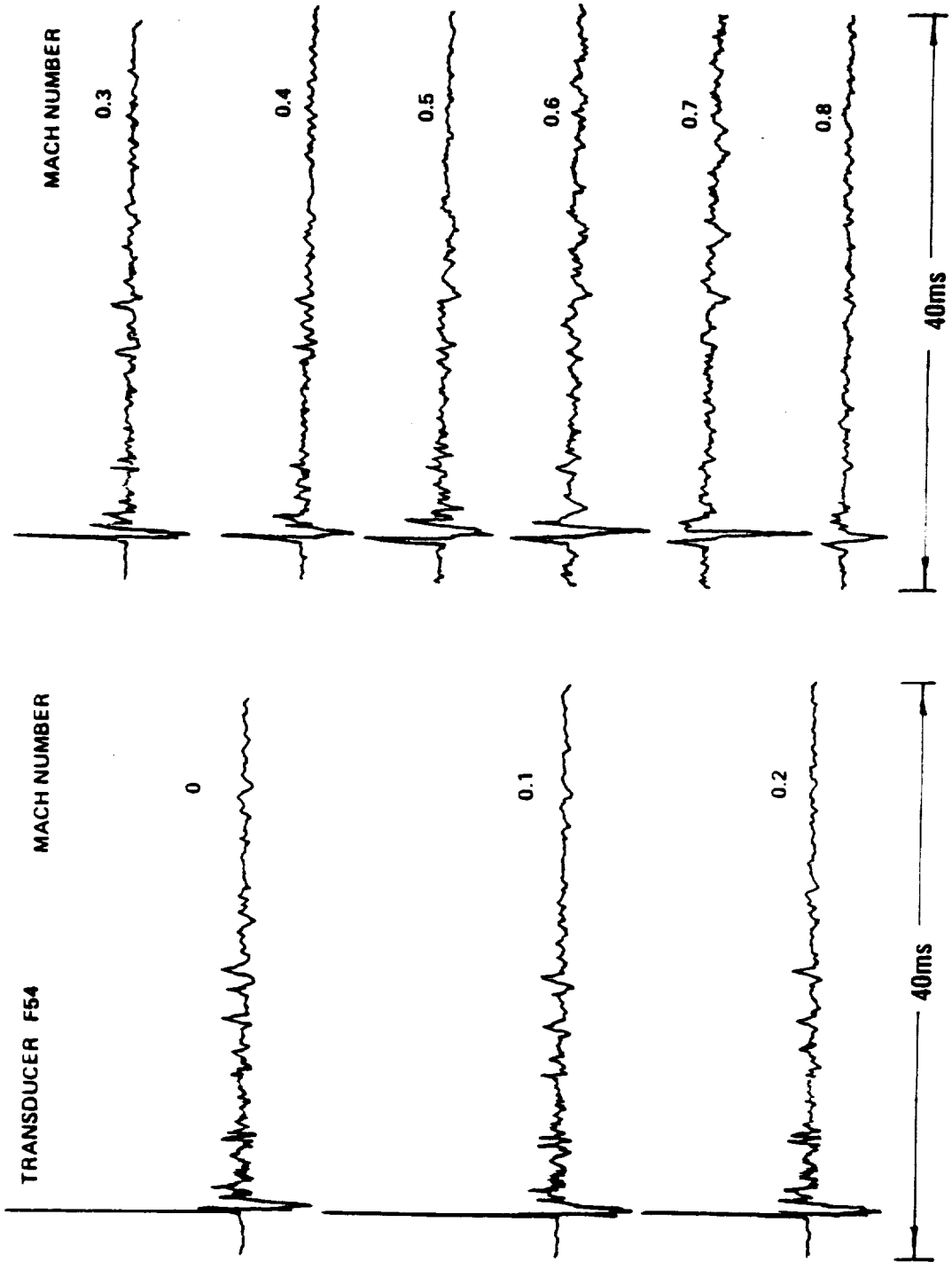


Figure A-7. Time-Domain Averaged Time Histories for Fuselage Transducer F54 at All Mach Numbers Tested

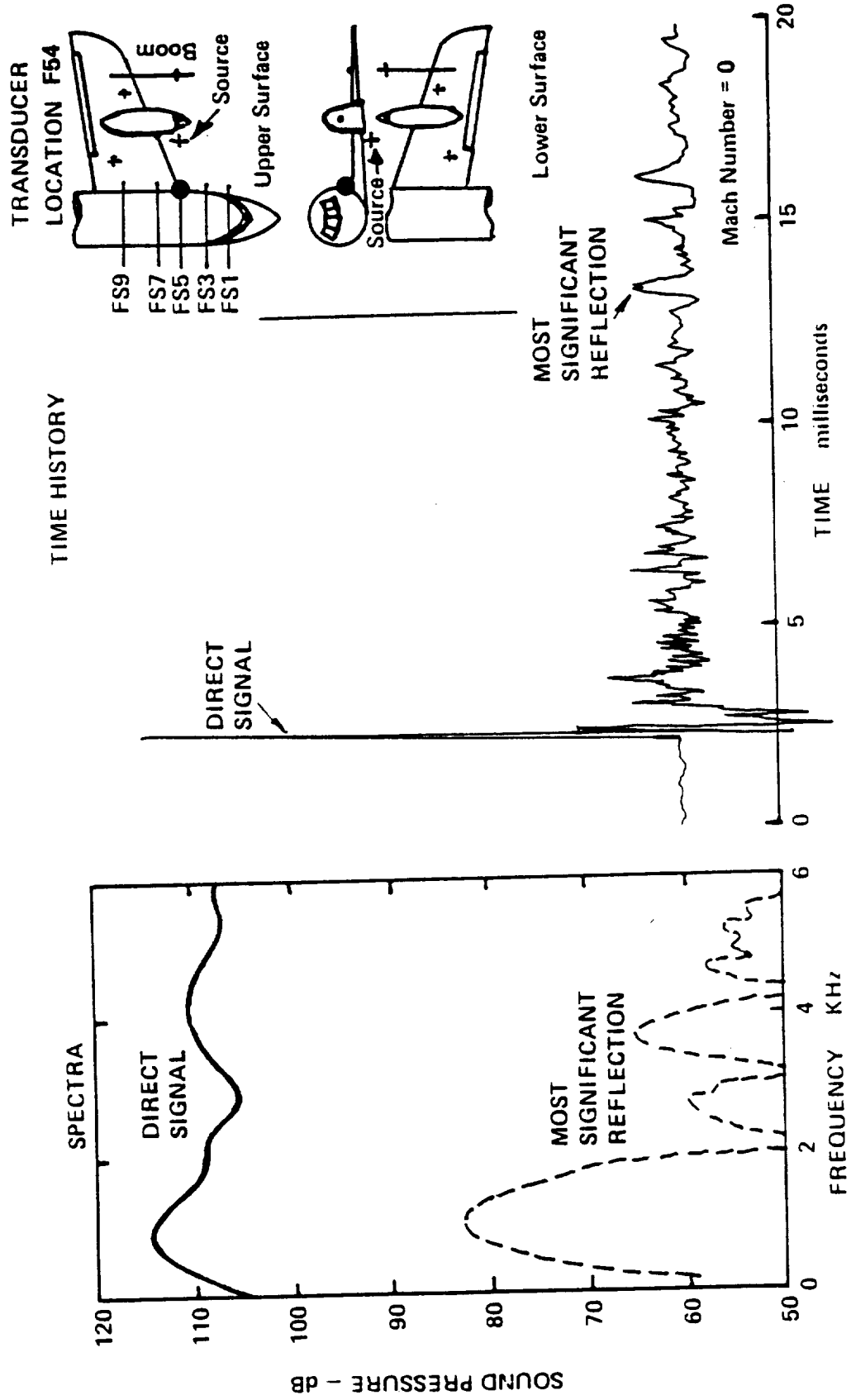


Figure A-8. Time History and Direct and Reflected Signal Spectra at M = 0 for the Unshielded Fuselage Transducer F54

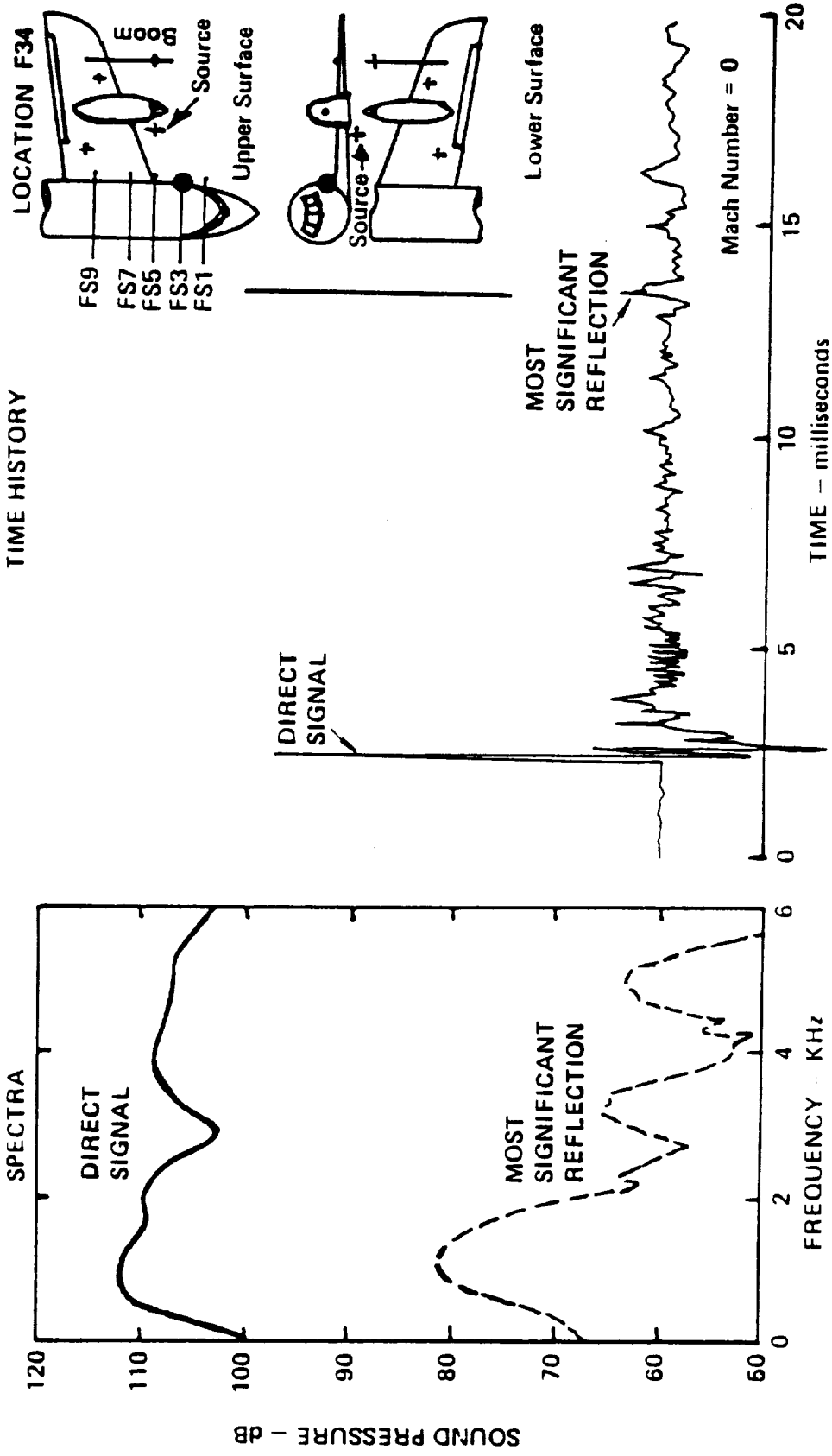


Figure A-9. Time History and Direct and Reflected Signal Spectra at M = 0 for the Unshielded Fuselage Transducer F34

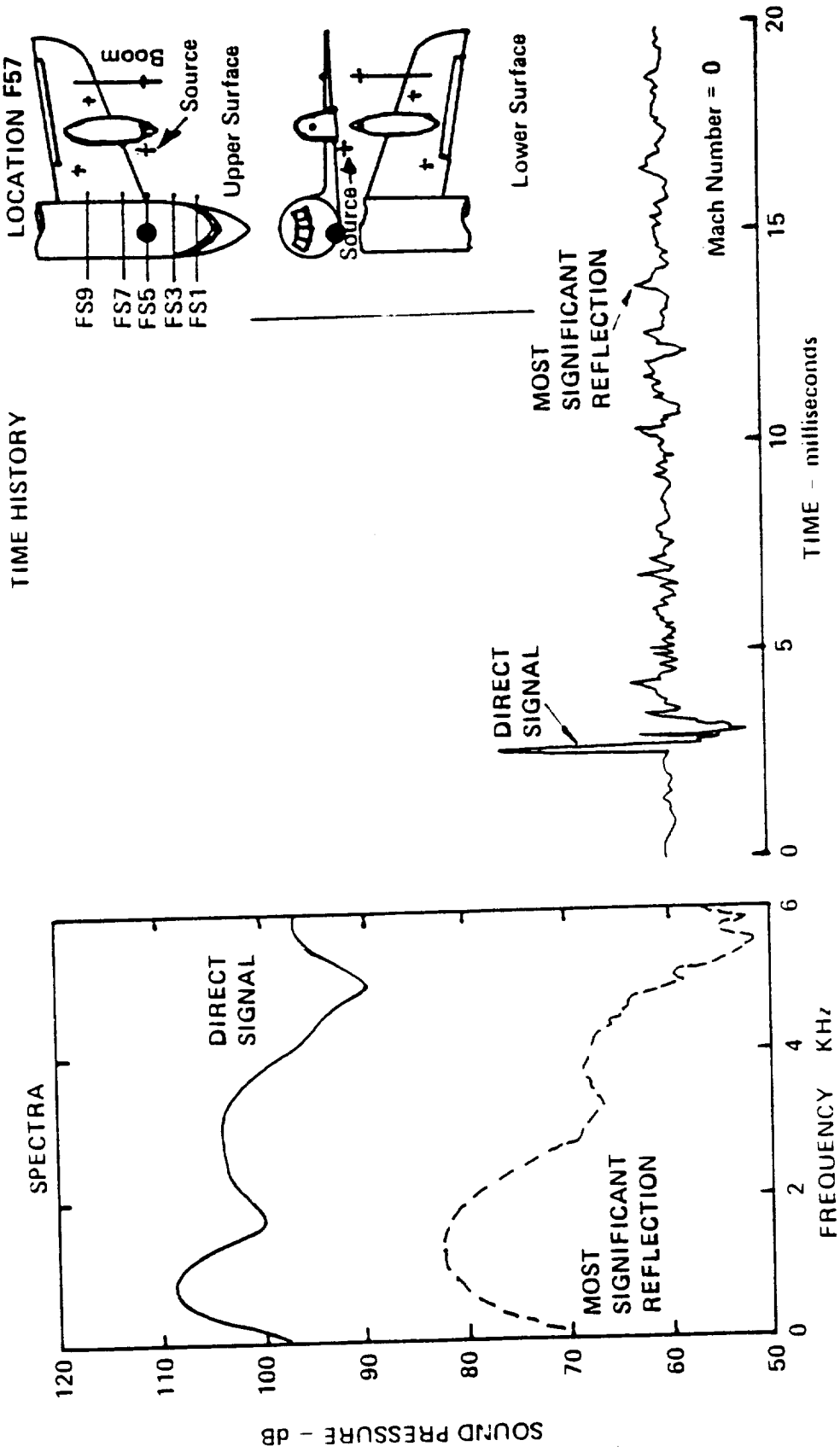


Figure A-10. Time History and Direct and Reflected Signal Spectra at M = 0 for the Unshielded Fuselage Transducer F57

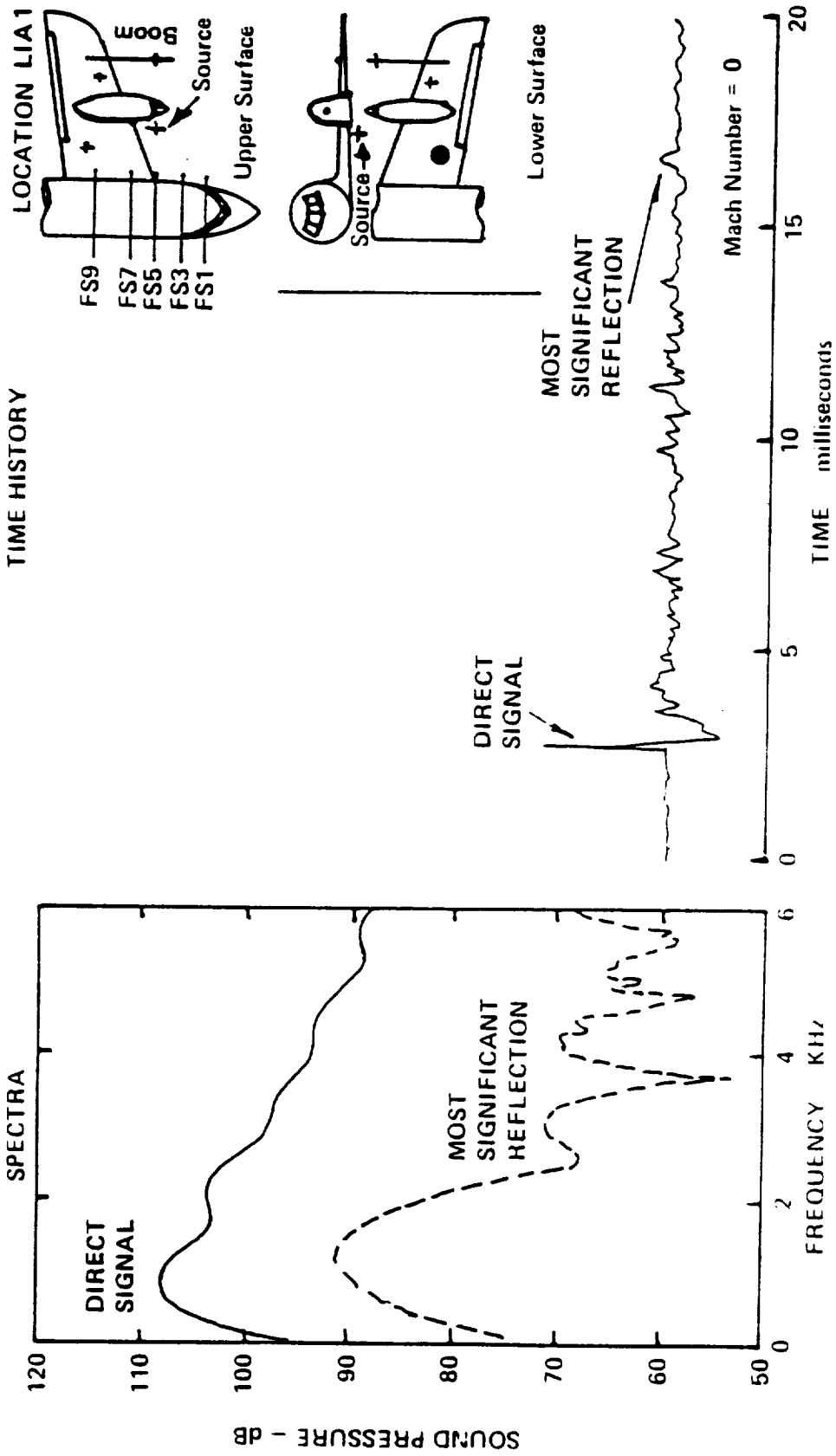


Figure A-11. Time History and Direct and Reflected Signal Spectra at M = 0 for the Unshielded Lower Surface Wing Transducer L1A1

ORIGINAL PAGE IS
OF POOR QUALITY

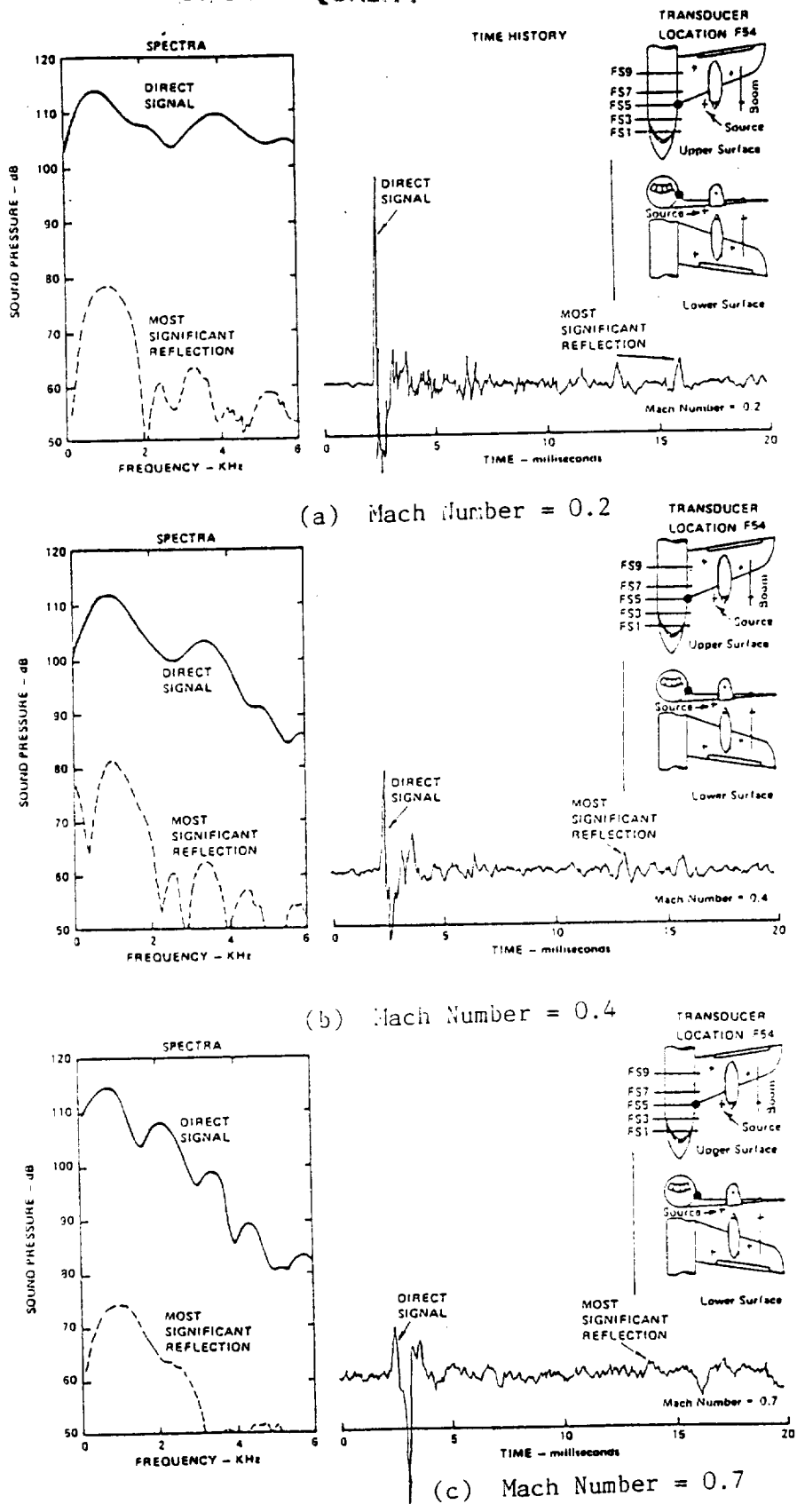


Figure A-12. Effect of Mach Number on Direct and Reflected Signals Measured at Fuselage Transducer F54

Conclusions

The primary objective was accomplished--the importance of reflection contamination of acoustic measurements made in the near-field of the source, in a hard-walled, high-speed, wind tunnel was investigated. The results showed that the reflections from the walls of the tunnel were insignificant compared to the direct signal from the source to the transducers in all important locations.

The pulse source directivity relative to the model propfan directivity was not assessed because the result would usually be to reduce the significance of the reflection even further. Since a margin of at least 20 dB of direct over reflected signal existed, it was considered unnecessary to include such corrections.

At first inspection, the data from some transducers showed the possibility of contamination, but a closer examination revealed that this occurred only at measurement locations where there was no direct line-of-sight between the transducer and the source, i.e., the transducer was shielded.

References

A-1. Salikuddin, M., et al, "Development of an Impulsive Noise Source to Study the Acoustic Reflection Characteristics of Hard-Walled Wind Tunnels," AIAA-86-1887, July 1986.

A-2. Salikuddin, M., et al, "An Impulse Test Technique with Application to Acoustic Measurements," Journal of Sound and Vibration, Vol. 70, 1980, pp. 487-501.

Lockheed

APPENDIX B
REVERSE ROTATION DESIGN STUDY

List of Figures

Figure	Title	Page
B-1	Opposite Rotation Gearbox Modification	B-4
B-2	Opposite Rotation Gearbox Nose Scavenge Pump	B-4

APPENDIX B
REVERSE ROTATION DESIGN STUDY

The preliminary design phase of the PTA program included a study of modifications to provide for a twin engine version of the PTA aircraft and the capability to operate one engine with rotation in either direction. As a result of this study, it was determined that only the gearbox would need to be modified to provide opposite rotation. The resultant design, however, would require a 20 rpm higher power section output speed than for base rotation. The modifications from the PTA configuration would include casting pattern changes, and changes to the accessory gear train, prop brake, nose scavenge pump, planet system, and lube system. These are summarized in Figure B-1.

The major changes from the PTA gearbox would be:

- Addition of reversing idler gear to the offset gear mesh to provide opposite rotation
- Widening of idler gear teeth to accommodate reverse bending loads and maintain infinite life bending stress
- New rear housing and center diaphragm castings to accommodate the added idler gear and its support bearings
- Increased capacity of the pressure oil pump

The rear housing would be lengthened 2 cm (0.8 in.), and the contour would be altered to provide clearance for the reversing idler gear. A boss would be added to support the bearing. The gearbox center diaphragm would be recontoured to provide attachment for the rear housing and to provide a boss for the front idler bearing. The helical splines of the prop brake would be machined in the opposite direction from the PTA gearbox splines in order to apply friction torque in the appropriate direction.

The nose scavenge pump would be inverted, as shown in Figure B-2, to permit it to mesh with the reversing idler gear and fit inside the gearbox case. The PTA gearbox oil pump would be modified by increasing tooth height and increasing pump speed 3.6 percent to increase the oil capacity from 87 liter/minute (23 GPM) for the PTA pump to 110 liter/minute (29 GPM) in order to add oil to the reversing idler gear teeth and bearings. Limiting the nose-up attitude to less than 10 degrees during propfan operation would prevent the aft scavenge pump from unporting and thus would provide sufficient scavenge capacity to accommodate the increase in pressure pump capacity/flow rate.

The opposite rotation planet gear system would rotate in the same direction as the production T56 gears but 66 percent faster. The resulting bearing loads would be the same as for the PTA design, which is lower than for the T56 application. The planet roller separators would exert 2.75 times the radial load on the journal due to the higher prop

shaft rotational speed. As for the PTA application, the journal land finish would be improved by "stoning" to 0.0000001 cm (0.000025 in.) peak-to valley.

The operational characteristics of the opposite rotation gearbox design are compared to the T56 and PTA gearboxes as follows:

	T56	PTA Opposite Rotation	PTA
Overall Ratio	13.54	6.8085	6.7967
Pinion Rotation	CCW	CW	CW
Prop Rotation	CW	CW	CCW
Input Speed	13,820	11,520	11,500
Prop Speed	1,020	1,692	1,692
Pump Rotation	+	+	+
Max Power	3,728 kw (5,000 shp)	4,474 kw (6,000 shp)	4,474 kw (6,000 shp)
Speed Variation	100%	75%-105%	75%-105%

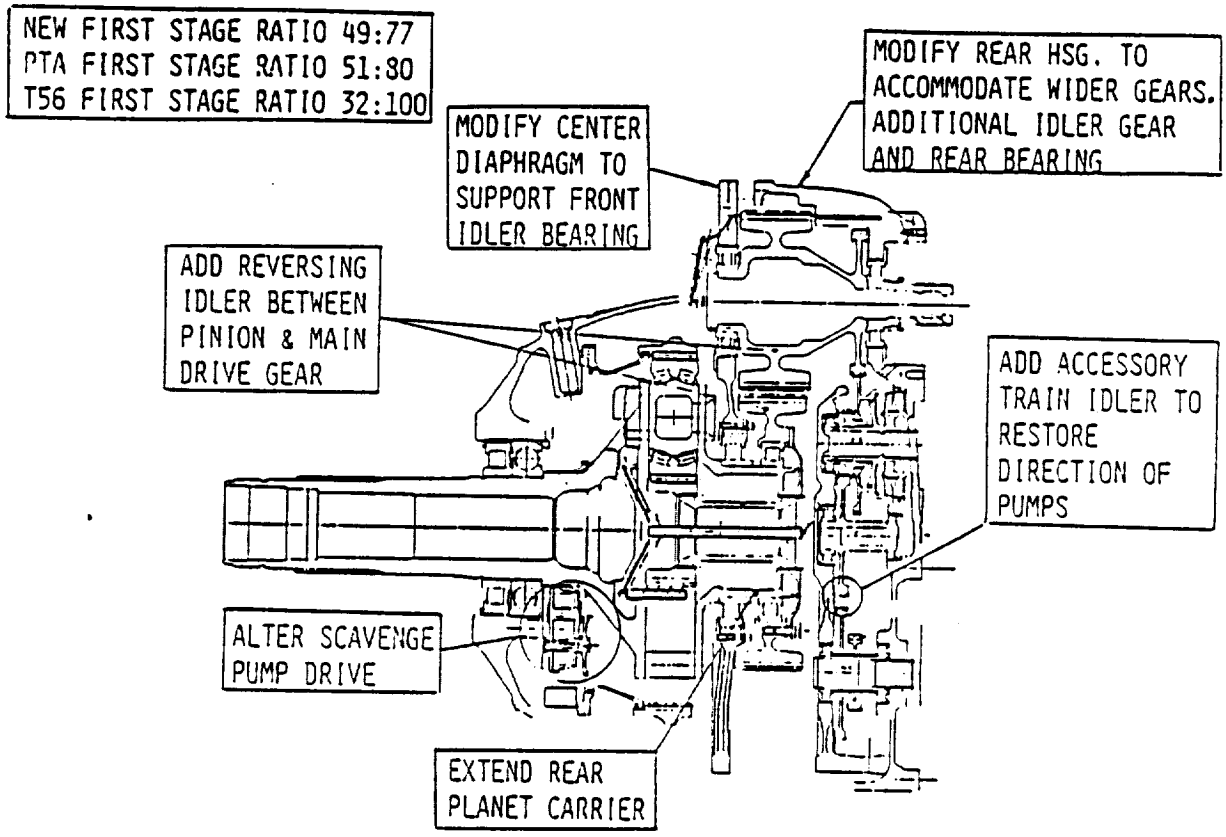


Figure B-1. Opposite Rotation Gearbox Modification

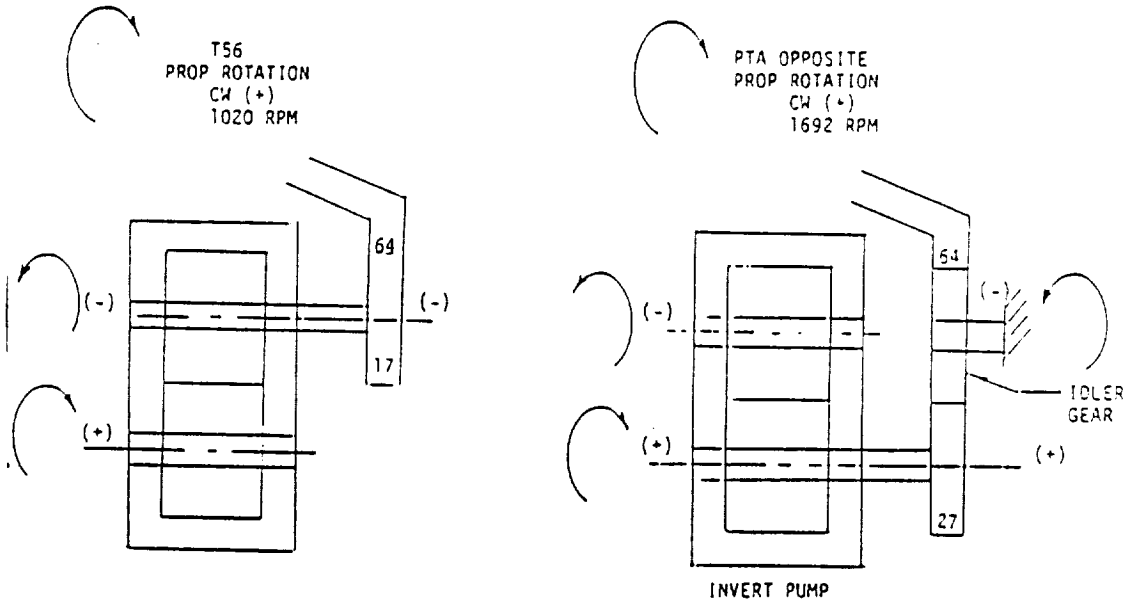


Figure B-2. Opposite Rotation Gearbox Nose Scavenge Pump

Lockheed

APPENDIX C
LOW-SPEED, FULL-SCALE WIND TUNNEL TESTS

List of Figures

Figure	Title	Page
C-1	PTA Model in NASA-Ames 40 x 80 Ft Wind Tunnel	C-5
C-2	Test Article Forward Fairing	C-5
C-3	Acoustic Cocoon	C-7
C-4	Test Article Support Structure	C-8
C-5	Test Article Installation	C-8
C-6	Test Article Plan View	C-9
C-7	Test Article Elevation View	C-9
C-8	Test Configurations	C-10
C-9	Wind Tunnel Wall Microphone Installation	C-13
C-10	Free-Field Microphone Locations	C-13
C-11	Wind Tunnel-to-Flight Noise Corrections	C-16
C-12	PTA Acoustic Geometry and LAP Design Point	C-17
C-13	Map of Propfan Noise Characteristics	C-18
C-14	Map of Propfan Wake Fluctuating Pressure Characteristics	C-19
C-15	Predicted Noise Levels on Wing and Fuselage Surfaces	C-22
C-16	Estimated Requirements for Cabin Noise Reduction	C-22
C-17	Test Parameter Limitations - Symmetric Configuration	C-27
C-18	Test Parameter Limitations - Asymmetric Configuration	C-27
C-19	Inboard Profile of Model and Platform Support	C-28
C-20	Plan View of Support Platform	C-29
C-21	Maximum Thrust for Loads Analysis	C-31

APPENDIX C
LOW-SPEED, FULL-SCALE WIND TUNNEL TESTS

1.0 INTRODUCTION

The PTA Program was originally structured in two phases--with the first phase culminating in a full-scale wind tunnel test, and with all flight tests relegated to the second phase. The reasons for this were: a degree of uncertainty about the final level of funding for the program, and the desire to get full-scale simulated flight data in the event that flight tests were not funded.

Shortly after the contract was awarded, however, the government decided to fund the flight tests. From that point, the need for the full-scale wind tunnel tests was less urgent, and subsequently this task was dropped from the PTA Program so that other tasks could be expanded.

The low-speed wind tunnel tests would have provided some valuable data, however, particularly in the area of cabin acoustics and on phenomena associated with airborne and structureborne noise propagation. It is believed, therefore, that the studies and analyses performed in preparing for these tests may have value to guide others in planning similar research programs. A complete report of this work may be found in Reference C-1.

2.0 TEST REQUIREMENTS

The objectives of the full-scale PTA wind tunnel tests were to:

- Provide propfan blade stress and acoustics data under simulated low-speed flight conditions
- Provide propfan inflow angle measurements to validate prediction methods
- Provide for systematic investigation of yaw and pitch inflow effects on propfan noise and blade stress
- Establish baseline noise and vibration data for comparison with flight test data
- Obtain data to evaluate the relative contribution of structure-borne and airborne noise
- Provide for mechanical checkout of the propfan drive system and control system at low airspeeds

3.0 TEST HARDWARE

3.1 TEST FACILITY

These tests were planned for the 40 x 80-Ft Wind Tunnel of the NASA-Ames Research Center. This facility and its requirements for model installation are described in Reference C-2.

3.2 TEST ARTICLE

Because the objectives of these tests included blade stress tests and acoustic measurements in a realistic environment, it was desired to use or simulate as much of the flight hardware as possible. It was also desired that provisions be made for isolating and identifying the propfan noise propagated through the air and that propagated through the aircraft structure.

To measure airborne noise alone, it was planned that the cabin and wing structure would be independently mounted from the wind tunnel floor so that no noise could be propagated through the aircraft structure. To measure structureborne noise alone, it was planned that the wing and fuselage would be joined with the normal attachment fittings and that a cocoon would be built around the fuselage to shield it from airborne noise.

The proposed test hardware is shown in Figure C-1. It included: (a) the propfan, nacelle, and drive system mounted on the flight hardware GII wing, (b) a cabin developed from a fuselage barrel section off the GIII production line, and (c) a double-wall cocoon. Preliminary design drawings were developed for all this hardware.

3.2.1 Wing and Drive System

The wing proposed for these tests was the wing that would be used in the flight test program. After all structural modifications were made, it was planned that the wing would be mated to the nacelle containing the propfan drive system and that this assembly would become the basic element of the test hardware.

3.2.2 Fuselage

It was not necessary to use an entire fuselage in these tests; it was necessary that the wing-fuselage attachment be realistic, that the cabin wall structure be accurately modeled, and that the cabin have pressurization capability. Since there were no spare GII fuselage sections available, it was decided to take a 9.1m (30-ft) long barrel section from the GIII assembly line and use it as the test fuselage. Pressure bulkheads were designed for each end, and aerodynamic fairings were designed to simulate the fuselage nose and tail sections. The nose fairing is shown in Figure C-2, and the tail fairing was similar.

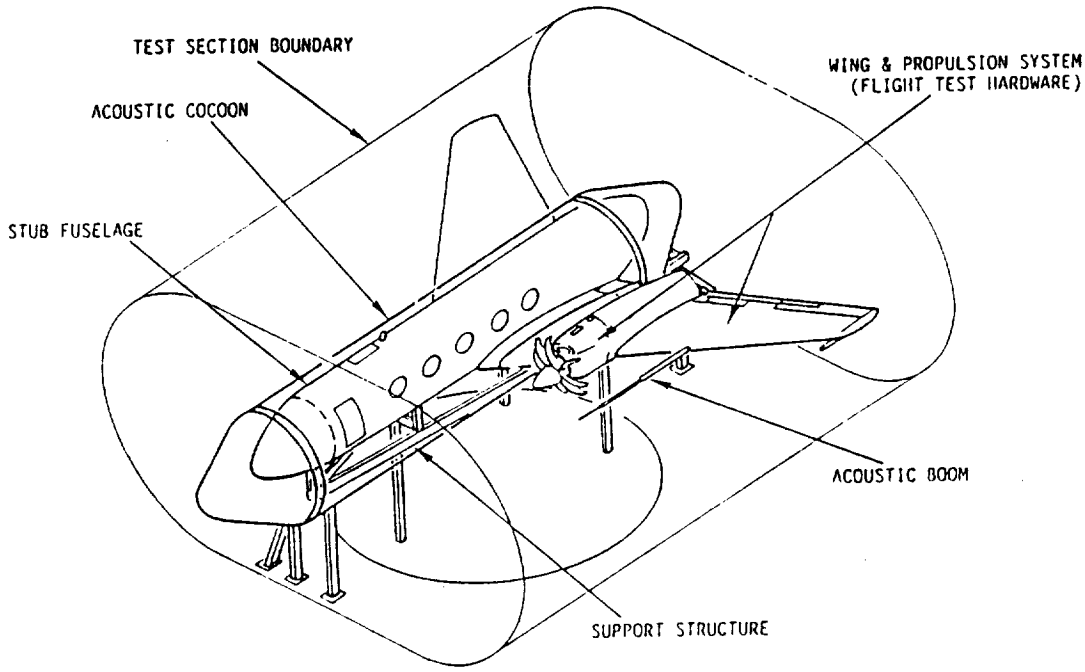


Figure C-1. PTA Model in NASA-Ames 40 x 80 Ft Wind Tunnel

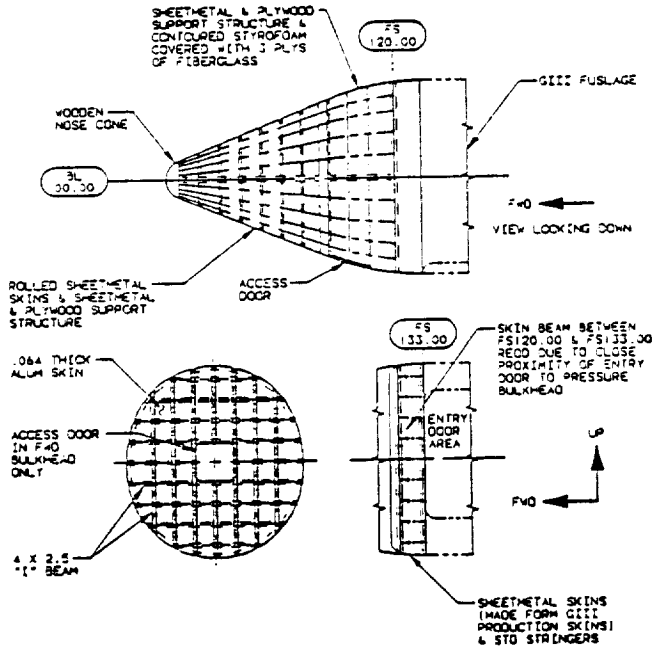


Figure C-2. Test Article Forward Fairing

ORIGINAL PAGE IS OF POOR QUALITY

3.2.3 Cocoon

The cocoon is shown in Figure C-3. It was a double-walled structure to obtain the required noise reduction and was designed to fit around the wing and fuselage without being structurally attached to either the wing or fuselage. It was designed in two parts with a horizontal split line along the wing chord line at the planes of intersection. The cocoon also had nose and tail aerodynamic fairings.

As shown in the cross section of Figure C-3, the cocoon was supported from the wind tunnel floor. A platform, independently mounted from the floor, supported the rest of the test hardware. This platform is shown in Figure C-4, and the platform and model without the cocoon is shown in Figures C-5 through C-7.

The walls of the cocoon were 4 mm (0.16 in.) aluminum lined with lead vinyl sheets. Seals that would not significantly transmit vibration were designed for the regions where the walls of the cocoon fit around the wings.

3.3 TEST PROCEDURES

Test procedures were developed by Lockheed with recommendations from Hamilton Standard, Allison, and Lockheed engineers. The test configurations are depicted in Figure C-8. Test sequences were developed as outlined below.

Order	Configuration	Consideration
1	Bare wing with propfan and microphone ring around fuselage	Obtain baseline data
2	As 1, with isolated fuselage and cocoon	If cocoon results are unacceptable (cabin interior noise too high), eliminate tests of Configurations 3 and 4
3	As 2, with fuselage connected to the wing	If structureborne noise (SBN) is very low, there is no need for Configuration 4
4	As 3, with massive damping of fuselage	Obtain SBN transmitted only through the floor
5	As 1, with fuselage attached to wing	Simulates the flight case; microphone ring can be eliminated if Configuration 1 results are satisfactory
6	As 2, without cocoon	If SBN is undetectable in cocoon tests, this configuration will be eliminated

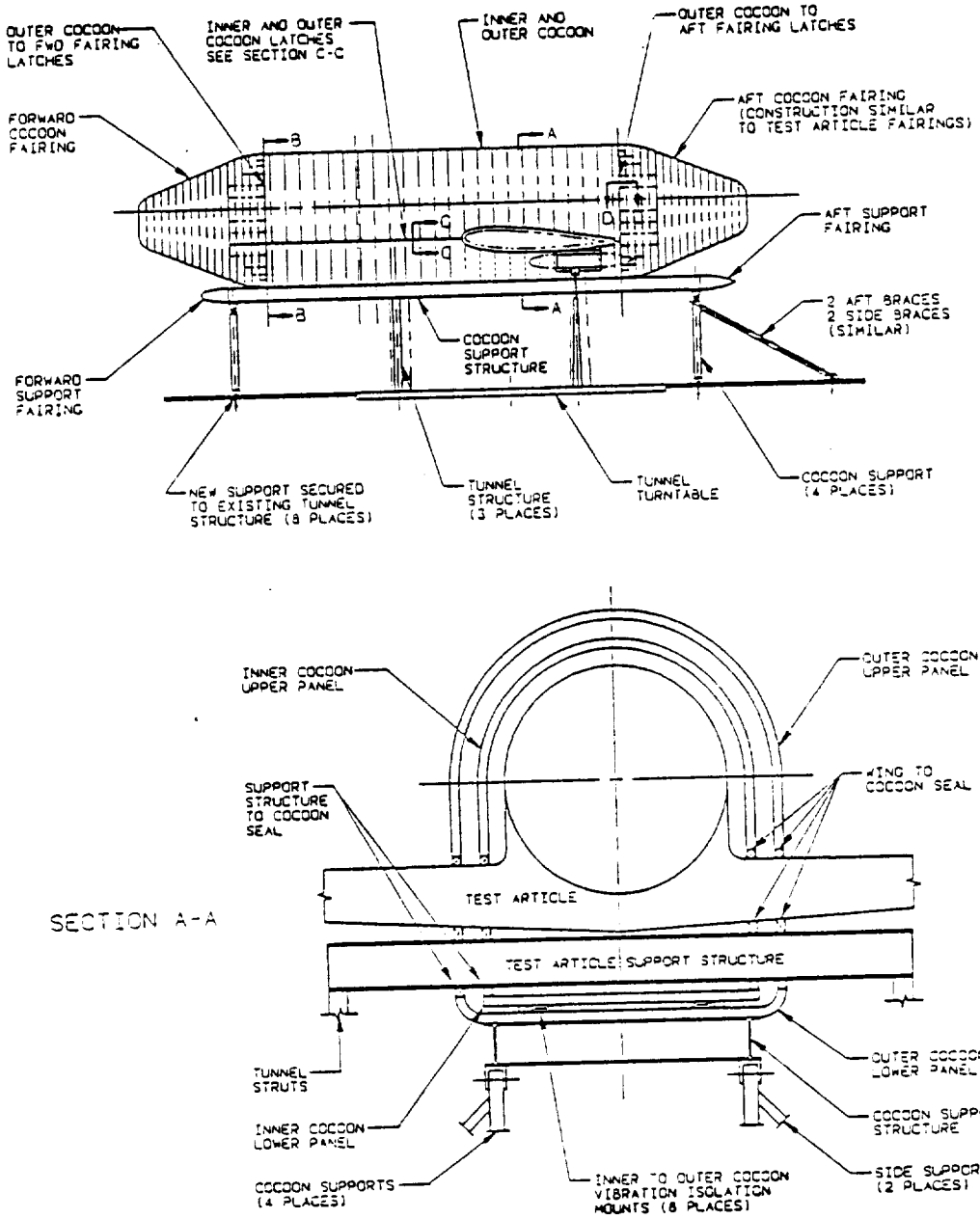


Figure C-3. Acoustic Cocoon

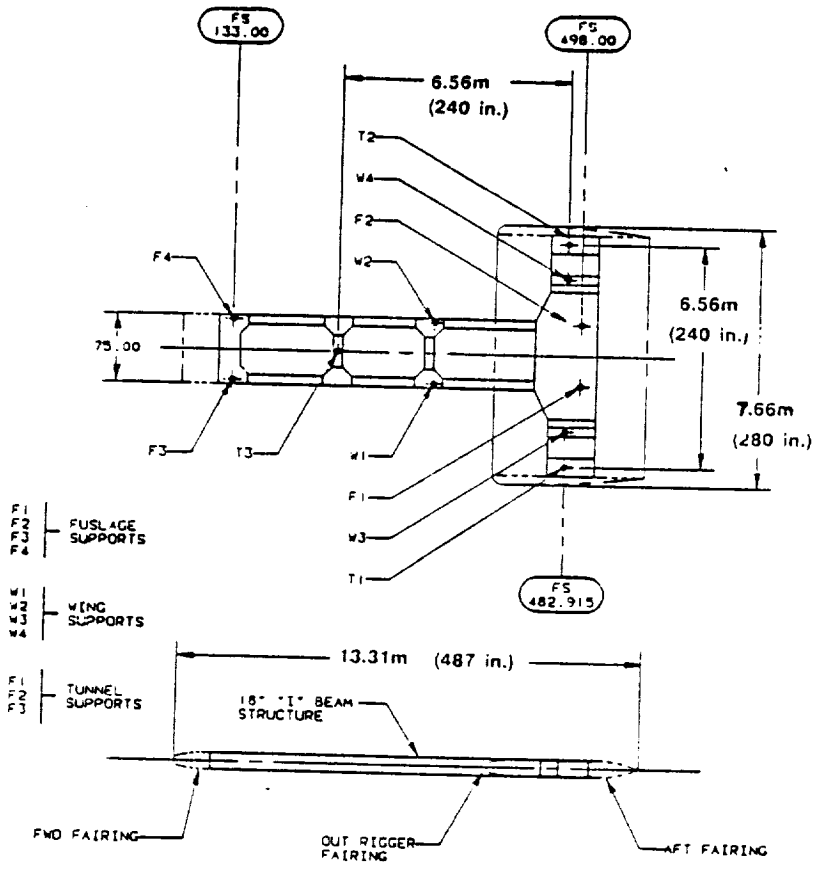


Figure C-4. Test Article Support Structure

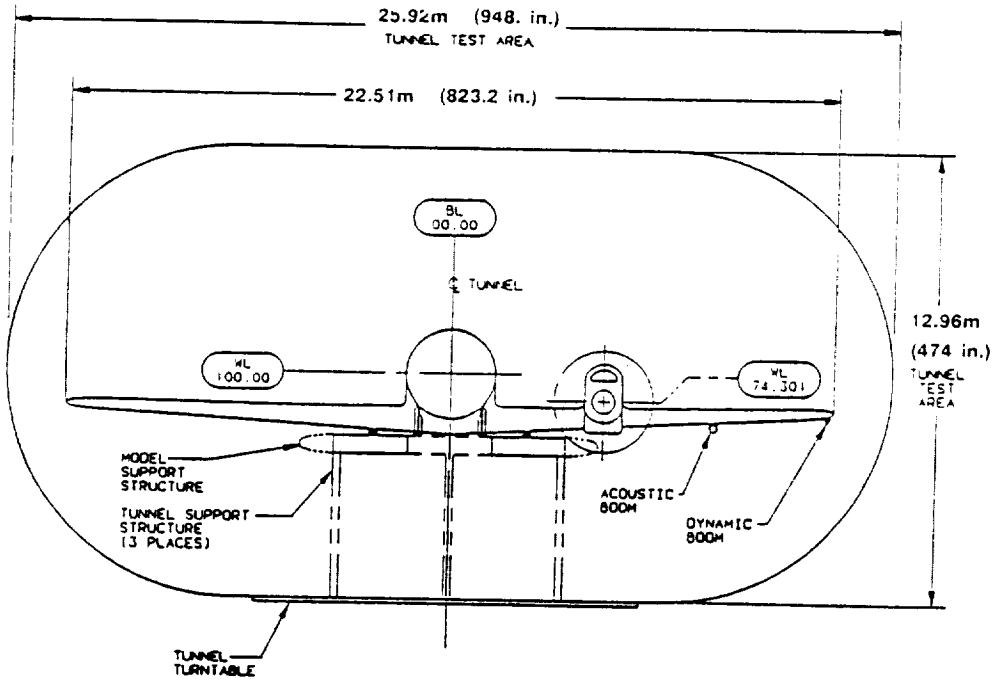


Figure C-5. Test Article Installation

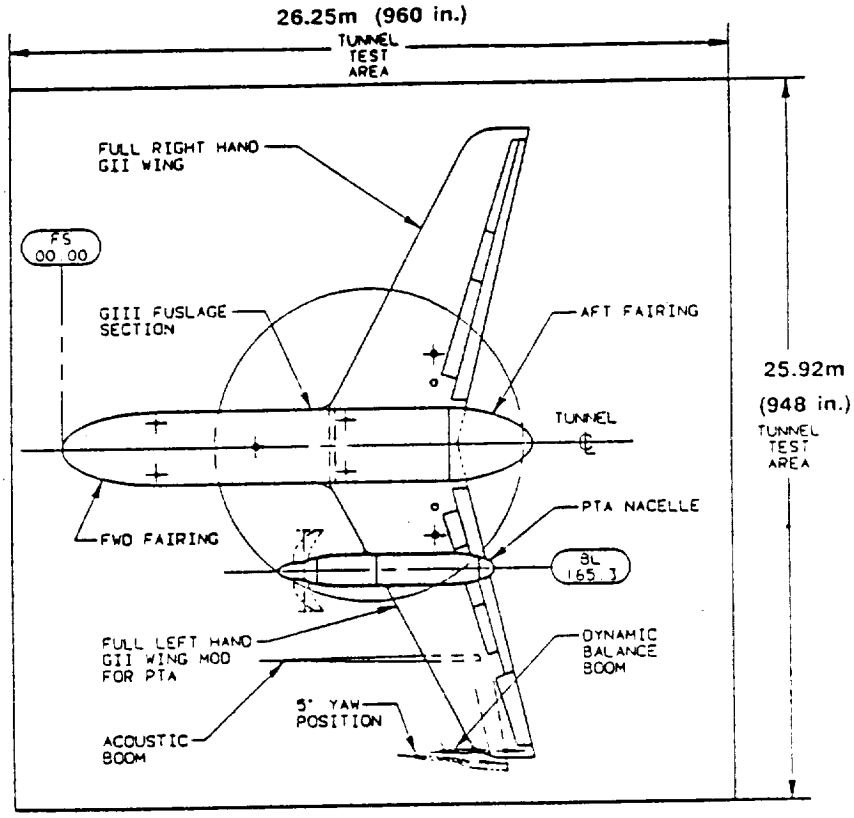


Figure C-6. Test Article Plan View

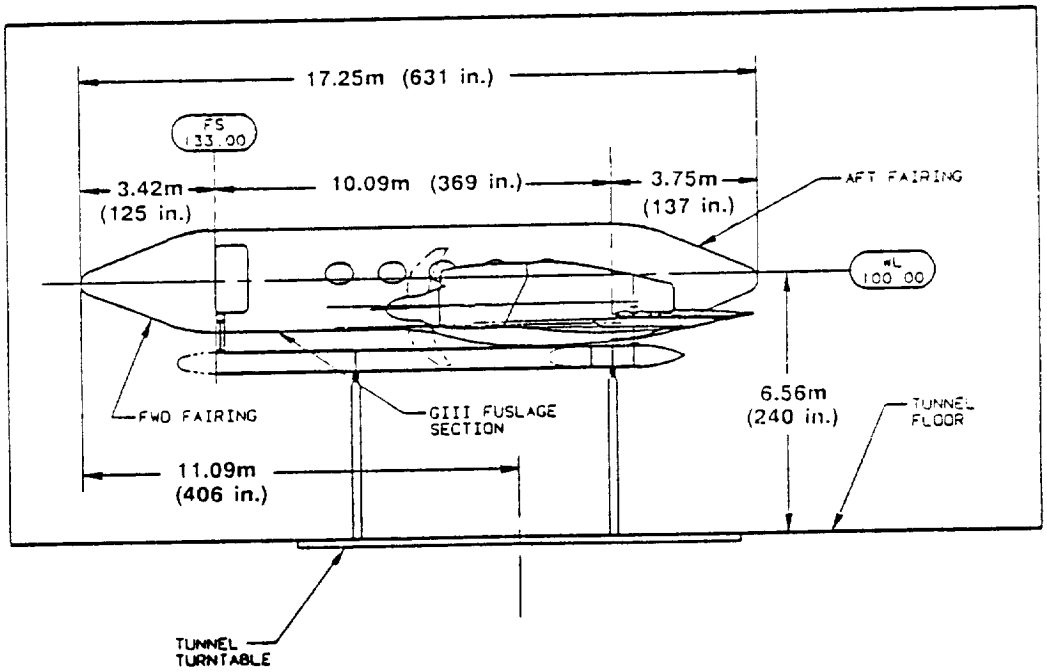
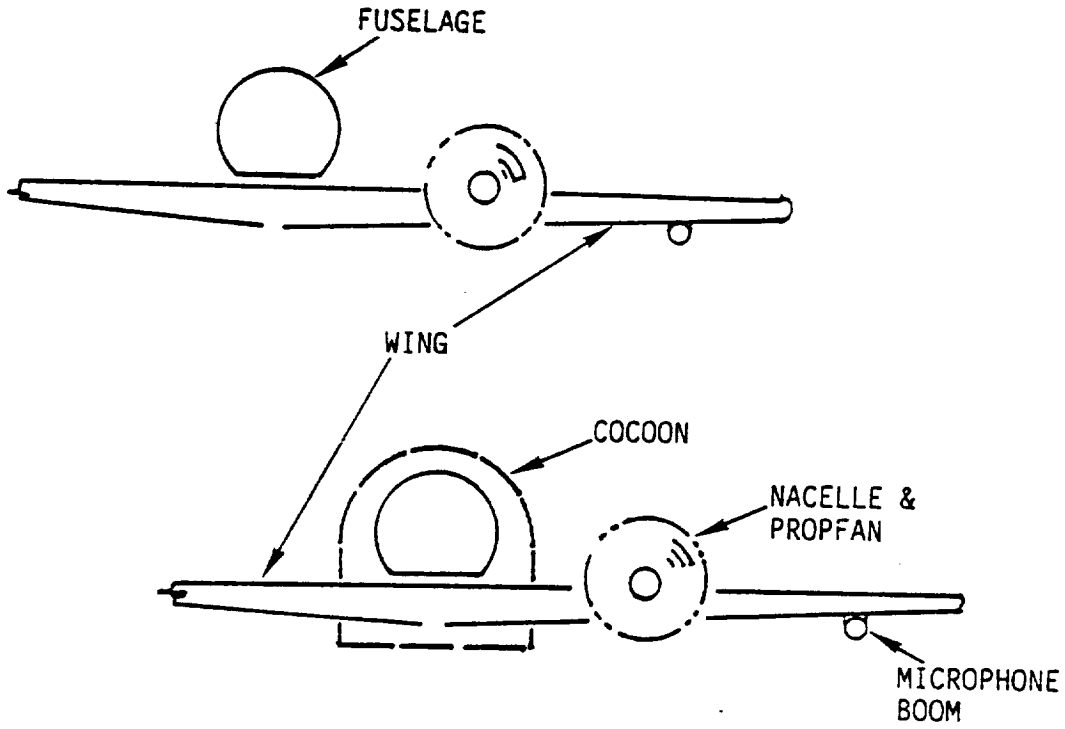


Figure C-7. Test Article Elevation View



CONFIGURATION	0	1	2	3	4	5	6
WING/NACELLE	X	X	X	X	X	X	X
PROPFAN		X	X	X	X	X	X
FUSELAGE ATTACHED		X	X	X			
FUSELAGE DETACHED					X	X	
COCOON AERO NOISE BARRIER			X	X	X		
FUSELAGE ACOUSTIC DEADENING				X			

Figure C-8. Test Configurations

This test program was designed for an allotted 10-week test span.

3.4 TEST INSTRUMENTATION

3.4.1 Instrumentation

The criteria for development of the research data system was that the same equipment be used for tests at the Ames tunnel and aboard the test airplane. There were, however, minor differences in the transducer makeup at the wind tunnel and on the airplane. The following instrumentation was unique to each test:

WIND TUNNEL TESTS	FLIGHT TESTS
Propeller Inflow Rake	Flutter Accelerometers
Acoustic Microphone Ring	Telemetry Down Link
Tunnel Floor Microphones	Airplane Basic Flight Parameters
	Far-Field Microphones
	FAR 36 Test Simulations

A complete listing was developed of test data parameters (with ranges and accuracies) which was almost identical to that for flight tests. Notable additions for the investigation of propfan noise are depicted in Figures C-9 and C-10. Microphones were arrayed along the tunnel floor to record the far-field noise signal, and a "microphone ring" placed microphones just beyond the propfan tips to record near-field noise. In addition, the velocity and direction of airflow in the propfan plane was to be measured by rake-mounted probes.

3.5 DATA SYSTEM

For these tests, data system consoles were to be exactly the same as for the flight tests, and there was to be approximately 90 percent commonality for the data system wiring diagrams. The principal differences were the transducer wiring for the acoustic microphone ring and an array of microphones on the tunnel floor.

Design for the data acquisition system focussed on three areas:

- Signal conditioning equipment
- Control panels and racks
- Cable harnesses

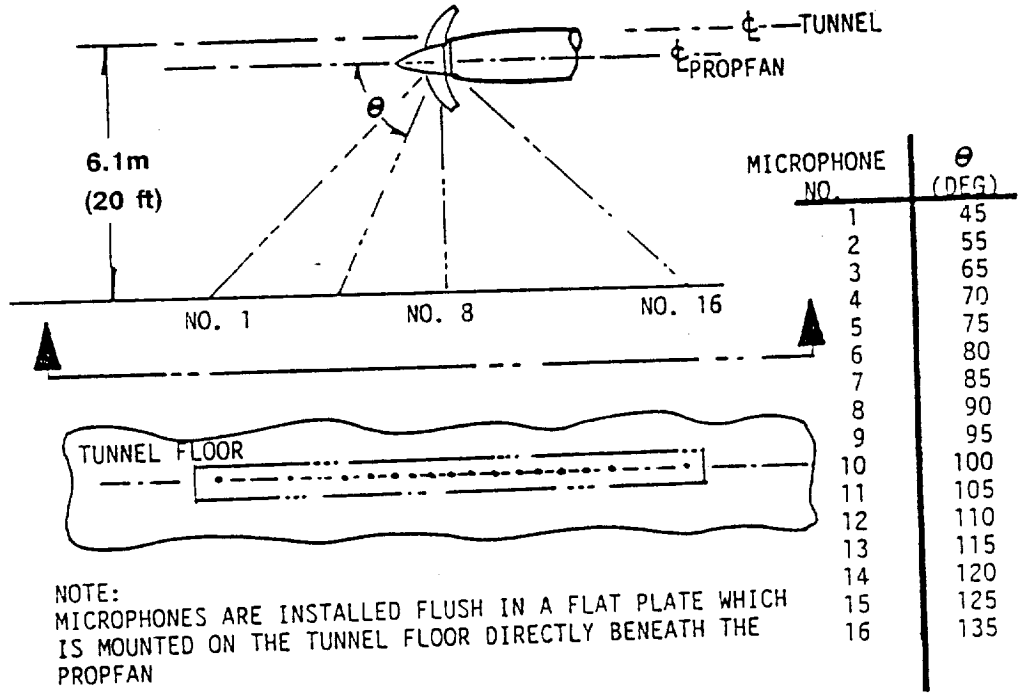
The eight signal conditioning modules were of standard design. The 70 constant-bandwidth frequency modulating (CBFM) cards were designed to handle 4 channels of data each with band-edge-overrun-limiting resistors on each "board." A standard (stand alone) remote controller was employed in the design. Existing designs were selected for the FM line driver/reference card, the decommutator, and approximately 172 signal conditioner cards.

The control panels and racks were as designed for flight tests. They included:

- Power supply/J box
- Data system control panel
- Data system consoles
- Power control and distribution panel
- Signal module containment boxes
- Dynamic monitor control panel

Several pieces of special test instrumentation were required to meet the test objectives: a propeller inflow rake, an acoustic ring, an acoustic wing boom, an acoustic traversing rake for the cabin, and a far-field noise measurement assembly. The wing boom and cabin traversing rake are described as part of the flight test program. The propeller inflow rake was not designed at the time this task was terminated; it was to be installed in place of the propfan to obtain precise measurement of the flow field in which the propfan was operating. The acoustic ring, also not designed at the termination of the task, was to locate microphones in a circle around the propfan and adjacent to the fuselage side wall. The far-field noise measurement assembly is depicted in Figure C-10.

Cables for data and power transmission were basically the same as for flight tests, but were designed to be fed through the tunnel floor and routed to the tunnel control room instead of being routed inside the fuselage. The tunnel propfan data system wiring was to be connected at the QEC disconnect and substituted for aircraft wiring. The PTA data system power control was to be located in the wind tunnel control room. Cables without disconnects were designed to provide circuit protection for the dynamic signal modules.



MICROPHONE NO.	θ (DEG)
1	45
2	55
3	65
4	70
5	75
6	80
7	85
8	90
9	95
10	100
11	105
12	110
13	115
14	120
15	125
16	135

Figure C-9. Wind Tunnel Wall Microphone Installation

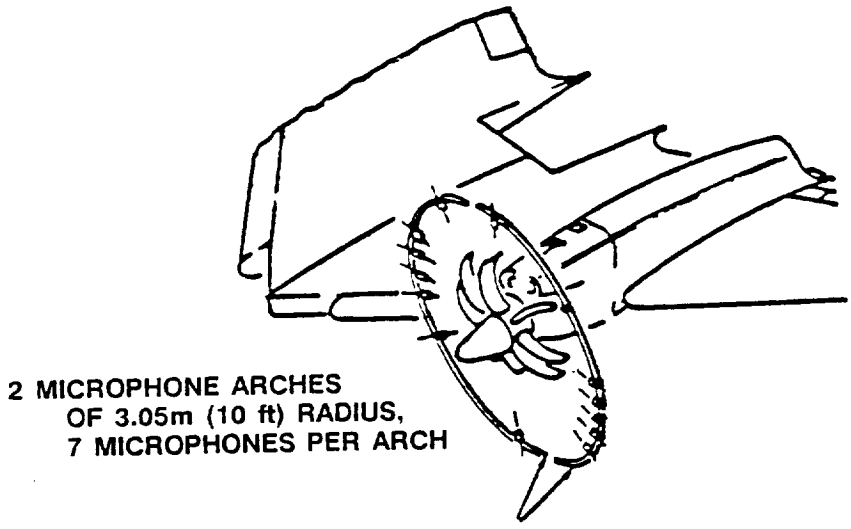


Figure C-10. Free-Field Microphone Locations

4.0 ANALYSIS

4.1 AERODYNAMIC ANALYSIS

The aerodynamic analysis activity was limited to prediction of aerodynamic forces on test hardware and to studies related to propfan flow field measurement and subsequent validation of flow field prediction methodology. Flow field measurements were to be used by Hamilton Standard to predict blade stresses for comparison with measured data and also to validate flow field prediction methods. Flow velocity vectors were to be measured with a rake of "5-hole probes" capable of accurately measuring the three-dimensional velocity components.

Planning and study of this work was performed only in sufficient depth to establish feasibility.

4.2 ACOUSTIC ANALYSIS

4.2.1 Objectives

The objectives in acoustic analysis were to obtain near-field noise and vibration data and cabin noise data in sufficient detail to:

a. Establish a data base for comparison with later flight test acoustic and vibration data and to make parametric assessments of these data

b. Verify predicted propfan and drive system near-field noise characteristics.

c. Determine the relative importance of structureborne noise in the cabin and provide an assessment of structureborne transmission mechanisms

d. Assess potential design concepts for the reduction of structureborne noise

e. Estimate cabin noise levels at PTA cruise conditions

f. Estimate the effect of two propfans (twin configuration) on cabin noise levels, including the effect(s) of propfan direction of rotation

g. Predict near- and far-field noise using measured propeller inflow fields and comparison with measured levels

h. Determine the absolute level of structureborne noise in the cabin

i. Validate predicted far-field noise characteristics by measurement of "far-field" noise data in the wind tunnel

4.2.2 Analysis

The experimental and analytical approach to meet the required objectives evolved to include:

a. Test plans development

b. Application of wind tunnel acoustic and vibration test data to airplane

c. Model, wind tunnel, and flight acoustic environment prediction

d. Model acoustic and vibration transducer locations and requirements

e. Test hardware acoustic design requirements

Prediction methods for the estimation of structureborne noise in aircraft cabins have not yet been developed. Limited flight test data from current propeller-driven aircraft suggest, however, that unattenuated structureborne noise may produce a cabin noise "floor" at a level greater than 80 dBA.

The wind tunnel acoustic and vibration data to issue from these tests would be almost directly applicable to the PTA airplane at low altitudes and Mach numbers up to 0.4. They would enable more precise acoustic conversions between tunnel and flight data to be developed based upon important propfan acoustic parameters and on acoustic impedance differences. A preliminary version of a sound pressure level (SPL) adjustment curve is shown in Figure C-11. Obtaining a low-speed "overlap" point between wind tunnel and flight tests is very important in relating data from the two sources.

Scaling of cabin noise levels is based on external excitation noise levels in terms of sound pressure levels (SPLs) and fluctuating pressure levels (FPLs). Predictions of fuselage SPLs and wing FPLs indicate different dependencies on propfan parameters. Because cabin total noise, structureborne noise, and airborne noise would be separately measured during the planned tests, it is expected that application of such a data base would result in a better understanding of the mechanism and importance of structureborne noise transmission into the cabin during PTA cruise conditions.

Propfan acoustic environment predictions were made for the fuselage and wing to determine expected noise levels for comparison with expected PTA flight noise levels and to determine noise reduction requirements for the fuselage acoustic cocoon. The geometries, fuselage SPLs, and wing FPL predictions are shown in Figure C-12 through C-14.

NOTES:

- ΔdB IS APPLIED TO MEASURED TUNNEL SPL TO OBTAIN FLIGHT SPL AT SAME M_0, J AND C_p, AND U FOR THE SAME GEOMETRIC LOCATION.
- ΔdB IS APPLICABLE TO ALL PROPELLER TONES.
- FREQUENCIES NEED TO BE REDUCED BY SCALE FACTOR

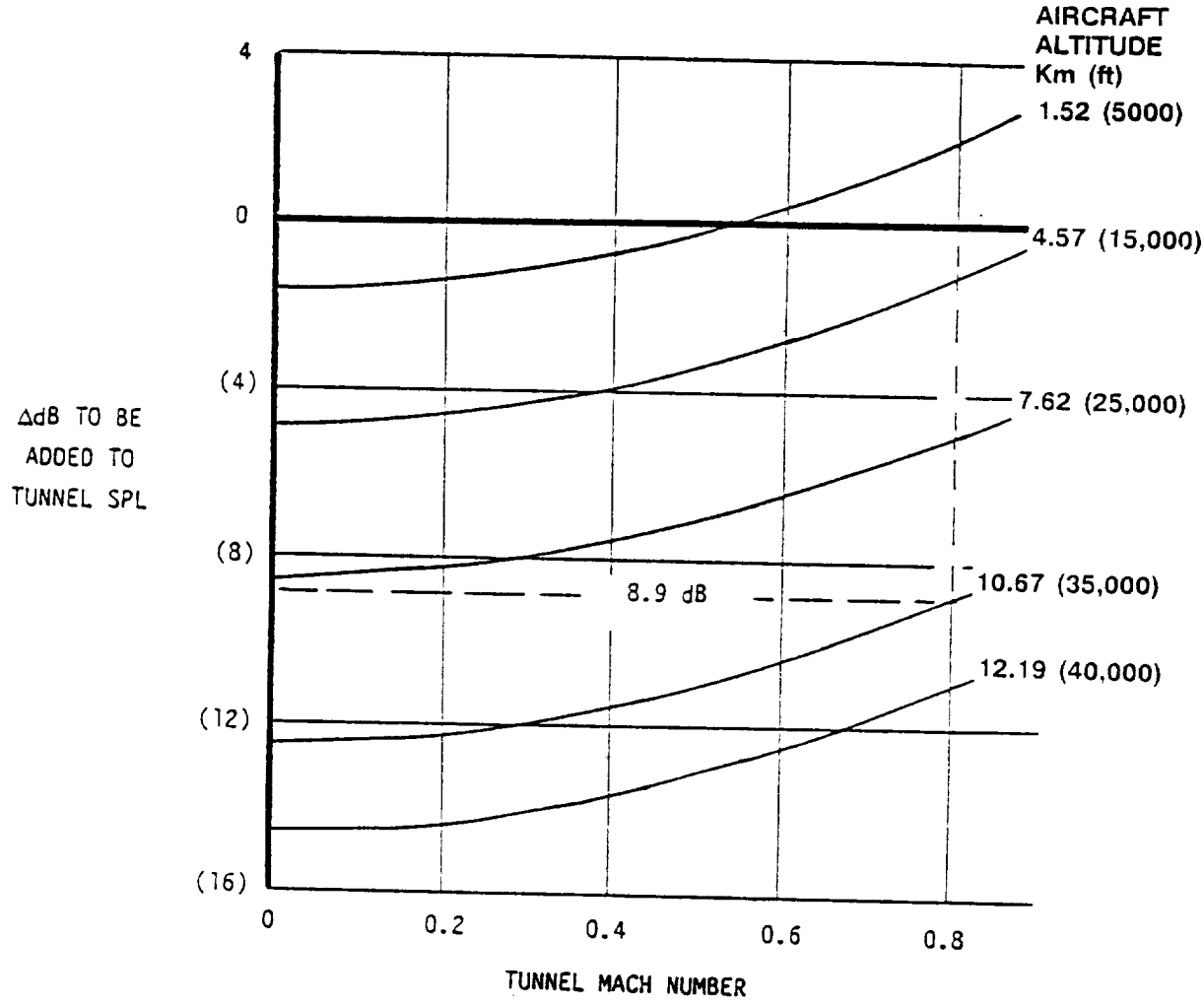
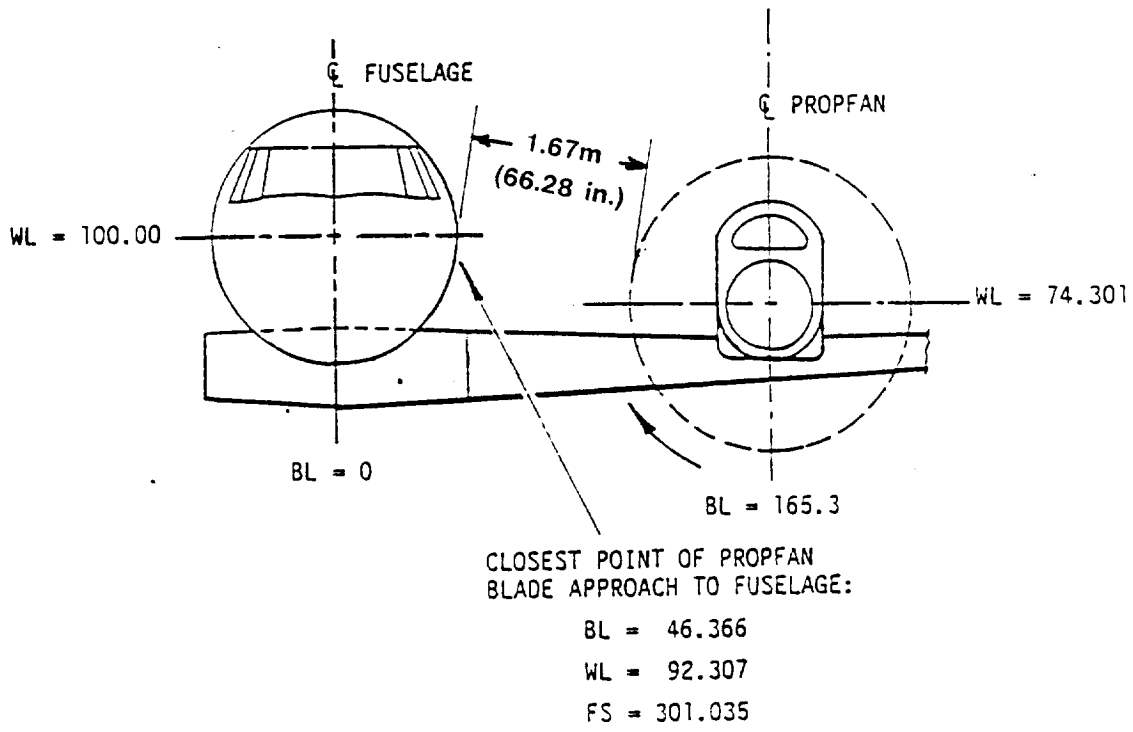


Figure C-11. Wind Tunnel-to-Flight Noise Corrections



LAP DESIGN POINT

ALTITUDE = 10,668m (35,000 ft)

MACH NO. = 0.8

V_{ROT} = 244 (800 fps)

J = 3.06

$PSHP/D_p^2$ = 256 $\frac{kw}{m^2}$ (32 HP/ft^2

C_p = 1.45

Figure C-12. PTA Acoustic Geometry and LAP Design Point

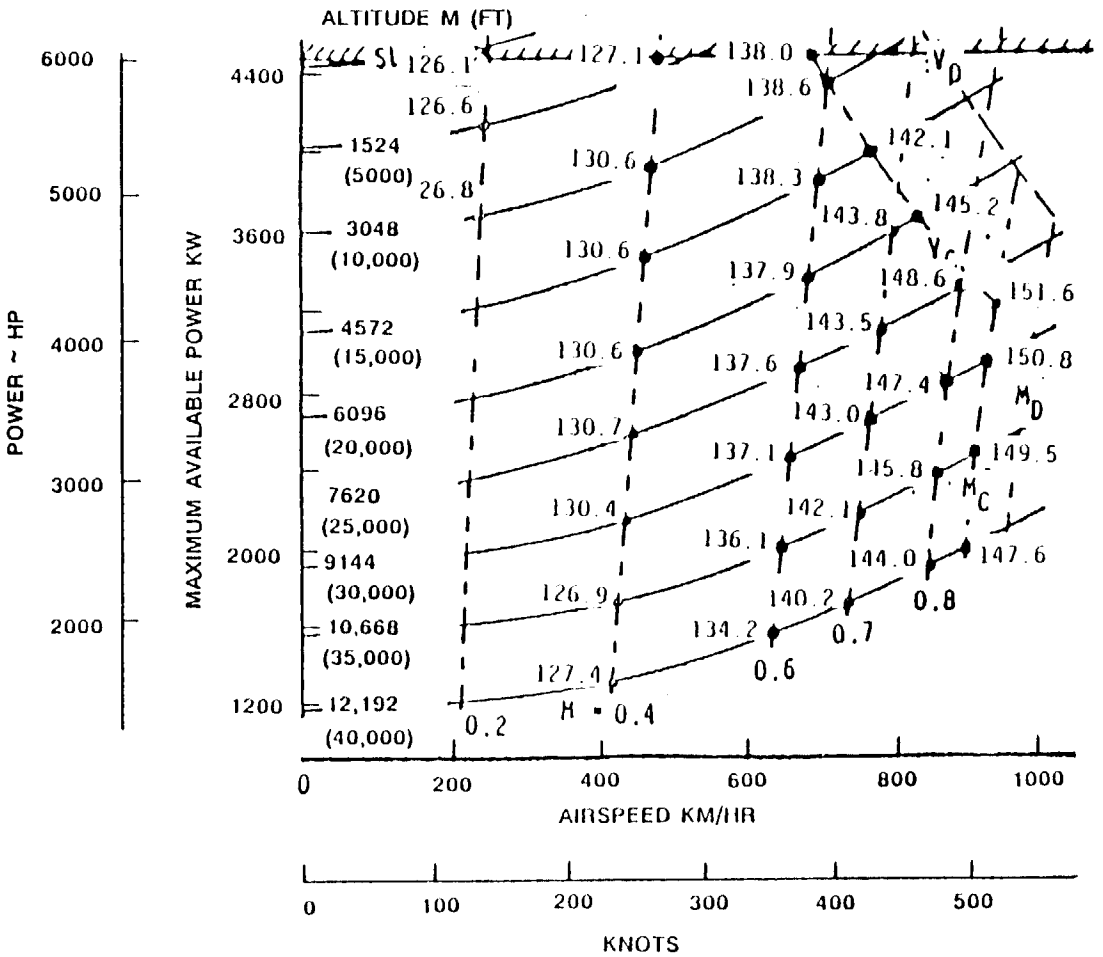


Figure C-13. Map of Propfan Noise Characteristics

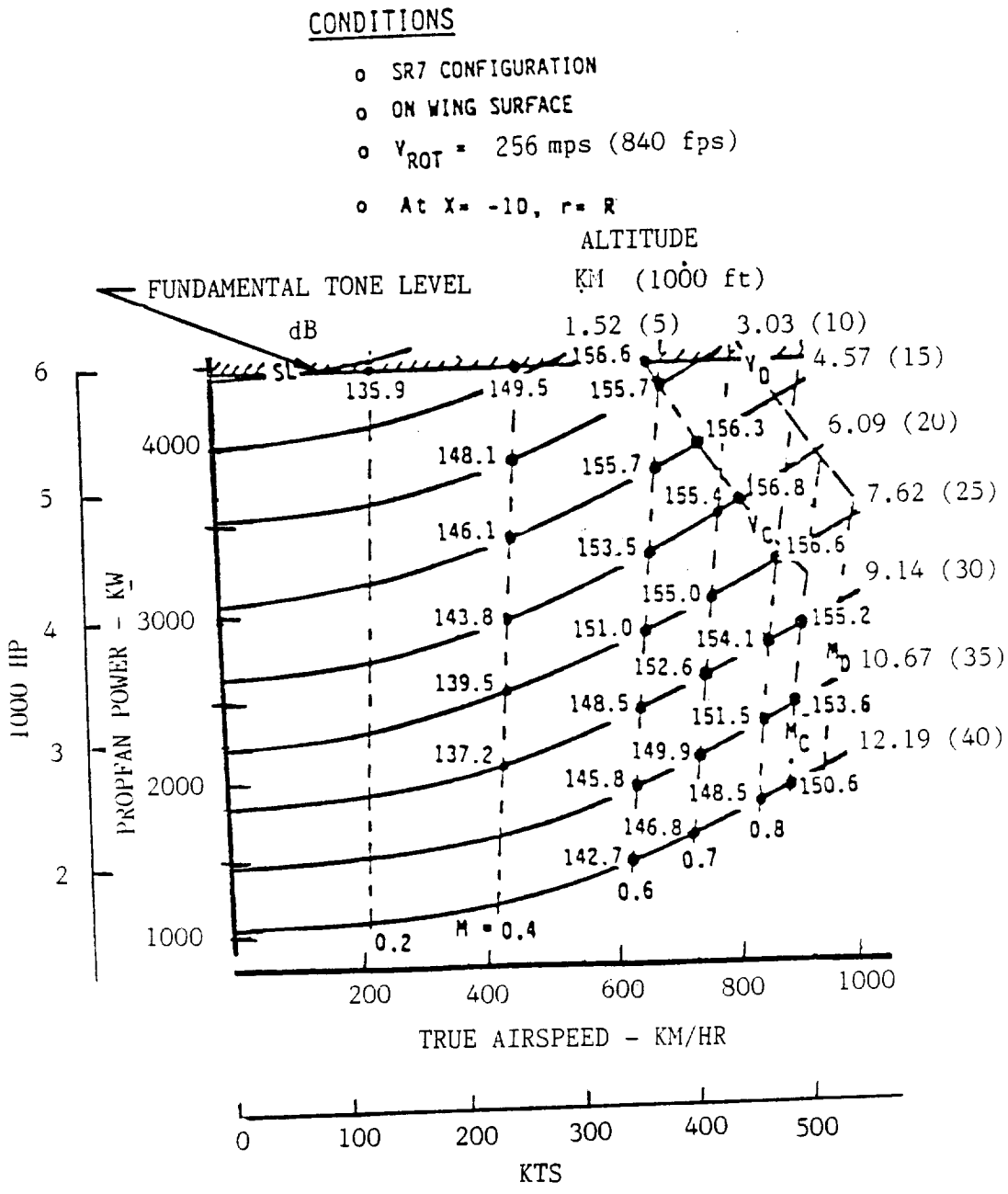


Figure C-14. Map of Propfan Wake Fluctuating Pressure Characteristics

The prediction methods used in these analyses were:

- For propeller-generated SPLs on the fuselage surface: "SR7 Near-Field Noise Prediction Program (PTANEAR)," prepared by Hamilton Standard (Reference C-2)

- For propeller-generated FPLs on the wing surface: an empirical method devised by Lockheed-Georgia Company

A comparison between predicted noise for wind tunnel and flight tests at the propfan design point reveals that the fuselage SPLs would reduce by 18 dB between flight and the wind tunnel, whereas the wing FPLs would reduce by only 4 dB. This indicates that the LSWT test, as proposed, was an excellent tool for the identification of cabin structureborne noise and for investigating structureborne noise mechanisms.

The tunnel reverberant acoustic SPLs on the fuselage and wing were also estimated and are shown in Figure C-15. The indication is that reverberant acoustic levels would be much less than the direct acoustic levels and, therefore, would not be a significant problem in the near-field tests. For the planned far-field tests, it is expected that the reverberant effects would be much more severe. However, as part of the wind tunnel test program, reverberant noise levels in the tunnel would be measured and their impact reassessed.

A peak noise level of 138 dB was predicted on the surface of the cocoon at the fundamental frequency.

4.2.3 Location of Instrumentation

The acoustic and vibration transducer locations were essentially the same as for the PTA airplane. In fact, the same instrumented wing, propulsion system, and wing acoustic boom were to be used in the PTA flight test program. The need for the propfan near-field noise survey in the LSWT required the addition of the special acoustic microphone ring. All transducer locations were carefully defined so as to obtain data required to satisfy the program objectives. The transducer types also were selected for best sensitivity, range, ruggedness, high-speed grazing flow, temperature environment static pressure, reliability, etc.

4.2.4 Test Hardware Acoustic Requirements

The mounting of the fuselage/wing specimen in the wind tunnel required that:

1. The fuselage and wing supports be designed to enable the fuselage to be physically separated from the wing. This was essential for the assessment of the relative magnitudes of structureborne and airborne noise and vibration.

2. No vibration be transmitted from the wind tunnel floor to either the fuselage or the wing.

3. The fuselage and wing support mounting attachments not adversely affect the structural vibration characteristics (local or overall) of the fuselage or the wing so that the structureborne noise propagation and distribution is significantly changed.

4. To avoid undue excitation, the wing support structure not be located in the propfan wake.

The requirement that structureborne noise be positively identified and measured in the fuselage cabin led to the need for the cocoon to completely surround the fuselage specimen. Special anti-vibration mounting of the cocoon from the floor was not necessary. The cocoon had to provide:

1. Sufficient acoustic attenuation of the propfan airborne noise that the measured noise level in the cabin would be in fact clearly dominated by structureborne noise. This led to a required cocoon wall noise reduction of at least 45 dB, in the vicinity of the propeller plane, for the propeller fundamental frequency of 226 Hz. The logic leading to this acoustical requirement is illustrated in Figure C-16.

2. Access for the wings, which would be subject to vertical static and vibratory displacement, without generating an acoustical flanking path.

3. Access for personnel into the cabin.

4. Access to microphones installed on the fuselage external surface for calibration and inspection purposes.

It was planned that the acoustic microphone ring around the propeller should be as large as possible without interfering with the fuselage, and the ring support system should not be subject to excitation by the propfan wake.

For far-field noise level measurements, microphones were to be installed directly beneath the centerline of the propulsion system, and flush-mounted on a flat plate.

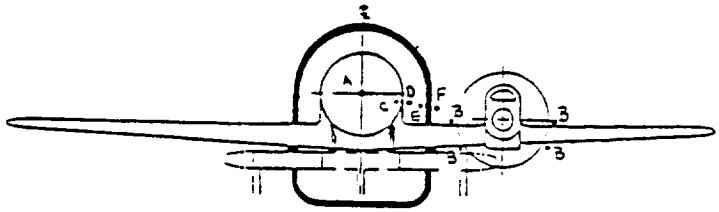
4.2.5 Acoustic Data Evaluation Plans

It was planned that the first acoustic analyses would be of a test conducted to determine tunnel background noise levels and the level of reverberant source noise at near- and far-field microphone locations. The data would be evaluated to determine the magnitude and extent of wind tunnel induced acoustic contamination at the various microphone locations for comparison with the later propfan acoustic signals.

	FUSELAGE SURFACE SPL'S(MAX)		WING SURFACE FPL'S (MAX)	WING SURFACE SPL'S (MAX)	
	DIRECT	REFLECTED		DIRECT	REFLECTED
CRUISE @ LAP DESIGN POINT	152	---	151	140	---
LSWT (NO COCOON)	134	122	147	122	121
CHANGE IN LEVEL, ΔdB CRUISE TO LSWT	-18	---	-4	---	---
	COCOON	SURFACE	WING	SURFACE	
LSWT (WITH COCOON)	138*	122*	147	122	121

*NO ALLOWANCE FOR EFFECT OF COCOON PROXIMITY ON PROPFAN ACOUSTICS

Figure C-15. Predicted Noise Levels on Wing and Fuselage Surfaces



	NOMINAL	RANGE
STRUCTUREBORNE NOISE FLOOR		
COMMERCIAL AIRCRAFT CABIN TOTAL ALLOWABLE PROPFAN NOISE, AT A	80 dBA	—
PROPFAN HIGHER-ORDER NOISE CONTRIBUTION TO TOTAL	3 dBA	0 to 5
CABIN ALLOWABLE PROPFAN NOISE AT 1ST ORDER FREQUENCY	77 dBA	75 to 80
"A" WEIGHTING AT 1ST ORDER	-10 dB	—
CABIN ALLOWABLE PROPFAN 1ST ORDER SPL	87 dB	85 to 90
LEVEL OF MINIMUM SBN OF INTEREST (WHERE PRESSURE OF SBN ADDS 1 dB)	80 dB	78 to 83
SBN INCREASE IN ABSENCE OF PAX, SEATS, TRIM, CARPET, BAGGAGE, ETC	3 dB	0 to 4
LEVEL OF MINIMUM SBN OF INTEREST, IN BARE COMMERCIAL AIRPLANE, AT A	83 dB	78 to 87
LSWT FUSELAGE SBN TARGET		
FLUCTUATING PRESSURE LEVEL AT B, DESIGN CRUISE, 1ST ORDER	151 dB	147 to 155
FPL AT B, LSWT TEST CONDITIONS	147 dB	143 to 151
REDUCTION IN FPL, FLIGHT-TO-LSWT	4 dB	—
RESULTING REDUCTION IN LSWT FUSELAGE SBN AT A (ASSUMPTION)	4 dB	—
LEVEL OF MINIMUM SBN OF INTEREST IN LSWT, AT A	79 dB	74 to 83
LSWT FUSELAGE ABN TARGET		
FOR SBN TO BE DETECTABLE, ABN MUST BE LOWER THAN SBN BY AT LEAST	6 dB	—
ABN DESIGN TARGET LEVEL, AT MIC LOCATION A	73 dB	68 to 77
NOISE REDUCTION		
ABN INCREASE FROM MIC LOCATIONS TO FUSELAGE INTERIOR SURFACE (A TO C)	4 dB	1 to 6
ABN TARGET LEVEL AT C	77 dB	69 to 83
FUSELAGE WALL NOISE REDUCTION (D TO C)	16 dB	8 to 24
ABN TARGET LEVEL AT FUSELAGE EXTERIOR SURFACE D	93 dB	77 to 107
ABN INCREASE ACROSS AIR GAP, D TO E (NO LIMP BARRIER OR ABSORPTION)	0 dB	0 to 1
ABN TARGET LEVEL AT COCOON INTERIOR SURFACE E	93 dB	77 to 108
COCOON EXTERIOR NOISE LEVEL AT F, 1ST ORDER	138 dB	135 to 141
COCOON WALL NOISE REDUCTION REQUIRED (LEVEL AT E MINUS LEVEL AT F)	45 dB	64 to 29

Figure C-16. Estimated Requirements for Cabin Noise Reduction

The propfan acoustic data evaluation would consist of identification of absolute noise levels and trends in the following areas:

a. Near-Field Acoustics - The analysis emphasis in near-field acoustics would be on propfan fundamental tone; however, the importance of the propfan harmonics would be determined. Analyses would focus on:

   - o Near-free-field sound pressure level (SPL)
   - o Near-field fuselage SPL and phase; baseline data would be analyzed parametrically
   - o Near-field wing FPL and phase; baseline data for FPL and phase would be analyzed parametrically

b. Far-Field Acoustics - The frequency range of concern was 50 to 10,000 Hz, which encompasses all the propfan tones and any propfan broadband noise. The far-field data would be acquired along a line parallel to and 6m (20 ft) beneath the propulsion centerline. Although the wind tunnel and the propfan could be operated at realistic operating conditions for far-field noise purposes, important questions needed to be resolved concerning possible interference with the propfan far-field noise. The microphones would be exposed to tunnel drive noise, propfan drive system noise (with muffler tailpipe installed), propfan noise, and tunnel reverberant acoustic effects on all these sources. They also would be exposed to grazing boundary layer flow. Considering these effects, the analysis would be aimed at:

   - o Source separation of the measured acoustic data
   - o Determination of the propfan-alone spectra sensitivity to significant operational parameters
   - o Determination of the drive system muffler effectiveness using measured and predicted data

The fuselage, wing, and cocoon configurations and test combinations were carefully defined so that the following cabin noise source levels and their previously discussed parametrics could be defined:

a. Total noise (airborne plus structureborne noise) - measured in the baseline configuration

b. Airborne noise - measured with the fuselage physically separated from the wing

c. Structureborne noise - measured with the cocoon surrounding the fuselage to suppress the airborne noise

d. Structureborne noise arising from the floor alone - measured as above but with massive sidewall soundproofing added

A test was planned with the cocoon surrounding the fuselage but physically separated from the wing. The fuselage would be unpressurized because it could be pressurized only when attached to the wing. The measured cabin noise levels should be very low so that a cabin sound pressure level increase of at least 10 dB must be obtained when the wing is reattached and the cocoon still in place. Demonstration of this increase would confirm that the test approach is valid; it was, therefore, an essential part of the acoustic test.

Cabin acoustic and vibration data on spatial distribution of noise would be acquired in a non-soundproof (no cocoon) fuselage cabin. The majority of the data would be acquired at a tunnel speed of M = 0.4. Results would be analyzed primarily to define the distribution of the fundamental tone and first few harmonics at cabin wall axial and circumferential sidewall locations and spatially at a height corresponding to the average seated head height. The survey would be obtained on a parametric basis, from which cabin sound sensitivities would be determined for:

- o Propeller tip rotation speed
- o Propeller shaft horsepower
- o Aircraft angle of attack
- o Nacelle tilt angle
- o Tunnel speed

Another essential part of the analysis was planned to be a comparison of cabin noise levels measured in the wind tunnel program and in the airplane at equivalent test conditions, e.g., the low-speed overlap point. Such a comparison would be made on a total noise basis.

An analysis was planned to determine the level of structureborne noise in the airplane cabin at the LAP cruise design point (H = 10,668m (35,000 ft) and M = 0.8). The approach would comprise the following steps:

a. Identification of the measured cabin structureborne noise level in the tunnel at M = 0.4, with the fuselage pressurized and unpressurized

b. Development of measured and predicted wing FPLs at both tunnel and flight conditions

c. Prediction of the cabin structureborne noise at the LAP condition

d. Identification of the measured cabin airborne noise levels in the tunnel at M = 0.4

e. Development of measured and predicted fuselage SPLs at both tunnel and flight conditions

f. Prediction of the cabin airborne noise at the design conditions

g. Prediction of the cabin total noise (airborne plus structureborne noise)

h. Comparison of predicted and measured PTA cabin noise total levels

After the level and distribution of structureborne noise in the PTA cabin at the LAP design point was determined, its importance would be assessed.

Objectives of the structureborne noise (SBN) evaluation were to:

- o Estimate the cabin structureborne noise level and assess its importance
- o Identify the source of cabin structureborne noise
- o Define structureborne noise mechanisms and transmission paths

The first objective was discussed under the cabin noise discussion. This discussion deals with the analysis approach to satisfy the last two objectives. The candidate sources of SBN noise are:

- o Propeller slipstream excitation of the wing
- o Engine mount excitation of the wing

The principal test configuration for this analysis was that in which the cocoon surrounded the fuselage (to block the airborne excitation) and the wing was attached to the fuselage. The test parameters varied would be: propfan tip rotational speed and shaft horsepower, tunnel speed, angle of attack, and nacelle tilt.

The acoustic data of interest would be the accelerations measured on the engine, engine mounts, wing, wing/fuselage interface, and the fuselage skin/stringer structure, and the fluctuating pressure levels measured on the wing surface behind the propeller.

The total structureborne noise contribution to interior noise for the LSWT test conditions would be identified, and the structureborne noise transmitted through the aircraft floor alone would also be identified. The variation of a single parameter such as angle of attack, rpm, or free-stream Mach number might cause a particular variable such as wing surface pressure loading or forces through the engine mounts to show a correlation with interior noise. The desired results would be a sensitivity of interior noise to both surface pressure loading and forces (mass or aerodynamic unbalance) through the engine mounts. The "mechanism" or transmission path might be identified by the wing strain and acceleration measurements. If the wing were excited by normal structural modes, the spar strain measurements should also correlate with interior noise. On the other hand, if there were a local wing panel response to the propeller wake and this response were transmitted via surface panel modal or forced response, then wing surface accelerations might correlate with interior noise. There is no validated method for identifying "mechanisms" and transmission paths. This effort was planned as an exercise in deduction and logic using the test measurements obtained for these controlled laboratory tests.

The relationships identified from the planned tests and analyses could be used to extrapolate to design point conditions. This would be accomplished by comparisons to demonstrate the similarity between the LSWT

measurements and flight test measurements, prediction of increased wing surface pressure and/or increased engine mount loads at design cruise, and estimations of the magnitude of the structureborne noise level that would occur. It would be assumed that the LSWT-determined transfer functions are valid in flight at cruise condition.

Some concerns exist about the approach to the structureborne noise study of this test. It would not be possible to identify the airborne noise transmission through the floor because there was no configuration planned that would block SBN, have a treated sidewall, but no cocoon. The possibility exists that airborne noise transmission through the floor could be greater than the SBN transmission. If this occurred, conclusions based only on SBN transmission would be in error. For example, the SBN transmission through the floor might be low enough to be ignored while the unmeasured ABN transmission through the floor might be significant. It must be emphasized that for cabin noise control purposes, the critical design information would be sidewall-radiated versus floor-radiated noise and not ABN versus SBN transmission.

4.3 STRUCTURAL ANALYSIS

A brief analysis was performed to derive the preliminary test parameter limitations required to assure support loads within allowable values for the fuselage, wing, cocoon, and tunnel mounting structure. Two test configurations were examined: (1) symmetric - complete wings on each side of the fuselage; (2) asymmetric - complete wing on the left/propfan side of the fuselage and a stub wing on the right side. The resulting limitations are shown in Figures C-17 and C-18. These findings are preliminary and would have to be updated to reflect subsequent data refinements and model support platform configuration changes that would accompany a continuation of the design effort.

4.3.1 Loads Analysis

The preliminary loads analysis effort was directed toward estimating the test parameter limitations required to assure model support loads (wind tunnel balance) within allowable values. These allowable applied loads are:

MOUNT	ALLOWABLE LOAD kN (LB)				
	DOWN	UP	SIDE	DRAG	THRUST
Front	80.1 (18,000)	80.1 (18,000)	-	-	-
Main (Left/Right)	155.7 (35,000)	66.7 (15,000)	17.8 (4,000)	35.6 (8,000)	35.6 (8,000)

The model platform and support system was analyzed as illustrated in Figures C-19 and C-20. This configuration would be subject to change with additional refinement/development of the model design.

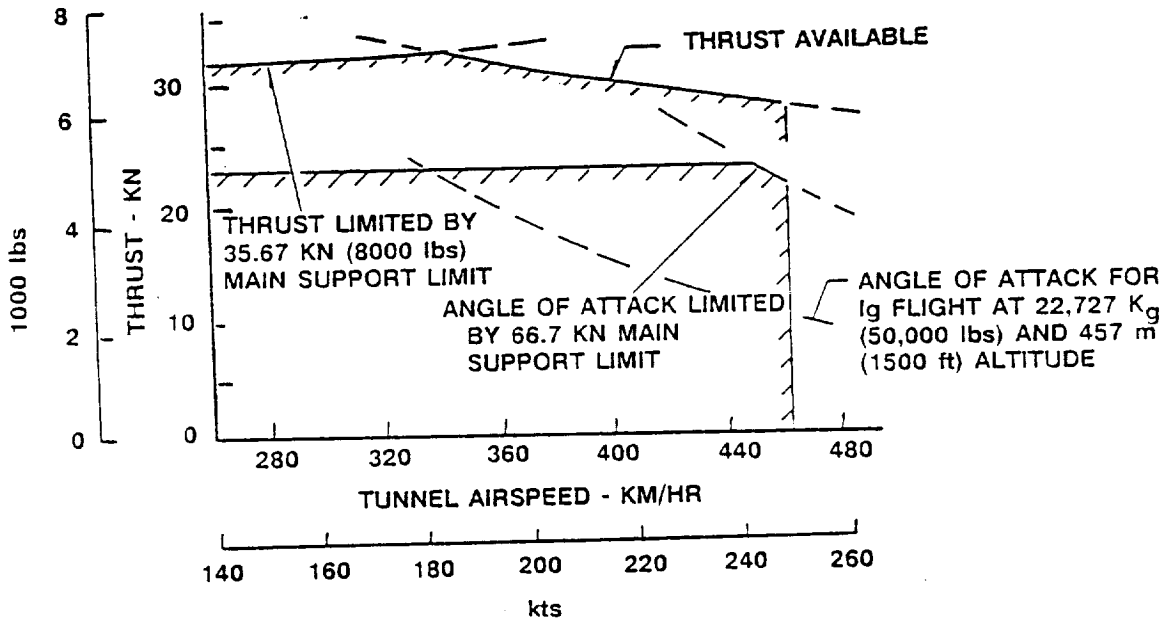


Figure C-17. Test Parameter Limitations - Symmetric Configuration

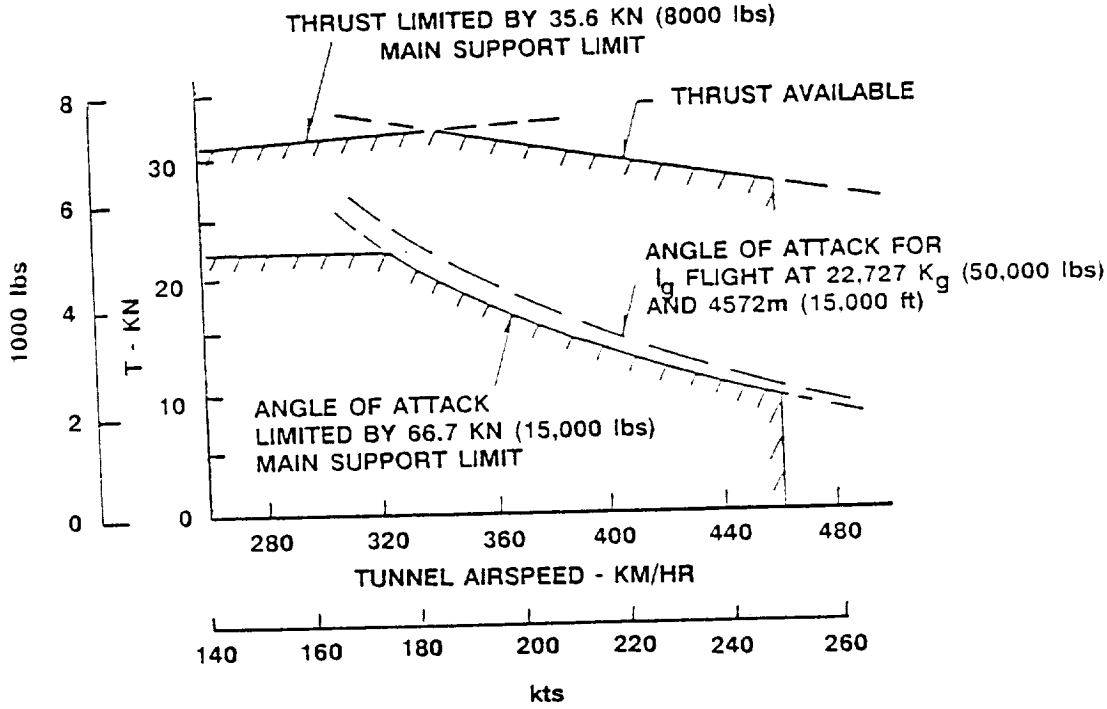


Figure C-18. Test Parameter Limitations - Asymmetric Configuration

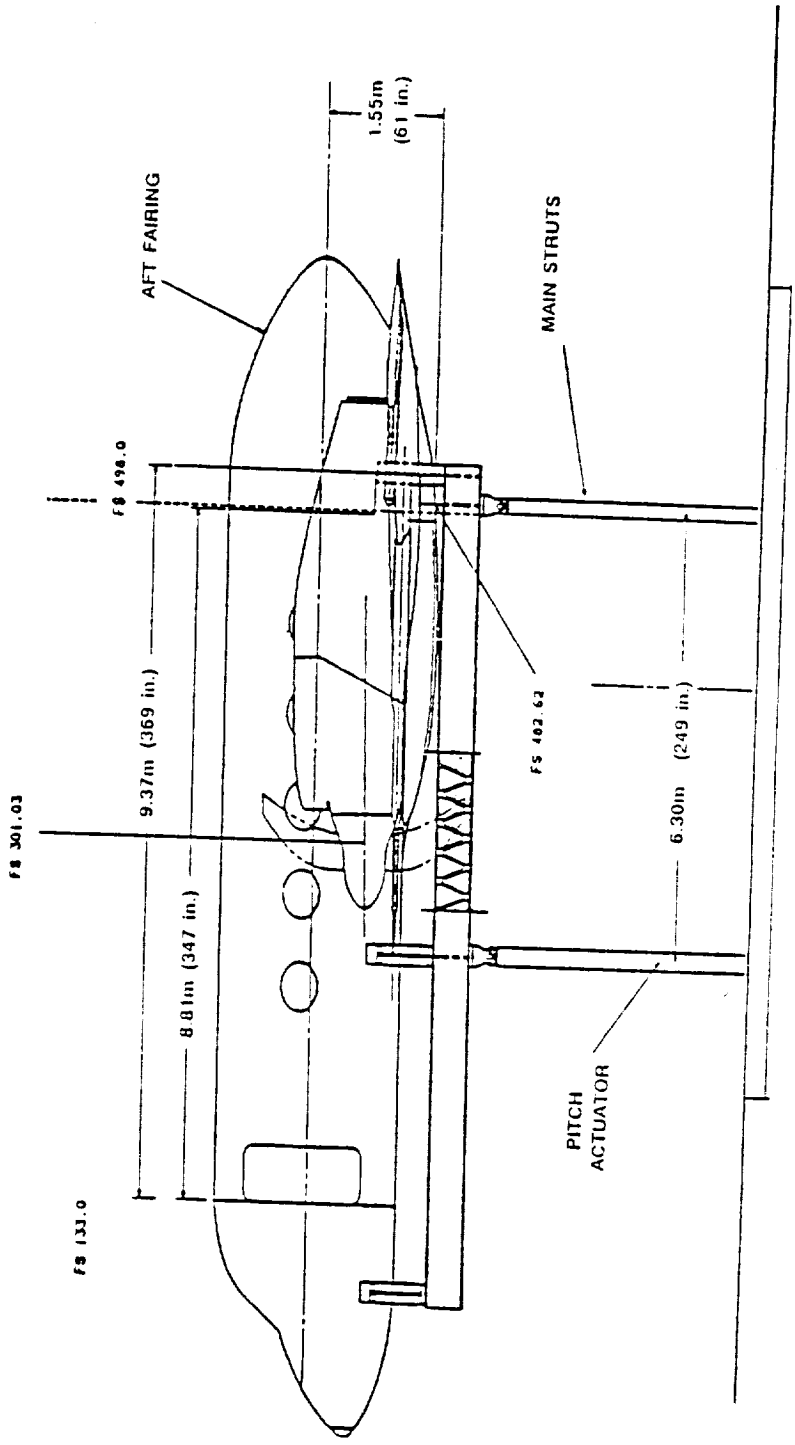


Figure C-19. Inboard Profile of Model and Platform Support

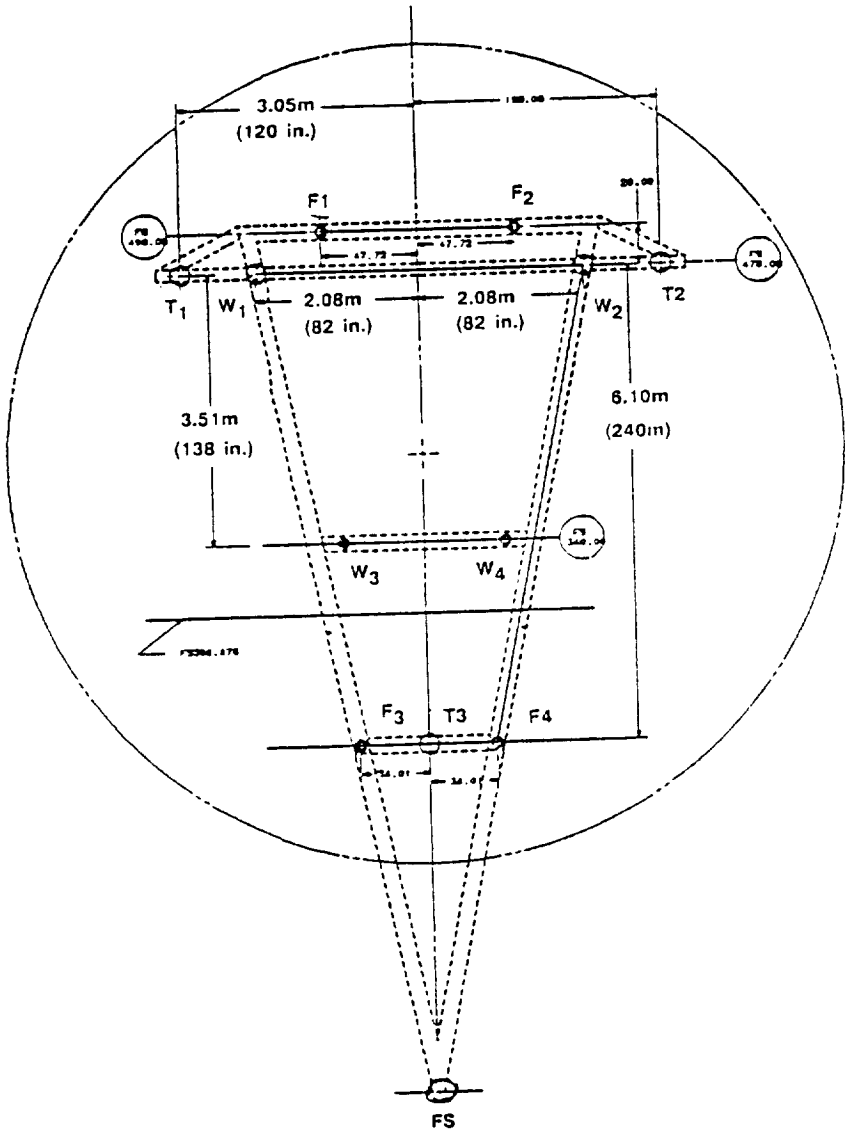


Figure C-20. Plan View of Support Platform

The following axes and sign conventions were used for all applied loads:

x - positive aft

y - positive left

z - positive up

Positive moments are left wing up, nose up, left wing forward. Convention origin was FS 451.3, BL 0, WL 100.

Aerodynamic loadings were estimated using a vortex-lattice solution for a paneled representation of the model:

Load	Symmetric Configuration	Asymmetric Configuration
P_x	$10.24q + .13q(\alpha + 1)^2$	$10.24q + .13q(\alpha + 1)^2$
P_y	0	0
P_z	$48.73q(\alpha + 2)$	$40.78q(\alpha + 1)$
M_x	$111.6q(\alpha + 1)$	$5689q(\alpha + 1)$
M_y	$2274q + 113.5q(\alpha + 1)$	$2274q + 602.9q(\alpha + 1)$
M_z	0	0

where: q = Tunnel dynamic pressure (psf)

α = Model angle of attack (deg)

Inertia data were:

Model:

Load	Symmetric Configuration	Asymmetric Configuration
P_z, kN (lb)	-73.2 (-16,446)	-69.9 (-15,718)
M_x, N-m (in.-lb)	-2,785 (-793,158)	-4,324 (-1,231,348)
M_y, N-m (in.-lb)	-2,900 (-826,083)	-2,423 (-690,000)

Platform: Weight = 36 kN (8100 lb) (apply as -12 kn (-2700 lb) at each support)

Propulsion data were estimated:

Thrust: Apply thrust levels shown in Figure C-21 irrespective of prop tip speed (conservative)

Prop Airloads: Use Hamilton Standard propeller force and moment derivatives for the SR3 propfan.

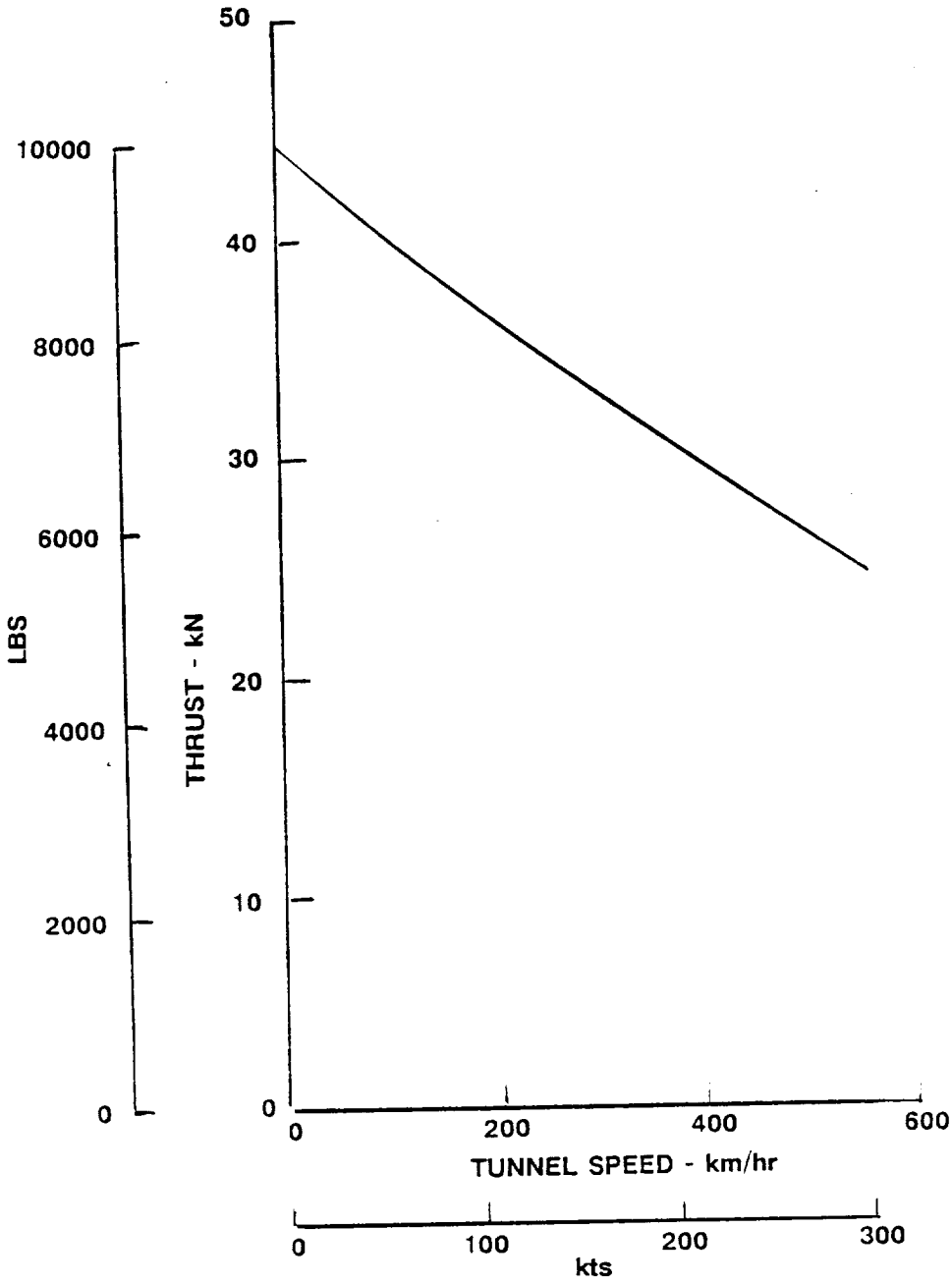


Figure C-21. Maximum Thrust for Loads Analysis

Torque: Use 4474 kw (6000 shp) for all conditions

($M_x = 1.782 \times 10^8 / V_{TIP}$)

where: M_x = Torque (in.-lb)

V_{TIP} = Propeller tip speed (fps)

Applied loads at each support were determined for combinations of the following parameters:

Tunnel airspeed, V_K: 0, 100, 150, 200, 250 knots

Propfan thrust: ± maximum available and zero

Prop tip speed, V_{TIP}: 183 (600), 244 (800), 256 (840) mps (fps)

Angle of attack, : 5, 3, 0, -3, -5 degrees

Nacelle tilt, NT: 3, -1, -5 degrees

A computer program was used to perform all calculations. The resulting support loads were extracted from the program output, tabulated for analysis and review, and are shown graphically in Figures C-17 and C-18.

4.3.2 Stress Analysis

The primary stress effort accomplished was: (1) stress design support to the preliminary layouts for the cocoon and platform configurations, (2) study of the LSWT requirements and load capabilities and their accommodation in the preliminary designs, and (3) modular additions to the aircraft modification finite element model to incorporate the LSWT requirements for internal loads and platform loads.

4.3.3 Stress Design Support

Stress support was provided to the preliminary design activities to integrate the requirements of the different test configurations and the associated structural support systems. These include the LSWT test specimen, cocoon, platform, the flat pressure bulkheads in the fuselage at FS 120 and FS 498, and interfaces. The test configurations were to be evaluated through a finite element model analysis to determine the internal loads and stresses and support loads. These are entirely different from those due to normal aircraft usage, such as the restraint of wing aerodynamic/propulsive loads at the trunnion points.

4.3.4 LSWT Requirements

The LSWT requirements were studied and reflected in the preliminary design of the test hardware and support system. Allowable loads on the tunnel struts dictated selection of the symmetric wing configuration to avoid large moments about the longitudinal axis. The test hardware design and test plans were oriented towards ensuring that the test article interfaced with the 40 x 80 Ft Wind Tunnel and toward the conduct of tests without damage to the test specimen, wind tunnel, and/or personnel.

4.3.5 Finite Element Model

The LSWT test article configurations were reflected in the overall aircraft modification finite element model by adding modules to represent the test configurations. Flat pressure bulkhead modules and the associated interface or transition areas were modeled for closure at the ends of the fuselage barrel section.

4.3.6 Vibration

Ground vibration tests would be required for the test article, as mounted in the Low-Speed Wind Tunnel, to meet the tunnel entry criteria. Additional tests would be required for variations of the test article and the associated variations in the test article mounting to the platform support structure.

5.0 CONCLUSIONS

5.1 CONCLUSIONS

It was concluded that it would be feasible to conduct the full-scale, low-speed wind tunnel test. The flight-weight wing, nacelle, and fuselage hardware could be safely tested in the NASA-Ames 40 x 80 Ft Low-Speed Wind Tunnel, and separate measures of structureborne noise and airborne noise could probably be obtained from this test.

REFERENCES

C-1. Poland, D. T., "Propfan Test Assessment (PTA) Program Low-Speed Wind Tunnel Test Evaluation," Lockheed Aeronautical Systems Company, LG87ER0032, February 1987.

C-2. "Guide for Planning Investigations in the Ames 40 x 80 Ft Wind Tunnel Operated by the Low Speed wind Tunnels Investigations Branch (FHW)," NASA-Ames Research Center, revised March 1984.

Lockheed

APPENDIX D
PREDICTED AIRPORT PERFORMANCE - PTA AIRCRAFT

As part of the aerodynamic analysis of the PTA aircraft, predictions were made of airport performance. Results of this analysis are given in the charts of this appendix.

List of Figures

Figure	Title	Page
D-1	Estimated PTA Stall Speed	D-2
D-2	Critical Engine Failure Speed - V_1	D-3
D-3	Rotation, Liftoff and Takeoff Speeds	D-4
D-4	Maximum Allowable Takeoff Weight Permitted by Second Segment Climb Requirements	D-5
D-5	FAA Takeoff Performance	D-6
D-6	Approach, Landing and Landing Climb Speed	D-7
D-7	Landing Field Length - Anti-Skid System Operative	D-8
D-8	Landing Field Length - Anti-Skid System Inoperative	D-9

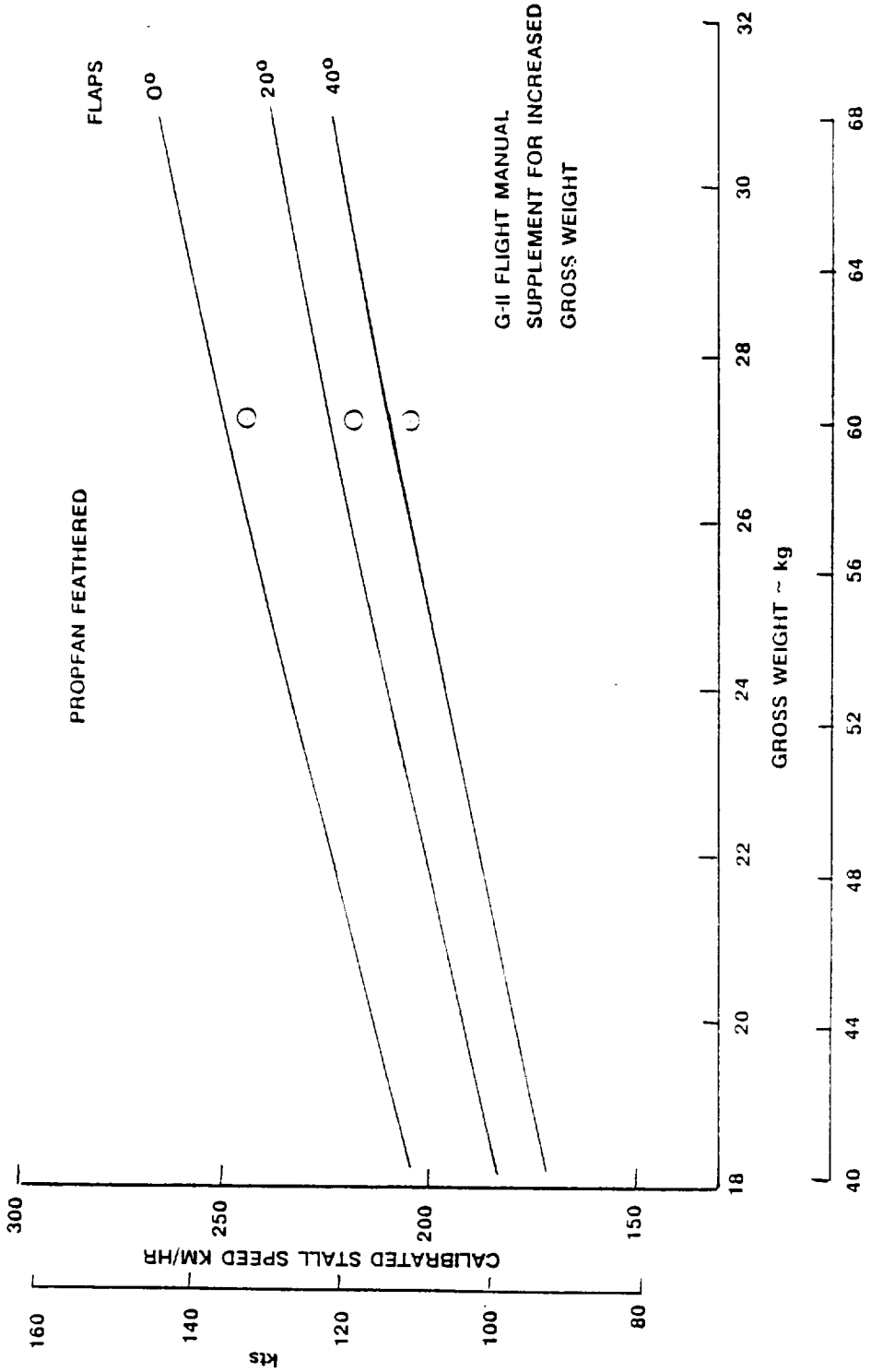


Figure D-1. Estimated PTA Stall Speed

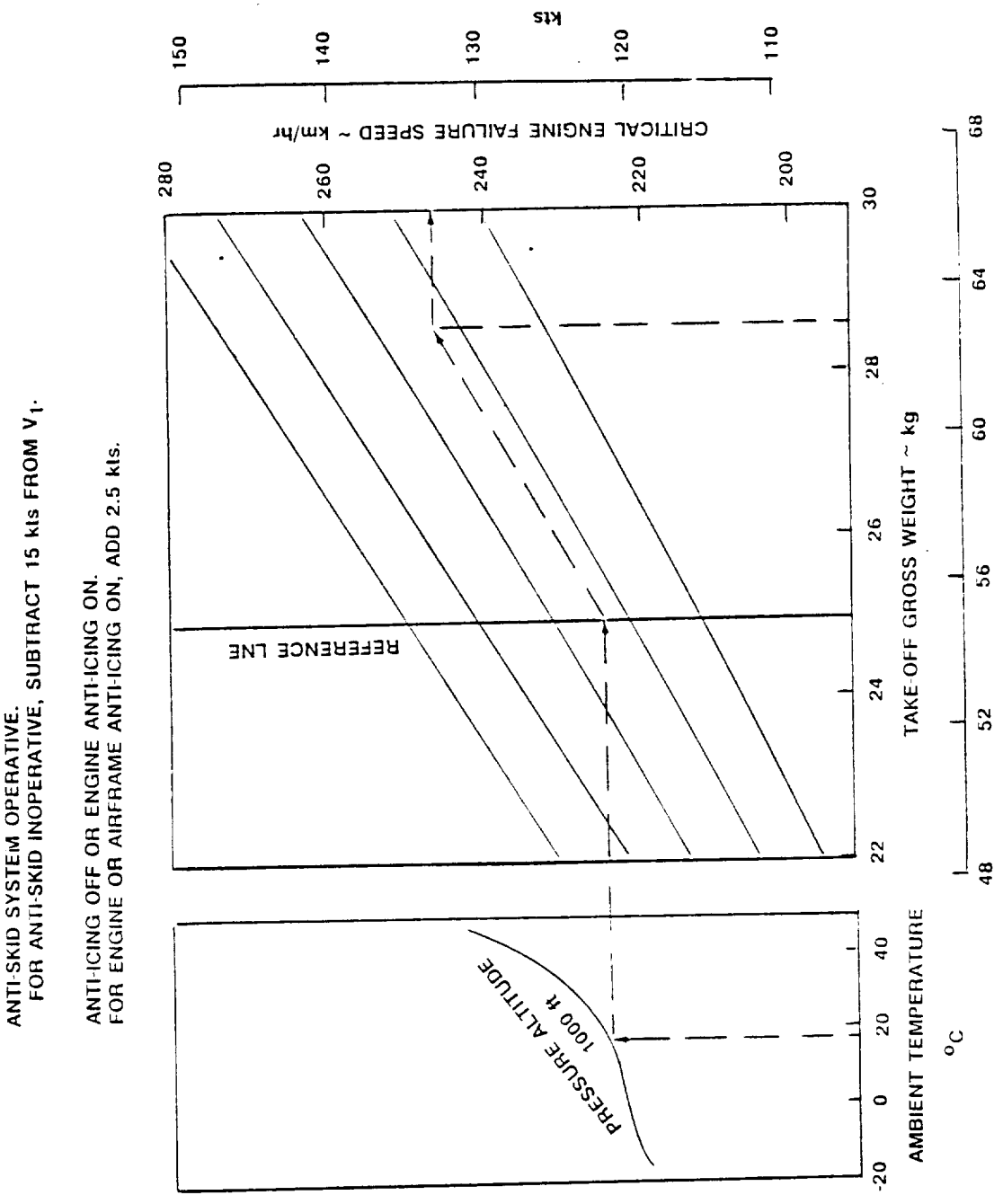


Figure D-2. Critical Engine Failure Speed - V_1

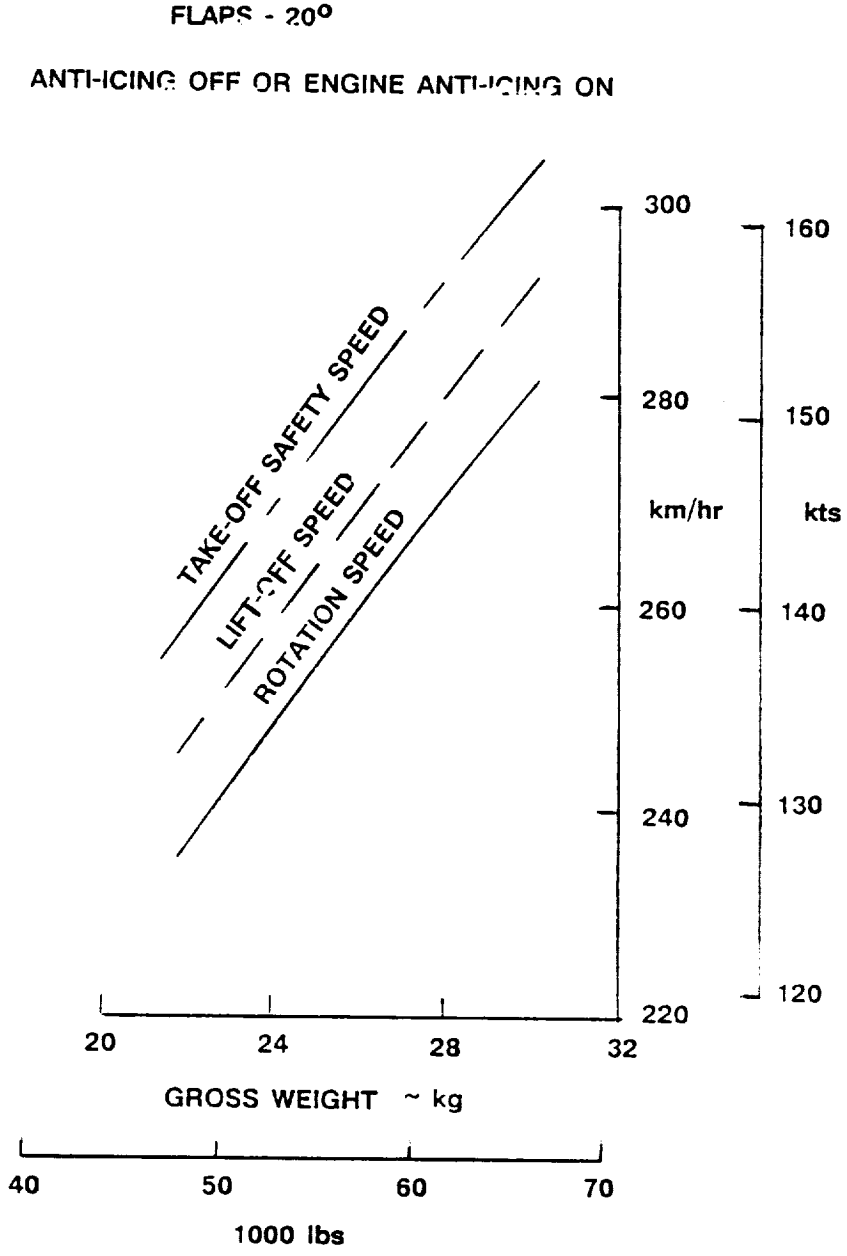


Figure D-3. Rotation, Liftoff and Takeoff Speeds

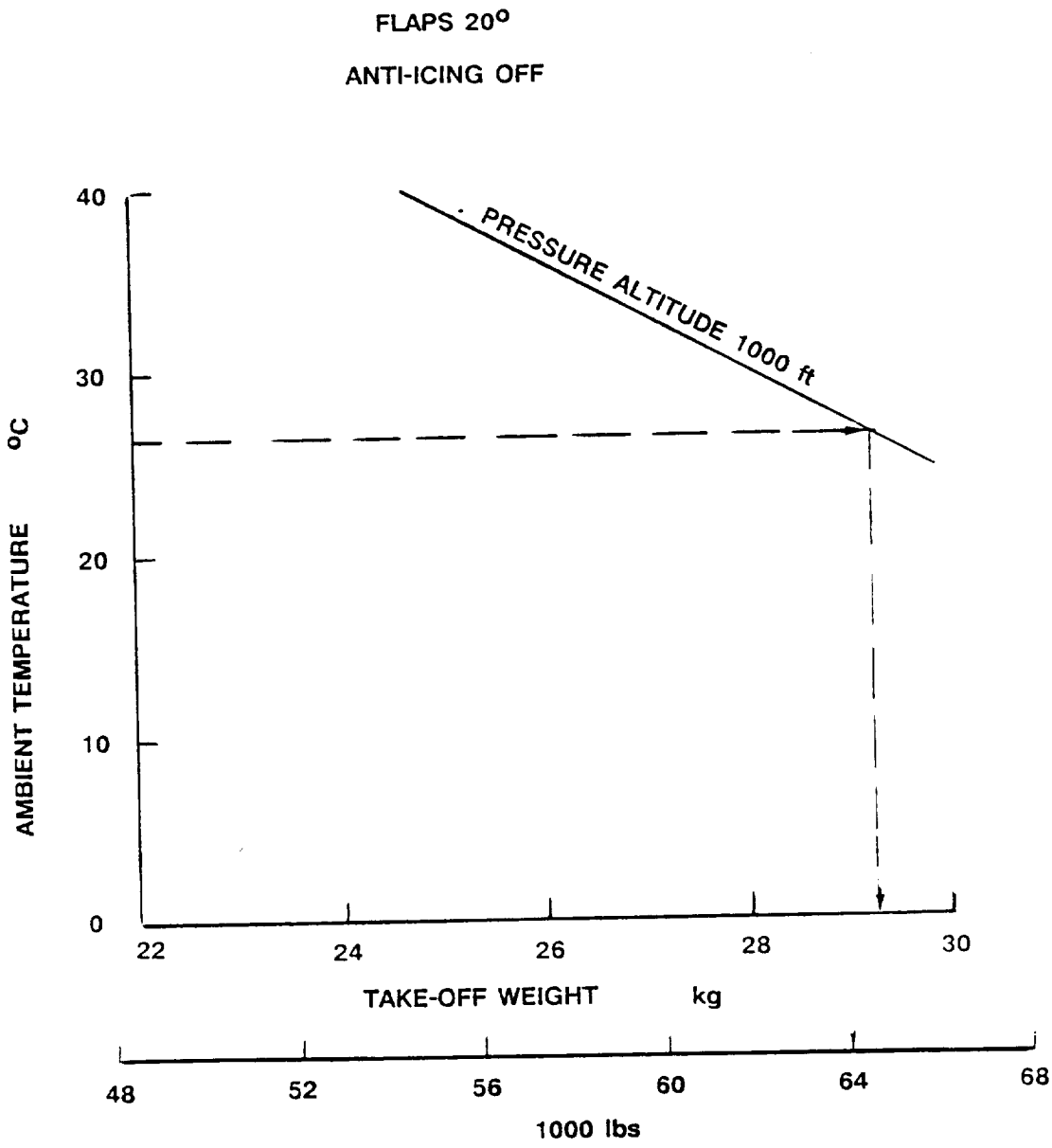


Figure D-4. Maximum Allowable Takeoff Weight Permitted by Second Segment Climb Requirements

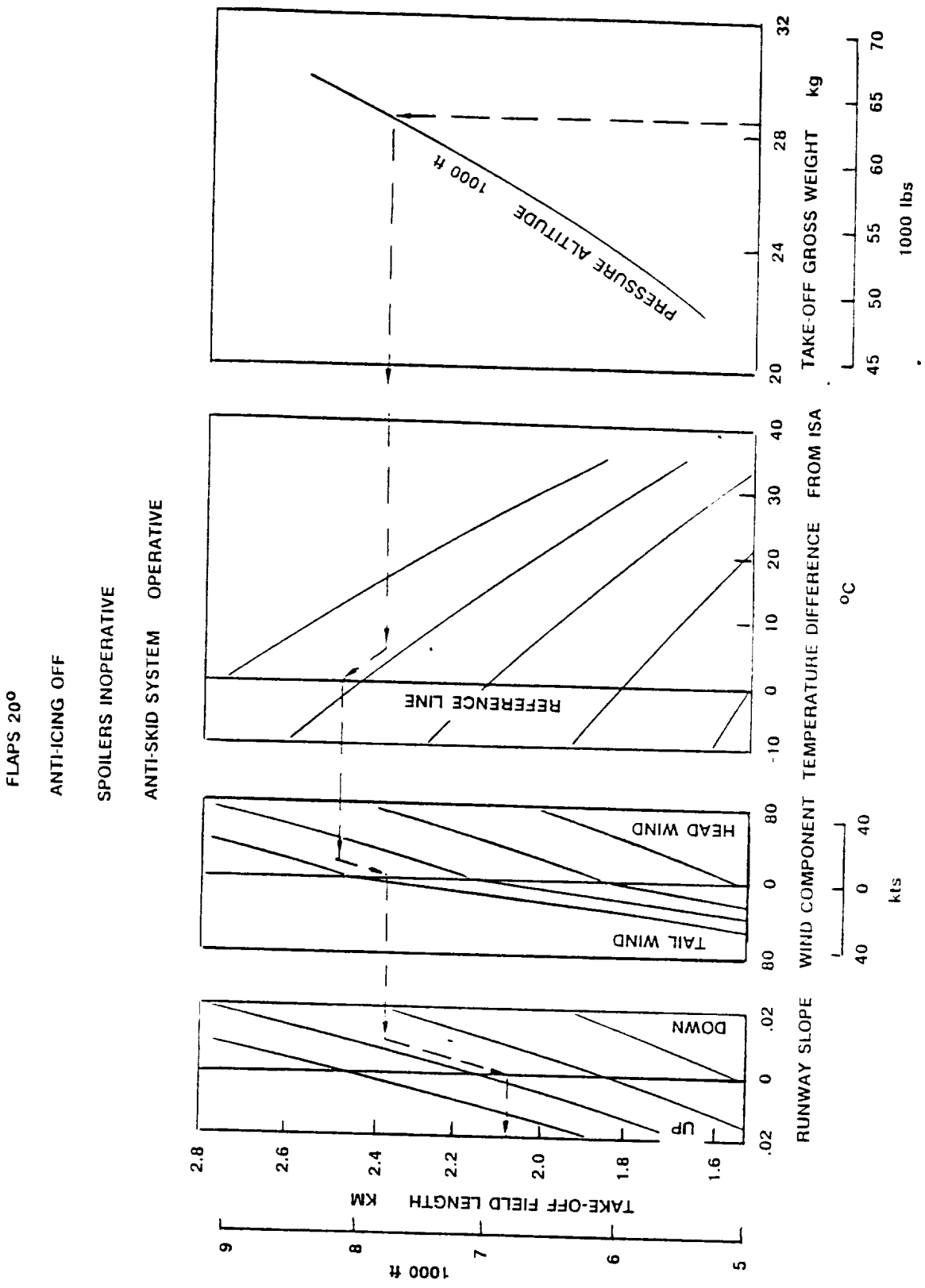


Figure D-5. FAA Takeoff Performance

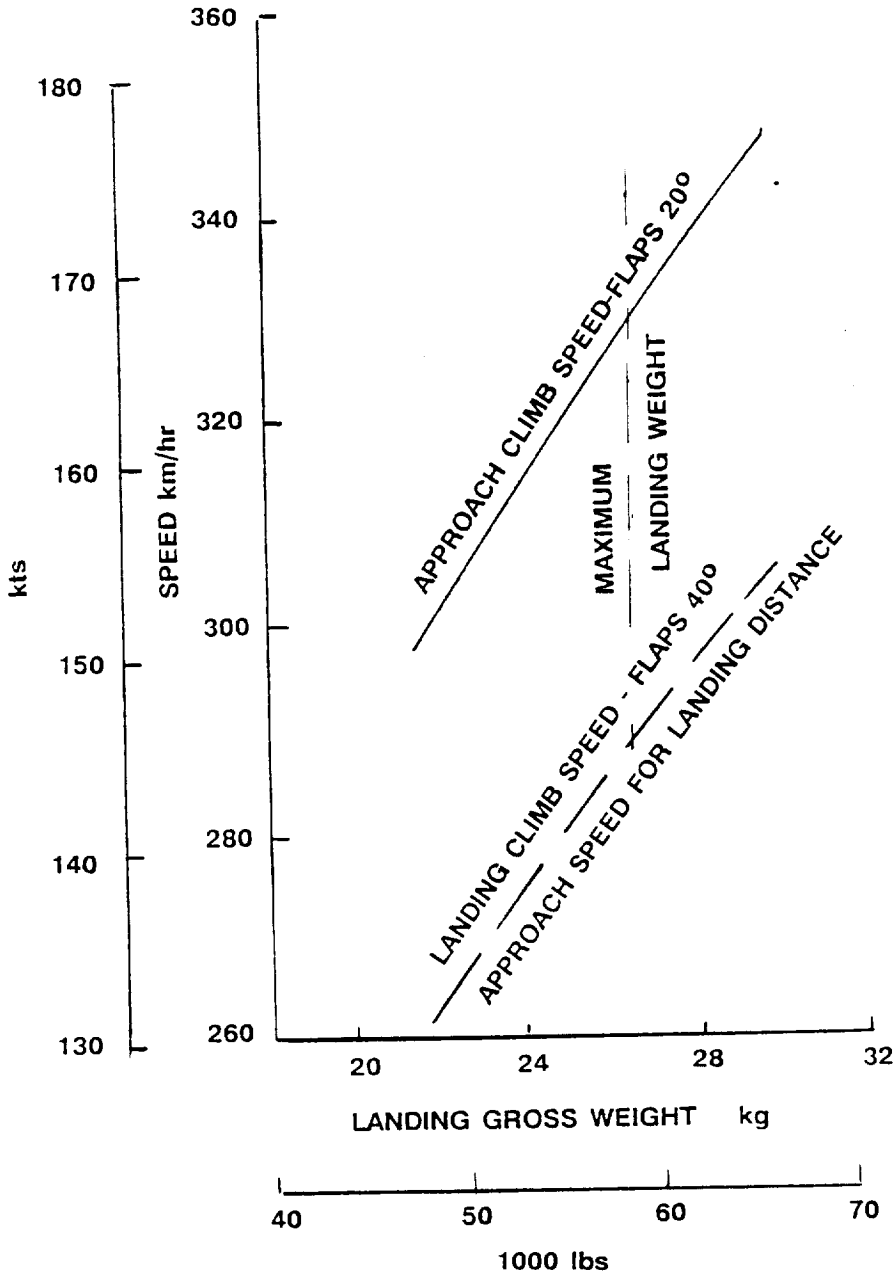


Figure D-6. Approach, Landing and Landing Climb Speeds

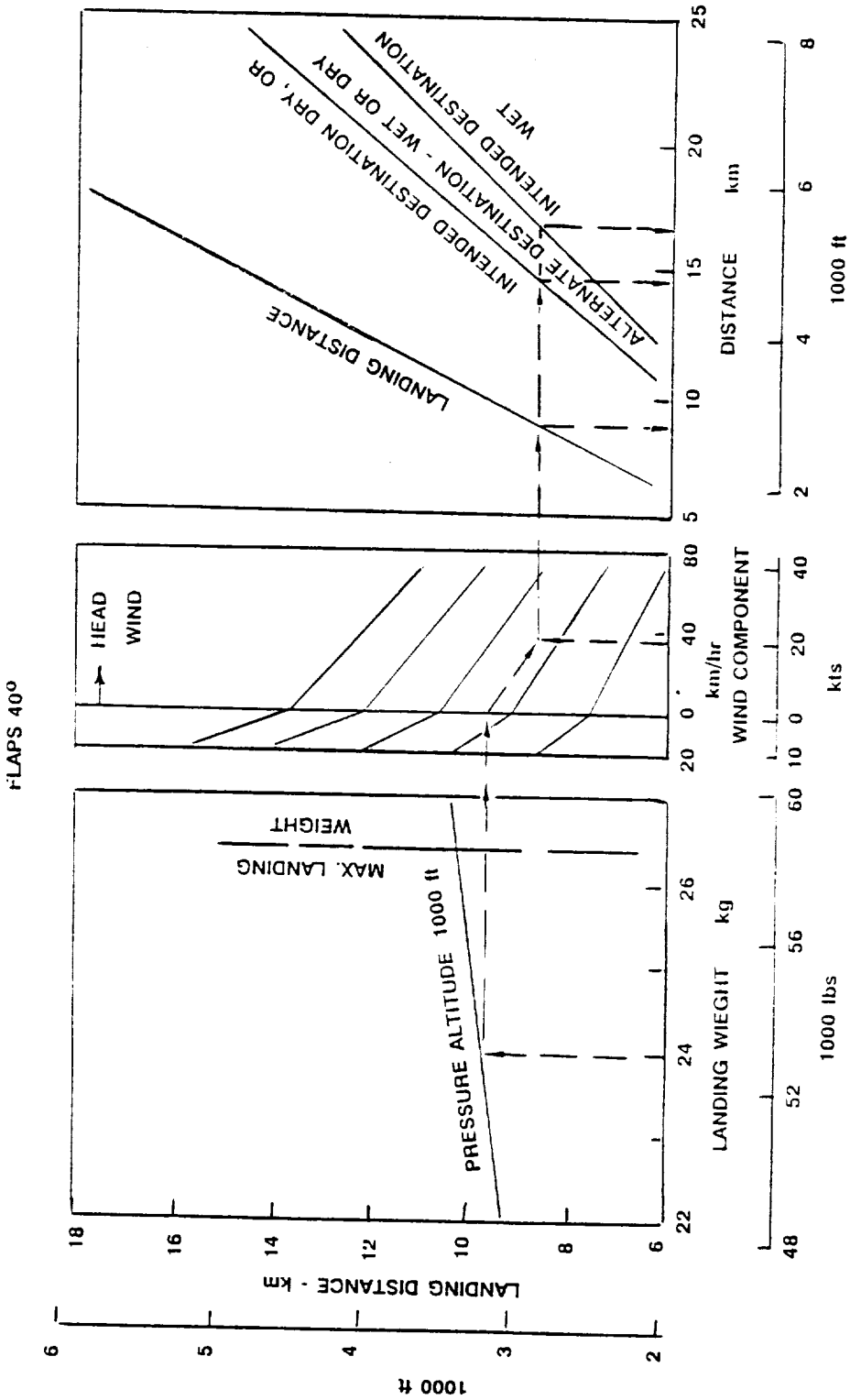


Figure D-7. Landing Field Length - Anti-Skid System Operative

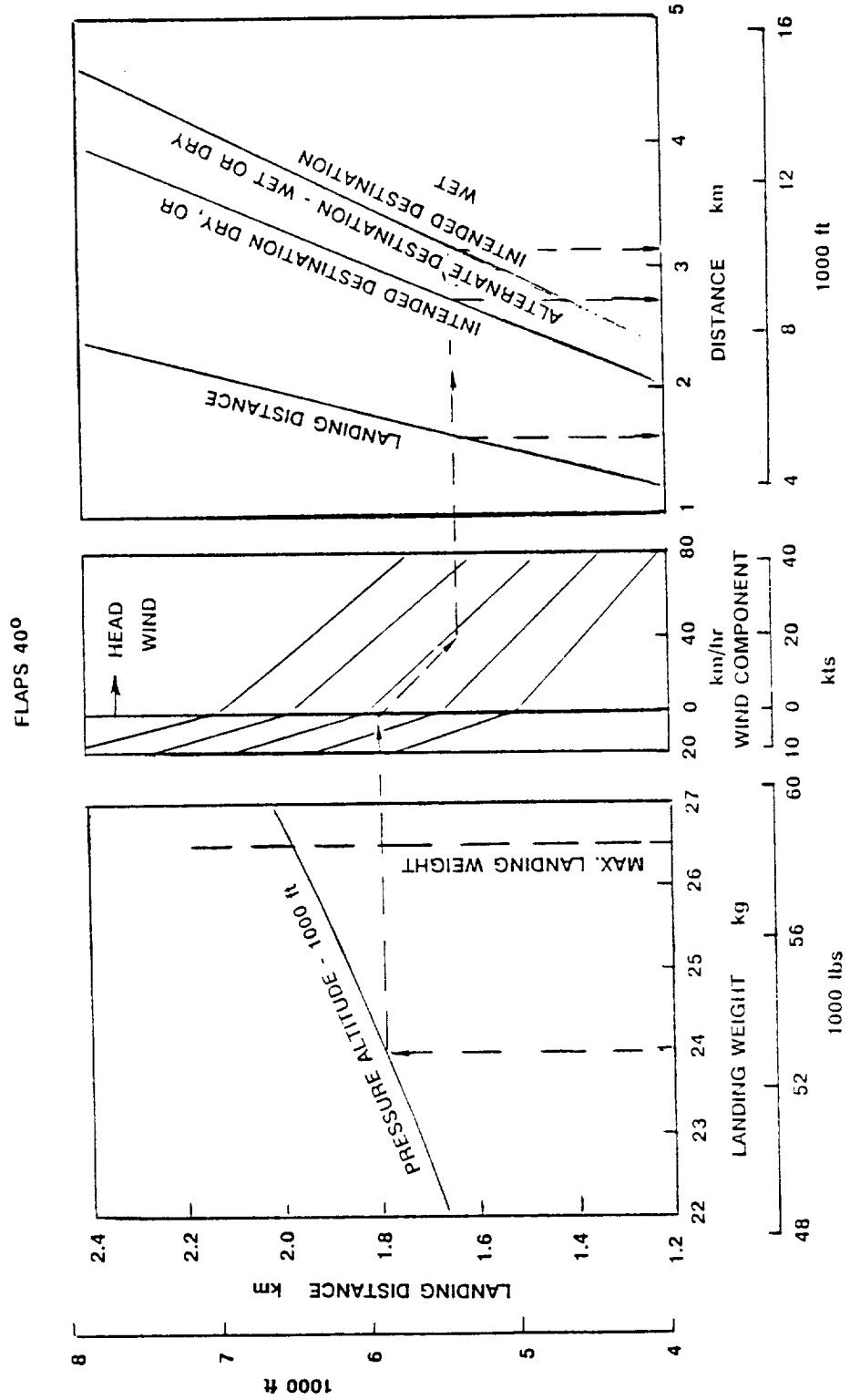


Figure D-8. Landing Field Length - Anti-Skid System Inoperative

APPENDIX E
SAMPLE OF A COMPUTERIZED SAFETY TRACKING LOG

A sample of a computerized safety tracking log is attached.

PTA

HAZARD

TRACKING

LOG

Lockheed

PTA HAZARD LOG AND RISK INDEX

As a means to monitor progress in elimination or mitigation of PTA hazards, this Hazard Tracking Log lists PTA program hazards by safety risk value, status, and required continuing actions. Column heading explanations follow:

HAZARD IDENT: Alpha-Numeric identifier of hazard.

HAZARD REMARKS: Hazard or potential problem.

IN HRI: Initial Hazard Risk Index (HRI) value given to each hazard.

MO HRI: Modified HRI value due to mitigating action or circumstances.

FI HRI: Final HRI value when hazard CLOSED.

HAZ STAT: Hazard status - OPEN; CLOS(ed).

VERIF: How hazard mitigating circumstances confirmed:

A = Analysis C = Comparability (off-the-shelf)
D = Design I = Inspection
P = Procedures T = Test

VOL NUM: PTA hazard analyses volume where hazard most recently analyzed.

01 = Preliminary Hazard Analysis
02F = Subsystem Hazard Analysis
02S = System Hazard Analysis
03 = Static Test Operating & Support Hazard Analysis
04 = Flight Test Operating & Support Hazard Analysis

CLOSE AUTH: Design/readiness review where hazard is recommended CLOSED. This means no additional actions are planned other than those identified in "corrective action/ remarks" column of the hazard analyses worksheets. Closure is recommended by Lockheed and formalized by NASA-LeRC approval of the review.

ORIGINAL PAGE IS
OF POOR QUALITY

PTA HAZARD LOG AND RISK INDEX
(Continued)

CNTG ACT: Continuing action(s) required to mitigate risk to an "acceptable" level, whether hazard is OPEN or CLOSED.

C = Conditional Maintenance or Inspection
D = Design
E = Emergency or Precautionary Procedures
I = Inspections - Routine or Pre-mission
M = Maintenance
P = Procedure - Operations/Training
R = Real-Time Monitoring
T = Test Results

PIA
HAZARD TRACKING LOG
IN ORDER OF RISK

HAZARD IDENT	HAZARD REMARKS	IN	HRI MO	FI	HAZARD STATUS	VERIF CODE	VOL NUM	CLOSE AUTH	CNTG ACT
SE-6	PPS TO B-60 STAND ADAPTER: SUPPORT EQUIPMENT PROCEDURAL ERROR	06	06	06	CLOS	IP	03	PSRRV	IPR
DS-4	REDUCTION GEARBOX: UNCONTAINED INTERNAL FAILURE	02	08	08	CLOS	AIPT	04	FTRRV	EIMR
DS-4-1a	REDUCTION GEARBOX MAIN DRIVE SPUR GEAR/TEETH FAIL: OVERSPEED	04	08	08	CLOS	ADP	04	FTRRV	CEMR
DS-4-1d	REDUCTION GEARBOX PINION SPUR SHAFT GEAR FAILS/FRACTURES/LOCKS	04	08	08	CLOS	ADP	04	FTRRV	EIMR
DS-10	MECHANICAL FUEL CONTROL (MFC) SOLENOID/VALVE FAILS OPEN	08	08	08	CLOS	AIT	03	PSRRV	P
PF-1-1	PROPFAN BARREL FRACTURE	04	08	08	CLOS	ACT	03	PSRRV	TIR
PF-1-2	PROPFAN BLADE TRUNION FRACTURES/FAILS	04	08	08	CLOS	ACT	03	PSRRV	TIR
FS-6	LUBE FUNCTIONAL COMPONENTS FAIL/MALFUNCTION	04	08	08	CLOS	CI	01	PFPDR	NONE
TI-35	HAM STAN TI DATA SYSTEM OPS: REAL TIME WARNING DEVICE INADEQUATE	08	08	08	CLOS	P	03	PSRRV	PE
FP-7	FIRE EXTINGUISHING SYSTEM: DESIGN/MATERIAL/MANUFACTURING/MAINTENA	04	08	08	CLOS	CA	02S	PFDDR	NONE
SSF-2-1	MAINTENANCE-ADJUSTMENT WHILE PPS OPERATING: DAMAGE/INJURY	08	08	08	CLOS	P	03	PSRRV	P
PMT-14	EMER RESPONSE TO EXCESS PROPFAN VIBRATION: PROC ERROR- TASK 5	08	08	08	CLOS	P	03	PSRRV	E
PF-1	PROPFAN BLADE/SPAR FAILS: DEPARTS PROPFAN PROPULSION SYSTEM	04	08	08	CLOS	CDIT	04	FTRRV	IR
CC-15	HUMAN FACTORS: HIGH NOISE LEVELS AT TEST POINTS	09	09	09	CLOS	A	04	FTRRV	P
CC-15-2	ADVERSE CABIN TEMP AT TEST POINTS	09	09	09	CLOS	A	04	FTRRV	P
DS-1-1a	HIGH PRESSURE TURBINE (HPT) WHEEL SPLINES FAILURE	06	10	10	CLOS	A	02F	PFDDR	MIC
DS-1-1b	HIGH PRESSURE TURBINE FRONT AIR SEAL FAIL FROM BOLT HOLE CRACKS	06	10	10	CLOS	A	02F	PFDDR	MIC
DS-1-1c	HIGH PRESSURE TURBINE 1ST/2ND STAGE SPACER RIM SEPARATION	06	10	10	CLOS	A	02F	PFDDR	MIC
DS-1-1d	HIGH PRESSURE TURB 1ST/2ND STAGE SPACER SEAL KNIVES WORN OR ERODE	06	10	10	CLOS	A	02F	PFDDR	MIC
DS-1-1e	HIGH PRESSURE TURBINE 1ST/2ND STAGE SPACER HOLES BLOCKED	06	10	10	CLOS	A	02F	PFDDR	MIC
DS-1-1f	HIGH PRESSURE TURBINE 1ST/2ND STAGE BLADES AIR FOIL FAILURE	06	10	10	CLOS	A	02F	PFDDR	MIC
DS-1-1g	HIGH PRESSURE TURBINE 1ST/2ND STAGE BLADES "FIR TREE" FAILURE	06	10	10	CLOS	A	02F	PFDDR	MIC
DS-1-1h	HIGH PRESSURE TURBINE 1ST/2ND STAGE VANES DEFORM/FAIL	06	10	10	CLOS	A	02F	PFDDR	MIC
DS-1-1i	HIGH PRESSURE TURBINE CASE LUGS FAIL: RADIAL ROTATION	06	10	10	CLOS	A	02F	PFDDR	IC
DS-1-1j	HIGH PRESSURE TURB REAR SUPPORT BEARING RACE/ROLLERS SKID/SPALL/C	06	10	10	CLOS	A	02F	PFDDR	IC
DS-1-1k	HIGH PRESSURE TURBINE REAR SUPPORT SEPARATOR BREAKS	06	10	10	CLOS	A	02F	PFDDR	MIC
DS-1-1l	HPT BEARING AND RACE: FATIGUE/CONTAMINATION/AXIAL SHAFT WHIPS	06	10	10	CLOS	A	02F	PFDDR	C
DS-3	REDUCTION GEARBOX (RGB) OVERLOAD: INTERNAL FAILURE	05	10	10	CLOS	A	02F	PFDDR	MIRC

PTA
HAZARD TRACKING LOG
IN ORDER OF RISK

HAZARD IDENT	HAZARD REMARKS	IN	HRI MO	HRI FI	HAZARD STATUS	VERIF CODE	VOL NUM	CLOSE AUTH	CNTG ACT
DS-3-1a	REDUCTION GEARBOX MAIN DRIVE GEAR CRACK/FAILS	05	10	10	CLOS	APT	03	PSRRV	MIRC
DS-3-1b	REDUCTION GEARBOX REAR HOUSING/MOUNTING PAD CRACKS/FAILS	10	10	10	CLOS	APT	03	PSRRV	MI
DS-3-1c	REDUCTION GEARBOX ALTERNATOR DRIVE GEAR CRACKS/FAILS	10	10	10	CLOS	APT	03	PSRRV	MIC
DS-3-1d	REDUCTION GEARBOX OIL PUMP DRIVE IDLER CRACKS/FAILS	10	10	10	CLOS	APT	03	PSRRV	MIC
DS-3-1e	TACHOMETER DRIVE SPUR GEAR CRACKS/FAILS	10	10	10	CLOS	APT	03	PSRRV	MIC
DS-3-1f	OIL PUMP GEAR BEARING CRACKS/FAILS	10	10	10	CLOS	APT	03	PSRRV	MIC
DS-3-2	OIL PUMP FAILS	10	10	10	CLOS	A	03	PSRRV	MIR
DS-4-2a	REDUCTION GEARBOX REAR HOUSING AT OR NEAR MOUNT PADS CRACKS/LOOSE	06	10	10	CLOS	A	03	PSRRV	I
DS-4-2b	REDUCTION GEARBOX MOUNT BOLTS CRACKS/LOOSE/FAILS	10	10	10	CLOS	A	03	PSRRV	I
DS-12	MECHANICAL FUEL CONTROL DRAIN VALVE REMAINS CLOSED ON SHUTDOWN	06	10	10	CLOS	A	02F	PFDDR	P
DS-13-1	MFC ENRICH SWITCH FAILS TO OPEN WHEN MANIFORD PRESSURE = 50 PSI	10	10	10	CLOS	AIP	03	PSRRV	P
DS-13-2	MECHANICAL FAILURE CONTROL ENRICHMENT VALVE REMAINS OPEN	10	10	10	CLOS	AIP	03	PSRRV	P
PF-6	PROPFAN CONTROL MALFUNCTION & PITCH LOCK FAILS	06	10	10	CLOS	A	04	FTRRV	NONE
PF-13-1	PROPFAN ACTUATOR SERVO-GOVERNOR SEIZES IN DECREASE PITCH POSITION	06	10	10	CLOS	A	02F	PFDDR	NONE
PF-13-2	PROPFAN GOVERNOR FLYWEIGHTS/DRIVE LOST	06	10	10	CLOS	A	02F	PFDDR	NONE
PF-13-3	PROPFAN DELTA PRESSURE REGULATING VALVES SEIZE TO INCREASE PRESS	06	10	10	CLOS	A	02F	PFDDR	NONE
PF-13-4	PF BALLSCREW QUILLSHAFT/PITCH LOCK SCREW/CONTROL ACT OVERSPEED	06	10	10	CLOS	A	02F	PFDDR	NONE
NA-4	NACELLE VENTING/COOLING INADEQUATE	06	10	10	CLOS	A	04	FTRRV	RT
NA-5	NACELLE FLUID DRAINS DRIP/LEAK/OVERFLOW	06	10	10	CLOS	AC	02F	ACDDR	NONE
FS-1	PTA UNIQUE FUEL SYSTEM COMPONENTS; LEAK/DRIP/FAIL/MALFUNCTION	06	10	10	CLOS	A	02F	PFDDR	M
FS-4	FLEXIBLE FUEL LINE CRACKS/FAILS	06	10	10	CLOS	IP	03	PSRRV	MI
FS-6-1	AIR TO OIL COOLER/EXIT FLAP ACTUATOR/CONTROL FAILS OR MALFUNCTION	06	10	10	CLOS	CI	02F	PFDDR	D
FS-6-2	OIL TANK/TANK SUMP SHUTOFF VALVE/DRAIN VALVE FAILS OR MALFUNCTION	06	10	10	CLOS	CI	02F	PFDDR	IR
FS-11	EXPOSED ELECTRICAL COMPONENT; DAMAGE/INJURY	04	10	10	CLOS	DIP	04	FTRRV	P
FS-12	ELECTRICAL CONNECTORS BENT/CORRODE/INSTALLATION ERROR	04	10	10	CLOS	DIP	04	FTRRV	P
FS-17-1	CIRCUIT BREAKERS FAIL OPEN	06	10	10	CLOS	DI	02S	PFDDR	EM
FS-17-2	CIRCUIT BREAKERS FAIL CLOSED	06	10	10	CLOS	DI	02S	PFDDR	EM
FS-32	AIR STARTER DUCT/SLIP JOINTS CRACK OR FAIL	06	10	10	CLOS	AC	02F	PFDDR	NONE
FS-35-1a	ELECTRONIC ENGINE CONTROL (EEC) FAILS/OVERSPEEDS	06	10	10	CLOS	C	02F	PFDDR	NONE

Lockheed

PTA
HAZARD TRACKING LOG
IN ORDER OF RISK

HAZARD IDENT	HAZARD REMARKS	IN	HRI MO	HRI FI	HAZARD STATUS	VERIF CODE	VOL NUM	CLOSE AUTH	CNTG ACT
FS-35-1b	ELECTROMECHANICAL ACTUATOR FAILS	05	10	10	CLOS	C	02F	PFDDR	NONE
FS-35-1c	FUEL CONTROL FAILS/OVERSPEEDS	06	10	10	CLOS	C	02F	PFDDR	NONE
FS-36	ENGINE EMERGENCY SHUTDOWN CONTROLS MALFUNCTION/FAIL	10	10	10	CLOS	CD	02S	PFDDR	NONE
FS-38-7e	PROPFAN AUX PUMP "PULL/FEATHER PUSH" SWITCH (#3 CONTACT) SHORTS	06	10	10	CLOS	A	02F	PFDDR	P
WFC-8	RUDDER/YAW DAMPNER SYSTEM: PTA FLIGHT TEST EFFECTS	06	10	10	CLOS	A	04	FTRRV	PTR
TI-24-1	FOD INTO GELAC TEST CONSOLE	06	10	10	CLOS	I	04	FTRRV	I
TI-28	CABIN MOVING MICROPHONE ARRAY BOOM: BINDS/DEFORMS/FAILS	06	10	10	CLOS	DI	04	FTRRV	NONE
TI-29	TEST INST SAFETY PARAMETERS/WARNING DEVICES INADEQUATE/INOPERATIV	06	10	10	CLOS	DA	02S	ACDDR	PIE
TI-29-1	GII EMERGENCY AUDIO WARNING DEVICE INADEQUATE	06	10	10	CLOS	AI	04	FTRRV	I
TI-31-1	CHECKOUT OF TEST INST PARAMETERS/PPS OPERATIONS: NO OBS/RESPONSE	10	10	10	CLOS	IPT	03	PSRRV	PI
AI-1	QEC TO DRIVE SYSTEM: DEGRADED INTERFACE	06	10	10	CLOS	DI	02S	ACDDR	NONE
AI-2	AFT NACELLE TO DRIVE SYSTEM: DEGRADED INTERFACE	06	10	10	CLOS	DI	02S	ACDDR	NONE
AI-4	QEC UNIT TO PROPFAN: DEGRADED INTERFACE	06	10	10	CLOS	DI	02S	ACDDR	NONE
CC-8	UTILITY AND SAFETY OF FLIGHT ENGINEER SEAT	05	10	10	CLOS	I	04	FTRRV	EI
CC-19-5a	HOT BRAKES-EXTENSIVE TAXI TESTS	06	10	10	CLOS	A	04	FTRRV	EP
CC-19-5b	GROUND SPOILER DISABLED-EFFECTS	06	10	10	CLOS	A	04	FTRRV	P
FP-2	FIRE WALLS: INADEQUATE/BREACHED	06	10	10	CLOS	AD	02F	PFDDR	NONE
FP-5	FLUID LINES/RESERVOIRS: LEAK/FAIL/RUPTURE	06	10	10	CLOS	DI	02F	PFDDR	I
FP-6	FIRE DETECT SYSTEM: INADEQUATE/MALFUNCTION/FAILS	06	10	10	CLOS	CD	04	FTRRV	EP
FP-6-1a	FIRE DETECTOR SENSE ELEMENT: SINGLE BREAK	10	10	10	CLOS	CA	02F	PFDDR	IE
FP-6-1b	FIRE DETECTOR SENSE ELEMENT: MULTI-BREAKS	10	10	10	CLOS	CA	02F	PFDDR	IE
FP-6-1c	FIRE DETECTOR SENSE ELEMENT: LATENT SHORT TO GROUND	10	10	10	CLOS	CA	02F	PFDDR	IE
FP-6-2b	FIRE DETECTOR CONTROL UNIT MALFUNCTION: FALSE NEGATIVE	06	10	10	CLOS	CAP	04	FTRRV	NONE
FP-6-2c	FIRE DETECTOR UNIT NOT INSTALLED FOR TASK 5	10	10	10	CLOS	AIP	03	PSRRV	NONE
FP-6-3c	FIRE DETECTOR WARNING INDICATION LIGHT NOT INSTALLED FOR TASK 5	10	10	10	CLOS	DI	03	PSRRV	NONE
FP-7-6b	FIRE BOTTLE DISCHARGE SQUIBS FAIL/SHORT: REDUCED CAPABILITY	06	10	10	CLOS	CA	02F	PFDDR	E
FP-8	FLAMMABLE FLUID SHUTOFF VALVES MALFUNCTION/STICK/FAIL	06	10	10	CLOS	CA	02S	PFDDR	E
FP-11	FACILITY FIRE EXTGUISHING SYS AT B-60 STAND: NOT INCORP/INADEQUAT	10	10	10	CLOS	AIP	03	PSRRV	NONE
SE-5	PROPFAN PROPULSION SYSTEM HANDLING ERROR	06	10	10	CLOS	IP	03	PSRRV	IPR

PTA
HAZARD TRACKING LOG
IN ORDER OF RISK

HAZARD IDENT	HAZARD REMARKS	IN	HRI MO	FI	HAZARD STATUS	VERIF CODE	VOL NUM	CLOSE AUTH	CNTG ACT
SSF-1	UNDETECTED FUEL LEAK (TASK 5): VISUAL/CCTV MONITOR	06	10	10	CLOS	I	03	PSRRV	EPR
SSF-1-1	VISUAL MONITOR OF GII/PTA PPS ON FLIGHTLINE	10	10	10	CLOS	I	04	FTRRV	EIPR
SSF-10-5A	AIRCRAFT PUSHED INTO HANGAR WALL/DOOR: GELAC/GAC	10	10	10	CLOS	A	04	PSRRV	IP
SSF-13-4A	FUEL & DEFUEL GII/PTA- GULFSTREAM- TASK 8/9- SPARK	10	10	10	CLOS	IP	04	FTRRV	E
PMT-20-3	PPS/SPEY RUNUP- UNPLANNED TAXI- GELAC	10	10	10	CLOS	P	04	FTRRV	P
PMT-20-7B	PERSONELL INJURY FROM WALKING INTO/AT PTA UNIQUE ITEMS	10	10	10	CLOS	P	04	FTRRV	IP
PMT-20-8	FLIGHTCREW AND MAINTENANCE ACTIVITY- SAME TIME	06	10	10	CLOS	P	04	FTRRV	P
PMT-20-9	UNAUTHORIZED AIRCRAFT CONFIGURATION CHANGE	06	10	10	CLOS	P	04	FTRRV	P
PMT-25	MAINTENANCE PER GELAC SUPPLEMENTS TO MAINTENANCE MANUAL	06	10	10	CLOS	EP	04	FTRRV	EP
PT-6	TRANSPORTING QEC UNIT TO & FROM BROWN FIELD: DAMAGE	10	10	10	CLOS	CI	03	PSRRV	NONE
PF-5	PROPFAN ADVERSE VIBRATION/STABILITY IN FLIGHT	04	10	10	CLOS	AI	04	FTRRV	RI
PF-2-1	PROPFAN BLADE DISBOND/DEFORM	11	11	11	CLOS	IP	04	FTRRV	CI
FS-34	AIR START DUCT BELLOWS CRACKS/FAILS	09	11	11	CLOS	DI	04	FTRRV	I
FS-39-3a	DRIVE SYS/RGB MAGNETIC PLUG WARNING LIGHT FALSE POSITIVE SIGNAL	09	11	11	CLOS	CI	02F	PFDDR	ERI
TI-4	INADEQUATE GROUNDING: DEGRADED OPERATIONS	09	11	11	CLOS	AI	04	FTRRV	I
TI-20	TEST INSTRUMENT HAS SHARP MATERIAL PROJECTION: INJURY	09	11	11	CLOS	I	01	ACPDR	NONE
TI-21	TEST INSTRUMENT HAS HIGH SURFACE TEMPERATURE: INJURY	09	11	11	CLOS	I	01	ACPDR	NONE
TI-23	TEST INSTRUMENT HIGH VOLTAGE (500 + VOLTS): SHOCK/INJURY/DAMAGE	09	11	11	CLOS	I	01	ACPDR	NONE
FP-7-5a	FIRE EXTINGUISHING AGENT BOTTLE LEAKS: REDUCED CAPABILITY	11	11	11	CLOS	C	02F	PFDDR	E
PMT-22	WRONG OR NO TEST CARDS- UNIQUE PARAMETERS	09	11	11	CLOS	I	04	FTRRV	IP
DS-2	ONE-THIRD TURBINE DISK FAILS	08	12	12	CLOS	A	02S	PFDDR	IC
DS-2-1a	HIGH PRESSURE TURBINE 1ST/2ND STAGE WHEEL MATERIAL DEFECT/FAILURE	08	12	12	CLOS	A	02S	PFDDR	IC
DS-2-1b	HIGH PRESSURE TURBINE WHEEL RIM FATIGUE:SEPARATES FROM WEB	08	12	12	CLOS	A	02S	PFDDR	IC
DS-2-1c	HIGH PRESSURE TURBINE WHEEL HUB FATIGUE/FAILS	08	12	12	CLOS	A	02S	PFDDR	IC
DS-2-2a	LOW PRESSURE TURBINE WHEEL FAILS AT WEB/RIB/FIR TREE	08	12	12	CLOS	A	02S	PFDDR	IC
DS-2-2b	LOW PRESSURE TURBINE WHEELS OUT OF BALANCE	08	12	12	CLOS	A	02S	PFDDR	IC
DS-2-3	POWER TURBINE DRIVE SHAFT FATIGUE/SHEARS	08	12	12	CLOS	A	02S	PFDDR	ICI
DS-4-1b	REDUCTION GEARBOX MAIN REDUCTION ROLLER BRNG FAIL/FRACTURE/LOCKS	08	12	12	CLOS	A	02S	PFDDR	C
DS-4-1c	REDUCTION GEARBOX SUN GEAR FAILS/FRACTURES/LOCKS	04	08	12	CLOS	ADP	04	FTRRV	CEMR
		04	08	12	CLOS	ADP	04	FTRRV	EIMR

Lockheed

PTA
HAZARD TRACKING LOG
IN ORDER OF RISK

HAZARD IDENT	HAZARD REMARKS	IN	HRI MO	FI	HAZARD STATUS	VERIF CODE	VOL NUM	CLOSE AUTH	CNTG ACT
DS-4-1f	REDUCTION GEARBOX FRONT PINION ROLLER BRNG FAILS/FRACTURES/LOCKS	04	08	12	CLOS	ADP	04	FTRRV	EIMR
DS-4-1g	REDUCTION GEARBOX PROPFAN SHAFT FAILS/FRACTURES/LOCKS	04	08	12	CLOS	ADP	04	FTRRV	EIMR
DS-4-1h	REDUCTION GEARBOX PROPFAN THRUST NUT FAILS/FRACTURES/LOCKS	04	08	12	CLOS	ADP	04	FTRRV	EIMR
DS-6	DRIVE SYSTEM CONTAINMENT RING STRUCK BY ONE-THIRD DISK	08	12	12	CLOS	AD	02S	PFDDR	NONE
DS-7	SAFETY COUPLING NOT INCORPORATED; LOSS OF SPEED CONTROL	04	12	12	CLOS	AD	01	PFPDR	NONE
DS-14	TORQUEMETER SLIPS/SHEARS/BREAKS	08	12	12	CLOS	A	02S	PFDDR	NONE
PF-12	PROPFAN UNCONTROLLED MOVEMENT TOWARD FLAT PITCH CONDITION	08	12	12	CLOS	A	04	FTRRV	EP
PF-17	PROPFAN BLADE STRUCK BY LIGHTNING	12	12	12	CLOS	A	04	FTRRV	CE
NA-1	NACELLE MOUNTS AND BRACES CRACK/FAIL	04	12	12	CLOS	AC	01	ACPDR	NONE
FS-1-6	QEC FUEL FIREWALL FITTING LEAKS/RUPTURE/DISCONNECTS	08	12	12	CLOS	I	02F	PFDDR	I
FS-13	ELECTRICAL COMPONENT IN CLOSE PROXIMITY WITH FLAMMABLE MIX; FIRE	04	12	12	CLOS	DI	02F	PFDDR	I
FS-37-9	DS/RGB VIBRATION INDICATOR; FLUCTUATES/FAILS/ERRONEOUS DATA	08	12	12	CLOS	CIP	03	PSRRV	ER
WFC-1	LEFT WING STRUCTURE OVERSTRESS - FAIL	04	12	12	CLOS	DAT	01	ACPDR	NONE
WFC-1-1	RIGHT WING STRUCTURE OVERSTRESS - CRACK/FAIL	08	12	12	CLOS	A	04	FTRRV	I
WFC-4	OUTBOARD FLIGHT SPOILERS; NO REDUNDANCY/BINDS/FAILS	08	12	12	CLOS	A	04	FTRRV	EIMP
WFC-4-1	OUTBOARD FLIGHT SPOILER ACTUATOR; NO REDUNDANCY/BINDS/FAILS	08	12	12	CLOS	A	04	FTRRV	IMP
WFC-6	LATERAL STABILITY REDUCED; PTA DESIGN EFFECTS	04	12	12	CLOS	AT	04	FTRRV	RT
WFC-7	LONGITUDINAL STABILITY REDUCED; DESIGN EFFECTS	04	12	12	CLOS	AT	04	FTRRV	IP
WFC-11	STATIC BALANCE BOOM/ATTACHMENT DEFORMS/FAILS	10	12	12	CLOS	AD	04	FTRRV	T
WFC-14-1	GII/PTA STRUCTURE IN HIGH GUSTS; STRAIN/CRACK/FAIL	08	12	12	CLOS	AD	04	FTRRV	CIPR
WFC-14-2	GII/PTA STRUCTURE IN HIGH SINK RATE LANDING; STRAIN/CRACK/FAIL	10	12	12	CLOS	AD	04	FTRRV	CP
WFC-15	OBJECT FALLS FROM WING/FLIGHT CONTROLS/AIRCRAFT	12	12	12	CLOS	I	04	FTRRV	PI
TI-25	TEST INSTRUMENT AIRSPEED NOSE BOOM VIBRATION/INSTALLATION; FAILS	06	12	12	CLOS	CD	04	FTRRV	CI
CC-1	CABIN AISLE WIDTH INADEQUATE; EMERGENCY EGRESS	08	12	12	CLOS	AIT	04	FTRRV	EP
CC-2	EMERGENCY EGRESS DURING DYNAMIC (OUT OF CONTROL) MANEUVER	08	12	12	CLOS	ADIT	04	FTRRV	EI
CC-2-1	INFLIGHT EGRESS-AIRCRAFT NOT OUT OF CONTROL	12	12	12	CLOS	ADIT	04	FTRRV	EI
CC-3	GROUND EMERGENCY EGRESS THRU CABIN WINDOWS	08	12	12	CLOS	I	04	FTRRV	I
CC-4	INFLIGHT EMERG EGRESS KICKOUT DOOR; NOT INCORP	08	12	12	CLOS	ACD	04	FTRRV	E
CC-5	BAGGAGE DOOR BLADDER SEAL/PRESSURE DIFFERENTIAL	08	12	12	CLOS	ATI	02S	ACDDR	D

PTA
HAZARD TRACKING LOG
IN ORDER OF RISK

Lockheed

HAZARD IDENT	HAZARD REMARKS	IN	HRI MO	FI	HAZARD STATUS	VERIF CODE	VOL NUM	CLOSE AUTH	CNTG ACT
CC-6	PARACHUTE/HARNESS AVAILABILITY FOR EMERGENCY EGRESS - FLIGHT	08	12	12	CLOS	A	04	FTRRV	EI
CC-6-1	CREW USE/STOWAGE OF PARACHUTE DURING NORMAL OPERATIONS	08	12	12	CLOS	A	04	FTRRV	EI
CC-11	OXYGEN FOR CREW EMERGENCY EGRESS/BAILOUT AT ALTITUDE	08	12	12	CLOS	AI	04	FTRRV	E
CC-11-1	CABIN DECOMPRESSION AT ALT FOR EMERG BAILOUT: OXYGEN INADEQUATE	08	12	12	CLOS	AI	04	FTRRV	E
CC-14	ACOUSTIC MIC ARRAY BOOM ASSY IN CABIN: EMERGENCY EGRESS BLOCKED	08	12	12	CLOS	DI	04	FTRRV	EP
CC-16-1	FUSELAGE STEEL SHIELD STRUCK BY FAILED PF/RGB ASSEMBLY (EFFECTS)	12	12	12	CLOS	A	04	FTRRV	NONE
CC-16-2	FUSELAGE, STEEL SHIELD COMES LOOSE: DAMAGE TO PPS/AIRCRAFT	12	12	12	CLOS	AD	04	FTRRV	I
CC-20-1	PPS AUDIO FIRE WARNING SAME AS SPEY	08	12	12	CLOS	D	04	FTRRV	E
CC-20-2	AURAL PPS/ GII SAFETY SIGNALS IN HIGH NOISE LEVEL	08	12	12	CLOS	D	04	FTRRV	E
FP-7-1d	FIRE EMERGENCY HANDLE: CONTACTS STAY OPEN AFTER PULLING	12	12	12	CLOS	C/A	02F	PFDDR	IE
FP-7-2a	FIRE EMERGENCY HANDLE: BREAK/FAILS WHEN PULLED	12	12	12	CLOS	AC	04	FTRRV	E
FP-7-7b	FIRE AGENT TRANSFER CHECK VALVE POPPET JAMS TO CENTER	12	12	12	CLOS	CA	02F	PFDDR	NONE
FP-7-8a	FIRE AGENT DISTRIBUTION SUPPLY LINES BREAK/RUPTURE/CRACK	12	12	12	CLOS	CA	02F	PFDDR	I
FP-7-8b	FIRE AGENT DISTRIBUTION QEC DISCHARGE NOZZLE BENT/CRIMPED/CLOGGED	12	12	12	CLOS	CA	02F	PFDDR	I
FP-7-8c	FIRE AGENT DISTRIBUTION AFT NACELLE DISCHARGE NOZZLE BENT/CLOGGED	12	12	12	CLOS	CA	02F	PFDDR	I
SSF-16	MEDIA DEMO OF PROPFAN PROPULSION SYSTEM: DAMAGE/INJURY- TASK 5	12	12	12	CLOS	P	03	PSRRV	EP
PMT-15-1	CRASH/FIRE AT OR NEAR AIRFIELD - GELAC	12	12	12	CLOS	P	04	FTRRV	E
PMT-15-2	CRASH/FIRE AT GAC	12	12	12	CLOS	P	04	FTRRV	E
PMT-20-2	WORKER HIT BY PROPFAN	08	12	12	CLOS	P	04	FTRRV	P
PMT-21	COCKPIT CREW TRAINING INADEQUACIES	08	12	12	CLOS	C	04	FTRRV	P
DS-4-1e	REDUCTION GEARBOX SUN GEAR HUB SPLINE FAILS/FRACTURES/LOCKS	04	12	12	CLOS	ADP	04	FTRRV	EIMR
CC-21-1	NO CHASE AIRCRAFT FOR FLIGHT CHECKOUT (TASK 9.8)	12	12	12	CLOS	A	04	FTRRV	PRT
PF-7	PROPFAN ACTUATOR UNCONTROLLED TO REVERSE PITCH IN FLIGHT	08	08	12	CLOS	DT	02F	PFDDR	NONE
WFC-3-4	EMERG DESCENT: NO SPEED BRAKES	13	13	13	CLOS	A	04	FTRRV	E
DS-1	TURBINE BLADE FAILURE	11	14	14	CLOS	A	02F	PFDDR	NONE
DS-1-2a	LOW PRESSURE TURBINE (LPT) WHEEL BLADES FATIGUE/FAIL	11	14	14	CLOS	A	02F	PFDDR	IC
DS-1-2b	LOW PRESSURE TURBINE WHEEL BLADES CORRODE/ERODE: REDUCED EFFICIEN	11	14	14	CLOS	A	02F	PFDDR	IC
DS-1-2c	POWER TURBINE VANE CORRODE/ERODE: REDUCED EFFICIENCY	11	14	14	CLOS	A	02F	PFDDR	IC
DS-1-2d	LOW PRESSURE TURBINE VANES SHROUD SEAL RING CRACKS	11	14	14	CLOS	A	02F	PFDDR	IC

PTA
HAZARD TRACKING LOG
IN ORDER OF RISK

HAZARD IDENT	HAZARD REMARKS	IN	HRI MO	FI	HAZARD STATUS	VERIF CODE	VOL NUM	CLOSE AUTH	CNTG ACT
DS-1-2e	LOW PRESSURE TURBINE CASE MOUNTING FLANGE/RING/BOLTS BREAK	11	14	14	CLOS	A	02F	PFDDR	IC
DS-1-2f	LOW PRESSURE TURBINE SUPPORT ASSEMBLY FLANGE/CONE/DISC FAILS	11	14	14	CLOS	A	02F	PFDDR	IC
DS-1-2g	LOW PRESSURE TURBINE SEALS/KNIFE POINT WEAR: REDUCED EFFICIENCY	11	14	14	CLOS	A	02F	PFDDR	IC
DS-1-2h	LOW PRESSURE TURBINE RETAINING BOLT FAILS	11	14	14	CLOS	A	02F	PFDDR	IC
DS-1-2i	LOW PRESSURE TURBINE OIL FEED TUBES BLOCKED OR FAIL	11	14	14	CLOS	A	02F	PFDDR	IC
DS-1-2j	LPT REAR SUPPORT ASSY/SHELL/FRONT FLANGE/CONE/STRUT FAIL	11	14	14	CLOS	A	02F	PFDDR	IC
DS-1-2k	LOW PRESSURE TURBINE DRIVE SHAFT ROLLER/THRUST BRNGS FATIGUE/FAIL	11	14	14	CLOS	A	02F	PFDDR	IC
DS-5-1a	PROPFAN BRAKE OUTER MEMBERS WEAR/FAIL	14	14	14	CLOS	1	03	PSRRV	E
DS-8-4a	DRIVE SYSTEM COMPRESSOR INLET HOUSING MOUNT PADS FATIGUE/FAIL	14	14	14	CLOS	A	02F	PFDDR	IR
DS-8-4b	DS COMPRESSOR INLET HOUSING MOUNT PAD THREAD INSERTS FATIGUE/FAIL	14	14	14	CLOS	A	02F	PFDDR	IR
DS-8-4c	DRIVE SYSTEM COMPRESSOR INLET HOUSING STRUT FATIGUE/FAILS	14	14	14	CLOS	A	02F	PFDDR	IR
DS-8-4d	DRIVE SYSTEM COMPRESSOR INLET HOUSING AFT HUB FATIGUE/FAILS	14	14	14	CLOS	A	02F	PFDDR	IR
DS-8-4e	DRIVE SYSTEM COMPRESSOR INLET HOUSING FRONT HUB FATIGUE/FAILS	14	14	14	CLOS	A	02F	PFDDR	IR
DS-8-4f	DRIVE SYSTEM COMPRESSOR INLET HOUSING FATIGUE/CRACKS	14	14	14	CLOS	A	02F	PFDDR	IR
DS-8-4g	DS COMPRESSOR INLET HOUSING FRONT OR REAR FLANGE FATIGUE/FAILS	14	14	14	CLOS	A	02F	PFDDR	IR
PF-8	PROPFAN MEDIUM (FLUID) PRESSURE LOST	11	14	14	CLOS	DA	02F	PFDDR	NONE
PF-8-1a	PROPFAN CONTROL SCAVENGE PUMP FAILS	11	14	14	CLOS	DA	02F	PFDDR	NONE
PF-8-1b	PROPFAN MAIN AND STANDBY PUMPS FAIL	11	14	14	CLOS	DA	02F	PFDDR	NONE
PF-8-1c	PROPFAN SUMP RELIEF VALVE FAILS CLOSED	11	14	14	CLOS	DA	02F	PFDDR	NONE
PF-8-1d	PROPFAN MAIN AND STBY REGULATING VALVES FAIL IN BYPASS POSITION	11	14	14	CLOS	DA	02F	PFDDR	NONE
PF-8-1e	PROPFAN PRESSURE SEAL LEAKS INTO SUMPS	11	14	14	CLOS	DA	02F	PFDDR	NONE
PF-10	PROPFAN OVERSPEED GOVERNOR MALFUNCTION	11	14	14	CLOS	CD	01	PFDDR	NONE
PF-15-1	PROPFAN AUX PUMP/AUX SCAVENGE PUMP: FAILS/LOSS OF OUTPUT	14	14	14	CLOS	A	04	FTRRV	EP
PF-15-2	PROPFAN MAIN PUMP/STANDBY PUMP CHECK VALVE: FAIL OPEN	14	14	14	CLOS	A	04	FTRRV	EP
PF-15-3	PROPFAN FEATHER VALVE SEIZES IN UNFEATHER POSITION	14	14	14	CLOS	A	04	FTRRV	EP
NA-5-1	NACELLE DRAIN COLLECTOR BOX OVERFILL	10	14	14	CLOS	D	04	FTRRV	IM
NA-6	NACELLE EXHAUST/STUB DUCTS & PIVOT SUPPORTS: POOR COOLING FLOW	11	11	14	CLOS	D	01	ACPDR	NONE
NA-10	NACELLE DYNAROHR ACOUSTIC MATERIAL HOLDS RESIDUAL FUEL	9	14	14	CLOS	C	02S	ACDDR	NONE
FS-1-2	FUEL TEMPERATURE SENSOR AT PROPFAN OIL/FUEL HEAT EXCHANGER FAILS	11	14	14	CLOS	CP	03	PSRRV	E

Lockheed

PTA
HAZARD TRACKING LOG
IN ORDER OF RISK

HAZARD IDENT	HAZARD REMARKS	IN	HRI MO	FI	HAZARD STATUS	VERIF CODE	VOL NUM	CLOSE AUTH	CNTG ACT
FS-1-4	FUEL PRESSURE RELIEF VALVE FAILS OPEN	11	14	14	CLOS	AIPT	03	PSRRV	M
FS-3-1	FUEL TO OIL COOLER (PF) FAILS/LEAKS	11	14	14	CLOS	I	02F	PFDDR	I
FS-3-2	FUEL TO OIL COOLER (DS) FAILS/LEAKS	11	14	14	CLOS	I	02F	PFDDR	I
FS-5	AIR TO OIL COOLER (DS) INADEQUATE TO NEEDS	11	14	14	CLOS	A	02F	PFDDR	NONE
FS-6-4	OIL SYSTEM ELECTROMAGNETIC DRAIN PLUG SHORTS/FAILS	11	14	14	CLOS	CIP	03	PSRRV	RI
FS-7	DRIVE SYSTEM LUBRICATION OIL LINES LEAK/FATIGUE/FAIL	11	14	14	CLOS	CDIP	03	PSRRV	RI
FS-10	PTA UNIQUE ELECTRICAL EQUIPMENT: INCOMPATABILITY WITH G-II	11	14	14	CLOS	C	02F	PFDDR	NONE
FS-14	ELECTRICAL CONTROLS UNGROUNDED/NOT ISOLATED	09	14	14	CLOS	D	01	PFPDR	NONE
FS-18	ELECTRICAL INSULATION BURNS: SMOKE/FUMES	11	14	14	CLOS	D	01	PFPDR	NONE
FS-23	ELECTRICAL SYSTEM MECHANICAL COMPONENT: DESIGN/MFG/MAINT ERROR	11	14	14	CLOS	DI	02F	PFDDR	I
FS-24-1a	AUXILIARY PUMP INVERTER FAILS WITH PROPFAN OPERATING	06	14	14	CLOS	DI	04	FTRRV	EIM
FS-24-2a	RIGHT ALTERNATOR BUS FAILS WITH PROPFAN OPERATING	06	10	14	CLOS	DI	04	FTRRV	EIM
FS-25	FLUID LINES-HAMILTON STANDARD EQUIPMENT: LEAK/RUPTURE/FAIL/MALF	11	14	14	CLOS	DI	02F	PFDDR	I
FS-26	OIL TEMPERATURE SENSOR LEAK/RUPTURE/FAIL/MALF	11	14	14	CLOS	DI	02F	PFDDR	I
FS-27	OIL TO FUEL PROPFAN HEAT COOLER: LEAK/MALF/RUPTURE	11	14	14	CLOS	CIP	03	PSRRV	I
FS-29	FUEL TO LUBE OIL COOLER: CONTAMINATION	14	14	14	CLOS	C	01	PFPDR	NONE
FS-31	AIR START ISOLATION VALVE FAILS OPEN AFTER START	11	14	14	CLOS	CD	02F	PFDDR	NONE
FS-33	AIR START CONTROL VALVE LEAKS/CRACKS/FAILS	11	14	14	CLOS	DI	02F	PFDDR	NONE
FS-35-4b	ENGINE OVERSPEED TEST SWITCH FAILS CLOSED	14	14	14	CLOS	AC	03	PSRRV	E
FS-35-6b	MANUAL FUEL VALVE SWITCH FAILS OPEN WITH ENGINE OPERATING	11	14	14	CLOS	A	02F	PFDDR	E
FS-35-6c	MANUAL FUEL VALVE SWITCH FAILS CLOSED PRIOR TO ENGINE START	11	14	14	CLOS	A	02F	PFDDR	E
FS-37-1a	DRIVE SYSTEM NP TACHOMETER INDICATOR FLUCTUATES/FAILS	11	14	14	CLOS	CI	03	PSRRV	ER
FS-37-1b	DRIVE SYSTEM NP TACHOMETER INDICATOR: FALSE ERRONEOUS READING	11	14	14	CLOS	CI	02F	PFDDR	ER
FS-37-2a	DRIVE SYSTEM NG TACHOMETER INDICATOR: FLUCTUATES/FAILS	11	14	14	CLOS	CI	02F	PFDDR	ER
FS-37-2b	DRIVE SYSTEM NG TACHOMETER INDICATOR: FALSE ERRONEOUS READING	11	14	14	CLOS	CI	02F	PFDDR	ER
FS-37-3a	DRIVE SYSTEM TORQUE INDICATOR FLUCTUATES/FAILS	11	14	14	CLOS	CI	03	PSRRV	ER
FS-37-3b	DRIVE SYSTEM TORQUE INDICATOR: FALSE ERRONEOUS READING	11	14	14	CLOS	CI	02F	PFDDR	ER
FS-37-4a	DRIVE SYSTEM TURBINE GAS TEMP (TGT) INDICATOR FLUCTUATES/FAILS	11	14	14	CLOS	CI	03	PSRRV	ER
FS-37-4b	DRIVE SYS TURBINE GAS TEMP INDICATOR FALSE ERRONEOUS READING	11	14	14	CLOS	CI	02F	PFDDR	ER

PTA
HAZARD TRACKING LOG
IN ORDER OF RISK

HAZARD IDENT	HAZARD REMARKS	IN	HRI MO	HRI FI	HAZARD STATUS	VERIF CODE	VOL NUM	CLOSE AUTH	CNTG ACT
FS-37-5a	DRIVE SYSTEM REDUCTION GEARBOX OIL PRESSURE INDICATOR: FLUX/FAILS	11	14	14	CLOS	CI	03	PSRRV	ER
FS-37-5b	DS REDUCTION GEARBOX OIL PRESS INDICATOR: FALSE ERRONEOUS READING	11	14	14	CLOS	CI	02F	PFDDR	ER
FS-37-6a	DRIVE SYSTEM/PROPFAN OIL TEMPERATURE INDICATOR FLUCUATES/FAILS	11	14	14	CLOS	CIP	03	PSRRV	ER
FS-37-6b	DRIVE SYSTEM/PF OIL TEMP INDICATOR: FALSE ERRONEOUS READING	11	14	14	CLOS	CI	02F	PFDDR	ER
FS-37-7a	DRIVE SYSTEM FUEL FLOW INDICATOR FLUCTUATES/FAILS	11	14	14	CLOS	CI	02F	PFDDR	ER
FS-37-7b	DRIVE SYSTEM FUEL FLOW INDICATOR: FALSE ERRONEOUS READING	11	14	14	CLOS	CI	03	PSRRV	ER
FS-37-8a	DRIVE SYSTEM FUEL TEMPERATURE INDICATOR: FLUCTUATES/FAILS	11	14	14	CLOS	AC	03	PSRRV	E
FS-37-8b	DRIVE SYSTEM FUEL TEMPERATURE INDICATOR: FALSE ERRONEOUS READING	11	14	14	CLOS	AC	03	PSRRV	E
FS-38-7c	PROPFAN AUX PUMP "PULL/FEATHER PUSH" SWITCH (#2 CONTACT) OPEN	11	14	14	CLOS	A	02F	PFDDR	E
FS-38-7d	PROPFAN AUX PUMP "PULL/FEATHER PUSH" SWITCH (#3 CONTACT) OPEN	11	14	14	CLOS	A	02F	PFDDR	E
FS-39-2a	DS/RGB LOW OIL PRESSURE WARNING LIGHT FALSE POSITIVE SIGNAL	11	14	14	CLOS	CI	02F	PFDDR	ERI
FS-39-2b	DRIVE SYS LOW FUEL PRESSURE WARNING LIGHT FALSE POSITIVE SIGNAL	11	14	14	CLOS	CI	02F	PFDDR	ERI
FS-39-5b	PROPFAN LOW OIL FLOW LIGHT: FALSE NEGATIVE SIGNAL	11	14	14	CLOS	CI	02F	PFDDR	EI
MFC-3-3	LNDG SPOILER: INCREASED ROLL DURING LANDING OR ABORTED TAKFOFF	14	14	14	CLOS	A	04	FTRRV	P
TI-1	WIRE/CABLES: WRONG SIZE/TYPE - OVERHEAT/BREAK/MALFUNCTION	11	14	14	CLOS	I	01	ACPDR	I
TI-2	WIRE BUNDLES ROUTING: DAMAGED DURING INSTALLATION OR TESTING	09	14	14	CLOS	I	03	PSRRV	NONE
TI-3	WIRE/CABLE MISIDENTIFIED OR UNIDENTIFIED: MISCONNECTED	11	14	14	CLOS	DI	03	PSRRV	NONE
TI-5	IMPROPER GROUNDING POINTS: SHOCK POTENTIAL	11	14	14	CLOS	AI	04	FTRRV	I
TI-6	TEST SWITCHES/EQUIPMENT/INSTRUMENTS NOT IDENT: OPERATOR CONFUSION	09	11	14	CLOS	I	04S	FTRRV	NONE
TI-7	TEST SWITCHES/EQUIP/INSTS-WRONG SIZE/COLOR: OPERATOR CONFUSION	11	14	14	CLOS	DI	03	PSRRV	NONE
TI-11	TEST INSTRUMENT WIRE/CABLE SUPPORTS INADEQUATE	11	14	14	CLOS	I	02S	ACDDR	I
TI-14	FLUID INGRESS INTO TEST EQUIPMENT: CORROSION/MALF/FAIL	11	14	14	CLOS	I	02S	ACDDR	I
TI-17	FLIGHT TEST ENGINEER INTERCOM/RADIO INTERFERENCE	11	14	14	CLOS	I	01	ACPDR	NONE
TI-18	TEST ENGINEER CONSOLE POWER SWITCH: WRONG POSITION SELECTED	11	14	14	CLOS	I	01	ACPDR	I
TI-19	TEST INST COMPUTER DROPS OFF LINE DURING POWER SWITCHING CHANGE	11	14	14	CLOS	I	01	ACPDR	NONE
TI-24	TEST INSTRUMENT ACCESS DOOR PROTECTION: NO INTERLOCK/WARNING	11	14	14	CLOS	I	01	ACPDR	I
TI-33	PPS NORMAL OR EMERGENCY PROCEDURES: IMPROPER/NOT DONE	11	14	14	CLOS	DIPT	03	PSRRV	PE
AI-3	QEC UNIT TO AFT NACELLE: DEGRADED INTERFACE	06	14	14	CLOS	DI	04	FTRRV	C
AI-10	QEC NACELLE TO AFT NACELLE INTERFACE: FUNCTIONAL SYSTEM DAMAGE	06	14	14	CLOS	AI	04	FTRRV	C

PTA
HAZARD TRACKING LOG
IN ORDER OF RISK

HAZARD IDENT	HAZARD REMARKS	IN	HRI MO	FI	HAZARD STATUS	VERIF CODE	VOL NUM	CLOSE AUTH	CNTG ACT
AI-11	ELECTRICAL AND ELECTRONIC COMPONENT COOLING INADEQUATE	11	14	14	CLOS	D	02S	ACDDR	NONE
CC-7	UTILITY OF PPS CONTROLS FOR FLIGHT ENGINEER USE	09	14	14	CLOS	A	02S	ACDDR	T
CC-8-1	UTILITY OF PPS MONITOR GAGES AND LIGHTS	07	14	14	CLOS	A	04	FTRRV	NONE
CC-8-3	FLIGHT ENGINEER: HUMAN ENGINEERING OF PPS CONTROLS	07	14	14	CLOS	A	04	FTRRV	NONE
CC-10	FLIGHT ENGINEER/CABIN CREW OXYGEN SYSTEM: MALF/NO PRESSURE/FAIL	11	14	14	CLOS	DI	04	FTRRV	E
CC-12	ICS AT CABIN FLIGHT STATIONS: NOT INSTALLED OR INADEQUATE	07	14	14	CLOS	ID	01	ACPDR	I
CC-18	CABIN WINDOWS: SONIC FATIGUE	11	14	14	CLOS	A	04	FTRRV	CI
CC-21	LOCATION OF RADIO/ ICS BUTTON- HUMAN FACTORS	07	14	14	CLOS	AD	04	FTRRV	NONE
FP-3	NACELLE/COWL MATERIAL FEEDS FIRE	09	14	14	CLOS	AD	01	PFPDR	NONE
FP-4	DUCTING/VENTING MATERIAL FEEDS FIRE	11	14	14	CLOS	AD	02F	PFDDR	NONE
FP-6-3b	FIRE WARNING INDICATION LIGHT SYSTEM: FALSE POSITIVE	14	14	14	CLOS	AC	04	FTRRV	E
FP-7-1a	FIRE DETECTOR PRESS-TO-TEST FAILS OPEN: NO SIGNAL (TASK 5)	14	14	14	CLOS	C	02F	PFDDR	I
FP-7-7a	FIRE AGENT TRANSFER CHECK VALVE POPPET JAMS TO END	11	14	14	CLOS	CA	02F	PFDDR	E
FP-9	FIRE ZONES VENT FLAMMABLE FUMES/FLUIDS	11	14	14	CLOS	DA	02S	PFDDR	E
SE-1	GEC DOLLY - UNWANTED MOVE DURING PPS INSTALLATION/REMOVAL	09	14	14	CLOS	A	01	ACPDR	NONE
SE-3	GEC SLING UNBALANCE: WRONG ATTACHMENT HOLE SELECTED	09	14	14	CLOS	IP	03	PSRRV	M
SSF-13-4B	FUEL/DEFUEL AT GAC - SPILL	14	14	14	CLOS	T	04	PSRRV	I
PMT-6	TASK INITIAL COMPLETION & VERIF CHECKOUT: PROC ERROR- TASK 5	14	14	14	CLOS	P	03	PSRRV	P
PMT-7	POST-AND PRE-RUN CHECKLISTS: PROCEDURAL ERROR- TASK 5	14	14	14	CLOS	P	03	PSRRV	P
PMT-8	END-TO-END FUNCTIONAL VERIF CHECKOUT: PROC ERROR- TASK 5	14	14	14	CLOS	P	03	PSRRV	P
PMT-9	ENGINE DRY MOTOR CHECKLIST: PROCEDURAL ERROR- TASK 5	14	14	14	CLOS	P	03	PSRRV	P
PMT-10	ENGINE WET MOTOR CHECKLIST: PROCEDURAL ERROR- TASK 5	14	14	14	CLOS	P	03	PSRRV	P
PMT-11	START UP PROCEDURE FOR FACILITY & PPS: PROCEDURAL ERROR- TASK 5	14	14	14	CLOS	P	03	PSRRV	P
PMT-12	SHUTDOWN PROCEDURE FOR FACILITY & PPS: PROCEDURAL ERROR- TASK 5	14	14	14	CLOS	P	03	PSRRV	P
PMT-13	PROPFAN TEST PROCEDURE: PROCEDURAL ERROR- TASK 5	14	14	14	CLOS	P	03	PSRRV	P
PMT-16	PRECIPITATION CLOG/PLUG T.I. PICKUPS	14	14	14	CLOS	IP	04	FTRRV	IP
PMT-17-1	TOWED AIRCRAFT HITS OBJECT- GELAC	11	14	14	CLOS	C	04	FTRRV	P
PMT-17-2	TOWED AIRCRAFT HITS OBJECT- GAC	14	14	14	CLOS	P	04	FTRRV	P
PMT-19	IMPROPER MAINTENANCE PROCEDURES- PARTS	11	14	14	CLOS	C	04	FTRRV	P

Lockheed

PTA
HAZARD TRACKING LOG
IN ORDER OF RISK

HAZARD IDENT	HAZARD REMARKS	IN	HRI MO	HRI FI	HAZARD STATUS	VERIF CODE	VOL NUM	CLOSE AUTH	CNTG ACT
PMT-20	HIGH NOISE LEVELS FOR OBSERVER- PPB RUNNING	09	14	14	CLOS	P	04	FTRRV	P
PMT-20-1	WORKER SLIPS/FALLS	11	14	14	CLOS	P	04	FTRRV	P
PMT-20-7A	MAINTENANCE STAND STRIKES TEST ARTICLE - GAC/GELAC	11	14	14	CLOS	P	04	FTRRV	PR
PMT-23	PTA TEST/FUNCTIONAL FLIGHT INTO ADVERSE WEATHER	11	14	14	CLOS	P	04	FTRRV	P
PMT-24	PARTS FALL OFF AIRCRAFT AFTER MAINTENANCE	14	14	14	CLOS	P	04	FTRRV	P
PT-3	BULKY END ITEM - HARD TO PACKAGE; PPS COMPONENT DAMAGE	11	14	14	CLOS	AI	01	ACPDR	NONE
DS-8	DRIVE SYSTEM COMPRESSOR BLADES FAIL AT ROOTS	10	15	15	CLOS	A	02F	PFDDR	R
DS-8-1a	DRIVE SYSTEM COMPRESSOR BLADE DOVETAIL TAB STRAIN/BLADE CREEP	10	15	15	CLOS	A	02F	PFDDR	R
DS-8-1b	DRIVE SYSTEM COMPRESSOR WHEEL FAILS	10	15	15	CLOS	A	02F	PFDDR	R
DS-8-1c	DRIVE SYSTEM COMPRESSOR TIE-BOLT THREADS RUPTURE/FAIL	10	15	15	CLOS	A	02F	PFDDR	R
DS-8-1d	DRIVE SYSTEM COMPRESSOR ROTOR FRONT CONE; BREAKS AT BRNG JOURNAL	10	15	15	CLOS	A	02F	PFDDR	R
DS-8-2a	DRIVE SYSTEM ACCESSORY DRIVE BOX SPLINE FATIGUE/FAILS	10	15	15	CLOS	A	02F	PFDDR	I
DS-8-2b	DRIVE SYSTEM COMPRESSOR ROTOR REAR CONE FLANGE/SPLINE FAILS	10	15	15	CLOS	A	02F	PFDDR	I
DS-8-2c	DRIVE SYSTEM COMPRESSOR REAR CONE SHAFT REAR THREADS FAIL	10	15	15	CLOS	A	02F	PFDDR	I
DS-8-2d	DRIVE SYSTEM COMPRESSOR REAR CONE SHAFT FRONT THREADS FAIL	10	15	15	CLOS	A	02F	PFDDR	I
DS-8-5b	DRIVE SYSTEM COMPRESSOR ACCESSORY DRIVE HUB BREAKS	10	15	15	CLOS	A	02F	PFDDR	IR
DS-8-5c	DRIVE SYSTEM COMPRESSOR ACCESSORY DRIVE SPLINE BREAKS	10	15	15	CLOS	A	02F	PFDDR	IR
DS-8-5d	DS COMPRESSOR ACCESSORY DRIVE PINION GEAR BEARING FATIGUE/FAILS	10	15	15	CLOS	A	02F	PFDDR	IR
DS-8-5e	DS COMPRESSOR ACCESSORY DRIVE FRONT BEARING SUPPORT FATIGUE/FAILS	10	15	15	CLOS	A	02F	PFDDR	IR
DS-8-5f	DS COMPRESSOR ACCESSORY DRIVE FRONT SUPPORT BEARING FAILS	10	15	15	CLOS	A	02F	PFDDR	IR
DS-9-2a	DIFFUSER/COMBUSTOR STRUT BREAKS	10	15	15	CLOS	A	02F	PFDDR	I
DS-9-2b	DIFFUSER/ASSEMBLY FLANGE FATIGUE/FAILS	10	15	15	CLOS	A	02F	PFDDR	I
DS-9-2c	DIFFUSER ASSEMBLY INNER OR OUTER SHELL BUCKLES/BENDS	10	15	15	CLOS	A	02F	PFDDR	I
DS-9-2d	DIFFUSER ASSEMBLY THRUST BEARING SUPPORT FATIGUE/FAILS	10	15	15	CLOS	A	02F	PFDDR	I
DS-9-2e	DIFFUSER SNUBBER ASSEMBLY CIRCUMFERENCE CRACKS	10	15	15	CLOS	A	02F	PFDDR	I
DS-9-2f	DIFFUSER/COMBUSTOR INNER BURNER CASE BREAKS	10	15	15	CLOS	A	02F	PFDDR	I
DS-9-2g	DIFFUSER/COMBUSTOR CONE FATIGUE/CRACKS/FAILS	10	15	15	CLOS	A	02F	PFDDR	I
PF-2	PROPFAN BLADE SHELL/SHEATH PORTION FAILS AND DEPARTS	14	15	15	CLOS	A	02F	PFDDR	MIC
PF-3	PROPFAN BLADE ASSEMBLY FOREIGN OBJECT DAMAGE	14	15	15	CLOS	IP	04	FTRRV	CI

PTA
HAZARD TRACKING LOG
IN ORDER OF RISK

HAZARD IDENT	HAZARD REMARKS	IN	HRI MO	FI	HAZARD STATUS	VERIF CODE	VOL NUM	CLOSE AUTH	CNTG ACT
PF-3-1	BIRD STRIKE OPERATING PROPFAN	15	15	15	CLOS	I	04	FTRRV	CI
PF-11	PROPFAN BLADE DYNAMIC EXCITATION: INTERFERENCE WITH PPS INLET	06	15	15	CLOS	AT	01	PFPDR	NONE
PF-13-6	PROPFAN ACTUATOR VALVES FAIL IN NULL POSITION	14	15	15	CLOS	A	04	FTRRV	EP
NA-2	NACELLE STRUCTURE/COWL PANELS/BULKHEADS FAIL	06	15	15	CLOS	ID	02F	ACDDR	NONE
NA-3	NACELLE FASTENERS LOOSE/FAIL: FOREIGH OBJECT DAMAGE	06	15	15	CLOS	I	01	ACPDR	I
FS-17	CIRCUIT BREAKERS FAIL: FUME/FIRE	06	15	15	CLOS	DI	02S	PFDDR	NONE
FS-35-6d	MANUAL FUEL VALVE SWITCH FAILS CLOSED WITH ENGINE OPERATING	10	15	15	CLOS	A	03	PSRRV	NONE
FS-38-1	PROPFAN SPEED CONTROL LEVER (FEATHER MICROSWITCH) FAILS CLOSED	10	15	15	CLOS	A	02F	PFDDR	E
FS-39-3b	DRIVE SYS/RGB MAGNETIC PLUG WARNING LIGHT FALSE NEGATIVE SIGNAL	10	15	15	CLOS	CIP	03	PSRRV	MRI
FS-39-4b	PROPFAN AUXILIARY PUMP OPERATES, BUT NO LIGHT	10	15	15	CLOS	CIP	03	PSRRV	EIR
FS-39-6	"FUEL ISOLATION VALVE CLOSED" - WARNING LIGHT ON BUT VALVE OPEN	10	15	15	CLOS	CI	02F	FFDDR	EIR
WFC-5	AILERONS: INSTALLATION EFFECTS/INTERFERENCE	10	15	15	CLOS	A	02S	ACDDR	NONE
WFC-10	DYNAMIC BALANCE BOOM/ATTACHMENT DEFORMS/FAILS	10	15	15	CLOS	AD	04	FTRRV	ITR
TI-9	TEST INSTRUMENT RACKS AND EQUIPMENT: INADEQUATE RESTRAINT	10	15	15	CLOS	D	02S	ACDDR	NONE
TI-10	FLIGHT TEST ENGINEER SEATS: INADEQUATE STRENGTH/RESTRAINTS	10	15	15	CLOS	D	02S	ACDDR	NONE
TI-17-1	TWO WAY AIR TO GROUND VOICE RADIO INOPERATIVE OR NOT INSTALLED	10	15	15	CLOS	T	02S	ACDDR	NONE
TI-25-1	TEST INST ACOUSTIC BOOM - LEFT WING VIBRATION/INSTALLATION: FAILS	06	15	15	CLOS	D	04	FTRRV	CI
TI-28-1	OUTGAS FROM CABIN MICROPHONE ARRAY	06	15	15	CLOS	DI	04	FTRRV	NONE
TI-31	RECONNECT TEST INST WIRES AFTER MAINTENANCE: IMPROPER/NOT CONNECT	10	15	15	CLOS	IPT	03	PSRRV	PI
TI-40	SETUP/OPERATE/MONITOR CCTV: DEGRADED READINESS	15	15	15	CLOS	I	03	PSRRV	NONE
TI-41	TEST EQUIPMENT SPARKS IN LOWERED PRESSURES	06	15	15	CLOS	D	04	FTRRV	P
AI-9	OEC NACELLE TO AFT NACELLE - VARIABLE INCIDENCE FITTINGS: FAIL	10	15	15	CLOS	AI	02S	ACDDR	I
CC-9	CABIN CREW SEATS INADEQUATE/MALFUNCTION: INJURY	10	15	15	CLOS	ID	02S	ACDDR	NONE
CC-9-1	CABIN CREW SEATS IMPROPER ATTACHMENT TO FLOOR	10	15	15	CLOS	ID	02S	ACDDR	NONE
CC-9-2	CABIN CREW SEATS EASY ACCESS TO CRITICAL CONTROLS	10	15	15	CLOS	ID	02S	ACDDR	NONE
CC-9-3	CABIN CREW SEATS FLIGHT TEST ENGINEER-MONITOR INTERFACE	10	15	15	CLOS	ID	02S	ACDDR	NONE
CC-14-1	ACOUSTIC MIC BOOM ARRAY ASSEMBLY IN CABIN: STRUCTURAL FAILURE	06	15	15	CLOS	DA	04	FTRRV	I
CC-19-1	NOSE LDG GEAR UP OR COLLAPSE: PPS NOT OPERATING	15	15	15	CLOS	A	04	FTRRV	EIMP
CC-19-1a	NOSE LDG GEAR UP OR COLLAPSE: PPS OPERATING	15	15	15	CLOS	A	04	FTRRV	EIMP

PTA
HAZARD TRACKING LOG
IN ORDER OF RISK

HAZARD IDENT	HAZARD REMARKS	IN	HRI MD	FI	HAZARD STATUS	VERIF CODE	VOL NUM	CLOSE AUTH	CNTG ACT
CC-19-2	RIGHT MLG UP OR COLLAPSE: PPS OPER/ NOT OPERATING	15	15	15	CLOS	A	04	FTRRV	EIMP
CC-19-3a	LEFT MLG UP OR COLLAPSE: PPS NOT OPERATING	15	15	15	CLOS	A	04	FTRRV	EIMP
CC-19-3b	LEFT MLG UP OR COLLAPSE: PPS OPERATING	15	15	15	CLOS	A	04	FTRRV	EIMP
CC-19-4a	ALL LDG GEAR UP OR COLLAPSE: PPS NOT OPERATING	15	15	15	CLOS	A	04	FTTRV	EIMP
CC-19-4b	ALL LDG GEAR UP OR COLLAPSE: PPS OPERATING	15	15	15	CLOS	A	04	FTRRV	EIMP
CC-22	BIRD STRIKES WINDSHIELD	15	15	15	CLOS	A	04	FTRRV	P
FP-6-4a	FIRE WARNING HORN/MALFUNCTION/FAILS: FALSE NEGATIVE (TASK 9)	10	15	15	CLOS	C	04	FTRRV	EI
FP-7-1c	FIRE EMERGENCY HANDLE: CONTACTS FAIL CLOSED PRIOR TO PULLING	15	15	15	CLOS	C	02F	PFDDR	E
FP-7-2b	FIRE EMERGENCY HANDLE: SOLENOID MALFUNCTION/FAILS-UNABLE TO PULL	10	15	15	CLOS	AC	04	FTRRV	E
FP-7-4a	FIRE EXTINGUISHING AGENT BOTTLE LEAKS: "AGENT DISC" LIGHT FALSE	10	15	15	CLOS	C	04	FTRRV	NONE
FP-7-5b	FIRE EXTINGUISHING AGENT BOTTLE OVERPRESSURIZED: BURST	10	15	15	CLOS	CA	02F	PFDDR	E
FP-7-6a	FIRE BOTTLE DISCHARGE SQUIBS: NO POWER SOURCE REDUNDANCY	08	15	15	CLOS	CA	04	FTRRV	C
SE-4	GEC SLING ATTACHMENT POINT ON GEC STRUCTURE: FAILS	10	15	15	CLOS	IPT	03	PSRRV	M
SE-7	MOVE PPS ONTO & OFF GII AIRCRAFT	10	15	15	CLOS	AIP	04	FTRRV	M
SSF-2	FACILITY DAMAGE/INJURY DUE TO PPS FAILURE EFFECTS	15	15	15	CLOS	AI	03	PSRRV	EP
SSF-7	B-60 TEST STAND: FATIGUE/OVERSTRESS/FAILURE- TASK 5	10	15	15	CLOS	I	03	PSRRV	I
SSF-10	ROHR CONTROL ROOM: SMOKE/FIRE- TASK 5	15	15	15	CLOS	IP	03	PSRRV	IEP
SSF-10-1	HAMILTON STANDARD/ROHR CONDOR MONITOR TRAILER: SMOKE/FIRE- TASK 5	15	15	15	CLOS	IP	03	PSRRV	IEP
SSF-10-2	ROHR PROPFAN PROPULSION SYSTEM BUILDUP SHOP: SMOKE/FIRE- TASK 5	15	15	15	CLOS	IP	03	PSRRV	IEP
SSF-10-3	ROHR ADMINISTRATIVE TRAILER: SMOKE/FIRE- TASK 5	15	15	15	CLOS	IP	03	PSRRV	I
SSF-11	ROHR TEST STAND WATER DELUGE SYSTEM: LOW QUANTITY/PRESSURE-TASK 5	15	15	15	CLOS	P	03	PSRRV	E
SSF-11-1	FIRE IN GELAC GII/PTA HANGAR- TASK 9	10	15	15	CLOS	I	04	FTRRV	E
SSF-11-2	FIRE IN GII/PTA HANGAR- GULFSTREAM- TASK 8/9	15	15	15	CLOS	I	04	FTRRV	E
SSF-13-5	FUEL CELL OPEN IN GELAC GII/PTA HANGAR- TASK 9	10	15	15	CLOS	P	04	FTRRV	P
SSF-17	COMM BETWEEN CONTROL ROOM & HAM STAN TRAILER: MALF/INOP- TASK 5	10	10	15	CLOS	P	03	PSRRV	EP
SSF-18	WING/NACELLE PROOF TEST AT GAC	10	15	15	CLOS	AT	04	PSRRV	PR
PMT-3	PPS-INSTALL/REMOVE FROM B-60 STAND: PROCEDURAL ERROR- TASK 5	15	15	15	CLOS	P	03	PSRRV	PIR
PMT-5	EMERGENCY RESPONSES TO FIRE: PROCEDURAL ERROR- TASK 5	15	15	15	CLOS	P	03	PSRRV	E
PMT-18	JACK, SCALES, SHORING MALFUNCTION/FAIL	15	15	15	CLOS	P	04	FTRRV	P

PIA
HAZARD TRACKING LOG
IN ORDER OF RISK

HAZARD IDENT	HAZARD REMARKS	IN	HRI MO	FI	HAZARD STATUS	VERIF CODE	VOL NUM	CLOSE AUTH	CNTG ACT
PMT-20-5	PRESSURE FUEL/DEFUEL- WING DAMAGE- GELAC	10	15	15	CLOS	P	04	FTRRV	P
PMT-20-6	PRESSURE FUEL/DEFUEL WING DAMAGE- GAC	10	10	15	CLOS	P	04	FTRRV	P
PMT-23-1	SPEY ENGINE FAILS ON TAKEOFF	15	15	15	CLOS	J	04	FTRRV	EM
PT-7	TRANSPORT PPS TO B-60 STAND FROM ENGINE BUILDUP ROOM/RETURN:DAMAG	15	15	15	CLOS	IP	03	PSRRV	IR
PT-8	TRANSPORTING QEC UNIT FROM ROHR TO GAC: DAMAGE	15	15	15	CLOS	IP	03	PSRRV	NONE
PT-8-1	TRANSPORT PPS FROM ROHR TO GULFSTREAM: DAMAGE	15	15	15	CLOS	IP	04	FTRRV	NONE
PT-9	TRANSPORTING PROPFAN ASSEMBLY FROM ROHR TO HAM STAN: DAMAGE	15	15	15	CLOS	IP	03	PSRRV	NONE
PT-9-1	TRANSPORT PROPFAN FROM GULFSTREAM TO LOCKHEED: DAMAGE	15	15	15	CLOS	IP	04	FTRRV	NONE
DS-5	STARTER SPUR GEAR SPLINE FAILS	14	17	17	CLOS	A	02F	PFDDR	MIR
DS-8-3a	DRIVE SYSTEM COMPRESSOR STATOR VANES FATIGUE/FAIL	14	17	17	CLOS	A	02F	PFDDR	R
DS-8-3b	DRIVE SYSTEM COMPRESSOR STATOR VANES ERRODE/CORRODE/FOD	14	17	17	CLOS	A	02F	PFDDR	R
DS-8-3c	DRIVE SYS COMPRESS STATOR VANES OUTER SPINDLE HIGH CYCLE FATIGUE	14	17	17	CLOS	A	02F	PFDDR	R
DS-9-1a	COMBUSTOR LINER WALL BUCKLES/BENDS	14	17	17	CLOS	A	02F	PFDDR	J
DS-9-1b	COMBUSTOR LINER WALLS FATIGUE/FAILS	14	17	17	CLOS	A	02F	PFDDR	I
DS-15	TORQUEMETER BEARINGS/REFERENCE SHAFT FAILS	17	17	17	CLOS	A	02F	PFDDR	E
DS-16	TORQUEMETER PICKUP COIL FAILS OPEN/SHORTS	17	17	17	CLOS	A	02F	PFDDR	E
PF-3-2	BIRD STRIKE PROPFAN NOT OPERATING	17	17	17	CLOS	I	04	FTRRV	CI
PF-4	PROPFAN SLIPSTREAM ENTERS LEFT SPEY ENGINE INTAKE	14	17	17	CLOS	AT	04	FTRRV	T
PF-13-5	PROPFAN ACTUATOR VALVES FAIL IN INCREASE POSITION	14	17	17	CLOS	A	04	FTRRV	EP
NA-7	NACELLE SOUND ATTENUATION AND INSULATION MATERIALS OVERHEAT	17	17	17	CLOS	A	02F	ACPDR	NONE
NA-8	NACELLE VARIABLE INCIDENCE: POOR PROPFAN-TO-GROUND CLEARANCE	14	17	17	CLOS	A	02S	ACDDR	NONE
FS-1-5	EMERGENCY FUEL MANUAL SHUTOFF HANDLE/CABLE BINDS OR BREAKS	14	17	17	CLOS	IT	02F	PFDDR	EO
FS-8	OIL/FUEL COOLER LEAKS/FAILS	14	17	17	CLOS	CI	02F	PFDDR	RI
FS-21	LIGHTNING STRIKE: INJURY/DAMAGE	14	17	17	CLOS	D	01	PFDDR	CP
FS-22	LUBRICATION FOR ELECTRICAL COMPONENT: SMOKE/HEAT	11	17	17	CLOS	D	01	PFPDR	D
FS-35-2a	ENGINE POWER LEVER ASSYEMBLY DRIVE BELT SLIPS/FAILS	14	17	17	CLOS	A	02F	PFDDR	PE
FS-35-2b	ENGINE POWER LEVER ASSEMBLY POTENTIOMETER FAILS OPEN/CLOSE	17	17	17	CLOS	AC	02F	PFDDR	NONE
FS-35-3a	ENGINE CONTROL RUN/STOP SWITCH FAILS IN "STOP"	14	17	17	CLOS	A	02F	PFDDR	E
FS-35-3b	ENGINE CONTROL RUN/STOP SWITCH FAILS IN "RUN"	14	17	17	CLOS	A	02F	PFDDR	E

Lockheed

PTA
HAZARD TRACKING LOG
IN ORDER OF RISK

HAZARD IDENT	HAZARD REMARKS	IN	HRI MO	FI	HAZARD STATUS	VERIF CODE	VOL NUM	CLOSE AUTH	CNTG ACT
FS-35-3c	ENGINE CONTROL RUN/STOP SWITCH SHORTS TO GROUND	14	17	17	CLOS	A	02F	PFDDR	E
FS-35-4a	ENGINE OVERSPEED TEST SWITCH FAILS OPEN	14	17	17	CLOS	ACP	04	FTRRV	IP
FS-38-2	PF SPEED CONTROL LVR (ROTARY VARIABLE DIFF TRANS-RVDT) FAILS OPEN	14	17	17	CLOS	AP	03	PSRRV	ER
FS-38-3	PROPFAN SPEED CONTROL LEVER DISCONNECTED FROM RVDT	14	17	17	CLOS	A	02F	PFDDR	ER
FS-38-4	PROPFAN SPEED CONTROL LEVER (FEATHER MICROSWITCH) FAILS OPEN	14	17	17	CLOS	AP	03	PSRRV	ER
FS-38-5a	PROPFAN SPEED CONTROL ON/OFF SWITCH (115 VAC CONTACT) FAILS OPEN	14	17	17	CLOS	A	02F	PFDDR	E
FS-38-5c	PROPFAN SPEED CONTROL ON/OFF SWITCH (28 VDC CONTACT) FAILS OPEN	14	17	17	CLOS	A	02F	PFDDR	NONE
FS-38-6a	PROPFAN RESET SWITCH FAILS OPEN	14	17	17	CLOS	A	02F	PFDDR	E
FS-38-8a	PF ELECTRONIC SPEED CONTROL UNIT 28 VDC POWER INTERRUPT; NO FAULT	14	17	17	CLOS	A	02F	PFDDR	E
FS-38-8b	PF ELECTRONIC SPEED CONTROL UNIT 115 VAC POWER/SERVO AMP FAILS	14	17	17	CLOS	A	02F	PFDDR	E
FS-38-8c	PROPFAN ELECTRONIC SPEED CONTROL UNIT FALSE POSITIVE SIGNALS	14	17	17	CLOS	A	02F	PFDDR	E
FS-38-8d	PROPFAN ELECTRONIC SPEED CONTROL UNIT FALSE NEGATIVE SIGNALS	14	17	17	CLOS	A	02F	PFDDR	E
FS-39-1a	DRIVE SYSTEM OVERSPEED WARNING LIGHT LATENT FAILURE	14	17	17	CLOS	CIP	03	PSRRV	ER
FS-39-1b	DRIVE SYSTEM OVERSPEED WARNING LIGHT FALSE POSITIVE SIGNAL	14	17	17	CLOS	CI	02F	PFDDR	PR
FS-39-1c	PROPFAN CONTROL WARNING LIGHT FALSE POSITIVE SIGNAL	14	17	17	CLOS	CI	02F	PFDDR	ER
FS-39-5a	PROPFAN LOW OIL FLOW LIGHT; FALSE POSITIVE SIGNAL	14	17	17	CLOS	CI	02F	PFDDR	E
WFC-3-1	LANDING SPOILERS; UNTIMELY OR LACK OF OPERATION/STRUCTURAL INTERF	14	14	17	CLOS	A	04	FTRRV	M
WFC-3-2	INBOARD FLIGHT SPOILERS; UNTIMELY/LACK OF OPS/STRUCT INTERFERENCE	14	17	17	CLOS	A	04	FTRRV	M
WFC-9	LEFT WING LEADING EDGE OVERPRESSURE DUE TO FUNCTIONAL SYS BURST	14	17	17	CLOS	AD	02S	ACDDR	NONE
WFC-12	LEFT WING FLAPS/SPOILERS/TRAILING EDGE; SONIC FATIGUE	11	17	17	CLOS	AD	04	FTRRV	IMP
WFC-13	LEFT WING MICROPHONE BOOM DEFORMS/FAILS	14	17	17	CLOS	A	02S	ACDDR	NONE
WFC-14-3	TAXI; HEAVY FUEL OR VERY LIGHT FUEL LOAD	14	17	17	CLOS	A	04	FTRRV	IMPO
TI-12	TEST INST-WIRE/CABLE SUPPORTS NEAR HEAT SOURCE; INSULATION DAMAGE	14	17	17	CLOS	I	02S	ACDDR	I
TI-16	TEST INSTRUMENT MASTER POWER SWITCH NOT INSTALLED	14	17	17	CLOS	D	01	ACPDR	NONE
TI-22	TEST INSTRUMENT CATHODE RAY TUBE IMPLOSION; INJURY	14	17	17	CLOS	I	01	ACPDR	NONE
TI-30	TEST INST SPLICED TO RDHR CONTROL ROOM; IMPROPER/FAULTY/DAMAGE	14	17	17	CLOS	IP	03	PSRRV	PIE
AI-6	NACELLE TILT ANGLES/PROPFAN GROUND CLEAR; DAMAGE	14	17	17	CLOS	DA	02S	ACDDR	NONE
AI-7	QEC TO PROPFAN PLANE OF ROTATION CLEARANCE; DAMAGE	14	17	17	CLOS	DA	01	ACPDR	NONE
AI-8	QEC NACELLE TO PROPFAN SPINNER CLEARANCE; DAMAGE	14	17	17	CLOS	DA	01	ACPDR	NONE

PTA
HAZARD TRACKING LOG
IN ORDER OF RISK

HAZARD IDENT	HAZARD REMARKS	IN	HRI MD	HRI FI	HAZARD STATUS	VERIF CODE	VOL NUM	CLOSE AUTH	CNTG ACT
CC-8-2	FLIGHT ENGINEER ACCESS TO OVERHEAD CIRCUIT BREAKERS AND INSTRUMEN	07	17	17	CLOS	I	04	FTRRV	NONE
CC-8-4	PPS CONTROL PEDESTAL SHARP EDGES; INJURY	07	17	17	CLOS	A	04	FTRRV	NONE
CC-15-1	LEFT FUSELAGE BETWEEN WINDOWS 2 & 3; SONIC FATIGUE	11	17	17	CLOS	A	04	FTRRV	CI
CC-16	FUSELAGE STEEL SHIELD STRUCK BY FAILED PROPFAN SEGMENT (EFFECTS)	17	17	17	CLOS	A	04	FTRRV	NONE
FP-1	FIRE ZONES; NOT DESIGNED/DESIGNATED FOR NACELLE	11	17	17	CLOS	D	01	PFPDR	NONE
FP-7-1b	FIRE DETECTOR PRESS-TO-TEST FAILS OPEN; NO SIGNAL (TASK 9)	14	17	17	CLOS	C	04	FTRRV	P
FP-7-6c	FIRE BOTTLE DISCHARGE SQUIBS SHORT TO POWER; UNPLANNED DISCHARGE	14	17	17	CLOS	CA	02F	PFDDR	E
FP-10	FLEXIBLE FIRE SHIELD BRITTLE/CRACK/SPLIT/TEAR	11	17	17	CLOS	DI	02S	PFDDR	M
SSF-10-4	GELAC GROUND TELEMETRY & MONITOR ROOM- TASK 9	14	17	17	CLOS	I	04	FTRRV	EIPR
SSF-10-5	GII/PTA MAINTENANCE IN GELAC HANGAR- TASK 9	14	17	17	CLOS	CIP	04	FTRRV	EIMP
SSF-10-6	GII/PTA MAINTENANCE IN GULFSTREAM HANGAR- TASK 8/9	17	17	17	CLOS	A	04	FTRRV	I
SSF-14	ROHR FACILITY AIRSTART SYSTEM; MALFUNCTION/INOPERATIVE- TASK 5	17	17	17	CLOS	CP	03	PSRRV	P
PT-1	PACKAGING NOT STURDY/RUGGED; PPS COMPONENT DAMAGE	11	17	17	CLOS	AI	01	ACPDR	NONE
PT-2	PACKAGING-IMPROPER MOUNTS/SHOCKS/DAMPENERS; PPS COMPONENT DAMAGE	11	17	17	CLOS	AI	01	ACPDR	NONE
DS-8-6a	DRIVE SYSTEM COMPRESSOR CASE ARM FAILS	18	18	18	CLOS	A	02F	PFDDR	R
DS-8-6b	DRIVE SYSTEM COMPRESSOR CASE BELLCRANK ACTUATOR FAILS	18	18	18	CLOS	A	02F	PFDDR	R
DS-8-6c	DRIVE SYSTEM COMPRESSOR CASE SUPPORT ASSEMBLY FAILS	18	18	18	CLOS	A	02F	PFDDR	R
DS-8-6d	DRIVE SYSTEM COMPRESSOR CASE END FLANGE CRACKS/FAILS	18	18	18	CLOS	A	02F	PFDDR	R
DS-8-6e	DRIVE SYSTEM COMPRESSOR CASE SHELL CRACKS/BREAKS	18	18	18	CLOS	A	02F	PFDDR	R
DS-11-2	MECHANICAL FUEL CONTROL LATCHING SHUTOFF FAILS OPEN/CLOSED	18	18	18	CLOS	A	02F	PFDDR	P
FS-2	PTA FUEL USE; ADVERSE EFFECTS ON SPEY ENGINE OPERATIONS	18	18	18	CLOS	A	01	PFPDR	NONE
FS-3	FUEL TO OIL COOLERS (PF AND DS LUBE) INADEQUATE TO NEEDS	18	18	18	CLOS	A	02F	PFDDR	NONE
FS-9	OIL TO FUEL/FUEL TO OIL CONTAMINATION	18	18	18	CLOS	C	01	PFPDR	NONE
FS-20	ELECTROMAGNETIC INTERFERENCE (EMI) WITH PTA ELECTRICAL COMPONENTS	18	18	18	CLOS	D	04	FTRRV	T
FS-40	FUNCTIONAL SYSTEM TEST AFTER LAYUP	18	18	18	CLOS	IP	04	FTRRV	IMP
TI-13	TEST INSTRUMENT CONNECTORS MISIDENTIFIED OR MISCONNECTED	18	18	18	CLOS	DI	02S	ACDDR	I
TI-36	ROHR TEST INSTRUMENTATION DATA SYS OPERATIONS; DEGRADED READINESS	16	18	18	CLOS	IPT	03	PSRRV	PECR
TI-36-1	ROHR NACELLE/ACOUSTIC TAILPIPE DATA; DEGRADED READINESS	16	18	18	CLOS	IPT	03	PSRRV	PECR
TI-37	ROHR ACOUSTIC DATA SYSTEM; DEGRADED READINESS	16	18	18	CLOS	IPT	03	PSRRV	MCR

PIA
HAZARD TRACKING LOG
IN ORDER OF RISK

HAZARD IDENT	HAZARD REMARKS	IN	HRI MO	FI	HAZARD STATUS	VERIF CODE	VOL NUM	CLOSE AUTH	CNTG ACT
TI-38	ROHR AMBIENT TEMPERATURE DATA: DEGRADED READINESS	16	18	18	CLOS	IPT	03	PSRRV	PECR
TI-39	OBSERVATION/RECORDING-PPS OPERATIONS INSTS: DEGRADED READINESS	16	18	18	CLOS	IPT	03	PSRRV	PECR
CC-23	COCKPIT COORDINATION TO ESTABLISH/HOLD TEST POINT	16	18	18	CLOS	A	04	FTRRV	P
SSF-9	B-60 ACOUSTIC ARRAY: MALFUNCTION/INOPERATIVE- TASK 5	18	18	18	CLOS	IP	03	PSRRV	I
SSF-9-1	GROUND AUDIO ARRAY AT FACILITY- GELAC/DOBBINS- TASK 9	18	18	18	CLOS	IP	04	FTRRV	IPR
SSF-13-1	FACILITY FUEL TO PF PROPULSION SYSTEM: LOSS OF CONTROL- TASK 5	18	18	18	CLOS	DP	03	PSRRV	P
PMT-1	DRIVE SYSTEM BUILDUP: PROCEDURE/TECHNIQUE ERROR- TASK 5	18	18	18	CLOS	P	03	PSRRV	PI
PMT-2	GEC UNIT INSTALL/REMOVE FROM DOLLY: PROCEDURAL ERROR- TASK 5	18	18	18	CLOS	P	03	PSRRV	P
PMT-4	TEST INST-ROUTINELY INSTALL/REMOVE FROM PPS: PROC ERROR- TASK 5	18	18	18	CLOS	P	03	PSRRV	PI
WFC-3	LAT CONTROL & DIVE BRAKE SYSTEM: REDUCED LAT CONTROL AUTHORITY	06	18	18	CLOS	A	04	FTRRV	EI
DS-5-1	PROPFAN BRAKE INNER MEMBERS FAIL/MALFUNCTION	19	19	19	CLOS	A	04	FTRRV	E
DS-11-1a	MECHANICAL FUEL CONTROL LATCHING SHUTOFF: IMPROPER METERING	18	19	19	CLOS	A	02F	PFDDR	NONE
DS-11-1b	MECHANICAL FUEL CONTROL SHUTOFF VALVE FAILS OPEN/CLOSED	18	19	19	CLOS	A	02F	PFDDR	NONE
PF-9	PROPFAN FEATHER SYSTEM ELECTRICAL CONTROL INOPERATIVE: NO FEATHER	16	19	19	CLOS	C	01	PFPDR	NONE
PF-14-1	PF CONTROL MAIN PUMP/STANDBY PUMPS/SCAV PUMPS: LOW/NO OUTPUT	18	19	19	CLOS	A	02F	PFDDR	E
PF-14-2a	PROPFAN SUMP RELIEF/AUXILIARY PUMP CHECK VALVES FAIL OPEN	18	19	19	CLOS	A	02F	PFDDR	E
PF-14-2b	PROPFAN PRESSURIZED SEAL LEAKS	18	19	19	CLOS	A	02F	PFDDR	E
PF-14-3	PROPFAN BLADE RETENTION BEARING FAILS	18	19	19	CLOS	A	02F	PFDDR	E
PF-16-1	PROPFAN FEATHER VALVE SEIZES IN FEATHER POSITION	19	19	19	CLOS	A	02F	PFDDR	E
PF-16-2	PROPFAN FEATHER SOLENOID FAILS CLOSED	19	19	19	CLOS	A	02F	PFDDR	E
NA-9	NACELLE FLEXIBLE FIRE SHIELD BENT/BRITTLE/CRACKS/FAILS	16	19	19	CLOS	A	04	FTRRV	C
FS-1-1a	MOTOR OPERATED FUEL SHUTOFF VALVE FAILS CLOSED	19	19	19	CLOS	AC1	04	FTRRV	NONE
FS-1-1b	MOTOR OPERATED FUEL SHUTOFF VALVE FAILS OPEN (ELECTRICALLY)	19	19	19	CLOS	AC1	04	FTRRV	NONE
FS-1-1c	MOTOR OPERATED FUEL SHUTOFF VALVE FAILS OPEN (MECHANICALLY)	19	19	19	CLOS	AC1	02F	PFDDR	NONE
FS-1-3	FUEL LOW PRESSURE SWITCH MALFUNCTIONS/FAILS	18	19	19	CLOS	AC	02F	PFDDR	P
FS-6-3	OIL TEMPERATURE SENSOR FAILS/MALFUNCTIONS	18	19	19	CLOS	C	02F	PFDDR	RE
FS-15	ELECTRICAL COMPONENTS SUSTAIN/MAINTAIN FIRE	16	19	19	CLOS	D	01	PFPDR	NONE
FS-16	CIRCUIT BREAKERS CONTAMINATED/CORRODED	19	19	19	CLOS	D	01	PFPDR	NONE
FS-19	ELECTRICAL COMPONENTS CAUSING ENVIRONMENTAL CONTAMINATION	16	19	19	CLOS	DI	02F	PFDDR	M

Lockheed

PTA
HAZARD TRACKING LOG
IN ORDER OF RISK

HAZARD IDENT	HAZARD REMARKS	IN	HRI MO	HRI FI	HAZARD STATUS	VERIF CODE	VOL NUM	CLOSE AUTH	CNTG ACT
FS-24-1b	AUXILIARY PUMP INVERTER FAILS WITH PROPFAN NOT OPERATING	18	19	19	CLOS	DI	04	FTRRV	EIM
FS-24-2b	RIGHT ALTERNATOR BUS FAILS WITH PROPFAN NOT OPERATING	18	19	19	CLOS	DI	02F	PFDDR	P
FS-24-3	INVERTER "G"/TRANSFORMER RECT./CONTROL RELAY/DATA SYS BUS FAILS	11	19	19	CLOS	DI	04	FTRRV	EIM
FS-24-4	LEFT ALTERNATING CURRENT MONITOR BUS/RELAY FAILS	11	19	19	CLOS	DI	04	FTRRV	EIM
FS-24-5	LEFT AC MONITOR BUS/CONTROL RELAY FAILS	06	10	19	CLOS	DI	04	FTRRV	EP
FS-24-6a	SECONDARY INVERTER BUS FAILS	19	19	19	CLOS	D	02F	PFDDR	E
FS-24-6b	SECONDARY INVERTER BUS CONTACTOR RELAY FAILS	19	19	19	CLOS	D	02F	PFDDR	E
FS-24-6c	INVERTER "C" FAILS	19	19	19	CLOS	A	04	FTRRV	EIP
FS-30	AIR START ISOLATION VALVE FAILS CLOSED	18	19	19	CLOS	CD	01	PFPDR	NONE
FS-35-5a	ENGINE FUEL MANIFOLD QUICK-FILL SWITCH FAILS OPEN	18	19	19	CLOS	AT	02F	PFDDR	E
FS-35-5b	ENGINE FUEL MANIFOLD QUICK-FILL SWITCH FAILS CLOSED	19	19	19	CLOS	A	02F	PFDDR	NONE
FS-35-6a	MANUAL FUEL VALVE SWITCH FAILS OPEN PRIOR TO ENGINE START	19	19	19	CLOS	A	02F	PFDDR	E
FS-38-7a	PROPFAN AUX PUMP "PULL/FEATHER PUSH" SWITCH (#8 CONTACT) OPEN	18	19	19	CLOS	A	02F	PFDDR	NONE
FS-38-7b	PROPFAN AUX PUMP "PULL/FEATHER PUSH" SWITCH (#1 CONTACT) OPEN	19	19	19	CLOS	A	02F	PFDDR	E
FS-38-7f	PROPFAN AUX PUMP "PULL/FEATHER PUSH" SWITCH (#4 CONTACT) OPEN	18	19	19	CLOS	A	02F	PFDDR	E
FS-38-7g	PROPFAN AUX PUMP "PULL/FEATHER PUSH" SWITCH (#6 CONTACT) OPEN	18	19	19	CLOS	A	02F	PFDDR	E
FS-38-7h	PROPFAN AUX PUMP "PULL/FEATHER PUSH" SWITCH (#5 CONTACT) OPEN	18	19	19	CLOS	A	02F	PFDDR	E
FS-39-4a	PROPFAN AUXILIARY PUMP LIGHT FALSE POSITIVE SIGNAL	16	19	19	CLOS	CIP	03	FSRRV	EIR
WFC-2	LEFT WING DOUBLERS: LIMITED ACCESS/INTERFERENCE/INJURY	18	19	19	CLOS	DI	01	ACPDR	NONE
WFC-2-1	RIGHT WING DOUBLERS: LIMITED ACCESS/INTERFERENCE/INJURY	18	19	19	CLOS	AI	02S	ACDDR	NONE
TI-15	WIRE ROUTING: G-II VS PTA TEST INST: MECH/ELECTRONIC INTERFERENCE	18	19	19	CLOS	IT	02S	ACDDR	I
TI-22	TEST INSTRUMENT WIRES REMOVED FROM PPS; NOT REINSTALLED PROPERLY	18	19	19	CLOS	IPT	03	FSRRV	ICPR
TI-24	FACILITY TEST INSTRUMENT CALIBRATION: NOT DONE/INADEQUATE	19	19	19	CLOS	P	03	FSRRV	PM
AI-5	DEC NACELLE TO AFT NACELLE: DEGRADED INTERFACE	18	19	19	CLOS	DA	01	ACPDR	NONE
CC-20-3	NO RECORDING OF AURAL SAFETY SIGNALS	19	19	19	CLOS	A	04	FTRRV	E
FF-6-2a	FIRE DETECTOR CONTROL UNIT MALFUNCTION: FALSE POSITIVE	19	19	19	CLOS	CA	02F	PFDDR	E
FF-6-3a	FIRE WARNING INDICATION LIGHT: FALSE NEGATIVE	19	19	19	CLOS	C	02F	PFDDR	E
FF-6-4b	FIRE WARNING HORN/MALFUNCTION/FAILS: FALSE POSITIVE (TASK 9)	19	19	19	CLOS	C	04	FTRRV	E
FF-7-4b	FIRE BOTTLE "AGENT DISC" LIGHT MALFUNCTION/FAILS	19	19	19	CLOS	C	02F	PFDDR	E

PTA
HAZARD TRACKING LOG
IN ORDER OF RISK

HAZARD IDENT	HAZARD REMARKS	IN	HRI MO	FI	HAZARD STATUS	VERIF CODE	VOL NUM	CLOSE AUTH	CNTG ACT
SSF-12	B-60 ACOUSTICAL FIELD TEMP MONITOR: MALFUNCTION/FAIL- TASK 5	19	19	19	CLOS	IP	03	PSRRV	
SSF-13	ROHR FACILITY FUEL: SPILL/CONTAMINATION/LEAK/WRONG TYPE- TASK 5	19	19	19	CLOS	IP	03	PSRRV	EIMT
SSF-13-2	FACILITY EMERGENCY FUEL TANK SYSTEM: LOSS OF CONTROL- TASK 5	19	19	19	CLOS	P	03	PSRRV	P
SSF-13-3	FUEL & DEFUEL GII/PTA- GELAC- TASK 9	19	19	19	CLOS	IP	04	FTRRV	EP
SSF-13-3A	WRONG TYPE FUEL/FOD INTRO GII FUEL SYSTEM	19	19	19	CLOS	CP	04	PSRRV	IP
SSF-15	FACILITY ELECT POWER FOR PF AUXILIARY PUMP: MALF/FAIL- TASK 5	19	19	19	CLOS	IP	03	PSRRV	P
PT-4	FRAGILE AND/OR NON-SYMMETRIC ITEM HARD TO PROTECT: DAMAGE	18	19	19	CLOS	AI	01	ACPDR	NONE
PT-5	ADVERSE ENVIRONMENTAL CONDITION: DAMAGE TO COMPONENT	18	19	19	CLOS	AI	01	ACPDR	NONE
PF-18	HIGH SPEED TAXI TEST WITH PROPFAN IN REVERSE PITCH	04	20	20	CLOS	A	04	FTRRV	NONE
FS-38-5b	PROPFAN SPEED CONTROL ON/OFF SWITCH (115 VAC CONTACT) FAILS CLOSE	19	20	20	CLOS	A	02F	PFDDR	NONE
FS-38-5d	PROPFAN SPEED CONTROL ON/OFF SWITCH (28 VDC CONTACT) FAILS CLOSED	19	20	20	CLOS	A	02F	PFDDR	NONE
FS-38-6b	PROPFAN RESET SWITCH FAILS CLOSED	19	20	20	CLOS	A	02F	PFDDR	NONE
TI-8	TEST INSTRUMENT CAUSES OUT OF LIMIT CENTER OF GRAVITY CONDITION	19	20	20	CLOS	I	01	ACPDR	I
TI-28-2	PVC OUTGASSING - NO COMBUSTION	16	20	20	CLOS	D	04	FTRRV	NONE
CC-21-2	NO COMPATIBLE COMMUNICATIONS- PTA TO CHASE AIRCRAFT	12	20	20	CLOS	P	04	FTRRV	NONE
SE-2	OEC DOLLY - STRUCTURAL FAILURE: DESIGN/MANUFACTURE ERROR	19	20	20	CLOS	CIT	01	ACPDR	NONE
PMT-20-4	PFS/SPEY RUNUP- UNPLANNED TAXI- GAC	20	20	20	CLOS	P	04	FTRRV	NONE
FS-24	DELETED - CLOSED ADMINISTRATIVELY			99	CLOS			ADMIN	
FS-28	DELETED - CLOSED ADMINISTRATIVELY			99	CLOS			ADMIN	
TI-26	DELETED - CLOSED ADMINISTRATIVELY - TASK 6			99	CLOS			ADMIN	
TI-27	DELETED - CLOSED ADMINISTRATIVELY - TASK 6			99	CLOS			ADMIN	
CC-13	CLOSED ADMINISTRATIVELY PER SSIG #2: PLAN DEPRESSURE-TEMP			99	CLOS			ADMIN	
CC-13-1	CLOSED ADMINISTRATIVELY PER SSIG #2: PLAN DEPRESSURE-02 FAIL			99	CLOS			ADMIN	
CC-17	CLOSED ADMINISTRATIVELY			99	CLOS			ADMIN	
CC-17-1	CLOSED ADMINISTRATIVELY			99	CLOS			ADMIN	
CC-17-2	CLOSED ADMINISTRATIVELY			99	CLOS			ADMIN	
FS-7-3a	CLOSED ADMINISTRATIVELY- DESIGN ELIMINATED			99	CLOS			ADMIN	
FS-7-3b	CLOSED ADMINISTRATIVELY- DESIGN ELIMINATED			99	CLOS			ADMIN	
SSF-3	DELETED - CLOSED ADMINISTRATIVELY: TASK 6			99	CLOS			ADMIN	

PTA
HAZARD TRACKING LOG
IN ORDER OF RISK

HAZARD IDENT	HAZARD REMARKS	IN	HRI MO	FI	HAZARD STATUS	VERIF CODE	VOL NUM	CLOSE AUTH	CNTG ACT
SSF-4	DELETED - CLOSED ADMINISTRATIVELY: TASK 6			99	CLOS			ADMIN	
SSF-5	DELETED - CLOSED ADMINISTRATIVELY: TASK 6			99	CLOS			ADMIN	
SSF-6	DELETED - CLOSED ADMINISTRATIVELY: TASK 6			99	CLOS			ADMIN	
SSF-8	DELETED - CLOSED ADMINISTRATIVELY: TASK 6			99	CLOS			ADMIN	